UNIVERSITÉ DE LORRAINE | BIBLIOTHÈQUES UNIVERSITAIRES

AVERTISSEMENT

Ce document est le fruit d'un long travail approuvé par le jury de soutenance et mis à disposition de l'ensemble de la communauté universitaire élargie.

Il est soumis à la propriété intellectuelle de l'auteur. Ceci implique une obligation de citation et de référencement lors de l'utilisation de ce document.

D'autre part, toute contrefaçon, plagiat, reproduction illicite encourt une poursuite pénale.

Contact bibliothèque : ddoc-theses-contact@univ-lorraine.fr
(Cette adresse ne permet pas de contacter les auteurs)

LIENS

Code de la Propriété Intellectuelle. articles L 122. 4
Code de la Propriété Intellectuelle. articles L 335.2- L 335.10
http://www.cfcopies.com/V2/leg/leg_droi.php
http://www.culture.gouv.fr/culture/infos-pratiques/droits/protection.htm

École Doctorale SIReNa - Laboratoire GeoRessources

Arethuse Geology - Géosciences Montpellier

THÈSE

Présentée et soutenue pour l'obtention du titre de

DOCTEUR DE L'UNIVERSITÉ DE LORRAINE

Mention : **Géosciences**

par **Célestine BERTHIER**

The Archean Sukumaland greenstone belt, Tanzania craton: crustal growth, gold fertilization and concentration

28 février 2025



Membres du jury:

Directeurs de thèse	Mme. Anne-Sylvie ANDRÉ-MAYER	Professeure, UMR 7359, Université de Lorraine
	M. Alain CHAUVET	Directeur de Recherche, UMR 5243, Université de Montpellier
	M. Julien FENEYROL	Géologue d'exploration senior, Arethuse Geology, Aix-en-Provence
Rapporteurs	M. Yannick BRANQUET	Maître de Conférences, UMR 6118, Geosciences Rennes
	Mme. Crystal LAFLAMME	Professeure, Université de Laval, Quebec
Président du jury	M. Stéphane GUILLOT	Directeur de Recherche, UMR 5275, ISTerre Grenoble
Examinateurs	M. Bruno DHUIME	Directeur de recherche, UMR 5243, Université de Montpellier
	M. Flavien CHOULET	Maître de Conférences, UMR 6249, Chrono Environnement
	Mme. Aude GÉBELIN	Professeure, UMR 7359, Université de Lorraine
Membres invités	M. Aurélien EGLINGER	Maître de Conférences, UMR 7359, Université de Lorraine
	M. Rémi BOSC	Gérant, Arethuse Geology, Aix-en-Provence

~ Abstract ~

Structurally-controlled, epigenetic gold deposits can be defined as small-scale expressions of a sequence of geological processes that occur across different temporal and spatial scales. Notably, some factors influencing mineralization may have involved lithospheric-scale processes, active well before the ore-forming events, up to one or more orogenic cycles. These processes governed the initial enrichment of the crust, the transport of ore-bearing fluids to deposition sites and controlled gold deposition. Conversely, insights into the mechanisms of deposit formation can significantly contribute to our understanding of the Earth's system, specifically mineral systems requiring large-scale and long-term processes such as orogenic gold. A multi-scale and multi-method approach was followed to reconstruct the gold mineral system and constrain crustal growth mechanisms in the northern Sukumaland granite-greenstone belt (SGGB) of the Archean Tanzania Craton, host of the Nyanzaga and Kilimani gold deposits.

The journey of gold in the northern SGGB, from initial fertilization of the crust to economic concentration at the Nyanzaga and Kilimani gold deposits, results from nearly 200 million years of magmatic activity, deformation, metamorphism and hydrothermal circulation. Gold was extracted from the mantle during the earliest record of crustal growth in the SGGB. This episode consisted of mantle-derived mafic-ultramafic magmatism in a mantle-plume oceanic plateau setting, between 2820 and 2800 Ma. Between 2800 and 2700 Ma, crustal reworking was likely driven by dripping processes, before transitioning to subduction-like processes around 2700 Ma. The convergent tectonics ultimately led to collision between the SGGB and an exotic terrane during the 2700-2660 Ma period. A hot and weak lithosphere controlled shortening and crustal thickening that resulted in transpression and vertical flattening, contrasting with the localized strain typical of modern cold orogens. The absence of crustal-scale thrusts and significant topography, along with the presence of granulite-facies metamorphism and lateral crustal flow suggests that the SGGB evolved through prolonged transpression in a hot orogen setting. Crustal anatexis is recorded between 2660 and 2620 Ma. The resulting partial melting, reworking and/or metamorphism of the gold-enriched mafic lithologies likely triggered gold release from its source rock around 2645 Ma. Refolding processes shaped the meta-volcanosediments of the SGGB to provide favorable geometries for strike-slip faulting with favorable opening rates for ore-bearing fluid circulation and gold precipitation after 2645 Ma. Gold fertilization and gold release and concentration processes are therefore temporally disconnected of more than 150 Ma. Mixing of fluids may have contributed to the precipitation of gold.

The mineral system approach had dual implications, synchronously constraining (i) the tectonic processes that drove crustal growth and differentiation in a Neoarchean granite-greenstone terrane and (ii) the magmatic, tectonic, hydrothermal and to a smaller extent metamorphic processes that controlled the journey of gold within this juvenile crustal segment.

~ Résumé étendu ~

Introduction

À la fin de l'ère archéenne, vers 2,5 milliards d'années (Ga), plus de la moitié du volume total de la croûte continentale se serait formée (Dhuime et al., 2018). Cette période est ainsi cruciale pour comprendre la croissance des continents. Toutefois, les roches témoins de la Terre primitive et juvénile sont beaucoup moins abondantes que celles d'époques plus récentes (Gerya, 2014). En raison de phénomènes majeurs de remaniement, de recyclage et de préservation de la croûte, moins de 8 % des continents actuels se sont formés avant 2,5 Ga (Korenaga, 2021).

Cet enregistrement partiel de la croûte continentale de plus de 2,5 Ga limite considérablement nos connaissances sur l'histoire Terre archéenne à hadéenne. Par conséquent, une attention croissante est portée à l'étude des différentes caractéristiques de la croûte archéenne – qu'elles soient pétrographiques, structurales ou métallogéniques – pour explorer les mécanismes de croissance de la croûte et les modèles tectoniques (Morris et Kirkland, 2014 ; Hastie et al., 2016 ; Jayananda et al., 2018 ; Mole et al., 2019, 2021 ; Diwu et al., 2024). L'Archéen est marqué par des transformations majeures du régime tectonique terrestre, souvent considérées comme l'empreinte des premières tectoniques des plaques (Condie et Kröner, 2008 ; Van Kranendonk, 2011 ; Shirey et Richardson, 2011 ; Laurent et al., 2018 ; Dhuime et al., 2015 ; Palin et al., 2020 ; Hawkesworth et al., 2024), provoquées par le refroidissement progressif du manteau terrestre (Labrosse et Jaupart, 2007 ; Herzberg et al., 2010 ; Cawood et al., 2018).

L'interprétation du cadre tectonique d'un segment de croûte dépend fortement des indicateurs utilisés, en effet un indicateur unique peut donner lieu à plusieurs interprétations tectoniques. Par exemple, les signatures géochimiques issues de processus non liés à la tectonique des plaques peuvent ressembler à celles observées dans les marges convergentes actuelles (Johnson et al., 2017 ; Cawood et al., 2018 ; Nebel et al., 2018 ; Chowdhury et al., 2021). De même, les géométries en dôme-et-bassin, souvent associées à une tectonique par sagduction, comme dans le craton de Pilbara, peuvent aussi résulter de la déformation d'une lithosphère chaude dans des environnements orogéniques chauds ou ultra-chauds, incluant des processus de subduction (Chardon et al., 2009). Une approche multi-proxy est donc de plus en plus utilisée pour contraindre les mécanismes de croissance crustale durant l'Archéen (Cawood et al., 2018, 2022 ; Mole et al., 2019, 2021, 2022 ; Brown et al., 2020 ; Dong et al., 2022 ; Hawkesworth et al., 2024 ; Liu et al., 2024 ; Schreefel et al., 2024).

Les croûtes continentales archéennes abritent certaines des plus importantes provinces aurifères mondiales, illustrées par les cratons de Yilgarn, Supérieur et Kaapvaal (Phillips et al., 2019 ; Dube et Mercier-Langevin, 2020 ; Frimmel et Nwaila, 2020 ; Tripp et al., 2020 ; Travers, 2024). L'exploration et exploitation aurifères dans le craton archéen de Tanzanie sont relativement récentes, en comparaison avec d'autres provinces aurifères africaines, telles que le craton archéen de Kaapvaal, le craton paléoprotérozoïque d'Afrique de l'Ouest et le Bouclier nubien néoprotérozoïque, où l'or a joué un rôle clé dans les cultures de l'âge du fer (Klemm et Klemm, 2013 ; Elbra, 2017). Les sociétés pastorales de l'Afrique centrale et orientale ont historiquement manifesté peu d'intérêt pour l'or, malgré la présence de ceintures de roches vertes riches en minéralisation (Kabete et al., 2012a). L'intérêt minier pour le craton de Tanzanie a débuté avec les prospecteurs allemands à la fin du XIX^{è} siècle, avant de connaître une hausse dans les années 1930, stimulée par l'augmentation des prix de

l'or (Henckel et al., 2016). D'importants gisements ont été découverts grâce à des études géochimiques, puis géophysiques, menant à l'ouverture de mines d'échelle mondiale, tel que le gisement de Geita. Entre 1935 et 1970, ces mines ont produit environ 2,6 millions d'onces troy (Moz) d'or. Cependant, l'activité d'exploration a considérablement ralenti ces dernières années, et la plupart des principaux gisements du craton, tels que Geita et Bulyanhulu, ont été découverts il y a maintenant plusieurs décennies. Le gisement d'or de Nyanzaga, identifié à la fin du XXè siècle, figure parmi les dernières découvertes significatives de la province. Aujourd'hui, certains considèrent le craton de Tanzanie comme une province aurifère mature, avec un potentiel limité pour la découverte de nouveaux grands gisements (Henckel et al., 2016).

Les gisements d'or structuraux et épigénétiques sont l'expressions à petite échelle d'une série de processus géologiques opérant à différentes échelles spatiales et temporelles (Wyborn, 1997 ; McCuaig et Hronsky, 2014 ; Champion et Huston, 2016). Certains facteurs influençant la minéralisation, tels que des processus à l'échelle lithosphérique, pourraient être actifs bien avant les événements minéralisateurs, couvrant jusqu'à un ou plusieurs cycles orogéniques (Meffre et al., 2016 ; Masurel et al., 2021 ; Sumail et al., 2024). Ces processus régissent l'enrichissement initial de la croûte, le transport des fluides minéralisateurs vers les sites de dépôt, et contrôlent la précipitation aurifère. Cette approche illustre le concept de système minéral, qui relie de nombreux processus contrôlant la formation et la préservation des gîtes minéralisés (Wyborn et al., 1994 ; McCuaig et Hronsky, 2014).

Bien que cette approche soit largement adoptée dans de nombreuses provinces aurifères (Champion et Huston, 2016 ; Joly et al., 2015 ; Mériaud et al., 2019 ; Groves et al., 2020 ; Makiba et al., 2020 ; Osei et al., 2021 ; Huston et al., 2023), elle n'a pas encore été appliquée au craton « mature » de Tanzanie. Dans cette région, les méthodes d'exploration traditionnelles, telles que les levés géochimiques et géophysiques, prédominent (Henckel et al., 2016 ; Dirks et al., 2020). Dans ce projet de thèse, une approche multi-échelle et multi-méthodes a été adoptée pour reconstruire le système minéral aurifère et contraindre les mécanismes de croissance crustale dans le nord de la ceinture de granites-roches vertes de Sukumaland (SGGB) du craton archéen de Tanzanie, hôte des gisements d'or de Nyanzaga et Kilimani.

Méthodes

Ce travail combine des études de terrain, pétrographiques, structurales, géochimiques, géochronologiques et isotopiques à différentes échelles : régionale/district, gisement, macroscopique et microscopique.

Un transect de 50 km à travers la partie nord-est de la ceinture de roches vertes de Sukumaland (SGGB), incluant les roches vertes et le socle environnants, a été réalisé dans la région du gisement d'or de Nyanzaga. Une carte géologique a été établie à partir d'observations de terrain, d'analyses microstructurales, d'images satellites (Bing, Landsat 8+) et de données aéromagnétiques, ces dernières couvrant uniquement les roches supracrustales de la ceinture. Les travaux de cartographie à l'échelle du district réalisés par OreCorp Ltd ont considérablement enrichi notre carte (communication personnelle de McIntyre). Des descriptions détaillées et des échantillonnages représentatifs ont été effectués sur des carottes de forage et des affleurements des gisement d'or de Nyanzaga et Kilimani. Des mesures structurales concernant les objets de déformation et les foliations ont été compilées.

Des études pétrographiques microscopiques ont été réalisées sur des lames minces, ciblant diverses caractéristiques, notamment les différentes lithologies, des échantillons fortement et faiblement déformés, les veines et leurs halos d'altération, ainsi que des éléments métamorphiques et hydrothermaux.

Des observations complémentaires ont été effectuées au microscope électronique à balayage, en modes d'imagerie en électrons rétrodiffusés, en diffraction d'électrons rétrodiffusés, ainsi qu'en cathodoluminescence (laboratoire GeoRessources, Université de Lorraine, et Curtin University, Perth). Des analyses géochimiques roche totale, pour les éléments majeurs et traces, y compris l'or, ont été effectuées sur des échantillons représentatifs de roches ignées et supracrustales prélevées le long du transect (laboratoire ALS, Séville, Espagne). Des datations U-Pb sur zircons et des analyses isotopiques Hf-O ont été réalisées sur sept échantillons magmatiques représentatifs de l'histoire magmatique de la SGGB. De plus, des datations U-Pb et des analyses Hf ont été réalisées sur trois échantillons sédimentaires. Des analyses des isotopes multiples du soufre ont été effectuées sur les trois générations de pyrite, stérile et aurifère, du gisement de Nyanzaga (CRPG, Université de Lorraine).

Chapitre 1 - Contexte géologique et métallogénique du craton de Tanzanie

Le craton tanzanien, datant du Méso- au Néoarchéen, est situé en Afrique centrale-orientale. Il s'étend de l'ouest du Kenya au centre de la Tanzanie et au sud-est de l'Ouganda, s'étendant probablement sous le lac Victoria (Borg et Shackleton, 1997 ; Sanislav et al., 2014). Il constitue l'un des quatre blocs crustaux archéens formant le Bouclier d'Afrique centrale, également appelé le craton du Grand Congo (Djeutchou et al., 2024). Le craton tanzanien se divise en deux régions géologiquement distinctes : La région aurifère du lac Victoria (LVG) au nord, constituée de nombreuses ceintures de roches vertes et granitoïdes associés, formant un superterrane granite-roches vertes, et la région centrale de Tanzanie (CTR) au sud, caractérisée par une faible proportion de roches vertes et des terrains de gneiss-migmatites fortement métamorphisés et déformés, représentant un superterrane de haute intensité métamorphique (Windley et Bridgewater, 1971 ; Windley, 1984 ; Myers et Kröner, 1994 ; Borg et Shackleton, 1997 ; Kwelwa et al., 2012a).

La LVG est dominée par des granitoïdes et paragneiss orientés E-W à NW-SE, intercalés avec six ceintures de roches vertes du Néoarchéen, plissées et présentant une distribution hétérogène de l'or. Par exemple, la ceinture du Sukumaland (SGGB) qui abrite de nombreux gisements, dont le gisement de classe mondiale de Geita, contraste avec la ceinture granitique de Kilimafedha, actuellement stérile (Borg et Shackleton, 1997 ; Kwelwa et al., 2018).

La SGGB est dominée par des méta-volcanosédiments de type Nyanzian, bordés par des granitoïdes syn-accrétionnaires à post-tectoniques de la série tonalite-trondhjémite-granodiorite (TTG) (Sanislav et al., 2015 ; Henkel et al., 2016 ; Kwelwa et al., 2018 ; Sanislav et al., 2018b). Des études approfondies menées dans la partie nord-ouest de la SGGB, autour du gisement d'or de Geita, ont révélé une histoire métamorphique et de déformation prolongée, composée de huit événements regroupés en trois phases tectoniques distinctes, nommées Évènement I à III (Borg et Shackleton, 1997 ; Kabete et al., 2012 ; Henckel et al., 2016 ; Dirks et al., 2022).

Événement I (2820-2700 Ma) : Phase d'accrétion marquée par la formation de grands volumes de roches volcanosédimentaires et l'intrusion de granitoïdes mafiques à felsiques en régime extensif (Cook et al., 2016 ; Sanislav et al., 2018a ; Mshiu et Maboko, 2022). Cet événement se caractérise par des failles normales listriques, des cisaillements parallèles aux couches et le plissement intrafolial des couches de chert (Sanislav et al., 2014, 2018a ; Dirks et al., 2022).

Événement II (ca. 2700-2660 Ma) : Une compression généralement orientée N-S à NW-SE, ou NE-SE, a plissé les roches accrétées antérieurement (Kabete et al., 2012 ; Dirks et al., 2022). Ce plissement est souvent

décrit comme polyphasé, impliquant jusqu'à cinq sous-événements de plissement et de replissement, associés à des cisaillements ductiles colatéraux (Sanislav et al., 2016 ; Dirks et al., 2022). Vers la fin de cet événement, des zones de cisaillement ductile-fragile et des failles décrochantes ont probablement décalé les plis (Kabete et al., 2012 ; Sanislav et al., 2016).

Événement III (2660-2620 Ma) : La compression a été remplacée par une extension orientée NW-SE, réactivant les zones de cisaillement et les failles (Borg, 1994 ; Kabete et al., 2012 ; Dirks et al., 2022).

Chapitre II : Croissance crustale et contrôle géodynamique dans la région nord de la SGGB

Dans ce chapitre, nous présentons de nouvelles analyses pétrographiques, géochimiques, géochronologiques (U-Pb) et isotopiques (O-Hf) sur des roches magmatiques et sédimentaires de la région nord de la ceinture de roches vertes et granitoïdes de Sukumaland (craton tanzanien). Ces données sont compilées avec la littérature existante (géochimie roche totale, datations U-Pb, isotopie Hf-Nd) pour améliorer et discuter notre compréhension de l'évolution géodynamique de cette portion de croûte archéenne.

La croissance crustale dans cette région débute autour de 2820 Ma, marquée par l'extrusion de croûte mafique dérivée d'un manteau primitif (εNd élevé) dans un contexte de panache mantellique (2820–2800 Ma). Entre 2800 et 2700 Ma, les roches de type tonalite-trondhjémite-granodiorite (TTG) montrent une diminution progressive des valeurs de εHf, suivant une tendance d'évolution crustale. Ces roches présentent également des signatures isotopiques $\delta^{18}O$ similaires au manteau, des rapports élevés Sr/Y et Gd/Yb, ainsi que de faibles rapports K_2O/Na_2O. Ces caractéristiques géochimiques et isotopiques indiquent un important recyclage de matériel mafique sous des conditions de grande profondeur, probablement induite par des processus de « dripping » crustal.

Entre 2700 et 2660 Ma, un changement significatif dans les régimes tectoniques est observé. Des indices de fusion à grande profondeur (rapports élevés Sr/Y et Gd/Yb) et un recyclage de matériel ayant atteint des niveaux supracrustaux est enregistré dans les TTG (augmentation des valeurs $\delta^{18}O$). Des signatures géochimiques de type sanukitoïde émergent également, accompagnées de preuves de mélange entre une croûte juvénile et des composants crustaux plus anciens et évolués, attestées par des valeurs négatives de εHf et des rapports K_2O/Na_2O élevés. Cette période enregistre également la sédimentation néoarchéenne dans des bassins syntectoniques de type molasse, dont la population de zircons est d'âge Éo- à Néoarchéen. Ces données suggèrent une différenciation crustale entraînée par des processus de subduction et l'amalgamation d'une terrane exotique entre 2700 et 2660 Ma.

Après 2660 Ma, l'activité tectonique évolue vers un magmatisme potassique, dérivé d'une fusion partielle intraplaque de la croûte (rapports faibles Sr/Y et Gd/Yb) durant une phase tardive à post-collisionelle. Nos résultats enrichissent les débats en cours sur la mise en place de la tectonique des plaques, en suggérant que des processus de subduction étaient actifs dans le craton tanzanien après 2700 Ma.

Chapitre III : Évolution magmato-tectonique de la partie nord de la SGGB et tectonique archéenne

La ceinture de roches vertes et granitoïdes de Sukumaland (SGGB), datée au Néoarchéen, présente une histoire magmato-tectonique étendue, marquée par 80 millions d'années de raccourcissement progressif et continu. Ce chapitre vise à reconstituer l'évolution tectonique du nord-est de la SGGB, en s'intéressant

à : (i) l'évolution des mécanismes de raccourcissement et des modes de flux crustal, (ii) l'intégration des caractéristiques magmatiques, sédimentaires, structurales, hydrothermales et métamorphiques dans une histoire cohérente, (iii) la caractérisation des styles de raccourcissement et d'épaississement crustal. Dans ce cadre, le modèle magmato-tectonique proposé permet d'examiner les périodes magmato-tectoniques lors desquelles l'or a été introduit dans la croûte puis concentré, conduisant à la formation des gisements d'or de Nyanzaga et Kilimani.

Les investigations structurales, pétrographiques et géochimiques détaillées, menées le long d'un transect de 50 km traversant les roches vertes et granitoïdes environnantes de la SGGB, révèlent une histoire de déformation progressive en trois étapes, contrôlée par un raccourcissement horizontal continu. La déformation évolue du fluage vertical (aplatissement) vers un « flow » crustal en décrochement, accompagné d'un refroidissement progressif de la croûte. Les mécanismes de raccourcissement et d'épaississement crustal observés dans la SGGB ne correspondent pas aux styles orogéniques collisionnels modernes, mais résultent plutôt d'une transpression prolongée d'une lithosphère archéenne faible, cohérente avec les caractéristiques d'un orogène chaud.

L'enrichissement en or de la croûte terrestre a été observé dans des roches altérées par des processus hydrothermaux. Cet enrichissement résulterait vraisemblablement de processus magmatiques, soit lors d'un événement magmatique juvénile associé à des intrusions mafiques-ultramafiques dérivées du manteau, daté d'environ 2820 à 2800 Ma (Chapitre II), soit au cours d'épisodes magmatiques felsiques survenus entre 2780 et 2700 Ma, puis entre 2660 et 2645 Ma. Par la suite, l'or s'est concentré dans les gisements de Nyanzaga et de Kilimani via des processus impliquant des interactions magmatiques et hydrothermales, survenues entre 2645 et 2620 Ma.

Chapitre IV : Source du soufre et processus de formation de la minéralisation dans le gisement d'or de Nyanzaga

Ce chapitre combine des analyses isotopiques du soufre ($\Delta^{33}S$-$\delta^{34}S$) avec des études pétro-texturales à différentes échelles (macroscopique et microscopique) des sulfures associés à l'or et des veines pour retracer les réservoirs de soufre, et indirectement d'or, ainsi que les processus des fluides métallifères au gisement néoarchéen de Nyanzaga.

L'histoire de la déformation en trois étapes, D_{1a}, D_{1b} et D_{1c}, révèle une circulation prolongée de fluides sulfurés, déposant divers sulfures porteurs d'éléments comme As, Sb, Ag, Mo, Pb, Cu et Zn. L'absence de fractionnement isotopique indépendant de la masse (MIF-S) dans ce gisement indique une origine unique du soufre, soit magmatique, soit mantellique, sur une période excédant 55 Ma. Les variations significatives de fractionnement isotopique dépendant de la masse (MDF-S), observées dans les pyrites, sont interprétées comme suit :

- Phase D_{1a} : les conditions des fluides sulfurés auraient subi une séparation rythmique de phases (liquide-vapeur) et/ou des variations locales de température.

- Phases D_{1b} et D_{1c} : au moins deux fluides distincts ont circulé et se sont mélangés, conduisant à des variations significatives dans les paragenèses des sulfures et les valeurs MDF-S.

Chapitre V : Influence des plis replissées sur le développement des structures minéralisées à Nyanzaga et Kilimani

Ce chapitre explore l'évolution structurale et hydrothermale des gisements d'or de Nyanzaga et Kilimani au sein de la ceinture de roches vertes de Sukumaland. Étape D_{1a} : le premier stade de compression crée des plis verticaux orientés E-O en réponse à un raccourcissement orienté N-S. Étape D_{1b} : les structures précédemment formées sont replissées lors d'une compression/transpression continue. Étape D_{1c} : la nature fragile de la déformation tardive entraîne l'apparition d'un réseau de failles, les failles NW-SE montrant un cisaillement dextre et contrôlant la formation de failles normales verticales orientées N-S. Une histoire hydrothermale prolongée est enregistrée. Elle débute par une phase stérile en or, riche en silicates disséminés et en pyrite, associée aux déformations D_{1a} et D_{1b}. Elle est suivie par le développement d'un système de veines aurifères lors des stades progressifs D_{1b} et D_{1c}. L'or est principalement concentré dans les failles verticales NW-SE (Kilimani) et N-S (Nyanzaga).

Conclusions générales

L'histoire de l'or dans le nord de la SGGB, depuis son introduction initiale dans la croûte jusqu'à sa concentration économique dans les gisements d'or de Nyanzaga et Kilimani, résulte de près de 200 millions d'années d'activité magmatique, de déformation, de métamorphisme et de circulation hydrothermale :

- 2820–2800 Ma : L'or est extrait du manteau lors de la croissance initiale de la croûte, marquée par du magmatisme mafique-ultramafique dérivé d'un panache mantellique.

- 2800–2700 Ma : le recyclage crustal est probablement dominée par des processus de « dripping » avant de passer à des processus semblables à la subduction vers 2700 Ma.

- 2700–2660 Ma : La tectonique convergente mène à une collision entre la SGGB et un terrane exotique. Une lithosphère chaude et faible contrôle le raccourcissement et l'épaississement crustal par transpression et aplatissement vertical, contrastant avec les orogènes froids modernes.

- 2660–2620 Ma : Une anatexie crustale provoque la fusion partielle et la libération d'or depuis les lithologies mafiques enrichies.

- Après 2645 Ma : La géométrie des structures replissées favorise la génération de failles dans lesquelles circulent des fluides métallifères qui précipitent l'or. La fertilisation de l'or et sa concentration sont ainsi déconnectées dans le temps d'environ 150 Ma. Les mélanges de fluides ont également joué un rôle clé dans la précipitation de l'or. Cette approche systémique apporte des contraintes à la fois sur les processus tectoniques ayant conduit à la croissance et à la différenciation crustale dans une ceinture archéenne, et sur les processus magmatiques, tectoniques, hydrothermaux, et métamorphiques ayant contrôlé l'évolution de l'or dans ce segment crustal juvénile.

~ Remerciements - Acknowledgement ~



Une thèse est une aventure qui dure trois longues années. Aucun aventurier ne peut réussir seul, sans une équipe brillante, indispensable.

Il y a d'abord les guides, ceux qui connaissent le chemin, qui évitent de se perdre, qui encouragent, conseillent, partagent et transmettent leurs connaissances, offrant ainsi les meilleures chances de succès. Anne-Sylvie, Alain, Julien et Aurélien, j'ai immensément appris au cours de ces trois années, nos échanges ont été une source inestimable de savoir et d'inspiration. Je suis infiniment reconnaissante d'avoir eu la chance de faire partie de cette équipe exceptionnelle.

Anne-Sylvie, ta positivité, ta bienveillance et ta disponibilité m'ont accompagné dès mon projet de M1. À cette époque déjà, j'étais convaincue que si je devais faire une thèse, ce serait avec toi. Tu as cru en moi, même lorsque je doutais de mes capacités. Merci pour ton dévouement et avoir toujours traité tes doctorants d'égale à égale.

Alain, tu as été un véritable pilier tout au long de cette aventure. Ta bienveillance, ton calme rassurant, et ta force tranquille ont toujours été là pour me soutenir. L'encadrement humain que tu m'as offert a été une source précieuse de motivation. Ton expérience sur le terrain a été une mine d'or, et j'ai énormément appris grâce à toi. Je suis profondément fière de t'avoir eu parmi mes encadrants de thèse et d'avoir pu bénéficier de ton expertise et de ta sagesse.

Merci Julien, depuis mon stage de fin d'études, tu as été bien plus qu'un simple accompagnant. Tu as toujours été là, à l'écoute, avec un regard critique constructif qui m'a permis de grandir. Merci d'avoir été un véritable soutien tout au long de cette thèse, de m'avoir guidée avec patience et bienveillance. Ton sens du détail, ta rigueur et ton exigence ont été des repères essentiels. Mais au-delà de tout cela, tu as enrichi ma vision de la géologie, m'offrant une compréhension plus profonde du travail de géologue, notamment sur le terrain. Merci pour ton indéfectible implication.

Aurélien, tu m'as poussé vers l'excellence et m'a encouragé à viser le meilleur. Tu as été un moteur essentiel tout au long de cette thèse, particulièrement au quotidien à Nancy. Quels bons moments inoubliables nous avons partagé au cœur de la savane parmi les éléphants, les lions et

les zèbres. Nicolas Thébaud, un grand merci d'avoir fait partie de cette aventure avec nous. Nos échanges ont été d'une grande richesse tout au long de cette thèse. Ta connaissance approfondie et ta compréhension de la géologie archéenne m'ont été d'une aide précieuse sur le terrain. Je te remercie également pour ton accueil chaleureux à Perth.

Il y a ensuite les sponsors, un maillon indispensable, qui accompagne et soutient l'aventurier. Rémi, aventurier de la première heure, tu as été l'instigateur de cette thèse, qui en premier à dit « oui c'est possible, je prends le risque ». Merci d'avoir cru en moi, même dans les moments difficiles. Rendez-vous pour de nouvelles grimpes et aller toujours plus haut, toujours plus loin ! I deeply thank OreCorp Limited and later Perseus Mining for financing part of this PhD project and the on-site team for such a warm welcome. My thoughts go especially to Deditius, Patrick, Lilian, David and the whole team of geologists. Asante sana! I am particularly grateful to Jim and John who deeply contributed to my understanding of the Nyanzaga and Kilimani deposits. Jim, thank you for the lovely evening in Perth, I wish you the very best. Ce projet de recherche a bénéficié de l'attribution d'une bourse par établissement d'une Convention Industrielle de Formation par la Recherche (CIFRE) de la part de l'Association Nationale pour la Recherche et la Technologie.

Je tiens également à remercier chaleureusement les rapporteurs et membres du jury — Crystal LaFlamme, Yannick Branquet, Aude Gébelin, Bruno Dhuime, Flavien Choulet et Stéphane Guillot — pour le temps et l'expertise que vous avez consacrés à l'évaluation de ce travail, qui en sera grandement enrichi. J'adresse également mes remerciements à Jean-Marc Montel, Bruno Dhuime et Flavien Choulet pour avoir fait partie de mon comité de suivi individuel. Vos discussions et vos conseils précieux ont grandement contribué à l'amélioration de mon travail de thèse.

Il y a les mentors qui ont allumé une étincelle et fait naitre une passion devenue vocation. Éric Asselborn, tu m'as initiée à la minéralogie, merci à toutes les journées et soirées cailloux, les bourses aux minéraux de SMAM et Millau, nos échanges ont été une source précieuse de savoir et de passion. Stéphane Guillot, merci d'avoir fait briller mes yeux de collégienne de 3e, d'avoir nourri et enrichi ma passion pour la géologie. À Fabrice Cotton que je remercie de m'avoir ouvert les portes de la recherche. Aimé Marion, tu m'as appris la rigueur, l'anticipation, tu m'as appris à ne pas lâcher même si on échoue et tu m'as poussée vers l'excellence. Je suis extrêmement fière d'avoir été ton élève. Éric Lewin, à toutes nos discussions passionnantes la tête dans les étoiles, de géologie, d'Islande.

Tout aventurier fait partie d'une communauté, et pour moi, ce fut d'abord la Gold Team. Quelle chance d'avoir appartenu à cette équipe dynamique et inspirante, qui m'a tant apporté. Julien Perret, tu as été mon modèle durant mon master, et je te suis profondément reconnaissante pour tous nos échanges enrichissants et les journées confinées passées à travailler ensemble sur notre très beau papier. Joffrey, Valentine, Atiq, Lucas, Bastien cette grande aventure se termine pour moi (place à la prochaine !), aussi je vous souhaite d'apprécier pleinement la vôtre. La relève de la Gold Team est là !

À cette première communauté s'ajoute celle d'Arethuse, un équipe qui m'a accueillie avec tout autant de chaleur et d'enthousiasme. Ça a été un réel plaisir de faire partie de cette team. Rémi, Julien, Naima, Virginie, Emmanuelle, Florian, Joffrey, Denis, Arnaud, Christophe, les moments passés avec vous furent épiques, parfois chaotiques, et surtout inoubliables. Dédicace aux belles d'Arethuse, je suis très fière de faire partie de ce groupe très select ! Et un merci tout particulier à Vivi, notre chief happiness officer, pour tous les moments que tu as ensoleillés.

Chaque expédition requiert des helpers, indispensables au bon déroulé de la mission. Mes travaux de thèse ont requis les compétences et savoir-faire de nombreuses personnes. À GeoRessources, merci aux lithopréparateurs Alexandre Flammang et John Moine pour votre disponibilité et votre efficacité. Merci également à Andreï Lecomte et Olivier Rouer au SCMEM. Au CRPG, merci à Pierre Bouilhol, Abdellah Zitouni, Virginie Moineau et Nordine Bouden. At the CET and CMCA, I'm particularly grateful to Chris Fischer, Denis Fougerouse, Matvei Aleshin and Laure Martin.

Il va de soi que les compagnons de cordée, ces camarades galériens embarqués sur le même navire, méritent des remerciements tout particuliers. À tous les membres de GeoRessources, merci pour votre accueil chaleureux et pour les merveilleux moments partagés ensemble. Un immense merci à tous : doctorants, post-doctorants, titulaires, stagiaires, administratifs, et Isabelle, qui avez contribué à faire de cette expérience une aventure aussi riche qu'inoubliable. Un remerciement tout particulier à mes co-bureaux, Sara et Marjo : vous avez été mon rayon de soleil quotidien. Je garde en mémoire les incroyables soirées passées au foyer, de jeux, bourguignon, bières et rires inoubliables avec Paul M, Paul B, Thomas, Martin, Laurie, Ahmed et Loris. Et bien sûr, toutes ces sorties d'escalade inoubliables avec Yann, Chloé, Matthieu, Étienne, Maxime et Hugo. Yann «la Légende» et Chloé, merci pour l'initiation à la falaise, nos soirées mémorables et ce terrain dans le Tarn qui restera gravé dans ma mémoire. Je tiens également à remercier Caroline et Alix pour tous les bons moments dans notre bureau – et pour ces fameuses chaises dino qui nous manqueront toujours. Enfin, Lucas, merci d'avoir partagé ce bout de chemin avec moi. Tu as su me maintenir à flots lorsque tout semblait sombrer.

À Montpellier, merci à toute l'équipe des doctorants pour votre accueil chaleureux à chacune de mes visites, et tout particulièrement Manon, je te souhaite le meilleur dans la suite de ta thèse et tes aventures canadiennes. Bruno Dhuime, un grand merci pour nos échanges passionnants sur l'isotopie et la croissance crustal à l'Archéen.

During my three-month stay in Perth, I had the privilege of meeting incredible people and creating memories that will last a lifetime. Sumail, Zulu, Lucas, Maddie, Ravi, Anne, Lauri, Fran, Vinicius, and Luke, I shared so many unforgettable moments with you, from eating and drinking to climbing, hiking, camping, swimming, playing, and watching football: it was hectic! Our climbing and drinking (thankfully not at the same time) trip to Margaret River stands out as a core memory — what an adventure! Julien, thank you for welcoming me to Perth, for the climbing sessions, and, most importantly, for inviting me to join your Rottnest Island adventure. I had a wonderful time there with you. Sumail, you've become a dear friend, and I cannot express how much I treasure the friendship that brightened my time in Perth. I'm especially grateful for your cricket lessons, even though I still haven't quite figured out the rules!

Il arrive qu'un aventurier croise sur sa route des gîtes d'étapes, des auberges de luxe et des parenthèses enchantées. Manu et Anne-Sylvie, un immense merci pour les merveilleux moments passés ensemble à Malleloy, mais aussi au Grand Bo ! Un aventurier se nourrit d'aventure partagées, merci les amis pour ces séjours incroyables à Annecy, Aix, Manchester, Bruxelles, Savines-le-Lac, le refuge de la Muzelle, l'Ariège, Toronto, la Galice, le Tarn, Zanzibar. À mes escapades inoubliables en famille : Floflo et Paul, merci pour votre accueil à Morges ; aux souvenirs impérissables sur le glacier de l'Étendard, à Corrençon-en-Vercors, aux Îles Féroé et en Jordanie.

Et vient enfin la famille : le phare dans la tempête, la ligne de vie, le pilier qui soutient l'aventurier. À ma famille alsacienne, merci pour ces chaleureux week-ends passés ensemble à Wangenbourg, les randonnées avec Jeff, et les délicieuses flammekueche des Stengels. Ces instants de partage restent gravés dans mon cœur. Un merci tout particulier à Nono et Janine, mes grands-parents d'adoption, et les plus grands aventuriers que je connaisse.

Mon Joffrey, à toutes ces aventures déjà vécues et à toutes celles à venir. Tu auras été ma bouée de sauvetage qui m'a gardé à flot dans les plus grosses tempêtes de la thèse.

Ma Floflo, la meilleure compagne d'aventure qui soit, il n'y a personne comme toi pour me redonner le sourire.

À mes parents, vous m'avez transmis dès mon plus jeune âge votre passion pour l'aventure, m'emmenant jusqu'aux confins du monde. Vous avez toujours été à mes côtés, pour me soutenir et m'encourager à poursuivre mes rêves. Vous m'avez donné des ailes, m'avez inculqué la détermination et le dépassement de soi. Ces mots ne rendront jamais pleinement hommage à l'amour et à la reconnaissance infinie que je ressens pour vous. Vous êtes ma boussole, ma source de force, et je vous en suis éternellement reconnaissante.

À mon petit Kili, tu as été mon rayon de soleil, tes câlins me redonnent le sourire et la détermination pour aller au bout de cette thèse. À Sydney et Smoky, mes deux autres compagnons à quatre pattes, merci pour votre présence réconfortante.

À Grand Michel,

À Abdou,

~ Table of content ~

GLOSSAIRE **XXVII**

INTRODUCTION **2**

1. Evolution of the continental crust in the Archean **3**
2. Archean tectonic evolution: a view from the rock record **5**
2.1. Nature of the Archean crust *5*
2.2. Tectonism recorded by igneous rocks *6*
2.3. Tectonism recorded by sedimentary basins *8*
3. Metamorphic marker of the Archean geodynamic **9**
4. Architecture of the Archean crust and tectonic implications **9**
5. Gold deposits as a tracer of the Archean geodynamic **11**
6. Defining the gold mineral system **13**
7. Defining orogenic gold deposits in the Archean **16**
8. PhD objectives and structure of the manuscript **17**
8.1. PhD objectives *17*
8.2. Overview of the manuscript organization *18*
9. Financial and scientific support, external collaborations **20**

CHAPTER I - GEOLOGICAL AND METALLOGENIC CONTEXT OF THE TANZANIA CRATON **22**

1. Geological context of the Tanzania craton **23**
1.1. Stratigraphic and tectonic subdivisions of the Tanzania craton *23*
1.1.1. Lithostratigraphic subdivision *23*
1.1.2. A tectono-stratigraphic and metallogenic subdivision of the LVG *26*
1.2. Crustal growth in the Tanzania craton *26*
1.2.1. Eo- to Paleoarchean *28*
1.2.2. Meso- to Neoarchean *30*
1.3. Tectonic models for crustal growth and differentiation in the LVG *33*
2. Metallogeny of the Tanzania craton **36**

CHAPTER II - NEOARCHEAN CONTINENTAL CRUSTAL GROWTH AND DIFFERENTIATION IN THE NORTHERN SUKUMALAND GREENSTONE-GRANITE BELT: CONSTRAINTS FROM ZIRCON U-PB AGE AND HF-O ISOTOPIC COMPOSITION 40

Abstract 44

1. Introduction 45

2. Geological and tectonic framework of the Tanzania craton 47

2.1. Geological setting of the Tanzania craton 47

2.2. The Sukumaland granite-greenstone belt 49

3. Methodology 49

3.1. Sampling and analyses 49

3.2. Data compilation in the Tanzania craton 50

3.3. Classification of the granitoids 51

4. Results 54

4.1. Lithologies 54

4.1.1. Igneous rocks 54

4.1.2. Supracrustal rocks 54

4.2. Whole-rock geochemistry of magmatic rocks 57

4.3. Zircon U-Pb ages and O-Hf isotope analyses 60

4.3.1. Magmatic record in the northeastern SGGB 60

4.3.2. Detrital record in the northeastern SGGB 63

5. Discussion 64

5.1. Petrogenesis of the magmatic record 64

5.2. Crustal growth and reworking in the Sukumaland granite-greenstone belt 66

5.3. Inputs from the U-Pb-Hf detrital record: Eo- to Neoarchean crustal growth and reworking 69

5.4. Geodynamic implications for the Archean crustal growth in the northern Sukumaland granite-greenstone belt 70

5.4.1. 2820-2700 Ma: mantle-plume and oceanic plateau environment 70

5.4.2. 2700-2660 Ma: hints of subduction-like processes? 72

5.4.3. 2700-2660 Ma: older crustal material records accretion with an exotic terrane 73

5.4.4. 2660-2620: crustal anatexis and stabilization 74

6. Conclusions 75

Acknowledgement 75

CHAPTER III - MAGMATO-TECTONIC EVOLUTION OF THE NORTHERN NEOARCHEAN SUKUMALAND GRANITE-GREENSTONE BELT (TANZANIA): TECTONIC AND GOLD-ENDOWMENT IMPLICATIONS 78

Abstract 82

1. Introduction 83
2. Geological setting (adapted from Chapter V) 85
3. Sampling and Methods 86
4. Results 87
4.1. Lithological framework 89
4.1.1. Meta-volcanosediments of the Nyanzian Supergroup 89
4.1.2. Clastic sediments of the Kavirondian stratigraphy 90
4.1.3. Granitoids 92
4.2. Deformation structures 92
4.2.1. Fabrics 92
4.2.2. Folds 94
4.2.3. Major shear zones 94
4.2.4. Minor shear zones 97
4.2.5. Faults and fractures 97
4.2.6. Veins 99
4.3. Gold mineralization 99
5. Discussion 101
5.1. Shortening direction and crustal flow modes 101
5.2. Tectonic evolution of the SGGB 103
5.3. Implications for crustal shortening and thickening style in the northern SGGB 106
5.4. Gold fertilization and concentration in the crust 106
6. Conclusion 107
Acknowledgement 107

CHAPTER IV - IN SITU MULTIPLE SULFUR ISOTOPES OF PYRITE IN THE NEOARCHEAN NYANZAGA GOLD DEPOSIT: FROM SULFUR SOURCE TO ORE-FLUID PROCESSES 110

Abstract 114

1. Introduction 115
2. Regional geological setting 116
3. Deposit geology 117
3.1. The Nyanzaga gold project 117
3.2. Deformation-hydrothermal framework 119
4. Methods 120
4.1. Sampling and sample preparation 120
4.2. Multiple sulfur isotope analyses and analyses processing 120
5. Results 122
5.1. Microstructural and textural features of pyrite grains and veins 122
5.2. Multiple sulfur isotope results 126
6. Discussion 128
6.1. A single sulfur reservoir 129
6.2. Evolution of the sulfur-bearing fluid conditions 131
6.2.1. Physical-chemical conditions recorded by microscale textures 131
6.2.2. $\delta^{34}S$ *constrains on fluid processes 132*
6.3. Implications for the gold system: from crustal fertilization to gold precipitation 134
7. Conclusion 136

Acknowledgement 136

Chapter V - Refold structures of the Archean Nyanzaga gold Project, Sukumaland greenstone belt, Tanzania: precursors to the gold-bearing fault system 138

Abstract 142

1. Introduction 143

2. Geological setting 144

2.1. Regional geology 144

2.2. The Nyanzaga gold Project 146

3. Methods 148

3.1. Sampling 148

3.2. Microscopy and mineralogical chemical characterization 148

4. Deformation, hydrothermal alteration and mineralization stages 149

4.1. Structural features of the Nyanzaga and Kilimani deposits 149

4.1.1. F_{1a} and F_{1b} folding 149

4.1.2. D_{1c}-related faults and fractures 152

4.2. Mineralogy and hydrothermal stages at the Nyanzaga and Kilimani deposits 154

4.3. Gold distribution and location 159

5. Discussion 160

5.1. Reconstructing the petro-structural history of the Nyanzaga and Kilimani gold deposits 160

5.2. Multi-phase or progressive deformation? 163

5.3. Influence of fold interference pattern on the geometry of the fault system and gold concentration 163

5.4. Regional comparison of the gold deposits in the Sukumaland greenstone belt (SGB) 165

6. Conclusion 166

Acknowledgement 167

Chapter VI - General conclusions 170

1. Main findings 172

2. Unraveling the gold mineral system: the journey of gold through the northern Sukumaland granite-greenstone belt 173

2.1. Fertile environment 174

2.2. Lithospheric architecture 174

2.3. Ore-forming processes 175

2.4. Ore preservation 175

3. Contributing to the plate tectonic onset conundrum: the case study of the Lake Victoria Goldfields 176

3.1. Tectonic setting of the northern SGGB: insights from multiple proxies 176

3.2. Zooming out at the Lake Victoria Goldfields to the Tanzania craton scales 177

3.3. Worldwide record of crustal evolution in the Archean and onset of plate tectonics 177

4. Translating the northern SGGB gold mineral system into an exploration targeting tool 180

SUPPLEMENTARY MATERIAL 184

REFERENCES 380

~

GLOSSAIRE

~

The term **anatexis** refers specifically to the partial melting of crustal rocks occurring within pressure-temperature (P-T) conditions between the solidus and liquidus. Anatexis lies beyond the metamorphic regime, marking the transition between metamorphism and magmatism. The resulting products are **migmatites**, composed of two distinct components, the refractory residue called the melanosome, and the melt, the leucosome.

A **collision** is the amalgamation between two continental blocks resulting from the closure of an oceanic segment (Foucault & Raoult, 2010; Laurent et al., 2014). Collision is accompanied by crustal thickening, intense metamorphism, deformation and magmatism.

A **craton** is an ancient and stable part of the continental lithosphere that has not undergone metamorphism or generalized deformation for at least 1 Ga (Neuendorf et al., 2005). It typically includes one or more Archean nuclei (ranging from 4000 to 2500 Ma) and features thick lithospheric roots (up to 400 km deep), often referred to as the "keel". Cratons represent the most stable and enduring segments of the Earth's continental crust.

Cratonization is the overarching process resulting in the formation of stable and enduring Archean cratons (Rowe, 2021; Rowe et al., 2022). It marks the onset of widespread partial melting of the mid-lower crust and result in a late, craton-wide, high-K granite magmatic event. It generally starts 5 to 20 Ma after convergence. It forms a cooler, stronger and more refractory lithosphere, thereby providing stability to the entire lithosphere (Pollack, 1986).

The **crust** is the upper most part of the solid Earth and account for less than 0.5 % of the Earth mass (Monroe et al., 2006). It ranges from almost inexistant in mid-oceanic ridges to over 80-kilometer thick under the Himalaya range (Gilligan et al., 2015). Based on chemical and mechanical properties, the crust is subdivided into continental and oceanic. Continental crust is generally 35- to 40-kilometer thick, ranging from less than 20- to over 80-kilometer thick. The continental crust has an average andesitic composition, *i.e.*, rich in SiO_2, Al_2O_3 and depleted in FeO and MgO. The oceanic crust is thinner than the continents, with an average thickness of 6-7 kilometers and can extend to over 40 kilometers in oceanic plateau environments (Furumoto et al., 1976; Kerr, 2003), and near zero at mid-oceanic ridges (Blackman et al., 2002). The bulk oceanic crust is mafic, with high FeO and MgO and low SiO_2 contents.

The crust is as old as the Hadean, with the oldest gneisses and detrital zircons dated between 4400 and 4000 Ma (Bowring and Williams, 1999; Wilde et al., 2001; Iizuka et al., 2006). Its composition and thickness has evolved through time. The **Archean continental crust** differs from its Phanerozoic counterpart in terms of petrographic and chemical compositions, with a more mafic composition (Condie, 1981, 1998; Keller and Schoene, 2012), P–T conditions of metamorphic provinces, notably with the absence of high P/low T facies (Percival, 1994; Brown, 2007), geometry of volcano-sedimentary basins (Chardon et al., 2009). The oceanic crust was thicker in the Archean, with an average 20-kilometer thickness (*e.g.*, Herzberg et al., 2010).

Crustal differentiation encompasses all processes of reworking, recycling, remelting and fractional crystallization of a crustal segment, leading to a more evolved crust and to higher silica compositions

(Hawkesworth et al., 2010 and references therein). Crustal differentiation therefore mainly involves igneous processes.

Crustal growth refers to the formation of new continental crust derived from the partial melting of the mantle. The crust is called juvenile if there is no addition of reworked or recycled crust. The term may also refer to the variation in crustal volume over geological time, i.e., the volume of new crust minus the crust recycled into the mantle (Hawkesworth et al., 2010; Cawood et al., 2013).

Crustal recycling occurs when a portion of the crust returns to the mantle. It includes subduction processes (*e.g.*, Cawood et al., 2006, 2018; Polat, 2012; Wyman, 2019), delamination (Johnson et al., 2014), subcretion (Bédard et al., 2013), or crustal drips often with an asymmetric component (*e.g.*, Nebel et al., 2018; Mole et al., 2019).

Crustal reworking involves within-crust remobilization of the crust, either by partial melting or erosion and subsequent sedimentation (Hawkesworth et al., 2010).

Deformation phase *vs* stage: based on Perret (2021). Deformation phases occur discretely over time and correspond to distinct tectonic regimes (with changes in the orientation of the main deformation directions, tectonic style, and geodynamic context). If multiple episodes are recognized, the deformation is described as **polyphase**. Within a given deformation episode, several stages of deformation may be considered. In this case, the observed structures result from a single tectonic event but must be separated because they reflect, for example, a progressive change in tectonic style (*e.g.*, from ductile to ductile-brittle) or the rotation of the main deformation directions during this event. The principle of parsimony suggests that all these structures should be integrated into a single "structural and kinematic model" rather than multiplying deformation episodes; the deformation is then described as progressive (Fossen et al., 2019). Finally, **events** are termed for deformation that is independent of interpretation regarding polyphase versus progressive deformation (Fossen et al., 2019; Oriolo et al., 2022).

Gold concentration refers to the amount of gold present in a specific volume or mass of rock. It is typically expressed in terms of weight per unit of mass, such as parts per billion (ppb), parts per million (ppm), or grams per ton (g/t). Here this concept is defined as its endowment in economic concentrations in gold deposits, leading to mineralized rocks. If the economic threshold varies in time with the mining techniques and gold price, the current gold average grade in gold deposits is 1.18 ppm (Croharé, 2015).

Gold fertilization/enrichment of a crustal segment is the result of geological and biological processes that abnormally endowed the crust (Frimmel, 2008, 2018; McCuaig and Hronsky, 2014). The concentration of gold in the enriched segment becomes higher than the crustal Clarke number, *i.e.*, its concentration in the crust (*e.g.*, up to 1.3 ppb in the upper continental crust, Rudnick and Gao, 2003). Gold fertilization is not to be confused with gold concentration, defined here as the enrichment in economic concentration of a restricted area of the crust (see gold concentration).

Following Anhaeusser (2014) definition, **greenstone belts** are Archean (4000-2500 Ma) metamorphosed and deformed volcanosedimentary stratigraphic sequences, bordered by gneissic rocks and granitoids. Are excluded the syn- to post-tectonic supracrustal basins such as the Witwatersrand Basins on the Kaapvaal Craton in South Africa or the Timiskaming and Cadillac basins in the Superior Craton in Canada. The **granite-greenstone belt** term is used to refer to the complex comprising all supracrustal rocks and surrounding granitoids related to the given greenstone belt (Anhaeusser, 2014).

Structurally controlled, epigenetic gold deposits in the Archean have many names, the most common are greenstone-hosted, quartz-carbonate vein, lode-, orogenic or mesothermal gold deposits (Dubé and Gosselin, 2007). These names may relate to distinct definitions, and we propose to follow the definition by Dubé and Gosselin (2007): "*these deposits occur as quartz and quartz-carbonate veins, with valuable amounts of gold and silver, in faults and shear zones located within deformed terranes of ancient to recent greenstone belts commonly metamorphosed at greenschist* facies. " They are distributed along major compressional to transtensional crustal-scale fault zones in deformed greenstone terranes commonly marking the convergent margins between major lithological boundaries, such as volcano-plutonic and sedimentary domains. The definition of these lode-gold deposits (nomenclature used in the PhD manuscript) encapsulate the orogenic gold deposit type as defined by Goldfarb et al. (2005) or Bierlein et al. (2006b), but may also apply for epithermal or some intrusion-related deposits (*e.g.*, Kelley et al., 1998; Thompson et al., 1999; Groves et al., 2003; Cook et al., 2009; Groves et al., 2019).

High-K granites are purely crustal-derived granites, generated by partial melting of TTGs and/or metasediments (Laurent et al., 2014). They are distinguished by their homogeneity, typically appearing as grey to pink equigranular granites and leucogranites. Their modal mineralogy is consistent, with K-feldspar, sodic plagioclase and quartz in relatively equal proportions, and biotite. These granites are widespread in late-Archean terranes across all major cratons (Sylvester, 1994). They occur as large batholiths, plutons, and smaller intrusive bodies associated with TTGs.

The **lithosphere** is the Earth's uppermost solid layer, distinguished from the underlying asthenosphere by differences in heat transfer (dominated by conduction in the lithosphere versus convection in the asthenosphere), chemical composition, and mechanical behavior. Acting as a rigid layer, it forms a thermal boundary separating Earth's hot interior from its surface, whereas the asthenosphere below is weaker and less viscous (Anderson, 1995; Pollack and Chapman, 1977; Fischer et al., 2010; Green et al., 2010). The lithosphere may be referred as a "lid", representing a strong thermal boundary layer, insulating the Earth's hot interior from the cold hydrosphere (Palin et al., 2020).

Partial melting occurs when a rock is exposed to temperatures high enough to melt part of its minerals while others remain solid.

Pre-, early-, syn-, late-, post-tectonic: based on Perret (2021). The relative chronology of structures, magmatic bodies, or mineral generations can be examined by considering a reference deformation stage or phase. By applying the fundamental principles of continuity, cross-cutting relationships, inclusion, and

superposition, it is possible to determine whether the objects of interest formed prior, early, during, late, or after the deformation features associated with the reference event. These are then classified as pre-, early-, syn-, late-, or post-tectonic, respectively. Importantly, while these terms are quite effective, their use requires a clear definition of the chosen reference deformation. Generally, this refers to the deformation event that controls the structural fabric at the relevant working scale.

Primitive *vs* depleted mantle: The **primitive mantle** refers to the portion of the Earth's mantle that retains the composition of the material from which the Earth originally formed, or close to it (Sun, 1982). It is considered the source from which the first magmas and crust formed and is rich in elements like magnesium and iron, with relatively low levels of incompatible elements such as potassium and thorium. This composition is thought to reflect the undifferentiated state of the mantle before any significant crustal differentiation or chemical processing occurred. The **depleted mantle** refers to a portion of the Earth's mantle that has undergone partial melting, resulting in the removal of certain elements, particularly those that are more incompatible during melting, such as potassium, thorium, and rare earth elements. This process creates a mantle that is less enriched in these elements compared to the primitive mantle, and it is typically associated with regions that have been subject to extensive magmatic extraction or have experienced a history of mantle depletion through mantle convection or plate tectonics. The depleted mantle is the source of mid-ocean ridge basalts (MORB) (Salters and Stracke, 2004).

The **sanukitoid suite** is a diverse group of granitoids formed through interactions between the Archean primitive mantle and an eclogitized sinking mafic crust results in a mantle peridotite, metasomatically enriched in incompatible elements (e.g., Shirey and Hanson, 1984; Martin et al., 2009; Laurent et al., 2014). Sanukitoids s.l. include mafic to felsic lithologies, often associated with lamprophyres or ultrapotassic rocks, and are characterized by mineral assemblages such as K-feldspar, plagioclase, biotite, and amphibole. Typically, their trace element signature aligns closely with that of TTGs, whereas their major element composition distinctly resembles post-Archean calc-alkaline granitoids (Laurent, 2012). They represent minor but widespread components of late-Archean terranes (between 3000 and 2500 Ma).

Scale: Based on Perret (2021). The different observation scales used in this study are defined laterally but correspond to a similar depth of investigation (Jébrak and Marcoux, 2008). These include the following geological scales and their metallogenic counterparts: (i) lithospheric and metallogenic province (up to several hundred km), (ii) crustal and district (tens of km to km), (iii) local and deposit (km to m), (iv) macroscopic and mineralized structure (dm to cm), and (v) microscopic and ore mineral (mm to μm).

Stress *vs* strain: based on Perret (2021). **Stress** refers to the effective force applied to a rock per unit area, similar to pressure, and describes the external forces acting on the rock (Fossen, 2016). On the other hand, **strain** refers to the measure of deformation that a rock undergoes in response to stress. Strain encompasses both changes in shape and volume, as well as the collective displacement of points within the rock relative to a fixed external reference frame. **Deformation** results from various types of displacement, including translation, rotation, distortion, and dilation (Fossen, 2016). While strain provides insight into the finite deformation experienced by a rock, interpreting stress from strain observations can be complex, often

requiring assumptions about the tectonic regime involved. To avoid over-interpretation, this manuscript primarily focuses on deformation rather than stress.

Tectonic mode refers to the geological processes, such as magmatism, deformation, metamorphism, and sedimentation, that define the global tectonic activity of Earth controlling crustal growth and differentiation, and govern how it loses heat (Lenardic, 2018; Palin et al., 2020; Cawood et al., 2022). Based on the degree of lithospheric interaction with mantle convection, three endmember tectonic modes have been proposed:

(i) Stagnant lid tectonics, where the lithosphere remains largely immobile, not participating in mantle convection (Moresi & Solomatov, 1998). This mode is characterized by limited horizontal surface movement and primarily vertical mass transport, with some interaction between the surface and interior via processes like magmatism and tectonic deformation. Stagnant lid tectonics can be divided into two sub-modes: a "hot" stagnant lid, where mantle convection and plume activity allow for volcanic processes (*e.g.*, Mars; Moore et al., 2017; Lenardic, 2018), and a "cold" stagnant lid, where the lithosphere sits atop a solid, non-convecting mantle (*e.g.*, the Moon; Stern, 2018).

(ii) Sluggish lid tectonics, where the lithosphere moves at slower speeds then the underlying mantle, driven by mantle convection (O'Neill et al., 2016; Lenardic, 2018). The lithosphere is composed of small, rigid segments separated by zones of melt-impregnated, non-rigid material. These zones allow for surface motion and compressional deformation, particularly around areas of mantle downwelling. This sub-mode, proposed for early Archean Earth and present-day Venus, exhibits some characteristics of active-lid tectonics, such as distributed deformation, but with slower lithospheric motion.

(iii) Active lid tectonics, where rigid lithospheric plates are in motion, primarily governed by mantle convection and subduction processes. This mode involves significant buoyancy-driven interactions between the lithosphere and mantle convection, which can occur through processes like lithospheric downwelling or subduction (Cawood et al., 2022). It includes two sub-modes: plate tectonics, with rigid plates and narrow deformation zones at plate boundaries, and distributed deformation, where wide deformation zones cover much of the surface with gradual changes in plate velocities.

A **terrane** is a crustal block or fragment characterized by a unique geologic history distinct from that of the surrounding regions, typically separated from them by large-scale structures. A **superterrane** are an assemblage of terranes that share a similar tectonic history compared to the surrounding. Superterranes are generally separated from one another by lithospheric-/crustal-scale structures.

The **tonalite-trondhjemite-granodiorite** (TTG) **suite** represents a series of plutonic rocks characterized by high Na_2O/K_2O ratios (between 0.3 and 0.6 wt.%, low in potassium and rich in sodium) and holocrystalline, leucocratic compositions (Jahn et al., 1981; Moyen and Martin, 2012). These rocks are typically characterized by mineral assemblages dominated by plagioclase (commonly oligoclase), quartz, and minor amounts of biotite, amphibole, epidote, and orthoclase. TTGs are formed through partial melting of tholeiitic and hydrous mafic rocks (*e.g.*, Halla et al., 2009; Moyen and Martin, 2012; Hastie et al., 2016; Moyen and Laurent, 2018).

~ Acronyms and mineral abbreviations ~

Geological-metallogenic acronyms

BIF = banded iron formation

Ga = giga-annum, i.e., billion years ago

Ma = mega-annum, i.e., million years ago

MDF-S = mass-dependent fractionation of sulfur

MIF-S = mass-independent fractionation of sulfur

Moz, koz = million/thousand troy ounces

TTG(s) = tonalite- trondhjemite-granodiorite rock(s)

Geographic-geologic acronyms

CTR = Central Tanzania Region

MMGB = Musoma Mara Greenstone Belt

SGB = Sukumaland Greenstone Belt

LVG = Lake Victoria Goldfield

Mineral abbreviations, following the IMA–CNMNC approved mineral symbols from Warr (2021):

Ab = albite
Act = actinolite
Amp = amphibole
Ank = ankerite
Ap = apatite
Apy = arsenopyrite
Ba = barite
Boul = boulangerite
Bour = bournonite
Bt = biotite
Cal = calcite
Cb = carbonate
Ccp = chalcopyrite
Chl = chlorite
Dol = dolomite
El = electrum
Ep = epidote
Flr = fluorite
Fsp-K = K-feldspar
Fsp-Ba = hyalophane
Ga = galena
Gu = gudmundite
Ilm = ilmenite
Jam = jamesonite
Mnz = monazite
Plg = plagioclase
Po = pyrrhotite
Py = pyrite
Qz = quartz
Rt = rutile
Sch = scheelite
Ser = sericite
Sph = sphalerite
Ttn = titanite
Ttr = tetrahedrite
Ulm = ullmannite
Zrn = zircon

~

INTRODUCTION

~

1. Evolution of the continental crust in the Archean

Over the course of 4.6 billion years, the Earth has evolved, from its chondritic and molten state after accretion, to a core-mantle-crust-atmosphere-structured planet, with crustal growth driven by plate tectonics (Elkins-Tanton, 2008, 2012; Mallard et al., 2016; Lenardic, 2018). After only a few millions of years, the Earth was already structured with a mafic to ultramafic proto-crust, resulting from a rapid cooling, density settling and crystallization (Elkins-Tanton, 2008, 2012; Carlson et al., 2019). Since then, the generation of crust was largely continuous throughout the Earth's history (Fig. 0-1).

Crustal growth is defined by the variation in crustal volume over geological time, *i.e.*, the volume of new, juvenile crust minus crustal destruction in the mantle (Hawkesworth et al., 2010; Cawood et al., 2013). Due to extensive recycling during continuous orogenic cycles, the oceanic crust record is highly limited, with the oldest oceanic crust dating back to approximately 280 Ma (Müller et al., 2008). Conversely, as early as the Hadean, the first eon of Earth's history, was witnessed the initial formation of felsic crust (detrital age of ~ 4.4 Ga recorded from the Jack Hills, Yilgarn Craton; Wilde et al., 2001; Harrison et al., 2017), providing the foundation for subsequent crustal evolution and continent formation. The continental crust is therefore the long-term archive of the Earth's history (Cawood et al., 2013; Hawkesworth et al., 2017; Buzenchi, 2023). These first fragments were produced between 4.45 and 3.8 Ga, either through reworking of mafic-ultramafic rocks, probably related to meteorite bombardments or with overthickening of a proto crust (Kemp et al., 2010; Laurent et al., 2021), or by shallow level magmatic differentiation (Reimink et al., 2014), or even by felsic melt production in a subduction-like setting (*e.g.*, Harrison et al., 2005, 2008; Hopkins et al., 2008, 2010; Turner et al., 2020).

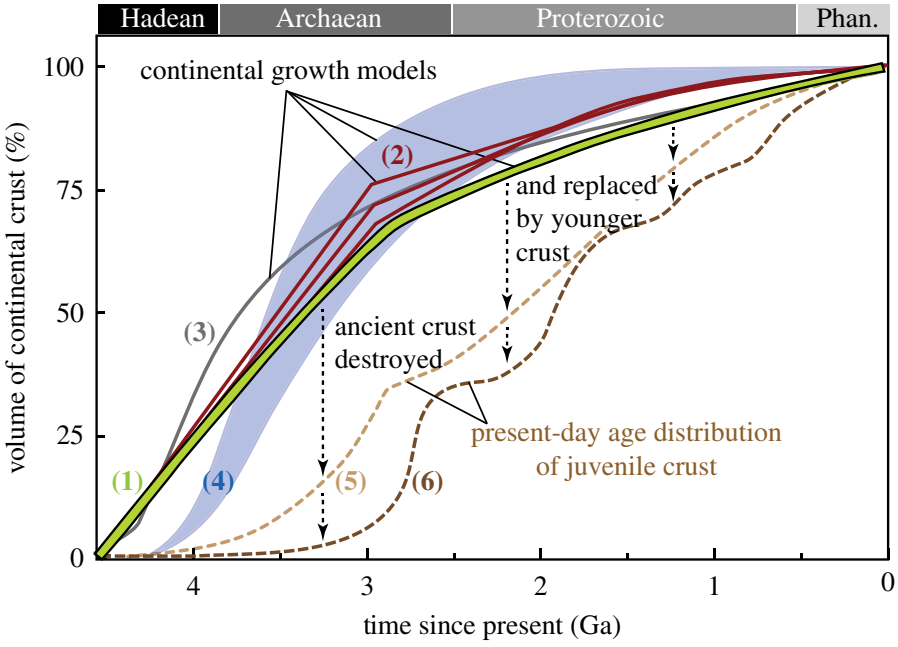

Figure 0-1. Selected continental growth curves (1: Dhuime et al., 2012; 2: Dhuime et al., 2017; 3: Campbell, 2003; 4: Pujol et al., 2013), estimating the total volume of present continental crust formed through time (Dhuime et al., 2018). Brown curves represent the evolution of the present-day continental crust (5: Condie and Aster, 2010; 6: Dhuime et al., 2017). Vertical arrows therefore represents the evolution of volume of continental crust destroyed during orogenic cycles.

By the end of the Archean Eon, at 2.5 Ga, more than half of the overall continental crust volume was likely generated (Fig. 0-1). The early Earth is therefore a key period of the continental growth history. However, the availability of the continental crust decreases with time, in other words, the rock record of the juvenile, primitive and primordial Earth is very limited compared to the present day (Gerya, 2014). As a result of major crustal reworking, recycling and preservation, less than 8 % of worldwide continents are older than 2.5 Ga (Fig. 0-2; Korenaga, 2021). Furthermore, less than 25 % of the overall volume of continental crust records contains rocks that were extracted from the mantle prior to 3 Ga (based on Hf-Nd isotope analyses, light brown dot curve in Fig. 0-1; Dhuime et al., 2018 and references therein). In other words, an important percentage of the early Earth continental crust was destroyed in the mantle and replaced by younger crust during orogenic cycles (represented by the black arrows in Fig. 0-1).

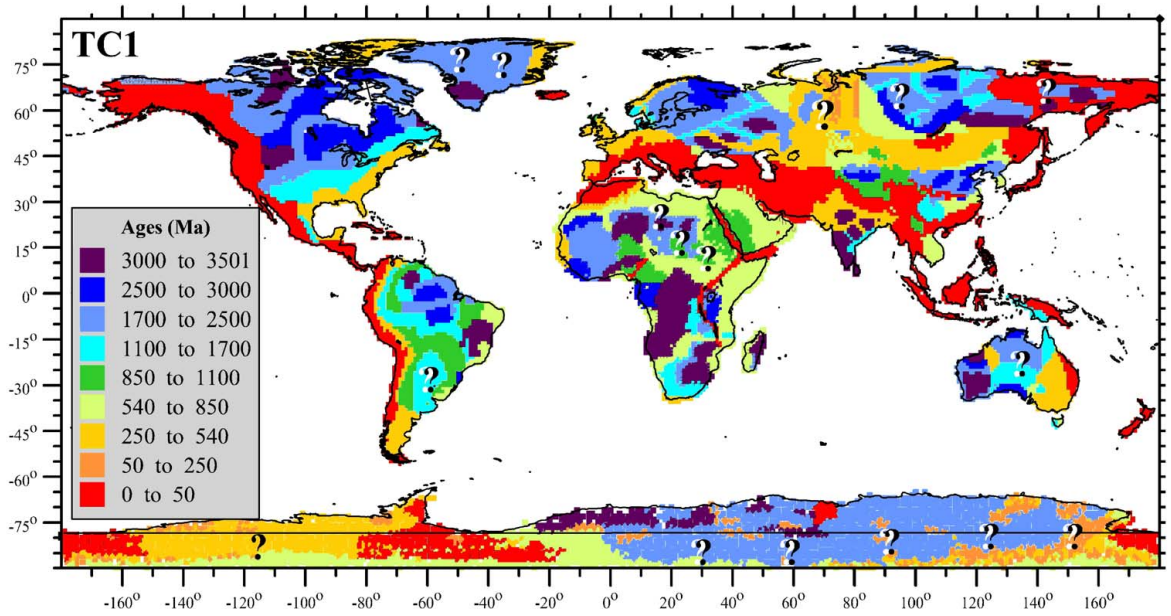

Figure 0-2. Worldwide age distribution of continental crustal segments (Artemieva, 2006).

The incomplete record of the > 2.5 Ga-old continental crust limits considerably our knowledge of the early Earth's history. As a result, there is a growing emphasis on using various characteristics of the Archean crust, whether they are petrographic, structural, metallogenic, to explore crustal growth and tectonic models (*e.g.*, Morris and Kirkland, 2014; Hastie et al., 2016; Jayananda et al., 2018; Mole et al., 2019, 2021; Diwu et al., 2024). The Archean is a period of major change in the tectonic regime of the Earth, generally accepted as the hallmark of plate tectonic (*e.g.,* Condie and Kröner, 2008; Van Kranendonk, 2011; Shirey and Richardson, 2011; Laurent et al., 2018; Dhuime et al., 2015; Palin et al., 2020; Hawkesworth et al., 2024), triggered by cooling of the mantle (Labrosse and Jaupart, 2007; Herzberg et al., 2010; Cawood et al., 2018). In the following are detailed the proxies and methods used for determining crustal growth processes in the Archean.

2. Archean tectonic evolution: a view from the rock record

2.1. Nature of the Archean crust

The Archean Eon, spanning from 4.0 to 2.5 Ga, represents the second major chapter in Earth's history and is considered by many as pivotal for crustal growth and the evolution of geodynamic processes (*e.g.*, van Kranendonk et al., 2007; Dhuime et al., 2015; Greber et al., 2017; Maruyama et al., 2018; Ernst, 2018; Palin et al., 2020). This Eon is the second longest period of the Earth evolution behind the Proterozoic and the Archean alone represent a third of the geological times. Its starting point is attributed to the oldest rocks ever recorded on Earth (Bowring and Williams, 1999). The primordial crust differentiated into early juvenile mafic crust and a more felsic, continental crust in the late Hadean or early Archean (Fig. 0-3; Kamber et al., 2005; Cawood et al., 2022). However, the composition of these mafic and continental crusts was quite different from the modern oceanic and continental ones (Fig. 0-3a-b; Herzberg et al., 2010; Dhuime et al., 2015; Tang et al., 2016; Chen et al., 2020; Hawkesworth & Jaupart, 2021).

In the hotter mantle conditions of the Archean Eon, the "*oceanic crust*" was likely thicker and mechanically weaker (*i.e.*, more ductile), and the oceanic lithosphere was more buoyant compared to the Phanerozoic (Fig. 0-3a; Herzberg et al., 2010). Remnants of the Archean continental crust are scattered across the globe and form cratonic nuclei within younger continents.

If the bulk composition of the Phanerozoic crust is similar to andesite, with granodiorite-granite-dominant crustal lithologies (Hawkesworth and Kemp., 2006), the Archean continental crust was predominantly mafic, and dominated by tonalite-trondhjemite-granodiorite rocks (TTGs), while granites are minor (Fig. 0-3b; Chen et al., 2020; Dhuime et al., 2015; O'Neil and Carlson, 2017; Reimink et al., 2018; Tang et al., 2016). The TTG suite represents a series of plutonic rocks characterized by minimal proportions of K-feldspar and high Na_2O/K_2O ratios (between 0.3 and 0.6 wt.% of feldspar, low in potassium and rich in sodium) (Jahn et al., 1981; Moyen and Martin, 2012). These rocks are typically characterized by mineral assemblages dominated by plagioclase (commonly oligoclase), quartz, and minor amounts of biotite, amphibole, epidote, and orthoclase. They form through partial melting of tholeiitic and hydrous mafic rocks in various tectonic contexts (*e.g.*, Halla et al., 2009; Moyen and Martin, 2012; Hastie et al., 2016; Moyen and Laurent, 2018). TTGS were highly deformed during the tectonic history of the craton, resulting in orthogneisses exhibiting pronounced foliation and migmatites. Late in the history of cratonic crust, high-K and low-Ca granitic rocks are recorded, resulting from the partial melting of the TTGs. The magmatic complexes, dominated by TTGs, form 90 to 95 % of the cratonic surface nowadays.

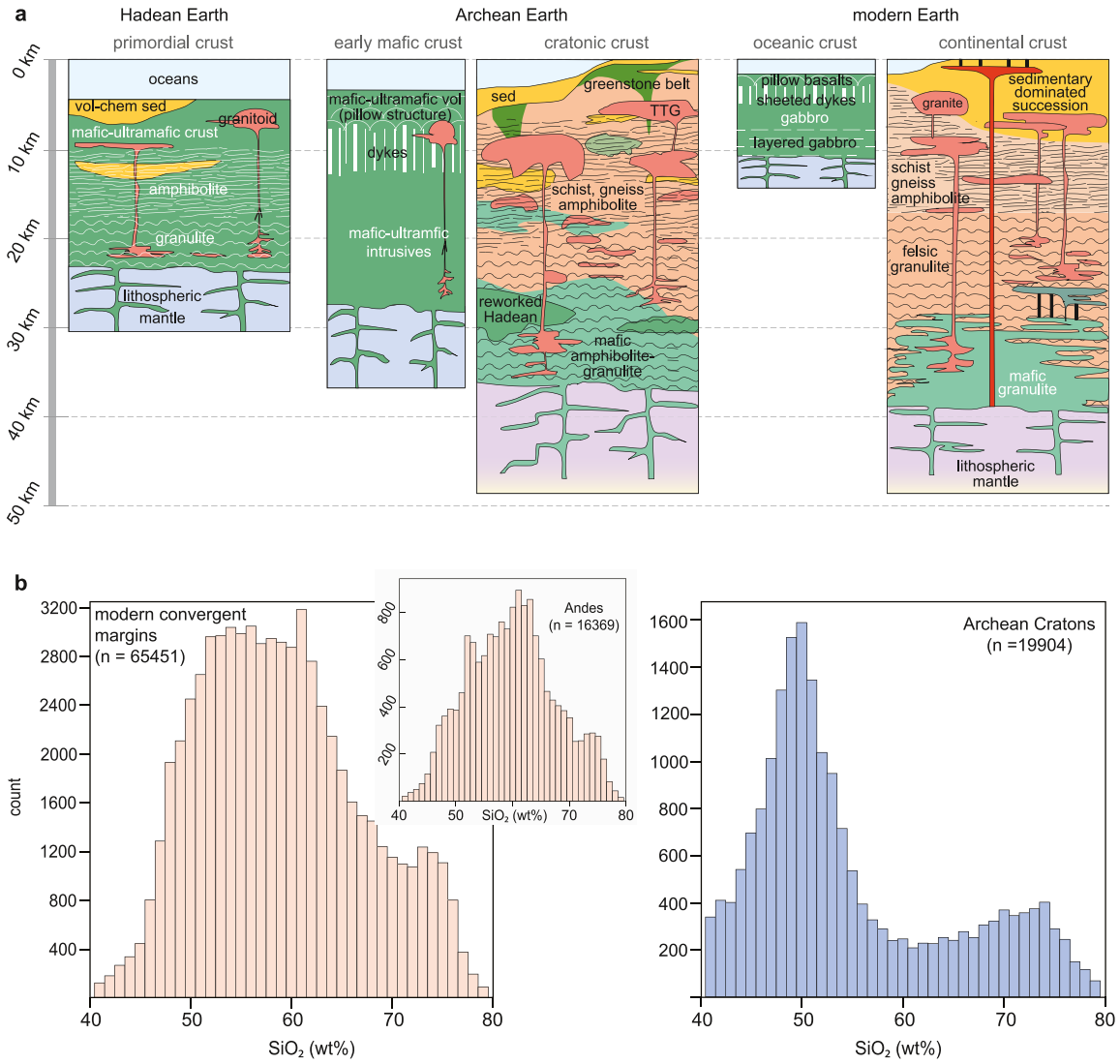

Figure 0-3. a. Schematic lithological sections of Hadean, Archean and modern crusts (Cawood et al., 2022, from Kamber et al., 2005; Hawkesworth and Kemp, 2006). **b.** Distribution of whole-rock SiO_2 from igneous rocks of modern convergent margins and from Archean cratons (Cawood et al., 2022, from GEOROC: http://georoc.mpch-mainz.gwdg.de/georoc/ and Gard et al., 2019).

2.2. Tectonism recorded by igneous rocks

Particular attention has been devoted to tonalite-trondhjemite-granodiorite suite rocks (TTGs) and sanukitoids, unique and widespread igneous rocks of the Archean continental crust (*e.g.*, Moyen and Martin, 2012; Hastie et al., 2016; Moreira et al., 2018, 2020; Moyen and Laurent, 2018; Nebel et al., 2018). TTGs are formed through partial melting of (non)-hydrated, alkali-rich and/or oceanic plateau basalts at various depths and therefore can be correlated to various Archean tectonic models including subduction-like processes with subducted oceanic slabs or plateaus (Fig. 0-4b; Martin and Moyen, 2002; Martin et al., 2014; Hastie et al., 2016), crustal drips resulting from the convection of asthenospheric mantle (Fig. 0-4a; François et al., 2014; Nebel et al., 2018; Mole et al., 2019), melting at the base of an overthickened oceanic plateau (Bédard, 2006), often implying delamination at the base of the crust (Bédard et al., 2003; Moyen, 2011; Johnson et al., 2014).

The interaction between the Archean primitive mantle and an eclogitized sinking mafic crust results in a mantle peridotite, metasomatically enriched in incompatible elements (e.g., Laurent et al., 2014). Subsequently, hydrous melts are generated from this hydrated/metasomatized mantle, in particular sanukitoid melts (Bédard, 2018). The emergence of sanukitoid igneous rocks are therefore evidence of the introduction of hydrated mafic crust into the mantle (Laurent et al., 2014; Bédard, 2018; Cawood et al., 2018; Nebel et al., 2018; Moreira et al., 2020). However, the geochemical signature of sanukitoids has also been tectonically interpreted in various ways, resulting from either subduction processes (Fig. 0-4b; *e.g.*, Laurent et al., 2014; Moyen and Laurent, 2018), or from dripping processes (Fig. 0-4a; *e.g.*, Nebel et al., 2018; Mole et al., 2019).

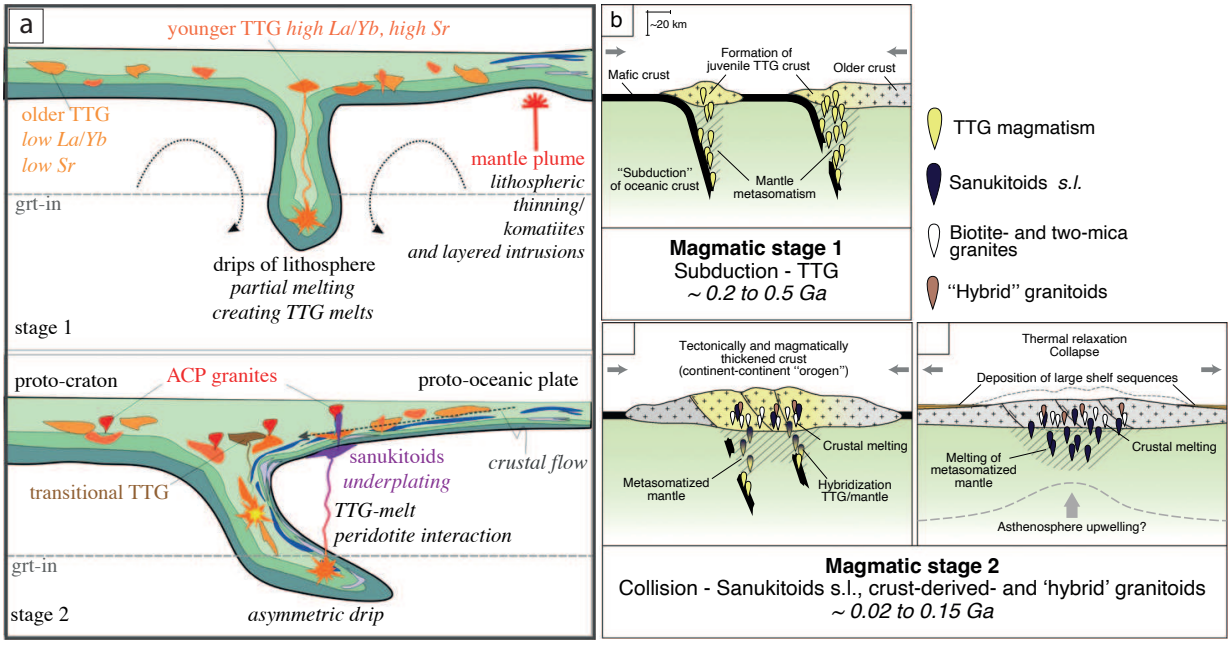

Figure 0-4. Schematic tectonic models showing **a.** lower crustal drip transitioning from TTG formation to sanukitoid magmatism via peridotite interaction (Nebel et al., 2018), **b.** TTG and sanukitoid generation in a subduction setting (Laurent et al., 2014).

The use of isotopic proxies on igneous rocks can further constrain the tectonic setting. Shifts in Hf, Nd and O isotopic arrays are indicators of magmatic contributions from different sources, in other words, the evolution in time of their signature may indicate changes in the source of the intrusives. Their use on magmatic zircon populations enables to identify fundamental changes in tectonic conditions, by measuring the mantle input and crustal reworking in the source of the intrusives, including supracrustal contributions (*e.g.*, DePaolo, 1981; Patchett 1983; Valley et al., 1998, 2005; Hawkesworth et al., 2006; Hawkesworth and Kemp 2006; Kemp et al., 2006; Collins et al., 2011; Dhuime et al., 2011; Dhuime, 2012; Iizuka et al., 2017; Bauer et al., 2020; Smithies et al., 2021).

2.3. *Tectonism recorded by sedimentary basins*

The geochronological study of detrital zircon populations in sedimentary basins provides a robust tool for constraining tectonic settings (Cawood et al., 2012). By comparing zircon crystallization ages with the depositional age of the sedimentary basin, one can distinguish whether they formed in convergent, collisional or extensional settings. Basins formed in convergent plate margins feature a high proportion of zircons with ages close to the depositional age (Fig. 0-5a). Conversely, collisional or extensional basins typically show a broader age distribution dominated by older zircons from reworked basement sources. Collisional and extensional settings can in turn be differentiated based on the gap recorded between crystallization age and deposition age that is almost null in collisional settings (Fig. 0-5b and c).

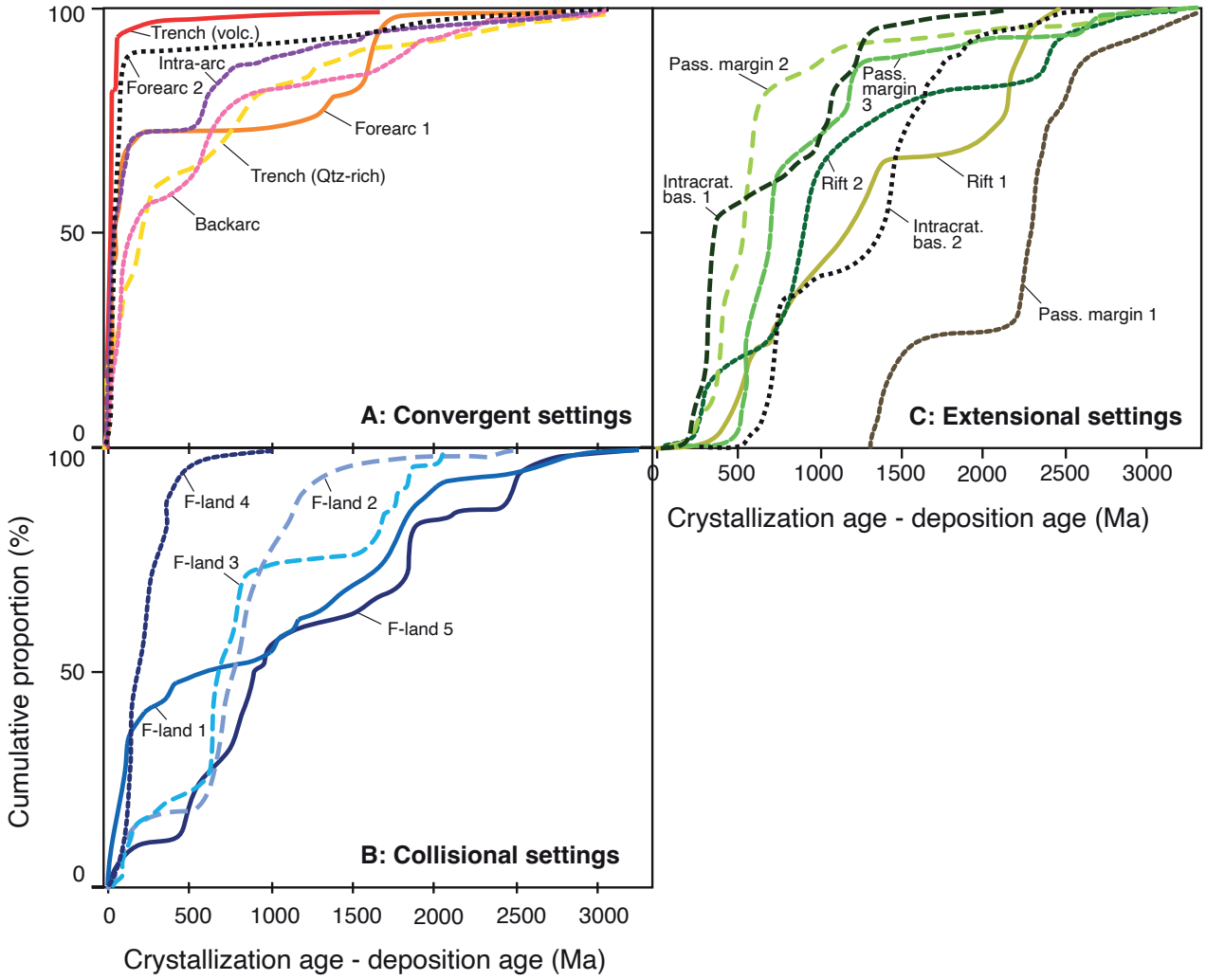

Figure 0-5. Cumulative diagram of the difference between detrital zircon crystallization ages and the depositional age of the sedimentary basin in **a.** convergent, **b.** collisional and **c.** extensional settings (Cawood et al., 2012).

3. Metamorphic marker of the Archean geodynamic

The Archean Eon also stands out from more recent geological eras for its higher temperature metamorphic record. Amphibolite, to granulite-facies metamorphism at high to ultra-high temperatures (≥ 850°C) was common during the Archean in both the magmatic complexes and greenstone belts (Fig. 0-6; Brown, 2007; Brown and Johnson, 2019). The Eon is also remarkable for the absence of blueschist metamorphism, with one of the oldest known occurrences dating to the Paleoproterozoic (Ganne et al., 2011).

The metamorphic differences between Archean and younger Earth reflect a significant shift in orogenic geodynamics, attributed to the thickening of the continental lithosphere and the progressive cooling of the Earth's mantle over time (Brown, 2007). The absence of blueschist facies metamorphism, a hallmark of cold subduction, suggests Archean tectonics styles involved either shorter subduction cycles and shallow-dipping slabs, or non-subduction tectonic processes (Brown and Johnson, 2019).

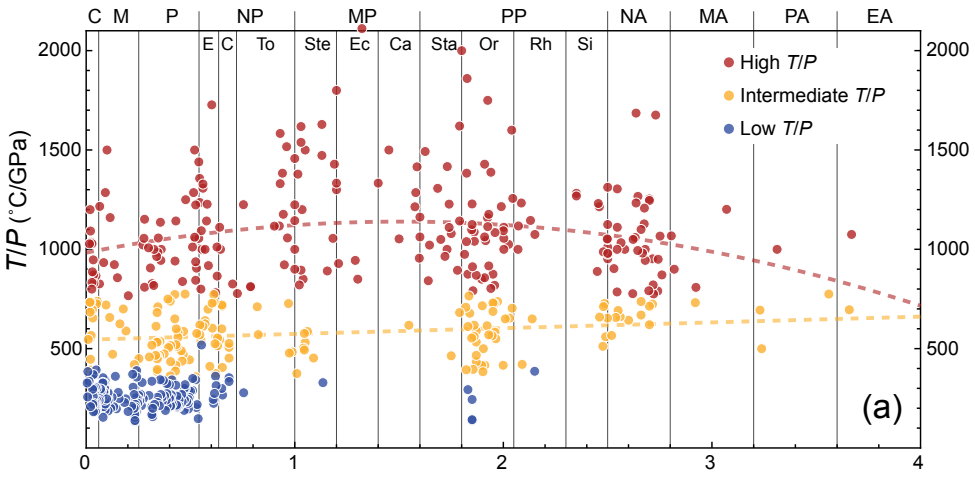

Figure 0-6. Temporal evolution of the metamorphic thermobaric ratios (T/P) for 564 localities (Brown and Johnson, 2019).

4. Architecture of the Archean crust and tectonic implications

The architecture of the Archean cratons is remarkable compared to younger continental segments.

Their internal structure reveals alternating domes, with granitoidic rock cores, surrounded by denser mafic volcanic and sedimentary rocks, forming basin-like keels (Suess, 1875; Kusky et al., 2018). Another major architectural distinction between the Archean and modern continental crust is the accommodation of shortening. In modern-day convergent zones such as the Andes, Alps and Himalayas, linear continental-scale collision belts are characterized by significant crustal thickening, often exceeding 40 kilometers, and accommodated by sub-horizontal thrust zones that concentration the deformation (*e.g.*, Gapais et al., 2009 and references therein). In the Archean granite-greenstone terranes, deformation is almost always ubiquitous, characterized by large-scale homogeneous sub-vertical foliations and large-scale subvertical ductile shear zones (Davis and Maidens, 2003; Chardon et al., 2009). Deformation is accommodated by both horizontal and vertical kinematics, and very little crustal thickening is interpreted (Bouhallier et al., 1995; Choukroune et al., 1995; Cagnard et al., 2007; Duclaux et al., 2007; Chardon et al., 2009).

Geodynamically, the Archean dome-and-keel architecture has been interpreted through both vertical and

horizontal tectonic models. The traditional model emphasizes vertical tectonics, driven by density contrast, where vertically ascending solid-state diapirs, as proposed by (Fig. 0-7b; Ramberg, 1967; Weinberg and Podladchikov, 1995) are accompanied by the downward movement of greenstone sequences (Van Kranendonk et al., 2015). The Eastern Pilbara Craton in Western Australia exemplifies this architectural style (Fig. 0-7a). The region's granitoid bodies exhibit complex dome-like deformation patterns interwoven with thick and folded volcanic and sedimentary sequences. Numerical models, such as those presented by Sizova et al. (2015) and Johnson et al. (2014, 2019), have demonstrated that specific conditions could allow the dense upper crust to sink into the mantle through a process known as drip tectonics, also known as sagduction (*e.g.*, Bouhallier, 1994; Bouhallier et al., 1995; Collins et al., 1998; Nebel et al., 2018).

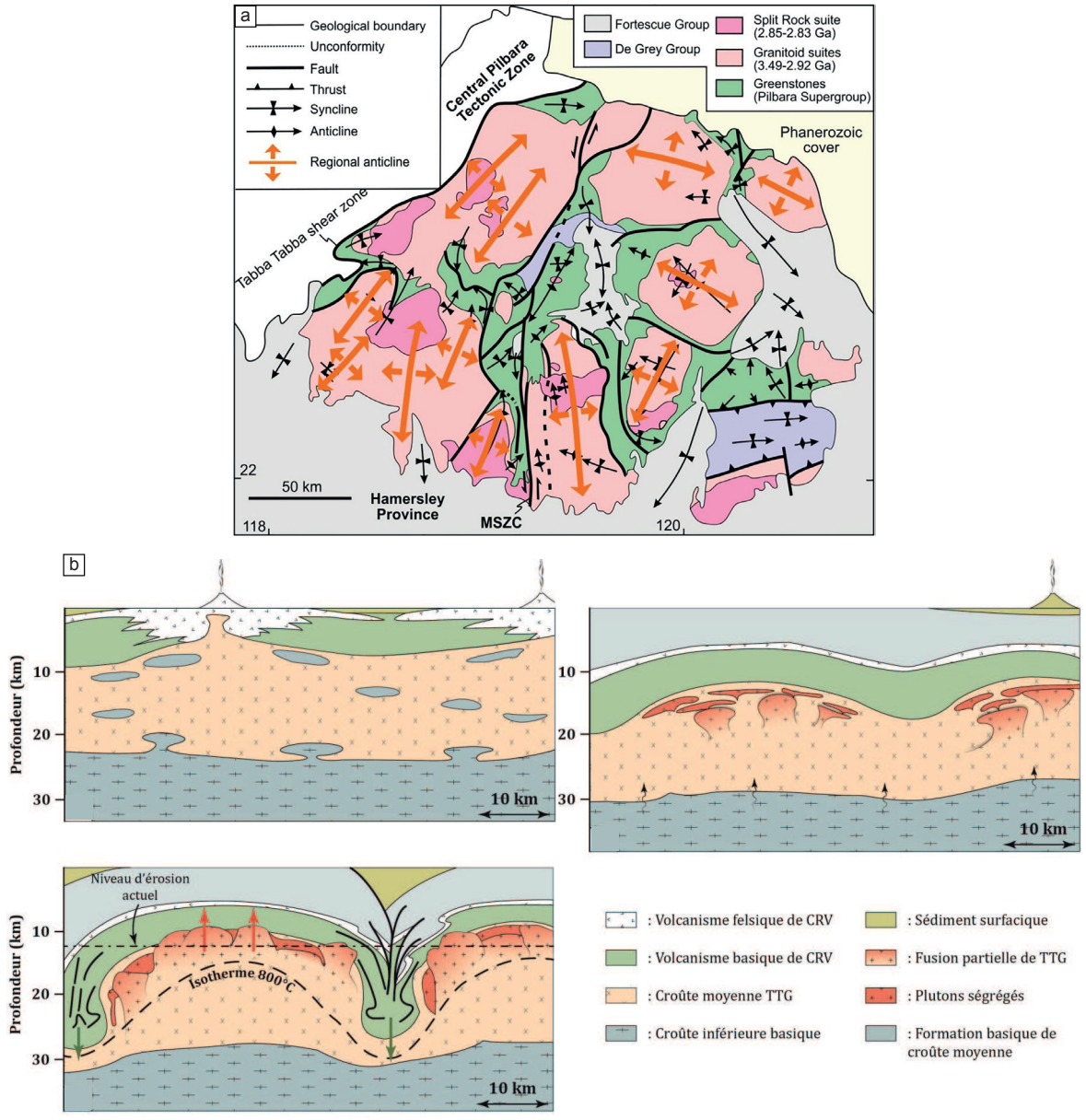

Figure 0-7. a. Simplified map of the Eastern Pilbara craton, where folds and overall structural patterns are highlighted for both domes (pinks) and basins (green) (Kusky et al., 2021). **b.** Schematic crustal-scale cross-sections of the diapiric geodynamic models for the dome-and-keel structures from the Eastern Pilbara craton (Vezinet, 2016; from Van Kranendonk et al., 2004). The eruption of ~ 10 km thick basaltic layer leads to positive thermal anomaly in the felsic middle crust triggering partial melting and inversion of the crustal density profile between the supracrustal lithologies and the lower crust. It results in the diapiric ascent of the low-density, partially melted felsic crust and sinking of dense basaltic lithologies into the lower crust.

The dome-and-keel patterns can also be explained by horizontal tectonic, *i.e.*, subduction-like processes (Fig. 0-8). This implies that these patterns were formed through crustal thickening, thrusting, and folding driven by plate tectonic activity, followed by the intrusion of magmatic bodies. Because of the hotter conditions within the Hadean and Archean Earth, the lithosphere was more buoyant and weaker, *i.e.*, more ductile, compared to its Phanerozoic counterpart (England and Bickle, 1984; Choukroune et al., 1995; Jackson, 2002; Neves et al., 2005; Cagnard et al., 2006). These Archean horizontal-driven tectonic models therefore adapt the accretionary orogeny model to the thermal regime at this time (Choukroune et al., 1995; Chardon et al., 2009; Mvondo et al., 2017; Traore et al., 2020). Subduction is flatter and generally less developed than in Phanerozoic times (*e.g.*, Capitanio et al., 2019 and references therein).

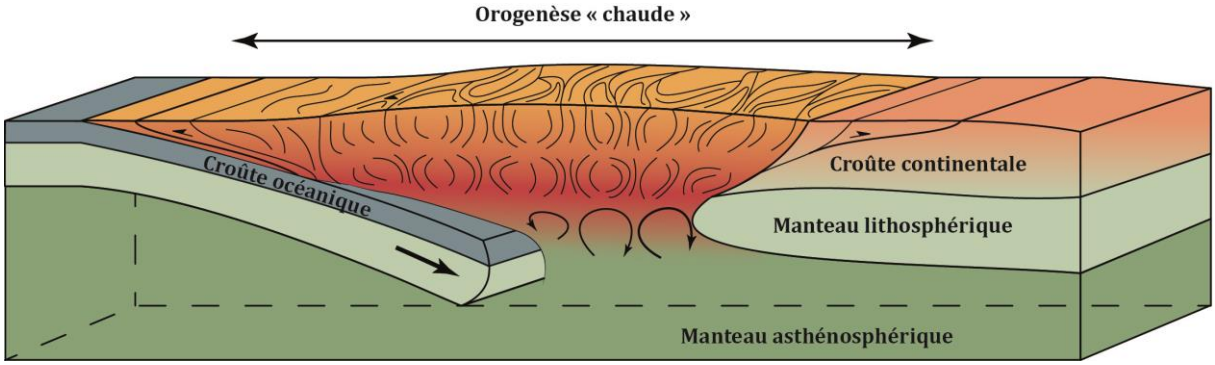

Figure 0-8. Hot orogen model showing both vertical and horizontal tectonic processes with dome structures and subduction process (Vezinet, 2019, after Chardon et al., 2009).

5. Gold deposits as a tracer of the Archean geodynamic

Archean geodynamics is also the cradle of a significant economic concentration of many elements, most notably gold. A major peak of gold mineralization is recorded as early as the Mesoarchean, between 2.9 and 2.8 Ga (Goldfarb et al., 2001; Frimmel, 2008, 2018). This event is the largest known gold anomaly in the crust and consists of conglomerate-hosted gold mineralization (*e.g.*, Witwatersrand, Kaapvaal). According to Frimmel (2018), this event represents the primary enrichment of gold in the crust, facilitated by "*photosynthesizing microbes under an oxygen-deficient atmosphere*". Subsequent gold deposits are believed to have formed through the recycling of these gold-enriched supracrustal segments via subduction processes (Frimmel, 2018). This recycling led to periodic episodes of major gold endowment during times of significant continental accretion, such as supercontinent formation, as exemplified by the peaks of crustal growth, gold peaks and supercontinent formations (Fig. 0-9; Goldfarb et al., 2010; after Goldfarb et al., 2001; Condie, 2005; Groves et al., 2005; Frimmel, 2018). However, the cyclicity of gold mineralization in the crust is also accompanied by significant episodes of juvenile crust formation (Fig. 0-9), such as hot spots (Goldfarb et al., 2001; Condie, 2007; Condie et al., 2009; Frimmel, 2018; Thébaud et al., 2018). The gold endowment of the crust is therefore also thought to result from mantle-crust transfer during juvenile magmatism. Overall, most of the gold hosted in the crust is interpreted to have enriched the crust during the Archean, and the addition of new mantle gold is limited after the Archean (Frimmel, 2008).

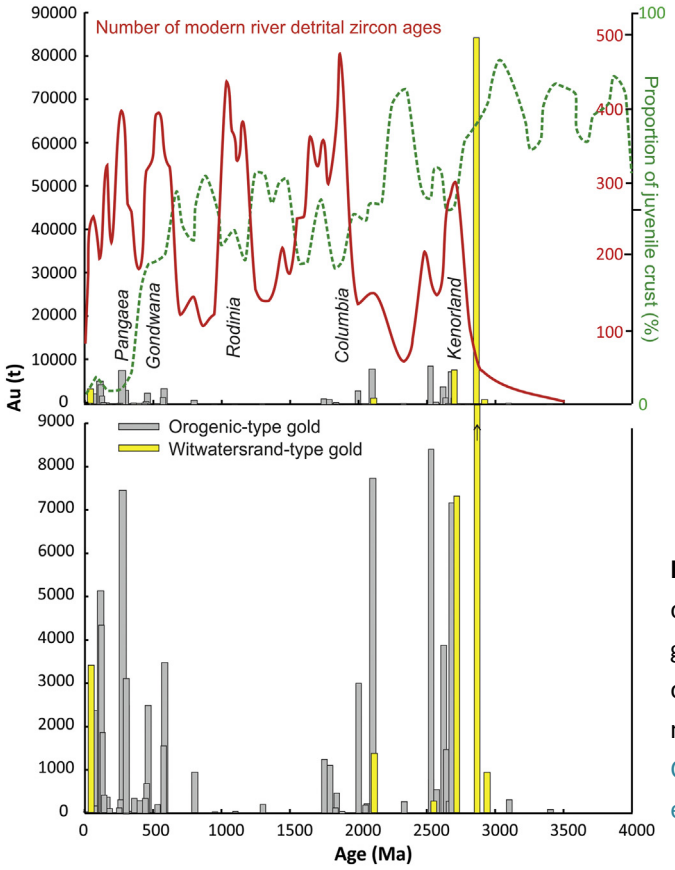

Figure 0-9. Temporal distribution of gold content (t) in orogenic gold deposits (grey) and conglomerate-hosted gold deposits (yellow), of the proportion of juvenile crust (%), of supercontinents, and of the number of modern river detrital zircon ages (Frimmel, 2018, from Goldfarb et al., 2005; Belousova et al., 2010; Spencer et al., 2017).

The mineral deposits can be defined as small-scale expressions of a sequence of geological processes that occur across different temporal and spatial scales (*e.g.*, Wyborn, 1997; McCuaig and Hronsky, 2014; Champion and Huston, 2016). Notably, some factors influencing mineralization may have involved lithospheric-scale processes (*e.g.*, Yang et al., 2024) and occurred well before the ore-forming events, up to one or more orogenic cycles (*e.g.*, Meffre et al., 2016; Masurel et al., 2021; Sumail et al., 2024). Compiling mineral deposits formed in convergent margins through geological times has proven an efficient tool in constraining the evolution of tectonic styles (Fig. 0-10; Huston et al., 2023). By studying the characteristics and spatial distribution of different mineral deposits, fingerprints of convergent margin processes can be identified. These fingerprints help in turn reconstruct the tectonic settings and thermal regimes of past geological periods.

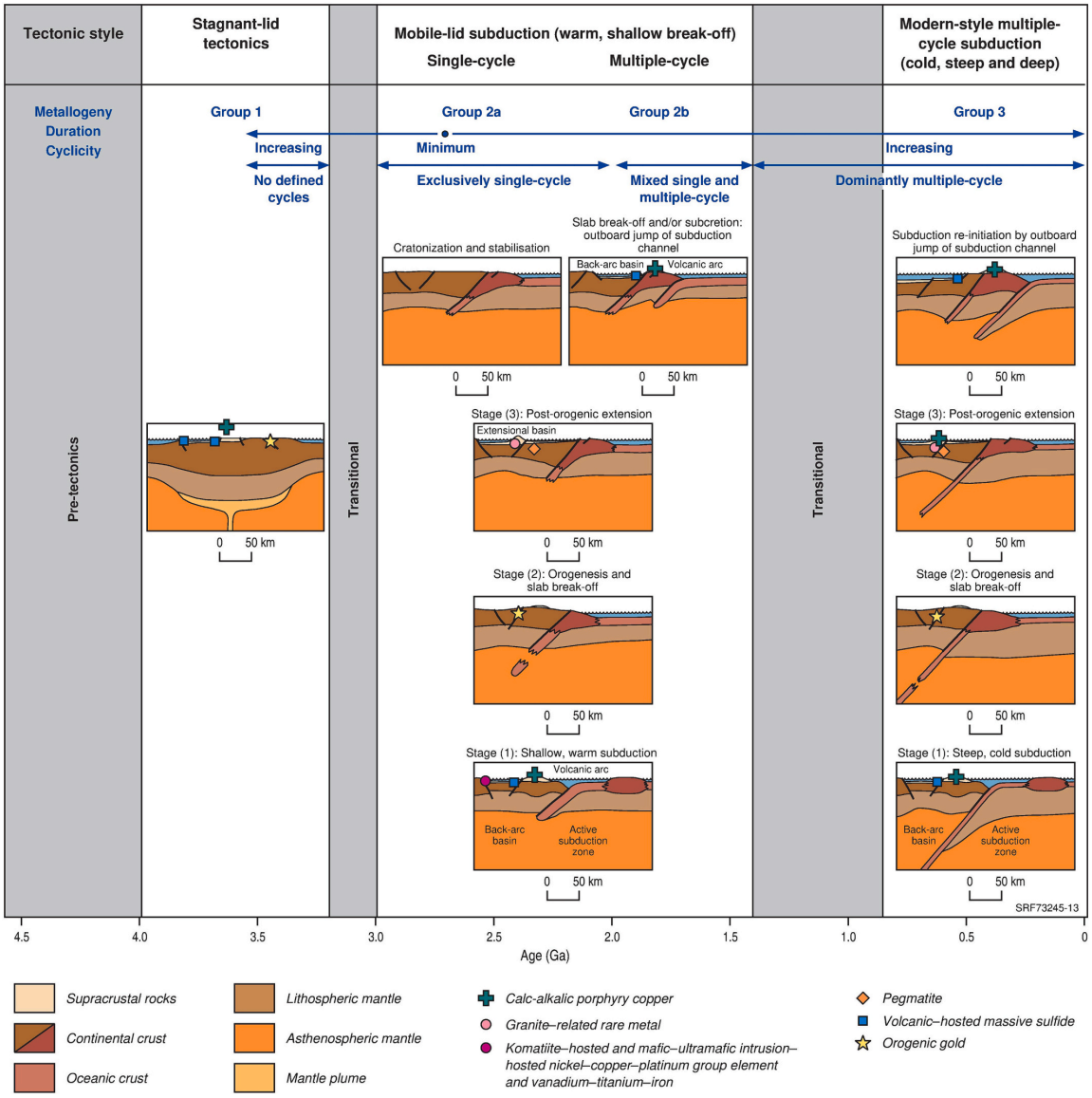

Figure 0-10. 4.0 to 0 Ga evolution of tectonic styles and their relationship with mineral deposits in convergent margins (Huston et al., 2023).

6. Defining the gold mineral system

Gold is a siderophile chemical element, meaning it has an affinity for iron. This geochemical property implies that gold was preferentially concentrated in the core during the differentiation of the Earth (Wood et al., 2006). As a result, gold is distributed only in trace amounts in the upper continental crust, with an average concentration of 1.3 ppb, corresponding to the Clarke value for gold (Rudnick and Gao, 2003). Gold deposits with concentrations on the order of ppm may nowadays be considered economic viable, and thus represent significant geochemical anomalies, with enrichment factors that can reach 1,000 to 10,000 times the Clarke value. Such anomalies therefore mean that geological processes at up to lithospheric scales were required to significantly enrich the crust.

Furthermore, the spatial and temporal distribution of gold deposits at all scales is intrinsically unevenly distributed, but not randomly (Barley and Groves, 1992; Kerrich et al., 2005; Goldfarb et al., 2001; 2010; Frimmel, 2008; 2018; Cawood and Hawkesworth, 2015). For instance, the worldwide orogenic-gold

concentration correlates with periods of massive crustal growth and supercontinent assemblies (Fig. 0-11; Goldfarb et al., 2001, 2010). This episodic distribution seems to reflect a direct link between orogenic gold deposit formation and preservation, and large-scale geological processes, including mantle-crust differentiation, as well as the recycling and/or remobilization of the crust during major crustal growth periods (Frimmel, 2008). Barley and Groves (1992) defined three major factors that controlled such heterogeneous distribution: (i) an evolving hydrosphere and atmosphere, (ii) significant changes of the Earth's heat flux through time and (iii) long-term tectonic trends.

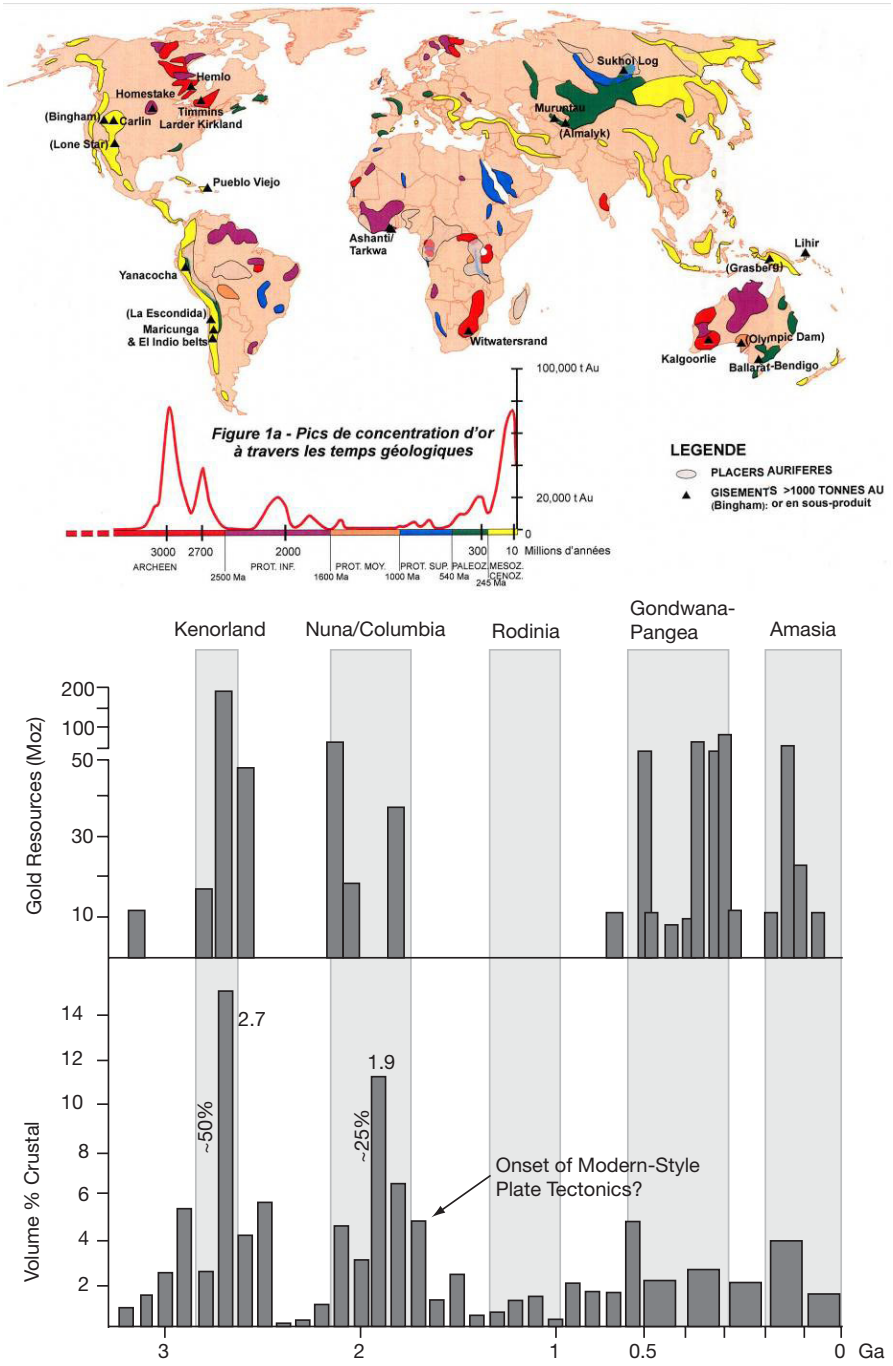

Figure 0-11. a. World repartition of gold provinces. Colors represent the Eon of formation of the provinces, and are represented in the gold resources distribution diagram. World-class deposits of more than 1000 tones gold resources are also highlighted on the map (Lescuyer, 2005). **b.** Distribution of gold resources in orogenic gold deposits (Moz) and comparison with the crustal growth volume (%) during the geological times (Goldfarb et al., 2010; after Goldfarb et al., 2001; Condie, 2005; Groves et al., 2005). Grey areas represent the periods of amalgamation of continental crust, forming supercontinents.

Notably, some factors influencing mineralization may have involved lithospheric-scale processes (*e.g.*, Yang et al., 2024) or microscopic-scale ones (*e.g.*, Sugiono et al., 2022, 2025; Fougerouse et al., 2024), and may have occurred well before the ore-forming events, up to one or more orogenic cycles (*e.g.*, Meffre et al., 2016; Masurel et al., 2021; Sumail et al., 2024) as well as after mineralization, preserving the ore during up to several billions of years (Fig. 0-12; Wyborn, 1997; McCuaig and Hronsky, 2014; Champion and Huston, 2016). These processes governed the initial enrichment of the crust, the transport of ore-bearing fluids to deposition sites and controlled gold deposition. This vision embodies the mineral system concept that links many processes that "*control the generation and preservation of mineral deposits*" (Wyborn et al., 1994; McCuaig and Hronsky, 2014). Ultimately, economically valuable elements were concentrated into relatively small volume compared to the Earth's crust, suitable for economic extraction (Jenkin et al., 2015).

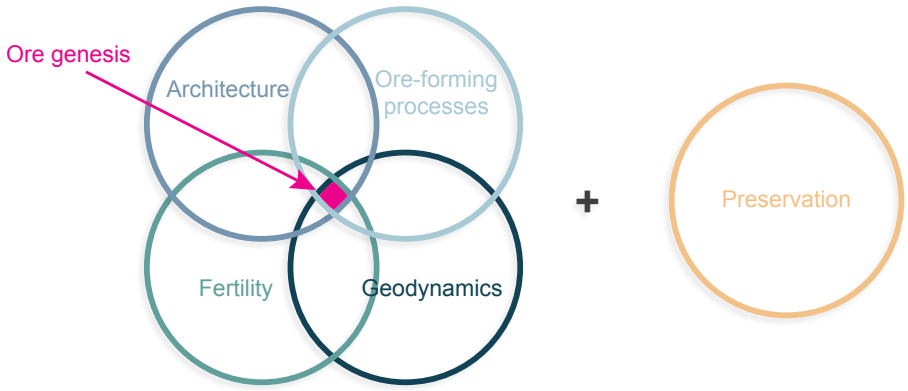

Figure 0-12. Key factors of the gold mineral system controlling ore genesis as defined by McCuaig and Hronsky (2014), and adapted after Occhipinti et al. (2020) and Perret (2021). The juncture of favorable transient geodynamics, fertile crust, architecture and ore-forming processes are critical in ore genesis. The post-mineralization preservation of the deposit is the fifth parameter of the mineral system.

If gold concentration into deposits is governed by geological processes, the mineral deposit distribution can therefore be predicted within the continental crust, where all the geological factors influencing the formation and preservation of mineral deposits meet: favorable geodynamic evolution, lithospheric architecture, ore-forming processes and deposit preservation (Fig. 0-12; Fyfe and Kerrich, 1976; Wyborn et al., 1994; McCuaig and Hronsky, 2014; André-Mayer et al., 2024). The system approach enables selecting new exploration targets relying on a deeper understanding of the overall geodynamic context, guided by the source-transport-trap paradigm (McCuaig et al., 2010; McCuaig and Hronsky, 2014). This integrated approach is especially achievable through the development of collaborative work between academic research and exploration industry, as exemplified by the West African Exploration Initiative ongoing since 2006 (*e.g.*, Thébaud et al., 2020; Masurel et al., 2021), or the THEIA common laboratory initiated in 2023 aiming at deepening our understanding of the genesis of Precambrian deposits in Africa and Arabia to enhance the accuracy of their prediction, and developing next-generation tools for mineral exploration to stay ahead in predictive capabilities and ensure the industry maintains a leading edge in geoscience and technology (André-Mayer et al., 2024). To accurately identify these deposits, a systematic, multi-scale, and multidisciplinary approach is required (Perret, 2021; Perret et al., 2021; André-Mayer et al., 2024). Conversely, insights into the mechanisms of deposit formation can significantly contribute to our understanding of the Earth's system, specifically mineral systems requiring large-scale and long-term processes such as orogenic gold (Fig. 0-13; Cawood and Hawkesworth, 2015; André-Mayer et al., 2024).

7. Defining orogenic gold deposits in the Archean

Structurally controlled, epigenetic gold deposits in the Archean have many names, the most common are greenstone-hosted, quartz-carbonate vein, lode-, orogenic or mesothermal gold deposits (Dubé and Gosselin, 2007 and references therein). These deposits are found in deformed greenstone belts of various ages and are characterized by networks of gold-bearing, laminated quartz-carbonate fault-fill veins formed within brittle-ductile shear zones and faults (Dubé and Gosselin, 2007 ; Groves et al., 2018 and references therein). They commonly occur in metamorphic rocks of greenschist to lower amphibolite facies, predominantly mafic in composition, and form at intermediate crustal depths (5–10 km). Associated features include iron-carbonate alteration, extensional veins, and hydrothermal breccias. Gold is primarily hosted in quartz-carbonate vein systems but may also occur in iron-rich, sulphidized wall-rock selvages or arsenopyrite-rich replacement zones.

Lode-gold deposits are epigenetic, meaning that the mineralized fluids might have circulated over large distances (Fig. 0-13; Tomkins, 2013; Gaboury, 2019 and references therein). The ore-bearing fluids, ligands and gold are not necessarily sourced from a single reservoir (Hagemann et al., 1994; Tomkins, 2013; LaFlamme et al., 2018a; Thébaud et al., 2018). Two distinct but not necessarily mutually exclusive sources of gold are mainly discussed, juvenile, mantle-derived magmas (*e.g.*, Pitcairn et al., 2015; Augustin and Gaboury, 2017) and volcanosedimentary series (*e.g.*, Large et al., 2007, 2011; Gaboury, 2013). The latter can be fertilized through primary processes such as mantle-derived volcanism (*e.g.*, Evans et al. 2010; Phillips and Powell 2010; Fu et al. 2012; Pitcairn et al. 2015), from microbial activity (Frimmel, 2018) or from the erosion of pre-enriched rocks. Finally, these fertile supracrustal units may be recycled into the mantle, where they act as a source of gold through metasomatism (Bierlein and McKnight, 2005; Hart, 2005; Eglinger et al., 2017; Masurel et al., 2019).

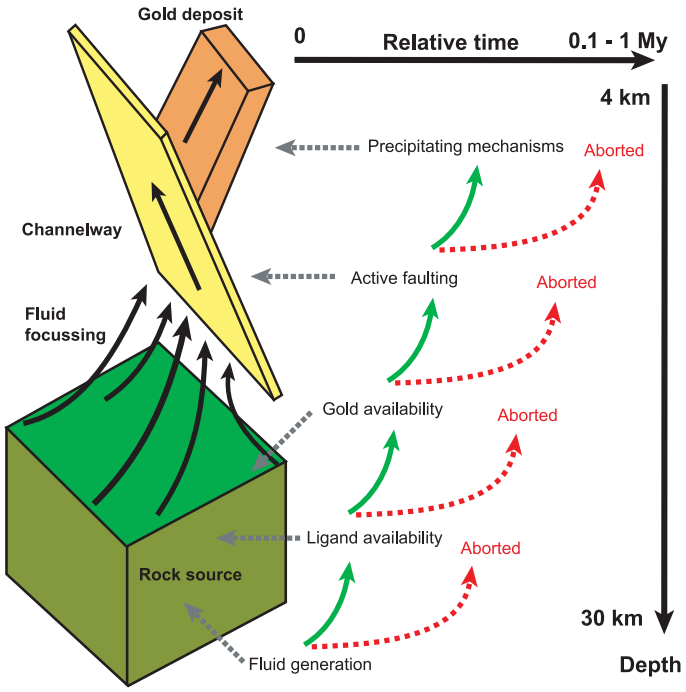

Figure 0-13. Genetic model for orogenic gold deposits, showing the path of gold in the crust from its source rock to its deposition site (Gaboury, 2019, after Ridley and Diamond, 2000 and Cox, 2016).

The deposits are related to low-salinity, H_2O-CO_2-rich hydrothermal fluids that transport gold along major crustal faults (Fig. 0-12). These fluids may originate from prograde metamorphism (*e.g.*, Phillips and Groves, 1983; Pitcairn et al., 2006; Lambeck et al. 2011; Gaboury, 2013; Zhong et al., 2015) and thermal re-equilibration of subducted volcano-sedimentary terranes during accretionary or collisional tectonic events (Groves et al., 1998a, 2018), during magma crystallization (*e.g.*, Rock and Groves, 1988; Robert, 2001; Salier et al., 2004; Bierlein and Pisarevsky, 2008; Doublier et al., 2014). As the fluid rises through the crust, it redeposits gold in second- and third-order structures through fluid-pressure cycling and variations in temperature and pH (Fig. 0-13).

Changes in the fluid physical-chemical conditions that trigger gold deposition include: fluid-rock interaction (Palin and Xu, 2000), mixing of fluids with different physical-chemical conditions (Cox, 1995; Goldfarb and Groves, 2015), rock buffering of the fluid pH (Evans et al., 2006; Petrella et al., 2020), mineral precipitation (Williams-Jones et al., 2009; Hu et al., 2017), and boiling/phase separation (Hodkiewicz et al., 2008; Voisey et al., 2020). As gold transport in the fluid is thought to be mainly achieved by complexing with sulfur (bi- or tri-sulfide complexes; Pokrovski et al., 2015) and its deposition by the complex destabilization through changes in the fluid conditions (*e.g.*, Gaboury, 2019), mineralized sulfide minerals therefore constitute direct tracers of ore-forming processes and are largely studied as such (*e.g.*, Cook and Chryssoulis, 1990; Deditius et al., 2014; Li et al., 2014; Velásquez et al., 2014; Fougerouse et al., 2016; Gourcerol et al., 2020; Voisey et al., 2020; Perret et al., 2021; Berthier et al., 2023; Sugiono et al., 2025).

8. PhD objectives and structure of the manuscript

8.1. PhD objectives

Archean continental crusts host the most important gold provinces and represent historic focus of mineral exploration, exemplified by the Yilgarn, Superior, and Kaapvaal cratons (*e.g.*, Phillips et al., 2019; Dube and Mercier-Langevin, 2020; Frimmel and Nwaila, 2020; Tripp et al., 2020; Travers, 2024). Exploration and mining in the Archean Tanzania Craton is recent, in comparison to most gold mineral provinces in Africa, such as the Archean Kaapvaal craton, the Paleoproterozoic West Africa craton and the Neoproterozoic Nubian Shield, where gold played an important role in Iron Age cultures (*e.g.*, Klemm et Klemm, 2013; Elbra, 2017). The pastoral societies of Central-East Africa historically exhibited little interest in gold, despite the region's abundant greenstone belts and highly gold-concentrated rocks (Kabete et al., 2012a). Systematic mining efforts in the Tanzania Craton began with German prospectors in the late 19th century, with increased activity later driven by gold price increases in the 1930s (Henckel et al., 2016). Exceptionally large ore bodies were discovered through geochemical and later geophysical surveys, and the interest in the Tanzania Craton led to the opening of significant mines, such as the world-class Geita deposit, which dominated production in the Lake Victoria Goldfields during the colonial era. Between 1935 and 1970, these mines, along with smaller operations, yielded approximately 2.6 million troy ounces (Moz) of gold. However, exploration activity has slowed significantly in recent years, and many of the craton's major deposits, such as Geita and Bulyanhulu, were discovered decades ago. The Nyanzaga gold deposit, identified in the late 20th century, is among the last significant discoveries in the province. The Tanzania Craton is now considered by some as a mature gold province, with limited potential for new, large-scale deposits (Henckel et al., 2016).

While the mineral system approach is widely adopted in many gold provinces (Champion and Huston, 2016; Joly et al., 2015; Mériaud et al., 2019; Groves et al., 2020; Makiba et al., 2020; Osei et al., 2021; Huston et al., 2023), it has not yet been applied to the so-called mature Tanzania Craton. In this region, traditional exploration methods such as geochemical and geophysical surveys have been predominantly used (Henckel et al., 2016; Dirks et al., 2020). This PhD work therefore aims at reconstructing the gold source(s) and fertilization in Archean juvenile crustal segments, up to its economic concentration and the geological and geochemical processes that control mantle-crust gold transfers in the Sukumaland Greenstone Belt of the Archean Tanzania Craton. A multi-scale and multidisciplinary approach is followed, enabling an integrative vision of gold mineralization through time and space, from the district and lithospheric scales to the deposit and microscopic scales.

8.2. Overview of the manuscript organization

This PhD manuscript contains 6 chapters including a geological and metallogenic context in Chapter I and a reappraisal of the main results and general discussion in Chapter VI. A multi-scale and multi-method approach was followed to reconstruct the gold mineral system (Figs. 0-12, 0-14) and tackle the question of crustal growth mechanisms in the Archean northern Sukumaland granite-greenstone belt and related Nyanzaga and Kilimani gold deposits:

Chapter I presents the current state of the art regarding the general geological and gold metallogenic context of the Tanzania Craton.

Chapter II reconstructs the crustal growth and differentiation mechanisms in the Sukumaland granite-greenstone belt (SGGB; geodynamic factor of the gold mineral deposit in Fig. 0-11; crustal differentiation and geodynamic processes in Fig. 0-14), by combining fieldwork along a transect across the SGGB, petrography, geochemistry, geochronology (zircon U-Pb) and isotopy (zircon O-Lu-Hf).

Chapter III enables first to reconstruct the crustal and tectono-magmatic evolution of the region through a district- and crustal-scale, petro-structural study of the architecture of the SGGB (architecture factor of the gold mineral deposit in Fig. 0-12; tectonic processes in Fig. 0-14), and second to discuss about the gold fertility (fertility factor of the gold mineral deposit in Fig. 0-12; initial enrichment in Fig. 0-14) of this newly juvenile Archean crust.

Chapter IV makes the link between the regional and the deposit scale by constraining the source of sulfur (and by proxy the gold reservoir; fertility factor of the gold mineral deposit in Fig. 0-12; sources of metal, ligands, fluid and sulfur and initial enrichment in Fig. 0-13) as well as the ore-forming processes (ore-forming processes factor of the gold mineral deposit in Fig. 0-12; gold deposition in Fig. 0-14) using the $\delta^{34}S$ and $\Delta^{33}S$ isotopic signature of gold-barren and -bearing pyrite of the Nyanzaga deposit, combined with thorough macroscopic- and microscopic-scale petro-textural study of veins and sulfide minerals.

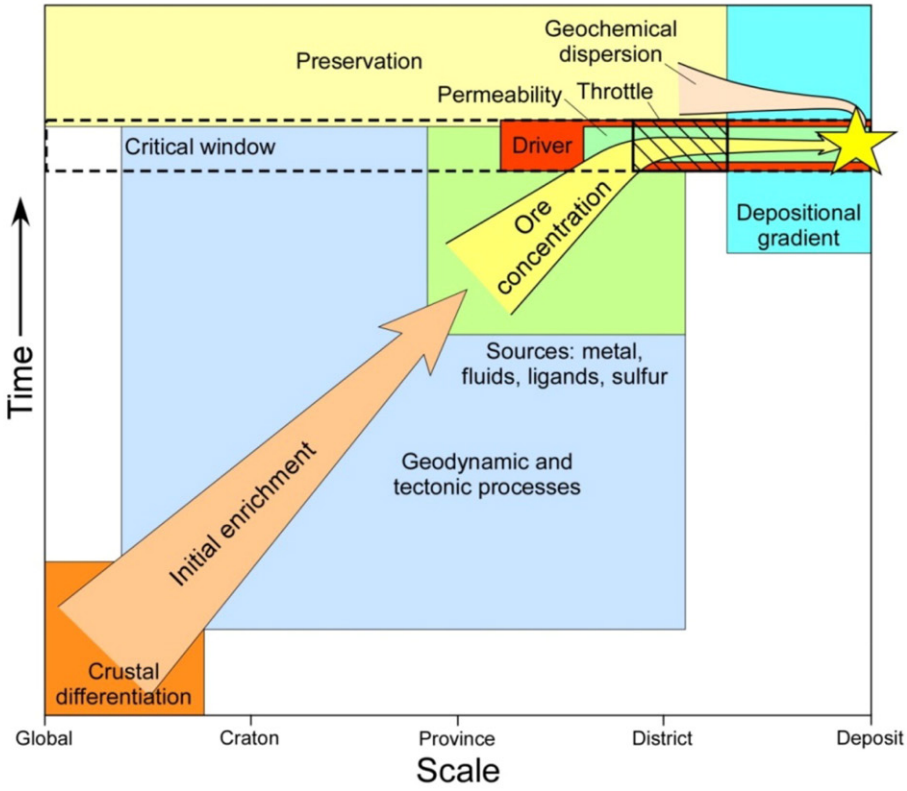

Figure 0-14. Space-time diagram showing key features and processes controlling the formation of mineral deposits (Champion and Huston, 2016).

Chapter V (article published in 2024) proposes an extensive deposit-scale structural study of the Nyanzaga and Kilimani deposits to characterize the local deformation history. Spatial and temporal relations between lithologies, deformation, alteration and gold mineralization highlight the strong structural controls of gold mineralization and give insights to the timing of barren and fertile hydrothermal stages (architecture and ore-forming processes factors of the gold mineral deposit in Fig. 0-12; permeability, throttle and ore concentration in Fig. 0-14).

Chapter VI combines all the results and partial conclusions to reconstruct the journey of gold through this Archean crust segment of the Tanzania craton from the timing and geodynamic context of gold fertilization of the crust, to the tectonic controls on its circulation and deposition (Figs. 0-12, 0-14). Perspectives regarding the global onset of plate tectonic, as well as exploration strategies in the Tanzania Craton concludes this PhD manuscript.

9. Financial and scientific support, external collaborations

This thesis was made possible through the scientific and financial support of several organizations. First, Arethuse Geology provided both scientific and financial supports. The National Association for Research and Technology (ANRT) provided funding through a grant awarded under the framework of an Industrial Agreement for Training through Research (CIFRE) No. n°2021/0546. OreCorp Limited and later Perseus Mining companies played a key role as project partners, financing part of the PhD project, hosting the research team at the Nyanzaga exploration camp and providing the necessary equipment for fieldwork. This work was partly supported by the French PIA project "Lorraine Université d'Excellence", reference ANR-15-IDEX-04-LUE. The PhD project has also benefited of the 2023 Student Research Grant – Hugh McKinstry Fund (SRG 23-94) from the Society of Economic Geology. GeoRessources and Geosciences Montpellier laboratories provided facilities necessary for the smooth running of the project over the course of the three-year PhD, as well as the Centre for Exploration Targeting for a three-month period (07/17/2023 to 10/17/2023). This work benefited of the framework of the LabCom ANR THEIA, created in January 2024, that binds GeoRessources with Arethuse Geology in a shared R&D trajectory on the understanding of Precambrian metallogenic systems, particularly in Africa.

~

CHAPTER I

~

1. Geological context of the Tanzania craton

The Tanzania craton extends from western Kenya to central Tanzania and southeastern Uganda, likely continuing beneath Lake Victoria (Borg and Shackleton, 1997; Sanislav et al., 2014). It constitutes one of the four Archean crustal blocks that form the Central African Shield, also referred to as the Greater Congo craton (Djeutchou et al., 2024), alongside the Congo craton, the Ugandan craton and the Bangweulu block (Fig. 1-1; Borg and Shackleton, 1997; Begg et al., 2009; Ganbat et al., 2020; Turnbull et al., 2021). The Tanzania craton is separated from other Archean crustal blocks by Proterozoic orogenic belts predominantly consisting of remobilized Archean crust (Fig. 1-1). These include the Paleoproterozoic belts of the Ubendian in the southwest, the Usagaran in the east, the Ruwenzory in the north, and the Mesoproterozoic Kibaran belt in the west (Borg and Shackleton, 1997; Muhongo et al., 2001; Reddy et al., 2003; Sommer et al., 2003; Begg et al., 2009; Manya, 2011; Lawley et al., 2013; Thomas et al., 2013; Ganbat et al., 2020). Archean cores were amalgamated between 2100 and 1800 Ma during the Eburnean orogeny and the formation of the Columbia supercontinent (e.g., Pinna et al., 1996; De Waele et al., 2008). To the east of the Tanzania craton and the Usagaran belt lies the Neoproterozoic Mozambique belt, which formed during the East African–Antarctic orogeny and contains remobilized Archean fragments (e.g., Kabete et al., 2012b; Thomas et al., 2013, 2016). The significant amount of remobilized Archean crust within the Proterozoic mobile belts, often interpreted as autochthonous (e.g., Vogt et al., 2006; Thomas et al., 2016), aligns closely with the metacraton concept as defined by Liégeois et al. (2013).

1.1. Stratigraphic and tectonic subdivisions of the Tanzania craton

The Tanzania craton comprises two geologically distinct regions (Fig. 1-1): (i) the Lake Victoria Goldfields(LVG) to the north, which consists of numerous greenstone belts and associated granitoids (Fig. 1-2a), *i.e.*, a granite-greenstone superterrane; and (ii) the Central Tanzania Region (CTR), in the south, characterized by a lower proportion of greenstone rocks and highly metamorphosed and deformed gneissic-migmatitic terranes, *i.e.*, a high-grade superterrane (Fig. 1-3; Windley and Bridgewater, 1971; Windley, 1984; Myers and Kröner, 1994; Borg and Shackleton, 1997; Kwelwa et al., 2012a).

1.1.1. Lithostratigraphic subdivision

The **lithostratigraphy** of the Tanzania craton is divided into three units, in chronological order: the Dodoman Supergroup, the Nyanzian Supergroup and the Kavirondian Supergroup (Fig. 1-2b; Quennell, 1956; Barth, 1990; Borg and Shackleton, 1997; Borg and Krogh, 1999). The **Dodoman Supergroup** is exclusively described in the CTR and is considered the basement of the craton, with some of the oldest rocks recorded in the region, from Meso- to Neo-Archean (Gabert, 1990; Manya, 2011; Sun et al., 2018). Granitoid-migmatite rocks underwent metamorphism under P-T conditions from the almandine-amphibolite facies to the granulite facies (Gabert, 1990; Kabete et al., 2012b; Thomas et al., 2016). They alternate with high-grade metamorphic supracrustal rocks forming WNW-trending belts, mainly granulite-facies metamorphites, locally migmatites, intruded by meta-mafic rocks (Gabert, 1990). Low-grade metamorphic rocks, talc-chlorite, sericite and corundum-bearing schists were also described in the supracrustal belts of the CTR (Quennel et al., 1956; Gabert, 1990).

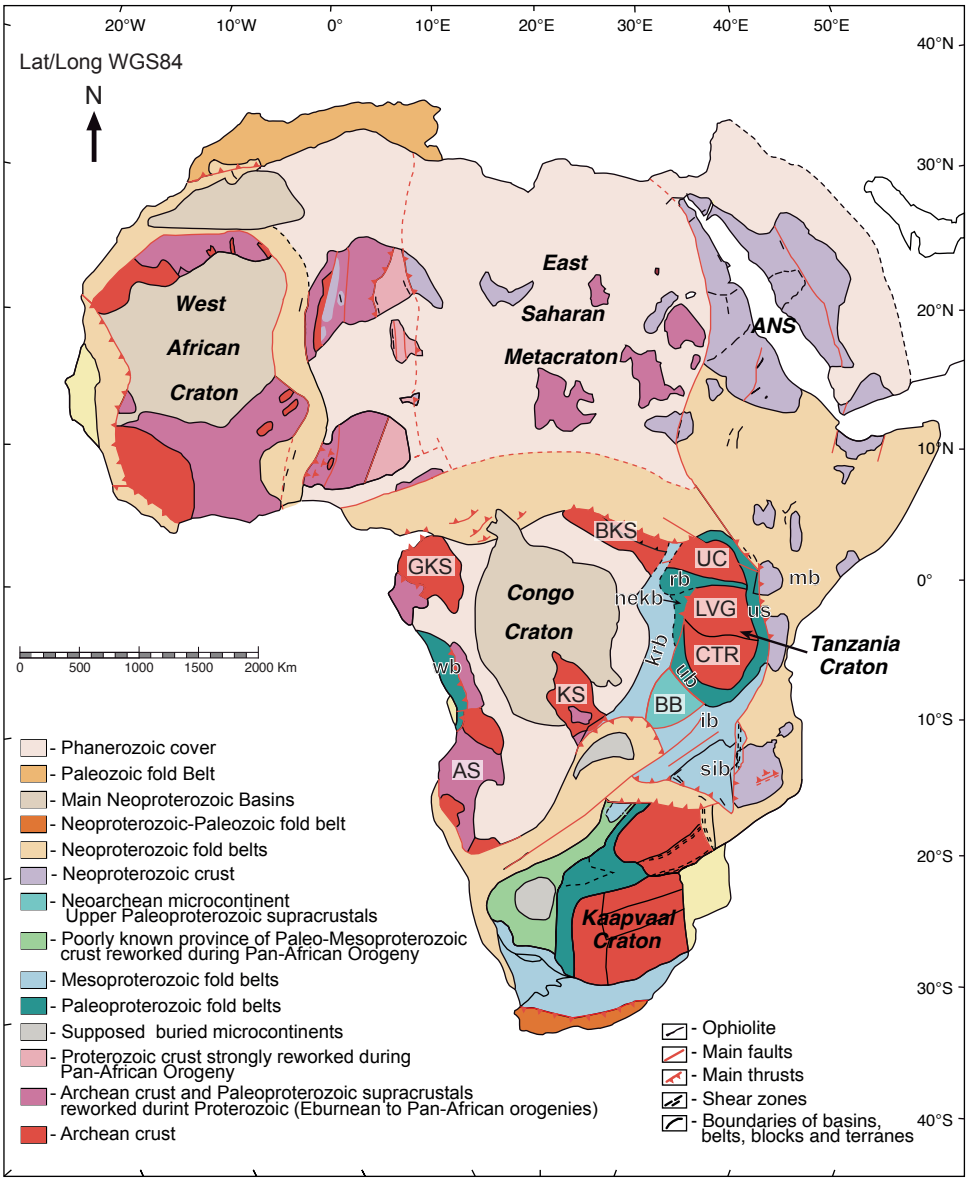

Figure 1-1. Map of the African litho-tectonic domains (from Begg et al., 2009). Cratons and microcontinents: Tanzania craton (LVG – Lake Victoria Goldfield; CTR – Central Tanzania Region); Congo craton (GKS – Gabon-Cameroon Shield; BKS – Bomu-Kibalian Shield; KS – Kasai Shield; AS – Angolan Shield); UC – Uganda craton; BB – Bangweulu block. Paleoproterozoic mobile belts: ub – Ubendian; us – Usagaran; rb – Ruwenzory; nekb – Northeastern Kibaran; wb – West Central Africa. Mesoproterozoic mobile belts: krb – Kibaran; ib – Irumide; sib – Southern Irumide. Neoproterozoic mobile belt: mb – Mozambique belt.

The **Nyanzian Supergroup** spans over 120 Ma of volcanic activity and sedimentation and was primarily described in the LVG, as well as in rare greenstone belts in the CTR (Fig. 1-2b; *e.g.*, Kabete et al., 2012a). Its stratigraphy is subdivided into two units:

- The **Lower Nyanzian** is dominated by mafic volcanics, *e.g.*, basalt, dolerite, and minor felsic volcanics and shales (Manya and Maboko, 2003, 2008). The base of the stratigraphy was dated at ca. 2823 Ma in meta-basalts (Cook et al., 2016). The volcanic sediments of the Nyanzian Supergroup formed in a marine environment, in an island arc or oceanic plateau setting (*e.g.*, Chamberlain, 2003; Cook et al., 2016).

- The **Upper Nyanzian** consists of a well bedded turbiditic sequence overlying banded iron formations (BIF) and black shales, with felsic volcanic and volcaniclastic intercalations (Quennel et al., 1956; Borg and Krogh, 1999). They deposited in an arc and back-arc setting (Chamberlain, 2003), or in a context of subduction beneath an oceanic plateau (Sanislav et al., 2018b).

The Nyanzian Supergroup underwent multiple stages of deformation and metamorphism, most often up to the greenschist facies and reaching the amphibolite facies near granitic intrusions and at the base of the stratigraphy (Lower Nyanzian). The volcano-sedimentary sequence was significantly disrupted by shear zones and granitoid intrusions (Borg and Shackleton, 1997; Sanislav et al., 2015). A major deformation event affected the region, folding the Nyanzian meta-sediments, which led to their uplift and the formation of a regional unconformity surface (Cahen and Snelling, 1966; Sanislav et al., 2015, 2016). This event is dated at around 2700 Ma (*e.g.,* Kwelwa et al., 2018; Sanislav et al., 2018a).

Conglomerates quartzite, sandstone and siltstone of the **Kavirondian Supergroup** deposited between ca. 2700 and 2640 Ma and unconformably overly the Upper Nyanzian (Gabert, 1990; Borg, 1992; Sanislav et al., 2015, 2018b). They form localized basins, generally no more than 1 km in length, and are interpreted as syn- to post-tectonic molassic basins that developed during and/or after the primary event of sediment shortening and folding (Sanislav et al., 2018b).

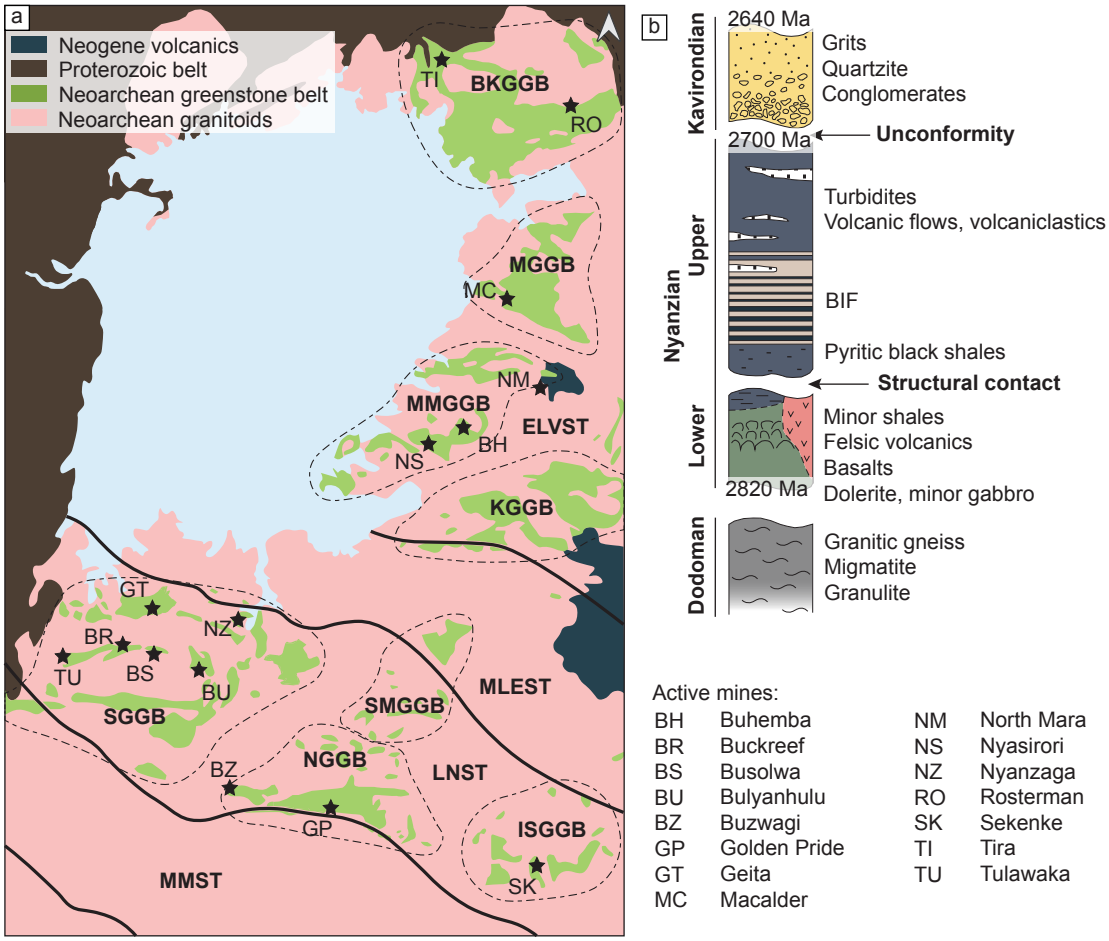

Figure 1-2. a. Simplified geological map of the LVG (from Borg and Shackleton, 1997; Cook et al., 2016). The subdivision in superterranes follows Kabete et al. (2012a). ELVST = East Lake Victoria, MLEST = Mwanza Lake Eyasi, LNST = Lake Nyanza, MMST = Moyowosi-Manyoni. Black doted lines represent the granite-greenstone belts: BKGGB = Busia-Kakamega, ISGGB = Iramba-Sekenke, KGGB = Kilimafedha, MGGB = Migori, MMGGB = Musoma-Mara, NGGB = Nzega, SGGB = Sukumaland, SMGGB = Shinyanga-Malita. Black stars highlight the main gold deposits. **b.** Stratigraphic column of the LVG (from Kwelwa et al., 2018 ; Sun et al., 2018).

1.1.2. A tectono-stratigraphic and metallogenic subdivision of the LVG

Several granite-greenstone belts have been identified in the LVG (Fig. 1-2a; Borg and Shackleton, 1997; Borg and Krogh, 1999), six of which are found in Tanzania, extending from the northeast to the southwest: Musoma-Mara, Kilimafedha, Shyninga-Malita, Iramba-Sekenke, Nzega, and Sukumaland. These belts consist of disconnected fragments of metamorphosed sedimentary and volcanic assemblages, surrounded by high-Ca and high-K granitoids, that have been grouped based on their geographic proximity and geophysical mapping. For instance, the Sukumaland granite-greenstone belt (SGGB) alone includes over 15 supracrustal fragments (Fig. 1-2a; Cook et al., 2016; Kwelwa et al., 2018). However, geological, isotopic, and geochronological studies question the definition of some of these belts. In particular, the Musoma-Mara granite-greenstone belt (MMGGB) is composed of the Suguti-Sirori and the North-Mara belts, the first being dominated by mafic magmatic rocks emplaced before 2750 Ma, 80 Ma before the volcanic activity of the latter, which is primarily felsic (Manya, 2007a, 2007b, 2008; Mtoro et al., 2009; Manya, 2012; Mshiu and Maboko, 2012). These two portions of the MMGGB might therefore not share a common geological history and should rather be described as separate terranes of the Tanzania craton (Kabete et al., 2012a).

Based on geological, geophysical, and geochronological evidence, several geological and tectonic subdivisions of the Tanzania craton have been proposed. Kabete et al. (2012a, 2012b) suggested a **tectono-stratigraphic and metallogenic division** based on the interpretation of regional geological maps (Quennell, 1956; Barth, 1990; BRGM, 2004), as well as geophysical and remote sensing data (Fig. 1-3). The authors subdivided the LVG and CTR into three superterranes, oriented WNW-ESE, and separated by crustal shear zones. These superterranes represent accretion blocks that amalgamated to form the Tanzania craton. They are further subdivided into terranes, which are areas dominated by greenstones or granitoids, separated by crustal-scale structures, some hosting gold deposits (Fig. 1-3; Kabete et al., 2012a). The geological history of the crustal blocks and litho-tectonic units, as well as their boundaries, is still not fully understood, and their delineation requires further geological, geochronological, and geochemical contributions (*e.g.*, Sanislav et al., 2014a, 2018b). Notably, most of the dating in the LVG comes from an unpublished report, with only a few ages made public and accessible in the literature (Supplementary Material 1.6 in Chapter II; Chamberlain and Tosdal, 2007; Kabete et al., 2012a). In light of these different classifications of the Tanzania craton, the following PhD manuscript will follow the classic and most used subdivision in the literature, which is the subdivision by greenstone belt (*e.g.*, Henckel et al., 2016; Sun et al., 2018; Wu et al., 2023).

1.2. Crustal growth in the Tanzania craton

The Tanzania craton provides a comprehensive record of crustal growth and differentiation, spanning from the Eoarchean to the Neoarchean (Kabete et al., 2012b; Thomas et al., 2016; Sun et al., 2018). This record offers valuable insight into the tectonic history of the Archaean Earth (Figs. 1-4 to 1-7; *e.g.*, Kabete et al., 2012b; Thomas et al., 2016; Sun et al., 2018; Wu et al., 2023). However, the geological evolution of this craton has been unevenly studied across its terranes, its understanding remains incomplete and is the subject of ongoing debate (*e.g.*, Borg and Krogh, 1999; Kabete et al., 2012a, 2012b; Sanislav et al., 2014a, 2018b; Manya, 2016; Thomas et al., 2016; Sun et al., 2018). Significant attention has been devoted to the cratonic margins and the history of the Proterozoic belts that delineate the craton (*e.g.*, Muhongo et al., 2001; Reddy et al., 2003; Sommer et al., 2003; Lawley et al., 2013; Thomas et al., 2013). In comparison to other Archaean cratons of similar age, such as those of Yilgarn in Australia and Dharwar in India, the Tanzania craton remains underexplored (*e.g.*, Jayananda et al., 2018, 2020; Mole et al., 2019; Osei et al., 2021; Masurel et al., 2022).

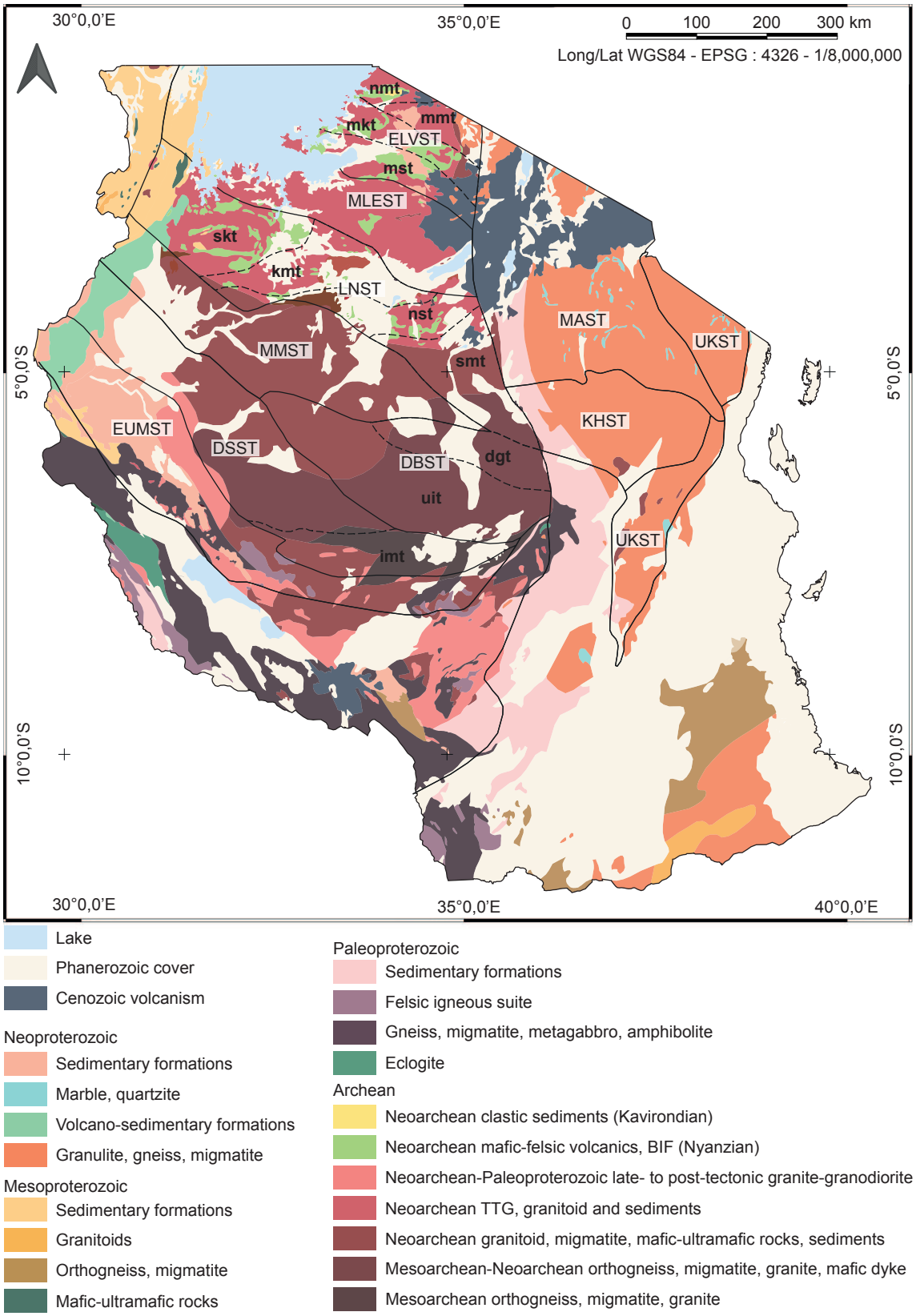

Figure 1-3. Geological map of Tanzania (after BRGM, 2004). Superterrane and terrane boundaries defined by Kabete et al. (2012a) are shown as solid and dashed lines, respectively. Superterranes: ELVST = East Lake Victoria, MLEST = Mwanza Lake Eyasi, LNST = Lake Nyanza, MMST = Moyowosi-Manyoni, DBST = Dodoman Basement, DSST = Dodoma Schist, EUMST = Eastern Ubendian-Mtera, MAST = Mbulu-Masai, UKST = Usagara–Usambara, KHST = Kilindi–Handeni. Terranes: nmt = North Mara, mmt = Mara-Mobrama, mkt = Musoma-Kilimafedha, mst = Maswa-Serengeti, skt = Sukumaland, kmt = Kahama-Mwadui, nst = Nzega-Sekenke, smt = Singida-Mayamaya, dgt = Dodoma Gneiss, uit = Undewa-Ilangali, imt = Isanga-Mtera.

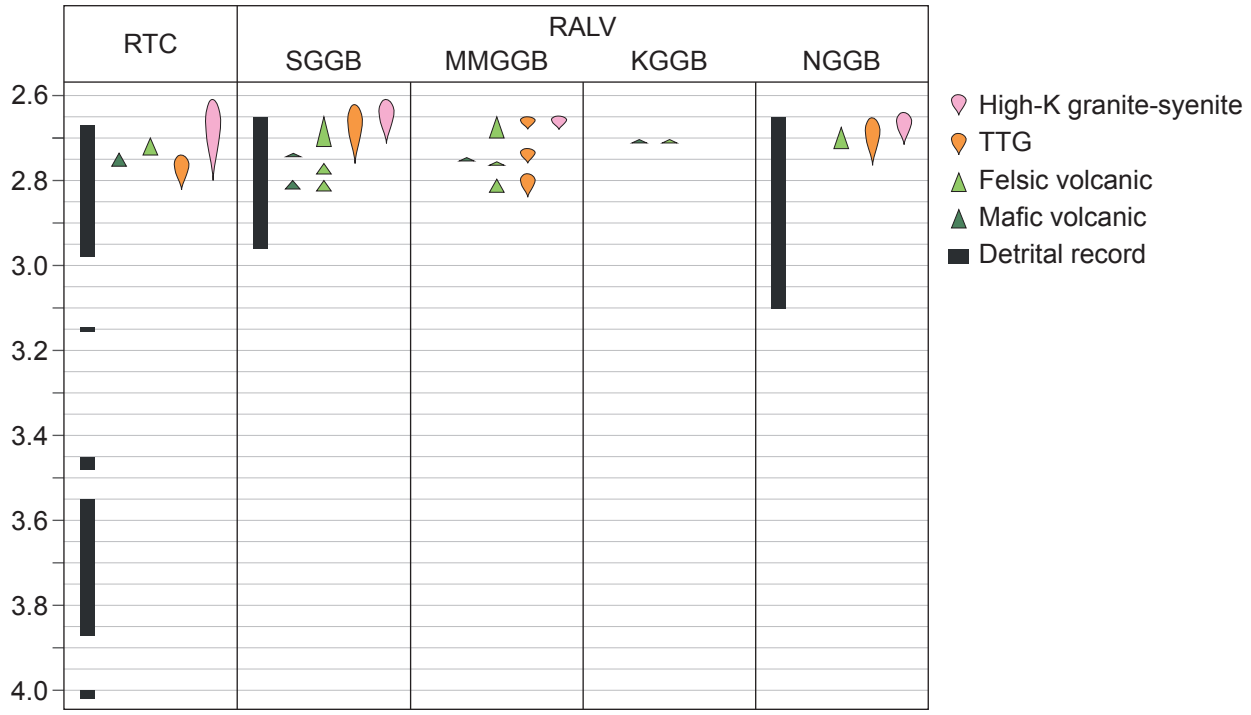

Figure 1-4. Detrital, volcanic and plutonic record in the CTR and in the granite-greenstone belts of the LVG. SGGB = Sukumaland granite-greenstone belt ; MMGGB = Musoma-Mara granite-greenstone belt ; KGGB = Kilimafedha granite-greenstone belt ; NGGB = Nzega granite-greenstone belt.

Some greenstone belts of the LVG have been extensively studied due to their significant potential for gold exploration. In particular, the Sukumaland and Musoma-Mara belts have received more detailed investigation due to the presence of large, world-class deposits (*e.g.*, Geita and North Mara gold deposits, Fig. 1-2a; see section 4; Henkel et al., 2019). These belts are thought to have developed in a variety of tectonic environments, such as back-arc basins, continental arcs, and even oceanic plateaus (Fig. 1-8; *e.g.*, Cloutier et al., 2005; Manya et al., 2007; Cook et al., 2016; Sanislav et al., 2018b).

1.2.1. Eo- to Paleoarchean

The oldest ages recorded in the Tanzania craton are detrital in origin and were exclusively dated in the CTR (Figs. 1-4, 1-5d, 1-6a; Kabete et al., 2012b; Thomas et al., 2016). Detrital zircon yield U-Pb ages between 4010 and 3450 Ma, while the deposition of the related sediments is dated between 3600 and 3230 Ma, and later between 2800 and 2720 Ma. The initial mantle extraction event is dated at 3900 Ma (Fig. 1-6a). The first magmatic event in the Tanzania craton therefore occurred between 4010 and 3600 Ma, and is interpreted as the earliest episode of crustal growth (Kabete et al., 2012b), leading to the formation of a (proto)-crust that was later entirely reworked and/or recycled through subsequent magmatic and erosional processes (Kabete et al., 2012b; Thomas et al., 2016; Sun et al., 2018).

The oldest Hf model ages are recorded in Meso- to Neoarchean magmatic rocks and range from 3600 to 3400 Ma (Thomas et al., 2016). They indicate a period of juvenile crustal growth that no magmatic are yet discovered or is preserved (Fig. 1-7d). Between 3600 and 3230 Ma, the CTR underwent weathering, erosion, and sedimentation of supracrustal materials (Fig. 1-4; Kabete et al., 2012b; Thomas et al., 2016).

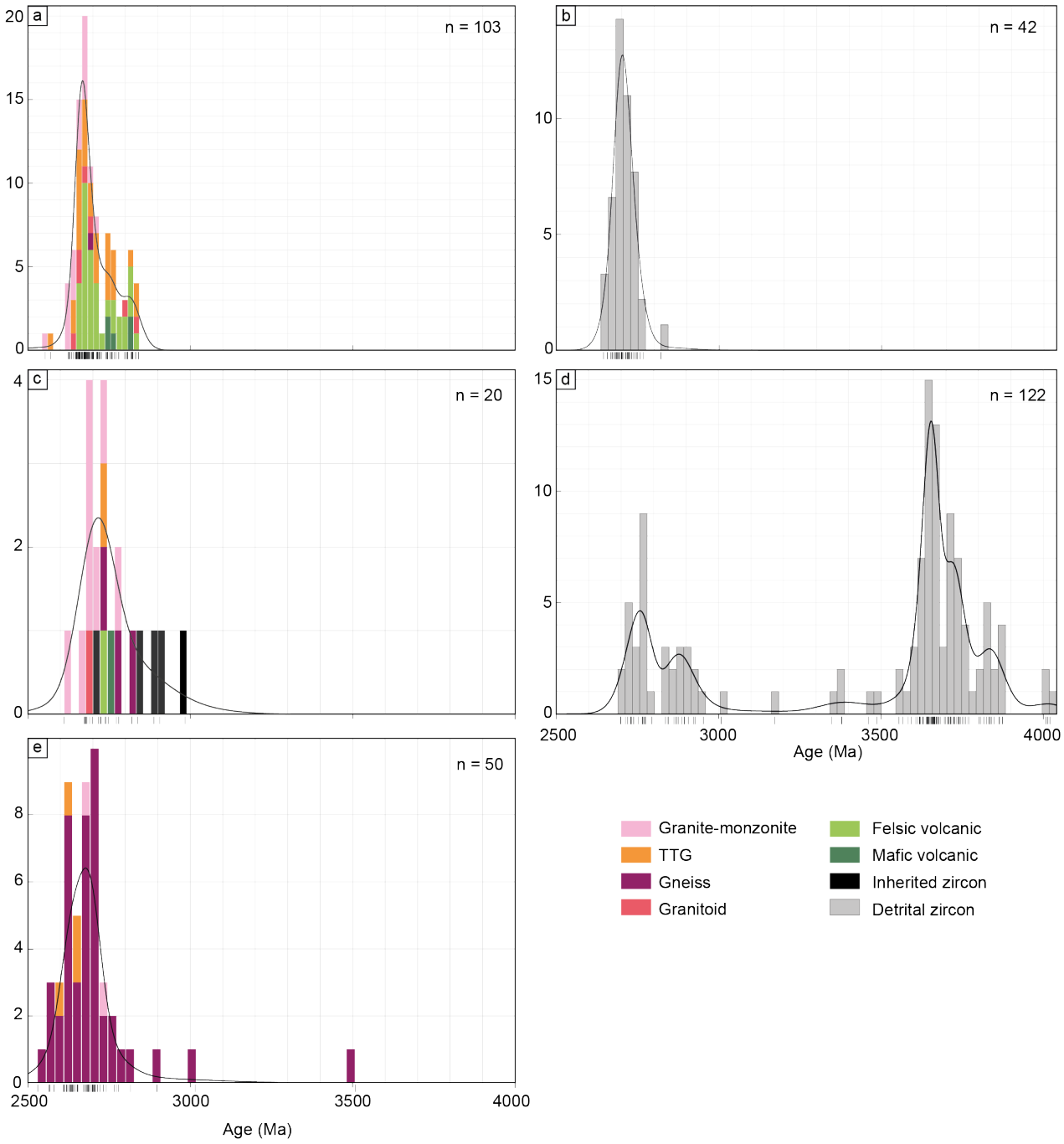

Figure 1-5. Histograms and Kernel density curves showing the age distribution of: **a.** magmatic ages in the LVG, **b.** detrital ages in the LVG, **c.** magmatic ages in the CTR, **d.** detrital ages in the CTR, and **e.** reworked Archaean magmatic rocks in the Proterozoic belts bordering the Tanzania craton. Data from Supplementary Material 1.6 in Chapter II (Maboko 1995; Maboko and Nakamura, 1996; Borg and Krogh, 1999; Muhongo et al. 2001; Johnson et al. 2003; Manya and Maboko, 2003, 2008a, 2008b; Reddy et al. 2004; Cloutier et al., 2005; Sommer et al. 2005; Tenczer et al. 2005, 2012; Cutten et al. 2006; Maboko et al., 2006; Vogt et al. 2006;Chamberlain and Tosdal, 2007; Manya et al., 2007a, 2007b; Manya, 2008, 2011, 2016a; Mtoro et al., 2009; Messo et al., 2012; Kabete et al., 2012b; Sanislav et al., 2014, 2018b; Thomas et al., 2016; Kwelwa et al., 2018; Wu et al., 2023), and Proterozoic ages from Sanislav et al. (2014a).

It is worth noting that Eoarchean detrital ages were obtained from two samples yielded predominantly discordant ages (Kabete et al., 2012b). The temporal range of crustal growth inferred from these data is likely incorrect due to significant Pb loss, as evidenced by Hf isotopic analysis on zircon from the schist (Thomas et al., 2016). Therefore, the first magmatic event on the craton could be restricted to the period between 3900 and 3600 Ma (Fig. 1-6a; Thomas et al., 2016).

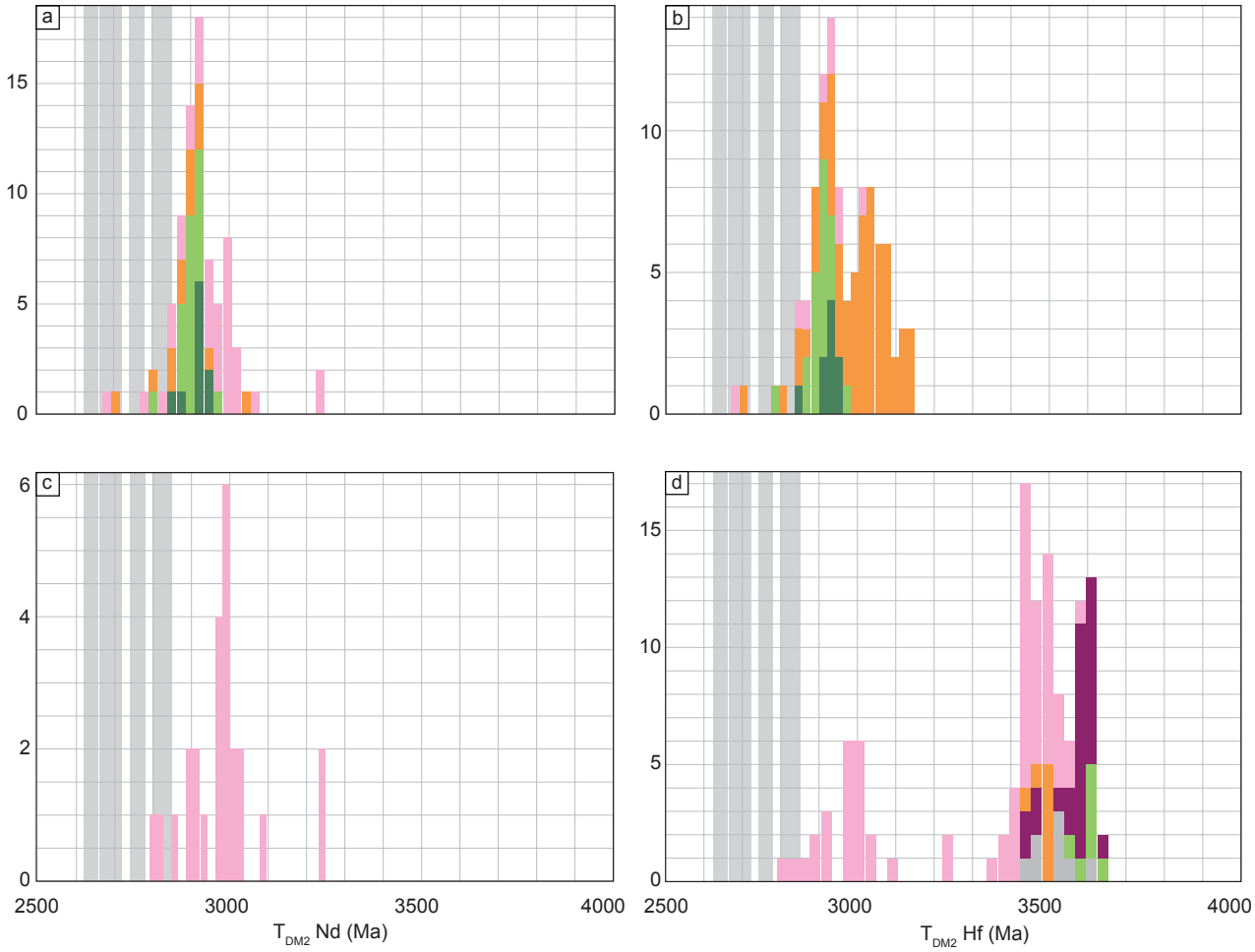

Figure 1-6. a. zircon εHf vs age diagram for magmatic and sedimentary samples of the Tanzania craton. **b.** zircon εNd vs age diagram for magmatic and sedimentary samples of the Tanzania craton (data from Supplementary Material 1.6 in Chapter II **;** Borg and Krogh, 1999; Maboko and Nakamura, 1996; Manya and Maboko, 2003, 2008a, 2008b; Cloutier et al., 2005; Maboko et al., 2006; Manya et al., 2007a, 2007b; Mtoro et al., 2009; Manya, 2011, 2016a; Messo et al., 2012; Sanislav et al., 2014, 2018b; Kwelwa et al., 2018; Thomas et al., 2016; Wu et al., 2023).

1.2.2. Meso- to Neoarchean

While the detrital record provides evidence of crustal differentiation in the Tanzania craton as early as the Eoarchean, the analyzed magmatic rocks in the region yield late Mesoarchean to late Neoarchean ages, between 2820 and 2550 Ma (Figs. 1-4, 1-5a, c; Maboko and Nakamura, 1996; Manya and Maboko, 2003; Cloutier et al., 2005; Maboko et al., 2006; Manya et al., 2007a, 2007b; Manya and Maboko, 2008a, 2008b; Mtoro et al., 2009; Manya, 2011; Kabete et al., 2012b; Messo et al., 2012; Sanislav et al., 2014a; Cook et al., 2016; Thomas et al., 2016; Kwelwa et al., 2018; Wu et al., 2023). The juvenile granite-greenstone belts, predominantly distributed in the LVG, formed during this period (Figs. 1-2a, 1-3). Rare sporadic magmatism in the CTR suggests episodes of crustal growth during this period as well (Fig. 1-5c; Manya and Maboko, 2003; Manya et al., 2006; Kabete et al., 2012a, 2012b; Thomas et al., 2016).

Central Tanzania Region (CTR)

In the Tanzania craton, the oldest magmatic rocks and oldest Nd model ages from Neoarchean granitoids are dated in the Mesoarchean period (3230 to 2900 Ma) (Figs. 1-4, 1-5c, 1-7c; Maboko and Nakamura, 1996; Manya, 2011; Kabete et al., 2012b; Sun et al., 2018). These ages are interpreted as evidence of the initiation of juvenile crust formation during the Mesoarchean.

The rock record in the CTR was largely emplaced within a range of 200 Ma, from the late Mesoarchean to the late Neoarchean (Figs. 1-4, 1-5c; Maboko and Nakamura, 1996; Manya, 2011; Kabete et al., 2012b; Thomas et al., 2016; Sun et al., 2018). An initial phase of crustal growth and differentiation occurred between 2900 and 2750 Ma, characterized by predominantly juvenile magmatism. Small volumes of juvenile mafic lavas were extruded around 2750 Ma (Thomas et al., 2016). Additionally, a series of tonalitic to granodioritic orthogneisses were emplaced between 2820 and 2750 Ma, derived from the reworking and/or recycling of Mesoarchean juvenile crust formed between 3230 and 2900 Ma (Thomas et al., 2016). A brief period of 20 Ma followed, during which supracrustal sedimentary and volcanic rocks were deposited, including explosive volcanism dated to 2725 ± 36 Ma (Thomas et al., 2016). Finally, significant crustal reworking and/or recycling characterized the last phase of crustal growth in the CTR, occurring between 2730 and 2610 Ma and dominated by granite and syenite magmatism (Manya, 2011; Kabete et al., 2012b; Thomas et al., 2016). Model ages and inherited zircons from plutons indicate reworking of Mesoarchean crust formed between 3000 and 2800 Ma (Fig. 1-5c; Sun et al., 2018).

Lake Victoria Goldfields(LVG)

Peaks of juvenile crustal growth and differentiation in the LVG are dated between 2850 and 2600 Ma, similar to crustal growth events in other major Neoarchean cratons such as the Yilgarn, Kaapvaal, and Superior (Figs. 1-4, 1-5a; Condie, 2000; Rino et al., 2004; Laurent et al., 2019; Witt et al., 2020; Mole et al., 2021). The northern half of the Tanzania craton underwent four episodes of magmatism, as inferred from petrographic, geochronological and isotopic studies on intrusives and volcanosediments from the Sukumaland, Nzega, and Musoma-Mara granite-greenstone belts, with a major peak recorded at 2700 Ma (Fig. 1-5a; Sanislav et al., 2014a; Kwelwa et al., 2018; Sanislav et al., 2018b; Sun et al., 2018).

The oldest magmatic activity in the LVG is characterized by widespread juvenile tholeiitic mafic to felsic volcanism between 2850 and 2800 Ma, including basaltic lava flows accompanied by the intrusion of rare granodiorites and tonalites in the MMGGB (Figs. 1-4, 1-5a, 1-6b; Borg and Krogh, 1999; Manya and Maboko, 2003; Manya, 2004; Cloutier et al., 2005; Chamberlain and Tosdal, 2007; Cook et al., 2016; Kwelwa et al., 2018). A second event of synchronous volcanism and plutonism occurred between 2780 and 2740 Ma, characterized by episodic TTG-diorites intrusion and felsic volcanism, derived from the partial melting of the mafic basement (Figs. 1-4, 1-5a, 1-6a; Borg and Krogh, 1999; Manya and Maboko, 2003; Chamberlain and Tosdal, 2007; Mtoro et al., 2009; Sanislav et al., 2014a, 2018b). A third growth phase between 2720 and 2660 Ma is evidenced by the accumulation of volcanic and sedimentary sequences alongside the intrusion of felsic plutons, including TTG-diorites, granites and monzonites (Borg and Krogh, 1999; Chamberlain and Tosdal, 2007; Manya et al., 2007a; Messo et al., 2012; Sanislav et al., 2014a, 2018b; Manya, 2016a; Kwelwa et al., 2018; Wu et al., 2023). The period between 2660 and 2620 Ma marks the cessation of volcanism and TTG-diorite magmatism, transitioning to the emplacement of high-K granites and monzonites (Borg and Krogh, 1999; Maboko et al., 2006; Chamberlain and Tosdal, 2007; Manya et al., 2007b; Sanislav et al., 2014a, 2018b; Kwelwa et al., 2018).

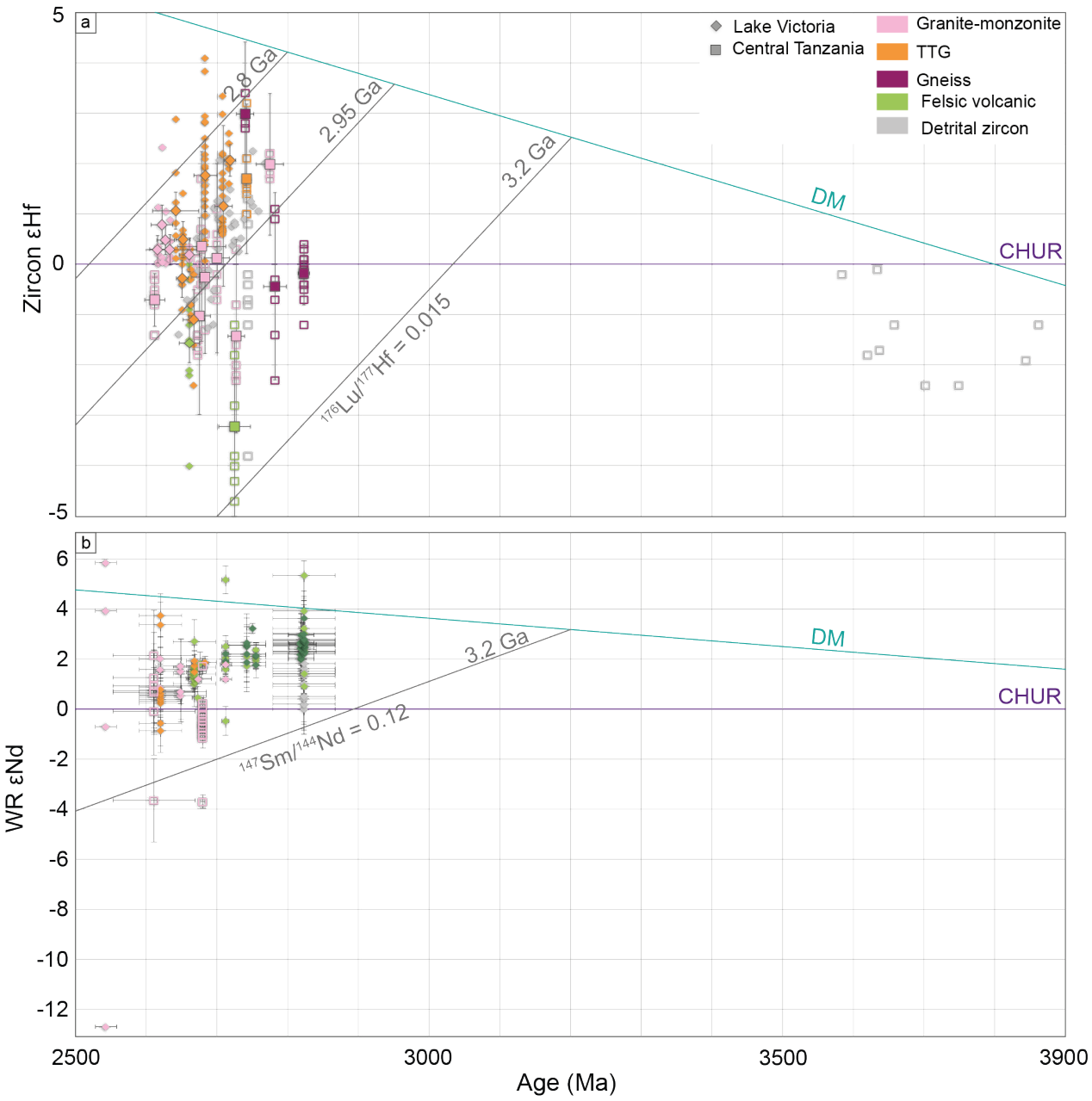

Figure 1-7. Probability density diagrams showing the distribution of Nd depleted mantle age in **a.** and **c.** and two-stage Hf model age in **b.** and **d**, from magmatic and detrital samples of the LVG (**a.** and **b.**) and in the CTR (**c.** and **d.**) (data from Supplementary Material 1.6 in Chapter II **;** Borg and Krogh, 1999; Maboko and Nakamura, 1996; Manya and Maboko, 2003, 2008a, 2008b; Cloutier et al., 2005; Maboko et al., 2006; Manya et al., 2007a, 2007b; Mtoro et al., 2009; Manya, 2011, 2016a; Messo et al., 2012; Sanislav et al., 2014, 2018b; Kwelwa et al., 2018; Thomas et al., 2016; Wu et al., 2023). Grey areas highlight crustal growth periods in the LVG as defined by Sanislav et al. (2014) et Kwelwa et al. (2018). Colors as in Fig. 1-6.

The majority of Neoarchean magmatic rocks in the LVG exhibit Nd and Hf isotopic signatures close to chondritic values, indicative of mantle extraction between 2950 and 2800 Ma followed by progressive differentiation of the juvenile rocks (Fig. 1-7a-b). However, rare magmatic rocks from the MMGGB and the Sukumaland granite-greenstone belt (SGGB) display isotopic signatures indicative of older crustal material reworking, similarly to the isotopic signature of magmatism in the CTR (Fig. 1-6a; Manya, 2006; Kwelwa et al., 2018). This reworking and/or recycling of older material is interpreted in the SGGB as resulting from the assimilation of minor amounts of sediments (Kwelwa et al., 2018), while crustal growth in the MMGGB is attributed to an active continental margin setting (Manya et al., 2007a, 2007b).

Two younger ages were obtained in the SGGB and the Migori greenstone belt, around ca. 2550 Ma. These ages may reflect a late post-tectonic thermal event that locally affected the Tanzania craton or represent unreliable analyses (Fig. 1-5a; Pinna et al., 2000; Chamberlain and Tosdal, 2007; Sanislav et al., 2014a).

Archean ages from reworked sequences within the Proterozoic mobile belts bordering the Tanzania craton to the east and south exhibit a distribution similar to most ages recorded in the craton, ranging between 2800 and 2600 Ma, with a peak around 2700 Ma. It suggests that the basement of these mobile belts was derived from the reworking of the Tanzania craton (Fig. 1-5e; Maboko, 1995; Muhongo et al., 2001; Johnson et al., 2003; Reddy et al., 2003, 2004; Collins et al., 2004; Sommer et al., 2005; Cutten et al., 2006; Tenczer et al., 2006, 2012; Vogt et al., 2006; Kabete et al., 2012b; Thomas et al., 2016).

The majority of the crust in the Tanzania craton formed between 2850 and 2600 Ma, beginning with juvenile, mafic-dominated magmatism that progressively differentiated over a period of 160 million years. The peak of crustal growth occurred around 2700 Ma, consistent with the timing observed in other Neoarchean cratons worldwide (Figs. 1-4, 1-5; e.g., Condie, 2000; Rino et al., 2004). Both the northern and southern regions of the Tanzania craton share a similar magmatic history, but while the CTR lies on a reworked and/or recycled Meso- to Eoarchean basement, the vast majority of the LVG formed from the progressive differentiation of a late Mesoarchean mantle extraction.

1.3. Tectonic models for crustal growth and differentiation in the LVG

The Neoarchean tectonic context of the LVG is generally interpreted as a sequence of geological processes comparable to modern plate tectonic scenarios (*e.g.*, Manya and Maboko, 2003; Manya, 2004; Cloutier et al., 2005; Manya et al., 2007; Manya and Maboko, 2008; Kabete et al., 2012a). However, the tectonic history of most greenstone belts within the LVG remains only partially understood. Geochemical studies of volcanic rocks in the Nzega, Kilimafedha, and Iramba-Sekenke belts have led to tectonic models suggesting arc or back-arc environments (Manya and Maboko, 2008a; Messo et al., 2012; Manya, 2016).

The evolution of the **Musoma-Mara granite-greenstone belt** (MMGGB) is attributed to a continental arc setting (Manya, 2006; Manya, 2012). Mantle plume activity is thought to have produced Mg-rich basalts dated at ca. 2700 Ma, exhibiting geochemical signatures interpreted as the result of komatiitic magma contamination by felsic crust (Manya, 2012). However, no komatiites have been identified in the Tanzania craton, possibly due to their recycling, limited exposure, or incomplete mapping. The subduction of a mid-ocean ridge between 2676 and 2670 Ma has been proposed by some authors as a mechanism that generated elevated thermal activity, promoting the formation of Mg-rich rocks and adakites (Manya et al., 2007a, 2007b; Manya, 2012). TTG rocks formed through partial melting of garnet amphibolites in an Andean-

type continental margin between 2850 and 2650 Ma. These were later recycled into potassic granites between 2670 and 2650 Ma through partial melting within the crust (Chamberlain and Tosdal, 2007; Manya et al., 2007a; Mshiu et al., 2009). Volcanosedimentary sequences were likely deposited in a back-arc basin environment between 2830 and 2650 Ma (Chamberlain and Tosdal, 2007; Mtoro et al., 2009). Evidence of older crustal material reworking and/or recycling includes: (i) Mg-rich andesites with geochemical signatures indicating contamination of parental magmas by ancient felsic crust, and (ii) Nd isotopic signatures in intrusive rocks pointing to limited mixing with crust older than the magmatic records of the MMGGB (Manya, 2006; Manya et al., 2007a, 2007b; Manya, 2012).

The **Sukumaland granite-greenstone belt** (SGGB) is the most studied belt within the Tanzania craton, with significant research focused on both its metallogenic potential and tectonic evolution. This includes a wide range of petrological, structural, metallogenic, geochemical, geochronological and isotopic studies (*e.g.*, Borg 1992; Chamberlain, 2003; Manya, 2005; Cloutier et al., 2005; Maboko et al., 2006; Sanislav et al., 2014, 2016, 2017, 2018b; Cook et al., 2016; Van Ryt et al., 2017; Kwelwa et al., 2018; Wu et al., 2023). These studies have led to hypotheses about crustal growth, which can be grouped into two tectonic models: a volcanic arc setting and modification through the subduction of an oceanic plateau.

The tectonic model of crustal growth in a volcanic arc and back-arc basin setting was first established by Manya and Maboko (2003), and later developed in Manya (2004), Cloutier et al. (2005), Maboko et al. (2006), Manya and Maboko (2008). Geochemical signatures of basalts, andesites, and rhyolites from the LVG were compared to those of Phanerozoic volcanic arc and back-arc basin units, and interpreted as resulting from the interaction between a depleted mantle and the partial melting of a subducted oceanic plate in a back-arc basin environment (Manya, 2004; Manya and Maboko, 2008). The geochemical and Nd isotopic signatures of granitoids reflect contamination of the source of certain intrusions by oceanic crustal sediments that underwent partial melting in the amphibolite and garnet stability fields. This process is also interpreted as a result of subduction, which would have led to the burial of these sediments (Cloutier et al., 2005; Maboko et al., 2006).

A second tectonic model for crustal growth in the SGGB was proposed by Sanislav et al. (2018b), involving the modification of an oceanic plateau through subduction (Fig. 1-8). A compilation of geochemical, U-Pb geochronological, and Nd and Hf isotopic data from magmatic and sedimentary samples shows a process where juvenile mafic crust, formed around 2850 Ma and 2800 Ma, gradually evolved through successive partial melting events into more evolved continental crust around 2600 Ma. The oldest magmatism in the SGGB, predating 2800 Ma, consists of widespread tholeiitic mafic volcanism in an oceanic plateau environment. A thick root of oceanic crust initially developed (Fig. 1-8a). The initiation of subduction above the oceanic plateau, prior to 2700 Ma, and the retreat of the subducting plate led to extension within the overlying plateau (Fig. 1-8b). Magmas generated by dehydration of the subducting plate accumulated at the base of the plateau due to its thickness. The partial melting of the eclogitized mafic root subsequently generated TTGs and diorites, synchronous with the deposition of volcaniclastics and ferruginous clastic sediments. Flattening of the subducting plate between 2700 and 2660 Ma led to compression in the plateau and a transition from TTG magmatism to more evolved, high-K monzonites and granites (Fig. 1-8c). This period of crustal shortening likely coincides with the assembly of the central and northern parts of the Tanzania craton. Finally, the thickened and eclogitized oceanic plateau underwent delamination, and its base sank

into the mantle after 2660 Ma (Fig. 1-8d). The upwelling of hot mantle material caused the heating and partial melting of the TTGs and associated sediments, resulting in the formation of the high-K granites. Magmatism from a metasomatized mantle also intruded the plateau in the form of rare lamprophyre dykes.

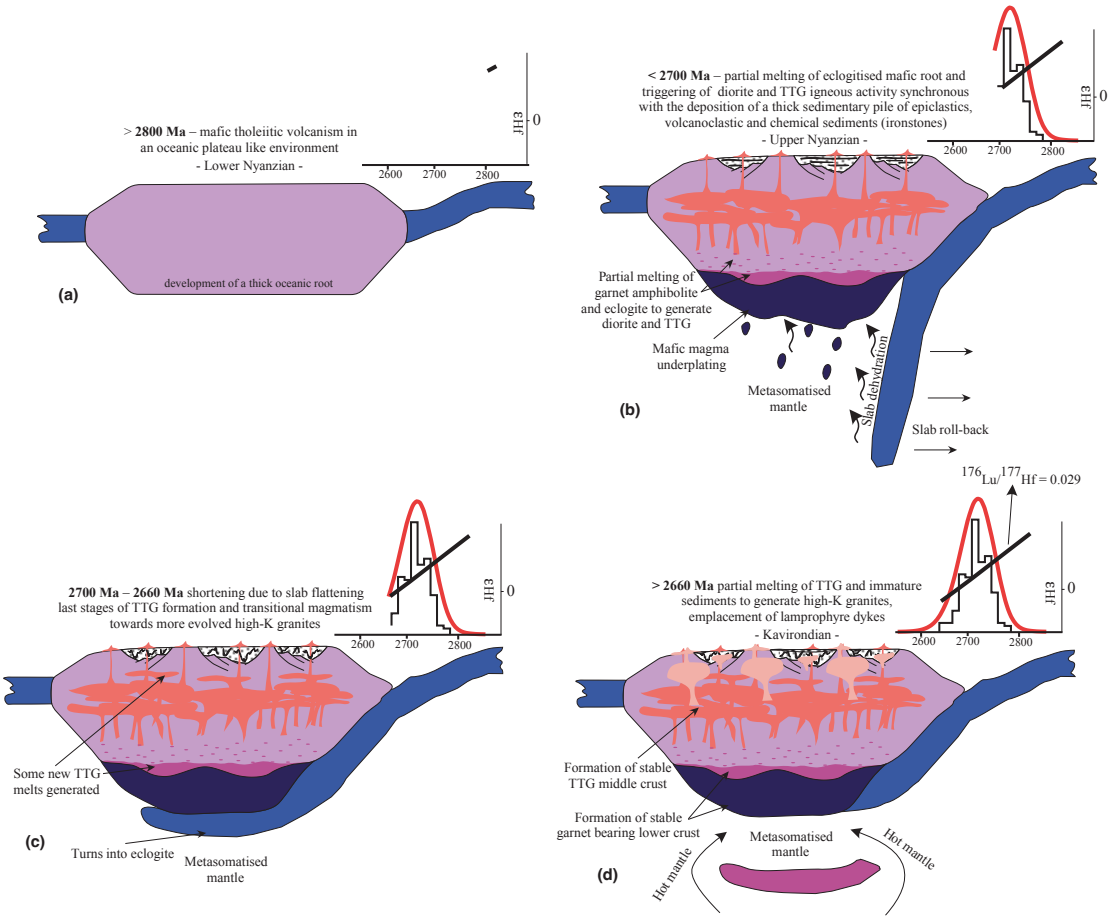

Figure 1-8. Tectonic model of crustal growth and differentiation in the Lake Victoria Goldfield, based on geochemical, U-Pb geochronological, and Nd and Hf isotopic data from magmatic and sedimentary samples from the SGGB (Sanislav et al., 2018b). Probability density diagrams show the distribution of detrital zircon and the evolution trend of the εHf during each tectono-magmatic event.

Overall, the geodynamic context of the LVG is complex, involving fractional crystallization of juvenile magma in both oceanic plateau and island arc or active continental margin settings. The recycling of both juvenile and ancient crust is gradual, linked to partial melting processes of mafic roots in plateau environments, as well as subduction or intraplate processes. Considering the ages of magmatism, most of the Tanzania craton appears to have formed during syn- or post-collisional tectonic events, following the extensive recycling of mafic rocks.

2. Metallogeny of the Tanzania craton

Three gold fields have been identified in Tanzania, two of which are located in the southwest and west of the Tanzania craton within Proterozoic mobile belts that record the reworking of the Archean craton (Van Straaten, 1984). The third, the Lake Victoria Goldfields (LVG), is the only one situated entirely within the craton itself. Few small-scale gold prospects were discovered in the Central Tanzania Region (CTR), within mafic-amphibolite belts and granitoid gneisses (Kabete et al., 2012a). Geochronological studies of a mafic amphibolite-hosted gold deposit in this region have constrained the timing of mineralization to between 2700 and 2660 Ma (Kabete et al., 2012a).

The LVG hosts numerous gold deposits with endowments exceeding 50 tons (Kabete et al., 2012a). Yet, many of these deposits lie within terranes whose tectonic evolution remains poorly understood due to a lack of detailed geological investigations and robust geochronological data, and lack of accessibility of the data (*e.g.*, Manya et al., 2006; Yuan et al., 2019). For instance, the timing of mineralization in some deposits was constrained by Chamberlain and Tosdal (2007) in an unpublished report, which is referenced only rarely in the literature (*e.g.*, Sanislav et al., 2014). Here is discussed the metallogenic setting of the best constrained gold deposits, located in Figure 9. The relationship between ore bodies and large-scale structures is not visible due to a lack of regional structural mapping.

Gold deposits in the LVG are predominantly located in the deformed and granitoid-intruded volcanosedimentary sequences of the greenstone belts, consistent with the distribution of most gold deposits in Archean cratons (*e.g.*, Yilgarn craton, Tripp et al., 2020; Canadian Shield, Poulsen et al., 2000). However, no mineralization has been identified in the syn-tectonic molasse basins of the Kavirondian Supergroup, unlike goldfields found in similar sediments in Archean cratons (*e.g.*, Timiskaming orogenic gold deposits in the Abitibi region; Bleeker, 2015; Dubé et al., 2020). Among the six greenstone belts of the LVG, gold endowment varies significantly. The Sukumaland (SGGB) and Musoma-Mara (MMGGB) belts are particularly notable for their exceptionally large deposits and numerous prospects. In the SGGB, the Geita gold camp boasts an estimated resource of 6.5 Moz Au, with over 8 Moz Au already extracted (Dirks et al., 2020), Bulyanhulu mine has an estimated resource of 6.2 Moz Au (Barrick, 2024), and the Nyanzaga deposit an estimated resource of 2.8 Moz Au (Perseus Mining, 2024). Similarly, the MMGGB hosts the North Mara mine, which has an estimated resource of 5.1 Moz Au (Barrick, 2024) or Buhemba deposit, with an estimated resource of 550 koz (Buhemba Gold Company Limited, 2020). In contrast, the Iramba-Sekenke and Nzega belts contain fewer but still significant gold deposits and prospects. The Sekenke mine produced 40 koz Au at an average grade of 34.6 g/t between 1909 and 1915 (Henckel et al., 2016). In the Nzega belt, the Buzwagi mine extracted approximately 900 koz by 2016 (Henckel et al., 2016), while the Golden Pride mine had an estimated total extraction of 2.2 Moz Au before its closure in 2014 (Henckel et al., 2016). Finally, no gold deposits have been identified in the Kilimafedha and Shyninga-Malita belts (Henckel et al., 2016).

Gold deposits within the LVG are hosted in various rock types and structures (Henckel et al., 2016 and references therein). Most ore bodies are observed in the Upper Nyanzian Supergroup, in alternating mafic to felsic volcaniclastics, BIF, cherts and clastic sediments (mudstones, sandstones) (*e.g.*, Geita, Bulyanhulu, Nyanzaga, Tulawaka, Golden Pride, Buhemba deposits; Magayane et al., 1998; Sanislav et al., 2015, 2016; Henckel et al., 2016; Brigden et al., 2017; Kwelwa et al., 2018). These deposits are generally classified as orogenic gold deposits (*e.g.*, Chamberlain, 2003; Henckel et al., 2016), but may also present geochemical and structural features closer to epithermal deposit types (Henckel et al., 2016; Dirks et al., 2020). More rarely, the mineralization is hosted in the Lower Nyanzian Supergroup, in mafic-ultramafic rocks (*e.g.*, Buckreef,

Busolwa deposits, IAMGOLD, 2009), or in granitoidic intrusive bodies in close proximity to the greenstone belts, dated between 2820 and 2680 Ma (*e.g.*, Nyabirama orebody in the North Mara mine, Buzwagi mine; Chamberlain and Tosdal, 2007; Henckel et al., 2016). In the LVG, gold mineralization formed late in the history of deformation, and, when dated, is interpreted to formed around 2680 Ma (Golden Pride and Buzwagi deposits, Vos et al., 2009; Manya, 2016a) or around 2640-2620 Ma (Geita, Bulyanhulu deposits, Chamberlain and Tosdal, 2007; Sanislav et al., 2018a). These two peak of mineralization correspond to a major period of Archean orogenic gold deposits formation in greenstone belt settings worldwide (*e.g.*, Yilgarn craton or Superior Province, Frimmel, 2018). Ore bodies are constrained in large-scale deformation structures, either shear zones or strike-slip faults, in both compressional and extensional settings (Chamberlain, 2003; Smith and Anderson, 2003; Vos et al., 2009; Sanislav et al., 2015, 2016; Henckel et al., 2016; Brigden et al., 2017; Manya, 2017; Yuan et al., 2019). Mineralization is primarily expressed in quartz-carbonate veins, a hallmark of orogenic gold deposits (Manya, 2017; Vos et al., 2009; Henckel et al., 2016; Brigden et al., 2017; Van Ryt et al., 2017; Yuan et al., 2019). Some deposits may be linked to volcanogenic massive sulfides or intrusions, although the genetic relationship to mineralization remains unclear (*e.g.*, Bulyanhulu, Golden Pride and Nyanzaga deposits; Chamberlain, 2003; Vos et al., 2009; Brigden et al., 2017). Gold is associated with important alteration, dominated by K-feldspar, quartz, carbonate, sericite, sulfide and chlorite (*e.g.*, Chamberlain, 2003; Smith and Anderson, 2003; Henckel et al., 2016; Brigden et al., 2017; Manya, 2017; Van Ryt, 2019; Yuan et al., 2019). Amongst the most common sulfides are observed pyrite, pyrrhotite, arsenopyrite and chalcopyrite, but Te, Sb, Pb, Zn, Bi, Ag or Ni–Co phases are also frequent in most deposits (Chamberlain, 2003; Vos et al., 2009; Henckel et al., 2016; Brigden et al., 2017; Van Ryt, 2019; Yuan et al., 2019). Buzwagi gold deposit is the exception with no geochemical relationship between Au and Ag, As, Sb, Bi and Te (Manya, 2017). These characteristics are typical of lode-gold deposits as defined by Dubé and Gosselin (2007), with the exception of gold deposits hosted in intrusions.

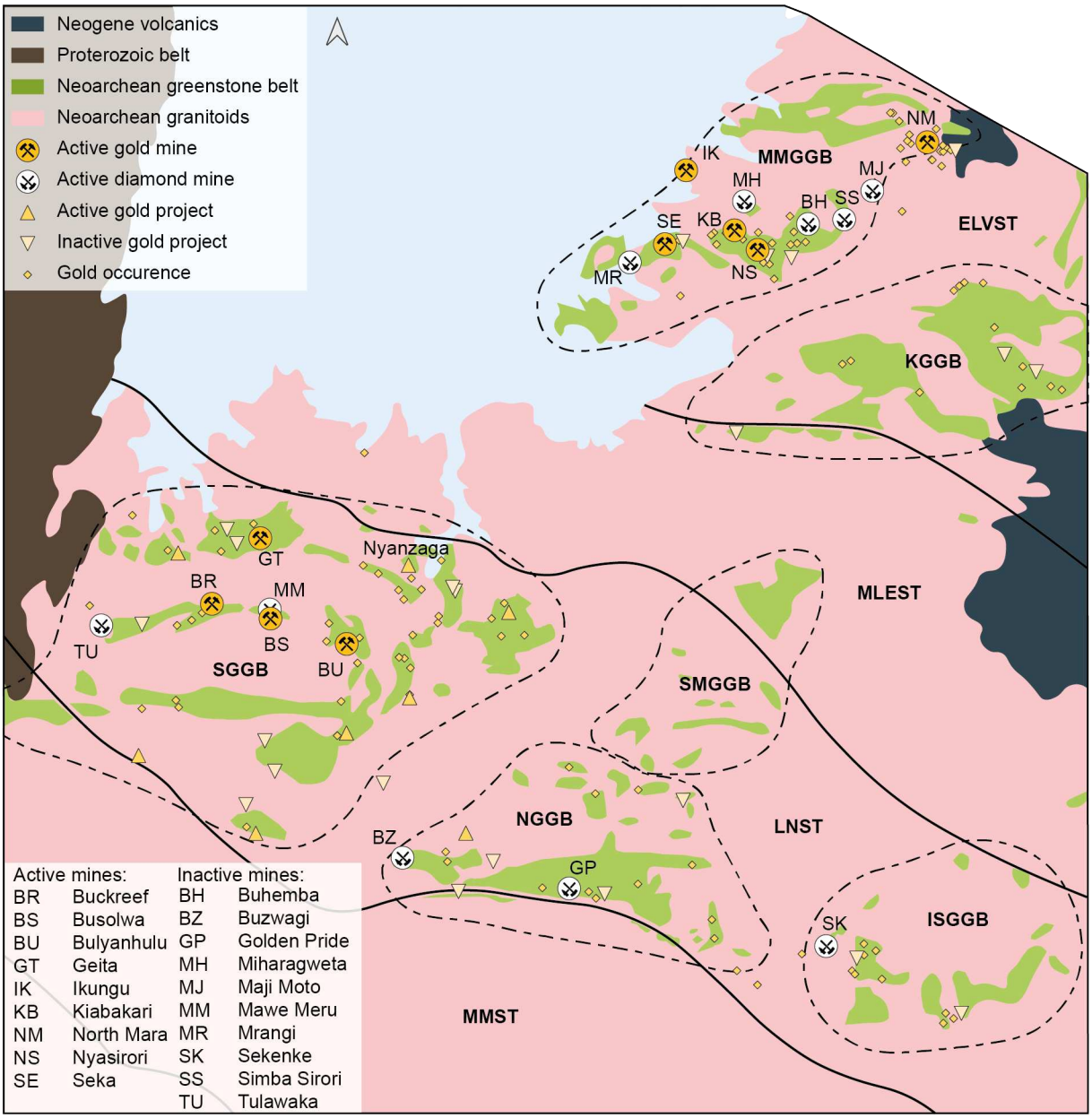

Figure 1-9. Geologic-metallogenic map of the Lake Victoria Goldfields(LVG), Tanzania craton (from Cook et al., 2016, Borg and Shackelton, 1997). Gold active and inactive mines are located in the different greenstone belts, as well as active and inactive projects, and occurrences (data from Henckel et al., 2016; Geological Survey of Tanzania, 2024). Subdivision by terrane is visible (Kabete et al., 2012a). ELVST = East Lake Victoria, MLEST = Mwanza Lake Eyasi, LNST = Lake Nyanza, MMST = Moyowosi-Manyoni. Black dotted lines highlight the six granite-greenstone belts of the LVG: ISGGB = Iramba-Sekenke, KGGB = Kilimafedha, MMGGB = Musoma-Mara, NGGB = Nzega, SGGB = Sukumaland, SMGGB = Shinyanga-Malita.

~

Chapter II

~

Neoarchean continental crustal growth and differentiation in the northern Sukumaland greenstone-granite belt: constraints from zircon U-Pb age and Hf-O isotopic composition

Article en préparation pour publication dans *Precambrian Research*

Célestine Berthier[a,b,c,*], Nicolas Thébaud[d], Aurélien Eglinger[b,e], Anne-Sylvie André-Mayer[b], Julien Feneyrol[a], Alain Chauvet[c], Christopher M. Fischer[d], Laure A.J. Martin[d], Rémi Bosc[a]

[a] Arethuse Geology SARL., 29 allées Saint Jean, Fuveau 13710, France

[b] GeoRessources, Université de Lorraine, CNRS, Nancy 54000, France

[c] Géosciences Montpellier, Université de Montpellier, CNRS, Montpellier 34095, France

[d] Centre for Exploration Targeting, School of Earth Sciences The University of Western Australia, WA 6009, Australia

[e] InnovExplo Inc, 560 3e Avenue, Val d'Or QC J3P 1S4, Canada

Abstract

The Meso- to Neoarchean period is considered by many researchers as a tipping point in the holistic tectonic regimes of the Earth, setting the premises of plate tectonics and still associated with intensive crustal accretion.In this study, we present new petrographic, geochemical, geochronological (U-Pb) and isotopic (O-Hf) analyses of magmatic and sedimentary rocks from the northern Sukumaland granite-greenstone belt (Tanzania craton), that we compiled with the existing literature (whole-rock geochemistry, U-Pb dating, Hf-Nd isotopy), with the aim to improve and discuss our knowledge about the geodynamic evolution of such a portion of the Archean crust.

Crustal growth in the region began around 2820 Ma, marked by the extrusion of mafic crust derived from a primitive mantle (high εNd) in a mantle-plume setting (2820–2800 Ma). Between 2800 and 2700 Ma, tonalite-trondhjemite-granodiorite rocks (TTGs) exhibited a progressive decrease in εHf values, following a crustal evolution trend, alongside mantle-like $\delta^{18}O$ values, high Sr/Y and Gd/Yb ratios, and low K_2O/Na_2O ratios. These geochemical and isotopic characteristics suggest increasing crustal reworking of mafic material under high-depth conditions, likely driven by dripping processes. The period from 2700 to 2660 Ma marks a significant shift in tectonic regimes, with evidence of high-depth melting (high Sr/Y and Gd/Yb ratios) and an increase in the $\delta^{18}O$ signatures of TTGs. Sanukitoid-like geochemical signatures also emerged during this time, alongside evidence of source mixing between juvenile crust and older, more evolved crustal components, indicated by low εHf values and high K_2O/Na_2O ratios. This period also witnessed the deposition of Neoarchean sediments in syn-tectonic molasse basins recording a Eo- to Neoarchean zircon population. Collectively, these data suggest crustal differentiation driven by subduction-like processes and the amalgamation of an exotic terrane during the 2700-2660 Ma period. After 2660 Ma, tectonic activity shifted towards potassic magmatism, derived from intraplate partial melting of the crust (low Sr/Y and Gd/Yb ratios) during a late- to post-collisional phase. Our findings contribute to ongoing debates about the timing of plate tectonic onset by proposing that subduction processes operated in the Tanzania craton after 2700 Ma.

1. Introduction

It is now generally accepted that modern plate tectonics did not operate during the early history of the Earth and its emergence was closely tied to the progressive cooling of the mantle (Labrosse and Jaupart, 2007; Herzberg et al., 2010; Cawood et al., 2018). In the hotter mantle conditions of early Earth, the oceanic crust was likely thicker and mechanically weaker (*i.e.*, more ductile), and the oceanic lithosphere was more buoyant compared to the Phanerozoic. These characteristics pose significant challenges for reconciling early Earth dynamics with modern plate tectonic and subduction models (Sleep and Windley, 1982; Rey et al., 2014). There remains considerable debate over when, where and how Earth's current tectonic regime was initiated as a consequence of mantle cooling (*e.g.*, Hawkesworth et al., 2016, 2024; Cawood et al., 2018; Bédard, 2020; Johnson, et al., 2019; Moreira et al., 2020; Palin & Santosh, 2021; Windley et al., 2021; Cawood et al., 2022). Some models suggest the onset of plate tectonic as early as Hadean (*e.g.*, Hopkins et al., 2008; Turner et al., 2014; Ernst, 2017; Maruyama et al., 2018), or as late as Neoproterozoic (*e.g.*, Stern, 2005; Hamilton, 2011). However, a growing number of studies point to major changes in the continental and oceanic crusts as markers of the initiation of mobile-lid tectonics and the precursor to Wilson cycle processes during the Mesoarchean, and more precisely around 3000 and 2900 Ma (*e.g.*, Condie and Kröner, 2008; Van Kranendonk, 2011; Shirey and Richardson, 2011; Laurent et al., 2018; Dhuime et al., 2015; Palin et al., 2020; Hawkesworth et al., 2024). A general consensus has emerged with identified widespread subduction-like processes at ca. 2700 Ma (Condie and Kröner, 2008; Van Kranendonk, 2011; Dhuime et al., 2012; Gerya, 2014; Cawood et al., 2018).

Importantly, the timing of these markers varies in space, resulting in coexisting geodynamic models, including or excluding subduction-like processes, in different cratons. For instance, based on petrographic, geochemical, geochronological and isotopic data, evidence of plate mobility are dated at 3350 Ma in the Dharwar (Jayananda et al., 2018), at 3120 Ma in the Pilbara (Smithies et al., 2005; Hawkesworth and Kemp, 2021), at 2990 Ma in the Kaapvaal (Schmitz et al., 2004), at 2700 Ma in the Superior and in the Yilgarn (Czanorta et al., 2010; Witt et al., 2020; Mole et al., 2021), or even at 2550 Ma in the North China cratons (Huang et al., 2018). Until the late Archean, plate tectonic and non-plate tectonic settings appear to have coexisted, as illustrated by plume-lid processes in the West Yilgarn Superterrane (as late as 2730-2620 Ma; Mole et al., 2019) alongside subduction-like tectonics in the Eastern Goldfields Superterrane of the East Yilgarn craton (Czarnota et al., 2010; Witt et al., 2020). Such spatial and temporal variations likely reflect the fragmented and incomplete rock archive in Precambrian times (Gerya et al., 2014) and emphasize the importance of distinguishing localized subduction-like processes from the global onset of plate tectonics (Cawood et al., 2018).

The period between 3800 and 2500 Ma therefore represents a transitional phase between stagnant lid and plate tectonics, characterized by the onset of sluggish to active lid processes (Cawood et al., 2018, 2022; Palin et al., 2020). Interestingly, transitional models during this period are diverse, but their common feature is the combination of lateral and vertical lithospheric movements in varying proportions. They are divided into squishy lid tectonics, defined as downwelling of lithospheric mantle and crust (drips, delamination, subcretion; Bédard et al., 2013; Johnson et al., 2014; Nebel et al., 2018), and mobile lid tectonics, such as subduction processes, which became increasingly prevalent after 3200 Ma (Martin and Moyen, 2002; Laurent et al., 2014; Martin et al., 2014; Cawood et al., 2022). The onset of modern-day plate tectonics is attributed to an increasingly rigid lithosphere, recorded at the craton and local scales by localization of deformation, shift from dome and basin to lateral tectonics, metamorphic record of convergent tectonics,

important crustal and supracrustal reworking, subduction- and subsequent cratonisation-like geochemical signature of igneous rocks, late dyke swarms (Hawkesworth et al., 2024 and references therein).

The combination of field work, petrological, structural, geochemical, geochronological, isotopic, geophysical and metallogenic studies are crucial in constraining the tectonic regimes of the early Earth (*e.g.*, Dhuime et al., 2012; Frimmel, 2018; Mole et al., 2019; Bauer et al., 2020; Hawkesworth et al., 2020; Gao et al., 2022; Rowe et al., 2022; Schreefel et al., 2024; Zhang et al., 2024). For instance, field work, structural and petrological studies provide constraints on tectono-metamorphic events and the evolution of orogenic flow modes (*e.g.*, Chardon et al., 2009). Major and trace element geochemical signatures of igneous rocks may inform on the nature of their source as well as the depth of melting (Jahn et al., 1981; Martin, 1986; Martin et al., 2005; Moyen and Laurent, 2018; Smithies et al., 2018; Schreefel et al., 2024). The combination of Hf/Nd and O isotope on U-Pb-constrained zircons characterizes juvenile vs recycled contributions in the source of the rock, and whether the melted source was altered by low- or high-temperature hydrothermal activity (*e.g.*, DePaolo, 1981; Patchett 1983; Valley et al., 1998, 2005; Hawkesworth and Kemp 2006; Kemp et al., 2006; Collins et al., 2011; Dhuime et al., 2011; Dhuime, 2012; Iizuka et al., 2017; Bauer et al., 2020; Smithies et al., 2021).

Particular attention has been devoted to tonalite-trondhjemite-granodiorite suite rocks (TTGs) and sanukitoids (*e.g.*, Moyen and Martin, 2012; Hastie et al., 2016; Moreira et al., 2018, 2020; Moyen and Laurent, 2018; Nebel et al., 2018). TTGs are formed through partial melting of hydrated, alkali-rich and/or oceanic plateau basalts and therefore can be correlated to various Archean tectonic models (*e.g.*, Moyen and Martin, 2012; Hastie et al., 2016; Moyen and Laurent, 2018). In contrast, sanukitoids derive from a mix between a crustal and a mantle peridotite source (Shirey and Hanson, 1984; Martin et al., 2009; Laurent et al., 2014). A transition from TTGs to sanukitoids therefore marks changes in the tectonic setting towards the introduction of hydrated mafic crust into the mantle (Laurent et al., 2014; Bédard, 2018; Cawood et al., 2018; Nebel et al., 2018; Moreira et al., 2020).

In the Tanzania craton, crustal growth scenarios have been discussed based on all the previously mentioned fields of geological studies. However, the Tanzania craton has not undergone the same attention as some other Archean cratons such as the Yilgarn, Pilbara, North China, Dharwar or the Superior (*e.g.*, Jayananda et al., 2018; Hawkesworth and Kemp, 2021; Mole et al., 2021; Diwu et al 2024; Schreefel et al., 2024), and the available geochemical and isotopic datasets remain incomplete and fragmented. The Sukumaland granite-greenstone belt (SGGB), located in the superterrane of the Lake Victoria Goldfields, is by far the most studied region in the Tanzania craton, mainly because of the world-class Geita gold deposit (Wu et al., 2023 and references therein). If a first tectonic model was constructed by Sanislav et al. (2018b), many uncertainties remain regarding the crustal growth and thickening in the SGGB. In this chapter, we propose to strengthen the petrological, geochemical, geochronological and isotopic knowledge of the SGGB by studying igneous and detrital rocks from the northeastern part of the belt. In particular, we present the first O isotope study of the Tanzania craton, as well as the largest U-Pb-Hf detrital record of the Lake Victoria Goldfields. Based on these analyses and a comprehensive compiled dataset, we constrain the temporal evolution of crustal growth and reworking in the northern SGGB and discuss their implications on geodynamic processes of the late Archean greenstone belt.

2. Geological and tectonic framework of the Tanzania craton

2.1. Geological setting of the Tanzania craton

The Tanzania craton constitutes one of the four Archean crustal blocks that form the Central African Shield, alongside the Congo craton, the Ugandan craton and the Bangweulu Block (Fig. 2-1a; Borg and Shackleton, 1997; Begg et al., 2009; Ganbat et al., 2020; Turnbull et al., 2021). The Tanzania craton is separated from these terranes by Proterozoic mobile belts (Borg and Shackleton, 1997; Begg et al., 2009; Ganbat et al., 2020). The craton extends from western Kenya to central Tanzania and south-eastern Uganda, and may spread under the Lake Victoria (Borg and Shackleton, 1997; Sanislav et al., 2014). The craton consists of two superterranes, the Lake Victoria Goldfields to the north and the Central Tanzania Region in the south (Fig. 2-1; Borg and Shackleton, 1997; Wade and Oates, 1938; Kabete et al., 2012b; Kwelwa et al., 2018).

The Central Tanzania Region (CTR) is considered the basement of the craton, with some of the oldest rocks recorded in the region, from early Paleo- to Neoarchean (Gabert, 1990; Manya, 2011; Sun et al., 2018). High-grade mafic and felsic gneissic granitoids form the vast majority of the region, consisting mainly of TTG, granite and syenite (Fig. 2-1b; Thomas et al., 2016). Scarce supracrustal rocks, generally metamorphosed at the amphibolite facies, rare occurrences of granulite and greenschist facies are also described (Quennel et al., 1956 ; Gabert, 1990; Kabete et al., 2012b). Kabete et al. (2012b) and Thomas et al. (2016) reported geochronological and isotopic studies on detrital zircon from supracrustal rocks of the CTR, with ages as old as 4013 ± 4 Ma, and ranging between 4010 to 3450 Ma (Fig. 2-1b). The magmatic record of the CTR extend between 3230 and 2600 Ma (Kabete et al., 2012b; Thomas et al., 2016).

The Lake Victoria Goldfields (LVG) is dominated by juvenile Neoarchean granitoids and supracrustal rocks forming regional-scale greenstone belts (Fig. 2-1b; Gabert, 1990; Borg and Shackleton, 1997; Manya, 2011; Kwelwa et al., 2018; Sun et al., 2018). The stratigraphy of the LVG is divided into the Nyanzian and Kavirondian Supergroups (Borg, 1992; Sanislav et al., 2015; Kwelwa et al., 2018). The Nyanzian Supergroup spans over 120 Ma of volcanic activity and sedimentation and is subdivided into a mafic volcanic-dominated Lower Group and an Upper Group dominated by turbiditic sequences interlayered with chert sediments, banded iron formations (BIF) and felsic volcanic and volcaniclastic intercalations (Quennell et al., 1956; Borg and Krogh, 1999; Manya and Maboko, 2003, 2008; Cook et al., 2016). The Nyanzian Supergroup underwent metamorphism, mostly up to the greenschist facies, reaching the amphibolite facies near granitic intrusions. The post-orogenic molassic basins of the Kavirondian Supergroup were deposited around 2640 Ma and unconformably overlie the Nyanzian Supergroup (Gabert, 1990; Borg, 1992; Sanislav et al., 2015, 2018b). The magmatic history of the LVG extends between 2850 and 2600 Ma, with a peak dated around 2700 Ma (Sanislav et al., 2014a ; Kwelwa et al., 2018 ; Sanislav et al., 2018b ; Sun et al., 2018).

Figure 2-1. a. Map of Africa with the location of the Archean litho-tectonic blocs and Proterozoic mobile belts (from Begg et al., 2009). **b.** Geological map of Tanzania (from BRGM, 2004). Superterranes and terranes limits as defined by Kabete et al. (2012a) are shown in continuous and dotted lines, respectively. The yellow dot locate the oldest detrital zircon ages from quartz schists. Superterranes : ELVST = East Lake Victoria, MLEST = Mwanza Lake Eyasi, LNST = Lake Nyanza, MMST = Moyowosi-Manyoni, DBST = Dodoman Basement, DSST = Dodoma Schist, EUMST = Eastern Ubendian-Mtera, MAST = Mbulu-Masai, UKST = Usagara–Usambara, KHST = Kilindi–Handeni. Terranes : nmt = North Mara, mmt = Mara-Mobrama, mkt = Musoma-Kilimafedha, mst = Maswa-Serengeti, skt = Sukumaland, kmt = Kahama-Mwadui, nst = Nzega-Sekenke, smt = Singida-Mayamaya, dgt = Dodoma Gneiss, uit = Undewa-Ilangali, imt = Isanga-Mtera.

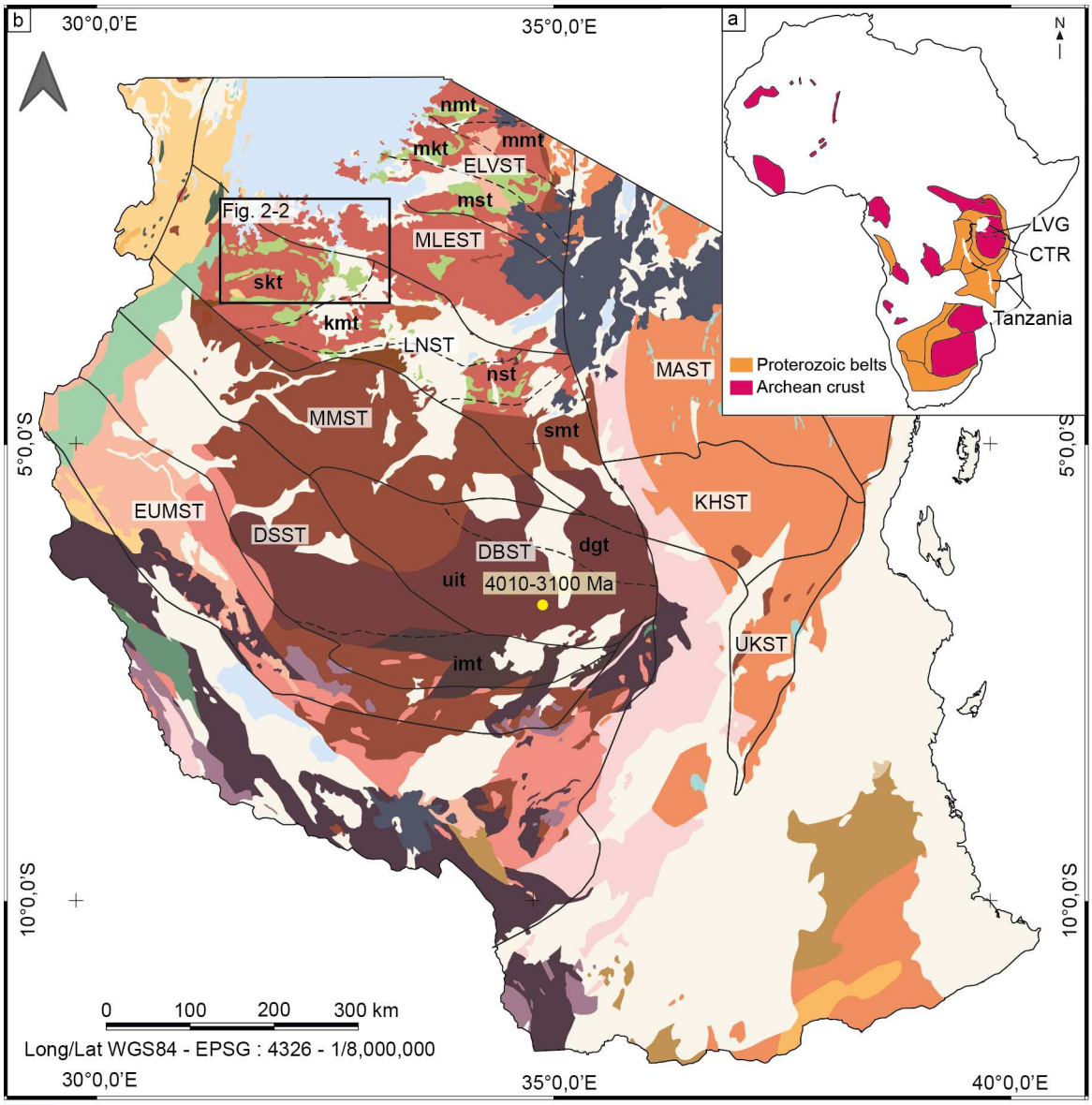

Lake
Phanerozoic cover
Cenozoic volcanism

Neoproterozoic
- Sedimentary formations
- Marble, quartzite
- Volcano-sedimentary formations
- Granulite, gneiss, migmatite

Mesoproterozoic
- Sedimentary formations
- Granitoids
- Orthogneiss, migmatite
- Mafic-ultramafic rocks

Paleoproterozoic
- Sedimentary formations
- Felsic igneous suite
- Gneiss, migmatite, metagabbro, amphibolite
- Eclogite

Archean
- Neoarchean clastic sediments (Kavirondian)
- Neoarchean mafic-felsic volcanics, BIF (Nyanzian)
- Neoarchean-Paleoproterozoic late- to post-tectonic granite-granodiorite
- Neoarchean TTG, granitoid and sediments
- Neoarchean granitoid, migmatite, mafic-ultramafic rocks, sediments
- Mesoarchean-Neoarchean orthogneiss, migmatite, granite, mafic dyke
- Mesoarchean orthogneiss, migmatite, granite

2.2. The Sukumaland granite-greenstone belt

The Sukumaland granite-greenstone belt (SGGB) is the largest one of the Tanzania craton and is located in southern part of the LVG (Fig. 2-2). The belt is dominated by Nyanzian meta-volcanosediments, flanked by syn-accretionary to post-tectonic granitoids of Tonalite–Trondhjemite–Granodiorite (TTG) affinity and high-K granites (Fig. 2-2; Sanislav et al., 2015; Henckel et al., 2016; Kwelwa et al., 2018; Sanislav et al., 2018b). The 200 Ma magmatic history of the SGGB show a progressive evolution from mafic to felsic igneous activity, between 2820 and 2620 Ma, and is subdivided into four phases (Sanislav et al., 2014a ; Kwelwa et al., 2018 ; Sanislav et al., 2018b ; Sun et al., 2018):

- 2820-2800 Ma: the earliest magmatic activity in the SGGB is characterized by widespread eruptions of juvenile tholeiitic mafic and rare felsic volcanic rocks (Borg and Krogh, 1999; Maboko et al., 2003, 2008b; Cloutier et al., 2005; Chamberlain and Tosdal, 2007; Cook et al., 2016).
- 2780-2700 Ma: synchronous volcanism and plutonism are marked by intermittent TTG-diorite magmatism and predominantly felsic volcanic rocks derived from the partial melting of the mafic basement (Borg and Krogh, 1999; Manya and Maboko, 2003a; Chamberlain and Tosdal, 2007; Sanislav et al., 2014a, 2018b).
- 2700-2660 Ma: This third phase is defined by the transition towards dominated felsic magmatism, including TTG-diorites and granite-monzonites, and the accumulation of volcanic and sedimentary sequences (Borg and Krogh, 1999; Chamberlain and Tosdal, 2007; Sanislav et al., 2014a, 2018b; Kwelwa et al., 2018; Wu et al., 2023).
- 2660-2620 Ma: This period marks the cessation of volcanism and TTG-diorite magmatism, transitioning to widespread high-K granites and monzonites (Borg and Krogh, 1999; Maboko et al., 2006; Chamberlain and Tosdal, 2007; Sanislav et al., 2014a, 2018b; Kwelwa et al., 2018).

Parallel to magmatism, three events of deformation are defined in the northwestern SGGB (Sanislav et al., 2018a; Dirks et al., 2022). The main event is dated between 2700 and 2660 Ma and correspond to important shortening and the development of crustal-scale shear zones and regional penetrative foliation (Sanislav et al., 2018a). Magmatic bodies synchronous to this major shortening stage is named syn-tectonic intrusives.

3. Methodology

3.1. Sampling and analyses

Multi-disciplinary approach was conducted, from fieldwork to micro-scale petrography (38 outcrops studied in the Fig. 2-3 delimitation), whole-rock (WR) geochemistry (21 samples, ICP-MS and ICP-OES), zircon O isotopes (10 samples, SIMS), zircon U-Pb geochronology and Lu-Hf isotopy (10 samples, LA-SF-ICPMS; Fig. 2-3). The detailed description of the methodology is provided in Supplementary Material 2-1. Sample location and the analytical analyses carried out for isotopically analyzed samples are summarized in Table 2-1 and detailed in Supplementary Material 2-2. Data tables are provided in Supplementary Materials 2-3 (WR geochemistry) and 2-4 (geochronology-isotopy). Note that the n number refers to the number of analyses and not the number of zircon grains (see Supplementary Material 2-2).

A 50 km-long transect across the SGGB, both in the greenstones and surrounding basement rocks, was conducted in the area of the Nyanzaga gold deposit (Figs. 2-2, 2-3). A field map (Fig. 2-3) was established using field observations, microstructural analysis, satellite imagery (Bing, Landsat 8+), and aeromagnetic

data, which cover only the supracrustal rocks of the greenstone belt (Fig. 2-3). Significant inputs from district-scale OreCorp Ltd. mapping improved our map (McIntyre, personal communication). Of all ten samples chosen for geochronology and isotopic studies, three are sandstones sampled in two distinct basins, while the remaining seven are deformed and undeformed igneous rocks (Table 2-1, Fig. 2-3). Note that plane orientations are written as "strike-dip" (*e.g.*, 026-77) with strike defined by the right-hand-rule convention. Lineations are written as "dip/dip direction" (*e.g.*, 81/075).

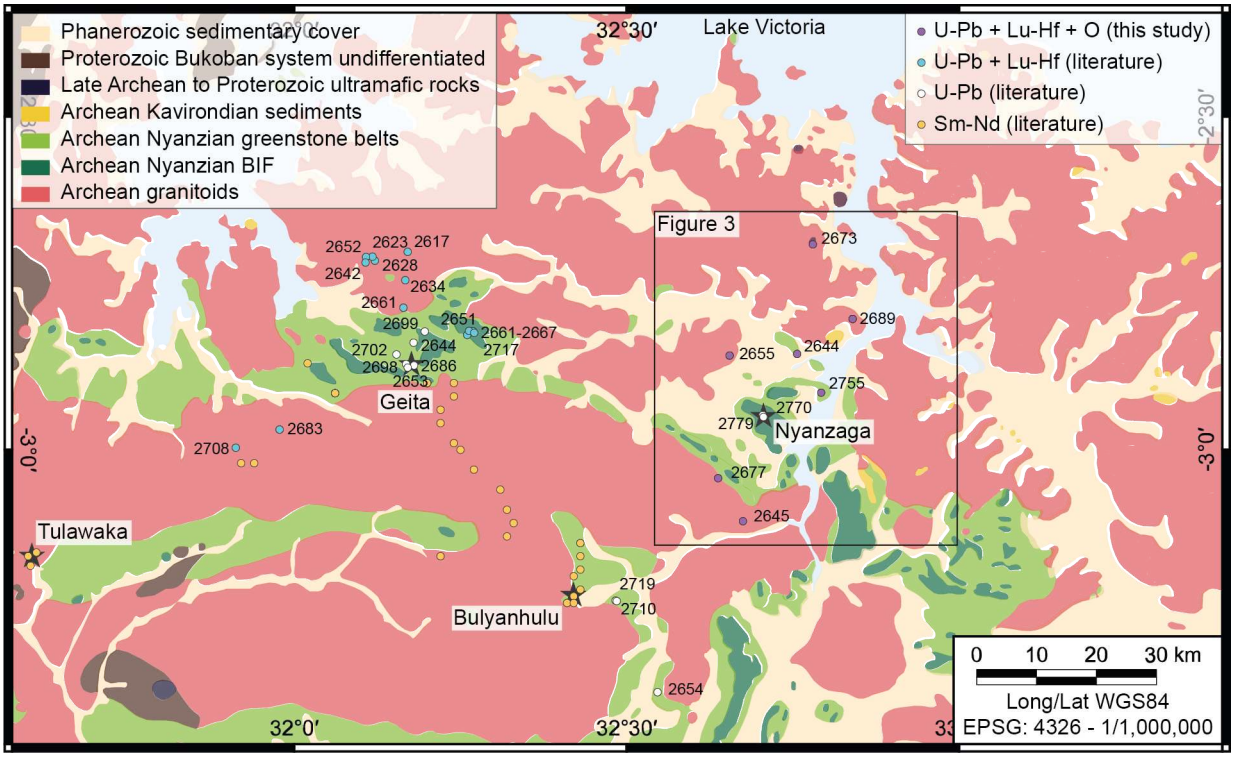

Figure 2-2. Geological map of the Sukumaland granite-greenstone belt (Barth, 1990). The sample locations analyzed for zircon U-Pb and Lu-Hf, and whole-rock Sm-Nd isotopy are indicated (Borg and Krogh, 1999; Manya and Maboko, 2003, 2008b; Cloutier et al., 2005; Maboko et al., 2006; Chamberlain and Tosdal, 2007; Sanislav et al., 2014, 2018b; Cook et al., 2016; Kwelwa et al., 2018; Wu et al., 2023). The main gold deposits of the greenstone belt are also located (stars).

3.2. *Data compilation in the Tanzania craton*

A compilation of whole-rock geochemistry, U-Pb geochronology and Sm-Nd and Lu-Hf isotopy was conducted on magmatic and detrital zircon grains from various lithologies across the entire Tanzania craton. Two separate datasets were created (Supplementary Materials 2-5 and 2-6): one for geochemical data (Manya, 2004; Cloutier et al., 2005; Maboko et al., 2006; Manva and Maboko, 2008b; Boniface and Mruma, 2012; Kazimoto and Ikingura, 2014; Sanislav et al., 2014a; Kwelwa, 2017; Cook et al., 2016; Wu et al., 2023), and another for geochronological and isotopic analyses (Borg and Krogh, 1999; Manva and Maboko, 2003, 2008b; Cloutier et al., 2005; Maboko et al., 2006; Chamberlain and Tosdal, 2007; Sanislav et al., 2014a, 2018b; Cook et al., 2016; Kwelwa et al., 2018; Wu et al., 2023). When available, U-Pb and Sm-Nd ages were included in the first dataset as well. The compiled geochronology-isotopy dataset underwent the same data-cleaning process as our data (see Supplementary Material 2-1). Some Lu-Hf isotopic analyses were performed on discordant zircon grains and the zircon age was not always matching the Lu-Hf analyses in the literature. Therefore, the crystallization age of the magmatic rock will be favored over the age of each zircon for the compiled datasets.

3.3. Classification of the granitoids

Four episodes of crustal growth in the SGGB are described by Kwelwa et al. (2018) and further discussed in Sanislav et al. (2018b): mafic volcanism prior to ca. 2800 Ma, pre-tectonic intrusives (prior to 2700 Ma), syn-tectonic intrusives (2700 – 2660 Ma), late- to post-tectonic intrusives (2660 – 2620 Ma). The three plutonic episodes (hence excluding the mafic volcanism around 2800 Ma) are used in our study to classify the granitoidic rocks. Granitoids are further subdivided based on their petrographic nature, as either TTG-diorite or granite-monzonite. If the majority of studies put temporal constrains on the analyzed intrusives, either from U-Pb geochronology or structural analyses, some did not enable us to match granitoids to our tectonic classification and an undifferentiated subdivision was therefore defined. If these intrusives presented a tectonic fabric, they were grouped in the pre- to syn-tectonic subdivision. Although all these intrusives exhibit metamorphism features, the prefix "meta-" is omitted for readability in the remaining of the text. However, since sedimentary and volcanosedimentary suites are not consistently metamorphosed, the prefix 'meta-' will be retained for clarity.

Table 2-1. Sample location, lithology, relation to deformation and analyses performed in this study, north-eastern SGGB. Inh Zrn = inherited zircon. 21 plutonic, sedimentary and volcanic samples were analyzed for WR geochemistry. 7 magmatic and 3 sedimentary samples were analyzed for U-Pb dating, Hf isotopy, and O isotopy only on the magmatic samples. One inherited zircon was found in SU06.

Sample	Easting (°)	Northing (°)	Lithology	Relation to deformation	WR geochemistry	U-Pb age weighted mean (Ma)	Hf isotopy εHf	O isotopy $\delta^{18}O$ (‰)
SU01A	32.9712	-2.7004	Granodiorite	Syn tectonic	X			
SU01B	32.9712	-2.7004	Bt-mag-rich enclave		X			
SU04	32.7797	-2.6916	Granodiorite	Syn tectonic	X	2673 ± 7	-1.90 ± 0.76	5.84 ± 0.139
SU05	32.8521	-2.7428	Granite	Post tectonic	X			
SU06 Inh Zrn	32.8399	-2.8030	Granodiorite	Syn tectonic	X	2689 ± 7 2798 ± 14	-1.61 ± 0.9 2.13 ± 0.7	5.68 ± 0.230 5.48 ± 0.228
SU08A	32.8263	-2.8401	Granodiorite	Pre to syn tectonic	X			
SU09	32.6318	-2.8264	Granodiorite	Late tectonic	X			
SU10A	32.8399	-2.8030	Sandstone	Undeformed basin		2808-2627	X	
SU10B	32.6544	-2.8583	Granodiorite	Late tectonic	X	2655 ± 5	0.26 ± 0.74	5.94 ± 0.230
SU11	32.6817	-2.8923	Sandstone	Folded basin	X	3820-2700	X	
SU12	32.7128	-2.9919	BIF	Folded sediments	X			
SU15A	32.6374	-3.0427	Bt-plg-rich enclave		X			
SU15B	32.6374	-3.0427	Qz-monzonite	Syn tectonic	X	2677 ± 4	1.37 ± 0.81	6.66 ± 0.229
SU16	32.6745	-3.1071	Granite	Post tectonic	X	2645 ± 4	0.44 ± 0.75	6.39 ± 0.231
SU17	32.7517	-3.0906	Monzogranite	Late tectonic	X			
SU18	32.5922	-3.0085	Granodiorite	Pre tectonic	X			
SU19	32.6582	-3.0367	Talc ultramafic rock		X			
SU20	32.7984	-2.9078	Sandstone	Folded basin		3568-2680	X	
SU21	32.7922	-2.9142	Weathered granitoid	Pre tectonic		2755 ± 11	2.25 ± 0.74	5.18 ± 0.139
SU25	32.7561	-2.8560	Monzogranite dyke	Post tectonic	X	2644 ± 7	0.20 ± 0.93	6.18 ± 0.230
SU31B	32.7407	-3.0426	Felsic volcanic rock	Pre tectonic	X			
SU31C	32.7407	-3.0426	Felsic volcanic rock	Pre tectonic	X			
SU32	32.7372	-3.0495	Felsic volcanic rock	Pre tectonic	X			
SU38	32.7378	-3.0518	Felsic volcanic rock	Pre tectonic	X			

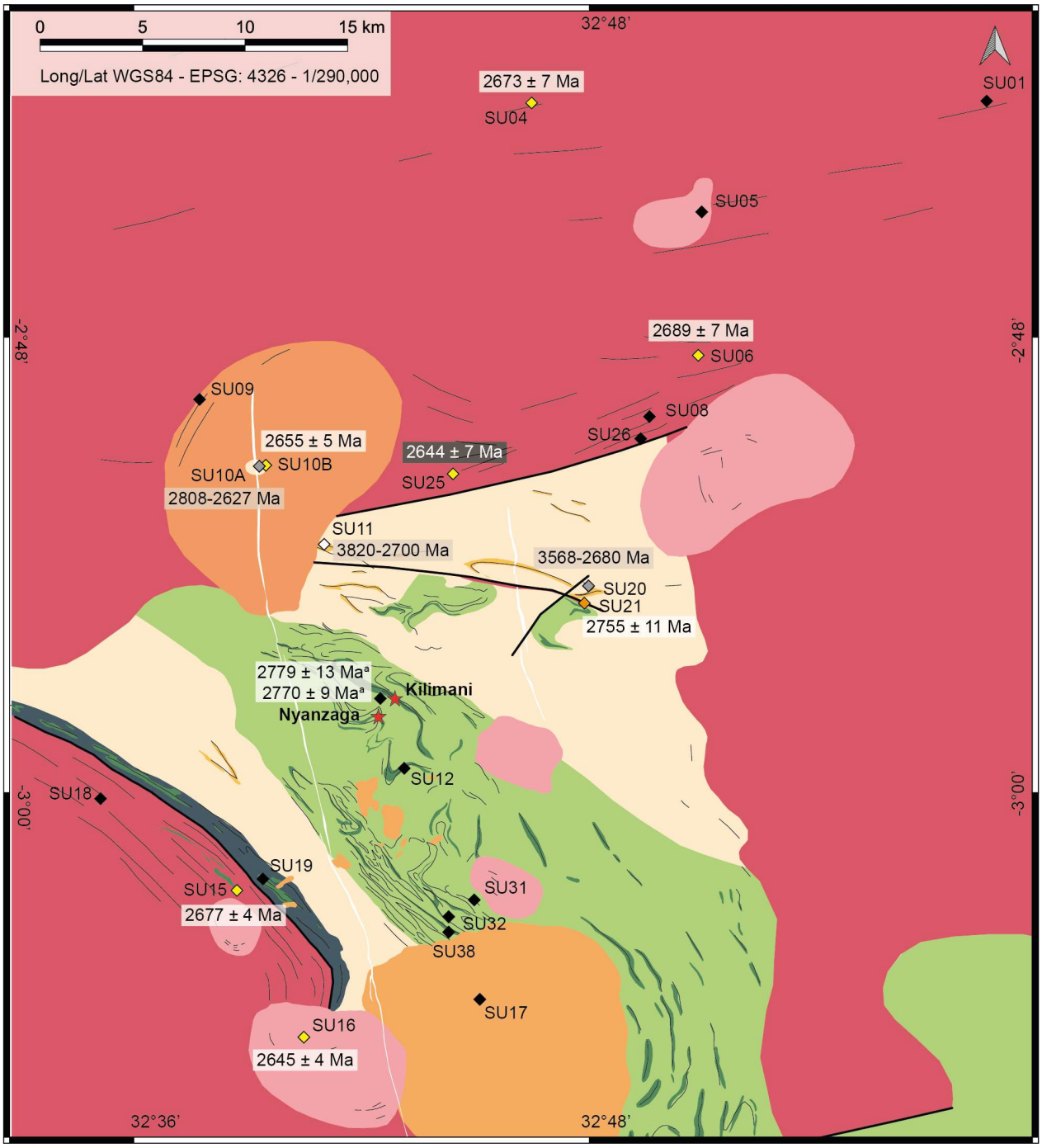

Dolerite dyke
Upper Kavirondian - Magnetic sediments
Lower Kavirondian - Magnetic sediments
Lower Kavirondian - Undifferentiated sediments
Upper Nyanzian - Volcanosediments
Nyanzian - BIF
Lower Nyanzian - Mafic/ultramafic rocks
Post-tectonic high-K granites
Late-tectonic granodiorite, granite
Pre- to syn-tectonic TTG
Major shear zone and fault
Lineaments

WR geochemistry + U-Pb-Hf-O
U-Pb-Hf-O
WR geochemistry + U-Pb-Hf
U-Pb-Hf
WR geochemistry
Gold deposit
2627-2808 Ma — Detrital ages
2655 ± 5 Ma — Magmatic age
2644 ± 7 Ma — Magmatic age (dyke)

Figure 2-3. Geological map of the transect area across the Sukumaland granite-greenstone belt, relying on field data, structural analyses and aeromagnetic data from McIntyre (personal communication). Location of samples that underwent WR geochemical, U-Pb, Lu-Hf, O isotope analyses. [a]: zircon U-Pb dating of felsic volcaniclastics from Chamberlain and Tosdal (2007).

4. Results

4.1. Lithologies

4.1.1. Igneous rocks

The pre- to syn-tectonic intrusions form a granitoidic complex surrounding the north-eastern Sukumaland greenstone belt to the north and south (Figs. 2-2, 2-3; Table 2-1). None of them intrudes the supracrustal units of the belt. They are affected by a penetrative tectonic fabric (Fig. 2-4a and h). Seven pre- to syn-tectonic intrusives were sampled, they consist of granodiorites and one quartz-monzonite. The distinction between pre- and syn-tectonic granitoids on the geological map was not possible due to a lack of outcrops and precise geophysical data. SU21 and SU18 are deformed, pre-tectonic granodiorites (Fig. 2-4a). SU21 is highly deformed and weathered, with almost complete sericitization of the feldspar, and recrystallization of the quartz. Biotite, rutile and ilmenite are present in small quantities. A biotite-rich enclave was encountered in SU18 granodiorite (Fig. 2-4a).

Of all the plutonic outcrops studied along the transect, the vast majority of them consisted of syn-tectonic intrusives, mainly granodiorites, more rarely quartz-monzonites and granites. SU01A, SU04, SU06 and SU08A are medium-grain granodiorites, affected by a well-expressed tectonic fabric, with quartz, sericitized plagioclase, rare biotite and K-feldspar (Fig. 2-4c). SU15B quartz-monzonite is slightly richer in K-felspar. Amphibole and magnetite were observed in SU01 granodiorite, while magnetite is present in SU15B quartz-monzonite. Local heterogeneities are common in syn-tectonic granitoids, with biotite ± plagioclase micro-granular enclaves, some of which preserved primitive fabrics (Fig. 2-4b).

Six late- to post-tectonic granodiorites and granites-monzogranites were sampled. They form 5- to 10-kilometer-large intrusions, crosscutting all magmatic bodies and the supracrustal units of the greenstone belt (Fig. 2-3). They show no tectonic fabrics, and rarely a magmatic one (Fig. 2-4d-f). SU09-SU10B granodiorites are amphibole-bearing and biotite-rich (Fig. 2-4e-f). SU17-SU36 monzogranites display biotite ± tourmaline – magnetite, variations in granulometry and biotite – plagioclase – tourmaline enclaves (Fig. 2-4d). SU05 granite exhibits heterogeneities with porphyritic to aplitic textures, and biotite – plagioclase micro-granular enclaves. SU16 is a pink granite with porphyritic texture (Fig. 2-4g). SU25 sample is a monzogranite pegmatitic dyke crosscutting syn-tectonic granodiorite and aplitic dykes (Fig. 2-4h).

4.1.2. Supracrustal rocks

Due to limited outcropping and artisanal mining, the mafic and ultramafic rocks of the base of the supracrustal formation were poorly studied along the transect (Lower Nyanzian Supergroup). Ultramafic rocks, highly altered into talc, and BIF were observed near an artisanal mining hole in the southernmost part of the greenstone belt (SU19; Fig. 2-3; Table 2-1).

The vast majority of the exposed greenstones consists of alternating felsic volcanics and sedimentary units of the Upper Nyanzian Supergroup, including volcaniclastic rocks, tuffs and porphyry dacite (SU31C; Table 2-1, Fig. 2-5b) intercalated with well-bedded pyrite-rich or poor, non-magnetic or magnetic BIF (SU12; Fig. 2-5a), sandstones, siltstones and mudstones. Chlorite and magnetite, as well as silica-dolomite, alterations are frequent. Greenschist facies metamorphism is widespread.

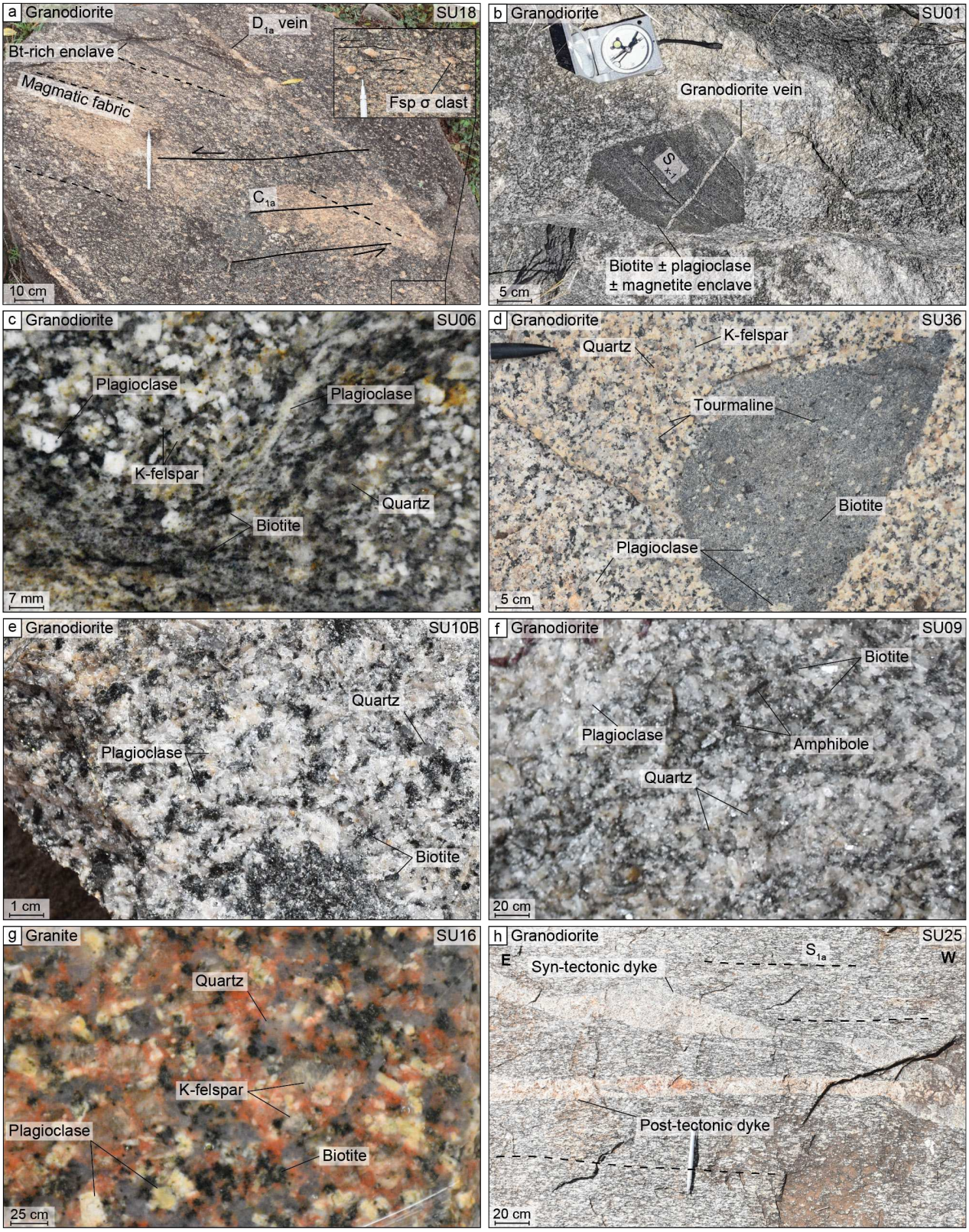

Figure 2-4. a. SU18 pre-tectonic granodiorite with magmatic fabric, affected by E-W C_{1a} shear bands (275-70). Clasts of sigma feldspar indicate an apparent sinistral kinematics. **b.** SU01 syn-tectonic granodiorite and biotite ± plagioclase ± magnetite enclave, affected by a granodiorite vein. **c.** SU06 syn-tectonic granodiorite with plagioclase, biotite, quartz and rare K-feldspar. **d.** SU36 late-tectonic tourmaline-bearing granodiorite. A biotite ± plagioclase-tourmaline enclave is shown. **e.** SU10B late-tectonic granodiorite with plagioclase, biotite and rare quartz. **f.** SU09 late-tectonic granodiorite with plagioclase, biotite, quartz and amphibole. **g.** SU16 post-tectonic granite with quartz, K-feldspar and plagioclase. **h.** Syn-tectonic granodiorite and aplitic dyke crosscut by SU25 post-tectonic monzogranite pegmatitic dyke.

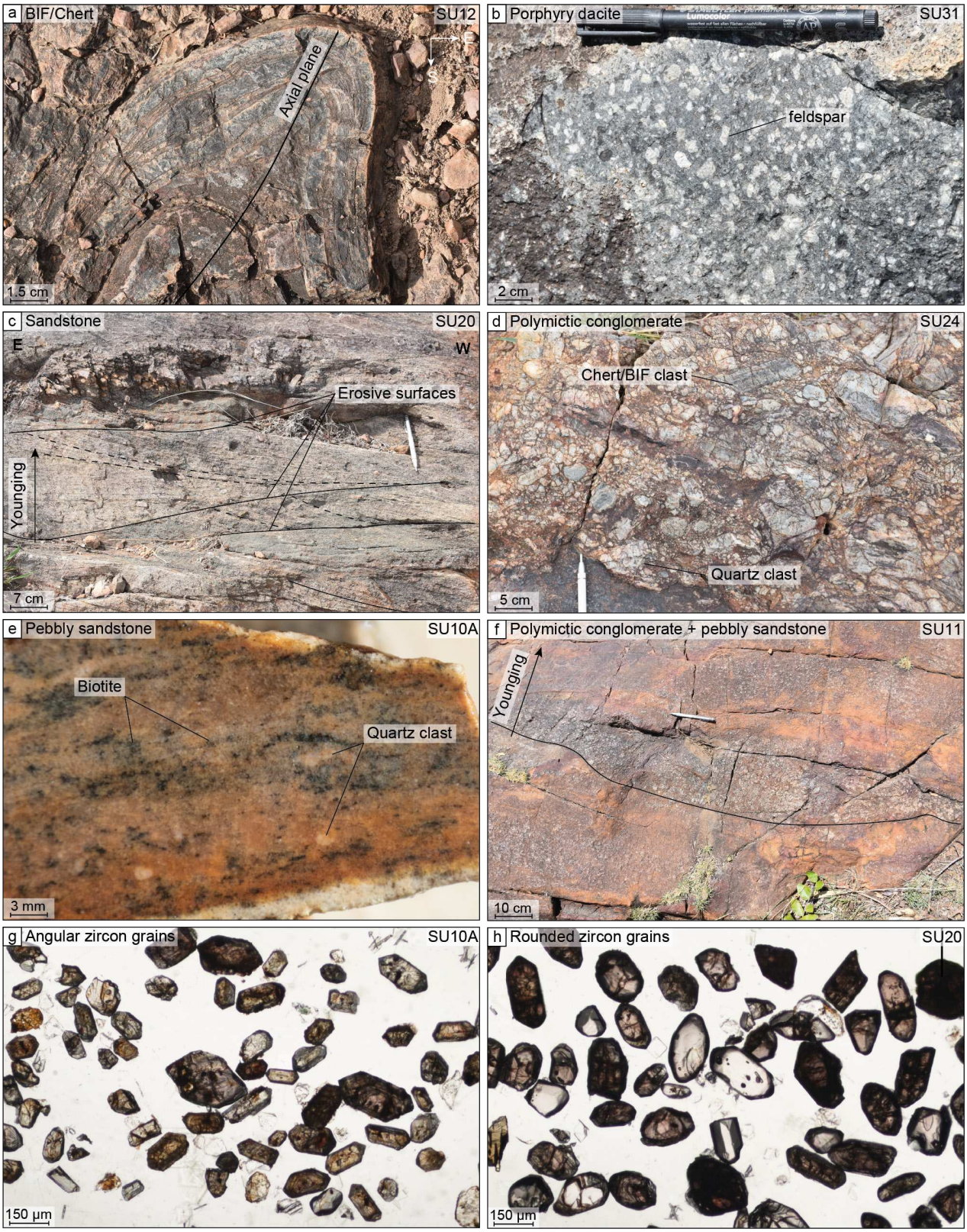

Figure 2-5. a. Folded cherts and BIF of the Upper Nyanzian. **b.** Porphyry dacite of the Upper Nyanzian. **c.** Kavirondian sandstone showing river current ripples and erosive surfaces that indicate south-directed sedimentation. **d.** Kavirondian polymictic conglomerate, showing Nyanzian chert and BIF clasts. **e.** Biotite-bearing pebbly sandstone. **f.** Pebbly sandstones eroded by polymictic conglomerate channels. **g.** Microphotograph of angular zircon grains from SU10A pebbly sandstone (transmitted light, non-polarized). **h.** Microphotograph of rounded zircon grains from SU20 sandstone (transmitted light, non-polarized).

The Kavirondian conglomerate and sandstone sediments unconformably overly the meta-volcanosedimentary suite and consist of unmetamorphosed, molasse basins oriented WNW-ESE, parallel to the Sukumaland belt (Fig. 2-3). The largest basin of the studied area is folded and about 10-kilometer large, while the smallest consists of an undeformed, narrow, 1-kilometer-long molasse basin (Fig. 2-3). Polymictic pebble conglomerates are primarily composed of angular chert and quartz clasts (Fig. 2-5d-f). Well-defined syn-sedimentary structures, such as cross-bedding, erosive surfaces and channels, with common quartz clasts, are common in pebble sandstones (Fig. 2-5c and f). Three sandstones were sampled: SU11 and SU20 from the largest, folded basin south of a crustal-scale shear zone (Figs. 2-3, 2-5c and f); and SU10A from the smallest, undeformed basin (Figs. 2-3, 2-5e). In the latter, the conglomerates are monogenic, and the sandstones bear biotite grains. These basins are unmetamorphosed, show no hydrothermal alteration, are poorly affected by deformation (syn-sedimentary structures are well preserved) and the samples are unweathered. They are therefore great candidates for isotopic analyses as detrital zircons were certainly not affected by Pb-loss after their sedimentation.

4.2. Whole-rock geochemistry of magmatic rocks

The SU31B, SU31C, SU32, and SU38 felsic volcanic samples exhibit dacitic to rhyolitic compositions (Fig. 2-6d). These volcanic samples are also notable for their relatively high nickel (Ni: 76–96 ppm) and slightly elevated chromium contents (Cr: 160–226 ppm), which are higher than those typically observed in felsic volcanics of the SGGB reported in the literature (Manya, 2004; Cloutier et al., 2005). SU32, in particular, shows a significantly higher chromium content, reaching 513 ppm. The rare-earth element (REE) patterns of these felsic volcanic samples display steep slopes (La_N/Yb_N: 17-45; Gd_N/Yb_N: 2.13-5.24) and no significant Eu anomalies, consistent with other felsic volcanics from the SGGB (Fig. 2-7c; Manya, 2004; Cloutier et al., 2005). They show slightly higher enrichment in LREE.

Six pre- to syn-tectonic intrusive samples were analyzed: SU01A, SU04, SU06, SU08A, SU15B, and SU18 (Table 2-1). In the feldspar diagram, samples are weakly potassic as they plot in the granitic and granodioritic fields, except SU15B, which plots in the quartz-monzonite field (Fig. 2-6a). These rocks are characterized by high silica content (SiO_2: 71.2–73.7 wt.%; Fig. 2-6c) and high sodium oxide (Na_2O: 3.74–4.62 wt.%). They are weakly peraluminous with an A/CNK ratio ranging from 1.13 to 1.18 (Fig. 2-6b), and while most of the samples are calc-alkalic, SU15B exhibits an alkali-calcic composition (Fig. 2-6e). The majority of the rocks are classified as A-type granitoids, with the exceptions of SU01A and SU08A, which exhibit I-, S-, and M-type affinities (Fig. 2-6f). All the samples exhibit low concentrations of ferromagnesian minerals, with total FeOt + MgO + MnO + TiO_2 content below 3.2 wt.%. They have elevated Mg# (mean value of 32.7; Fig. 2-6j) and high concentrations of Ni (50–115 ppm) and Cr (96–473 ppm), much higher than typically observed in other intrusives from the region, with the exception of SU04, which shows very low Ni (5 ppm) and Cr (2.5 ppm) contents.

These samples can be subdivided in two distinct geochemical groups. The first cluster, comprising SU01A, SU15B and SU18, is characterized by high Sr/Y ratios (> 40), low K_2O/Na_2O ratios (< 1; Fig. 2-6i), steep light and heavy rare-earth element (LREE and HREE) patterns with La_N/Yb_N ratios of 68–175 and Gd_N/Yb_N ratios of 4.8–6.1, and only minor negative Eu anomalies (Eu/Eu* = 0.65–0.74; Fig. 2-7a). The second cluster, consisting of SU04, SU06 and SU08A, shows lower Sr/Y ratios (20–28), K_2O/Na_2O ratios between 0.8 and 1.1 (Fig. 2-6i), less steep LREE and HREE patterns (La_N/Yb_N = 25.5–30.8, Gd_N/Yb_N = 2.12–2.75), and similarly minor Eu anomalies (Eu/Eu* = 0.62–0.77; Fig. 2-7a).

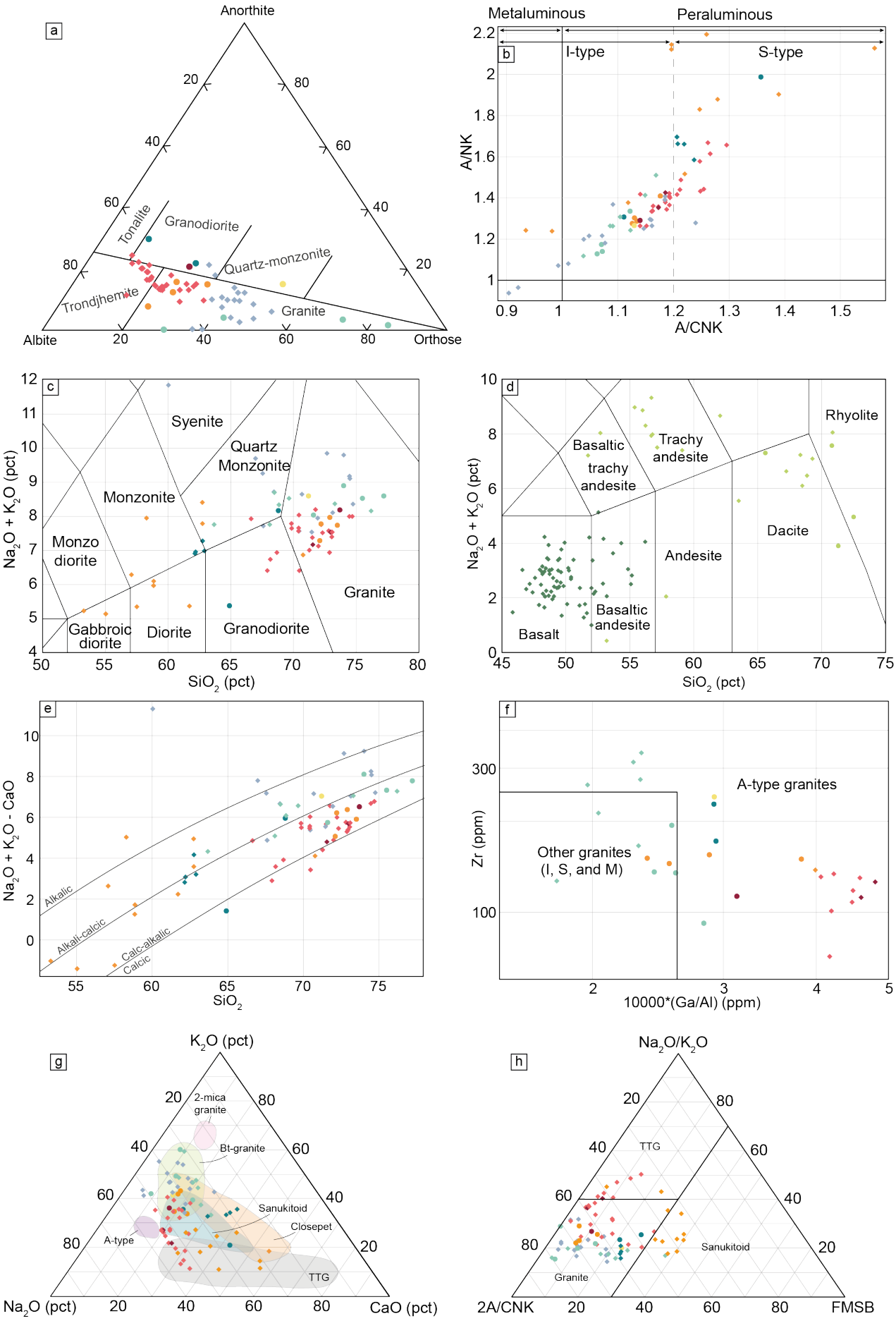
a
Anorthite
Albite
Orthose
Tonalite
Granodiorite
Quartz-monzonite
Trondjhemite
Granite
b
Metaluminous
Peraluminous
I-type
S-type
A/NK
A/CNK
c
Syenite
Quartz Monzonite
Monzonite
Monzo diorite
Granite
Gabbroic diorite
Diorite
Granodiorite
Na2O + K2O (pct)
SiO2 (pct)
d
Rhyolite
Basaltic trachy andesite
Trachy andesite
Dacite
Andesite
Basaltic andesite
Basalt
Na2O + K2O (pct)
SiO2 (pct)
e
Alkalic
Alkali-calcic
Calc-alkalic
Calcic
Na2O + K2O - CaO
SiO2
f
A-type granites
Other granites (I, S, and M)
Zr (ppm)
10000*(Ga/Al) (ppm)
g
K2O (pct)
2-mica granite
Bt-granite
Sanukitoid
Closepet
A-type
TTG
Na2O (pct)
CaO (pct)
h
Na2O/K2O
TTG
Sanukitoid
Granite
2A/CNK
FMSB

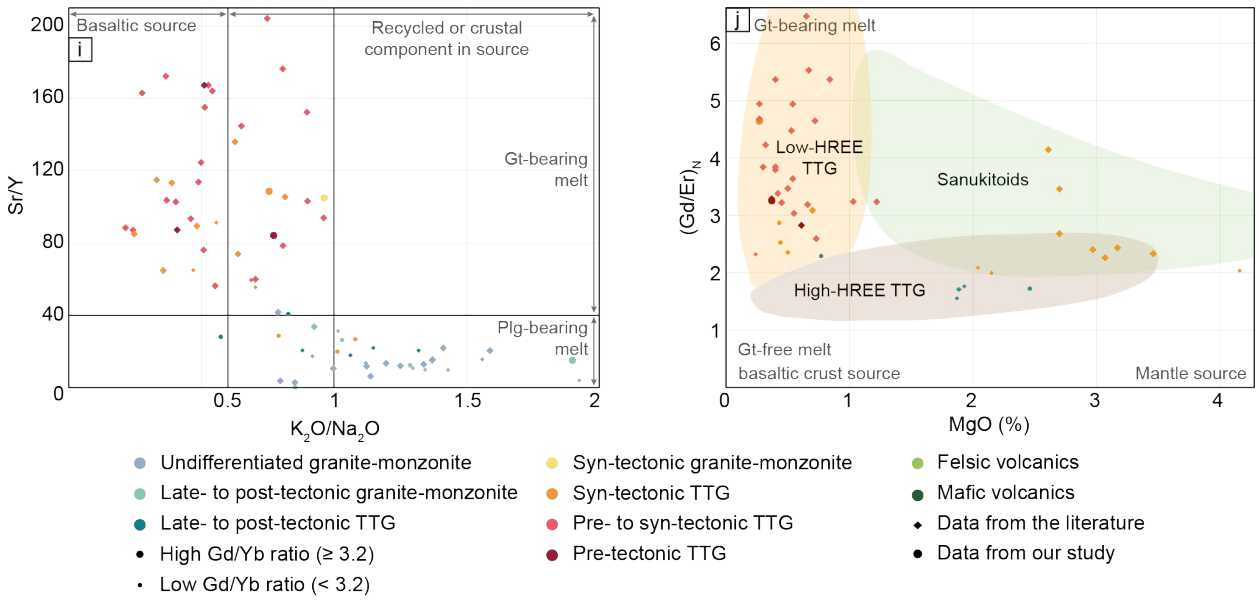

Figure 2-6. Whole-rock geochemical analyses on magmatic rocks of the SGGB of this study (circles) and from the literature (diamonds). **a.** Feldspar triangle for plutonic rocks with > 10% modal quartz (O'Connor, 1965). **b.** A/CNK vs A/NK diagram (Shand, 1943) with I-type and S-type boundaries (Chappell and White, 1974). **c.** TAS diagram for plutonic rocks (Middlesmost, 1994). **d.** TAS diagram for volcanic rocks (Le Maitre et al., 1989). **e.** MALI diagram (MALI = Na_2O + K_2O – CaO wt ‰; Frost et al., 2001). **f.** Granite A- and I-, S-, M-type differentiation (Whalen et al., 1987). **g.** K_2O-Na_2O-CaO ternary diagram (Moyen et al., 2003). **h.** K_2O/Na_2O-2A/CNK-FMSB diagram (Laurent et al., 2014). FMSB = 2 × (FeOt + MgO) × (Sr + Ba) (wt.%). **i.** Sr/Y vs K_2O/Na_2O diagram (Smithies et al., 2021). **j.** (Gd/Er) vs MgO diagram for TTGs and sanukitoids (Halla et al., 2009).

The late- to post-tectonic intrusives consist of the SU09 and SU10B granodiorites, SU17 monzogranite, SU05 and SU16 granites and SU25 monzogranite pegmatitic dyke (Table 2-1). The two granodiorites display lower silica contents (65 – 69 wt.%; Fig. 2-6c), while the granite-monzonite intrusives show higher silica contents (72 – 77.2 wt.%). They record varying K_2O/Na_2O ratios, the lowest being in SU10B (0.57), then increasing in SU09 and SU25 (0.83-0.85), and being the highest in SU05, SU16 and SU25 (1.03-1.90; Fig. 2-6i). They are weakly peraluminous to metaluminous and exhibit calc-alkalic to alkali-felsic compositions, except for a calcic composition for SU10B granodiorite (Fig. 2-6b and e). SU10B, SU09 and SU25 are classified as A-type, while SU05, SU16 and SU17 exhibit S-, M-, and I-type characteristics (Fig. 2-6f). SU09, SU10B and SU17 show the highest ferromagnesian content and Mg# values of all studied samples (FeOt + MgO + MnO + TiO_2: 3.56–3.84 wt.%; Mg#: 34.0–36.6), while SU05, SU16 and SU25 are poorer in ferromagnesian minerals and have low Mg# values (FeOt + MgO + MnO + TiO_2: 0.61–2.30 wt.%; Mg#: 12.2–26.1; Fig. 2-6j). Ni and Cr concentrations are elevated in SU05 and SU09 (Ni: 75-81 ppm; Cr: 180-200 ppm), compared to SU10B, SU16, SU17 and SU25 (Ni: 37-44 ppm; Cr: 87-135 ppm). Late- to post-tectonic intrusives have a low Sr/Y ratio (< 40; Fig. 2-6i). With the exception of SU25, the REE patterns of late- to post-tectonic intrusives are gentler compared to the pre- to syn-tectonic intrusives, with La_N/Yb_N ratios of 11.8–62.8 and Gd_N/Yb_N ratios of 1.5–3.4 (Fig. 2-7b). They also show varying Eu anomalies, from insignificant in SU09 (Eu/Eu*: 0.91), slightly negative in SU16, SU10B and SU17 (Eu/Eu*: 0.61-0.77), and significantly negative in SU05 (Eu/Eu*: 0.34). SU25 exhibits a unique REE pattern among the studied samples, showing a relatively flat REE distribution with low LREE and high HREE concentrations. It also has the most pronounced Eu anomaly, with Eu/Eu* of 0.14.

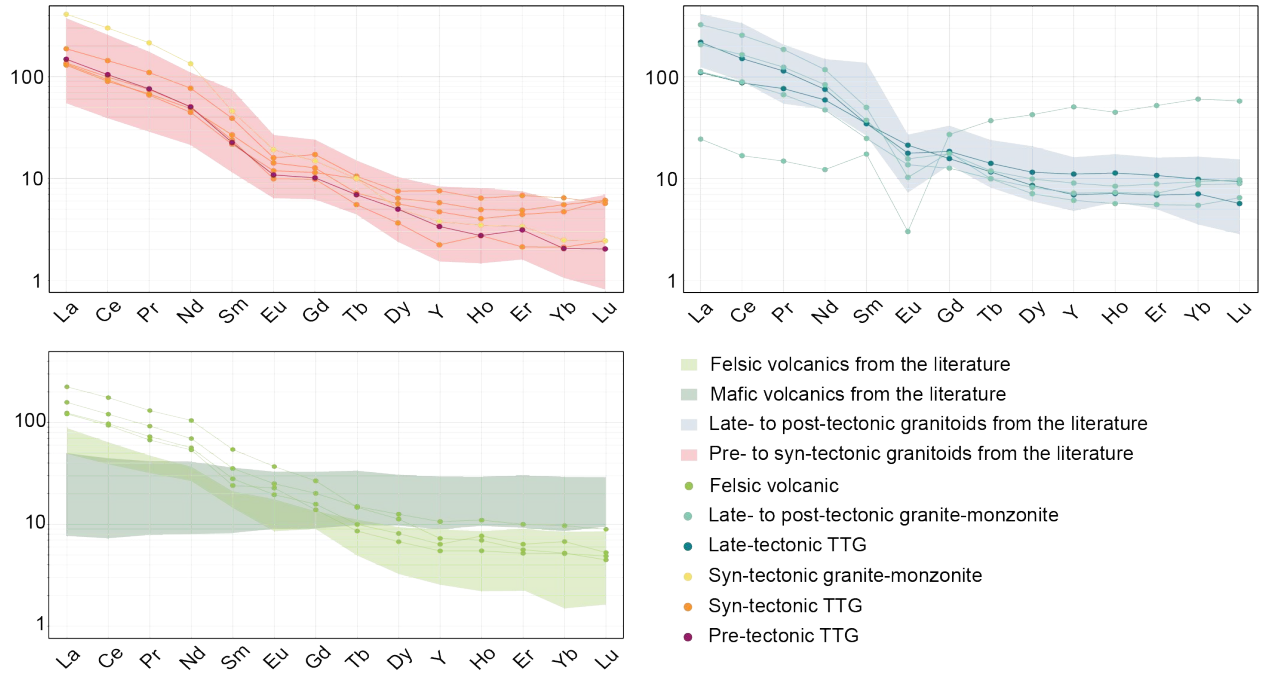

Figure 2-7. C1 chondrite normalized rare-earth element (REE) diagrams (McDonough and Sun, 1995) for **a.** pre- to syn-tectonic intrusives, **b.** late- to post-tectonic intrusives, **c.** felsic volcanics. The halos outline the REE patterns of all the pre- to syn-tectonic TTGs (orange), late- to post-tectonic granite-monzonite (pink), mafic volcanics (dark green) and felsic volcanics (light green) from the literature in the SGGB.

4.3. Zircon U-Pb ages and O-Hf isotope analyses

We conducted zircon U-Pb analyses on 7 magmatic samples, showing concordant data clusters and one inherited zircon in SU06, as well as 3 sandstones. Weighted mean $^{207}Pb/^{206}Pb$ dates with 95% confidence intervals uncertainties are presented in Figure 2-8. εHf and $\delta^{18}O$ versus U-Pb ages are shown in Figure 2-9. Two-stage model ages were calculated and are used here as an indicator of older/younger inputs in the source, not as an absolute age for mantle extraction.

4.3.1. Magmatic record in the northeastern SGGB

The SU21 pre- to syn-tectonic intrusive is the oldest lithology analyzed in this study, dated at 2751 ± 12 Ma (MSWD = 3.7, n = 7; Fig. 2-8e). Two-stage model age spans from 2975 to 2941 Ma. The granitoid yields the highest average εHf values at 2.25 ± 0.74 (ranging from 2.6 ± 0.71 to 1.9 ± 0.76, n = 12; Fig. 2-9b), and the lowest average $\delta^{18}O$ at 5.18 ± 0.139 ‰ (ranging from 5.38 ± 0.134 ‰ to 4.96 ± 0.147 ‰, n = 17, Fig. 2-9c). A single inherited zircon from SU06 syn-tectonic granodiorite was dated at 2798 ± 14 Ma (MSWD = 1.2, n = 2; Fig. 2-8b), with high εHf values of mean 2.13 ± 0.7 (2.2 ± 0.71 and 2.0 ± 0.69; Fig. 2-9b), and low $\delta^{18}O$ mean at 5.48 ± 0.228 ‰ (5.62 ± 0.225 ‰ and 5.33 ± 0.230 ‰; Fig. 2-9b). Two-stage model age of the single inherited zircon is comprised between 3001 and 2994 Ma. SU04 and SU06 pre- to syn-tectonic granodiorites are dated at 2673 ± 7 Ma (MSWD = 0.99, n = 7; Fig. 2-8a) and 2684 ± 7 Ma (MSWD = 0.91, n = 12; Fig. 2-8b), respectively. They yield rather similar average $\delta^{18}O$ and εHf values (SU04: $\delta^{18}O$ at 5.84 ± 0.139 ‰, n = 7; εHf at -1.90 ± 0.76, n = 12; SU06: $\delta^{18}O$ at 5.68 ± 0.230 ‰, n = 18; εHf at -1.61 ± 0.9, n = 14; Fig. 2-9b-c), and similar two-stage model ages (SU04: 3107 and 2997 Ma; SU06: between 3118 and 2957 Ma). SU15B

pre- to syn-tectonic quartz-monzonite is dated at 2677 ± 4 Ma (MSWD = 0.97, n = 22; Fig. 2-8c) and records the highest $\delta^{18}O$ mean of the 7 analyzed samples, at 6.66 ± 0.229 ‰ (ranging from 7.34 ± 0.232 ‰ to 5.94 ± 0.226 ‰, n = 23; Fig. 2-9c), a high εHf mean at 1.37 ± 0.81 (ranging from 1.9 ± 1.25 to 0.9 ± 1.42, n = 14; Fig. 2-9b), and two-stage model ages between 2948 and 2899 Ma.

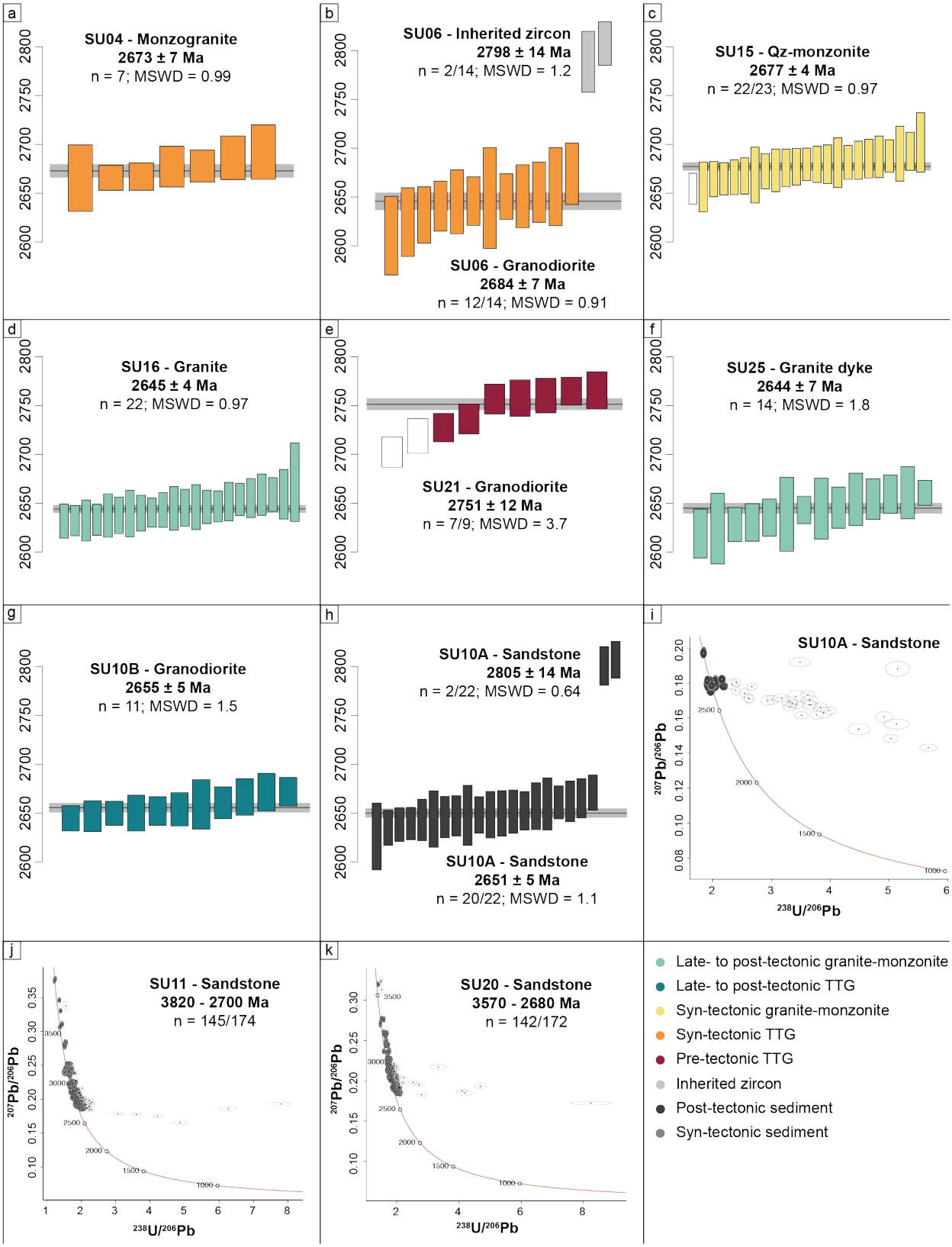

Figure 2-8. Zircon U-Pb data from this study analyzed using LA-ICP-MS. Interpreted ages are reported with 95% confidence intervals, uncertainties of single analyses represent 2SE. Tera Wasserburg concordia diagrams are shown for sedimentary samples.

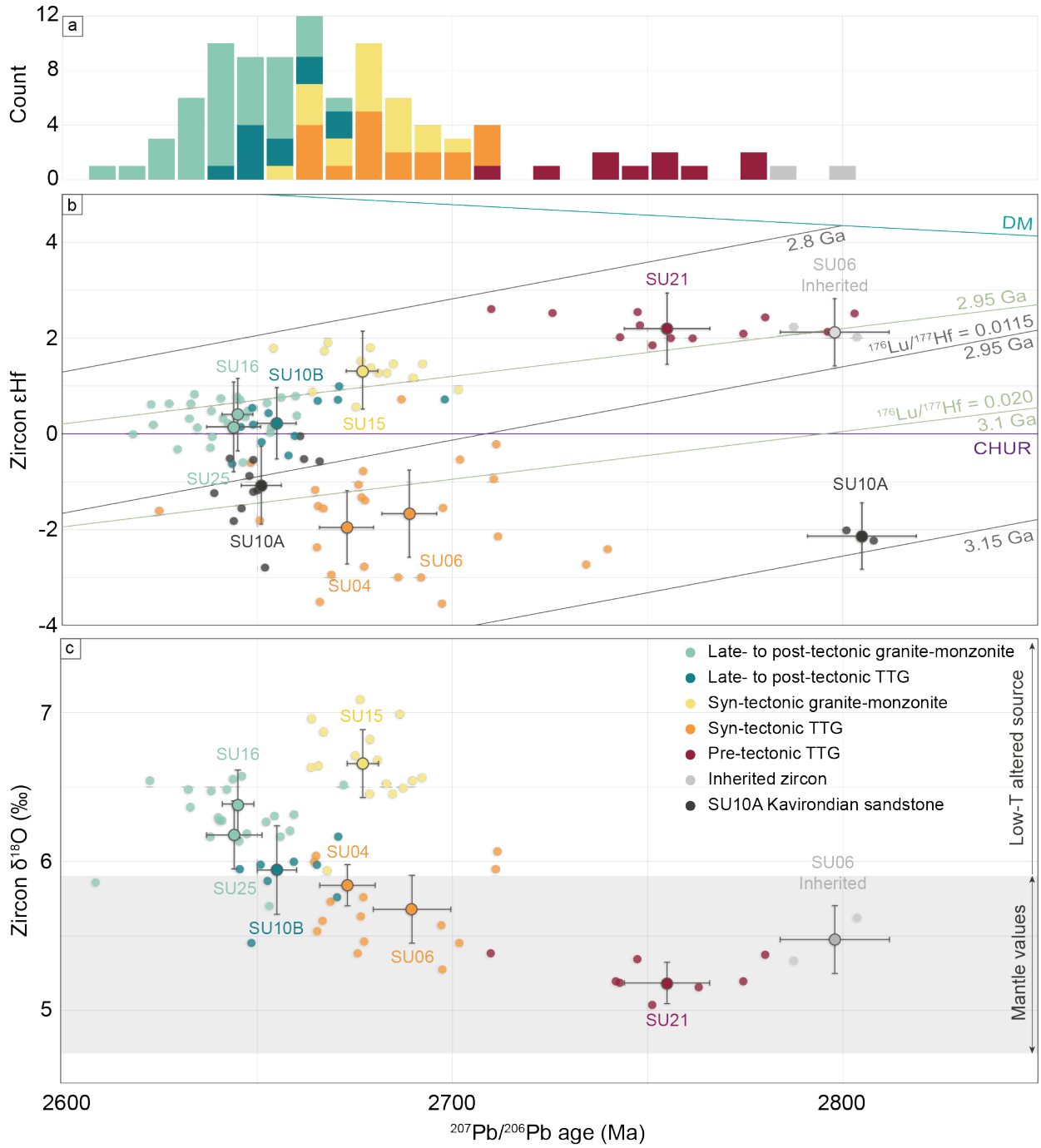

Figure 2-9. a. Probability distribution plot, **b.** zircon εHf vs age diagram and **c.** zircon $\delta^{18}O$ vs age for magmatic samples of the north-eastern Sukumaland granite-greenstone belt, Tanzania craton, data from this study. Individual zircon ages are shown as well as average of magmatic samples. Error bars represent 95 % confidence interval (ages) and 2SD (εHf and $\delta^{18}O$). In the zircon εHf vs age diagram is shown the SU10A Kavirondian sandstone.

Late- to post-tectonic SU10B granodiorite crystallized at 2655 ± 5 Ma (MSWD = 1.5, n = 11; Fig. 2-8g). Zircon εHf values for this sample are near the chondritic value, with a mean at 0.26 ± 0.74 (ranging from 1.0 ± 0.66 to -0.6 ± 0.69, n = 12; Fig. 2-9b). Two-stage model age for this sample is comprised between 2982 and 2916 Ma. SU10B yields average $\delta^{18}O$ value of 5.94 ± 0.230 ‰ (ranging between 6.26 ± 0.225 ‰ and 5.45 ± 0.222 ‰, n = 19; Fig. 2-9c). Finally, the youngest age for magmatism recorded in the study area is 2645 Ma, from SU16 granite (2645 ± 4 Ma, MSWD = 0.97, n = 22; Fig. 2-8d) and SU25 monzogranite pegmatitic dyke (2644 ± 7 Ma, MSWD = 1.8, n = 14; Fig. 2-8f). They show similar high $\delta^{18}O$ and near-chondritic εHf means: SU16

at 6.39 ± 0.231 ‰ $\delta^{18}O$ (range between 6.90 ± 0.252 ‰ and 6.16 ± 0.222 ‰, n = 25; Fig. 2-9c) and 0.44 ± 0.75 εHf (range between 0.8 ± 0.74 and -0.6 ± 1.00; n = 15; Fig. 2-9b); SU25 at 6.18 ± 0.230 ‰ $\delta^{18}O$ (range between 6.59 ± 0.230 ‰ and 5.70 ± 0.229 ‰; n = 9; Fig. 2-9c) and 0.20 ± 0.93 εHf (range between 0.8 ± 0.85 and -0.3 ± 1.06; n = 13; Fig. 2-9b). Two-stage model age for SU16 and SU25 samples have a similar range, between 2966 and 2912 Ma.

4.3.2. Detrital record in the northeastern SGGB

Kavirondian sandstones yield a wide range of zircon U-Pb ages, between 3822 and 2639 Ma (Fig. 2-10). Three samples were analyzed, SU11 and SU20 were sampled in a syn-tectonic molasse basin, SU10A in a restricted post-tectonic molasse basin (Fig. 2-3). The latter records a restricted age range, with a single concordant age at 2651 ± 5 Ma (MSWD = 1.1, n = 20; Fig. 2-8h-i). The εHf for this age group varies between -0.1 ± 0.82 and -2.8 ± 0.88, with a mean value at -1.1 ± 0.8 (n = 14; Figs. 2-9b, 2-10b). One older zircon is dated at 2805 ± 14 Ma (MSWD = 0.64, n = 2; Fig. 2-8h-i), with εHf of -2.0 ± 0.71 and -2.2 ± 0.69 (Figs. 2-9b, 2-10b).

SU11 and SU20 were sampled from the same Kavirondian basin, 13km apart (Fig. 2-3). They yield similar age and εHf trends and will therefore be described together. They contain zircon ages ranging from 3820 Ma to 2680 Ma (n = 287; Figs. 2-8j-k, 2-10a). A few grains were dated between 3820 and 3340 Ma (n = 6) following an εHf trend from 7.1 ± 0.76 to -4.9 ± 0.66, with two-stage model age between 3925 and 3735 Ma (Fig. 2-10). A large and continuous number of zircon grains were dated between 3245 and 2680 Ma, with a peak at ca. 2875 Ma. The εHf values for the analyzed zircon grains varies between -8.3 ± 0.74 and 4.3 ± 0.76, with 67 % of them showing positive values.

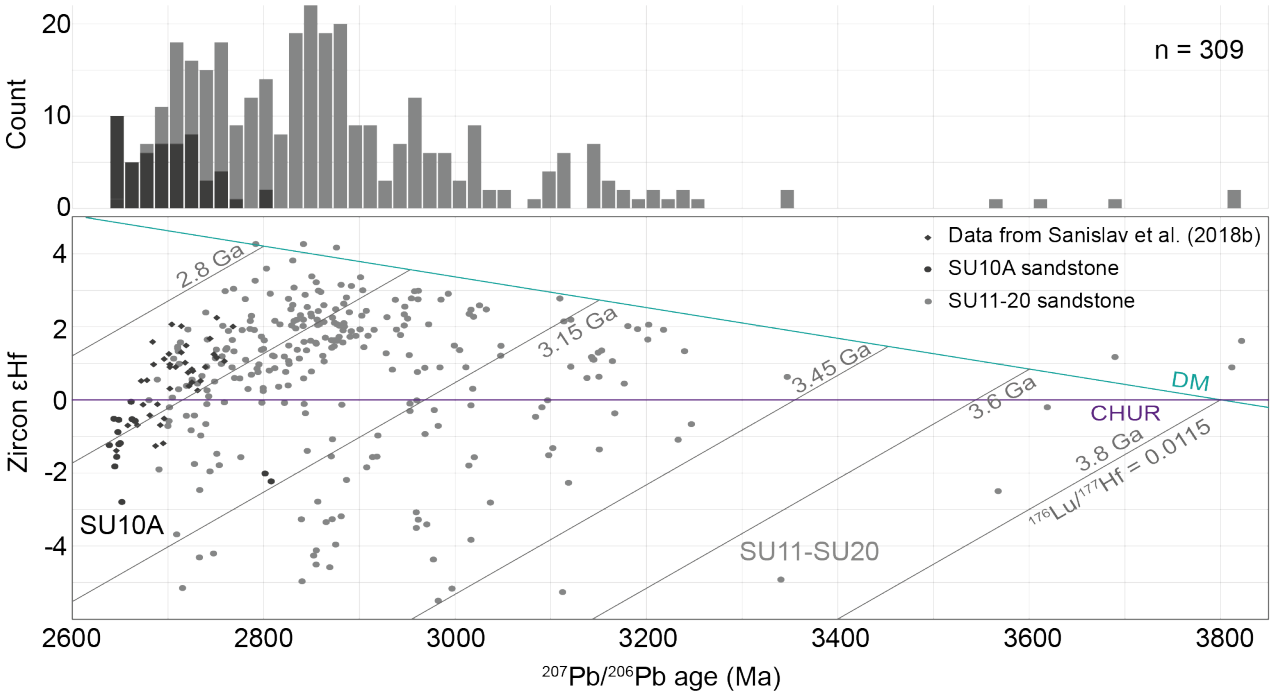

Figure 2-10. a. Probability distribution plot and **b.** zircon εHf vs age diagram for detrital zircons of the northern Sukumaland granite-greenstone belt, Tanzania craton, data from this study and Sanislav et al. (2018b).

5. Discussion

5.1. Petrogenesis of the magmatic record

Whole-rock geochemical analyses combined with a study of the relationship between granitoids and tectonism allow for investigating temporal variations of source composition and melting depth during crustal growth in the SGGB (*e.g.*, Smithies et al., 2018; Schreefel et al., 2024). In this section are discussed the changes over time of magma sources and the depths of melting based on petrography, U-Pb geochronology and whole-rock geochemical compositions of four magmatic phases: ≥ 2800 Ma mafic, 2780-2700 Ma pre-tectonic, 2700-2660 syn-tectonic, and 2660-2620 Ma late- to post-tectonic magmatism. Our studied intrusives are combined with the compiled dataset of petrography and geochemical analyses on volcanic and plutonic rocks from the SGGB (Manya, 2004; Cloutier et al., 2005; Maboko et al., 2006; Manya and Maboko, 2008b; Boniface and Mruma, 2012; Sanislav et al., 2014a; Cook et al., 2016; Wu et al., 2023). Such complete dataset enables to reconstruct the overall petrographic-geochemical evolution of the SGGB, notably the mafic extrusions at ca. 2820 Ma, not sampled in our studied area.

Certain trace elements and element ratios in magmatic rocks are sensitive to the source composition and pressure during melting and are hence widely used to constrain the depth and nature of the melted source (Jahn et al., 1981; Martin, 1986; Martin et al., 2005; Moyen and Laurent, 2018; Smithies et al., 2018; Schreefel et al., 2024). For instance, Th, Yb, Nb, Ti and Zr contents fingerprint oceanic basalt tectonic settings, whether they derive from a depleted or primitive mantle, in a context of mantle-plume (Ti/Yb), with crustal inputs (Th/Nb) (e.g., Kamenetsky et al., 2000; Pearce, 2008, 2014). In intrusive rocks, trace elements and element ratios inform whether their source was mafic or felsic (*e.g.*, K_2O/Na_2O ratio, Mg#, Ni, Cr contents), whether it melted at high (*i.e.*, in garnet stability fields) or low depth (*i.e.*, plagioclase stability field) environments (*e.g.*, Martin et al., 2005; Smithies et al., 2018). Melting at high depths (> 7-8 kbar, Johnson et al., 2017) results in garnet-rich restites, which tend to sequester Y and HREE, and high Sr/Y and Gd/Yb melts (Taylor and McLennan, 1985; Moyen, 2009; Hoffmann et al., 2011). On the other hand, melting at low depths leads to plagioclase-rich restites, which preferentially capture Sr and Eu, leading to low Sr/Y and Gd/Yb melts. However, the Sr/Y ratio can be impacted by the nature of the source rock (Moyen, 2009). Specifically, a crustal source has significantly higher Sr/Y ratio compared to mafic crust and will lead to high Sr/Y (up to 80), even when melting at low depth. It led us to pair Sr/Y and K_2O/Na_2O ratios (Fig. 2-6i), showing for the SGGB dataset no evolved source (high K_2O/Na_2O) with high Sr/Y, concluding that the depth of melting can be deduced for the intrusives in the northern SGGB based on their Sr/Y ratios. Furthermore, the combination of the Sr/Y and Gd/Yb ratios, based on distinct proxies, also resolve the potential issue.

The magmatic history of the SGGB begins with Na-rich, low-Th, mafic and minor felsic volcanism formed between 2820 and 2800 Ma (Manya, 2004; Cloutier et al., 2005; Manya and Maboko, 2008b; Boniface and Mruma, 2012; Cook et al., 2016; Kwelwa et al., 2018). Such low-Th signature and the high (Th/Yb)/(Nb/Yb) and (Nb/Th)/(Zr/Nb) trends of the basalts (Fig. 2-11) are widely observed in other Archean cratons, as outlined by the overlap of the SGGB basalts with the low-Th basalts of the Eastern Goldfield in Pearce (2014) diagram (Barnes et al., 2012; Schreefel et al., 2024). Neither strongly enriched nor depleted compositions are found, and the trend shows progressive evolution from a primitive mantle composition towards the arc field. These geochemical characteristics reflect plume-head volcanism from a primitive mantle-dominated source and progressive contamination of the mantle-derived magma by crustal material (Pearce, 2008, 2014; Barnes et al., 2012; Moyen and Laurent, 2018; Smithies et al., 2018; Schreefel et al., 2024).

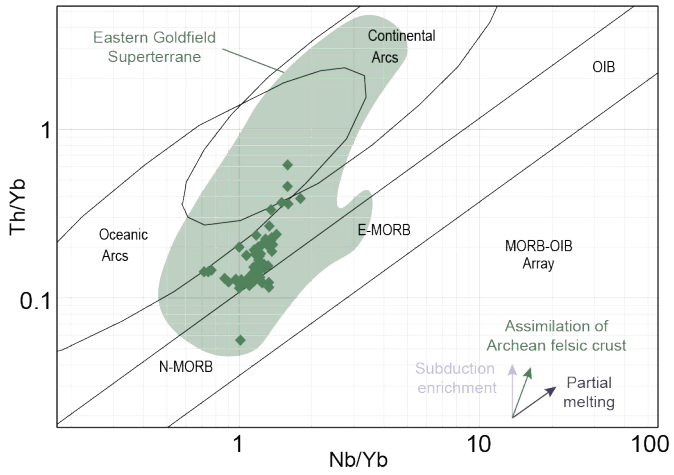

Figure 2-11. Nb/Yb vs Th/Yb diagram for the mafic volcanics of the northern SGGB (Pearce, 2008, 2014). Data from Manya (2004), Cloutier et al. (2005), Manya and Maboko (2008b), Boniface and Mruma (2012), Cook et al. (2016) and Kwelwa et al. (2018). The mafic volcanics of the Eastern Goldfield Superterrane, Yilgarn, are outlined (Barnes et al., 2012; Schreefel et al., 2024).

Pre- to syn-tectonic granitoids were emplaced between 2780 and 2660 Ma, and can be subdivided into three groups based on their geochemical signatures: high-Sr/Y TTGs; low-Sr/Y TTGs; sanukitoid-like TTGs. The vast majority of them fall into the first category, that corresponds to the typical Archean low-HREE TTGs defined by Halla et al. (2009), with elevated Sr and Eu, low Yb and Y contents, hence, high Sr/Y and Gd/Yb ratios (Fig. 2-6i). They show low to moderate K_2O/Na_2O and strongly fractionated REE patterns (Fig. 2-6i, 7a). These features can be interpreted as reflecting partial melting of metamorphosed basaltic crust at depths high enough to stabilize garnet and hornblende (*e.g.*, Smithies et al., 2018). Furthermore, the presence of magnetite and amphibole in some syn-tectonic granitoids indicates that the melted basaltic crust was hydrated, at least after 2700 Ma.

A cluster of three pre- to syn-tectonic granodiorites from our study falls into the second group that shows significantly lower Sr/Y and Gd/Yb ratios compared to the other syn-tectonic intrusives, and a moderate to high K_2O/Na_2O ratio (Fig. 2-6i). They also show flatter HREE pattern compared to other pre- to syn-tectonic granodiorites, and small Eu anomalies, all pointing out to partial melting of a more evolved, continental crust at low depths, in the plagioclase stability field (Martin et al., 2005; Smithies et al., 2018). Finally, some syn-tectonic TTG rocks from the literature (Kwelwa, 2017) show similarities with sanukitoid-like granitoids (Balakrishnan and Rajamani, 1987; Jayananda et al., 1995, 2000; Martin et al., 2005,; Heilimo et al., 2010; Laurent et al., 2014). Their signature is characterized by low SiO_2, high ferromagnesian, CaO, MgO and Sr contents (Fig. 2-6g-i). They also present high Sr/Y and Gd/Yb and are rich in amphibole, overall concordant with a derivation from the interaction between a TTG-like melt and mantle peridotite (Fig. 2-6i; Martin et al., 2009; Moyen and Martin, 2012).

Late- to post-tectonic intrusives, formed between 2660 and 2620 Ma, show distinctively low Sr/Y and Gd/Yb, indicative of low-pressure melting, in the stability field of plagioclase (Fig. 2-6i). The SU10B granodiorite shares similarities with Archean sanukitoid-like granitoids, notably with the presence of amphibole, low SiO_2, high Sr, Ba and ferromagnesian contents, high Mg number, relatively low K_2O/Na_2O, high Ba/Rb ratios, and minor to negligeable Eu anomalies (*e.g.*, Balakrishnan and Rajamani, 1987; Jayananda et al., 1995, 2000; Martin et al., 2005, 2010; Heilimo et al., 2010; Laurent et al., 2014). However, the low Sr/Y and Gd/Yb ratios are less common and hard to reconcile with the tectonic setting of sanukitoid melts involving interaction with the peridotite mantle, *i.e.*, at high depths (Martin et al., 2009; Moyen and Martin, 2012). The granitic bodies

and dykes show higher K_2O/Na_2O ratio signatures and well pronounced Eu anomalies (Figs. 2-6i, 2-7b). Such signature is indicative of protracted crustal reworking (Halla et al., 2009; Moyen, 2011). In particular, SU25 post-tectonic monzogranite pegmatitic dyke shows a unique flat REE pattern accompanied by the strongest Eu anomaly of all intrusives from the SGGB, resulting from weak partial melting of a granitoid that had already been partially melted before (Fig. 2-7b).

Overall, a global geochemical trend emerges from the magmatic record in the SGGB, beginning with mafic magmatism from a primitive mantle in a mantle-plume setting. Granitoids followed, showing increasing K_2O/Na_2O ratios and HREE contents, and decreasing Sr/Y, Gb/Yb ratios. Their geochemical signature is interpreted as crustal thickening first from the melting at high depth of mafic crust between 2780 and 2660 Ma, that was hydrated at least after 2700 Ma, to reworking of more or less evolved continental crust at low depth leading to the intrusion of late- to post-tectonic high-K granitoids after 2660 Ma.

5.2. Crustal growth and reworking in the Sukumaland granite-greenstone belt

Shifts in Hf, Nd and O isotopic arrays are indicators of magmatic contributions from different sources, in other words, the evolution in time of their signature may indicate changes in the source of the intrusives. Their use on magmatic zircon populations enables to identify fundamental changes in tectonic conditions, by measuring the mantle input and crustal reworking in the source of the intrusives, including supracrustal contributions (*e.g.*, DePaolo, 1981; Patchett 1983; Valley et al., 1998, 2005; Hawkesworth et al., 2006; Hawkesworth and Kemp 2006; Kemp et al., 2006; Collins et al., 2011; Dhuime et al., 2011; Dhuime, 2012; Iizuka et al., 2017; Bauer et al., 2020; Smithies et al., 2021). The Hf isotopic composition of a zircon grain, similarly to whole-rock Nd isotopic composition, is commonly used to determine the mantle and/or crustal contribution in the melt source (*e.g.*, DePaolo, 1981; Dhuime et al., 2011; Bauer et al., 2020). Indeed, crust has a lower Lu/Hf ratio than the mantle and accumulates less radiogenic ^{176}Hf, resulting in a lower εHf signature (Gardiner et al., 2018; Spencer et al., 2020). At a regional scale, arrays of decreasing εHf and εNd values with time may suggest repeated crustal reworking that traces back to a single episode of mantle extraction, often referred as model age of crust formation (T_{DM}; *e.g.*, Blichert-Toft and Albarède, 2008; Henderson 2016). εHf signatures may also reflect new mantle inputs and mixing between several sources extracted from the upper mantle at different times, detail that may be lost using whole-rock Nd data (*e.g.*, Hawkesworth and Kemp, 2006; Belousova et al., 2009; Bauer et al., 2020). $\delta^{18}O$ signature of a zircon may reflect derivation from a mantle-derived source (5.3‰ ± 0.6‰ 2σ), but also significant input in the source of rocks that experienced weathering and low-temperature alteration, *i.e.*, rocks that reached supracrustal levels prior to melting, translated through increase of the $\delta^{18}O$ signature (Valley et al., 1998, 2005; Smithies et al., 2021). On the contrary, a decrease of the $\delta^{18}O$ signature indicates contributions of rocks hydrothermally altered at high temperature.

The ≥ 2800 Ma basalts show positive εNd values, with a spread near the depleted mantle evolution line (Fig. 2-12c; Manya and Maboko, 2003; Cloutier et al., 2005; Cook et al., 2016). The mantle-like isotopic signature demonstrates (near)-direct derivation from mantle material, in agreement with their geochemical signature (section 5.1; Cook et al., 2016).

The pre- to syn-tectonic SU21 granodiorite is the oldest dated intrusive in our area, at 2751 ± 12 Ma, and shows homogeneous mantle-like signature with the lowest $\delta^{18}O$ of the studied samples (5.18 ± 0.139 ‰; Fig. 2-12d) and high εHf values, plotting near the depleted mantle array (mean: 2.25 ± 0.74; Fig. 2-12b).

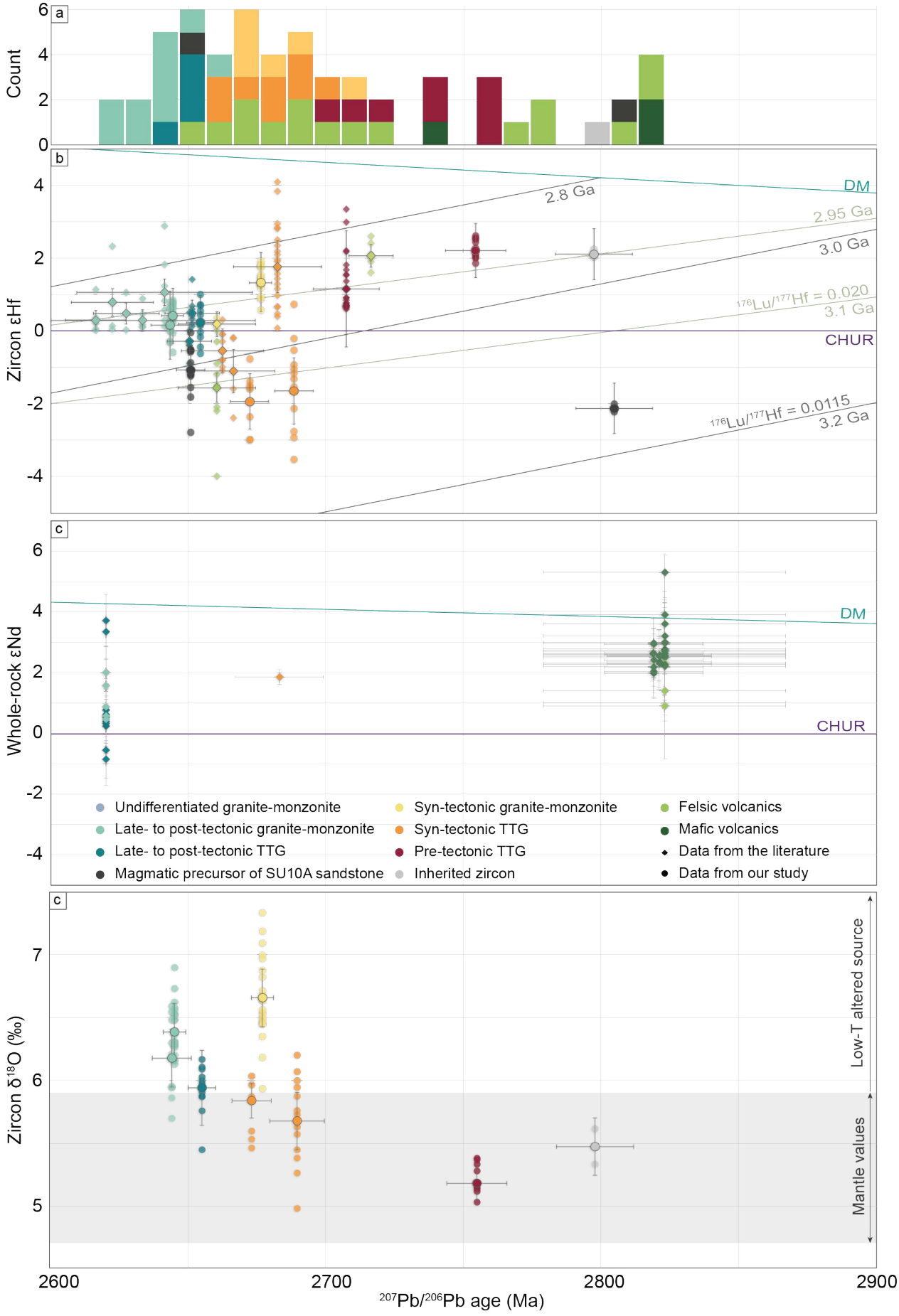
a
Count
b
Zircon εHf
DM
2.8 Ga
2.95 Ga
3.0 Ga
176Lu/177Hf = 0.020
3.1 Ga
CHUR
176Lu/177Hf = 0.0115
3.2 Ga
c
Whole-rock εNd
DM
CHUR
Undifferentiated granite-monzonite
Late- to post-tectonic granite-monzonite
Late- to post-tectonic TTG
Magmatic precursor of SU10A sandstone
Syn-tectonic granite-monzonite
Syn-tectonic TTG
Pre-tectonic TTG
Inherited zircon
Felsic volcanics
Mafic volcanics
Data from the literature
Data from our study
c
Zircon δ18O (‰)
Low-T altered source
Mantle values
207Pb/206Pb age (Ma)

Figure 2-12. a. Probability distribution plot of magmatic $^{207}Pb/^{206}Pb$ age, **b.** Zircon εHf vs age diagram, **c.** whole-rock εNd vs age diagram and **d.** zircon $\delta^{18}O$ vs age for magmatic samples of the Sukumaland granite-greenstone belt, Tanzania craton, data from this study and literature (Borg and Krogh, 1999; Manya and Maboko, 2003, 2008b; Cloutier et al., 2005; Maboko et al., 2006; Chamberlain and Tosdal, 2007; Sanislav et al., 2014, 2018b; Cook et al., 2016; Kwelwa et al., 2018; Wu et al., 2023). The ages correspond to the average of magmatic samples. Error bars represent 95 % confidence interval (ages) and 2SD (εHf, εNd and $\delta^{18}O$). In the zircon εHf vs age diagram is shown the SU10A Kavirondian sandstone.

In the literature, two trondhjemites formed prior to 2700 Ma were isotopically constrained in the SGGB, yielding similarly elevated εHf means of 1.35 ± 0.23 and 2.12 ± 0.11 (Fig. 2-12b; Kwelwa et al., 2018; Wu et al., 2023). All three TTGs fall between the ca. 3000 and 2800 Ma crustal evolution lines, meaning that pre-tectonic magmatism resulted from the melting of an isotopically juvenile source, similarly to the mafic magmatism at ca. 2820-2800 Ma. The ca. 2800 Ma inherited zircon from the syn-tectonic SU06 granodiorite follows a similar crustal evolution trend and mantle-like O signature (Fig. 2-12b and d).

Between 2700 and 2660 Ma, two trends can be highlighted from our samples and the literature. SU15 monzogranite and most pre- to syn-tectonic TTG rocks from the literature show positive or near zero εHf and positive εNd values, falling along the same crustal evolution trends as the pre-tectonic intrusives and the ca. 2820-2800 Ma mafic volcanics (Fig. 2-12b-c; Maboko et al., 2006; Sanislav et al., 2014; Kwelwa et al., 2018; Wu et al., 2023). SU15 also yields a $\delta^{18}O$ signature well above the pre-tectonic SU21 signature and the mantle value range, marking the onset of reworking of rocks that reached supracrustal levels (Fig. 2-12d; Valley et al., 1998, 2005; Smithies et al., 2021).

SU04 and SU06 granodiorites show a large spread of much lower εHf and $\delta^{18}O$ values compared to SU15 monzogranite (Fig. 2-12b and d). Similar low εHf values are also recorded in a granodiorite and a tuff sampled in the Geita region (Fig. 2-12b; Kwelwa et al., 2018). While most zircon oxygen isotope analyses and the $\delta^{18}O$ means of SU04 and SU06 fall within the mantle value range, they still show an increase relative to the SU06 inherited zircon and SU21 values, potentially from the mixing of at least two sources, one with a mantle-like signature and another with a supracrustal signature. Combined with the εHf signature, the isotopic signature of both granodiorites underscores significant recycling of matured ancient crust with long crustal residual time (*e.g.*, Dong et al., 2017). The presence of the SU06 inherited zircon falling on the same crustal evolution trend as the mafic rocks and most of the pre- to syn-tectonic intrusives indicates that the SU04 and SU06 granodiorites resulted from mixing between the Neoarchean juvenile crust and older crustal component.

After 2660 Ma, the granodiorites and granites from the northern SGGB show near zero εHf values, falling once again along the same crustal evolution trend as most magmatic rocks from the area (Fig. 2-12b). Furthermore, their $\delta^{18}O$ signature is slightly above the mantle values (Fig. 2-12d). The late- to post-tectonic intrusives therefore resulted from the ongoing reworking of the juvenile crust formed from the ca. 3000-2800 Ma mantle-upwelling magmatism.

In summary, crustal growth in the northern SGGB evolved from a mantle-upwelling episode and mafic-dominated magmatism prior to 2800 Ma, to purely crustal reworking after 2780 Ma of the magmatic rocks formed from this mantle plume. After 2700 Ma, shifts in Hf and O isotopic signatures of the granitoids mark the onset of reworking of rocks that reached supracrustal levels and of much older crust component. Based on the overall scarce magmatic dataset in the SGGB, the shift from mantle-derived to purely crustal magmatism cannot be precisely dated. Similarly, the lack of analytical data for the period between 2750 and 2690 Ma prevents us from constraining the onset of supracrustal reworking.

5.3. Inputs from the U-Pb-Hf detrital record: Eo- to Neoarchean crustal growth and reworking

The syn-sedimentation tectonic setting of the Kavirondian molasse basins can be deduced based on the age spectrum of the detrital record (Cawood et al., 2012). The large basin in which were sampled SU11 and SU20 sandstones shows a widespread range of zircon ages (between 3820 and 2680 Ma), of which more than 55 % of them are older than the regional magmatic history, *i.e.*, the SGGB (between 2820 and 2620 Ma; Fig. 2-10a). A short period of time is observed between the youngest zircon dated (ca. 2680 Ma) and the age of sediment deposition (prior to 2660 Ma; see Chapter III), concluding to sedimentary deposition in a collisional setting (Cawood et al., 2012).

The detrital zircon ages offer a broad snapshot of Eo- to Neoarchean magmatism throughout the region that surrounded the SGGB at ca. 2700 Ma. Their U-Pb-Hf isotopic signatures highlight several episodes of magmatism and crustal growth and reworking (Fig. 2-10b). The oldest crustal trend (3820-3340 Ma, n = 6 analyses) show mantle-derived magmatism around 3800 Ma, followed by crustal reworking with low εHf values (down to -4.9 at 3340 Ma). Then, almost continuous juvenile magmatism is recorded between 3350 and 2800 Ma by the detrital record, as well as overlapping evolution crustal trend, with εHf ranging from ~ 4.3 to ~ - 5.5. The peak of magmatism is recorded around 2900 and 2820 Ma (Fig. 2-10a). The end of mantle-derived magmatism is marked by a shift in the detrital εHf signature to purely crustal evolution trend ($^{176}Lu/^{177}Hf$ = 0.0115) at 2800 Ma.

Investigating the detrital zircon provenance is out of the scope of this study, yet some observations can be made. The wide and old detrital population from SU11 and SU20 sandstones was never dated before in the Lake Victoria Goldfields (Sanislav et al., 2018b). The zircon population predominantly comprises well-rounded grains consistent with long transport before deposition in the Kavirondian basin (Fig. 2-5h). Eo- to Neoarchean detrital zircon grains were sampled in the Central Tanzania Region (CTR) of the craton, as old as 4020 Ma and could be a first potential source of the basins (Fig. 2-1; Kabete et al., 2012; Thomas et al., 2016). However, a hiatus of ages between 3450 and 2930 Ma in the RTC does not match with our dataset, and could either be explained by an absence of magmatism in the region or by the too scarce geochronological dataset collected in the RTC. Then, the studied Kavirondian basin is located a few tens of kilometers south of the Lake Victoria, under which Archean crust is inferred. Finally, the basin is located 130 km east of the western border of the Tanzania craton and of the Kibaran Paleoproterozoic mobile belt (*e.g.*, Begg et al., 2009). All of these crustal segments are potential sources of the syn-tectonic Kavirondian basins. No study has yet investigated the surrounding crust that may have lied west of the SGGB at 2700 Ma, prior to the events that formed the Proterozoic belt.

The smaller basin sampled in the studied area, SU10A, presents monogenic conglomerates and biotite-bearing sandstones with angular quartz clasts and sigmoidal crossbeds (Fig. 2-5e). The zircons from the sampled population are very angular (Fig. 2-5g). All of these observations reflect short distances between erosion and sedimentation, via small alluvial fans and talus slopes (Krapez et al., 2000; Sanislav et al., 2018b; Masurel et al., 2022). Furthermore, they appear to come from a single granitoidic source as only one population of detrital zircon was retrieved (2651 ± 5 Ma, n = 20), apart from one single older zircon that can be interpreted as an inherited zircon (2805 ± 14 Ma, n = 2). SU10A sandstone was sampled a few hundreds of meters away from the late-tectonic SU10B granodiorite, dated at 2655 ± 5 Ma (Fig. 2-3). We can therefore postulate that SU10A sandstone is monogenic and resulted from the erosion of the late-tectonic intrusive surrounding the sediment, and its zircon U-Pb-Hf isotopic analyses reflect the isotopic signature of this magmatic precursor. SU10A magmatic precursor yields heterogenous εHf values, with a similar range to

the SU04 and SU06 granodiorites (Fig. 2-12b). The inherited zircon from the SU10A precursor yields an age of 2805 ± 14 Ma and a low εHf values, falling on a crustal evolution trend with a model age approximating 3150 Ma (Fig. 2-12b). The lowest εHf values of SU04 and SU06 zircon grains also follow this trend that is considered a strong argument favoring the mixing of sources with input of much older crust during crustal growth of the Neoarchean crust in the SGGB.

5.4. Geodynamic implications for the Archean crustal growth in the northern Sukumaland granite-greenstone belt

In the Tanzania craton, crustal growth scenarios have been proposed and discussed in the past. Notably, Sanislav et al. (2018b) proposed a thick oceanic plateau subsequently affected by subduction as the driver of crustal growth in the Lake Victoria Goldfields. However, the region has not undergone the same attention as some other Archean cratons such as the Yilgarn, Pilbara, North China, Dharwar or the Superior, and the geochemical and isotopic datasets remain fragmentary (*e.g.*, Jayananda et al., 2018; Hawkesworth and Kemp, 2021; Mole et al., 2021; Diwu et al 2024; Schreefel et al., 2024). In this section, we propose to review the characteristics of the magmatic episodes of the northern SGGB, based on magmatic and detrital records, and discuss if they fit into tectonic models driven by crustal drip (squishy lid tectonics) or subduction-like processes (mobile lid tectonics; see Cawood et al., 2022 and references therein). To do so, we combine geochemical constraints on the source and depths of melting (described in section 5.1; Fig. 2-13d) with the evolution in time of the Hf-Nd-O isotopic signatures of the magmatic rocks (described in section 5.2; Fig. 2-13a-b).

5.4.1. 2820-2700 Ma: mantle-plume and oceanic plateau environment

In the northern SGGB, mafic crust is extracted from (near)-direct derivation of the depleted mantle between 2820 and 2800 Ma (Fig. 2-13a; Manya, 2004; Cloutier et al., 2005; Manya and Maboko, 2008b; Boniface and Mruma, 2012; Cook et al., 2016; Kwelwa et al., 2018). The geochemical and isotopic signature of the basalts is characteristic of Archean mantle plume systems (Bédard, 2018; Moyen and Laurent, 2018). Basalts and ultramafic rocks are accompanied by the sedimentation of BIF, the primary juvenile crust was therefore formed in a submarine oceanic plateau setting.

A progressive crustal contamination trend of the basalts is unlike modern-day trends and reflects thickening of the submarine mafic plateau, ultimately leading to the burial and partial melting of the newly formed juvenile mafic crust (Fig. 2-11; Moyen and Laurent, 2018; Smithies et al., 2018; Mole et al., 2019, 2021). Mafic crust typically melts at depths above 20 to 45 kilometers (Johnson et al., 2017; Wiemer et al., 2018) and Hayman et al. (2015) demonstrated that 45-kilometer-thick basalt-komatiite formations in the Yilgarn craton can form in only 30 Ma. Between 2820 and 2800 Ma, partial melting of the mafic crust in the northern SGGB can therefore be reasonably interpreted from a mantle plume activity leading to thickening of an oceanic plateau and burial of the juvenile crust (*e.g.*, Bédard et al., 2012; Mole et al., 2019).

Between 2800 and 2700 Ma, the Nd-Hf-O isotopic signature of pre-tectonic TTGs and the SU06 inherited zircon demonstrates a juvenile origin, with source rocks that did not reach supracrustal levels prior to melting (mantle-like $\delta^{18}O$), in other words, no evidence of subducted component (Fig. 2-13a-b). Geochemical

proxies indicate that a mafic crust melted at high depth (Fig. 2-13d). The partial melting of mafic crust at the root of a thickened plume-related oceanic plateau at depth high enough to stabilize garnet has been shown to generate similar high-depth TTGs (Smithies et al., 2009; Pourteau et al., 2020; Johnson et al., 2017). The ongoing activity of a mantle plume is generally inferred to explain the high heat required for the melting of the crust (*e.g.*, Vandenburg et al., 2023; Liu et al., 2024).

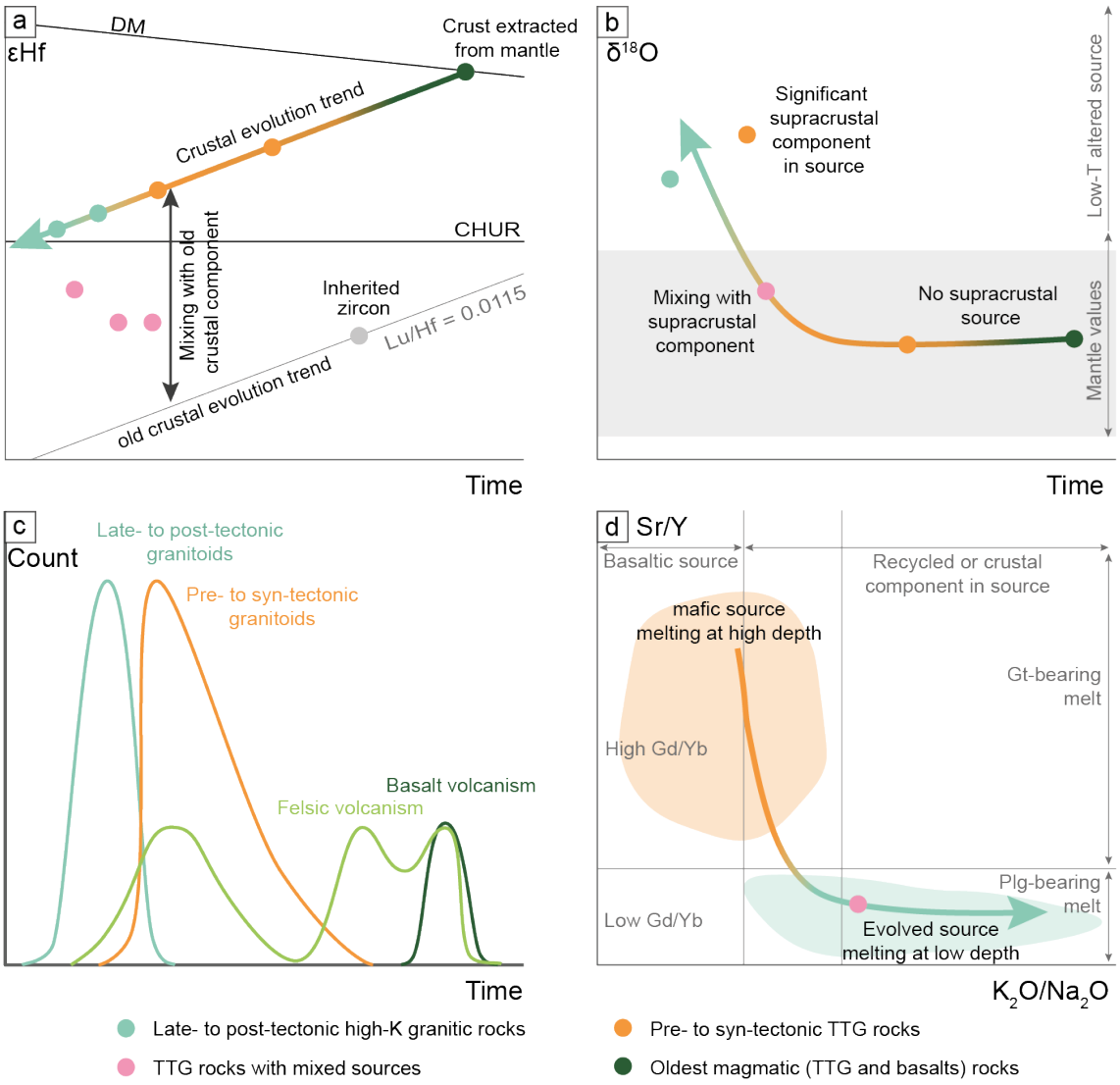

Figure 2-13. Schematic evolution of the Lu-Hf, O isotopic and Sr/Y, K_2O/Na_2O geochemical trends of the magmatic record from the northern SGGB. **a.** Mafic crust was extracted from the mantle and progressively reworked along a crustal evolution trend. Pink dots show mixing between the juvenile crust and an older crustal component. **b.** The crust was originally sourced from rocks with a mantle $\delta^{18}O$ signature. Then, a progressive increase of values indicate inputs of rocks that reached supracrustal levels prior to melting. **c.** Evolution of zircon $^{207}Pb/^{206}Pb$ age from magmatic rocks. **d.** Evolution from pre- to syn-tectonic intrusives formed from a mafic source melted at high depth, to late- to post-tectonic intrusives formed from an evolved source melted at low depth.

Such scenario implies the activity of a mantle plume at least between 2820 and 2750 Ma (youngest mantle-like $\delta^{18}O$ signature), which would be unlikely in the Phanerozoic (Condie, 1998), yet such long-lived plumes have been discussed in the Archean (Bédard, 2006). The detrital Hf signature show no mantle-derived magmatic record after 2800 Ma, indicating that mantle-plume magmatism ceased at ca. 2800 Ma, making unlikely a long-lasting mantle-plume activity. An alternative would be the onset of dripping process or delamination,

which would explain the absence of new mantle-derived magmatism, the high Sr/Y, Gd/Yb, low K_2O/Na_2O and mantle-like $\delta^{18}O$ of TTGs, as well as the Hf-Nd crustal evolution trend after ca. 2800 Ma (*e.g.*, Bédard et al., 2003; Mole et al., 2019, 2021). However, drips and crust delamination eclogitized the mantle and led to sanukitoid-like magmatism that are is yet observed in the SGGB between 2800 and 2750 Ma (Nebel et al., 2018; Mole et al., 2019). In light of the scarce geochemical and isotopic dataset between 2800 and 2700 Ma in the SGGB, the tectonic setting of that time period remains highly uncertain, with evidence that favor processes involving dripping or delamination of the crust and no evidence for subduction-like tectonics.

5.4.2. 2700-2660 Ma: hints of subduction-like processes?

TTG generation involves the melting of tholeiitic and mafic rocks at various depths (Rapp et al., 1991; Halla et al., 2009; Moyen and Martin, 2012; Laurent et al., 2014; Moyen and Laurent, 2018). In light of their geochemical signature, they are considered to form in various tectonic settings, including subduction-like processes with subducted oceanic slabs or plateaus (Martin and Moyen, 2002; Martin et al., 2014; Hastie et al., 2016), crustal drips resulting from the convection of asthenospheric mantle (François et al., 2014; Moyen and Laurent, 2018; Nebel et al., 2018; Mole et al., 2019), melting at the base of an overthickened oceanic plateau (Bédard, 2006), often implying delamination at the base of the crust (Bédard et al., 2003; Moyen, 2011; Johnson et al., 2014). In the northern SGGB, a subduction above a thick oceanic plateau is proposed as the driver of TTG magmatism between 2700 and 2660 Ma (Sanislav et al., 2018b). In light of our compiled dataset in the SGGB and the new data presented here, we discuss suitable tectonic settings for the evolution of the continental crust in the northern SGGB between 2700 and 2660 Ma. The syn-tectonic granitoids can be subdivided into three groups based on their geochemical and isotopic signatures: high-Sr/Y TTGs and sanukitoids discussed in this sub-section, low-Sr/Y TTGs that will be the focus of sub-section 5.4.3.

The interaction between the Archean primitive mantle and an eclogitized sinking mafic crust results in a mantle peridotite, metasomatically enriched in incompatible elements (e.g., Laurent et al., 2014). Subsequently, hydrous melts are generated from this hydrated/metasomatized mantle, in particular sanukitoid melts (Bédard, 2018). The emergence of sanukitoid igneous rocks therefore marks changes in the tectonic setting with the introduction of hydrated mafic crust into the mantle (Laurent et al., 2014; Bédard, 2018; Cawood et al., 2018; Nebel et al., 2018; Moreira et al., 2020). This transition is observed in the syn-tectonic magmatic record in the northern SGGB, between 2700 and 2660 Ma. Intrusives (high-Sr/Y TTGs and sanukitoids) were sourced from the melting of a hydrated mafic crust at high depth, resulting in amphibole- and magnetite-bearing TTGs and sanukitoid-like granitoids (Fig. 2-13d). The generation of sanukitoids are described in various tectonic contexts. In subduction-like processes, they form from the emergence of a mantle wedge by fluid circulation from the subducted crust (*e.g.*, Martin et al., 2005, 2010; Laurent et al., 2014; Mole et al., 2021). The presence of supracrustal rocks and high temperature altered crust in the slab result in significant increase or decrease of the $\delta^{18}O$ signature of the granitoids, respectively (*e.g.*, Valley et al., 1998, 2005; Van Kranendonk et al., 2015; Moreira et al., 2020; Mole et al., 2021; Smithies et al., 2021). On the other hand, asymmetric dripping and delamination of a thickened plateau can also generate sanukitoids with similar geochemical signatures (*e.g.*, Johnson et al., 2014; Nebel et al., 2018; Mole et al., 2019; Piccolo et al., 2019). However, no significant O isotope variations of granitoids are recorded in such tectonic settings (mantle-like $\delta^{18}O$; Mole et al., 2019), unless there is mixing with older crustal material, typically older felsic crust at lower levels (*e.g.*, Mole et al., 2019). In the northern SGGB, syn-tectonic granitoids were generated from the reworking of rocks that reached supracrustal levels prior to melting (high $\delta^{18}O$; Fig. 2-13b). Their source results from the reworking of juvenile material, recorded by high εHf values that fall along the same crustal

evolution trend as mafic and pre-tectonic TTGs (Fig. 2-13a). The covariance of all these characteristics favors scenarios of subduction-like processes rather than dripping and continuous crustal reworking in a thickened oceanic plateau (Laurent et al., 2014; Hastie et al., 2016; Nebel et al., 2018; Mole et al., 2021; Schreefel et al., 2024).

5.4.3. 2700-2660 Ma: older crustal material records accretion with an exotic terrane

The period between 2700 and 2660 Ma is also marked by the emergence of older, more evolved crustal material in the northern SGGB. They are recorded in the old detrital zircon-dominated Kavirondian molasse basins (SU11 and SU20; Fig. 2-10), as well as in the syn-tectonic low-Sr/Y TTGs (SU04 and SU06; Figs. 2-8, 2-9) and in the late- to post-tectonic magmatic precursor of SU10A sandstone (Figs. 2-8 to 2-12). Similar mixing between juvenile and older crustal material in igneous rocks is described in other Archean cratons. In the Yilgarn and the Superior for instance, the older crustal components are interpreted as remnants of a rifted continental crust and are recorded as early as the juvenile mantle-derived magmatism (Percival et al., 2012; Osei et al., 2021 and references therein; Mole et al., 2019, 2021). Instead, the old evolved crustal components are recorded late in the history of crustal growth in the northern SGGB, after 2690 Ma (Fig. 2-13a). Additionally, we demonstrate in section 5.3 that the syn-tectonic Kavirondian basins, deposited after 2680 Ma, developed in collisional settings (Cawood et al., 2012). Overall, these observations and interpretation not only show that the older crustal component might be sourced from an exotic terrane, *i.e.*, crustal segment that did not formed from the same magmatic events as the SGGB, that amalgamated with the SGGB around 2680 Ma, but also favor active lid tectonics with horizontal movements and therefore subduction-like processes. The southern part of the SGGB is bordered by the Central Tanzania Region in which old basement is inferred (*e.g.*, Kabete et al., 2012a, 2012b). As discussed in section 5.3, the region is a potential source for the Kavirondian old zircon grains and could also be the exotic terrane that amalgamated with the Lake Victoria Goldfields and the SGGB. The age of the Archean terranes located below the Lake Victoria are also unknown, and could also account for the amalgamated exotic terrane.

The syn-tectonic low-Sr/Y TTGs show clear mixing between at least two sources (sections 5.1 and 5.2). The SU06 inherited zircon reveals that the first source was likely the juvenile mafic crust formed at 2800 Ma (Fig. 2-12). The SU10A zircon dated at 2800 Ma was inherited from a much older and more evolved crust (Fig. 2-12). Some $\delta^{18}O$ values of these low-Sr/Y TTGs are significantly higher than the SU06 inherited zircon (Fig. 2-12d), which indicate that the older source reached supracrustal levels prior to melting. These observations point out to three most probable sources, firstly by (i) melting of older supracrustal component in the subducted slab that mixed with the lower overriding crust. However, the low Sr/Y and Gd/Yb ratios indicate low depth melting, not concordant with slab melting (*e.g.*, Moyen, 2009). Then, (ii) burial of the Kavirondian sediments that are the only known record of older crustal material in the Lake Victoria Goldfields could have reached depth high enough for their partial melting. During underplating during subduction-like processes or slab breakoff in collisional settings would heat enough the crust for its reworking (Sims et al., 1997). Yet, the TTGs are A-type and weakly peraluminous, not concordant with a derivation from sediments (Gao et al., 2016 and references therein). The generation of these low-Sr/Y TTGs that incorporated older crustal material is difficult to explain, and a third origin can be proposed: (iii) the absence of evidence of mixing trends prior to 2700 Ma is not evidence of absence (Fig. 2-13a), and can be due to the limited rock record in the northern SGGB. Mole et al. (2021) described similar low Sr/Y TTGs with clear mixing trends between mantle-derived, rift-related magmas and pre-existing Mesoarchean crust. In that hypothesis of rifting around 2800 Ma in the

northern SGGB, the source of the low-Sr/Y TTGs could be remnants of the older crust.

Finally, the period between 2700 and 2660 Ma is marked by peak of magmatism and deformation in the SGGB (Fig. 2-12a; Sanislav et al., 2015, 2016, 2018a). It also marks the shift toward potassic magmatism and low-depth melting (Fig. 2-13c-d). This change is attributed to compressional deformation with increasing crustal thickness and rigidity (Cawood et al., 2022).

5.4.4. 2660-2620: crustal anatexis and stabilization

After 2660 Ma, high-K granites become dominant. The geochemical and isotopic signatures of the late- to post-tectonic intrusives reflect partial melting of mafic to felsic sources at low depts, resulting in granodioritic to granitic compositions (sections 5.1 and 5.2). This voluminous magmatism in late Archean cratons reflects intraplate partial melting of the mid-lower crust after the amalgamation between terranes (*e.g.*, Laurent et al., 2014; Clos et al., 2019; Rowe, 2021; Rowe et al., 2022). This period of anatexis implies significant increase of temperature within the crust to produce partial melting of the TTG and mafic rocks (*e.g.*, Sylvester, 1994; Laurent et al., 2014). Such heating is generally assigned to terrane amalgamation, followed by crustal thickening and decompression of the hot lithosphere (Guo et al., 2015; Jayananda et al., 2018; Rowe et al., 2022), slab break off and sinking into the mantle, leading to mantle upwelling (*e.g.*, Heilimo et al., 2010; Jayananda et al., 2018; Sanislav et al., 2018b), or crustal delamination (Almeida et al., 2013). In the last two scenarios, large volume of sanukitoid melts are produced, contemporaneous to high-K granites, which are not recorded in the SGGB (Almeida et al., 2013; Jayananda et al., 2018). The first scenario is therefore favored.

The evolution from convergence around 2700 Ma to intraplate granitic magmatism between 2660 and 2620 is consistent with the magmatic and tectonic history of other Archean terranes and cratons such as the Eastern Goldfield and Narryer terranes in the Yilgarn craton (Czarnota et al., 2010; Rowe et al., 2022; Schreefel et al., 2024), or the south-east Superior craton (Mole et al., 2021) reflecting late Archean cratonization and stabilization of cratons (Cawood et al., 2022).

In light of these observations, (i) thickening of a submarine oceanic plateau above a mantle plume and dripping processes best explain the magmatic record between 2820 and 2700 Ma; (ii) plate tectonic and subduction-like processes may have occurred at or prior to ca. 2700 Ma, resulting in sanukitoid magmas and recycling of supracrustal rocks; (iii) collision between the SGGB and an exotic terrane with old crustal material likely happened between 2680 and 2660 Ma; (iv) intraplate plutonism between 2660 and 2620 Ma with widespread high-K granitic intrusives in response to heating of the thickened crust.

Striking similarities are observed between the northern SGGB and the Neoarchean south-east Superior craton geodynamic evolution. Similar transition from dripping to subduction-like processes is postulated by Mole et al. (2021), with similar timing: dripping process dominated crustal growth between 2750 and 2704 Ma, succeeded by subduction processes after 2704 Ma, until 2685 Ma, age of the inferred continental collision. Furthermore, the evolution of petrographic, geochemical and O-Hf-Nd isotopic data share many similarities with our dataset.

6. Conclusions

This chapter focused on the crustal growth and differentiation of the late Archean northern Sukumaland granite-greenstone belt, located in the poorly constrained Lake Victoria Goldfields Superterrane of the Tanzania craton. Our study presents the first O isotope analyses in the Tanzania craton as well as the first geochronological and isotopic study of large syn-tectonic molasse basins. Thanks to thorough petrological, geochemical, geochronological (U-Pb) and isotopic (O-Hf) studies on volcanic, plutonic and sedimentary rocks and compilation of the existing literature, key features of crustal evolution were unraveled:

- Crustal growth in the northern SGGB can be constrained between 2820 and 2620 Ma and progressively evolved from mafic magmatism derived from a primitive mantle in a mantle-plume setting (2820-2800 Ma), to pure crustal reworking at high depth of mafic rocks resulting in TTG-sanukitoid plutonism (2780-2660 Ma), to reworking of more or less evolved continental crust at low depth leading to the intrusion of potassic granitoids (2660-2620 Ma).
- Mixed isotopic signatures in several < 2700 Ma magmatic rocks indicate the incorporation of an older crustal component in their source, at low depth. The crustal material is more evolved (high K_2O/Na_2O and negative εHf) and show supracrustal-like $\delta^{18}O$ signatures. We also present the first detrital record of older crustal material in the Lake Victoria Goldfields. Sediments in large syn-tectonic molasse basins show a widespread age range, as old as 3820 Ma.
- We proposed new constraints on the geodynamic evolution of the northern SGGB, favoring mobile lid tectonics and subduction-like processes over stagnant and squishy lid tectonics. (i) thickening of a submarine oceanic plateau above a mantle plume and dripping processes best explain the mafic-TTG magmatic record between 2820 and 2700 Ma; (ii) plate tectonic and subduction-like processes may have occurred at or prior to ca. 2700 Ma, resulting in sanukitoid magmas and recycling of supracrustal rocks; (iii) collision between the SGGB and an exotic terrane with old crustal material likely happened between 2680 and 2660 Ma.

Acknowledgement

The authors are grateful to the OreCorp's team for their welcome and scientific exchanges. The authors are thankful to Denis Fougerouse who assisted with the imaging of the zircon grains, and Matvei Aleshin who assisted with the O-OH SIMS analyses. Special thanks to Bruno Dhuime for his scientific inputs. This work is part of Célestine Berthier's PhD project which benefited of a CIFRE funding, reference CIFRE n°2021/0546, attributed by the French National Research and Technology Agency (ANRT). This work was partly supported by the French PIA project "Lorraine Université d'Excellence", reference ANR-15-IDEX-04-LUE, and also benefited of the 2023 Student Research Grant – Hugh McKinstry Fund (SRG 23-94) from the Society of Economic Geology.

~

Chapter III

~

Magmato-tectonic evolution of the northern Neoarchean Sukumaland granite-greenstone belt (Tanzania): tectonic and gold-endowment implications

Article en préparation pour publication dans *Journal of African Earth Sciences*

Célestine Berthier[a,b,c,*], Aurélien Eglinger[b,d], Nicolas Thébaud[e], Alain Chauvet[c], Anne-Sylvie André-Mayer[b], Julien Feneyrol[a], Rémi Bosc[a]

[a] Arethuse Geology SARL., 29 allées Saint Jean, Fuveau 13710, France

[b] GeoRessources, Université de Lorraine, CNRS, Nancy 54000, France

[c] Géosciences Montpellier, Université de Montpellier, CNRS, Montpellier 34095, France

[d] InnovExplo Inc, 560 3e Avenue, Val d'Or QC J3P 1S4, Canada

[e] Centre for Exploration Targeting, School of Earth Sciences The University of Western Australia, WA 6009, Australia

Abstract

The Neoarchean Sukumaland granite-greenstone belt (SGGB) presents a protracted magmato-tectonic history of 80 Ma of progressive and continuous shortening. This chapter attempts to reconstruct the tectonic evolution of the northeastern SGGB, including (i) constraining the evolution of shortening and crustal flow modes, (ii) linking magmatic, sedimentary, structural, hydrothermal and metamorphic features into a coherent history, and (iii) characterizing the style of crustal shortening and thickening. In light of this magmato-tectonic model, we will examine the timing of crustal gold fertilization and concentration event(s) that ultimately led to the formation of the Nyanzaga and Kilimani gold deposits.

Detailed structural, petrographic and geochemical investigations along a 50-kilometer transect across the greenstones and surrounding granitoids of the SGGB reveal a progressive, three-stage deformation history driven by continuous horizontal shortening. Deformation evolves from vertical flattening to strike-slip crustal flow, accompanied by gradual cooling of the crust. The crustal shortening and thickening observed in the SGGB do not conform to modern-day collisional orogen style, but rather result from protracted transpression of a weak Archean-type lithosphere, consistent with the characteristics of a hot orogen.

Gold content in magmatic and sedimentary lithologies of the granite-greenstone belt provides insights into the timing of crustal fertilization episodes and potential sources for the Nyanzaga and Kilimani gold deposits. Gold fertilization was driven by magmatic processes either during the juvenile and mantle-derived mafic-ultramafic magmatic event at ca. 2820-2800 Ma, or through felsic magmatic episodes between 2780-2700 Ma and 2660-2645 Ma. Gold concentration at the Nyanzaga and Kilimani deposits is temporally disconnected from fertilization event(s), and was controlled by magmatic-hydrothermal processes dated between 2645 and 2620 Ma.

1. Introduction

A lode-gold deposit is the small-scale expression of a sequence of geological processes that occur across different temporal and spatial scales (Wyborn et al., 1994; Wyborn, 1997; McCuaig and Hronsky, 2014; Champion and Huston, 2016). This vision embodies the concept of mineral system that examines mineral deposit generation through the source-transport-trap paradigm (McCuaig et al., 2010; McCuaig and Hronsky, 2014). The first stage of the gold mineral system requires fertilization of the crust, either through magmatic or sedimentary processes (Large et al., 2007, 2011; Gaboury, 2013; Pitcairn et al., 2015; Augustin and Gaboury, 2017). Gold is then transported from its source rock to its deposition site, requiring a fluid source, appropriate ligands, gold availability, *i.e.*, solubility, permeable conduits and finally favorable mechanisms precipitating gold (Cox, 2016; Gaboury, 2019). In particular, gold extraction and fluid circulation imply specific magmatic, metamorphic and hydrothermal conditions, while ore-bearing fluid circulation requires a favorable architecture, *i.e.*, specific a tectonic setting. Understanding the gold mineral system therefore requires insights into the magmatic, tectonic, metamorphic and hydrothermal evolution of a terrane, and inversely can be used as a tracer of the tectonic evolution (Cawood and Hawkesworth, 2015; André-Mayer et al., 2024).

Accretionary orogen tectonic styles are greatly influenced by the thermal state of the lithosphere, hence its rheology (England and Bickle, 1984; Jackson, 2002; Cagnard et al., 2006; Chardon et al., 2009). Heating of the latter can happen in various contexts, generally described in Precambrian accretionary orogens or magmatic arcs (*e.g.*, Chardon et al., 2009, 2020; Mvondo et al., 2017; Perchuk et al., 2018; Traore et al., 2022), but also in orogenic plateaus, mature collision zones, Cordilleras or back arc domains (Chardon et al., 2009, 2011). In particular, the overall temperature of the mantle has strongly evolved during geological times, and its progressive cooling over time is interpreted as the main trigger of onset of subduction processes and plate tectonics (Labrosse and Jaupart, 2007; Herzberg et al., 2010; Cawood et al., 2018). In cold, modern-day collisional orogens, shortening is expected to lead to strong strain localization along thrust systems and high relief building (*e.g.*, Davy and Cobbold, 1991; Guillot et al., 1995, 2003; Pilia et al., 2023).

In the Archean, hot and weak lithospheres favors large-scale homogeneous deformation accompanied by ubiquitous transpressive shear zones and little crustal thickening (Davis and Maidens, 2003; Chardon et al., 2009). The resulting architecture of the Archean granite-greenstone terranes typically forms dome-and-keel structures, where alternating domes, with granitoidic rock cores, are surrounded by denser mafic volcanic and sedimentary rocks, forming basin-like keels (Suess, 1875; Kusky et al., 2018). Geodynamically, the Archean dome-and-keel architecture may be interpreted through vertical tectonism, *e.g.*, sagduction, driven by density contrast with solid-state diapirs ascending and coeval sinking of the greenstone sequences, well exemplified by the Eastern Pilbara craton (Ramberg, 1967; Weinberg and Podladchikov, 1995; Van Kranendonk et al., 2015). However, most Archean terranes do not fit with the tectono-metamorphic constrains of such vertical tectonics. Alternative models propose to apply the accretionary orogeny model and adapt them to the Archean thermal regime (Choukroune et al., 1995; Chardon et al., 2009; Mvondo et al., 2017; Traore et al., 2020). Deformation accommodated by both horizontal and vertical kinematics, *i.e.*, lateral flow (Bouhallier et al., 1995; Choukroune et al., 1995; Vanderhaeghe and Teyssier, 2001; Cagnard et al., 2007; Duclaux et al., 2007; Chardon et al., 2009). These models first introduced by Chardon et al. (2009) are subdivided into ultra-hot, hot and mixed-hot orogens.

Examining the mechanisms of crustal growth and thickening provides a framework within which the timing of crustal gold fertilization and concentration can be ultimately constrained. Such approach will be followed

in this chapter, focusing on the northeastern section of the Neoarchean Sukumaland granite-greenstone belt (SGGB), in the Lake Victoria Goldfield Superterrane, Tanzania craton (Figs. 3-1, 3-2). A 50 kilometer-long transect was conducted across the supracrustal units and associated granitoids of the SGGB. Detailed macroscopic- and microscopic-scale petro-structural analyses are coupled with the geochronological results from Chapter II, enabling to reconstruct the crustal flow modes and the magmato-tectono-metamorphic evolution of the northeastern SGGB over the 80-Ma-long deformation history. This study will provide direct hints on the tectonic styles of crustal growth and thickening during the protracted deformation history of the SGGB. Finally, the addition of whole-rock gold content geochemical analyses on granitoids and supracrustal units ultimately enable delineating the timing of crustal gold fertilization and concentration.

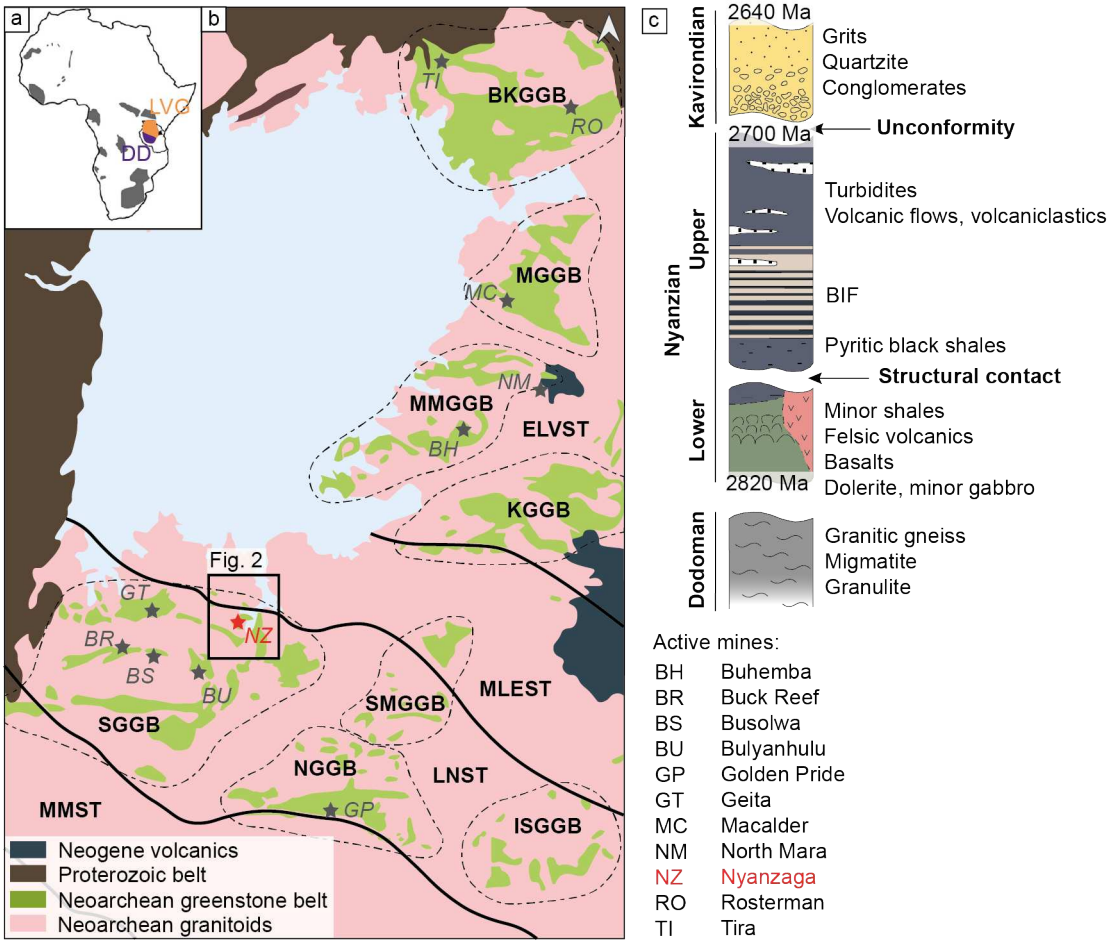

Figure 3-1. a. Present-day location of the Tanzania Craton within the African continent. Orange = Lake Victoria Goldfields, Purple = Dodoman Domain. **b.** Location of the Sukumaland granite-greenstone belt and of the transect, Lake Victoria Goldfields (from Cook et al., 2016, after Borg and Shackelton, 1997). Bold black lines represent super-terrane boundaries as proposed by Kabete et al (2012): ELVST = East Lake Victoria, MLEST = Mwanza Lake Eyasi, LNST = Lake Nyanza, MMST = Moyowosi-Manyoni. Black dotted lines represents the main granite-greenstone belts: ISGGB = Iramba Sekenke, KFGGB = Kilimafedha, MMGGB = Musoma-Mara, NZGGB = Nzega, SGGB = Sukumaland , SMGGB = Shinyanga-Malita. grey stars represent the principal gold deposits. Nyanzaga gold project is highlighted with a red star. **c.** Lithostratigraphic sequence of the LVG (from Kwelwa et al., 2018; Sun et al., 2018).

2. Geological setting (adapted from Chapter V)

The Meso- to Neoarchean Tanzanian craton, located in east-central Africa (Fig. 3-1a), consists of two superterranes: the Lake Victoria Goldfield (LVG) to the north and the Dodoman Belt in the south (Fig. 3-1a; Borg and Shackleton, 1997; Kabete et al., 2012; Kwelwa et al., 2018). The LVG is dominated by W- to NW-trending syn- to late-tectonic granitoids and paragneissic rocks, intercalated with W- to NW-trending, complexly folded greenstone belts of Neoarchean age, showing apparent heterogeneous gold distributions, *e.g.*, the highly endowed Sukumaland granite-greenstone belt (SGGB) hosting the world-class Geita deposit and the currently barren Kilimafedha granite-greenstone belt (Fig. 3-1b; Borg and Shackleton, 1997; Kwelwa et al., 2018). The stratigraphy of the LVG is divided into the Nyanzian and Kavirondian Supergroups (Fig. 3-1b; Borg, 1992; Sanislav et al., 2015; Kwelwa et al., 2018). The older Nyanzian Supergroup spans over 120 Ma of volcanic activity and sedimentation and is subdivided into Lower and Upper Groups. The Lower Nyanzian is dominated by mafic volcanics, *e.g.,* basalt, dolerite, and minor felsic volcanics and shales (Manya and Maboko, 2003, 2008) in which the oldest mafic volcanics have been dated at ca. 2823 Ma (Cook et al., 2016). They formed in a marine environment, either in an island arc setting or an oceanic plateau (*e.g.*, Chamberlain, 2003; Cook et al., 2016). The Upper Nyanzian consists of a well bedded turbiditic sequence interlayered with chert-sediment intercalations, banded iron formations (BIF) and pyritic black shales, with felsic volcanic and volcaniclastic intercalations (Quennell et al., 1956; Borg and Krogh, 1999). They are interpreted to have formed either in arc and back-arc setting (Chamberlain, 2003) or by initiation of subduction under an oceanic plateau (Sanislav et al., 2018b). The Nyanzian Supergroup underwent metamorphism, most often up to the greenschist facies and reaching the amphibolite facies near granitic intrusions. Conglomerates, quartzite sandstone, sandstone and siltstone of the Kavirondian Supergroup deposited between ca. 2450-2762 Ma unconformably overly the Upper Nyanzian Supergroup (Gabert, 1990; Borg, 1992; Sanislav et al., 2015). They are interpreted as molassic post-tectonic basins.

Six granite-greenstone terranes have been identified in the Tanzanian portion of the LVG (black dotted lines in Fig. 3-1b; Borg and Krogh, 1999). The Sukumaland granite-greenstone belt is the largest and most gold-endowed of all greenstone belts in the LVG, hosting some world-class deposits (Fig. 3-1b; i.e., Geita and Bulyanhulu deposits, Sanislav et al., 2014b, Chamberlain, 2003, respectively). The belt is dominated by the Nyanzian meta-volcanosediments, flanked by syn-accretionary to post-tectonic granitoid of tonalite–trondhjemite–granodiorite (TTG) affinity (Sanislav et al., 2015; Henkel et al., 2016; Kwelwa et al., 2018; Sanislav et al., 2018b). Extensive work has been undertaken in the northwestern part of the SGGB, around the world-class Geita gold deposit, revealing a protracted, multiphase metamorphic-deformation history consisting of eight events, grouped into three tectonically distinct phases, named Event I to III (*e.g.,* Borg and Shackleton, 1997; Kabete et al., 2012; Henckel et al., 2016 and references therein; Dirks et al., 2022).

- Event I (2820-2700 Ma) corresponds to a phase of accretion with the formation of large volumes of volcanosedimentary rocks and granitoids emplacement in an extensional regime (Cook et al., 2016; Sanislav et al., 2018a; Mshiu and Maboko, 2022). Event I is characterized by listric normal faulting, layer-parallel shearing and intrafolial folding of chert layers (Sanislav et al., 2014, 2018a; Dirks et al., 2022 and references therein);
- During Event II (ca. 2700-2660 Ma), generally N-S to NW-SE or NE-SW compression folded the previously accreted rocks (Kabete et al., 2012; Dirks et al., 2022 and references therein). Folding during Event II is often described as polyphase, involving up to five folding and refolding sub-events, associated with co-lateral? ductile shearing (*e.g.,* Sanislav et al., 2016; Dirks et al., 2022). Late in

Event II, ductile-brittle shear zones and brittle strike-slip faults are interpreted to offset the folds (*e.g.,* Kabete et al., 2012; Sanislav et al., 2016);

- Lastly, the compression is transposed into a NW-SE extension during Event III (2660-2620 Ma), reactivating shears and faults (*e.g.,* Borg, 1994; Kabete et al., 2012; Dirks et al., 2022 and references therein).

A recent work undertaken by Berthier et al. (2024) (Chapter V) at the Nyanzaga and Kilimani gold deposits proposed a progressive deformation evolution of three stages, named D_{1a}, D_{1b} and D_{1c}. Progressive folding and refolding under ductile conditions is described during D_{1a} and D_{1b} stages under N-S compression to transpression, followed by a brittle N-S transpression forming a network of NW-oriented dextral, NE-oriented sinistral and N-oriented normal-sinistral strike-slip faults hosting the gold mineralization.

3. Sampling and Methods

A 50 km-long transect across supracrustal rocks and surrounding granitoids of the SGGB was conducted in the area of the Nyanzaga gold deposit (Fig. 3-2a). A field map was developed using field observations, microstructural analysis, satellite imagery (Bing, Landsat 8+), and aeromagnetic data, which cover only the supracrustal rocks of the greenstone belt. Significant inputs from district-scale OreCorp Ltd. mapping improved our map (McIntyre, personal communication). Note that no structural data was available in the literature in the transect area. A three-dimensional cross-section was created based on petro-structural observations (Fig. 3-2b). Plane orientations are written as "strike-dip" (*e.g.*, 026-77) with strike defined by the right-hand-rule convention. Lineations are written as "dip/dip direction" (*e.g.*, 81/075).

A total of thirty-eight outcrops were visited, mainly in the granitoids scattered both north and south of the greenstone belt, but also in the supracrustal rocks (Fig. 3-2a). Twenty-four of them were sampled for further petrographic investigation (Table 3-1). Twenty-two polished thin sections were made and studied using optical microscope with transmitted and reflected light (GeoRessources laboratory, Université de Lorraine). Further observations were undertaken using a scanning electron microscope (SEM) in backscattered electron (BSE) and energy-dispersive (EDS) modes (GeoRessources laboratory, Université de Lorraine).

The paragenetic sequence of hydrothermal and metamorphic stages, presented in Figure 3-8, is derived from mineralogy and the observed relationships between shearing, fracturing, veining, and hydrothermal alteration along the transect. The upper section shows the distribution of hydrothermal alteration and metamorphic minerals, while the lower section details the evolution of hydrothermal vein mineralogy.

This work also relies on whole-rock geochemical and U-Pb geochronological analyses conducted on seven plutonic and three sedimentary samples, detailed in Chapter II. The zircon U-Pb ages for these ten samples are visible in Figure 3-2a and summarized in Table 3-1. Furthermore, whole-rock gold content of nineteen samples were determined by fire assay and inductively coupled plasma atomic emission spectroscopy analysis, with a limit of detection of 0.5 ppb (ALS Laboratory, Sevilla, Spain). Sample preparation is detailed in Supplementary Material 2-1 in Chapter II.

Outcrop ID	Easting ; Northing (°)	Brief description	U-Pb dating (Chapter II)
SU01	32.97124; -2.70051	Syn-tectonic granodiorite	
SU04	32.77989; -2.69165	Syn-tectonic quartz-monzonite	2673 ± 7 Ma
SU05	32.85159; -2.74236	Late-tectonic granite	
SU06	32.83957; -2.80347	Syn-tectonic granodiorite	2689 ± 7 Ma Inherited 2798 ± 14 Ma
SU08	32.82629; -2.84028	Syn-tectonic gneissic granodiorite	
SU09	32.63172; -2.82656	Late-tectonic granodiorite	
SU10A	32.65364; -2.85736	Upper Kavirondian sandstone	2808 – 2627 Ma
SU10B	32.65364; -2.85736	Late-tectonic granodiorite	2655 ± 5 Ma
SU11	32.68163; -2.89256	Lower Kavirondian sandstone	3820 – 2700 Ma
SU12	32.71298; -2.99151	Upper Nyanzian BIF	
SU15	32.63737; -3.04272	Syn-tectonic granodiorite	2677 ± 4 Ma
SU16	32.67462; -3.10722	Post-tectonic granite	2645 ± 4 Ma
SU17	32.75174; -3.09065	Late-tectonic granodiorite	
SU18	32.59221; -3.00858	Pre-tectonic granodiorite	
SU19	32.65824; -3.03665	Talc ultramafic rock – artisanal mine site	
SU20	32.79825; -2.90777	Lower Kavirondian sandstone	3568 – 2680 Ma
SU21	32.79217; -2.91425	Pre-tectonic granodiorite	2755 ± 11 Ma
SU25	32.75594; -2.85595	Post-tectonic monzogranite pegmatitic dykes	2644 ± 7 Ma
SU26	32.82824; -2.84293	Late-tectonic granodiorite dyke and Qz-Py vein	
SU29	32.73947; -2.83001	Syn-tectonic granodiorite	
SU31	32.74072; -3.04956	Felsic volcanic rock	
SU32	32.73719; -3.04956	Felsic volcanic rock and D_{1b} vein stockwork	
SU36	32.77322; -3.06419	Late-tectonic granodiorite	
SU38	32.73785; -3.05155	Felsic volcanic rock and D_{1b} vein stockwork	

Table 3-1. Geographic coordinates (WGS84) and brief description of the key outcrops discussed in the text. Zircon U-Pb ages are reported as described in Chapter II. See Fig. 3-2a for location of the samples.

4. Results

Three deformation stages were defined based on the petro-structural investigation detailed in this section. They are named D_{1a}, D_{1b} and D_{1c} and are related to periods of magmatism, sedimentation, folding, shearing, veining and circulation of gold-bearing fluids succeeded and overlapping one another. In this study, phases will refer to discrete and tectonically distinct deformations, *i.e.*, polyphase deformation; stages will be considered as resulting from progressive deformation; events will be independent of interpretation regarding polyphase versus progressive deformation (Fossen et al., 2019; Oriolo et al., 2022).

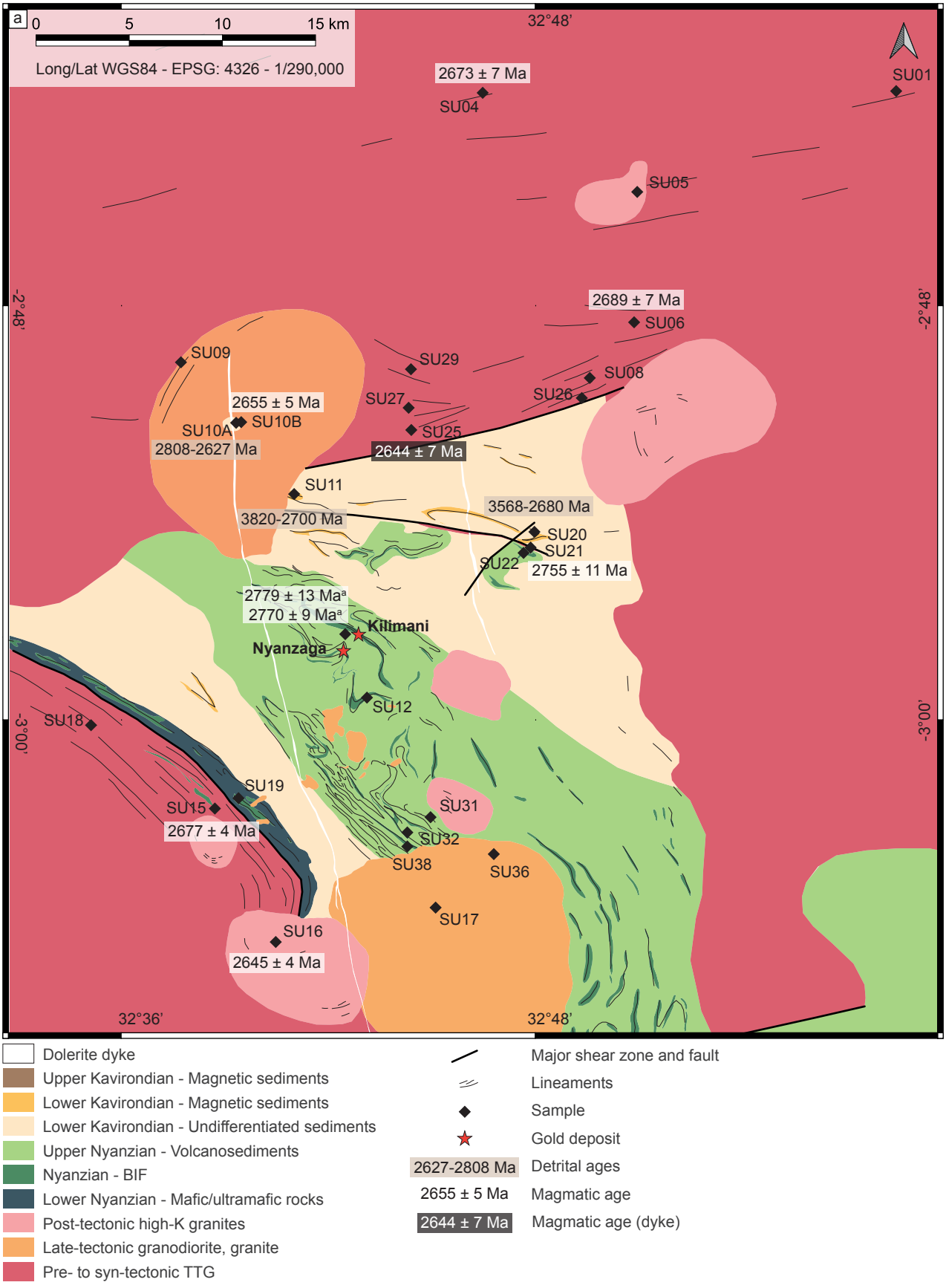

Figure 3-2. a. Location of samples from the transect across the Sukumaland granite-greenstone belt (SGGB). Zircon U-Pb dating are presented. [a]: Zircon U-Pb dating of felsic volcaniclastics from Chamberlain and Tosdal (2007).

Furthermore, the ductile and brittle nature of structures is based on macro-scale observations. Because such terms are scale sensitive, they may not fit micro-scale observations (Rutter, 1986; Snoke et al., 1998; Perret et al., 2021). In other terms, a brittle structure may present at the microscopic scale features considered to develop under ductile conditions.

4.1. Lithological framework

Lithologies observed along the transect are variably deformed and metamorphosed. In particular, the intrusives are classified as pre-, syn-, late- or post-tectonic based on their relative timing with the main, penetrative D_{1a} deformation stage in the studied area. The lithological framework of the along the studied transect can be subdivided into three types: the metamorphosed supracrustal rocks that form the greenstone belt (Nyanzian Supergroup), clastic sediments formed from the erosion of the greenstone belt and granitoids (Kavirondian Supergroup), and a large variety of intrusive rocks found on both sides of the greenstone belt, as well as intruding it. Although all these intrusives exhibit metamorphism, *e.g.*, chloritization of biotite, the prefix "meta-" has been omitted for readability. Because not all sedimentary and volcanic rocks are metamorphosed, the prefix will be kept for supracrustal lithologies.

4.1.1. Meta-volcanosediments of the Nyanzian Supergroup

The greenstone sequence in the transect area comprises alternating volcaniclastic and sedimentary units, metamorphosed, highly folded, and host of gold mineralization (Figs. 3-1c, 3-3a-b, 3-4a). From bottom to top, the lithological assemblage is composed of:

- Alternating mafic to ultramafic rocks and banded iron formations (BIF) of the Lower Nyanzian Supergroup found in the southern part of the Sukumaland greenstone belt. Poor outcropping and the activity of artisanal miners hindered detailed study of this lower section of the stratigraphic sequence. Along the southern sheared boundary with granitoids, fine-grained meta-sediments were observed in association with BIF, exhibiting strong talc alteration, indicative of a possible ultramafic origin.
- Upper Nyanzian meta-volcanosedimentary sequence forming the majority of the belt and consisting of cherts, BIF, mudstones, sandstones, tuffs and felsic volcaniclastics (Fig. 3-3a-b). These rocks have generally undergone metamorphism to the greenschist facies, with common chlorite and epidote. The most prevalent layers are alternating sequences of BIF, felsic volcaniclastics and tuffs, with BIF commonly overlying the volcaniclastics and tuffs. These units are the host of the ore bodies at the Nyanzaga and Kilimani gold deposits (Berthier et al., 2024, Chapter V). BIF are typically composed of iron oxides interlayered with cherts of variable thicknesses. Dacitic rocks crop out locally, often associated with finely banded felsic volcaniclastics and tuffs. The overall volcanosedimentary sequence suggest a marine environment. Greenschist facies metamorphism is recorded in the meta-volcanosediments by disseminated chlorite, epidote and albite.

Two volcaniclastic samples located near the Nyanzaga and Kilimani deposits were dated by zircon U-Pb dating and yielded ages at 2779 ± 13 Ma and 2770 ± 9 Ma (Chamberlain and Tosdal, 2007). The meta-volcanosedimentary sequence of the SGGB in the Nyanzaga area is fairly similar to the lithostratigraphy described at Geita deposit, with common occurrences of tuffs, volcaniclastics and BIF (*e.g.*, Borg, 1993; Sanislav et al., 2015, 2016). The Lower Nyanzian sequence is present at the southern extent of the SGGB's

greenstones in both areas, with occurrences of basalts and gabbros dominating the base of the stratigraphy at Geita (Cook et al., 2016; Sanislav et al., 2018a). They are affected by the major Geita Shear Zone and display a tectonic foliation (Sanislav et al., 2018a). Geochemical studies have been undertaken on the Geita basalts and have been interpreted as oceanic plateau basalts with a primitive mantle composition (Cook et al., 2016).

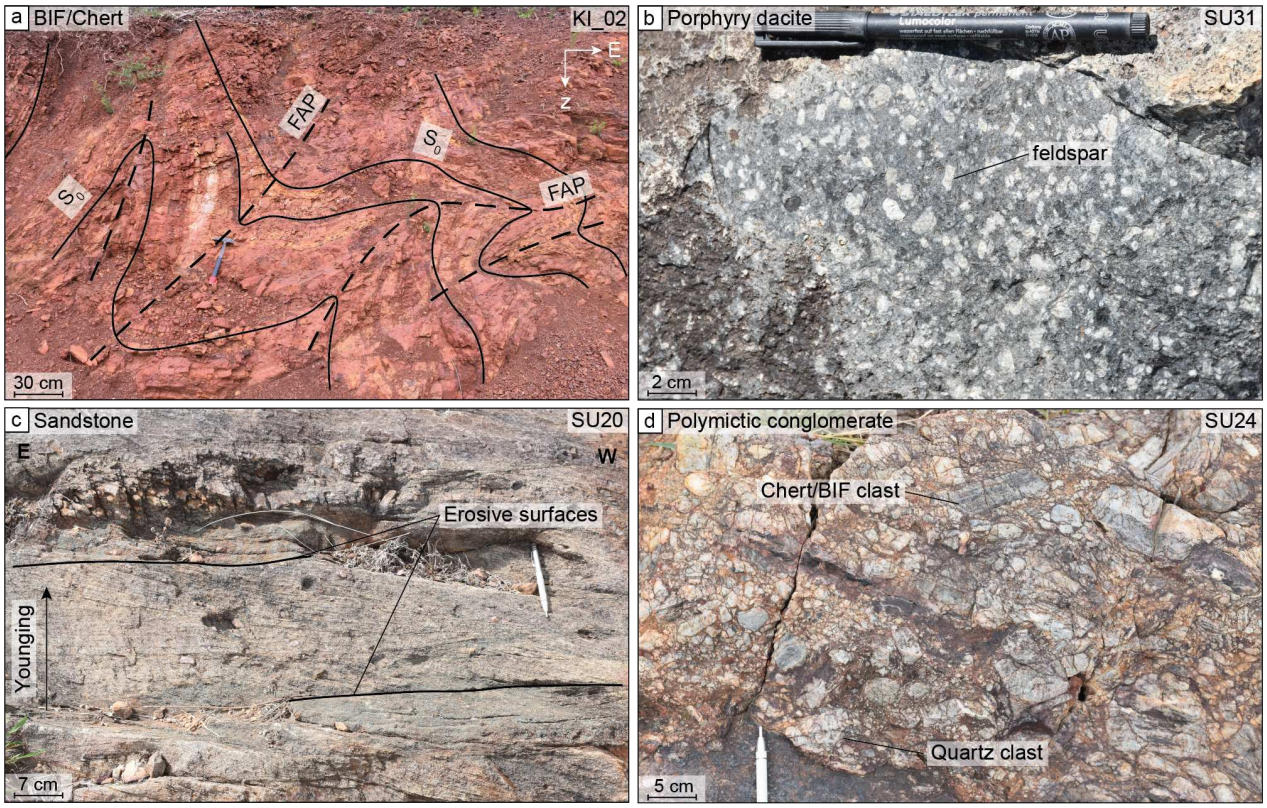

Figure 3-3. a. Folded cherts of the Upper Nyanzian. **b.** Porphyry dacite of the Upper Nyanzian. A slightly green color is indicative of greenschist facies metamorphism. **c.** Lower Kavirondian sandstone showing river current ripples and erosive surfaces indicating south-directed sedimentation. **d.** Lower Kavirondian polymictic conglomerate, showing Nyanzian chert and BIF clasts.

4.1.2. Clastic sediments of the Kavirondian stratigraphy

Polymictic pebble conglomerates and sandstones of the Kavirondian Supergroup unconformably overlie the Nyanzian meta-sedimentary sequence of the SGGB (Figs. 3-1c, 3-4a-b). The conglomerates are primarily composed of angular chert and BIF clasts, and less commonly quartz clasts (Fig. 3-4d). Well-defined syn-sedimentary structures, such as cross-bedding, erosive surfaces and channels, with common quartz clasts, indicate the orientation of sedimentation (Fig. 3-4c). These features suggest a fluviatile environment with medium to high energy during deposition.

The Kavirondian sediments are generally folded, forming three narrow molasse basins, aligned parallel to the belt and intercalated between the highly folded Nyanzian meta-volcanosedimentary sequences (Fig. 3-4c). The clastic sediments seem to have resulted from the erosion of the Nyanzian meta-volcanosediments and granitoids. Zircon U-Pb dating from the folded basins yield detrital ages between 3820 and 2620 Ma (Table 3-1; Chapter II).

A restricted basin developed in a late-tectonic intrusive, formed from the erosion of the latter (in SU09-10B granodiorite, Fig. 3-2). The undeformed sediments consist of conglomerates are monogenic, and biotite-bearing sandstones. Zircon U-Pb dating show a monogenic source with restricted age range and a single concordant age at 2651 ± 5 Ma and one older zircon at 2805 ± 14 Ma (Chapter II).

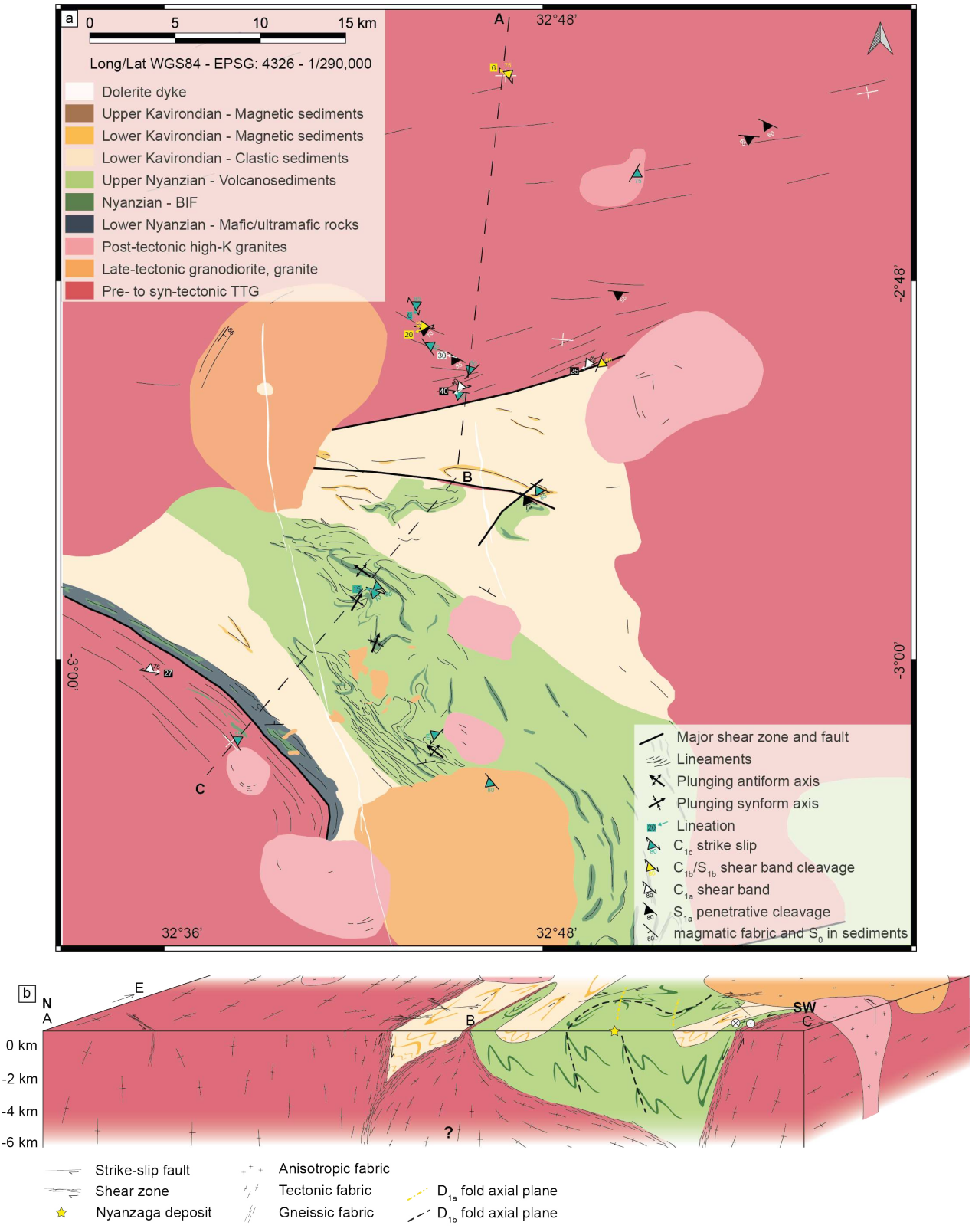

Figure 3-4. a. Map and **b.** cross-section of the geological and structural features of the SGGB. Their construction relies on field data, microstructural analyses and aeromagnetic data of the supracrustal rocks.

4.1.3. Granitoids

Different types of granitoid and gneissic rocks flank the Archean supracrustal rocks to the north and south of the belt in the studied area, from highly deformed, pre- to syn-tectonic granodiorite and quartz-monzonite, to late-tectonic granodiorite and granite, to undeformed, post-tectonic granitic bodies and dykes (Fig. 3-2).

Pre- to syn-tectonic intrusives primarily consist of granodiorite and gneisses that form the basement of the SGGB (Fig. 3-2; Table 3-1). Rare quartz-monzonite occur (SU15; Fig. 3-2). One pre-tectonic and three syn-tectonic intrusives were dated (see Chapter II), yielding respectively ages at 2755 ± 11 Ma, and between 2689 ± 7 Ma and 2673 ± 6 Ma (Table 3-1). These rocks display well-defined tectonic fabrics, often overprinting magmatic fabrics in pre-tectonic intrusives (Fig. 3-6g). Their contacts with the greenstones of the SGGB are highly sheared, resulting in migmatitic gneiss. Some granodiorites also exhibit local heterogeneities with biotite ± feldspar – quartz micro-granular enclaves, some of which preserved primitive fabrics. Highly sheared pre- or syn-tectonic aplite dykes cut across the gneissic granodiorite near the northern boundary between granitoids and the supracrustal rocks of the SGGB. Pre-tectonic intrusives are dated prior to 2700 Ma, while syn-tectonic intrusives formed between 2700 and 2660 Ma (Chapter II; Sanislav et al., 2018a). Their distinction on the geological map was not possible due to a lack of outcrops.

Late-tectonic granodiorites and monzogranites form 10-kilometer-large intrusives, intruding both the pre-/syn-tectonic complexes and the greenstone belt (Fig. 3-4a). SU10B late-tectonic granodiorite was dated at 2655 ± 11 Ma (Table 3-1; Chapter II). They show no tectonic fabric, and rarely a magmatic one. Granodiorites are amphibole-bearing. Monzogranites display biotite ± tourmaline – magnetite, variations in granulometry and biotite – plagioclase – tourmaline enclaves. Late-tectonic granodiorites are dated between 2660 and 2645 Ma (Chapter II; Sanislav et al., 2018a, 2018b).

Post-tectonic granites crosscut earlier magmatic bodies, the Nyanzian and Kavirondian units, and existing tectonic fabrics. SU16 granite is dated at 2645 ± 4 Ma (Table 3-1; Chapter II). Some intrusives display magmatic fabrics. Monzogranite pegmatitic dykes, though rare, are also present. Post-tectonic magmatic rocks are dated at 2644 ± 7 Ma (Table 3-1; Chapter II).

4.2. Deformation structures

4.2.1. Fabrics

The S_{1a} tectonic fabric is the main penetrative foliation and affects all pre- to syn-tectonic intrusives. In the northern SGGB, S_{1a} varies between WNW-ESE-, to E-W-, to ENE-WSW-oriented (this study and Sanislav et al., 2018a; Figs. 3-4, 3-5), yet progressively rotates towards the orientation of the major shear zones at the boundary between the greenstones and granitoids, where S_{1a} shifts to a migmatitic foliation (Figs. 3-4a, 3-5a). SU18 pre-tectonic intrusive preserved a magmatic fabric crosscut by the S_{1a} tectonic fabric (Fig. 3-6g). At the microscopic scale, the S_{1a} in granitoids is highlighted by recrystallized elongated quartz grains, biotite and sericite wrapping around feldspar clasts (Fig. 3-7a and d).

D_{1a} deformation also affects the supracrustal lithologies, as recorded by the S_{1a} syn-folding cleavage, observed locally in the F_{1a} fold hinge zones in the Nyanzian meta-volcanosediments (Berthier et al., 2024, Chapter V). The cleavage is highlighted by sericite, carbonate and arsenopyrite. Its initial orientation in the supracrustal rocks cannot be deduced due to subsequent refolding during the posterior deformation

stages. In the folded Kavirondian sandstones, a local, poorly defined cleavage crosscut the S_0 bedding and crossbeds, accompanied by quartz-rich tension veins. Due to folding of the sediments, the origin of the cleavage remains uncertain.

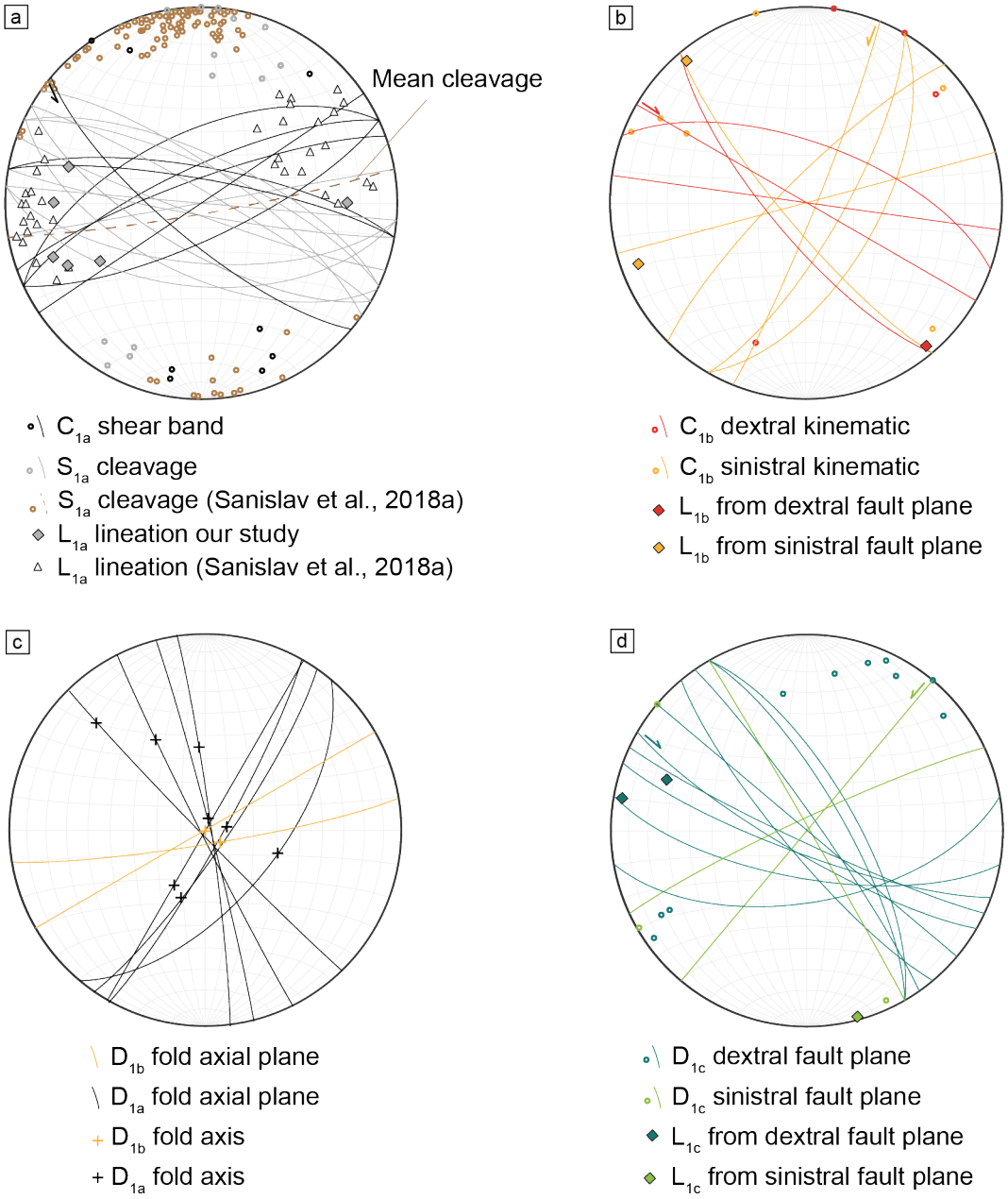

Figure 3-5. a. S_{1a}, C_{1a} and L_{1a} orientations measured in granitoids of the studied area. S_{1a} and L_{1a} measured in both granitoids and supracrustal units at Geita Shear Zone are outlined (from Sanislav et al., 2018a). **b.** C_{1b} conjugate shear zone and L_{1b} lineation orientation. **c.** F_{1a} and F_{1b} fold axial planes and axes affecting the supracrustal units in the Sukumaland greenstone belt. **d.** D_{1c}-related fault planes and lineation

4.2.2. Folds

The migmatitic gneisses observed in major shear zones show syn-melting flow folding of the leucosome (Fig. 3-6f). The fold is asymmetric, forming a z shape, indicative of a dextral flow.

The meta-volcanosediments of the Nyanzian Supergroup are folded during the D_{1a} and D_{1b} deformation stages, resulting in complex refold geometries visible as fold interference patterns on maps (Figs. 3-4b, 3-5c). Folding was studied in Berthier et al. (2024, see Chapter V) and will not be further detailed here. The refold structure is defined by (i) F_{1a} with vertical axial plane and shallow plunging axis, *i.e.*, an upright fold, with varying axis generally moderately dipping (around 25° in varying directions) but is locally steeply dipping. F_{1a} is affected by (ii) F_{1b} with vertical axial plane and vertical fold axis, *i.e.*, a vertical fold (Berthier et al., 2024, Chapter V and Supplementary Material 5-1). The axial plane of the F_{1a} synclines and anticlines is curved due to refolding, forming an overall interference pattern in the shape of a z (Figs. 3-4a-b; Berthier et al., 2024). The northernmost Kavirondian sedimentary basin is also folded, forming WNW-oriented upright asymmetrical to overturned F_{1a} folds (Fig. 3-4a-b).

4.2.3. Major shear zones

Shear strain localization in the SGGB led to the development of major shear zones, ranging from several hundred meters to a kilometer in width and extending over several kilometers in length. These structures border the greenstone belt on its northern and southern extents, juxtaposing the migmatitic gneiss basement to the Nyanzian meta-volcanosediments and Kavirondian sedimentary basins (Fig. 3-4a). All shear zones show ductile deformation with well-expressed S_{1a} gneissic to migmatitic foliation and stretching lineation, localized at the center of the structure and rapidly attenuated to tectonic foliation within the granitoids (Figs. 3-4b, 3-6a-j).

At the northern margin of the belt, the deformation zone is nearly two kilometers wide and is exposed for about ten kilometers in length (Fig. 3-4a-b). The deformation zone is primarily hosted in gneisses and migmatitic gneiss, and is characterized by a migmatitic foliation near the boundary between the greenstones and granodiorites (Fig. 3-6d-f), which evolves into a well-developed tectonic foliation within the granodiorite and granite, rapidly attenuating towards the north (*e.g.*, from SU25 to SU27 outcrops, Fig. 3-2 for location, Fig. 3-6j, c, g-h). Syn-tectonic aplite dykes are highly folded and sheared (Fig. 3-6c). The shear zone is globally oriented ENE-WSW (shear planes: 250-75, Figs. 3-2, 3-6a, d-f), and contains indicators of dextral shear sense, notably C/S planes with a dextral-inverse kinematic and apparent dextral asymmetric flow folds (Fig. 3-6a, f). More rarely, sinistral shear sense are recorded, with feldspar sigma clasts showing both kinematics. At the micro-scale, feldspar sigma clasts record dominantly dextral shear senses, and to a lesser extent sinistral shear senses (Fig. 3-7a). The L_{1a} lineation is represented by biotite and amphibole mineral lineation and stretched K-feldspar and plagioclase (Fig. 3-6a-b). L_{1a} moderately plunges eastward (Figs., 3-5a, 3-6b). At the southern margin of the shear zone, the Kavirondian clastic sediments show minor deformation, with F_{1a} folding of the sequence but no tectonic fabric nor D_{1a}-related shearing indicators were observed (Figs. 3-2, 3-5c).

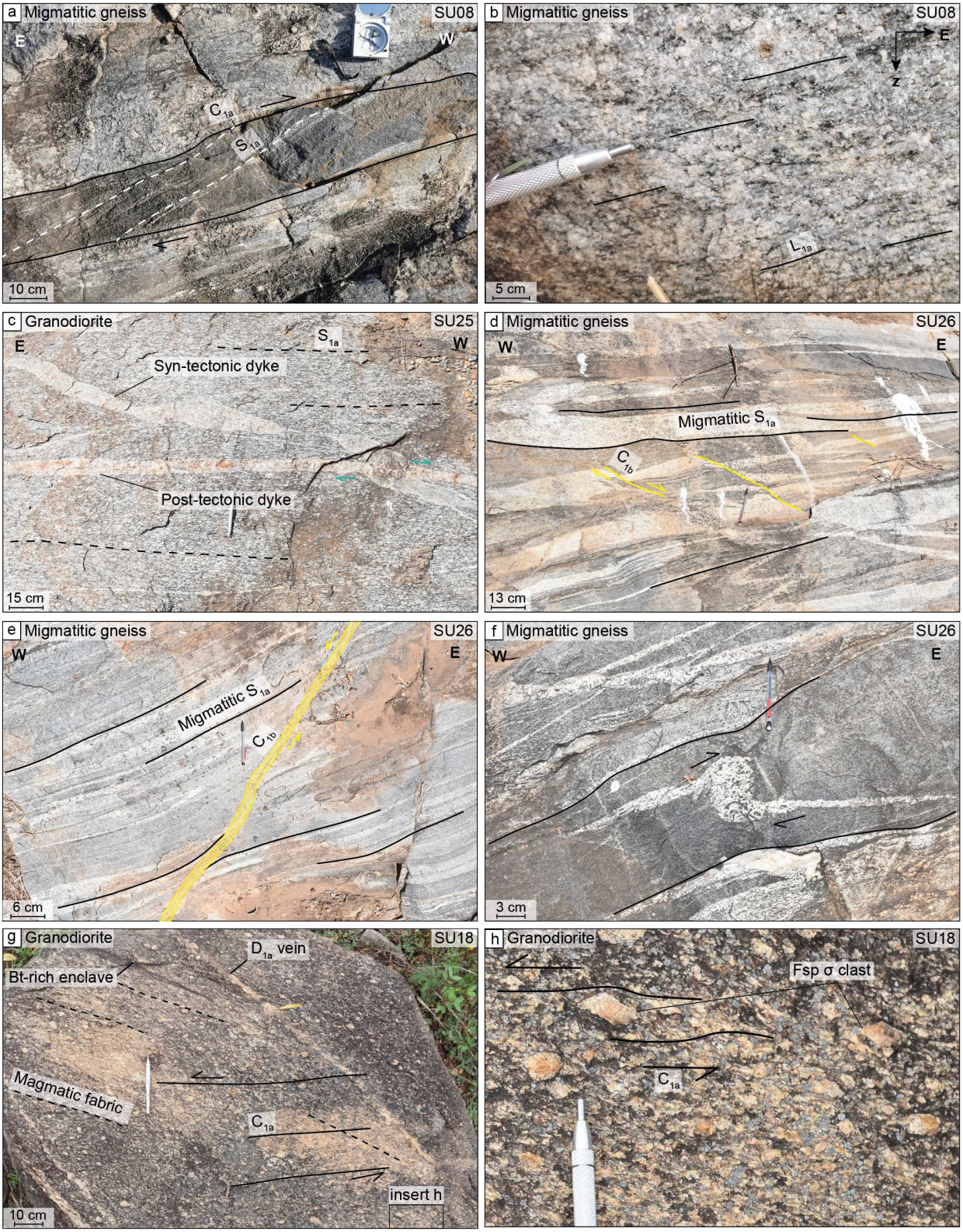

Figure 3-6. a. Migmatitic gneiss showing a migmatitic foliation and S_{1a}/C_{1a} shear band cleavage. **b.** 245/75 shear plane view of previous outcrop, showing the L_{1a} stretching lineation (25/250), indicating dextral-reverse kinematics. **c.** Syn-tectonic dyke crosscut by a post-tectonic pegmatitic granite dyke with minor dextral strike-slip. **d.** C_{1a} shear band of the northern shear zone, affected by D_{1b}-related minor dextral NW-SE shear zones. **e.** Migmatitic gneiss affected by the D1a-related major shear zones, subsequently affected by a D_{1b}-related NE-SW sinistral shear zone. **f.** Drag fold with dextral kinematics in the migmatitic gneiss affected by D_{1a}-related major shear zone. **g.** Granodiorite with magmatic fabric, affected by E-W C_{1a} shear bands (275-70). **h.** Zoom from the outcrop in Fig. 3-6g, clasts of sigma feldspar indicating an apparent sinistral kinematics.

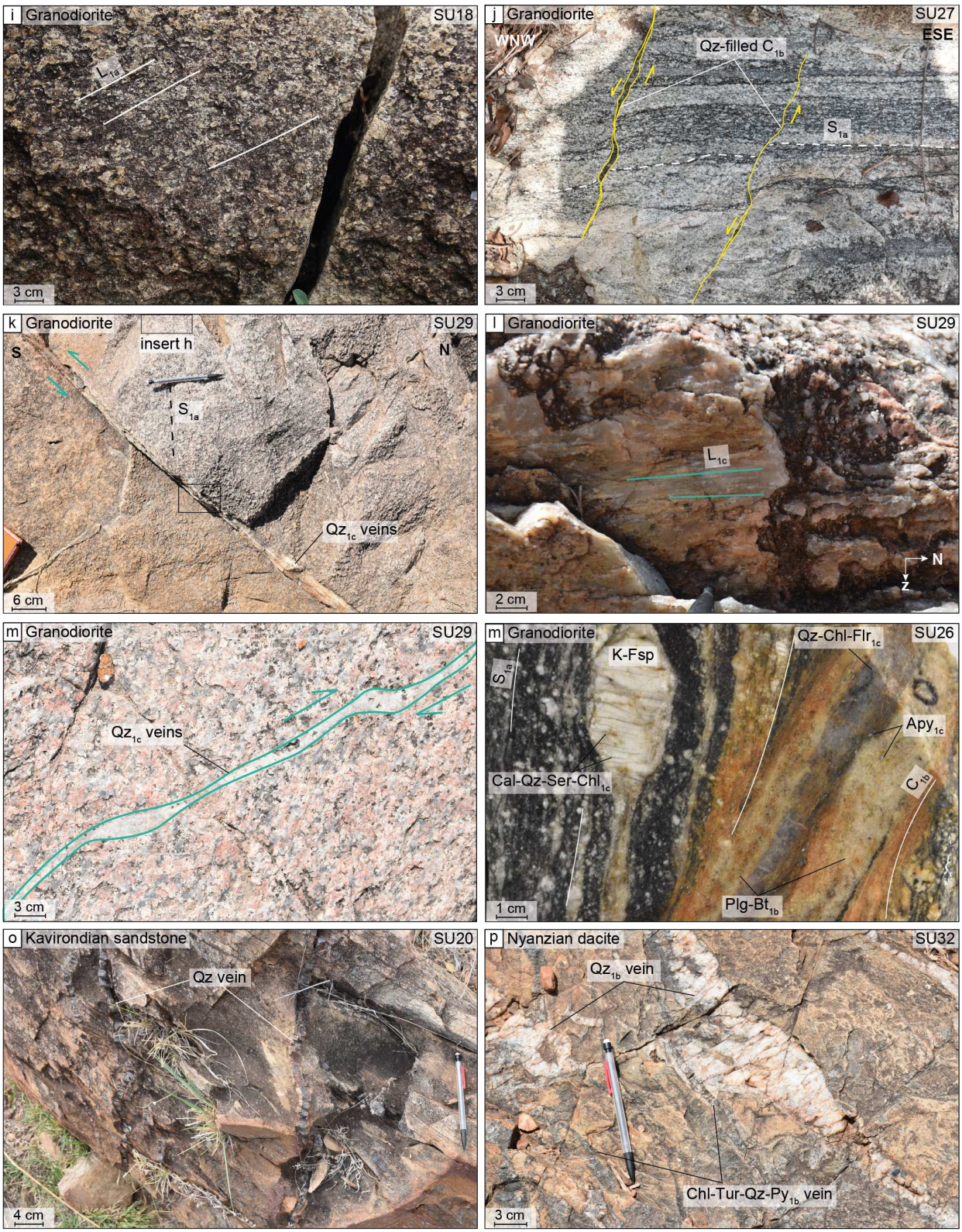

Figure 3-6. (continued) i. Zoom from the outcrop in **g**, L_{1a} stretching lineation (28/088). **j.** Granodiorite located north of the D_{1a}-related northern major shear zone, showing a WNW-ESE oriented S_{1a} tectonic foliation. D_{1b}-related NE-SW sinistral shear zones filled with quartz affect the intrusive. **k.** D_{1c}-related NE-SW sinistral small fault in a syn-tectonic granodiorite affected by the S_{1a} E-W tectonic cleavage. **l.** Zoom in on the fault mirror (L_{1c}: 20/250). **m.** Zoom in on pull-aparts within NW-SE quartz veins with dextral kinematics. **n.** Zoom from Fig. 3-6e on the D_{1b}-related Plg-Bt dyke, itself affected by a D_{1c}-related Qz-Ser-Flr-Apy vein. A Ser-Apy alteration halo from the vein affect the dyke. The S_{1a} tectonic foliation in the granodiorite is affected by the D_{1b}-related shearing. **o.** Folded syn-sedimentary or syn-folding veins in Kavirondian sandstone. **p.** D_{1b}-related Qz vein stockwork affected a Nyanzian dacite from the greenstone belt, and affected by a D_{1c}-related Chl-Tur-Qz-Py vein stockwork.

A second WNW-ESE shear zone, scarcely exposed, was observed approximately five kilometers south of the first one (located near the "B" of the cross-section in Fig. 3-4a-b). Highly sheared granodioritic rocks are juxtaposed to the Nyanzian meta-volcanosediments to the south against the Kavirondian sandstones and conglomerates to the north. Kinematics could not be determined due to the poor exposure of the deformation zone and strong weathering.

The southern margin of the greenstone belt is bordered by an NW-SE shear zone (Fig. 3-4a), and is scarcely exposed. The greenstone belt-granitoid boundary was delineated using magnetic data due to poor outcropping. A pre-tectonic granodiorite observed approximately one kilometer south of the margin displays a magmatic foliation (120-90), intersected by E-W shear planes (280-70; Fig. 3-6g). Biotite- sericite-quartz wrapped around feldspar sigma clasts and an L_{1a} stretching lineation (28/088) indicate a sinistral-reverse kinematics (Fig. 3-6h-i).

Microscopic-scale mineral textures constrain the peak temperature near these shear zones (*e.g.*, Passchier and Trouw, 2005). Quartz and feldspar grains display high-temperature recrystallization textures (Fig. 3-7b, d): (i) quartz grain boundary migration (GBM, > 500 °C, Fig. 3-7b-d); (ii) feldspar grain boundary area reduction (GBAR, T ≥ 450 °C, Fig. 3-7b, d; Passchier and Trouw, 2005). The latter is mostly effective after deformation ceased, indicative of high-temperature conditions after D_{1a} penetrative deformation stage. Myrmekite may align along the tectonic foliation plane during crystallization of the magma (Passchier and Trouw, 2005 and references therein). Some feldspar grains exhibit quartz myrmekites and deformation twins repeatedly aligned along the same plane interpreted as the tectonic foliation (Fig. 3-7d;).

4.2.4. Minor shear zones

Smaller ductile-brittle shear zones forms localized vertical deformation zones of tens of meter long and a few decimeters wide (Fig. 3-6j, d-e). They affects pre- to late-tectonic intrusives and displaces the major shear zones (Fig. 3-6d-e). These ductile-brittle shear zones developed at varied angles to the foliation, and occur either as parallel sets with a same shear sense or as a single localized structure. Regionally they form a conjugate set of NW-striking dextral and NE-striking sinistral structures (Figs. 3-4a, 3-5b). C_{1b} shear bands, highlighted by biotite and sericite, penetrate intrusives and crosscut and affect the penetrative S_{1a} (Fig. 3-7c). The asymmetry of shear bands is a reliable shear sense indicator. L_{1b} stretching lines are subhorizontal (Fig. 3-5b). Deformation zones are filled with quartz-feldspar recrystallization. An aplitic diorite dyke was observed in one of these minor shear zones, formed synchronous to the D_{1b} deformation (Fig. 3-6e, m).

4.2.5. Faults and fractures

The last deformation recorded in the SGGB consists of brittle faulting (Fig. 3-4b). These structures intersect all lithologies and both folds and shear zones. Networks of conjugate faults exhibit NW-striking dextral-(reverse) and dextral-(normal) kinematics, and NE-striking sinistral kinematics (Figs. 3-6d, 3-7h). They are generally restricted to a few centimeters in width and a few meters in length in the granitoids, while larger faults of a kilometer long and a few meters large crosscut the supracrustal rocks of the SGGB, the latter are further described at the Nyanzaga and Kilimani gold deposits in Berthier et al. (2024) (Chapter V). A third set of N-S to NNW-SSE-oriented faults and fractures are observed locally, including at the Nyanzaga deposit, recording normal-(sinistral) kinematics (Berthier et al., 2024, Chapter V). The extensive network of faults at

the Nyanzaga and Kilimani deposits affecting the Nyanzian meta-volcanosediments is detailed in Berthier et al. (2024) (Chapter V). Subhorizontal slickenside lineation demonstrate pure strike-slip shearing (Figs. 3-5d, 3-6l). The filling of these fractures is dominated by an assemblage of transparent quartz, chlorite, sulfide minerals such as pyrite and pyrrhotite, sericite and calcite (Fig. 3-6m; Berthier et al., 2024, Chapter V).

A second and rare network of faults and fractures with opposite kinematics are also observed, *i.e.*, NW-striking sinistral and NE-striking dextral kinematics. Their infilling is usually dominated by epidote and quartz.

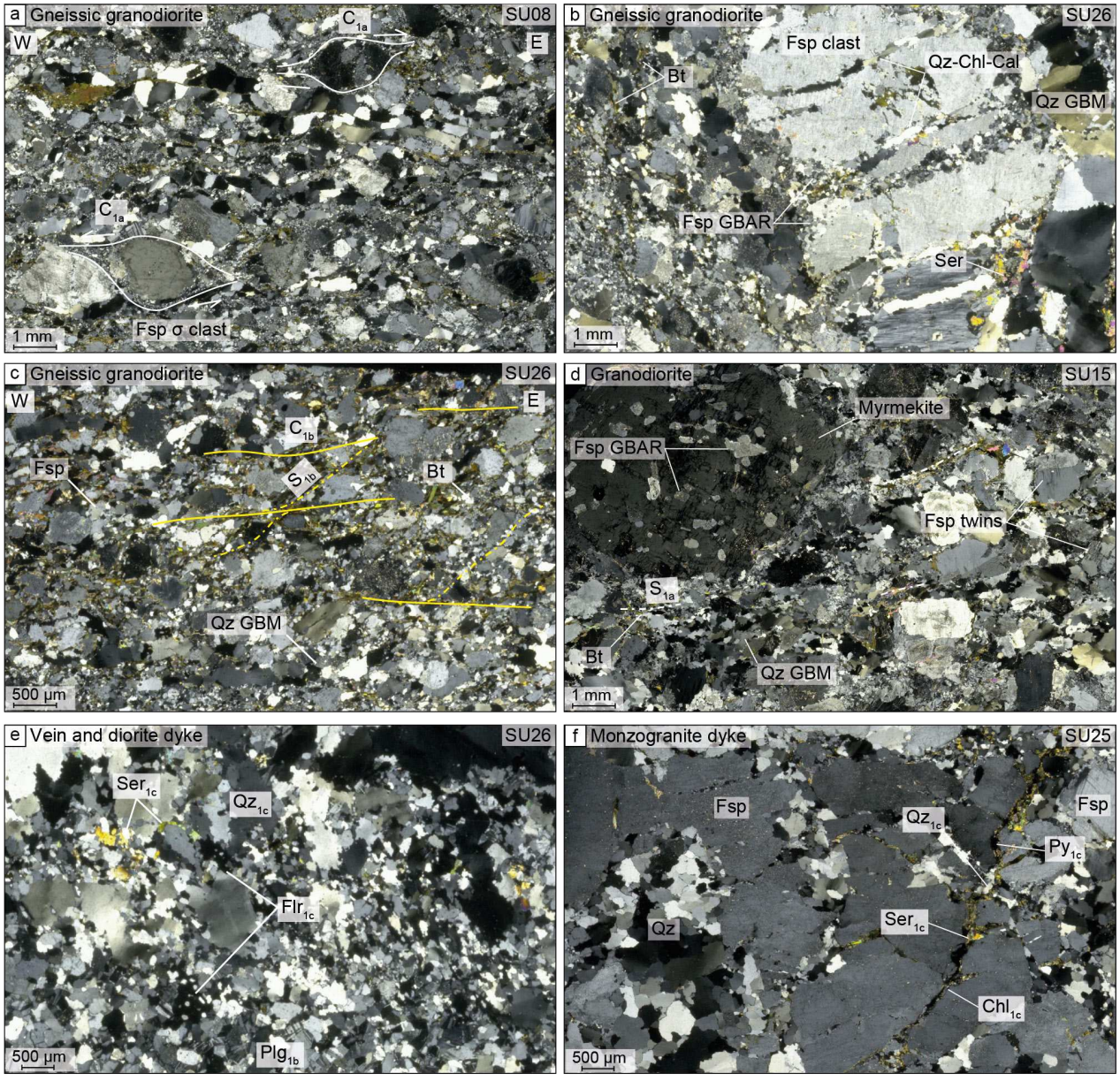

Figure 3-7. Microstructural features **a.** Sinistral and dextral kinematics recorded from Qz-Bt bands wrapped around Fsp clasts. **b.** GBM and GBAR textures in Qz and Fsp affected by the D_{1a}-related major shear zone. Fractures in Fsp clasts are filled with D_{1b}-related Qz-Cal-Chl-Ser. **c.** Biotite grains aligning along C_{1b}/S_{1b} planes, highlighting a sinistral kinematics. **d.** GBAR textures, quartz myrmekites, and deformation twins in feldspar grains. Quartz exhibits a recrystallization texture of GBM. **e.** Zoom on the D_{1c}-related Qz-Ser-Flr-Py veins affecting the D_{1b}-related Plg-dominated dyke from Fig. 3-6m. **f.** D_{1c}-related Qz-Ser-Py-Chl veins affected the SU25 post-tectonic monzogranite pegmatitic dyke.

4.2.6. Veins

Four types of veins have been identified in the north-eastern SGGB (this study and Berthier et al., 2024, Chapter V):

- Syn-sedimentary or syn-folding veins in the meta-volcanosedimentary pile are highly folded and stretched, forming boudins (Fig. 3-6o; Berthier et al., 2024, Chapter V). They are principally filled with quartz presenting recrystallization textures with grain boundary migration (GBM; Fig. 3-8; Passchier and Trouw, 2005; Berthier et al., 2024, Chapter V).
- Intensely sheared D_{1a}-related extension veins in granitoids affected by the major shear zones (Figs. 3-6g, 3-8). Their infilling is dominated by quartz.
- Large stockworks of D_{1b-1c}-related milky quartz veins with GBM and subgrain rotation (SGR) are observed in the meta-volcanosediments (Figs. 3-6p, 3-8; Passchier and Trouw, 2005).
- Large stockworks of veinlets and extension veins form around the D_{1c}-related brittle faults (Fig. 3-6l-k; Berthier et al., 2024, Chapter V), affecting D_{1b}-related vein stockworks (Fig. 3-6p) and dykes (Fig. 3-6n), and post-tectonic intrusions and dykes (Fig. 3-7f). Those observed along the transect are mainly infilled with an assemblage dominated by quartz, chlorite, tourmaline and sulfide, mainly pyrite (Figs. 3-6m, n, p and 3-7e, f, 3-8). At the Nyanzaga and Kilimani gold deposits, they are gold-bearing and show a wide variety of composition, with quartz, carbonate calcite, chlorite, tourmaline and various sulfide minerals such as pyrite, pyrrhotite, arsenopyrite, gudmundite, galena (Berthier et al., 2024, Chapter V). Rare and restricted alteration halos of carbonate and pyrite, pyrrhotite, arsenopyrite formed around the veins. Bulging (BLG) dynamic quartz recrystallization textures and the fracturing of feldspar clasts attest to deformation temperatures at the brittle-ductile transition of quartz (300 < T < 450 °C; Passchier and Trouw, 2005).

4.3. Gold mineralization

The average amount of gold in the upper continental crust is 1.3 ppb, corresponding to the Clarke value for gold (Rudnick and Gao, 2003). Several samples from the transect show gold enrichment above the Clarke (Fig. 3-2; Table 3-2). The most gold endowed sample is SU19 talc-altered ultramafic rock from the Lower Nyanzian Supergroup, found in the southernmost part of the SGGB, with 30 ppb gold content. Further east, SU32 felsic volcanic rock from the Upper Nyanzian Supergroup is affected by an important D_{1b}-related quartz and D_{1c}-related chlorite-tourmaline-epidote-calcite-pyrite vein stockworks and yield 6 ppb gold content. Finally, smaller gold enrichment is recorded in SU26 sample, with 2 ppb gold content. It consists of a shear zone filled with a granodiorite aplitic dyke, crosscut by a cm-wide D_{1c}-related quartz – sericite – chlorite – fluorite – pyrite.

At Nyanzaga and Kilimani gold deposits, gold mainly concentrated along the D_{1c}-related NW-striking and N-striking subvertical faults. A network of quartz-chlorite-sulfide-dominated veinlets concentrate most of the mineralization. The detailed description of gold distribution and location at Nyanzaga and Kilimani is presented in Berthier et al. (2024) (Chapter V).

Sample	Brief description	U-Pb dating (Chapter II)	Gold content in ppb
SU01	Syn-tectonic granodiorite		0.5
SU04	Syn-tectonic quartz-monzonite	2673 ± 7 Ma	0.5
SU05	Late-tectonic granite		0.5
SU06	Syn-tectonic granodiorite	2689 ± 7 Ma Inherited 2798 ± 14 Ma	0.5
SU08	Syn-tectonic gneissic granodiorite		0.5
SU09	Late-tectonic granodiorite		0.5
SU10B	Late-tectonic granodiorite	2655 ± 5 Ma	0.5
SU11	Lower Kavirondian sandstone	3820 – 2700 Ma	1
SU12	Upper Nyanzian BIF		1
SU15	Syn-tectonic granodiorite	2677 ± 4 Ma	0.5
SU16	Post-tectonic granite	2645 ± 4 Ma	0.5
SU17	Late-tectonic granodiorite		1
SU18	Pre-tectonic granodiorite		0.5
SU19	Talc ultramafic rock – artisanal mine site		**30**
SU25	Post-tectonic monzogranite pegmatitic dyke	2644 ± 7 Ma	0.5
SU26	Shear zone infilled with late-tectonic granodiorite dyke and D_{1b} quartz-pyrite vein		**2**
SU31	Felsic volcanic rock		0.5
SU32	Felsic volcanic rock affected by D_{1b}-related vein stockwork		**6**
SU38	Felsic volcanic rock affected by D_{1b}-related vein stockwork		1

Table 3-2. Gold content from whole-rock analyses in rock samples from the transect and brief description of the key outcrops discussed in the text. Zircon U-Pb ages are reported as described in Chapter II. See Fig. 3-2a for the location of the samples.

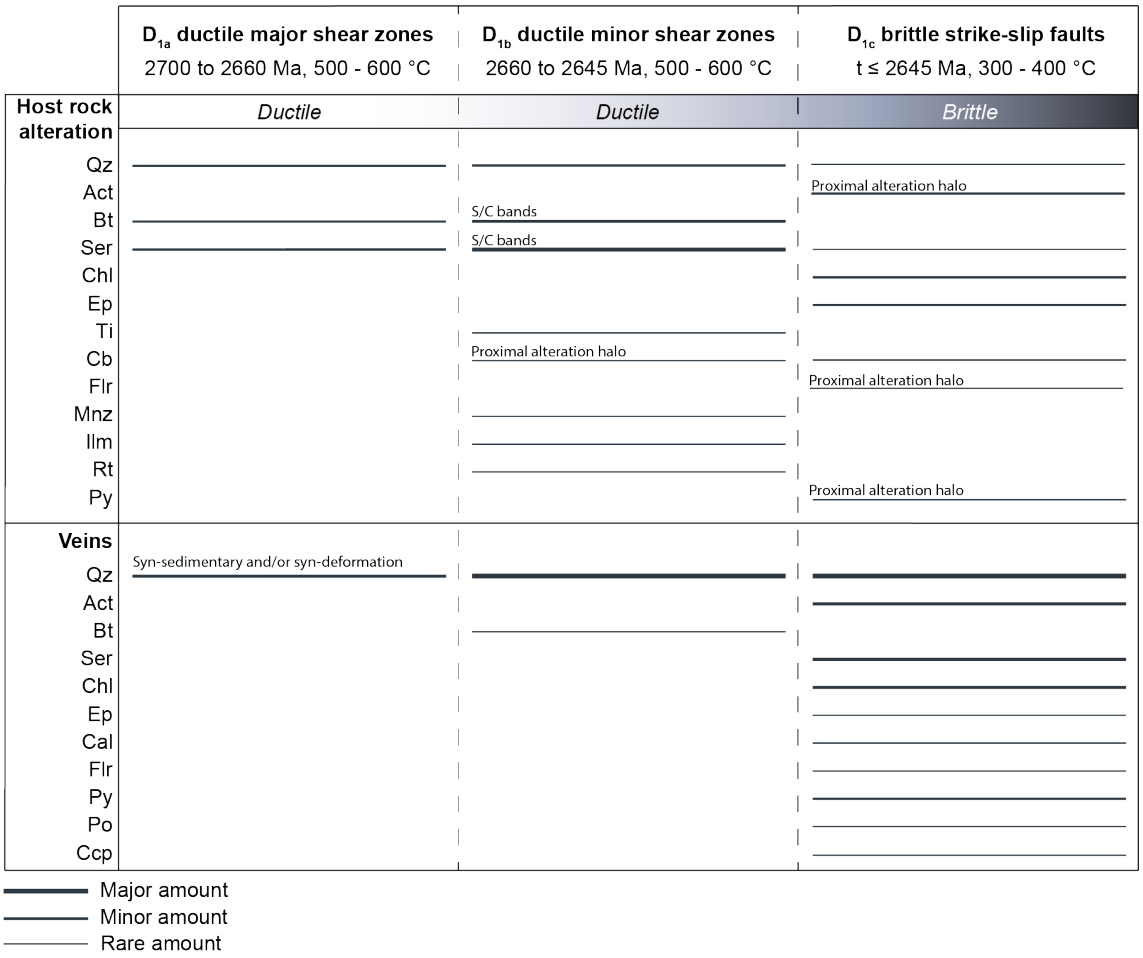

Figure 3-8. Paragenetic sequence of the hydrothermal and metamorphic stages observed along the transect.

5. Discussion

5.1. Shortening direction and crustal flow modes

In this section is discussed the evolution of shortening, and the strain ellipsoid's orientation when possible, during the tectono-hydrothermal history of the SGGB. During the D_{1a} deformation stage, strain ellipsoid indicators include: (i) a steeply dipping to subvertical S_{1a} fabric generally oriented ENE-WSW away from deformation zones and varying from WNW-ESE to E-W near the major shear zones, (ii) shallowly dipping ENE-WSW L_{1a} lineations, (iii) E-W boudin structures in syn-tectonic dykes, (iv) presence of both kinematics along the major shear zones, and (v) dextral-reverse-dominated and sinistral-reverse-dominated kinematics along the northern and southern major shear zones, respectively. These observations suggest a global subhorizontal NNW-SSE maximal shortening direction (Z), characterized by oblique ENE-WSW maximum stretching (X). This aligns, within the crustal flow model proposed by Chardon et al. (2009; after Balé and Brun, 1989), in Figure 3-9, constructed based on the L_{1a} lineation measured along the transect. The latter plot in the domain of vertical flattening field and in the domain of transpression that links vertical orogen-parallel flow with orogen-parallel strike-slip flow (Fig. 3-9).

Regional-scale folding was recorded in the supracrustal units of the SGGB (Borg, 1992; Chamberlain, 2003; Boniface and Mruma, 2012; Sanislav et al., 2015, 2016, 2018b; Berthier et al., 2024, Chapter V). The first generation of folding affects lithologies as young as the Kavirondian sediments dated between 3820 and

2680 Ma (Fig. 3-4a-b). they are shallowly plunging and upright, characterized by subvertical axial planes and generally shallow plunging fold axes (Figs. 3-4b, 3-5c; Berthier et al., 2024, Chapter V). Due to their subsequent refolding, their original orientation cannot be easily reconstructed. However, their geometry show they formed in a compressional-transpressional regime, similar to the D_{1a} regime. Moreover, they represent the main deformation stage in the supracrustal units (Berthier et al., 2024, Chapter V), and fit with the D_{1a} main deformation stage. We therefore propose to temporally link these folds with the D_{1a} deformation stage.

D_{1b} deformation is marked by NW-striking dextral and NE-striking sinistral subvertical conjugate shear zones. The subhorizontal L_{1b} lineation suggests that D_{1b} stage developed by strike-slip deformation (Fig. 3-5b). Note that rare D_{1b} shear zones showed normal kinematics, with a moderately L_{1b} slickenside lineation measured along a sinistral-normal shear zone (Fig. 3-9). Local extension might have occurred during the global shortening stage. When plotted in the crustal flow mode diagram by Chardon et al. (2009; after Balé and Brun, 1989), in Figure 3-9, the L_{1b} lineation falls in the orogen-parallel strike-slip flow.

Once again, this deformation stage can be associated with a folding stage in the supracrustal units of the SGGB. Indeed, refolding of the meta-volcanosediments is characterized by subvertical geometries, *i.e.*, subvertical axis and axial plane, with an ENE-oriented axial plane (Figs. 3-4b, 3-5c; Berthier et al., 2024, Chapter V). Their orientation and geometry is therefore in line with the orientation of the D_{1b} stage, defining a subhorizontal NNW-SSE-oriented maximum shortening (Z). Their relative timing, after F_{1a} folding and before D_{1b}-related faulting (affecting both fold generations) fits with the interpretation.

The D_{1c} stage is dominated by conjugate NW-striking dextral-(reverse and normal) and NE-striking sinistral subvertical strike-slip faults, as well as N-S normal-sinistral faults, with subhorizontal L_{1c} lineations (Fig. 3-5d). A significant stockwork of veins at the Nyanzaga and Kilimani deposits is characterized by N-S and NNW-SSE subvertical veinlets (Berthier et al., 2024, Chapter V). Like D_{1b}, D_{1c} deformation formed under a strike-slip regime and a NNW-SSE-oriented maximum shortening (Z) fits best with all D_{1c} features. At Geita, this event was interpreted under extensional regime, while in our studied area, strike-slip, reverse and normal kinematics were recorded. At the Nyanzaga and Kilimani deposits, D_{1c} is interpreted as a transpressional stage, during which local extension was recorded as normal faulting bounded by purely strike-slip faults. Therefore, strike-slip deformation is inferred for D_{1c} stage, which locally deviate to transpressional and transtensional regimes.

Shortening is therefore relatively constant from D_{1a} to D_{1c}, remaining subhorizontal and NNW-SSE oriented (Z), evolving from a transpressional regime with oblique ENE-WSW maximum stretching (X) during the D_{1a} stage, to strike-slip flow with subhorizontal maximum stretching (X). Deformation is accompanied by a progressive decrease of temperature, from ductile to ductile-brittle, to brittle fields of deformation. The structural framework of the SGGB reflects a progressive evolution, as defined by Oriolo et al. (2022), resulting from relatively uniform flow parameters, regardless of the transition from ductile to brittle conditions. The evolution of deformation at this regional scale is in line with the progressive deformation history proposed by Berthier et al. (2024) (Chapter V) at the scale of the Nyanzaga and Kilimani gold deposits.

Discussing shortening orientations has enabled to compare and associate deformations in in the granitoids and in the supracrustal rocks of the SGGB. We propose to first present the tectonic evolution of the northern SGGB based on these interpretation and observations made along the transect and from the available literature (section 5.2). In turn, the reconstruction of the evolution of deformation and shortening directions allows discussing the geodynamic implications for the tectonic evolution of the northern SGGB (section 5.3).

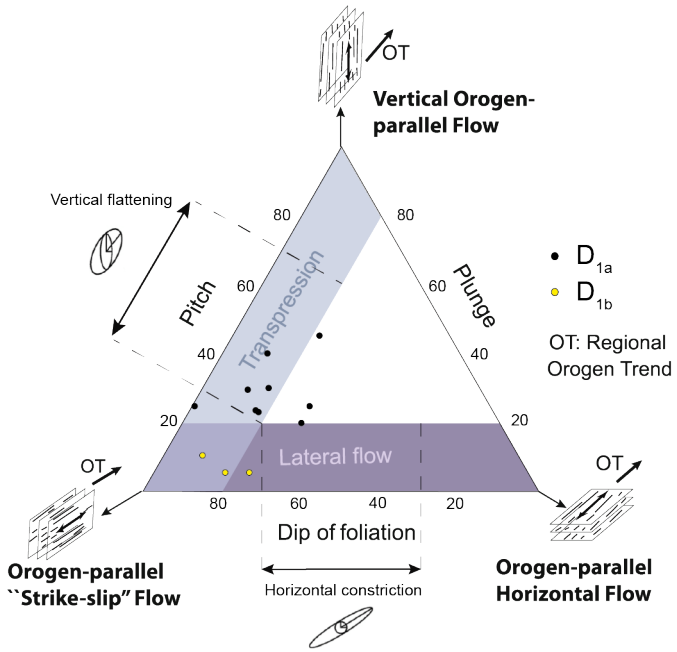

Figure 3-9. Fabric data (dip of foliation, pitch and plunge of related lineation) plotted in the crustal flow mode diagram from Chardon et al. (2009; modified from Balé and Brun, 1989).

5.2. Tectonic evolution of the SGGB

The magmato-tectono-hydrothermal history of the SGGB comprises four magmatic stages and three deformation stages (Fig. 3-10; Chapter II). Prior to shortening recorded along the transect, significant pre-tectonic magmatism occurred, dated between 2780 and 2700 Ma (Chapter II), primarily forming granodiorite plutons, synchronous to the deposition of the Nyanzian volcanosedimentary pile. A cryptic deformation stage, associated with extensional normal faulting and localized shearing, has been identified at the Geita gold deposit and interpreted to coincide with the volcanosediment deposition (Sanislav et al., 2015, 2016). If this first deformation stage happened in the transect area, it was entirely obliterated by subsequent tectonic events. The first deformation stage identified in the study area, referred to as D_{1a}, represents the earliest observable deformation event at this local scale. It is important to note that this designation does not imply that D_{1a} corresponds to the first regional deformation event. Instead, D_{1a} reflects the initial deformation stage preserved in the structural history of the studied area, which may differ from the broader regional tectonic framework.

The D_{1a} deformation stage marks the onset of shortening in the SGB around 2700 Ma, characterized by shallowly plunging upright folds in the supracrustal rocks and shearing. Widespread and extensive syn-tectonic magmatism occurred during this period, alongside the deposition of Kavirondian clastic sediments in molassic basins, synchronous with their folding. The regional S_{1a} penetrative cleavage affected pre- to syn-tectonic intrusives, and was transposed along C_{1a} shear bands near the major shear zones developed at the boundary between the belt and the pre- to syn-tectonic granitoids. At the heart of the major shear zones, migmatitic gneisses and S_{1a} are indicative of granulitic P-T conditions. In the granodiorite, microstructural analysis of quartz and feldspar textures indicates deformation temperatures between 500°C and 600°C, consistent with the ductile nature of the major shear zones (Passchier and Trouw, 2005). This temperature range is further supported by the presence of homogeneous strain pattern and ductile C_{1a} shear bands

throughout outcrops, indicative of thermal conditions above 500 °C (Gapais, 1989). A metamorphic gradient is therefore recorded from granulitic at the heart of the deformation zones, to amphibolitic in the granitoids and amphibolitic to greenschist in the meta-volcanosediments of the belt. The absence of the S_{1a} penetrative fabric in late-tectonic intrusives dated at 2655 ± 5 Ma constrain the minimum age of D_{1a} deformation stage.

Shortening continued during D_{1b}, after 2660 Ma (Fig. 3-10), and is characterized by more localized strain along conjugate sets of minor shear zones. Subvertical folding further affects the supracrustal rocks, resulting in complex refold structures (Berthier et al., 2024, Chapter V). This period also marks the transition toward high-K-dominated magmatism and a gradual decrease in deformation temperatures. The absence of ductile-brittle deformation in the post-tectonic intrusives dated at 2645 ± 4 Ma marks the minimum age of D_{1b} deformation stage. The presence of both grain boundary migration (GBM) and subgrain rotation (SGR) recrystallization textures in quartz from D_{1b}-related veins, combined with the near absence of ductile deformation in feldspar within late-tectonic intrusives and quartz vein stockworks, suggests a temperature range of 400°C to 500°C (Passchier and Trouw, 2005).

Finally, following post-tectonic high-K granite magmatism at ca. 2645 Ma, deformation temperatures decreased to brittle conditions during the D_{1c} stage, leading to the formation of strike-slip faults, affecting the sedimentary units, and to a lesser extent the granitoids. L_{1c} lineations are shallowly plunging and record both reverse and normal kinematics. The presence of bulging (BLG) recrystallization texture in quartz constrains deformation temperatures to between 300°C and 350°C.

Restricted post-folding Kavirondian basins developed, likely after D_{1b} deformation stage (Fig. 3-10). These basins can be differentiated from the earlier, syn-tectonic counterparts by the absence of folding and the restricted zircon population range: SU10A show a monogenic source, while a similar basin yielded ages between 2790 and 2640 Ma near the Geita deposit (Sanislav et al., 2018b; Chapter II). Based on the observation of two generations of clastic sedimentary basins, we propose distinguishing them, into Lower Kavirondian, formed between 2680 and 2660 Ma and the Upper Kavirondian, formed after 2640 Ma (Fig. 3-10).

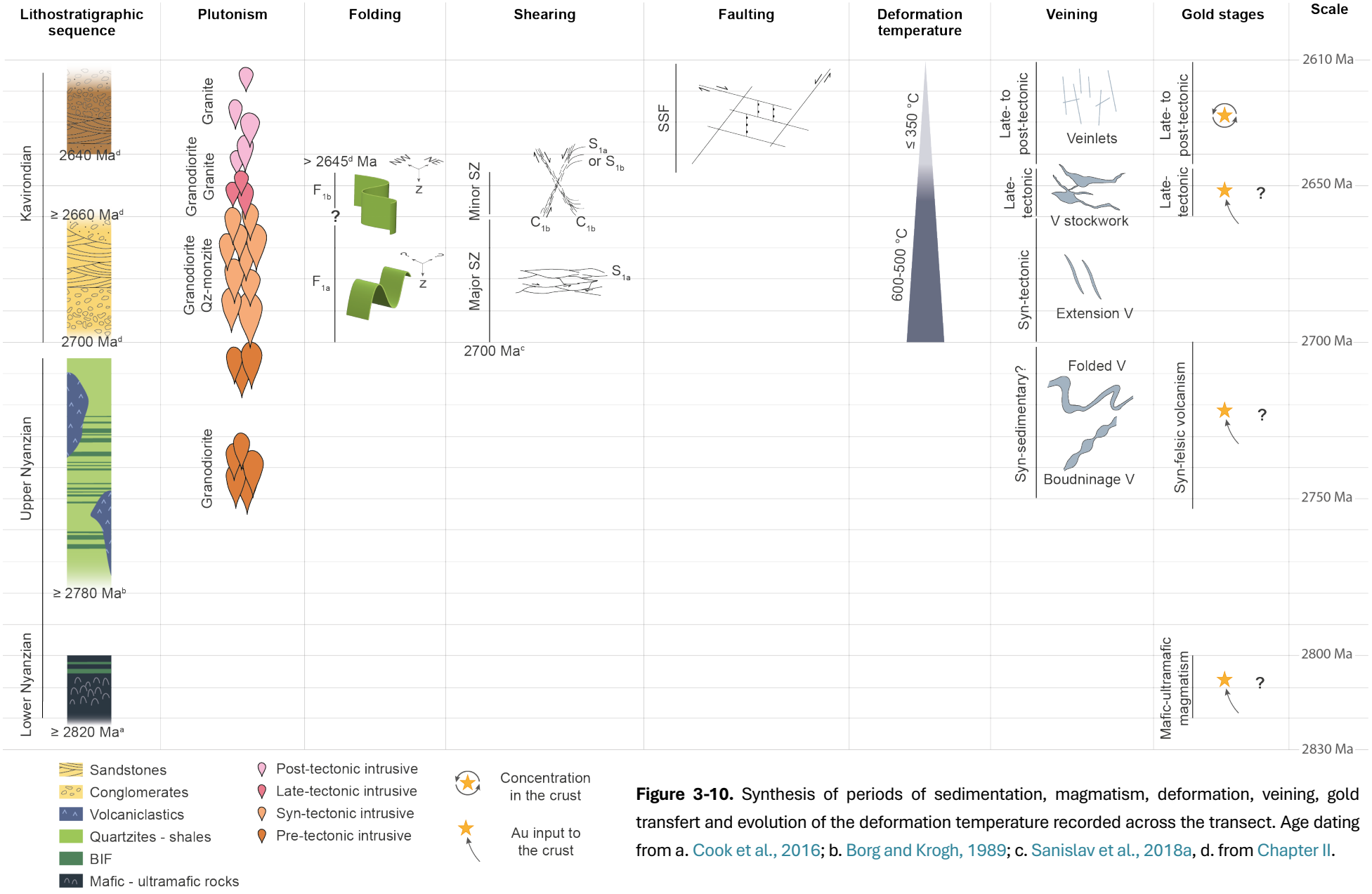

Figure 3-10. Synthesis of periods of sedimentation, magmatism, deformation, veining, gold transfert and evolution of the deformation temperature recorded across the transect. Age dating from a. Cook et al., 2016; b. Borg and Krogh, 1989; c. Sanislav et al., 2018a, d. from Chapter II.

5.3. Implications for crustal shortening and thickening style in the northern SGGB

The petro-structural study of the northern SGGB hint on the tectonic regimes that controlled crustal shortening and thickening during the Neoarchean, between 2700 and 2620 Ma. Firstly, not much localized crustal thickening is observed, notably no crustal-scale thrusts that act as major agents for crustal thickening in present-day orogens (*e.g.*, Gillet et al., 1986; Guillot et al., 2003). The heterogeneous and extensive provenance of detrital zircons (from 3820 to 2820 Ma) indicate a wide drainage basin, not restricted to the SGGB or LVG (Chapter II), meaning that relief was rather low (*e.g.*, Parra et al., 2010). This is further supported by little post-tectonic extension recorded in the northern SGGB. Rather, crustal thickening was leveled by syn-shortening erosion developed near the major shear zones, and syn- to late-shortening lateral flow (Fig. 3-9). Secondly, crustal flow is also characterized by vertical flattening. The lower crust (migmatite) was uplifted, synchronous with sinking of supracrustal rocks, as recorded by moderately dipping L_{1a} along the boundary between the SGGB and granitoids. Crustal shortening and thickening in the northern SGGB is therefore controlled by both transpression and vertical flattening, hence combining E-W horizontal and vertical escape during N-S compression. These characteristics are not shared with modern-day collisional orogen style, where shortening is expected to lead to strong strain localization along thrust systems, but rather share similarities with hot and weak lithospheres that favor lateral flow and distributed deformation (Davy and Cobbold, 1991; Cagnard et al., 2004; Chardon et al., 2009; Mvondo et al., 2017). Crustal shortening and thickening in the northern SGGB therefore result from protracted transpression of a weak Archean-type lithosphere falling in the hot orogen type (Chardon et al., 2009).

5.4. Gold fertilization and concentration in the crust

Gold content analyses in the samples collected along the transect enable preliminary discussion on the gold-fertile and/or -endowed lithologies in the northern SGGB (Table 3-2). Three samples show anomalous gold content, but all are affected by hydrothermal alteration, gold endowment could therefore either be syngenetic, i.e., originating from a gold-enriched magmatic, or epigenetic, i.e., related to the circulation a gold-bearing fluid. SU19 in particular, show strong anomalies (30 ppb Au, compared to the 1.3 ppb Au Clarke, Rudnick and Gao, 2003), that could be related to the juvenile mafic magmatism that formed the Lower Nyanzian mafic-ultramafic volcanic rocks and related mafic plutons, dated between 2820 and 2800 Ma (Fig. 3-10; Cook et al., 2016; Chapter II), or related to the talc alteration that was not temporally constrained. Similarly the SU32 dacite from the Upper Nyanzian shows slight enrichment (6 ppb, Table 3-2; compared to the 0.48 ± 0.45 ppb average Au content in dacite, Pitcairn, 2011), that could either be related to (i) felsic volcanism dated between 2780 and 2700 Ma, (ii) the D_{1b}-related quartz stockwork (Fig. 3-6p), or (iii) the D_{1c}-related chlorite – tourmaline – quartz – pyrite vein stockwork (Fig. 3-6p). Finally, SU26 late-tectonic granodiorite dyke show even smaller enrichment (2 ppb, Table 3-2; compared to the 0.45 ± 0.4 ppb average Au content in late-tectonic granitoids, Pitcairn, 2011), that could either be related to (i) a late-tectonic fertile granodiorite, emplaced between 2660 and 2645 Ma (Fig. 3-10), or (ii) the D_{1c}-related quartz – sericite – chlorite – fluorite – pyrite veins and related alteration (Figs. 3-6m, 3-7e). Based on the existing data, no gold-fertile lithologies are of sedimentary origin, the fertilization of the crust seems therefore to have resulted from magmatic processes prior to 2645 Ma.

At the Nyanzaga, Kilimani, and Geita gold deposits, ore zones are concentrated along D_{1c}-related subvertical strike-slip faults (Sanislav et al., 2015, 2016; Van Ryt et al., 2017; Berthier et al., 2024, Chapter V). Indirect

dating of gold mineralization suggests a timeframe between 2645 and 2620 Ma, synchronous with post-tectonic high-K granite magmatism. Based on the geochemical dataset from this study, gold fertilization of the crust is temporally disconnected from gold concentration processes, as commonly discussed for lode-gold, or orogenic gold deposits (*e.g.,* Frimmel, 2008, 2018; McCuaig and Hronsky, 2014). This interpretation disagrees with the previous assumptions from studies at the Geita gold deposit (western SGGB) that gold might be sourced from the post-tectonic high-K granites due to (i) the potassic alteration associated with gold, (ii) biotite geochemical signatures indicative of fluid magmatic source, and (iii) the granitophilic element association with gold (Van Ryt et al., 2017, 2019, 2020). If we agree with a potential magmatic source for gold, we believe that fertilization processes happened before 2645 Ma.

6. Conclusion

The structural framework of the northeastern Sukumaland granite-greenstone belt is defined by a three-stage progressive deformation history. D_{1a} stage (2700-2660 Ma) involved N-S-directed crustal shortening, resulting in upright folds, steep ESE-WNW S_{1a} fabrics, and wide ductile shear zones with shallow E-W plunging lineations. This phase was characterized by vertical flattening and oblique E-W maximum stretching under subhorizontal N-S compression. D_{1b} stage (2660-2645 Ma) introduced localized NW-striking dextral and NE-striking sinistral subvertical shear zones under ductile-brittle conditions. This phase produced complex refold structures and subvertical ENE-WSW folds, driven by a shift to strike-slip deformation under NNW-SSE-directed shortening. D_{1c} stage, following post-tectonic magmatism (ca. 2645 Ma), was dominated by brittle strike-slip faults with conjugate NW- and NE-striking systems. Both normal and reverse faulting occurred, with shallow plunging lineations, reflecting strike-slip deformation under NNW-SSE strain, locally deviated into transpressional and transtensional regimes. Overall, deformation was driven by a progressive transition from vertical flattening to strike-slip shearing, alongside progressive decrease of deformation temperature.

In the northeastern SGGB, a hot and weak lithosphere controlled shortening and crustal thickening that resulted in transpression and vertical flattening, contrasting with the localized strain typical of modern cold orogens. The absence of crustal-scale thrusts and significant topography, along with lateral crustal flow suggests that the SGGB evolved through prolonged transpression in a hot orogen setting.

Gold enrichment in the crust was recorded in hydrothermally-altered rocks. Gold fertilization of the crust likely resulted from magmatic processes, either during the juvenile and mantle-derived mafic-ultramafic magmatic event at ca. 2820-2800 Ma (Chapter II), or through felsic magmatic episodes between 2780-2700 Ma and 2660-2645 Ma. Gold was later concentrated at the Nyanzaga and Kilimani gold deposits through processes that involved magmatic-hydrothermal processes between 2645 and 2620 Ma.

Acknowledgement

The authors are grateful to the OreCorp's team for their welcome and scientific exchanges. The authors are also thankful to Abdellah Zitouni and Virginie Moineau for their contribution on the sample preparation. This work is part of Célestine Berthier's PhD project which benefited of a CIFRE funding, reference CIFRE n°2021/0546, attributed by the French National Research and Technology Agency (ANRT).

~

CHAPTER IV

~

In situ multiple sulfur isotopes of pyrite in the Neoarchean Nyanzaga gold deposit: from sulfur source to ore-fluid processes

Article en préparation pour publication dans *Geochimica et Cosmochimica Acta*

Célestine Berthier[a,b,c,*], Anne-Sylvie André-Mayer[b], Alain Chauvet[c], Julien Feneyrol[a], Nicolas Thébaud[d], Aurélien Eglinger[b,e], Rémi Bosc[a]

[a] Arethuse Geology SARL., 29 allées Saint Jean, Fuveau 13710, France

[b] GeoRessources, Université de Lorraine, CNRS, Nancy 54000, France

[c] Géosciences Montpellier, Université de Montpellier, CNRS, Montpellier 34095, France

[d] Centre for Exploration Targeting, School of Earth Sciences The University of Western Australia, WA 6009, Australia

[e] InnovExplo Inc, 560 3e Avenue, Val d'Or QC J3P 1S4, Canada

Abstract

This study combines sulfur isotope analyses ($\Delta^{33}S$-$\delta^{34}S$) and macroscopic- to microscopic-scale petro-textural studies of gold-associated sulfides and veins to trace sulfur, and indirectly gold, reservoir alongside ore-fluid processes at the Neoarchean Nyanzaga gold deposit, Tanzania. The deposit is hosted in volcanosediments metamorphosed at the greenschist facies and located in the Sukumaland greenstone belt, Tanzania craton. Progressive three-stage deformation history recorded the circulation of sulfur-bearing fluids for ~ 55 Ma, that deposited various As-, Sb-, Ag-, Mo-, Pb-, Cu-, Zn-bearing sulfide minerals. The absence of mass independent fractionation of sulfur (MIF-S) at the Nyanzaga deposit reflects sourcing of sulfur from a single source, either magmatic or mantle-derived during more than 55 Ma. Based on macro and microtextural study of veins and sulfides, combined with analyses of ^{32}S, ^{33}S and ^{34}S isotopes in pyrite, significant variations in the mass dependent fractionation (MDF-S) are interpreted as followed: during D_{1a} stage, the sulfur-bearing fluid condition likely underwent a combination of rhythmic fluid phase separation and/or local temperature variations; during the D_{1b} and D_{1c} stages, at least two fluids circulated and mixed, with one carrying gold, leading to large variation in sulfide parageneses and MDF-S values.

1. Introduction

The use of multiple sulfur isotopes is of interest for tracing Earth's deep sulfur cycle, with sulfur isotopic compositions of crustal and mantle reservoirs showing distinct signatures (Fig. 4-1; Farquhar and Wing, 2013; LaFlamme et al., 2018b, 2018c; Li et al., 2020; Lewis et al., 2021; Genot et al., 2024). Over Earth's history, significant links have been observed between the sulfur cycle and ore deposits (*e.g.*, Tomkins, 2010; Mullet et al., 2017; Thébaud et al., 2018; Hutchison et al., 2020; Walker et al., 2021; Caruso et al., 2022; Virnes et al., 2024). One critical question is how sulfur species are transformed and transferred between different reservoirs, first from mantle to crust and then within the crust. The combination of mass-dependent and mass-independent sulfur isotope signatures, respectively monitored through $d^{34}S$ and $D^{33}S$, provides valuable insights into the origins and transformations of sulfur in Earth's geological history, particularly in relation to the formation of orogenic deposits (*e.g.*, Xue et al., 2013; Selvaraja et al., 2017; LaFlamme et al., 2018a, 2018b; Sugiono et al., 2021). These lode-gold deposits are mainly associated with hydrothermal systems that develop in collisional settings at deep crustal levels, with a strong structural control (Dubé and Gosselin, 2007; Groves et al., 2018).

The diversity of host rocks and subtypes of these lode-gold deposits still leaves many open debates, particularly regarding the duration of activity of such systems, the fertility factors, the conditions for gold mobilization, the sources of fluids, and the truly favorable crustal levels for their formation (Tomkins, 2013; Gaboury, 2019). The lode-gold deposits are hydrothermal deposits, meaning epigenetic ore deposits, with the mineralized fluids that might have circulated over large distances (Tomkins, 2013; Gaboury, 2019 and references therein). Two main mechanisms of gold extraction from the source reservoir are mostly considered, from fluid release during either prograde metamorphism in fertile rocks (*e.g.*, Phillips and Groves, 1983; Pitcairn et al., 2006; Lambeck et al. 2011; Gaboury, 2013; Zhong et al., 2015), or during magma crystallization (*e.g.*, Rock and Groves, 1988; Salier et al., 2004; Bierlein and Pisarevsky, 2008; Doublier et al., 2014). Differentiating between magmatic and metamorphic sources can sometimes be achieved by analyzing the elemental assemblages of deposits. Magmatic-hydrothermal gold deposits are typically enriched in a broad range of elements such as S, Cu, Mo, Sb, Bi, W, Pb, Zn, Te, Hg, As, and Ag (*e.g.*, Goldfarb et al., 2005; Richards, 2009; Goldfarb and Pitcairn, 2023). However, many lode-gold deposits are gold-only systems with high S and As contents, rendering their origins more enigmatic and necessitating alternative approaches to identify their sources.

As sulfur plays a critical role in gold transport, the study of sulfur isotopes in sulfide minerals from orogenic gold deposits has proven to be efficient in recording ore-forming processes (e.g., Palin and Xu, 2000; Seal 2006; Kresse et al., 2018; Laflamme et al., 2018a; Sugiono et al., 2022), and fingerprinting sulfur and indirectly gold sources and reservoirs (*e.g.*, Alt et al. 1993; Chang et al. 2008; Chen et al., 2015; LaFlamme et al., 2018a, b; Virnes et al., 2024). Firstly, sulfide minerals constitute direct tracers of ore-forming processes and are largely studied as such (*e.g.*, Cook and Chryssoulis, 1990; Deditius et al., 2014; Li et al., 2014; Velásquez et al., 2014; Fougerouse et al., 2016; Gourcerol et al., 2020; Voisey et al., 2020; Perret et al., 2021; Berthier et al., 2023). Changes in the fluid physical-chemical conditions that trigger gold deposition include: fluid-rock interaction (Palin and Xu, 2000), mixing of fluids with different physical-chemical conditions (Cox, 1995; Goldfarb and Groves, 2015), rock buffering of the fluid pH (Evans et al., 2006; Petrella et al., 2020), mineral precipitation (Williams-Jones et al., 2009; Hu et al., 2017), and boiling/phase separation (Hodkiewicz et al., 2008; Voisey et al., 2020). The $\delta^{34}S$ signature on sulfide represents a monitoring of the ore-forming processes and the related changes in the physical-chemical conditions of the fluid during the crystallization of the sulfur

(*e.g.*, Ohmoto, 1972; Li and Liu, 2006; Seal 2006; Deditius et al., 2009; Phillips and Powell, 2010; Marini et al., 2011; Fiorentini et al., 2018; Hutchison et al., 2020).

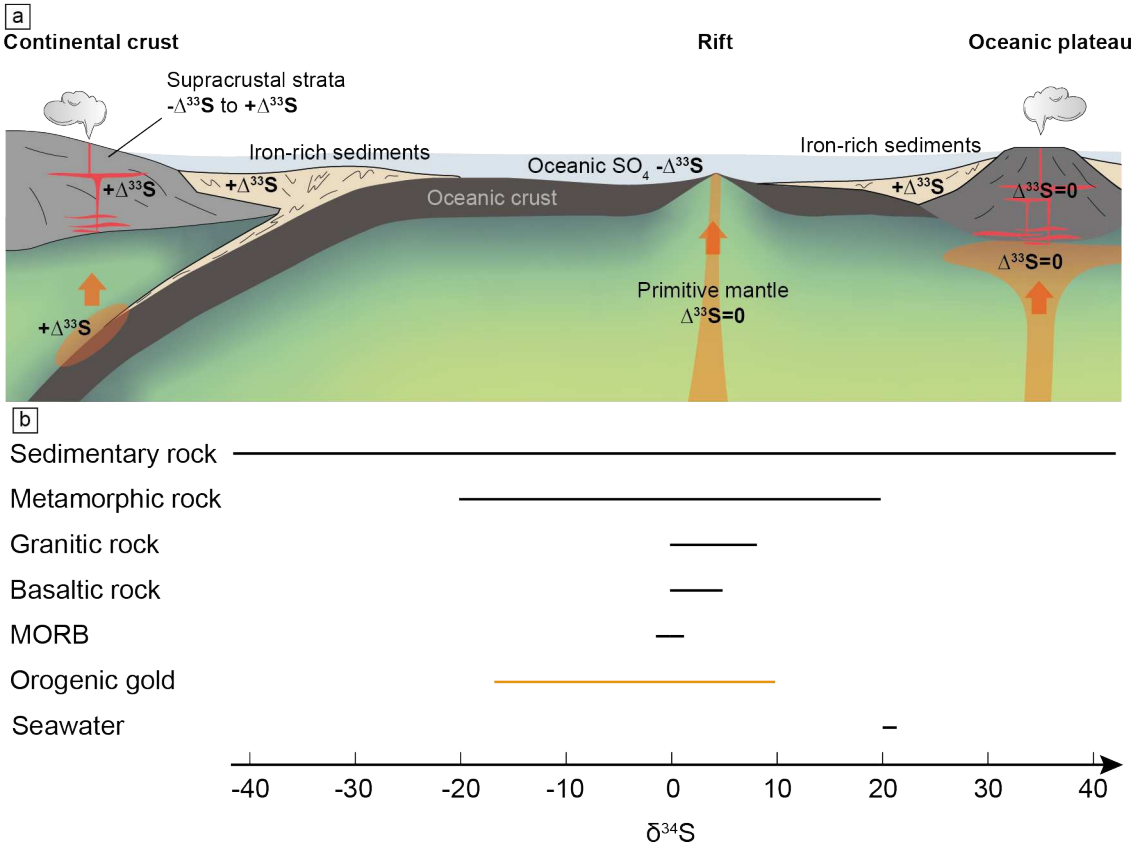

Figure 4-1. a. Schematic lithospheric-scale crossection showing the sulfur isotope composition of the main sulfur reservoirs (modified after Farquhar and Wing, 2013; LaFlamme et al., 2018b, 2018c). **b.** Generally accepted range of $\delta^{34}S$ values for various rock types, orogenic gold deposits and in seawater (Seal, 2006; Hoefs, 2009; Bark et al., 2021, orogenic gold range from Xue et al., 2013; LaFlamme et al., 2018a).

- While $\delta^{34}S$ is highly sensitive to variations in thermodynamic conditions affecting fluid during circulation and deposition, this sensitivity limits its use for reliably tracing the sulfur source (Palin and Xu, 2000; LaFlamme et al., 2016). Over the years, substantial variations in $\delta^{34}S$ have been documented in gold deposits (Fig. 4-1b), suggesting that isotopic values are more reflective of fluid physical-chemical conditions than of the source reservoir of sulfur (Hodkiewicz et al., 2008). On the contrary, mass independent fractionation of sulfur (MIF-S), monitored by $\Delta^{33}S$, is chemically conservative of the sulfur source and is not affected by dynamic chemical processes (Farquhar et al., 2000, 2002). The use of such proxy is particularly efficient for differentiating sulfur sourced from primitive mantle ($\Delta^{33}S \approx 0‰$) and crustal ($\Delta^{33}S \neq 0‰$) reservoirs through complex geological processes (Fig. 4-1a; *e.g.*, Hofman et al., 2009; LaFlamme et al., 2018c; Genot et al., 2024; Virnes et al., 2024).
- In petro-structurally constrained gold deposits, coupling the study of $\delta^{34}S$ and $\Delta^{33}S$ allows to unravel the source of sulfur and the evolution of the ore fluid, and ultimately allow discussing potential sources for gold (*e.g.*, LaFlamme et al., 2018b; Thébaud et al., 2018; Sugiono et al., 2021, 2022; Caruso et al., 2022). This chapter investigates the source of sulfur and the evolution of fluid conditions by an integrated study of multi-sulfur isotopes in three pyrite generations from the well-constrained

Nyanzaga gold deposit of the Neoarchean Sukumaland granite-greenstone belt (SGGB) in Tanzania (Berthier et al., 2024, Chapter V). Here, we combine MIF-S and MDF-S signatures of pyrite grains to constrain the source of sulfur and to adjust in time and space with the current knowledge of crustal growth recorded in the northern SGGB during Neoarchean (Chapter II and III). With the addition of detailed study of sulfide and vein paragenesis, and mineral textures of each deformation-hydrothermal stage, we discuss the physical-chemical evolution of the sulfur-bearing fluid. Ultimately, the multi-sulfur isotope signature and petro-textural study constrains the source of gold and the timing of circulation of the mineralized fluid.

2. Regional geological setting

The Tanzania craton consists of two main regions: the granitoid-dominated Central Tanzania Region and the greenstone-rich, gold-endowed Lake Victoria Goldfields (LVG; Fig. 4-2a; Borg and Shackleton, 1997; Kabete et al., 2012; Kwelwa et al., 2018). The Nyanzaga gold project is located in the Neoarchean Sukumaland granite-greenstone Belt (SGGB), the largest and most gold-endowed belt in the LVG (Fig. 4-2b; Henkel et al., 2016). The stratigraphy in the greenstone belt is divided into the Nyanzian and Kavirondian Supergroups (Fig. 4-2c; Borg, 1992; Sanislav et al., 2015; Kwelwa et al., 2018). The base of the Nyanzian consists of mafic volcanics, *e.g.,* basalt, dolerite, and minor felsic volcanics and banded-iron formations (BIF) dated between 2820 and 2800 Ma (Manya and Maboko, 2003, 2008; Cook et al., 2016). They formed in a marine environment, either in an island arc setting or an oceanic plateau (*e.g.*, Chamberlain, 2003; Cook et al., 2016). The Upper Nyanzian consists of a well bedded turbiditic sequence interlayered with chert-sediment intercalations, banded iron formations (BIF) and pyritic black shales, with felsic volcanic and volcaniclastic intercalations, dated between 2780 and 2650 Ma (Quennell et al., 1956; Borg and Krogh, 1999). At the Nyanzaga deposit, felsic volcaniclastics were dated at ca. 2775 Ma (Chamberlain and Tosdal, 2007). The Nyanzian Supergroup underwent generalized metamorphism, mostly to the greenschist facies, reaching the amphibolite facies near granitic intrusions. The Kavirondian Supergroup consists of syn-tectonic and post-tectonic molasse basins, deposited between 2700-2660 Ma and after 2640 Ma, respectively (Gabert, 1990; Borg, 1992; Sanislav et al., 2015; Chapter III). They are dominated by polymictic conglomerates and well-bedded pebble sandstones. Different types of granitoids flank the Archean supracrustal rocks to the north and south of the Sukumaland belt, from highly deformed, pre- to syn-tectonic granodiorites and quartz-monzonites (2780-2660 Ma), to late-tectonic granodiorites and granites (2660-2645 Ma), to undeformed, post-tectonic granitic bodies (2645-2620 Ma; Chapters I, II).

3. Deposit geology

3.1. The Nyanzaga gold project

The Nyanzaga project is located in the northeastern part of the SGGB and is hosted within volcanosedimentary units of the Nyanzian Supergroup (Fig. 4-2b-c; Henckel et al., 2016). The project comprises two gold deposits in development, operated by Perseus Mining: Nyanzaga (combined indicated and inferred mineral resources of 23.7 Mt @ 4.03 g/t Au for 3.07 Moz Au, at a 1.5 g/t Au cut-off grade; OreCorp, 2017) and Kilimani (inferred mineral resources of 6.3 Mt @ 1.06 g/t Au for 213 koz Au, with a 0.40 g/t Au cut-off grade; OreCorp, 2022).

Three major formations have been defined at the Nyanzaga deposit: the Lower Volcaniclastic, the Central

Formation and the Upper Volcaniclastic (Fig. 4-2c-d; Henckel et al., 2016; OreCorp, 2017, 2022). The Lower Volcaniclastic Formation is dominated by thick package of dacitic volcaniclastic rocks (> 300 m), capped by a 20-50 meter-thick chert unit. The Central Formation consists of chert-, sandstone- and mudstone-dominated units that comprise alternating cherts, siltstones, sandstones and mudstones (270-290 m). Massive sulfide lenses are encountered locally in mudstones and cherts. The Nyanzaga Upper Volcaniclastic Formation consists of a thick package of dacitic to intermediate volcaniclastic rocks (250-300 m). The sequence in the Nyanzaga area is topped by the Kilimani Iron Formation, comprising BIF and interbedded mudstone and siltstone (310-420 m). Sedimentation is characterized by lateral variations in facies occurring across hundreds of meters. No granitoid intrusions have been identified within the Nyanzaga mineralization area, with the nearest granitic bodies located 3 km to the south and 5 km to the east. Note that all units of the volcanosediments exhibiting greenschist facies metamorphism, the prefix 'meta-' has been removed from the name of the units for readability purpose in the rest of the chapter.

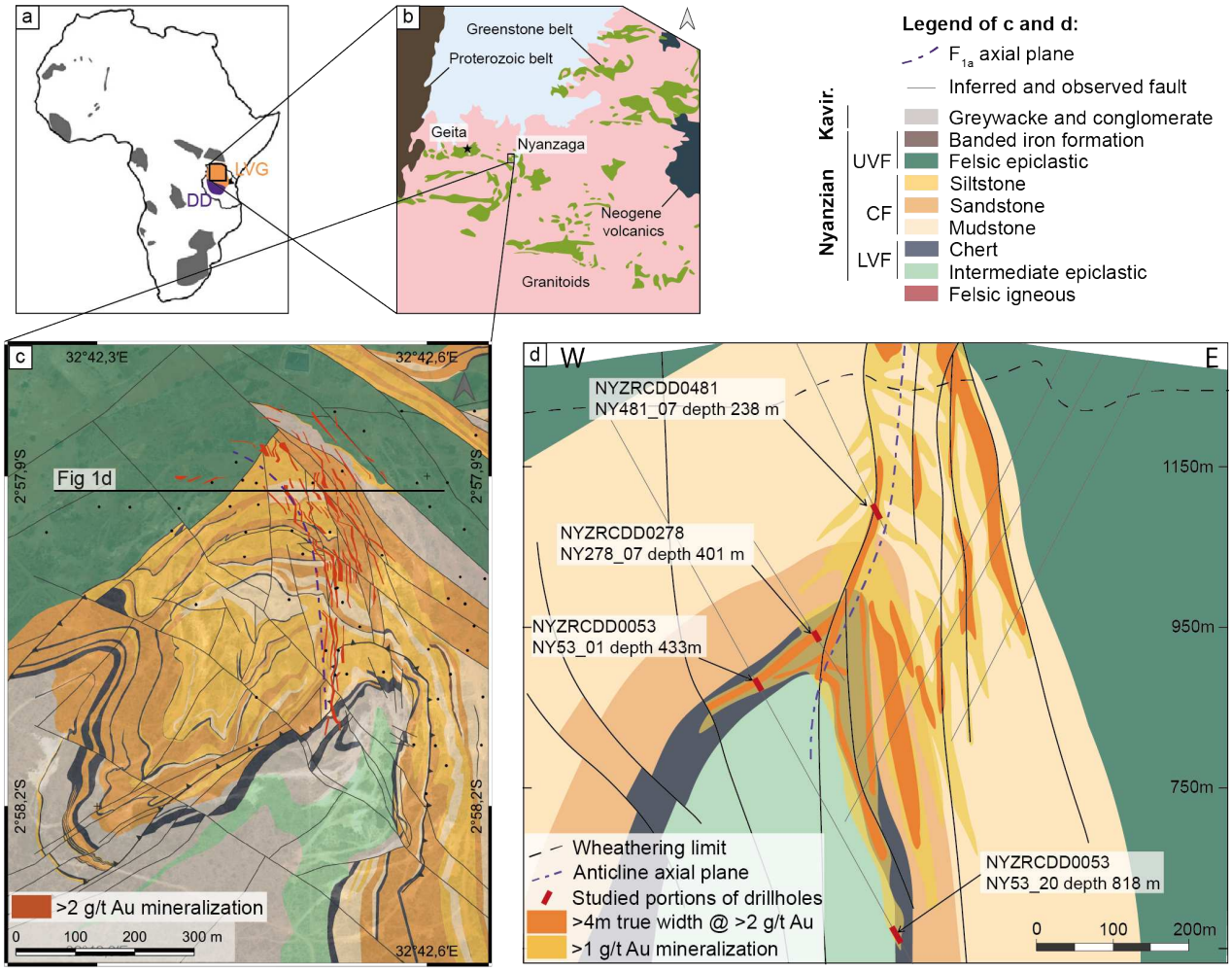

Figure 4-2. a. Present-day location of the Tanzania craton within the African continent. Orange = Lake Victoria Goldfields, Purple = Dodoman Domain. **b.** Location of the Nyanzaga project and Geita gold deposit within the Sukumaland granite-greenstone belt (SGGB), Lake Victoria Goldfields (from Cook et al., 2016, after Borg and Shackelton, 1997). **c.** Geological map of the Nyanzaga deposit (based on field mapping and geophysical data, OreCorp, 2017, 2022). **d. 2°57'54.5"S vertical section of the Nyanzaga deposit. The main ore zones are indicated. Studied sections of cores are outlined** in red on the drillholes. Kavir. = Kavirondian; LVF = Lower Volcaniclastic Formation; CF = Central Formation; UVF = Upper Volcaniclastic Formation; KIF = Kilimani Iron Formation.

Alteration processes including silicification or silica-dolomite alteration are extensive in the Nyanzaga deposit, replacing sandstones and siltstones, and locally replacing mudstone (OreCorp, 2017). The cherts from the Lower Volcaniclastic Formation are demagnetized at Nyanzaga, but preserved magnetite to the east and west of the deposit. The Kilimani gold deposits is deeply weathered and very little of the hydrothermal mineral assemblages are preserved. At the Nyanzaga deposit, the bulk of the gold mineralization is hosted in siliceous rocks such as cherts or silicified sandstone and siltstone, more rarely in mudstones (OreCorp, 2017). At Kilimani, mineralization is hosted in volcaniclastics of the Upper Volcaniclastic (OreCorp, 2022).

3.2. Deformation-hydrothermal framework

Berthier et al. (2024, Chapter V) conducted a detailed petro-structural study of the deformation-hydrothermal evolution of the Nyanzaga and Kilimani gold deposits. The main features for Nyanzaga is summed up in this section.

Both deposits underwent three-stage progressive and continuous shortening. The first compressional stage, D_{1a}, created upright E-W folds in the volcanosedimentary sequence, in response to N-S-oriented shortening. Transpressional regime then dominated deformation during the ongoing N-S shortening, leading to the refolding of volcanosediments by D_{1b}-related subvertical folds. Due to the brittle nature of late deformation during D_{1c}, a set of faults emerged, with the NW-SE ones exhibiting dextral shearing and controlling the formation of normal N-S vertical faults.

Indirect dating of deformation stages, based on regional petro-structural observations is detailed in Chapter III, starting with the ductile D_{1a} regional penetrative deformation stage dated between 2700 and 2660 Ma, followed by ductile-brittle D_{1b} strike-slip deformation between 2660 and 2645 Ma. The brittle D_{1c} stage affected all lithologies formed prior to 2645 Ma, providing a maximum age for deformation.

Associated with deformation, five stages of disseminated alteration and veins developed in response to hydrothermal circulation (Berthier et al., 2024, Chapter V). D_{1a} and D_{1b} stages are dominated by disseminated alteration of silicate and sulfide minerals (Fig. 4-3c-d and j) and associated with quartz- and ankerite-dominated veining (Fig. 4-3a-b and i). Hydrothermal alteration then transitioned to vein-dominated and minor sulfide dissemination during D_{1c} stage (Fig. 4-3m-o). Three veining stages are described during D_{1c}: (i) V_3 smoky quartz ± ankerite – sulfide veinlets and tectonic breccias, (ii) V_4 milky quartz large veins and tectonic breccias, and (iii) V_5 late calcite-chlorite-dominated veinlets.

Within this hydrothermal history, Berthier et al. (2024, Chapter V) discriminated four generations of sulfide minerals, associated with distinct mineral assemblages and alteration styles. The two first generations consist of mainly disseminated pyrite aggregates to pyrite veinlets associated to D_{1a} and D_{1b} deformation stages.

(i) The first generation consists of D_{1a}-related, pyrite-dominated, dense disseminated aggregates developed near parallel to the S_0 bedding in fine-grained layers, such as cherts and mudstones (Fig. 4-3c-d). Pyrite is associated with quartz, sericite and rare tourmaline, monazite, scheelite and chlorite and forms pluri-centimeter-thick bands.

(ii) This first set of sulfide minerals is overgrown by late-D_{1b}-related pyrite, accompanied by rare folded ankerite ± pyrrhotite – pyrite veinlets and pseudo-boudins with the same mineralogy (Fig. 4-3c, i-j).

Finally, two major incomes of sulfide minerals are associated with D_{1c} hydrothermal alteration, related to two veining stages:

(iii) the first one consists of V_3 smoky quartz ± carbonate – pyrrhotite – pyrite – arsenopyrite – gudmundite – electrum – galena – jamesonite – bournonite veinlets and crackle breccias (Fig. 4-3m-n), and associated with minor disseminated hydrothermal alteration with pyrite – pyrrhotite – arsenopyrite ± gudmundite – electrum (Fig. 4-3o).

(iv) The second V_3 is a complex assemblage of calcite – chlorite ± barite – galena – pyrrhotite – jamesonite – boulangerite – bournonite – chalcopyrite – sphalerite – tetrahedrite – ullmannite – molybdenite – electrum in V_5 veins. No pyrite has been observed in this stage.

No gold is associated with D_{1a}- and D_{1b}-related hydrothermal stages that are hence interpreted barren. The petrographic and structural observations consistently indicate that gold mineralization is spatially and temporally associated with the hydrothermalism stages associated both to D_{1c}-related fault zones at the deposit scale, and to D_{1c}-related sulfide minerals at macro- to microscopic scales (Berthier et al., 2024, Chapter V).

4. Methods

4.1. Sampling and sample preparation

The detailed petro-structural analyses of the Nyanzaga and Kilimani gold deposits undertaken by Berthier et al., (2024) concluded that the two deposits share the same tectono-hydrothermal history, including the same sulfurization stages. Because strong weathering affected the vast majority of the Kilimani deposit, we therefore sampled sulfide minerals from the Nyanzaga deposit alone. Gold grades analyzed by fire assay on one-meter drill cores by OreCorp Limited are reported on sample macro- and microphotographs (Fig. 4-3).

Four pyrite-bearing samples were selected for multiple sulfur isotope analyses: Py_{1a} and Py_{1b} disseminated aggregates (samples NY53_01 and NY53_20), Py_{1c} grains in pyrite-pyrrhotite-dominated vein (sample NY481_07) and in galena-bearing vein (sample NY278_07; Fig. 4-3). These four samples were processed into thin sections for micro-scale petrographic, structural and textural study, and rock mounts for multiple sulfur isotope analyses. The round rock mounts are 24.5 mm large and 5 mm deep. The samples were carefully mounted so that the targeted pyrite grains would sit in the center of the mount and avoid analytical artefacts in the 5 mm wide outer ring of the mount (as detailed in LaFlamme et al., 2016). Pyrite micro-textures, internal zoning and mineral inclusions were highlighted in both thin sections and rock mounts by scanning electron microscope in backscattered electron mode at the GeoRessources laboratory (Université de Lorraine, Nancy, France). The mounts were then gold coated (30 nm thickness) for multiple sulfur isotope analyses. Note that analytical uncertainty is given in 2SD.

4.2. Multiple sulfur isotope analyses and analyses processing

Multiple sulfur isotope analyses of pyrite were conducted on a CAMECA IMS 1270 Secondary Ion Mass Spectrometer (SIMS) at the Centre de Recherches Pétrographiques et Géochimiques (CRPG), Université de Lorraine-CNRS, France. Multi-collection mode using three off-axis Faraday cups using amplifiers with 10^{10} Ω (L '2), 10^{11} Ω (C), and 10^{11} Ω (H1) enabled the simultaneous measurements of ^{32}S, ^{33}S and ^{34}S ion beams.

A Cs+ primary ion beam of 2.5 nA was focused to a 15 µm diameter, under a $2.21.10^{-8}$ pressure chamber. Electrons were bombarded to compensate positive charges accumulated on the surface. The Spain pyrite ($\delta^{34}S$ = -1.56 ± 0.26 ‰ (σ), $\delta^{33}S$ = -0.78 ± 13 ‰ (σ), $\Delta^{33}S$ = 0.03 ± 0.01 ‰ (σ); Kitayama, 2018) was analyzed as reference material at the beginning, middle and end of the session to correct time drift, monitor external standard repeatability, and correct for instrumental mass fractionation (IMF). Mean measurement errors on the pyrite analyses are for $\delta^{34}S$ and $\Delta^{33}S$ of 0.08‰ and 0.10 ‰, respectively. Measurements performed over 40 integration cycles for a total of 117 and 19 analyses on our samples and standards, respectively. The analyzes are listed in Supplementary Material 3.1.

Calculation process for the sulfur mass dependent fractionation of $\delta^{34}S$, $\delta^{33}S$ and sulfur mass independent fractionation of $\Delta^{33}S$ values are described in Farquhar and Wing (2003) and LaFlamme et al. (2016) as followed:

$$\delta^{x}S\ (‰) = \left(\frac{\left({}^{x}S/{}^{32}S\right)_{Sample} - \left({}^{x}S/{}^{32}S\right)_{V-CDT}}{\left({}^{x}S/{}^{32}S\right)_{V-CDT}}\right)$$

Standardized to the Vienna-Cañon Diablo Troilite (V-CDT; Ding et al., 2001). Analytical uncertainty:

$$\sigma_{\delta^{x}S} = \left(\frac{1000}{\alpha \times R_{V-CDT}}\right) \times \sqrt{\left(\sigma_{R_i}\right)^2 + \left(\frac{-R_i}{\alpha}\sigma_{\alpha}\right)^2}$$

Where α is the correction factor to account for instrumental mass fractionation, R_i is the drift-corrected sample measurement, $R_{V\text{-}CDT}$ is the drift-corrected sample measurement standardized to the Vienna-Cañon Diablo Troilite. Their calculation process is detailed in LaFlamme et al. (2016).

$$\Delta^{33}S = \left(\delta^{33}S - 1000\left(\left(1 + \frac{\delta^{34}S}{1000}\right)^{0.515} - 1\right)\right)$$

Analytical uncertainty:

$$\sigma_{\Delta^{33}S} = \sqrt{\begin{array}{c}\sigma^2_{\delta^{33}S} + \sigma^2_{\delta^{34}S} \times \left[0.515 \times \left(1 + \frac{\delta^{34}S}{1000}\right)^{-0.485} \times \sigma^2_{\delta^{34}S}\right]^2 \\ +2 \times \sigma_{\delta^{34}S\delta^{33}S} \times \left[0.515 \times \left(1 + \frac{\delta^{34}S}{1000}\right)^{-0.485}\right]\end{array}}$$

Where corresponds to the $\delta^{33}S$ and $\delta^{34}S$ covariance.

5. Results

5.1. Microstructural and textural features of pyrite grains and veins

As described in section 3.2., pyrite is observed in all three deformation stages and will therefore be subdivided in Py_{1a}, Py_{1b} and Py_{1c} in the following. In this section we develop the microscopic-scale study of the pyrite textures and associated veins (Fig. 4-3, Table 4-1). We summarized the macroscopic and microscopic characteristics of both sulfide minerals and veins in Figure 4.

Disseminated Py_{1a} aggregates (Figs. 4-3c-d, 4-4a-b): they form dense pyrite-dominated aggregates in which they present two textural styles (Fig. 4-3g-h). The first one consists of intricate textures with an imbrication of 5 to 12 µm-large 3D hexagonal cores, overgrown by 13 to 30 µm-large cubic dark and light rims (Fig. 4-3g-h). The second style formed 60 to 80 µm-large hexagonal cores surrounded by up to 100 µm-large cubic pyrite (Fig. 4-3g). Networks of carbonate ± quartz veins developed, with carbonate crustiform textures (Fig. 4-3a), and quartz comb veins with inner carbonate infilling (Fig. 4-3b and f). The crustiform bands show variations in carbonate grain sizes but no mineral assemblage variations. Carbonate grains show dense and thick patchy twins, locally curved (Fig. 4-3e). Quartz grains show recrystallization texture, with grain boundary migration (GBM, Fig. 4-3f; Passchier and Trouw, 2005).

Disseminated Py_{1b} overgrowths (Figs. 4-3c, j and l, 4-4c-e): during the D_{1b} deformation stage, the aggregates of Py_{1a} grains are overgrown by anhedral and homogeneous Py_{1b}. Py_{1b} grains are associated with small amounts of other sulfide minerals, and can be subdivided into two distinct pyrite-dominated assemblages: (i) pyrite associated with various amounts of pyrrhotite and very rare arsenopyrite grains, named $Py_{1b\text{-}PP}$ (Figs. 4-3j, 4-4d); (ii) pyrite and minor amounts of arsenopyrite, gudmundite, Ag-bearing tetrahedrite and chalcopyrite, named $Py_{1b\text{-}PG}$ (Figs. 4-3l, 4-4e). Rare veins are observed during the D_{1b} stage, infilled with ankerite with no distinctive primary or recrystallisation texture (Berthier et al., 2024, Chapter V).

Vein-dominated Py_{1c} (Figs. 4-3m-n, 4-4f-h): during the D_{1c} deformation stage, Py_{1c} is dominantly observed in V_3 veinlets, that express a large diversity of mineral assemblages, which can be grouped into two main types. These two veins are D_{1c}, however no crosscutting relationship are observed between them and no temporal constrain can be proposed for the two vein types.

(i) *Pyrite-pyrrhotite-dominated veins* consist of quartz ± pyrrhotite ± pyrite ± ankerite ± electrum assemblages, which are either quartz- or pyrrhotite-pyrite-dominated (Figs. 4-3m, 4-4g), some showing rare association with ankerite. The pyrite grains, named $Py_{1c\text{-}pp}$, are up to 5.5 millimeter large, subhedral to euhedral and show no zoning (Fig. 4-3r). Trace amounts of arsenopyrite grains were observed in the veins.

(ii) *Galena-bearing veins* are characterized by a large spectrum of sulfide minerals, associated with quartz, ankerite and chlorite (Figs. 4-3n, 4-4h). The pyrite grains, named $Py_{1c\text{-}PG}$, range from 40 µm-large aggregates to 400 µm-large grains (Fig. 4-3q and s). They show no zoning, or small two-rim zoning at the edges of the grains (Fig. 4-3s). The metallic mineral assemblage consists of pyrrhotite, pyrite, arsenopyrite, gudmundite, galena, jamesonite, boulangerite, bournonite, chalcopyrite, tetrahedrite and electrum (Fig. 4-3n and q). Arsenopyrite grains are often associated with gudmundite and can show dense oscillatory zoning, fractured by an assemblage of jamesonite ± galena – boulangerite – electrum.

$Py_{1c\text{-}PP}$ is also encountered in alteration halos around D_{1c}-related pyrite-pyrrhotite-dominated veins, disseminated in the host rock (Fig. 4-3o). They form very small aggregates, associated with pyrrhotite and arsenopyrite, showing rare electrum inclusions. Quartz grains in veins may present bulging recrystallization textures (BLG, Fig. 4-3e; Passchier and Trouw, 2005).

Figure 4-3. petro-textural characteristics of veins and sulfide minerals at the Nyanzaga deposit, from D_{1a}, D_{1b}, D_{1c} deformation stages. Features are divided into macro- and microscale observations. **a.** and **b.** Macroscale textures of D_{1a}-related Cb crustiform vein and Qz comb veins infilled by inner Cb, respectively. They are crosscut by D_{1c}-related Qz ± Py-Po veinlets. **c.** and **d.** Macroscale texture of D_{1a}-related disseminated pyrite bands. They crosscut the S_0 bedding and are affected by folding. Py_{1b} overgrows the Py_{1a} bands. **e.** and **f.** Microscale mineral texture of D_{1a}-related Cb crustiform and Qz-Cb comb veins, respectively, and crosscut by D_{1c}-related Qz-Py-Po veins (cross-polarized, transmitted light). Cb in the comb veins locally shows zonal texture, while Qz in the comb vein presents grain boundary recrystallization texture. **g.** and **h.** Microscale mineral texture of D_{1a}-related Py bands, with complex assemblage of D_{1a}-related hexagonal Py cores and cubic rims (BSE-SEM image). **i.** D_{1b}-related Ank vein stockwork crosscutting D_{1a}-related Py bands at the macroscale. **j.** Py_{1a} bands overgrown by D_{1b}-related Py grains, and affected by D_{1b}-related Po bands. D_{1b}-related Ank veins crosscut Py_{1a} bands and are crosscut by D_{1b}-related sulfide minerals. **k.** Zoom at the microscale on the D_{1b}-related Ank veins (cross-polarized, transmitted light). **l.** D_{1b}-related homogenous Py_{1b} overgrowing the hexagonal-cubic Py_{1a} aggregates (BSE-SEM image). **m.** and **n.** Macroscale texture of the D_{1c}-related Py-Po-dominated and Ga-bearing veins, respectively. **n.** The mineral assemblage of the vein consist of Ga-Jam-Boul-Apy-Gu-Py-Po-Qz-Cb-Chl. The limits of the veins are highlighted with dotted lines. **o.** Macroscale texture of D_{1c}-related disseminated Py and Po. They are associated with D_{1c}-related Py-Po-Qz veins crosscutting D_{1a}-related Cb comb veins. **p.** and **q.** microscale mineral texture and assemblage in D_{1c}-related veins. **p.** Bulging recrystallization texture in Qz grains from a D_{1c}-related Qz vein. **q.** Sulfide assemblage in a Ga-bearing vein, with Ga-Jam-Boul-Apy-Py-Po-Gu (reflected light). **r.** and **s.** Microscale textures of D_{1c}-related Py, in Py-Po-dominated and Ga-bearing veins, respectively. **r.** Py grains are homogeneous and are associated with El grains (reflected light). **s.** Small Py_{1c} grains with a single slight chemical zoning (BSE-SEM image). Note that fire assay gold grades reported here were conducted on one-meter sample and therefore may not reflect the gold content of the pyrite or vein generation observed on the photographs. Ank = ankerite; Apy = arsenopyrite; Ba = barite; Boul = boulangerite; Cb = carbonate; Chl = chlorite; El = electrum; Ga = galena; Gu = gudmundite; Jam = jamesonite; Po = pyrrhotite; Py = pyrite; Qz = quartz; Tur = tourmaline.

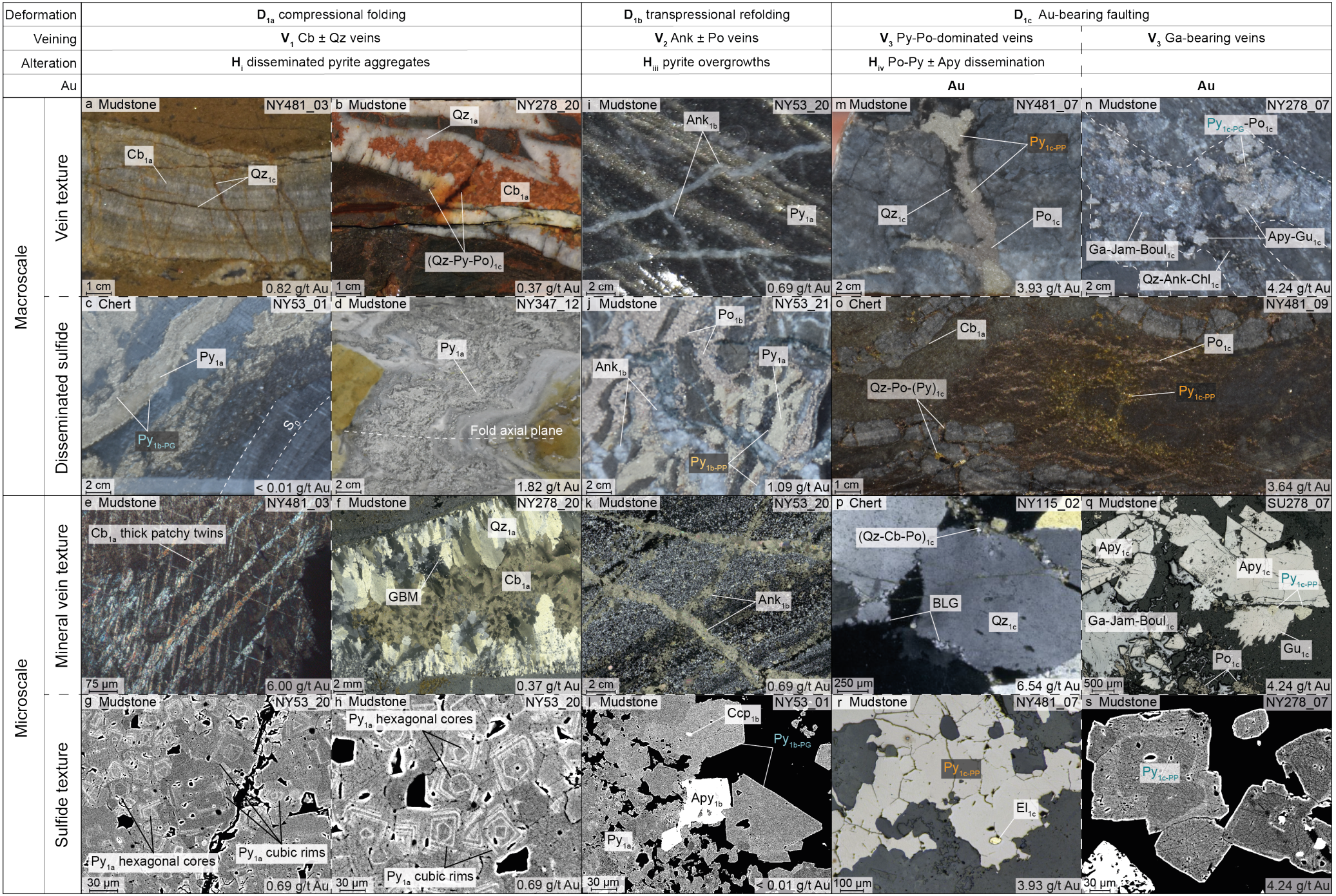
Deformation
D_{1a} compressional folding
D_{1b} transpressional refolding
D_{1c} Au-bearing faulting
Veining
V_1 Cb ± Qz veins
V_2 Ank ± Po veins
V_3 Py-Po-dominated veins
V_3 Ga-bearing veins
Alteration
H_i disseminated pyrite aggregates
H_{iii} pyrite overgrowths
H_{iv} Po-Py ± Apy dissemination
Au
Au
Au
Macroscale
Vein texture
Disseminated sulfide
Microscale
Mineral vein texture
Sulfide texture
a Mudstone NY481_03
Cb_{1a}
Qz_{1c}
1 cm
0.82 g/t Au
b Mudstone NY278_20
Qz_{1a}
Cb_{1a}
$(Qz\text{-}Py\text{-}Po)_{1c}$
1 cm
0.37 g/t Au
i Mudstone NY53_20
Ank_{1b}
Py_{1a}
2 cm
0.69 g/t Au
m Mudstone NY481_07
$Py_{1c\text{-}PP}$
Qz_{1c}
Po_{1c}
2 cm
3.93 g/t Au
n Mudstone NY278_07
$Py_{1c\text{-}PG}$-Po_{1c}
Apy-Gu_{1c}
Ga-Jam-$Boul_{1c}$
Qz-Ank-Chl_{1c}
2 cm
4.24 g/t Au
c Chert NY53_01
Py_{1a}
$Py_{1b\text{-}PG}$
S_0
2 cm
< 0.01 g/t Au
d Mudstone NY347_12
Py_{1a}
Fold axial plane
2 cm
1.82 g/t Au
j Mudstone NY53_21
Po_{1b}
Py_{1a}
Ank_{1b}
$Py_{1b\text{-}PP}$
2 cm
1.09 g/t Au
o Chert NY481_09
Cb_{1a}
Po_{1c}
$Qz\text{-}Po\text{-}(Py)_{1c}$
$Py_{1c\text{-}PP}$
1 cm
3.64 g/t Au
e Mudstone NY481_03
Cb_{1a} thick patchy twins
75 µm
6.00 g/t Au
f Mudstone NY278_20
Qz_{1a}
Cb_{1a}
GBM
2 mm
0.37 g/t Au
k Mudstone NY53_20
Ank_{1b}
2 cm
0.69 g/t Au
p Chert NY115_02
$(Qz\text{-}Cb\text{-}Po)_{1c}$
BLG
Qz_{1c}
250 µm
6.54 g/t Au
q Mudstone SU278_07
Apy_{1c}
Apy_{1c}
$Py_{1c\text{-}PP}$
Ga-Jam-$Boul_{1c}$
Gu_{1c}
Po_{1c}
500 µm
4.24 g/t Au
g Mudstone NY53_20
Py_{1a} hexagonal cores
Py_{1a} cubic rims
30 µm
0.69 g/t Au
h Mudstone NY53_20
Py_{1a} hexagonal cores
Py_{1a} cubic rims
30 µm
0.69 g/t Au
l Mudstone NY53_01
Ccp_{1b}
$Py_{1b\text{-}PG}$
Apy_{1b}
Py_{1a}
30 µm
< 0.01 g/t Au
r Mudstone NY481_07
$Py_{1c\text{-}PP}$
El_{1c}
100 µm
3.93 g/t Au
s Mudstone NY278_07
$Py_{1c\text{-}PP}$
30 µm
4.24 g/t Au

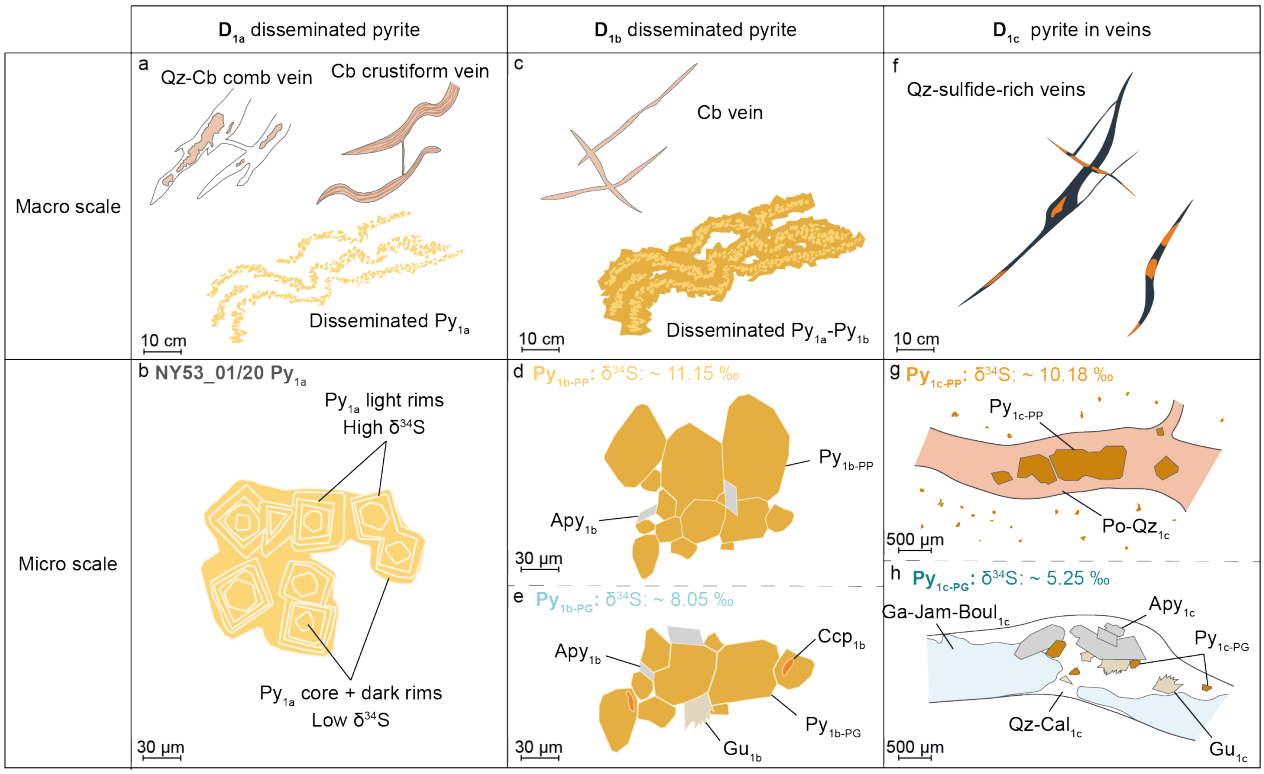

Figure 4-4. Schematic representation of vein and sulfide structures and textures at the Nyanzaga gold deposit. $\delta^{34}S$ values for each pyrite texture is shown. Apy = arsenopyrite; Boul = boulangerite; Cal = calcite; Cb = carbonate; Ccp = chalcopyrite; Ga = galena; Gu = gudmundite; Jam = jamesonite; Qz = quartz; Po = pyrrhotite; Py = pyrite.

Deformation	**D_{1a} stage**	**D_{1b} stage**	**D_{1c} stage**
Veining	V_1 Dol-Qz	V_2 Ank	V_3 Qz-sulfide
Alteration	Py_{1a} aggregates	Py_{1b} overgrowths	Disseminated Py-Po-(Apy-El)$_{1c}$
Au			Au
Host rock alteration	Py_{1a} aggregates with hexagonal cores and cubic rims ***NY53_01_20***	Py_{1b} overgrowths around Py_{1a} aggregates, 2 types: (i) Py-Po-(Apy) assemblage ***$Py_{1b\text{-}PP}$ in NY53_20*** (ii) Py-(Apy-Gu-Tet-Ccp) ***$Py_{1b\text{-}PG}$ in NY53_01***	Minor dissemination of Py-Po-(Apy-El)
Veins	Cb crustiform veins with dense, thick, curved twins. Qz comb veins with GBM textures. Cb inner infilling.	Rare Ank veins	2 types: (i) Py-Po-dominated veins: Qz-Py-Po-(Ank-El) ***$Py_{1c\text{-}PP}$ in NY481_07*** (ii) Ga-dominated veins: Ga-Jam-Boul-Apy-Gu-Py-Po-Qz-Cb-Chl ***$Py_{1c\text{-}PG}$ in NY278_07***

Table 4-1. Summary of veins and host rock alterations associated with all three pyrite-bearing hydrothermal stages.

5.2. *Multiple sulfur isotope results*

In situ multiple sulfur isotope were analyzed in pyrite grains from the three pyrite-bearing hydrothermal stages previously described: (Table 4-2, Figs. 4-5, 4-7). Thirty-nine analyses were performed on thirty-seven Py_{1a} grains, yielding $\delta^{34}S$ analyses that range from 2.35 ± 0.07 ‰ to 22.72 ± 0.09 ‰, and $\Delta^{33}S$ values that range from -0.18 ± 0.10 ‰ to 0.17 ± 0.10 ‰, with a weighted mean of -0.0059 ± 0.0153 ‰ (MSWD = 2.9 ; n = 39; Figs. 4-5, 4-6). Analysis spots are often larger than the smallest of hexagonal core-cubic rims pyrite, resulting in a sulfur signature of a mix of cores, dark and light rims. Yet, in the larger Py_{1a} grains, a trend is highlighted, with higher $\delta^{34}S$ values recorded in spots with large proportion of light rims and lower values in cores and dark rims (Fig. 4-5). $\Delta^{33}S$ values in Py_{1b} range between -0.08 ± 0.10 and 0.17 ± 0.11 ‰, with a $\Delta^{33}S$ weighted mean of 0.026 ± 0.017 ‰ (MSWD = 1; n = 31 on 28 grains; Figs. 4-6, 4-7a). $\delta^{34}S$ in $Py_{1b\text{-}PP}$ and in $Py_{1b\text{-}PG}$ range respectively between 10.78 ± 0.08 ‰ and 12.97 ± 0.07 ‰, and between 5.64 ± 0.07 ‰ and 10.05 ± 0.07 ‰ (Fig. 4-7).

Py_{1c} generation shows two clusters of $\delta^{34}S$ based on the vein type (Fig. 4-7). In galena-bearing veins, twenty-six analyses on twelve $Py_{1c\text{-}PG}$ grains yield $\delta^{34}S$ values ranging between 4.50 ‰ ± 0.08 ‰ and 5.83 ± 0.08 ‰ (Table 4-2, Fig. 4-7). Twenty analyses were conducted on seven $Py_{1c\text{-}PP}$ grains in pyrite-pyrrhotite-dominated veins and record $\delta^{34}S$ values that range from 9.78 ± 0.08 ±‰ to 11.71 ± 0.08 ‰ (Table 4-2, Fig. 4-7). The $\Delta^{33}S$ values in Py_{1c} range from -0.11 ± 0.13 ‰ to 0.11 ± 0.10 ‰, with a weighted mean of -0.0011 ± 0.0143 (MSWD = 1.2; n = 46, Fig. 4-6). The overall $\Delta^{33}S$ weighted mean for all generations is 0.0048 ± 0.0089 ‰ (MSWD = 1.7; n = 117, Fig. 4-6).

Sample	Py generation	N of analyses	$\delta^{34}S$ range (‰) $\delta^{34}S$ mean (‰)	$\Delta^{33}S$ range (‰) $\Delta^{33}S$ weighted mean (‰)
NY53_01	Py_{1a} aggregates	17	2.35 ± 0.07 to 22.72 ± 0.09	-0.13 ± 0.09 to 0.09 ± 0.09 -0.02 ± 0.024 (MSWD = 2.1)
	$Py_{1b\text{-}PG}$ aggregates	13	5.64 ± 0.07 to 10.05 ± 0.07 8.05 ± 0.02	-0.06 ± 0.09 to 0.08 ± 0.14 0.024 ± 0.027 (MSWD = 1.1)
NY53_20	Py_{1a} aggregates	22	5.28 ± 0.07 to 22.33 ± 0.08	-0.18 ± 0.10 to 0.17 ± 0.11 0.004 ± 0.020 (MSWD = 3.5)
	$Py_{1b\text{-}PP}$ aggregates	18	10.78 ± 0.08 to 12.97 ± 0.07 11.15 ± 0.02	-0.08 ± 0.10 to 0.11 ± 0.15 0.027 ± 0.023 (MSWD = 0.97)
NY278_07	Py_{1c} in Ga-bearing vein	26	4.50 ± 0.08 to 5.83 ± 0.08 5.25 ± 0.01	-0.08 ± 0.11 to 0.10 ± 0.11 0.0021 ± 0.0187 (MSWD = 1.2)
NY481_07	Py_{1c} in Po-Py-dominated vein	20	9.78 ± 0.08 to 11.71 ± 0.08 10.18 ± 0.02	-0.11 ± 0.13 to 0.11 ± 0.10 -0.0031 ± 0.0217 (MSWD = 1.2)

Table 4-2. Summary of multiple sulfur isotope analyses on pyrite at the Nyanzaga gold deposit.

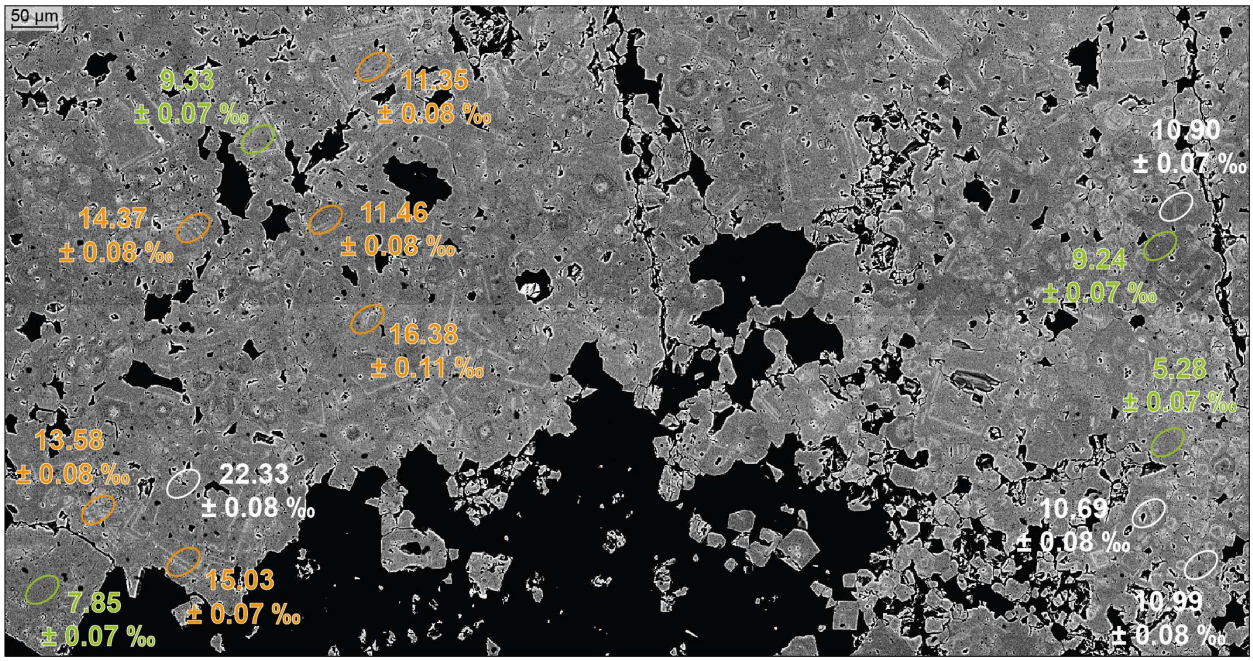

Figure 4-5. Location of multiple sulfur isotope analyses in Py_{1a} from NY53_20 sample. $\delta^{34}S$ values of each spot are marked in green when analyzing Py cores and dark rims, in orange when analyzing Py light rim-rich zones and in white when analyzing both at the same time.

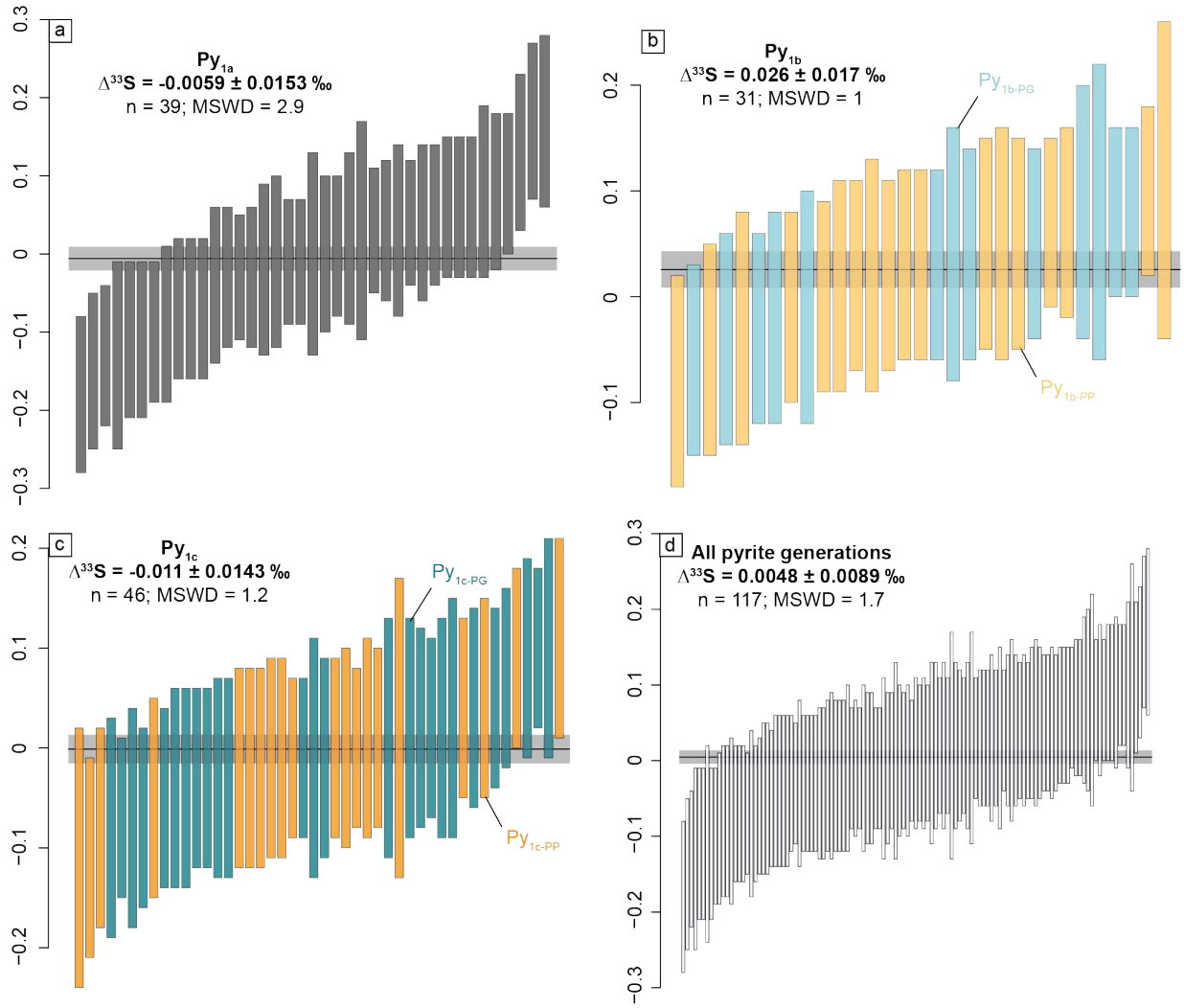

Figure 4-6. Weighted-mean diagrams of $\Delta^{33}S$ for **a.** Py_{1a} (from samples NY53_01, NY53_20), **b.** Py_{1b} (from samples NY53_01, NY53_20), **c.** Py_{1c} (from samples NY278_07, NY481_07) and for **d.** all generations.

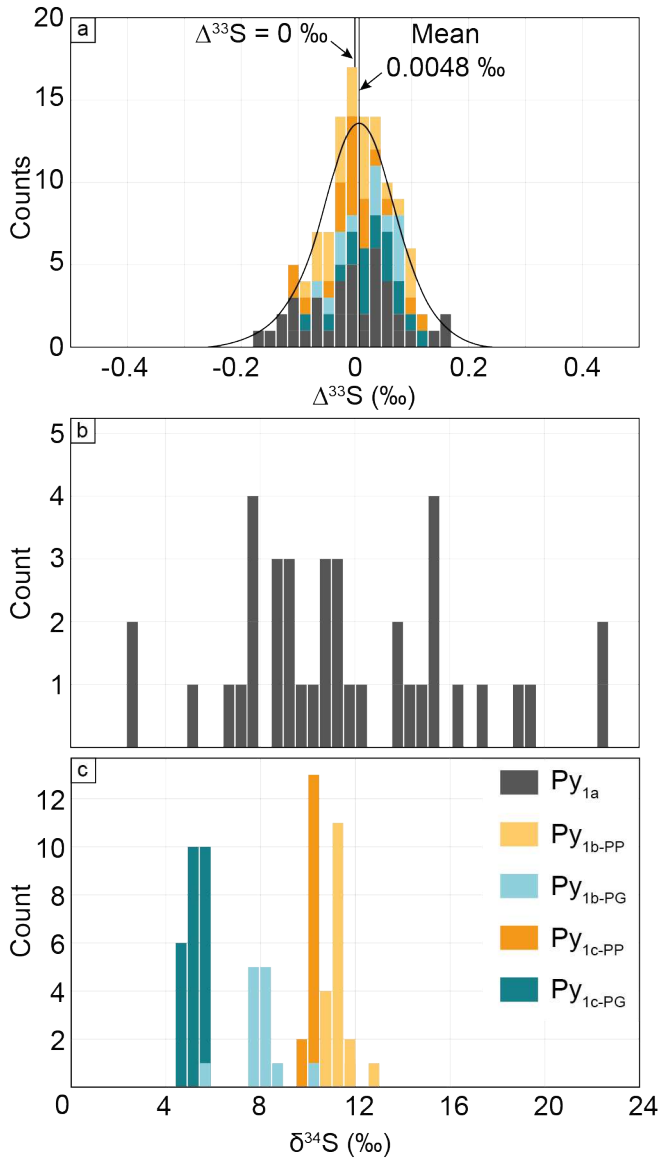

Figure 4-7. a. Histogram of $\Delta^{33}S$ in all pyrite generations. The kernel density estimation line is shown. The weighted mean of all pyrite generations is also shown, at 0.0048 ‰. Histograms of $\delta^{34}S$ in **b.** Py_{1a} (from samples NY53_01, NY53_20) and in **c.** Py_{1b} and Py_{1c} (from samples NY53_01, NY53_20, NY278_07, NY481_07).

6. Discussion

Combining the deformation-hydrothermal features, mainly micro-structures and textures of veins and pyrite, and the sulfur isotopes signatures ($\Delta^{33}S$-$\delta^{34}S$) helps to discuss the source of sulfur from the pyrite, as well as deciphering the evolution of fluid physical-chemical conditions at the Nyanzaga deposit. In light of these information, we will be able to discuss the source of gold and the timing of ore-bearing fluid circulation in the deposit.

As a reminder, mass dependent fractionation of sulfur (MDF-S) is monitored by $\delta^{34}S$ and is affected by physical-chemical evolution of the fluid and post precipitation mechanisms. On the other hand, mass independent fractionation of sulfur (MIF-S) is monitored by $\Delta^{33}S$ and is conservative, its signature gives direct hints on the source of the sulfur (Fig. 4-1a). In the following, the source of sulfur from the Nyanzaga pyrite is first discussed, followed by the deciphering of the evolution of fluid physical-chemical conditions at the Nyanzaga deposit. In light of these information, we will be able to discuss the source of gold and the timing of ore-bearing fluid circulation in the deposit.

6.1. A single sulfur reservoir

At the Nyanzaga deposit, the $\Delta^{33}S$ signature is homogeneous within each pyrite generation of each sample (Table 4-2) and constant both temporally, *i.e.*, from one generation to the next (Figs. 4-6, 4-8), and spatially, across 380 meters of stratigraphy (Fig. 4-2d). The $\Delta^{33}S$ range is evenly distributed near the 0 value (Fig. 4-7a), and $\Delta^{33}S$ weighted mean of all pyrite generations equals to 0.0048 ± 0.0089 ‰, which is within the error of zero and falls within the mantle range of +/- 0.03 ‰ (Bekker et al., 2016) and in the MDF-derived $\Delta^{33}S$ estimates by LaFlamme et al. (2018b; grey zones in Fig. 4-8). All values also fall within the MDF-derived $\Delta^{33}S$ estimates by LaFlamme et al. (2018b), with the exception of one value from a Py_{1a} (Fig. 4-8).

$\Delta^{33}S$ is an indelible tracer of the source of sulfur, that can be preserved in the mantle for prolonged periods of time (Cabral et al., 2013; Farquhar et al., 2013; Delavault et al., 2016; LaFlamme et al., 2018c; Smit et al. 2019). In other words, magmas generated in subduction settings typically inherit a positive MIF-S signature ($+\Delta^{33}S$) from supracrustal rocks in the subducting slab (Cabral et al., 2013; Farquhar et al., 2013; Delavault et al., 2016; LaFlamme et al., 2018c; Smit et al., 2019). The absence of evidence of a MIF-S signature at the Nyanzaga deposit (*i.e.*, $\Delta^{33}S = 0$) therefore reflects sourcing of sulfur from a purely mantle-derived source at depth, either the mantle itself or magmatic rocks that did not partially melt from supracrustal rocks (*e.g.*, sediments or hydrothermally altered oceanic crust that would yield positive and negative $\Delta^{33}S$ values, respectively; Fiorentini et al., 2012; Cabral et al., 2013; Farquhar et al., 2013; Chen et al 2015; Lewis et al., 2021). The homogeneity of the $\Delta^{33}S$ signature between each pyrite generation (Figs. 4-6, 4-7) might indicate that sulfur was sourced from a single reservoir during more than 55 Ma, *i.e.*, from D_{1a} (2700-2660 Ma) to D_{1c} (after 2645 Ma) (Berthier et al., 2024, Chapter V; Chapters I and II).

Furthermore, various elements are recognized in the hydrothermal mineral assemblage at the Nyanzaga deposit, including As, Sb, Ag, Mo, Pb, Cu, Zn during the D_{1b} and D_{1c} deformation and related hydrothermalism stages (Figs. 4-3 and 4-4, Table 4-1; Brigden et al., 2017; Berthier et al., 2024, Chapter V). This granitophilic suite of elements demonstrates a magmatic-like affinity consistent with a mantellic or magmatic provenance of the sulfur and more generally of the metal assemblage (*e.g.*, Thompson et al. 1999; Helt et al. 2014; Voute and Thébaud, 2014). Interestingly, similar granitophilic element suites associated with mineralization are observed in other gold deposits of several greenstone belts of the Lake Victoria Goldfields (Smith, 2003; Vos et al., 2009; Manya, 2017; Yuan et al., 2019; Van Ryt et al., 2020). At the world-class Geita deposit, located about 50 kilometers west of Nyanzaga in the greenstones of the SGGB, biotite, pyrite and magnetite geochemical signatures are also consistent with a magmatic-hydrothermal origin of the ore-bearing fluid (Van Ryt et al., 2019, 2020). In the Yilgarn craton, regional compilations of multiple sulfur isotope data and metallogenic studies on gold deposits indicate that fluids may originate from homogenized reservoirs at the scale of a Province (Thébaud et al., 2018; Sugiono et al., 2021). The observations in the Lake Victoria Goldfields may also indicate that fluids and metals that formed gold deposits originate from a homogenized reservoir, at least during the ore stage (D_{1c}, after 2645 Ma). Regional-scale multiple sulfur isotope analyses would be a great tool to assess such hypothesis.

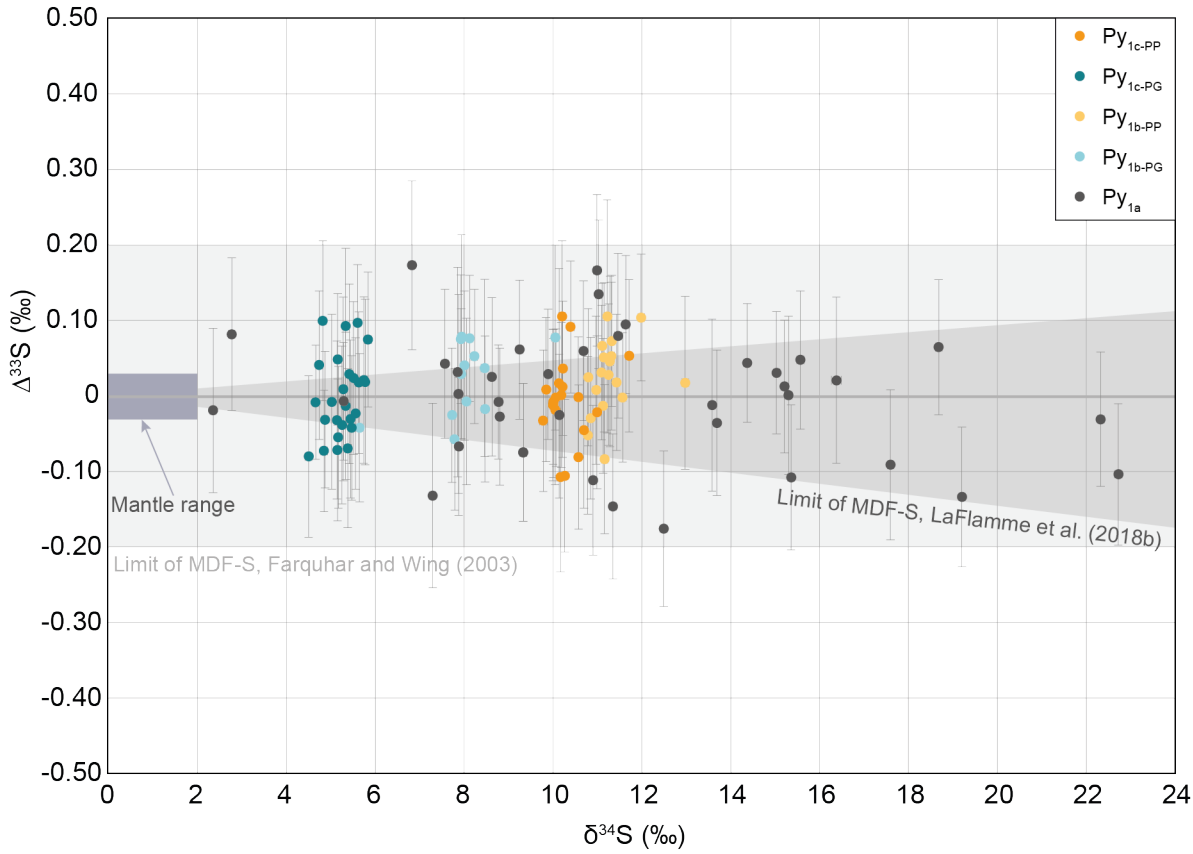

Figure 4-8. Diagram showing $\delta^{34}S$ vs $\Delta^{33}S$ values for all pyrite generations at the Nyanzaga deposit. The theoretical mantle range is shown (Kanehira et al., 1973; Labidi et al., 2013; Bekker et al., 2016). Mass-dependent fractionation lines (MDF-S) based on Farquhar and Wing (2003) and LaFlamme et al. (2018b).

In the northern SGGB, mantle-like geochemical and O-Hf-Nd isotopic signatures were observed in several magmatic episodes (Chapter II): during juvenile, mantle-plume mafic magmatism between 2820 and 2800 Ma and in TTGs emplaced between 2780 and 2700 Ma from the melting of the ca. 2800 Ma-old juvenile mafic crust. In light of our current knowledge of the northern SGGB, we can conclude that sulfur in the hydrothermal pyrite generations at the Nyanzaga deposit was most likely sourced from one of these three magmatic reservoirs, and was extracted from the mantle during mantle plume magmatism between 2820 and 2800 Ma.

Considering either a mantle-like or magmatic sources, $\delta^{34}S$ values should be constrained between -2 ‰ and +2 ‰ (*e.g.*, Kanehira et al., 1973; Labidi et al., 2013). At Nyanzaga, they are all above 2 ‰, with a range between 2.35 ± 0.07 ‰ and 22.72 ± 0.09 ‰ (Figs. 4-7, 4-8). These $\delta^{34}S$ values reflect certainly the thermochemical conditions in which hydrothermal fluids have been submitted, involving changes in fluid conditions during transport and deposition, within the metamorphic and hydrothermal evolution (Palin and Xu, 2000).

6.2. *Evolution of the sulfur-bearing fluid conditions*

The specific precipitation mechanisms of barren and gold-bearing pyrite are out of the scope of this study as it would require minor and trace element composition analyses. Yet, if MIF-S is a reliable and conservative tracer of the source(s) of sulfur as discussed in the previous section, the MDF-S, monitored by $\delta^{34}S$, proves to be a powerful marker of the changes of the fluid thermochemical conditions that triggered sulfide and related metallic ore precipitation (*e.g.*, Hodkiewicz et al., 2008; Xue et al., 2013; Fiorentini et al., 2018; LaFlamme et al., 2018a; Thébaud et al., 2018; Walker et al., 2021; Virnes et al., 2024). To discuss the evolution of fluid physical-chemical (P-T-χ) conditions recorded by the $\delta^{34}S$ values, we first present constrains from mineral textures and assemblages, presented in Figure 3 and summarized in Figure 4.

6.2.1. *Physical-chemical conditions recorded by microscale textures*

The metamorphic and hydrothermal mineral assemblage, petrogenesis and textures of veins and related disseminated alteration are essential markers in constraining the thermodynamic and tectonic conditions under which fluid circulated and elements precipitated (*e.g.*, Ramsay, 1980; Dong et al., 1995; McCuaig and Kerrich, 1998; Goldfarb et al., 2001; Passchier and Trouw, 2005; Bons et al., 2012; Goldfarb and Groves, 2015; Chauvet, 2019). At the Nyanzaga gold deposit, the D_{1a}-related mineral assemblage associated with peak metamorphism consists of chlorite ± sericite ± carbonate ± K- and Ba-feldspar ± pyrite (Berthier et al., 2024, Chapter V), indicating greenschist facies conditions, regionally encountered in the SUKUMALAND BELT (*e.g.,* Van Ryt et al., 2017).

The various vein textures further constrain the thermodynamic conditions. D_{1a}-related quartz ± carbonate combs in veins are primary textures resulting from infilling of fractures by overpressured fluids (*e.g.*, crack-seal fracturing; Cox and Etheridge, 1983; Ficher and Brantley, 1992; Dong et al., 1995; Hilgers et al., 2003), or from slow and synchronous fracture opening and crystal growth rates (Dowling and Morrison, 1990; Hilgers et al., 2001; Chauvet, 2019). These veins show at least two events of opening and infilling, generally a first one with quartz, followed by carbonate (Figs. 4-3f, 4-4). Furthermore, the multiple bands with varying mineral textures in the D_{1a}-related crustiform carbonate ± quartz veins are symmetric from both sides of the veins and characterize several cycles of opening-infilling at the center of the vein (Figs. 4-3a and e, 4-4; Ramsay, 1980; Dong et al., 1995; Passchier and Trouw, 2005; Bons et al., 2012). Cooling, fluid mixing, host rock-fluid interaction and boiling can account for changes in vein texture and mineralogy (*e.g.*, Chauvet, 2019), yet the complex crustiform texture requires repetitive changes in the conditions and episodic boiling induced by pressure fluctuation is the most feasible mechanism accounting for the textural evolution of the veins (*e.g.*, Buchanan, 1981; Cox, 1995; Dong et al., 1995). Contrastingly, D_{1c}-related veins seem to each have formed from one single fracturing event.

At the microscopic scale, mineral textures, in particular in quartz grains, are useful temperature gauge during deformation-hydrothermal stages, minus minor variations due to strain rate (Stipp et al., 2002; Passchier and Trouw, 2005; Berthier et al., 2023). As discussed in Berthier et al. (2024), evolution in quartz recrystallization textures in veins at the Nyanzaga deposit attests of progressive decrease of temperature during deformation, from grain boundary migration (GBM, T ~ 500-550 °C; Fig. 4-3f) during D_{1a} to bulging (BLG, T ~ 300-350°C Fig. 4-3p) in D_{1c} stage. The oscillatory zoning in D_{1a}-related pyrite exhibits sharp boundaries between alternating light and dark rims, suggesting abrupt shifts in conditions rather than gradual changes typically associated with diffuse transitions between pyrite zones (Velásquez et al., 2014). The oscillatory zoning with alternating

light and dark rims (Figs. 4-3g-h, 4-4) is widely interpreted to reflect either sudden pressure fluctuations and subsequent fluid boiling, where As-rich light rims formed during boiling (*e.g.*, Velásquez et al., 2014, 2018; Peterson and Mavrogenes, 2014; Berthier et al., 2023), or abrupt changes in the composition of the fluid through rhythmic mixing of fluids with distinct compositions (*e.g.*, Deditius et al., 2009). Py_{1b} and Py_{1c} grains show no or weak zoning, indicative of homogeneous or slowly changing physical-chemical conditions (Figs. 4-3l and r-s, 4-4).

Finally, the mineral paragenesis of the hydrothermal stages also contribute to constrain the thermochemical conditions of the fluid(s). The sulfide mineral assemblages described during the D_{1b} and D_{1c} stages can be grouped into two distinct paragenetic groups: the first consists of pyrite ± pyrrhotite and rare arsenopyrite, *i.e.*, $Py_{1b\text{-}PP}$ and $Py_{1c\text{-}PP}$ (Figs. 4-3j, m and r, 4-4d and g), while the second shows a complex signature with As-, Sb-, Pb-, Cu- and Ag-bearing sulfide minerals, *i.e.*, $Py_{1b\text{-}PG}$ and $Py_{1c\text{-}PG}$ (Figs. 4-3l, n and q, 4-4e and h). Spatial chemical variations in D_{1b} and D_{1c} stages could be attributed to fluid interaction with the host rock, yet no Sb, Pb or Cu enrichment were encountered in the volcanosedimentary pile. Moreover, marine volcanosedimentary sequences akin to those hosting the Nyanzaga deposit are commonly sulfur-rich (*e.g.*, Selvaraja et al., 2017). Consequently, metal leaching from these units would very likely mobilize volcanosedimentary sulfur, thereby influencing the $\Delta^{33}S$ signature of subsequently precipitated sulfide minerals. These variations could also be explained by local variations in pressure and/or temperature, but based on the textural study of quartz, the P-T conditions during D_{1b} and D_{1c} were likely stable (Berthier et al., 2024, Chapter V), and the studied samples are not spatially far enough to account for significant P-T variations (Fig. 4-2d). Therefore, the most plausible mechanism appears to be the circulation of several fluids with distinct chemical signatures (at least two).

Overall, the metamorphic and hydrothermal mineral parageneses, combined with the variations in mineral textures in veins and pyrite grains demonstrate that D_{1a} stage occurred at around 500 °C, with either local and episodic variations in pressure leading to fluid boiling or rhythmic fluid mixing extracted from a magmatic source (accounting for the $\Delta^{33}S = 0$ signature). Cooling, down to 300 – 350 °C, and homogeneous or slowly changing pressure conditions define D_{1b} and D_{1c} stages, with a possible circulation of at least two fluids with distinct chemical signatures but similar magmatic provenance of sulfur accounting for the $\Delta^{33}S = 0$. This might also reflects a retrograde metamorphic path from amphibolite to greenschist facies during the ~ 55 Ma from D_{1a} to D_{1c}.

6.2.2. $\delta^{34}S$ constrains on fluid processes

In addition to the physical-chemical conditions provided by the micro-textures of the metamorphic/hydrothermal mineral assemblages, the $\delta^{34}S$ signature of the different generation of the hydrothermal pyrite can be cross-referenced with the major mechanisms that control variations in $\delta^{34}S$ signature of sulfide. Major shifts of MDF-S can be explained by fluid-rock interaction (Palin and Xu, 2000), rock buffering of the fluid pH (Petrella et al., 2020), temperature variations (Hutchison et al., 2020), fluid boiling and phase separation (Hodkiewicz et al., 2008), and fluid mixing (Cameron and Hattori, 1987; Cooke and McPhail, 2001; Goldfarb and Groves, 2015). Importantly, the $\delta^{34}S$ signature of pyrite at the Nyanzaga deposit record significant shifts within the Py_{1a} generation, but is quite steady within pyrite grains from a single sulfide assemblage (Py_{PG} *vs* Py_{PP}) within each Py_{1b} and Py_{1c} generations (Figs. 4-7, 4-8).

S-bearing fluid interaction with the host rock is a major process accounted for MDF-S variations, resulting in local and significant shifts of $\delta^{34}S$ values due to mixing with the S-bearing host rock (*e.g.*, Phillips and Powell,

2010; Fiorentini et al., 2018). The Nyanzaga deposit is hosted in a volcanosedimentary sequence, deposited in a marine environment (Sanislav et al., 2018 and references therein; Berthier et al., 2024, Chapter V) that are commonly sulfur-rich (*e.g.*, Selvaraja et al., 2017; Brigden et al., 2017; Brigden, 2020). Fluid interaction with the host rock at the Nyanzaga deposit would therefore result in significant increase of the $\Delta^{33}S$ signature in both time and space, over short distances, as outlined by LaFlamme et al. (2018a). On the contrary, the absence of a MIF-S signature ($\Delta^{33}S = 0$) is a strong argument supporting thermodynamic changes at the origin of $\delta^{34}S$ significant variations (Figs. 4-6, 4-8).

The temperature effect on the MDF-S is substantial, as demonstrated by Ohmoto (1972) and further detailed in Hutchison et al. (2020). In oxidized conditions, fluid cooling leads to significant decrease of $\delta^{34}S$ in sulfide minerals. At the Nyanzaga deposit, temperature decrease between D_{1a} and D_{1c} stages is recorded by quartz microscale recrystallization textures. Yet, the large variations in Py_{1a} $\delta^{34}S$ (from 2.35 ± 0.07 ‰ to 22.72 ± 0.09 ‰; Table 4-2) prevent from studying the influence of temperature over temporal variations in the MDF-S.

The variation in $\delta^{34}S$ values within Py_{1a} generation are significant, exceeding 20 ‰ (Figs. 4-7b, 4-8). Such large variations are typically observed in sedimentary and metamorphic rocks (*e.g.*, Seal, 2006; Hoefs, 2009). However, a sedimentary origin can be ruled out due to the absence of a MIF-S signature (section 6.1). The Py_{1a} generation has undergone retrograde metamorphism, transitioning from high temperature (T ~ 500-550 °C; section 6.2.1) to lower temperature (T ~ 300-350 °C; section 6.2.1). While metamorphic processes might account for the observed $\delta^{34}S$ variation (*e.g.*, Hoefs, 2009), they cannot easily explain the oscillatory zoning within Py_{1a} grains. This zoning implies repetitive changes in physical and chemical conditions during formation, conditions that are inconsistent with the gradual and uniform effects typically associated with metamorphism (Hutchison et al., 2020). Finally, the $\delta^{34}S$ spatial variations in Py_{1c} are not related to temperature effects as temperature is interpreted as constant during the D_{1c} stage (Berthier et al., 2024, Chapter V).

Pressure fluctuations in the upper crust are considered to play no significant role on the fractionation of $\delta^{34}S$ in sulfide minerals (*e.g.*, Li and Liu, 2006; Seal 2006; Marini et al., 2011), yet this statement does not account for local drastic pressure drops that lead to fluid boiling and phase separation, generally described in fault-valve system when cyclic (*e.g.*, Sibson et al., 1988; Cox, 1995; Wilkinson and Johnston, 1996). The influence of fluid boiling on the $\delta^{34}S$ signature of pyrite was described by Martinez Serrano et al. (1996), González-Partida et al. (2005) and Sugiono et al. (2022) and all three studies reached the same conclusion: sulfur fractionation during fluid boiling leads to significant drop in the $\delta^{34}S$ values (decrease of up to - 8 ‰) in pyrite. If cyclic pressure drops leading to fluid boiling is a feasible mechanism explaining the Py_{1a} oscillatory zoning and the several opening-infilling episodes recorded in D_{1a}-related veins, it would also lead to significant decrease of $\delta^{34}S$ compared to the core and dark rims, contradictory with our observations.

Finally, we investigate the implications of fluid mixing on the MDF-S in pyrite. Rhythmic mixing of magmatic-derived fluids, such as fluid and vapor separation from the same magmatic-hydrothermal fluid, was previously proposed as a mechanism to explain oscillatory zoning in pyrite (Deditius et al., 2009). It would result in a homogeneous $\Delta^{33}S$ signature in both the liquid and vapor phases, as the MIF-S is an indelible tracer (Cabral et al., 2013; Farquhar et al., 2013; Delavault et al., 2016; LaFlamme et al., 2018c; Smit et al. 2019). In Deditius et al. (2009) paper, the studied high-sulfidation gold-silver deposits are interpreted to result from the interaction between a hydrothermal-magmatic system and a magmatic vapor plume. With the support of experimental analyses on elemental partitioning in vapor-rich hydrothermal systems, they concluded that episodic circulation of the vapor phase led to precipitation of As-rich pyrite rims under higher

temperature compared to the As-poor liquid phase. The combination of rhythmic local temperature and fluid phase variations could be a feasible mechanism for the major variations in D_{1a}-related $\delta^{34}S$ values and mineral texture of veins and pyrite aggregates. However, it appears crucial to combine this study with trace element analyses in pyrite in order to conclude on the viability of this scenario during the D_{1a} stage at the Nyanzaga deposit.

Fluid mixing is further investigated for the D_{1b}-related and D_{1c}-related pyrite. Variations in $\delta^{34}S$ values align with changes in the sulfide assemblages (Figs. 4-4, 4-8), with:

(i) The lowest $\delta^{34}S$ values in $Py_{1c\text{-}PG}$ formed in galena-bearing veins (4.50-5.83 ‰, mean: 5.25 ± 0.01 ‰), associated with a complex assemblage of As-, Pb-, Sb-, Cu-bearing minerals.
(ii) Intermediate $\delta^{34}S$ values in disseminated $Py_{1b\text{-}PG}$ (range: 7.74-8.47 ‰, two outliers: 5.64 ‰ and 10.05 ‰, mean: 8.05 ± 0.02 ‰), that are more rarely associated with As-, Pb-, Sb-, Ag- and Cu-bearing minerals.
(iii) Highest $\delta^{34}S$ signature in disseminated $Py_{1b\text{-}PP}$ and $Py_{1c\text{-}PP}$ in pyrite-pyrrhotite-dominated veins (9.78 to 12.97 ‰, mean: 10.77 ± 0.02 ‰), associated with rare pyrrhotite and pyrite.

If we have demonstrated in section 6.1 that sulfur was extracted from mantle or magmatic reservoir(s), but the rock source was not necessarily constant over time. For instance, mafic rocks formed between 2820 and 2800 Ma, and TTG intrusives emplaced between 2780 and 2700 Ma in the northern SGGB record mantle-like geochemical and isotopic signatures, with no evidence of subduction and supracrustal input (Chapter II). In other words, sulfur extracted from these two magmatic units will very likely hold a mantle-like S isotopic signature, *i.e.*, $\Delta^{33}S = 0$, but the metallic cortege associated with S will not necessarily be similar between a mafic or an intermediate magmatic rock. As previously discussed, the mineralogical variations associated with Py_{1b} and Py_{1c} are could result from the circulation of at least two fluids with distinct chemical signatures (sub-section 6.2.1). In such case, fluids would have to be sourced from magmatic reservoirs with no MIF-S ($\Delta^{33}S = 0$), but possibly be sourced from distinct magmatic episodes (*e.g.*, mafic magmatism between 2820-2800 Ma and TTG magmatism between 2780-2700 Ma). The fluids could also have different $\delta^{34}S$ signatures explaining the variations observed in Py_{1b} and Py_{1c}. However, in the scenario of fluid mixing, these variations in the MDF-S of Py_{1b} and Py_{1c} could also result from sulfur isotope partitioning in sulfide minerals during their precipitation (*e.g.*, Grootenboer and Schwarcz, 1969; Thode, 1970; Li and Liu, 2006; Seal, 2006; Zhang, 2021). The precipitation of various amounts of sulfide minerals associated with Py_{1b} and Py_{1c} could therefore partition $\delta^{34}S$ between the different minerals.

6.3. Implications for the gold system: from crustal fertilization to gold precipitation

Sulfur may prove to be a good isotopic tracer for tectonic settings controlling crustal growth (Fig. 4-1a). In this section we demonstrate that the combination of thorough petro-textural study and multiple sulfur isotope analyses at the Nyanzaga deposit enable to reconstruct the journey of gold through the crust, from its initial mantle extraction to its circulation in the ore-bearing fluid, and even hint on the ore-forming processes.

When considering a mineral system, the sources of ore-bearing fluids, sulfur and metals, including gold, are not necessarily the same. At the Nyanzaga deposit, the multiple sulfur isotope analyses reveal no evidence of a MIF-S signature (Figs. 4-6, 4-7), in other words, sourcing of sulfur solely from a mantle reservoir or a magmatic reservoir that did not partially melt from supracrustal rocks (section 6.1). We propose to first

explore the hypothesis of a distinct reservoirs for gold, for instance the volcanosedimentary sequence of the Sukumaland belt, that are often presented as the most likely source of gold in greenstone-hosted gold deposits (Pitcairn et al., 2006; Thomas et al., 2011; Gaboury, 2013), or subduction-related intermediate and felsic intrusives (*e.g.*, the syn- to post-tectonic intrusives described in Chapter II), also viewed as a good candidate for gold sourcing (Tomkins, 2013). All of these rocks contain sulfur with positive and/or negative $\Delta^{33}S$ signatures (*e.g.*, LaFlamme et al., 2018b, 2018c). It is highly unconceivable that gold would be leached from these sulfur-bearing rocks without any extraction of sulfur, therefore in such scenario, the ore-bearing fluid would present a nonzero $\Delta^{33}S$ signature. Based on all previous assumptions, gold was therefore not extracted from volcanosedimentary or subduction-related magmatic rocks but from the same mantle-derived magmatic source as the sulfur.

As previously discussed in section 6.1 and based on our study of crustal growth in Chapter II, three potential sulfur reservoirs exist in the northern SGGB: juvenile, mantle-plume-derived mafic rocks (2820-2800 Ma) and TTGs formed from the reworking of the mafic crust from two distinct tectonic processes at different times (2780-2700 Ma and 2660-2645 Ma). In any case, gold was hence extracted from the mantle during the 2820-2800 Ma magmatic period. Additionally, the latter records evidence of gold enrichment (19 ppb Au in talc-altered ultramafic rocks; Chapter III), strengthening the hypothesis of gold fertilization of the SGGB crustal segments through mantle-derived magmatic processes.

Furthermore, the detailed petro-structural study of the deformation-hydrothermal evolution of the Nyanzaga deposit has concluded that gold was concentrated during the D_{1c} deformation stage (Berthier et al., 2024, Chapter V), dated after 2645 Ma (Chapter III). Importantly, Py_{1a} has recorded drastic variations in the fluid physical-chemical conditions during the D_{1a} deformation stage, either rhythmic fluid boiling or mixing (section 6.2.2). These condition variations are effective mechanisms triggering gold precipitation, as demonstrated by decades of research (*e.g.*, Sibson et al., 1988; Deditius et al., 2009; Velásquez et al., 2014, 2018; Peterson and Mavrogenes, 2014; Berthier et al., 2023). Consequently, it is unlikely that fluid(s) circulating at the Nyanzaga deposit during the D_{1a} stage were gold bearing. Consequently, significant diachronism exists between the gold fertilization of the crust, between 2820 and 2800 Ma, and the circulation of the ore-bearing fluid and economic concentration in the Nyanzaga deposit. The shift in the mineral assemblage between D_{1a} and D_{1b}-D_{1c} stages, from pyrite-only assemblage to the As, Sb, Ag, Mo, Pb, Cu, Zn-bearing signature (Table 4-1, Fig. 4-4; Chapter V), further strengthen the hypothesis of either an evolution of the element composition of the fluid reservoir, or tapping in different reservoirs.

This temporal disconnect implies that magmatic, metamorphic, or hydrothermal events triggered gold mobilization and the release of ore-bearing fluids after 2660 Ma. The period between 2660 and 2645 Ma corresponds to cratonization and anatexis of the crust, during which TTGs were generated through partial melting of mafic rocks (Chapter II). A first hypothesis suggests that gold, initially hosted in mafic rocks, migrated into melts during partial melting and was subsequently released into ore-bearing fluids during magma crystallization (Tomkins, 2013; Chapter II). This scenario is supported by the granitophilic suite of elements associated with gold at the Nyanzaga deposit that are typical of intermediate to felsic magmatic rocks (Goldfarb et al., 2005; Richards, 2009; Tomkins, 2013). Cratonization processes, such as slab break-off or crustal delamination, likely increased crustal temperatures, led to local partial melting of TTG and mafic rocks (*e.g.*, Maury et al., 2000; Chapter II). Such high-temperature conditions may have induced amphibolite-facies metamorphism described in the mafic rocks of the SGGB (Chapter III; Quennel et al., 1956 ; Gabert, 1990; Kabete et al., 2012b). High-temperature metamorphism in metabasaltic rocks is known to result in

gold depletion (Pitcairn et al., 2015). Yet, the release of certain elements, such as Sb, during metamorphism requires prior seafloor alteration of the mafic crust (Pitcairn et al., 2015). This process would likely influence the MIF-S signature (+/- $\Delta^{33}S$; Xue et al., 2013; Lewis et al., 2021). While metamorphic fluid release from amphibolite-facies mafic crust is a feasible explanation for gold mobilization, it does not fully account for the diverse suite of metals deposited at Nyanzaga and Kilimani.

Lastly, several gold-bearing fluids are inferred to have circulated during the D_{1b} and D_{1c} deformation stages at Nyanzaga (section 6.2). These fluids, both mantle-derived and with $\Delta^{33}S = 0$, exhibit distinct elemental compositions: (i) one enriched in granitophile elements (As, Sb, Pb, Cu, Ag) and (ii) another with only trace amounts of As. These compositions align with the sourcing of elements from (i) late- to post-tectonic granitoids generated by partial melting of the mafic crust (Goldfarb et al., 2005; Richards, 2009) and (ii) metamorphosed mafic magmatic rocks from ca. 2800 Ma (Pitcairn et al., 2015), respectively.

7. Conclusion

The sulfur isotopic study of sulfide minerals at the Nyanzaga gold deposit provides insights into the sources of sulfur and the evolution of ore-forming fluids in a structurally complex setting. The data reveal that sulfur was primarily sourced from a magmatic or mantle-derived reservoir, as evidenced by the absence of mass-independent sulfur fractionation (MIF-S). The record of crustal growth in the northern Sukumaland granite-greenstone belt (SGGB) constrain the timing of sulfur extraction from the mantle between 2820 and 2800 Ma.

$\delta^{34}S$ variations in both time and space imply physical-chemical variations of the sulfur-bearing fluid conditions during the progressive, three-stage, history of deformation. During the D_{1a} stage, key features indicate rhythmic shifts in the fluid conditions: crack-seal and crustiform veins, oscillatory zoning in pyrite and higher $\delta^{34}S$ values in light rims compared to cores and dark rims in pyrite. We propose a scenario involving rhythmic local temperature and fluid phase variations. During the D_{1b} and D_{1c} stages, spatial variations in $\delta^{34}S$ signatures of pyrite were accompanied by variations of sulfide mineral assemblages. Fluid mixing with distinct chemical signatures and likely distinct $\delta^{34}S$ signatures is the most feasible scenario.

By combining multiple sulfur isotope analyses with detailed petrographic and textural studies of an Archean gold deposit, we have unraveled the timing and origin of gold enrichment in the crust. This approach has further allowed us to examine the timing and potential mechanisms of gold extraction from its reservoir and its subsequent precipitation at the Nyanzaga deposit.

Acknowledgement

The authors are grateful to the OreCorp's team for their welcome and scientific exchanges. The authors are also thankful to Nordine Bouden for the acquisition of multiple S isotope analyses. This work is part of Célestine Berthier's PhD project which benefited of a CIFRE funding, reference CIFRE n°2021/0546, attributed by the French National Research and Technology Agency (ANRT).

~

Chapter V

~

Refold structures of the Archean Nyanzaga gold Project, Sukumaland greenstone belt, Tanzania: precursors to the gold-bearing fault system

Article publié en août 2024 dans Journal of Structural Geology 187

https://doi.org/10.1016/j.jsg.2024.105233

Célestine Berthier[a,b,c,*], Alain Chauvet[c], Julien Feneyrol[a], Anne-Sylvie André-Mayer[b], Aurélien Eglinger[b,d], John McIntyre[e], Rémi Bosc[a]

[a] Arethuse Geology SARL., 29 allées Saint Jean, Fuveau 13710, France

[b] GeoRessources, Université de Lorraine, CNRS, Nancy 54000, France

[c] Géosciences Montpellier, Université de Montpellier, CNRS, Montpellier 34095, France

[d] InnovExplo Inc, 560 3e Avenue, Val d'Or QC J3P 1S4, Canada

[e] OreCorp Ltd, 513 Hay St, Suite 22, Subiaco WA 6008, Australia

Keywords:

Structural control; refold structures; progressive deformation; lode gold deposit; Sukumaland greenstone belt.

Abstract

This study presents a complete investigation into the structural-hydrothermal evolution of the Nyanzaga and Kilimani gold deposits within the Neoarchean Sukumaland greenstone belt, Tanzania craton. The first compressional stage, D_{1a}, creates upright E-W folds in response to N-S-oriented shortening. The second stage, D_{1b}, refolds the previously formed structures during ongoing compression/transpression under N-S-oriented shortening. Due to the brittle nature of late deformation, during D_{1c}, a set of faults emerges, with the NW-SE ones exhibit dextral shearing and control the formation of normal N-S vertical faults.

A protracted hydrothermal history is recorded, beginning with a disseminated silicate mineral- and pyrite-rich, gold-barren stage associated with the D_{1a} and D_{1b} deformations, followed by the development of a gold-endowed vein system during progressive D_{1b} and D_{1c} stages. Gold was mainly concentrated within vertical NW-SE (Kilimani) and N-S (Nyanzaga) faults. Our findings challenge traditional polyphase deformation models presented in the other gold deposits of the area, by proposing a progressive and continuous deformation-hydrothermal history. In addition, we highlight the influence of refold structures on fault geometry, which is crucial in concentrating gold mineralization under continuous N-S compression and transpression.

1. Introduction

Structural features are fundamental in shaping the distribution and controlling the formation of lode-gold deposits worldwide, and have been intensively studied for decades (Robert and Brown, 1986; Sawkins, 1990; Groves et al., 1998, 2019; Goldfarb et al., 2001; Robb, 2005; Bierlein et al., 2006; Richards, 2011, 2013; Gaboury, 2019). Investigating the protracted structural setting of gold deposits, including their features (local state of strain, relative timing, timing of hydrothermal activity, etc.) and the geometry of both pre-mineralization structures and gold traps, provides a better understanding of the final geometry of gold mineralization within geological terranes (Groves et al., 2018; Chauvet, 2019; Perret et al., 2020) and can be fundamental for a complete understanding of the regional tectonic history (*e.g.*, Perret et al., 2021; Travers et al., 2023; Shaw et al., 2022). In cases where the pre-existing structures, which may include shear zones, faults, fractures, and/or fold structures, exhibit a preferred orientation or specific geometrical relationships with respect to mineralization, new geological structures may form and propagate along these pre-established pathways, focusing mineralized fluids.

The formation of an economic deposit remains an exceptional phenomenon (*e.g.*, Haxel et al., 2002), and not only results from a protracted structural history, but from the convergence of several parameters, such as the nature of the surrounding rocks, and the physical-chemical conditions (e.g., Sawkins, 1990; Hronsky et al., 2012; Gaboury, 2019). A last fundamental parameter regarding lode-gold deposits is the geological period, as it has been claimed that the Archaean is the most favorable period for the development of world-class deposits (Goldfarb et al., 2001; Frimmel, 2008, 2018). The reasons advanced include the higher gold potential within the dominant mafic material, the higher thermal conditions and the voluminous magmas potentially involved within the Archaean geodynamic setting (*e.g.*, Frimmel, 2008; Kolb et al., 2015; Dong and Santosh, 2016; Groves et al., 2019).

Each of the parameters leading to the formation of economic deposits needs to be identified and their relation to mineralization clarified in order to fully understand the mineralized system, the tectonic meaning behind the forming of a deposit, and providing keys for regional ore exploration (*e.g.*, Goldfarb et al., 2001; Goldfarb and Groves, 2015; Gaboury, 2019). However, if based on petrologic, petrochronologic and/or purely geometric approaches at a local scale, the deconvolution of deformation-hydrothermal history of these economic deposits may lead to complex polyphase deformation histories that may not reflect the regional-scale tectonic processes (Faleiros et al., 2016; Fossen et al., 2019; Wang et al., 2019; Oriolo et al., 2022). The discussion regarding progressive versus polyphase deformation is therefore particularly relevant when reconciling deposit- and regional-scale tectonic frameworks (Fossen et al., 2019; Perret et al., 2021; Oriolo et al., 2022; Shaw et al., 2022). The concept of progressive deformation is well defined and widely studied, but interpreting overprinting patterns in natural examples as the result of either progressive or polyphase deformation is far from trivial. For instance, strain partitioning and localization often lead to refold patterns during progressive deformation but the superposition of folds and the resulting complex geometries may be wrongly attributed to separate deformation events, especially when observed at a local scale (*e.g.*, Tikoff and Teyssier, 1994; Allibone et al., 2002; Santos et al., 2017; Fossen et al., 2019 and references therein). Differentiating progressive to polyphase deformation proves to be scale dependent, in particular time dependent (*e.g.*, Sibson, 2004; Oriolo et al., 2022). Progressive deformation may last 10 to 20 million years in the Himalayas or the Andes (*e.g.*, Burg and Bouilhol, 2019; Fennell et al., 2019), knowing that given stress field and metamorphism conditions may be steady for up to tens of millions of years (Viete and Liester, 2017). However, timing in the Archean is recorded at a much larger scale. This can result from two distinct causes:

(i) greater uncertainty in available dating; (ii) drastically different rheologic conditions during the Archaean leading to longer tectono-metamorphic events. For instance, an extension event defined in the Sukumaland greenstone belt (SGB), Tanzania craton, is marked by the deposition of volcanosediments between ca. 2820 Ma and 2700 Ma, meaning an extension of at least 120 Ma (Cook et al., 2016; Kwelwa et al., 2018). Extension is followed by shortening, notably recorded by intense shearing along the Geita Shear Zone, active during 40 Ma (between 2700-2660 Ma; Sanislav et al., 2018b).

In this study, we track the deformation-metallogenic evolution and discuss the possibility of protracted structural patterns as the result of progressive deformation at the Nyanzaga and Kilimani gold deposits, located in the Neoarchean SGB (Fig. 5-1). The key role that pre-existing structures played in the focus of late-stage gold-bearing structures will also be addressed. Based on field observations and a large set of outcrops and drill core samples, a comprehensive description of the relationship between lithologies, structures, alterations and mineralization from deposit to microscopic scales provides insights into the history of deformation and the main factors controlling the spatial distribution and local endowment of gold within the two deposits of the Nyanzaga Project. We will specifically focus on the significant role of protracted fold geometry, involving interference between at least two folding stages, as a fundamental factor in the genesis and evolution of structures that host mineralization. Such a result holds broader implications and can be extrapolated at the scale of the SGB, presenting a cohesive geological-tectonic framework that can help understand other complex gold deposits within the region, such as the major Geita and Bulyanhulu deposits. These deposits, sharing a similar geological context with Nyanzaga and Kilimani, stand as notable examples for comparative analysis. In this study, phases will refer to discrete and tectonically distinct deformations, i.e., polyphase deformation; stages will be considered as resulting from progressive deformation; events will be independent of interpretation regarding polyphase versus progressive deformation (Fossen et al., 2019; Oriolo et al., 2022).

2. Geological setting

2.1. Regional geology

The Meso- to Neoarchean Tanzanian craton, located in east-central Africa (Fig. 5-1a), consists of two superterranes: the Lake Victoria Goldfields (LVG) to the north and the Dodoman Belt in the south (Fig. 5-1a), separated by the NW-striking Dodoma Schist Belt (not visible in Fig. 5-1a; Borg and Shackleton, 1997; Kabete et al., 2012; Kwelwa et al., 2018). The LVG is dominated by syn- to late-tectonic granitoids and paragneissic rocks, which separate W- to NW-trending, complexly folded greenstone belts of Neoarchean age (Fig. 5-1b; Borg and Shackleton, 1997; Kwelwa et al., 2018). The stratigraphy of the LVG is divided into the Nyanzian and Kavirondian Supergroups (Fig. 5-1b; Borg, 1992; Sanislav et al., 2015; Kwelwa et al., 2018). The Nyanzian Supergroup spans over 120 Ma of volcanic activity and sedimentation and is subdivided into a mafic volcanic-dominated Lower Group and an Upper Group dominated by turbiditic sequences interlayered with chert sediments, banded iron formations (BIF) and felsic volcanic and volcaniclastic intercalations (Quennell et al., 1956; Borg and Krogh, 1999; Manya and Maboko, 2003, 2008; Cook et al., 2016). The Nyanzian Supergroup underwent metamorphism, mostly up to the greenschist facies, reaching the amphibolite facies near granitic intrusions. The post-orogenic molassic basins of the Kavirondian Supergroup were deposited between ca. 2450-2762 Ma and unconformably overlie the Nyanzian Supergroup (Gabert, 1990; Borg, 1992; Sanislav et al., 2015).

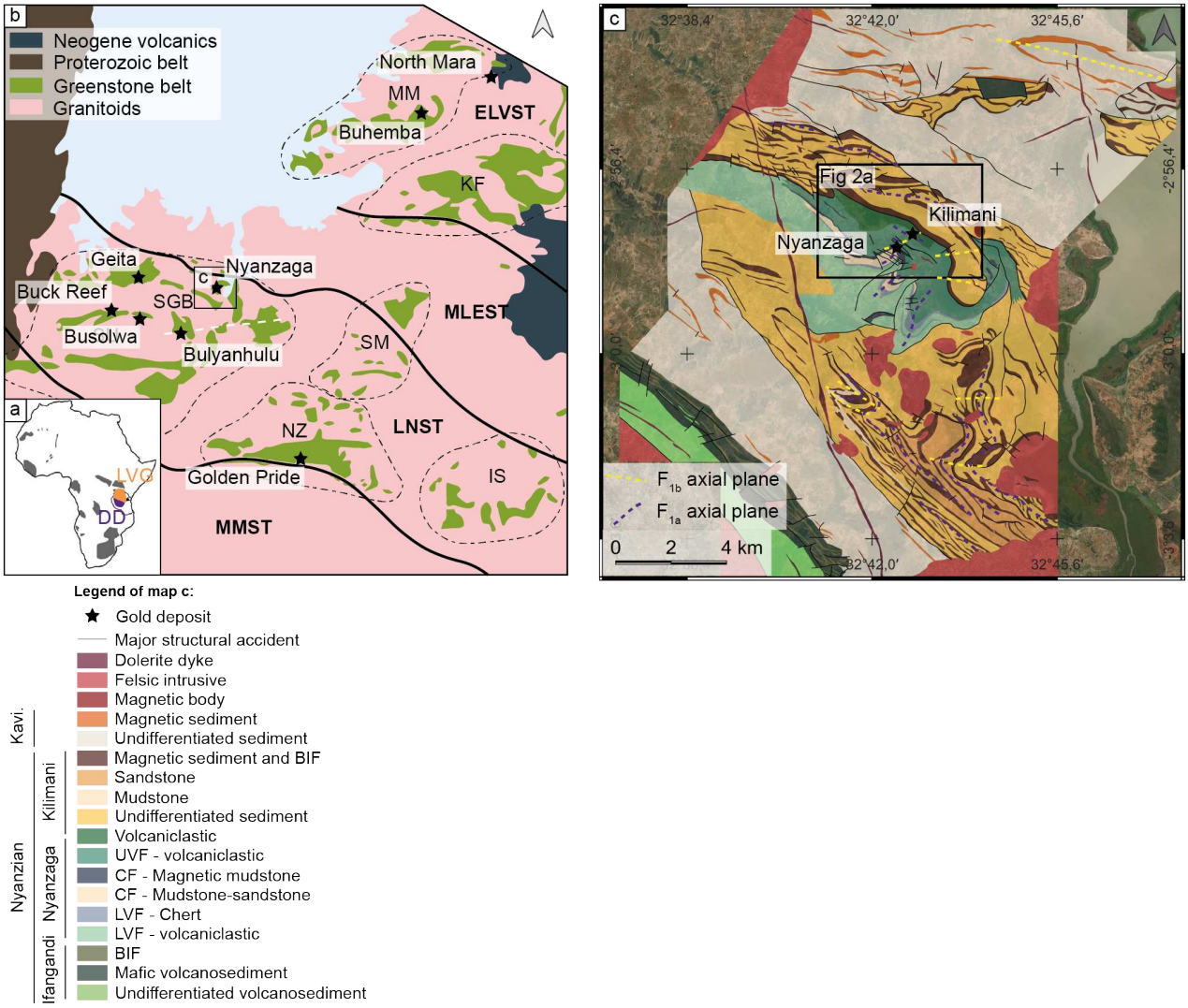

Figure 5-1. a. Present-day location of the Tanzania craton within the African continent. Orange = Lake Victoria Goldfields, Purple = Dodoman Domain. **b.** Location of the Nyanzaga Project within the Sukumaland greenstone belt (SGB), Lake Victoria Goldfields (from Cook et al., 2016, after Borg and Shackelton, 1997). Bold black lines represent super-terrane boundaries as proposed by Kabete et al (2012): ELVST = East Lake Victoria, MLEST = Mwanza Lake Eyasi, LNST = Lake Nyanza, MMST = Moyowosi-Manyoni. Black dotted lines represents the main greenstone belts: SU = Sukumaland, SM = Shinyanga-Malita greenstone belt, MM = Musoma-Mara, KF = Kilimafedha, NZ = Nzega, IS = Iramba Sekenke. White dotted line = hypothetical fold axial plane of the SGB. **c.** Geological and structural framework near the Nyanzaga Project, based on field geology and geophysical data (McIntyre, pers. com.). Dotted lines represent the fold axes in the meta-volcanosediments, purple = first set, yellow = second set of folds.

The Sukumaland greenstone belt (SGB) is the largest and most gold-endowed of all greenstone belts in the LVG, hosting some world-class deposits (Fig. 5-1b; i.e., Geita and Bulyanhulu deposits, Sanislav et al., 2014, Chamberlain, 2003, respectively). The belt is dominated by Nyanzian meta-volcanosediments, flanked by syn-accretionary to post-tectonic granitoids of tonalite–trondhjemite–granodiorite (TTG) affinity (Sanislav et al., 2015; Henckel et al., 2016; Kwelwa et al., 2018; Sanislav et al., 2018b). Extensive work has been undertaken in the northwestern part of the SGB, around the world-class Geita gold deposit, revealing a protracted, multiphase metamorphic-deformation history consisting of eight events, grouped into three tectonically-distinct phases, named Event I to III (*e.g.,* Borg and Shackleton, 1997; Kabete et al., 2012; Henckel et al., 2016 and references therein; Dirks et al., 2022). Event I (2820-2700 Ma) corresponds to a

phase of accretion of large volumes of volcanosedimentary rocks and granitoids in an extensional regime (Cook et al., 2016; Sanislav et al., 2018a; Mshiu and Maboko, 2022). Event I is characterized by listric normal faulting, layer-parallel shearing and intrafolial folding of chert layers (Sanislav et al., 2014, 2018a; Dirks et al., 2022 and references therein). During Event II (ca. 2700-2660 Ma), generally N-S to NW-SE or NE-SW compression folded the previously accreted rocks (Kabete et al., 2012; Dirks et al., 2022 and references therein). Folding during Event II is often described as polyphase, involving up to five folding and refolding sub-events, associated with ductile shearing (*e.g.,* Sanislav et al., 2016; Dirks et al., 2022). Late in Event II, ductile-brittle shear zones and brittle strike-slip faults are interpreted to offset the folds (*e.g.,* Kabete et al., 2012; Sanislav et al., 2016). Lastly, the compression is transposed into a NW-SE extension during Event III (2660-2620 Ma), reactivating shears and faults (*e.g.,* Borg, 1994; Kabete et al., 2012; Dirks et al., 2022 and references therein). At the Bulyanhulu deposit, a two-event compressive deformation history is proposed, with a first folding event, followed by refolding of the volcanosediments and development of ore-bearing subvertical NW-trending reverse-oblique shear zones and strike-slip faults (Chamberlain, 2003).

2.2. The Nyanzaga gold Project

The Nyanzaga Project is located in the northern part of the SGB and is hosted within volcanosedimentary units of the Nyanzian Supergroup (Fig. 5-1b-c; Henckel et al., 2016). The Project comprises two gold deposits in development, operated by Sotta Mining Limited, a Tanzanian operating company owned by OreCorp Limited and the Government of Tanzania (Figs. 5-1c, 5-2): Nyanzaga (combined indicated and inferred mineral resources of 23.7 Mt @ 4.03 g/t Au for 3.07 Moz Au, at a 1.5 g/t Au cut-off grade; OreCorp, 2017) and Kilimani (inferred mineral resources of 6.3 Mt @ 1.06 g/t Au for 213 koz Au, with a 0.40 g/t Au cut-off grade; OreCorp, 2022).

The Nyanzaga and Kilimani gold deposits are hosted in a volcaniclastic sediment-dominated stratigraphic sequence within the Upper Nyanzian Group (Borg, 1992; Borg and Krogh, 1999). Three major formations have been defined at the Nyanzaga deposit: the Lower Volcaniclastic, the Central Formation and the Upper Volcaniclastic (Fig. 5-2c; Henckel et al., 2016; OreCorp, 2017, 2022). The Lower Volcaniclastic Formation consists of a thick package of dacitic volcaniclastic rocks, capped by a thick (20-50m) chert unit. Massive sulfide lenses are encountered locally in mudstones and cherts. A lower Sandstone Member forms the base of the Central Formation, comprising three cycles of sandstone and siltstone (with rare chlorite-magnetite mudstone) capped by cherts, overlayed by an upper Mudstone Member, comprising five cycles of siltstone and chlorite-magnetite mudstone, capped by cherts. The Nyanzaga Upper Volcaniclastic Formation consists of a thick package of dacitic to intermediate volcaniclastic rocks, with a distinctive high Cr and Ni whole rock geochemical signature, overlain by a felsic volcanoclastic unit. The sequence in the Nyanzaga area is topped by the Kilimani Formation, comprising BIF and interbedded mudstone and siltstone. Sedimentation is characterized by lateral variations in facies occurring across hundreds of meters. No granitoid intrusions have been identified within the Nyanzaga mineralization area, with the nearest granitic bodies located 3 km to the south and 5 km to the east (Fig. 5-1c). Note that all units of the volcanosediments exhibit metamorphism, the prefix ‘meta-‘ has been removed from the name of the units for readability purpose.

Alteration processes including silicification or silica-dolomite alteration are extensive in the Nyanzaga deposit, replacing sandstones and siltstones, and locally replacing mudstone (OreCorp, 2017). The cherts from the Lower Volcaniclastic Formation are non-magnetic at the Nyanzaga deposit, and preserved magnetite along strike to the east and west.

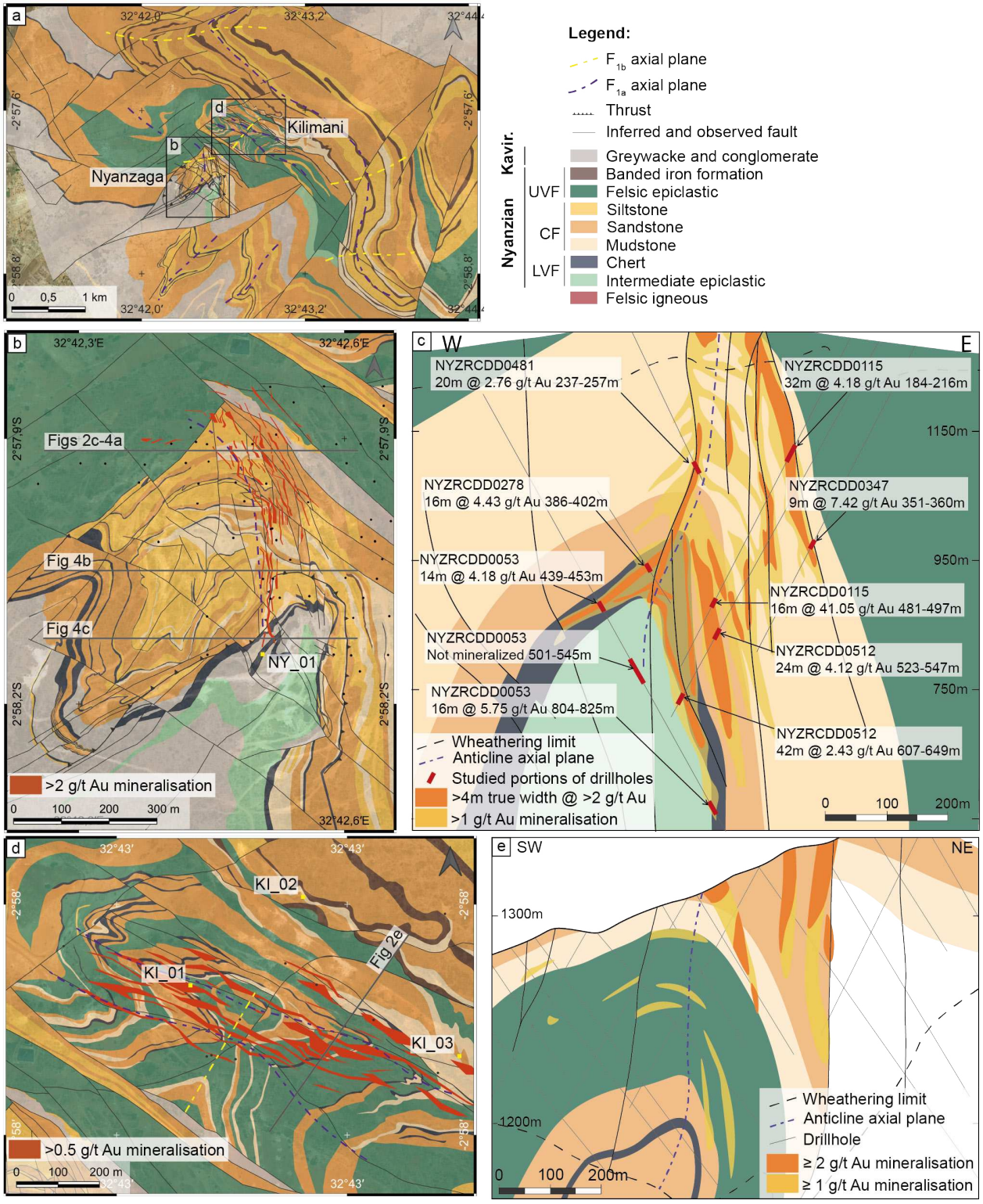

Figure 5-2. a. Geological and structural framework of the Nyanzaga gold Project (based from field mapping and geophysical data, OreCorp, 2017, 2022). **b.** Geological map of the Nyanzaga deposit. **c.** 2°57'54.5"S vertical section of the Nyanzaga deposit. **d.** Geological map of the Kilimani deposit **e.** Vertical section of the Kilimani deposit. The main ore zones are indicated. Studied sections of cores are outlined on the drillholes (from OreCorp, personal communication). Kavir. = Kavirondian; LVF = Lower Volcaniclastic Formation; CF = Central Formation; UVF = Upper Volcaniclastic Formation; KIF = Kilimani Iron Formation.

The bulk of the gold mineralization is hosted in siliceous rocks such as cherts or silicified sandstone and siltstone, some lodes in the upper part of the orebody are hosted in altered mudstones (OreCorp, 2017). At Kilimani, mineralization is hosted in volcaniclastics of the Upper Volcaniclastic and the Upper Felsic Volcaniclastic (OreCorp, 2022). Gold mineralization consists of native gold and electrum grains in quartz ± sulfide ± carbonate ± chlorite veins. Weathering has affected both deposits, being limited to around the top of the mineralized system at Nyanzaga, but nearly completely overprinting mineralization in Kilimani, masking the primary alteration and mineralization style (Fig. 5-2c and e).

According to Brigden et al. (2017), the area is affected by two folding events. A first subvertical, N-NE- and NW-striking tight, isoclinal folding event formed the NW-Nyanzaga and NW-Kilimani anticlines (Figs. 5-1c, 5-2). A second folding event with open W-NE axial planes seems to have affected the first ones. In addition, numerous subvertical NNW-/NW-, N- and NNE-/NE-trending subvertical faults offset the Nyanzaga and Kilimani anticline hinges (Fig. 5-2b-e; OreCorp, 2017). A thrusting event towards the NE has also been suggested, covering the SE part of the Nyanzaga Hill (Fig. 5-2c). A last faulting event is described, with three NW-trending faults south of the Nyanzaga deposit and the ore bodies offsetting the thrusting and the volcanosediments below with a dextral kinematics (Brigden et al., 2017). Evidence for the late thrusting and faulting events remains presently difficult to identify in the field.

3. Methods

3.1. Sampling

Detailed logging and representative sampling were performed on, respectively, 13 and 6 segments of drill cores at the Nyanzaga deposit (Fig. 5-2c) and the Kilimani deposit. Oriented thin sections were prepared from these samples, targeting different features including lithology, highly and weakly deformed samples, veins and their alteration halos and all sulfide assemblages.

96 bedding and 334 vein orientations were measured on the cores using a "Rocket Launcher" core orientation tool, based on orientation and downhole survey data collected during the drilling process. A database provided by OreCorp served as a source of additional structural data. Prior to analysis, rigorous efforts were undertaken to ensure the quality and accuracy of the database. The data classification, *i.e.*, bedding versus different types of veins, underwent a thorough checking process to eliminate any inconsistencies. As the classification of veins in the database differs from the one described in this paper, only the structural measures from the bedding (2522 + 628 data at Nyanzaga and Kilimani respectively) and the easily distinguishable late calcite-chlorite veins (17 data) were added to our 430 bedding and vein measures. Note that plane orientations are written as "strike-dip" (*e.g.*, 026-77) with strike defined by the right-hand-rule convention. Lineations are written as "dip/dip direction" (*e.g.*, 81/075).

3.2. Microscopy and mineralogical chemical characterization

A total of 59 polished thin sections were examined in detail under transmitted and reflected light microscopy, to determine mineral assemblages, mineral fabrics and associated deformation stages, and the relative timing of the main silicate and sulfide minerals regarding deformation stages defined at the deposit to macroscopic scales. Internal zoning and textures of sulfide minerals and the relationship between sub-microscopic ore-

bearing mineralogical assemblage were observed using a scanning electron microscope in back-scattered electron mode (BSE-SEM) at the GeoRessources research center (Vandœuvre-lès-Nancy, France).

4. Deformation, hydrothermal alteration and mineralization stages

This section covers the structural history, along with the hydrothermal and mineralization features, found at the Nyanzaga and Kilimani gold deposits. These insights are derived from field, core and thin section observations, as well as a comprehensive dataset of structural measurements on oriented core samples. Geological mapping of the two deposits undertaken by OreCorp (Figs. 5-1c and 5-2, 2017, 2022) was a significant input in deciphering the deformation history. Three stages in a progressive deformation have been identified on the basis of three types of structures that are listed and described below, being named D_{1a}, D_{1b} and D_{1c}.

4.1. Structural features of the Nyanzaga and Kilimani deposits

4.1.1. F_{1a} and F_{1b} folding

Previous structural analysis already mentioned the existence of two folding types within the Nyanzaga and Kilimani district (Brigden et al., 2017), here confirmed and detailed in our study. A first major set of folds, named F_{1a}, developed in the volcanosedimentary units of the Upper Nyanzian at the Nyanzaga and Kilimani deposits, with upright, moderately-plunging, asymmetric folds with a wavelength in the order of 500 meters (Figs. 5-2, 5-3, 5-4). At the district scale, F_{1a} antiforms and synforms show folded axial planes and axes (see purple dotted lines in Figs. 5-1c, 5-2a, b and d), with a progressive shift in their orientations from north to south:

- F_{1a} folds are WNW-ESE-dominated in the north-western part of the belt (Fig. 5-1c), including the Kilimani Anticline (FAP: 137-90, FA: 26/310; Figs. 5-2d-e, 5-4d). A slight curving of the hinge is responsible for the mushroom shape of the fold visible on the geological map (Fig. 5-2d).
- F_{1a} axial planes are N-S- to NE-SW-trending in the center of the belt (Fig. 5-1c). At the Nyanzaga deposit, the change in F_{1a} fold orientation is recorded over 400m from north to south, from a NW-oriented cylindrical fold (FAP: 144-89, FA: 47/327, Fig. 5-4a), to a N-oriented cylindrical fold (FAP: 082-88; FA: 53/357, Fig. 5-4b), to a NNE-oriented non-cylindrical fold (FAP: 026-77, FA: 81/075, Fig. 5-4c).
- In the south-eastern part of the belt, folds curve back to NW-SE-trending axial planes (Fig. 5-1c).

A wide range of F_{1a} geometries are observed on metric second-order folds at the outcrop to core scales, from overturned and asymmetric tight folds (Fig. 5-3a), to open and gentle, kink-style and symmetric folds (Figs. 5-3b and c, respectively). All of these folds have sub-horizontal to slightly plunging fold axes, consistent with the geometry of F_{1a} folds described at larger scales.

The important shift in the orientation of the F_{1a} folds is interpreted as the result of superimposed folding stages (Figs. 5-1c, 5-2a). F_{1b} folds have subvertical fold axes and axial planes and present slight variations in the orientation of their axial planes, from ENE-WSW striking in the northern part of the belt, to ESE-WNW striking in the south, rotating through an E-W orientation (yellow dotted lines in Figs. 5-1c, 5-2a). The F_{1b} folds are rather open, with a wavelength in the order of 7 kilometers (Fig. 5-1c). The curving of the F_{1a} axial planes

forms an overall z-shaped folding pattern at the district scale (Fig. 5-1c). The interference pattern of the F_{1a-1b} refold structures at the Nyanzaga and Kilimani deposits can be classified as Type 2 in Grasemann et al. (2004) classification, *i.e.*, a first fold with horizontal axis affected by a second one with vertical axis (Ramsay, 1962; Grasemann et al., 2004).

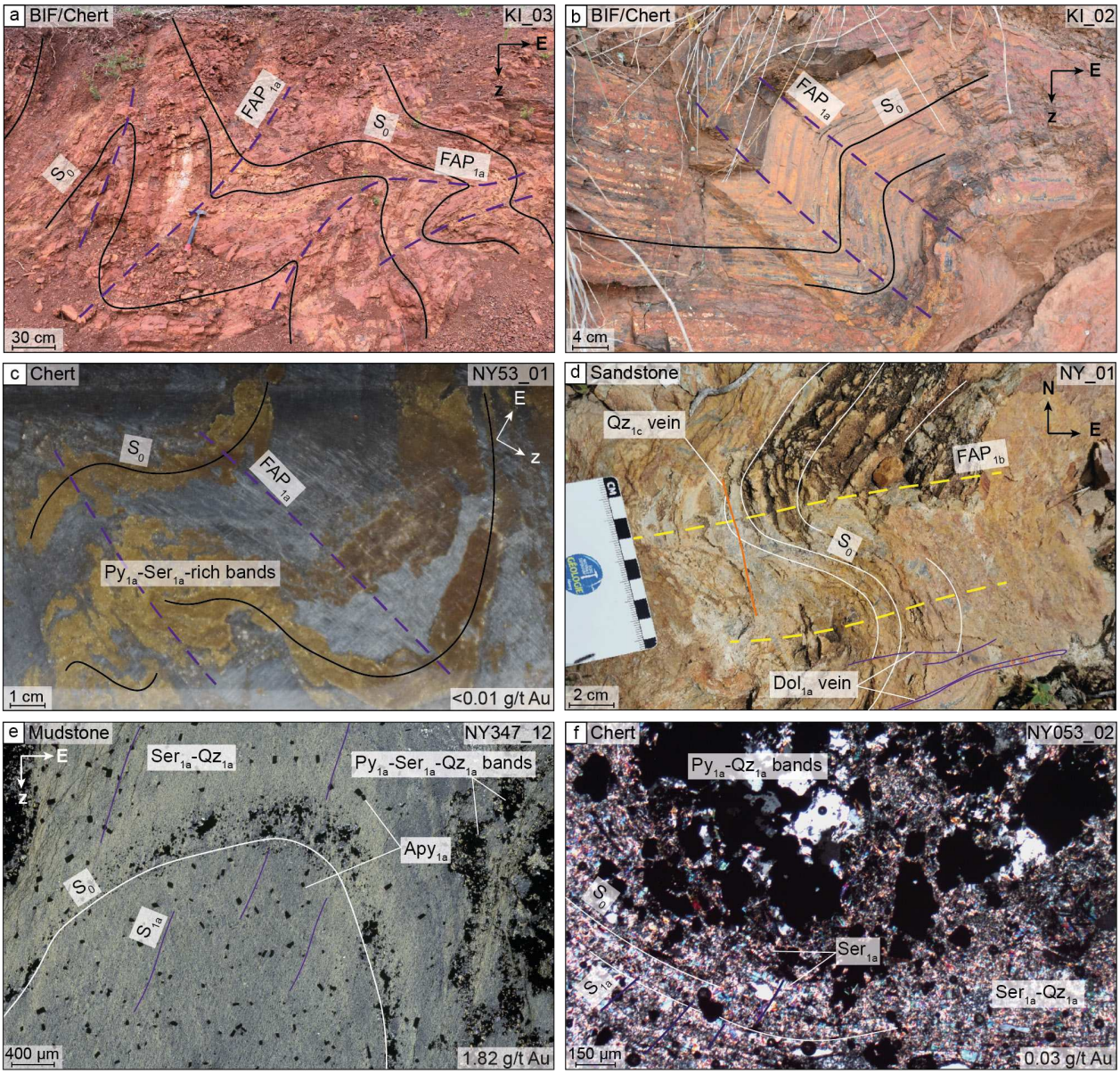

Figure 5-3. D_{1a}- and D_{1b}-related folding event observed at the outcrop- and core-scales. **a.** Asymmetric close F_{1a} folds in cherts on the Kilimani hillside. **b.** Kink-style F_{1a} fold in the cherts on the Kilimani hillside. **c.** D_{1a}-related folded cherts and Hi Py-rich bands on cores from the Nyanzaga deposit. **d.** NE-SW F_{1b} folds in sandstones, crosscut by D_{1c}-related V_3 Qz veins (FAP: 070-90). **e.** Apy grains aligned along the S_{1a} in a fold hinge zone (cross-polarized, transmitted light). **f.** S_0 bedding wrapping around H_i Py-Qz bands (cross-polarized, transmitted light). An S_{1a} cleavage is outlined by D_{1a}-related H_{ii} Ser grains. Dotted line = fold axial plane, strait line = foliation, purple = D1a-related features, yellow = D_{1b}-related features. FAP = fold axial plane.

In refold structures, the F_{1a} folded axial planes represent folded surfaces of the second generation of folds, similar to lithological contacts in a simple cylindrical fold. At the Nyanzaga deposit, the F_{1a} axial planes of the Nyanzaga Anticline at different latitudes record the D_{1b}-related refolding, showing changes in their orientation (Fig. 5-4a-c). F_{1a} axial planes have been measured at 15 different latitudes along the Nyanzaga Anticline, their planes and their poles were plotted in Figure 5-4e. The F_{1b} axis, β_{1b}, can be deduced by the intersection of all F_{1a} axial planes (Ramsay and Hubert, 1987). The poles of the F_{1a} axial planes align along a great circle and, perpendicular to it, the surface containing the β_{1b} is the F_{1b} axial plane (Ramsay and Hubert, 1987). The F_{1b} fold at the Nyanzaga deposit is therefore almost E-W oriented, with a subvertical axial plane and axis (FAP: 260-83, FA 82/135; Fig. 5-4e). Figure 5-3d illustrates an F_{1b} second-order, asymmetric, s-shaped fold with vertical axial plane and axis, with an ENE-oriented axial plane.

At the microscopic scale, folding is accompanied by an S_{1a} syn-folding cleavage. This cleavage is only visible at this scale, sub-parallel to the F_{1a} fold axial surface and restricted to the fold hinge zones. The foliation is highlighted by carbonate, sericite and arsenopyrite grains (Fig. 5-3e-f). No S_{1b} has been observed at the microscopic scale. Modeling of refold structures affecting the Nyanzaga deposit area is proposed in Supplementary Material 5-1.

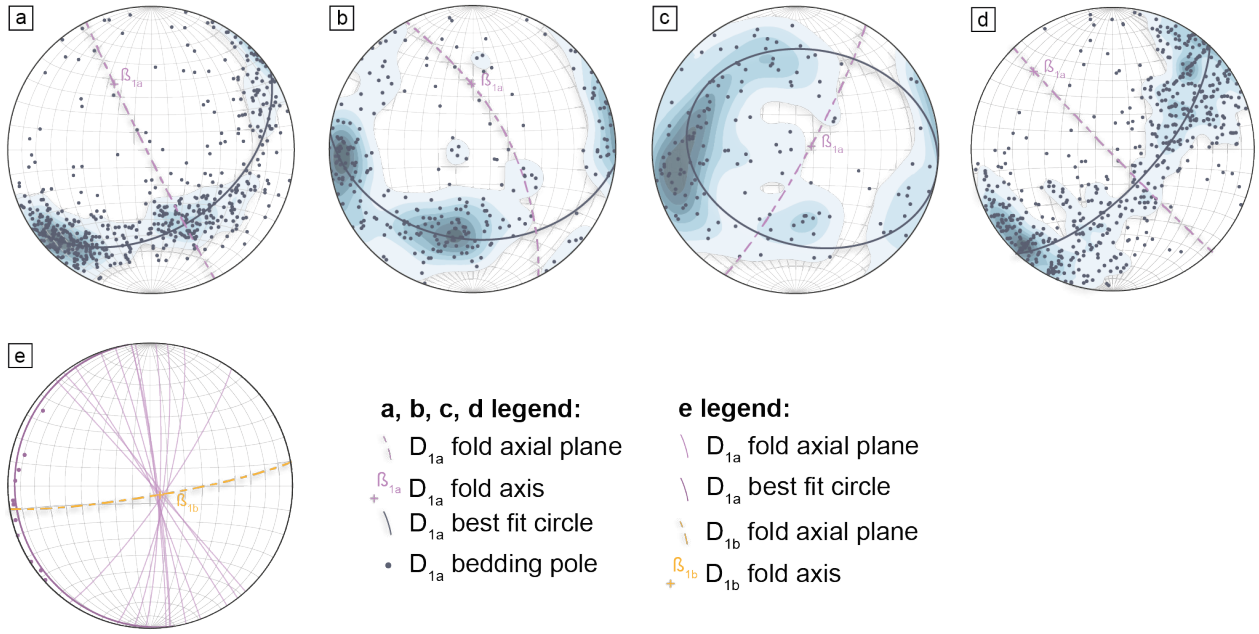

Figure 5-4. Stereograms of the bedding a-c at the Nyanzaga and d Kilimani deposits. **a.** S_0 bedding poles, F_{1a} fold axis and fold axial plane from the drillhole section 2°57'54.5''S (FAP: 144-89; FA: 47/327; 760 data). **b.** S_0 bedding poles, F_{1a} fold axis and fold axial plane from the drillhole section 2°58'03.8''S (FAP: 082-88; FA: 53/357; 423 data). **c.** S_0 bedding poles, F_{1a} fold axis and fold axial plane from the drillhole section 2°58'08.7S (FAP: 026-77; FA: 81/075; 157 data). Note that the S_0 bedding poles outlines a folded hinge line, hence a best fit small circle. **d.** S_0 bedding poles, F_{1a} fold axis and fold axial plane from all the drillhole at the Kilimani deposit (FAP: 137-90, FA: 26/310; 628 data). **e.** F_{1a} fold axial planes of the Nyanzaga Anticline at various latitudes and depths (15 data), outlining the F_{1b} fold axis and axial plane (FAP: 260-83; FA: 82/135).

4.1.2. D_{1c}-related faults and fractures

At the deposit scale, subvertical fault and fracture networks crosscut both folding generations. This fault-fracture network is shown on maps and cross-sections (Fig. 5-2), and can be subdivided into three groups: (i) NE- to NNE-oriented strike-slip faults with an apparent sinistral-reverse kinematics (Fig. 5-2a and d; OreCorp, 2017, 2020); (ii) N-S to NNW-SSE-oriented faults and fractures, their kinematic has not been described at the deposit scale (Figs. 5-2a, 5-5b); and (iii) NW-trending strike-slip faults with an apparent dextral kinematic (Figs. 5-2b and d, 5-5a) that appear to restrain the N-S fault system. The first two faults groups seem restricted to the central part of the studied domain, *i.e.*, coinciding with the Nyanzaga gold deposit location, where the Nyanzaga Anticline is N-S oriented (Fig. 5-2b). Regardless of its orientation, faults developed preferentially along the lithological contacts and on the subvertical limbs of the Nyanzaga and Kilimani anticlines (Fig. 5-2b-e).

At the outcrop scale, only a few faults and fractures were observed (Fig. 5-5a-b). N-S striking extensional veins along the NW-SE shear are consistent with the dextral kinematics along the shear zones (Fig. 5-5a-b). Extensional veins are filled with quartz, accompanied by small epidote-chlorite alteration halos. The outcrop in Figure 5-5b yields the relationship between the three directions of faults and fractures. The formation of N-S faults and extensional veins clearly appears to be a response to dextral motion along the NW-SE faults (Figs. 5-2b, 5-5a-b).

At the core scale, shear veins developed at lithological contacts, accompanied by networks of extensional veins (Fig. 5-5c). N-trending features are also characterized by several types of structures such as, fractures with normal-(sinistral) kinematics and minor pyrite-pyrrhotite infillings (Fig. 5-5d), pull-aparts (Fig. 5-5e) and extensional veins (Fig. 5-5f). All of these structures record normal kinematics. Near and within fault zones, large silicification, crackle and tectonic breccias are common (Fig. 5-5g-h). If fracturing and veining is widespread throughout the deposits, they are more concentrated in intensely silicified zones and silica-rich layers such as cherts and sandstone (Fig. 5-2c). The thin section analysis allows determining that no fabric developed during the D_{1c} fracturing stage, concordant with the brittle nature of this late stage.

Figure 5-5. D_{1c}-related faults and veins observed at the outcrop- and core-scales. **a**. NW-SE strike-slip fault in meta-sediments at the Kilimani deposit. Syn-faulting subvertical N-S quartz extension veins indicate a dextral kinematics of the fault. **b.** Relationship between small fractures on the outcrop. NW-SE fractures in red constrains N-S fractures in orange. The NE-SW fractures are in blue. **c.** Strike-slip fault developped at the lithological contact between volcaniclastics and cherts, observed on a core from the Kilimani deposit. V_3 Py-Chl-Qz veinlets formed during the faulting, indicating an apparent dextral kinematics. **d.** D_{1a}-related V_1 Dol crustiform vein crosscut by subvertical V_3 Qz-Po-(Py) veins. Py and Po are disseminated in the meta-sediments and are part of H_{Iv} alteration. A N-S D_{1c}-related fracture records a normal kinematics. **e.** Subvertical V_3 Qz vein forming a pull-apart with gold-bearing Po grain at the center, normal kinematics. **f.** En echelon V_3 Py-Po-(Cb-Qz) veins with a N-S orientation and normal kinematics (non-polarized, transmitted light). **g.** Crackle breccia of V_3 smoky Qz in sandstones. **h.** V_4 tectonic breccia in a normal N-S fault zone with fragments of cherts and V_3 Py-Po-smoky Qz veins. White milky Qz forms the breccia matrix. NY = sample and outcrop from Nyanzaga, KI = sample and outcrop from Kilimani. See Fig. 5-6 for mineral abbreviations.

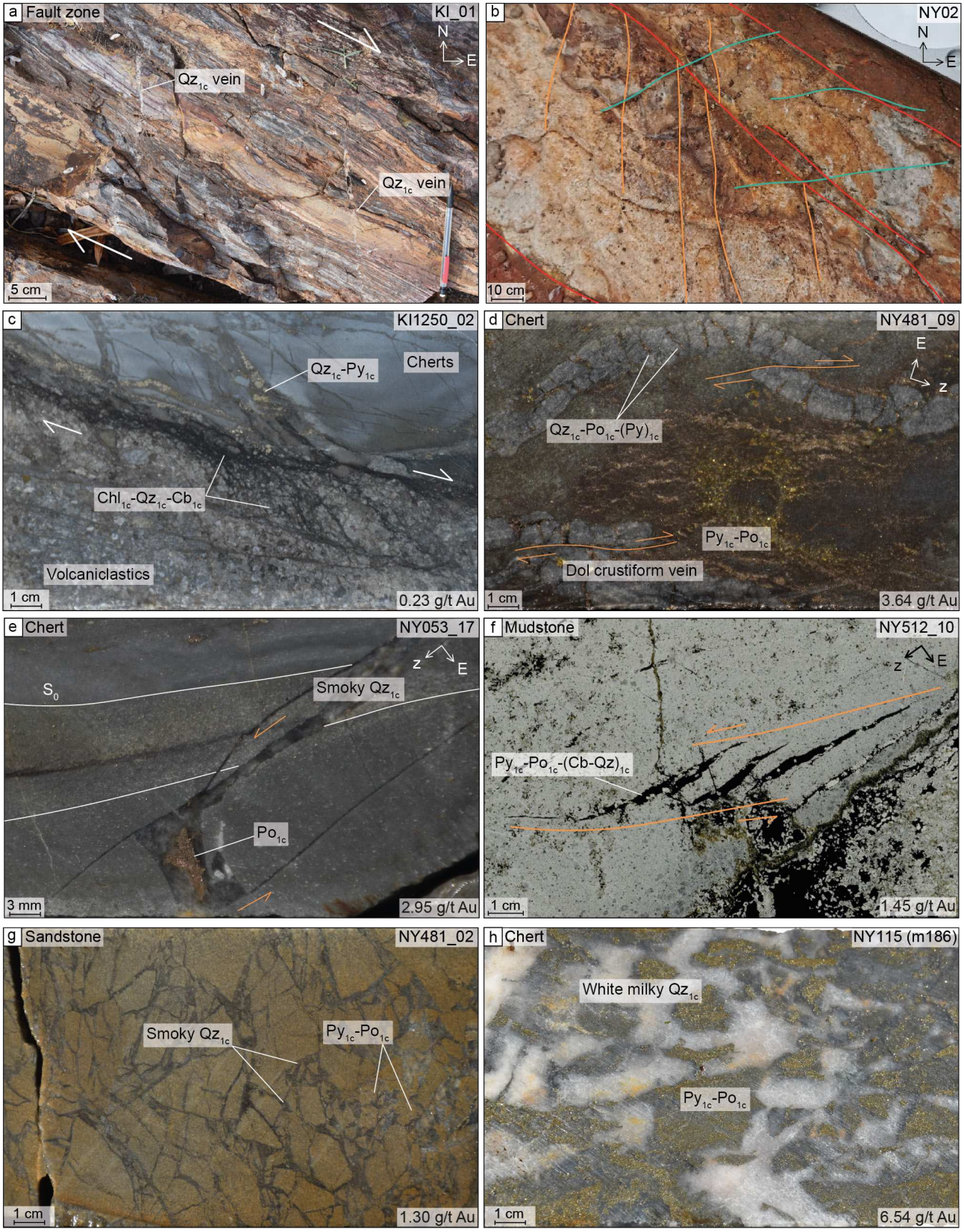
a Fault zone
KI_01
N
E
Qz1c vein
Qz1c vein
5 cm
b
NY02
N
E
10 cm
c
KI1250_02
Qz1c-Py1c
Cherts
Chl1c-Qz1c-Cb1c
Volcaniclastics
1 cm
0.23 g/t Au
d Chert
NY481_09
E
z
Qz1c-Po1c-(Py)1c
Py1c-Po1c
Dol crustiform vein
1 cm
3.64 g/t Au
e Chert
NY053_17
z
E
S0
Smoky Qz1c
Po1c
3 mm
2.95 g/t Au
f Mudstone
NY512_10
z
E
Py1c-Po1c-(Cb-Qz)1c
1 cm
1.45 g/t Au
g Sandstone
NY481_02
Smoky Qz1c
Py1c-Po1c
1 cm
1.30 g/t Au
h Chert
NY115 (m186)
White milky Qz1c
Py1c-Po1c
1 cm
6.54 g/t Au

4.2. Mineralogy and hydrothermal stages at the Nyanzaga and Kilimani deposits

Based on mineralogy, the relationship between fracturing, veining, hydrothermal alteration and deformation stages at the Nyanzaga and Kilimani deposits is depicted in the paragenetic sequence in Figure 5-6, with the upper part illustrating the distribution of minerals from hydrothermal alteration and the lower part the evolution of hydrothermal vein mineralogy (Fig. 5-6). Table 5-1 summarizes the deformation, veining, hydrothermal alteration and gold mineralization features at the Nyanzaga and Kilimani deposits.

Following the habit, textures and crosscutting relationships, veins have been divided into five successive sets, named V_1 to V_5 (Fig. 5-6, Table 5-1). Disseminated alteration halos, named H_i to H_{iv}, accompany veining; H_{ii} is dominated by silicate minerals while the three others are characterized by sulfide minerals. The first two vein sets formed during folding, widely spread along Nyanzaga and Kilimani anticlines, with early-D_{1a}-related highly folded dolomite ± quartz V_1 veins, associated with few centimeter-wide quartz – dolomite – K felspar – rutile alteration halos, named VH_1 (Fig. 5-8a). Microscopically, quartz grains in the V_1 veins present recrystallisation textures, as grain boundary migration (GBM, Fig. 5-8b; Passchier and Trouw, 2005). V_2 veins are late-D_{1b}-folding-related, ankerite ± pyrrhotite – pyrite veinlets (Fig. 5-8d-e), or more rarely pseudo-boudins perpendicular to the S_0 (Fig. 5-8f).

The three first hydrothermal alterations are also related to folding stages, with H_i consisting of early-D_{1a}-related pluri-centimeter-thick bands of pyrite – quartz – sericite ± tourmaline – monazite – chlorite dense disseminated aggregates, subparallel to the highly folded S_0 bedding, and overgrown by late-D_{1b}-related pyrite of H_{iii} alteration (Figs. 5-3c, e-f, 5-4c, e-f, 5-8b and c). Various amounts of quartz, carbonate, hyalophane, sericite, chlorite and albite emplaced within the volcanosediments during D_{1a} and D_{1b} stages, forming the dominated assemblage of widespread H_{ii} alteration (Fig. 5-6).

V_3 to V_5 are post-folding veins, related to D_{1c} faulting, with V_3 veins infilled with smoky quartz ± carbonate – pyrrhotite – pyrite – arsenopyrite – gudmundite, forming dense stockworks and crackle breccia in fault damage zones (Figs. 5-5c and e-f, 5-8g). V_3 veins display a major preferred subvertical, N-trending orientation (Fig. 5-7a). V_4 is filled with white milky quartz (Figs. 5-5h, 5-8d and h), and forms pluri-centimetric-wide extension veins and tectonic breccias, located solely in fault zones and damage-related areas. V_4 vein set is distributed following two distinct clusters, trending N100° and dipping vertically and NNW-SSE with low dips towards the ENE (Fig. 5-7b). Quartz grains present recrystallisation texture, with distinctive grain boundary migration, attesting of bulging (BLG, Fig. 5-8i; Passchier and Trouw, 2005). Finally, V_5, consists of rare late-D_{1c}-related calcite-chlorite-dominated veinlets associated with small chlorite alteration halos, named VH_5 (Fig. 5-8m-n). Calcite veins can present fibrous crystal texture (Fig. 5-8m). A mineral assemblage with barite – galena – pyrrhotite – jamesonite – boulangerite – bournonite – chalcopyrite – sphalerite – tetrahedrite – ullmannite – molybdenite – electrum fills these veinlets (Figs. 5-6, 5-8j-l and p, 5-9b and d). They are consistently subvertical and NNW-SSE-oriented (Fig. 5-7c). A last hydrothermal alteration is related to D_{1c} faulting, with an assemblage of pyrite – pyrrhotite – arsenopyrite ± gudmundite – electrum named H_{iv} alteration and disseminated in the volcanosediments (Figs. 5-5d, 5-8h), preferentially oriented in subvertical N-S trails (Fig. 5-5d). Among the five vein sets, V_1, V_2 and V_4 exhibit no association with gold, while V_3 and V_5 vein sets display various amounts of electrum (Fig. 5-6, Table 5-1).

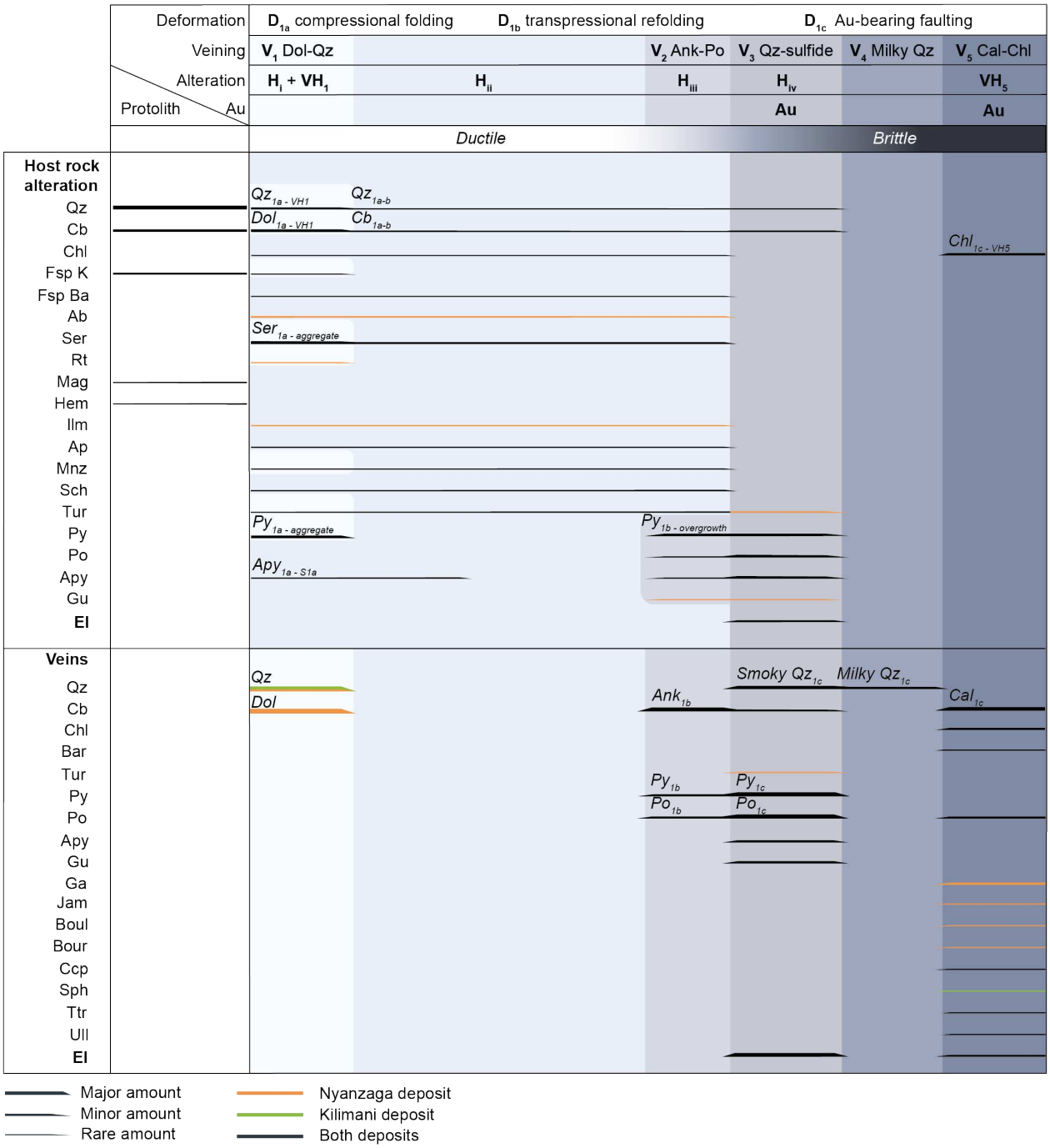

Figure 5-6. Mineral paragenetic sequence at the Nyanzaga and Kilimani gold deposits, based on macro- and micro-scale petro-structural work. V = veins; VH = vein-related alteration halo; H = hydrothermal alteration. Mineral abbreviations: Ab = albite; Ank = ankerite; Ap = apatite; Apy = arsenopyrite; Ba = barite; Boul = boulangerite; Bour = bournonite; Cal = calcite; Cb = carbonate; Ccp = chalcopyrite; Chl = chlorite; Dol = dolomite; El = electrum; Fsp-K±Ba = K-feldspar and hyalophane; Ga = galena; Gu = gudmundite; Ilm = ilmenite; Jam = jamesonite; Mnz = monazite; Po = pyrrhotite; Py = pyrite; Qz = quartz; Rt = rutile; Sch = scheelite; Ser = sericite; Sph = sphalerite; Ttr = tetrahedrite; Ulm = ullmannite.

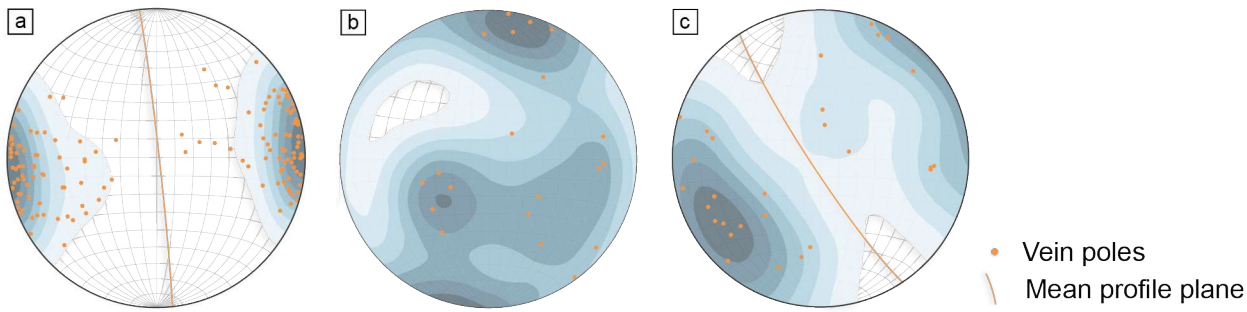

Figure 5-7. a. Stereogram of D_{1c}-related V_3 smoky Qz ± Py ± Po veins showing a consistent N-S subvertical orientation (145 data). **b.** Stereogram of D_{1c}-related V_4 white milky quartz veins showing clusters of veins, the main ones with a NW-SE orientation (20 data). **c.** Stereogram of D_{1c}-related strike of the V_5 Cal-Chl veins showing a global NW-SE trend (28 data).

	Deformation	Veining, mineralogy Hydrothermal alteration	Gold mineralization
D_{1a}	**Ductile deformation, F_{1a} folding:** Upright folds, wavelength 500m Cylindrical, locally non-cylindrical Folded axis and axial plane, varying from NW-SE to N-S, to NE-SW Second-order folds varying from overturn and tight, to open, kink-style symmetrical Rare S_{1a} parallel to the F_{1a} axial plane	**Veining:** V_1 folded Qz-Dol parallel or perpendicular to the S_0, Crustiform or comb, boudinaged, Qz GBM **Hydrothermal alteration:** VH_1 Qz-Dol-KFsp-Rt around V_1 H_i Py-Ser-Qz ± Tur-Mnz-Chl aggregates subparallel to the S_0 in cherts and mudstones H_{ii} Qz-BaFsp-Ser-Chl-Ab widespread alteration	None
D_{1b}	**Ductile deformation, F_{1b} folding:** Open, z-shaped refolds, wavelenght 7km Subvertical axis and axial plane FAP: 260-83, FA: 82/135	**Veining:** V_2 Ank ± Po veinlets, Ank ± Po-Py pseudo-boudins perpendicular to the S_0 **Hydrothermal alteration:** H_{iii} Py ± Apy-Gun-Ser overgrowths around H_i-related Py	None
D_{1c}	**Brittle deformation, D_{1c} fault network:** NE-SW to NNE-SSW sinistral-reverse strike slip faults NW-SE dextral strike-slip faults N-S to NNW-SSE normal-(sinistral), only present at the Nyanzaga deposit	**Veining:** V_3 smoky Qz ± Cb-Po-Py-Apy-Gun stockworks, extension veins, pull-aparts crackle breccias, subvertical and N-S oriented V_4 white milky Qz extension veins and tectonic breccias, Qz BLG V_5 Cal-Chl ± Ba-Ga-Po-Jam-Boul-Bour-Ccp-Sph-Tet-Ull-Mo-El, rare **Hydrothermal alteration:** H_{iv} Py-Po-Apy ± Gun-El widespread, locally along N-S trails VH_5 Chl around V_5	Orebodies concentrated mainly along the D_{1c}-related vertical NW-SE in both deposits and N-S faults at Nyanzaga El inclusions in H_{iv} and V_3 sulfides, associated with V_5 Ga ± Ba-Po Disseminated El in V_3 and V_5

Table 5-1. Summary of the deformation, veining and hydrothermal alteration, and gold mineralization features observed at the district- to micro-scales at the Nyanzaga Gold Project. See Fig. 5-6 for abbreviations.

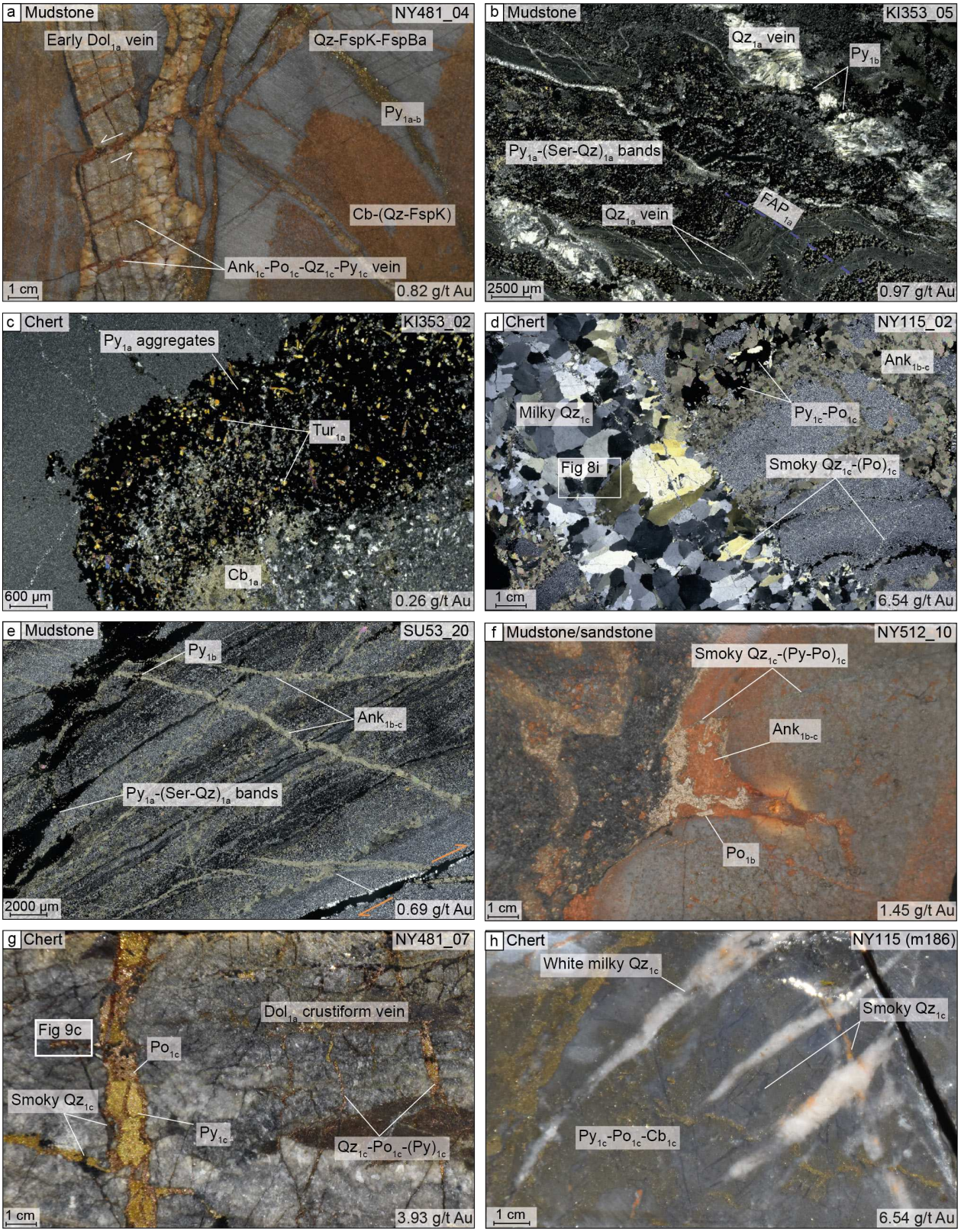
a Mudstone
NY481_04
Early Dol1a vein
Qz-FspK-FspBa
Py1a-b
Cb-(Qz-FspK)
Ank1c-Po1c-Qz1c-Py1c vein
1 cm
0.82 g/t Au
b Mudstone
KI353_05
Qz1a vein
Py1b
Py1a-(Ser-Qz)1a bands
FAP1a
Qz1a vein
2500 µm
0.97 g/t Au
c Chert
KI353_02
Py1a aggregates
Tur1a
Cb1a
600 µm
0.26 g/t Au
d Chert
NY115_02
Ank1b-c
Milky Qz1c
Py1c-Po1c
Fig 8i
Smoky Qz1c-(Po)1c
1 cm
6.54 g/t Au
e Mudstone
SU53_20
Py1b
Ank1b-c
Py1a-(Ser-Qz)1a bands
2000 µm
0.69 g/t Au
f Mudstone/sandstone
NY512_10
Smoky Qz1c-(Py-Po)1c
Ank1b-c
Po1b
1 cm
1.45 g/t Au
g Chert
NY481_07
Dol1a crustiform vein
Fig 9c
Po1c
Smoky Qz1c
Py1c
Qz1c-Po1c-(Py)1c
1 cm
3.93 g/t Au
h Chert
NY115 (m186)
White milky Qz1c
Smoky Qz1c
Py1c-Po1c-Cb1c
1 cm
6.54 g/t Au

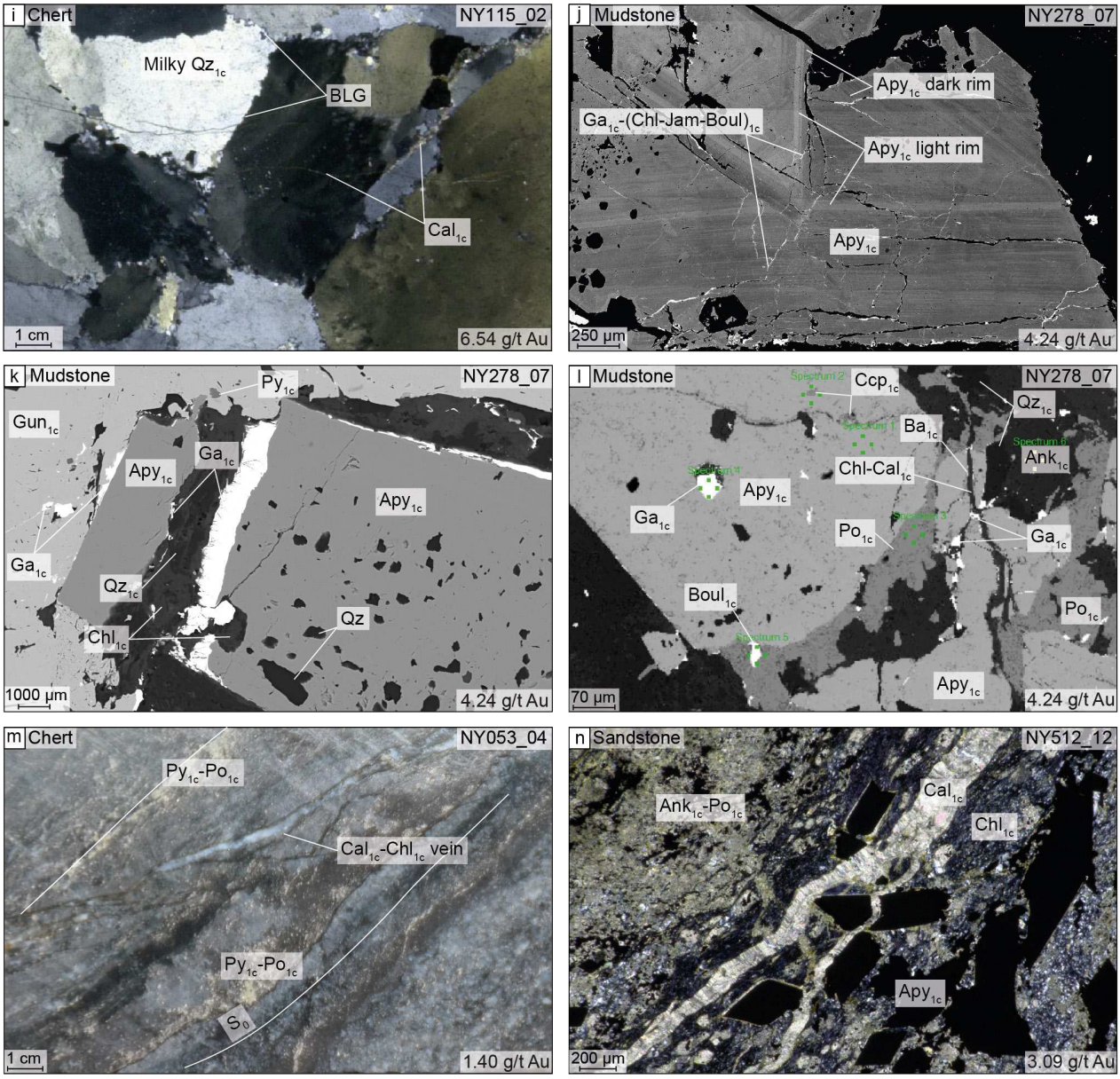

Figure 5-8. Vein features at the outcrop- and core-scales. **a.** Early D_{1a}-related V_1 Dol-dominated crustiform veins, crosscut and offset by V_3 Ank-Po-Qz-Py veinlets. VH_1 alteration halo is visible proximal to the V_1 vein, with a Qz-FspK-FspBa assemblage. Distal to the vein, quartz and Fsp are rarer. **b.** Boudinaged and folded V_1 comb Qz veins, crosscut by H_i Py-(Ser-Qz) bands. The purple dotted line represents the F_{1a} fold axial plane (cross-polarised, transmitted light). **c.** Folded H_i Py-Tur-rich aggregate (cross-polarised, transmitted light). **d.** Late-D_{1b}-early-D_{1c}-related V_2 Ank ± Py-Po stockwork crosscut by V_4 milky Qz vein, itself crosscut by V_3 smoky Qz ± Po veinlets (cross-polarised, transmitted light). **e.** V_2 Ank veins crosscutting the H_i Py aggregates and crosscut by the H_{iii} homogenous Py overgrowths. A V_3 smoky Qz-Po-Py vein offset the V_2 veins (cross-polarised, transmitted light). **f.** V_2 Ank-Po pseudo-boudin developed at the lithological contact between mudstone and sandstone, and affecting the sandstone unit. **g.** V_3 Po-Py-Qz vein crosscutting a V_1 Dol crustiform vein. Po infill a fracture in a Py grain. **h.** V_4 Milky white Qz extensional veins crosscutting a V_3 smoky Qz veinlet stockwork. H_{iv} Py-Po-Cb alteration is observed in the cherts. **i.** Bulging recrystallisation texture (BLG) of V_4 milky Qz grains. Zoom from Fig. 5-8d (cross-polarised, transmitted light). **j.** Multiple oscillatory zonation in an Apy grain from a V_3 vein. H_v Ga ± Chl-Jam-Boul alteration fills fractures in the Apy (BSE-SEM). **k.** H_{iv} Gun grain associated with a fractured Apy grain, the fracture is infilled with H_v Ga-Qz-Chl (BSE-SEM). **l.** H_{iv} Apy grains fractured and filled with a H_v Po-Chl-Cal-Ga-Ccp-(Boul-Bour) assemblage (BSE-SEM). **m.** V_5 Cal-Chl vein crosscutting H_{iv} disseminated Py-Po. **n.** V_5 veins of fibrous crystals of Cal fracturing H_{iv} large disseminated euhedral Apy grains. VH_5 Chl alteration halo formed around the V_5 veins (cross-polarised, transmitted light). See Fig. 5-6 for mineral abbreviations.

4.3. Gold distribution and location

At the deposit scale, the projection at the surface of the ore zones at depth not only follows the orientations of the Nyanzaga and Kilimani F_{1a} anticline axial planes, but also shows a strong correlation with the NW-SE strike-slip dextral faults at the Kilimani deposit (Fig. 5-2d-e), with the N-S to NNW-SSE-oriented faults, and with the NW-SE strike-slip faults at the Nyanzaga deposit (Fig. 5-2b-c). At the Nyanzaga deposit, mineralized lodes, above 2 g/t Au, are mainly located along the vertical faults, commonly parallel to the S_0 layering on the eastern limb of the anticline. To a lesser extent, economic gold lodes formed in the subvertical fault zones on the western limb of the anticline, and from there permeated through the subhorizontal lithological contacts (Fig. 5-2c). In these lodes, gold is hosted in small D_{1c}-related sets of subvertical veins and veinlets, mainly within the most competent layers such as silicified rocks, cherts or at contacts between units. At the Kilimani deposit, ore bodies are hosted in the Upper Volcaniclastic and Upper Felsic Volcaniclastic Formations with highest gold endowments in the upper sandstone and mudstone, vertically oriented near faults, and in some slightly dipping layer-parallel lodes on the southern limb of the deposit (Fig. 5-2e). Less endowed bodies, *i.e.*, between 1 g/t and 2 g/t, are scattered within volcaniclastics, near the anticline hinge, following the lithostratigraphy.

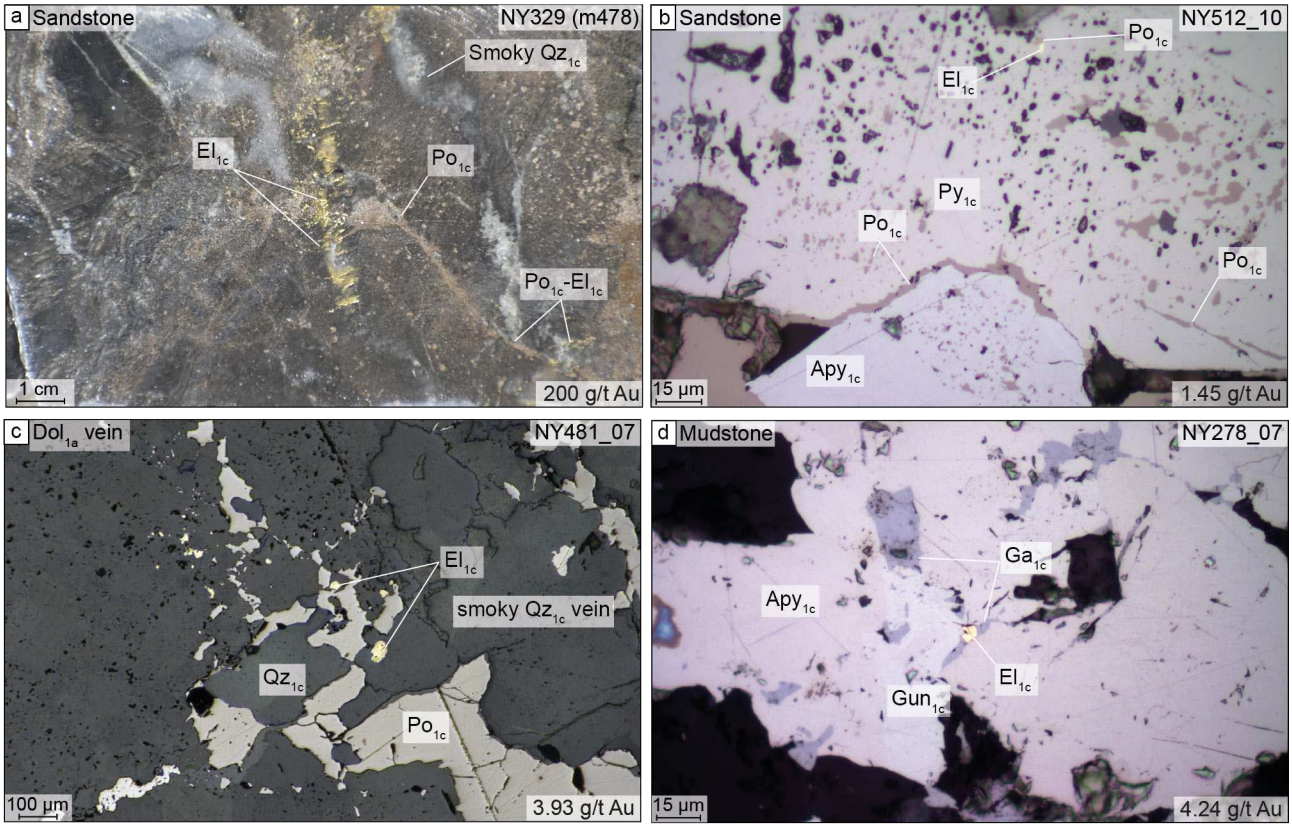

Figure 5-9. D_{1c}-related mineralization features. **a.** H_v El ± Po grains filling fractures in sandstone. **b.** El-Po grains in inclusion in H_{iv} Py (reflected light). **c.** Disseminated El grains in V_3 smoky Qz-Po veinlet crosscutting a V_1 Dol vein. Zoom from Fig. 5-8g (reflected light). **d.** El grains associated with H_v Gal infilling fractures in H_{iv} Gun-Apy grains (reflected light). See Fig. 5-6 for mineral abbreviations.

At the core scale, the V_1 veins and H_i pyrite aggregates appear to be barren, as indicated by the low amounts of gold where no other hydrothermal stage overprinted them (< 0.01 g/t Au; Figs. 5-3c and f, 5-8c). The highest gold grades, above 2 g/t, are always observed where a large number of the V_3 veins set formed (Figs. 5-5 d-e and g-h, 5-8f-h and m). Visible gold is always associated with V_3 and V_5 veins sets and sulfide grains within the veins (Fig. 5-9).

At the microscopic scale, gold mineralization is expressed in the form of: (i) disseminated electrum grains in V_3 and V_5 veins (Figs. 5-6, 5-9c); (ii) electrum inclusions in H_{iv} sulfide grains (Fig. 5-9b); (iii) electrum infillings in fractures associated with V_5 galena ± barite and pyrrhotite in H_{iv} sulfide minerals (Fig. 5-9d).

5. Discussion

5.1. Reconstructing the petro-structural history of the Nyanzaga and Kilimani gold deposits

The structural, mineralogical and textural investigation at the deposit to microscopic scales described above has allowed us to establish the deformation and hydrothermal evolution of the Nyanzaga and Kilimani gold deposits, as well as the relative chronology between both gangue and ore minerals within the ore-hosting volcanosedimentary sequence (Fig. 5-6, Table 5-1). Relying on these observations, a 3D petro-structural evolutionary model from the district to the core scales is provided in Figure 5-10. The model aims at reconciling the protracted deformation and hydrothermal history to the emplacement with the gold mineralization.

Deformation stage 1a: The ductile D_{1a} is a well-expressed deformation stage in the studied area, forming the moderately plunging upright, NE-striking, asymmetric Nyanzaga and Kilimani F_{1a} anticlines (Figs. 5-2, 5-4, 5-10a$_1$). Folds with such geometry are formed as the result of a D_{1a}-related compressional regime, where the maximum and intermediate principal strains are horizontal, and the minimum principal strain is vertical (Fig. 5-10a$_1$).

The S_{1a} cleavage is poorly expressed across the volcanosediments and is restricted to the F_{1a} second-order fold hinge zones, highlighted by sericite ± arsenopyrite grains (Fig. 5-10a$_2$). Dolomite ± quartz V_1 veins were affected by the folding stages (Figs. 5-3c and f, 5-7b, 5-10a$_2$). They demonstrates high temperature recrystallisation textures with grain boundary migration, formed at T ≥ 500 °C (Fig. 5-7b; Passchier and Trouw, 2005). Such high temperature is consistent with the ductile nature of the D_{1a} deformation stage. The H_i pyritization forms dense, folded aggregates, parallel to the S_0 cleavage (Fig. 5-4c and f). No gold is related to D_{1a}.

Deformation stage 1b: The D_{1b} ductile stage is characterized by the refolding of the F_{1a} folds. The vertical fold axis and vertical E-W-oriented axial plane of the F_{1b} characterize a transpressional regime with a vertical intermediate principal strain, and horizontal N-S maximum and E-W minimum principal strains (Figs. 5-4e, 5-10b$_1$). The N-S transpression rotated clockwise the earlier folds, resulting in the formation of asymmetric z-shaped F_{1a} folds (Fig. 5-1c; Carreras and Druguet, 2019). The WNW-ESE to NW-SE orientation of long limbs of the z-shaped folds observed at the district scale (Fig. 5-1c) records the original orientation of the F_{1a} folds, hence a D_{1a} NNE- to NE-oriented maximum shortening (Fig.10a$_1$).

Late in the folding history, ankerite ± pyrrhotite – pyrite V_2 veins crosscut the H_i pyrite and V_1 veins (Fig. 5-10b$_2$). Due to folding, the highly silicified units, *e.g.*, cherts, are progressively boudinaged, resulting in ankerite – pyrrhotite ± pyrite V_2 veins in the low pressure inter-boudin necking area (Fig. 5-10b$_2$). H_{iii} homogenous pyrite

overgrows the H_i pyrite aggregates and crosscut the V_1 and V_2 veins (Fig. 5-10b$_2$). No gold is related to D_{1b}.

Deformation stage 1c: With continuing N-S to NNW-oriented shortening, the conjugate NE-SW and NW-SE strike-slip faults form, affect and offset the refold structures, exhibiting, respectively, reverse-sinistral and dextral shearing motions (Fig. 5-10c$_1$).

During this stage, and in relation with the z-shape of the D_{1b} fold in the zone of the future Nyanzaga deposit, NW-SE dextral shearing planes, parallel to the long limb of the fold, control the opening and formation of N-S-trending sub-vertical normal faults and veins where the Nyanzaga Anticline is N-S-oriented, focusing most of the hydrothermal fluid circulation and gold deposition (Fig. 5-10c$_{1-2}$). Simultaneously, a similar NW-SE dextral fault network formed at the Kilimani deposit, yet lacking the N-S normal faults due to its location far from the N-S trending part of the F_{1a} fold geometry (Fig. 5-10c$_{1-2}$). Note that no gold is recorded along the NE-SW reverse-sinistral faults.

If faults preferentially formed along lithological contacts, they also crosscut them (*e.g.*, NW-SE faults in the southern part of the Nyanzaga Anticline where lithological contacts are NE-SW, and NE-SW faults crosscutting the NW-SE Kilimani Anticline, Fig. 5-2b and d). Therefore, lithological contacts functioned as weakness surfaces in fault formation and do not seem to have controlled the orientation of the NW-SE and NE-SW conjugated pair of faults.

Three main hydrothermal sub-stages occurred during the D_{1c} deformation stage (Fig. 5-10c$_3$), with (i) smoky quartz ± ankerite – sulfide V_3 veinlets, stockworks and crackle breccias; (ii) milky white quartz V_4 veins and tectonic breccias; (iii) late assemblage of calcite – chlorite-dominated V_5 fractures mostly localized in both previous veins and sulfide grains (Fig. 5-10c$_3$). Quartz in V_{3-4} veins records bulging recrystallisation textures, indicating that the temperature of the system decreased from ~ 500-550°C during the D_{1a} deformation stage to ~ 300-400°C during the D_{1c} stage, consistent with the shift from ductile- to brittle-dominated deformations (Fig. 5-10a$_2$-b$_2$; e.g., Stipp et al., 2002; Passchier and Trouw, 2005). In parallel to vein formation, disseminated alteration is recorded within the host rock, with widespread H_{iv} assemblage of pyrite – pyrrhotite – arsenopyrite – gudmundite developed in various amounts and formed parallel to V_3 veins (Fig. 5-10c$_3$).

Gold mineralization is spatially related to the D_{1c}-related hydrothermal features (Figs. 5-6, 5-9, 5-10c$_2$). Electrum grains formed: (i) in the smoky quartz ± ankerite – sulfide V_3 veins, either as inclusion in the sulfide minerals or disseminated in the quartz (Fig. 5-9c); (ii) disseminated in the late calcite – chlorite V_5 veins; and (iii) in association with V_5 galena ± pyrrhotite minerals, in fractures in H_{iv} disseminated pyrite, pyrrhotite, arsenopyrite, gudmundite grains (Fig. 5-9b and d).

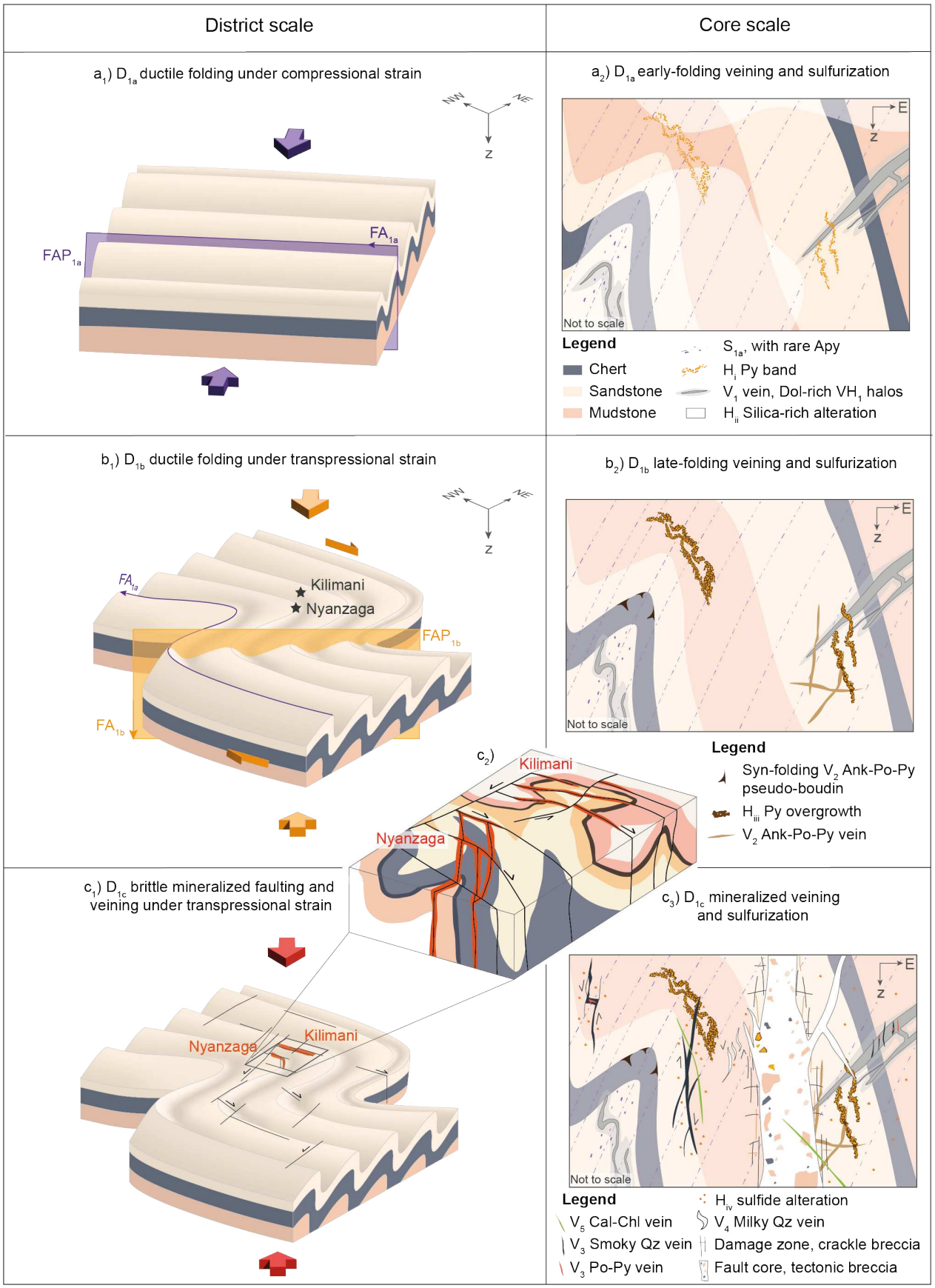

Figure 5-10. 3D petro-structural evolutionary model of **a** D_{1a}, **b** D_{1b} and **c** D_{1c} at the Nyanzaga and Kilimani gold deposits, Sukumaland greenstone belt. **a_1**, **b_1** and **c_1** present the structural evolution at the district scale. **a_2**, **b_2** and **c_3** present the hydrothermal evolution at the core scale. **c_2** present the structural features during the D_{1c} deformation stage at the two deposits scale. Refer to the text for explanations.

5.2. *Multi-phase or progressive deformation?*

Oriolo et al. (2022) proposed a new definition of progressive deformation, as the result of rather homogenous flow parameters, independently of ductile or brittle conditions. In this section we question whether the three-stage deformation at the Nyanzaga and Kilimani gold deposits results from discrete phases or from a progressive history.

At the Nyanzaga Project, the refold structure is defined by (i) F_{1a} upright fold affected by (ii) F_{1b} vertical folding, hence the overall z shape of the F_{1a} synclines and anticlines (Figs. 5-1c, 5-2). Such refold structure is classified as Type 2 in Ramsay (1962) and Grasemann et al. (2004) classifications and has been widely interpreted as resulting from a progressive non-coaxial deformation history, whether from flow perturbations, strain partitioning or local layer irregularities (Holdsworth and Pinheiro, 2000; Alsop et al., 2010; Carreras and Druguet, 2019).

A transpressional regime is suggested when initial folds develop parallel to the extension direction, such as the WNW-ESE F_{1a} folds, and are then rotated by shearing (Holdsworth and Pinheiro, 2000; Carreras and Druguet, 2019). Therefore, at the Nyanzaga and Kilimani gold deposits, the shift from F_{1a} to F_{1b} folds resulted in a strain field change with a switch from a D_{1a} compressional regime to a D_{1b} transpressional regime under a consistent roughly N-S to NNE maximum shortening orientation (Fig. 5-10; *e.g.*, Perret et al., 2021). Furthermore, the $D_{1a\text{-}1b}$ N-S maximum shortening persists during the brittle-(ductile) D_{1c} deformation stage. The reverse-sinistral kinematics described on the NE-SW faults and dextral kinematics on the NW-SE faults fit into the same transpressional regime as F_{1b} folding stage (Fig. 5-10; Brigden et al., 2017; OreCorp, 2022).

The rather homogenous flow parameters during ductile folding-refolding $D_{1a\text{-}1b}$ and brittle fracturing-faulting D_{1c} could therefore be merged into a single-stage progressive deformation history as defined by Oriolo et al. (2022). The continuum of deformation is accompanied by a continuum of hydrothermal alteration, with overlapping of disseminated alteration and vein sets from one deformation stage to the next. An overall progressive shift from disseminated-dominated alteration of the host rock and minor veining during the $D_{1a\text{-}1b}$ stages to alteration linked to strong veining and to a lesser extent dissemination during the D_{1c} stage (Fig. 5-6) is in line with the progressive shift from ductile to brittle deformation, and progressive decrease in temperature of the system as demonstrated by quartz textures evolution in V_1 to $V_{3\text{-}4}$ veins (Fig. 5-8b and i).

The history of progressive deformation interpreted here primarily relies on structural-petrographic and kinematic evidence at the micro to district scales. To fully reconstruct the deformation history, whether it involves a single continuous phase or multiple phases, links with the regional-scale tectonic evolution of the SGB are essential. Combining structural, micro-structural, textural information with direct or indirect dating may help to accurately place each deformation event within the constrained tectonic framework of the area (Fossen et al., 2019; Süssenberger et al., 2018a; Oriolo et al., 2022).

5.3. *Influence of fold interference pattern on the geometry of the fault system and gold concentration*

The petrographic observations and geochemical analyzes consistently indicate that gold mineralization is spatially and temporally associated with the D_{1c}-related sulfide minerals, mainly formed in veins (Fig. 5-9). At the core to deposit scales, ore-related hydrothermal alteration is focused in and near the D_{1c}-related fault zones (Figs. 5-2, 5-5g-h, 5-10c_1-c_2).

However, an heterogeneous distribution of gold is observed between and within both deposits, correlated to the orientation of faults: (i) the NE-SW reverse-sinistral strike-slip faults are barren, (ii) the NW-SE dextral strike-slip faults are moderately gold-endowed, hosting most of the poorly-endowed Kilimani mineralization and a minor amount of the Nyanzaga mineralization, (iii) the N-S normal faults concentrate most of the gold mineralization, explaining the high-gold values at Nyanzaga (Figs. 5-2, 5-10c_2). These N-S faults were created in response to the dextral shearing along the main NW-SE faults (see Fig. 5-10c_1-c_2), and are principally normal-sinistral structures, a few N-S dilational jogs and extensional veins have been observed (Fig. 5-5e-f). The development of dilational structures, *i.e.*, local extension, and high-opening rates along them constitute excellent conditions for gold precipitation as widely documented in the literature in transpressional regimes, such as relay ramps, jogs and extensional duplexes (*e.g.*, Bierlein et al., 2006 and references therein; Dressel et al., 2018; Chauvet, 2019; Murray et al., 2019). Indeed, the correlation between structure orientations and gold endowment at the Nyanzaga and Kilimani gold deposits can therefore be interpreted as resulting from a shortening orientation that favored transpression during the D_{1c} deformation stage, transpression that led to numerous localized open or dilational features. Processes of deposition of gold in relation with infilling of open space seems to dominate.

A small part of the mineralization is hosted in layer-parallel lodes near the subvertical fault zones on the western limb of the Nyanzaga Anticline (Fig. 5-2c). In these lodes, gold is hosted in small D_{1c}-related sets of subvertical veins and veinlets, mainly within the most competent layers such as silicified rocks, cherts or at contacts between units. Therefore, if faults have acted as major conduits for the circulation and precipitation of the mineralized fluid, minor circulation permeated through the lithological units and contacts, and precipitation was controlled by competency of the host rock.

Furthermore, an heterogeneous distribution of faults along both deposits can be linked to the geometry of the refold structures (Figs. 5-2b and d, 5-3, 5-4). If lithological contacts constitute weak planes favorable for fracturing and faulting, the D_{1c}-related subvertical fault network appears to be preferentially developed along vertical limbs of the asymmetric inclined F_{1a} Nyanzaga and Kilimani anticlines, *i.e.*, the east and north limbs, respectively (Figs. 5-2, 5-10c_2). Their refolding during the D_{1b} deformation stage affected them differently. At the Kilimani deposit, the anticline reoriented towards a NW-SE direction and the gold mineralization focused along NW-SE subvertical faults (Figs. 5-2d-e, 5-10c_1-c_2). At the Nyanzaga deposit however, the curving of the anticline led to (i) a NW-SE orientation of the lithological contacts on the northern part of the deposit, mainly affected by NW-SE gold-endowed faults, (ii) a N-S-oriented anticline at the heart of the Nyanzaga deposit, where N-S to NNW-SSE faults have concentrated most of the gold, and (iii) a NE-SW-oriented anticline in the south of the deposit, crosscut and offset by barren NE-SW faults (Figs. 5-2b-c, 5-10c_1-c_2).

The crucial role of z-shaped folding in localizing gold mineralization is also highlighted by the fact that only the NW-SE trending structures were mineralized within the conjugated pair of NW-SE and NE-SW faults. The focus of NW-SE faults along pre-existing structures, *i.e.*, stratification planes, favors the concentration of shearing along these planes, unlike the NE-SW faults. This results in gold lode heterogeneity within the conjugated pair of faults.

These observations and interpretations favor a model in which the structural complexity, and in particular the geometry of the refold structures, is the main control of the gold mineralization. The history of deformation leading to gold mineralization is then as follows (Fig. 5-10): (i) the D_{1a}-related folding stage verticalized the stratigraphy on the east limb of the Nyanzaga Anticline and the north limb of the Kilimani Anticline, (ii) the D_{1b}-related refolding stage reoriented the Nyanzaga Anticline along a N-S axial plane, where (iii) major subvertical

NW-SE dextral strike-slip and N-S normal faults developed, preferentially along the lithological contacts that constitute weak planes favorable for fracturing and focusing most of the ore-bearing fluid(s) (Fig. 5-10c$_2$).

It is worth noting that the original description of the Nyanzaga gold deposit includes the presence of a thrust south of the mineralization, crosscut and offset by NW-trending brittle faults with a dextral kinematics (Fig. 5-2b; Brigden et al., 2017). The thrust shows no link to the gold lodes and was hence interpreted to have formed after the mineralizing stage, similar to the NW-trending faults affecting the thrust. This suggests that these faults could have resulted from a later deformation stage (Brigden et al., 2017). However, given that the thrust is positioned above the NE-trending Nyanzaga Anticline, the absence of mineralization in this part of the fold may instead be explained by its unfavorable orientation for the development of ore-bearing structures with opening kinematics, such as the mineralized N-S faults. The NW-trending faults offsetting the thrust recorded a dextral kinematics, similarly to the NW-trending faults in the northern part of the Nyanzaga deposit (Fig. 5-2b). Consequently, these faults are interpreted as D_{1c}-related structures that did not channel mineralizing fluids due to their location within the NE-trending section of the Nyanzaga Anticline.

5.4. Regional comparison of the gold deposits in the Sukumaland greenstone belt (SGB)

Comprehensive studies on the petro-structural and mineralization context of other gold deposits in the SGB have been undertaken and discussed in other works (Borg, 1994; Chamberlain, 2003; Vos et al., 2009; Sanislav et al., 2015, 2016; Van Ryt et al., 2017; Kwelwa et al., 2018). The results and model obtained on the Nyanzaga and Kilimani gold deposits are here compared to some of the other deposits of the belt, including: the Geita and Bulyanhulu deposits.

The progressive and continuous three-stage deformation history described at the Nyanzaga and Kilimani gold deposits is a concept newly introduced in the SGB. Multi-phase deformation histories have been proposed at the Geita and Bulyanhulu gold deposits, with three phases and up to eight deformation events (Borg, 1994; Chamberlain, 2003; Sanislav et al., 2015, 2016; Kwelwa et al., 2018). In these cases, at least two to four folding events are described, all starting with upright tight folds formed during a compressional regime and affected by reclined to vertical folds (e.g., Borg, 1994; Chamberlain, 2003; Sanislav et al., 2015). At the Bulyanhulu deposit, while the second set of folds is E-W-oriented and share similar characteristics to the F_{1b} folds described in this paper, the earliest set of folds is mostly N-S-oriented (Chamberlain, 2003), similar to the F_{1a} rotated under the effects of the F_{1b} folding within the Nyanzaga area. Several authors have described the geometry of the SGB as arcuate or curved, based on geological and lineament mapping, and interpreted it as resulting from large-scale folding during a N-S-directed transpression (e.g., Borg, 1994; Chamberlain, 2003). The spatial changes in the global orientation of the first-generation fold could therefore explain the location of the Bulyanhulu deposit, near the hinge zone of the E-W SGB fold, where the belt is N-S oriented (Fig. 5-1b), the Nyanzaga and Kilimani deposits being then located on the north-eastern limb of the similar SGB fold (Fig. 5-1b). At the Geita deposit, the first set of major folds is NE-verging, refolded by NE-SW folds, leading to s-shaped refold structures, with NE-SW long limbs (Sanislav et al., 2016). Such a structure is close to the refold structure modelled at Nyanzaga (Fig. 5-6e), and could be interpreted as a conjugate of the z-shape refold structures with NW-SE long limbs described at the Nyanzaga district (Fig. 5-1c). The Geita and Bulyanhulu deposits are also crosscut by ductile-brittle shear zones that exhibit a steep dip and NW and NE trends, formed during a N-S transpression and later reactivated under transtension. If that last event has not been observed at the Nyanzaga and Kilimani gold deposits, the first one is similar to the D_{1c}

stage at the Nyanzaga and Kilimani deposits (Sanislav et al., 2015, 2016; Kwelwa et al., 2018). Late strike-slip and normal reactivations through N-S extensional events are described at the Geita deposit, that were not recorded at the Nyanzaga and Kilimani deposits (Sanislav et al., 2015, 2016), yet normal kinematics are found along the N-trending mineralized faults and fractures (Fig. 5-5d-f).

The shift from compression to transpression is observed and described throughout the whole SGB since Borg (1992) (*e.g.*, Borg and Krogh, 1999; Chamberlain, 2003; Sanislav et al., 2018a). At the Geita deposit, the overall compression is interpreted as being driven by slab flattening of subduction underneath an oceanic plateau around 2700 and 2660 Ma (Sanislav et al., 2018b). The horizontal shortening, dominated by coaxial deformation, and developed along major shear zone such as the Geita Shear Zone would imply lateral extrusion of material, as classically proposed (Fossen and Tikoff, 1998; Sanislav et al., 2018a). While the start of this shearing is dated around ca. 2690 Ma, *i.e.*, ca. 10 Ma after the start of the compression (Sanislav et al., 2018b; Dirks et al., 2020), no explanation is yet proposed to explain the accommodation of the compression by transpression under the ductile regime. We suggest that strain localization along shear zones and non-coaxial deformation may have been strongly favored by (i) evolution towards more brittle conditions and (ii) the influence of specific external geometry, for example the limits of the SGB margin, the difference in rheology of specific lithologies such as the BIF or granitic rocks.

At the Geita deposit, transtension follows the transpression, contemporaneous to the gold-bearing strike-slip faults (Borg, 1992; Sanislav et al., 2015). The geometry and kinematics of faults and veins at the Nyanzaga and Kilimani gold deposits are more in line with a transpressive regime, in particular the reverse nature of the NE-SW faults. The localized distribution of normal N-S faults at Nyanzaga, bounded by NW-SE dextral ones, could be explained by the activation of local extension within a global transpression (*e.g.*, Woodcock and Fischer, 1986; Poli and Renner, 2004).

Regionally, the mineralizing event is interpreted as a single stage of mineralization in all deposits of the area, focused along the fault zones, hence classified as lode-gold deposits (e.g., Chamberlain, 2003; Van Ryt et al., 2017). Gold is associated with a wide variety of sulfide minerals, showing similarities with the Nyanzaga and Kilimani ore-related mineralogical assemblage (Chamberlain, 2003; Vos et al., 2009). A barren sulfurization of the host rocks is linked to syn-sedimentary and volcanic-exhalative events at both the Geita and Bulyanhulu deposits, that can be correlated with the Nyanzaga H_i early pyrite aggregates as previously suggested (Chamberlain, 2003, Van Ryt et al., 2017). Geochemical analyses are required at Nyanzaga to test the hypothesis of volcanic-exhalative-related pyrite, rather than early disseminated hydrothermal alteration as interpreted in our study.

6. Conclusion

Our structural and petrographic investigation from the district to the microscopic scales at the Nyanzaga and Kilimani gold deposits suggest that:

- The Nyanzaga and Kilimani gold deposits share a similar deformation-hydrothermal history that challenges the prevailing notion of polyphase deformation in lode-gold deposits and proposes here a progressive and continuous history. The ductile D_{1a} and D_{1b} stages, characterized by F_{1a} and F_{1b} folds, transition into the brittle-(ductile) D_{1c} stage, marked by faulting and gold mineralization. The absence of separate hydrothermal stages during folding stages, coupled with continuous fluid emplacement,

supports this progressive model;

- The influence of fold interference patterns on the fault mode of formation was crucial in concentrating gold mineralization under continuous N-S compression and transpression. The heterogeneous spatial distribution of gold mineralization, mainly along the N-S normal faults, and to a lesser extent along the NW-SE faults, is intricately linked to the geometry of refold structures, whose vertical lithological contacts constituted weak planes favorable for fracturing and trapping. The refolding process responsible for the current orientation of the Nyanzaga Anticline led to the folding of the axial plane, producing segments with a N-S strike, suitable for reactivation and focusing N-S normal fracturing and faulting with favorable opening rates for high concentration of gold;
- Comparisons with other gold deposits in the Sukumaland greenstone belt, such as Geita and Bulyanhulu, highlight the novelty of our petro-structural model at the Nyanzaga and Kilimani deposits. The single-phase deformation-hydrothermal-mineralization model proposed in our study challenges previous polyphase interpretations in other gold deposits and contributes to the regional geological understanding of deposits.

Acknowledgement

The authors are grateful to the OreCorp's team for their welcome and scientific exchanges. Special thanks to Jim Brigden who has deeply contributed to the knowledge of the studied area through the years, and for the stimulative exchanges. We gratefully acknowledge T. Torvela and the anonymous reviewer for their constructive comments that helped to greatly improve the manuscript. This work is part of Célestine Berthier's PhD project which benefited of a CIFRE funding, reference CIFRE n°2021/0546, attributed by the French National Research and Technology Agency (ANRT).

~

Chapter VI
General conclusions

~

1. Main findings

This three-year PhD project attempted to reconstruct the journey of gold within the northern Sukumaland granite-greenstone belt (SGGB), tracing its path, from initial crustal fertilization from magmatic processes, controlled by geodynamic and tectonic settings during crustal growth, to its economic concentration from magmatic-hydrothermal processes in the upper crust at the Nyanzaga and Kilimani deposits. This project relied on a multi-scale (spatial and temporal) and multidisciplinary approach, combining fieldwork, petrographic, structural, geochemical, geochronological, and isotopic studies at the crustal/district, local/deposit, macroscopic/mineralized, and microscopic/ore mineral scales. Such approach and main results are summarized in a schematic representation of the evolution of the northern SGGB, with the attempt of merging both temporal and spatial scales (Fig. 6-1). In this first section, I briefly summarize the main results uncovered in each chapter, with specified spatial and temporal scales of study:

- Chapter II: Crustal growth and differentiation of the SGGB was unraveled based on crustal -scale fieldwork, petrographic, whole-rock geochemical, U-Pb geochronological, and O-Hf isotopic data on magmatic and sedimentary samples collected across the SGGB, combined with the compilation of the existing literature. Evolving tectonic settings shaped the crustal growth during 200 Ma, with a progressive evolution from mafic magmatism derived from a primitive mantle in a mantle-plume setting (2820-2800 Ma), to pure crustal reworking of mafic rocks in dripduction and later subduction settings, resulting in TTG-sanukitoid plutonism (2780-2660 Ma), to crustal anatexis resulting from the collision with an exotic terrane and leading to the intrusion of potassic granitoids (2660-2620 Ma).
- Chapter III: Magmato-tectonic evolution of the northern SGGB was investigated through fieldwork, petrographic and structural study at the crustal/district scale. A three-stage progressive and continuous deformation history was unraveled. 80 Ma of NNW-SSE shortening, between 2700 and 2620 Ma, accommodated first by ductile transpressional regime, then by orogen-parallel strike-slip flow in ductile-brittle to brittle conditions. The tectonic style shares many similarities with hot orogen setting. Whole-rock geochemical analyses on intrusive and supracrustal rocks of the northeastern SGGB show that crustal gold fertilization most likely resulted from magmatic processes prior to 2645 Ma. Gold concentration stage is dated after 2645 Ma and was temporally disconnected from fertilization.
- Chapter IV: Petrographic, textural studies and pyrite multiple sulfur isotope analyses were carried out at the Nyanzaga gold deposit, from local to ore mineral scales, unraveling the source of sulfur, ore fluids and gold, as well as the physical-chemical conditions of the fluid that led to sulfide deposition. This approach enabled to examine the timing and potential mechanisms of gold extraction from its reservoir and its subsequent precipitation at the Nyanzaga deposit. Sulfur, fluid and gold were sourced from a magmatic or mantle-derived reservoir(s). Sulfur and gold were extracted from the mantle between 2820 and 2800 Ma. Fluid mixing during the mineralizing stage was likely involved in the precipitation of gold.
- Chapter V: The petro-structural evolution of the Nyanzaga and Kilimani gold deposits was investigated through fieldwork, petrographic and structural study at the deposit to ore mineral scales. A three-stage progressive deformation history was unraveled, under continuous N-S compression and transpression. Protracted two-folding deformation of the SGGB meta-volcanosediments influenced the formation of strike-slip faults and focused gold mineralization in N-S normal fracturing and faulting with favorable opening rates for high concentration of gold.

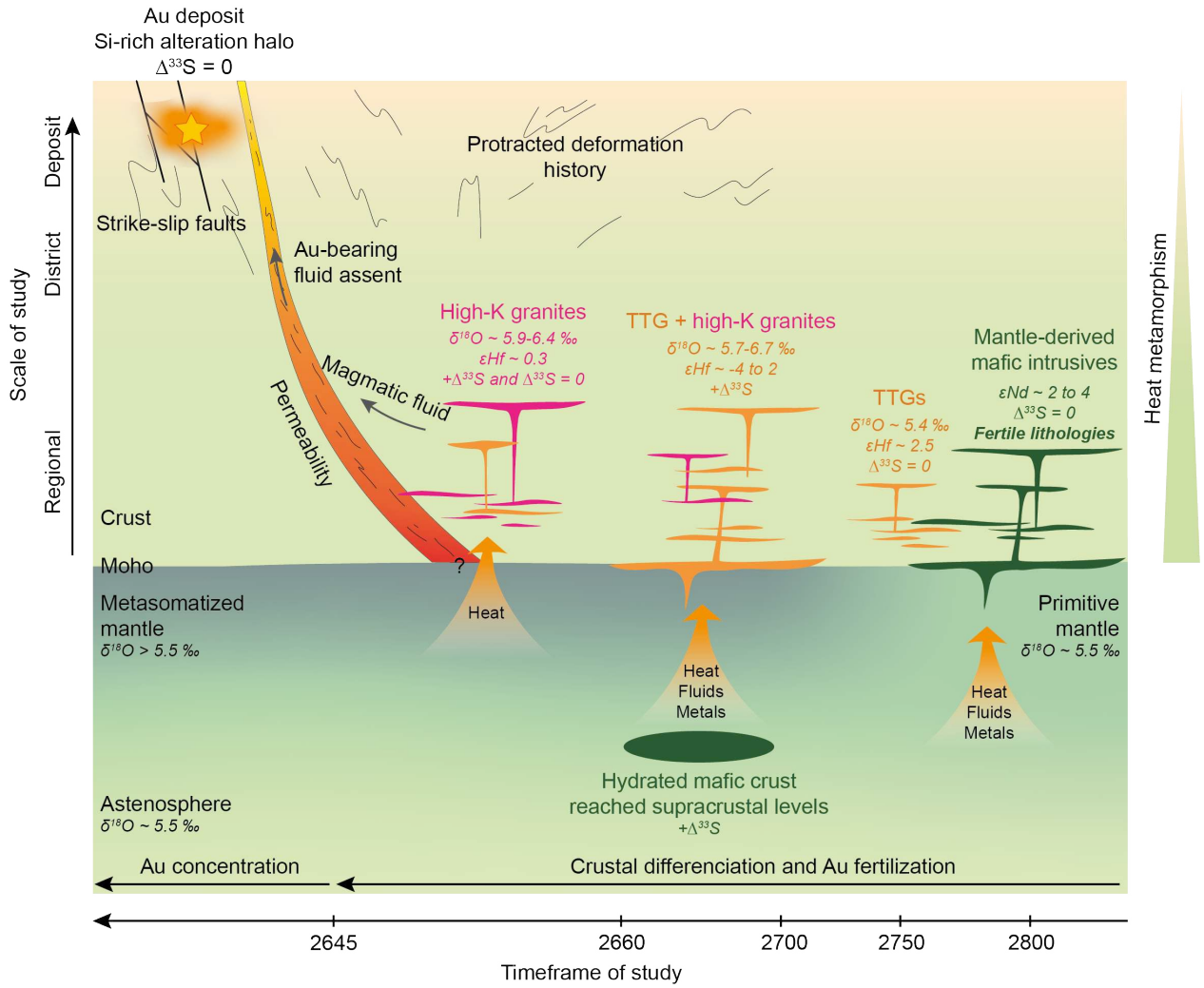

Figure 6-1. Schematic illustration summarizing magmatic, tectonic, hydrothermal, metamorphic and metallogenic processes evolution in space and time that controlled the formation of gold deposits in the northern Sukumaland granite-greenstone belt, unraveled in this PhD study. Ranges of measured and expected Hf-O-S isotopic signatures are indicated.

2. Unraveling the gold mineral system: the journey of gold through the northern Sukumaland granite-greenstone belt

The journey of gold in the northern SGGB, from initial fertilization of the crust to economic concentration at the Nyanzaga and Kilimani gold deposits, results from nearly 200 million years of magmatic activity, deformation, metamorphism and hydrothermal circulation. In the following, the key factors analyzed throughout this study are integrated into a cohesive model of crustal growth, gold enrichment and economic concentration in the northern SGGB, following the mineral system approach as defined by McCuaig and Hronsky (2014) (Fig. 6-2).

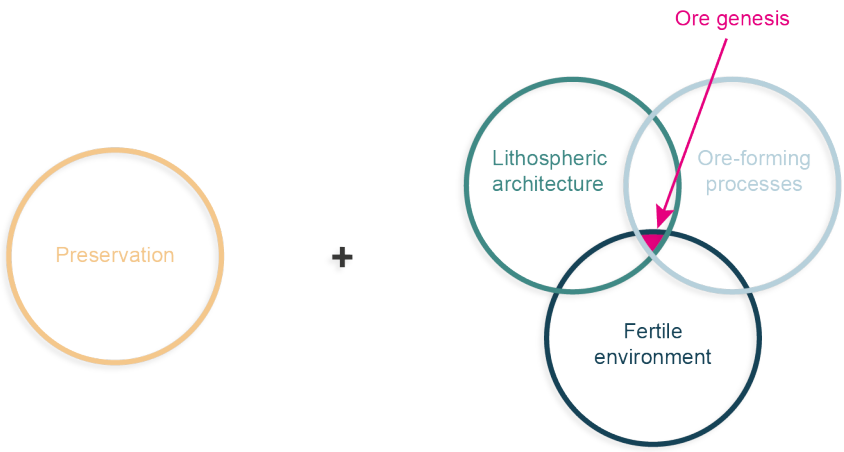

Figure 6-2. Key factors of the gold mineral system controlling ore genesis in the northern SGGB, adapted from McCuaig and Hronsky (2014), Eglinger et al. (2023) and André-Mayer et al. (2024). The juncture of favorable fertile environment, architecture and ore-forming processes are critical in ore genesis. The post-mineralization preservation of the deposit is the fifth parameter of the mineral system.

2.1. Fertile environment

Favorable geodynamic environment resulted in the gold fertilization of the SGGB crust. This first stage of the mineral system is dominated by magmatic processes (Chapter II). Characterizing the geodynamic style of crustal growth will be detailed in part 3 of the discussion.

Our findings reveal that gold was extracted from the mantle during the earliest record of crustal growth in the SGGB. This episode consisted of mantle-derived mafic-ultramafic magmatism in a mantle-plume oceanic plateau setting, between 2820 and 2800 Ma. The resulting juvenile mafic crust is characterized by elevated εNd (~ 2 to 4) values and a Th-Nb geochemical proxy indicative of primitive mantle sources (Fig. 6-1; Chapter II; Manya, 2004; Manya and Maboko, 2003, 2008b; Cloutier et al., 2005; Boniface and Mruma, 2012; Cook et al., 2016; Kwelwa et al., 2018). No evidence of mass-independent fractionation of sulfur (MIF-S; $\Delta^{33}S = 0$) is expected during this stage.

Subduction-like processes ultimately led to collision between the SGGB and an exotic terrane, that led to crustal anatexis between 2660 and 2620 Ma (Chapter II). The resulting partial melting, reworking and/or metamorphism of the gold-enriched mafic lithologies likely triggered gold release from its source rock (Fig. 6-1; Chapter III). The timing of gold mineralization at the Nyanzaga and Kilimani deposits, after ca. 2645 Ma (Chapter III), suggests that gold release processes likely happened around a similar timing. Gold fertilization and gold release and concentration processes are therefore temporally disconnected of more than 150 Ma (Fig. 6-1).

2.2. Lithospheric architecture

A favorable tectonic setting enabled hydrothermal ore-bearing fluid to ascent from the source rock to the upper crust and gold deposition site during the late D_{1b} and/or D_{1c} deformation stages, *i.e.*, around 2645 Ma (Figs 6-1, 6-2). Favorable permeable pathways were crucial for fluid circulation. During this period, deformation is controlled by strike-slip crustal flow (Chapter III) that enables fluid vertical ascent along the intermediate principal strain (Y). Crustal-scale structures developed at the boundary between greenstones

and granitoids and could be favorable draining systems, yet they were active between 2700 and 2660 Ma. Instead, subvertical shear zones and strike-slip faults of unknown depth dominated deformation during the cratonization period, between 2660 and 2645 Ma and could have channeled the ore-bearing fluids to the deposition sites.

2.3. Ore-forming processes

The ore-bearing fluid circulated in the upper crustal levels and met favorable physical-chemical conditions for gold precipitation in economic concentration (Figs. 6-1, 6-2). While this PhD project did not focus on a thorough study of ore-forming processes of the SGGB gold deposits, some insights into the physical-chemical conditions responsible for gold precipitation at the Nyanzaga and Kilimani deposits were retrieved from the deposit- to microscopic-scale petro-structural studies (Chapters III and V) and the multiple S isotope studies on mineralized pyrite (Chapter IV).

The gold deposits of the northern SGGB formed during the brittle D_{1c} deformation stage, after 2645 Ma (Chapters III and V; Sanislav et al., 2015, 2016). While some minor gold is hosted in layer-parallel lodes, the majority of the mineralization at the Nyanzaga and Kilimani deposits is located in a D_{1c}-related subvertical faults network (Chapter V). The protracted, progressive deformation history of the Nyanzaga and Kilimani gold deposits significantly influenced the development of such network that served as ore-bearing fluids conduits and subsequent traps for gold mineralization. The heterogeneous spatial distribution of gold mineralization, mainly along the N-S normal faults, and to a lesser extent along the NW-SE faults, is intricately linked to the geometry of refold structures, whose vertical lithological contacts constituted weak planes favorable for fracturing and trapping. The refolding process responsible for the current orientation of the Nyanzaga Anticline led to the folding of the axial plane, producing segments with a N-S strike, suitable for reactivation and focusing N-S normal fracturing and faulting with favorable opening rates for high concentration of gold.

The paragenetic sequence, and the textural characteristics and $\delta^{34}S$ signatures of gold-bearing pyrite suggests that at least two ore fluids circulated at the Nyanzaga deposit (Chapter IV). Their mixing may have contributed to the precipitation of gold.

2.4. Ore preservation

Post-mineralization preservation of the ore deposit is the last crucial factor of the mineral system. The Nyanzaga and Kilimani gold mineralization formed more than 2600 Ma ago at upper crustal levels (300–400°C during the gold-concentrating D_{1c} brittle stage) and has been remarkably well-preserved from erosion. This can be attributed primarily to minimal post-ore uplift and erosion, likely linked to the mechanically weakened hot lithosphere that controlled crustal growth and thickening in the SGGB, resulting in negligible topography (Chapter III).

Additionally, prolonged fluid circulation and hydrothermal mineral deposition extensively silicified the host rocks, preserving the deposits from erosion and contributing to the formation of prominent buttes in the landscape. Moreover, the Kilimani gold deposit is capped with BIF, lithologies resistant to erosion.

3. Contributing to the plate tectonic onset conundrum: the case study of the Lake Victoria Goldfields

The gold mineral system approach followed in the northern SGGB has implied deciphering the geodynamic settings that controlled crustal growth and differentiation. I have summarized in the previous section how such approach enabled to reconstruct the gold journey through the crust, in this section I will focus on its contributions on the understanding of the geodynamic context in the northern SGGB.

This study focused on the northern Sukumaland granite-greenstone belt (SGGB), but areas lacking economic interest, without significant gold deposits, are underexplored. This results in uneven petrographic, structural, geochemical, geochronological, and isotopic coverage at various scales. Our ability to trace the evolution of tectonic processes is therefore limited at the superterrane scale, late alone the Tanzania craton scale. Even within the SGGB, the southern portion remains poorly understood. In this section, I propose to first summarize the key tectonic processes for crustal growth in the northern SGGB, based on various proxies compiled during this PhD project. I will then evaluate the current understanding of tectonism in the Lake Victoria Goldfields (LVG) and the Central Tanzania Region (CTR) superterranes. Finally, I will reposition these episodes of crustal growth-differentiation, sedimentation, deformation, and metamorphism within a compiled global dataset and compare our findings with global onset of plate tectonics and supercontinent debates.

3.1. Tectonic setting of the northern SGGB: insights from multiple proxies

Key elements constraining crustal growth and reworking in the northern SGGB, when considered collectively, strongly support a model of subduction-driven tectonics (*e.g.*, Hastie et al., 2016; Cawood et al., 2018; Brown et al., 2020):

- Partial melting of hydrated, supracrustal mafic rocks that interacted with metasomatized mantle (2700-2660 Ma, D_{1a} deformation stage): hydrated minerals and sanukitoid-like geochemical signature in syn-tectonic TTGs, high Sr/Y and Gd/Yb ratios, low K_2O/Na_2O ratio in TTGs, εHf trend falling along a crustal evolution line, $\delta^{18}O$ signature of rocks that reached supracrustal levels prior to melting.
- Horizontal shortening and transpressional belt architecture (2700-2620 Ma, D_{1a} to D_{1c} deformation stages): folding of the supracrustal rocks, steep and constant tectonic fabric across the greenstone belt and granitoids, constant and moderately dipping lineation showing transpression along crustal-scale shear zones during pure shearing.
- Collisional setting (2680-2660 Ma, D_{1a} deformation stage): synchronous melting of hydrated mafic rocks at high depth and beginning of reworking of the lower crust, ongoing shortening stage and crustal-scale structures, granulite facies metamorphism, large range of detrital zircon ages.
- Amalgamation with an exotic terrane (< 2690 Ma, D_{1a} deformation stage): geochronological detrital record of a large dataset of exotic ages, reworking of older and more evolved crustal material than previously found.
- Anatexis and crust stabilization (2660-2620 Ma, D_{1b} to D_{1c} deformation stages): voluminous high-K granites, partial melting of the crust at low pressure.

It is worth mentioning that multi-sulfur isotopic analysis did not provide evidence for subduction, instead indicating sourcing from a purely mantle-derived reservoir (no MIF-S, $\Delta^{33}S = 0$). If sulfur was sourced from magmatic rocks formed in a subduction setting, MIF-S signature preserved in the subducted slab would have influenced the multiple sulfur analyses in pyrite (Cabral et al., 2013; Farquhar et al., 2013; Delavault et

al., 2016; LaFlamme et al., 2018c; Smit et al., 2019). However, the absence of evidence does not equate to evidence of absence. Collectively, fieldwork, petrographic, structural, geochemical, geochronological, and isotopic studies of the northern SGGB converge on a tectonic history characterized by subduction-driven processes around 2700 Ma. This period was marked by crustal shortening, ultimately leading to collision and the amalgamation of the SGGB with an exotic terrane. Nevertheless, the current findings and available dataset do not yet allow for insights into the location of the subduction zone, the exact timing of the collision, or the nature of the exotic terrane involved.

3.2. Zooming out at the Lake Victoria Goldfields to the Tanzania craton scales

The SGGB is the best-constrained terrane of the Tanzania craton. The Musoma-Mara Greenstone Belt (MMGB) has also been the focus of geochemical, geochronological, and isotopic studies, revealing a magmatic history closely resembling that of the SGGB (Chamberlain and Tosdal, 2007; Manya et al., 2007a, 2007b; Mtoro et al., 2009). Juvenile magmatism in the MMGB began between 2850 and 2800 Ma with the emplacement of mafic to felsic volcanic rocks and TTGs, followed by a phase of crustal reworking and the emplacement of additional mafic to felsic volcanic rocks and TTGs between 2750 and 2650 Ma. The final magmatic episode consisted of high-K granites, culminating around 2600 Ma. Some Sm-Nd isotopic analyses of high-Mg andesites suggest potential mixing with older crustal material, but no age constraints for the volcanic rocks are available (Manya et al., 2007b). Despite these insights, the deformation, metamorphic, and sedimentary histories of the MMGB remain poorly understood. Limited datasets from five studies on the geochemical and isotopic evolution of the Kilimafedha and Nzega greenstone belts highlight magmatic patterns similar to those of the SGGB (Manya and Maboko, 2018a; Messo et al., 2012; Manya, 2016a, 2016b; Manya et al., 2017). Nonetheless, the overall understanding of the LVG remains insufficient to propose a unified tectonic history for the superterrane.

The CTR has recorded a similar timing of late Mesoarchean to Neoarchean crustal growth as the LVG (Manya, 2011; Kabete et al., 2012b; Thomas et al., 2016). The magmatic rock record in the CTR spans from 2900 to 2610 Ma, encompassing mafic to felsic volcanism and the progression from TTGs to high-K granites and syenites. However, a significant distinction between the two superterranes is the presence of an older basement in the CTR, as evidenced by Hf isotopic signatures in intrusives and Hf-U-Pb isotopy in sediments (Figs. 0-5 and 0-6; Chapter I). The basement could be Eo- to Mesoarchean (Chapter I).

At the scale of the craton, high-K, low-Ca magmatism is recorded and result from intraplate partial melting. This magmatic episode is particularly widespread in the LVG. This stage could be interpreted as the cratonization of the Tanzania craton (Rowe et al., 2022).

3.3. Worldwide record of crustal evolution in the Archean and onset of plate tectonics

Discussions about the global onset of plate tectonics increasingly rely on comparing the timing of proxies indicative of subduction-like processes worldwide (*e.g.*, Cawood et al., 2018, 2022; Brown et al., 2020; Hawkesworth et al., 2024). A great way to provide clear evidence of plate tectonics is by identifying synchronous, large horizonal displacements between continental blocks contemporaneous with the creation and destruction of oceanic lithosphere and the amalgamation of these crustal fragments (*e.g.*, Mitchell et al., 2014; Cawood et al., 2018, 2022; Brown et al., 2020). To do so, researchers have compiled and investigated

magmatic, sedimentary, metamorphic and metallogenic local datasets of Archean cratons worldwide to propose a global prediction regarding the onset of plate tectonics (Cawood et al., 2022; Hawkesworth et al., 2024). I propose in this section to add our acquired and compiled dataset from the Tanzania craton, though mostly focused on the best-constrained terrane of the craton, the SGGB (Fig. 6-3).

Crustal growth and thickening in the Tanzania Craton share striking similarities with other Archean cratons, in particular the south-east Superior and Eastern Yilgarn superterranes (Fig. 6-3; Czarnota et al., 2010 and Mole et al., 2021 for reviews and construction of geodynamic models, and see references therein). Both regions show rifting of a continental crust in the late Mesoarchean to the early Neoarchean, around 2800 and 2750 Ma in the south-east Superior, and between ca. 2810 and 2760 Ma in the Eastern Yilgarn. This episode result in the formation of mantle-derived mafic-ultramafic volcanism-(plutonism) at the center of the rift, with the thickening of a juvenile crust similar to the crust formed in the LVG. At the borders of the rift, the older basement is affected by magmatism showing a more evolved geochemical-isotopic signature recording the mixing between the mantle-plume and the basement, similar to the RTC. In the south-east Superior craton, dripping processes is inferred as the tectonic setting driving crustal recycling, still under the influence of the mantle plume. In the LVG, we also propose dripping tectonics between 2780 and 2700 Ma, but with no mantle plume (Chapter II). Subduction initiation is dated around 2704-2695 Ma and around 2715-2690 Ma in the south-east Superior and Eastern Yilgarn craton, respectively. Subduction maturation follows, dated between 2695-2685 Ma and 2690-2663 Ma in the south-east Superior and Eastern Yilgarn craton, respectively. The geochemical and Hf-Nd isotopic signatures of intrusives once again show striking similarities with the LVG, with increasing O, decreasing Hf, and high Sr/Y, low K_2O/Na_2O TTGs and sanukitoids. Finally, continental collision, crustal thickening and cratonization terminate the magmato-tectonic history of the two cratons, with progressive decrease of the magmatic record between ca. 2660 and 2620 in the Eastern Yilgarn.

Furthermore, similarities between the three cratons can be further extrapolated to (i) deformation, evolving from extension prior to ca. 2700 Ma, to contraction and transpression around 2695 in the south-east Superior and intermittent between 2715-2670 Ma in the Eastern Yilgarn, and later strike-slip after 2665-2660 Ma in the south-east Superior and 2650 Ma in the Eastern Yilgarn, accompanied by progressive decrease of the temperature of deformation, (ii) granulite-facies metamorphism, dated around 2700-2680 Ma, (iii) the geometry of structures, with widespread crustal-scale subvertical shear zones accommodating shortening through lateral flow, (iv) the history of sedimentation, with marine sedimentation, to syn-tectonic and later post-tectonic clastic sedimentary basins, and finally (v) the late-orogenic gold mineralization after 2660 Ma in the south-east Superior and after 2645 Ma in the Eastern Yilgarn (*e.g.*, Czarnota et al., 2010; Bleeker, 2015; Mole et al., 2021; Sumail et al., 2024; Hawkesworth et al., 2024; and references therein).

At the worldwide scale, the period between 2700 and 2600 Ma coincides with a peak of magmatism and horizontal shortening tectonics in several cratons, accompanied with syn-tectonic sedimentation and granulite facies metamorphism (Fig. 6-3; *e.g.*, Cawood et al., 2022; Hawkesworth et al., 2024 and references therein). It also coincides with a metallogenic pattern highlighting a convergent margin metallogenic cycle (Frimmel, 2018; Huston et al., 2023), with a succession of (i) volcanic-hosted massive sulfide (VHMS) and calc-alkalic porphyry copper, (ii) orogenic gold and (iii) alkalic porphyry copper, granite-related rare metal and pegmatite (Huston et al., 2023 and references therein). All of these factors are interpreted as evidence of the onset of plate tectonics in the late Mesoarchean to Neoarchean, but also the potential amalgamation of the cratons into supercontinent(s) (Soderlund et al., 2010; Whymark and Frimmel, 2018; Cawood et al., 2022; Huston et al., 2023).

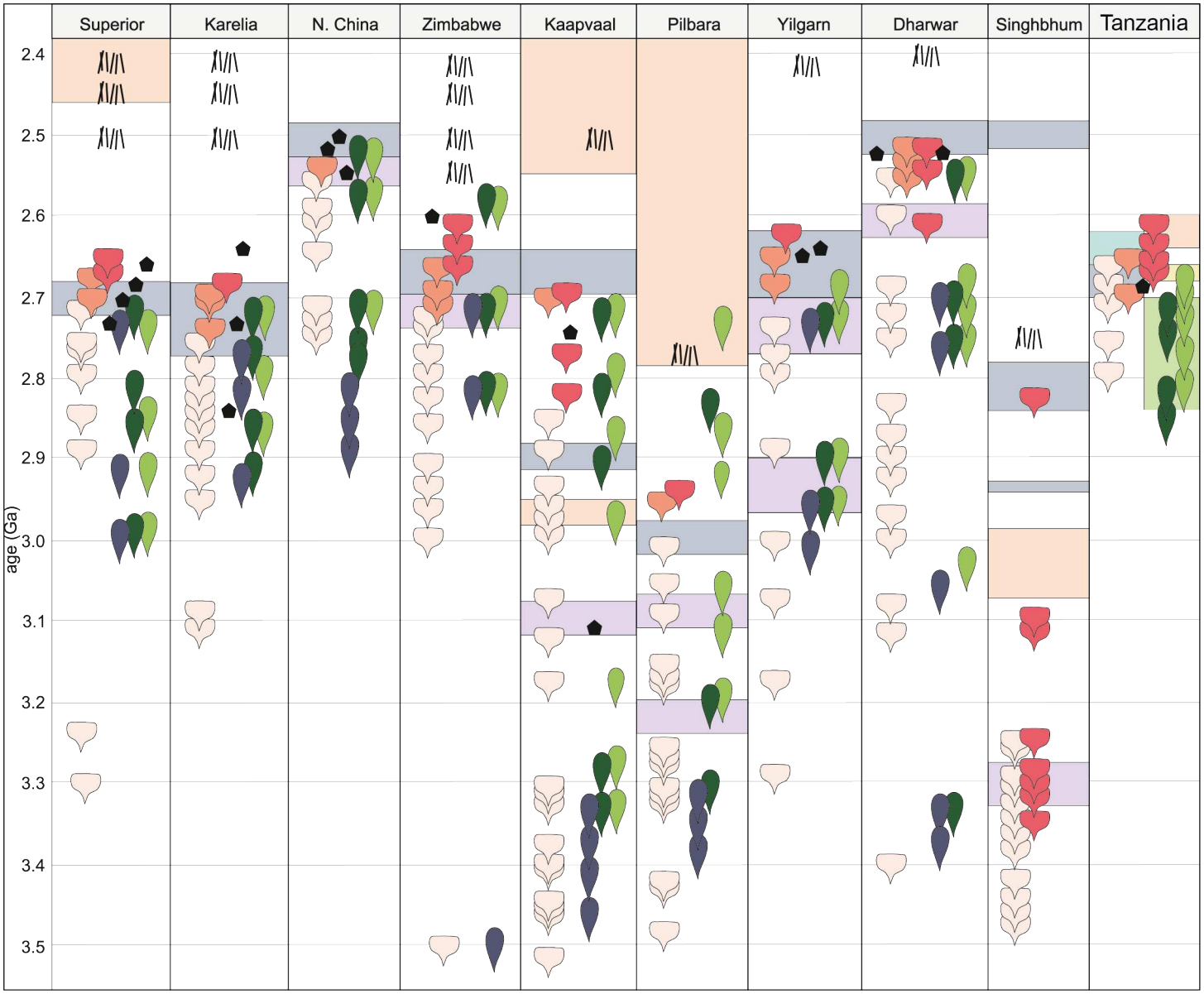

Figure 6-3. Time-space plot for the Superior, Karelian, Dharwar, North China, Pilbara, Yilgarn, Zimbabwe, Kaapvaal and Tanzania cratons for the period 3.5 – 2.4 Ga, showing the time of major felsic and mafic/ ultramafic igneous activity, deformational events that are late stage in the orogenic cycle of the craton, granulite facies metamorphism, mafic dyke emplacement and major late sedimentary basin deposition, after Cawood et al. (2022) and Hawkesworth et al. (2024). Distribution of felsic magmatism adapted from Laurent et al. (2014) and for mafic magmatism from Gao et al. (2022).

4. Translating the northern SGGB gold mineral system into an exploration targeting tool

The LVG is considered mature from an exploration perspective (Henckel et al., 2016). Most large mines and prospects were identified either during the colonial era in the early 20th century or through geophysics, remote sensing, radiometric and soil geochemical surveys initiated in the late 1980s (Henckel et al., 2016). For instance, the Nyanzaga prospect was first described in 1937, and later explored in 1997, with Kilimani prospect discovered through soil anomalies. Golden Ridge, the most recently find major deposit in the Tanzanian LVG, also originated from soil and stream geochemical analyses that have been the most effective exploration tool in the region. The apparent maturity of the LVG may originate from a reliance on empirical methods like regional geochemical surveys, which have limited effectiveness in identifying deeper anomalies. New exploration targeting ideas and tools may arise from studying the gold mineral system and contribute to the LVG, and more generally to the Tanzania craton.

Translating the gold mineral system into an exploration targeting tool enables linking ore deposit formation to large-scale geological processes, increasing the probability of discovering new camps and prospects (McCuaig et al., 2010; McCuaig and Hronsky, 2014; Champion and Huston, 2016; Groves et al., 2020; Perret, 2021). However, such approach is not straightforward (McCuaig et al., 2010). The complexity indeed arises from the scale dependency of geological processes and the challenge of mapping them with available data at various scales (Champion and Cassidy, 2008; McCuaig et al., 2010; Groves et al., 2020). Critical elements like geodynamic triggers and fluid pathways often have subtle or indirect expressions, making their identification reliant on proxies and integrated datasets (Masurel et al., 2021; Mole et al., 2021, 2022; Sumail et al., 2024). A great tool for province-scale exploration is prospective mapping, using Sm-Nd, Lu-Hf, O isotopes or zircon trace elements to highlight the spatial and genetic relationship between ore prospects and geodynamic features (Champion and Cassidy, 2008; Champion and Huston, 2016; Mole et al., 2021, 2022; Smithies et al., 2023). When combining the spatial relationship between several proxies, one may construct a predictive map that has proved effective (*e.g.*, Watine et al., 2023). Achieving such maps require systematic and long-term research, but result in a robust geodynamic-tectonic-metallogenic framework that ultimately significantly enhance the efficiency of mineral exploration (*e.g.*, Masurel et al., 2022; Mole et al., 2021, 2022). The understanding of the gold mineral system and the availability of extensive geochemical, geochronological and isotopic datasets in the Yilgarn or Superior cratons far surpass what is currently available for the LVG. Furthermore, relying on a limited number of deposits and deposit types, as may be the case in the LVG, can bias exploration efforts toward these known systems, potentially overlooking other critical factors that could highlight prospective areas. Still, we summarizes in Figure 6-4 key factors of the gold mineral system from this PhD project and from the available literature on gold deposits in the LVG (Smith, 2003; Cloutier et al., 2005; Vos et al., 2009; Sanislav et al., 2015, 2016; Manya, 2016a, 2016b, 2017; Van Ryt et al., 2017, 2019, 2020; Yuan et al., 2019). The result is a scale-dependent table summarizing the key targeting elements for gold deposits in the LVG (Fig. 6-4; based on McCuaig et al., 2010).

	Source	Pathway	Fluid throttle (physical)	Deposition (chemical)
Province	Juvenile magmatism Protracted magmatic and tectonic history Critical	Collisional tectonic setting (fold and thrust belt) Crustal-scale structures	Large-scale damage zones and structures	Greenstone belts
Camp	Juvenile mafic crust Reworking of the mafic crust Metamorphism greenschist to amphibolite Important	Protracted deformation history (folding and faulting) Favorable crustal flow and geometries for permeability	Protracted deformation history (folding and faulting) Favorable geometries for local dilational sites	Local magnetic weakening Si, Cb, Chl alteration Metal anomaly (As, Sb, Ag, Pb, Cu, Hg, W, Mo)
Prospect	Minor	Subvertical crustal-scale structures Favorable crustal flow	Favorable geometries Damage zones and vein stockworks Contractional and local dilational sites	Si, Cb, Chl alteration Metal anomaly (As, Sb, Ag, Au, Pb, Cu, Hg, W, Mo)

Figure 6-4. Table summarizing the key targeting elements for lode-gold deposits in the LVG, based on McCuaig et al. (2010). Colors represent the relative importance of each factor: red = critical, orange = important, green = less important.

~

SUPPLEMENTARY MATERIAL

~

List of supplementary materials

Chapter II:

Supplementary Material 2-1 – Methodology 188

Supplementary Material 2-2 – Comprehensive petrographic sample description and U-Pb-O-Hf results 196

Supplementary Material 2-3 – Whole-rock analyses 262

Supplementary Material 2-4 – U-Pb-O-Hf analyses 268

Supplementary Material 2-5 – Whole-rock analyses from the literature 322

Supplementary Material 2-6 – U-Pb-Nd-Hf analyses from the literature 352

Chapter IV:

Supplementary Material 4-1 – Multiple-sulfur isotope analyses 370

Chapter V:

Supplementary Material 4-1 – Matlab 3D-modeling of fold interference patterns 376

Supplementary Material 2-1 – Methodology

This Supplementary Material details the data collection, sample preparation, analysis techniques and data processing from this study. A multi-disciplinary approach was followed, combining field work (38 outcrops visited along the ca. 50 km-long transect), macro- and micro-scale petrography (33 hand samples and 22 thin sections), whole-rock (WR) geochemistry (21 samples), in-situ zircon Lu-Hf isotope analyses and U-Pb geochronology on 7 magmatic and 3 sedimentary samples. Additionally, in-situ zircon O isotopes were analyzed in the same 7 magmatic samples.

1. Field work and sampling

A 50 km-long transect across the northeastern Sukumaland granite-greenstone belt (SGGB, Lake Victoria Goldfield, Tanzania Craton) and surrounding granitoids was conducted in the area of the Nyanzaga gold deposit in October-November 2022. The aim was to sample magmatic and sedimentary rocks representative of the different episodes of crustal growth in the SGGB. Relatively good outcropping of the bedrock enabled sampling of poorly weathered rocks, with all generations of intrusives (pre-, syn-, late- and post-tectonic; see Chapter III for detailed description), felsic meta-volcanic rocks and clastic meta-sediments from the Lower and Upper Nyanzian Supergroup, as well as unmetamorphosed sediments from the Kavirondian Supergroup. Due to limited outcropping and the presence of artisanal mining sites, only one outcrop of the mafic-ultramafic unit of the Lower Nyanzian was visited and sampled (SU19; Table 2-1).

2. Petrography

Petrographic investigations were conducted on 22 polished thin sections using optical microscope with transmitted and reflected light (GeoRessources laboratory, Université de Lorraine and School of Earth Sciences, The University of Western Australia). Further observations were undertaken using a scanning electron microscope (SEM) in backscattered electron (BSE) and energy-dispersive (EDS) modes (GeoRessources laboratory, Université de Lorraine).

3. Whole-rock geochemistry

The twenty-one whole-rock samples were crushed and pulverized at the CRPG and GeoRessources laboratory (Université de Lorraine). Any vein and/or weathered material were removed using a diamond saw. Each crushed sample was quartered to obtain a representative 100-gram sample, followed by pulverization, down to minus 75 µm. Samples were analyzed by ALS geochemistry (Sevilla, Spain), by the following methods: major and minor oxides (Al_2O_3, BaO, CaO, Cr_2O_3, Fe_2O_3, K_2O, MgO, MnO, Na_2O, P_2O_5, SO_3, SiO_2, SrO, TiO_2, TiO_2) by inductively coupled plasma optical emission spectrometry (ICP-AES) using four-acid digestion, and loss on ignition (LOI) at T > 500 °C, trace elements (Ba, Ce, Cr, Cs, Dy, Er, Eu, Ga, Gd, Hf, Ho, La, Lu, Nb, Nd, Pr, Rb, Sm, Sn, Sr, Ta, Tb, Th, Tm, U, V, W, Y, Yb, Zr) by Li borate fusion and inductively coupled plasma mass spectrometry (ICP-MS), and gold by fire assay and ICP-AES (detection limit at 0.5 ppb).

4. Geochronology-isotopy on zircon: sample preparation and imaging

3 to 5 kg of unweathered and poorly altered rocks were broken down to small pieces by a diamond saw (GeoRessources), then crushed using a steel jaw crusher and a roller mill (GeoRessources and CRPG). Density separation was undertaken on the – 1 mm/+ 250 µm powder fraction, using a shaking table (CRPG). The non-magnetic fraction was then separated using a Franz (CRPG), followed by density separation using diiodomethane solution (GeoRessources). Representative zircon grains were hand-picked under a binocular microscope. When possible, at least 80 zircon grains per magmatic sample, and at least 200 grains per detrital sample were selected, ensuring a variety in size and morphology (see also Supplementary Material 2-2).

The rest of the sample preparation was conducted at the UWA, and follows the same protocol as Schreefel et al. (2024) detailed in their Supplementary Data A:

"To reduce any edge effect, zircon grains were centrally mounted in the inner 12 mm area of a 25 mm epoxy-resin mount (n = 4; Struers EpoFix) along with zircon reference materials (91500, OGC, FC-1, and QGNG; see references below). UWA sample material is used for the Owens Gully Diorite reference standard, and is here abbreviated as OGC (also named OG1). The epoxy- grain mounts were hand-polished (Struers Largo Grinding Discs with Struers DiaPro 9, 3, and 1 µm Diamond Suspensions) to expose zircon and to minimize the relief and scratches. Lastly, the mounts were cut to a thickness of 4 mm (Buehler IsoMet 1000 Precision Saw). Prior to coating or analysis, the mounts were carefully cleaned with detergent, distilled water and ethanol in an ultrasonic bath. If the mounts were already coated, the coat was removed using 1 µm diamond wax (Struers DP-Stick) and then cleaned.

The polished mounts were microscopically assessed to facilitate optimal spot placement (i.e. inclusion-, fracture-, and inheritance-free zones). The mounts were first imaged using an optical microscope (transmitted and reflected light) to examine the grains for fractures, inclusions and irregular surfaces. After carbon coating, the mounts were imaged with a SEM using the BSE and cathodoluminescence (CL) modes to identify internal growth patterns and other compositional irregularities (Curtin University, Perth). An accelerating voltage of 15 to 20 kV together with a working distance of 15 mm and a beam intensity of 1.5 nA was used to obtain the SEM images. Spots for the various analysis were chosen as closely as possible to each other and in the same zircon domain based on cathodoluminescence imagery.

In-situ zircon petrochronology analyses were performed in sequence, based on the spot diameter used for the analytical techniques: O isotopes (10 µm), U-Pb geochronology (15 µm), and lastly Lu-Hf isotopes (50 µm)."

An overview of zircon grains from individual samples including analytical spots is provided in Supplementary Material 2-2. Metamict zircon grains, showing no luminescence in cathodoluminescence (SEM) were avoided for isotope analyses.

5. Zircon O isotopy

The oxygen isotope ratios ($^{18}O/^{16}O$) and $^{16}O^{1}H/^{16}O$ in zircon were analyzed using secondary ion mass spectrometry (SIMS; CAMECA IMS 1280) at the CMCA, UWA. These measurements were conducted during two separate analytical sessions on zircon mounts TAN1 and TAN2, on the 7 magmatic samples. Before the analyses, the mounts underwent thorough cleaning (see section 4) and were coated with a 20 nm layer of

high-purity gold in a vacuum environment. To minimize degassing during analysis, the samples were stored in a vacuum oven for a minimum of two days and placed in the instrument's storage chamber 24 hours prior to the session.

The instrument analytical parameters and protocol was the same as in Schreefel et al. (2024) Supplementary Material A:

"A static ~2.8 nA Gaussian Cs+ beam with a total impact energy of 20 kV was focused to a 10 x 10 µm spot area on the sample surface. A normal incidence electron gun was used for charge compensation at the sample surface during analysis. The analysis area was pre-sputtered for 40 seconds using a 15 x 15 µm raster to remove gold coating and any other contamination. This was followed by automatic secondary peak-centering in the 3000 µm field aperture. Other instrument parameters were as follows: ~45 µm entrance slit, and for energy filtering a 30-eV band pass for the energy slit with a 5-eV gap. Secondary O-ions (^{16}O and ^{18}O) were analyzed on the multi-collection axis with a nominal mass resolving power of ~2,400 using dual Faraday cup detectors with 1010 Ω (L'2) and 1011 Ω (H1) resistors for ^{16}O and ^{18}O, respectively. OH- ions were analyzed with a mass resolving power of ~6000 using an on-axis, low background Faraday cup with 1011 Ω (FC2) resistors (Pidgeon et al., 2013). To avoid interference from ^{17}O- on the OH-peak, the magnetic field was slightly offset to the high-mass side.

Analyses consisted of 20 four-second cycles, which gave an average external precision of 0.11 ‰ on zircon 91500 during all analytical sessions. The two analytical sessions were monitored for drift and precision using the primary reference standard zircon 91500 ($\delta^{18}O$ = 9.86 ± 0.22 (2SD); Wiedenbeck et al., 2004), which was measured every six sample analyses. Bracketing of standards permitted to monitor the stability of the analytical session (precision and drift) and to correct the instrumental mass fractionation (IMF). Uncertainty on each $\delta^{18}O$ spot has been calculated by propagating the errors on the IMF determination, which include the internal error on each sample data point and the standard deviation of the average O isotope ratio measured on the primary standard during the session. The IMF-correction procedure follows that of Kita et al. (2009)."

Analyses on zircon OGC (5.88 ± 0.06 ‰; Petersson et al., 2019) and FC1 (+5.61 ± 0.04‰, Ávila et al., 2020) standards every 6 sample analyses were used to verify the accuracy. OGC returned an average $\delta^{18}O$ of 5.68 ± 0.23 ‰ (n = 15; mount TAN1), 5.80 ± 0.15 ‰ (n = 22; mount TAN2). FC1 returned an average $\delta^{18}O$ of 5.55 ± 0.15 ‰ (n = 15; mount TAN1) and 5.69 ± 0.23 ‰ (n = 21; mount TAN2). They deviate by 3.4 % and 1 % from the reported values, respectively.

The stability of $^{16}O^{1}H/^{16}O$ analyses was monitored by measuring the $^{16}O^{1}H/^{16}O$ in the primary and secondary reference standards. No drift was measured.

$^{16}O^{1}H/^{16}O$ values for each spot are used to quantitively assess whether the zircon is altered (Pidgeon et al., 2017). Elevated $^{16}O^{1}H/^{16}O$ would generally correlates with increasingly high or low $\delta^{18}O$ values. $^{16}O^{1}H/^{16}O$ vs $\delta^{18}O$ diagrams for each sample are visible in Supplementary Material 2-2. The $^{16}O^{1}H/^{16}O$ cut off value is set at 0.0007, based on the upper limit from the zircon reference chips in both mounts (OGC and FC1). Any sample analyses above the threshold are not further considered. Similarly, individual analyses with significantly different $\delta^{18}O$ values compared to the main sample population were omitted from average calculations (n = 1). Finally, zircon grains that were later identified as having discordant U-Pb ages were also excluded from the dataset.

6. Zircon U-Pb geochronology

U-Pb isotope compositions in zircon were determined during two analytical sessions on the two mounts TAN1 and TAN2, on all 10 samples, by laser ablation sector field inductively coupled plasma mass spectrometry (LA-SF-ICPMS) at CMCA, UWA. Once again, the instrument analytical parameters and protocol was the same as in Schreefel et al. (2024) Supplementary Material A:

"The LA-SF-ICPMS system used in this study consisted of a Thermo Fisher Scientific Element XR SF- ICPMS coupled to a Teledyne CETAC (Photon Machines) Analyte G2 193 nm excimer argon-fluoride (ArF) laser ablation system. Laser ablation analyses were carried out using a fluence of 4 J/cm^2, a laser repetition rate of 7 Hz, and a laser spot diameter of 15 µm. Each analysis consisted of a 10 s gas blank, while the laser was firing on the shutter, followed by 40 seconds of ablation time for a total of 280 laser pulses. Every analysis also consisted of a 20 s washout period with He-gas before the next analysis began. This routine measured masses ^{204}Hg+Pb (10 ms), ^{206}Pb (20 ms), ^{207}Pb (20 ms), ^{208}Pb (10 ms), ^{232}Th (10 ms), and ^{238}U (10 ms).

Daily ThO^+/Th^+ was routinely less than 0.3% percent. All U-Th-Pb isotope analyses were calibrated to the (primary) reference zircon FC-1 (1099.0 ± 0.6 Ma; weighted mean ^{207}Pb/^{206}Pb age; Paces and Miller, 1993). Semi-quantitative Th and U concentrations were determined in Iolite based on analyses of 91500 (Wiedenbeck et al., 1995)."

Sample zircon grains were analyzed in groups of ~10 analyses. Between each standard block were analyzed several samples from FC1 (1099.0 ± 0.6 Ma; weighted mean ^{207}Pb/^{206}Pb age; Paces and Miller, 1993), 91500 (1065.4 ± 0.3 Ma; weighted mean ^{207}Pb/^{206}Pb age; Wiedenbeck et al., 1995) and OGC (3465.4 ± 0.6 Ma; weighted mean ^{207}Pb/^{206}Pb age; Stern et al., 2009) enabling for correction of mass bias, instrumental drift, and laser-induced elemental fractionation. U-Pb isotope analyses were then reduced using the "U-Pb Geochronology" data reduction scheme in Iolite 4 as outlined in Paton et al. (2010). Final ages and ratios reflect the Iolite U-Pb error propagation method described in Paton et al. (2010). Weighted mean and intercept ages as well as concordia diagrams were generated using IsoplotR Version 6.4.2 (Ludwig, 2003).

Measured weighted mean ^{207}Pb/^{206}Pb ages were 1074 ± 6 for 91500 (n = 42; MSWD = 0.78), 1098 ± 1.7 Ma for FC1 (n = 159; MSWD = 0.69) and 3468 ± 1.4 Ma for OGC (n = 99; MSWD = 1). They deviate by 0.8 %, 0.01 % and 0.09% from the reported ages, respectively.

Analyses were only considered valid if they displayed stable Pb/Pb and U/Pb ratios for at least ten seconds. Samples with excess ^{204}Pb beyond background levels were rejected, as no common-Pb correction was applied. U-Pb data for zircon in each sample typically included both concordant and discordant analyses, with discordant (or imprecise/unreliable) data excluded as they were considered geologically insignificant. Concordant clusters of U-Pb data near or on concordia were interpreted differently based on the sample type: for magmatic samples, these clusters represent the age of igneous crystallization and ages were calculated using weighted mean ^{207}Pb/^{206}Pb dates from these concordant clusters and are presented with 95% confidence intervals; for sedimentary samples, the youngest concordant cluster indicates the maximum depositional age, each individual ^{207}Pb/^{206}Pb dates are reported with two standard error (2SE) uncertainties. Data is presented in Supplementary Material 2-2. In the SU06 granodiorite, two concordant analyses yielded older ^{207}Pb/^{206}Pb dates than the primary population. These outliers were interpreted as inherited grains, reflecting zircon that predated the main crystallization event.

7. Zircon Lu-Hf isotopy

Zircon Lu-Hf isotope compositions were analyzed during two sessions using laser ablation multi-collector inductively coupled plasma mass spectrometry (LA-MC-ICPMS) on all 10 samples of the two mounts TAN1 and TAN2. The analytical setup comprised a Thermo Fisher Scientific Neptune Plus MC-ICPMS integrated with a Teledyne CETAC (Photon Machines) Analyte G2 193 nm excimer argon-fluoride (ArF) laser ablation system. All measurements were conducted at the CMCA, UWA. Once again, the instrument analytical parameters and protocol was the same as in Schreefel et al. (2024) Supplementary Material A:

"The MC-ICPMS was operated in low resolution and all masses were measured on 10^{11} Ω amplifiers, with the exception of ^{180}Hf which was measured using a 10^{10} Ω amplifier. The instrument set- up employed the Jet sample cone and X skimmer cone configuration, along with the addition of 10 to 12 mL/min N_2 for increased sensitivity. A total of 1 L/min of He-carrier gas was added through the laser cell and Helix sample cup. Laser ablation analyses were carried out using a fluence of 5 J/cm^2, a laser repetition rate of 4 Hz, and laser spot diameter of 50 µm. Each analysis consisted of a ~50 s gas blank and a 10 s laser "warm up" period, followed by 60 s of ablation time for a total of 240 laser pulses. Every analysis also consisted of a 50 s washout period with He-gas before the next analysis began. Daily HfO^+/Hf^+ was routinely less than 0.1%.

Data reduction was done in Iolite 3 using the methodology described in Fisher et al. (2014), with the exception that the synthetic MUNZirc zircon standard (Fisher et al., 2011) was used to calibrate the invariant isotope compositions utilized for the Yb-interference correction. This was done by adopting the $^{173}Yb/^{171}Yb$ ratio of Segal et al. (2003) and iteratively adjusting the $^{176}Yb/^{171}Yb$ ratio to achieve the correct $^{176}Hf/^{177}Hf$ ratio for MUNZirc 0-4 on a session-by-session basis, which yielded after correction an average $^{176}Hf/^{177}Hf$ ratio of 0.282135 ± 0.000027 (2SD; n = 189) and a 176Yb/177Hf ratio range between 0.000028 ± 0.000006 (2SD; MUNZirc 1) and 0.368800 ± 0.005900 (2SD; MUNZirc 4). The (primary) zircon reference standard Mud Tank Zircon (MTZ; n = 239) was used to normalize the mass bias and interference corrected 176Hf/177Hf ratios using an accepted value of 0.282507 ± 6 (2SD; Woodhead and Hergt, 2005); the magnitude of this correction is typically ~0.5 εHf units. Unknowns were analysed in groups of ~10 analyses, interspersed with a standard block including zircon MTZ, MUNZirc 0-4, FC1, 91500, and OGC."

The method's accuracy and reproducibility were verified by using secondary reference standards with Hf contents, including FC1 ($^{176}Hf/^{177}Hf$ = 0.282184 ± 16 (2SD); Woodhead and Hergt, 2005), 91500 ($^{176}Hf/^{177}Hf$ = 0.282308 ± 6 (2SD); Blichert-Toft, 2008), and repeated analyses of zircon OGC ($^{176}Hf/^{177}Hf_{(i)}$ = 0.280560 ± 21 (2SD); Kemp et al., 2017). The average $^{176}Hf/^{177}Hf$ ratio obtained for FC1 was 0.282185 ± 20 (n = 32), while for 91500 it was 0.282311 ± 21 (n = 18). For OGC, the initial $^{176}Hf/^{177}Hf$ ratio was 0.280636 ± 23 (n = 17).

Similarly to Schreefel et al. (2024), the decay constant of ^{176}Lu, taken from Söderlund et al. (2004) (1.867 x 10^{-11} a^{-1}) was used to calculate the initial $^{176}Hf/^{177}Hf$ ratios, as it best fits terrestrial rocks (Albarède et al., 2006; Amelin and Davis, 2005). Initial εHf values were calculated using the chondritic uniform reservoir (CHUR) parameters from Bouvier et al. (2008), with $^{176}Hf/^{177}Hf$ = 0.282785 and $^{176}Lu/^{177}Hf$ = 0.0336. Each analysis also involved calculating a two-stage depleted mantle model age (T_{DM}^2), assuming that zircon's parental magma originated from average continental crust ($^{176}Lu/^{177}Hf$ = 0.015) extracted from a depleted mantle (Griffin et al., 2002, 2000). The T_{DM}^2 age, which estimates the crustal source age of the igneous rocks, was derived for mantle depletion at 3.8 Ga (Vervoort et al., 2018; $^{176}Hf/^{177}Hf$ = 0.283238; $^{176}Lu/^{177}Hf$ = 0.03976).

Metamorphosed zircon grains have typically low Th/U ratio and any analyses with a ratio under 0.1 were removed (Yakymchuk et al., 2018). None of the analyses showed $^{176}Yb/^{177}Hf$ exceeding 0.2 or εHf 2SE greater

than 4 epsilon units. Few detrital analyses showed Pb loss in Lu/Hf vs Age diagram and were removed (n = 8). Lu-Hf data from individual analyses (samples and standards), as well as εHf and T_{DM}^{2} calculations are provided in Supplementary Material 2-4.

Supplementary Material 2-2

Comprehensive petrographic sample description and U-Pb-O-Hf results

This Supplementary Material provides a petrographic overview, zircon imagery and U-Pb-O-Hf results of all seven magmatic and three sedimentary samples from this study. The location of samples is given in Figure 2-3 (Chapter II).

SGGB = Sukumaland granite-greenstone belt

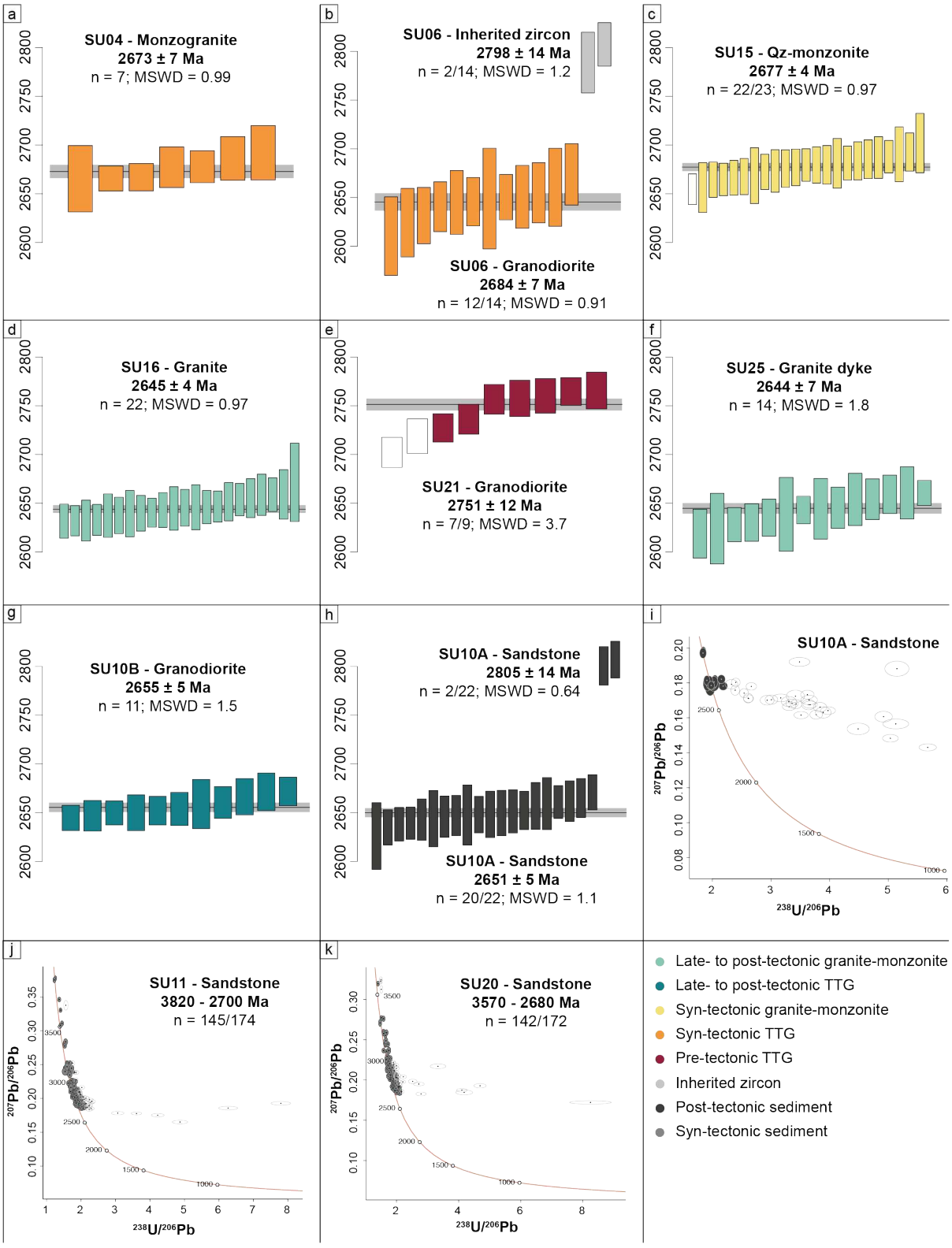

Figure SM2-2.1. Zircon U-Pb data from this study analyzed using LA-ICP-MS. Interpreted ages are reported with 95% confidence intervals, uncertainties of single analyses represent 2SE. Tera Wasserburg concordia diagrams are shown for sedimentary samples.

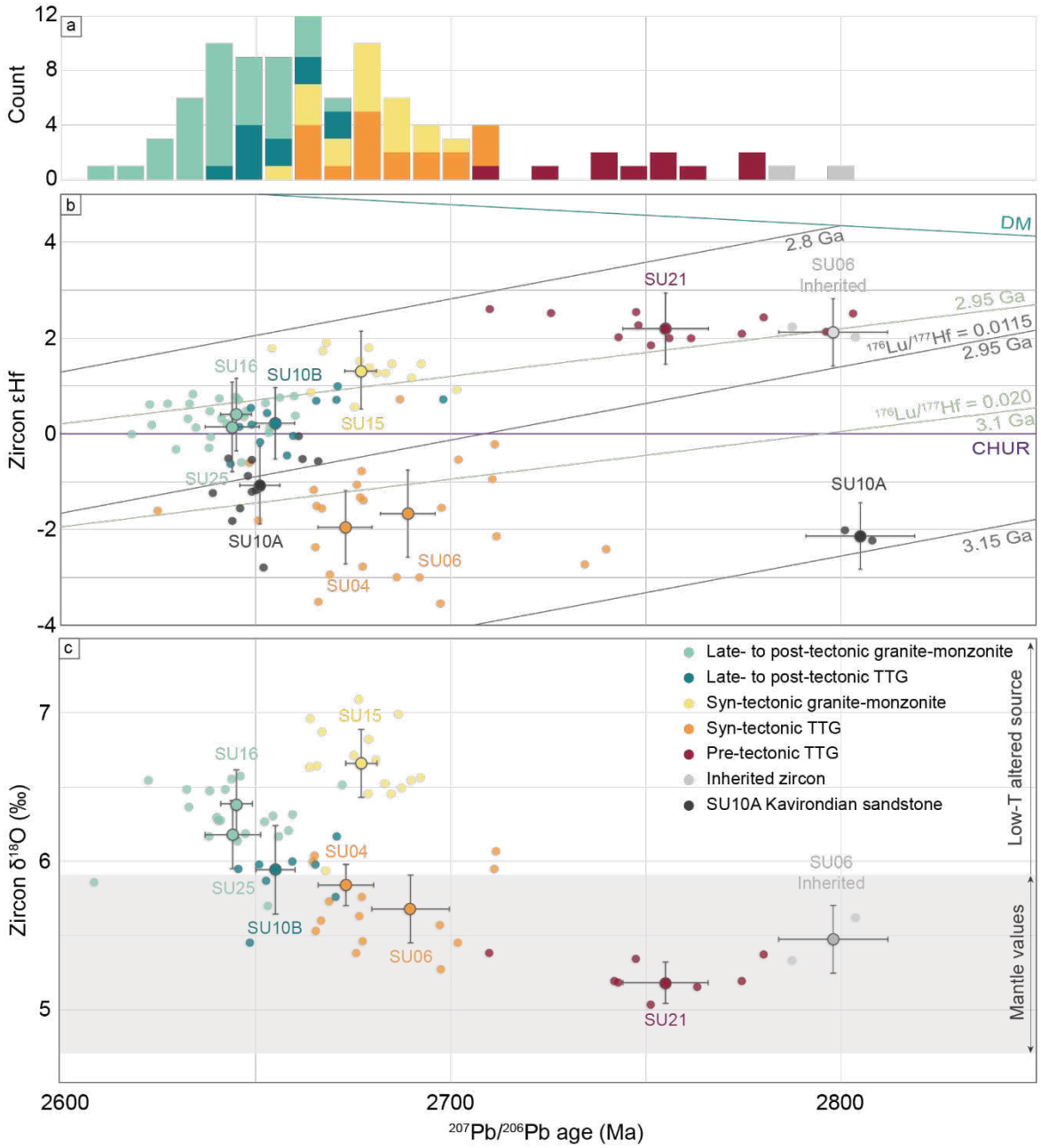

Figure SM2-2.2 a. Probability distribution plot, **b.** zircon εHf vs age diagram and **c.** zircon $\delta^{18}O$ vs age for magmatic samples of the north-eastern SGGB, Tanzania Craton, data from this study. Individual zircon ages are shown as well as average of magmatic samples. Error bars represent 95 % confidence interval (ages) and 2SE (εHf and $\delta^{18}O$).

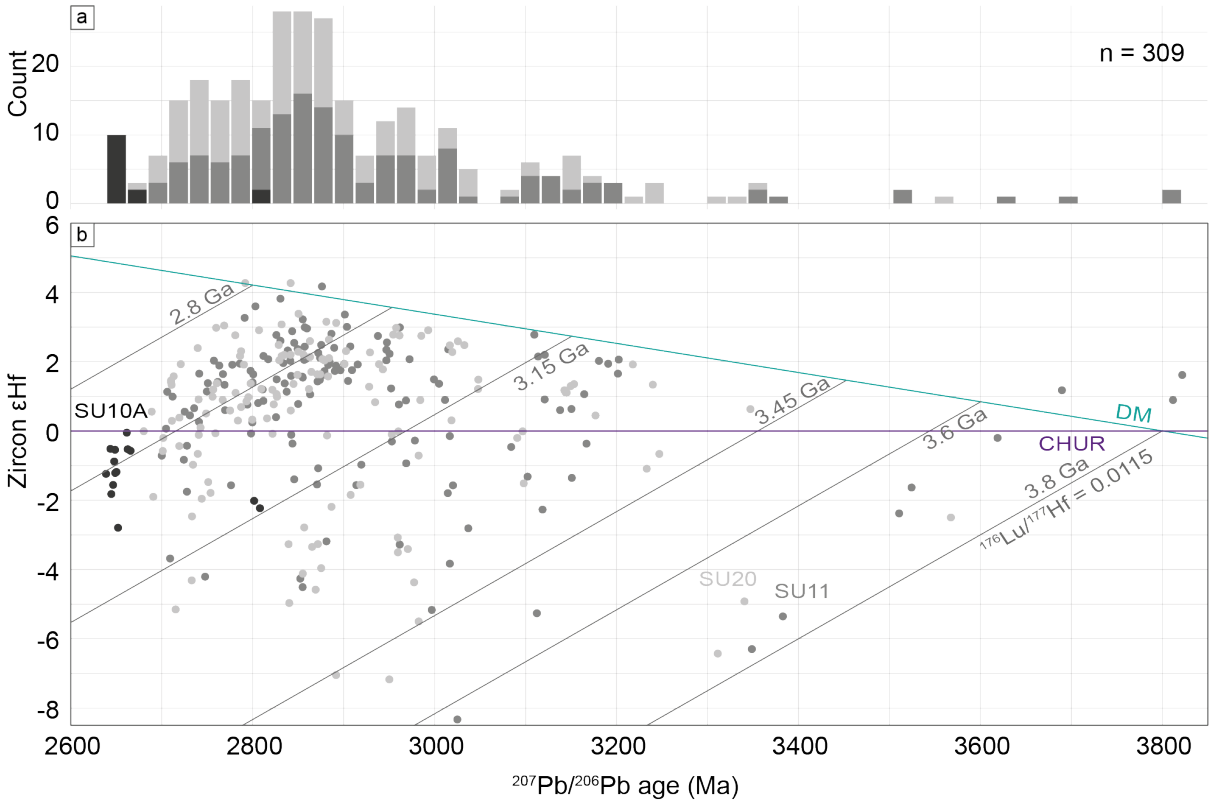

Figure SM2-2.3 a. Probability distribution plot, **b.** zircon εHf vs age diagram for detrital zircon grains of the north-eastern SGGB, Tanzania Craton, data from this study. Error bars represent 95 % confidence interval (ages) and 2SE (εHf).

SU04

Sample Localization regional context

(32.7797; -2.6916)

Sampled on a hill, 20 km north of the northern limit between the SGGB and granitoids. Syn-tectonic granodiorite with an E-W S_{1a} tectonic fabric, affected by D_{1b} strike-slip shear zones and D_{1c} strike-slip faults.



Figure SM2-2.3: SU04 outcrop and sample photographs.

Sample description

SU04 consists of a syn-tectonic granodiorite with a granoblastic texture and an E-W S_{1a} tectonic fabric, highlighted by Ser-Bt. SU04 is affected by D_{1b}-related, Plg-rich, strike-slip shear zone. GBM and GBAR textures are observed in Qz and Plg, respectively.

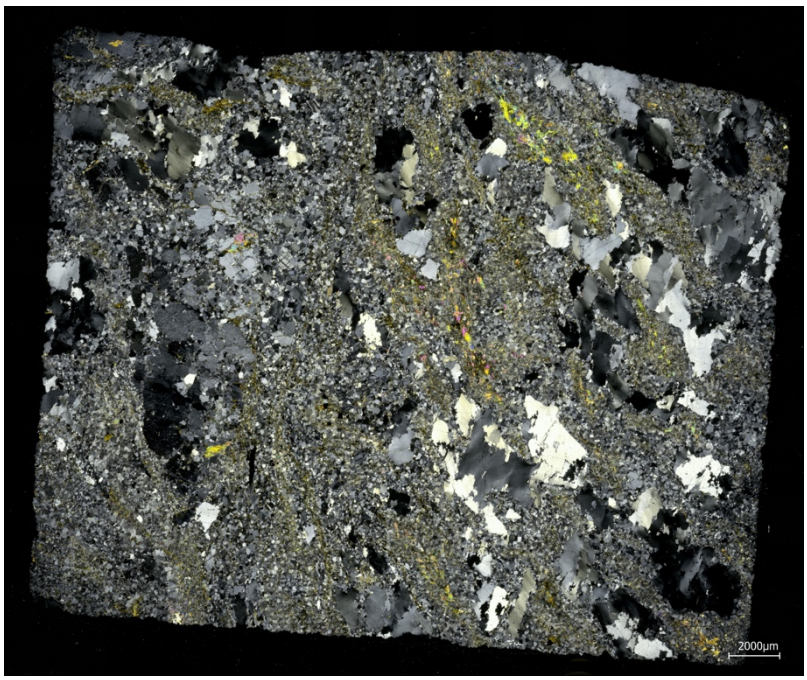

Figure SM2-2.4: Micrographs of sample SU04 in cross-polarized analyzed light.

Zircon morphology

85 zircon crystals were isolated from this sample, with as many colorless as dark brown grains, euhedral with few fractures. Grains can be up to 500 µm long, equant and prismatic. In cathodoluminescence images, zircon grains present either oscillatory zoning or a simple zoning with a core and a rim.



Figure SM2-2.5: Above: cathodoluminescence and transmitted light images of representative zircons from sample SU04. **Below**: location of O-Hf-U-Pb analyses.

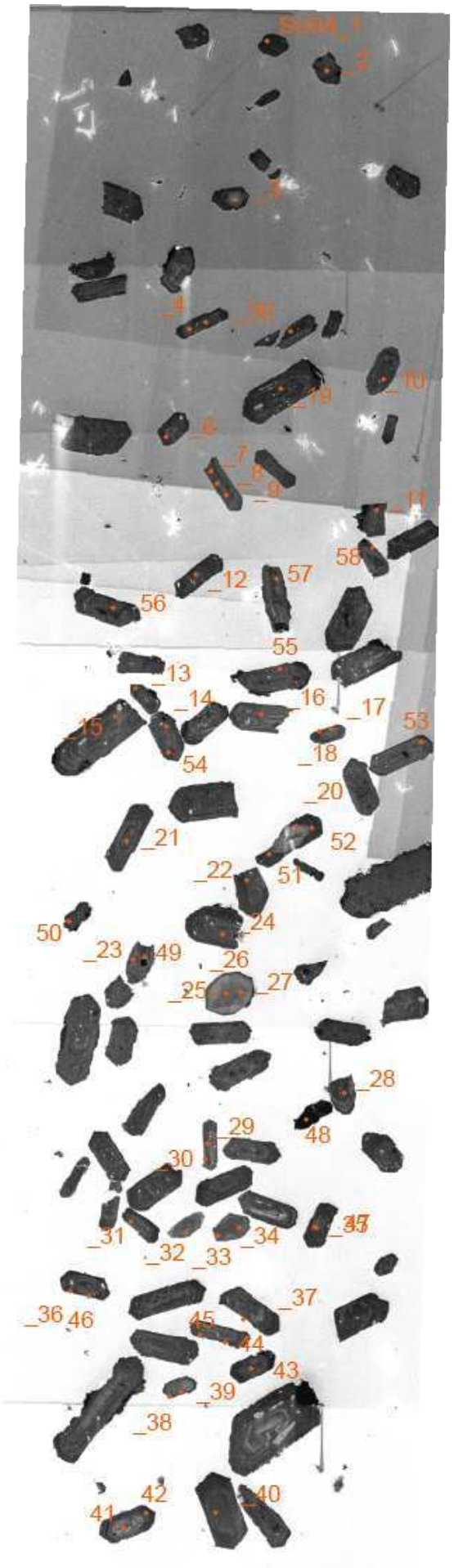
_1
_2
_3
_4
_5
_6
_7
_8
_9
_10
_11
_12
_13
_14
_15
_16
_17
_18
_20
_21
_22
_23
_24
_25
_26
_27
_28
_29
_30
_31
_32
_33
_34
_36
_37
_38
_39
40
41
42
43
44
45
46
47
48
49
50
51
52
53
54
55
56
57
58

Analytical details

O isotope ratios ($^{16}O/^{18}O$ and $^{16}O^{1}H/^{16}O$) were determined using SIMS at CMCA (UWA) the 05/09/2023. U-Pb isotope compositions in zircon were analyzed by LA-ICP-MS at CMCA (UWA) the 03/10/2023. Lu-Hf isotope compositions in zircon were analyzed by LA-ICP-MS at CMCA (UWA) the 20/10/2023.

Results

O isotopy

40 spots were analyzed on 31 zircon grains. 8 analyses show low $^{16}O^{1}H/^{16}O$, the 32 others are considered as outliers. Results are shown in a $\delta^{18}O$ - $^{16}O^{1}H/^{16}O$ diagram.

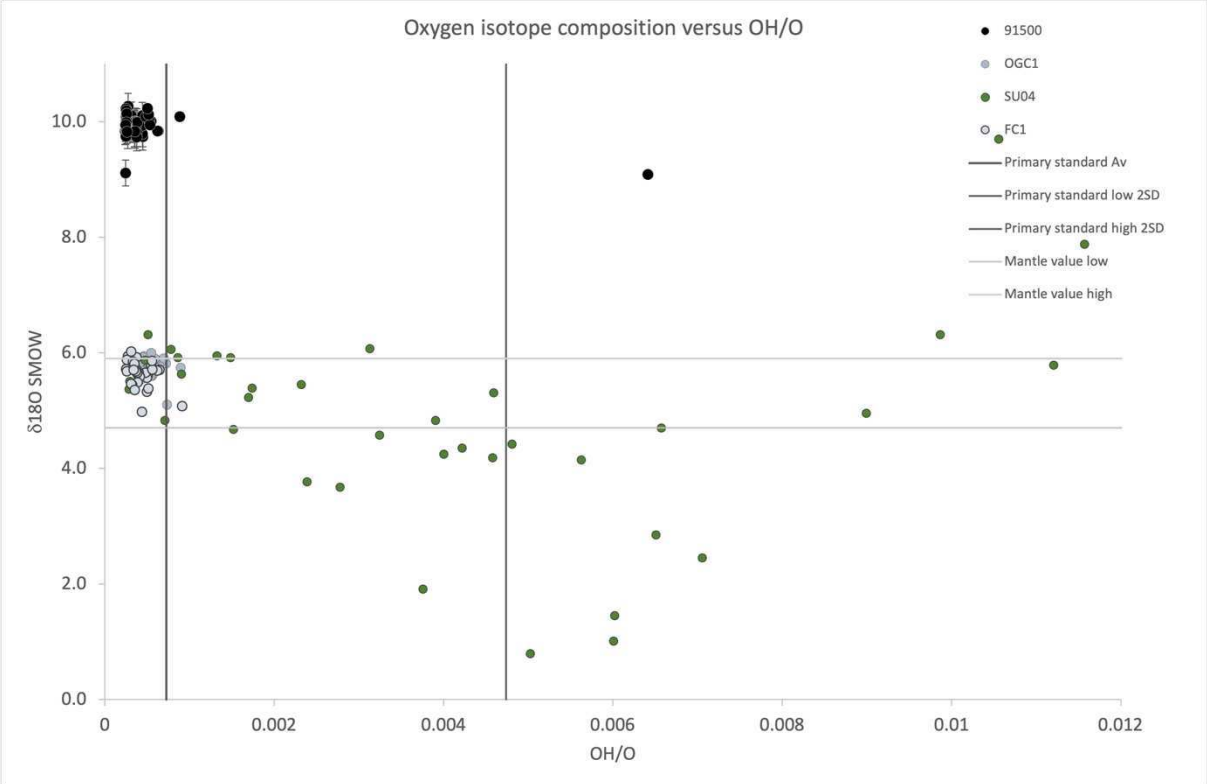

Figure SM2-2.6: $\delta^{18}O$ vs $^{16}O^{1}H/^{16}O$ analyses results for sample SU04.

U-Pb isotopy

35 spots were analyzed on 25 zircon grains. 7 analyses fall onto the concordia, 6 are discordant and 22 failed (inclusions or fractures). Results are shown in a Tera-Wasserburg and weighted mean diagrams.

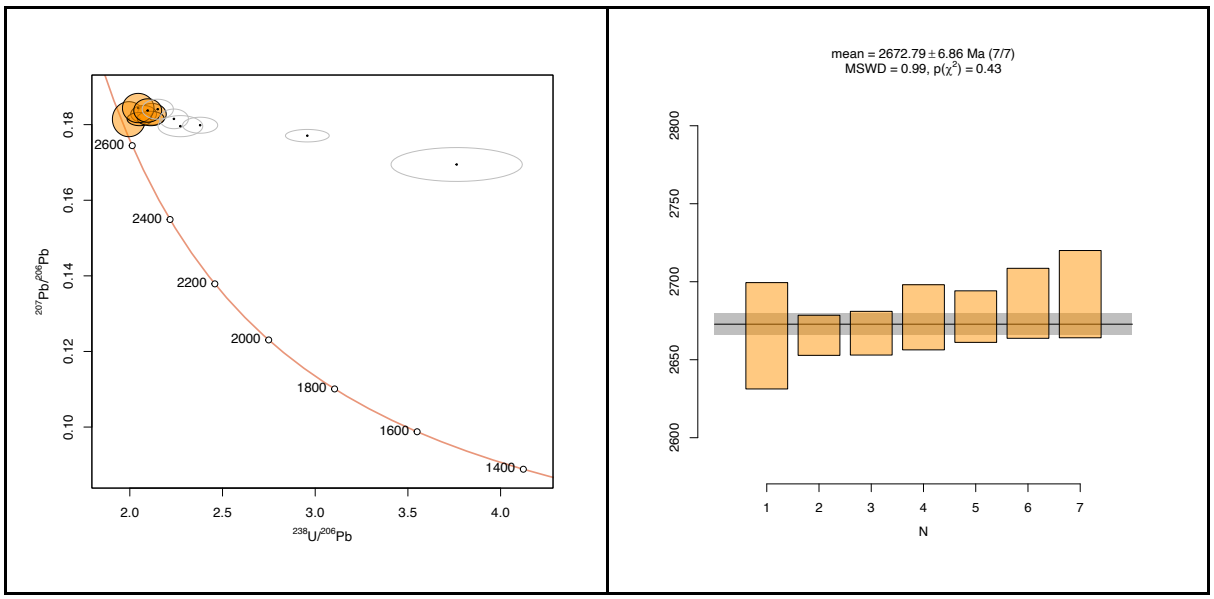

Figure SM2-2.7: U-Pb analyses results for sample SU04. Left: shows the Tera-Wasserburg plots (orange ellipses show the concordant and near concordant data, transparent ellipses show the discordant analyses (> 8% discordant). Right: Weighted mean averages calculated using the concordant analyses.

Interpretation

O isotopy

The mean value is 5.64 ± 0.14 ‰. The analyses fall at the upper limit of the mean mantle values, indicating that the source of SU04 includes material that has undergone low temperature oxygen exchanges in the hydrosphere (volcano-sediments or rock that went to supra-crustal depths before melting).

U-Pb isotopy

The analyses range from concordant to strongly discordant. 6 analyses were > 8% discordant. The weighed mean shows a concordant age of 2673 ± 7 Ma, MSWD = 0.99, based on the $^{207}Pb/^{206}Pb$ ratios. The age is interpreted as the crystallization of the SU04 granodiorite.

Lu-Hf analyses

Lu-Hf analyses were acquired on 10 near concordant zircons, they returned $^{176}Hf/^{177}Hf_i$ of 0.281065 ± 0.000016. The corresponding εHf_t for this dataset is comprised between -3.5 and -0.6 an individual error of (2s) 0.8. Hf model age calculated for this analysis is estimated between ca. 2950 and 3140 Ga (using $^{176}Hf/^{177}Hf$ =0.0115).

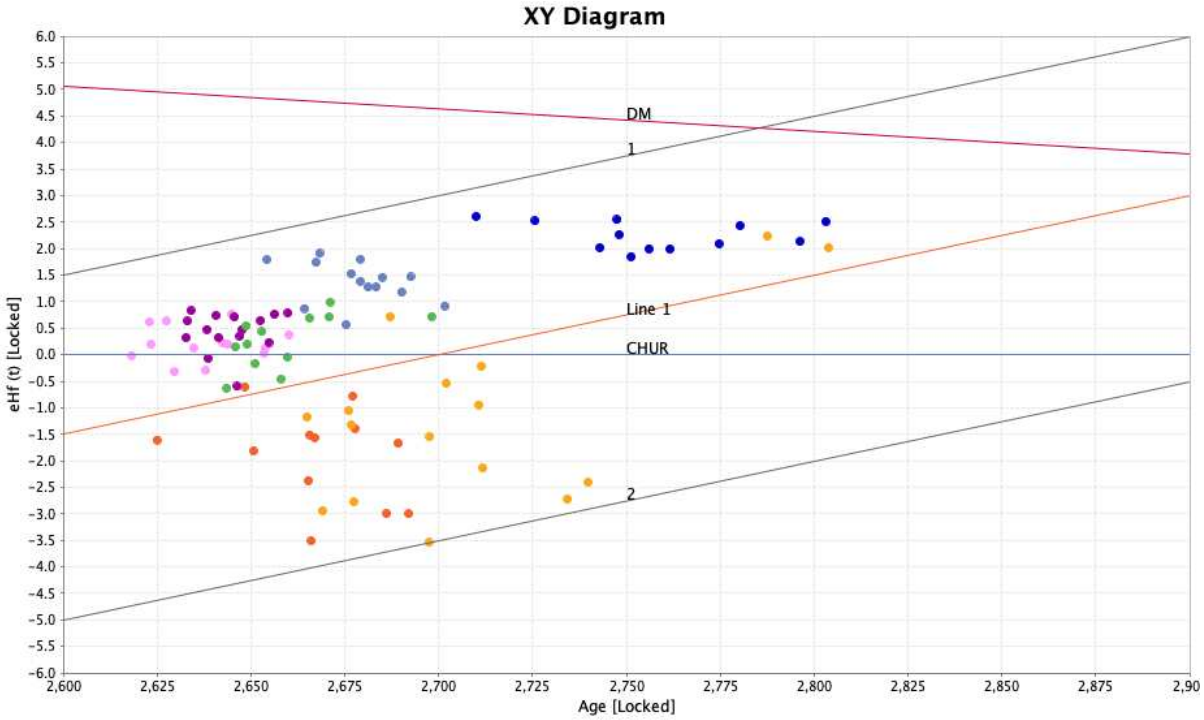

Figure SM2-2.8: εHf vs Age of magmatic samples. Dark blue: SU21, light blue: SU15, green: SU10B, purple: SU16, pink: SU25, yellow: SU06, orange: SU04.

SU06

Sample Localization regional context

(32.8399; -2.8030)

Sampled on a hill, 4 km north of the northern limit between the SGGB and granitoids. Syn-tectonic granodiorite with an E-W S_{1a} tectonic fabric, affected by D_{1b} strike-slip shear zones. Few undeformed pegmatitic dykes crosscut the foliation.



Figure SM2-2.9: SU06 sample photographs.

Sample description

SU06 consists of a granodiorite with quartz, albite, biotite, chlorite and rare monazite grains. Quartz and feldspar grains present grain boundary area reduction (GBAR), resulting in polygonal-shaped grains. Grain boundary migration (GBM) and subgrain rotation (SGR) also affected the coarser quartz grains that often display lamellar extinctions.

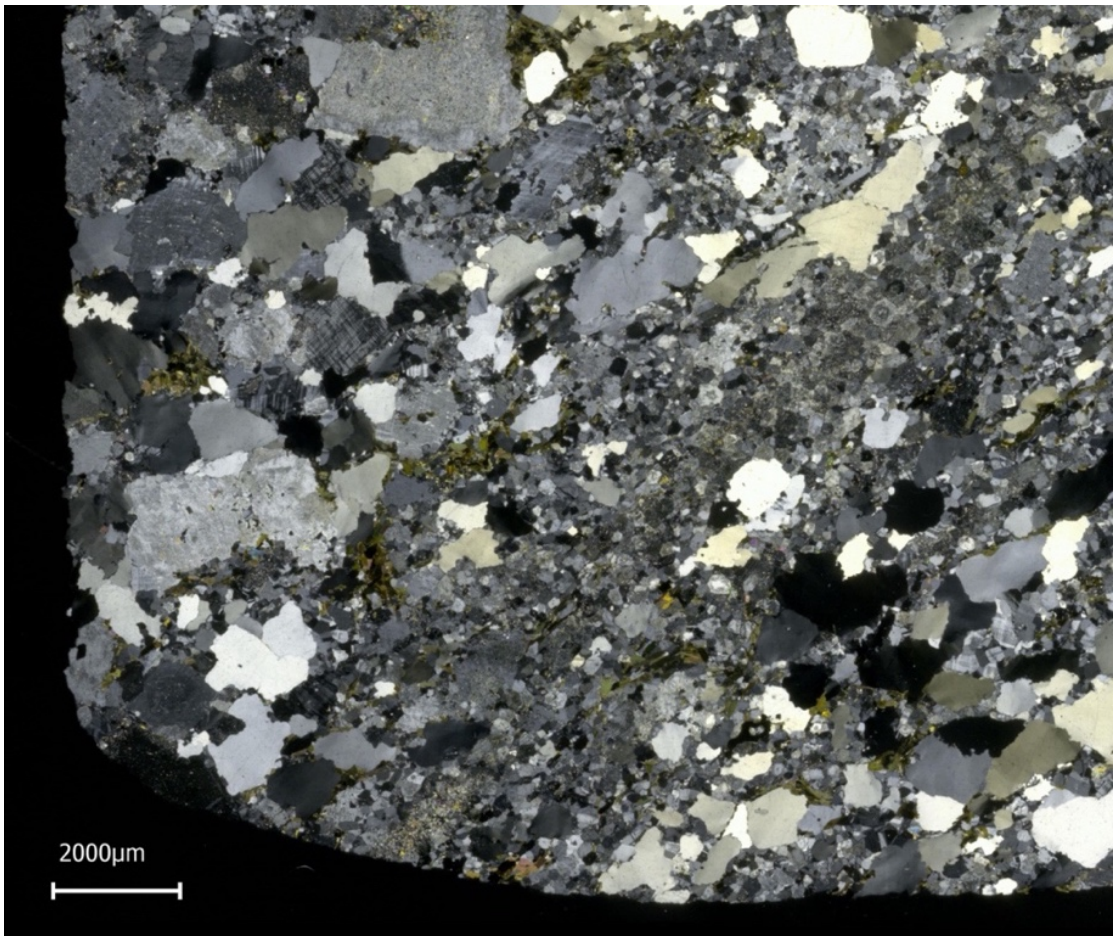

Figure SM2-2.10: Micrographs of sample SU06 in cross-polarized analyzed light.

Zircon morphology

123 zircon crystals were isolated from this sample, all colourless to light brown, euhedral with few fractures. Grains can be up to 300 µm long, and mainly prismatic and elongated. In cathodoluminescence images, zircon grains present oscillatory zoning with light cores and few thin rims.

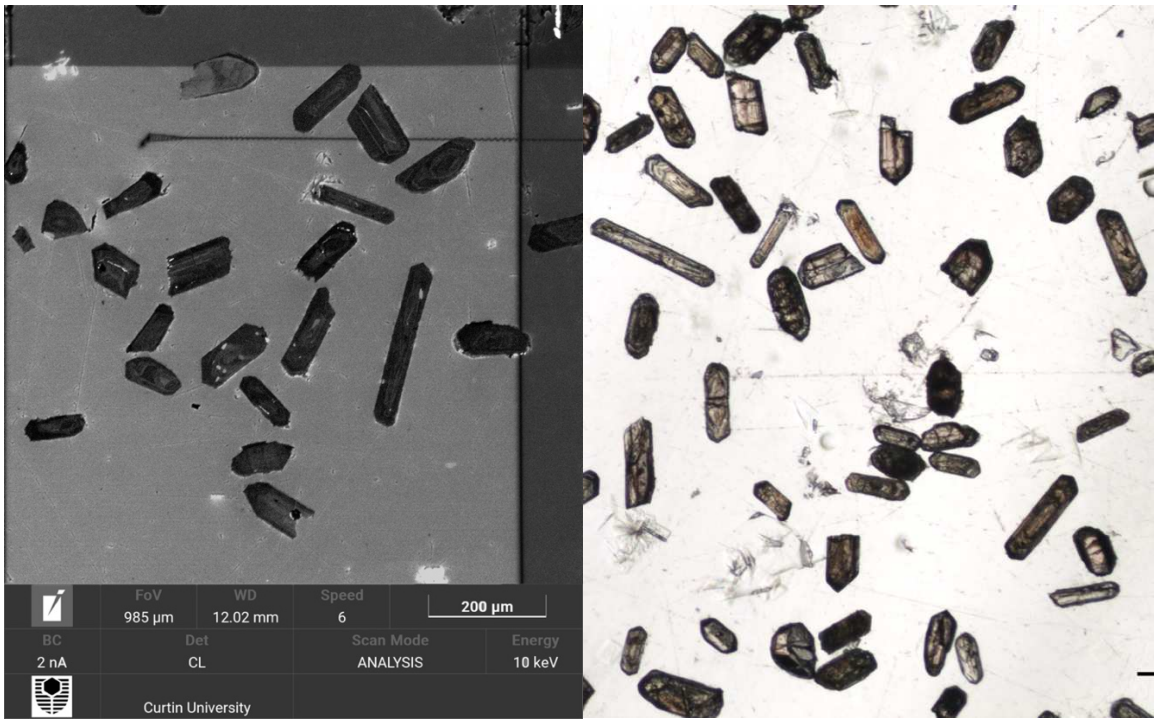

Figure SM2-2.11: Above: cathodoluminescence and transmitted light images of representative zircons from sample SU06. **Below**: location of O-Hf-U-Pb analyses.

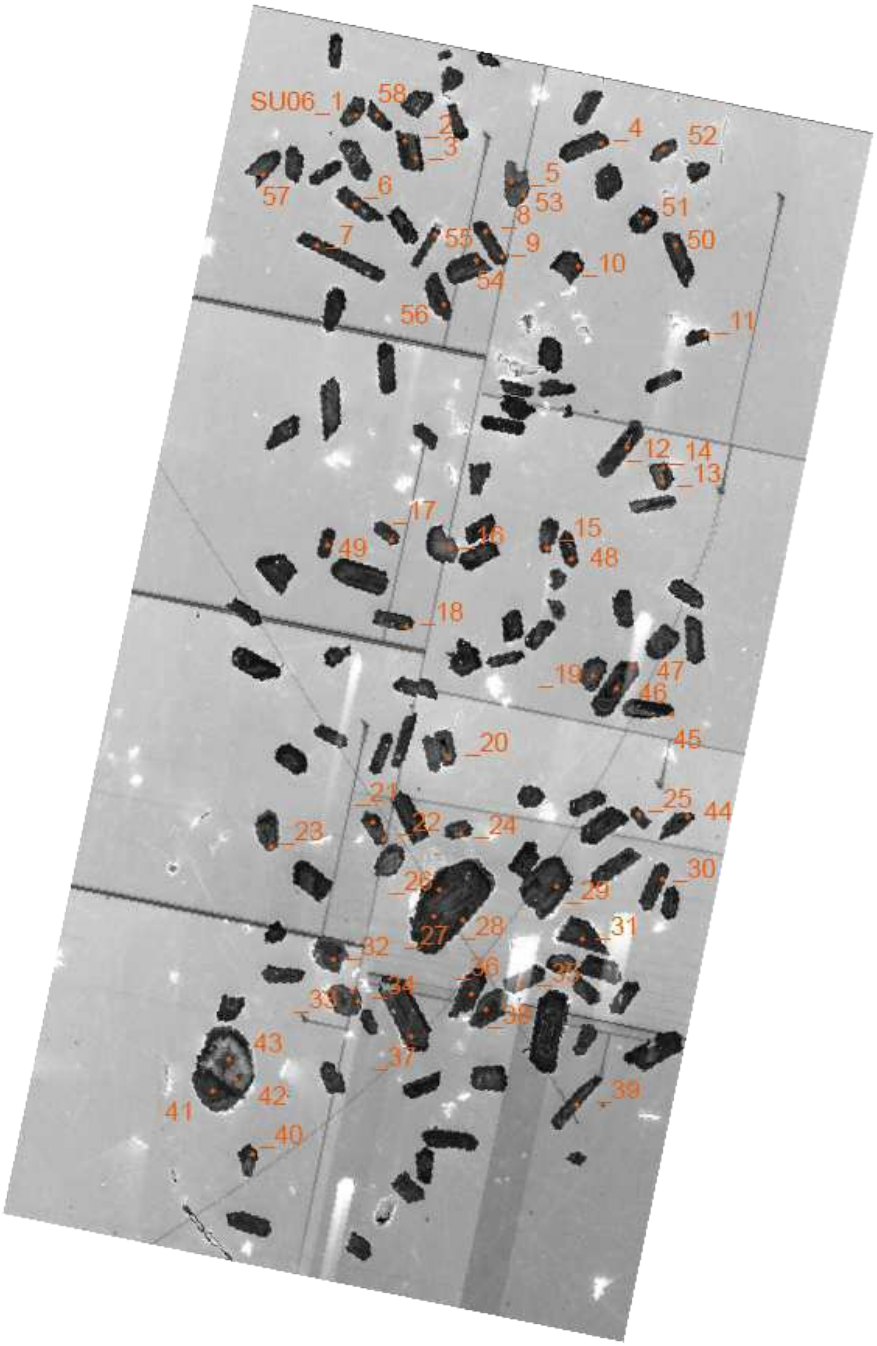
SU06_1
58
4
52
3
5
57
6
53
51
7
55
9
50
10
54
56
11
12
14
13
17
15
49
16
48
18
47
46
20
45
21
25
44
23
22
24
30
29
28
31
32
27
34
43
37
39
42
41
40

Analytical details

O isotope ratios ($^{16}O/^{18}O$ and $^{16}O^{1}H/^{16}O$) were determined using SIMS at CMCA (UWA) the 06/09/2023. U-Pb isotope compositions in zircon were analyzed by LA-ICP-MS at CMCA (UWA) the 16/09/2023. Lu-Hf isotope compositions in zircon were analyzed by LA-ICP-MS at CMCA (UWA) the 20/10/2023.

Results

O isotopy

40 spots were analyzed on 33 zircon grains. 15 analyses show low $^{16}O^{1}H/^{16}O$, the 25 others are considered as outliers. Results are shown in a $\delta^{18}O$ - $^{16}O^{1}H/^{16}O$ diagram.

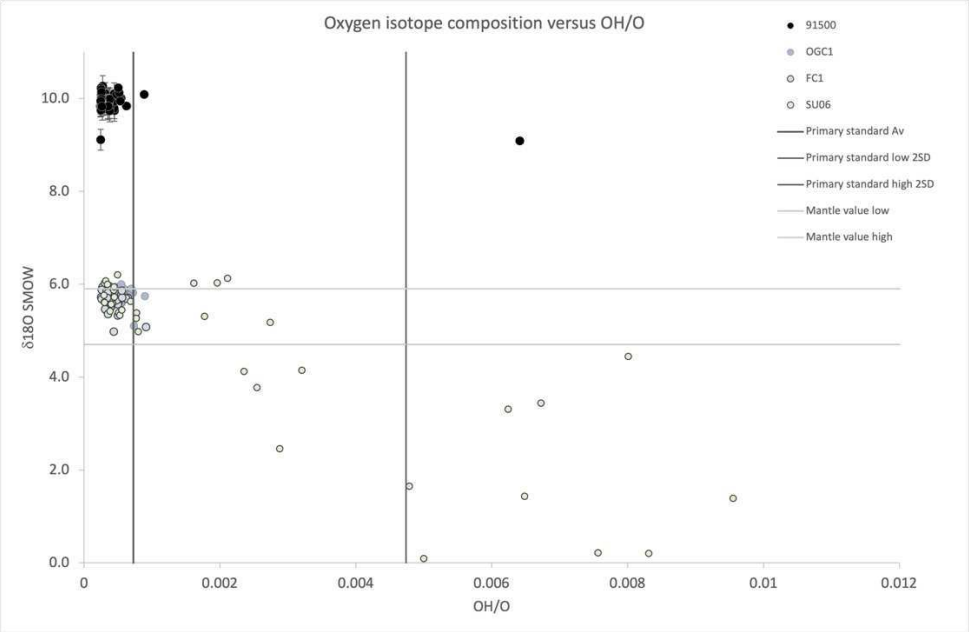

Figure SM2-2.12: $\delta^{18}O$ vs $^{16}O^{1}H/^{16}O$ analyses results for sample SU06.

U-Pb isotopy

39 spots were analyzed on 32 zircon grains. 14 analyses fall onto the concordia, 8 are discordant and 17 failed (inclusions or fractures). Results are shown in a Tera-Wasserburg and weighted mean diagrams.

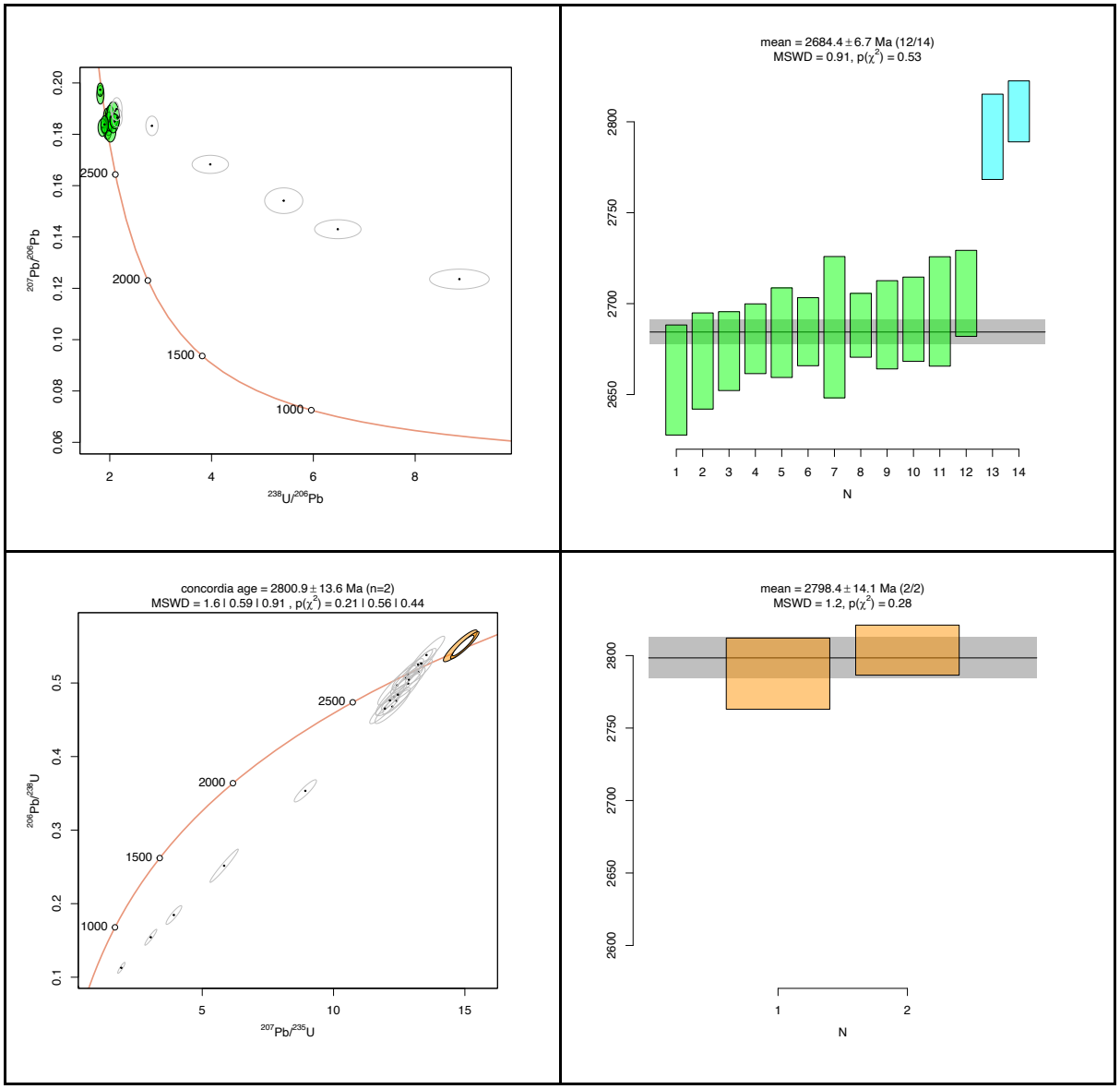

Figure SM2-2.13: U-Pb analyses results for sample SU06. Left: shows the Tera-Wasserburg plots (green and orange ellipses show the concordant and near concordant data, transparent ellipses show the discordant analyses (> 8% discordant). Right: Weighted mean averages calculated using the concordant analyses.

Interpretation

O isotopy

The mean value is 5.79 ± 0.23 ‰. An inherited zircon has a mean value at 5.44 ± 0.23 ‰. The analyses fall in the mantle value range, near the upper limit of the mean mantle values, indicating that the source of SU06 is mantle-derived and includes material that

has undergone low temperature oxygen exchanges in the hydrosphere (volcano-sediments or rock that went to supra-crustal depths before melting).

U-Pb isotopy

The analyses range from concordant to strongly discordant. 8 analyses were > 8 % discordant. The dates obtained from the 14 analyses have a good precision and form two groups, based on their $^{207}Pb/^{206}Pb$ ratios: group A comprises 12 analyses which yield a weighted mean date of 2684 ± 7 Ma (MSWD = 0.91). The discordia plot with 20 data returned an upper intersection at 2705 ± 21 Ma (MSWD = 4). Group B comprises 2 analyses which yield a weighted mean date of 2798 ± 14 Ma (MSWD = 1.2).

Group A age is interpreted as the crystallization age of the SU06 granite. Group B appears to be inherited zircon grains.

Lu/Hf analyses

Lu-Hf analyses were acquired on 14 near concordant zircons forming two groups:

	Group 1	Group 2
Pb-Pb age	2798 ± 14 Ma	2684 ± 7 Ma
$^{176}Hf/^{177}Hfi$	0.281084 ± 0.000014	0.281064 ± 0.000021
εHf_t (2s)	2.0 to 2.2 (0.7)	-3.5 to 0.7 (0.9)
Hf model age (using $^{176}Hf/^{177}Hf$ =0.0115)	2900 to 3140 Ma	

SU10A

Sample Localization regional context

(32.8399; -2.8030)

Sampled in the valley, 4 km north of the northern limit between the SGGB and granitoids. Sandstone in a post-tectonic basin in near contact to the undeformed SU10B granodiorite.

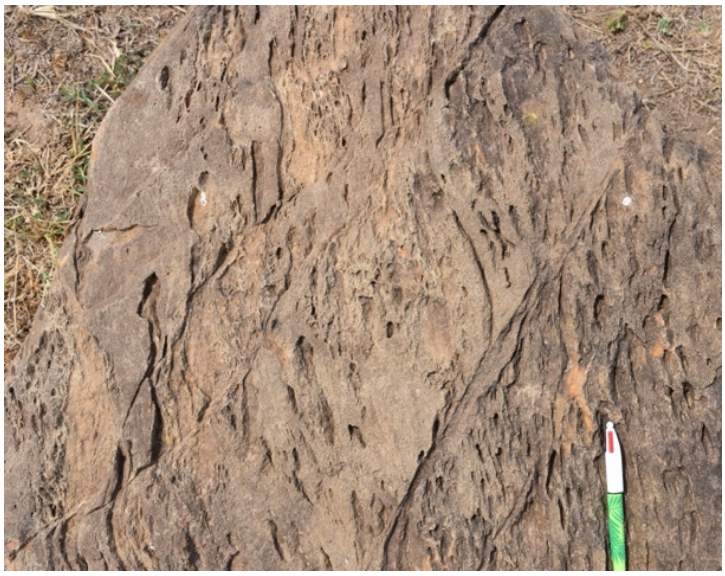

Figure SM2-2.15: Sample SU10A photograph.

Sample description

SU10A consists of a greywacke with quartz-rich polymictic clasts. Sedimentary crossbeddings are well visible.

Zircon morphology

Around 250 zircon crystals were isolated from this sample, all light brown to dark brown, mainly euhedral and not very rounded, frequent fractures. Grains can be up to 500 µm long, and mainly equant. In cathodoluminescence images, zircon grains present oscillatory zoning, either very light or dark.

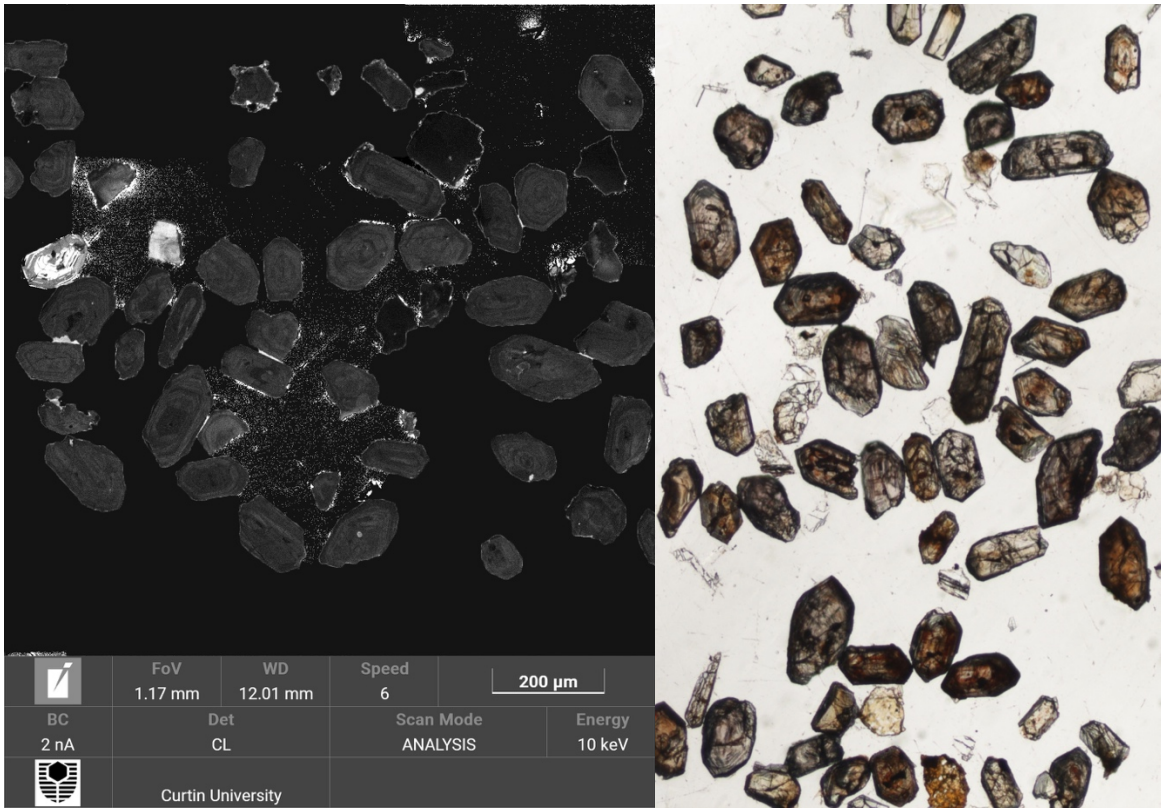

Figure SM2-2.16: Above: cathodoluminescence and transmitted light images of representative zircons from sample SU10A. **Below**: location of Hf-U-Pb analyses.

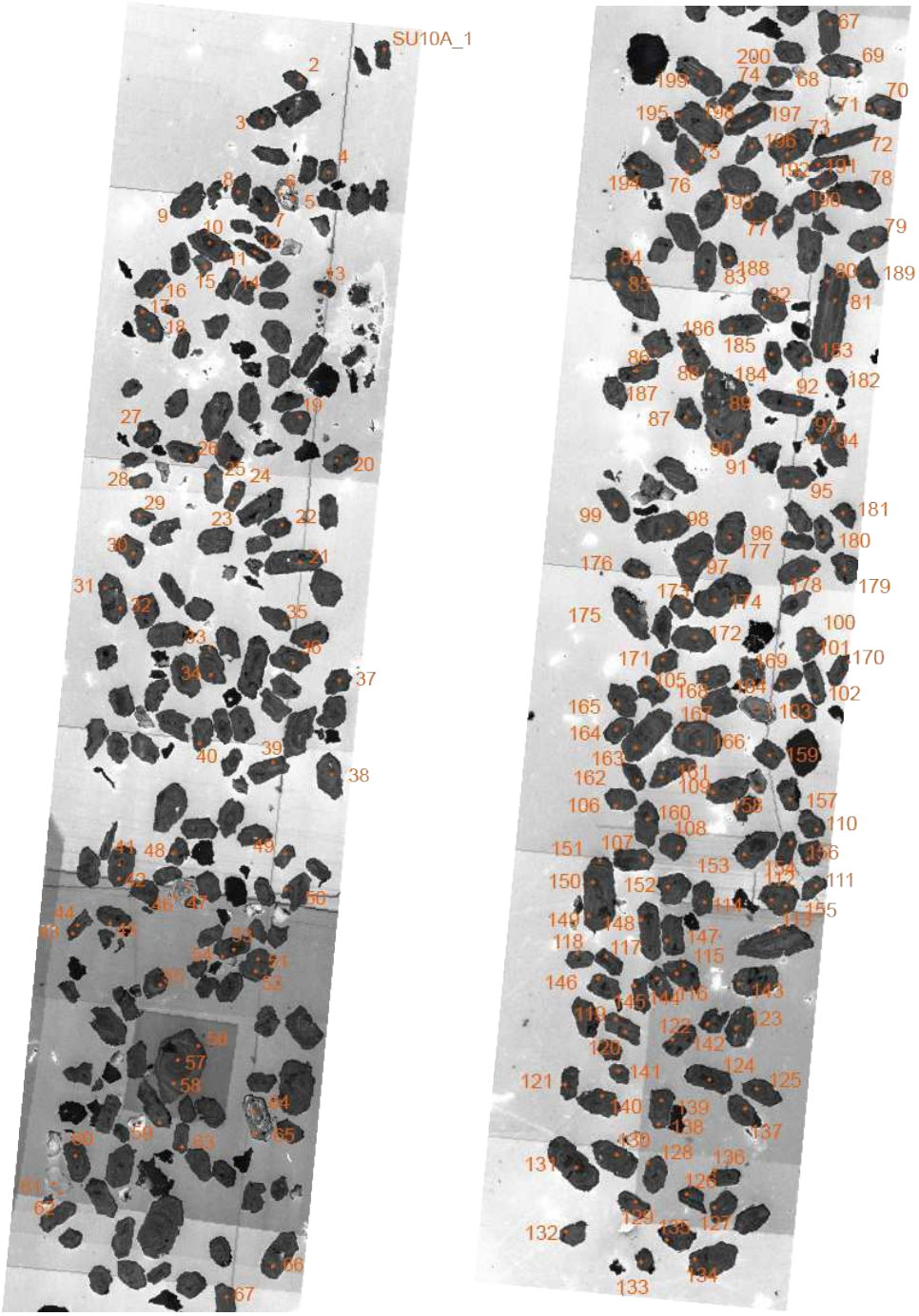
SU10A_1

Analytical details

O isotope ratios ($^{16}O/^{18}O$ and $^{16}O^{1}H/^{16}O$) were determined using SIMS at CMCA (UWA) the 05/09/2023. U-Pb isotope compositions in zircon were analyzed by LA-ICP-MS at CMCA (UWA) the 16/09/2023. Lu-Hf isotope compositions in zircon were analyzed by LA-ICP-MS at CMCA (UWA) the 20/10/2023.

Results

U-Pb isotopy

200 spots were analyzed on zircon grains. 22 analyses fall onto the concordia, 31 are discordant and 147 failed (inclusions or fractures). Results are shown in a Tera-Wasserburg and weighted mean diagrams.

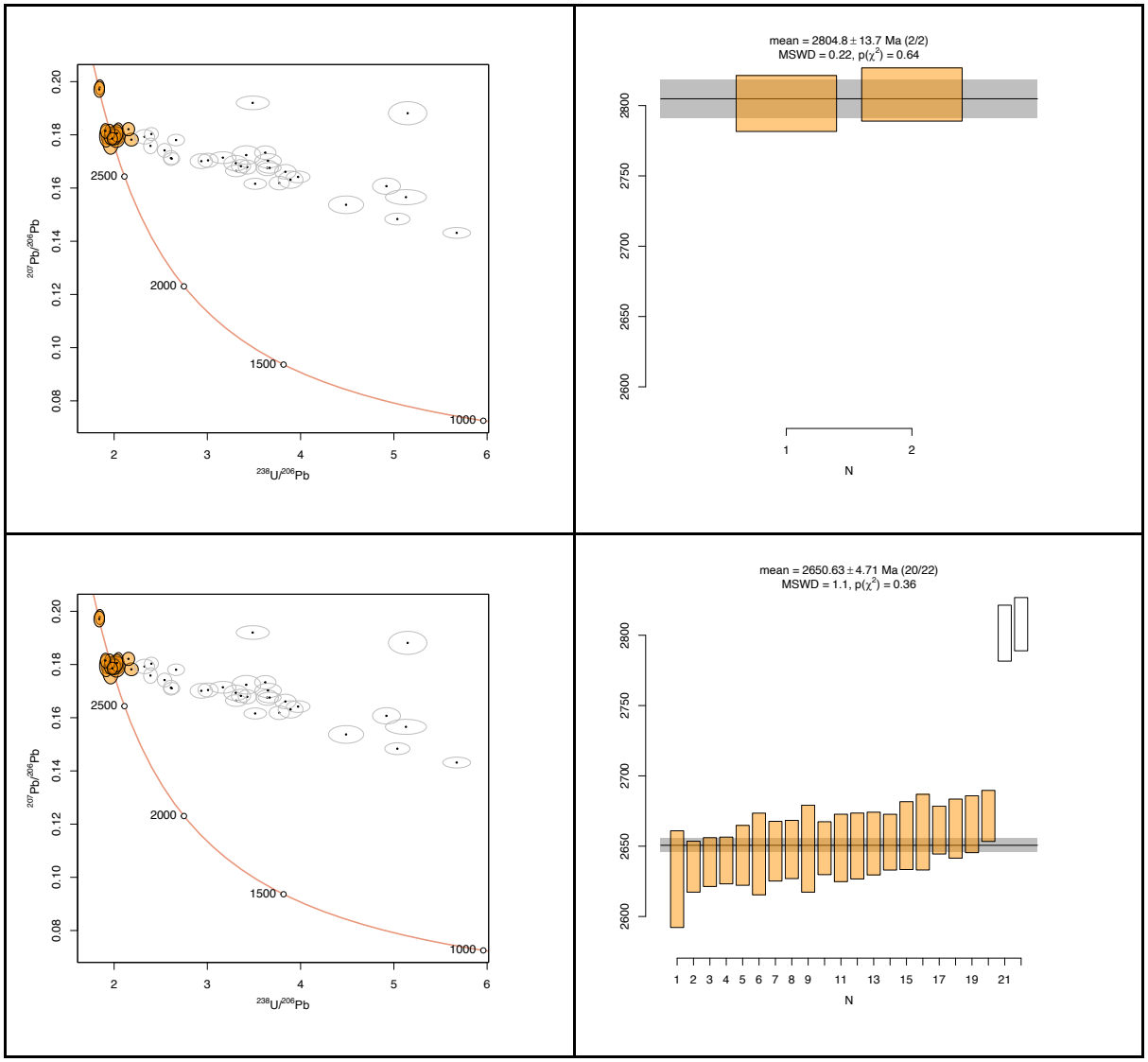

Figure SM2-2.17: U-Pb analyses results for sample SU10A. Left: shows the Tera-Wasserburg plots (orange ellipses show the concordant and near concordant data, transparent ellipses show the discordant analyses (> 8% discordant). Right: Weighted mean averages calculated using the concordant analyses

Interpretation

U-Pb isotopy

The analyses range from concordant to strongly discordant. The dates obtained from the 22 analyses have a good precision and form two groups, based on their $^{207}Pb/^{206}Pb$ ratios: group A comprises 18 analyses which yield a weighted mean date of 2651 ± 5 Ma (MSWD = 1.1). The discordia plot with 51 data returned an upper intersection at 2660 ± 5 Ma (MSWD = 25). Group B comprises 2 analyses which yield a weighted mean date of 2805 ± 14 Ma (MSWD = 0.22).

Group A age is interpretated as the maximum age of deposition in the basin.

Lu/Hf analyses

Lu-Hf analyses were acquired on 13 near concordant zircons of Group A and Group B.

	Group A	Group B
Pb-Pb age	2805 ± 14 Ma	2651 ± 5 Ma
$^{176}Hf/^{177}Hfi$	0.280940 ± 0.000014	0.281119 ± 0.000018
εHf_t (2s)	-2.0 to -2.2 (0.7)	-2.8 to -0.1 (0.8)
Hf model age (using $^{176}Hf/^{177}Hf$ =0.0115)	3120 to 3160 Ma	2920 to 3070 Ma

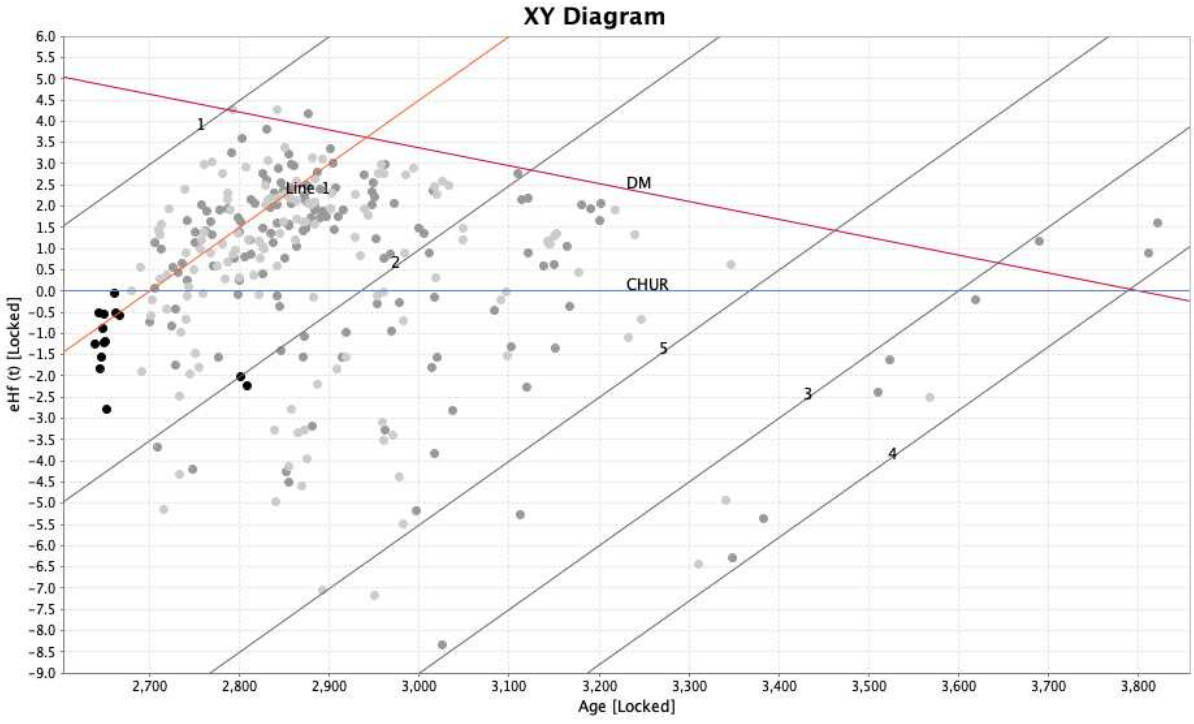

Figure SM2-2.18: εHf vs Age of magmatic samples. Light grey: SU20, dark grey: SU11, black: SU10A.

SU10B

Sample Localization regional context

(32.6544; -2.8583)

Sampled in a crop, 2 km north of the northern limit between the SGGB and granitoids. Late-tectonic granodiorite with a Bt-rich enclave and no tectonic fabric. Crosscut by a granodioritic aplite dyke.

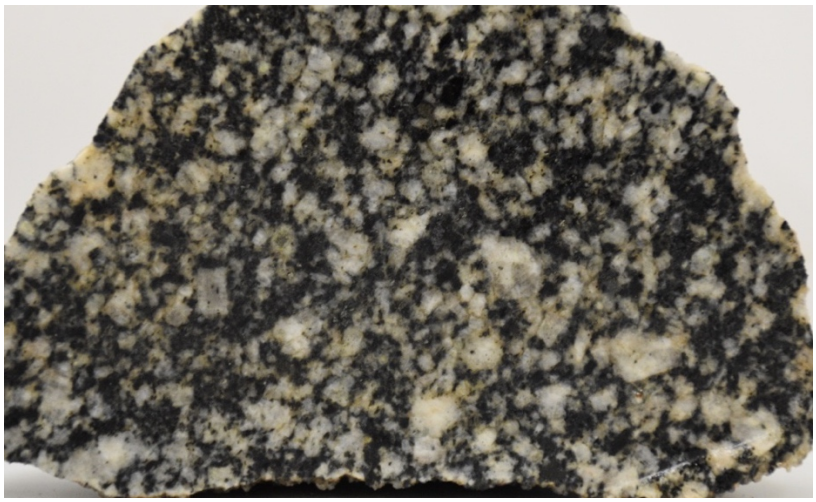

Figure SM2-2.19: Sample SU10B photograph.

Sample description

SU10B consists of a granodiorite with quartz, plagioclase, chloritised biotite and rare oxide grains. Heterogenous with coarse and fine grain areas.

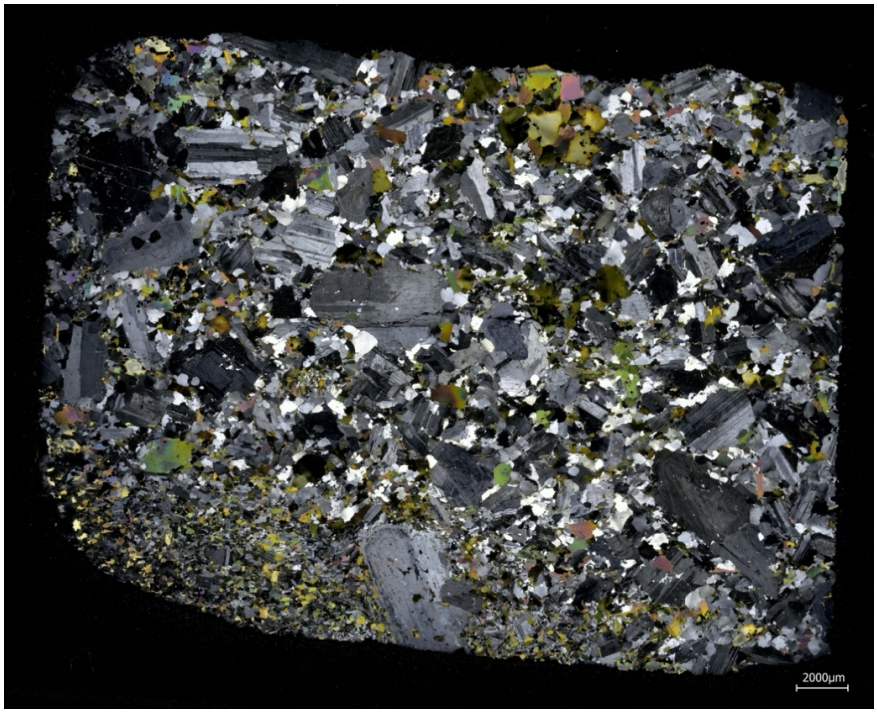

Figure SM2-2.20: Micrographs of sample SU10B in cross-polarized analyzed light.

Zircon morphology

94 zircon crystals were isolated from this sample, mainly dark brown, few light browns, euhedral with few fractures. Grains can be up to 250 µm long, and mainly prismatic. In cathodoluminescence images, zircon grains present oscillatory zoning with light cores and few thin rims. The last rim is light and rather large.

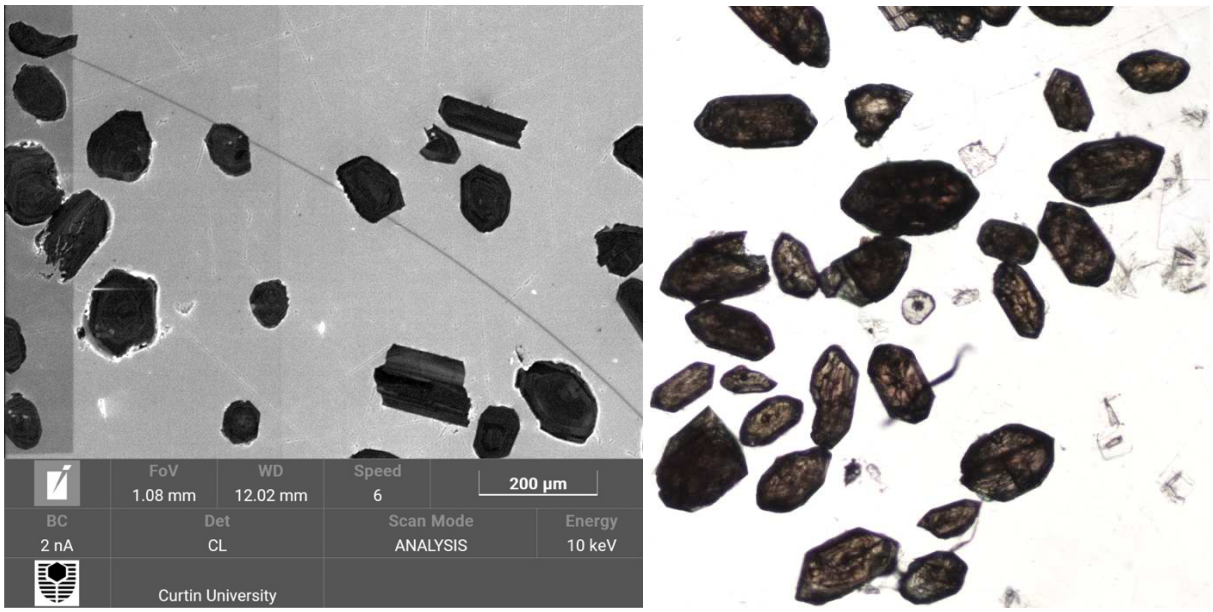

Figure SM2-2.21: Above: cathodoluminescence and transmitted light images of representative zircons from sample SU10B. **Below**: location of O-Hf-U-Pb analyses.

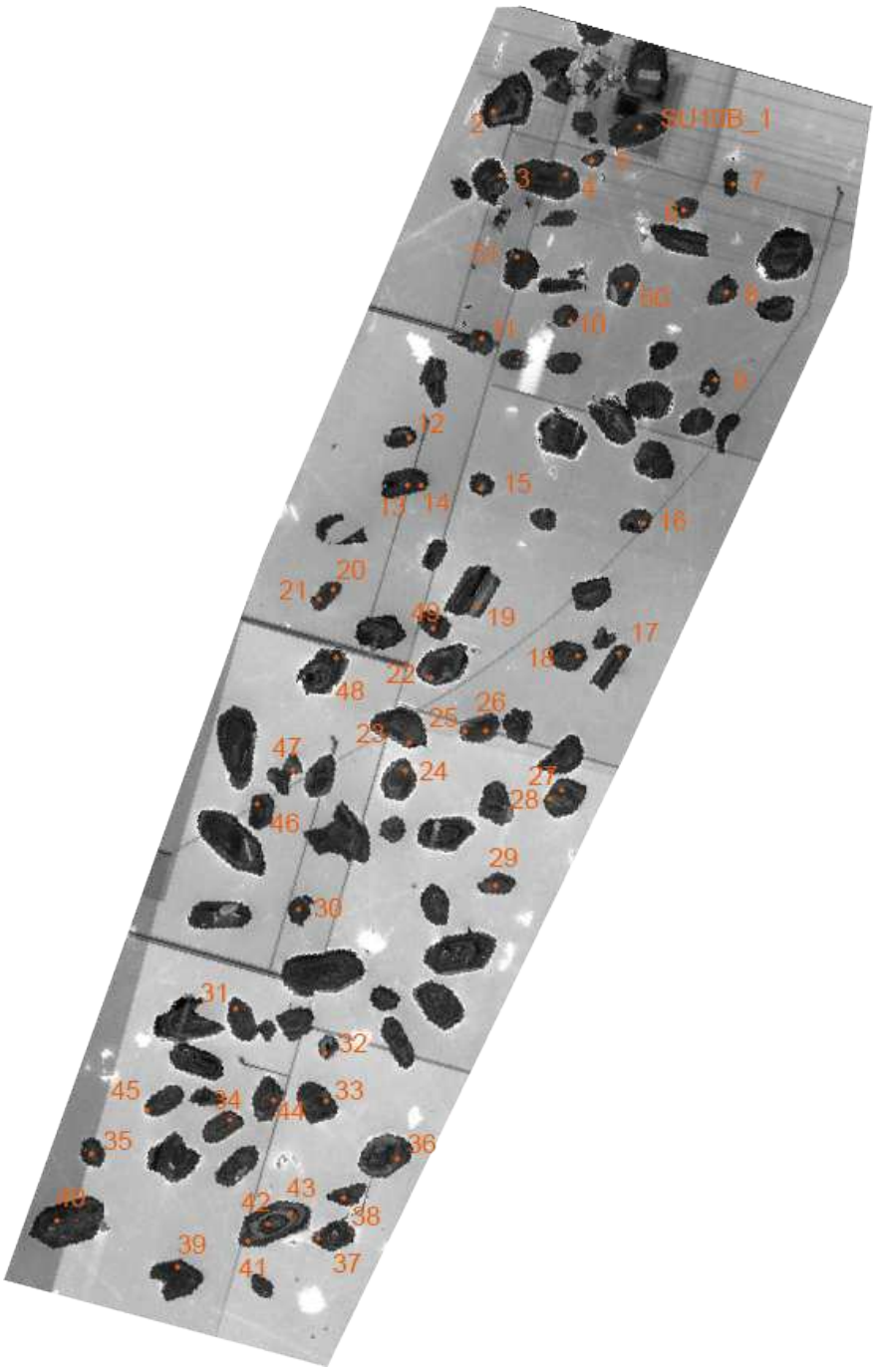
SUHDB_1
1
2
3
4
5
6
7
8
9
10
11
12
13
14
15
16
17
18
19
20
21
22
23
24
25
26
27
28
29
30
31
32
33
34
35
36
37
38
39
40
41
42
43
44
45
46
47
48

Analytical details

O isotope ratios ($^{16}O/^{18}O$ and $^{16}O^{1}H/^{16}O$) were determined using SIMS at CMCA (UWA) the 06/09/2023. U-Pb isotope compositions in zircon were analyzed by LA-ICP-MS at CMCA (UWA) the 16/09/2023. Lu-Hf isotope compositions in zircon were analyzed by LA-ICP-MS at CMCA (UWA) the 20/10/2023.

Results

O isotopy

40 spots were analyzed on 36 zircon grains. 15 analyses show low $^{16}O^{1}H/^{16}O$, the 25 others are considered as outliers. Results are shown in a $\delta^{18}O$ - $^{16}O^{1}H/^{16}O$ diagram.

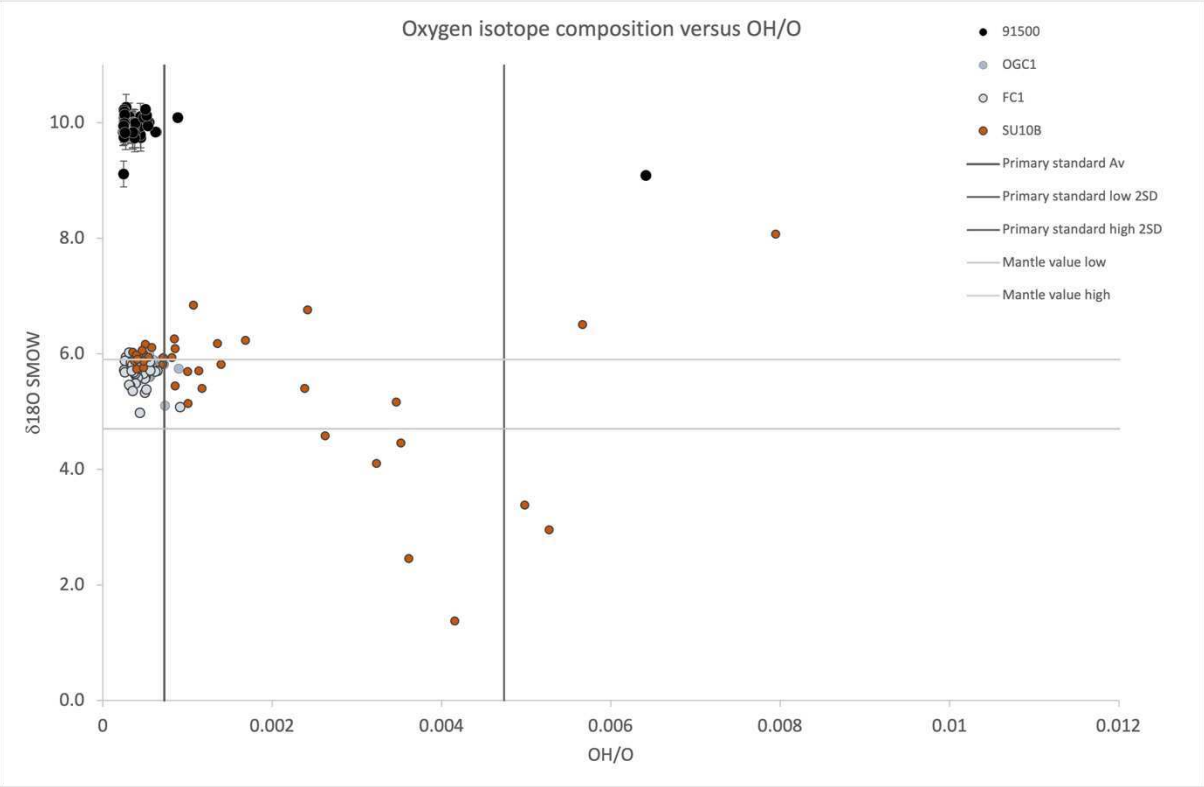

Figure SM2-2.22: $\delta^{18}O$ vs $^{16}O^{1}H/^{16}O$ analyses results for sample SU10B.

U-Pb isotopy

36 spots were analyzed on 30 zircon grains. 11 analyses fall onto the concordia, 13 are discordant and 12 failed (inclusions or fractures). Results are shown in a Tera-Wasserburg and weighted mean diagrams.

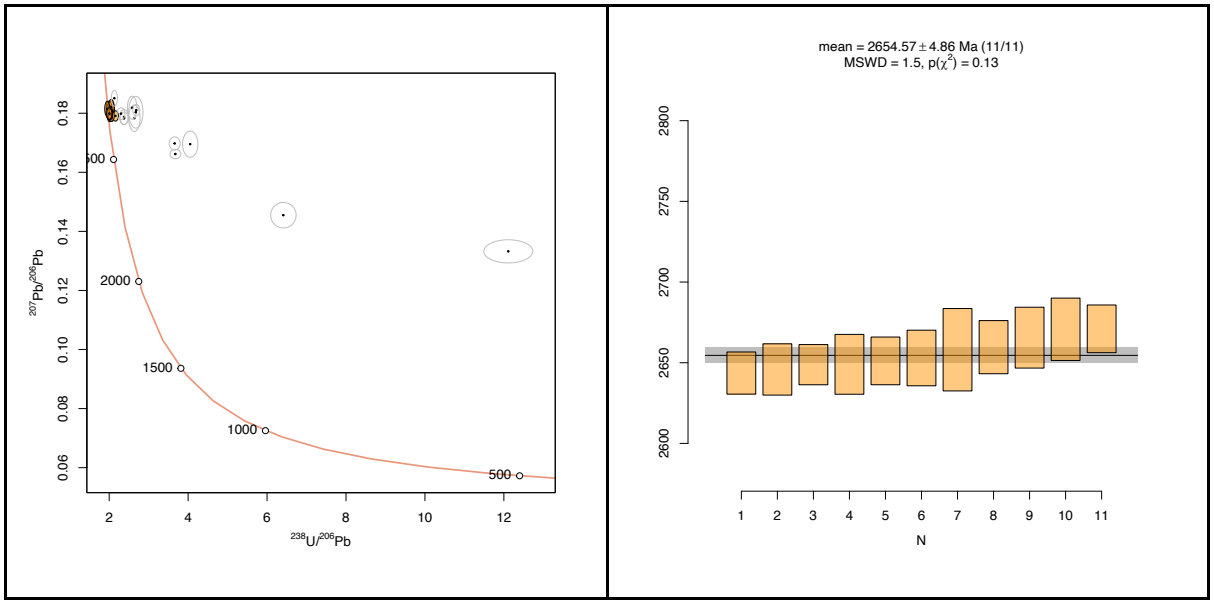

Figure SM2-2.23: U-Pb analyses results for sample SU10B. Left: shows the Tera-Wasserburg plots (orange ellipses show the concordant and near concordant data, transparent ellipses show the discordant analyses (> 8% discordant). Right: Weighted mean averages calculated using the concordant analyses.

Interpretation

O isotopy

Mean value at 5.95 ± 0.23 ‰. The analyses fall around the upper mean mantle values limit, indicating that the source of the granodiorite includes material that has undergone low temperature oxygen exchanges in the hydrosphere (volcano-sediments or rock that went to supracrustal depths before melting).

U-Pb isotopy

The analyses range from concordant to strongly discordant. 13 analyses were > 8% discordant. The date obtained from the 11 analyses has a good precision, based on its $^{207}Pb/^{206}Pb$ ratios: it yields a weighted mean date of 2655 ± 5 Ma (MSWD = 1.5). The discordia plot with 24 data returned an upper intersection at 2666 ± 5 Ma (MSWD = 4.8). The age is interpreted as the crystallization age of the SU10B granodiorite.

Lu/Hf analyses

Lu-Hf analyses were acquired on 11 near concordant zircons, they returned $^{176}Hf/^{177}Hf_i$ of 0.281128 ± 0.000015. The corresponding εHf_t for this dataset is comprised between -0.6 and 1.0 an individual error of (2s) 0.7. Hf model age calculated for this analysis is estimated between ca. 2850 and 2950 Ga (using $^{176}Hf/^{177}Hf$ =0.0115).

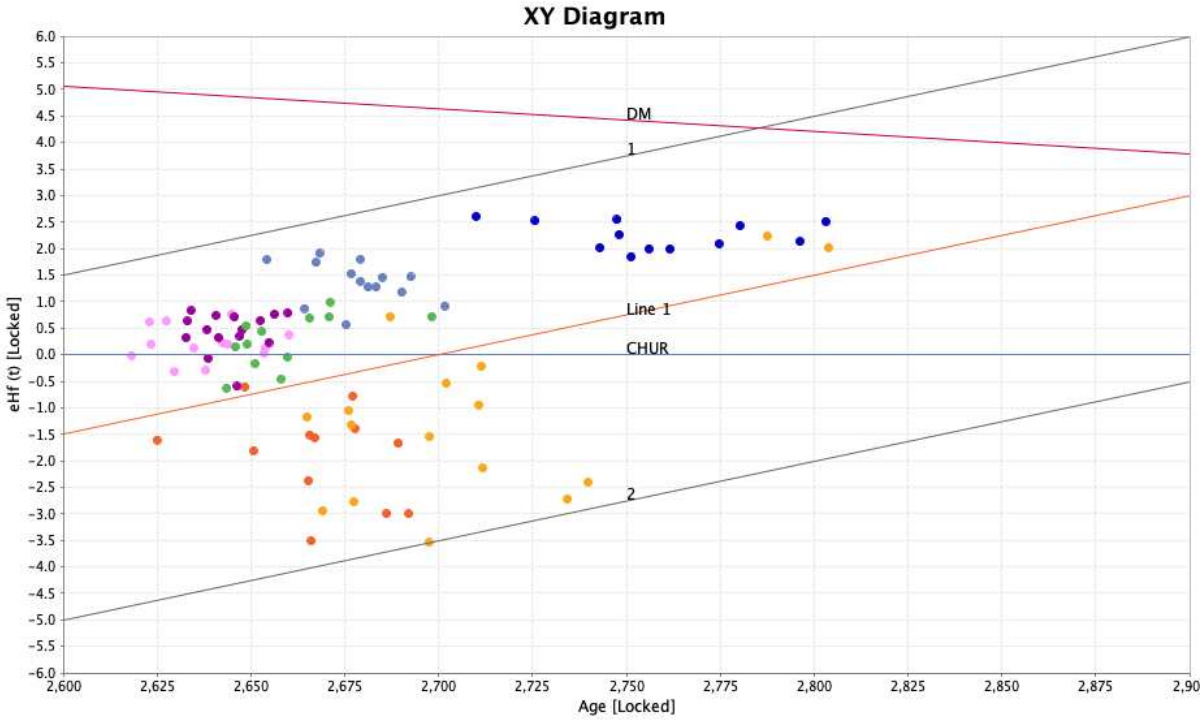

Figure SM2-2.24: εHf vs Age of magmatic samples. Dark blue: SU21, light blue: SU15, green: SU10B, purple: SU16, pink: SU25, yellow: SU06, orange: SU04.

SU11

Sample Localization regional context

(32.6817; -2.8923)

Sampled on a hill, 2 km south of the northern limit between the SGGB and granitoids. Conglomerates with quartz pebbles and sandstones in a syn-tectonic basin. Sedimentary structures of canals, unconformities, typical of fluvial context. N030-75 bedding.



Figure SM2-2.25: Sample SU11 photographs.

Sample description

SU11 consists of a quartz-rich meta-greywacke. No thin section.

Zircon morphology

More than 200 zircon crystals were isolated from this sample, from transparent and colourless to opaque and dark brown, mainly euhedral to rounded with few fractures. Grains can be up to 250 µm long, and mainly prismatic and elongated. In cathodoluminescence images, zircon grains present various patterns, from very light grains with 1 or 2 rims, to light grains with oscillatory zoning, to dark to very dark grains with more or less defined oscillatory zoning.

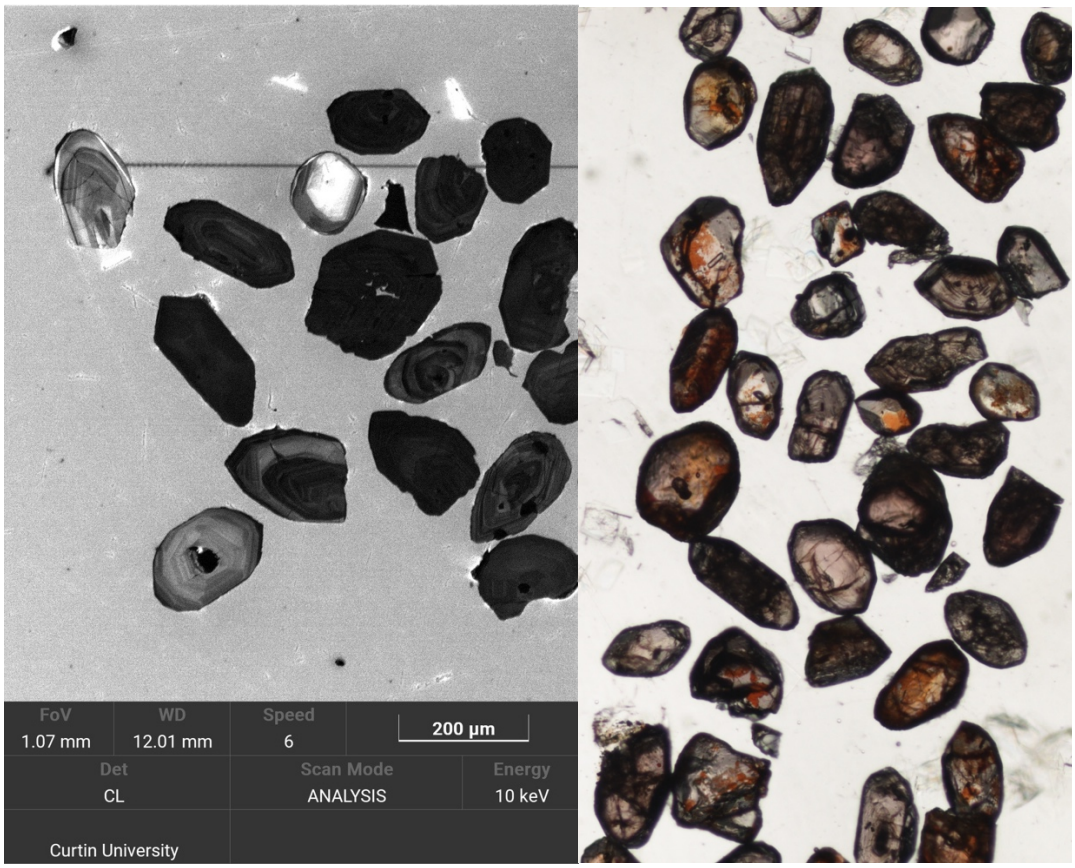

Figure SM2-2.26: **Above**: cathodoluminescence and transmitted light images of representative zircons from sample SU11. **Below**: location of O-Hf-U-Pb analyses.

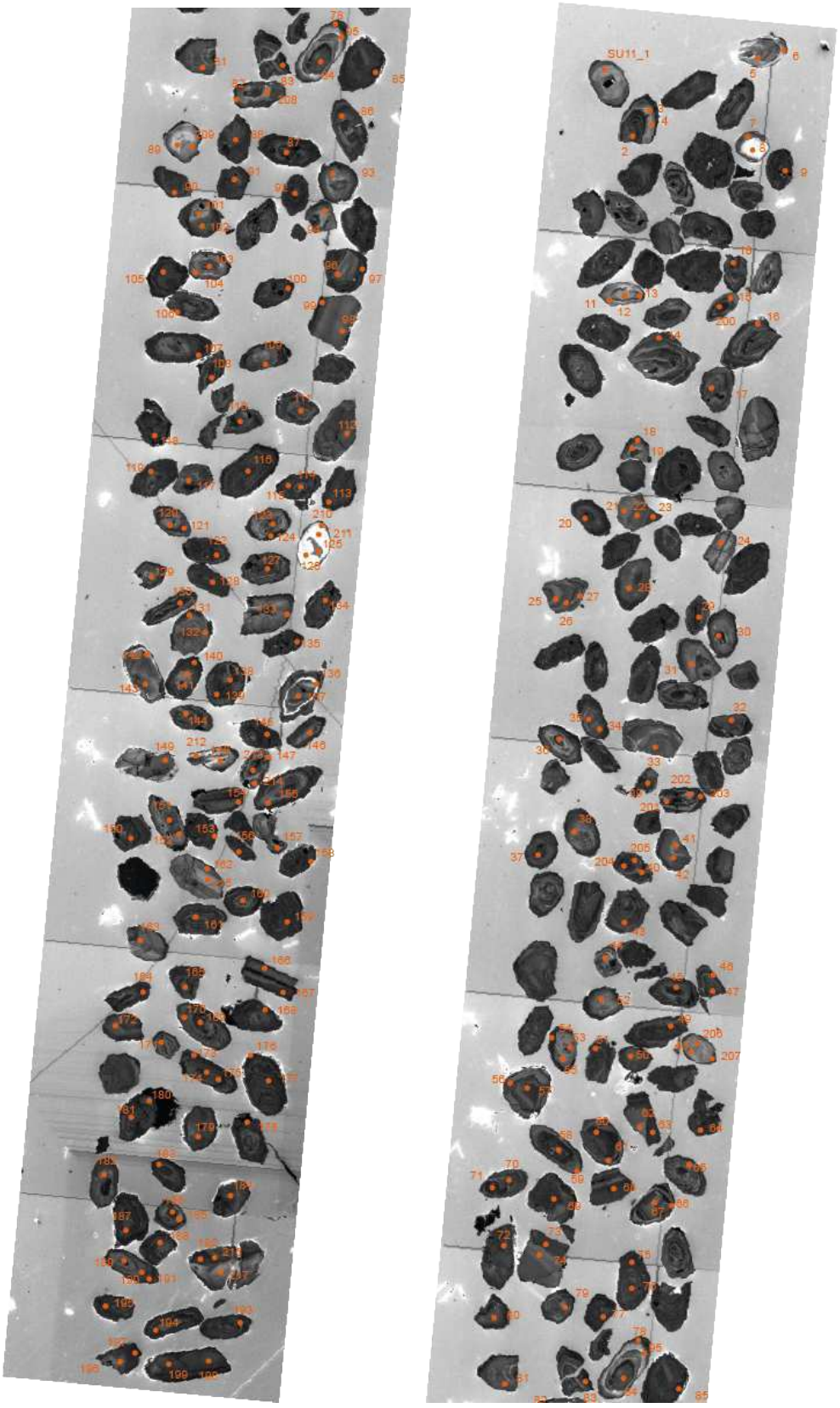
SU11_1

Analytical details

U-Pb isotope compositions in zircon were analyzed by LA-ICP-MS at CMCA (UWA) the 03/10/2023. Lu-Hf isotope compositions in zircon were analyzed by LA-ICP-MS at CMCA (UWA) the 20/10/2023.

Results

U-Pb

217 spots were analyzed on numerous zircon grains. 145 analyses fall onto the concordia, 29 are discordant and 43 failed (inclusions or fractures). Results are shown in a Tera-Wasserburg and weighted mean diagrams.

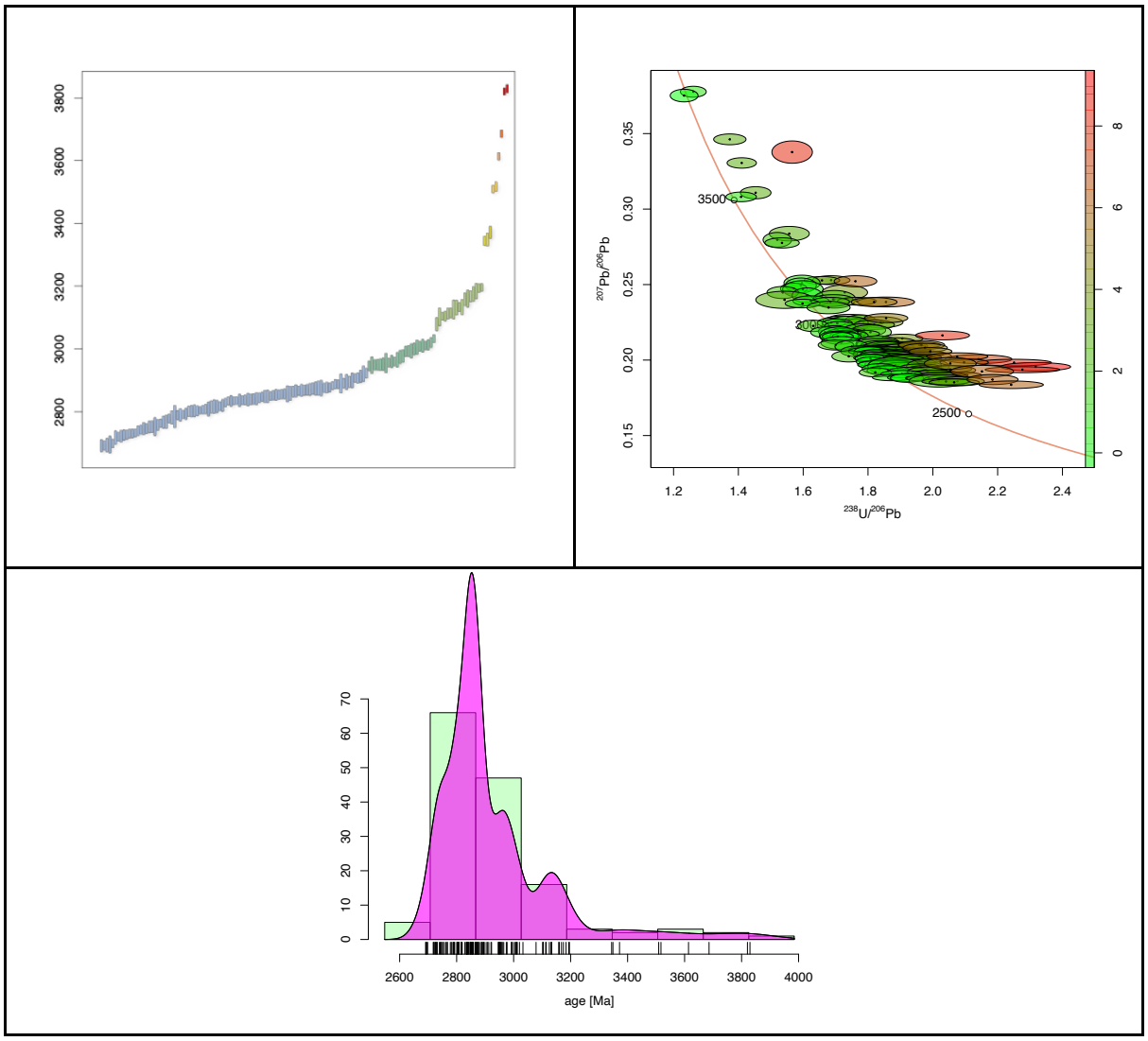

Figure SM2-2.27: U-Pb analyses results for sample SU11. Left: temporal repartition of the 145 concordant zircon analyses (< 8%). Right: shows the Tera-Wasserburg plots (green and orange ellipses show the concordant and near

concordant data, red ellipses show the discordant analyses, > 8 % discordant). Bottom: Distribution of concordant ages (KDE).

Interpretation

U-Pb isotopy

The analyses range from concordant to strongly discordant. 29 analyses were > 8% discordant. The dates obtained from the 145 analyses have a good precision and spread from 3820 to 2700 Ma. The youngest age is interpreted to date the maximum age of sedimentation in the basin.

Lu/Hf analyses

Lu-Hf analyses were acquired on near concordant zircons, they returned $^{176}Hf/^{177}Hf_i$ of 0.280951 ± 0.000016. The corresponding εHf_t for this dataset is comprised between -8.3 and 7.1 an individual error of (2s) 0.8. Three trends can be highlighted from the analyses, the Hf model ages calculated for these trends are estimated between: 2830 and 3060 Ma, 3060 and 3420 Ma; 3620 and 3800 Ma (using $^{176}Hf/^{177}Hf$ =0.0115).

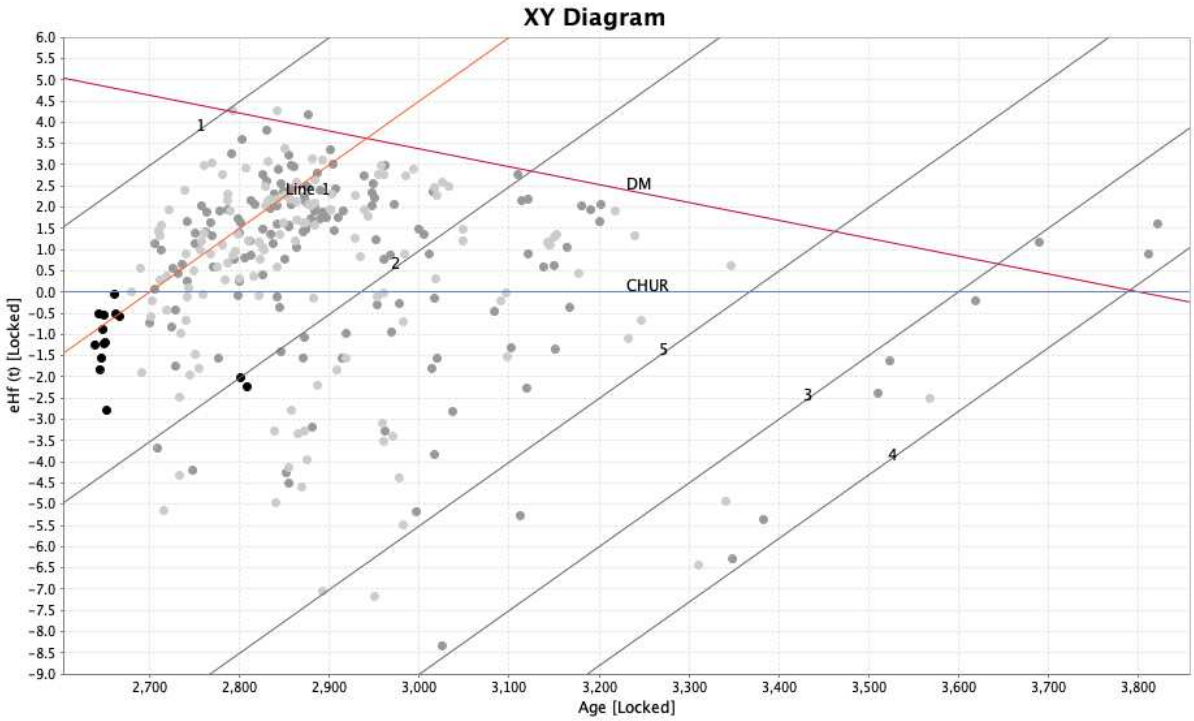

Figure SM2-2.28: εHf vs Age of magmatic samples. Light grey: SU20, dark grey: SU11, black: SU10A.

SU15

Sample Localization regional context

(32.6374; -3.0427)

Sampled in a crop, less than 1km south of the southern limit between the SGGB and granitoids. Quartz-monzonite with a tectonic fabric: N297-70. Tension quartz veins (245-50) and small brittle fractures (330-75) with dextral kinematics.



Figure SM2-2.29: Sample SU15 photographs.

Sample description

SU15 consists of a quartz-monzonite with quartz, plagioclase, K-feldspar, chloritised biotite and sericite grains. Tectonic fabric highlighted by Ser and chloritised Bt grains. Textures: quartz GBM and plagioclase GBAR.

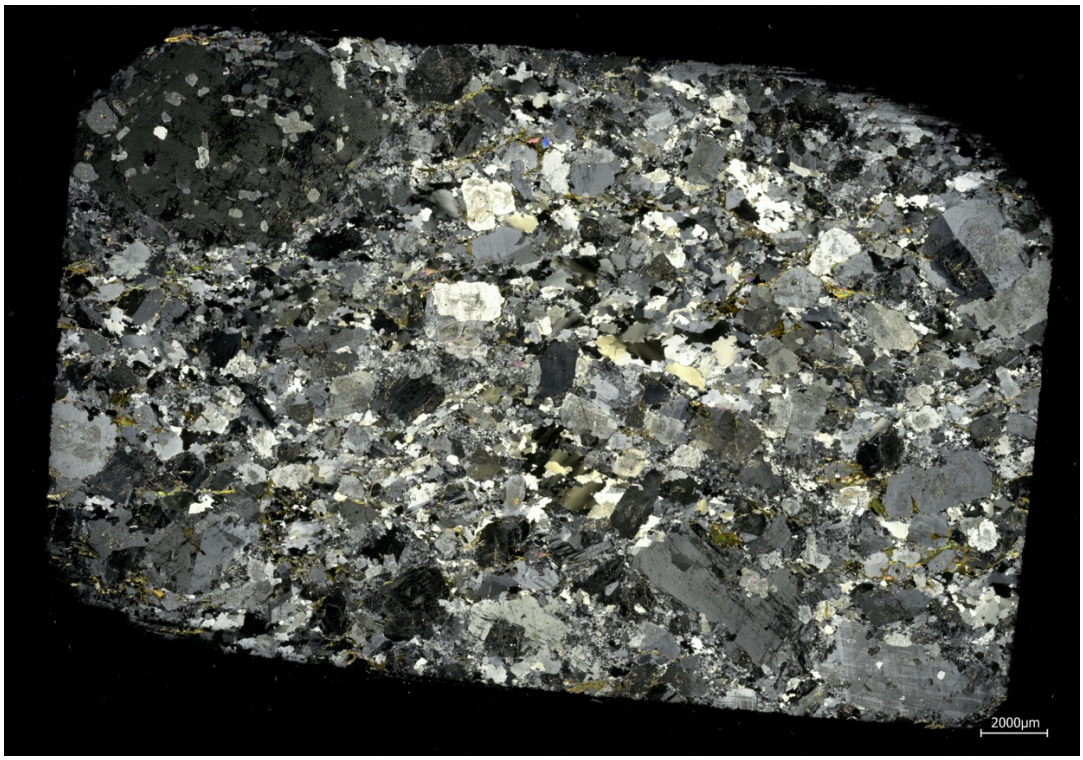

Figure SM2-2.30: Micrograph of sample SU15 in cross-polarized analyzed light.

Zircon morphology

101 zircon crystals were isolated from this sample, all colourless to light brown, mainly euhedral. Grains can be up to 150 µm long, and mainly elongated and prismatic. In cathodoluminescence images, zircon grains present oscillatory zoning with light cores and few thin rims.



Figure SM2-2.31: Above: cathodoluminescence and transmitted light images of representative zircons from sample SU15.

Below: location of O-Hf-U-Pb analyses.

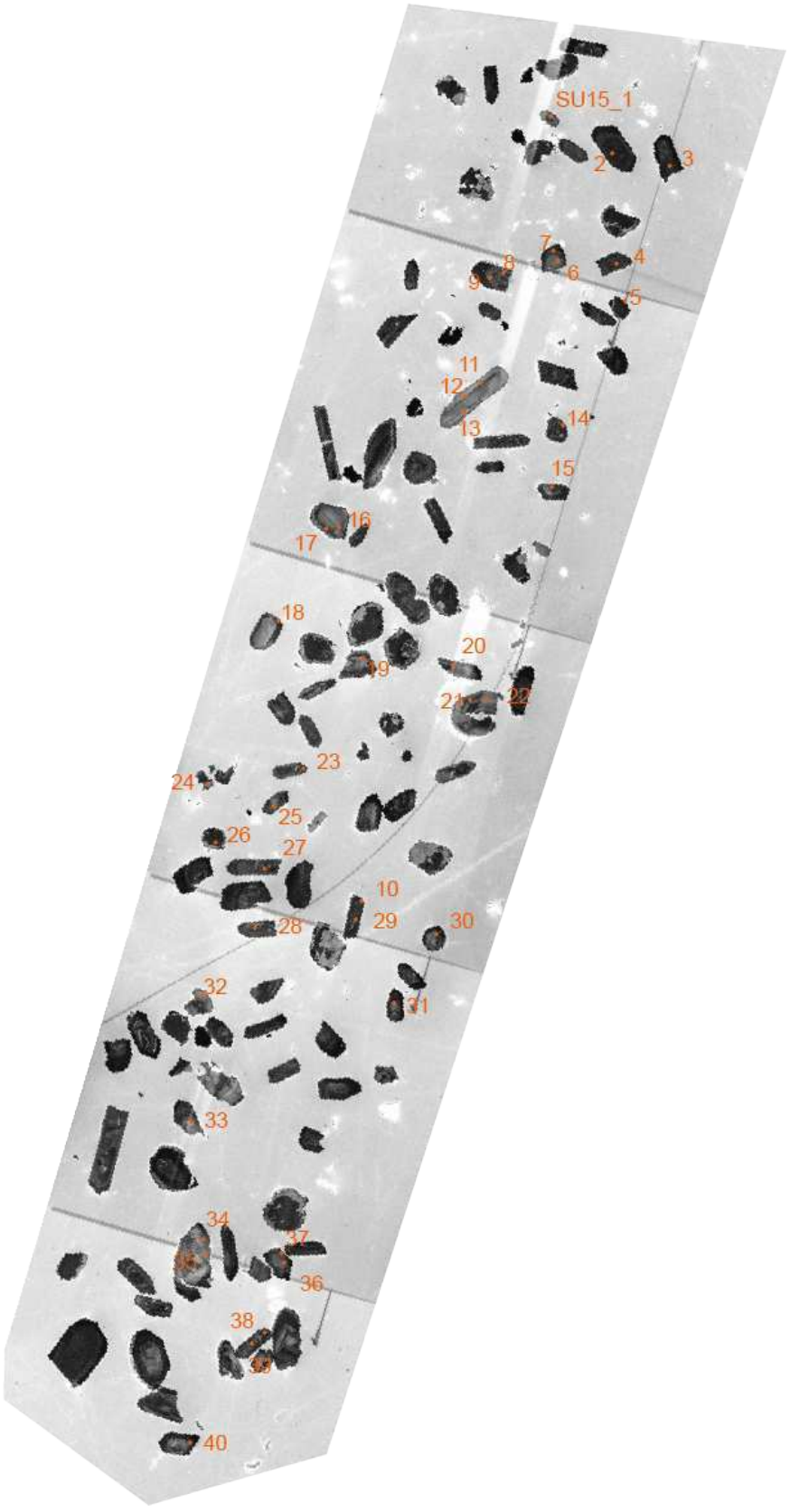

Analytical details

O isotope ratios ($^{16}O/^{18}O$ and $^{16}O^{1}H/^{16}O$) were determined using SIMS at CMCA (UWA) the 06/09/2023. U-Pb isotope compositions in zircon were analyzed by LA-ICP-MS at CMCA (UWA) the 16/09/2023. Lu-Hf isotope compositions in zircon were analyzed by LA-ICP-MS at CMCA (UWA) the 20/10/2023.

Results

O isotopy

40 spots were analyzed on 30 zircon grains. 22 analyses show low $^{16}O^{1}H/^{16}O$, the 18 others are considered as outliers. Results are shown in a $\delta^{18}O$ - $^{16}O^{1}H/^{16}O$ diagram.

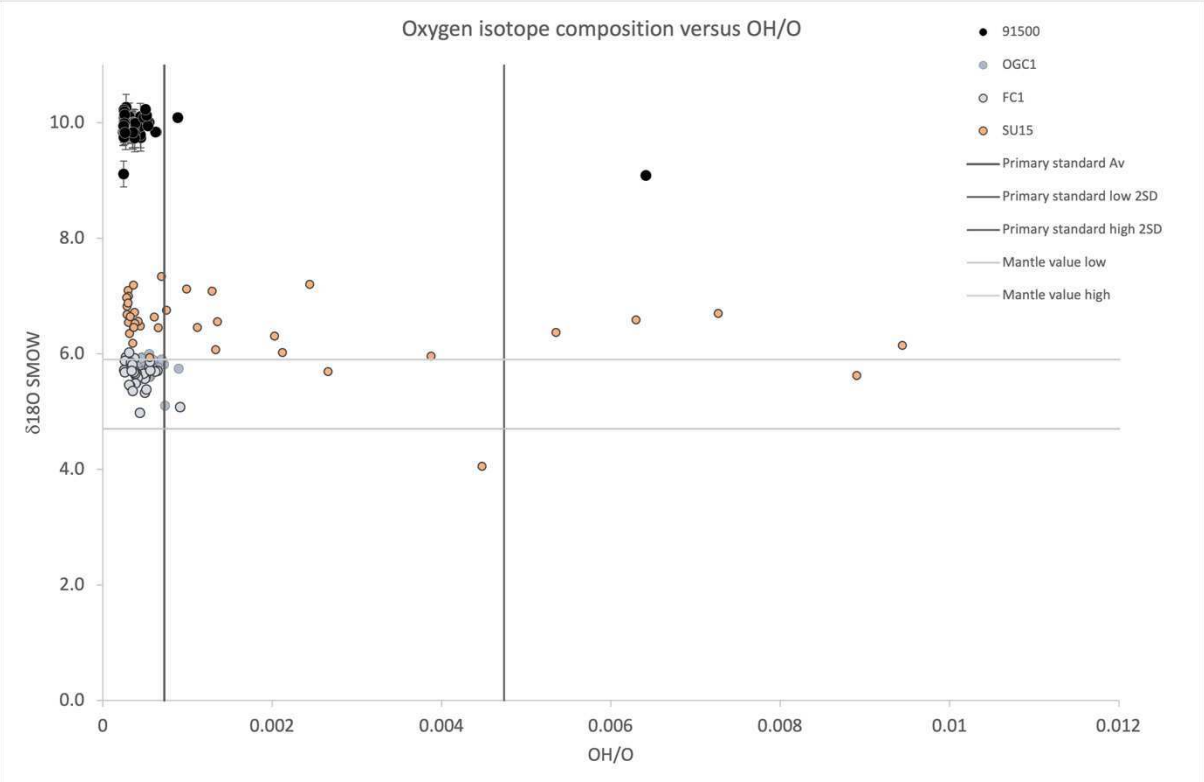

Figure SM2-2.32: $\delta^{18}O$ vs $^{16}O^{1}H/^{16}O$ analyses results for sample SU15

U-Pb isotopy

31 spots were analyzed on 24 zircon grains. 23 analyses fall onto the concordia, 1 is discordant and 7 failed (inclusions or fractures). Results are shown in a Tera-Wasserburg and weighted mean diagrams.

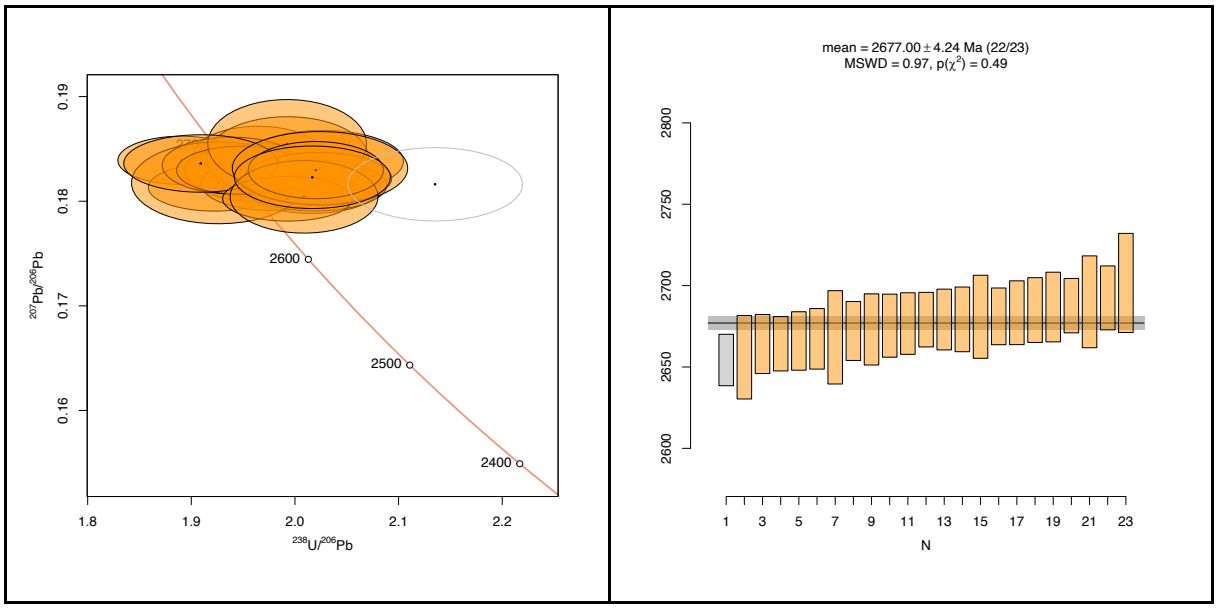

Figure SM2-2.33: U-Pb analyses results for sample SU15. Left: shows the Tera-Wasserburg plots (orange ellipses show the concordant and near concordant data, transparent ellipses show the discordant analyses > 3% discordant). Right: Weighted mean averages calculated using the concordant analyses.

Interpretation

O isotopy

Mean value at 6.66 ± 0.23 ‰. The analyses fall around the upper mean mantle values limit, indicating that the source of the granite includes material that has undergone low temperature oxygen exchanges in the hydrosphere (volcano-sediments or rock that went to supra-crustal depths before melting).

U-Pb isotopy

The analyses range from concordant to slightly discordant. One analysis is 7 % discordant, the rest is ≤ 3 % discordant. The dates obtained from the 23 analyses have a good precision, based on their $^{207}Pb/^{206}Pb$ ratios: they yield a weighted mean date of 2677 ± 4 Ma (MSWD = 0.97). The discordia plot with 24 data returned an upper intersection at 2680 ± 7 Ma (MSWD = 1.1). The age is interpreted to represent the crystallization age of SU15 quartz-monzonite.

Lu/Hf analyses

Lu-Hf analyses were acquired on 11 near concordant zircons, they returned $^{176}Hf/^{177}Hf_i$ of 0.281117 ± 0.000017. The corresponding εHf_t for this dataset is comprised between -0.6

and 1.0 an individual error of (2s) 0.7. Hf model age calculated for this analysis is estimated between ca. 2820 and 2910 Ma (using $^{176}Hf/^{177}Hf$ =0.0115).

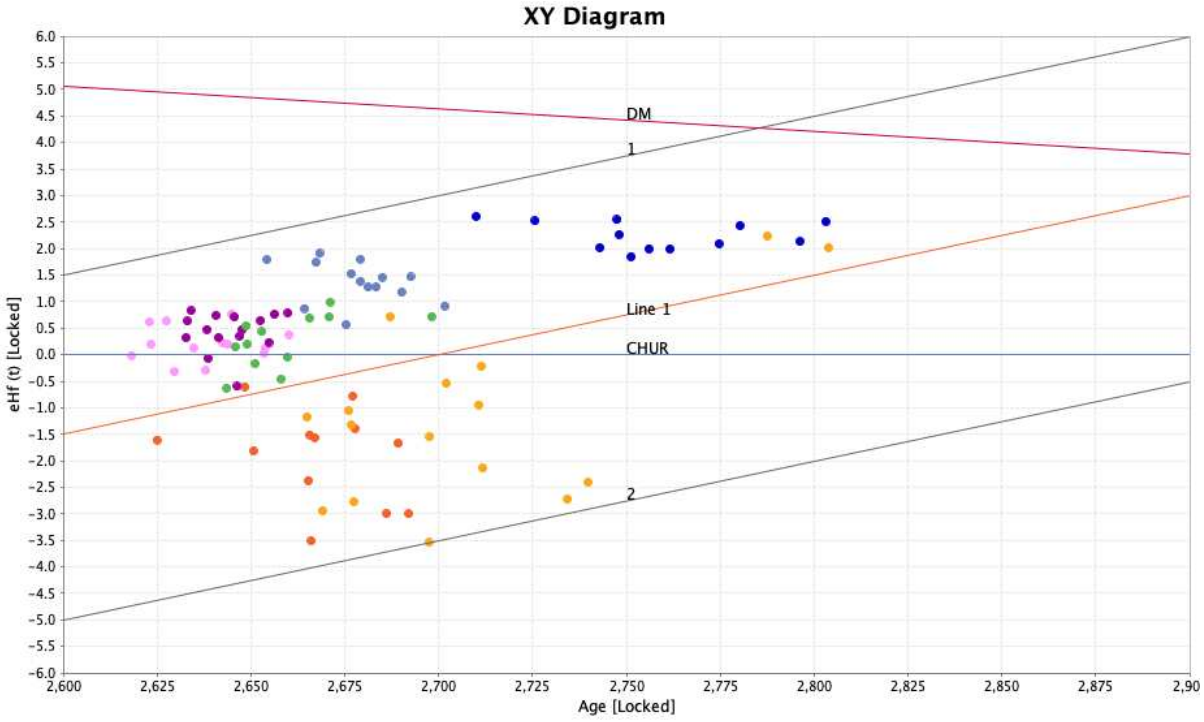

Figure SM2-2.34: εHf vs Age of magmatic samples. Dark blue: SU21, light blue: SU15, green: SU10B, purple: SU16, pink: SU25, yellow: SU06, orange: SU04.

SU16

Sample Localization regional context

(32.6745; -3.1071)

Sampled on a hill, less than 1km south of the southern limit between the SGGB and granitoids. Granite with no deformation.

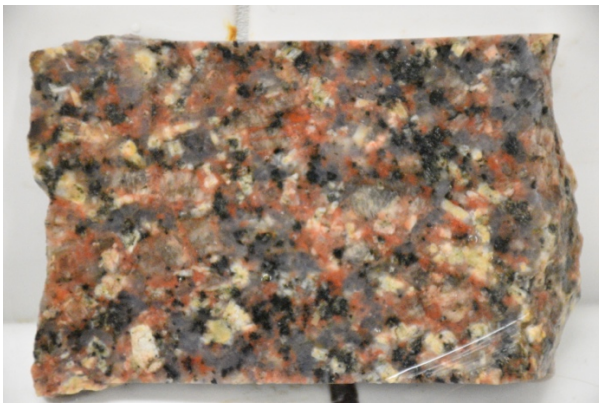

Figure SM2-2.35: Sample SU16 photograph.

Sample description

SU16 consists of a granite with quartz, K-feldspar, plagioclase, biotite, ± sericite grains and rare pyrite. Small late fractures are filled with sericite and chlorite.

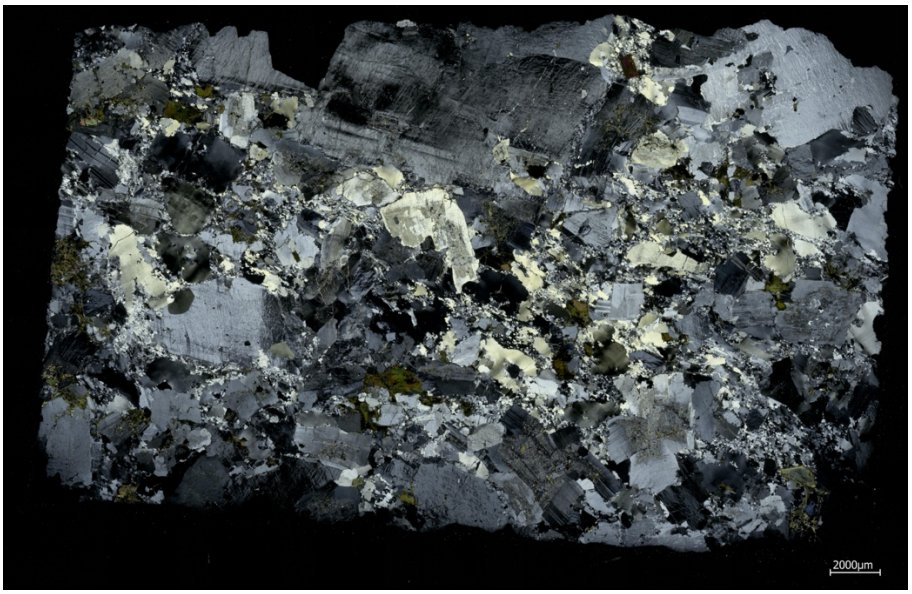

Figure SM2-2.36: Micrographs of sample SU16 in cross-polarized analyzed light.

Zircon morphology

133 zircon crystals were isolated from this sample, all light to dark brown, mainly euhedral with quite a few fractures. Grains can be up to 300 µm long, and mainly prismatic and more rarely elongated. In cathodoluminescence images, zircon grains present oscillatory zoning with light cores and few thin rims.

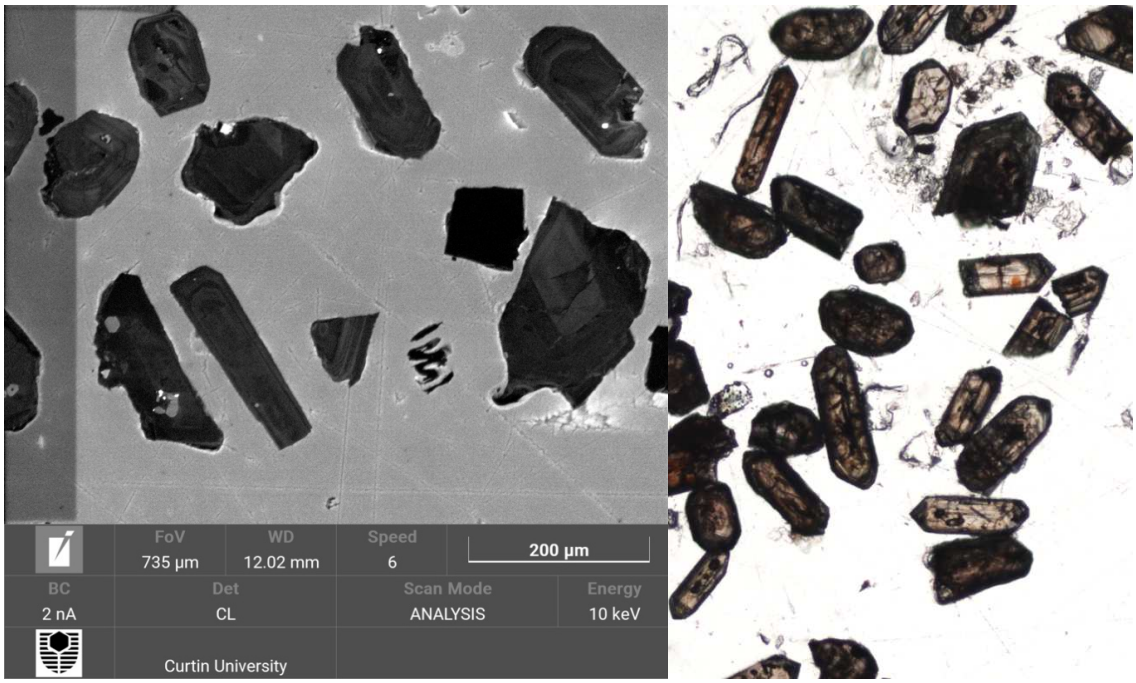

Figure SM2-2.37: **Above**: cathodoluminescence and transmitted light images of representative zircons from sample SU16. **Below**: location of O-Hf-U-Pb analyses.

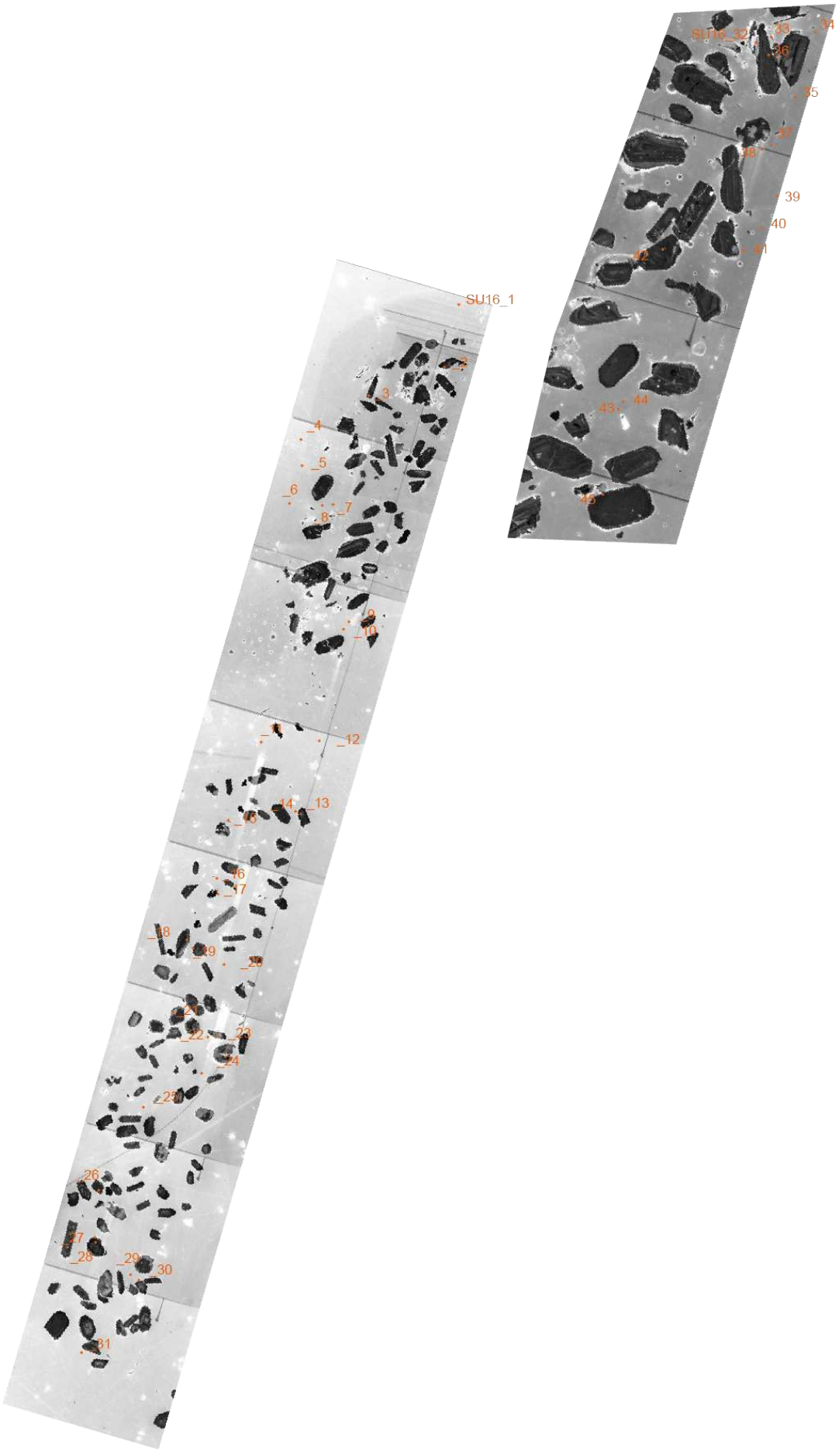
SU16_1
SU16_32

Analytical details

O isotope ratios ($^{16}O/^{18}O$ and $^{16}O^{1}H/^{16}O$) were determined using SIMS at CMCA (UWA) the 06/09/2023. U-Pb isotope compositions in zircon were analyzed by LA-ICP-MS at CMCA (UWA) the 16/09/2023. Lu-Hf isotope compositions in zircon were analyzed by LA-ICP-MS at CMCA (UWA) the 20/10/2023.

Results

O isotopy

45 spots were analyzed on 35 zircon grains. 23 analyses show low $^{16}O^{1}H/^{16}O$, the 17 others are considered as outliers. Results are shown in a $\delta^{18}O$ - $^{16}O^{1}H/^{16}O$ diagram.

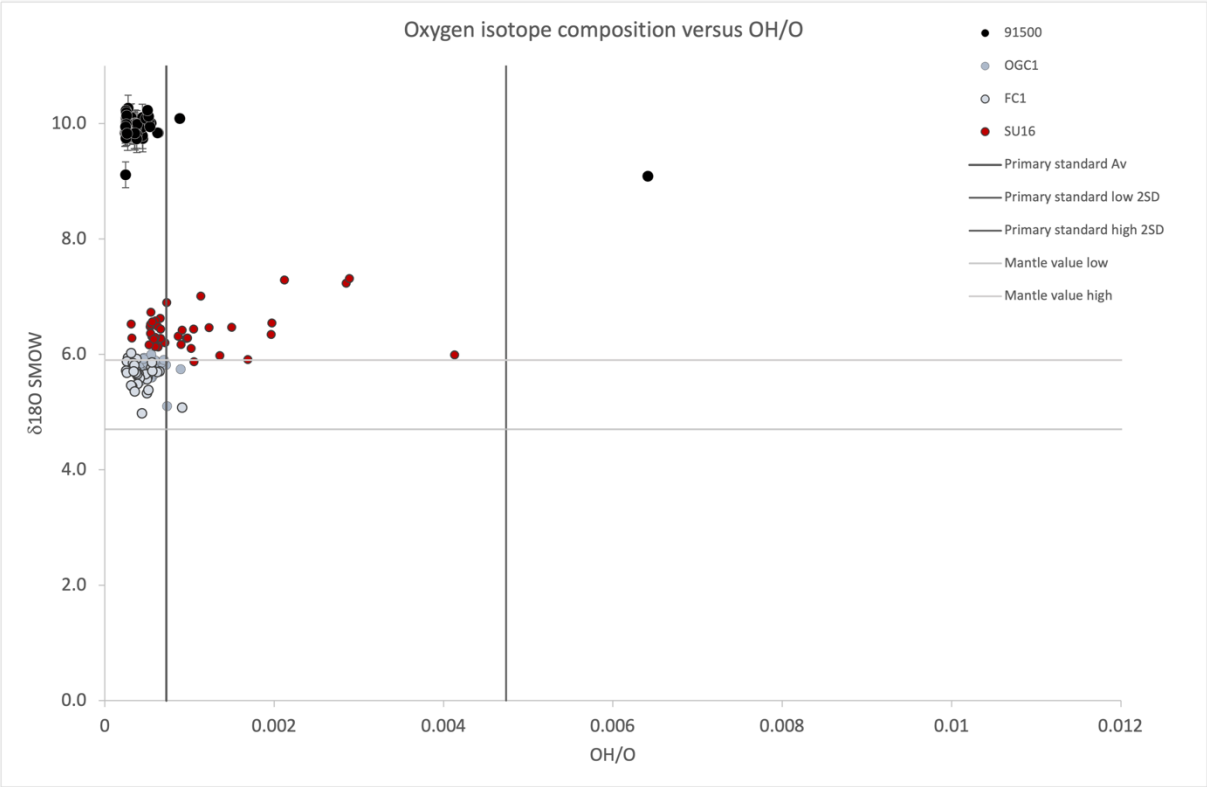

Figure SM2-2.38: $\delta^{18}O$ vs $^{16}O^{1}H/^{16}O$ analyses results for sample SU16.

U-Pb isotopy

41 spots were analyzed on 32 zircon grains. 22 analyses fall onto the concordia, 11 are discordant and 8 failed (inclusions or fractures). Results are shown in a Tera-Wasserburg and weighted mean diagrams.

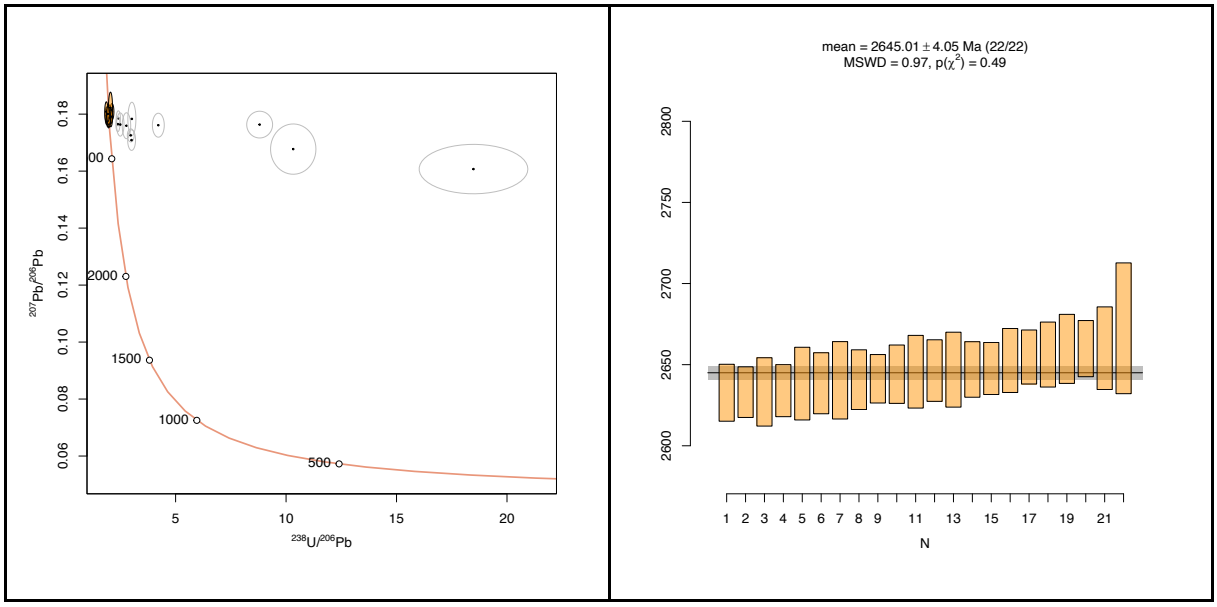

Figure SM2-2.39: U-Pb analyses results for sample SU16. Left: shows the Tera-Wasserburg plots (orange ellipses show the concordant and near concordant data, transparent ellipses show the discordant analyses (> 8% discordant). Right: Weighted mean averages calculated using the concordant analyses.

Interpretation

O isotopy

Mean value at 6.40 ± 0.23 ‰. The analyses fall around the upper mean mantle values limit, indicating that the source of the granite includes material that has undergone low temperature oxygen exchanges in the hydrosphere (volcano-sediments or rock that went to supra-crustal depths before melting).

U-Pb isotopy

The analyses range from concordant to strongly discordant. 11 analyses were > 8% discordant. The dates obtained from the 22 analyses have a good precision, based on their $^{207}Pb/^{206}Pb$ ratios: they yield a weighted mean date of 2645 ± 4 Ma (MSWD = 0.97). The discordia plot with 35 data returned an upper intersection at 2641 ± 4 Ma (MSWD = 2.7). The age is interpreted as the crystallization age of the SU16 granite.

Lu/Hf analyses

Lu-Hf analyses were acquired on 13 near concordant zircons, they returned $^{176}Hf/^{177}Hf_i$ of 0.281140 ± 0.000015. The corresponding εHf_t for this dataset is comprised between -0.6 and 0.8 an individual error of (2s) 0.8. Hf model age calculated for this analysis is estimated between ca. 2850 and 2950 Ga (using $^{176}Hf/^{177}Hf$ =0.0115).

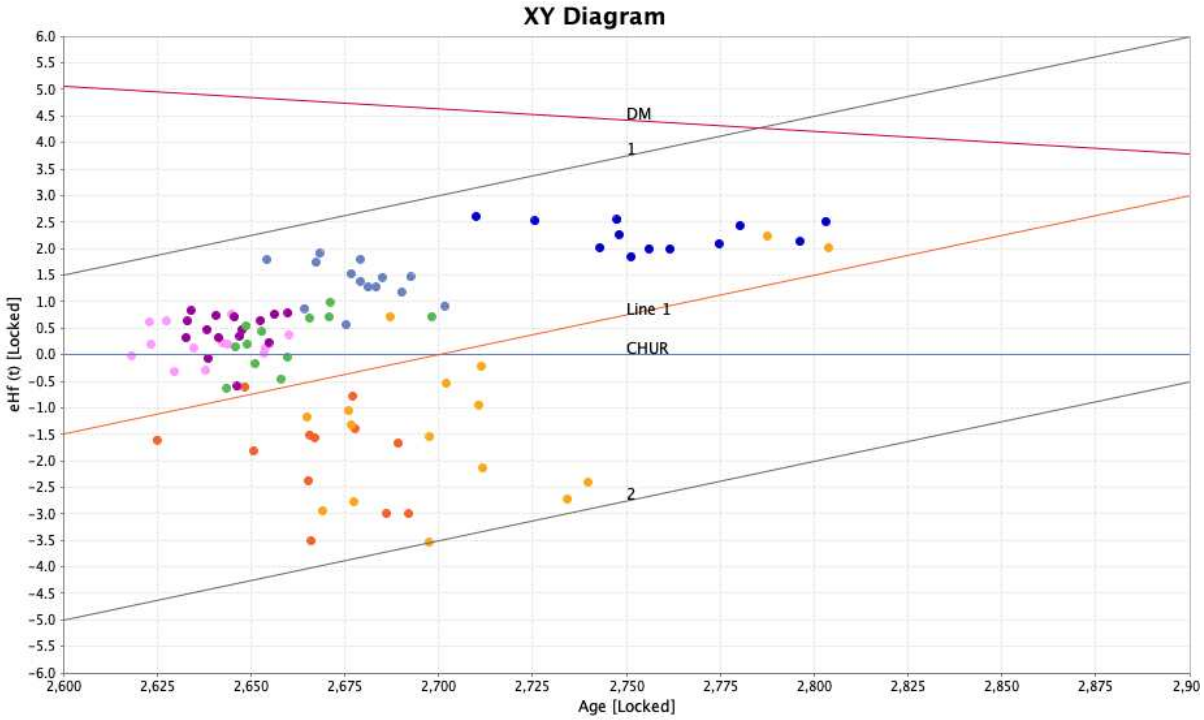

Figure SM2-2.40: εHf vs Age of magmatic samples. Dark blue: SU21, light blue: SU15, green: SU10B, purple: SU16, pink: SU25, yellow: SU06, orange: SU04.

SU20

Sample Localization regional context

(32.7984; -2.9078)

Sampled on a hill, less than 1 km south of the northern limit between the SGGB and granitoids. Folded meta-graywacke and conglomerates with quartz pebbles in a syn-orogenic basin. Crossbedding visible, S_0 = 090/105-60. Late tension quartz veins more or less folded, dextral shearing S_x = 115-85.



Figure SM2-2.41: Sample SU20 photographs.

Sample description

SU20 consists of a metagreywacke with quartz clasts in a quartz-sericite matrix. The S_0 and S_x are outlined by the fine sericitized matrix.

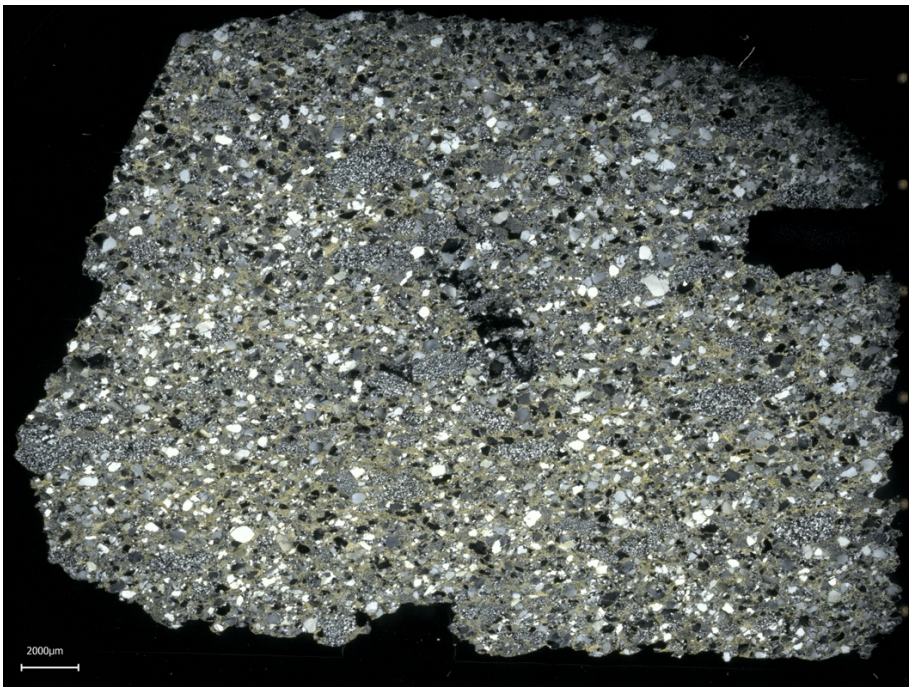

Figure SM2-2.42: Micrograph of sample SU20 in cross-polarized analyzed light.

Zircon morphology

More than 200 zircon crystals were isolated from this sample, some transparent with no fracture, others light to dark brown with quite a few fractures. Grains are more or less rounded and can be up to 400 µm long, mainly prismatic and very rarely elongated. In cathodoluminescence images, zircon grains present various patterns, from very light grains with 1 or 2 rims, to light grains with oscillatory zoning, to dark to very dark grains with more or less defined oscillatory zoning.

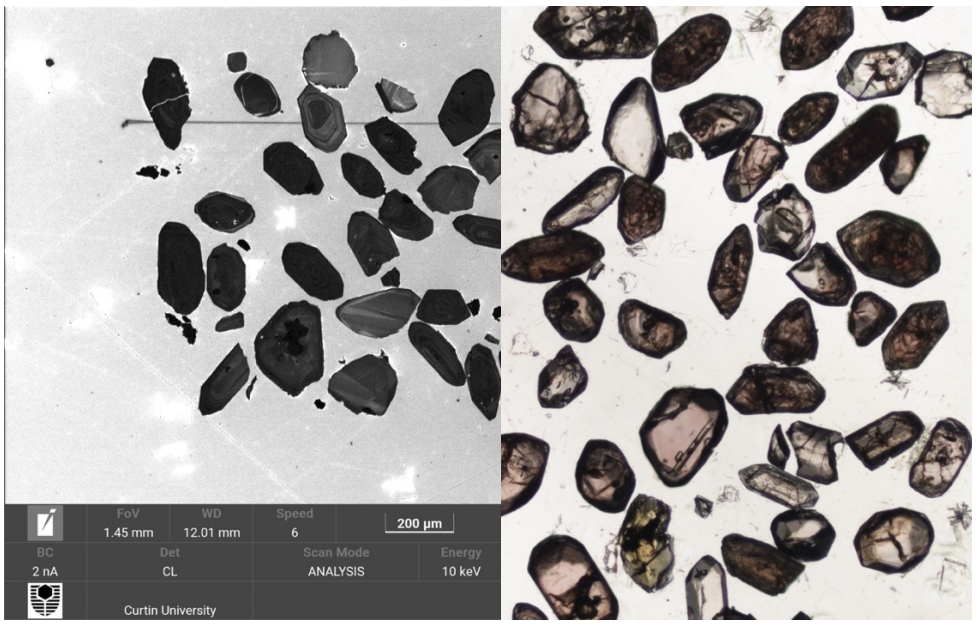

Figure SM2-2.43: Above: cathodoluminescence and transmitted light images of representative zircons from sample SU20. **Below**: location of O-Hf-U-Pb analyses.

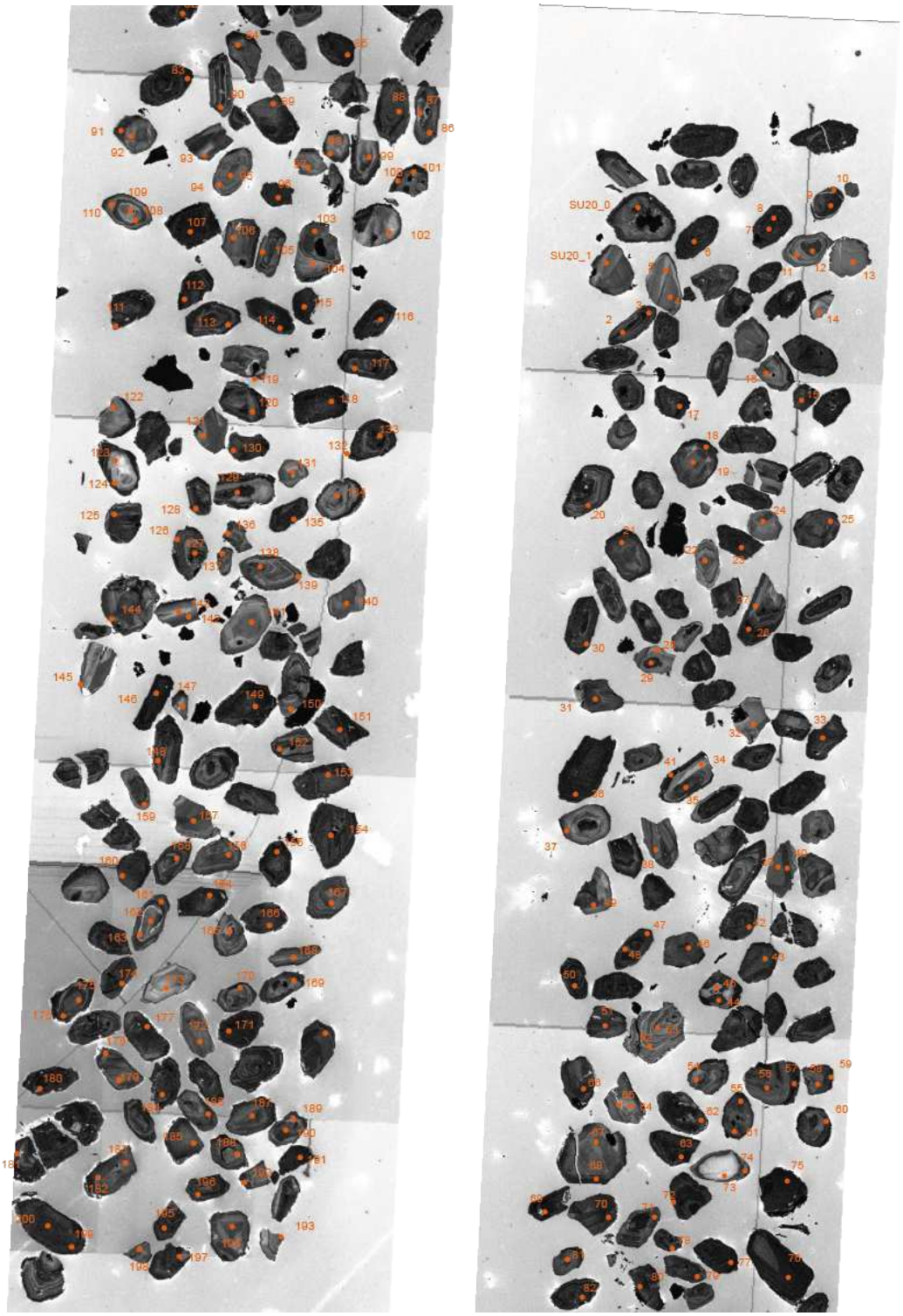
SU20_0
SU20_1

Analytical details

U-Pb isotope compositions in zircon were analyzed by LA-ICP-MS at CMCA (UWA) the 03/10/2023. Lu-Hf isotope compositions in zircon were analyzed by LA-ICP-MS at CMCA (UWA) the 20/10/2023.

Results

200 spots were analyzed. 142 analyses fall onto the concordia, 30 are discordant and 29 failed (inclusions or fractures). Results are shown in a Tera-Wasserburg and weighted mean diagrams.

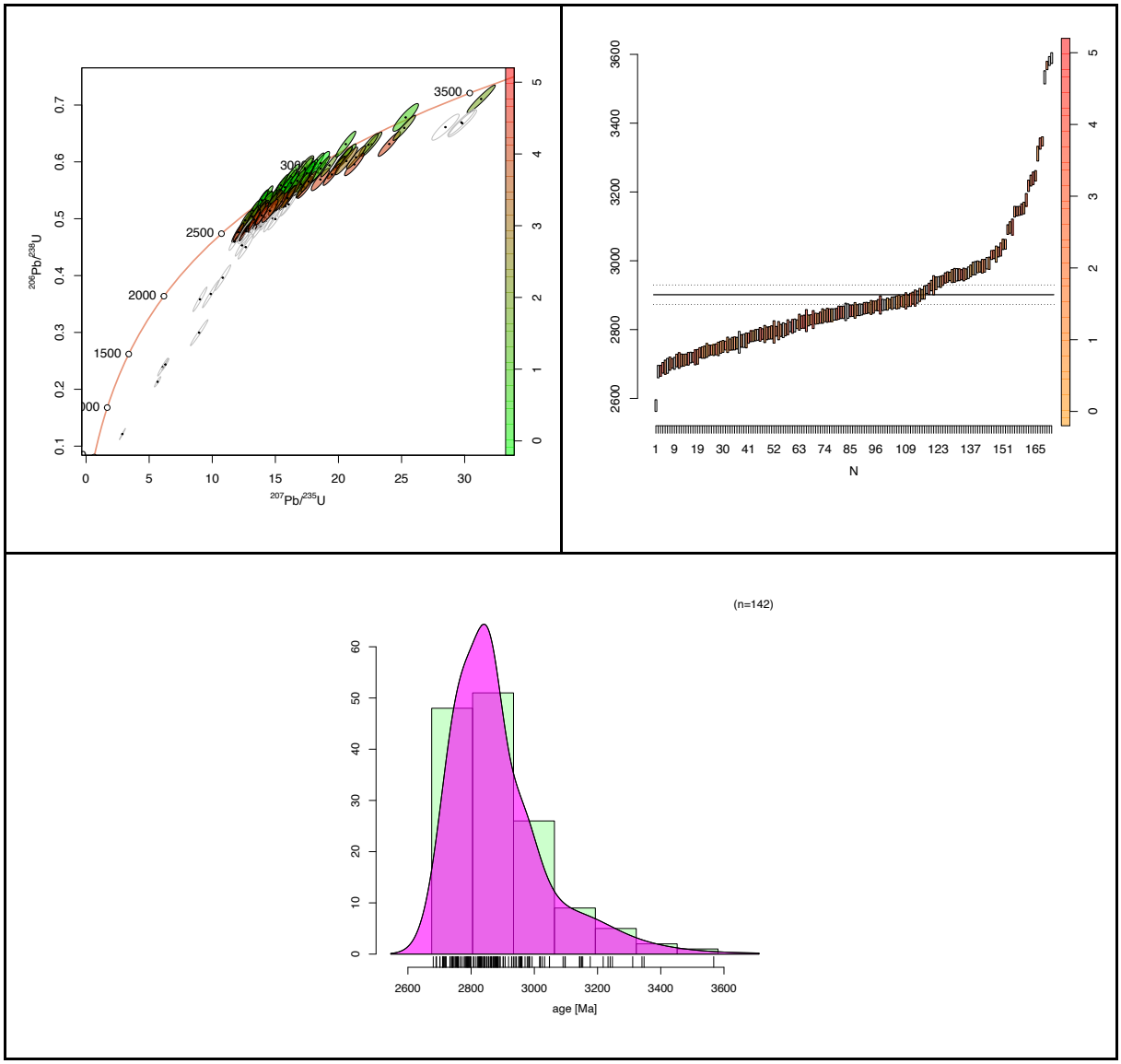

Figure SM2-2.44: U-Pb analyses results for sample SU11. Left: temporal repartition of the 145 concordant zircon analyses (< 8%). Right: shows the Tera-Wasserburg plots (green to red ellipses show the concordant and near concordant data, transparent ellipses show the discordant analyses, > 8 % discordant). Bottom: Distribution of concordant ages (KDE).

Interpretation

U-Pb analyses

The analyses range from concordant to strongly discordant. 30 analyses were > 8% discordant. The dates obtained from the 142 analyses have a good precision and spread from 3568 to 2680 Ma. The youngest age is interpreted to date the maximum age of sedimentation in the basin.

Lu/Hf analyses

Lu-Hf analyses were acquired on near concordant zircons, they returned $^{176}Hf/^{177}Hf_i$ of 0.280972 ± 0.000015. The corresponding εHf_t for this dataset is comprised between -7.2 and 4.3 an individual error of (2s) 0.7. Three trends can be highlighted from the analyses, the Hf model ages calculated for these trends are estimated between: 2820 and 3100 Ma, 3100 and 3420 Ma, 3610 and 3800 Ma (using $^{176}Hf/^{177}Hf$ =0.0115).

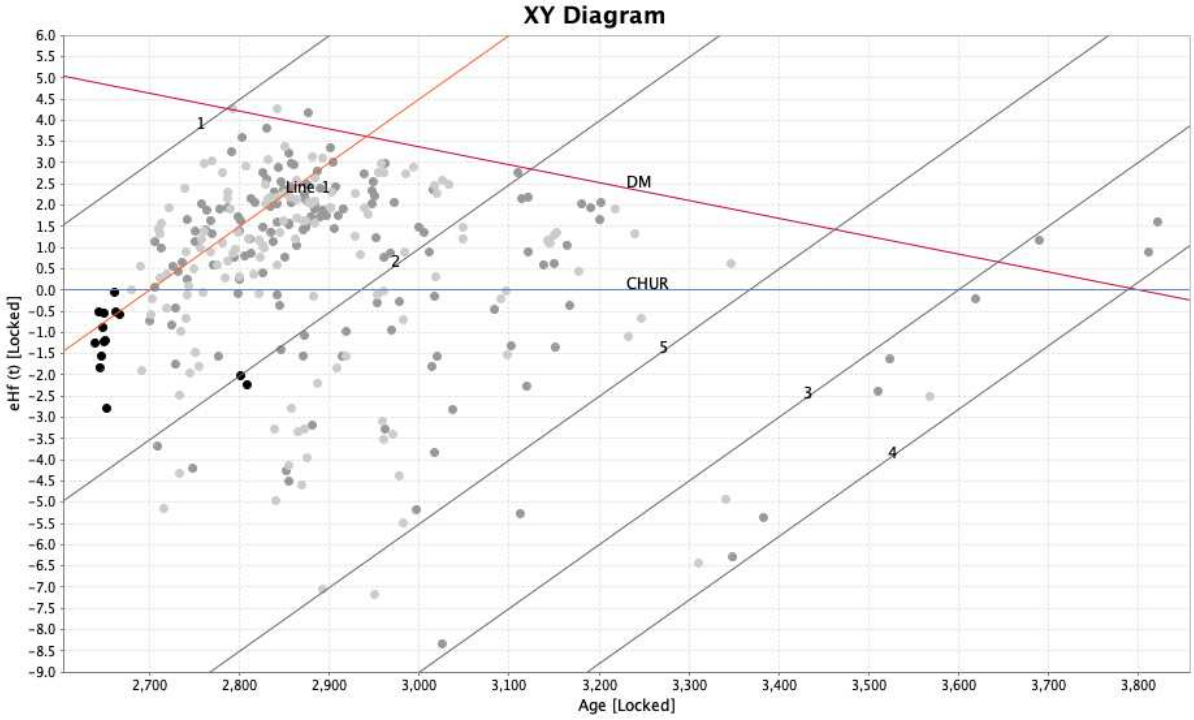

Figure SM2-2.45: εHf vs Age of magmatic samples. Light grey: SU20, dark grey: SU11, black: SU10A.

SU21

Sample Localization regional context

(32.7922; -2.9142)

Sampled between two hills, at the heart of a crustal-scale shear zone. Highly deformed and weathered granitoid.

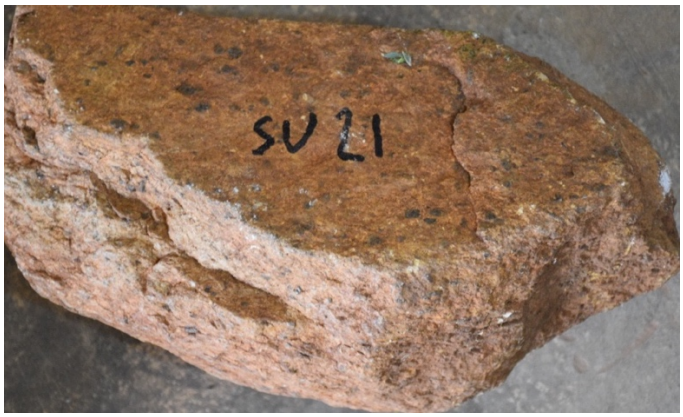

Figure SM2-2.46: Sample SU21 photograph.

Sample description

SU21 consists of a highly weathered granitoid with quartz, K-feldspar, biotite grains. Weathering is expressed by strong carbonatation of K-feldspar grains and chloritisation in the C/S shear bands.

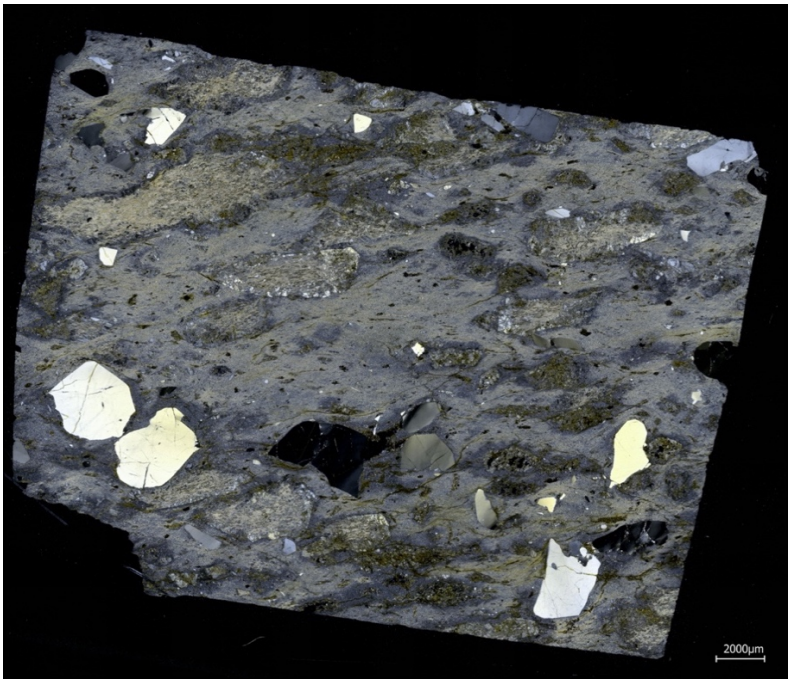

Figure SM2-2.47: Micrograph of sample SU21 in cross-polarized analyzed light.

Zircon morphology

101 zircon crystals were isolated from this sample, mainly light to dark brown, euhedral with few fractures. Grains can be up to 300 µm long, and mainly prismatic. In cathodoluminescence images, zircon grains present oscillatory zoning with light cores and few thin rims. A very light rim in the middle of the oscillatory zoning presents irregularities.

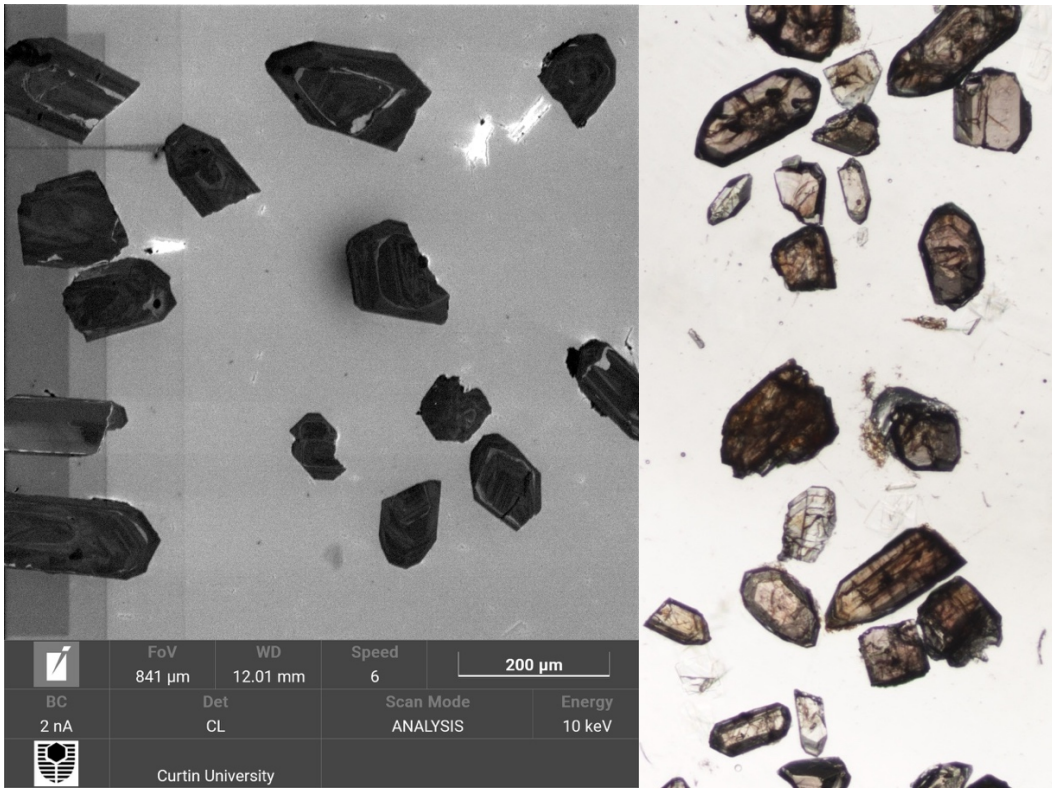

Figure SM2-2.48: Above: cathodoluminescence and transmitted light images of representative zircons from sample SU21. **Below**: location of O-Hf-U-Pb analyses.

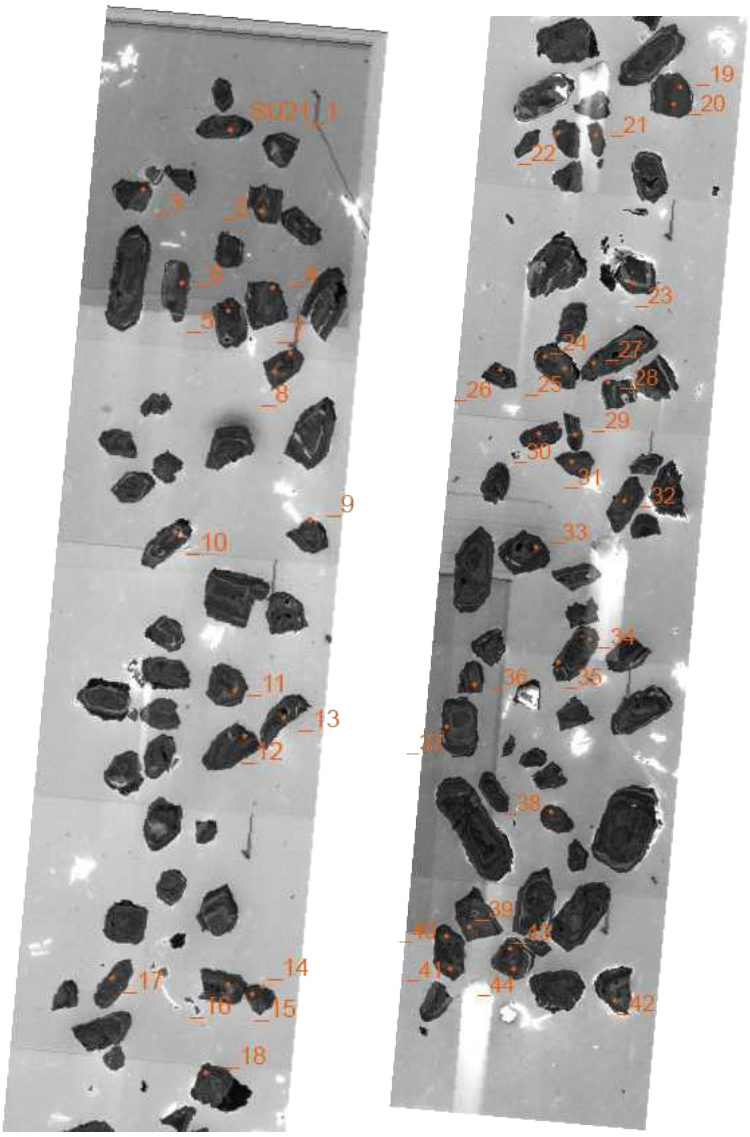
_1
_2
_3
_4
_5
_6
_7
_8
_9
_10
_11
_12
_13
_14
_15
_16
_17
_18
_19
_20
_21
_22
_23
_24
_25
_26
_27
_28
_29
_30
_31
_32
_33
_34
_35
_36
_37
_38
_39
_40
_41
_42
_43
_44

Analytical details

O isotope ratios ($^{16}O/^{18}O$ and $^{16}O^{1}H/^{16}O$) were determined using SIMS at CMCA (UWA) the 06/09/2023. U-Pb isotope compositions in zircon were analyzed by LA-ICP-MS at CMCA (UWA) the 03/10/2023. Lu-Hf isotope compositions in zircon were analyzed by LA-ICP-MS at CMCA (UWA) the 20/10/2023.

Results

O isotopy

44 spots were analyzed on 37 zircon grains. 20 analyses show low $^{16}O^{1}H/^{16}O$, the 24 others are considered as outliers. Results are shown in a $\delta^{18}O$ - $^{16}O^{1}H/^{16}O$ diagram.

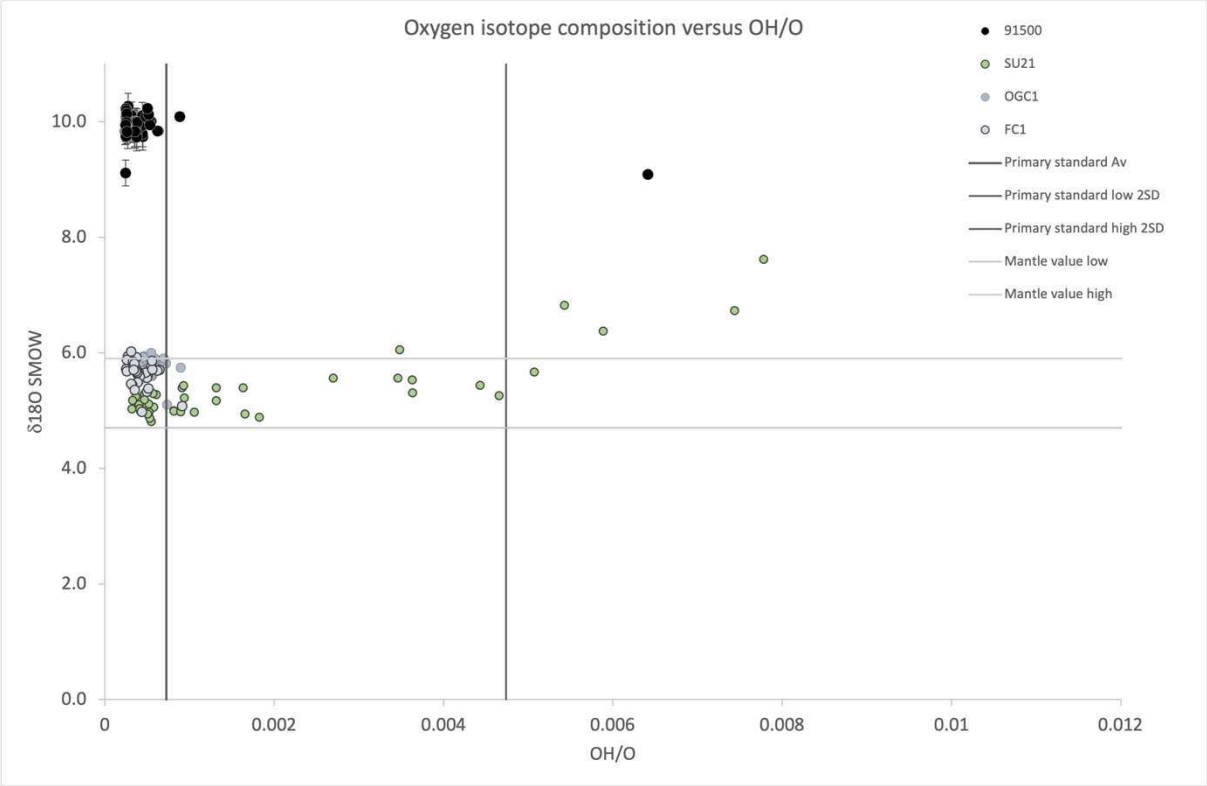

Figure SM2-2.50: $\delta^{18}O$ vs $^{16}O^{1}H/^{16}O$ analyses results for sample SU21.

U-Pb isotopy

36 spots were analyzed on 37 zircon grains. 11 analyses fall onto the concordia, 17 are discordant and 4 failed (inclusions or fractures). Results are shown in a Tera-Wasserburg and weighted mean diagrams.

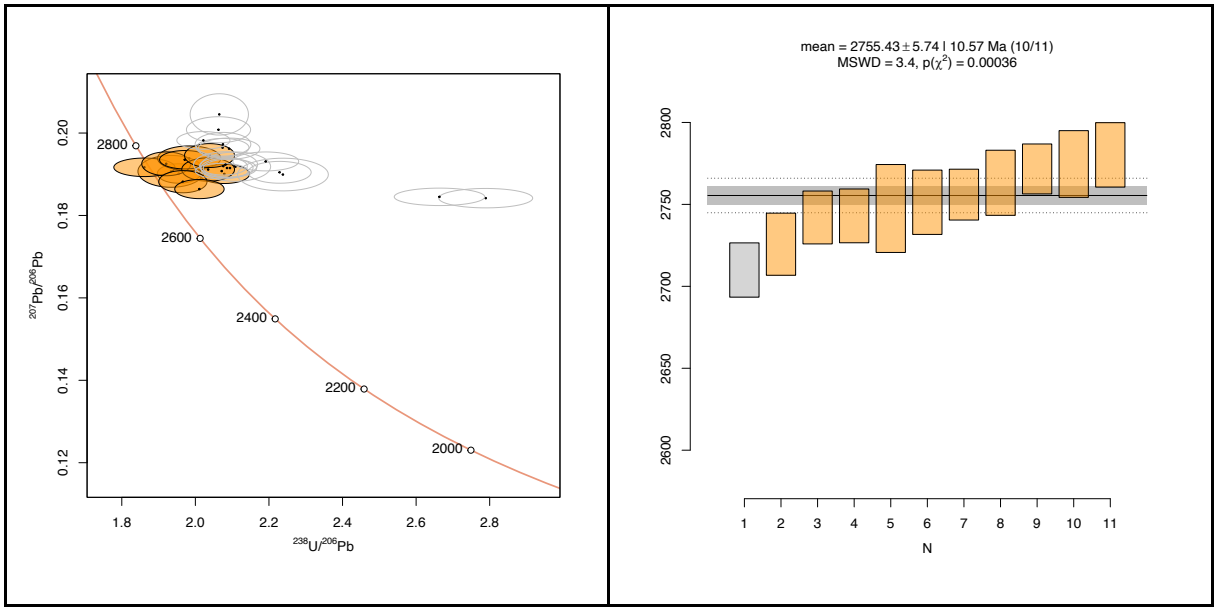

Figure SM2-2.51: U-Pb analyses results for sample SU21. Left: shows the Tera-Wasserburg plots (orange ellipses show the concordant and near concordant data, transparent ellipses show the discordant analyses (> 8% discordant). Right: Weighted mean averages calculated using the concordant analyses.

Interpretation

O isotopy

Mean value at 5.12 ± 0.14 ‰. The analyses all fall within the mean mantle values, indicating that the source of SU21 is mantle-derived.

U-Pb isotopy

The analyses range from concordant to strongly discordant. 17 analyses were > 8 % discordant. The dates obtained from the 11 analyses have a good precision, based on their $^{207}Pb/^{206}Pb$ ratios: they yield a weighted mean date of 2755 ± 11 Ma (MSWD = 3.4). The age is interpreted as the crystallization age of the SU21 granitoid.

Lu/Hf analyses

Lu-Hf analyses were acquired on 13 near concordant zircons, they returned 176Hf/177Hfi of 0.281128 ± 0.000015. The corresponding εHft for this dataset is

comprised between 1.9 and 2.6 an individual error of (2s) 0.7. Hf model age calculated for this analysis is estimated between ca. 2850 and 2900 Ga (using $^{176}Hf/^{177}Hf$ =0.0115).

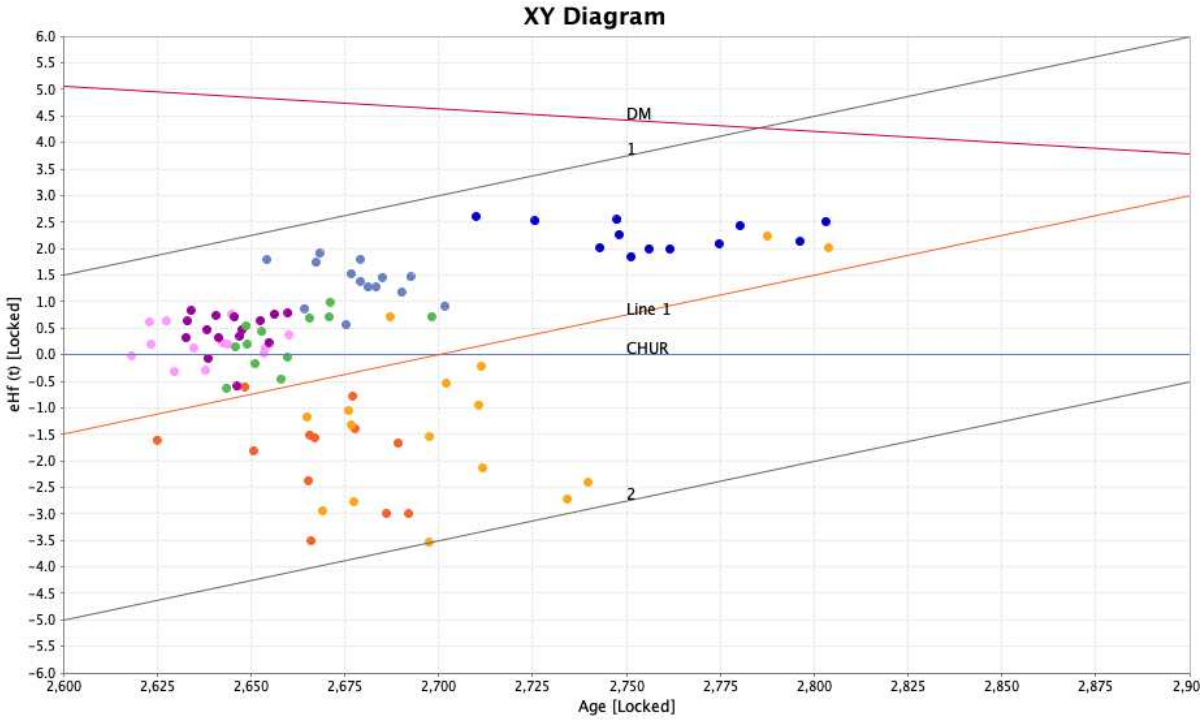

Figure SM2-2.52: εHf vs Age of magmatic samples. Dark blue: SU21, light blue: SU15, green: SU10B, purple: SU16, pink: SU25, yellow: SU06, orange: SU04.

SU25

Sample Localization regional context

(32.7561; -2.8560)

Sampled on a hill, within the northern limit between the SGGB and granitoids. It consists of a late undeformed granodiorite pegmatitic dyke (horizontal left to right on picture below) crosscutting an early deformed aplitic dyke (diagonal top-left to bottom-right on picture below) and orthogneiss.

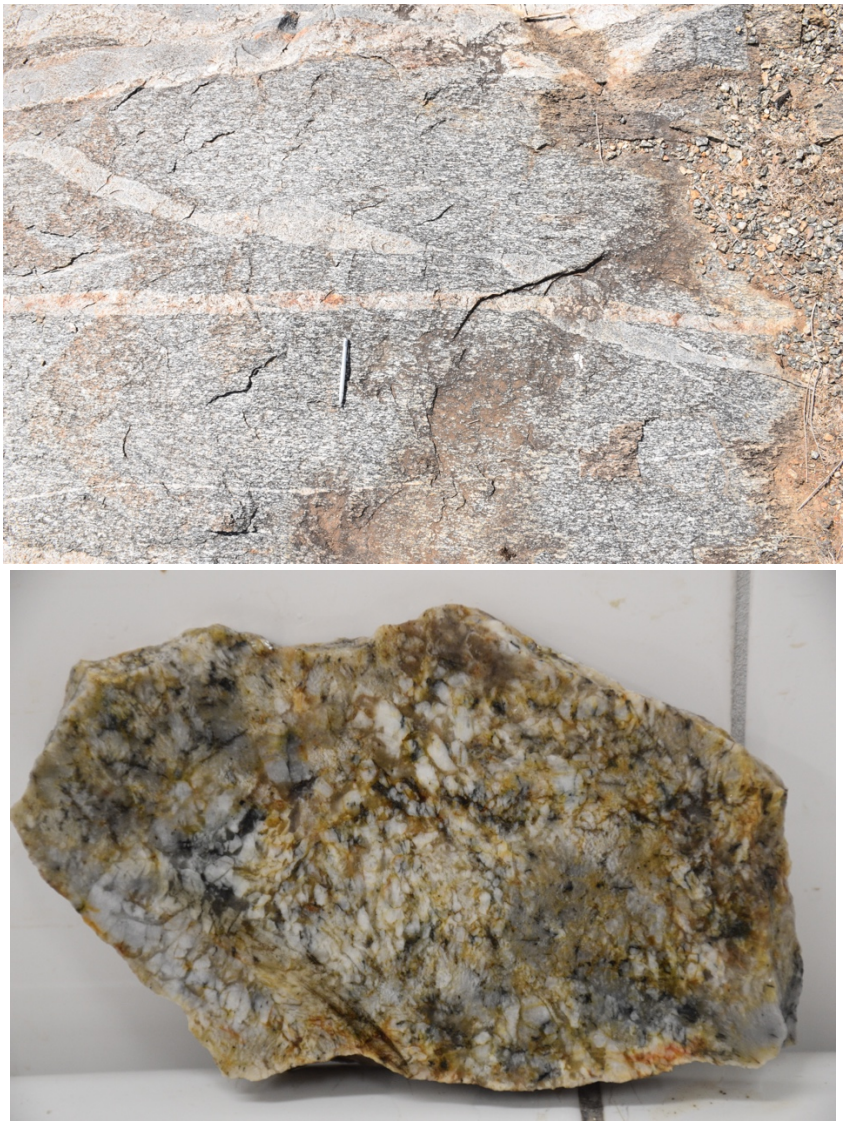

Figure SM2-2.53: Sample SU25 photographs.

Sample description

SU25 consists of a granodiorite pegmatitic dyke with granoblastic texture, affected by small sericite-chlorite-quartz-pyrite fractures.

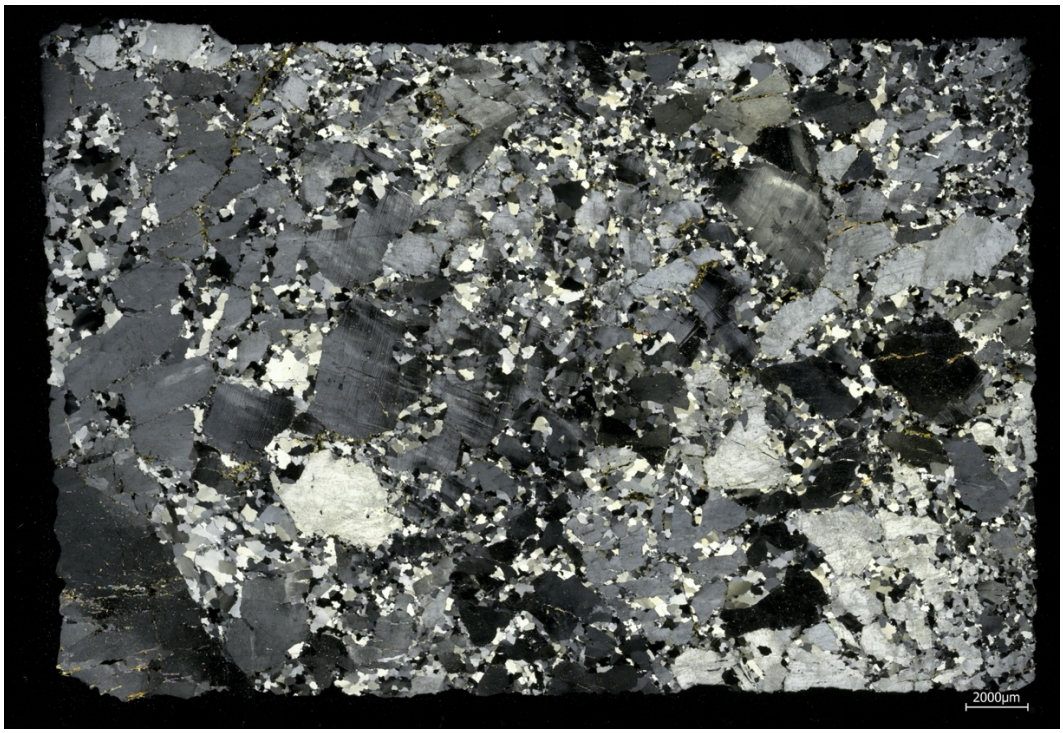

Figure SM2-2.54: Micrograph of sample SU25 in cross-polarized analyzed light.

Zircon morphology

40 zircon crystals were isolated from this sample, mainly light brown, a few are dark brown, euhedral with few fractures. Grains can be up to 200 µm long, and mainly prismatic and elongated. In cathodoluminescence images, zircon grains present few oscillatory zonings with light cores and few thin rims.

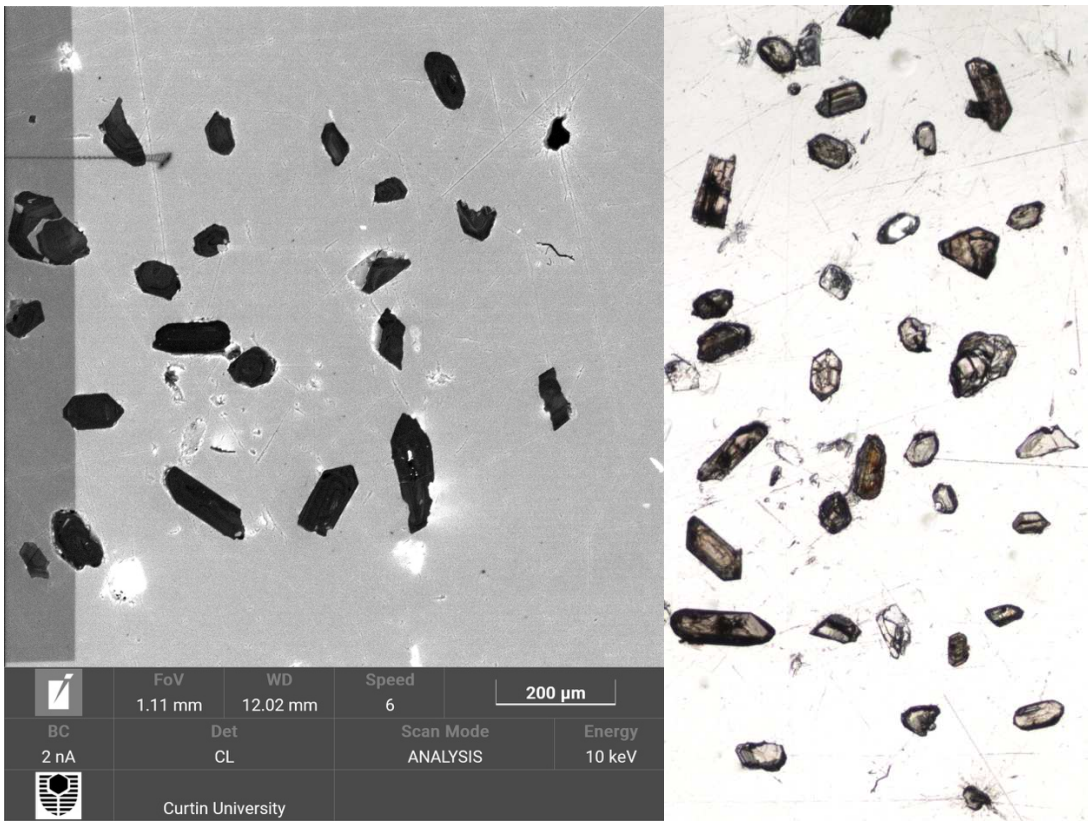

Figure SM2-2.55: **Above**: cathodoluminescence and transmitted light images of representative zircons from sample SU25. **Below**: location of O-Hf-U-Pb analyses.

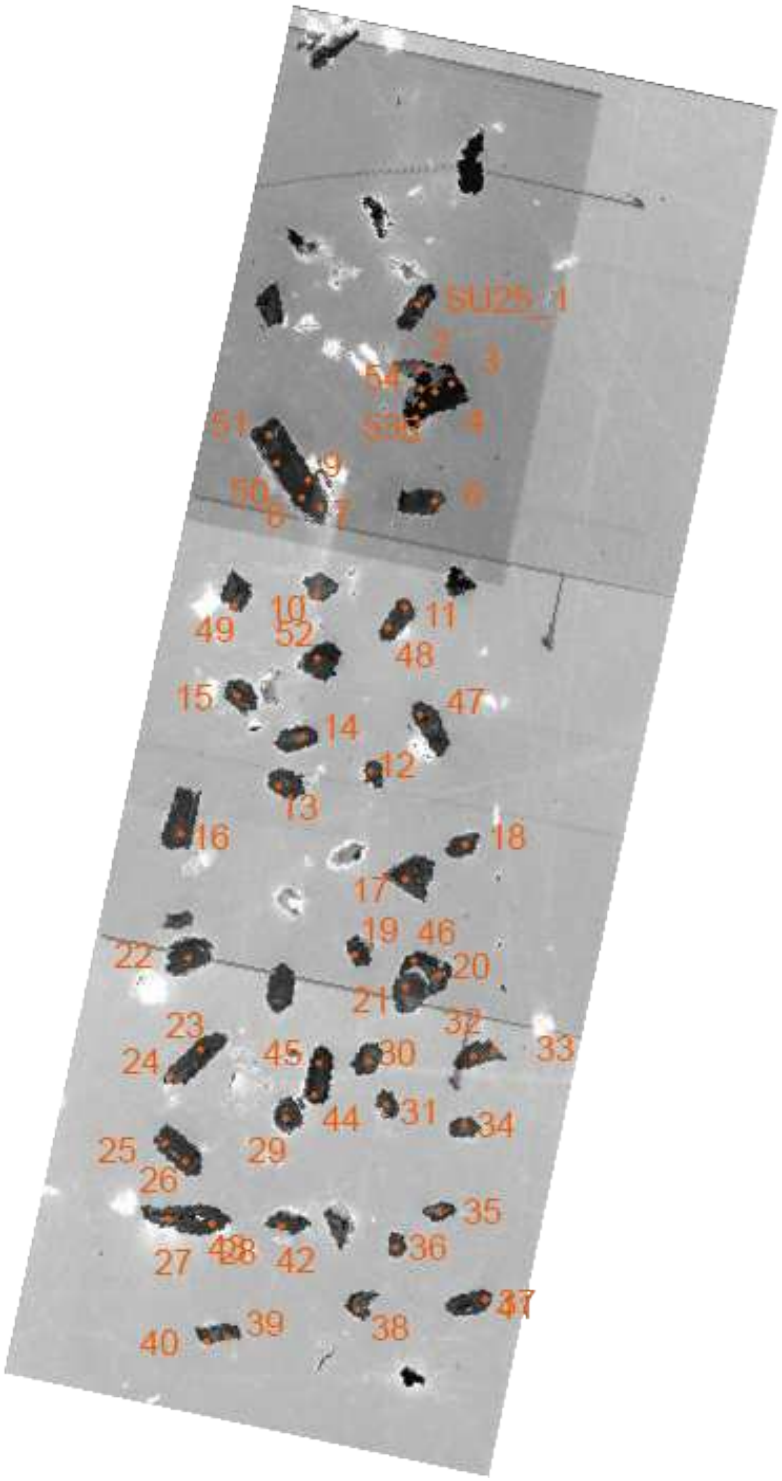
SU25 1
2
3
54
51
4
9
50
6
7
8
49
10
52
11
48
15
47
14
12
13
16
18
17
19
46
22
20
21
23
32
33
24
45
30
44
31
34
25
29
26
35
27
42
36
40
39
38

Analytical details

O isotope ratios ($^{16}O/^{18}O$ and $^{16}O^{1}H/^{16}O$) were determined using SIMS at CMCA (UWA) the 06/09/2023. U-Pb isotope compositions in zircon were analyzed by LA-ICP-MS at CMCA (UWA) the 03/10/2023. Lu-Hf isotope compositions in zircon were analyzed by LA-ICP-MS at CMCA (UWA) the 20/10/2023.

Results

O isotopy

36 spots were analyzed on 29 zircon grains. 12 analyses show low $^{16}O^{1}H/^{16}O$, the 24 others are considered as outliers. Results are shown in a $\delta^{18}O$ - $^{16}O^{1}H/^{16}O$ diagram.

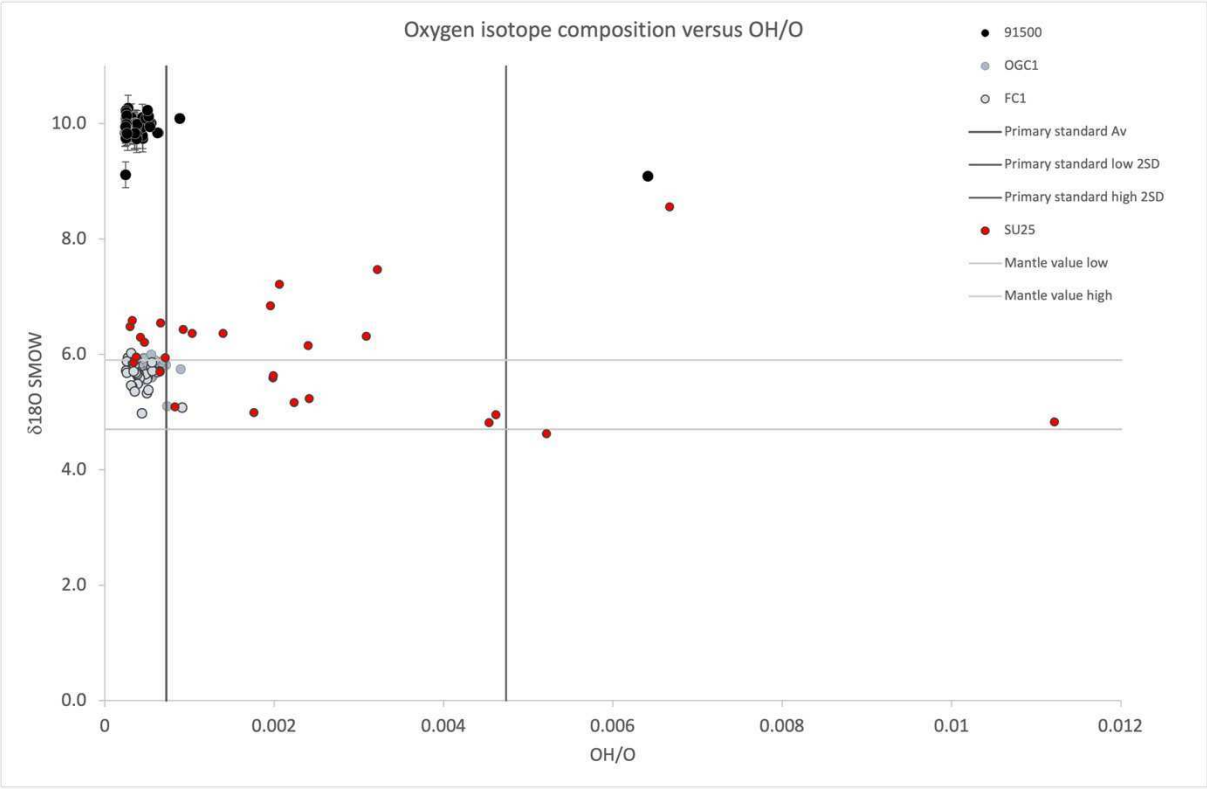

Figure SM2-2.56: $\delta^{18}O$ vs $^{16}O^{1}H/^{16}O$ analyses results for sample SU25.

U-Pb isotopy

34 spots were analyzed on 24 zircon grains. 14 analyses fall onto the concordia, 9 are discordant and 11 failed (inclusions or fractures). Results are shown in a Tera-Wasserburg and weighted mean diagrams.

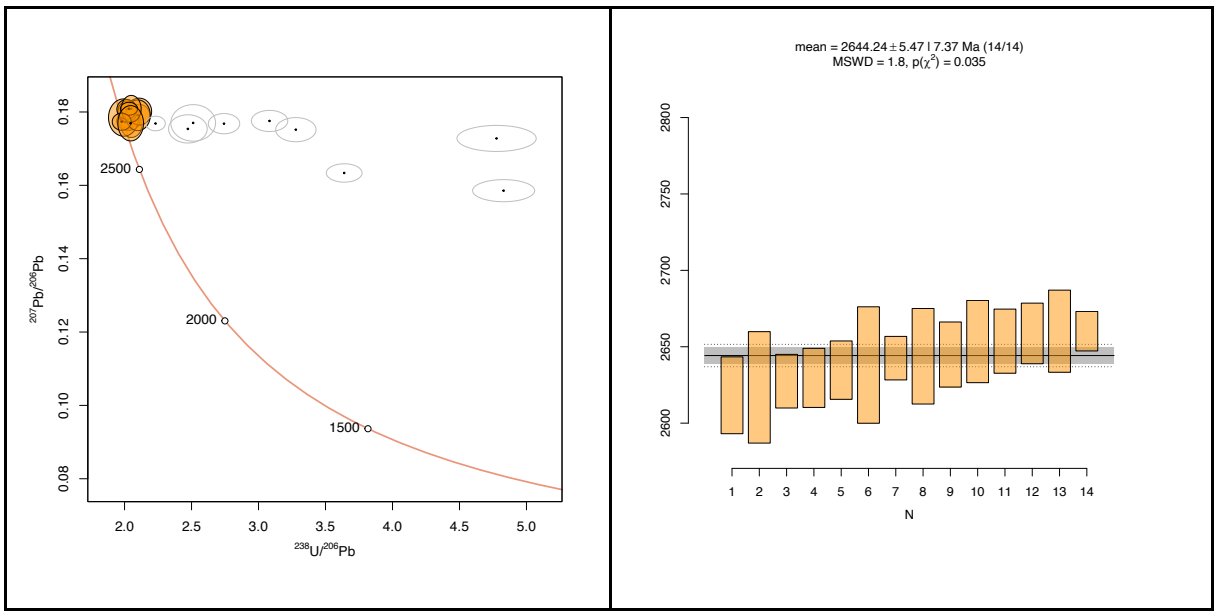

Figure SM2-2.57: U-Pb analyses results for sample SU25. Left: shows the Tera-Wasserburg plots (orange ellipses show the concordant and near concordant data, transparent ellipses show the discordant analyses (> 8% discordant)). Right: Weighted mean averages calculated using the concordant analyses.

Interpretation

O isotopy

Mean value at 5.98 ± 0.23 ‰. The analyses fall around the upper mean mantle values limit, indicating that the source of the dyke includes material that has undergone low temperature oxygen exchanges in the hydrosphere (volcano-sediments or rock that went to supra-crustal depths before melting).

U-Pb isotopy

The analyses range from concordant to strongly discordant. 9 analyses were > 8% discordant. The dates obtained from the 14 analyses have a good precision, based on their $^{207}Pb/^{206}Pb$ ratios: they yield a weighted mean date of 2644 ± 7 Ma (MSWD = 1.8). The discordia plot with 23 data returned an upper intersection at 2648 ± 6 Ma (MSWD = 6.5). The age is interpreted as the crystallization age of the SU25 and gives a minimum age for the shear zone.

Lu/Hf analyses

Lu-Hf analyses were acquired on 13 near concordant zircons, they returned $^{176}Hf/^{177}Hf_i$ of 0.281134 ± 0.000021. The corresponding εHf_t for this dataset is comprised between -0.3 and 0.8 an individual error of (2s) 0.9. Hf model age calculated for this analysis is estimated between ca. 2850 and 2950 Ma (using $^{176}Hf/^{177}Hf$ =0.0115).

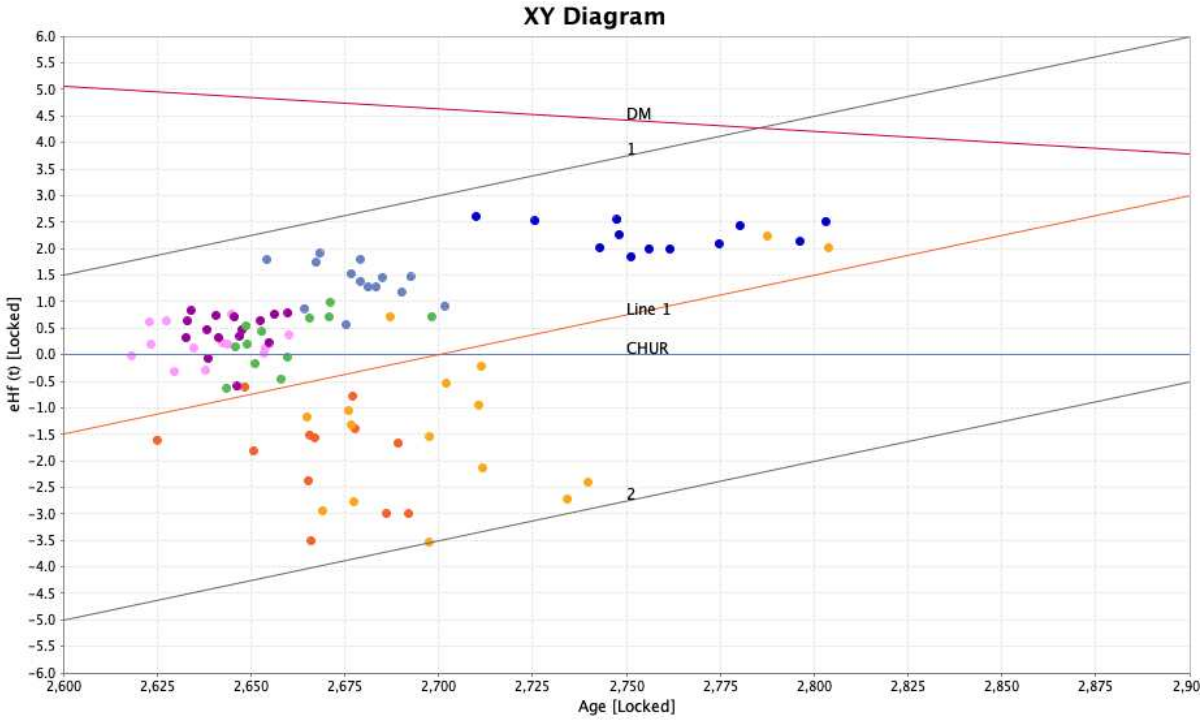

Figure SM2-2.57: εHf vs Age of magmatic samples. Dark blue: SU21, light blue: SU15, green: SU10B, purple: SU16, pink: SU25, yellow: SU06, orange: SU04.

Supplementary Material 2-3

Whole-rock analyses

Sample	Lithology	SiO2	Al2O3	Fe2O3	FeO	CaO	MgO	Na2O	K2O	Cr2O3	TiO2	MnO	P2O5	SrO	BaO	LOI	Total	Mg#
		%	%	%		%	%	%	%	%	%	%	%	%	%	%	%	-
SU01A	Granodiorite	73.50	14.15	1.06	0.95	1.83	0.27	4.41	3.33	0.01	0.13	0.02	0.05	0.04	0.07	0.52	99.39	22.06
SU01B	Bt-mag-rich enclave	53.00	17.45	8.98	8.08	6.03	3.32	4.91	1.92	0.03	1.16	0.17	0.53	0.10	0.07	0.86	98.53	29.12
SU04	Granodiorite	72.20	13.55	1.66	1.49	1.56	0.43	3.74	4.04	<0.002	0.22	0.03	0.09	0.02	0.07	0.72	98.33	22.35
SU05	Granite	74.00	12.95	1.44	1.30	0.79	0.18	3.07	5.83	0.03	0.17	0.04	0.04	0.01	0.05	0.57	99.17	12.20
SU06	Granodiorite	72.90	13.85	1.68	1.51	1.59	0.44	3.96	4.01	0.01	0.21	0.03	0.08	0.02	0.08	0.77	99.63	22.54
SU08A	Granodiorite	72.10	14.35	2.00	1.80	2.22	0.50	4.07	3.22	0.03	0.24	0.03	0.08	0.03	0.12	0.56	99.55	21.74
SU08B	Granodiorite	59.50	17.90	5.58	5.02	4.68	2.26	4.81	2.11	0.02	0.73	0.09	0.25	0.06	0.05	0.88	98.92	31.04
SU09	Sandstone	68.80	14.85	2.96	2.66	2.21	0.77	4.47	3.70	0.02	0.35	0.06	0.11	0.04	0.12	0.51	98.97	22.42
SU10B	Granodiorite	64.90	15.40	5.47	4.92	3.96	2.46	3.42	1.96	0.02	0.53	0.09	0.18	0.05	0.08	0.45	98.97	33.32
SU11	Sandstone	90.00	4.94	1.38	1.24	0.02	0.03	0.07	1.31	0.02	0.12	<0.01	0.02	<0.01	0.03	1.04	98.98	2.36
SU12	BIF	55.40	20.60	13.00	11.70	0.03	0.24	0.04	2.19	0.01	0.63	<0.01	0.03	<0.01	0.08	7.51	99.76	2.01
SU15A	Bt-plg-rich enclave	73.90	14.85	1.44	1.30	1.70	0.33	4.75	3.42	0.01	0.19	0.02	0.05	0.05	0.12	0.66	101.49	20.30
SU15B	Qz-monzonite	71.20	14.90	2.54	2.29	1.56	0.52	4.38	4.22	0.06	0.40	0.03	0.13	0.07	0.16	0.54	100.71	18.53
SU16	Granite	75.50	13.30	1.85	1.67	1.20	0.33	3.73	4.80	0.02	0.27	0.04	0.06	0.01	0.09	0.57	101.77	16.54
SU17	Monzogranite	71.60	14.60	2.71	2.44	2.29	0.79	3.96	4.08	0.01	0.28	0.05	0.08	0.04	0.07	0.56	101.12	24.47
SU18	Granodiorite	73.70	14.80	1.51	1.36	1.67	0.37	4.62	3.57	0.02	0.19	0.03	0.06	0.04	0.11	0.75	101.44	21.40
SU19	Talc ultramafic rock	49.90	33.40	3.21	2.89	0.04	0.20	0.13	0.01	0.00	0.38	<0.01	0.02	0.01	<0.01	12.40	99.70	6.47
SU21	Weathered granitoid				0.00													
SU25	Monzogranite dyke	77.20	13.45	0.57	0.51	0.81	0.04	4.64	3.96	0.01	0.03	0.03	0.01	<0.01	<0.01	0.42	101.17	7.23
SU26	Vein and dyke	74.70	12.95	1.56	1.40	1.44	0.31	3.18	5.05	0.02	0.16	0.04	0.03	0.01	0.05	0.04	99.54	18.09
SU31B	Felsic volcanic rock	70.80	16.05	2.81	2.53	2.09	0.47	5.52	2.05	0.03	0.29	0.03	0.16	0.11	0.13	1.39	101.93	15.67
SU31C	Felsic volcanic rock	65.60	16.60	4.09	3.68	3.96	1.22	4.24	3.06	0.02	0.50	0.06	0.15	0.06	0.13	1.20	100.89	24.89
SU32	Felsic volcanic rock	71.30	11.85	4.43	3.99	4.83	1.47	3.03	0.87	0.07	0.41	0.07	0.10	0.05	0.03	1.77	100.28	26.94
SU38	Felsic volcanic rock	72.50	14.20	4.14	3.73	2.22	1.34	3.44	1.52	0.03	0.48	0.05	0.10	0.04	0.06	1.30	101.42	26.45

	Lithology	Au	Ba	Ce	Cr	Cs	Dy	Er	Eu	Ga	Gd	Hf	Ho	La	Lu	Nb	Nd	Pr	Rb	Sc	Sm	Sn	Sr	Ta	Tb	Th	Ti
		ppm	ppm	ppm	ppm	ppm	ppm	ppm	ppm	ppm	ppm	ppm	ppm	ppm	ppm	ppm	ppm	ppm	ppm	ppm	ppm	ppm	ppm	ppm	ppm	ppm	%
SU01A	Granodiorite	0.001	676	61.0	111	5.32	0.90	0.34	0.56	19.0	1.96	4.40	0.15	32.3	0.06	2.87	23.1	6.93	112.0	2.7	3.54	1.40	380	0.60	0.20	18.8	0.09
SU01B	Bt-mag-rich enclave	0.001	643	109.5	205	10.75	5.57	2.46	2.59	23.6	8.73	4.99	0.96	49.0	0.34	8.55	63.1	15.30	141.5	20.1	12.15	3.20	891	0.70	1.04	7.5	0.75
SU04	Granodiorite	0.001	685	55.2	<5	6.84	1.39	0.71	0.80	20.6	2.53	4.76	0.22	30.8	0.15	6.00	22.2	6.30	139.5	5.8	3.97	1.80	198	0.50	0.26	19.2	0.15
SU05	Granite	0.001	449	157.0	200	3.35	1.75	0.89	0.58	16.6	3.59	4.10	0.31	77.1	0.16	6.72	53.8	17.25	206.0	3.4	7.41	0.90	145	0.50	0.36	49.2	0.11
SU06	Granodiorite	0.001	715	88.2	96	12.55	1.85	1.09	0.90	28.0	3.42	4.89	0.35	44.6	0.14	8.55	35.2	10.20	163.0	6.1	5.78	2.70	237	1.10	0.38	29.2	0.15
SU08A	Granodiorite		1110	57.2	185	4.30	1.57	0.78	0.67	18.0	2.28	3.78	0.27	31.6	0.15	6.83	20.4	6.13	91.2	5.5	3.21	1.30	261	0.50	0.36	13.3	0.16
SU08B	Granodiorite	0.001	426	65.7	135	35.60	3.37	1.75	1.21	25.7	4.33	4.83	0.67	36.4	0.24	7.79	26.6	7.35	193.5	14.0	4.81	3.60	571	0.60	0.59	11.9	0.50
SU09	Sandstone	0.001	1100	92.6	180	4.67	2.11	1.10	1.20	22.9	3.13	6.51	0.39	51.9	0.14	8.05	34.4	10.60	118.5	7.8	5.13	1.10	444	0.60	0.42	12.0	0.21
SU10B	Granodiorite	0.001	715	53.5	124	3.64	2.84	1.72	1.00	23.9	3.68	4.68	0.62	26.1	0.23	7.38	27.1	7.11	116.5	15.0	5.15	1.80	489	0.60	0.51	6.6	0.33
SU11	Sandstone	0.001	243	16.7	125	0.76	0.73	0.40	0.29	6.4	0.85	1.35	0.14	9.2	0.06	1.52	6.8	1.93	32.8	3.4	1.06	<0.5	56	0.20	0.14	2.4	0.08
SU12	BIF	0.001	754	17.1	107	1.39	2.15	1.40	0.79	28.6	2.38	3.06	0.42	9.6	0.20	7.22	8.3	2.09	62.3	21.7	1.79	1.40	76	0.40	0.40	7.8	0.43
SU15A	Bt-plg-rich enclave	0.001	1100	52.3	88	6.44	0.62	0.30	0.59	25.0	1.40	3.14	0.10	27.5	0.04	3.81	18.0	5.57	120.0	3.6	2.17	0.70	463	0.30	0.13	8.5	0.12
SU15B	Qz-monzonite	0.001	1480	184.5	473	3.50	1.24	0.54	1.08	23.0	2.96	5.49	0.19	97.4	0.06	6.47	61.3	20.00	153.0	3.7	6.78	1.50	619	0.30	0.36	18.9	0.27
SU16	Granite	0.001	779	101.0	135	4.90	2.44	1.42	0.88	18.0	3.50	5.82	0.46	49.0	0.24	9.00	38.3	11.55	167.0	3.8	5.55	2.00	177	0.70	0.43	14.3	0.18
SU17	Monzogranite	0.001	669	54.6	87	11.55	2.02	1.15	0.77	20.0	2.52	4.17	0.40	26.7	0.22	7.61	21.6	6.20	195.0	7.7	3.67	1.50	298	1.00	0.36	30.0	0.18
SU18	Granodiorite		1010	64.2	156	3.61	1.23	0.50	0.61	24.5	2.02	3.27	0.15	35.2	0.05	5.82	23.1	7.05	129.0	4.0	3.34	0.70	446	0.50	0.25	13.9	0.13
SU19	Talc ultramafic rock	0.030	28	28.5	24	0.30	2.73	1.69	0.79	22.5	3.44	4.13	0.54	15.0	0.32	3.62	7.7	2.60	0.7	7.9	2.55	0.90	109	0.20	0.47	5.2	0.26
SU21	Weathered granitoid	0.001																									
SU25	Monzogranite dyke	0.001	17	10.3	105	6.09	10.45	8.36	0.17	20.1	5.40	4.29	2.45	5.8	1.42	23.30	5.6	1.38	203.0	3.5	2.58	1.20	17	3.10	1.34	20.5	0.02
SU26	Vein and dyke	0.002	475	74.8	183	10.35	4.30	2.59	0.53	18.0	4.75	3.22	0.84	37.8	0.40	14.30	29.2	8.21	211.0	3.9	5.72	24.40	77	1.90	0.78	16.2	0.11
SU31B	Felsic volcanic rock	0.001	1205	107.5	226	3.60	2.77	0.90	2.08	19.2	5.32	3.34	0.38	53.1	0.11	7.07	47.9	12.15	71.8	6.1	8.04	0.70	1035	0.30	0.53	11.7	0.18
SU31C	Felsic volcanic rock		1165	73.9	160	4.56	3.09	1.60	1.41	20.6	4.01	4.52	0.60	37.4	0.22	7.10	31.8	8.54	100.0	10.4	5.24	2.10	617	0.50	0.54	9.7	0.31
SU32	Felsic volcanic rock	0.001	246	57.4	513	2.00	1.66	0.83	1.28	15.6	2.76	3.76	0.30	28.7	0.12	3.66	24.6	6.23	34.8	8.9	3.56	1.10	578	0.30	0.31	5.6	0.25
SU38	Felsic volcanic rock	0.006	531	59.6	204	3.25	2.00	1.02	1.10	17.6	3.14	3.87	0.42	29.4	0.13	4.69	25.8	6.75	50.9	11.5	4.14	2.40	491	0.50	0.36	6.0	0.30

	Lithology	Tm	U	V	W	Y	Yb	Zr	Ag	As	Cd	Co	Cu	Li	Mo	Ni	Pb	Sc	Tl	Zn
		ppm	ppm	ppm	ppm	ppm	ppm	ppm	ppm	ppm	ppm	ppm	ppm	ppm	ppm	ppm	ppm	ppm	ppm	ppm
SU01A	Granodiorite	0.02	7.55	8.0	1.6	3.5	0.34	145	<0.5	<5	<0.5	3	3	30	2	50	25	2	<10	23
SU01B	Bt-mag-rich enclave	0.33	9.64	156.0	2.8	27.7	2.31	202	<0.5	<5	0.80	22	31	130	2	62	17	15	<10	146
SU04	Granodiorite	0.11	6.52	16.0	2.3	7.4	0.76	155	<0.5	<5	<0.5	3	6	50	1	5	31	4	<10	43
SU05	Granite	0.13	11.70	5.0	1.7	9.6	0.88	136	<0.5	<5	<0.5	5	3	20	3	75	47	2	<10	46
SU06	Granodiorite	0.13	4.52	16.0	1.6	11.9	1.04	150	<0.5	5.00	<0.5	4	8	90	2	49	32	4	<10	41
SU08A	Granodiorite	0.10	3.83	21.0	1.3	9.1	0.89	151	<0.5	<5	<0.5	5	5	40	2	105	21	4	<10	41
SU08B	Granodiorite	0.28	4.45	97.0	2.4	17.5	1.71	212	<0.5	<5	0.50	13	3	90	2	76	15	11	<10	107
SU09	Sandstone	0.15	4.08	31.0	<0.5	10.9	1.14	228	<0.5	<5	<0.5	7	7	20	2	81	19	4	<10	59
SU10B	Granodiorite	0.26	1.86	95.0	<0.5	17.4	1.59	172	<0.5	<5	<0.5	14	11	60	<1	37	11	11	<10	76
SU11	Sandstone	0.04	0.73	14.0	1.6	4.3	0.36	51	<0.5	47.00	<0.5	1	4	<10	1	38	7	1	<10	7
SU12	BIF	0.17	1.65	168.0	2.3	11.7	1.12	121	<0.5	11.00	0.50	4	16	20	1	18	10	17	<10	15
SU15A	Bt-plg-rich enclave	0.01	4.29	10.0	1.1	3.4	0.24	114	<0.5	<5	<0.5	3	2	50	1	40	21	1	<10	42
SU15B	Qz-monzonite	0.02	1.41	25.0	1.8	5.9	0.40	241	<0.5	<5	<0.5	6	4	60	2	115	28	3	<10	62
SU16	Granite	0.21	6.64	9.0	1.5	14.2	1.50	194	<0.5	<5	<0.5	4	3	40	2	44	26	3	<10	44
SU17	Monzogranite	0.15	9.42	30.0	1.1	11.3	1.40	135	<0.5	<5	<0.5	7	6	50	1	38	24	5	<10	43
SU18	Granodiorite	0.02	2.59	11.0	1.6	5.3	0.33	113	<0.5	<5	<0.5	5	4	40	2	84	21	3	<10	46
SU19	Talc ultramafic rock	0.27	1.91	18.0	28.9	17.1	1.74	144	<0.5	51.00	<0.5	2	5	<10	1	7	7	6	<10	3
SU21	Weathered granitoid																			
SU25	Monzogranite dyke	1.38	29.30	<5	1.6	79.5	9.74	92	<0.5	9.00	<0.5	2	13	10	1	39	54	3	<10	11
SU26	Vein and dyke	0.39	10.25	10.0	7.0	28.1	2.65	107	1.40	3590	<0.5	6	12	60	4	113	120	3	<10	57
SU31B	Felsic volcanic rock	0.10	3.65	45.0	1.5	11.4	0.84	149	<0.5	7.00	<0.5	8	12	20	2	96	15	5	<10	33
SU31C	Felsic volcanic rock	0.20	2.95	49.0	2.5	16.7	1.56	190	<0.5	12.00	<0.5	10	3	30	3	76	18	8	<10	54
SU32	Felsic volcanic rock	0.14	1.46	59.0	1.9	8.6	0.83	148	<0.5	6.00	<0.5	11	21	20	2	95	14	7	<10	54
SU38	Felsic volcanic rock	0.15	1.74	65.0	1.8	10.0	1.09	166	<0.5	<5	<0.5	15	38	30	3	96	10	8	<10	68

Supplementary Material 2-4

U-Pb-O-Hf analyses

	$^{206}Pb/^{204}Pb$	$^{207}Pb/^{235}U$	2SE	$^{206}Pb/^{238}U$	2SE	rho	$^{238}U/^{206}Pb$	2SE	$^{207}Pb/^{206}Pb$	2SE	$^{207}Pb/^{235}U$ Age (Ma)	2SE	$^{206}Pb/^{238}U$ Age (Ma)	2SE	$^{207}Pb/^{206}Pb$ Age (Ma)	2SE	U (ppm)	Th (ppm)	Th/U	TW conc %
SU04																				
SU04-3	780	13	0.40883	0.50322	0.01721	0.57840	1.99496	0.07163	0.18144	0.00373	2645	39	2619	77	2665	34	127.6	8.2	0.1	2
SU04-20	667	12	0.36755	0.47256	0.01419	0.19624	2.11863	0.06267	0.18274	0.00231	2596	30	2492	61	2677	21	92.1	11.2	0.1	7
SU04-25	1248	12	0.32833	0.48185	0.01257	0.36761	2.07443	0.05601	0.18279	0.00183	2616	27	2536	57	2678	17	96.5	8.8	0.1	5
SU04-26	1121	12	0.33181	0.48734	0.01301	0.19254	2.05277	0.05435	0.18147	0.00141	2619	26	2558	56	2666	13	132.9	10.4	0.1	4
SU04-27	1377	12	0.32214	0.47344	0.01257	0.46818	2.11262	0.05842	0.18162	0.00154	2592	27	2498	57	2667	14	161.5	16.3	0.1	6
SU04-42	857	12	0.47356	0.49058	0.01777	0.16159	2.04522	0.06849	0.18439	0.00312	2637	35	2566	71	2692	28	113.5	11.6	0.1	4
SU04-55	5068	12	0.34780	0.47756	0.01353	0.44885	2.09653	0.06055	0.18374	0.00249	2611	30	2514	60	2686	22	169.3	11.6	0.1	6
SU04-22	*6371*	*11*	*0.31460*	*0.44689*	*0.01315*	*0.48267*	*2.23805*	*0.06272*	*0.18152*	*0.00209*	*2538*	*28*	*2381*	*56*	*2666*	*19*	*444.0*	*33.6*	*0.1*	*11*
SU04-23	*5317*	*10*	*0.33518*	*0.42307*	*0.01343*	*0.25530*	*2.37939*	*0.07618*	*0.17985*	*0.00171*	*2473*	*31*	*2262*	*61*	*2651*	*16*	*720.3*	*69.7*	*0.1*	*14*
SU04-37	*168371*	*11*	*0.42228*	*0.44587*	*0.01703*	*0.26886*	*2.27277*	*0.09719*	*0.17960*	*0.00225*	*2514*	*41*	*2351*	*84*	*2648*	*21*	*661.4*	*97.2*	*0.1*	*10*
SU04-14	*4055*	*12*	*0.34512*	*0.46691*	*0.01433*	*0.54373*	*2.15074*	*0.06790*	*0.18408*	*0.00212*	*2588*	*31*	*2461*	*65*	*2689*	*19*	*465.3*	*41.5*	*0.1*	*8*
SU04-53	*991*	*8*	*0.26626*	*0.33954*	*0.01116*	*0.36585*	*2.95753*	*0.09511*	*0.17708*	*0.00133*	*2259*	*30*	*1878*	*52*	*2625*	*13*	*1415.4*	*124.9*	*0.1*	*28*
SU04-56	*5024*	*6*	*0.56990*	*0.27472*	*0.02207*	*-0.18968*	*3.76303*	*0.28510*	*0.16946*	*0.00361*	*2005*	*69*	*1519*	*103*	*2552*	*36*	*1290.7*	*38.6*	*0.0*	*39*
SU06																				
SU06-13	-5134	15	0.37584	0.55214	0.01629	0.63786	1.81634	0.05747	0.19542	0.00293	2804	33	2827	72	2788	25	257.1	115.8	0.5	-2
SU06-15	10899	13	0.34705	0.51484	0.01509	0.56320	1.94080	0.05243	0.18649	0.00293	2697	29	2679	59	2711	26	289.2	410.3	1.4	1
SU06-16	-3129	15	0.36873	0.55047	0.01445	0.35919	1.81370	0.04932	0.19736	0.00208	2815	28	2831	62	2804	17	125.0	86.9	0.7	-1
SU06-20	-6906	13	0.40807	0.51276	0.01771	0.43240	1.95379	0.06563	0.18185	0.00312	2667	36	2664	73	2669	28	123.4	96.5	0.8	0
SU06-22	5640	13	0.39245	0.50087	0.01917	0.51993	2.00258	0.07083	0.18656	0.00375	2668	38	2611	76	2711	33	276.3	344.9	1.2	3
SU06-23	7860	13	0.37573	0.51162	0.01690	0.56769	1.97341	0.06757	0.18270	0.00253	2662	35	2643	74	2677	23	344.8	287.3	0.8	1
SU06-24	14931	13	0.34323	0.52772	0.01534	0.38090	1.90521	0.05951	0.18277	0.00218	2696	32	2720	69	2677	20	206.7	178.2	0.9	-2
SU06-32	2079	12	0.37564	0.49718	0.01970	0.65050	2.01297	0.08730	0.18139	0.00356	2637	45	2600	93	2665	32	308.6	154.3	0.5	2
SU06-33	6252	13	0.33011	0.50100	0.01502	0.62166	1.98171	0.05902	0.18499	0.00296	2670	32	2634	64	2697	26	110.8	133.5	1.2	3
SU06-57	12710	13	0.47609	0.49062	0.02278	0.59129	2.06553	0.09842	0.18661	0.00488	2639	51	2545	100	2712	43	160.6	127.9	0.8	5
SU06-17	32510	14	0.52936	0.54272	0.02065	0.03392	1.85866	0.07115	0.18261	0.00276	2718	39	2775	86	2676	25	154.7	147.2	1.0	-4
SU06-21	1539	12	0.32468	0.48270	0.01392	0.39024	2.07796	0.06102	0.18551	0.00216	2628	30	2533	62	2702	19	252.4	343.7	1.4	6
SU06-36	2563	13	0.38431	0.52770	0.01691	0.44187	1.89922	0.05939	0.18383	0.00271	2704	33	2727	70	2687	24	138.0	47.6	0.3	-2
SU06-39	4610	12	0.35901	0.47983	0.01568	0.44701	2.09911	0.07169	0.18502	0.00230	2616	34	2512	71	2698	21	361.7	533.5	1.5	7
SU06-54	*4274*	*12*	*0.34530*	*0.46902*	*0.01691*	*0.68505*	*2.14933*	*0.07644*	*0.18645*	*0.00298*	*2601*	*37*	*2463*	*73*	*2710*	*26*	*337.1*	*293.9*	*0.9*	*8*
SU06-34	*2517*	*12*	*0.33675*	*0.47887*	*0.01506*	*0.59789*	*2.10267*	*0.06416*	*0.18919*	*0.00288*	*2635*	*32*	*2508*	*63*	*2734*	*25*	*144.9*	*137.6*	*0.9*	*8*
SU06-19	*1596*	*12*	*0.38171*	*0.47289*	*0.01783*	*0.68063*	*2.13774*	*0.08415*	*0.18982*	*0.00359*	*2623*	*41*	*2474*	*81*	*2740*	*31*	*225.2*	*225.3*	*1.0*	*9*
SU06-14	*6220*	*9*	*0.26583*	*0.35226*	*0.01105*	*0.45251*	*2.82996*	*0.09718*	*0.18329*	*0.00306*	*2330*	*35*	*1951*	*58*	*2682*	*28*	*393.2*	*242.8*	*0.6*	*27*
SU06-41	*1182*	*3*	*0.14428*	*0.15681*	*0.00796*	*0.42293*	*6.48026*	*0.36761*	*0.14302*	*0.00297*	*1418*	*46*	*925*	*49*	*2263*	*36*	*1759.8*	*103.1*	*0.1*	*58*
SU06-44	*824*	*7*	*0.53088*	*0.28173*	*0.01976*	*-0.14479*	*3.97530*	*0.28804*	*0.16828*	*0.00284*	*1952*	*64*	*1446*	*94*	*2540*	*28*	*678.7*	*879.3*	*1.3*	*38*
SU06-56	*1383*	*2*	*0.10288*	*0.11500*	*0.00545*	*0.02483*	*8.86926*	*0.47202*	*0.12358*	*0.00313*	*1088*	*39*	*689*	*35*	*2008*	*45*	*2742.4*	*1633.6*	*0.6*	*65*
SU06-58	*952*	*4*	*0.23018*	*0.18630*	*0.01081*	*0.42420*	*5.41821*	*0.30196*	*0.15413*	*0.00402*	*1618*	*50*	*1092*	*56*	*2391*	*44*	*1383.1*	*877.6*	*0.6*	*53*
SU10A																				
SU10A-21	1824	12	0.35648	0.49429	0.01305	0.81190	2.01840	0.04920	0.17978	0.00254	2626	26	2594	52	2650	23	216.5	223.3	1.0	2
SU10A-30	3701	13	0.33256	0.52259	0.01307	0.78087	1.92095	0.04711	0.17939	0.00230	2670	26	2702	54	2646	21	154.6	81.6	0.5	-2
SU10A-44	3722	12	0.38752	0.51184	0.01726	0.72670	1.96299	0.06724	0.17725	0.00366	2639	38	2654	75	2627	34	372.1	260.8	0.7	-1
SU10A-46	4385	13	0.29995	0.50477	0.01159	0.70669	1.97662	0.04499	0.18008	0.00215	2647	24	2639	49	2653	20	248.7	122.3	0.5	0
SU10A-58	37689	12	0.28484	0.50345	0.01030	0.57895	1.98903	0.04080	0.17962	0.00204	2639	22	2626	44	2649	19	146.9	70.9	0.5	1

	$^{206}Pb/^{204}Pb$	$^{207}Pb/^{235}U$	2SE	$^{206}Pb/^{238}U$	2SE	rho	$^{238}U/^{206}Pb$	2SE	$^{207}Pb/^{206}Pb$	2SE	$^{207}Pb/^{235}U$ Age (Ma)	2SE	$^{206}Pb/^{238}U$ Age (Ma)	2SE	$^{207}Pb/^{206}Pb$ Age (Ma)	2SE	U (ppm)	Th (ppm)	Th/U	TW conc %
SU10A-61	12842	15	0.33265	0.54174	0.01122	0.56763	1.84671	0.03927	0.19786	0.00229	2800	23	2790	48	2808	19	130.9	97.3	0.7	1
SU10A-62	-11029	15	0.35786	0.54556	0.01324	0.74609	1.84070	0.04599	0.19709	0.00240	2800	26	2797	57	2801	20	191.7	141.2	0.7	0
SU10A-73	5952	13	0.36460	0.52478	0.01599	0.67228	1.91539	0.05735	0.17958	0.00335	2674	33	2708	66	2648	31	216.0	120.0	0.6	-3
SU10A-75	6286	13	0.29437	0.50201	0.01074	0.72169	1.99709	0.04299	0.18102	0.00186	2642	22	2617	46	2661	17	178.3	158.6	0.9	1
SU10A-77	18101	12	0.34254	0.50219	0.01264	0.81113	1.99406	0.04995	0.17997	0.00242	2638	27	2620	54	2652	22	246.2	204.1	0.8	1
SU10A-80	2081	12	0.30887	0.48787	0.01171	0.59107	2.04563	0.04663	0.18086	0.00294	2619	26	2566	48	2660	27	125.7	61.2	0.5	4
SU10A-89	-12990	12	0.30388	0.49337	0.01197	0.86896	2.03636	0.05084	0.17867	0.00179	2612	25	2575	53	2640	17	155.3	107.1	0.7	2
SU10A-94	2664	12	0.43123	0.49718	0.01727	0.85196	2.02427	0.07521	0.17917	0.00314	2620	39	2588	79	2644	29	283.0	176.3	0.6	2
SU10A-110	-5058	13	0.33876	0.51323	0.01299	0.73055	1.95421	0.04866	0.17964	0.00259	2655	27	2664	54	2649	24	66.0	34.0	0.5	-1
SU10A-114	18484	12	0.30478	0.49959	0.01127	0.75939	2.00404	0.04776	0.17952	0.00224	2631	25	2609	51	2648	21	138.6	67.7	0.5	1
SU10A-143	-6477	12	0.34947	0.50195	0.01375	0.84425	2.00315	0.05642	0.17907	0.00230	2629	29	2610	60	2643	21	131.4	73.2	0.6	1
SU10A-159	-20695	12	0.31486	0.49281	0.01294	0.75276	2.03030	0.05148	0.18059	0.00263	2624	27	2582	54	2658	24	247.6	143.4	0.6	3
SU10A-192	1392	13	0.32742	0.51107	0.01268	0.77982	1.95255	0.04441	0.18113	0.00230	2664	25	2666	50	2662	21	163.2	103.1	0.6	0
SU10A-199	12213	13	0.31069	0.52510	0.01142	0.62413	1.90658	0.04219	0.18147	0.00222	2688	24	2718	49	2666	20	148.1	60.4	0.4	-2
SU10A-200	5060	12	0.28541	0.50355	0.01043	0.68061	1.98065	0.04466	0.17855	0.00187	2637	23	2635	49	2639	17	141.9	97.7	0.7	0
SU10A-79	2850	11	0.34212	0.46047	0.01307	0.89195	2.18552	0.05969	0.17820	0.00194	2543	27	2429	55	2635	18	703.4	536.1	0.8	7
SU10A-47	1240	12	0.30915	0.46712	0.01221	0.86996	2.15428	0.05303	0.18212	0.00200	2577	25	2458	50	2672	18	266.4	141.9	0.5	8
SU10A-5	*749*	*8*	*0.34923*	*0.29632*	*0.01236*	*0.96803*	*3.48688*	*0.14278*	*0.19202*	*0.00206*	*2184*	*38*	*1625*	*59*	*2759*	*18*	*727.7*	*716.9*	*1.0*	*40*
SU10A-9	*3224*	*8*	*0.28695*	*0.32413*	*0.01128*	*0.95946*	*3.16708*	*0.11266*	*0.17143*	*0.00179*	*2168*	*33*	*1769*	*55*	*2571*	*17*	*619.6*	*1074.1*	*1.7*	*30*
SU10A-15	*5833*	*8*	*0.28237*	*0.34382*	*0.01159*	*0.91681*	*2.93547*	*0.09622*	*0.17010*	*0.00223*	*2229*	*32*	*1890*	*54*	*2558*	*22*	*1201.6*	*432.7*	*0.4*	*26*
SU10A-16	*3343*	*11*	*0.41260*	*0.43475*	*0.01672*	*0.94718*	*2.32668*	*0.08636*	*0.17926*	*0.00218*	*2490*	*36*	*2305*	*72*	*2645*	*20*	*482.0*	*803.4*	*1.7*	*12*
SU10A-18	*3407*	*6*	*0.20907*	*0.27589*	*0.00742*	*0.85304*	*3.64253*	*0.09523*	*0.16756*	*0.00234*	*2024*	*26*	*1564*	*36*	*2533*	*23*	*1067.1*	*1700.1*	*1.6*	*38*
SU10A-19	*2217*	*7*	*0.20706*	*0.30248*	*0.00797*	*0.91375*	*3.30944*	*0.09261*	*0.16644*	*0.00176*	*2103*	*27*	*1702*	*42*	*2521*	*18*	*816.8*	*646.7*	*0.8*	*32*
SU10A-29	*3000*	*6*	*0.14861*	*0.26568*	*0.00621*	*0.72191*	*3.77131*	*0.08675*	*0.16186*	*0.00206*	*1963*	*23*	*1516*	*31*	*2474*	*21*	*962.5*	*595.1*	*0.6*	*39*
SU10A-38	*9553*	*9*	*0.24868*	*0.38556*	*0.01014*	*0.82876*	*2.61008*	*0.06611*	*0.17128*	*0.00225*	*2342*	*26*	*2091*	*45*	*2569*	*22*	*918.9*	*447.9*	*0.5*	*18*
SU10A-45	*3825*	*5*	*0.19189*	*0.22540*	*0.00791*	*0.87756*	*4.48790*	*0.15189*	*0.15371*	*0.00267*	*1771*	*32*	*1297*	*40*	*2387*	*30*	*989.4*	*870.7*	*0.9*	*45*
SU10A-55	*6645*	*7*	*0.23303*	*0.27658*	*0.00814*	*0.93016*	*3.65119*	*0.11418*	*0.17024*	*0.00217*	*2036*	*30*	*1560*	*43*	*2559*	*21*	*761.8*	*1073.4*	*1.4*	*38*
SU10A-71	*344*	*5*	*0.14500*	*0.19548*	*0.00629*	*0.73916*	*5.14821*	*0.16584*	*0.18813*	*0.00349*	*1825*	*31*	*1144*	*34*	*2725*	*31*	*2057.2*	*2552.9*	*1.2*	*58*
SU10A-76	*2249*	*9*	*0.26699*	*0.37930*	*0.01070*	*0.93077*	*2.66499*	*0.07285*	*0.17803*	*0.00175*	*2359*	*27*	*2054*	*48*	*2634*	*16*	*313.0*	*695.4*	*2.2*	*21*
SU10A-83	*3078*	*4*	*0.09636*	*0.19861*	*0.00429*	*0.66582*	*5.03762*	*0.10842*	*0.14835*	*0.00178*	*1646*	*20*	*1167*	*23*	*2326*	*21*	*908.4*	*550.4*	*0.6*	*50*
SU10A-95	*3895*	*7*	*0.24872*	*0.29459*	*0.01064*	*0.87807*	*3.41781*	*0.12489*	*0.17238*	*0.00283*	*2105*	*36*	*1654*	*53*	*2580*	*27*	*578.2*	*634.0*	*1.1*	*35*
SU10A-108	*1907*	*6*	*0.16443*	*0.25418*	*0.00666*	*0.90136*	*3.97385*	*0.10221*	*0.16418*	*0.00177*	*1930*	*24*	*1447*	*33*	*2498*	*18*	*444.2*	*370.7*	*0.8*	*42*
SU10A-118	*17785*	*9*	*0.24225*	*0.38213*	*0.00945*	*0.88277*	*2.61859*	*0.06889*	*0.17105*	*0.00177*	*2338*	*26*	*2085*	*47*	*2567*	*17*	*771.1*	*765.2*	*1.0*	*19*
SU10A-119	*4136*	*8*	*0.23889*	*0.33476*	*0.00945*	*0.88664*	*3.00762*	*0.08673*	*0.17041*	*0.00213*	*2209*	*28*	*1850*	*46*	*2561*	*21*	*813.3*	*559.7*	*0.7*	*27*
SU10A-126	*3535*	*7*	*0.17718*	*0.29200*	*0.00667*	*0.64432*	*3.42808*	*0.07772*	*0.16789*	*0.00213*	*2079*	*23*	*1650*	*33*	*2536*	*21*	*767.6*	*571.6*	*0.7*	*35*
SU10A-141	*2938*	*10*	*0.27810*	*0.42003*	*0.01045*	*0.76803*	*2.39012*	*0.05929*	*0.17585*	*0.00236*	*2448*	*26*	*2253*	*47*	*2613*	*22*	*907.9*	*600.9*	*0.7*	*13*
SU10A-142	*2970*	*7*	*0.20720*	*0.30342*	*0.00899*	*0.87304*	*3.30506*	*0.10335*	*0.16934*	*0.00233*	*2119*	*30*	*1704*	*47*	*2550*	*23*	*952.3*	*573.1*	*0.6*	*33*
SU10A-144	*10939*	*6*	*0.14480*	*0.25774*	*0.00696*	*0.61968*	*3.89246*	*0.10714*	*0.16313*	*0.00261*	*1943*	*28*	*1474*	*36*	*2488*	*27*	*1110.3*	*1037.9*	*0.9*	*41*
SU10A-153	*2381*	*7*	*0.16708*	*0.27610*	*0.00686*	*0.83987*	*3.62141*	*0.09221*	*0.17331*	*0.00204*	*2059*	*25*	*1572*	*36*	*2589*	*20*	*735.5*	*1072.6*	*1.5*	*39*
SU10A-154	*1614*	*4*	*0.13028*	*0.19704*	*0.00647*	*0.89164*	*5.12972*	*0.17738*	*0.15656*	*0.00228*	*1675*	*31*	*1148*	*36*	*2418*	*25*	*1053.7*	*1286.8*	*1.2*	*52*
SU10A-157	*2079*	*5*	*0.11468*	*0.20381*	*0.00508*	*0.64040*	*4.92104*	*0.12032*	*0.16070*	*0.00247*	*1731*	*24*	*1193*	*27*	*2462*	*26*	*963.2*	*1834.5*	*1.9*	*51*
SU10A-160	*3394*	*6*	*0.16511*	*0.26060*	*0.00655*	*0.79067*	*3.83718*	*0.09248*	*0.16611*	*0.00220*	*1971*	*24*	*1493*	*32*	*2518*	*22*	*864.5*	*996.2*	*1.2*	*41*
SU10A-167	*2141*	*10*	*0.27577*	*0.41953*	*0.01030*	*0.80396*	*2.39983*	*0.06026*	*0.18031*	*0.00195*	*2467*	*25*	*2245*	*48*	*2655*	*18*	*271.8*	*432.9*	*1.6*	*15*
SU10A-172	*7498*	*6*	*0.20712*	*0.28813*	*0.00793*	*0.94859*	*3.51328*	*0.09791*	*0.16159*	*0.00167*	*2024*	*26*	*1615*	*40*	*2472*	*17*	*730.1*	*399.4*	*0.5*	*34*

	$^{206}Pb/^{204}Pb$	$^{207}Pb/^{235}U$	2SE	$^{206}Pb/^{238}U$	2SE	rho	$^{238}U/^{206}Pb$	2SE	$^{207}Pb/^{206}Pb$	2SE	$^{207}Pb/^{235}U$ Age (Ma)	2SE	$^{206}Pb/^{238}U$ Age (Ma)	2SE	$^{207}Pb/^{206}Pb$ Age (Ma)	2SE	U (ppm)	Th (ppm)	Th/U	TW conc %
SU10A-178	*9281*	*9*	*0.23168*	*0.39473*	*0.00951*	*0.72926*	*2.54135*	*0.06160*	*0.17415*	*0.00209*	*2382*	*25*	*2139*	*44*	*2597*	*20*	*644.6*	*240.1*	*0.4*	*17*
SU10A-181	*2079*	*3*	*0.08708*	*0.17603*	*0.00387*	*0.75445*	*5.67374*	*0.11965*	*0.14314*	*0.00164*	*1522*	*19*	*1046*	*20*	*2265*	*20*	*700.0*	*353.2*	*0.5*	*54*
SU10A-183	*5705*	*6*	*0.17586*	*0.27427*	*0.00700*	*0.91882*	*3.66850*	*0.09858*	*0.16758*	*0.00161*	*2018*	*25*	*1554*	*37*	*2533*	*16*	*668.4*	*501.7*	*0.8*	*38*
SU10A-198	*3402*	*7*	*0.18011*	*0.29820*	*0.00736*	*0.77744*	*3.36039*	*0.08338*	*0.16823*	*0.00200*	*2099*	*24*	*1679*	*37*	*2539*	*20*	*426.1*	*576.4*	*1.4*	*34*
SU10B																				
SU10B-1	4564	12	0.33905	0.49349	0.01713	0.72787	2.04618	0.07449	0.18065	0.00278	2617	37	2565	77	2658	26	256.3	95.5	0.4	3
SU10B-4	4597	12	0.31168	0.49712	0.01338	0.27411	2.01080	0.05466	0.17966	0.00201	2629	28	2602	58	2649	19	256.9	116.4	0.5	2
SU10B-11	4546	13	0.34039	0.50248	0.01514	0.38744	1.99582	0.05774	0.18206	0.00163	2648	28	2618	62	2671	15	395.7	203.4	0.5	2
SU10B-12	-45767	13	0.27955	0.50288	0.01274	0.57407	1.98790	0.05098	0.18082	0.00180	2645	26	2627	55	2660	16	114.1	37.2	0.3	1
SU10B-16	1490	12	0.33126	0.48645	0.01521	0.44904	2.05785	0.06159	0.17932	0.00172	2605	29	2553	63	2646	16	177.6	105.9	0.6	3
SU10B-19	-1162	12	0.30661	0.48953	0.01391	0.46659	2.05088	0.06025	0.18203	0.00212	2622	30	2560	62	2671	19	106.9	46.1	0.4	4
SU10B-20	5994	12	0.36807	0.50080	0.01526	0.29799	2.00615	0.06430	0.18009	0.00187	2633	32	2607	69	2653	17	378.8	164.4	0.4	2
SU10B-21	-7216	12	0.30099	0.49568	0.01349	0.40658	2.02233	0.05361	0.17964	0.00135	2623	26	2590	57	2649	12	250.4	100.1	0.4	2
SU10B-24	19250	13	0.32192	0.51171	0.01419	0.49335	1.95161	0.05201	0.18146	0.00207	2666	27	2667	58	2666	19	251.5	126.2	0.5	0
SU10B-25	30970	12	0.28162	0.50081	0.01291	0.60746	2.00093	0.05243	0.17989	0.00160	2634	26	2613	56	2651	15	204.9	188.3	0.9	1
SU10B-50	9161	11	0.29282	0.46501	0.01302	0.40322	2.15821	0.06083	0.17908	0.00141	2559	27	2454	58	2644	13	618.2	333.5	0.5	7
SU10B-3	*5624*	*11*	*0.34278*	*0.42806*	*0.01477*	*0.26601*	*2.37630*	*0.08292*	*0.17824*	*0.00173*	*2465*	*34*	*2264*	*67*	*2636*	*16*	*325.3*	*235.3*	*0.7*	*13*
SU10B-10	*14781*	*9*	*0.32661*	*0.38367*	*0.01657*	*0.63060*	*2.63775*	*0.11645*	*0.17831*	*0.00360*	*2370*	*45*	*2072*	*78*	*2636*	*34*	*279.8*	*144.0*	*0.5*	*21*
SU10B-13	*-61229*	*6*	*0.21045*	*0.27540*	*0.00908*	*0.09285*	*3.65965*	*0.11081*	*0.16978*	*0.00180*	*2031*	*28*	*1557*	*42*	*2555*	*18*	*531.6*	*387.4*	*0.7*	*39*
SU10B-18	*4940*	*6*	*0.19557*	*0.24608*	*0.01100*	*0.48205*	*4.05363*	*0.15669*	*0.16952*	*0.00359*	*1941*	*38*	*1421*	*49*	*2552*	*35*	*1067.2*	*484.5*	*0.5*	*45*
SU10B-27	*-11016*	*11*	*0.37096*	*0.42680*	*0.01598*	*0.25092*	*2.37736*	*0.08726*	*0.17872*	*0.00204*	*2468*	*36*	*2263*	*70*	*2640*	*19*	*345.3*	*161.7*	*0.5*	*13*
SU10B-28	*1712*	*12*	*0.30921*	*0.47017*	*0.01402*	*0.52054*	*2.13172*	*0.06217*	*0.18507*	*0.00217*	*2602*	*29*	*2480*	*60*	*2698*	*19*	*304.6*	*146.9*	*0.5*	*8*
SU10B-31	*11976*	*6*	*0.16745*	*0.27350*	*0.00797*	*0.32129*	*3.67774*	*0.11118*	*0.16618*	*0.00130*	*2008*	*27*	*1550*	*42*	*2519*	*13*	*838.3*	*638.2*	*0.8*	*38*
SU10B-35	*2324*	*10*	*0.29808*	*0.38941*	*0.01344*	*0.53211*	*2.58261*	*0.09651*	*0.18185*	*0.00315*	*2407*	*38*	*2110*	*67*	*2669*	*29*	*1001.8*	*1171.4*	*1.2*	*21*
SU10B-36	*-28059*	*9*	*0.52250*	*0.37808*	*0.02237*	*0.24439*	*2.67443*	*0.14702*	*0.18033*	*0.00432*	*2367*	*55*	*2048*	*96*	*2655*	*40*	*409.8*	*235.5*	*0.6*	*22*
SU10B-43	*4429*	*11*	*0.33037*	*0.44005*	*0.01383*	*0.20858*	*2.30053*	*0.08018*	*0.17986*	*0.00162*	*2504*	*33*	*2327*	*68*	*2651*	*15*	*202.3*	*101.3*	*0.5*	*11*
SU10B-45	*-64605*	*2*	*0.05947*	*0.08257*	*0.00311*	*0.36398*	*12.11235*	*0.49968*	*0.13324*	*0.00316*	*937*	*29*	*511*	*20*	*2140*	*41*	*3868.0*	*2641.8*	*0.7*	*76*
SU10B-46	*1706*	*3*	*0.13973*	*0.15631*	*0.00698*	*0.28241*	*6.41396*	*0.25993*	*0.14548*	*0.00348*	*1439*	*36*	*934*	*35*	*2293*	*41*	*1628.2*	*1238.3*	*0.8*	*59*
SU10B-51	*10051*	*9*	*0.20661*	*0.37284*	*0.00983*	*0.61013*	*2.68570*	*0.07139*	*0.18102*	*0.00157*	*2367*	*26*	*2040*	*46*	*2661*	*14*	*3487.9*	*49231.5*	*14.1*	*23*
SU11																				
SU11-1	3880	15	0.38276	0.54894	0.01232	0.65615	1.82608	0.03991	0.20365	0.00270	2838	24	2815	50	2855	22	34.7	18.0	0.5	1
SU11-2	-6503	17	0.41284	0.57312	0.01263	0.65698	1.75165	0.03922	0.21634	0.00231	2936	24	2911	52	2953	17	106.5	31.1	0.3	1
SU11-3	-401	18	0.45330	0.58931	0.01303	0.61337	1.69693	0.04037	0.21897	0.00306	2978	27	2987	57	2972	22	21.6	8.5	0.4	-1
SU11-4	21313	18	0.43818	0.60131	0.01292	0.58041	1.66775	0.03604	0.21843	0.00287	2992	24	3028	52	2968	21	26.5	11.5	0.4	-2
SU11-5	803	22	0.62865	0.62992	0.01871	0.77493	1.59638	0.04491	0.25106	0.00417	3169	32	3135	70	3191	26	36.2	20.0	0.6	1
SU11-6	771	18	0.48239	0.56354	0.01308	0.61815	1.77687	0.03969	0.22556	0.00355	2962	26	2878	52	3020	25	21.5	11.2	0.5	5
SU11-7	66887	22	0.62265	0.65311	0.01619	0.83507	1.53695	0.03925	0.24475	0.00322	3181	28	3231	65	3150	21	22.1	14.1	0.6	-3
SU11-8	362	21	0.54881	0.62195	0.01425	0.56320	1.61269	0.03755	0.24283	0.00400	3127	28	3110	57	3138	26	12.0	7.6	0.6	1
SU11-10	-74326	14	0.34888	0.50734	0.01242	0.68185	1.97193	0.04582	0.19322	0.00244	2716	25	2644	50	2769	21	109.0	68.2	0.6	4
SU11-11	375	16	0.50017	0.54844	0.01611	0.14943	1.83073	0.05487	0.21055	0.00441	2868	35	2809	68	2909	34	51.6	79.4	1.5	3
SU11-12	-1864	17	0.55863	0.58550	0.01756	0.72634	1.71767	0.05070	0.21137	0.00340	2933	32	2958	70	2915	26	49.4	86.7	1.8	-2
SU11-13	628	17	0.44169	0.57396	0.01412	0.58085	1.74987	0.04173	0.20891	0.00336	2904	28	2914	56	2896	26	57.5	106.3	1.8	-1
SU11-14	-3650	13	0.35290	0.50423	0.01207	0.79419	1.98318	0.04970	0.19234	0.00242	2706	27	2632	54	2762	21	147.4	116.6	0.8	4
SU11-15	16437	22	0.49848	0.63708	0.01358	0.59620	1.57091	0.03300	0.24731	0.00292	3170	23	3176	53	3167	19	146.7	86.0	0.6	0

	$^{206}Pb/^{204}Pb$	$^{207}Pb/^{235}U$	2SE	$^{206}Pb/^{238}U$	2SE	rho	$^{238}U/^{206}Pb$	2SE	$^{207}Pb/^{206}Pb$	2SE	$^{207}Pb/^{235}U$ Age (Ma)	2SE	$^{206}Pb/^{238}U$ Age (Ma)	2SE	$^{207}Pb/^{206}Pb$ Age (Ma)	2SE	U (ppm)	Th (ppm)	Th/U	TW conc %
SU11-16	-12874	15	0.41865	0.55026	0.01314	0.77179	1.82143	0.04377	0.20194	0.00269	2833	26	2821	55	2841	22	112.2	59.0	0.5	1
SU11-17	11821	18	0.42545	0.59343	0.01230	0.67614	1.68696	0.03502	0.22477	0.00242	3009	23	3001	50	3014	17	67.8	36.3	0.5	0
SU11-18	2585	15	0.35916	0.55242	0.01134	0.64039	1.81300	0.03791	0.20385	0.00235	2846	23	2832	48	2857	19	52.6	37.3	0.7	1
SU11-19	-1010	16	0.43326	0.57642	0.01417	0.69008	1.74082	0.04217	0.20248	0.00300	2879	27	2926	57	2846	24	53.1	34.6	0.7	-3
SU11-20	3357	15	0.42447	0.54551	0.01519	0.88546	1.83015	0.04865	0.19698	0.00232	2805	28	2810	61	2801	19	94.8	116.2	1.2	0
SU11-21	1488	17	0.39027	0.57991	0.01183	0.48112	1.72678	0.03506	0.21601	0.00269	2948	23	2945	48	2950	20	53.4	37.0	0.7	0
SU11-22	-2495	17	0.38826	0.57591	0.01197	0.72211	1.73419	0.03572	0.21554	0.00225	2942	22	2935	49	2947	17	82.2	72.6	0.9	0
SU11-23	64241	17	0.41542	0.58548	0.01271	0.75603	1.70680	0.03861	0.21553	0.00239	2957	24	2973	54	2947	18	165.9	118.5	0.7	-1
SU11-24	-31511	15	0.40230	0.54337	0.01286	0.73626	1.84910	0.04465	0.20394	0.00260	2828	26	2787	55	2857	21	74.7	32.3	0.4	2
SU11-25	1906	15	0.37925	0.52892	0.01239	0.72854	1.89903	0.04494	0.20061	0.00263	2787	26	2727	53	2830	21	69.2	32.6	0.5	3
SU11-26	-2726	15	0.33880	0.54521	0.01160	0.41975	1.83861	0.03850	0.19726	0.00251	2802	23	2800	48	2803	21	58.9	17.0	0.3	0
SU11-27	1766	14	0.38371	0.50612	0.01396	0.47952	1.98451	0.05271	0.19584	0.00392	2722	31	2631	57	2791	33	73.0	36.3	0.5	5
SU11-28	46859	15	0.35396	0.55298	0.01180	0.65163	1.80750	0.03828	0.20099	0.00227	2836	23	2839	49	2834	18	73.6	86.4	1.2	0
SU11-29	3289	16	0.48037	0.53925	0.01489	0.77911	1.85214	0.05519	0.20803	0.00347	2845	33	2783	67	2890	27	103.4	63.2	0.6	4
SU11-30	-734	17	0.47996	0.59306	0.01554	0.82403	1.70106	0.04425	0.21000	0.00269	2936	28	2981	62	2905	21	90.8	44.8	0.5	-3
SU11-31	3254	16	0.38046	0.55962	0.01285	0.73170	1.79240	0.04246	0.20621	0.00246	2868	25	2858	55	2875	19	67.8	37.2	0.5	0
SU11-32	1174	16	0.36270	0.54935	0.01181	0.72523	1.82211	0.04006	0.20602	0.00223	2852	23	2820	50	2874	18	101.9	28.7	0.3	2
SU11-33	819	14	0.34940	0.53072	0.01206	0.68364	1.88522	0.04311	0.19662	0.00258	2775	25	2743	51	2798	21	52.0	40.1	0.8	2
SU11-34	5124	14	0.53060	0.53266	0.01960	0.52902	1.87922	0.06423	0.19606	0.00476	2775	40	2750	77	2793	40	124.6	97.4	0.8	1
SU11-35	-4221	15	0.35696	0.54413	0.01324	0.66287	1.83684	0.04426	0.19422	0.00273	2788	26	2802	55	2778	23	84.6	76.7	0.9	-1
SU11-38	1679	15	0.36524	0.55279	0.01204	0.63712	1.81125	0.03818	0.19896	0.00251	2824	23	2834	48	2817	21	56.0	49.7	0.9	-1
SU11-39	5662	18	0.42335	0.58380	0.01259	0.61012	1.71348	0.03872	0.22231	0.00261	2983	24	2963	54	2997	19	82.0	187.6	2.3	1
SU11-40	-179754	25	0.64145	0.65897	0.01589	0.57180	1.52015	0.03540	0.27964	0.00392	3322	27	3259	60	3360	22	144.0	17.5	0.1	3
SU11-41	-1159	16	0.38300	0.55484	0.01218	0.61876	1.80506	0.03898	0.20563	0.00267	2859	24	2842	50	2871	21	42.6	35.0	0.8	1
SU11-42	870	16	0.42195	0.56719	0.01347	0.72690	1.77051	0.04428	0.20578	0.00285	2878	27	2886	58	2872	23	35.2	34.0	1.0	-1
SU11-43	-3086	15	0.34804	0.55064	0.01225	0.65401	1.82261	0.04001	0.19184	0.00241	2783	24	2820	50	2757	21	79.8	57.4	0.7	-3
SU11-44	-827	18	0.45895	0.59088	0.01379	0.74425	1.70179	0.03977	0.21561	0.00279	2961	26	2980	56	2948	21	46.2	21.3	0.5	-2
SU11-46	14380	18	0.41180	0.58803	0.01271	0.76910	1.70549	0.03712	0.22434	0.00233	2997	23	2975	52	3011	17	172.0	114.3	0.7	1
SU11-47	-3190	19	0.47585	0.61276	0.01457	0.61727	1.63098	0.03864	0.22265	0.00303	3032	26	3083	58	2999	22	53.9	21.6	0.4	-3
SU11-48	-1118	22	0.56575	0.63106	0.01554	0.65396	1.59278	0.03836	0.24946	0.00395	3165	28	3141	60	3181	25	37.4	23.0	0.6	1
SU11-50	2253	14	0.32194	0.52189	0.01107	0.63765	1.92019	0.04120	0.18813	0.00229	2715	23	2703	47	2725	20	74.7	73.3	1.0	1
SU11-52	*5347*	*14*	*0.37868*	*0.52643*	*0.01443*	*0.47646*	*1.90433*	*0.05215*	*0.19072*	*0.00191*	*2736*	*28*	*2721*	*61*	*2748*	*16*	*51.3*	*2.1*	*0.0*	*1*
SU11-53	1386	14	0.37745	0.51983	0.01391	0.37208	1.92456	0.05056	0.19253	0.00210	2735	27	2697	58	2763	18	69.7	6.3	0.1	2
SU11-55	1448	14	0.41647	0.53846	0.01504	0.22508	1.86201	0.05240	0.19301	0.00258	2769	30	2771	63	2767	22	38.0	2.7	0.1	0
SU11-56	1261	15	0.45618	0.54344	0.01586	0.30870	1.84415	0.05522	0.20365	0.00196	2829	30	2793	68	2855	16	69.3	5.9	0.1	2
SU11-57	44003	15	0.40374	0.53020	0.01396	0.40083	1.87982	0.04847	0.20359	0.00196	2811	26	2750	58	2854	16	104.9	16.5	0.2	4
SU11-59	-3616	14	0.39210	0.52762	0.01363	0.25367	1.89448	0.04960	0.19685	0.00228	2771	27	2732	58	2800	19	41.4	2.5	0.1	2
SU11-60	4240	15	0.38305	0.53227	0.01407	0.44878	1.87807	0.05151	0.19762	0.00140	2783	27	2752	61	2806	12	219.9	24.2	0.1	2
SU11-61	39351	14	0.39869	0.50903	0.01408	0.10298	1.95996	0.05383	0.19668	0.00167	2738	27	2658	60	2798	14	116.0	6.6	0.1	5
SU11-62	1016	16	0.45539	0.54619	0.01501	0.18897	1.83402	0.05072	0.20605	0.00257	2845	29	2805	63	2874	20	45.4	3.0	0.1	2
SU11-65	-5685	17	0.49816	0.57866	0.01658	0.46596	1.73183	0.04930	0.21752	0.00278	2952	30	2938	67	2962	21	88.4	4.4	0.1	1
SU11-66	3443	41	1.11922	0.79296	0.02137	0.40763	1.26102	0.03211	0.37771	0.00292	3802	26	3764	73	3822	12	69.5	4.6	0.1	2
SU11-67	-913	42	1.15244	0.81119	0.02155	0.28464	1.23263	0.03461	0.37517	0.00335	3818	29	3829	81	3812	14	44.3	4.3	0.1	0
SU11-68	-13760	14	0.41480	0.52426	0.01507	0.52844	1.90882	0.05460	0.20001	0.00257	2779	30	2716	63	2826	21	263.6	16.3	0.1	4

	$^{206}Pb/^{204}Pb$	$^{207}Pb/^{235}U$	2SE	$^{206}Pb/^{238}U$	2SE	rho	$^{238}U/^{206}Pb$	2SE	$^{207}Pb/^{206}Pb$	2SE	$^{207}Pb/^{235}U$ Age (Ma)	2SE	$^{206}Pb/^{238}U$ Age (Ma)	2SE	$^{207}Pb/^{206}Pb$ Age (Ma)	2SE	U (ppm)	Th (ppm)	Th/U	TW conc %
SU11-69	-3254	16	0.40633	0.54676	0.01419	0.38642	1.82920	0.04701	0.20764	0.00169	2855	26	2811	59	2886	13	157.0	16.8	0.1	3
SU11-70	27070	18	0.47986	0.57499	0.01525	0.43101	1.74141	0.04714	0.22794	0.00185	2992	27	2925	64	3037	13	141.0	10.0	0.1	4
SU11-71	110323	17	0.48767	0.56168	0.01560	0.36737	1.78602	0.05072	0.22508	0.00199	2955	29	2866	66	3017	14	315.6	27.6	0.1	5
SU11-72	21935	14	0.43926	0.51149	0.01529	0.17375	1.96011	0.05964	0.20408	0.00186	2773	30	2657	66	2858	15	152.1	12.0	0.1	7
SU11-73	-4699	30	0.79496	0.70908	0.01829	0.40322	1.40855	0.03794	0.30809	0.00257	3492	28	3458	72	3511	13	85.5	7.9	0.1	2
SU11-74	-20904	29	0.78041	0.68881	0.01822	0.53314	1.45341	0.03807	0.31082	0.00323	3469	28	3375	69	3524	16	43.8	3.6	0.1	4
SU11-77	-2462	17	0.44900	0.57512	0.01504	0.55709	1.73942	0.04467	0.21750	0.00193	2948	26	2928	60	2962	14	112.4	8.4	0.1	1
SU11-80	24963	16	0.41359	0.55010	0.01433	0.49431	1.81869	0.04742	0.20667	0.00193	2856	26	2825	60	2879	15	79.3	6.6	0.1	2
SU11-81	15072	15	0.42157	0.54698	0.01488	0.25098	1.82886	0.04915	0.19689	0.00209	2805	27	2812	61	2800	17	66.6	3.7	0.1	0
SU11-82	856	15	0.42926	0.53335	0.01492	0.43838	1.87830	0.05260	0.20248	0.00264	2806	29	2752	63	2846	21	70.8	5.3	0.1	3
SU11-84	2564	16	0.43038	0.54736	0.01492	0.48302	1.82867	0.05055	0.20829	0.00186	2859	28	2812	63	2892	14	107.1	11.5	0.1	3
SU11-85	-7254	21	0.54080	0.62506	0.01641	0.55167	1.59816	0.04330	0.23744	0.00230	3114	28	3133	67	3102	15	173.7	19.6	0.1	-1
SU11-86	-10567	17	0.45799	0.56310	0.01482	0.31232	1.77791	0.04634	0.21738	0.00196	2926	26	2877	60	2961	15	86.1	6.3	0.1	3
SU11-87	-7108	13	0.36249	0.49259	0.01426	0.40114	2.04074	0.06016	0.18581	0.00163	2646	29	2571	62	2705	15	132.1	11.7	0.1	5
SU11-88	21146	14	0.36359	0.53343	0.01373	0.43846	1.87242	0.04730	0.18841	0.00167	2741	25	2759	57	2728	15	116.8	11.0	0.1	-1
SU11-89	258	17	0.52041	0.56105	0.01659	0.18768	1.78787	0.05366	0.21977	0.00346	2931	32	2864	69	2978	25	13.9	1.0	0.1	3
SU11-90	18281	16	0.42310	0.54610	0.01484	0.44780	1.83610	0.04999	0.20694	0.00195	2849	27	2803	62	2881	15	165.8	13.6	0.1	2
SU11-92	8349	12	0.39592	0.48157	0.01615	0.30394	2.07625	0.06673	0.18596	0.00240	2631	33	2534	67	2706	21	87.1	5.4	0.1	6
SU11-93	-1042	15	0.41263	0.52826	0.01424	0.34383	1.89737	0.05131	0.20631	0.00207	2814	27	2729	60	2876	16	48.1	3.1	0.1	5
SU11-94	7127	18	0.52944	0.57517	0.01571	0.30186	1.73834	0.05006	0.22482	0.00337	2980	31	2929	68	3015	24	23.8	1.8	0.1	3
SU11-95	*-225*	*16*	*0.49929*	*0.54910*	*0.01672*	*0.35189*	*1.83196*	*0.05385*	*0.21031*	*0.00337*	*2866*	*32*	*2808*	*67*	*2907*	*26*	*18.4*	*0.8*	*0.0*	*3*
SU11-96	-1221	13	0.36423	0.52059	0.01403	0.51697	1.92517	0.05213	0.18841	0.00204	2714	28	2697	60	2728	18	52.8	4.1	0.1	1
SU11-98	-993	14	0.38212	0.51549	0.01397	0.50367	1.94183	0.05410	0.19831	0.00207	2755	28	2678	61	2812	17	49.1	4.1	0.1	5
SU11-100	-16868	15	0.38671	0.52821	0.01390	0.44789	1.89317	0.05195	0.20160	0.00167	2794	27	2734	61	2838	13	162.4	14.5	0.1	4
SU11-101	7583	16	0.43235	0.55627	0.01497	0.46170	1.80195	0.04948	0.20570	0.00226	2861	28	2846	63	2871	18	46.3	3.8	0.1	1
SU11-102	-3476	15	0.43063	0.54017	0.01491	0.44381	1.85808	0.05275	0.20736	0.00232	2839	29	2776	64	2884	18	45.0	5.7	0.1	4
SU11-103	2220	14	0.39053	0.52305	0.01404	0.47382	1.91306	0.05209	0.20118	0.00176	2783	27	2711	60	2835	14	78.6	7.7	0.1	4
SU11-104	-2233	15	0.41945	0.53675	0.01486	0.40026	1.86678	0.05192	0.20206	0.00205	2810	28	2765	63	2842	17	47.9	4.4	0.1	3
SU11-109	-2176	15	0.43813	0.53816	0.01504	0.34387	1.86223	0.05079	0.20579	0.00232	2830	28	2771	61	2872	18	98.7	15.1	0.2	3
SU11-112	8575	32	0.84562	0.70969	0.01842	0.45978	1.41042	0.03648	0.33054	0.00278	3559	27	3455	69	3619	13	62.8	4.1	0.1	4
SU11-113	-17394	14	0.38311	0.52362	0.01402	0.41765	1.91183	0.05145	0.19620	0.00184	2759	27	2712	60	2794	15	120.3	9.6	0.1	3
SU11-117	3221	13	0.36424	0.49077	0.01382	0.42647	2.04094	0.05727	0.18662	0.00270	2650	30	2571	59	2712	24	45.4	2.3	0.1	5
SU11-118	-22430	13	0.33346	0.48990	0.01305	0.52550	2.04280	0.05272	0.18993	0.00155	2666	26	2569	55	2741	13	279.4	25.7	0.1	6
SU11-124	5679	14	0.43730	0.51682	0.01539	0.34119	1.94069	0.05748	0.20010	0.00303	2764	32	2679	65	2826	25	44.7	2.8	0.1	5
SU11-125	-1094	17	0.45607	0.55175	0.01502	0.52469	1.81914	0.05021	0.22342	0.00248	2931	29	2824	63	3005	18	52.2	4.1	0.1	6
SU11-131	-2308	15	0.41029	0.52563	0.01445	0.45088	1.91092	0.05251	0.20364	0.00256	2795	29	2713	61	2855	21	53.0	4.0	0.1	5
SU11-132	6966	14	0.40191	0.51970	0.01415	0.44573	1.93195	0.05316	0.20331	0.00232	2783	28	2689	61	2852	19	60.6	5.6	0.1	5
SU11-133	-1943	15	0.46980	0.52384	0.01701	0.50800	1.91507	0.06365	0.20648	0.00360	2806	36	2708	74	2877	28	98.5	9.9	0.1	6
SU11-135	977	13	0.45121	0.49901	0.01977	0.40872	2.01833	0.07376	0.18631	0.00336	2659	38	2594	78	2709	30	276.2	16.9	0.1	4
SU11-136	252	20	0.62832	0.59176	0.01839	0.43805	1.69664	0.05273	0.24027	0.00469	3068	35	2987	74	3121	31	26.0	2.0	0.1	4
SU11-138	900	16	0.43692	0.55349	0.01537	0.32501	1.81622	0.05057	0.20392	0.00192	2845	28	2828	64	2857	15	87.3	11.6	0.1	1
SU11-139	2308	15	0.41032	0.53872	0.01448	0.43347	1.85774	0.04789	0.20423	0.00194	2825	26	2776	58	2860	15	149.3	14.2	0.1	3
SU11-141	1138	20	0.55595	0.59247	0.01675	0.37843	1.69256	0.04892	0.24025	0.00247	3070	30	2993	69	3121	16	56.1	2.5	0.0	4
SU11-142	1393	20	0.55868	0.61805	0.01689	0.43200	1.62387	0.04462	0.23917	0.00270	3106	29	3093	68	3114	18	60.2	4.9	0.1	0

	$^{206}Pb/^{204}Pb$	$^{207}Pb/^{235}U$	2SE	$^{206}Pb/^{238}U$	2SE	rho	$^{238}U/^{206}Pb$	2SE	$^{207}Pb/^{206}Pb$	2SE	$^{207}Pb/^{235}U$ Age (Ma)	2SE	$^{206}Pb/^{238}U$ Age (Ma)	2SE	$^{207}Pb/^{206}Pb$ Age (Ma)	2SE	U (ppm)	Th (ppm)	Th/U	TW conc %
SU11-143	4909	20	0.54824	0.59698	0.01661	0.28312	1.68422	0.04738	0.23854	0.00240	3068	29	3005	68	3110	16	63.7	10.2	0.2	3
SU11-144	1149	15	0.42100	0.53632	0.01491	0.37872	1.86774	0.04922	0.20302	0.00206	2814	27	2764	59	2850	17	52.4	4.5	0.1	3
SU11-149	2445	16	0.42003	0.52676	0.01427	0.50492	1.90578	0.05124	0.21430	0.00227	2846	28	2719	60	2938	17	47.7	4.6	0.1	7
SU11-152	-3299	16	0.42017	0.54292	0.01444	0.45573	1.84435	0.04709	0.21117	0.00193	2864	26	2793	58	2914	15	76.2	9.2	0.1	4
SU11-153	7427	17	0.50155	0.54522	0.01609	0.42751	1.83922	0.05535	0.22508	0.00291	2927	31	2799	68	3017	21	68.8	3.9	0.1	7
SU11-155	1125	13	0.36264	0.48804	0.01334	0.25836	2.05365	0.05347	0.19406	0.00174	2681	26	2557	55	2776	15	71.4	4.4	0.1	8
SU11-159	7424	13	0.37914	0.50661	0.01472	0.37967	1.98829	0.05866	0.18803	0.00171	2682	29	2626	64	2724	15	120.0	12.7	0.1	3
SU11-162	-640	15	0.40466	0.53036	0.01389	0.49801	1.88616	0.05057	0.20295	0.00228	2804	28	2742	60	2849	18	48.6	4.5	0.1	4
SU11-163	1723	15	0.43077	0.53643	0.01470	0.42975	1.86757	0.04912	0.20719	0.00264	2833	28	2764	59	2883	21	20.3	1.9	0.1	4
SU11-166	17321	14	0.39282	0.52979	0.01455	0.48989	1.89491	0.05325	0.19850	0.00196	2779	28	2732	63	2813	16	75.7	8.5	0.1	3
SU11-167	7006	14	0.37464	0.52416	0.01376	0.52479	1.91103	0.05118	0.19822	0.00168	2769	27	2713	59	2811	14	175.3	17.6	0.1	3
SU11-170	17488	15	0.44817	0.53518	0.01550	0.49628	1.87249	0.05475	0.20813	0.00317	2835	31	2758	66	2890	25	45.9	2.8	0.1	4
SU11-171	7457	16	0.43767	0.54433	0.01532	0.51555	1.84154	0.05114	0.20983	0.00246	2859	29	2796	63	2904	19	55.1	4.8	0.1	4
SU11-172	5942	14	0.41640	0.51324	0.01513	0.39955	1.95783	0.05698	0.20006	0.00190	2755	29	2660	63	2826	16	75.9	4.7	0.1	6
SU11-178	*-3909*	*13*	*0.42649*	*0.48888*	*0.01513*	*0.15148*	*2.05407*	*0.06284*	*0.19328*	*0.00247*	*2677*	*31*	*2557*	*65*	*2770*	*21*	*75.0*	*2.1*	*0.0*	*7*
SU11-179	2032	13	0.36067	0.49643	0.01344	0.36187	2.01988	0.05465	0.18932	0.00184	2674	27	2593	58	2736	16	100.0	9.5	0.1	5
SU11-180	3179	15	0.44652	0.55155	0.01638	0.44374	1.82275	0.05403	0.20145	0.00176	2830	29	2819	68	2837	14	129.1	13.7	0.1	0
SU11-182	630	18	0.48238	0.58332	0.01542	0.53356	1.71691	0.04477	0.22624	0.00235	2998	27	2959	62	3025	17	54.4	5.3	0.1	2
SU11-183	8775	13	0.39775	0.49741	0.01578	0.49256	2.02436	0.06654	0.18879	0.00265	2669	34	2588	70	2731	23	157.3	11.8	0.1	5
SU11-184	1406	16	0.42861	0.53215	0.01422	0.52259	1.88327	0.05187	0.21189	0.00231	2847	28	2746	62	2919	18	72.3	6.6	0.1	6
SU11-187	1586	14	0.37447	0.50980	0.01376	0.43475	1.96257	0.05108	0.19520	0.00177	2730	26	2655	57	2786	15	104.7	8.3	0.1	5
SU11-188	-4477	15	0.42420	0.53253	0.01399	0.32767	1.87990	0.04978	0.20953	0.00216	2838	27	2750	59	2901	17	106.6	10.4	0.1	5
SU11-189	*878*	*13*	*0.36942*	*0.50022*	*0.01355*	*0.36164*	*2.00069*	*0.05560*	*0.19106*	*0.00179*	*2691*	*28*	*2613*	*60*	*2751*	*15*	*69.5*	*3.1*	*0.0*	*5*
SU11-190	4165	13	0.36133	0.49724	0.01315	0.34870	2.01123	0.05516	0.19094	0.00194	2686	28	2602	59	2750	17	76.9	6.8	0.1	5
SU11-191	17811	13	0.36315	0.48255	0.01371	0.30873	2.07628	0.06001	0.18997	0.00174	2651	29	2534	61	2741	15	230.4	26.2	0.1	7
SU11-192	-1812	15	0.41461	0.53778	0.01469	0.49471	1.86471	0.05095	0.20467	0.00214	2823	28	2768	61	2863	17	81.9	9.5	0.1	3
SU11-193	-2821	12	0.37706	0.48562	0.01355	-0.07205	2.06585	0.06247	0.18528	0.00176	2632	30	2545	64	2700	16	143.5	15.1	0.1	6
SU11-195	1250	19	0.49979	0.56719	0.01529	0.49998	1.76595	0.04826	0.23896	0.00207	3024	28	2892	64	3112	14	158.4	13.2	0.1	7
SU11-196	1805	21	0.55561	0.59278	0.01559	0.38874	1.68630	0.04680	0.25291	0.00238	3123	28	3002	67	3202	15	82.7	6.3	0.1	6
SU11-197	-5352	21	0.55458	0.60373	0.01589	0.48352	1.65802	0.04414	0.25277	0.00207	3139	27	3042	65	3201	13	180.2	19.7	0.1	5
SU11-198	-5438	14	0.37475	0.51052	0.01331	0.45765	1.95718	0.05081	0.20224	0.00160	2766	26	2661	57	2844	13	219.6	17.5	0.1	6
SU11-199	3270	14	0.39181	0.51170	0.01391	0.30338	1.95902	0.05393	0.20207	0.00163	2764	27	2659	60	2842	13	199.4	13.7	0.1	6
SU11-200	-2398	20	0.64047	0.57990	0.01904	0.41579	1.72827	0.05663	0.24481	0.00398	3068	35	2943	77	3151	26	86.7	15.5	0.2	7
SU11-202	*736*	*22*	*1.11626*	*0.65771*	*0.03280*	*0.23293*	*1.54273*	*0.07156*	*0.23990*	*0.00458*	*3158*	*49*	*3221*	*118*	*3119*	*30*	*66.5*	*3.3*	*0.0*	*-4*
SU11-204	4074	25	0.81611	0.64517	0.02062	0.38633	1.55721	0.04970	0.28372	0.00387	3313	34	3198	80	3383	21	115.8	15.7	0.1	5
SU11-205	13790	25	0.73087	0.65273	0.01788	-0.06825	1.53468	0.04285	0.27760	0.00273	3305	29	3234	71	3349	15	178.3	13.0	0.1	3
SU11-206	-296	21	0.70652	0.62344	0.01959	0.40626	1.59910	0.05029	0.24692	0.00453	3151	35	3131	78	3164	29	22.0	2.5	0.1	1
SU11-207	*37264*	*20*	*0.65438*	*0.59524*	*0.01828*	*0.35912*	*1.67822*	*0.05361*	*0.23477*	*0.00330*	*3056*	*34*	*3013*	*77*	*3084*	*22*	*28.1*	*1.0*	*0.0*	*3*
SU11-209	909	17	0.53338	0.55538	0.01575	0.30283	1.80768	0.05179	0.21846	0.00392	2915	32	2838	66	2969	29	17.4	2.3	0.1	4
SU11-210	-377	17	0.57203	0.58323	0.01677	0.29764	1.71149	0.04943	0.21623	0.00462	2958	34	2966	69	2952	34	14.1	2.0	0.1	-1
SU11-212	313	14	0.41404	0.50472	0.01423	0.41743	1.98837	0.05628	0.20221	0.00300	2751	30	2626	61	2843	24	24.0	1.2	0.1	7
SU11-214	2449	35	0.98011	0.73153	0.02111	0.47874	1.37365	0.04021	0.34619	0.00289	3631	30	3526	80	3690	13	80.2	5.3	0.1	4
SU11-217	1555	15	0.40799	0.52054	0.01353	0.26696	1.92030	0.05105	0.20946	0.00212	2817	27	2702	59	2901	16	41.8	2.2	0.1	7
SU11-54	*2083*	*12*	*0.34478*	*0.44491*	*0.01349*	*0.49374*	*2.25322*	*0.07029*	*0.18991*	*0.00269*	*2574*	*32*	*2368*	*62*	*2741*	*23*	*285.9*	*18.4*	*0.1*	*13*

	$^{206}Pb/^{204}Pb$	$^{207}Pb/^{235}U$	2SE	$^{206}Pb/^{238}U$	2SE	rho	$^{238}U/^{206}Pb$	2SE	$^{207}Pb/^{206}Pb$	2SE	$^{207}Pb/^{235}U$ Age (Ma)	2SE	$^{206}Pb/^{238}U$ Age (Ma)	2SE	$^{207}Pb/^{206}Pb$ Age (Ma)	2SE	U (ppm)	Th (ppm)	Th/U	TW conc %
SU11-64	*-24590*	*15*	*0.40947*	*0.51083*	*0.01373*	*0.19196*	*1.95914*	*0.05243*	*0.20997*	*0.00165*	*2801*	*27*	*2658*	*58*	*2905*	*13*	*262.2*	*23.2*	*0.1*	*8*
SU11-79	*-29045*	*12*	*0.55966*	*0.45470*	*0.01944*	*-0.13301*	*2.25066*	*0.09279*	*0.19833*	*0.00177*	*2616*	*40*	*2370*	*82*	*2812*	*15*	*175.1*	*19.3*	*0.1*	*14*
SU11-83	*-4164*	*13*	*0.49406*	*0.47677*	*0.01728*	*0.12852*	*2.14116*	*0.08270*	*0.20061*	*0.00235*	*2673*	*38*	*2471*	*79*	*2830*	*19*	*102.9*	*11.4*	*0.1*	*11*
SU11-97	*17615*	*6*	*0.20537*	*0.23689*	*0.00813*	*0.00182*	*4.22859*	*0.15299*	*0.17533*	*0.00208*	*1934*	*33*	*1368*	*45*	*2608*	*20*	*875.2*	*104.2*	*0.1*	*47*
SU11-105	*-6066*	*12*	*0.42497*	*0.44809*	*0.01599*	*0.16917*	*2.27639*	*0.09275*	*0.19363*	*0.00158*	*2583*	*39*	*2347*	*80*	*2772*	*13*	*174.8*	*16.8*	*0.1*	*14*
SU11-107	*1257*	*3*	*0.09462*	*0.12793*	*0.00352*	*0.55780*	*7.79859*	*0.23426*	*0.19287*	*0.00224*	*1506*	*25*	*778*	*22*	*2766*	*19*	*825.3*	*54.8*	*0.1*	*72*
SU11-110	*9508*	*17*	*0.48061*	*0.53883*	*0.01504*	*0.37674*	*1.85593*	*0.05388*	*0.22779*	*0.00243*	*2930*	*30*	*2778*	*66*	*3036*	*17*	*195.4*	*16.4*	*0.1*	*8*
SU11-114	*6697*	*13*	*0.36862*	*0.47845*	*0.01380*	*0.47439*	*2.09662*	*0.06034*	*0.19848*	*0.00187*	*2683*	*29*	*2514*	*60*	*2813*	*15*	*203.7*	*19.6*	*0.1*	*10*
SU11-120	*-4656*	*12*	*0.38762*	*0.45382*	*0.01502*	*0.38442*	*2.23064*	*0.07387*	*0.18879*	*0.00147*	*2578*	*32*	*2388*	*66*	*2731*	*13*	*107.3*	*5.3*	*0.0*	*12*
SU11-127	*-5310*	*12*	*0.37594*	*0.46382*	*0.01508*	*0.54396*	*2.15189*	*0.07825*	*0.19247*	*0.00322*	*2630*	*38*	*2460*	*74*	*2763*	*27*	*218.5*	*15.7*	*0.1*	*11*
SU11-129	*3122*	*12*	*0.46362*	*0.43881*	*0.01647*	*0.03038*	*2.31756*	*0.08669*	*0.19555*	*0.00224*	*2575*	*37*	*2312*	*73*	*2789*	*19*	*95.0*	*8.7*	*0.1*	*16*
SU11-137	*1797*	*18*	*0.55070*	*0.55415*	*0.01699*	*0.40001*	*1.81897*	*0.05691*	*0.23845*	*0.00238*	*2993*	*32*	*2824*	*72*	*3109*	*16*	*103.5*	*3.0*	*0.0*	*9*
SU11-145	*1687*	*8*	*0.42300*	*0.33611*	*0.01549*	*-0.42423*	*3.06746*	*0.14947*	*0.17834*	*0.00215*	*2232*	*45*	*1819*	*77*	*2637*	*20*	*362.4*	*43.9*	*0.1*	*29*
SU11-150	*2369*	*20*	*0.57476*	*0.56894*	*0.01699*	*0.54170*	*1.76132*	*0.05307*	*0.25220*	*0.00295*	*3078*	*31*	*2899*	*70*	*3198*	*19*	*76.2*	*5.3*	*0.1*	*9*
SU11-151	*-2963*	*15*	*0.46706*	*0.51127*	*0.01531*	*0.16144*	*1.96500*	*0.05768*	*0.20995*	*0.00242*	*2798*	*30*	*2652*	*64*	*2904*	*19*	*70.6*	*6.7*	*0.1*	*8*
SU11-156	*130257*	*7*	*0.24186*	*0.27802*	*0.00971*	*0.14095*	*3.61286*	*0.12532*	*0.17789*	*0.00181*	*2084*	*32*	*1575*	*48*	*2633*	*17*	*478.5*	*46.5*	*0.1*	*40*
SU11-157	*-10646*	*13*	*0.40153*	*0.48821*	*0.01462*	*0.50407*	*2.05398*	*0.06456*	*0.19775*	*0.00316*	*2699*	*33*	*2557*	*66*	*2807*	*26*	*56.4*	*4.7*	*0.1*	*9*
SU11-160	*4429*	*11*	*0.40646*	*0.45290*	*0.01527*	*0.05536*	*2.24203*	*0.07976*	*0.18365*	*0.00202*	*2547*	*35*	*2378*	*71*	*2685*	*18*	*57.1*	*5.8*	*0.1*	*10*
SU11-161	*-10279*	*15*	*0.47836*	*0.49454*	*0.01623*	*0.25068*	*2.02988*	*0.06699*	*0.21633*	*0.00237*	*2795*	*33*	*2582*	*70*	*2953*	*18*	*165.5*	*18.7*	*0.1*	*12*
SU11-168	*-2873*	*11*	*0.37637*	*0.43971*	*0.01438*	*0.18054*	*2.29869*	*0.07340*	*0.18517*	*0.00183*	*2532*	*31*	*2328*	*62*	*2699*	*16*	*90.8*	*6.7*	*0.1*	*13*
SU11-173	*2728*	*4*	*0.15052*	*0.15981*	*0.00567*	*0.25849*	*6.26966*	*0.22685*	*0.18585*	*0.00222*	*1651*	*31*	*954*	*32*	*2705*	*20*	*626.7*	*63.8*	*0.1*	*65*
SU11-174	*-2116*	*12*	*0.34669*	*0.45723*	*0.01462*	*0.55069*	*2.18430*	*0.06335*	*0.18708*	*0.00266*	*2589*	*30*	*2430*	*59*	*2716*	*23*	*196.4*	*11.2*	*0.1*	*11*
SU11-176	*1790*	*5*	*0.18578*	*0.20735*	*0.00754*	*0.10609*	*4.87435*	*0.18384*	*0.16524*	*0.00220*	*1762*	*33*	*1203*	*41*	*2509*	*22*	*709.5*	*58.7*	*0.1*	*52*
SU11-181	*-2813*	*14*	*0.45376*	*0.48993*	*0.01644*	*0.20987*	*2.07517*	*0.07634*	*0.20235*	*0.00195*	*2711*	*36*	*2535*	*77*	*2845*	*16*	*107.5*	*11.3*	*0.1*	*10*
SU11-186	*-2705*	*18*	*0.68895*	*0.54627*	*0.02096*	*0.16437*	*1.85554*	*0.07097*	*0.23845*	*0.00263*	*2974*	*38*	*2779*	*86*	*3109*	*18*	*197.6*	*21.0*	*0.1*	*10*
SU11-213	*-1857*	*30*	*0.91523*	*0.64032*	*0.02043*	*0.56226*	*1.56593*	*0.05031*	*0.33773*	*0.00595*	*3478*	*36*	*3184*	*81*	*3652*	*27*	*55.3*	*4.5*	*0.1*	*13*
SU11-215	*1222*	*15*	*0.40925*	*0.50734*	*0.01464*	*0.52106*	*1.97621*	*0.05535*	*0.20806*	*0.00242*	*2784*	*29*	*2640*	*61*	*2890*	*19*	*54.7*	*4.8*	*0.1*	*8*
SU11-216	*2800*	*14*	*0.39696*	*0.50236*	*0.01339*	*0.26396*	*1.99223*	*0.05359*	*0.20574*	*0.00205*	*2765*	*27*	*2622*	*58*	*2872*	*16*	*127.1*	*13.8*	*0.1*	*9*
SU15																				
SU15-1	1731	13	0.32034	0.50907	0.01354	0.34238	1.96512	0.05236	0.18255	0.00214	2665	27	2652	58	2675	19	83.4	46.4	0.6	1
SU15-3	1774	13	0.30169	0.50827	0.01310	0.51434	1.96460	0.05029	0.18444	0.00219	2675	27	2652	56	2692	20	167.6	24.3	0.1	2
SU15-4	10368	12	0.28942	0.49607	0.01316	0.64116	2.01608	0.05320	0.18130	0.00199	2635	27	2597	56	2664	18	254.4	197.4	0.8	2
SU15-6	3294	13	0.30352	0.50884	0.01342	0.58515	1.96849	0.05529	0.18318	0.00193	2667	28	2648	61	2681	17	84.8	49.7	0.6	1
SU15-7	8644	13	0.32386	0.52839	0.01389	0.41686	1.89048	0.04940	0.18391	0.00186	2709	26	2737	58	2688	17	82.6	36.5	0.4	-2
SU15-11	-2473	13	0.30003	0.51110	0.01291	0.46315	1.95775	0.05121	0.18269	0.00209	2669	27	2660	57	2677	19	56.8	24.2	0.4	1
SU15-12	-1166	13	0.33726	0.49841	0.01491	0.53863	2.02658	0.06291	0.18381	0.00238	2643	32	2586	66	2687	21	81.5	41.8	0.5	3
SU15-13	-29406	13	0.33001	0.52061	0.01371	0.35095	1.92283	0.05180	0.18132	0.00183	2679	27	2699	59	2664	17	65.5	40.9	0.6	-1
SU15-16	2243	13	0.30303	0.51202	0.01382	0.64666	1.96229	0.05574	0.18296	0.00206	2669	29	2655	62	2679	19	95.5	55.1	0.6	1
SU15-17	814	13	0.29976	0.50698	0.01362	0.58313	1.97622	0.05372	0.18166	0.00204	2655	28	2640	59	2667	19	88.1	56.4	0.6	1
SU15-18	-1249	13	0.31991	0.50330	0.01645	0.74460	1.99268	0.06297	0.18417	0.00315	2660	34	2622	68	2690	28	58.3	21.9	0.4	2
SU15-19	1277	12	0.30797	0.49295	0.01388	0.55429	2.01888	0.05612	0.18151	0.00197	2634	28	2594	59	2666	18	103.4	59.4	0.6	3
SU15-20	-4791	13	0.38978	0.52063	0.01832	0.58184	1.92594	0.06735	0.18176	0.00315	2680	37	2696	77	2668	29	196.4	164.5	0.8	-1
SU15-21	3255	13	0.30354	0.51645	0.01370	0.48872	1.93872	0.05382	0.18342	0.00218	2682	28	2681	61	2683	20	62.2	35.1	0.6	0
SU15-22	1435	13	0.31451	0.51267	0.01302	0.31557	1.94787	0.04998	0.18295	0.00185	2676	26	2671	56	2679	17	88.8	54.4	0.6	0

	$^{206}Pb/^{204}Pb$	$^{207}Pb/^{235}U$	2SE	$^{206}Pb/^{238}U$	2SE	rho	$^{238}U/^{206}Pb$	2SE	$^{207}Pb/^{206}Pb$	2SE	$^{207}Pb/^{235}U$ Age (Ma)	2SE	$^{206}Pb/^{238}U$ Age (Ma)	2SE	$^{207}Pb/^{206}Pb$ Age (Ma)	2SE	U (ppm)	Th (ppm)	Th/U	TW conc %
SU15-23	2471	13	0.36984	0.50261	0.01542	0.56044	1.99247	0.06168	0.18547	0.00342	2667	34	2622	67	2702	30	174.2	77.1	0.4	3
SU15-25	4491	12	0.29970	0.49495	0.01373	0.59837	2.02244	0.05714	0.18218	0.00199	2636	28	2590	60	2672	18	113.0	65.9	0.6	3
SU15-27	-5112	13	0.35232	0.52718	0.01658	0.59730	1.90913	0.05986	0.18361	0.00221	2698	32	2715	69	2685	20	191.6	133.3	0.7	-2
SU15-30	2035	12	0.28350	0.50186	0.01296	0.54143	1.99277	0.05038	0.18023	0.00172	2640	25	2622	54	2654	16	87.2	68.0	0.8	1
SU15-33	921	13	0.38996	0.49684	0.01694	0.14512	2.02415	0.06815	0.18315	0.00283	2640	35	2588	72	2681	26	70.4	43.7	0.6	3
SU15-34	4209	12	0.37124	0.49792	0.01454	0.22768	2.00879	0.05741	0.18042	0.00279	2634	31	2604	61	2656	26	54.4	31.2	0.6	2
SU15-35	-2254	12	0.30090	0.49363	0.01287	0.44746	2.02011	0.05251	0.18297	0.00220	2641	27	2592	55	2679	20	66.2	37.9	0.6	3
SU15-36	5995	12	0.30757	0.49716	0.01435	0.52835	2.01679	0.06063	0.18229	0.00241	2639	31	2596	64	2673	22	140.6	38.6	0.3	3
SU15-40	*1018*	*12*	*0.33836*	*0.46903*	*0.01462*	*0.42465*	*2.13525*	*0.06791*	*0.18162*	*0.00282*	*2582*	*33*	*2476*	*65*	*2667*	*26*	*95.9*	*64.3*	*0.7*	*7*
SU16																				
SU16-1	4468	12	0.37202	0.47393	0.01627	0.37183	2.11904	0.07114	0.18083	0.00232	2586	34	2492	69	2660	21	139.4	136.9	1.0	6
SU16-5	11900	12	0.30526	0.50488	0.01422	0.50407	1.98791	0.05459	0.17938	0.00205	2638	28	2627	59	2646	19	100.8	85.8	0.9	0
SU16-7	10068	12	0.32446	0.49952	0.01432	0.48081	2.00999	0.05646	0.18085	0.00189	2635	28	2603	60	2660	17	239.4	190.8	0.8	2
SU16-8	8360	13	0.36413	0.50988	0.01639	0.45895	1.97897	0.06415	0.18045	0.00218	2648	33	2637	70	2656	20	238.6	191.3	0.8	0
SU16-9	13702	13	0.30704	0.51463	0.01385	0.42794	1.94047	0.04943	0.17883	0.00161	2658	25	2679	56	2641	15	236.0	126.5	0.5	-1
SU16-10	-11140	13	0.28592	0.50964	0.01304	0.46934	1.95970	0.05255	0.17795	0.00167	2644	27	2658	58	2633	16	189.9	118.3	0.6	-1
SU16-11	20758	13	0.30409	0.51020	0.01347	0.34189	1.95593	0.04971	0.17945	0.00185	2654	26	2662	55	2647	17	141.9	81.8	0.6	0
SU16-15	3041	12	0.27949	0.49667	0.01301	0.55377	2.01706	0.05318	0.17951	0.00174	2625	26	2596	56	2648	16	126.1	67.3	0.5	2
SU16-16	2206	13	0.35181	0.53535	0.01716	0.60835	1.88041	0.06004	0.17944	0.00250	2691	33	2749	71	2647	23	120.0	81.9	0.7	-4
SU16-17	3519	13	0.30916	0.51848	0.01314	0.23588	1.92687	0.04846	0.17790	0.00188	2659	26	2695	55	2633	18	70.9	50.5	0.7	-2
SU16-23	1209	12	0.30333	0.50150	0.01317	0.38570	1.99273	0.05367	0.17853	0.00202	2631	27	2622	58	2639	19	87.1	42.1	0.5	1
SU16-24	-4974	12	0.31663	0.50348	0.01514	0.59436	1.99428	0.05980	0.17930	0.00242	2634	31	2620	65	2646	22	129.8	120.7	0.9	1
SU16-25	967	12	0.27684	0.49786	0.01311	0.64138	2.00987	0.05075	0.18028	0.00181	2632	26	2603	54	2655	17	124.4	58.1	0.5	2
SU16-26	2848	12	0.28517	0.50321	0.01296	0.51007	1.98900	0.05198	0.17804	0.00172	2630	26	2626	56	2634	16	125.8	63.1	0.5	0
SU16-27	962	12	0.35996	0.48915	0.01736	0.65030	2.05264	0.07417	0.18222	0.00444	2623	41	2558	76	2672	40	161.4	102.1	0.6	4
SU16-28	1029	12	0.31183	0.48490	0.01390	0.51006	2.06604	0.06141	0.17873	0.00257	2598	31	2545	62	2640	24	69.4	39.0	0.6	3
SU16-30	-6945	12	0.27170	0.48252	0.01249	0.57318	2.07436	0.05394	0.17913	0.00194	2597	26	2536	55	2644	18	77.2	37.4	0.5	4
SU16-33	2334	13	0.32848	0.51033	0.01435	0.38373	1.96700	0.05665	0.17796	0.00226	2640	30	2650	63	2633	21	115.9	90.3	0.8	-1
SU16-37	928	13	0.37931	0.53759	0.01695	0.42219	1.86496	0.05898	0.18087	0.00278	2706	33	2768	71	2660	25	58.5	40.5	0.7	-4
SU16-38	842	12	0.34654	0.50414	0.01584	0.45403	1.98428	0.05936	0.17851	0.00241	2635	31	2631	65	2638	22	117.2	90.1	0.8	0
SU16-40	-4806	12	0.34259	0.50890	0.01596	0.42429	1.97937	0.06106	0.17877	0.00198	2639	31	2636	67	2641	18	108.1	76.2	0.7	0
SU16-41	5927	13	0.34296	0.51674	0.01526	0.44890	1.93659	0.05443	0.18005	0.00214	2666	29	2684	62	2653	20	154.8	64.6	0.4	-1
SU16-4	*1897*	*3*	*0.15499*	*0.11615*	*0.00670*	*0.32487*	*8.80410*	*0.47163*	*0.17633*	*0.00378*	*1345*	*43*	*694*	*35*	*2618*	*36*	*918.6*	*784.1*	*0.9*	*73*
SU16-6	*7016*	*10*	*0.28648*	*0.41901*	*0.01341*	*0.59545*	*2.40723*	*0.07709*	*0.17852*	*0.00212*	*2455*	*32*	*2240*	*61*	*2638*	*20*	*307.4*	*205.3*	*0.7*	*15*
SU16-12	*15860*	*1*	*0.08270*	*0.05768*	*0.00567*	*0.80428*	*18.48366*	*1.97977*	*0.16072*	*0.00698*	*800*	*64*	*340*	*35*	*2462*	*73*	*2524.0*	*1550.2*	*0.6*	*85*
SU16-13	*1892*	*6*	*0.26698*	*0.24079*	*0.01266*	*0.49921*	*4.21805*	*0.21628*	*0.17611*	*0.00338*	*1940*	*47*	*1371*	*63*	*2616*	*32*	*392.1*	*333.8*	*0.9*	*47*
SU16-14	*14196*	*2*	*0.16171*	*0.10166*	*0.00872*	*0.55027*	*10.32441*	*0.82638*	*0.16773*	*0.00710*	*1193*	*64*	*596*	*46*	*2534*	*71*	*1906.2*	*2362.7*	*1.2*	*75*
SU16-20	*-97366*	*9*	*0.43581*	*0.37217*	*0.02100*	*0.55699*	*2.77535*	*0.15427*	*0.17593*	*0.00366*	*2311*	*54*	*1984*	*95*	*2614*	*35*	*381.0*	*440.9*	*1.2*	*22*
SU16-32	*2829*	*8*	*0.38899*	*0.33462*	*0.01535*	*0.21965*	*3.02061*	*0.14660*	*0.17833*	*0.00471*	*2246*	*50*	*1844*	*78*	*2637*	*44*	*395.8*	*418.5*	*1.1*	*29*
SU16-34	*3420*	*8*	*0.34510*	*0.34608*	*0.01455*	*-0.00185*	*2.97047*	*0.12520*	*0.17255*	*0.00185*	*2232*	*39*	*1871*	*68*	*2582*	*18*	*206.0*	*90.9*	*0.4*	*26*
SU16-36	*-31541*	*8*	*0.33742*	*0.33540*	*0.01435*	*0.07385*	*3.00832*	*0.14340*	*0.17089*	*0.00291*	*2212*	*46*	*1850*	*77*	*2566*	*28*	*389.7*	*260.3*	*0.7*	*27*
SU16-39	*5457*	*10*	*0.29360*	*0.42023*	*0.01385*	*0.51953*	*2.38688*	*0.07611*	*0.17650*	*0.00210*	*2452*	*31*	*2256*	*61*	*2619*	*20*	*685.2*	*303.6*	*0.4*	*14*
SU16-45	*4858*	*10*	*0.43802*	*0.41095*	*0.01993*	*0.56677*	*2.49567*	*0.13632*	*0.17635*	*0.00328*	*2410*	*53*	*2172*	*101*	*2618*	*31*	*600.3*	*278.2*	*0.5*	*16*
SU20																				

	^{206}Pb / ^{204}Pb	^{207}Pb / ^{235}U	2SE	^{206}Pb / ^{238}U	2SE	rho	$^{238}U/^{206}Pb$	2SE	^{207}Pb / ^{206}Pb	2SE	$^{207}Pb/^{235}U$ Age (Ma)	2SE	$^{206}Pb/^{238}U$ Age (Ma)	2SE	$^{207}Pb/^{206}Pb$ Age (Ma)	2SE	U (ppm)	Th (ppm)	Th/U	TW conc %
SU20-0	2272	13	0.36524	0.50636	0.01362	0.30721	1.97185	0.05294	0.18905	0.00192	2695	27	2644	58	2733	17	222.9	30.0	0.1	3
SU20-1	1827	17	0.46329	0.56607	0.01499	0.28826	1.76865	0.04732	0.21746	0.00209	2932	27	2889	62	2961	16	58.8	4.5	0.1	2
SU20-2	1145	15	0.43380	0.53790	0.01455	0.21430	1.85952	0.05173	0.20385	0.00201	2822	28	2774	63	2857	16	111.0	9.2	0.1	3
SU20-3	7306	15	0.49391	0.54169	0.01907	0.39913	1.85466	0.06477	0.20171	0.00262	2815	35	2780	79	2839	21	106.5	12.1	0.1	2
SU20-4	1279	18	0.51566	0.59739	0.01618	0.22020	1.67734	0.04409	0.22177	0.00247	3002	27	3014	63	2993	18	75.6	10.8	0.1	-1
SU20-5	2764	17	0.47016	0.56537	0.01523	0.44873	1.77218	0.04778	0.22073	0.00257	2944	28	2884	63	2985	19	53.3	3.1	0.1	3
SU20-9	2124	25	0.88694	0.68025	0.02052	-0.14547	1.47452	0.04274	0.27102	0.00371	3321	31	3337	76	3311	21	138.3	13.3	0.1	-1
SU20-11	-21929	14	0.39978	0.52053	0.01432	0.31144	1.92343	0.05273	0.19316	0.00256	2739	29	2699	60	2769	22	49.6	4.9	0.1	2
SU20-12	2246	14	0.40395	0.51305	0.01531	0.49378	1.95459	0.05872	0.19592	0.00230	2737	31	2664	66	2792	19	149.1	11.0	0.1	4
SU20-13	1121	24	0.69896	0.63015	0.01769	0.31179	1.58369	0.04399	0.27615	0.00289	3270	29	3155	69	3341	16	42.1	3.3	0.1	6
SU20-14	1538	15	0.42877	0.54954	0.01481	0.42266	1.81992	0.04679	0.20201	0.00235	2834	27	2823	59	2842	19	39.3	2.7	0.1	1
SU20-15	8123	15	0.41727	0.54093	0.01463	0.50779	1.84642	0.04696	0.20829	0.00226	2849	26	2790	58	2892	18	137.1	14.8	0.1	4
SU20-16	2986	17	0.48055	0.56324	0.01552	0.35470	1.78151	0.05034	0.21698	0.00272	2923	30	2872	65	2958	20	60.0	6.6	0.1	3
SU20-17	*2255*	*13*	*0.37886*	*0.50260*	*0.01383*	*0.21184*	*1.98972*	*0.05765*	*0.18988*	*0.00166*	*2691*	*29*	*2625*	*62*	*2740*	*14*	*144.3*	*6.0*	*0.0*	*4*
SU20-18	4817	21	0.55127	0.61110	0.01650	0.59031	1.63797	0.04573	0.24519	0.00261	3121	29	3072	68	3153	17	133.7	14.5	0.1	2
SU20-19	1775	20	0.57233	0.60599	0.01633	0.26542	1.65137	0.04528	0.24356	0.00240	3107	28	3052	67	3143	16	83.5	6.7	0.1	3
SU20-20	*4011*	*19*	*0.55758*	*0.56908*	*0.01581*	*0.35640*	*1.75748*	*0.04886*	*0.23680*	*0.00349*	*3020*	*30*	*2904*	*65*	*3098*	*24*	*153.6*	*7.2*	*0.0*	*6*
SU20-21	-6490	14	0.38394	0.51409	0.01394	0.31747	1.94098	0.05532	0.19175	0.00190	2723	29	2679	62	2757	16	99.2	9.4	0.1	3
SU20-22	-16934	16	0.44080	0.54988	0.01475	0.38892	1.81914	0.04930	0.20666	0.00240	2856	28	2824	62	2879	19	66.0	5.1	0.1	2
SU20-24	582	13	0.36051	0.50274	0.01367	0.43502	1.99146	0.05628	0.18643	0.00209	2672	29	2623	61	2710	18	46.3	3.0	0.1	3
SU20-25	1143	15	0.42016	0.55520	0.01492	0.56073	1.80516	0.04799	0.20014	0.00196	2833	27	2842	61	2827	16	92.6	9.8	0.1	-1
SU20-27	14285	13	0.37833	0.49939	0.01531	0.46588	2.00309	0.05782	0.18764	0.00244	2673	30	2610	62	2721	21	242.5	21.6	0.1	4
SU20-28	9245	17	0.49230	0.59239	0.01695	0.57261	1.69468	0.04792	0.21314	0.00367	2953	32	2990	68	2929	28	28.6	2.4	0.1	-3
SU20-29	1637	17	0.49622	0.57516	0.01698	0.51706	1.74233	0.05260	0.21670	0.00257	2943	31	2924	71	2956	19	78.1	9.7	0.1	1
SU20-30	1284	18	0.48479	0.57997	0.01575	0.41547	1.72638	0.04756	0.22033	0.00237	2968	28	2946	65	2982	17	96.7	6.2	0.1	1
SU20-31	4379	16	0.43109	0.56244	0.01474	0.39373	1.77711	0.04596	0.20717	0.00222	2881	27	2878	60	2883	17	119.3	11.5	0.1	0
SU20-32	2461	14	0.39061	0.53148	0.01417	0.26901	1.88197	0.04898	0.19221	0.00202	2755	27	2747	58	2760	17	59.0	4.9	0.1	0
SU20-33	2044	25	0.68848	0.66116	0.01769	0.40395	1.51544	0.04108	0.27730	0.00236	3317	28	3267	69	3347	13	135.0	10.4	0.1	2
SU20-34	2780	16	0.48121	0.56184	0.01622	0.26815	1.78655	0.05020	0.21037	0.00249	2890	29	2866	65	2908	19	44.5	2.3	0.1	1
SU20-37	-2585	16	0.47126	0.56777	0.01619	0.33049	1.76590	0.04833	0.20376	0.00285	2871	29	2893	64	2856	23	35.0	3.1	0.1	-2
SU20-38	2976	18	0.49127	0.58361	0.01590	0.48133	1.71305	0.04898	0.21965	0.00254	2972	30	2964	68	2977	19	61.2	5.0	0.1	0
SU20-39	890	14	0.38358	0.52176	0.01436	0.32107	1.92187	0.05317	0.19111	0.00202	2730	28	2701	61	2751	17	61.0	4.3	0.1	2
SU20-40	1645	14	0.37886	0.51809	0.01386	0.30860	1.93071	0.04920	0.19028	0.00229	2721	27	2690	56	2744	20	72.1	7.2	0.1	2
SU20-42	1885	13	0.37813	0.51223	0.01419	0.36369	1.95295	0.05589	0.18918	0.00204	2705	29	2665	62	2734	18	101.5	10.0	0.1	2
SU20-43	3168	13	0.37413	0.50699	0.01407	0.40028	1.97245	0.05864	0.18654	0.00197	2682	30	2644	64	2711	17	82.8	6.9	0.1	2
SU20-44	3499	19	0.52069	0.59427	0.01591	0.45804	1.68391	0.04634	0.23575	0.00209	3057	28	3005	66	3091	14	138.7	10.5	0.1	3
SU20-45	1759	21	0.60553	0.63252	0.01844	0.39038	1.58426	0.04601	0.23663	0.00249	3119	30	3154	72	3097	17	87.8	9.4	0.1	-2
SU20-46	1274	15	0.44901	0.52341	0.01641	0.52717	1.91887	0.05749	0.20765	0.00247	2810	31	2704	66	2887	19	96.0	5.2	0.1	6
SU20-47	2003	14	0.42004	0.52782	0.01587	0.16163	1.89210	0.05473	0.19495	0.00197	2763	29	2735	64	2784	17	129.6	11.5	0.1	2
SU20-48	6750	14	0.40107	0.52640	0.01512	0.32898	1.90523	0.05510	0.19662	0.00214	2765	29	2720	64	2798	18	80.3	5.0	0.1	3
SU20-49	3269	15	0.51205	0.52220	0.01744	0.06267	1.94246	0.07380	0.20703	0.00190	2795	37	2677	83	2882	15	101.2	9.0	0.1	6
SU20-50	693	14	0.42555	0.52299	0.01529	0.31638	1.91100	0.06022	0.19167	0.00262	2738	33	2713	70	2756	22	59.0	4.7	0.1	2
SU20-51	10094	17	0.47132	0.58097	0.01554	0.36326	1.72548	0.04678	0.21654	0.00169	2951	27	2947	64	2954	13	154.4	12.2	0.1	0
SU20-52	1013	13	0.41469	0.51112	0.01580	0.27855	1.97029	0.05980	0.19213	0.00221	2711	31	2646	66	2760	19	67.9	7.4	0.1	4

	^{206}Pb / ^{204}Pb	^{207}Pb / ^{235}U	2SE	^{206}Pb / ^{238}U	2SE	rho	$^{238}U/^{206}Pb$	2SE	^{207}Pb / ^{206}Pb	2SE	$^{207}Pb/^{235}U$ Age (Ma)	2SE	$^{206}Pb/^{238}U$ Age (Ma)	2SE	$^{207}Pb/^{206}Pb$ Age (Ma)	2SE	U (ppm)	Th (ppm)	Th/U	TW conc %
SU20-53	417	14	0.40763	0.53297	0.01457	0.29990	1.87574	0.05073	0.18978	0.00235	2746	28	2755	61	2739	20	39.8	2.5	0.1	-1
SU20-54	*1287*	*15*	*0.43384*	*0.54282*	*0.01489*	*0.20948*	*1.84673*	*0.05065*	*0.20566*	*0.00209*	*2837*	*28*	*2790*	*62*	*2871*	*17*	*97.1*	*4.6*	*0.0*	*3*
SU20-55	1790	15	0.42545	0.54319	0.01476	0.27036	1.83859	0.05158	0.20465	0.00192	2837	28	2800	64	2863	15	109.0	9.4	0.1	2
SU20-56	2051	18	0.49613	0.58179	0.01511	0.47815	1.72101	0.04472	0.22952	0.00204	3010	26	2953	62	3048	14	104.8	9.6	0.1	3
SU20-58	1553	14	0.41088	0.51392	0.01430	0.35332	1.95176	0.05581	0.20304	0.00224	2772	29	2667	62	2850	18	75.1	5.0	0.1	6
SU20-59	1594	16	0.41839	0.56023	0.01502	0.39936	1.79032	0.04931	0.20077	0.00188	2844	28	2861	64	2832	15	129.3	10.5	0.1	-1
SU20-60	3043	14	0.40227	0.54069	0.01471	0.39648	1.85340	0.05068	0.19204	0.00217	2768	28	2782	62	2759	19	95.8	6.4	0.1	-1
SU20-61	1978	16	0.42883	0.55057	0.01498	0.28624	1.81956	0.05133	0.20639	0.00229	2855	29	2823	64	2877	18	98.4	7.1	0.1	2
SU20-62	-1910	19	0.53886	0.59903	0.01696	0.41681	1.67249	0.04589	0.22546	0.00330	3020	30	3021	66	3019	23	70.2	5.9	0.1	0
SU20-63	4493	14	0.45465	0.50442	0.01631	0.05171	1.98830	0.06606	0.19955	0.00224	2738	33	2626	72	2822	18	181.7	12.8	0.1	6
SU20-64	699	16	0.43549	0.55455	0.01505	0.36938	1.81068	0.04913	0.20730	0.00218	2863	28	2835	62	2884	17	59.7	6.0	0.1	1
SU20-65	441	16	0.48808	0.57673	0.01665	0.29499	1.73951	0.05168	0.20484	0.00256	2890	31	2928	70	2864	20	36.0	3.2	0.1	-2
SU20-66	14674	16	0.43520	0.56879	0.01488	0.30273	1.75991	0.04523	0.20620	0.00169	2886	26	2900	60	2875	13	143.8	11.5	0.1	-1
SU20-67	1717	16	0.45635	0.55405	0.01516	0.30835	1.81324	0.04912	0.20693	0.00250	2860	28	2831	62	2881	20	50.3	5.0	0.1	1
SU20-68	-105186	15	0.43919	0.53405	0.01551	0.34665	1.87354	0.05239	0.20198	0.00254	2806	29	2757	63	2842	20	217.4	14.7	0.1	3
SU20-69	4766	13	0.35956	0.48992	0.01341	0.30117	2.04782	0.05800	0.19013	0.00185	2665	28	2563	60	2743	16	143.5	7.5	0.1	6
SU20-70	1035	14	0.37252	0.53412	0.01409	0.45624	1.87807	0.04930	0.18991	0.00186	2745	27	2752	59	2741	16	92.8	7.8	0.1	-1
SU20-72	1478	14	0.38499	0.52154	0.01418	0.52202	1.91823	0.04803	0.19684	0.00213	2759	26	2705	55	2799	18	177.9	10.0	0.1	3
SU20-74	1546	14	0.40417	0.51945	0.01443	0.30938	1.93397	0.05245	0.20238	0.00212	2778	28	2687	60	2845	17	93.0	6.1	0.1	5
SU20-75	8562	15	0.40023	0.54687	0.01433	0.58143	1.83124	0.05009	0.20543	0.00179	2844	27	2809	62	2869	14	320.6	27.1	0.1	2
SU20-76	6800	17	0.48442	0.58917	0.01625	0.42097	1.69963	0.04408	0.21388	0.00248	2954	27	2983	62	2934	19	88.9	19.1	0.2	-2
SU20-78	1962	14	0.40170	0.52281	0.01548	0.63090	1.92099	0.05701	0.19953	0.00285	2771	31	2702	65	2822	23	141.1	8.2	0.1	4
SU20-79	11287	15	0.38775	0.53533	0.01391	0.35732	1.87166	0.04905	0.19880	0.00156	2792	26	2759	59	2816	13	154.2	10.8	0.1	2
SU20-80	-241436	14	0.40078	0.53327	0.01491	0.26427	1.88398	0.05183	0.19465	0.00188	2766	28	2745	61	2781	16	127.2	11.4	0.1	1
SU20-81	1136	13	0.35846	0.49321	0.01326	0.32329	2.03556	0.05524	0.18540	0.00219	2647	28	2576	58	2701	20	69.0	6.1	0.1	4
SU20-83	3195	19	0.53753	0.59192	0.01736	0.45335	1.70069	0.05078	0.22948	0.00216	3021	30	2981	71	3048	15	226.3	19.2	0.1	2
SU20-84	90549	16	0.43193	0.55658	0.01505	0.39840	1.80074	0.04885	0.20606	0.00226	2863	28	2847	62	2874	18	85.9	9.8	0.1	1
SU20-85	3223	13	0.34475	0.50338	0.01342	0.44063	1.99303	0.05275	0.18650	0.00207	2672	27	2621	57	2711	18	169.6	16.4	0.1	3
SU20-86	*3002*	*15*	*0.40289*	*0.52554*	*0.01443*	*0.45527*	*1.91143*	*0.05157*	*0.20038*	*0.00181*	*2780*	*27*	*2713*	*60*	*2829*	*15*	*93.6*	*3.2*	*0.0*	*4*
SU20-87	10547	14	0.43884	0.51908	0.01580	0.38136	1.93966	0.05943	0.20077	0.00197	2767	31	2680	67	2832	16	108.4	14.6	0.1	5
SU20-88	2466	17	0.47371	0.57488	0.01557	0.39954	1.74612	0.04905	0.22033	0.00211	2957	28	2919	66	2982	15	90.6	7.4	0.1	2
SU20-90	5077	13	0.44542	0.48776	0.01693	0.19293	2.07499	0.07382	0.19141	0.00150	2659	34	2536	75	2754	13	178.5	16.9	0.1	7
SU20-91	1470	17	0.48449	0.58106	0.01583	0.39001	1.72433	0.04949	0.21871	0.00233	2962	29	2948	68	2971	17	83.7	9.5	0.1	1
SU20-92	1164	16	0.46351	0.55208	0.01526	0.43007	1.81924	0.05001	0.21721	0.00235	2904	28	2824	63	2959	17	53.0	4.1	0.1	4
SU20-93	1132	17	0.48809	0.56210	0.01570	0.33792	1.78448	0.05129	0.22057	0.00273	2937	30	2868	67	2984	20	65.8	7.7	0.1	4
SU20-94	-2581	23	0.62155	0.63277	0.01757	0.48863	1.58458	0.04325	0.26016	0.00252	3211	28	3154	68	3247	15	96.5	6.0	0.1	3
SU20-95	1473	22	0.59879	0.63013	0.01744	0.49160	1.58760	0.04075	0.25788	0.00261	3201	27	3149	64	3233	16	121.2	12.7	0.1	3
SU20-96	14084	20	0.53120	0.60781	0.01580	0.45551	1.64505	0.04141	0.24393	0.00204	3112	26	3062	61	3145	13	166.0	16.8	0.1	3
SU20-97	1660	14	0.45427	0.52273	0.01563	0.27765	1.91708	0.05522	0.19653	0.00320	2758	31	2706	64	2797	27	61.7	9.0	0.1	3
SU20-98	4573	14	0.41842	0.52775	0.01507	0.45401	1.89056	0.05336	0.19537	0.00299	2766	30	2737	63	2787	25	58.6	5.8	0.1	2
SU20-99	704	15	0.45250	0.53345	0.01537	0.23358	1.88300	0.05651	0.20307	0.00225	2806	30	2746	67	2850	18	72.4	8.9	0.1	3
SU20-100	5259	17	0.45519	0.55922	0.01511	0.27074	1.78744	0.04936	0.21633	0.00205	2917	28	2864	64	2953	15	193.9	16.1	0.1	3
SU20-101	1184	16	0.46548	0.54663	0.01477	0.44361	1.82729	0.04827	0.21731	0.00252	2900	28	2814	60	2960	19	80.0	5.7	0.1	5
SU20-102	-364	14	0.46760	0.51244	0.01454	0.22063	1.94948	0.05998	0.19609	0.00391	2740	35	2669	67	2793	33	11.0	0.7	0.1	4

	$^{206}Pb/^{204}Pb$	$^{207}Pb/^{235}U$	2SE	$^{206}Pb/^{238}U$	2SE	rho	$^{238}U/^{206}Pb$	2SE	$^{207}Pb/^{206}Pb$	2SE	$^{207}Pb/^{235}U$ Age (Ma)	2SE	$^{206}Pb/^{238}U$ Age (Ma)	2SE	$^{207}Pb/^{206}Pb$ Age (Ma)	2SE	U (ppm)	Th (ppm)	Th/U	TW conc %
SU20-103	1425	13	0.35920	0.51536	0.01377	0.41072	1.94475	0.05283	0.18675	0.00182	2697	27	2675	59	2713	16	70.5	5.0	0.1	1
SU20-104	-3940	13	0.36052	0.48886	0.01318	0.35770	2.04039	0.05436	0.18643	0.00260	2650	28	2571	56	2710	23	27.6	2.5	0.1	5
SU20-105	9832	14	0.40316	0.50601	0.01427	0.13403	1.98647	0.05974	0.20111	0.00202	2747	30	2628	65	2834	16	71.6	7.6	0.1	7
SU20-106	-2182	13	0.34769	0.48474	0.01309	0.36837	2.06835	0.05612	0.18700	0.00210	2640	28	2542	57	2715	19	95.5	7.9	0.1	6
SU20-109	5202	14	0.43388	0.51141	0.01582	0.26966	1.97489	0.06117	0.20199	0.00233	2756	31	2641	67	2842	19	80.4	6.7	0.1	6
SU20-111	1376	12	0.33987	0.47688	0.01306	0.04960	2.10424	0.05979	0.18307	0.00177	2604	28	2506	59	2680	16	98.4	9.7	0.1	6
SU20-112	1202	14	0.38361	0.51554	0.01389	0.47542	1.93717	0.05614	0.19298	0.00217	2731	29	2683	64	2767	18	133.6	19.2	0.1	3
SU20-115	3487	17	0.45490	0.55520	0.01460	0.40255	1.80153	0.04834	0.22533	0.00176	2948	27	2846	62	3018	13	162.9	14.7	0.1	6
SU20-117	1135	14	0.43610	0.50501	0.01686	0.54276	1.99258	0.06551	0.20046	0.00322	2741	35	2622	71	2829	26	138.7	7.3	0.1	7
SU20-120	1287	15	0.40789	0.52917	0.01435	0.43559	1.89550	0.05172	0.20465	0.00208	2808	28	2731	61	2863	17	46.9	4.3	0.1	4
SU20-121	5663	15	0.43546	0.52748	0.01457	0.18125	1.90325	0.05262	0.20494	0.00224	2805	28	2722	61	2865	18	51.8	5.3	0.1	5
SU20-122	1110	14	0.39528	0.51213	0.01413	0.40969	1.95637	0.05187	0.19774	0.00263	2745	28	2662	58	2807	22	29.0	2.7	0.1	5
SU20-123	431	14	0.48633	0.50552	0.01547	0.17302	1.98594	0.05693	0.20008	0.00394	2742	33	2629	62	2826	32	9.9	1.0	0.1	6
SU20-126	1464	15	0.39111	0.51918	0.01379	0.49139	1.92422	0.05104	0.20365	0.00211	2789	27	2698	58	2855	17	68.0	5.5	0.1	6
SU20-130	6013	13	0.41297	0.49729	0.01524	-0.00910	2.02750	0.06877	0.18902	0.00168	2669	33	2585	72	2733	15	123.9	12.5	0.1	5
SU20-131	718	13	0.38453	0.49681	0.01370	0.25895	2.02016	0.05543	0.19523	0.00239	2703	28	2592	59	2786	20	28.8	1.8	0.1	7
SU20-134	*11659*	*16*	*0.46152*	*0.55944*	*0.01583*	*0.39686*	*1.79618*	*0.05082*	*0.21302*	*0.00202*	*2897*	*29*	*2853*	*65*	*2928*	*15*	*47.5*	*2.4*	*0.0*	*2*
SU20-135	-17258	31	0.86747	0.71204	0.01941	0.30529	1.40716	0.03893	0.31967	0.00252	3529	28	3461	74	3568	12	102.2	11.9	0.1	3
SU20-136	*-4914*	*12*	*0.36447*	*0.47747*	*0.01338*	*0.30193*	*2.09839*	*0.06145*	*0.18747*	*0.00251*	*2629*	*30*	*2512*	*61*	*2719*	*22*	*64.3*	*2.8*	*0.0*	*7*
SU20-138	3246	17	0.47741	0.56811	0.01611	0.32684	1.76511	0.05000	0.21445	0.00219	2920	29	2894	66	2939	16	98.7	17.7	0.2	1
SU20-139	1962	16	0.44255	0.54053	0.01454	0.31987	1.85115	0.05053	0.21502	0.00193	2877	27	2784	62	2943	15	72.0	6.5	0.1	5
SU20-140	1381	21	0.57398	0.59507	0.01607	0.51414	1.67896	0.04534	0.25898	0.00302	3150	29	3012	65	3240	18	51.8	5.7	0.1	7
SU20-141	4501	17	0.47193	0.55553	0.01506	0.47601	1.80453	0.04820	0.22734	0.00271	2955	28	2842	61	3033	19	49.7	6.7	0.1	6
SU20-142	752	16	0.44273	0.53878	0.01501	0.32518	1.86016	0.05292	0.20949	0.00244	2848	29	2773	64	2901	19	50.7	7.6	0.1	4
SU20-146	2909	13	0.39186	0.50633	0.01432	0.19327	1.97755	0.05734	0.19084	0.00204	2701	29	2638	63	2749	18	127.7	12.8	0.1	4
SU20-147	459	15	0.46431	0.52570	0.01467	0.04785	1.90961	0.05298	0.20728	0.00302	2813	30	2715	61	2884	24	29.6	4.1	0.1	6
SU20-149	-4497	15	0.42591	0.52895	0.01519	0.45803	1.88391	0.05536	0.20451	0.00213	2813	30	2745	66	2862	17	239.8	23.3	0.1	4
SU20-152	*-10257*	*14*	*0.40290*	*0.51264*	*0.01415*	*0.39394*	*1.95337*	*0.05373*	*0.20293*	*0.00240*	*2771*	*28*	*2665*	*60*	*2849*	*19*	*54.9*	*2.2*	*0.0*	*6*
SU20-155	2030	13	0.34618	0.48805	0.01314	0.29827	2.04636	0.05523	0.18745	0.00162	2652	27	2565	57	2719	14	97.8	9.4	0.1	6
SU20-156	-2445	13	0.35618	0.50359	0.01330	0.42685	1.98600	0.05585	0.18978	0.00180	2692	28	2629	61	2740	16	98.5	12.5	0.1	4
SU20-158	-8485	15	0.42891	0.52817	0.01573	0.45961	1.90126	0.05222	0.20180	0.00212	2791	28	2724	61	2840	17	129.3	13.9	0.1	4
SU20-160	-16024	16	0.42233	0.53490	0.01400	0.51742	1.87142	0.04862	0.21723	0.00200	2877	26	2760	58	2960	15	176.4	12.0	0.1	7
SU20-163	-4933	14	0.39952	0.51365	0.01443	0.42738	1.94709	0.05375	0.19574	0.00216	2740	28	2672	60	2790	18	83.8	8.9	0.1	4
SU20-166	2957	12	0.35751	0.48433	0.01378	0.14697	2.07024	0.06730	0.18546	0.00159	2631	32	2540	68	2702	14	148.3	14.7	0.1	6
SU20-169	2000	13	0.35261	0.49781	0.01321	0.43251	2.01166	0.05376	0.18424	0.00231	2652	28	2601	57	2691	21	51.4	4.5	0.1	3
SU20-171	-21833	14	0.37425	0.50640	0.01376	0.30121	1.97543	0.05262	0.19632	0.00172	2729	27	2640	58	2795	14	198.8	24.6	0.1	6
SU20-172	*1815*	*14*	*0.39120*	*0.50743*	*0.01477*	*0.63713*	*1.96829*	*0.06418*	*0.19804*	*0.00244*	*2741*	*33*	*2648*	*71*	*2809*	*20*	*130.1*	*4.6*	*0.0*	*6*
SU20-175	2650	16	0.47471	0.54090	0.01597	0.41101	1.86354	0.06133	0.21597	0.00200	2875	33	2769	74	2950	15	130.6	14.3	0.1	6
SU20-177	-5939	16	0.44749	0.56448	0.01539	0.33758	1.77669	0.05022	0.20970	0.00183	2893	28	2878	66	2903	14	158.0	18.8	0.1	1
SU20-179	-4577	15	0.42057	0.52942	0.01425	0.46935	1.88540	0.04743	0.21177	0.00216	2845	26	2743	56	2918	17	79.4	7.6	0.1	6
SU20-182	-8332	20	0.52798	0.58948	0.01530	0.40000	1.69418	0.04605	0.24378	0.00211	3083	28	2990	65	3144	14	110.8	10.5	0.1	5
SU20-183	1674	20	0.51862	0.57825	0.01530	0.58218	1.73089	0.04613	0.24463	0.00247	3066	28	2940	63	3150	16	71.0	6.1	0.1	7
SU20-185	-11675	15	0.44878	0.52664	0.01564	0.43081	1.90367	0.05671	0.20831	0.00302	2820	32	2722	66	2892	24	99.3	9.7	0.1	6
SU20-186	-3961	13	0.37539	0.49342	0.01387	0.39896	2.02719	0.05607	0.19537	0.00185	2700	28	2585	59	2787	16	84.3	5.6	0.1	7

	$^{206}Pb/^{204}Pb$	$^{207}Pb/^{235}U$	2SE	$^{206}Pb/^{238}U$	2SE	rho	$^{238}U/^{206}Pb$	2SE	$^{207}Pb/^{206}Pb$	2SE	$^{207}Pb/^{235}U$ Age (Ma)	2SE	$^{206}Pb/^{238}U$ Age (Ma)	2SE	$^{207}Pb/^{206}Pb$ Age (Ma)	2SE	U (ppm)	Th (ppm)	Th/U	TW conc %
SU20-188	-2022	14	0.40885	0.51074	0.01500	0.44260	1.95662	0.05813	0.19460	0.00192	2730	30	2661	65	2781	16	105.1	11.9	0.1	4
SU20-190	1929	12	0.33509	0.47586	0.01280	0.34685	2.09976	0.05765	0.18404	0.00173	2611	27	2511	57	2689	16	104.2	11.2	0.1	7
SU20-191	4548	15	0.44051	0.51449	0.01589	0.54254	1.94614	0.06165	0.20575	0.00338	2788	34	2673	69	2872	27	372.9	28.2	0.1	7
SU20-192	745	14	0.38011	0.51074	0.01372	0.40245	1.96035	0.05228	0.19560	0.00223	2733	27	2657	58	2789	19	71.5	10.9	0.2	5
SU20-193	1417	14	0.41774	0.50598	0.01394	0.17279	1.97660	0.05276	0.19970	0.00235	2745	28	2639	58	2823	19	72.0	10.0	0.1	6
SU20-194	2295	21	0.58818	0.60813	0.01659	0.42747	1.64482	0.04400	0.25540	0.00267	3157	28	3062	65	3218	16	65.0	3.8	0.1	5
SU20-197	809	21	0.64668	0.60042	0.01836	0.25185	1.66231	0.05415	0.24886	0.00295	3121	34	3036	79	3177	19	46.2	2.7	0.1	5
SU20-198	*-9246*	*13*	*0.37051*	*0.49713*	*0.01350*	*0.17494*	*2.00639*	*0.05772*	*0.19394*	*0.00177*	*2703*	*29*	*2607*	*62*	*2775*	*15*	*80.4*	*3.0*	*0.0*	*6*
SU20-199	13845	17	0.45978	0.55696	0.01490	0.47400	1.79721	0.04920	0.22508	0.00184	2949	27	2852	63	3017	13	241.5	22.3	0.1	5
SU20-200	-5697	18	0.48303	0.56479	0.01501	0.30761	1.76873	0.04583	0.22633	0.00205	2970	26	2889	60	3026	15	133.9	23.7	0.2	5
SU20-8	*3677*	*6*	*0.31277*	*0.24731*	*0.01228*	*0.19852*	*4.18148*	*0.22234*	*0.18467*	*0.00243*	*1988*	*48*	*1382*	*66*	*2695*	*22*	*1051.9*	*112.7*	*0.1*	*47*
SU20-10	*2678*	*16*	*0.49502*	*0.52311*	*0.01560*	*0.18165*	*1.91655*	*0.05574*	*0.21980*	*0.00265*	*2865*	*30*	*2707*	*64*	*2979*	*19*	*222.3*	*19.1*	*0.1*	*9*
SU20-77	*7087*	*6*	*0.24180*	*0.24842*	*0.00914*	*0.10412*	*4.10539*	*0.14233*	*0.18739*	*0.00179*	*2017*	*32*	*1405*	*44*	*2719*	*16*	*669.8*	*60.5*	*0.1*	*47*
SU20-108	*1034*	*14*	*0.40098*	*0.50763*	*0.01377*	*0.40856*	*1.97528*	*0.05277*	*0.20399*	*0.00215*	*2765*	*27*	*2641*	*58*	*2858*	*17*	*57.5*	*4.4*	*0.1*	*7*
SU20-110	*1304*	*14*	*0.38993*	*0.50079*	*0.01451*	*0.48498*	*2.00860*	*0.05623*	*0.20362*	*0.00216*	*2748*	*28*	*2605*	*60*	*2855*	*17*	*69.9*	*4.4*	*0.1*	*8*
SU20-113	*3526*	*15*	*0.52804*	*0.51100*	*0.01805*	*0.23450*	*1.99867*	*0.07607*	*0.21444*	*0.00200*	*2802*	*37*	*2615*	*82*	*2939*	*15*	*104.2*	*6.8*	*0.1*	*10*
SU20-118	*13880*	*6*	*0.24869*	*0.21541*	*0.00790*	*-0.42360*	*4.69182*	*0.16075*	*0.19302*	*0.00227*	*1927*	*31*	*1246*	*39*	*2767*	*19*	*540.0*	*38.4*	*0.1*	*54*
SU20-119	*3108*	*10*	*0.64537*	*0.32828*	*0.02043*	*-0.06444*	*3.33869*	*0.20587*	*0.21718*	*0.00243*	*2334*	*57*	*1689*	*92*	*2959*	*18*	*140.1*	*21.0*	*0.2*	*39*
SU20-124	*3448*	*14*	*0.42946*	*0.49856*	*0.01437*	*0.13898*	*2.01031*	*0.06026*	*0.20321*	*0.00317*	*2745*	*32*	*2603*	*64*	*2851*	*25*	*19.4*	*2.0*	*0.1*	*8*
SU20-128	*14552*	*3*	*0.16139*	*0.12876*	*0.00692*	*0.28408*	*8.24517*	*0.54832*	*0.17228*	*0.00176*	*1377*	*51*	*738*	*46*	*2579*	*17*	*911.7*	*95.6*	*0.1*	*70*
SU20-133	*2505*	*14*	*0.40761*	*0.48851*	*0.01369*	*0.07283*	*2.04879*	*0.05596*	*0.20229*	*0.00206*	*2723*	*28*	*2562*	*58*	*2844*	*17*	*105.5*	*7.6*	*0.1*	*10*
SU20-137	*-2935*	*30*	*0.85247*	*0.66759*	*0.01937*	*0.44492*	*1.49803*	*0.04298*	*0.32419*	*0.00330*	*3481*	*30*	*3296*	*74*	*3589*	*16*	*142.1*	*13.1*	*0.1*	*8*
SU20-143	*-2092*	*14*	*0.39316*	*0.49655*	*0.01351*	*0.37135*	*2.01579*	*0.05306*	*0.20865*	*0.00230*	*2768*	*27*	*2597*	*56*	*2894*	*18*	*56.9*	*1.1*	*0.0*	*10*
SU20-144	*-3468*	*16*	*0.48038*	*0.52843*	*0.01584*	*0.47739*	*1.90346*	*0.05913*	*0.22176*	*0.00230*	*2880*	*31*	*2722*	*69*	*2993*	*17*	*86.5*	*4.2*	*0.0*	*9*
SU20-145	*-4686*	*29*	*0.83996*	*0.66171*	*0.01790*	*0.17643*	*1.51275*	*0.04226*	*0.31263*	*0.00389*	*3436*	*30*	*3271*	*72*	*3533*	*19*	*45.5*	*4.2*	*0.1*	*7*
SU20-150	*8889*	*14*	*0.43260*	*0.50725*	*0.01484*	*0.31408*	*1.97458*	*0.05543*	*0.20575*	*0.00209*	*2774*	*28*	*2641*	*61*	*2872*	*16*	*103.0*	*10.3*	*0.1*	*8*
SU20-153	*-20184*	*30*	*0.79318*	*0.67008*	*0.01816*	*0.59499*	*1.49381*	*0.04225*	*0.32239*	*0.00273*	*3478*	*29*	*3304*	*73*	*3581*	*13*	*133.7*	*10.7*	*0.1*	*8*
SU20-157	*-4156*	*14*	*0.46931*	*0.48770*	*0.01565*	*-0.00731*	*2.05558*	*0.07022*	*0.20579*	*0.00192*	*2736*	*34*	*2555*	*72*	*2872*	*15*	*109.0*	*10.2*	*0.1*	*11*
SU20-161	*-1260*	*11*	*0.54601*	*0.41451*	*0.01850*	*-0.13326*	*2.52379*	*0.11551*	*0.19835*	*0.00228*	*2509*	*44*	*2152*	*84*	*2812*	*19*	*68.1*	*9.8*	*0.1*	*21*
SU20-162	*-4635*	*12*	*0.39861*	*0.45904*	*0.01473*	*0.26510*	*2.20693*	*0.07464*	*0.19788*	*0.00174*	*2632*	*33*	*2409*	*68*	*2808*	*14*	*91.1*	*6.3*	*0.1*	*13*
SU20-165	*-14080*	*10*	*0.53471*	*0.38700*	*0.01922*	*0.04009*	*2.72007*	*0.14455*	*0.19510*	*0.00190*	*2424*	*50*	*2018*	*92*	*2785*	*16*	*163.2*	*17.8*	*0.1*	*25*
SU20-167	*1129*	*13*	*0.44037*	*0.48205*	*0.01665*	*0.33297*	*2.09787*	*0.07374*	*0.19669*	*0.00258*	*2674*	*35*	*2513*	*73*	*2798*	*21*	*169.8*	*13.8*	*0.1*	*10*
SU20-168	*-472*	*14*	*0.38866*	*0.50090*	*0.01347*	*0.48099*	*1.99681*	*0.05424*	*0.20666*	*0.00212*	*2767*	*28*	*2617*	*58*	*2879*	*17*	*57.8*	*4.1*	*0.1*	*9*
SU20-170	*-3613*	*13*	*0.46649*	*0.45808*	*0.01579*	*0.00273*	*2.22214*	*0.08335*	*0.20406*	*0.00199*	*2654*	*36*	*2395*	*75*	*2858*	*16*	*158.4*	*13.7*	*0.1*	*15*
SU20-173	*-2396*	*14*	*0.40969*	*0.50346*	*0.01394*	*0.32506*	*1.98805*	*0.05221*	*0.20351*	*0.00263*	*2757*	*28*	*2627*	*57*	*2854*	*21*	*32.8*	*1.6*	*0.0*	*8*
SU20-178	*6172*	*15*	*0.39916*	*0.51754*	*0.01365*	*0.45604*	*1.93418*	*0.05084*	*0.21156*	*0.00159*	*2820*	*26*	*2687*	*58*	*2917*	*12*	*174.8*	*12.7*	*0.1*	*8*
SU20-181	*1471*	*15*	*0.43799*	*0.49747*	*0.01396*	*0.21430*	*2.00234*	*0.06133*	*0.21800*	*0.00229*	*2816*	*31*	*2611*	*66*	*2965*	*17*	*216.0*	*10.1*	*0.0*	*12*
SU20-187	*-5546*	*13*	*0.47305*	*0.48061*	*0.01724*	*0.40818*	*2.09127*	*0.07682*	*0.19253*	*0.00370*	*2657*	*39*	*2519*	*77*	*2763*	*32*	*201.0*	*21.6*	*0.1*	*8*
SU20-189	*-1672*	*12*	*0.32172*	*0.46009*	*0.01235*	*0.44831*	*2.17619*	*0.05805*	*0.18549*	*0.00196*	*2584*	*27*	*2437*	*54*	*2702*	*17*	*85.0*	*3.2*	*0.0*	*10*
SU20-196	*126480*	*9*	*0.44738*	*0.36939*	*0.01641*	*-0.13244*	*2.79122*	*0.13555*	*0.18282*	*0.00200*	*2341*	*46*	*1974*	*83*	*2678*	*18*	*288.8*	*56.8*	*0.2*	*25*
SU21																				
SU21-3	-9644	13	0.38059	0.50693	0.01476	0.39500	1.95495	0.04706	0.19018	0.00190	2709	24	2663	52	2743	16	127.5	12.2	0.1	4
SU21-4	*-1457*	*14*	*0.41486*	*0.51524*	*0.01695*	*0.60908*	*1.93386*	*0.07247*	*0.19070*	*0.00311*	*2722*	*38*	*2687*	*81*	*2748*	*26*	*204.0*	*10.1*	*0.0*	*2*
SU21-6	5276	14	0.55857	0.54696	0.02035	-0.01279	1.86136	0.06688	0.19169	0.00181	2763	35	2772	79	2756	15	111.4	6.4	0.1	-2

	$^{206}Pb/^{204}Pb$	$^{207}Pb/^{235}U$	2SE	$^{206}Pb/^{238}U$	2SE	rho	$^{238}U/^{206}Pb$	2SE	$^{207}Pb/^{206}Pb$	2SE	$^{207}Pb/^{235}U$ Age (Ma)	2SE	$^{206}Pb/^{238}U$ Age (Ma)	2SE	$^{207}Pb/^{206}Pb$ Age (Ma)	2SE	U (ppm)	Th (ppm)	Th/U	TW conc %
SU21-8	-8036	14	0.42348	0.50826	0.01730	0.61236	1.98323	0.06914	0.19388	0.00241	2713	34	2632	74	2775	20	183.6	12.2	0.1	5
SU21-14	1035	14	0.41416	0.51906	0.01635	0.54086	1.92088	0.05365	0.19253	0.00233	2737	28	2702	60	2763	20	224.1	32.0	0.1	2
SU21-18	2722	14	0.38019	0.50679	0.01420	0.51029	1.97128	0.05527	0.19353	0.00180	2717	27	2645	60	2772	15	185.4	13.4	0.1	5
SU21-19	5821	13	0.33696	0.48084	0.01304	0.48134	2.07893	0.05515	0.19007	0.00187	2650	26	2532	54	2742	16	166.3	13.0	0.1	8
SU21-24	*694515*	*13*	*0.37865*	*0.49127*	*0.01395*	*0.29709*	*2.03472*	*0.05776*	*0.19114*	*0.00228*	*2676*	*28*	*2577*	*59*	*2751*	*19*	*190.6*	*4.6*	*0.0*	*6*
SU21-28	768	13	0.37204	0.50845	0.01386	0.24411	1.96598	0.05280	0.18819	0.00217	2694	27	2651	57	2726	19	103.7	9.6	0.1	3
SU21-35	3193	13	0.34796	0.49477	0.01405	0.66043	2.01104	0.05404	0.18640	0.00187	2663	27	2602	56	2710	16	158.2	13.3	0.1	4
SU21-43	879	13	0.36173	0.49113	0.01309	0.34099	2.03854	0.05473	0.19454	0.00233	2691	27	2573	56	2780	19	160.7	17.4	0.1	7
SU21-2	*1292*	*14*	*0.40816*	*0.48400*	*0.01543*	*0.62686*	*2.06501*	*0.06382*	*0.20453*	*0.00404*	*2726*	*34*	*2546*	*64*	*2862*	*32*	*464.8*	*28.0*	*0.1*	*11*
SU21-5	*4133*	*12*	*0.57490*	*0.45101*	*0.01994*	*-0.08516*	*2.23800*	*0.09938*	*0.18993*	*0.00319*	*2580*	*44*	*2381*	*87*	*2741*	*27*	*643.4*	*15.8*	*0.0*	*13*
SU21-7	*1536*	*13*	*0.40212*	*0.47978*	*0.01519*	*0.46262*	*2.09164*	*0.06750*	*0.19621*	*0.00207*	*2674*	*31*	*2519*	*66*	*2794*	*17*	*237.4*	*21.2*	*0.1*	*10*
SU21-11	*1117*	*13*	*0.39519*	*0.48199*	*0.01444*	*0.33107*	*2.07505*	*0.06092*	*0.19728*	*0.00231*	*2687*	*29*	*2536*	*60*	*2803*	*19*	*149.8*	*12.0*	*0.1*	*9*
SU21-12	*918*	*13*	*0.36249*	*0.48277*	*0.01381*	*0.47131*	*2.07404*	*0.05779*	*0.19645*	*0.00180*	*2684*	*27*	*2537*	*57*	*2796*	*15*	*242.4*	*23.8*	*0.1*	*9*
SU21-13	*1666*	*13*	*0.35442*	*0.48413*	*0.01363*	*0.36365*	*2.07172*	*0.05798*	*0.19077*	*0.00150*	*2657*	*27*	*2539*	*58*	*2748*	*13*	*217.7*	*22.3*	*0.1*	*8*
SU21-15	*2031*	*13*	*0.38455*	*0.47981*	*0.01530*	*0.53614*	*2.08214*	*0.07002*	*0.19234*	*0.00250*	*2660*	*33*	*2529*	*69*	*2762*	*21*	*452.9*	*22.5*	*0.0*	*9*
SU21-16	*2717*	*12*	*0.36432*	*0.45302*	*0.01449*	*0.44477*	*2.22896*	*0.06908*	*0.19047*	*0.00213*	*2587*	*30*	*2389*	*61*	*2746*	*18*	*104.2*	*3.6*	*0.0*	*12*
SU21-20	*-11986*	*13*	*0.34620*	*0.47808*	*0.01309*	*0.44140*	*2.09412*	*0.05841*	*0.19151*	*0.00177*	*2651*	*27*	*2517*	*57*	*2754*	*15*	*222.9*	*13.9*	*0.1*	*9*
SU21-22	*67942*	*13*	*0.41125*	*0.47605*	*0.01709*	*0.58157*	*2.10907*	*0.07689*	*0.19184*	*0.00286*	*2645*	*36*	*2502*	*74*	*2757*	*24*	*420.3*	*38.9*	*0.1*	*9*
SU21-26	*1076*	*13*	*0.45246*	*0.48865*	*0.01695*	*0.21891*	*2.06290*	*0.07024*	*0.20081*	*0.00254*	*2709*	*34*	*2548*	*70*	*2832*	*20*	*281.7*	*26.7*	*0.1*	*9*
SU21-31	*-7969*	*14*	*0.38757*	*0.49588*	*0.01400*	*0.24291*	*2.02178*	*0.05814*	*0.19822*	*0.00173*	*2716*	*28*	*2591*	*60*	*2811*	*14*	*221.5*	*20.7*	*0.1*	*8*
SU21-32	*1341*	*12*	*0.39305*	*0.45713*	*0.01604*	*0.44581*	*2.19133*	*0.07207*	*0.19311*	*0.00185*	*2616*	*32*	*2423*	*65*	*2768*	*15*	*248.0*	*36.9*	*0.1*	*12*
SU21-37	*4897*	*13*	*0.34043*	*0.48109*	*0.01257*	*0.46110*	*2.07609*	*0.05243*	*0.19197*	*0.00174*	*2661*	*25*	*2535*	*52*	*2758*	*15*	*187.3*	*15.5*	*0.1*	*8*
SU21-42	*1081*	*13*	*0.34485*	*0.47973*	*0.01276*	*-0.03744*	*2.08610*	*0.05694*	*0.19152*	*0.00191*	*2654*	*27*	*2525*	*56*	*2755*	*16*	*103.0*	*5.6*	*0.1*	*8*
SU21-23	*1598*	*9*	*0.35453*	*0.36415*	*0.01360*	*0.11603*	*2.78928*	*0.10279*	*0.18420*	*0.00190*	*2348*	*34*	*1975*	*61*	*2690*	*17*	*528.5*	*36.4*	*0.1*	*26*
SU21-21	*7966*	*10*	*0.37247*	*0.37850*	*0.01381*	*-0.13467*	*2.66354*	*0.09904*	*0.18452*	*0.00170*	*2392*	*35*	*2055*	*64*	*2693*	*15*	*637.3*	*53.5*	*0.1*	*23*
SU25																				
SU25-8	1072	12	0.30660	0.48966	0.01455	0.58507	2.05116	0.06296	0.17637	0.00267	2593	32	2560	65	2618	25	205.0	111.9	0.5	2
SU25-9	3286	12	0.29484	0.49683	0.01502	0.65745	2.02500	0.06136	0.17812	0.00205	2614	30	2587	65	2635	19	255.0	133.0	0.5	1
SU25-10	-12300	12	0.31284	0.47591	0.01496	0.58146	2.10953	0.06222	0.17922	0.00230	2581	30	2501	61	2645	21	176.8	89.8	0.5	5
SU25-11	6898	12	0.33841	0.49609	0.01640	0.61024	2.02883	0.07024	0.17758	0.00207	2609	34	2583	74	2630	19	344.4	184.8	0.5	1
SU25-12	1687	12	0.48485	0.50570	0.02322	0.54719	1.99296	0.09077	0.17848	0.00409	2631	48	2621	98	2638	38	239.1	133.4	0.6	0
SU25-20	-2463	12	0.35029	0.47701	0.01621	0.52054	2.10914	0.07485	0.18014	0.00292	2586	37	2502	74	2653	27	161.3	98.3	0.6	5
SU25-21	2272	12	0.27675	0.49543	0.01252	0.48216	2.02077	0.05112	0.17896	0.00154	2620	25	2592	54	2643	14	104.9	72.3	0.7	2
SU25-23	955	12	0.32185	0.49442	0.01364	0.31768	2.02134	0.05682	0.18017	0.00228	2626	29	2591	60	2654	21	139.7	53.6	0.4	2
SU25-30	2150	12	0.35048	0.47776	0.01640	0.55680	2.09972	0.07461	0.17910	0.00337	2585	38	2511	74	2644	31	253.9	160.4	0.6	5
SU25-33	1027	12	0.31499	0.49721	0.01446	0.56473	2.01544	0.05851	0.18072	0.00216	2632	30	2597	62	2659	20	153.1	75.5	0.5	2
SU25-42	-4377	12	0.32952	0.48780	0.01417	0.43377	2.05002	0.05946	0.18088	0.00293	2617	31	2561	61	2660	27	217.2	108.1	0.5	4
SU25-43	6798	12	0.27315	0.49164	0.01244	0.53196	2.03310	0.05174	0.18088	0.00141	2625	25	2579	54	2660	13	314.3	167.5	0.5	3
SU25-50	3743	12	0.29853	0.50477	0.01382	0.55621	1.97895	0.05708	0.17735	0.00187	2631	29	2637	62	2627	18	157.3	74.0	0.5	0
SU25-51	1588	12	0.40301	0.48989	0.02023	0.62800	2.04566	0.07709	0.17691	0.00388	2598	41	2566	80	2623	36	279.1	151.4	0.5	2
SU25-7	*5720*	*6*	*0.16571*	*0.27548*	*0.00808*	*0.39530*	*3.63966*	*0.10740*	*0.16337*	*0.00202*	*2003*	*28*	*1565*	*41*	*2490*	*21*	*478.4*	*226.2*	*0.5*	*37*
SU25-13	*1065*	*5*	*0.23707*	*0.21440*	*0.01078*	*0.38641*	*4.77690*	*0.23823*	*0.17279*	*0.00286*	*1817*	*44*	*1225*	*56*	*2584*	*28*	*990.8*	*1630.8*	*1.6*	*52*
SU25-24	*3018*	*10*	*0.46069*	*0.40940*	*0.01987*	*0.20736*	*2.47289*	*0.11614*	*0.17539*	*0.00310*	*2414*	*46*	*2189*	*87*	*2609*	*29*	*308.0*	*146.3*	*0.5*	*15*
SU25-27	*2483*	*5*	*0.16464*	*0.20790*	*0.00771*	*0.25465*	*4.82934*	*0.18663*	*0.15855*	*0.00243*	*1735*	*35*	*1213*	*43*	*2439*	*26*	*1086.8*	*1181.5*	*1.1*	*50*

	$^{206}Pb/^{204}Pb$	$^{207}Pb/^{235}U$	2SE	$^{206}Pb/^{238}U$	2SE	rho	$^{238}U/^{206}Pb$	2SE	$^{207}Pb/^{206}Pb$	2SE	$^{207}Pb/^{235}U$ Age (Ma)	2SE	$^{206}Pb/^{238}U$ Age (Ma)	2SE	$^{207}Pb/^{206}Pb$ Age (Ma)	2SE	U (ppm)	Th (ppm)	Th/U	TW conc %
SU25-39	*2267*	*11*	*0.25498*	*0.44759*	*0.01158*	*0.48769*	*2.23161*	*0.05838*	*0.17686*	*0.00160*	*2517*	*26*	*2387*	*52*	*2623*	*15*	*171.6*	*73.4*	*0.4*	*9*
SU25-41	*2244*	*10*	*0.45447*	*0.40278*	*0.02070*	*0.31174*	*2.51230*	*0.13441*	*0.17702*	*0.00401*	*2408*	*53*	*2160*	*98*	*2624*	*38*	*611.7*	*294.8*	*0.5*	*17*
SU25-46	*-8462*	*7*	*0.23955*	*0.30771*	*0.01164*	*0.57000*	*3.27868*	*0.12140*	*0.17518*	*0.00266*	*2157*	*36*	*1716*	*56*	*2607*	*25*	*260.7*	*177.1*	*0.7*	*34*
SU25-49	*7165*	*9*	*0.29645*	*0.36587*	*0.01349*	*0.47148*	*2.74247*	*0.09452*	*0.17681*	*0.00222*	*2326*	*33*	*2004*	*59*	*2622*	*21*	*312.8*	*236.2*	*0.8*	*23*
SU25-52	*1572*	*8*	*0.24731*	*0.32675*	*0.01160*	*0.50552*	*3.08252*	*0.10947*	*0.17755*	*0.00232*	*2224*	*34*	*1811*	*56*	*2629*	*22*	*523.4*	*396.8*	*0.8*	*31*

	$^{206}Pb/^{204}Pb$	$^{207}Pb/^{235}U$	2SE	$^{206}Pb/^{238}U$	2SE	rho	$^{238}U/^{206}Pb$	2SE	$^{207}Pb/^{206}Pb$	2SE	$^{207}Pb/^{235}U$ Age (Ma)	2SE	$^{206}Pb/^{238}U$ Age (Ma)	2SE	$^{207}Pb/^{206}Pb$ Age (Ma)	2SE	U (ppm)	Th (ppm)	Th/U	TW conc %
TAN1																				
91500																				
35	628	1.7	0.05489	0.16189	0.00436	0.23803	6.18473	0.16690	0.07565	0.00155	1003	22	966	24	1085	41	80	7	0.1	9
1	1752	1.7	0.05585	0.16665	0.00441	0.25313	6.00525	0.15848	0.07547	0.00166	1021	22	993	24	1080	44	79	6	0.1	7
10	235	1.7	0.05547	0.16379	0.00447	0.37666	6.12417	0.17123	0.07649	0.00166	1017	23	975	25	1107	43	80	7	0.1	10
100	-2687	1.9	0.05634	0.17821	0.00481	0.37942	5.61591	0.14739	0.07878	0.00198	1093	24	1056	26	1166	50	81	32	0.4	8
101	615	1.8	0.04963	0.17586	0.00453	0.16211	5.69612	0.14860	0.07526	0.00141	1053	21	1043	25	1075	38	81	30	0.4	3
102	538	1.8	0.05261	0.17893	0.00455	0.20557	5.59545	0.14448	0.07516	0.00139	1064	21	1060	25	1072	37	80	30	0.4	0
103	927	1.8	0.04966	0.17731	0.00458	0.29773	5.65003	0.14586	0.07474	0.00131	1054	20	1051	25	1061	35	82	30	0.4	0
11	-2161	1.7	0.06030	0.16562	0.00462	0.22612	6.05668	0.17123	0.07554	0.00182	1016	24	985	26	1082	48	80	6	0.1	7
12	1015	1.8	0.06086	0.17386	0.00486	0.11065	5.75241	0.16710	0.07514	0.00158	1046	23	1033	28	1071	42	79	6	0.1	2
13	555	1.7	0.05567	0.16856	0.00475	0.42573	5.93292	0.17474	0.07460	0.00149	1021	23	1004	27	1057	40	82	7	0.1	5
14	462	1.7	0.05697	0.16957	0.00479	0.38245	5.91919	0.16119	0.07453	0.00151	1022	22	1006	25	1055	41	79	7	0.1	3
15	1080	1.7	0.05478	0.16805	0.00461	0.32098	5.96985	0.15859	0.07483	0.00140	1019	21	998	25	1063	38	80	7	0.1	5
16	-431	1.7	0.05582	0.16347	0.00476	0.11471	6.15877	0.18953	0.07639	0.00151	1012	23	970	28	1104	40	80	6	0.1	11
17	275	1.8	0.05349	0.17341	0.00469	0.56847	5.75558	0.14538	0.07454	0.00152	1040	21	1033	24	1055	41	80	7	0.1	2
18	-841	1.8	0.04843	0.17527	0.00373	0.25472	5.71939	0.12287	0.07495	0.00153	1048	19	1039	21	1066	41	80	30	0.4	1
19	1894	1.8	0.04865	0.17724	0.00364	0.25816	5.65094	0.11724	0.07514	0.00134	1057	18	1050	20	1071	36	80	30	0.4	1
2	-4788	1.7	0.05601	0.16685	0.00451	0.15195	5.99652	0.15554	0.07528	0.00141	1020	21	994	24	1075	38	81	7	0.1	7
20	900	1.9	0.05025	0.17676	0.00364	0.36561	5.66006	0.12117	0.07581	0.00130	1062	18	1049	21	1089	34	80	30	0.4	3
21	-2091	1.8	0.05209	0.17948	0.00369	0.37726	5.58046	0.11505	0.07430	0.00148	1058	19	1063	20	1049	40	80	30	0.4	-3
22	2074	1.9	0.05119	0.18036	0.00384	0.39296	5.54961	0.11543	0.07483	0.00143	1066	19	1068	20	1063	38	79	30	0.4	-1
23	1231	1.8	0.06178	0.17605	0.00472	0.61356	5.66352	0.13394	0.07603	0.00170	1064	21	1048	23	1095	45	81	30	0.4	4
24	532	1.8	0.05611	0.17640	0.00440	0.36428	5.69484	0.14243	0.07581	0.00192	1058	23	1043	24	1089	51	79	30	0.4	2
25	-1435	1.8	0.05029	0.17720	0.00364	0.32145	5.64513	0.11929	0.07448	0.00145	1052	19	1051	21	1054	39	80	30	0.4	-1
26	1530	1.8	0.04991	0.17212	0.00365	0.27193	5.81101	0.12852	0.07396	0.00157	1029	20	1024	21	1039	43	80	30	0.4	1
27	-717	1.8	0.05381	0.17575	0.00362	0.40482	5.69061	0.11482	0.07446	0.00150	1047	19	1044	19	1053	41	80	30	0.4	0
27	1665	1.8	0.05282	0.17312	0.00460	0.27745	5.79395	0.15635	0.07525	0.00119	1042	20	1026	26	1074	32	80	7	0.1	3
3	-1971	1.8	0.05697	0.16436	0.00443	0.21901	6.08180	0.16576	0.07994	0.00147	1050	22	981	25	1195	36	80	7	0.1	17
4	-3720	1.7	0.05546	0.16276	0.00457	0.19391	6.15468	0.17321	0.07450	0.00150	997	22	971	25	1054	41	80	7	0.1	7
5	-715	1.7	0.05708	0.16749	0.00451	0.25853	5.97472	0.15750	0.07591	0.00162	1028	22	998	24	1092	43	80	7	0.1	7
6	1020	1.7	0.05678	0.16557	0.00466	0.30670	6.04509	0.17547	0.07476	0.00163	1010	23	987	27	1061	44	79	7	0.1	6
7	280	1.8	0.06343	0.16634	0.00491	0.39245	6.02455	0.17423	0.07689	0.00212	1030	26	990	27	1117	55	82	6	0.1	10
8	810	1.8	0.06022	0.16959	0.00455	0.02061	5.90377	0.15488	0.07601	0.00160	1036	22	1009	25	1095	42	79	6	0.1	7
9	684	1.7	0.05444	0.15868	0.00456	0.22810	6.31571	0.18476	0.07570	0.00151	990	22	948	26	1086	40	81	7	0.1	11
FC1																				
102	-17955	1.9	0.05169	0.18361	0.00481	0.46622	5.44718	0.14676	0.07600	0.00080	1089	19	1087	27	1094	21	889	94	0.1	0
104	-48157	2.0	0.05313	0.18708	0.00492	0.34030	5.35177	0.14151	0.07609	0.00077	1102	19	1104	27	1097	20	758	67	0.1	-1
105	8370	2.0	0.05181	0.18723	0.00488	0.47883	5.34194	0.14374	0.07646	0.00070	1106	19	1106	27	1106	18	1124	141	0.1	0
108	-9057	1.9	0.05262	0.18565	0.00498	0.47493	5.39133	0.14454	0.07594	0.00076	1095	19	1097	27	1093	20	970	107	0.1	-1
109	7838	1.9	0.05184	0.18471	0.00486	0.46888	5.41444	0.14451	0.07650	0.00062	1098	19	1093	27	1107	16	1591	99	0.1	1
110	19924	2.0	0.05136	0.18645	0.00487	0.42071	5.36189	0.14123	0.07598	0.00059	1099	18	1102	27	1094	16	977	80	0.1	-1

	$^{206}Pb/^{204}Pb$	$^{207}Pb/^{235}U$	2SE	$^{206}Pb/^{238}U$	2SE	rho	$^{238}U/^{206}Pb$	2SE	$^{207}Pb/^{206}Pb$	2SE	$^{207}Pb/^{235}U$ Age (Ma)	2SE	$^{206}Pb/^{238}U$ Age (Ma)	2SE	$^{207}Pb/^{206}Pb$ Age (Ma)	2SE	U (ppm)	Th (ppm)	Th/U	TW conc %
111	-40873	1.9	0.05168	0.18546	0.00485	0.39113	5.39351	0.14180	0.07580	0.00062	1094	18	1097	27	1089	16	1404	155	0.1	-1
114	5666	2.0	0.05265	0.18732	0.00490	0.41828	5.34273	0.13900	0.07643	0.00070	1106	19	1106	26	1106	18	1071	97	0.1	0
115	200187	2.0	0.05187	0.18694	0.00493	0.52668	5.35206	0.14223	0.07604	0.00069	1101	19	1104	27	1095	18	832	75	0.1	-1
116	6324	2.0	0.05194	0.18535	0.00500	0.51161	5.40304	0.14555	0.07664	0.00065	1100	19	1095	27	1111	17	1339	111	0.1	1
117	7713	2.0	0.05202	0.18688	0.00488	0.43186	5.35045	0.13928	0.07581	0.00074	1099	19	1105	26	1089	20	605	62	0.1	-2
118	2991	1.9	0.05177	0.18464	0.00482	0.40405	5.41523	0.14226	0.07614	0.00078	1094	19	1092	26	1098	20	322	27	0.1	0
1	-14821	1.9	0.04543	0.18582	0.00365	0.40484	5.38324	0.10699	0.07592	0.00099	1096	16	1098	20	1092	26	244	136	0.6	-1
1	-5671	1.9	0.05338	0.18560	0.00473	0.10347	5.38382	0.13785	0.07589	0.00073	1096	18	1098	26	1091	19	348	32	0.1	-1
10	-5563	1.9	0.04284	0.18176	0.00356	0.43004	5.50334	0.10825	0.07684	0.00087	1090	15	1076	20	1116	23	335	209	0.6	3
10	-17639	2.0	0.05185	0.18826	0.00487	0.46916	5.31565	0.13657	0.07588	0.00080	1104	19	1111	26	1091	21	415	38	0.1	-2
100	-6175	2.0	0.05334	0.18699	0.00492	0.30242	5.34474	0.13826	0.07659	0.00078	1107	19	1106	26	1110	20	557	50	0.1	0
101	5010	1.9	0.05091	0.18478	0.00481	0.49818	5.40392	0.14398	0.07573	0.00069	1092	19	1095	27	1087	18	780	74	0.1	-1
11	73943	1.9	0.04337	0.18553	0.00356	0.43680	5.38290	0.09964	0.07608	0.00086	1098	15	1098	19	1096	23	419	263	0.6	0
12	-12515	2.0	0.04406	0.18545	0.00358	0.46447	5.39190	0.10426	0.07681	0.00082	1103	15	1097	20	1115	21	484	313	0.6	1
13	3949	1.9	0.04322	0.18637	0.00364	0.44415	5.36642	0.10384	0.07565	0.00084	1096	15	1102	20	1085	22	567	356	0.6	-2
14	4405	1.9	0.04326	0.18387	0.00361	0.48683	5.42693	0.09911	0.07556	0.00088	1088	14	1090	18	1082	23	506	337	0.7	-1
15	1861	2.0	0.04520	0.18554	0.00358	0.22932	5.38893	0.10254	0.07666	0.00098	1102	15	1097	19	1111	25	373	213	0.6	1
16	-1922	2.0	0.04607	0.18760	0.00375	0.49242	5.33450	0.10591	0.07592	0.00096	1102	16	1108	20	1092	25	301	166	0.5	-2
17	-1008674	1.9	0.04883	0.18358	0.00403	0.40081	5.45298	0.12031	0.07635	0.00122	1091	18	1085	22	1103	32	304	163	0.5	2
18	12530	2.0	0.04480	0.18662	0.00368	0.52052	5.36061	0.10544	0.07659	0.00086	1105	15	1103	20	1110	22	410	254	0.6	0
19	3812	1.9	0.04443	0.18424	0.00369	0.60517	5.42434	0.10567	0.07658	0.00086	1097	15	1091	20	1109	22	381	236	0.6	1
2	1978	2.0	0.04331	0.18698	0.00359	0.33293	5.34180	0.10429	0.07618	0.00085	1104	15	1106	20	1099	22	397	264	0.7	-1
2	-19828	1.9	0.05148	0.18423	0.00467	0.29178	5.42949	0.14369	0.07653	0.00071	1096	19	1090	27	1108	18	486	43	0.1	1
20	5541	1.9	0.04506	0.18450	0.00364	0.44485	5.41605	0.11094	0.07587	0.00093	1092	16	1092	21	1091	25	289	162	0.6	0
200	55304	1.9	0.05149	0.18456	0.00472	0.31868	5.41924	0.14345	0.07626	0.00059	1095	19	1092	27	1101	15	785	64	0.1	1
201	5010	1.9	0.05071	0.18515	0.00479	0.43144	5.40484	0.14452	0.07601	0.00058	1094	19	1094	27	1095	15	779	55	0.1	0
21	1688	1.9	0.04502	0.18563	0.00370	0.44716	5.39104	0.10755	0.07596	0.00095	1096	16	1097	20	1093	25	291	169	0.6	-1
22	64164	1.9	0.04366	0.18393	0.00364	0.46532	5.43295	0.10479	0.07581	0.00090	1089	15	1089	19	1089	24	359	235	0.7	0
23	-2572	1.9	0.05052	0.18520	0.00411	0.61600	5.40510	0.11885	0.07585	0.00103	1093	17	1094	22	1090	27	363	218	0.6	-1
24	1453	2.0	0.04722	0.18495	0.00375	0.39488	5.39978	0.10350	0.07647	0.00116	1099	16	1095	19	1106	30	199	118	0.6	1
25	2247	1.9	0.04646	0.18507	0.00361	0.43858	5.39755	0.10212	0.07581	0.00102	1094	16	1096	19	1089	27	150	80	0.5	-1
26	-3180	1.9	0.04454	0.18558	0.00379	0.38004	5.38799	0.10809	0.07534	0.00099	1091	16	1097	20	1077	26	148	80	0.5	-2
27	-49190	2.0	0.04293	0.18758	0.00374	0.43846	5.33486	0.10723	0.07589	0.00083	1102	15	1108	20	1091	22	514	380	0.7	-2
28	-5545	2.0	0.04412	0.18727	0.00370	0.51112	5.34223	0.10599	0.07665	0.00085	1108	15	1106	20	1111	22	525	394	0.7	0
29	-16779	2.0	0.04374	0.18548	0.00365	0.64521	5.39338	0.10601	0.07639	0.00076	1099	15	1096	20	1104	20	695	544	0.8	0
3	-4039	1.9	0.04303	0.18529	0.00355	0.48202	5.39571	0.10402	0.07617	0.00078	1097	15	1096	19	1099	21	539	377	0.7	0
3	8130	1.9	0.05222	0.18536	0.00477	0.31935	5.40389	0.14044	0.07609	0.00080	1095	19	1095	26	1097	21	694	61	0.1	0
30	-2202	1.9	0.04490	0.18545	0.00384	0.55005	5.39292	0.10936	0.07560	0.00087	1092	16	1097	20	1084	23	393	196	0.5	-1
31	-2200	1.9	0.04656	0.18715	0.00369	0.33420	5.33947	0.10687	0.07471	0.00103	1091	16	1107	20	1060	28	334	196	0.6	-4
32	-10437	1.9	0.04404	0.18664	0.00376	0.46694	5.35537	0.10410	0.07578	0.00090	1098	15	1104	20	1088	24	461	300	0.7	-1
33	-10634	2.0	0.04397	0.18716	0.00373	0.48713	5.34668	0.10624	0.07616	0.00084	1103	15	1105	20	1098	22	522	268	0.5	-1
34	16047	2.0	0.04511	0.18799	0.00377	0.65983	5.32399	0.10762	0.07667	0.00079	1110	15	1110	21	1112	21	793	534	0.7	0
35	-16213	2.0	0.04370	0.18794	0.00368	0.65078	5.31520	0.10568	0.07682	0.00076	1113	15	1111	20	1116	20	950	617	0.6	0
37	-5694	2.0	0.04454	0.18862	0.00377	0.52586	5.30566	0.10577	0.07634	0.00090	1110	16	1113	20	1103	24	573	403	0.7	-1

	$^{206}Pb/^{204}Pb$	$^{207}Pb/^{235}U$	2SE	$^{206}Pb/^{238}U$	2SE	rho	$^{238}U/^{206}Pb$	2SE	$^{207}Pb/^{206}Pb$	2SE	$^{207}Pb/^{235}U$ Age (Ma)	2SE	$^{206}Pb/^{238}U$ Age (Ma)	2SE	$^{207}Pb/^{206}Pb$ Age (Ma)	2SE	U (ppm)	Th (ppm)	Th/U	TW conc %
38	-44118	2.0	0.04467	0.18897	0.00375	0.62266	5.29475	0.10429	0.07591	0.00077	1107	15	1115	20	1092	20	598	448	0.8	-2
39	9763	2.0	0.04425	0.18702	0.00373	0.67249	5.34306	0.10162	0.07647	0.00074	1106	14	1106	19	1107	19	651	497	0.8	0
4	2663	2.0	0.04397	0.18857	0.00362	0.56707	5.30190	0.10061	0.07582	0.00078	1106	15	1114	19	1089	21	533	375	0.7	-2
4	4021	2.0	0.05154	0.18762	0.00486	0.49872	5.34167	0.13915	0.07613	0.00068	1103	19	1106	27	1098	18	664	62	0.1	-1
40	-9158	2.0	0.04516	0.18746	0.00381	0.43301	5.33236	0.10513	0.07636	0.00092	1106	16	1108	20	1104	24	535	382	0.7	-1
41	2799	2.0	0.04473	0.18681	0.00366	0.57342	5.34846	0.10908	0.07647	0.00081	1105	15	1105	21	1106	21	535	392	0.7	0
42	24971	2.0	0.04685	0.18553	0.00391	0.36255	5.40147	0.11393	0.07673	0.00101	1101	17	1095	21	1113	26	306	208	0.7	1
43	1682	2.0	0.04495	0.18787	0.00381	0.42202	5.32826	0.10660	0.07612	0.00094	1105	16	1109	20	1097	25	304	210	0.7	-2
44	2191	1.9	0.04658	0.18308	0.00377	0.44444	5.46264	0.11829	0.07609	0.00107	1088	17	1084	22	1097	28	223	135	0.6	1
45	2944	2.0	0.04728	0.18653	0.00385	0.55117	5.36160	0.10825	0.07657	0.00099	1105	16	1102	20	1109	26	356	233	0.7	0
46	7629	2.0	0.04843	0.18906	0.00403	0.55406	5.30235	0.11313	0.07618	0.00106	1109	17	1114	22	1099	28	345	222	0.6	-2
47	-4342	2.0	0.04675	0.18905	0.00399	0.52536	5.28385	0.11121	0.07649	0.00100	1114	17	1117	22	1107	26	307	189	0.6	-1
48	14672	1.9	0.04510	0.18129	0.00380	0.50248	5.51877	0.12164	0.07661	0.00105	1086	17	1074	22	1110	27	333	215	0.6	3
49	-24611	1.9	0.05250	0.18210	0.00489	0.38894	5.50189	0.14634	0.07600	0.00087	1082	19	1077	26	1094	23	346	32	0.1	1
5	3692	1.9	0.04314	0.18486	0.00363	0.65406	5.39444	0.09588	0.07585	0.00076	1094	14	1096	18	1090	20	661	451	0.7	-1
5	6121	2.0	0.05227	0.18658	0.00486	0.27689	5.37207	0.14221	0.07595	0.00064	1098	19	1101	27	1093	17	678	62	0.1	-1
51	-76655	2.0	0.05748	0.19212	0.00539	0.39321	5.21465	0.14699	0.07619	0.00067	1120	20	1131	29	1099	18	1383	234	0.2	-3
52	31238	2.0	0.05592	0.18683	0.00529	0.33408	5.36423	0.14893	0.07612	0.00064	1100	20	1102	28	1097	17	2702	410	0.2	-1
53	73197	2.0	0.05306	0.18658	0.00485	0.25264	5.35518	0.13776	0.07604	0.00075	1101	19	1104	26	1095	20	442	40	0.1	-1
54	-8100	2.0	0.05415	0.18531	0.00490	0.32943	5.39848	0.14290	0.07649	0.00091	1099	20	1096	27	1107	24	418	32	0.1	1
55	-8845	2.0	0.05229	0.18519	0.00476	0.32721	5.39473	0.14065	0.07636	0.00073	1099	19	1096	26	1104	19	416	36	0.1	0
56	41389	1.9	0.05213	0.18460	0.00488	0.41075	5.42452	0.14225	0.07599	0.00076	1092	19	1091	26	1094	20	398	41	0.1	0
57	-5691	1.9	0.05164	0.18407	0.00476	0.36931	5.43568	0.14015	0.07600	0.00074	1091	18	1089	26	1094	20	361	27	0.1	0
58	-2411	1.9	0.05369	0.18570	0.00477	0.26133	5.38665	0.13984	0.07596	0.00099	1096	20	1098	26	1093	26	236	22	0.1	-1
59	13268	2.0	0.05089	0.18762	0.00485	0.50747	5.33663	0.13788	0.07613	0.00065	1104	18	1107	26	1098	17	924	75	0.1	-1
6	23084	1.9	0.04301	0.18428	0.00357	0.58530	5.42637	0.10527	0.07612	0.00076	1093	15	1090	19	1097	20	496	349	0.7	0
6	-10733	2.0	0.05222	0.18969	0.00497	0.44615	5.26902	0.12923	0.07599	0.00070	1111	18	1120	25	1094	18	595	51	0.1	-2
60	8945	2.0	0.05200	0.18895	0.00492	0.47407	5.29388	0.13589	0.07617	0.00056	1110	18	1115	26	1099	15	1162	96	0.1	-2
61	4019	1.9	0.05040	0.18487	0.00472	0.37791	5.40889	0.13532	0.07621	0.00057	1096	18	1094	25	1100	15	737	71	0.1	1
63	5501	1.9	0.05133	0.18608	0.00482	0.43936	5.37812	0.14172	0.07599	0.00060	1098	18	1099	27	1094	16	764	76	0.1	-1
64	11629	2.0	0.05153	0.18776	0.00481	0.35678	5.32710	0.13145	0.07628	0.00058	1107	17	1109	25	1102	15	849	74	0.1	-1
67	-1311337	1.9	0.05735	0.18291	0.00537	0.33762	5.47480	0.15916	0.07655	0.00091	1091	21	1082	29	1109	24	1381	83	0.1	2
68	-26433	2.0	0.05393	0.18606	0.00480	0.26935	5.37819	0.13828	0.07644	0.00086	1102	19	1099	26	1106	22	262	17	0.1	0
69	5079	1.9	0.05351	0.18475	0.00486	0.34838	5.39465	0.12598	0.07609	0.00082	1096	17	1096	24	1096	22	313	24	0.1	0
7	-3628	1.9	0.04366	0.18334	0.00358	0.45853	5.45553	0.10717	0.07639	0.00089	1091	15	1085	20	1104	23	380	233	0.6	2
7	-11204	2.0	0.05287	0.18651	0.00480	0.35873	5.36262	0.13400	0.07655	0.00083	1104	18	1102	25	1109	22	285	24	0.1	0
70	4241	1.9	0.05204	0.18666	0.00490	0.47944	5.36402	0.14315	0.07553	0.00079	1095	19	1102	27	1082	21	317	27	0.1	-2
71	8017	2.0	0.05241	0.18701	0.00487	0.44362	5.34941	0.13753	0.07595	0.00081	1101	19	1105	26	1093	21	370	32	0.1	-2
72	-66135	2.0	0.05342	0.18554	0.00480	0.27172	5.39025	0.13895	0.07665	0.00083	1102	19	1097	26	1111	22	369	31	0.1	1
73	-3396	1.9	0.05361	0.18574	0.00490	0.33829	5.38908	0.14207	0.07591	0.00089	1095	19	1097	27	1092	23	366	31	0.1	-1
74	1282	1.9	0.05313	0.18393	0.00481	0.47784	5.43993	0.14031	0.07618	0.00095	1092	19	1088	26	1099	25	354	30	0.1	1
75	-3465	2.0	0.05383	0.18807	0.00494	0.44147	5.31569	0.13594	0.07588	0.00096	1104	19	1111	26	1091	25	355	32	0.1	-2
76	1849	2.0	0.05239	0.18685	0.00480	0.50571	5.34667	0.14287	0.07652	0.00081	1106	19	1105	27	1108	21	358	33	0.1	0
77	3401	1.9	0.05164	0.18419	0.00474	0.36784	5.43057	0.14005	0.07604	0.00075	1092	19	1090	26	1095	20	310	27	0.1	0

	$^{206}Pb/^{204}Pb$	$^{207}Pb/^{235}U$	2SE	$^{206}Pb/^{238}U$	2SE	rho	$^{238}U/^{206}Pb$	2SE	$^{207}Pb/^{206}Pb$	2SE	$^{207}Pb/^{235}U$ Age (Ma)	2SE	$^{206}Pb/^{238}U$ Age (Ma)	2SE	$^{207}Pb/^{206}Pb$ Age (Ma)	2SE	U (ppm)	Th (ppm)	Th/U	TW conc %
78	1643	2.0	0.05403	0.18543	0.00483	0.18874	5.39750	0.14185	0.07631	0.00083	1098	19	1096	27	1102	22	314	29	0.1	0
79	1606	1.9	0.05353	0.18584	0.00480	0.34260	5.38433	0.14039	0.07545	0.00092	1092	19	1098	26	1080	25	268	24	0.1	-2
8	-1993	1.9	0.04323	0.18524	0.00353	0.41326	5.39649	0.10374	0.07595	0.00082	1095	15	1096	19	1093	22	338	214	0.6	-1
8	-31001	1.9	0.05396	0.18270	0.00478	0.23014	5.47785	0.14714	0.07650	0.00089	1090	20	1081	27	1107	23	253	23	0.1	2
80	-5071	2.0	0.05410	0.18567	0.00482	0.33233	5.38362	0.14841	0.07660	0.00086	1102	20	1098	28	1110	22	286	24	0.1	1
81	16530	2.0	0.05447	0.18861	0.00498	0.43742	5.31463	0.14103	0.07587	0.00091	1104	20	1111	27	1091	24	317	27	0.1	-3
82	-5840	2.0	0.05291	0.18662	0.00483	0.49191	5.35866	0.14382	0.07629	0.00089	1103	20	1103	27	1102	23	405	33	0.1	0
83	-10027	1.9	0.05338	0.18175	0.00482	0.44664	5.50352	0.15910	0.07609	0.00099	1083	21	1076	29	1097	26	292	15	0.1	1
84	-14010	2.0	0.05294	0.18879	0.00503	0.51221	5.30714	0.13534	0.07647	0.00083	1111	19	1113	26	1107	22	447	35	0.1	-1
85	5885	2.0	0.05245	0.18635	0.00500	0.58397	5.38441	0.14394	0.07658	0.00091	1102	20	1098	27	1109	24	413	38	0.1	0
86	8402	1.9	0.05318	0.18530	0.00476	0.33473	5.39796	0.14469	0.07567	0.00084	1092	19	1096	27	1085	22	293	27	0.1	-1
87	21327	1.9	0.05161	0.18290	0.00486	0.50264	5.47102	0.14876	0.07597	0.00080	1086	19	1082	27	1093	21	550	39	0.1	1
88	-8541	1.9	0.05168	0.18531	0.00485	0.34271	5.39659	0.14451	0.07609	0.00064	1096	19	1096	27	1097	17	629	64	0.1	0
9	-2344	1.9	0.04506	0.18215	0.00357	0.50890	5.47879	0.11426	0.07547	0.00097	1081	16	1081	21	1080	26	262	146	0.6	0
9	-4834	1.9	0.05359	0.18419	0.00478	0.34027	5.43398	0.13919	0.07628	0.00091	1093	19	1089	26	1101	24	287	25	0.1	1
90	3666	2.0	0.05297	0.18804	0.00497	0.47057	5.32657	0.14179	0.07664	0.00070	1110	19	1109	27	1111	18	692	82	0.1	0
91	15620	1.9	0.05222	0.18556	0.00483	0.43419	5.39532	0.14036	0.07575	0.00074	1093	19	1096	26	1088	20	524	51	0.1	-1
92	-32742	2.0	0.05201	0.18917	0.00484	0.45473	5.28161	0.13893	0.07605	0.00061	1110	19	1118	27	1096	16	983	89	0.1	-2
93	-9670	1.9	0.05325	0.18423	0.00483	0.40873	5.43371	0.14253	0.07640	0.00090	1094	19	1089	26	1105	24	276	27	0.1	1
94	-3998	1.9	0.05246	0.18507	0.00478	0.32011	5.40575	0.14050	0.07617	0.00081	1096	19	1094	26	1099	21	317	30	0.1	0
95	2897	1.9	0.05222	0.18291	0.00473	0.38442	5.47019	0.14224	0.07633	0.00091	1089	19	1082	26	1103	24	305	23	0.1	1
96	-6646	2.0	0.05390	0.19077	0.00510	0.42435	5.24663	0.14017	0.07616	0.00071	1116	19	1125	28	1098	19	1339	106	0.1	-2
97	-2790	1.9	0.05400	0.18521	0.00497	0.34726	5.40317	0.15974	0.07590	0.00088	1094	21	1095	30	1092	23	325	31	0.1	-1
98	-1719	1.9	0.05352	0.18522	0.00478	0.42103	5.40010	0.13628	0.07591	0.00095	1094	19	1095	25	1092	25	303	28	0.1	-1
99	4834	2.0	0.05241	0.18595	0.00481	0.41728	5.37948	0.14025	0.07627	0.00077	1100	19	1099	26	1101	20	707	67	0.1	0
KARA																				
51	1186	11.4	0.31194	0.46599	0.01227	0.39072	2.14711	0.05728	0.17682	0.00186	2552	27	2465	55	2623	18	118	8	0.1	6
52	36214	11.7	0.33226	0.48409	0.01376	0.47199	2.07257	0.05771	0.17578	0.00205	2580	28	2538	58	2613	19	121	12	0.1	3
53	4525	10.8	0.29097	0.43597	0.01155	0.34601	2.28884	0.06073	0.17968	0.00136	2508	26	2337	52	2649	13	313	24	0.1	12
54	2056	12.2	0.41811	0.49977	0.01542	0.16415	2.00054	0.06104	0.17720	0.00315	2621	33	2613	66	2626	30	153	13	0.1	0
55	10754	10.9	0.31290	0.44341	0.01259	0.33799	2.25424	0.06234	0.17841	0.00169	2515	27	2367	55	2637	16	548	64	0.1	10
56	-2140	12.1	0.27256	0.49616	0.01006	0.61965	2.01778	0.04120	0.17751	0.00189	2614	22	2595	44	2629	18	146	85	0.6	1
57	3539	12.0	0.26636	0.49116	0.01027	0.75799	2.03621	0.04138	0.17801	0.00174	2608	21	2575	43	2634	16	108	64	0.6	2
58	140786	11.7	0.27031	0.47718	0.01030	0.68992	2.10160	0.04537	0.17813	0.00187	2579	22	2509	45	2635	17	165	103	0.6	5
59	2628	11.9	0.26936	0.48882	0.01032	0.71222	2.05030	0.04363	0.17718	0.00182	2597	22	2561	45	2626	17	149	94	0.6	2
60	26738	12.0	0.26822	0.49182	0.01043	0.69485	2.03804	0.04351	0.17712	0.00181	2603	22	2574	45	2625	17	130	73	0.6	2
61	1986	12.2	0.30227	0.49746	0.01156	0.73568	2.01089	0.04973	0.17777	0.00217	2619	26	2602	53	2631	20	160	97	0.6	1
62	4930	11.3	0.30535	0.46000	0.01224	0.44788	2.17547	0.05705	0.17840	0.00172	2548	26	2438	53	2637	16	156	12	0.1	7
63	2314	11.2	0.30792	0.45659	0.01230	0.48102	2.19073	0.05828	0.17716	0.00199	2535	27	2424	54	2626	19	103	10	0.1	8
64	-2513	11.0	0.29934	0.44866	0.01203	0.47969	2.22792	0.06164	0.17646	0.00160	2516	27	2390	55	2619	15	138	10	0.1	9
1	-4046	12.0	0.27154	0.49529	0.01034	0.73524	2.02273	0.04201	0.17636	0.00173	2606	22	2590	44	2618	16	140	99	0.7	1
1	-2481	12.2	0.32511	0.49688	0.01319	0.48909	2.01171	0.05210	0.17813	0.00155	2620	26	2601	55	2635	15	135	9	0.1	1
10	-4919	12.2	0.28574	0.49861	0.01075	0.69312	2.00917	0.04258	0.17692	0.00199	2615	23	2604	45	2623	19	118	54	0.5	1

	$^{206}Pb/^{204}Pb$	$^{207}Pb/^{235}U$	2SE	$^{206}Pb/^{238}U$	2SE	rho	$^{238}U/^{206}Pb$	2SE	$^{207}Pb/^{206}Pb$	2SE	$^{207}Pb/^{235}U$ Age (Ma)	2SE	$^{206}Pb/^{238}U$ Age (Ma)	2SE	$^{207}Pb/^{206}Pb$ Age (Ma)	2SE	U (ppm)	Th (ppm)	Th/U	TW conc %
10	-1884	11.9	0.33201	0.48560	0.01323	0.47317	2.06523	0.05550	0.17834	0.00192	2597	27	2546	57	2637	18	156	17	0.1	3
11	-2565	12.0	0.27248	0.49170	0.01022	0.72745	2.03136	0.04275	0.17687	0.00177	2604	22	2581	45	2623	17	144	73	0.5	2
11	3487	11.9	0.36474	0.48842	0.01554	0.65585	2.06393	0.06421	0.17741	0.00147	2592	30	2547	66	2628	14	238	18	0.1	3
13	-2848	12.2	0.28527	0.49997	0.01104	0.74666	2.00009	0.04175	0.17680	0.00186	2619	22	2614	45	2622	17	119	60	0.5	0
14	-6946	12.2	0.30990	0.49414	0.01097	0.71818	2.02317	0.04598	0.17845	0.00227	2617	24	2589	48	2638	21	130	54	0.4	2
15	13536	11.5	0.26763	0.47034	0.01053	0.71026	2.13032	0.04733	0.17774	0.00204	2564	23	2481	46	2631	19	149	70	0.5	6
16	-2108	11.9	0.28720	0.48509	0.01142	0.66287	2.06694	0.04716	0.17782	0.00245	2593	25	2544	48	2632	23	120	54	0.4	3
17	-3397	11.9	0.26394	0.48483	0.00990	0.52999	2.06018	0.04021	0.17762	0.00202	2595	21	2551	41	2630	19	167	71	0.4	3
18	27613	11.8	0.27002	0.48554	0.01032	0.70235	2.06098	0.04446	0.17637	0.00191	2588	23	2550	45	2618	18	90	38	0.4	3
19	2748	11.6	0.30793	0.47444	0.01241	0.42140	2.10337	0.05473	0.17805	0.00170	2578	26	2507	54	2634	16	111	9	0.1	5
2	-840928	11.9	0.26532	0.48696	0.01033	0.72129	2.05516	0.04575	0.17698	0.00176	2594	23	2556	47	2624	17	141	88	0.6	3
2	-1305	12.2	0.32962	0.49984	0.01313	0.35615	2.00291	0.05328	0.17691	0.00155	2618	26	2611	57	2623	15	139	10	0.1	0
20	-2037	11.9	0.32430	0.49244	0.01312	0.44956	2.03337	0.05428	0.17502	0.00210	2594	27	2578	57	2606	20	61	7	0.1	1
21	6246	11.9	0.33213	0.49280	0.01431	0.68704	2.03315	0.05873	0.17680	0.00216	2603	29	2579	61	2622	20	262	32	0.1	1
22	24115	12.3	0.33858	0.50441	0.01464	0.65051	1.98477	0.05971	0.17663	0.00252	2625	31	2630	65	2621	24	209	21	0.1	-1
23	14471	11.3	0.29943	0.45769	0.01177	0.23095	2.18560	0.05534	0.17927	0.00144	2549	25	2429	51	2645	13	129	10	0.1	8
24	1504	11.3	0.30414	0.46149	0.01219	0.33744	2.16795	0.05430	0.17805	0.00162	2550	25	2445	51	2634	15	150	17	0.1	7
25	-4310	11.6	0.32818	0.47132	0.01397	0.58883	2.12083	0.05824	0.17910	0.00248	2576	29	2490	57	2644	23	179	18	0.1	6
26	2410	10.9	0.28755	0.44537	0.01148	0.34954	2.24342	0.06214	0.17726	0.00128	2514	27	2376	55	2627	12	133	11	0.1	10
27	-35102	11.8	0.31353	0.48378	0.01279	0.47194	2.07176	0.05507	0.17636	0.00156	2583	26	2539	56	2618	15	129	12	0.1	3
28	-10586	11.4	0.31946	0.46339	0.01291	0.35236	2.16400	0.06159	0.17803	0.00165	2551	28	2449	58	2634	15	162	11	0.1	7
29	-11388	11.6	0.30471	0.47530	0.01228	0.47687	2.10219	0.05246	0.17733	0.00160	2575	25	2509	52	2627	15	167	16	0.1	5
3	4162	11.9	0.27024	0.48851	0.01047	0.70197	2.05208	0.04278	0.17754	0.00194	2598	22	2559	44	2629	18	141	94	0.7	2
3	3584	11.7	0.30982	0.47896	0.01282	0.59407	2.09159	0.05668	0.17667	0.00155	2576	27	2519	57	2621	15	143	10	0.1	4
30	-17988	11.4	0.31024	0.46182	0.01230	0.37660	2.16850	0.05800	0.17885	0.00156	2554	26	2445	54	2642	15	185	16	0.1	7
31	-22748	11.8	0.31194	0.48185	0.01286	0.52990	2.07518	0.05463	0.17805	0.00161	2591	26	2536	55	2634	15	189	19	0.1	4
32	5402	11.6	0.32062	0.47222	0.01258	0.29479	2.11383	0.05364	0.17813	0.00202	2574	26	2497	53	2635	19	186	4	0.0	5
33	3418	12.1	0.31953	0.49934	0.01298	0.42327	2.00423	0.05265	0.17652	0.00156	2615	26	2609	56	2620	15	147	14	0.1	0
36	2959	11.7	0.31944	0.47663	0.01288	0.36178	2.10724	0.05646	0.17798	0.00170	2576	27	2504	56	2633	16	142	13	0.1	5
37	3090	11.4	0.31736	0.46867	0.01201	0.30947	2.13627	0.05468	0.17709	0.00207	2559	26	2475	53	2625	19	78	6	0.1	5
38	13214	11.2	0.30016	0.46007	0.01234	0.53356	2.17595	0.05757	0.17728	0.00182	2542	27	2438	54	2627	17	198	16	0.1	7
39	3264	11.0	0.29308	0.44600	0.01165	0.42183	2.24129	0.05672	0.17856	0.00167	2521	25	2378	50	2639	16	105	9	0.1	10
4	2242	12.2	0.27705	0.49593	0.01092	0.77979	2.01571	0.04340	0.17783	0.00184	2617	22	2597	46	2632	17	141	94	0.7	1
4	-1364	11.6	0.30798	0.47387	0.01241	0.44895	2.11256	0.05660	0.17796	0.00152	2574	26	2498	56	2633	14	150	9	0.1	5
40	2295	10.9	0.28995	0.44498	0.01179	0.44136	2.25156	0.05969	0.17758	0.00150	2512	26	2369	53	2630	14	153	9	0.1	10
41	7465	11.5	0.31826	0.46833	0.01301	0.43611	2.14358	0.06114	0.17771	0.00146	2559	28	2468	59	2631	14	176	14	0.1	6
42	-3654	11.3	0.30816	0.46374	0.01223	0.37695	2.15928	0.05598	0.17691	0.00178	2548	26	2453	53	2623	17	143	17	0.1	6
43	737	11.8	0.33410	0.45992	0.01255	0.31507	2.17675	0.05641	0.18738	0.00235	2594	27	2437	53	2719	21	398	45	0.1	10
44	3796	10.9	0.31713	0.44011	0.01223	0.23838	2.27245	0.06176	0.17926	0.00214	2512	28	2351	54	2645	20	210	3	0.0	11
45	10763	12.1	0.27100	0.48752	0.01006	0.72375	2.04615	0.04635	0.17909	0.00184	2609	23	2565	48	2644	17	258	99	0.4	3
46	-2842	12.0	0.29048	0.49190	0.01093	0.65545	2.03484	0.04575	0.17759	0.00244	2607	25	2577	48	2630	23	203	96	0.5	2
47	4287	12.3	0.30364	0.49321	0.01059	0.61491	2.03039	0.04344	0.17914	0.00214	2617	23	2582	46	2644	20	213	102	0.5	2
48	-2391	12.2	0.31926	0.50107	0.01454	0.62819	2.00288	0.05657	0.17687	0.00331	2618	32	2611	61	2623	31	229	132	0.6	0
49	1722	11.7	0.26948	0.47625	0.01045	0.73325	2.10680	0.04649	0.17897	0.00195	2581	23	2504	46	2643	18	139	84	0.6	5

	$^{206}Pb/^{204}Pb$	$^{207}Pb/^{235}U$	2SE	$^{206}Pb/^{238}U$	2SE	rho	$^{238}U/^{206}Pb$	2SE	$^{207}Pb/^{206}Pb$	2SE	$^{207}Pb/^{235}U$ Age (Ma)	2SE	$^{206}Pb/^{238}U$ Age (Ma)	2SE	$^{207}Pb/^{206}Pb$ Age (Ma)	2SE	U (ppm)	Th (ppm)	Th/U	TW conc %
5	26903	11.8	0.27680	0.47976	0.01036	0.74341	2.09022	0.04477	0.17897	0.00191	2589	22	2520	45	2643	18	154	103	0.7	4
5	-5362	11.8	0.32542	0.48128	0.01298	0.36746	2.08164	0.05733	0.17823	0.00170	2589	27	2529	58	2636	16	130	9	0.1	4
50	3151	12.1	0.27677	0.49539	0.01084	0.74603	2.02518	0.04445	0.17733	0.00181	2610	23	2587	47	2627	17	132	81	0.6	1
6	-2727	12.1	0.27199	0.49523	0.01013	0.64223	2.01900	0.03998	0.17793	0.00186	2616	21	2594	42	2633	17	144	89	0.6	1
6	-98794	11.7	0.31763	0.48059	0.01278	0.35516	2.08650	0.05441	0.17710	0.00167	2581	26	2524	55	2625	16	139	9	0.1	4
7	-3890	12.0	0.26869	0.48864	0.01007	0.69259	2.04669	0.04342	0.17809	0.00183	2604	22	2565	45	2634	17	143	89	0.6	3
7	-4587	11.7	0.31509	0.47768	0.01259	0.31029	2.09871	0.05494	0.17782	0.00147	2579	26	2512	55	2632	14	132	7	0.1	4
8	-2977	12.2	0.27376	0.50081	0.01025	0.69668	1.99346	0.04034	0.17682	0.00182	2622	21	2621	44	2623	17	107	46	0.4	0
8	1113	11.8	0.31784	0.47907	0.01236	0.38027	2.09039	0.05364	0.17920	0.00183	2590	26	2520	54	2645	17	71	5	0.1	5
80	-14079	12.1	0.32219	0.48861	0.01275	0.48435	2.04320	0.05553	0.17829	0.00161	2606	27	2568	58	2636	15	130	14	0.1	3
9	-3204	12.1	0.26724	0.49298	0.00976	0.57657	2.02726	0.04194	0.17869	0.00187	2616	22	2585	44	2640	17	115	58	0.5	2
9	-1979	11.9	0.31471	0.48292	0.01267	0.46300	2.07576	0.05473	0.17826	0.00154	2592	26	2535	55	2636	14	96	9	0.1	4
OGC																				
52	-37245	28.9	0.87087	0.70547	0.02415	0.68571	1.42736	0.04658	0.29878	0.00396	3448	35	3423	87	3463	21	283	18	0.1	1
53	4562	28.5	0.95207	0.69370	0.02572	0.55097	1.44784	0.05195	0.29855	0.00415	3434	38	3385	95	3462	22	461	10	0.0	2
54	4257	27.9	0.80193	0.68005	0.02079	0.67765	1.46586	0.04996	0.29704	0.00377	3417	36	3353	89	3454	20	212	9	0.0	3
55	-9852	29.0	0.82632	0.69927	0.02072	0.63968	1.42602	0.04601	0.30029	0.00388	3454	34	3425	86	3471	20	228	28	0.1	2
56	-10210	30.2	0.71200	0.72639	0.01605	0.74937	1.38002	0.03016	0.30212	0.00329	3492	24	3513	59	3480	17	186	192	1.0	-1
57	-17794	29.2	0.67806	0.70517	0.01519	0.76150	1.42052	0.03055	0.29915	0.00298	3454	23	3436	57	3465	15	191	206	1.1	1
58	40125	29.7	0.70326	0.72628	0.01638	0.79038	1.38047	0.03118	0.29760	0.00313	3477	24	3512	61	3457	16	216	197	0.9	-2
59	7840	29.6	0.69333	0.71394	0.01539	0.66888	1.40095	0.03115	0.30083	0.00340	3473	25	3473	60	3474	18	174	183	1.1	0
60	15596	29.1	0.70613	0.70504	0.01564	0.78560	1.42088	0.03098	0.29951	0.00310	3455	24	3435	58	3467	16	161	91	0.6	1
61	-25069	29.5	0.70698	0.72091	0.01612	0.70765	1.39246	0.03104	0.29849	0.00343	3472	25	3489	60	3462	18	93	84	0.9	-1
63	3805	28.2	0.75562	0.68674	0.01858	0.58368	1.45736	0.04062	0.29815	0.00271	3426	29	3368	73	3460	14	173	14	0.1	3
64	8658	28.5	0.74420	0.68629	0.01788	0.45562	1.45511	0.03643	0.30024	0.00227	3434	26	3372	66	3471	12	186	15	0.1	3
67	-4003	27.3	0.73469	0.65861	0.01770	0.45486	1.51753	0.04152	0.30057	0.00273	3394	28	3263	70	3473	14	138	6	0.0	6
1	4994	29.4	0.70506	0.71731	0.01713	0.63493	1.39740	0.03256	0.29809	0.00330	3467	25	3480	63	3460	17	322	415	1.3	-1
1	3277	28.5	0.83623	0.69033	0.02100	0.53195	1.45506	0.04465	0.30035	0.00396	3435	33	3372	81	3471	20	359	38	0.1	3
10	9456	29.3	0.66027	0.71650	0.01500	0.76629	1.39737	0.02925	0.29739	0.00283	3465	23	3480	56	3456	15	152	173	1.1	-1
10	10253	29.2	0.75790	0.71000	0.01861	0.57212	1.40864	0.03917	0.29846	0.00230	3460	28	3458	74	3462	12	163	12	0.1	0
11	-1956	30.0	0.66700	0.72099	0.01512	0.76323	1.38742	0.02805	0.30155	0.00279	3485	22	3499	55	3478	14	108	100	0.9	-1
11	3738	28.6	0.75247	0.69668	0.01809	0.44581	1.43491	0.03811	0.29791	0.00243	3440	27	3409	70	3459	13	159	13	0.1	1
12	14341	29.9	0.66972	0.71710	0.01520	0.59532	1.39373	0.02869	0.30190	0.00323	3482	23	3487	55	3479	17	159	173	1.1	0
13	2520	28.3	0.77636	0.69171	0.01988	0.80559	1.44998	0.04099	0.29934	0.00450	3435	31	3381	74	3466	23	406	429	1.1	2
14	4161	29.7	0.69220	0.72134	0.01555	0.76790	1.38485	0.02766	0.29906	0.00316	3479	22	3504	54	3465	16	165	163	1.0	-1
15	-3213	29.4	0.68503	0.71898	0.01564	0.72359	1.39516	0.03061	0.29660	0.00319	3464	24	3484	59	3452	17	126	120	1.0	-1
16	-19415	28.8	0.65991	0.70069	0.01567	0.75327	1.43282	0.03238	0.29729	0.00302	3440	24	3413	60	3455	16	168	152	0.9	1
17	24929	29.7	0.67375	0.71803	0.01546	0.69219	1.39424	0.02923	0.30087	0.00326	3478	23	3486	56	3474	17	156	176	1.1	0
18	23692	29.2	0.80928	0.70005	0.02032	0.68896	1.42756	0.04620	0.30303	0.00515	3462	36	3423	86	3485	26	319	357	1.1	2
19	4165	28.6	0.77079	0.69834	0.01930	0.47202	1.43513	0.03819	0.29761	0.00237	3439	27	3409	71	3457	12	133	3	0.0	1
2	1071	28.6	0.67842	0.67615	0.01554	0.74983	1.48313	0.03428	0.30682	0.00350	3437	25	3322	60	3504	18	356	388	1.1	5
2	5106	29.3	0.91246	0.70125	0.02422	0.63729	1.43388	0.04784	0.30466	0.00433	3463	36	3411	88	3493	22	445	45	0.1	2
20	5781	28.2	0.75895	0.68485	0.01907	0.59701	1.46350	0.03965	0.29895	0.00293	3424	28	3357	71	3464	15	151	4	0.0	3
21	6499	29.7	0.78636	0.71404	0.01892	0.54493	1.39894	0.03833	0.30132	0.00265	3476	28	3477	74	3476	14	142	3	0.0	0

	$^{206}Pb/^{204}Pb$	$^{207}Pb/^{235}U$	2SE	$^{206}Pb/^{238}U$	2SE	rho	$^{238}U/^{206}Pb$	2SE	$^{207}Pb/^{206}Pb$	2SE	$^{207}Pb/^{235}U$ Age (Ma)	2SE	$^{206}Pb/^{238}U$ Age (Ma)	2SE	$^{207}Pb/^{206}Pb$ Age (Ma)	2SE	U (ppm)	Th (ppm)	Th/U	TW conc %
22	-46753	29.1	0.78864	0.70021	0.01914	0.46339	1.42908	0.03794	0.30146	0.00278	3456	28	3420	71	3477	14	184	6	0.0	2
23	-2170	27.9	0.74810	0.67609	0.01851	0.54355	1.48120	0.03930	0.29959	0.00251	3415	27	3326	69	3467	13	135	9	0.1	4
24	1854	28.7	0.75329	0.69541	0.01855	0.57454	1.43752	0.03626	0.29935	0.00247	3443	26	3404	67	3466	13	130	11	0.1	2
25	4951	27.5	0.72094	0.66536	0.01737	0.51287	1.50112	0.03975	0.30095	0.00244	3406	27	3291	68	3474	13	104	6	0.1	5
26	1884	28.7	0.86436	0.69433	0.01999	0.47700	1.44247	0.04182	0.29872	0.00452	3438	32	3395	77	3463	23	208	17	0.1	2
27	-2182	28.3	1.29610	0.69635	0.03220	0.19558	1.45901	0.05830	0.29565	0.00401	3417	41	3365	105	3447	21	71	6	0.1	2
28	-4083	29.0	0.84192	0.69693	0.02009	0.33135	1.43321	0.03941	0.30178	0.00314	3454	29	3412	73	3479	16	143	5	0.0	2
29	-8658	28.8	0.75275	0.69411	0.01834	0.43832	1.44303	0.03977	0.30069	0.00235	3444	28	3394	73	3473	12	174	16	0.1	2
3	5388	28.8	0.70999	0.69122	0.01619	0.81416	1.44526	0.03666	0.30233	0.00344	3448	27	3390	67	3482	18	301	208	0.7	3
3	10273	29.0	0.90843	0.69836	0.02308	0.59919	1.43585	0.04817	0.30177	0.00615	3452	39	3407	89	3479	32	539	23	0.0	2
30	-2283	28.3	0.86949	0.67825	0.02091	0.42752	1.46594	0.04380	0.30195	0.00389	3433	32	3353	78	3480	20	203	15	0.1	4
31	6149	28.7	0.74972	0.69404	0.01791	0.41134	1.43912	0.03620	0.29970	0.00226	3443	26	3401	67	3468	12	126	11	0.1	2
32	4270	28.6	0.75471	0.69641	0.01850	0.62159	1.43647	0.04005	0.29937	0.00257	3444	29	3406	74	3466	13	164	18	0.1	2
33	4806	28.4	0.75853	0.68670	0.01845	0.53917	1.45723	0.03895	0.30064	0.00290	3434	28	3368	70	3473	15	121	13	0.1	3
34	3548	29.0	0.78892	0.70200	0.01974	0.67670	1.42013	0.04013	0.30020	0.00380	3458	30	3436	75	3471	20	126	11	0.1	1
35	-3153	28.3	0.77234	0.69041	0.01921	0.50674	1.45443	0.04041	0.29700	0.00326	3424	29	3373	73	3454	17	94	4	0.0	2
36	3076	28.3	0.77332	0.68641	0.01892	0.45783	1.46210	0.03976	0.30116	0.00321	3433	29	3360	71	3476	17	194	14	0.1	3
37	8701	28.8	0.76995	0.69973	0.01908	0.68873	1.43127	0.04052	0.29967	0.00290	3449	29	3416	75	3468	15	384	46	0.1	1
38	6445	28.3	0.74954	0.68927	0.01828	0.46964	1.44875	0.03544	0.29785	0.00258	3431	26	3384	64	3458	14	175	21	0.1	2
39	-7661	27.1	0.73263	0.66064	0.01848	0.61685	1.52031	0.04271	0.29820	0.00298	3385	29	3259	72	3460	16	96	8	0.1	6
4	-19832	29.4	0.74010	0.70946	0.01844	0.78086	1.41225	0.03574	0.30263	0.00396	3471	28	3451	68	3483	20	206	176	0.9	1
4	2478	29.1	0.86657	0.69858	0.02221	0.45715	1.43933	0.04751	0.30163	0.00363	3450	35	3401	87	3478	19	199	12	0.1	2
40	1869	26.6	0.69484	0.64665	0.01686	0.65843	1.54600	0.04338	0.29942	0.00256	3372	29	3216	71	3467	13	106	8	0.1	7
41	-12819	27.5	0.72424	0.66928	0.01789	0.58079	1.49688	0.03946	0.29877	0.00271	3402	27	3298	68	3463	14	158	13	0.1	5
42	118399	28.1	0.73565	0.68583	0.01799	0.57259	1.45980	0.03880	0.29903	0.00237	3427	27	3364	70	3465	12	232	20	0.1	3
43	-70059	27.3	0.72688	0.66323	0.01816	0.60561	1.51176	0.04319	0.29928	0.00268	3394	29	3273	73	3466	14	241	22	0.1	5
44	11136	27.9	0.73787	0.67065	0.01856	0.67449	1.49121	0.04112	0.30182	0.00386	3415	30	3308	71	3479	20	250	10	0.0	5
45	4048	28.9	0.81894	0.69643	0.01815	0.87519	1.44015	0.03791	0.30036	0.00336	3445	28	3399	70	3471	17	248	209	0.8	2
46	-6942	28.8	0.86206	0.70114	0.02022	0.85927	1.43823	0.04233	0.29845	0.00389	3440	32	3403	78	3461	20	223	230	1.0	1
47	23780	30.1	0.74177	0.72530	0.01637	0.77149	1.37894	0.02973	0.30079	0.00340	3489	24	3515	58	3474	18	191	187	1.0	-1
48	3200	29.5	0.75036	0.71814	0.01735	0.78657	1.39540	0.03487	0.29727	0.00359	3466	27	3483	67	3455	19	156	146	0.9	-1
49	3493	28.9	0.66914	0.70451	0.01557	0.72039	1.41864	0.02919	0.29873	0.00335	3454	23	3439	55	3463	17	207	267	1.3	1
5	11273	29.2	0.79971	0.70764	0.01752	0.69004	1.41694	0.03620	0.29808	0.00412	3453	29	3442	68	3460	21	205	206	1.0	0
5	10046	28.4	0.78594	0.68680	0.01954	0.50656	1.45945	0.04066	0.30080	0.00360	3433	30	3364	73	3474	19	200	7	0.0	3
50	1531	29.5	0.71420	0.71242	0.01606	0.67651	1.40755	0.03164	0.30087	0.00372	3469	25	3460	60	3474	19	72	57	0.8	0
51	1012	28.6	0.76840	0.69384	0.01800	0.18941	1.44225	0.03744	0.29847	0.00237	3437	27	3395	69	3462	12	88	6	0.1	2
6	34593	29.4	0.65960	0.71251	0.01459	0.67610	1.40441	0.02911	0.29859	0.00277	3464	22	3466	56	3462	14	196	224	1.1	0
6	8757	29.8	0.80320	0.72492	0.01940	0.49040	1.38304	0.03721	0.29983	0.00287	3483	28	3507	73	3469	15	139	12	0.1	-1
7	7554	29.5	0.68645	0.71307	0.01512	0.70256	1.40157	0.03086	0.29873	0.00307	3466	24	3472	59	3463	16	131	135	1.0	0
7	2399	29.4	0.78833	0.71034	0.01909	0.53874	1.40682	0.03788	0.30121	0.00270	3471	28	3462	72	3476	14	132	11	0.1	0
70	-15068	28.5	0.77434	0.68571	0.01864	0.49102	1.45796	0.03784	0.30138	0.00232	3436	27	3367	68	3477	12	99	6	0.1	3
71	7824	29.3	0.81522	0.70994	0.01956	0.44408	1.41013	0.03841	0.29961	0.00240	3463	28	3455	73	3468	12	192	11	0.1	0
8	-56594	29.3	0.66229	0.71146	0.01503	0.80523	1.40720	0.02933	0.29908	0.00271	3463	22	3461	56	3465	14	142	153	1.1	0
8	9620	29.3	0.75303	0.71574	0.01896	0.62660	1.40014	0.03786	0.29903	0.00256	3468	28	3474	73	3465	13	161	10	0.1	0

	$^{206}Pb/^{204}Pb$	$^{207}Pb/^{235}U$	2SE	$^{206}Pb/^{238}U$	2SE	rho	$^{238}U/^{206}Pb$	2SE	$^{207}Pb/^{206}Pb$	2SE	$^{207}Pb/^{235}U$ Age (Ma)	2SE	$^{206}Pb/^{238}U$ Age (Ma)	2SE	$^{207}Pb/^{206}Pb$ Age (Ma)	2SE	U (ppm)	Th (ppm)	Th/U	TW conc %
9	-19531	29.4	0.66294	0.70969	0.01492	0.67558	1.40818	0.03124	0.30036	0.00324	3467	24	3459	59	3471	17	186	198	1.1	0
9	15341	29.1	0.78274	0.70251	0.01904	0.46292	1.42733	0.03824	0.30158	0.00242	3458	28	3423	71	3478	12	229	19	0.1	1
TAN2																				
91500																				
10	6267	1.8	0.05767	0.17478	0.00474	0.07005	5.71850	0.16006	0.07564	0.00150	1054	23	1039	27	1085	40	80	30	0.4	3
11	754	1.8	0.05016	0.17709	0.00490	0.46795	5.61526	0.13998	0.07550	0.00150	1065	21	1057	24	1081	40	77	30	0.4	1
12	-8163	1.8	0.05068	0.17843	0.00473	0.38709	5.60632	0.14461	0.07447	0.00148	1057	21	1058	25	1053	40	79	30	0.4	-2
13	-2413	1.8	0.04959	0.17044	0.00457	0.36489	5.88685	0.15741	0.07554	0.00154	1034	22	1011	25	1082	41	80	31	0.4	5
14	935	1.8	0.04925	0.17581	0.00441	0.32098	5.69227	0.14544	0.07475	0.00145	1049	21	1043	25	1061	39	79	29	0.4	1
15	636	1.8	0.05066	0.17699	0.00455	0.25434	5.64745	0.14262	0.07485	0.00132	1055	20	1051	24	1064	35	79	30	0.4	1
16	-527	1.8	0.05081	0.17617	0.00478	0.51449	5.65533	0.15772	0.07499	0.00159	1055	23	1050	27	1067	43	80	30	0.4	2
7	-3771	1.8	0.05085	0.17311	0.00475	0.32792	5.79012	0.15791	0.07455	0.00154	1036	22	1027	26	1055	42	81	31	0.4	1
8	-12031	1.8	0.05077	0.17232	0.00456	0.36552	5.80649	0.14912	0.07606	0.00152	1047	21	1024	24	1096	40	83	31	0.4	6
9	15372	1.9	0.06240	0.17811	0.00514	0.28705	5.62187	0.15085	0.07685	0.00212	1075	26	1055	26	1116	55	80	29	0.4	3
FC1																				
1	-4710	2.0	0.04504	0.18537	0.00489	0.52757	5.40915	0.14332	0.07650	0.00081	1098	19	1094	27	1107	21	315	185	0.6	1
10	-5306	1.9	0.04769	0.18079	0.00480	0.39082	5.52277	0.14003	0.07630	0.00091	1082	19	1073	25	1102	24	430	279	0.6	2
11	-25533	2.0	0.04987	0.18780	0.00508	0.58395	5.30403	0.14507	0.07617	0.00093	1108	20	1113	28	1099	24	346	197	0.6	-1
12	2810	2.0	0.04580	0.18518	0.00489	0.48297	5.40185	0.13596	0.07694	0.00093	1103	19	1095	25	1119	24	285	159	0.6	2
13	7067	2.0	0.04846	0.18687	0.00507	0.49274	5.36154	0.14519	0.07635	0.00094	1103	20	1102	27	1103	25	334	219	0.7	-1
14	-10715	2.0	0.04721	0.18778	0.00493	0.51397	5.31429	0.13987	0.07622	0.00077	1108	19	1111	27	1100	20	402	262	0.7	-1
15	-22826	2.0	0.04905	0.18716	0.00524	0.58343	5.37277	0.15319	0.07630	0.00086	1101	21	1100	29	1102	22	348	241	0.7	0
16	1801	2.0	0.04743	0.18864	0.00508	0.70145	5.28175	0.15051	0.07526	0.00092	1103	21	1118	29	1074	24	428	285	0.7	-4
17	4803	2.0	0.05062	0.18692	0.00498	0.05252	5.32572	0.12413	0.07578	0.00104	1102	18	1109	24	1088	27	421	275	0.7	-2
18	13383	1.9	0.04852	0.18367	0.00511	0.45561	5.45999	0.15404	0.07620	0.00105	1089	21	1084	28	1099	28	493	337	0.7	1
19	-5944	2.0	0.04912	0.18706	0.00521	0.56377	5.34268	0.13682	0.07539	0.00085	1097	19	1106	26	1078	23	516	358	0.7	-3
2	-690742	1.9	0.04640	0.18336	0.00501	0.59553	5.46358	0.14330	0.07600	0.00096	1087	19	1084	26	1094	25	468	259	0.6	1
20	11824	2.0	0.04597	0.18620	0.00479	0.46559	5.36206	0.14501	0.07572	0.00079	1097	19	1102	27	1087	21	492	340	0.7	-2
21	6469	2.0	0.04864	0.18814	0.00507	0.30810	5.33440	0.14238	0.07557	0.00092	1099	20	1108	27	1083	25	466	311	0.7	-3
22	6270	2.0	0.04857	0.18958	0.00501	0.62361	5.26714	0.15243	0.07581	0.00093	1110	21	1121	30	1089	25	497	345	0.7	-3
23	-5174	2.0	0.04871	0.18742	0.00502	0.36318	5.33960	0.13707	0.07560	0.00075	1099	18	1107	26	1084	20	561	390	0.7	-2
24	-25570	1.9	0.04888	0.18306	0.00478	0.27308	5.47596	0.14520	0.07623	0.00098	1088	20	1081	26	1100	26	530	369	0.7	1
25	6555	2.0	0.04747	0.18711	0.00484	0.46157	5.34429	0.14115	0.07554	0.00104	1098	20	1106	27	1082	28	440	292	0.7	-3
26	5618	1.9	0.04824	0.18294	0.00489	0.35010	5.46243	0.14700	0.07584	0.00094	1086	20	1084	27	1090	25	534	366	0.7	0
27	15571	2.0	0.04955	0.18679	0.00496	0.26964	5.35932	0.14698	0.07637	0.00088	1103	20	1103	28	1104	23	620	441	0.7	0
28	8014	2.0	0.04789	0.18707	0.00495	0.43235	5.34498	0.14388	0.07628	0.00094	1104	20	1106	27	1102	25	657	461	0.7	-1
29	-6280	1.9	0.05092	0.18403	0.00513	0.44317	5.43648	0.15564	0.07586	0.00099	1089	21	1088	29	1090	26	521	352	0.7	0
3	390921	2.0	0.04482	0.18738	0.00482	0.52844	5.33610	0.14005	0.07608	0.00094	1104	20	1107	27	1096	25	304	204	0.7	-2
32	3752	1.9	0.04908	0.18302	0.00525	0.59697	5.44033	0.15326	0.07625	0.00112	1092	21	1088	28	1101	29	732	505	0.7	1
33	4637	1.9	0.05204	0.18272	0.00563	0.54994	5.46954	0.16978	0.07560	0.00081	1083	22	1082	31	1084	22	714	499	0.7	0
34	-11121	2.0	0.04861	0.18611	0.00481	0.46215	5.38376	0.14264	0.07648	0.00100	1101	20	1098	27	1107	26	404	280	0.7	0
35	-3984	2.0	0.04573	0.18878	0.00472	0.50627	5.30002	0.13394	0.07603	0.00080	1108	18	1114	26	1095	21	379	261	0.7	-2
36	-782630	2.0	0.04640	0.18714	0.00478	0.45873	5.34153	0.13766	0.07656	0.00091	1107	19	1106	26	1109	24	546	414	0.8	0

	$^{206}Pb/^{204}Pb$	$^{207}Pb/^{235}U$	2SE	$^{206}Pb/^{238}U$	2SE	rho	$^{238}U/^{206}Pb$	2SE	$^{207}Pb/^{206}Pb$	2SE	$^{207}Pb/^{235}U$ Age (Ma)	2SE	$^{206}Pb/^{238}U$ Age (Ma)	2SE	$^{207}Pb/^{206}Pb$ Age (Ma)	2SE	U (ppm)	Th (ppm)	Th/U	TW conc %
39	-3513	2.0	0.04826	0.18810	0.00498	0.45245	5.33159	0.14105	0.07624	0.00094	1106	20	1108	27	1100	25	344	248	0.7	-1
4	14459	1.9	0.04963	0.18190	0.00503	0.43330	5.49732	0.15216	0.07644	0.00097	1087	20	1077	27	1106	25	337	226	0.7	2
40	2044	2.0	0.04518	0.18766	0.00490	0.49824	5.33047	0.14052	0.07636	0.00090	1107	19	1108	27	1104	24	367	266	0.7	-1
43	1694	2.0	0.05009	0.18505	0.00490	0.43842	5.40780	0.15237	0.07703	0.00109	1103	21	1094	28	1121	28	215	154	0.7	2
44	-16653	1.9	0.04788	0.18795	0.00492	0.45356	5.32094	0.13395	0.07563	0.00094	1102	19	1110	26	1084	25	325	213	0.7	-3
5	-523498	2.0	0.04614	0.18427	0.00488	0.48851	5.39722	0.14023	0.07673	0.00094	1102	19	1096	26	1113	25	304	206	0.7	1
53	-5016	2.0	0.05168	0.18473	0.00585	0.66229	5.39990	0.17069	0.07658	0.00122	1100	24	1095	32	1109	32	455	250	0.5	1
54	2080	2.0	0.04615	0.19048	0.00499	0.49975	5.23837	0.12653	0.07642	0.00088	1119	18	1126	25	1105	23	397	208	0.5	-2
6	42403	1.9	0.04852	0.18461	0.00487	0.36955	5.42135	0.15048	0.07631	0.00093	1095	20	1091	28	1102	24	318	219	0.7	0
7	5078	1.9	0.04607	0.18048	0.00468	0.45287	5.53154	0.15575	0.07642	0.00090	1082	20	1071	28	1105	24	360	239	0.7	3
8	-3157	1.9	0.04794	0.18541	0.00496	0.48176	5.40103	0.15082	0.07611	0.00088	1096	20	1095	28	1097	23	336	226	0.7	0
9	2685	2.0	0.04892	0.18605	0.00492	0.49056	5.36859	0.15188	0.07648	0.00094	1103	21	1101	29	1107	24	334	215	0.6	1
KARA																				
1	7663	12.5	0.28585	0.50905	0.01271	0.41756	1.96512	0.04798	0.17729	0.00165	2638	25	2652	53	2627	15	101	61	0.6	-1
10	-14313	12.0	0.28618	0.48925	0.01278	0.48054	2.04882	0.05475	0.17888	0.00184	2607	27	2562	57	2642	17	88	47	0.5	3
11	-39901	12.0	0.33195	0.49658	0.01421	-0.01213	2.02620	0.05599	0.17826	0.00210	2614	28	2586	59	2636	20	155	109	0.7	1
12	1860	12.3	0.41634	0.50327	0.01888	0.41207	2.00129	0.07353	0.17780	0.00343	2623	39	2612	79	2632	32	121	47	0.4	0
13	-2193	11.7	0.32454	0.47955	0.01483	0.13115	2.09671	0.06883	0.17716	0.00302	2576	35	2514	68	2626	28	103	44	0.4	4
14	-2378	12.2	0.29086	0.49561	0.01339	0.49639	2.02469	0.05266	0.17815	0.00188	2614	26	2588	55	2635	18	145	73	0.5	1
15	-3127	13.0	0.31420	0.52788	0.01395	0.29864	1.89969	0.05045	0.17807	0.00193	2674	27	2726	59	2634	18	69	37	0.5	-4
16	9913	12.0	0.28231	0.49447	0.01293	0.57138	2.02309	0.05638	0.17684	0.00183	2608	28	2589	59	2623	17	256	125	0.5	1
17	4427	12.5	0.31199	0.51640	0.01485	0.55875	1.94411	0.05403	0.17642	0.00199	2643	28	2675	61	2619	19	252	147	0.6	-2
18	4348	12.3	0.29943	0.50094	0.01399	0.52138	2.00719	0.05677	0.17907	0.00178	2627	28	2606	61	2644	16	327	204	0.6	1
19	19627	12.3	0.30024	0.49937	0.01363	0.34540	2.00671	0.05452	0.17842	0.00186	2624	27	2607	58	2637	17	254	158	0.6	1
2	-2639	12.3	0.31114	0.50293	0.01388	0.38024	1.99330	0.05348	0.17772	0.00175	2627	27	2621	58	2631	16	103	68	0.7	0
20	-23237	12.3	0.31169	0.49778	0.01392	0.36057	2.01018	0.05486	0.17894	0.00191	2625	28	2603	58	2642	18	181	89	0.5	1
21	3281	12.2	0.29170	0.49532	0.01346	0.48597	2.01797	0.05866	0.17858	0.00196	2620	29	2595	62	2639	18	177	93	0.5	2
27	-11595	11.9	0.28629	0.49546	0.01334	0.53358	2.02116	0.05309	0.17494	0.00191	2599	27	2591	56	2605	18	122	53	0.4	0
29	2492	13.0	0.34139	0.51391	0.01504	0.66847	1.93667	0.05565	0.18048	0.00250	2668	30	2684	63	2657	23	168	86	0.5	-1
3	325	14.8	0.74912	0.50303	0.01495	0.04799	1.98508	0.05395	0.21650	0.00936	2817	49	2630	59	2954	70	90	64	0.7	10
30	-1501	12.4	0.31147	0.50105	0.01373	0.30332	2.00493	0.05625	0.17987	0.00208	2632	29	2609	60	2651	19	82	36	0.4	1
31	3830	12.2	0.31856	0.49600	0.01310	0.18853	2.01832	0.05458	0.17836	0.00191	2618	27	2594	58	2637	18	80	34	0.4	1
32	2264	12.4	0.30496	0.50553	0.01374	0.50145	1.98168	0.05531	0.17809	0.00202	2634	28	2634	60	2634	19	104	51	0.5	0
4	1839	12.5	0.28907	0.51024	0.01310	0.45423	1.95915	0.04849	0.17689	0.00170	2638	25	2658	54	2623	16	86	54	0.6	-1
5	-6046	12.4	0.30107	0.50600	0.01365	0.45462	1.97912	0.05254	0.17849	0.00181	2637	27	2636	57	2638	17	99	51	0.5	0
6	-11722	12.4	0.29670	0.50200	0.01291	0.40750	1.98766	0.05133	0.17877	0.00181	2635	26	2627	56	2641	17	84	50	0.6	1
7	4482	12.2	0.29663	0.49905	0.01399	0.55438	2.01005	0.05581	0.17753	0.00180	2618	28	2603	59	2629	17	140	68	0.5	1
8	154386	12.6	0.28751	0.51392	0.01348	0.58241	1.94211	0.05052	0.17687	0.00160	2647	26	2678	57	2623	15	163	105	0.6	-2
9	-3357	11.7	0.28104	0.47700	0.01278	0.44598	2.09890	0.05379	0.17774	0.00175	2578	26	2512	53	2631	16	97	57	0.6	4
OGC																				
1	14445	29.0	0.63398	0.69986	0.01709	0.49170	1.42834	0.03529	0.30028	0.00228	3453	25	3421	66	3471	12	185	170	0.9	1
10	-305427	28.9	0.71129	0.70140	0.01829	-0.39892	1.43160	0.03259	0.29876	0.00220	3445	23	3415	60	3463	11	158	166	1.1	1
11	4125	26.1	0.80686	0.63776	0.02173	0.31582	1.58391	0.05546	0.29619	0.00270	3338	35	3155	87	3450	14	185	188	1.0	8

	$^{206}Pb/^{204}Pb$	$^{207}Pb/^{235}U$	2SE	$^{206}Pb/^{238}U$	2SE	rho	$^{238}U/^{206}Pb$	2SE	$^{207}Pb/^{206}Pb$	2SE	$^{207}Pb/^{235}U$ Age (Ma)	2SE	$^{206}Pb/^{238}U$ Age (Ma)	2SE	$^{207}Pb/^{206}Pb$ Age (Ma)	2SE	U (ppm)	Th (ppm)	Th/U	TW conc %
12	2773	28.5	0.65780	0.68734	0.01851	0.58539	1.45427	0.04068	0.29931	0.00297	3432	29	3374	73	3466	15	122	116	1.0	3
13	-7728	29.1	0.68431	0.70846	0.01983	0.66620	1.41657	0.04126	0.29747	0.00308	3452	30	3443	78	3456	16	123	128	1.0	0
14	5304	28.9	0.65410	0.69720	0.01852	0.68102	1.43311	0.04053	0.29968	0.00299	3447	29	3412	75	3468	15	91	76	0.8	2
15	8538	28.9	0.71846	0.69737	0.01845	0.07385	1.44828	0.05429	0.30042	0.00208	3439	37	3384	99	3472	11	140	123	0.9	2
16	2177	29.1	0.62329	0.70622	0.01726	0.60253	1.41546	0.03452	0.29899	0.00240	3457	25	3445	65	3464	12	139	135	1.0	1
17	4339	29.0	0.63403	0.70123	0.01762	0.63614	1.42712	0.03585	0.30008	0.00271	3453	26	3423	67	3470	14	137	135	1.0	1
18	-4111	29.2	0.62958	0.70287	0.01730	0.54954	1.42049	0.03390	0.30142	0.00224	3462	25	3436	64	3477	11	125	120	1.0	1
19	18557	29.5	0.67435	0.71226	0.01797	-0.08048	1.40501	0.03457	0.29969	0.00208	3467	25	3465	66	3468	11	143	138	1.0	0
2	3343	27.7	0.66256	0.67252	0.01817	0.43137	1.48243	0.03775	0.29912	0.00227	3412	26	3323	66	3465	12	173	164	0.9	4
20	3237	29.4	0.66225	0.71280	0.01833	0.55746	1.39956	0.03537	0.29900	0.00218	3468	26	3475	68	3464	11	133	127	1.0	0
21	-10240	29.0	0.64362	0.69940	0.01793	0.63551	1.42901	0.03567	0.30101	0.00230	3455	26	3420	66	3475	12	189	218	1.2	2
27	-70210	29.1	0.63691	0.70225	0.01744	0.48709	1.42433	0.03534	0.30058	0.00206	3456	25	3429	66	3473	11	164	117	0.7	1
29	-16092	28.9	0.64351	0.70113	0.01752	0.42995	1.42437	0.03434	0.29956	0.00213	3453	25	3428	64	3467	11	111	118	1.1	1
3	-7994	26.0	0.98987	0.63010	0.02511	0.18330	1.64183	0.08139	0.29983	0.00224	3315	49	3066	121	3469	12	265	205	0.8	10
30	114552	28.8	0.65136	0.70036	0.01796	0.51670	1.42989	0.03599	0.29865	0.00246	3446	26	3418	67	3463	13	169	183	1.1	1
31	2843	29.0	0.63302	0.70816	0.01793	0.65054	1.41065	0.03407	0.29796	0.00218	3457	25	3454	65	3459	11	207	262	1.3	0
32	5577	28.8	0.68430	0.69842	0.02023	0.74385	1.43749	0.04027	0.29948	0.00309	3444	29	3404	74	3467	16	192	221	1.2	2
4	2935	29.5	0.66778	0.71429	0.01750	0.13045	1.39953	0.03373	0.29964	0.00205	3471	25	3476	65	3468	11	114	93	0.8	0
5	5226	29.3	0.70222	0.70572	0.01860	-0.00924	1.45381	0.09165	0.30054	0.00229	3436	62	3374	166	3472	12	118	88	0.7	1
6	-5255	29.3	0.69442	0.70843	0.01837	0.16217	1.41501	0.03969	0.30070	0.00230	3463	29	3446	75	3473	12	132	105	0.8	1
7	4545	28.8	0.65702	0.69870	0.01818	0.52196	1.43121	0.03701	0.29994	0.00246	3450	27	3416	69	3469	13	151	151	1.0	2
8	2942	28.7	0.63370	0.69809	0.01755	0.65127	1.43379	0.03755	0.29927	0.00230	3446	27	3411	69	3466	12	150	159	1.1	2
9	6313	28.6	0.62504	0.69372	0.01703	0.47453	1.44127	0.03539	0.29944	0.00191	3441	25	3397	65	3467	10	157	166	1.1	2

Mount	Analysis #	Ip (nA)	$^{18}O/^{16}O$	± rel (%)	$^{16}O^{1}H/^{16}O$	± rel (%)	Row delta ^{18}O	± per mil	Drift corrected $d^{18}O$	± per mil	$^{18}O/^{16}O$	1σ error	SIMS corrected $d^{18}O$	± per mil	Drift corrected OH/O	± rel (%)	$^{207}Pb/^{206}Pb$ age per spot
91500																	
TAN1	91500@01	3.0069	0.0020	0.0058	0.0004	0.1054	9.67	0.058	9.672	0.058	0.0020247	0.000000269	9.736	0.133	0.00045	0.10541	
TAN1	91500@02	3.0034	0.0020	0.0058	0.0004	0.1146	10.04	0.058	10.043	0.058	0.0020255	0.000000270	10.108	0.133	0.00044	0.11457	
TAN1	91500@03	3.0059	0.0020	0.0063	0.0004	0.1800	9.88	0.063	9.878	0.063	0.0020251	0.000000274	9.943	0.135	0.00044	0.18001	
TAN1	91500@04	3.0104	0.0020	0.0060	0.0004	0.2553	9.73	0.060	9.726	0.060	0.0020248	0.000000272	9.791	0.134	0.00044	0.25528	
TAN1	91500@05	3.0068	0.0020	0.0070	0.0004	0.3563	9.86	0.070	9.864	0.070	0.0020251	0.000000281	9.928	0.139	0.00044	0.35629	
TAN1	91500@06	2.9794	0.0020	0.0058	0.0003	0.2670	9.69	0.058	9.693	0.058	0.0020248	0.000000269	9.758	0.133	0.00027	0.26695	
TAN1	91500@07	2.9816	0.0020	0.0050	0.0003	0.3398	9.86	0.050	9.862	0.050	0.0020251	0.000000263	9.926	0.130	0.00027	0.33980	
TAN1	91500@08	2.9660	0.0020	0.0061	0.0002	0.2224	10.01	0.061	10.006	0.061	0.0020254	0.000000272	10.071	0.134	0.00027	0.22242	
TAN1	91500@09	2.9736	0.0020	0.0070	0.0002	0.3026	9.95	0.070	9.945	0.070	0.0020253	0.000000281	10.010	0.139	0.00027	0.30265	
TAN1	91500@10	2.9538	0.0020	0.0050	0.0002	0.2120	9.82	0.050	9.816	0.050	0.0020250	0.000000263	9.881	0.130	0.00027	0.21204	
TAN1	91500@11	2.9518	0.0020	0.0076	0.0002	0.1902	10.20	0.076	10.204	0.076	0.0020258	0.000000287	10.269	0.142	0.00027	0.19017	
TAN1	91500@12	2.9460	0.0020	0.0095	0.0002	0.2263	10.04	0.095	10.039	0.095	0.0020255	0.000000309	10.104	0.153	0.00028	0.22628	
TAN1	91500@13	2.9478	0.0020	0.0064	0.0002	0.2515	9.92	0.064	9.918	0.064	0.0020252	0.000000275	9.982	0.136	0.00028	0.25145	
TAN1	91500@14	2.9283	0.0020	0.0077	0.0002	0.2854	9.88	0.077	9.884	0.077	0.0020251	0.000000289	9.948	0.143	0.00029	0.28539	
TAN1	91500@15	2.9161	0.0020	0.0092	0.0002	0.3365	10.03	0.092	10.030	0.092	0.0020254	0.000000306	10.095	0.151	0.00030	0.33655	
TAN1	91500@16	2.8874	0.0020	0.0079	0.0002	0.2790	9.84	0.079	9.843	0.079	0.0020251	0.000000291	9.907	0.144	0.00030	0.27899	
TAN1	91500@17	2.8935	0.0020	0.0056	0.0002	0.3098	9.88	0.056	9.875	0.056	0.0020251	0.000000268	9.940	0.132	0.00030	0.30978	
TAN1	91500@18	2.8307	0.0020	0.0051	0.0002	0.3077	9.89	0.051	9.892	0.051	0.0020252	0.000000264	9.957	0.130	0.00031	0.30765	
TAN1	91500@19	2.8321	0.0020	0.0052	0.0002	0.2295	10.04	0.052	10.041	0.052	0.0020255	0.000000265	10.105	0.131	0.00031	0.22948	
TAN1	91500@20	2.7844	0.0020	0.0074	0.0002	0.2984	9.91	0.074	9.906	0.074	0.0020252	0.000000285	9.970	0.141	0.00032	0.29838	
TAN1	91500@21	2.7863	0.0020	0.0115	0.0002	0.2799	9.93	0.115	9.927	0.115	0.0020252	0.000000337	9.992	0.166	0.00032	0.27989	
TAN1	91500@22	2.7726	0.0020	0.0052	0.0002	0.2792	9.81	0.052	9.810	0.052	0.0020250	0.000000264	9.875	0.131	0.00033	0.27916	
TAN1	91500@23	2.7752	0.0020	0.0074	0.0002	0.1903	9.81	0.074	9.807	0.074	0.0020250	0.000000285	9.871	0.141	0.00033	0.19031	
TAN1	91500@24	2.7559	0.0020	0.0072	0.0002	0.2587	9.86	0.072	9.865	0.072	0.0020251	0.000000284	9.929	0.140	0.00034	0.25872	
TAN1	91500@25	2.7537	0.0020	0.0069	0.0002	0.2712	9.81	0.069	9.807	0.069	0.0020250	0.000000280	9.871	0.138	0.00034	0.27121	
TAN1	91500@26	2.7403	0.0020	0.0072	0.0003	0.1945	9.72	0.072	9.717	0.072	0.0020248	0.000000283	9.782	0.140	0.00036	0.19449	
TAN1	91500@27	2.7368	0.0020	0.0085	0.0002	0.2406	9.73	0.085	9.734	0.085	0.0020248	0.000000297	9.799	0.147	0.00035	0.24059	
TAN1	91500@28	2.7235	0.0020	0.0052	0.0002	0.2735	9.94	0.052	9.943	0.052	0.0020253	0.000000265	10.007	0.131	0.00036	0.27354	
TAN1	91500@29	2.7260	0.0020	0.0071	0.0002	0.2221	9.90	0.071	9.896	0.071	0.0020252	0.000000282	9.961	0.139	0.00036	0.22214	
TAN1	91500@30	2.7193	0.0020	0.0061	0.0002	0.2144	9.93	0.061	9.928	0.061	0.0020252	0.000000272	9.992	0.134	0.00036	0.21437	
TAN1	91500@31	2.7201	0.0020	0.0053	0.0002	0.2427	9.85	0.053	9.855	0.053	0.0020251	0.000000265	9.919	0.131	0.00037	0.24271	
TAN1	91500@32	2.6799	0.0020	0.0068	0.0002	0.2426	9.75	0.068	9.747	0.068	0.0020249	0.000000279	9.812	0.138	0.00038	0.24262	
TAN1	91500@33	2.6768	0.0020	0.0055	0.0002	0.2131	9.67	0.055	9.666	0.055	0.0020247	0.000000267	9.730	0.132	0.00038	0.21311	
TAN1	91500@34	2.6747	0.0020	0.0055	0.0002	0.2140	9.92	0.055	9.925	0.055	0.0020252	0.000000267	9.989	0.132	0.00038	0.21397	
TAN2	91500add@01	2.5657	0.0020	0.0083	0.0002	0.1171	9.14	0.083	9.137	0.083	0.0020235	0.000000466	9.113	0.230	0.00024	0.11714	
TAN2	91500add@02	2.5644	0.0020	0.0073	0.0002	0.3399	9.86	0.073	9.859	0.073	0.0020249	0.000000460	9.835	0.227	0.00024	0.33993	
TAN2	91500add@03	2.5580	0.0020	0.0061	0.0002	0.1762	9.87	0.061	9.865	0.061	0.0020249	0.000000453	9.842	0.224	0.00024	0.17624	

Mount	Analysis #	Ip (nA)	$^{18}O/^{16}O$	± rel (%)	$^{16}O^{1}H/^{16}O$	± rel (%)	Row delta ^{18}O	± per mil	Drift corrected $d^{18}O$	± per mil	$^{18}O/^{16}O$	1σ error	SIMS corrected $d^{18}O$	± per mil	Drift corrected OH/O	± rel (%)	Pb/Pb age per spot
TAN2	91500@08	2.5419	0.0020	0.0073	0.0002	0.3426	9.90	0.073	9.903	0.073	0.0020250	0.000000460	9.879	0.227	0.00024	0.34257	
TAN2	91500@09	2.5387	0.0020	0.0072	0.0002	0.2082	9.99	0.072	9.995	0.072	0.0020252	0.000000459	9.971	0.227	0.00025	0.20820	
TAN2	91500@10	2.5236	0.0020	0.0073	0.0002	0.2586	9.94	0.073	9.939	0.073	0.0020251	0.000000460	9.915	0.227	0.00025	0.25857	
TAN2	91500@11	2.5178	0.0020	0.0089	0.0003	0.1945	9.87	0.089	9.870	0.089	0.0020249	0.000000472	9.846	0.233	0.00026	0.19446	
TAN2	91500@12	2.5049	0.0020	0.0058	0.0003	0.1502	9.97	0.058	9.975	0.058	0.0020252	0.000000451	9.951	0.223	0.00025	0.15017	
TAN2	91500@13	2.5058	0.0020	0.0069	0.0002	0.3456	9.95	0.069	9.953	0.069	0.0020251	0.000000457	9.929	0.226	0.00025	0.34562	
TAN2	91500@14	2.5016	0.0020	0.0054	0.0002	0.2295	10.08	0.054	10.077	0.054	0.0020254	0.000000449	10.054	0.222	0.00025	0.22951	
TAN2	91500@15	2.4895	0.0020	0.0058	0.0003	0.0755	10.04	0.058	10.038	0.058	0.0020253	0.000000451	10.015	0.223	0.00025	0.07550	
TAN2	91500@16	2.4908	0.0020	0.0073	0.0003	0.2775	9.77	0.073	9.771	0.073	0.0020247	0.000000460	9.748	0.227	0.00025	0.27754	
TAN2	91500@17	2.4936	0.0020	0.0070	0.0002	0.4384	9.93	0.070	9.929	0.070	0.0020251	0.000000458	9.905	0.226	0.00025	0.43840	
TAN2	91500@18	2.4816	0.0020	0.0089	0.0003	0.2357	9.96	0.089	9.965	0.089	0.0020251	0.000000472	9.941	0.233	0.00026	0.23568	
TAN2	91500@19	2.4702	0.0020	0.0084	0.0002	0.1855	10.04	0.084	10.040	0.084	0.0020253	0.000000468	10.017	0.231	0.00025	0.18554	
TAN2	91500@20	2.4562	0.0020	0.0055	0.0002	0.2998	10.04	0.055	10.037	0.055	0.0020253	0.000000449	10.014	0.222	0.00025	0.29979	
TAN2	91500@21	2.4531	0.0020	0.0066	0.0003	0.1972	10.12	0.066	10.118	0.066	0.0020254	0.000000455	10.094	0.225	0.00025	0.19719	
TAN2	91500@22	2.4314	0.0020	0.0056	0.0003	0.1685	10.02	0.056	10.023	0.056	0.0020253	0.000000450	9.999	0.222	0.00026	0.16850	
TAN2	91500@23	2.4130	0.0020	0.0101	0.0003	0.1028	9.96	0.101	9.961	0.101	0.0020251	0.000000481	9.938	0.237	0.00026	0.10277	
TAN2	91500@24	2.3902	0.0020	0.0074	0.0002	0.1792	10.25	0.074	10.249	0.074	0.0020257	0.000000460	10.226	0.227	0.00025	0.17920	
TAN2	91500@25	2.3884	0.0020	0.0093	0.0003	0.2875	10.17	0.093	10.168	0.093	0.0020255	0.000000474	10.144	0.234	0.00025	0.28747	
TAN2	91500@26	2.3760	0.0020	0.0093	0.0003	0.1117	9.93	0.093	9.926	0.093	0.0020251	0.000000474	9.903	0.234	0.00026	0.11169	
TAN2	91500@27	2.3594	0.0020	0.0070	0.0003	0.2016	10.06	0.070	10.061	0.070	0.0020253	0.000000458	10.038	0.226	0.00026	0.20159	
TAN2	91500@28	2.3553	0.0020	0.0055	0.0003	0.3156	10.10	0.055	10.102	0.055	0.0020254	0.000000450	10.079	0.222	0.00025	0.31558	
TAN2	91500@29	2.3534	0.0020	0.0083	0.0003	0.2291	10.05	0.083	10.050	0.083	0.0020253	0.000000467	10.027	0.231	0.00026	0.22914	
TAN2	91500@30	2.3473	0.0020	0.0108	0.0003	0.1978	10.22	0.108	10.217	0.108	0.0020256	0.000000487	10.194	0.241	0.00025	0.19775	
TAN2	91500@31	2.3372	0.0020	0.0094	0.0003	0.1932	10.16	0.094	10.158	0.094	0.0020255	0.000000476	10.134	0.235	0.00026	0.19319	
TAN2	91500@32	2.3331	0.0020	0.0084	0.0003	0.1655	9.98	0.084	9.979	0.084	0.0020252	0.000000467	9.955	0.231	0.00025	0.16554	
TAN2	91500@33	2.3337	0.0020	0.0080	0.0003	0.2648	9.98	0.080	9.982	0.080	0.0020252	0.000000465	9.958	0.229	0.00025	0.26483	
TAN2	91500@34	2.3295	0.0020	0.0087	0.0002	0.2145	9.95	0.087	9.947	0.087	0.0020251	0.000000470	9.923	0.232	0.00025	0.21453	
TAN2	91500@35	2.3184	0.0020	0.0066	0.0003	0.2156	9.88	0.066	9.877	0.066	0.0020250	0.000000456	9.853	0.225	0.00025	0.21556	
TAN2	91500@36	2.3100	0.0020	0.0109	0.0003	0.2655	10.01	0.109	10.012	0.109	0.0020252	0.000000489	9.989	0.241	0.00025	0.26553	
TAN2	91500@37	2.3125	0.0020	0.0094	0.0002	0.3970	9.97	0.094	9.968	0.094	0.0020251	0.000000475	9.945	0.235	0.00025	0.39702	
TAN2	*91500@38*	*2.3265*	*0.0020*	*0.0095*	*0.0064*	*2.2907*	*9.11*	*0.095*	*9.109*	*0.095*	*0.0020234*	*0.000000475*	*9.085*	*0.235*	*0.00641*	*2.29070*	
TAN2	91500@39	2.3158	0.0020	0.0056	0.0009	0.1821	10.11	0.056	10.109	0.056	0.0020254	0.000000450	10.085	0.222	0.00089	0.18211	
TAN2	91500@40	2.2989	0.0020	0.0082	0.0006	0.4057	9.86	0.082	9.862	0.082	0.0020249	0.000000466	9.839	0.230	0.00063	0.40566	
TAN2	91500@41	2.2984	0.0020	0.0091	0.0006	0.1862	9.86	0.091	9.864	0.091	0.0020249	0.000000473	9.841	0.234	0.00062	0.18619	
TAN2	91500@42	2.3104	0.0020	0.0056	0.0005	0.0932	10.03	0.056	10.032	0.056	0.0020253	0.000000450	10.008	0.222	0.00055	0.09324	
TAN2	91500@43	2.2967	0.0020	0.0091	0.0005	0.2985	10.04	0.091	10.036	0.091	0.0020253	0.000000473	10.012	0.234	0.00052	0.29846	
TAN2	91500@44	2.2920	0.0020	0.0081	0.0005	0.3338	10.11	0.081	10.113	0.081	0.0020254	0.000000465	10.089	0.230	0.00048	0.33375	
TAN2	91500@45	2.2917	0.0020	0.0067	0.0005	0.3246	9.97	0.067	9.970	0.067	0.0020251	0.000000456	9.946	0.225	0.00053	0.32459	

Mount	Analysis #	Ip (nA)	$^{18}O/^{16}O$	± rel (%)	$^{16}O^{1}H/^{16}O$	± rel (%)	Row delta ^{18}O	± per mil	Drift corrected $d^{18}O$	± per mil	$^{18}O/^{16}O$	1σ error	SIMS corrected $d^{18}O$	± per mil	Drift corrected OH/O	± rel (%)	Pb/Pb age per spot
TAN2	91500@46	2.2797	0.0020	0.0087	0.0005	0.1927	10.15	0.087	10.149	0.087	0.0020255	0.000000470	10.125	0.232	0.00051	0.19266	
TAN2	91500@47	2.2756	0.0020	0.0095	0.0005	0.1303	10.25	0.095	10.254	0.095	0.0020257	0.000000476	10.230	0.235	0.00050	0.13031	
TAN2	91500@48	2.2752	0.0020	0.0112	0.0004	0.2877	9.86	0.112	9.858	0.112	0.0020249	0.000000491	9.835	0.242	0.00036	0.28768	
TAN2	91500@49	2.2665	0.0020	0.0077	0.0003	0.2685	9.85	0.077	9.850	0.077	0.0020249	0.000000462	9.826	0.228	0.00026	0.26851	
OGC																	
TAN2	OGCadd@01	2.5573	0.0020	0.0084	0.0006	0.0991	5.62	0.084	5.621	0.084	0.0020164	0.000000466	5.598	0.231	0.00056	0.09909	
TAN2	OGCadd@2	2.5563	0.0020	0.0081	0.0005	0.1152	5.85	0.081	5.853	0.081	0.0020169	0.000000463	5.829	0.230	0.00055	0.11525	
TAN2	OGCadd@3	2.5556	0.0020	0.0085	0.0005	0.3058	5.68	0.085	5.678	0.085	0.0020165	0.000000466	5.654	0.231	0.00055	0.30575	
TAN2	OGC@05	2.5360	0.0020	0.0075	0.0005	0.0359	5.85	0.075	5.846	0.075	0.0020169	0.000000459	5.822	0.228	0.00051	0.03587	
TAN2	OGC@06	2.5160	0.0020	0.0061	0.0005	0.1914	5.87	0.061	5.872	0.061	0.0020169	0.000000451	5.849	0.224	0.00054	0.19143	
TAN2	OGC@07	2.4989	0.0020	0.0064	0.0006	0.0497	5.86	0.064	5.856	0.064	0.0020169	0.000000452	5.832	0.224	0.00056	0.04968	
TAN2	OGC@08	2.4890	0.0020	0.0075	0.0006	0.2581	5.82	0.075	5.817	0.075	0.0020168	0.000000459	5.794	0.228	0.00057	0.25805	
TAN2	OGC@09	2.4719	0.0020	0.0102	0.0005	0.0260	5.91	0.102	5.910	0.102	0.0020170	0.000000480	5.886	0.238	0.00052	0.02598	
TAN2	OGC@10	2.4248	0.0020	0.0066	0.0005	0.2411	5.77	0.066	5.771	0.066	0.0020167	0.000000454	5.748	0.225	0.00054	0.24114	
TAN2	OGC@11	2.3866	0.0020	0.0056	0.0005	0.0973	5.83	0.056	5.825	0.056	0.0020168	0.000000448	5.802	0.222	0.00047	0.09727	
TAN2	OGC@12	2.3625	0.0020	0.0087	0.0005	0.3887	5.74	0.087	5.745	0.087	0.0020167	0.000000468	5.721	0.232	0.00054	0.38874	
TAN2	OGC@13	2.3436	0.0020	0.0065	0.0006	0.3672	5.67	0.065	5.672	0.065	0.0020165	0.000000453	5.649	0.225	0.00058	0.36722	
TAN2	OGC@14	2.3307	0.0020	0.0093	0.0005	0.1843	5.85	0.093	5.847	0.093	0.0020169	0.000000472	5.823	0.234	0.00054	0.18433	
TAN2	OGC@15	2.3171	0.0020	0.0061	0.0005	0.2002	6.01	0.061	6.008	0.061	0.0020172	0.000000451	5.985	0.224	0.00054	0.20018	
TAN2	*OGC@16*	*2.3322*	*0.0020*	*0.0085*	*0.0176*	*1.6152*	*4.01*	*0.085*	*4.007*	*0.085*	*0.0020132*	*0.000000466*	*3.983*	*0.231*	*0.01760*	*1.61517*	
TAN2	OGC@17	2.3006	0.0020	0.0087	0.0009	0.2222	5.76	0.087	5.760	0.087	0.0020167	0.000000467	5.737	0.232	0.00090	0.22223	
TAN2	OGC@18	2.2937	0.0020	0.0060	0.0007	0.2439	5.83	0.060	5.835	0.060	0.0020169	0.000000450	5.811	0.223	0.00072	0.24388	
TAN2	OGC@19	2.2972	0.0020	0.0066	0.0007	0.1994	5.88	0.066	5.882	0.066	0.0020169	0.000000454	5.859	0.225	0.00067	0.19936	
TAN2	OGC@23	2.2690	0.0020	0.0094	0.0005	0.3267	5.61	0.094	5.615	0.094	0.0020164	0.000000473	5.592	0.235	0.00054	0.32671	
TAN2	OGC@20	2.2672	0.0020	0.0068	0.0004	0.1143	5.83	0.068	5.832	0.068	0.0020168	0.000000455	5.809	0.226	0.00041	0.11434	
TAN2	OGC@21	2.2664	0.0020	0.0089	0.0004	0.2975	5.56	0.089	5.561	0.089	0.0020163	0.000000469	5.537	0.233	0.00043	0.29748	
TAN2	OGC@22	2.2669	0.0020	0.0107	0.0006	0.2214	5.73	0.107	5.726	0.107	0.0020166	0.000000484	5.703	0.240	0.00056	0.22138	
TAN1	OGC@01	2.9937	0.0020	0.0078	0.0007	0.1997	5.03	0.078	5.033	0.078	0.0020154	0.000000288	5.097	0.143	0.00074	0.19972	
TAN1	OGC@2	2.9862	0.0020	0.0086	0.0006	0.0723	5.77	0.086	5.769	0.086	0.0020169	0.000000298	5.834	0.148	0.00058	0.07233	
TAN1	OGC@03	2.9884	0.0020	0.0088	0.0006	0.0539	5.82	0.088	5.816	0.088	0.0020170	0.000000300	5.881	0.149	0.00061	0.05386	
TAN1	OGC@04	2.9789	0.0020	0.0055	0.0004	0.2080	5.63	0.055	5.634	0.055	0.0020166	0.000000266	5.698	0.132	0.00043	0.20795	
TAN1	OGC@05	2.9618	0.0020	0.0065	0.0004	0.1235	5.87	0.065	5.871	0.065	0.0020171	0.000000275	5.936	0.136	0.00046	0.12354	
TAN1	OGC@06	2.9114	0.0020	0.0067	0.0005	0.1241	5.76	0.067	5.762	0.067	0.0020169	0.000000276	5.826	0.137	0.00051	0.12410	
TAN1	OGC@07	2.8179	0.0020	0.0083	0.0005	0.1077	5.84	0.083	5.841	0.083	0.0020170	0.000000294	5.906	0.146	0.00057	0.10774	
TAN1	OGC@08	2.7756	0.0020	0.0099	0.0003	0.0508	5.77	0.099	5.775	0.099	0.0020169	0.000000313	5.839	0.155	0.00042	0.05083	
TAN1	OGC@09	2.7339	0.0020	0.0077	0.0005	0.0386	5.83	0.077	5.829	0.077	0.0020170	0.000000287	5.893	0.142	0.00059	0.03861	
TAN1	OGC@10	2.7157	0.0020	0.0100	0.0004	0.2700	5.93	0.100	5.928	0.100	0.0020172	0.000000315	5.992	0.156	0.00055	0.27005	
TAN1	OGC@11	2.6763	0.0020	0.0072	0.0006	0.4559	5.83	0.072	5.833	0.072	0.0020170	0.000000282	5.898	0.140	0.00070	0.45594	

Mount	*Analysis #*	*Ip (nA)*	*$^{18}O/^{16}O$*	*± rel (%)*	*$^{16}O^{1}H/^{16}O$*	*± rel (%)*	*Row delta ^{18}O*	*± per mil*	*Drift corrected $d^{18}O$*	*± per mil*	*$^{18}O/^{16}O$*	*1σ error*	*SIMS corrected $d^{18}O$*	*± per mil*	*Drift corrected OH/O*	*± rel (%)*	Pb/Pb age per spot
TAN1	OGC@12	2.6716	0.0020	0.0095	0.0005	0.0608	5.66	0.095	5.660	0.095	0.0020167	0.000000308	5.725	0.153	0.00061	0.06082	
TAN1	OGC@13	2.6756	0.0020	0.0053	0.0005	0.0741	5.67	0.053	5.674	0.053	0.0020167	0.000000264	5.738	0.131	0.00060	0.07412	
TAN1	OGC@14	2.6741	0.0020	0.0089	0.0004	0.0474	5.78	0.089	5.784	0.089	0.0020169	0.000000301	5.849	0.149	0.00050	0.04736	
TAN1	OGC@15	2.6718	0.0020	0.0055	0.0003	0.0776	5.85	0.055	5.852	0.055	0.0020171	0.000000266	5.917	0.132	0.00045	0.07760	
FC1																	
TAN1	FC1@01	2.9948	0.0020	0.0061	0.0005	0.1695	5.54	0.061	5.541	0.061	0.0020164	0.000000271	5.605	0.134	0.00051	0.16948	
TAN1	FC1@2	3.0037	0.0020	0.0070	0.0005	0.2176	5.50	0.070	5.501	0.070	0.0020164	0.000000280	5.565	0.139	0.00050	0.21765	
TAN1	FC1@03	2.9995	0.0020	0.0074	0.0005	0.3431	5.58	0.074	5.585	0.074	0.0020165	0.000000284	5.649	0.141	0.00048	0.34308	
TAN1	FC1@04	2.9712	0.0020	0.0072	0.0004	0.0937	5.53	0.072	5.526	0.072	0.0020164	0.000000282	5.590	0.140	0.00041	0.09374	
TAN1	FC1@05	2.9436	0.0020	0.0090	0.0004	0.0948	5.60	0.090	5.596	0.090	0.0020165	0.000000302	5.660	0.150	0.00040	0.09475	
TAN1	FC1@06	2.8903	0.0020	0.0076	0.0003	0.1075	5.55	0.076	5.549	0.076	0.0020165	0.000000286	5.613	0.142	0.00039	0.10747	
TAN1	FC1@07	2.7916	0.0020	0.0080	0.0003	0.0542	5.52	0.080	5.521	0.080	0.0020164	0.000000290	5.585	0.144	0.00041	0.05422	
TAN1	FC1@08	2.7494	0.0020	0.0085	0.0006	0.3225	5.64	0.085	5.638	0.085	0.0020166	0.000000296	5.702	0.147	0.00065	0.32252	
TAN1	FC1@09	2.7212	0.0020	0.0088	0.0004	0.4008	5.70	0.088	5.704	0.088	0.0020168	0.000000300	5.768	0.149	0.00055	0.40082	
TAN1	FC1@10	2.6714	0.0020	0.0076	0.0004	0.0959	5.26	0.076	5.261	0.076	0.0020159	0.000000286	5.326	0.142	0.00050	0.09591	
TAN1	FC1@11	2.6706	0.0020	0.0102	0.0002	0.2024	5.58	0.102	5.579	0.102	0.0020165	0.000000318	5.644	0.157	0.00038	0.20237	
TAN1	FC1@12	2.6671	0.0020	0.0070	0.0003	0.1830	5.42	0.070	5.420	0.070	0.0020162	0.000000280	5.485	0.139	0.00039	0.18302	
TAN1	FC1@13	2.6707	0.0020	0.0116	0.0002	0.2190	5.59	0.116	5.591	0.116	0.0020165	0.000000337	5.655	0.167	0.00038	0.21896	
TAN1	FC1@14	2.6735	0.0020	0.0082	0.0004	0.9545	5.31	0.082	5.313	0.082	0.0020160	0.000000292	5.377	0.145	0.00052	0.95447	
TAN1	FC1@15	2.6699	0.0020	0.0083	0.0003	0.6573	4.91	0.083	4.910	0.083	0.0020152	0.000000294	4.974	0.146	0.00044	0.65725	
TAN2	FC1add@01	2.5569	0.0020	0.0057	0.0003	0.2533	5.74	0.057	5.742	0.057	0.0020167	0.000000448	5.718	0.222	0.00032	0.25330	
TAN2	FC1add@2	2.5544	0.0020	0.0068	0.0003	0.2423	5.46	0.068	5.462	0.068	0.0020161	0.000000455	5.439	0.226	0.00032	0.24231	
TAN2	FC1add@3	2.5557	0.0020	0.0058	0.0003	0.3781	5.48	0.058	5.485	0.058	0.0020162	0.000000449	5.461	0.223	0.00031	0.37813	
TAN2	FC1@05	2.5207	0.0020	0.0062	0.0004	0.1203	5.72	0.062	5.723	0.062	0.0020166	0.000000451	5.700	0.224	0.00038	0.12032	
TAN2	FC1@06	2.5027	0.0020	0.0078	0.0004	0.2427	5.70	0.078	5.700	0.078	0.0020166	0.000000461	5.677	0.229	0.00037	0.24268	
TAN2	FC1@07	2.4893	0.0020	0.0090	0.0004	0.2506	5.74	0.090	5.742	0.090	0.0020167	0.000000470	5.719	0.233	0.00037	0.25057	
TAN2	FC1@08	2.4811	0.0020	0.0074	0.0004	0.2548	5.94	0.074	5.941	0.074	0.0020171	0.000000459	5.918	0.227	0.00038	0.25482	
TAN2	FC1@09	2.4492	0.0020	0.0061	0.0003	0.2328	5.96	0.061	5.964	0.061	0.0020171	0.000000451	5.941	0.224	0.00028	0.23276	
TAN2	FC1@10	2.4161	0.0020	0.0074	0.0003	0.2535	5.90	0.074	5.896	0.074	0.0020170	0.000000459	5.873	0.227	0.00026	0.25348	
TAN2	FC1@11	2.3711	0.0020	0.0082	0.0003	0.1571	5.87	0.082	5.866	0.082	0.0020169	0.000000464	5.843	0.230	0.00033	0.15713	
TAN2	FC1@12	2.3536	0.0020	0.0099	0.0003	0.4593	6.04	0.099	6.042	0.099	0.0020173	0.000000477	6.018	0.237	0.00031	0.45933	
TAN2	FC1@13	2.3364	0.0020	0.0073	0.0003	0.5085	5.74	0.073	5.738	0.073	0.0020167	0.000000458	5.714	0.227	0.00025	0.50849	
TAN2	FC1@14	2.3291	0.0020	0.0089	0.0003	0.2119	5.70	0.089	5.699	0.089	0.0020166	0.000000469	5.675	0.233	0.00026	0.21186	
TAN2	FC1@15	2.3143	0.0020	0.0077	0.0004	0.2663	5.38	0.077	5.377	0.077	0.0020159	0.000000461	5.353	0.228	0.00035	0.26633	
TAN2	FC1@16	2.3145	0.0020	0.0092	0.0009	0.2944	5.10	0.092	5.095	0.092	0.0020154	0.000000471	5.072	0.234	0.00092	0.29443	
TAN2	FC1@17	2.3084	0.0020	0.0061	0.0006	0.2849	5.71	0.061	5.714	0.061	0.0020166	0.000000451	5.690	0.223	0.00062	0.28489	
TAN2	FC1@18	2.2890	0.0020	0.0096	0.0006	0.2848	5.73	0.096	5.733	0.096	0.0020166	0.000000475	5.710	0.235	0.00056	0.28479	
TAN2	FC1@19	2.2701	0.0020	0.0077	0.0006	0.1971	5.88	0.077	5.880	0.077	0.0020169	0.000000461	5.856	0.228	0.00056	0.19706	

Mount	*Analysis #*	*Ip (nA)*	*$^{18}O/^{16}O$*	*± rel (%)*	*$^{16}O^{1}H/^{16}O$*	*± rel (%)*	*Row delta ^{18}O*	*± per mil*	*Drift corrected $d^{18}O$*	*± per mil*	*$^{18}O/^{16}O$*	*1σ error*	*SIMS corrected $d^{18}O$*	*± per mil*	*Drift corrected OH/O*	*± rel (%)*	Pb/Pb age per spot
TAN2	FC1@20	2.2674	0.0020	0.0067	0.0004	0.2915	5.70	0.067	5.701	0.067	0.0020166	0.000000454	5.677	0.225	0.00037	0.29154	
TAN2	FC1@21	2.2636	0.0020	0.0076	0.0004	0.2365	5.83	0.076	5.829	0.076	0.0020168	0.000000460	5.806	0.228	0.00035	0.23650	
TAN2	FC1@22	2.2684	0.0020	0.0121	0.0003	0.2781	5.73	0.121	5.728	0.121	0.0020166	0.000000497	5.705	0.247	0.00034	0.27806	
SU06																	
TAN2	SU06@01	2.5039	0.0020	0.0081	0.0004	0.3040	5.90	0.081	5.900	0.081	0.0020170	0.000000463	5.877	0.230	0.00044	0.30399	
TAN2	*SU06@2*	*2.5033*	*0.0020*	*0.0070*	*0.0067*	*0.1732*	*3.46*	*0.070*	*3.463*	*0.070*	*0.0020121*	*0.000000455*	*3.440*	*0.226*	*0.00672*	*0.17320*	
TAN2	SU06@03	2.4998	0.0020	0.0056	0.0021	1.0354	6.15	0.056	6.155	0.056	0.0020175	0.000000448	6.132	0.222	0.00211	1.03536	
TAN2	*SU06@4*	*2.4997*	*0.0020*	*0.0115*	*0.0042*	*0.2129*	*-0.26*	*0.115*	*-0.260*	*0.115*	*0.0020046*	*0.000000489*	*-0.283*	*0.244*	*0.00416*	*0.21287*	
TAN2	SU06@5	2.5032	0.0020	0.0055	0.0003	0.1247	6.10	0.055	6.096	0.055	0.0020174	0.000000448	6.072	0.222	0.00032	0.12471	
TAN2	*SU06@6*	*2.4983*	*0.0020*	*0.0097*	*0.0083*	*0.1534*	*-1.94*	*0.097*	*-1.941*	*0.097*	*0.0020013*	*0.000000472*	*-1.965*	*0.236*	*0.00827*	*0.15343*	
TAN2	*SU06@7*	*2.4991*	*0.0020*	*0.0082*	*0.0025*	*1.1008*	*3.80*	*0.082*	*3.800*	*0.082*	*0.0020128*	*0.000000463*	*3.777*	*0.230*	*0.00254*	*1.10079*	
TAN2	*SU06@8*	*2.4938*	*0.0020*	*0.0067*	*0.0096*	*0.0607*	*1.41*	*0.067*	*1.413*	*0.067*	*0.0020080*	*0.000000452*	*1.390*	*0.225*	*0.00955*	*0.06067*	
TAN2	*SU06@09*	*2.4894*	*0.0020*	*0.0109*	*0.0076*	*0.2187*	*0.24*	*0.109*	*0.242*	*0.109*	*0.0020056*	*0.000000483*	*0.219*	*0.241*	*0.00756*	*0.21869*	
TAN2	*SU06@10*	*2.4937*	*0.0020*	*0.0095*	*0.0048*	*0.2704*	*1.68*	*0.095*	*1.679*	*0.095*	*0.0020085*	*0.000000472*	*1.655*	*0.235*	*0.00479*	*0.27039*	
TAN2	*SU06@11*	*2.4929*	*0.0020*	*0.0148*	*0.0080*	*0.2366*	*4.47*	*0.148*	*4.468*	*0.148*	*0.0020141*	*0.000000525*	*4.445*	*0.261*	*0.00801*	*0.23664*	
TAN2	*SU06@12*	*2.4920*	*0.0020*	*0.0100*	*0.0174*	*0.9001*	*4.13*	*0.100*	*4.134*	*0.100*	*0.0020134*	*0.000000477*	*4.110*	*0.237*	*0.01735*	*0.90009*	
TAN2	SU06@13	2.4887	0.0020	0.0082	0.0005	0.5542	5.36	0.082	5.358	0.082	0.0020159	0.000000464	5.334	0.230	0.00052	0.55418	2788
TAN2	SU06@14	2.4917	0.0020	0.0073	0.0004	0.3206	5.45	0.073	5.448	0.073	0.0020161	0.000000458	5.425	0.227	0.00038	0.32062	2682
TAN2	SU06@15	2.4834	0.0020	0.0078	0.0016	0.4136	6.05	0.078	6.046	0.078	0.0020173	0.000000462	6.022	0.229	0.00161	0.41364	2711
TAN2	SU06@16	2.4826	0.0020	0.0067	0.0003	0.3324	5.64	0.067	5.640	0.067	0.0020165	0.000000454	5.617	0.225	0.00030	0.33236	2804
TAN2	SU06@17	2.4819	0.0020	0.0103	0.0008	1.0246	5.41	0.103	5.407	0.103	0.0020160	0.000000480	5.384	0.238	0.00077	1.02461	2676
TAN2	*SU06@18*	*2.4835*	*0.0020*	*0.0100*	*0.0008*	*0.8028*	*5.01*	*0.100*	*5.007*	*0.100*	*0.0020152*	*0.000000478*	*4.984*	*0.237*	*0.00080*	*0.80276*	*2739.9*
TAN2	SU06@19	2.4824	0.0020	0.0109	0.0004	0.1138	5.99	0.109	5.992	0.109	0.0020172	0.000000486	5.969	0.241	0.00038	0.11384	2669
TAN2	SU06@20	2.4835	0.0020	0.0076	0.0004	0.1465	5.75	0.076	5.752	0.076	0.0020167	0.000000460	5.729	0.228	0.00044	0.14651	2702
TAN2	SU06@21	2.4801	0.0020	0.0067	0.0006	0.5951	5.47	0.067	5.473	0.067	0.0020161	0.000000454	5.449	0.225	0.00055	0.59513	2711
TAN2	SU06@22	2.4802	0.0020	0.0055	0.0004	0.3164	5.97	0.055	5.970	0.055	0.0020171	0.000000447	5.947	0.222	0.00044	0.31636	2677
TAN2	SU06@23	2.4787	0.0020	0.0076	0.0007	1.0511	5.65	0.076	5.654	0.076	0.0020165	0.000000460	5.631	0.228	0.00068	1.05113	2678
TAN2	SU06@24	2.4786	0.0020	0.0115	0.0003	0.3584	5.79	0.115	5.785	0.115	0.0020168	0.000000492	5.762	0.244	0.00029	0.35838	
TAN2	SU06@25	2.4742	0.0020	0.0077	0.0020	0.1950	6.05	0.077	6.053	0.077	0.0020173	0.000000461	6.029	0.228	0.00196	0.19504	
TAN2	*SU06@26*	*2.4722*	*0.0020*	*0.0087*	*0.0083*	*0.1677*	*0.23*	*0.087*	*0.229*	*0.087*	*0.0020056*	*0.000000465*	*0.206*	*0.232*	*0.00831*	*0.16769*	
TAN2	*SU06@27*	*2.4681*	*0.0020*	*0.0147*	*0.0027*	*0.9004*	*5.20*	*0.147*	*5.204*	*0.147*	*0.0020156*	*0.000000525*	*5.181*	*0.261*	*0.00274*	*0.90045*	
TAN2	*SU06@28*	*2.4675*	*0.0020*	*0.0120*	*0.0024*	*3.9270*	*4.15*	*0.120*	*4.149*	*0.120*	*0.0020135*	*0.000000496*	*4.125*	*0.246*	*0.00235*	*3.92698*	
TAN2	SU06@29	2.4643	0.0020	0.0060	0.0005	0.2339	6.23	0.060	6.227	0.060	0.0020176	0.000000450	6.203	0.223	0.00049	0.23387	
TAN2	*SU06@30*	*2.4629*	*0.0020*	*0.0080*	*0.0032*	*0.1638*	*4.17*	*0.080*	*4.174*	*0.080*	*0.0020135*	*0.000000462*	*4.150*	*0.230*	*0.00320*	*0.16382*	
TAN2	*SU06@31*	*2.4608*	*0.0020*	*0.0099*	*0.0029*	*1.5322*	*2.48*	*0.099*	*2.484*	*0.099*	*0.0020101*	*0.000000476*	*2.460*	*0.237*	*0.00288*	*1.53220*	
TAN2	SU06@32	2.4601	0.0020	0.0067	0.0003	0.0675	6.03	0.067	6.025	0.067	0.0020172	0.000000454	6.002	0.225	0.00034	0.06754	2665
TAN2	SU06@33	2.4439	0.0020	0.0102	0.0004	0.2019	5.60	0.102	5.598	0.102	0.0020164	0.000000480	5.575	0.238	0.00040	0.20189	2697
TAN2	SU06@34	2.4413	0.0020	0.0064	0.0003	0.2889	5.63	0.064	5.635	0.064	0.0020165	0.000000452	5.612	0.224	0.00030	0.28894	2734

Mount	Analysis #	Ip (nA)	$^{18}O/^{16}O$	± rel (%)	$^{16}O^{1}H/^{16}O$	± rel (%)	Row delta ^{18}O	± per mil	Drift corrected $d^{18}O$	± per mil	$^{18}O/^{16}O$	1σ error	SIMS corrected $d^{18}O$	± per mil	Drift corrected OH/O	± rel (%)	Pb/Pb age per spot
TAN2	*SU06@35*	*2.4415*	*0.0020*	*0.0056*	*0.0065*	*0.2620*	*1.46*	*0.056*	*1.461*	*0.056*	*0.0020081*	*0.000000446*	*1.438*	*0.222*	*0.00648*	*0.26199*	*2687*
TAN2	SU06@36	2.4403	0.0020	0.0089	0.0018	0.6247	5.33	0.089	5.331	0.089	0.0020158	0.000000469	5.308	0.233	0.00177	0.62472	2687
TAN2	*SU06@37*	*2.4365*	*0.0020*	*0.0094*	*0.0050*	*0.2061*	*0.12*	*0.094*	*0.118*	*0.094*	*0.0020054*	*0.000000471*	*0.094*	*0.235*	*0.00500*	*0.20611*	
TAN2	*SU06@38*	*2.4375*	*0.0020*	*0.0101*	*0.0069*	*0.2745*	*-2.05*	*0.101*	*-2.046*	*0.101*	*0.0020011*	*0.000000475*	*-2.069*	*0.237*	*0.00689*	*0.27452*	
TAN2	SU06@39	2.4198	0.0020	0.0064	0.0008	0.1846	5.29	0.064	5.289	0.064	0.0020158	0.000000452	5.266	0.224	0.00077	0.18457	2698
TAN2	*SU06@40*	*2.4212*	*0.0020*	*0.0073*	*0.0062*	*0.2296*	*3.33*	*0.073*	*3.334*	*0.073*	*0.0020118*	*0.000000457*	*3.311*	*0.227*	*0.00624*	*0.22956*	
SU25																	
TAN3	*SU25@01*	*2.6261*	*0.0020*	*0.0089*	*0.0072*	*0.4469*	*0.60*	*0.089*	*0.604*	*0.089*	*0.0020064*	*0.000000467*	*0.581*	*0.233*	*0.00724*	*0.44686*	
TAN8	SU25@6	2.6294	0.0020	0.0104	0.0013	0.3051	6.09	0.104	6.092	0.104	0.0020174	0.000000482	6.068	0.239	0.00127	0.30508	
TAN9	SU25@07	2.6355	0.0020	0.0081	0.0006	0.2009	6.00	0.081	5.999	0.081	0.0020172	0.000000463	5.976	0.230	0.00055	0.20093	
TAN10	SU25@8	2.6363	0.0020	0.0058	0.0007	0.2052	5.89	0.058	5.889	0.058	0.0020170	0.000000449	5.865	0.223	0.00066	0.20516	2618
TAN11	*SU25@9*	*2.6371*	*0.0020*	*0.0054*	*0.0020*	*2.6313*	*5.28*	*0.054*	*5.276*	*0.054*	*0.0020157*	*0.000000447*	*5.252*	*0.222*	*0.00196*	*2.63128*	
TAN12	SU25@10	2.6343	0.0020	0.0099	0.0003	0.0892	5.95	0.099	5.953	0.099	0.0020171	0.000000478	5.929	0.237	0.00032	0.08925	2645
TAN13	*SU25@11*	*2.6328*	*0.0020*	*0.0093*	*0.0019*	*1.3371*	*5.67*	*0.093*	*5.671*	*0.093*	*0.0020165*	*0.000000473*	*5.648*	*0.234*	*0.00192*	*1.33715*	
TAN14	SU25@12	2.6340	0.0020	0.0079	0.0010	1.0174	6.23	0.079	6.234	0.079	0.0020177	0.000000462	6.210	0.229	0.00103	1.01744	2630
TAN2	SU25@13	2.5534	0.0020	0.0068	0.0024	0.0830	6.18	0.068	6.178	0.068	0.0020175	0.000000455	6.155	0.226	0.00240	0.08296	
TAN2	SU25@14	2.5514	0.0020	0.0054	0.0004	0.2281	6.32	0.054	6.324	0.054	0.0020178	0.000000447	6.301	0.222	0.00042	0.22807	
TAN2	*SU25@15*	*2.5511*	*0.0020*	*0.0067*	*0.0067*	*0.9638*	*8.58*	*0.067*	*8.585*	*0.067*	*0.0020224*	*0.000000456*	*8.561*	*0.225*	*0.00667*	*0.96379*	
TAN2	*SU25@16*	*2.5449*	*0.0020*	*0.0079*	*0.0008*	*0.5400*	*5.12*	*0.079*	*5.119*	*0.079*	*0.0020154*	*0.000000461*	*5.096*	*0.229*	*0.00082*	*0.54003*	
TAN2	*SU25@17*	*2.5478*	*0.0020*	*0.0065*	*0.0020*	*0.0889*	*5.62*	*0.065*	*5.618*	*0.065*	*0.0020164*	*0.000000453*	*5.595*	*0.225*	*0.00198*	*0.08888*	
TAN2	*SU25@18*	*2.5477*	*0.0020*	*0.0064*	*0.0022*	*1.3309*	*5.19*	*0.064*	*5.191*	*0.064*	*0.0020156*	*0.000000452*	*5.168*	*0.224*	*0.00223*	*1.33088*	
TAN2	*SU25@19*	*2.5337*	*0.0020*	*0.0084*	*0.0046*	*0.2103*	*4.98*	*0.084*	*4.983*	*0.084*	*0.0020151*	*0.000000465*	*4.959*	*0.231*	*0.00462*	*0.21029*	
TAN2	SU25@20	2.5288	0.0020	0.0079	0.0006	0.5150	5.72	0.079	5.724	0.079	0.0020166	0.000000462	5.701	0.229	0.00065	0.51501	2653
TAN2	SU25@21	2.5284	0.0020	0.0091	0.0003	0.2567	6.51	0.091	6.511	0.091	0.0020182	0.000000471	6.487	0.233	0.00029	0.25674	2643
TAN2	*SU25@22*	*2.5319*	*0.0020*	*0.0086*	*0.0020*	*1.2008*	*6.87*	*0.086*	*6.868*	*0.086*	*0.0020189*	*0.000000468*	*6.844*	*0.232*	*0.00196*	*1.20079*	
TAN2	SU25@23	2.5303	0.0020	0.0057	0.0031	9.5515	6.34	0.057	6.338	0.057	0.0020179	0.000000449	6.314	0.223	0.00308	9.55151	
TAN2	SU25@24	2.5424	0.0020	0.0089	0.0003	0.1489	5.89	0.089	5.888	0.089	0.0020170	0.000000469	5.864	0.233	0.00034	0.14887	
TAN2	*SU25@25*	*2.5183*	*0.0020*	*0.0084*	*0.0045*	*0.3052*	*4.85*	*0.084*	*4.846*	*0.084*	*0.0020149*	*0.000000465*	*4.823*	*0.231*	*0.00454*	*0.30518*	
TAN2	*SU25@26*	*2.5176*	*0.0020*	*0.0063*	*0.0052*	*0.3544*	*4.65*	*0.063*	*4.650*	*0.063*	*0.0020145*	*0.000000451*	*4.627*	*0.224*	*0.00521*	*0.35441*	
TAN2	SU25@27	2.5181	0.0020	0.0060	0.0007	0.6672	5.97	0.060	5.969	0.060	0.0020171	0.000000450	5.946	0.223	0.00071	0.66716	
TAN2	*SU25@28*	*2.5193*	*0.0020*	*0.0074*	*0.0024*	*0.0612*	*5.26*	*0.074*	*5.261*	*0.074*	*0.0020157*	*0.000000458*	*5.237*	*0.227*	*0.00241*	*0.06116*	
TAN2	SU25@29	2.5186	0.0020	0.0061	0.0014	0.7139	6.39	0.061	6.388	0.061	0.0020180	0.000000451	6.365	0.224	0.00139	0.71388	
TAN2	SU25@30	2.5211	0.0020	0.0084	0.0010	0.7427	6.39	0.084	6.391	0.084	0.0020180	0.000000466	6.368	0.231	0.00103	0.74272	2644
TAN2	*SU25@31*	*2.5158*	*0.0020*	*0.0076*	*0.0021*	*1.0048*	*7.24*	*0.076*	*7.240*	*0.076*	*0.0020197*	*0.000000460*	*7.217*	*0.228*	*0.00206*	*1.00482*	*2658.7*
TAN2	*SU25@32*	*2.5200*	*0.0020*	*0.0086*	*0.0018*	*0.0795*	*5.02*	*0.086*	*5.016*	*0.086*	*0.0020152*	*0.000000467*	*4.993*	*0.231*	*0.00176*	*0.07950*	
TAN2	SU25@33	2.5130	0.0020	0.0063	0.0005	0.2603	6.24	0.063	6.235	0.063	0.0020177	0.000000452	6.212	0.224	0.00047	0.26033	2659
TAN2	*SU25@34*	*2.5117*	*0.0020*	*0.0056*	*0.0020*	*0.2594*	*5.66*	*0.056*	*5.657*	*0.056*	*0.0020165*	*0.000000448*	*5.633*	*0.222*	*0.00199*	*0.25936*	
TAN2	SU25@35	2.5134	0.0020	0.0082	0.0003	0.1324	6.62	0.082	6.616	0.082	0.0020184	0.000000464	6.593	0.230	0.00032	0.13237	

Mount	Analysis #	Ip (nA)	$^{18}O/^{16}O$	± rel (%)	$^{16}O^{1}H/^{16}O$	± rel (%)	Row delta ^{18}O	± per mil	Drift corrected $d^{18}O$	± per mil	$^{18}O/^{16}O$	1σ error	SIMS corrected $d^{18}O$	± per mil	Drift corrected OH/O	± rel (%)	Pb/Pb age per spot
TAN2	*SU25@36*	*2.5110*	*0.0020*	*0.0087*	*0.0112*	*0.3679*	*4.85*	*0.087*	*4.853*	*0.087*	*0.0020149*	*0.000000467*	*4.830*	*0.232*	*0.01121*	*0.36792*	
TAN2	*SU25@37*	*2.5016*	*0.0020*	*0.0086*	*0.0032*	*0.6594*	*7.49*	*0.086*	*7.494*	*0.086*	*0.0020202*	*0.000000468*	*7.471*	*0.232*	*0.00322*	*0.65938*	
TAN2	SU25@38	2.5021	0.0020	0.0082	0.0009	0.8602	6.46	0.082	6.460	0.082	0.0020181	0.000000465	6.436	0.230	0.00092	0.86024	
TAN2	SU25@39	2.5028	0.0020	0.0103	0.0007	0.2063	6.57	0.103	6.571	0.103	0.0020183	0.000000481	6.548	0.238	0.00066	0.20632	
TAN2	SU25@40	2.5003	0.0020	0.0094	0.0004	0.1950	5.98	0.094	5.978	0.094	0.0020171	0.000000473	5.955	0.235	0.00037	0.19500	
SU10B																	
TAN2	SU10B@01	2.4197	0.0020	0.0064	0.0010	0.4274	5.72	0.064	5.720	0.064	0.0020166	0.000000452	5.696	0.224	0.00100	0.42738	2658
TAN2	SU10B@2	2.4170	0.0020	0.0072	0.0008	0.1217	5.96	0.072	5.960	0.072	0.0020171	0.000000457	5.936	0.227	0.00081	0.12167	
TAN2	SU10B@3	2.4097	0.0020	0.0075	0.0003	0.2935	6.05	0.075	6.052	0.075	0.0020173	0.000000459	6.028	0.228	0.00035	0.29355	
TAN2	SU10B@4	2.4091	0.0020	0.0103	0.0012	0.6463	5.43	0.103	5.425	0.103	0.0020160	0.000000481	5.402	0.238	0.00117	0.64631	
TAN2	*SU10B@05*	*2.4095*	*0.0020*	*0.0093*	*0.0024*	*0.7695*	*5.43*	*0.093*	*5.425*	*0.093*	*0.0020160*	*0.000000472*	*5.402*	*0.234*	*0.00238*	*0.76952*	
TAN2	*SU10B@6*	*2.4079*	*0.0020*	*0.0091*	*0.0035*	*0.2254*	*4.49*	*0.091*	*4.486*	*0.091*	*0.0020141*	*0.000000470*	*4.463*	*0.233*	*0.00352*	*0.22541*	
TAN2	*SU10B@7*	*2.4102*	*0.0020*	*0.0117*	*0.0057*	*0.4211*	*6.53*	*0.117*	*6.534*	*0.117*	*0.0020183*	*0.000000494*	*6.510*	*0.245*	*0.00566*	*0.42115*	
TAN2	*SU10B@8*	*2.4082*	*0.0020*	*0.0073*	*0.0042*	*0.1529*	*1.40*	*0.073*	*1.404*	*0.073*	*0.0020080*	*0.000000456*	*1.381*	*0.227*	*0.00415*	*0.15288*	
TAN2	*SU10B@9*	*2.4043*	*0.0020*	*0.0078*	*0.0053*	*0.3040*	*2.98*	*0.078*	*2.982*	*0.078*	*0.0020111*	*0.000000460*	*2.958*	*0.229*	*0.00527*	*0.30399*	
TAN2	SU10B@10	2.4034	0.0020	0.0079	0.0004	0.3447	5.76	0.079	5.764	0.079	0.0020167	0.000000462	5.741	0.229	0.00040	0.34474	
TAN2	SU10B@11	2.3865	0.0020	0.0097	0.0005	0.3622	6.19	0.097	6.193	0.097	0.0020176	0.000000476	6.170	0.236	0.00050	0.36216	2671
TAN2	SU10B@12	2.3803	0.0020	0.0069	0.0005	0.2997	6.03	0.069	6.025	0.069	0.0020172	0.000000456	6.002	0.226	0.00048	0.29967	2660
TAN2	SU10B@13	2.3788	0.0020	0.0075	0.0007	0.9229	5.85	0.075	5.847	0.075	0.0020169	0.000000459	5.824	0.228	0.00071	0.92286	
TAN2	*SU10B@14*	*2.3776*	*0.0020*	*0.0074*	*0.0024*	*1.1135*	*6.79*	*0.074*	*6.789*	*0.074*	*0.0020188*	*0.000000459*	*6.765*	*0.227*	*0.00241*	*1.11349*	
TAN2	*SU10B@15*	*2.3791*	*0.0020*	*0.0087*	*0.0032*	*0.9206*	*4.13*	*0.087*	*4.129*	*0.087*	*0.0020134*	*0.000000467*	*4.106*	*0.232*	*0.00323*	*0.92058*	
TAN2	SU10B@16	2.3773	0.0020	0.0101	0.0005	0.6225	5.97	0.101	5.970	0.101	0.0020171	0.000000479	5.947	0.237	0.00054	0.62247	2646
TAN2	*SU10B@17*	*2.3709*	*0.0020*	*0.0089*	*0.0011*	*2.5699*	*6.87*	*0.089*	*6.867*	*0.089*	*0.0020189*	*0.000000469*	*6.843*	*0.233*	*0.00107*	*2.56992*	
TAN2	SU10B@18	2.3701	0.0020	0.0070	0.0009	0.1248	6.12	0.070	6.116	0.070	0.0020174	0.000000456	6.093	0.226	0.00085	0.12483	
TAN2	SU10B@19	2.3695	0.0020	0.0056	0.0005	0.0916	5.78	0.056	5.784	0.056	0.0020168	0.000000448	5.761	0.222	0.00048	0.09159	2671
TAN2	SU10B@20	2.3686	0.0020	0.0108	0.0005	0.5091	5.90	0.108	5.897	0.108	0.0020170	0.000000485	5.873	0.241	0.00048	0.50914	2653
TAN2	SU10B@21	2.3651	0.0020	0.0085	0.0008	0.7492	5.47	0.085	5.473	0.085	0.0020161	0.000000466	5.450	0.231	0.00085	0.74921	2649
TAN2	SU10B@22	2.3648	0.0020	0.0065	0.0004	0.2724	5.90	0.065	5.900	0.065	0.0020170	0.000000453	5.877	0.225	0.00037	0.27237	
TAN2	SU10B@23	2.3611	0.0020	0.0090	0.0006	0.1627	6.13	0.090	6.133	0.090	0.0020175	0.000000471	6.109	0.233	0.00057	0.16274	
TAN2	SU10B@24	2.3578	0.0020	0.0091	0.0004	0.2228	6.00	0.091	6.001	0.091	0.0020172	0.000000471	5.978	0.233	0.00042	0.22275	2666
TAN2	SU10B@25	2.3585	0.0020	0.0074	0.0004	0.0775	6.01	0.074	6.006	0.074	0.0020172	0.000000459	5.983	0.227	0.00039	0.07750	2651
TAN2	SU10B@26	2.3576	0.0020	0.0084	0.0004	0.1725	5.93	0.084	5.930	0.084	0.0020170	0.000000466	5.906	0.231	0.00041	0.17250	
TAN2	SU10B@27	2.3591	0.0020	0.0078	0.0007	0.3826	5.96	0.078	5.960	0.078	0.0020171	0.000000461	5.936	0.229	0.00071	0.38260	
TAN2	SU10B@28	2.3563	0.0020	0.0068	0.0008	0.1964	6.28	0.068	6.284	0.068	0.0020178	0.000000455	6.261	0.225	0.00084	0.19645	
TAN2	*SU10B@29*	*2.3531*	*0.0020*	*0.0075*	*0.0036*	*0.1891*	*2.48*	*0.075*	*2.482*	*0.075*	*0.0020101*	*0.000000458*	*2.459*	*0.228*	*0.00361*	*0.18914*	
TAN2	*SU10B@30*	*2.3502*	*0.0020*	*0.0097*	*0.0035*	*0.6551*	*5.19*	*0.097*	*5.190*	*0.097*	*0.0020156*	*0.000000476*	*5.167*	*0.236*	*0.00346*	*0.65509*	
TAN2	SU10B@31	2.3479	0.0020	0.0074	0.0013	0.5812	6.20	0.074	6.202	0.074	0.0020176	0.000000459	6.179	0.227	0.00135	0.58122	
TAN2	*SU10B@32*	*2.3479*	*0.0020*	*0.0098*	*0.0010*	*0.5562*	*5.16*	*0.098*	*5.165*	*0.098*	*0.0020155*	*0.000000476*	*5.141*	*0.236*	*0.00100*	*0.55618*	

Mount	Analysis #	Ip (nA)	$^{18}O/^{16}O$	± rel (%)	$^{16}O^{1}H/^{16}O$	± rel (%)	Row delta ^{18}O	± per mil	Drift corrected $d^{18}O$	± per mil	$^{18}O/^{16}O$	1σ error	SIMS corrected $d^{18}O$	± per mil	Drift corrected OH/O	± rel (%)	Pb/Pb age per spot
TAN2	*SU10B@33*	*2.3475*	*0.0020*	*0.0119*	*0.0074*	*0.7788*	*12.05*	*0.119*	*12.047*	*0.119*	*0.0020293*	*0.000000499*	*12.023*	*0.246*	*0.00744*	*0.77878*	
TAN2	*SU10B@34*	*2.3458*	*0.0020*	*0.0067*	*0.0026*	*0.9843*	*4.60*	*0.067*	*4.605*	*0.067*	*0.0020144*	*0.000000454*	*4.581*	*0.225*	*0.00262*	*0.98426*	
TAN2	SU10B@35	2.3445	0.0020	0.0086	0.0011	1.4515	5.73	0.086	5.734	0.086	0.0020167	0.000000467	5.710	0.232	0.00113	1.45155	
TAN2	SU10B@36	2.3438	0.0020	0.0096	0.0005	0.3975	6.09	0.096	6.087	0.096	0.0020174	0.000000475	6.063	0.236	0.00046	0.39746	
TAN2	*SU10B@37*	*2.3426*	*0.0020*	*0.0057*	*0.0050*	*0.2964*	*3.41*	*0.057*	*3.409*	*0.057*	*0.0020120*	*0.000000447*	*3.386*	*0.222*	*0.00498*	*0.29640*	
TAN2	SU10B@38	2.3416	0.0020	0.0074	0.0014	0.3725	5.85	0.074	5.846	0.074	0.0020169	0.000000458	5.823	0.227	0.00139	0.37245	
TAN2	SU10B@39	2.3410	0.0020	0.0057	0.0017	2.2305	6.26	0.057	6.261	0.057	0.0020177	0.000000449	6.237	0.222	0.00168	2.23052	
TAN2	*SU10B@40*	*2.3420*	*0.0020*	*0.0087*	*0.0079*	*4.0965*	*8.10*	*0.087*	*8.100*	*0.087*	*0.0020214*	*0.000000469*	*8.077*	*0.232*	*0.00794*	*4.09647*	
SU15																	
TAN2	SU15@01	2.3382	0.0020	0.0074	0.0004	0.1246	6.74	0.074	6.742	0.074	0.0020187	0.000000459	6.719	0.227	0.00037	0.12460	2675
TAN2	SU15@2	2.3385	0.0020	0.0078	0.0004	0.5819	6.51	0.078	6.507	0.078	0.0020182	0.000000462	6.484	0.229	0.00044	0.58193	
TAN2	SU15@3	2.3359	0.0020	0.0056	0.0004	0.2349	6.59	0.056	6.589	0.056	0.0020184	0.000000448	6.566	0.222	0.00041	0.23490	2693
TAN2	SU15@4	2.3344	0.0020	0.0056	0.0006	0.4044	6.66	0.056	6.662	0.056	0.0020185	0.000000449	6.639	0.222	0.00061	0.40444	2664
TAN2	*SU15@5*	*2.3339*	*0.0020*	*0.0076*	*0.0063*	*0.3850*	*6.61*	*0.076*	*6.614*	*0.076*	*0.0020184*	*0.000000460*	*6.590*	*0.228*	*0.00629*	*0.38500*	
TAN2	SU15@6	2.3346	0.0020	0.0067	0.0003	0.2343	6.71	0.067	6.709	0.067	0.0020186	0.000000455	6.686	0.225	0.00028	0.23428	2681
TAN2	SU15@07	2.3327	0.0020	0.0078	0.0004	0.1461	6.52	0.078	6.523	0.078	0.0020182	0.000000462	6.500	0.229	0.00037	0.14608	2688
TAN2	SU15@8	2.3307	0.0020	0.0088	0.0007	0.2888	7.36	0.088	7.363	0.088	0.0020199	0.000000470	7.339	0.232	0.00069	0.28882	
TAN2	*SU15@9*	*2.3303*	*0.0020*	*0.0056*	*0.0053*	*0.1142*	*6.40*	*0.056*	*6.397*	*0.056*	*0.0020180*	*0.000000448*	*6.374*	*0.222*	*0.00535*	*0.11418*	
TAN2	*SU15@10*	*2.3306*	*0.0020*	*0.0111*	*0.0039*	*0.6101*	*5.99*	*0.111*	*5.986*	*0.111*	*0.0020172*	*0.000000488*	*5.963*	*0.242*	*0.00387*	*0.61011*	
TAN2	SU15@11	2.3333	0.0020	0.0086	0.0003	0.3932	7.12	0.086	7.121	0.086	0.0020194	0.000000467	7.098	0.231	0.00029	0.39318	2677
TAN2	SU15@12	2.3328	0.0020	0.0097	0.0003	0.4235	7.02	0.097	7.023	0.097	0.0020192	0.000000476	6.999	0.236	0.00030	0.42348	2687
TAN2	SU15@13	2.3295	0.0020	0.0055	0.0003	0.1641	7.00	0.055	6.996	0.055	0.0020192	0.000000448	6.972	0.222	0.00028	0.16411	2664
TAN2	SU15@14	2.3247	0.0020	0.0072	0.0004	0.4024	7.21	0.072	7.215	0.072	0.0020196	0.000000458	7.191	0.227	0.00036	0.40243	
TAN2	SU15@15	2.3225	0.0020	0.0108	0.0003	0.3388	6.38	0.108	6.377	0.108	0.0020179	0.000000485	6.354	0.241	0.00031	0.33877	
TAN2	SU15@16	2.3223	0.0020	0.0081	0.0003	0.4982	6.85	0.081	6.849	0.081	0.0020189	0.000000464	6.825	0.230	0.00028	0.49819	2679
TAN2	SU15@17	2.3198	0.0020	0.0096	0.0003	0.1561	6.90	0.096	6.904	0.096	0.0020190	0.000000476	6.880	0.236	0.00029	0.15608	2667
TAN2	SU15@18	2.3185	0.0020	0.0086	0.0003	0.2148	6.57	0.086	6.569	0.086	0.0020183	0.000000468	6.546	0.232	0.00030	0.21482	2690
TAN2	SU15@19	2.3158	0.0020	0.0067	0.0003	0.4488	6.67	0.067	6.670	0.067	0.0020185	0.000000455	6.646	0.225	0.00032	0.44877	2666
TAN2	*SU15@20*	*2.3193*	*0.0020*	*0.0070*	*0.0005*	*0.1238*	*5.96*	*0.070*	*5.962*	*0.070*	*0.0020171*	*0.000000456*	*5.938*	*0.226*	*0.00055*	*0.12383*	*2668.2*
TAN2	SU15@21	2.3184	0.0020	0.0056	0.0004	0.3370	6.55	0.056	6.552	0.056	0.0020183	0.000000449	6.529	0.222	0.00037	0.33698	2683
TAN2	SU15@22	2.3181	0.0020	0.0077	0.0004	0.1536	6.48	0.077	6.483	0.077	0.0020182	0.000000461	6.459	0.228	0.00036	0.15356	2679
TAN2	SU15@23	2.3151	0.0020	0.0082	0.0013	0.9675	6.10	0.082	6.099	0.082	0.0020174	0.000000464	6.076	0.230	0.00133	0.96754	2702
TAN2	SU15@24	2.3153	0.0020	0.0073	0.0004	0.1702	6.21	0.073	6.209	0.073	0.0020176	0.000000458	6.186	0.227	0.00035	0.17015	
TAN2	SU15@25	2.3110	0.0020	0.0081	0.0024	0.3865	7.23	0.081	7.225	0.081	0.0020196	0.000000464	7.202	0.230	0.00244	0.38652	2672
TAN2	*SU15@26*	*2.3091*	*0.0020*	*0.0065*	*0.0094*	*0.3691*	*6.18*	*0.065*	*6.175*	*0.065*	*0.0020175*	*0.000000453*	*6.152*	*0.225*	*0.00944*	*0.36909*	
TAN2	SU15@27	2.3104	0.0020	0.0082	0.0004	0.5335	6.48	0.082	6.483	0.082	0.0020182	0.000000465	6.460	0.230	0.00036	0.53354	2685
TAN2	SU15@28	2.3100	0.0020	0.0065	0.0007	1.3120	6.47	0.065	6.475	0.065	0.0020181	0.000000453	6.451	0.225	0.00065	1.31204	
TAN2	*SU15@29*	*2.3151*	*0.0020*	*0.0082*	*0.0045*	*0.1298*	*4.08*	*0.082*	*4.077*	*0.082*	*0.0020133*	*0.000000463*	*4.054*	*0.230*	*0.00447*	*0.12980*	

Mount	Analysis #	Ip (nA)	$^{18}O/^{16}O$	± rel (%)	$^{16}O^{1}H/^{16}O$	± rel (%)	Row delta ^{18}O	± per mil	Drift corrected $d^{18}O$	± per mil	$^{18}O/^{16}O$	1σ error	SIMS corrected $d^{18}O$	± per mil	Drift corrected OH/O	± rel (%)	Pb/Pb age per spot
TAN2	SU15@30	2.3220	0.0020	0.0060	0.0021	2.2892	6.05	0.060	6.050	0.060	0.0020173	0.000000451	6.027	0.223	0.00212	2.28917	2654
TAN2	*SU15@31*	*2.3310*	*0.0020*	*0.0079*	*0.0316*	*0.5328*	*3.58*	*0.079*	*3.578*	*0.079*	*0.0020123*	*0.000000461*	*3.554*	*0.229*	*0.03155*	*0.53276*	
TAN2	*SU15@32*	*2.3298*	*0.0020*	*0.0100*	*0.0027*	*1.3110*	*5.72*	*0.100*	*5.721*	*0.100*	*0.0020166*	*0.000000479*	*5.698*	*0.237*	*0.00266*	*1.31105*	
TAN2	SU15@33	2.3258	0.0020	0.0063	0.0020	0.4743	6.34	0.063	6.336	0.063	0.0020179	0.000000452	6.313	0.224	0.00203	0.47430	2681
TAN2	SU15@34	2.3226	0.0020	0.0064	0.0014	0.1937	6.58	0.064	6.584	0.064	0.0020184	0.000000453	6.561	0.224	0.00135	0.19370	2656
TAN2	SU15@35	2.3200	0.0020	0.0089	0.0011	0.1828	6.48	0.089	6.480	0.089	0.0020181	0.000000470	6.457	0.233	0.00111	0.18285	2679
TAN2	SU15@36	2.3161	0.0020	0.0088	0.0010	0.3386	7.15	0.088	7.145	0.088	0.0020195	0.000000469	7.122	0.232	0.00099	0.33864	2673
TAN2	SU15@37	2.3073	0.0020	0.0059	0.0013	0.2076	7.11	0.059	7.109	0.059	0.0020194	0.000000450	7.086	0.223	0.00129	0.20762	
TAN2	*SU15@38*	*2.3056*	*0.0020*	*0.0067*	*0.0073*	*0.4685*	*6.72*	*0.067*	*6.723*	*0.067*	*0.0020186*	*0.000000455*	*6.699*	*0.225*	*0.00726*	*0.46854*	
TAN2	*SU15@39*	*2.3043*	*0.0020*	*0.0067*	*0.0089*	*0.2414*	*5.65*	*0.067*	*5.653*	*0.067*	*0.0020165*	*0.000000454*	*5.629*	*0.225*	*0.00890*	*0.24136*	
TAN2	SU15@40	2.3053	0.0020	0.0086	0.0007	0.2248	6.78	0.086	6.778	0.086	0.0020187	0.000000467	6.755	0.231	0.00075	0.22475	2667
SU16																	
TAN2	SU16@01	2.3017	0.0020	0.0082	0.0009	0.2114	6.34	0.082	6.339	0.082	0.0020179	0.000000465	6.316	0.230	0.00086	0.21141	
TAN2	SU16@02	2.2998	0.0020	0.0131	0.0007	0.4362	6.92	0.131	6.924	0.131	0.0020190	0.000000509	6.901	0.252	0.00073	0.43618	
TAN2	SU16@03	2.3004	0.0020	0.0057	0.0007	0.2300	6.65	0.057	6.650	0.057	0.0020185	0.000000449	6.626	0.223	0.00065	0.23004	
TAN2	SU16@5	2.3047	0.0020	0.0065	0.0006	0.2337	6.60	0.065	6.604	0.065	0.0020184	0.000000454	6.581	0.225	0.00060	0.23367	2646
TAN2	SU16@6	2.3041	0.0020	0.0100	0.0007	0.3657	6.23	0.100	6.228	0.100	0.0020176	0.000000478	6.204	0.237	0.00071	0.36570	
TAN2	SU16@7	2.3081	0.0020	0.0060	0.0010	0.8950	6.31	0.060	6.305	0.060	0.0020178	0.000000450	6.282	0.223	0.00096	0.89504	2660
TAN2	SU16@8	2.3111	0.0020	0.0067	0.0009	0.6024	6.20	0.067	6.195	0.067	0.0020176	0.000000454	6.172	0.225	0.00090	0.60242	2656
TAN2	SU16@09	2.3063	0.0020	0.0063	0.0007	0.4418	6.30	0.063	6.302	0.063	0.0020178	0.000000452	6.279	0.224	0.00066	0.44178	2641
TAN2	SU16@10	2.3076	0.0020	0.0087	0.0010	0.3397	6.31	0.087	6.309	0.087	0.0020178	0.000000468	6.285	0.232	0.00097	0.33972	2633
TAN2	SU16@11	2.3048	0.0020	0.0098	0.0010	0.1071	6.46	0.098	6.465	0.098	0.0020181	0.000000477	6.441	0.236	0.00105	0.10708	2647
TAN2	SU16@12	2.3050	0.0020	0.0077	0.0012	0.2712	6.49	0.077	6.488	0.077	0.0020182	0.000000461	6.465	0.228	0.00123	0.27119	
TAN2	SU16@13	2.3014	0.0020	0.0104	0.0006	0.2485	6.18	0.104	6.179	0.104	0.0020175	0.000000482	6.156	0.239	0.00059	0.24854	
TAN2	SU16@14	2.2997	0.0020	0.0057	0.0006	0.2690	6.15	0.057	6.155	0.057	0.0020175	0.000000449	6.132	0.222	0.00062	0.26901	
TAN2	SU16@15	2.2951	0.0020	0.0083	0.0006	0.3004	6.21	0.083	6.210	0.083	0.0020176	0.000000465	6.187	0.231	0.00058	0.30043	2648
TAN2	SU16@16	2.2952	0.0020	0.0080	0.0014	0.9055	6.01	0.080	6.005	0.080	0.0020172	0.000000463	5.982	0.229	0.00136	0.90550	
TAN2	SU16@17	2.2920	0.0020	0.0074	0.0005	0.3770	6.51	0.074	6.510	0.074	0.0020182	0.000000459	6.487	0.227	0.00053	0.37697	2633
TAN2	SU16@18	2.2937	0.0020	0.0111	0.0006	0.4639	6.56	0.111	6.560	0.111	0.0020183	0.000000489	6.537	0.242	0.00057	0.46391	
TAN2	*SU16@19*	*2.2929*	*0.0020*	*0.0081*	*0.0028*	*3.3257*	*7.26*	*0.081*	*7.261*	*0.081*	*0.0020197*	*0.000000464*	*7.238*	*0.230*	*0.00285*	*3.32572*	
TAN2	SU16@20	2.2941	0.0020	0.0074	0.0020	0.6734	6.57	0.074	6.571	0.074	0.0020183	0.000000459	6.548	0.227	0.00197	0.67337	
TAN2	*SU16@21*	*2.2918*	*0.0020*	*0.0101*	*0.0029*	*0.5838*	*7.34*	*0.101*	*7.340*	*0.101*	*0.0020199*	*0.000000480*	*7.317*	*0.237*	*0.00289*	*0.58380*	
TAN2	SU16@22	2.2874	0.0020	0.0078	0.0010	0.1585	6.13	0.078	6.128	0.078	0.0020174	0.000000462	6.105	0.229	0.00102	0.15855	
TAN2	SU16@23	2.2860	0.0020	0.0068	0.0006	0.3882	6.51	0.068	6.508	0.068	0.0020182	0.000000455	6.484	0.226	0.00062	0.38820	2639
TAN2	SU16@24	2.2885	0.0020	0.0077	0.0006	0.2018	6.16	0.077	6.162	0.077	0.0020175	0.000000461	6.139	0.228	0.00059	0.20184	2646
TAN2	SU16@25	2.2848	0.0020	0.0081	0.0006	0.1801	6.33	0.081	6.332	0.081	0.0020178	0.000000463	6.308	0.230	0.00055	0.18009	2655
TAN2	SU16@26	2.2818	0.0020	0.0071	0.0015	0.3608	6.50	0.071	6.497	0.071	0.0020182	0.000000457	6.473	0.226	0.00150	0.36079	2634
TAN2	SU16@27	2.2920	0.0020	0.0070	0.0005	0.1863	6.54	0.070	6.543	0.070	0.0020183	0.000000456	6.520	0.226	0.00054	0.18629	

Mount	Analysis #	Ip (nA)	$^{18}O/^{16}O$	± rel (%)	$^{16}O^{1}H/^{16}O$	± rel (%)	Row delta ^{18}O	± per mil	Drift corrected $d^{18}O$	± per mil	$^{18}O/^{16}O$	1σ error	SIMS corrected $d^{18}O$	± per mil	Drift corrected OH/O	± rel (%)	Pb/Pb age per spot
TAN2	SU16@28	2.2866	0.0020	0.0102	0.0006	0.1205	6.32	0.102	6.320	0.102	0.0020178	0.000000480	6.297	0.238	0.00059	0.12055	2640
TAN2	SU16@29	2.2844	0.0020	0.0079	0.0009	0.5778	6.45	0.079	6.447	0.079	0.0020181	0.000000462	6.423	0.229	0.00091	0.57776	
TAN2	SU16@30	2.2844	0.0020	0.0065	0.0006	0.4391	6.59	0.065	6.588	0.065	0.0020184	0.000000454	6.565	0.225	0.00056	0.43910	2644
TAN2	*SU16@31*	*2.2830*	*0.0020*	*0.0098*	*0.0041*	*0.7310*	*6.02*	*0.098*	*6.019*	*0.098*	*0.0020172*	*0.000000477*	*5.996*	*0.236*	*0.00413*	*0.73098*	
TAN2	SU16@32	2.2826	0.0020	0.0083	0.0011	0.3512	7.04	0.083	7.036	0.083	0.0020193	0.000000465	7.012	0.230	0.00113	0.35121	
TAN2	SU16@33	2.2741	0.0020	0.0081	0.0005	0.3282	6.39	0.081	6.390	0.081	0.0020180	0.000000464	6.367	0.230	0.00054	0.32821	2633
TAN2	SU16@34	2.2767	0.0020	0.0080	0.0007	0.4836	6.46	0.080	6.462	0.080	0.0020181	0.000000463	6.438	0.229	0.00066	0.48361	
TAN2	*SU16@35*	*2.2770*	*0.0020*	*0.0075*	*0.0021*	*0.4402*	*7.31*	*0.075*	*7.313*	*0.075*	*0.0020198*	*0.000000460*	*7.290*	*0.228*	*0.00212*	*0.44018*	
TAN2	SU16@36	2.2763	0.0020	0.0106	0.0010	0.4983	5.90	0.106	5.898	0.106	0.0020170	0.000000483	5.874	0.240	0.00105	0.49831	
TAN2	SU16@38	2.2745	0.0020	0.0083	0.0005	0.2800	6.19	0.083	6.192	0.083	0.0020176	0.000000465	6.169	0.230	0.00052	0.28002	2638
TAN2	SU16@39	2.2724	0.0020	0.0079	0.0020	1.2310	6.37	0.079	6.371	0.079	0.0020179	0.000000462	6.348	0.229	0.00196	1.23103	
TAN2	SU16@40	2.2718	0.0020	0.0070	0.0003	0.1863	6.31	0.070	6.307	0.070	0.0020178	0.000000456	6.283	0.226	0.00032	0.18629	2641
TAN2	SU16@41	2.2750	0.0020	0.0070	0.0006	0.3255	6.29	0.070	6.292	0.070	0.0020178	0.000000456	6.268	0.226	0.00057	0.32551	2653
TAN2	SU16@42	2.2693	0.0020	0.0064	0.0017	0.3654	5.94	0.064	5.937	0.064	0.0020171	0.000000453	5.913	0.224	0.00169	0.36541	
TAN2	SU16@43	2.2691	0.0020	0.0105	0.0003	0.3193	6.55	0.105	6.548	0.105	0.0020183	0.000000483	6.525	0.239	0.00031	0.31932	
TAN2	SU16@44	2.2680	0.0020	0.0115	0.0005	0.3591	6.76	0.115	6.758	0.115	0.0020187	0.000000492	6.735	0.244	0.00054	0.35908	
SU04																	
TAN1	*SU04@01*	*2.9957*	*0.0020*	*0.0054*	*0.0112*	*0.2535*	*5.82*	*0.054*	*5.816*	*0.054*	*0.0020168*	*0.000000265*	*5.793*	*0.131*	*0.01120*	*0.25352*	
TAN1	*SU04@2*	*2.9830*	*0.0020*	*0.0068*	*0.0071*	*0.3327*	*2.48*	*0.068*	*2.481*	*0.068*	*0.0020101*	*0.000000277*	*2.457*	*0.138*	*0.00705*	*0.33274*	
TAN1	SU04@3	2.9772	0.0020	0.0062	0.0003	0.2299	5.97	0.062	5.973	0.062	0.0020171	0.000000272	5.950	0.135	0.00033	0.22986	
TAN1	*SU04@4*	*2.9732*	*0.0020*	*0.0065*	*0.0060*	*0.9481*	*1.04*	*0.065*	*1.038*	*0.065*	*0.0020072*	*0.000000274*	*1.015*	*0.136*	*0.00600*	*0.94812*	
TAN1	*SU04@5*	*2.9731*	*0.0020*	*0.0092*	*0.0050*	*0.1176*	*0.82*	*0.092*	*0.823*	*0.092*	*0.0020068*	*0.000000303*	*0.800*	*0.151*	*0.00502*	*0.11762*	
TAN1	*SU04@6*	*2.9742*	*0.0020*	*0.0081*	*0.0040*	*0.5589*	*4.28*	*0.081*	*4.275*	*0.081*	*0.0020137*	*0.000000291*	*4.252*	*0.144*	*0.00400*	*0.55886*	
TAN1	SU04@07	2.9685	0.0020	0.0078	0.0005	0.4366	5.90	0.078	5.903	0.078	0.0020170	0.000000288	5.879	0.143	0.00047	0.43655	
TAN1	SU04@8	2.9632	0.0020	0.0073	0.0015	2.6444	5.95	0.073	5.949	0.073	0.0020171	0.000000283	5.925	0.140	0.00148	2.64437	
TAN1	*SU04@9*	*2.9481*	*0.0020*	*0.0067*	*0.0056*	*0.9014*	*4.17*	*0.067*	*4.174*	*0.067*	*0.0020135*	*0.000000276*	*4.150*	*0.137*	*0.00562*	*0.90140*	
TAN1	*SU04@10*	*2.9494*	*0.0020*	*0.0075*	*0.0007*	*0.5945*	*4.86*	*0.075*	*4.858*	*0.075*	*0.0020149*	*0.000000285*	*4.835*	*0.142*	*0.00071*	*0.59450*	
TAN1	*SU04@11*	*2.9502*	*0.0020*	*0.0070*	*0.0042*	*0.1087*	*4.38*	*0.070*	*4.384*	*0.070*	*0.0020139*	*0.000000280*	*4.360*	*0.139*	*0.00421*	*0.10874*	
TAN1	*SU04@12*	*2.9556*	*0.0020*	*0.0075*	*0.0046*	*0.7093*	*5.34*	*0.075*	*5.340*	*0.075*	*0.0020159*	*0.000000285*	*5.316*	*0.141*	*0.00459*	*0.70930*	
TAN1	*SU04@13*	*2.9618*	*0.0020*	*0.0065*	*0.0099*	*0.1109*	*6.34*	*0.065*	*6.341*	*0.065*	*0.0020179*	*0.000000275*	*6.318*	*0.136*	*0.00986*	*0.11087*	
TAN1	SU04@14	2.9588	0.0020	0.0051	0.0017	0.3633	5.26	0.051	5.255	0.051	0.0020157	0.000000262	5.232	0.130	0.00169	0.36327	
TAN1	*SU04@15*	*2.9668*	*0.0020*	*0.0111*	*0.0046*	*0.4447*	*4.21*	*0.111*	*4.211*	*0.111*	*0.0020136*	*0.000000329*	*4.188*	*0.164*	*0.00458*	*0.44470*	
TAN1	*SU04@16*	*2.9760*	*0.0020*	*0.0059*	*0.0032*	*0.0903*	*4.60*	*0.059*	*4.605*	*0.059*	*0.0020144*	*0.000000269*	*4.581*	*0.134*	*0.00324*	*0.09031*	
TAN1	SU04@17	2.9724	0.0020	0.0082	0.0023	0.7532	5.48	0.082	5.481	0.082	0.0020161	0.000000293	5.458	0.145	0.00232	0.75321	
TAN1	*SU04@18*	*2.9584*	*0.0020*	*0.0072*	*0.0065*	*0.5179*	*2.88*	*0.072*	*2.879*	*0.072*	*0.0020109*	*0.000000281*	*2.856*	*0.140*	*0.00651*	*0.51794*	
TAN1	*SU04@19*	*2.9725*	*0.0020*	*0.0293*	*0.0106*	*1.6510*	*9.73*	*0.293*	*9.728*	*0.293*	*0.0020247*	*0.000000641*	*9.705*	*0.316*	*0.01055*	*1.65100*	
TAN1	SU04@20	2.9651	0.0020	0.0075	0.0031	0.4663	6.10	0.075	6.102	0.075	0.0020174	0.000000285	6.079	0.141	0.00313	0.46625	
TAN1	*SU04@21*	*2.9529*	*0.0020*	*0.0078*	*0.0116*	*0.4551*	*7.91*	*0.078*	*7.907*	*0.078*	*0.0020210*	*0.000000289*	*7.884*	*0.143*	*0.01157*	*0.45512*	

Mount	Analysis #	Ip (nA)	$^{18}O/^{16}O$	± rel (%)	$^{16}O^{1}H/^{16}O$	± rel (%)	Row delta ^{18}O	± per mil	Drift corrected $d^{18}O$	± per mil	$^{18}O/^{16}O$	1σ error	SIMS corrected $d^{18}O$	± per mil	Drift corrected OH/O	± rel (%)	Pb/Pb age per spot
TAN1	SU04@22	2.9306	0.0020	0.0069	0.0005	0.4105	6.34	0.069	6.345	0.069	0.0020179	0.000000279	6.321	0.138	0.00051	0.41047	
TAN1	SU04@23	2.9363	0.0020	0.0082	0.0017	1.0276	5.42	0.082	5.418	0.082	0.0020160	0.000000293	5.395	0.145	0.00174	1.02757	
TAN1	SU04@24	2.9409	0.0020	0.0065	0.0013	0.7000	5.98	0.065	5.977	0.065	0.0020171	0.000000275	5.954	0.136	0.00132	0.69996	
TAN1	SU04@25	2.9344	0.0020	0.0055	0.0003	0.2504	5.40	0.055	5.400	0.055	0.0020160	0.000000266	5.377	0.132	0.00028	0.25044	
TAN1	SU04@26	2.9255	0.0020	0.0091	0.0003	0.3609	5.47	0.091	5.469	0.091	0.0020161	0.000000304	5.445	0.151	0.00032	0.36091	
TAN1	SU04@27	2.9204	0.0020	0.0082	0.0003	0.1458	5.54	0.082	5.535	0.082	0.0020163	0.000000293	5.512	0.145	0.00029	0.14584	
TAN1	*SU04@28*	*2.9257*	*0.0020*	*0.0085*	*0.0066*	*0.3625*	*4.73*	*0.085*	*4.726*	*0.085*	*0.0020146*	*0.000000296*	*4.702*	*0.147*	*0.00657*	*0.36249*	
TAN1	*SU04@29*	*2.9192*	*0.0020*	*0.0077*	*0.0015*	*1.0773*	*4.71*	*0.077*	*4.705*	*0.077*	*0.0020146*	*0.000000287*	*4.682*	*0.142*	*0.00151*	*1.07732*	
TAN1	*SU04@30*	*2.9145*	*0.0020*	*0.0077*	*0.0028*	*0.5773*	*3.71*	*0.077*	*3.707*	*0.077*	*0.0020126*	*0.000000287*	*3.684*	*0.142*	*0.00277*	*0.57728*	
TAN1	*SU04@31*	*2.9022*	*0.0020*	*0.0084*	*0.0048*	*0.3479*	*4.45*	*0.084*	*4.447*	*0.084*	*0.0020141*	*0.000000295*	*4.424*	*0.146*	*0.00481*	*0.34794*	
TAN1	*SU04@32*	*2.9012*	*0.0020*	*0.0087*	*0.0038*	*0.0845*	*1.94*	*0.087*	*1.938*	*0.087*	*0.0020090*	*0.000000297*	*1.915*	*0.148*	*0.00375*	*0.08452*	
TAN1	SU04@33	2.9049	0.0020	0.0069	0.0009	0.1461	5.66	0.069	5.659	0.069	0.0020165	0.000000278	5.635	0.138	0.00090	0.14611	
TAN1	SU04@34	2.9005	0.0020	0.0051	0.0008	0.1671	6.09	0.051	6.088	0.051	0.0020174	0.000000263	6.065	0.130	0.00078	0.16712	
TAN1	*SU04@35*	*2.8964*	*0.0020*	*0.0138*	*0.0090*	*1.0904*	*4.98*	*0.138*	*4.985*	*0.138*	*0.0020151*	*0.000000368*	*4.961*	*0.183*	*0.00899*	*1.09038*	
TAN1	*SU04@36*	*2.8927*	*0.0020*	*0.0059*	*0.0039*	*0.0958*	*4.86*	*0.059*	*4.858*	*0.059*	*0.0020149*	*0.000000269*	*4.835*	*0.134*	*0.00390*	*0.09582*	
TAN1	SU04@37	2.8916	0.0020	0.0108	0.0009	0.6965	5.95	0.108	5.947	0.108	0.0020171	0.000000325	5.923	0.161	0.00086	0.69651	
TAN1	*SU04@38*	*2.8933*	*0.0020*	*0.0055*	*0.0024*	*0.4104*	*3.79*	*0.055*	*3.794*	*0.055*	*0.0020128*	*0.000000265*	*3.771*	*0.132*	*0.00238*	*0.41043*	
TAN1	SU04@39	2.8673	0.0020	0.0056	0.0003	0.0563	5.81	0.056	5.809	0.056	0.0020168	0.000000267	5.786	0.132	0.00030	0.05633	
TAN1	*SU04@40*	*2.8617*	*0.0020*	*0.0052*	*0.0060*	*0.2128*	*1.48*	*0.052*	*1.480*	*0.052*	*0.0020081*	*0.000000262*	*1.456*	*0.131*	*0.00602*	*0.21276*	
SU21																	
TAN1	*SU21@01*	*2.8552*	*0.0020*	*0.0078*	*0.0036*	*0.3974*	*5.56*	*0.078*	*5.560*	*0.078*	*0.0020163*	*0.000000289*	*5.537*	*0.143*	*0.00363*	*0.39742*	
TAN1	SU21@2	2.8454	0.0020	0.0077	0.0005	0.8039	4.84	0.077	4.839	0.077	0.0020149	0.000000287	4.816	0.142	0.00055	0.80388	
TAN1	SU21@03	2.8141	0.0020	0.0055	0.0004	0.0999	5.12	0.055	5.116	0.055	0.0020154	0.000000266	5.093	0.132	0.00037	0.09988	
TAN1	SU21@4	2.8196	0.0020	0.0085	0.0004	0.0861	5.27	0.085	5.271	0.085	0.0020157	0.000000296	5.247	0.147	0.00036	0.08613	
TAN1	SU21@5	2.8075	0.0020	0.0085	0.0005	0.0274	4.90	0.085	4.895	0.085	0.0020150	0.000000296	4.872	0.147	0.00053	0.02736	
TAN1	SU21@6	2.8029	0.0020	0.0060	0.0011	0.3867	5.00	0.060	4.998	0.060	0.0020152	0.000000270	4.975	0.134	0.00105	0.38672	
TAN1	SU21@7	2.8064	0.0020	0.0079	0.0013	0.1189	5.20	0.079	5.198	0.079	0.0020156	0.000000289	5.175	0.143	0.00131	0.11887	
TAN1	SU21@8	2.7978	0.0020	0.0092	0.0004	0.0587	5.12	0.092	5.125	0.092	0.0020154	0.000000304	5.101	0.151	0.00042	0.05865	
TAN1	SU21@09	2.7934	0.0020	0.0080	0.0018	0.6171	4.91	0.080	4.913	0.080	0.0020150	0.000000290	4.889	0.144	0.00182	0.61715	
TAN1	SU21@10	2.7791	0.0020	0.0074	0.0008	0.0743	5.02	0.074	5.022	0.074	0.0020152	0.000000284	4.999	0.141	0.00081	0.07433	
TAN1	SU21@11	2.7887	0.0020	0.0061	0.0009	0.2777	5.42	0.061	5.420	0.061	0.0020160	0.000000271	5.397	0.135	0.00091	0.27769	
TAN1	SU21@12	2.7795	0.0020	0.0068	0.0004	0.1120	5.11	0.068	5.115	0.068	0.0020154	0.000000278	5.091	0.138	0.00044	0.11203	
TAN1	SU21@13	2.7769	0.0020	0.0083	0.0016	0.4770	5.42	0.083	5.419	0.083	0.0020160	0.000000294	5.396	0.146	0.00163	0.47696	
TAN1	SU21@14	2.7716	0.0020	0.0078	0.0006	0.0413	5.09	0.078	5.087	0.078	0.0020154	0.000000288	5.064	0.143	0.00058	0.04132	
TAN1	SU21@15	2.7673	0.0020	0.0078	0.0004	0.4605	5.01	0.078	5.010	0.078	0.0020152	0.000000288	4.987	0.143	0.00042	0.46055	
TAN1	SU21@16	2.7628	0.0020	0.0053	0.0005	0.0855	5.14	0.053	5.139	0.053	0.0020155	0.000000264	5.116	0.131	0.00052	0.08546	
TAN1	*SU21@17*	*2.7635*	*0.0020*	*0.0082*	*0.0051*	*0.3964*	*5.70*	*0.082*	*5.695*	*0.082*	*0.0020166*	*0.000000292*	*5.672*	*0.145*	*0.00507*	*0.39637*	
TAN1	SU21@18	2.7618	0.0020	0.0080	0.0008	0.4655	5.02	0.080	5.015	0.080	0.0020152	0.000000290	4.992	0.144	0.00081	0.46551	

Mount	Analysis #	Ip (nA)	$^{18}O/^{16}O$	± rel (%)	$^{16}O^{1}H/^{16}O$	± rel (%)	Row delta ^{18}O	± per mil	Drift corrected $d^{18}O$	± per mil	$^{18}O/^{16}O$	1σ error	SIMS corrected $d^{18}O$	± per mil	Drift corrected OH/O	± rel (%)	Pb/Pb age per spot
TAN1	SU21@19	2.7589	0.0020	0.0073	0.0004	0.0554	5.13	0.073	5.127	0.073	0.0020154	0.000000283	5.104	0.140	0.00040	0.05541	
TAN1	SU21@20	2.7552	0.0020	0.0084	0.0004	0.0916	5.06	0.084	5.060	0.084	0.0020153	0.000000295	5.037	0.146	0.00041	0.09156	
TAN1	SU21@21	2.7498	0.0020	0.0067	0.0017	0.3215	4.97	0.067	4.968	0.067	0.0020151	0.000000276	4.945	0.137	0.00165	0.32146	
TAN1	SU21@22	2.7468	0.0020	0.0074	0.0009	0.6520	5.25	0.074	5.250	0.074	0.0020157	0.000000284	5.227	0.141	0.00093	0.65201	
TAN1	SU21@23	2.7428	0.0020	0.0071	0.0005	0.5500	5.00	0.071	5.000	0.071	0.0020152	0.000000280	4.977	0.139	0.00052	0.54996	
TAN1	SU21@24	2.7461	0.0020	0.0065	0.0005	0.3994	4.97	0.065	4.969	0.065	0.0020151	0.000000275	4.946	0.136	0.00050	0.39940	
TAN1	*SU21@25*	*2.7440*	*0.0020*	*0.0075*	*0.0035*	*0.1914*	*6.08*	*0.075*	*6.082*	*0.075*	*0.0020173*	*0.000000285*	*6.058*	*0.141*	*0.00348*	*0.19144*	
TAN1	SU21@26	2.7412	0.0020	0.0089	0.0009	0.1175	5.46	0.089	5.458	0.089	0.0020161	0.000000301	5.434	0.150	0.00093	0.11745	
TAN1	*SU21@27*	*2.7348*	*0.0020*	*0.0078*	*0.0035*	*0.1690*	*5.59*	*0.078*	*5.586*	*0.078*	*0.0020164*	*0.000000288*	*5.563*	*0.143*	*0.00346*	*0.16899*	
TAN1	SU21@28	2.7333	0.0020	0.0073	0.0006	0.6808	5.31	0.073	5.306	0.073	0.0020158	0.000000282	5.282	0.140	0.00061	0.68083	
TAN1	*SU21@29*	*2.7311*	*0.0020*	*0.0053*	*0.0074*	*0.2034*	*6.76*	*0.053*	*6.758*	*0.053*	*0.0020187*	*0.000000264*	*6.735*	*0.131*	*0.00743*	*0.20342*	
TAN1	SU21@30	2.7326	0.0020	0.0066	0.0009	0.3693	5.01	0.066	5.006	0.066	0.0020152	0.000000276	4.983	0.137	0.00089	0.36931	
TAN1	SU21@31	2.7273	0.0020	0.0074	0.0004	0.0899	5.72	0.074	5.718	0.074	0.0020166	0.000000284	5.695	0.141	0.00040	0.08991	
TAN1	SU21@32	2.7247	0.0020	0.0071	0.0013	0.2848	5.42	0.071	5.424	0.071	0.0020160	0.000000281	5.401	0.139	0.00131	0.28482	
TAN1	*SU21@33*	*2.7254*	*0.0020*	*0.0101*	*0.0054*	*1.1629*	*6.85*	*0.101*	*6.848*	*0.101*	*0.0020189*	*0.000000316*	*6.824*	*0.157*	*0.00543*	*1.16292*	
TAN1	*SU21@34*	*2.7263*	*0.0020*	*0.0081*	*0.0059*	*2.5565*	*6.40*	*0.081*	*6.403*	*0.081*	*0.0020180*	*0.000000292*	*6.379*	*0.145*	*0.00588*	*2.55650*	
TAN1	SU21@35	2.7256	0.0020	0.0059	0.0006	0.3274	5.32	0.059	5.319	0.059	0.0020158	0.000000270	5.296	0.134	0.00057	0.32740	
TAN1	*SU21@36*	*2.7206*	*0.0020*	*0.0086*	*0.0047*	*0.1985*	*5.28*	*0.086*	*5.284*	*0.086*	*0.0020157*	*0.000000297*	*5.260*	*0.147*	*0.00465*	*0.19847*	
TAN1	SU21@37	2.7235	0.0020	0.0059	0.0003	0.1564	5.21	0.059	5.205	0.059	0.0020156	0.000000269	5.182	0.134	0.00033	0.15638	
TAN1	*SU21@38*	*2.7223*	*0.0020*	*0.0072*	*0.0036*	*1.7475*	*5.33*	*0.072*	*5.333*	*0.072*	*0.0020158*	*0.000000282*	*5.310*	*0.140*	*0.00363*	*1.74745*	
TAN1	*SU21@39*	*2.7167*	*0.0020*	*0.0070*	*0.0027*	*0.9203*	*5.59*	*0.070*	*5.586*	*0.070*	*0.0020164*	*0.000000280*	*5.563*	*0.139*	*0.00270*	*0.92033*	
TAN1	*SU21@40*	*2.7118*	*0.0020*	*0.0069*	*0.0078*	*0.2147*	*7.64*	*0.069*	*7.642*	*0.069*	*0.0020205*	*0.000000279*	*7.619*	*0.138*	*0.00778*	*0.21472*	
TAN1	*SU21@41*	*2.7085*	*0.0020*	*0.0062*	*0.0044*	*0.1104*	*5.47*	*0.062*	*5.465*	*0.062*	*0.0020161*	*0.000000272*	*5.442*	*0.135*	*0.00443*	*0.11043*	
TAN1	SU21@42	2.6815	0.0020	0.0053	0.0003	0.0613	5.05	0.053	5.054	0.053	0.0020153	0.000000264	5.031	0.131	0.00032	0.06126	
TAN1	SU21@43	2.6812	0.0020	0.0059	0.0005	0.4437	5.31	0.059	5.307	0.059	0.0020158	0.000000270	5.283	0.134	0.00047	0.44370	
TAN1	SU21@44	2.6821	0.0020	0.0062	0.0005	0.0978	5.22	0.062	5.217	0.062	0.0020156	0.000000272	5.194	0.135	0.00047	0.09782	

	$^{176}Hf/^{177}Hf$	2SE	$^{176}Lu/^{177}Hf$	2SE	$^{176}Yb/^{177}Hf$	2SE	$^{178}Hf/^{177}Hf$	2SE	$^{180}Hf/^{177}Hf$	2SE	Total Hf beam	Age per spot	2SE	Initial	EHfpd	eHf (t)	2SE	CHUR	TDM
MUDTANK																			
1	0.282516	1.30E-05	9.01E-06	1.50E-07	3.06E-04	9.3E-06	1.46719	2.6E-05	1.887	3.1E-04	17.7	730		0.282516	-9.51	6.80	0.690	0.28232	1014
10	0.282515	1.20E-05	8.18E-06	9.50E-08	2.72E-04	6.8E-06	1.46724	2.5E-05	1.886	1.8E-04	20.0	730		0.282515	-9.55	6.76	0.667	0.28232	1016
11	0.282503	1.20E-05	8.33E-06	8.80E-08	2.75E-04	6.9E-06	1.46722	2.6E-05	1.886	2.0E-04	20.2	730		0.282503	-9.97	6.34	0.667	0.28232	1032
12	0.282529	1.10E-05	8.67E-06	1.30E-07	2.82E-04	6.5E-06	1.46723	3.2E-05	1.886	1.8E-04	20.3	730		0.282529	-9.05	7.26	0.645	0.28232	997
13	0.282502	1.30E-05	8.55E-06	9.30E-08	2.91E-04	7.4E-06	1.46722	2.8E-05	1.886	2.1E-04	19.7	730		0.282502	-10.01	6.30	0.690	0.28232	1034
14	0.282509	1.30E-05	8.72E-06	1.10E-07	2.93E-04	8.4E-06	1.46721	2.1E-05	1.886	1.7E-04	19.9	730		0.282509	-9.76	6.55	0.690	0.28232	1024
15	0.282513	1.40E-05	8.34E-06	9.60E-08	2.76E-04	8.4E-06	1.46722	2.5E-05	1.886	2.3E-04	19.3	730		0.282513	-9.62	6.69	0.715	0.28232	1018
16	0.282506	1.30E-05	8.41E-06	1.20E-07	2.76E-04	7.9E-06	1.46718	2.4E-05	1.886	1.8E-04	20.0	730		0.282506	-9.87	6.44	0.690	0.28232	1028
17	0.282509	1.40E-05	8.39E-06	1.10E-07	2.74E-04	7.8E-06	1.46721	3.2E-05	1.886	2.1E-04	20.2	730		0.282509	-9.76	6.55	0.715	0.28232	1024
18	0.282512	1.20E-05	8.20E-06	9.80E-08	2.68E-04	6.6E-06	1.46722	3.0E-05	1.886	2.0E-04	20.1	730		0.282512	-9.65	6.66	0.667	0.28232	1020
19	0.282510	1.40E-05	8.21E-06	9.50E-08	2.76E-04	5.2E-06	1.46722	2.8E-05	1.886	1.9E-04	19.6	730		0.282510	-9.72	6.59	0.715	0.28232	1023
2	0.282507	1.50E-05	8.15E-06	9.80E-08	2.74E-04	7.2E-06	1.46721	3.0E-05	1.887	2.4E-04	17.5	730		0.282507	-9.83	6.48	0.740	0.28232	1027
20	0.282493	1.20E-05	7.76E-06	8.60E-08	2.68E-04	7.5E-06	1.46721	2.2E-05	1.887	2.2E-04	19.0	730		0.282493	-10.33	5.98	0.667	0.28232	1046
21	0.282508	1.10E-05	7.80E-06	1.10E-07	2.65E-04	6.9E-06	1.46722	2.5E-05	1.886	1.9E-04	19.3	730		0.282508	-9.80	6.52	0.644	0.28232	1025
22	0.282518	1.40E-05	7.34E-06	9.20E-08	2.49E-04	7.5E-06	1.46719	3.0E-05	1.886	2.0E-04	19.3	730		0.282518	-9.44	6.87	0.715	0.28232	1012
23	0.282512	1.20E-05	7.66E-06	9.50E-08	2.45E-04	7.2E-06	1.46720	2.4E-05	1.886	2.0E-04	19.9	730		0.282512	-9.65	6.66	0.667	0.28232	1020
24	0.282512	1.10E-05	7.70E-06	8.80E-08	2.50E-04	7.6E-06	1.46723	2.6E-05	1.886	1.5E-04	20.8	730		0.282512	-9.65	6.66	0.644	0.28232	1020
25	0.282503	1.20E-05	8.20E-06	1.00E-07	2.67E-04	6.4E-06	1.46722	2.6E-05	1.887	1.7E-04	21.4	730		0.282503	-9.97	6.34	0.667	0.28232	1032
26	0.282512	1.20E-05	8.37E-06	1.00E-07	2.73E-04	8.2E-06	1.46720	2.8E-05	1.886	1.8E-04	21.5	730		0.282512	-9.65	6.66	0.667	0.28232	1020
27	0.282506	1.00E-05	8.53E-06	1.00E-07	2.70E-04	5.6E-06	1.46719	2.2E-05	1.886	1.4E-04	21.6	730		0.282506	-9.87	6.44	0.623	0.28232	1028
28	0.282515	1.10E-05	8.02E-06	8.80E-08	2.57E-04	6.0E-06	1.46723	2.4E-05	1.886	1.7E-04	21.4	730		0.282515	-9.55	6.76	0.644	0.28232	1016
29	0.282516	1.40E-05	8.60E-06	1.10E-07	2.80E-04	8.5E-06	1.46723	2.5E-05	1.887	1.7E-04	21.2	730		0.282516	-9.51	6.80	0.715	0.28232	1014
3	0.282523	1.40E-05	7.91E-06	9.70E-08	2.60E-04	8.0E-06	1.46720	2.8E-05	1.887	2.9E-04	17.5	730		0.282523	-9.26	7.05	0.715	0.28232	1005
30	0.282506	1.20E-05	8.54E-06	9.10E-08	2.72E-04	6.1E-06	1.46719	2.2E-05	1.886	1.7E-04	21.5	730		0.282506	-9.87	6.44	0.667	0.28232	1028
31	0.282504	1.30E-05	9.42E-06	9.70E-08	3.13E-04	7.2E-06	1.46721	2.8E-05	1.887	2.2E-04	20.9	730		0.282504	-9.94	6.37	0.690	0.28232	1031
32	0.282512	1.30E-05	9.77E-06	1.50E-07	3.12E-04	6.7E-06	1.46719	2.2E-05	1.886	1.9E-04	21.6	730		0.282512	-9.65	6.66	0.690	0.28232	1020
33	0.282515	1.30E-05	8.78E-06	9.30E-08	2.90E-04	7.2E-06	1.46721	2.2E-05	1.886	1.4E-04	21.4	730		0.282515	-9.55	6.76	0.690	0.28232	1016
34	0.282517	1.30E-05	8.65E-06	1.20E-07	2.80E-04	7.7E-06	1.46718	2.9E-05	1.886	2.0E-04	21.0	730		0.282517	-9.48	6.83	0.690	0.28232	1013
35	0.282505	1.30E-05	8.58E-06	9.40E-08	2.79E-04	6.8E-06	1.46722	3.0E-05	1.886	1.6E-04	21.3	730		0.282505	-9.90	6.41	0.690	0.28232	1029
36	0.282507	1.50E-05	8.49E-06	9.30E-08	2.81E-04	7.5E-06	1.46719	2.5E-05	1.886	1.9E-04	21.1	730		0.282507	-9.83	6.48	0.740	0.28232	1027
37	0.282503	1.30E-05	8.33E-06	8.70E-08	2.75E-04	6.4E-06	1.46721	2.3E-05	1.886	1.7E-04	21.2	730		0.282503	-9.97	6.34	0.690	0.28232	1032
38	0.282508	1.10E-05	7.91E-06	1.10E-07	2.56E-04	6.0E-06	1.46722	2.7E-05	1.886	1.9E-04	21.3	730		0.282508	-9.80	6.52	0.644	0.28232	1025
39	0.282507	1.20E-05	7.76E-06	9.00E-08	2.49E-04	7.0E-06	1.46720	2.8E-05	1.886	2.0E-04	20.5	730		0.282507	-9.83	6.48	0.667	0.28232	1027
4	0.282506	1.40E-05	7.59E-06	1.10E-07	2.55E-04	7.6E-06	1.46721	3.7E-05	1.887	2.4E-04	17.9	730		0.282506	-9.87	6.45	0.715	0.28232	1028
40	0.282516	1.50E-05	7.57E-06	9.20E-08	2.44E-04	7.7E-06	1.46719	2.4E-05	1.887	1.7E-04	19.9	730		0.282516	-9.51	6.80	0.740	0.28232	1014
41	0.282503	1.30E-05	7.58E-06	9.80E-08	2.52E-04	7.9E-06	1.46720	2.9E-05	1.886	1.7E-04	20.6	730		0.282503	-9.97	6.34	0.690	0.28232	1032
5	0.282497	1.50E-05	7.85E-06	1.20E-07	2.70E-04	8.5E-06	1.46720	3.0E-05	1.887	2.2E-04	18.2	730		0.282497	-10.18	6.13	0.740	0.28232	1040
50	0.282499	1.40E-05	8.56E-06	9.20E-08	2.87E-04	7.1E-06	1.46719	3.2E-05	1.886	2.1E-04	21.6	730		0.282499	-10.11	6.20	0.715	0.28232	1038
51	0.282499	1.30E-05	8.61E-06	7.90E-08	2.74E-04	6.2E-06	1.46717	2.8E-05	1.886	2.2E-04	21.1	730		0.282499	-10.11	6.20	0.690	0.28232	1038
52	0.282506	1.20E-05	8.05E-06	9.90E-08	2.60E-04	6.8E-06	1.46719	2.9E-05	1.886	2.0E-04	21.3	730		0.282506	-9.87	6.45	0.667	0.28232	1028
53	0.282495	1.40E-05	8.06E-06	9.20E-08	2.64E-04	7.1E-06	1.46722	2.2E-05	1.887	1.8E-04	21.6	730		0.282495	-10.26	6.06	0.715	0.28232	1043
54	0.282511	1.10E-05	7.93E-06	7.40E-08	2.59E-04	6.2E-06	1.46724	2.8E-05	1.887	2.0E-04	21.2	730		0.282511	-9.69	6.62	0.644	0.28232	1021
6	0.282511	1.10E-05	8.20E-06	1.10E-07	2.74E-04	7.9E-06	1.46719	3.4E-05	1.886	2.2E-04	18.3	730		0.282511	-9.69	6.62	0.644	0.28232	1021
7	0.282504	1.50E-05	8.01E-06	9.30E-08	2.70E-04	8.1E-06	1.46720	2.2E-05	1.886	2.0E-04	18.3	730		0.282504	-9.94	6.37	0.740	0.28232	1031
8	0.282514	1.40E-05	8.23E-06	1.00E-07	2.73E-04	7.6E-06	1.46723	2.9E-05	1.887	1.8E-04	19.3	730		0.282514	-9.58	6.73	0.715	0.28232	1017
9	0.282519	1.50E-05	8.17E-06	1.10E-07	2.65E-04	7.9E-06	1.46720	3.0E-05	1.887	1.8E-04	19.6	730		0.282519	-9.41	6.91	0.740	0.28232	1010

MUNZirc	$^{176}Hf/^{177}Hf$	2SE	$^{176}Lu/^{177}Hf$	2SE	$^{176}Yb/^{177}Hf$	2SE	$^{178}Hf/^{177}Hf$	2SE	$^{180}Hf/^{177}Hf$	2SE	Total Hf beam	Age per spot	2SE	Initial	EHfpd	eHf (t)	2SE	CHUR	TDM
1	0.282151	1.20E-05	5.12E-04	4.00E-06	1.48E-02	2.4E-04	1.46721	2.3E-05	1.886	2.5E-04	26.3	0		0.282151	-22.42	-22.42	0.666	0.28279	1532
10	0.282137	8.40E-06	4.74E-04	8.30E-06	1.46E-02	6.0E-04	1.46721	2.4E-05	1.887	2.3E-04	33.9	0		0.282137	-22.90	-22.90	0.592	0.28279	1549
11	0.282148	1.10E-05	4.06E-04	6.80E-07	1.23E-02	1.5E-04	1.46720	2.3E-05	1.887	1.7E-04	33.2	0		0.282148	-22.53	-22.53	0.644	0.28279	1531
12	0.282136	1.10E-05	4.02E-04	5.20E-07	1.22E-02	1.2E-04	1.46720	2.5E-05	1.886	1.6E-04	33.3	0		0.282136	-22.95	-22.95	0.644	0.28279	1548
2	0.282134	1.30E-05	6.30E-04	3.80E-05	1.85E-02	1.0E-03	1.46719	2.1E-05	1.886	1.8E-04	28.1	0		0.282134	-23.02	-23.02	0.690	0.28279	1560
3	0.282142	9.40E-06	4.74E-04	3.20E-05	1.41E-02	8.5E-04	1.46723	2.5E-05	1.886	1.4E-04	29.0	0		0.282142	-22.73	-22.73	0.611	0.28279	1542
4	0.282143	1.20E-05	4.76E-04	3.60E-05	1.45E-02	9.7E-04	1.46720	2.2E-05	1.886	1.7E-04	29.6	0		0.282143	-22.70	-22.70	0.666	0.28279	1541
5	0.282125	1.00E-05	5.64E-04	4.10E-05	1.69E-02	1.1E-03	1.46722	2.2E-05	1.887	1.7E-04	30.2	0		0.282125	-23.34	-23.34	0.623	0.28279	1569
6	0.282147	8.70E-06	7.99E-04	7.60E-06	2.43E-02	1.7E-04	1.46721	2.4E-05	1.886	1.7E-04	29.5	0		0.282147	-22.56	-22.56	0.597	0.28279	1549
7	0.282142	1.10E-05	8.26E-04	2.80E-06	2.54E-02	1.5E-04	1.46718	2.3E-05	1.886	1.6E-04	28.9	0		0.282142	-22.74	-22.74	0.644	0.28279	1557
8	0.282138	1.30E-05	8.70E-04	3.20E-06	2.66E-02	1.7E-04	1.46718	2.2E-05	1.886	1.8E-04	29.2	0		0.282138	-22.88	-22.88	0.690	0.28279	1564
9	0.282144	1.30E-05	1.02E-03	5.40E-06	3.08E-02	4.7E-04	1.46720	2.4E-05	1.886	2.0E-04	29.0	0		0.282144	-22.67	-22.67	0.690	0.28279	1562
1	0.282126	2.10E-05	4.25E-03	3.50E-05	1.46E-01	3.7E-03	1.46722	3.2E-05	1.887	2.1E-04	19.7	0		0.282126	-23.30	-23.30	0.907	0.28279	1735
10	0.282141	1.70E-05	3.08E-03	1.30E-05	1.06E-01	1.9E-03	1.46719	2.6E-05	1.887	1.9E-04	25.9	0		0.282141	-22.77	-22.77	0.793	0.28279	1656
11	0.282144	1.90E-05	3.59E-03	1.50E-04	1.22E-01	4.3E-03	1.46718	2.5E-05	1.886	1.9E-04	24.9	0		0.282144	-22.67	-22.67	0.849	0.28279	1675
12	0.282125	1.90E-05	3.84E-03	1.00E-04	1.32E-01	5.0E-03	1.46720	2.5E-05	1.887	2.0E-04	24.1	0		0.282125	-23.34	-23.34	0.849	0.28279	1716
2	0.282115	1.80E-05	3.14E-03	1.20E-05	1.06E-01	1.6E-03	1.46720	2.8E-05	1.887	2.4E-04	22.6	0		0.282115	-23.69	-23.69	0.821	0.28279	1697
3	0.282141	2.00E-05	3.11E-03	1.90E-05	1.05E-01	1.3E-03	1.46721	2.5E-05	1.886	2.3E-04	21.6	0		0.282141	-22.77	-22.77	0.878	0.28279	1657
4	0.282150	2.00E-05	3.09E-03	1.70E-05	1.06E-01	1.3E-03	1.46722	2.8E-05	1.887	2.0E-04	22.7	0		0.282150	-22.46	-22.46	0.878	0.28279	1643
5	0.282116	2.00E-05	3.08E-03	1.70E-05	1.05E-01	1.3E-03	1.46720	2.6E-05	1.886	2.0E-04	23.7	0		0.282116	-23.66	-23.66	0.878	0.28279	1693
6	0.282121	1.70E-05	3.06E-03	1.40E-05	1.03E-01	1.2E-03	1.46718	2.6E-05	1.886	2.0E-04	25.2	0		0.282121	-23.48	-23.48	0.793	0.28279	1684
7	0.282155	2.10E-05	3.06E-03	1.20E-05	1.03E-01	1.1E-03	1.46718	2.2E-05	1.887	1.4E-04	24.5	0		0.282155	-22.28	-22.28	0.907	0.28279	1634
8	0.282122	2.00E-05	3.09E-03	1.20E-05	1.05E-01	1.4E-03	1.46720	2.9E-05	1.887	1.7E-04	24.7	0		0.282122	-23.45	-23.45	0.878	0.28279	1684
9	0.282122	1.60E-05	3.09E-03	1.30E-05	1.05E-01	1.8E-03	1.46718	2.3E-05	1.887	1.8E-04	26.2	0		0.282122	-23.45	-23.45	0.766	0.28279	1684
1	0.282133	3.20E-05	8.70E-03	5.50E-05	2.70E-01	3.4E-03	1.46717	3.0E-05	1.887	2.7E-04	23.0	0		0.282133	-23.06	-23.06	1.252	0.28279	1977
10	0.282135	3.20E-05	8.40E-03	6.00E-05	2.62E-01	1.9E-03	1.46718	2.4E-05	1.887	2.5E-04	26.5	0		0.282135	-22.99	-22.99	1.252	0.28279	1955
11	0.282124	2.80E-05	8.48E-03	5.20E-05	2.65E-01	2.3E-03	1.46720	2.3E-05	1.887	2.2E-04	27.1	0		0.282124	-23.37	-23.37	1.123	0.28279	1978

	$^{176}Hf/^{177}Hf$	2SE	$^{176}Lu/^{177}Hf$	2SE	$^{176}Yb/^{177}Hf$	2SE	$^{178}Hf/^{177}Hf$	2SE	$^{180}Hf/^{177}Hf$	2SE	Total Hf beam	Age per spot	2SE	Initial	EHfpd	eHf (t)	2SE	CHUR	TDM
12	0.282145	2.40E-05	8.51E-03	4.70E-05	2.63E-01	2.1E-03	1.46720	2.3E-05	1.887	1.8E-04	28.0	0		0.282145	-22.63	-22.63	0.998	0.28279	1944
2	0.282096	2.70E-05	8.60E-03	5.80E-05	2.66E-01	3.0E-03	1.46722	2.5E-05	1.887	1.8E-04	24.1	0		0.282096	-24.36	-24.36	1.091	0.28279	2035
3	0.282131	3.20E-05	7.90E-03	5.20E-05	2.51E-01	2.3E-03	1.46719	3.0E-05	1.887	1.8E-04	23.4	0		0.282131	-23.13	-23.13	1.252	0.28279	1930
4	0.282128	3.10E-05	7.65E-03	5.90E-05	2.41E-01	1.6E-03	1.46719	2.1E-05	1.887	2.0E-04	24.4	0		0.282128	-23.23	-23.23	1.219	0.28279	1919
5	0.282122	3.00E-05	7.80E-03	4.10E-05	2.46E-01	2.0E-03	1.46720	2.4E-05	1.886	1.9E-04	24.7	0		0.282122	-23.45	-23.45	1.187	0.28279	1939
6	0.282114	2.70E-05	8.53E-03	4.20E-05	2.62E-01	1.7E-03	1.46719	2.1E-05	1.887	2.2E-04	27.1	0		0.282114	-23.73	-23.73	1.091	0.28279	1999
7	0.282139	2.10E-05	8.53E-03	4.30E-05	2.65E-01	2.1E-03	1.46719	2.7E-05	1.887	1.8E-04	27.5	0		0.282139	-22.84	-22.84	0.907	0.28279	1956
8	0.282131	2.00E-05	5.12E-03	1.80E-05	1.55E-01	3.0E-03	1.46721	2.5E-05	1.886	2.1E-04	25.3	0		0.282131	-23.13	-23.13	0.878	0.28279	1771
9	0.282155	2.20E-05	8.52E-03	6.90E-05	2.64E-01	1.9E-03	1.46720	2.2E-05	1.886	1.9E-04	27.2	0		0.282155	-22.28	-22.28	0.937	0.28279	1928
TAN1																			
91500																			
1	0.282336	2.20E-05	3.23E-04	9.40E-07	9.47E-03	1.5E-04	1.46719	3.5E-05	1.887	2.6E-04	10.2	1065		0.282330	-15.88	7.77	0.937	0.28211	1271
10	0.282308	1.90E-05	3.23E-04	5.70E-07	9.45E-03	8.6E-05	1.46725	3.9E-05	1.887	1.9E-04	11.8	1065		0.282302	-16.87	6.78	0.849	0.28211	1309
2	0.282284	2.20E-05	3.24E-04	6.40E-07	9.41E-03	9.3E-05	1.46716	4.2E-05	1.887	1.8E-04	11.0	1065		0.282278	-17.72	5.93	0.937	0.28211	1342
3	0.282324	2.10E-05	3.23E-04	7.00E-07	9.49E-03	6.9E-05	1.46720	3.2E-05	1.886	2.3E-04	11.1	1065		0.282318	-16.30	7.35	0.907	0.28211	1287
4	0.282311	1.90E-05	3.22E-04	4.60E-07	9.69E-03	8.1E-05	1.46721	3.3E-05	1.887	2.1E-04	11.4	1065		0.282305	-16.76	6.89	0.849	0.28211	1305
5	0.282302	1.60E-05	3.21E-04	4.70E-07	9.59E-03	6.4E-05	1.46719	3.7E-05	1.886	1.8E-04	11.8	1065		0.282296	-17.08	6.57	0.766	0.28211	1317
6	0.282309	1.60E-05	3.16E-04	4.10E-07	9.24E-03	6.5E-05	1.46721	3.5E-05	1.887	2.0E-04	11.8	1065		0.282303	-16.83	6.82	0.766	0.28211	1307
7	0.282324	1.80E-05	3.18E-04	6.40E-07	9.21E-03	6.7E-05	1.46718	3.7E-05	1.886	1.8E-04	12.5	1065		0.282318	-16.30	7.35	0.821	0.28211	1287
8	0.282319	1.90E-05	3.24E-04	5.40E-07	9.42E-03	8.7E-05	1.46721	3.4E-05	1.886	1.7E-04	12.6	1065		0.282312	-16.48	7.17	0.849	0.28211	1294
9	0.282295	2.00E-05	3.25E-04	8.00E-07	9.50E-03	9.0E-05	1.46718	3.7E-05	1.886	2.0E-04	11.7	1065		0.282288	-17.33	6.32	0.878	0.28211	1327
FC1																			
102	0.282172	1.80E-05	8.04E-04	3.70E-05	2.82E-02	1.3E-03	1.46726	3.1E-05	1.886	2.7E-04	21.5	1099		0.282155	-21.68	2.37	0.821	0.28209	1514
106	0.282187	1.30E-05	1.40E-03	5.00E-05	4.49E-02	1.9E-03	1.46722	2.5E-05	1.886	2.0E-04	22.2	1099		0.282158	-21.15	2.47	0.690	0.28209	1517
110	0.282187	1.50E-05	1.74E-03	1.10E-05	5.47E-02	6.9E-04	1.46720	2.7E-05	1.886	1.6E-04	23.7	1099		0.282151	-21.15	2.22	0.740	0.28209	1531
116	0.282193	1.70E-05	1.70E-03	2.60E-05	5.50E-02	5.5E-04	1.46720	2.8E-05	1.886	2.1E-04	21.3	1099		0.282158	-20.93	2.45	0.793	0.28209	1521
118	0.282183	1.50E-05	1.21E-03	2.80E-06	3.84E-02	2.9E-04	1.46721	2.9E-05	1.887	2.2E-04	22.0	1099		0.282158	-21.29	2.46	0.740	0.28209	1515
1	0.282177	1.90E-05	8.78E-04	6.10E-06	2.67E-02	3.2E-04	1.46720	3.3E-05	1.886	2.2E-04	17.9	1099		0.282159	-21.50	2.49	0.849	0.28209	1510
100	0.282175	1.30E-05	1.08E-03	5.10E-06	3.24E-02	2.8E-04	1.46722	2.6E-05	1.886	1.9E-04	25.2	1099		0.282153	-21.57	2.28	0.690	0.28209	1521
51	0.282178	1.40E-05	4.82E-04	1.90E-05	1.71E-02	5.0E-04	1.46722	3.4E-05	1.887	2.2E-04	14.8	1099		0.282168	-21.47	2.82	0.714	0.28209	1493
56	0.282181	1.60E-05	9.40E-04	4.30E-05	2.90E-02	9.6E-04	1.46720	2.8E-05	1.886	1.8E-04	19.1	1099		0.282162	-21.36	2.59	0.766	0.28209	1507
59	0.282181	1.30E-05	1.13E-03	7.10E-06	3.69E-02	4.3E-04	1.46723	2.9E-05	1.887	2.2E-04	18.6	1099		0.282158	-21.36	2.45	0.690	0.28209	1515
63	0.282207	1.50E-05	1.72E-03	1.60E-05	5.49E-02	9.8E-04	1.46720	2.4E-05	1.887	2.3E-04	20.1	1099		0.282171	-20.44	2.94	0.740	0.28209	1502
69	0.282195	1.80E-05	1.45E-03	2.00E-05	4.69E-02	4.5E-04	1.46721	2.8E-05	1.886	2.2E-04	17.2	1099		0.282165	-20.86	2.71	0.821	0.28209	1508
73	0.282190	1.50E-05	1.32E-03	2.10E-06	4.48E-02	3.0E-04	1.46720	2.7E-05	1.887	2.2E-04	19.6	1099		0.282163	-21.04	2.63	0.740	0.28209	1510
75	0.282176	1.80E-05	1.36E-03	2.30E-06	4.61E-02	3.6E-04	1.46719	2.8E-05	1.887	2.2E-04	19.4	1099		0.282148	-21.54	2.10	0.821	0.28209	1531
78	0.282216	1.40E-05	1.40E-03	2.20E-06	4.81E-02	5.1E-04	1.46721	2.7E-05	1.887	2.5E-04	19.1	1099		0.282187	-20.12	3.49	0.714	0.28209	1476
80	0.282178	1.40E-05	7.55E-04	5.50E-06	2.41E-02	4.2E-04	1.46719	2.9E-05	1.887	2.7E-04	20.2	1099		0.282162	-21.47	2.62	0.714	0.28209	1504
82	0.282172	1.30E-05	7.44E-04	6.40E-06	2.26E-02	8.6E-05	1.46720	2.5E-05	1.887	2.0E-04	20.6	1099		0.282157	-21.68	2.41	0.690	0.28209	1512
84	0.282174	1.40E-05	5.45E-04	1.20E-05	1.67E-02	3.4E-04	1.46723	2.7E-05	1.886	2.0E-04	22.6	1099		0.282163	-21.61	2.63	0.714	0.28209	1501

	$^{176}Hf/^{177}Hf$	2SE	$^{176}Lu/^{177}Hf$	2SE	$^{176}Yb/^{177}Hf$	2SE	$^{178}Hf/^{177}Hf$	2SE	$^{180}Hf/^{177}Hf$	2SE	Total Hf beam	Age per spot	2SE	Initial	EHfpd	eHf (t)	2SE	CHUR	TDM
86	0.282191	1.40E-05	1.36E-03	1.80E-06	4.73E-02	4.4E-04	1.46725	2.4E-05	1.886	1.9E-04	20.3	1099		0.282163	-21.01	2.63	0.714	0.28209	1510
88	0.282199	1.30E-05	1.20E-03	3.80E-05	3.86E-02	1.0E-03	1.46722	2.4E-05	1.886	1.9E-04	24.4	1099		0.282174	-20.72	3.04	0.690	0.28209	1492
90	0.282201	1.90E-05	2.33E-03	3.90E-05	7.52E-02	9.7E-04	1.46723	3.0E-05	1.886	1.7E-04	22.5	1099		0.282153	-20.65	2.28	0.849	0.28209	1535
94	0.282163	1.20E-05	1.19E-03	5.40E-06	3.70E-02	5.4E-04	1.46721	2.5E-05	1.886	1.6E-04	21.0	1099		0.282138	-22.00	1.77	0.666	0.28209	1542
96	0.282195	1.50E-05	7.32E-04	6.20E-05	2.71E-02	2.2E-03	1.46722	3.0E-05	1.886	2.1E-04	18.6	1099		0.282180	-20.86	3.24	0.740	0.28209	1480
KARA																			
1	0.280943	1.40E-05	4.81E-04	4.30E-06	1.42E-02	2.0E-04	1.46723	2.5E-05	1.887	1.7E-04	19.6	2631		0.280919	-65.14	-6.21	0.713	0.28109	3163
11	0.280964	1.20E-05	6.75E-04	6.10E-05	1.99E-02	1.8E-03	1.46723	2.3E-05	1.886	2.0E-04	23.7	2631		0.280930	-64.40	-5.81	0.665	0.28109	3151
2	0.281004	1.60E-05	1.33E-03	5.90E-05	4.27E-02	1.6E-03	1.46721	3.1E-05	1.887	1.8E-04	20.4	2631		0.280937	-62.98	-5.55	0.765	0.28109	3150
3	0.280971	1.70E-05	8.91E-04	8.00E-06	2.90E-02	5.7E-04	1.46723	2.7E-05	1.886	2.0E-04	18.2	2631		0.280926	-64.15	-5.95	0.792	0.28109	3159
4	0.280952	1.40E-05	4.50E-04	6.40E-06	1.32E-02	1.4E-04	1.46723	3.1E-05	1.886	2.1E-04	20.4	2631		0.280929	-64.82	-5.83	0.713	0.28109	3149
5	0.280962	1.50E-05	5.60E-04	1.00E-05	1.67E-02	2.2E-04	1.46720	2.5E-05	1.886	2.2E-04	20.8	2631		0.280934	-64.47	-5.68	0.738	0.28109	3144
6	0.280939	1.20E-05	3.29E-04	3.60E-06	9.96E-03	1.9E-04	1.46722	2.7E-05	1.886	2.2E-04	25.8	2631		0.280922	-65.28	-6.08	0.665	0.28109	3156
8	0.280966	1.70E-05	7.70E-04	6.90E-06	2.31E-02	1.7E-04	1.46718	2.5E-05	1.887	1.8E-04	19.8	2631		0.280927	-64.32	-5.91	0.792	0.28109	3156
9	0.280933	1.20E-05	4.23E-04	9.50E-06	1.23E-02	3.1E-04	1.46719	2.6E-05	1.886	2.0E-04	23.7	2631		0.280912	-65.49	-6.46	0.665	0.28109	3172
OGC																			
1	0.280609	1.50E-05	5.30E-04	2.60E-05	1.40E-02	6.0E-04	1.46721	2.6E-05	1.887	2.0E-04	16.4	3465		0.280574	-76.95	1.21	0.738	0.28054	3611
10	0.280664	1.60E-05	1.31E-03	2.50E-05	4.06E-02	1.0E-03	1.46722	2.8E-05	1.887	1.9E-04	18.4	3465		0.280577	-75.00	1.33	0.764	0.28054	3610
11	0.280672	1.70E-05	1.63E-03	6.20E-05	5.08E-02	2.1E-03	1.46721	2.7E-05	1.886	2.2E-04	18.3	3465		0.280563	-74.72	0.84	0.791	0.28054	3630
13	0.280617	1.50E-05	7.88E-04	2.00E-05	2.24E-02	2.1E-04	1.46722	3.0E-05	1.887	2.2E-04	16.8	3465		0.280564	-76.67	0.88	0.738	0.28054	3624
2	0.280657	3.20E-05	1.96E-03	2.70E-04	5.60E-02	7.0E-03	1.46724	2.9E-05	1.885	4.9E-04	14.2	3465		0.280526	-75.25	-0.48	1.250	0.28054	3682
5	0.280673	1.90E-05	1.37E-03	3.00E-05	4.27E-02	6.3E-04	1.46722	3.2E-05	1.887	2.3E-04	14.7	3465		0.280581	-74.69	1.49	0.847	0.28054	3604
7	0.280618	1.40E-05	7.27E-04	1.60E-05	1.86E-02	4.3E-04	1.46722	2.5E-05	1.886	1.8E-04	19.6	3465		0.280569	-76.63	1.07	0.712	0.28054	3617
8	0.280625	1.40E-05	9.04E-04	2.40E-05	2.49E-02	1.0E-03	1.46722	2.4E-05	1.887	2.3E-04	18.3	3465		0.280565	-76.38	0.89	0.712	0.28054	3624
9	0.280683	2.20E-05	1.48E-03	3.90E-05	4.69E-02	1.8E-03	1.46720	3.3E-05	1.887	2.7E-04	14.2	3465		0.280584	-74.33	1.60	0.935	0.28054	3600
TAN2																			
91500																			
1	0.282304	2.20E-05	3.42E-04	7.10E-07	1.00E-02	7.6E-05	1.46722	3.8E-05	1.886	2.6E-04	11.9	1065		0.282297	-17.01	6.63	0.937	0.28211	1315
2	0.282308	2.20E-05	3.40E-04	6.30E-07	1.03E-02	6.8E-05	1.46720	5.2E-05	1.886	3.4E-04	12.2	1065		0.282301	-16.87	6.77	0.937	0.28211	1310
3	0.282310	2.30E-05	3.41E-04	7.70E-07	1.00E-02	6.3E-05	1.46722	4.3E-05	1.886	4.7E-04	13.2	1065		0.282303	-16.80	6.84	0.967	0.28211	1307
4	0.282328	2.10E-05	3.42E-04	6.30E-07	9.78E-03	6.1E-05	1.46722	5.0E-05	1.886	4.7E-04	13.0	1065		0.282321	-16.16	7.48	0.907	0.28211	1282
5	0.282307	2.20E-05	3.41E-04	8.30E-07	9.91E-03	1.0E-04	1.46718	4.3E-05	1.886	3.6E-04	13.3	1065		0.282300	-16.90	6.73	0.937	0.28211	1311
6	0.282308	2.30E-05	3.44E-04	1.50E-06	9.56E-03	6.4E-05	1.46719	6.6E-05	1.886	4.5E-04	12.8	1065		0.282301	-16.87	6.77	0.967	0.28211	1310
7	0.282328	2.40E-05	3.42E-04	3.00E-06	1.01E-02	1.3E-04	1.46726	5.7E-05	1.886	4.9E-04	12.9	1065		0.282321	-16.16	7.48	0.998	0.28211	1282
8	0.282302	2.50E-05	3.43E-04	2.80E-06	9.99E-03	1.1E-04	1.46724	5.6E-05	1.886	4.0E-04	13.1	1065		0.282295	-17.08	6.55	1.029	0.28211	1318
FC1																			
1	0.282183	1.40E-05	1.20E-03	1.10E-05	3.97E-02	6.4E-04	1.46721	2.1E-05	1.886	1.6E-04	28.3	1099		0.282158	-21.29	2.47	0.714	0.28209	1515
2	0.282182	1.40E-05	1.14E-03	2.70E-06	3.81E-02	3.2E-04	1.46720	2.2E-05	1.886	2.2E-04	27.2	1099		0.282158	-21.32	2.48	0.714	0.28209	1514
3	0.282185	1.30E-05	1.14E-03	3.00E-06	3.83E-02	4.2E-04	1.46720	2.3E-05	1.886	1.7E-04	27.7	1099		0.282161	-21.22	2.59	0.690	0.28209	1509
4	0.282180	1.20E-05	1.15E-03	7.60E-06	3.88E-02	1.9E-04	1.46721	2.1E-05	1.886	1.9E-04	26.6	1099		0.282156	-21.39	2.40	0.666	0.28209	1517
5	0.282187	1.30E-05	9.47E-04	1.40E-05	2.91E-02	6.3E-04	1.46722	2.3E-05	1.886	2.0E-04	27.4	1099		0.282167	-21.15	2.80	0.690	0.28209	1499
6	0.282175	1.40E-05	8.65E-04	2.00E-05	2.63E-02	7.8E-04	1.46719	2.3E-05	1.886	2.0E-04	27.3	1099		0.282157	-21.57	2.43	0.714	0.28209	1512
7	0.282193	1.60E-05	5.96E-04	6.50E-07	1.88E-02	1.9E-04	1.46721	2.8E-05	1.886	1.9E-04	20.4	1099		0.282181	-20.93	3.27	0.766	0.28209	1477
8	0.282194	1.50E-05	1.40E-03	2.30E-06	4.47E-02	3.9E-04	1.46721	3.8E-05	1.887	1.8E-04	19.3	1099		0.282165	-20.90	2.72	0.740	0.28209	1507
9	0.282174	1.90E-05	1.37E-03	1.40E-06	4.35E-02	2.7E-04	1.46720	2.9E-05	1.886	2.0E-04	19.3	1099		0.282146	-21.61	2.02	0.849	0.28209	1534
OGC																			
1	0.280622	1.60E-05	9.92E-04	7.90E-06	2.84E-02	3.8E-04	1.46718	2.6E-05	1.887	1.9E-04	20.8	3465		0.280556	-76.49	0.58	0.764	0.28054	3637

	$^{176}Hf/^{177}Hf$	2SE	$^{176}Lu/^{177}Hf$	2SE	$^{176}Yb/^{177}Hf$	2SE	$^{178}Hf/^{177}Hf$	2SE	$^{180}Hf/^{177}Hf$	2SE	Total Hf beam	Age per spot	2SE	Initial	EHfpd	eHf (t)	2SE	CHUR	TDM
2	0.280624	1.40E-05	1.04E-03	2.80E-05	2.98E-02	7.4E-04	1.46722	2.6E-05	1.886	2.0E-04	20.5	3465		0.280555	-76.42	0.54	0.712	0.28054	3638
3	0.280642	1.40E-05	1.22E-03	1.00E-04	3.59E-02	3.1E-03	1.46720	2.8E-05	1.886	2.0E-04	23.2	3465		0.280560	-75.78	0.75	0.712	0.28054	3631
4	0.280673	2.00E-05	1.64E-03	1.00E-04	4.96E-02	3.5E-03	1.46722	2.6E-05	1.886	1.8E-04	19.9	3465		0.280563	-74.69	0.85	0.876	0.28054	3629
5	0.280610	1.30E-05	7.59E-04	1.70E-05	2.14E-02	5.6E-04	1.46721	2.8E-05	1.886	1.9E-04	21.6	3465		0.280559	-76.91	0.70	0.688	0.28054	3631
6	0.280634	1.70E-05	1.04E-03	8.70E-05	2.87E-02	2.1E-03	1.46722	2.2E-05	1.886	1.8E-04	22.6	3465		0.280564	-76.06	0.89	0.791	0.28054	3625
7	0.280638	1.40E-05	9.80E-04	2.70E-05	2.53E-02	9.9E-04	1.46718	2.9E-05	1.887	2.0E-04	20.8	3465		0.280573	-75.92	1.18	0.712	0.28054	3614
8	0.280639	1.60E-05	1.05E-03	3.20E-05	3.02E-02	1.0E-03	1.46720	3.0E-05	1.886	1.8E-04	21.8	3465		0.280569	-75.89	1.05	0.764	0.28054	3619
SU04																			
14	0.281074	1.60E-05	1.08E-03	5.40E-05	3.10E-02	1.5E-03	1.46721	2.7E-05	1.886	2.7E-04	21.7	2689	19	0.281019	-60.51	-1.67	0.765	0.28107	3035
20	0.281079	1.60E-05	6.88E-04	3.60E-05	1.99E-02	1.2E-03	1.46722	3.0E-05	1.887	1.7E-04	17.5	2677	21	0.281044	-60.33	-0.78	0.765	0.28107	2998
22	0.281028	1.40E-05	1.19E-03	5.50E-05	3.57E-02	1.4E-03	1.46722	2.9E-05	1.886	2.2E-04	22.1	2666	19	0.280967	-62.13	-3.51	0.713	0.28107	3107
23	0.281073	1.80E-05	1.14E-03	3.10E-05	3.17E-02	6.0E-04	1.46725	3.7E-05	1.886	5.5E-04	18.7	2651	16	0.281015	-60.54	-1.81	0.820	0.28107	3041
25	0.281070	9.70E-06	8.48E-04	1.90E-05	2.40E-02	6.1E-04	1.46723	2.9E-05	1.886	1.6E-04	20.6	2678	17	0.281027	-60.65	-1.39	0.615	0.28107	3023
26	0.281076	1.50E-05	1.03E-03	8.80E-06	2.94E-02	1.9E-04	1.46721	3.1E-05	1.887	1.8E-04	20.0	2666	13	0.281023	-60.43	-1.51	0.738	0.28107	3029
27	0.281071	1.50E-05	9.60E-04	3.60E-05	2.77E-02	1.0E-03	1.46719	2.6E-05	1.887	1.9E-04	18.7	2667	14	0.281022	-60.61	-1.56	0.738	0.28107	3030
3	0.281057	2.70E-05	1.13E-03	2.40E-05	3.18E-02	4.2E-04	1.46733	5.9E-05	1.884	7.6E-04	12.3	2665	34	0.280999	-61.11	-2.37	1.090	0.28107	3063
37	0.281117	1.60E-05	1.34E-03	2.70E-05	3.78E-02	9.0E-04	1.46721	3.1E-05	1.886	2.4E-04	17.8	2648	21	0.281049	-58.98	-0.60	0.765	0.28107	2997
42	0.281023	1.20E-05	8.14E-04	1.60E-05	2.37E-02	4.3E-04	1.46721	2.4E-05	1.886	2.3E-04	22.2	2692	28	0.280981	-62.31	-3.00	0.665	0.28107	3083
53	0.281083	1.50E-05	1.22E-03	2.60E-05	3.47E-02	9.3E-04	1.46721	2.6E-05	1.886	1.9E-04	22.1	2625	13	0.281021	-60.19	-1.61	0.738	0.28107	3034
55	0.281029	1.60E-05	9.29E-04	5.90E-05	2.76E-02	2.1E-03	1.46720	2.2E-05	1.887	1.7E-04	21.6	2686	22	0.280981	-62.10	-3.00	0.765	0.28107	3084
SU10A																			
110	0.281117	1.70E-05	1.37E-03	1.40E-04	4.65E-02	5.9E-03	1.46721	2.7E-05	1.887	1.6E-04	16.2	2649	24	0.281048	-58.98	-1.21	0.792	0.28108	3000
114	0.281132	1.50E-05	1.47E-03	2.70E-05	4.44E-02	6.8E-04	1.46720	3.0E-05	1.886	2.0E-04	18.2	2648	21	0.281058	-58.45	-0.88	0.739	0.28108	2987
143	0.281105	2.00E-05	6.80E-04	6.90E-05	2.10E-02	2.3E-03	1.46721	3.8E-05	1.886	2.2E-04	13.8	2643	21	0.281071	-59.41	-0.52	0.877	0.28109	2962
192	0.281152	2.20E-05	1.85E-03	7.30E-05	6.48E-02	2.8E-03	1.46720	3.1E-05	1.886	2.0E-04	16.9	2662	21	0.281058	-57.75	-0.53	0.936	0.28107	2989
199	0.281109	1.60E-05	1.07E-03	9.70E-05	3.56E-02	3.3E-03	1.46720	3.0E-05	1.886	2.2E-04	18.3	2666	20	0.281054	-59.27	-0.57	0.765	0.28107	2987
200	0.281101	1.80E-05	9.42E-04	4.40E-05	3.32E-02	1.7E-03	1.46721	2.7E-05	1.886	1.9E-04	18.7	2639	17	0.281053	-59.55	-1.24	0.820	0.28109	2988
21	0.281102	1.30E-05	1.08E-03	4.10E-05	3.74E-02	1.8E-03	1.46720	3.1E-05	1.886	1.7E-04	18.6	2650	23	0.281047	-59.52	-1.18	0.688	0.28108	2997
30	0.281140	1.70E-05	1.99E-03	6.80E-05	6.74E-02	2.6E-03	1.46721	2.6E-05	1.886	2.0E-04	16.4	2646	21	0.281039	-58.17	-1.56	0.792	0.28108	3017
58	0.281093	1.40E-05	5.24E-04	5.50E-05	1.68E-02	2.3E-03	1.46719	3.3E-05	1.887	1.8E-04	16.9	2649	19	0.281066	-59.83	-0.54	0.713	0.28108	2967
61	0.280941	1.30E-05	4.26E-04	7.50E-06	1.20E-02	2.9E-04	1.46722	2.9E-05	1.886	2.2E-04	19.8	2808	19	0.280919	-65.21	-5.77	0.688	0.28108	3162
62	0.280939	1.40E-05	3.54E-04	1.20E-05	9.00E-03	2.1E-04	1.46723	3.4E-05	1.886	1.8E-04	18.2	2801	20	0.280921	-65.28	-5.42	0.713	0.28107	3158
75	0.281132	1.80E-05	1.18E-03	7.60E-05	4.12E-02	3.1E-03	1.46719	3.0E-05	1.887	1.7E-04	18.8	2661	17	0.281072	-58.45	-0.05	0.820	0.28107	2964
77	0.281133	2.00E-05	2.60E-03	1.10E-04	1.04E-01	5.9E-03	1.46719	2.7E-05	1.886	1.6E-04	17.4	2652	22	0.281001	-58.42	-2.79	0.877	0.28108	3077
94	0.281114	2.30E-05	1.60E-03	6.10E-05	5.01E-02	3.6E-03	1.46726	3.7E-05	1.886	5.7E-04	16.3	2644	29	0.281033	-59.09	-1.82	0.966	0.28108	3022
SU11																			
1	0.281055	1.40E-05	3.48E-04	1.70E-05	9.19E-03	4.7E-04	1.46720	2.1E-05	1.887	1.8E-04	21.3	2855	22	0.281036	-61.18	3.22	0.713	0.28095	3004
10	0.281073	1.50E-05	6.27E-04	3.60E-05	1.78E-02	1.2E-03	1.46718	2.1E-05	1.886	1.8E-04	23.0	2769	21	0.281040	-60.54	1.33	0.738	0.28100	3001
11	0.280994	2.80E-05	6.28E-04	2.40E-05	1.54E-02	4.7E-04	1.46730	5.2E-05	1.886	3.1E-04	8.7	2909	34	0.280959	-63.33	1.76	1.122	0.28091	3107
12	0.281006	1.90E-05	8.33E-04	5.50E-05	2.29E-02	1.8E-03	1.46722	3.9E-05	1.886	1.9E-04	10.3	2915	26	0.280959	-62.91	1.92	0.848	0.28091	3108
13	0.281011	1.60E-05	7.86E-04	5.30E-05	2.25E-02	1.7E-03	1.46721	4.0E-05	1.886	2.5E-04	19.1	2896	26	0.280967	-62.73	1.75	0.765	0.28092	3097
14	0.281094	1.40E-05	8.87E-04	2.80E-05	2.84E-02	1.3E-03	1.46722	3.1E-05	1.887	1.8E-04	19.1	2762	21	0.281047	-59.80	1.42	0.713	0.28101	2993
15	0.280779	2.60E-05	8.35E-04	5.90E-05	2.79E-02	2.6E-03	1.46718	3.8E-05	1.886	1.9E-04	22.4	3167	19	0.280728	-70.94	-0.37	1.058	0.28074	3412
16	0.281046	1.50E-05	6.34E-04	4.40E-06	1.77E-02	1.9E-04	1.46719	2.6E-05	1.887	1.5E-04	21.4	2841	22	0.281011	-61.50	2.03	0.738	0.28095	3038
17	0.280816	1.50E-05	4.60E-04	3.00E-05	1.36E-02	1.1E-03	1.46721	2.4E-05	1.887	2.4E-04	20.0	3014	17	0.280789	-69.63	-1.80	0.738	0.28084	3330
18	0.281024	1.60E-05	4.02E-04	9.00E-06	1.02E-02	1.7E-04	1.46721	3.0E-05	1.886	1.8E-04	18.2	2857	19	0.281002	-62.27	2.05	0.765	0.28094	3049
19	0.281060	2.80E-05	6.75E-04	3.30E-05	1.65E-02	6.6E-04	1.46720	4.3E-05	1.886	2.2E-04	6.7	2846	24	0.281023	-61.00	2.54	1.122	0.28095	3022

	$^{176}Hf/^{177}Hf$	2SE	$^{176}Lu/^{177}Hf$	2SE	$^{176}Yb/^{177}Hf$	2SE	$^{178}Hf/^{177}Hf$	2SE	$^{180}Hf/^{177}Hf$	2SE	Total Hf beam	Age per spot	2SE	Initial	EHfpd	eHf (t)	2SE	CHUR	TDM
2	0.280915	1.50E-05	7.58E-04	5.40E-05	1.94E-02	1.2E-03	1.46720	2.7E-05	1.886	1.7E-04	20.1	2953	17	0.280872	-66.13	-0.30	0.738	0.28088	3224
20	0.281046	1.30E-05	3.48E-04	6.30E-06	9.96E-03	2.2E-04	1.46722	2.8E-05	1.886	1.7E-04	18.5	2801	19	0.281027	-61.50	1.63	0.688	0.28098	3016
21	0.280969	1.80E-05	4.27E-04	5.40E-06	1.22E-02	2.8E-04	1.46721	2.9E-05	1.887	2.4E-04	18.9	2950	20	0.280945	-64.22	2.23	0.819	0.28088	3124
22	0.280987	1.40E-05	6.48E-04	9.50E-06	1.92E-02	5.4E-04	1.46722	2.8E-05	1.887	2.3E-04	20.5	2947	17	0.280950	-63.58	2.34	0.713	0.28088	3118
23	0.280979	1.70E-05	6.57E-04	2.20E-05	1.90E-02	8.4E-04	1.46720	3.3E-05	1.887	1.8E-04	24.4	2947	18	0.280942	-63.86	2.04	0.792	0.28088	3130
24	0.281045	1.50E-05	3.10E-04	1.00E-05	8.66E-03	2.8E-04	1.46721	2.8E-05	1.887	2.7E-04	25.7	2857	21	0.281028	-61.53	2.99	0.738	0.28094	3014
25	0.281089	1.10E-05	3.69E-04	4.60E-07	1.01E-02	9.6E-05	1.46719	2.7E-05	1.887	1.6E-04	23.9	2830	21	0.281069	-59.97	3.82	0.642	0.28096	2960
26	0.281101	1.10E-05	3.73E-04	9.20E-06	1.06E-02	2.2E-04	1.46721	2.3E-05	1.887	1.6E-04	25.2	2803	21	0.281081	-59.55	3.60	0.642	0.28098	2944
27	0.281095	9.50E-06	2.84E-04	1.90E-06	8.43E-03	1.3E-04	1.46719	2.5E-05	1.886	1.9E-04	26.4	2791	33	0.281079	-59.78	3.27	0.611	0.28099	2946
28	0.281027	1.50E-05	2.27E-04	1.40E-06	6.96E-03	8.9E-05	1.46719	3.6E-05	1.887	2.4E-04	18.2	2834	18	0.281015	-62.17	1.96	0.738	0.28096	3032
29	0.281069	2.50E-05	1.43E-03	7.00E-05	4.57E-02	3.4E-03	1.46722	3.4E-05	1.886	2.0E-04	20.9	2890	27	0.280990	-60.68	2.40	1.027	0.28092	3070
3	0.280932	1.20E-05	1.08E-04	3.20E-06	3.04E-03	7.6E-05	1.46722	1.8E-05	1.887	1.7E-04	21.5	2972	22	0.280926	-65.53	2.07	0.665	0.28087	3148
30	0.280989	2.00E-05	6.45E-04	2.80E-05	1.90E-02	8.8E-04	1.46723	3.6E-05	1.887	1.9E-04	12.8	2905	21	0.280953	-63.51	1.44	0.877	0.28091	3115
31	0.281022	1.40E-05	3.66E-04	5.10E-06	1.03E-02	8.5E-05	1.46719	2.9E-05	1.887	1.6E-04	19.4	2875	19	0.281002	-62.34	2.48	0.713	0.28093	3049
32	0.281007	1.40E-05	5.91E-04	1.90E-06	1.61E-02	2.2E-04	1.46722	2.4E-05	1.887	2.1E-04	20.8	2874	18	0.280974	-62.87	1.47	0.713	0.28093	3087
33	0.281051	1.70E-05	3.51E-04	1.30E-06	9.83E-03	5.3E-05	1.46719	3.0E-05	1.886	2.5E-04	20.3	2798	21	0.281032	-61.32	1.74	0.792	0.28098	3009
35	0.281084	1.70E-05	6.32E-04	1.70E-05	1.79E-02	3.8E-04	1.46720	3.0E-05	1.887	2.0E-04	19.3	2778	23	0.281050	-60.15	1.91	0.792	0.28100	2987
38	0.281059	1.20E-05	5.60E-04	1.30E-05	1.56E-02	4.5E-04	1.46722	2.2E-05	1.887	1.6E-04	20.6	2817	21	0.281029	-61.04	2.07	0.665	0.28097	3015
39	0.280837	2.30E-05	2.27E-03	1.00E-04	7.18E-02	3.6E-03	1.46720	3.1E-05	1.887	1.8E-04	15.6	2997	19	0.280706	-68.89	-5.17	0.966	0.28085	3463
4	0.280909	1.30E-05	2.46E-04	1.10E-05	6.83E-03	2.5E-04	1.46720	2.6E-05	1.887	1.6E-04	23.2	2968	21	0.280895	-66.34	0.88	0.688	0.28087	3189
40	0.280863	1.60E-05	8.50E-04	3.80E-05	2.97E-02	1.4E-03	1.46721	3.1E-05	1.887	2.1E-04	24.0	3360	22	0.280808	-67.97	7.07	0.765	0.28061	3301
41	0.280911	1.60E-05	3.51E-04	4.50E-06	9.18E-03	1.7E-04	1.46723	2.7E-05	1.886	1.9E-04	16.4	2871	21	0.280892	-66.27	-1.55	0.765	0.28094	3195
42	0.280925	1.30E-05	3.82E-04	8.60E-06	9.82E-03	4.2E-04	1.46721	2.1E-05	1.887	2.2E-04	17.7	2872	23	0.280904	-65.77	-1.08	0.688	0.28093	3179
43	0.281081	1.50E-05	2.63E-04	4.50E-06	7.40E-03	2.7E-04	1.46720	2.6E-05	1.886	2.0E-04	21.0	2757	21	0.281067	-60.26	2.03	0.738	0.28101	2963
44	0.280991	1.50E-05	6.20E-04	2.50E-05	1.60E-02	5.7E-04	1.46721	2.8E-05	1.886	1.7E-04	18.3	2948	21	0.280956	-63.44	2.55	0.738	0.28088	3111
46	0.280932	1.40E-05	1.13E-03	2.60E-05	3.42E-02	1.1E-03	1.46719	2.8E-05	1.886	2.1E-04	19.4	3011	17	0.280867	-65.53	0.89	0.713	0.28084	3231
47	0.280962	1.60E-05	1.22E-03	2.20E-05	3.76E-02	5.9E-04	1.46720	2.9E-05	1.886	2.1E-04	19.0	2999	22	0.280892	-64.47	1.49	0.765	0.28085	3199
48	0.280809	1.60E-05	3.74E-04	3.10E-05	1.19E-02	1.1E-03	1.46721	3.1E-05	1.886	2.0E-04	16.9	3181	25	0.280786	-69.88	2.02	0.764	0.28073	3332
5	0.280820	1.50E-05	7.00E-04	1.30E-05	2.01E-02	5.0E-04	1.46722	2.8E-05	1.887	1.8E-04	16.4	3191	26	0.280777	-69.49	1.94	0.738	0.28072	3346
50	0.281081	1.20E-05	6.53E-04	4.30E-06	1.85E-02	2.8E-04	1.46722	2.4E-05	1.887	1.9E-04	21.1	2725	20	0.281047	-60.26	0.56	0.665	0.28103	2993
6	0.280817	1.50E-05	4.32E-04	1.50E-05	1.13E-02	3.8E-04	1.46719	2.5E-05	1.886	1.9E-04	21.3	3020	25	0.280792	-69.59	-1.57	0.738	0.28084	3327
7	0.280805	1.20E-05	6.23E-04	2.00E-05	1.84E-02	5.1E-04	1.46720	2.4E-05	1.887	1.6E-04	19.9	3150	21	0.280767	-70.02	0.63	0.664	0.28075	3359
79	0.281078	1.50E-05	8.00E-04	2.00E-05	2.29E-02	5.6E-04	1.46719	2.8E-05	1.887	2.2E-04	21.4	2812	15	0.281035	-60.36	2.17	0.738	0.28097	3008
8	0.280818	1.90E-05	7.19E-04	2.00E-05	2.10E-02	4.1E-04	1.46723	2.9E-05	1.887	1.8E-04	17.0	3138	26	0.280775	-69.56	0.60	0.848	0.28076	3350
83	0.281056	1.30E-05	3.91E-04	5.20E-06	1.17E-02	2.3E-04	1.46723	2.0E-05	1.886	1.4E-04	24.2	2830	19	0.281035	-61.14	2.60	0.688	0.28096	3006
100	0.281040	1.50E-05	3.38E-04	9.20E-06	1.04E-02	3.8E-04	1.46719	3.4E-05	1.887	2.4E-04	16.0	2838	13	0.281022	-61.71	2.32	0.738	0.28096	3023
101	0.280995	1.60E-05	3.66E-04	5.10E-06	1.10E-02	1.6E-04	1.46720	3.3E-05	1.886	2.3E-04	17.8	2871	18	0.280975	-63.30	1.43	0.765	0.28093	3085
102	0.280994	1.50E-05	2.08E-04	1.60E-06	5.65E-03	5.7E-05	1.46721	2.4E-05	1.886	1.6E-04	18.8	2884	18	0.280982	-63.33	2.01	0.738	0.28093	3074
103	0.281038	1.60E-05	7.51E-04	3.70E-05	2.21E-02	1.1E-03	1.46720	2.9E-05	1.887	2.3E-04	18.9	2835	14	0.280997	-61.78	1.37	0.765	0.28096	3058
104	0.281031	1.10E-05	5.95E-04	1.40E-05	1.72E-02	3.5E-04	1.46721	2.8E-05	1.886	2.6E-04	18.6	2842	17	0.280999	-62.03	1.59	0.642	0.28095	3055
109	0.281034	1.70E-05	6.63E-04	1.50E-05	1.93E-02	3.4E-04	1.46724	2.8E-05	1.886	2.4E-04	15.8	2872	18	0.280997	-61.92	2.25	0.792	0.28093	3056
112	0.280465	1.50E-05	4.90E-04	8.90E-06	1.52E-02	2.9E-04	1.46721	3.0E-05	1.887	1.8E-04	19.0	3619	13	0.280431	-82.04	-0.20	0.738	0.28044	3797
113	0.281026	1.60E-05	3.53E-04	8.40E-06	9.91E-03	2.0E-04	1.46718	2.9E-05	1.886	2.1E-04	17.6	2794	15	0.281007	-62.20	0.76	0.765	0.28099	3043
117	0.281090	1.40E-05	4.26E-04	7.20E-06	1.26E-02	2.0E-04	1.46722	3.2E-05	1.887	1.7E-04	16.3	2712	24	0.281068	-59.94	0.99	0.713	0.28104	2963
118	0.281094	2.10E-05	1.25E-03	7.70E-05	4.78E-02	2.9E-03	1.46720	3.1E-05	1.886	2.8E-04	16.9	2741	13	0.281028	-59.80	0.26	0.906	0.28102	3022
124	0.281056	1.60E-05	9.17E-04	1.30E-05	2.66E-02	4.5E-04	1.46725	3.4E-05	1.887	1.7E-04	16.8	2826	25	0.281006	-61.14	1.49	0.765	0.28096	3047
125	0.280898	1.60E-05	2.35E-04	3.70E-06	6.19E-03	9.9E-05	1.46724	3.1E-05	1.887	1.7E-04	14.6	3005	18	0.280884	-66.73	1.36	0.765	0.28085	3203

	$^{176}Hf/^{177}Hf$	2SE	$^{176}Lu/^{177}Hf$	2SE	$^{176}Yb/^{177}Hf$	2SE	$^{178}Hf/^{177}Hf$	2SE	$^{180}Hf/^{177}Hf$	2SE	Total Hf beam	Age per spot	2SE	Initial	EHfpd	eHf (t)	2SE	CHUR	TDM
131	0.280843	1.60E-05	4.40E-04	6.80E-06	1.29E-02	1.5E-04	1.46719	2.8E-05	1.887	1.9E-04	16.6	2855	21	0.280819	-68.67	-4.51	0.765	0.28095	3293
132	0.280873	1.40E-05	8.32E-04	1.20E-05	2.45E-02	5.0E-04	1.46720	3.5E-05	1.887	2.4E-04	16.1	2852	19	0.280827	-67.61	-4.26	0.713	0.28095	3286
133	0.281022	1.40E-05	8.30E-04	1.50E-05	2.57E-02	4.1E-04	1.46722	2.7E-05	1.887	1.8E-04	19.2	2877	28	0.280976	-62.34	1.62	0.713	0.28093	3086
135	0.280998	1.50E-05	1.15E-03	1.40E-04	3.93E-02	5.3E-03	1.46724	2.5E-05	1.886	2.1E-04	17.3	2709	30	0.280938	-63.19	-3.68	0.738	0.28104	3144
136	0.280869	1.50E-05	6.39E-04	3.10E-05	1.76E-02	7.1E-04	1.46721	3.0E-05	1.887	1.8E-04	19.9	3121	31	0.280831	-67.75	2.20	0.738	0.28077	3275
138	0.281078	2.00E-05	1.20E-03	1.40E-05	3.51E-02	6.9E-04	1.46718	3.3E-05	1.887	2.9E-04	15.3	2857	15	0.281012	-60.36	2.43	0.877	0.28094	3039
139	0.281117	2.00E-05	1.67E-03	3.80E-05	4.81E-02	1.6E-03	1.46720	3.3E-05	1.887	2.2E-04	15.7	2860	15	0.281025	-58.98	2.96	0.877	0.28094	3023
141	0.280821	1.40E-05	4.41E-04	2.80E-05	1.23E-02	8.0E-04	1.46721	3.2E-05	1.887	2.2E-04	18.0	3121	16	0.280795	-69.45	0.91	0.713	0.28077	3322
142	0.280937	1.70E-05	1.72E-03	2.40E-05	5.29E-02	4.0E-04	1.46722	3.3E-05	1.886	2.7E-04	16.7	3114	18	0.280834	-65.35	2.15	0.792	0.28077	3275
143	0.280976	1.90E-05	2.03E-03	1.80E-05	6.29E-02	8.4E-04	1.46722	2.9E-05	1.886	1.8E-04	18.2	3110	16	0.280855	-63.97	2.78	0.848	0.28078	3248
144	0.281021	1.60E-05	9.21E-04	4.40E-05	2.91E-02	1.8E-03	1.46719	2.3E-05	1.887	2.2E-04	16.6	2850	17	0.280971	-62.38	0.78	0.765	0.28095	3094
149	0.281041	1.90E-05	1.30E-03	4.50E-05	4.11E-02	2.0E-03	1.46720	3.0E-05	1.887	2.0E-04	16.2	2938	17	0.280968	-61.67	2.74	0.848	0.28089	3098
152	0.280896	1.40E-05	5.98E-04	9.30E-06	1.71E-02	4.6E-04	1.46722	2.8E-05	1.887	2.6E-04	17.6	2914	15	0.280863	-66.80	-1.56	0.713	0.28091	3236
153	0.280883	1.50E-05	8.43E-04	2.90E-05	2.55E-02	5.2E-04	1.46721	3.0E-05	1.886	2.4E-04	17.8	3017	21	0.280834	-67.26	-0.15	0.738	0.28084	3274
155	0.280974	1.50E-05	3.85E-04	1.50E-05	1.10E-02	5.7E-04	1.46720	3.5E-05	1.887	2.5E-04	16.5	2776	15	0.280954	-64.04	-1.57	0.738	0.28100	3114
159	0.281027	1.20E-05	3.55E-04	8.20E-06	1.10E-02	3.9E-04	1.46718	3.0E-05	1.887	2.6E-04	18.7	2724	15	0.281008	-62.17	-0.83	0.665	0.28103	3042
162	0.281060	1.60E-05	8.13E-04	2.50E-05	2.45E-02	6.2E-04	1.46722	3.3E-05	1.887	2.3E-04	16.3	2849	18	0.281016	-61.00	2.36	0.765	0.28095	3033
163	0.281000	1.30E-05	3.54E-04	1.70E-05	9.65E-03	6.0E-04	1.46719	2.7E-05	1.886	2.2E-04	18.9	2883	21	0.280980	-63.12	1.90	0.688	0.28093	3077
167	0.281052	1.70E-05	8.12E-04	6.30E-05	2.30E-02	2.9E-03	1.46724	3.5E-05	1.887	1.9E-04	11.7	2811	14	0.281008	-61.28	1.20	0.792	0.28097	3044
170	0.281001	1.40E-05	5.47E-04	1.00E-05	1.64E-02	4.7E-04	1.46719	3.0E-05	1.887	1.9E-04	19.1	2890	25	0.280971	-63.09	1.73	0.713	0.28092	3091
171	0.281032	1.50E-05	6.16E-04	3.10E-05	1.73E-02	8.8E-04	1.46722	3.1E-05	1.887	2.1E-04	16.9	2904	19	0.280998	-61.99	3.00	0.738	0.28091	3055
172	0.281096	1.70E-05	9.88E-04	5.60E-05	2.81E-02	1.6E-03	1.46721	2.6E-05	1.886	2.6E-04	18.7	2826	16	0.281042	-59.73	2.77	0.792	0.28096	2998
178	0.281070	1.70E-05	9.64E-04	2.10E-05	2.94E-02	7.1E-04	1.46721	3.1E-05	1.886	2.4E-04	18.3	2770	21	0.281019	-60.65	0.60	0.792	0.28100	3032
179	0.281061	1.40E-05	3.47E-04	4.20E-06	1.02E-02	8.0E-05	1.46723	2.7E-05	1.886	1.9E-04	16.7	2736	16	0.281043	-60.97	0.66	0.713	0.28102	2996
180	0.281019	1.20E-05	5.52E-04	4.10E-06	1.56E-02	1.8E-04	1.46722	2.9E-05	1.887	2.0E-04	19.9	2837	14	0.280989	-62.45	1.13	0.665	0.28096	3068
182	0.280624	1.50E-05	4.31E-04	5.50E-06	1.26E-02	1.6E-04	1.46721	2.4E-05	1.887	2.2E-04	20.1	3025	17	0.280599	-76.42	-8.33	0.738	0.28083	3582
183	0.281059	1.60E-05	3.62E-04	7.90E-06	1.07E-02	2.3E-04	1.46723	2.5E-05	1.886	2.6E-04	20.9	2731	23	0.281040	-61.04	0.45	0.765	0.28103	3000
184	0.280914	1.70E-05	6.88E-04	1.80E-05	2.06E-02	8.6E-04	1.46719	2.6E-05	1.886	2.5E-04	19.2	2919	18	0.280875	-66.16	-0.97	0.792	0.28090	3219
187	0.281066	1.60E-05	3.77E-04	3.20E-06	1.08E-02	1.4E-04	1.46721	2.5E-05	1.886	2.1E-04	18.9	2786	15	0.281046	-60.79	1.94	0.765	0.28099	2991
188	0.281071	1.80E-05	1.11E-03	3.70E-05	3.66E-02	1.8E-03	1.46720	2.9E-05	1.887	2.0E-04	18.1	2901	17	0.281009	-60.61	3.36	0.820	0.28091	3042
189	0.281089	1.60E-05	6.79E-04	4.50E-05	2.06E-02	1.4E-03	1.46721	3.3E-05	1.886	1.9E-04	18.9	2751	15	0.281053	-59.97	1.38	0.765	0.28101	2984
190	0.281074	1.60E-05	5.10E-04	9.20E-06	1.54E-02	3.7E-04	1.46721	2.3E-05	1.886	2.6E-04	19.2	2750	17	0.281047	-60.51	1.14	0.765	0.28102	2991
191	0.281094	1.70E-05	5.11E-04	1.40E-05	1.48E-02	5.7E-04	1.46722	3.1E-05	1.886	1.9E-04	15.8	2741	15	0.281067	-59.80	1.65	0.792	0.28102	2964
192	0.281042	1.90E-05	1.32E-03	2.00E-05	3.73E-02	9.1E-04	1.46721	3.9E-05	1.886	1.6E-04	16.0	2863	17	0.280970	-61.64	1.05	0.848	0.28094	3098
193	0.281059	1.30E-05	6.03E-04	1.80E-05	1.75E-02	6.2E-04	1.46719	3.0E-05	1.887	1.7E-04	21.8	2700	16	0.281028	-61.04	-0.71	0.688	0.28105	3018
195	0.280674	1.50E-05	7.86E-04	2.90E-05	2.59E-02	1.4E-03	1.46722	2.8E-05	1.887	2.3E-04	19.1	3112	14	0.280627	-74.65	-5.26	0.738	0.28077	3548
196	0.280791	1.30E-05	2.97E-04	1.60E-05	8.65E-03	6.7E-04	1.46721	2.7E-05	1.886	2.7E-04	20.4	3202	15	0.280773	-70.51	2.06	0.688	0.28071	3350
197	0.280776	1.10E-05	2.30E-04	4.10E-06	5.74E-03	1.8E-04	1.46720	2.3E-05	1.887	1.6E-04	25.8	3201	13	0.280762	-71.04	1.65	0.642	0.28072	3364
198	0.281023	1.30E-05	1.47E-03	4.00E-05	4.64E-02	1.1E-03	1.46723	2.6E-05	1.886	1.9E-04	18.6	2844	13	0.280943	-62.31	-0.37	0.688	0.28095	3137
199	0.281035	1.80E-05	1.55E-03	2.00E-05	4.96E-02	7.9E-04	1.46720	2.7E-05	1.887	2.4E-04	18.1	2842	13	0.280951	-61.88	-0.11	0.819	0.28095	3126
200	0.280777	2.80E-05	1.09E-03	6.10E-05	3.56E-02	2.8E-03	1.46719	3.4E-05	1.886	3.7E-04	20.0	3151	26	0.280711	-71.01	-1.36	1.122	0.28075	3437
202	0.280801	2.00E-05	1.57E-03	1.10E-04	4.87E-02	3.6E-03	1.46717	2.7E-05	1.887	2.0E-04	16.6	3119	30	0.280707	-70.16	-2.27	0.876	0.28077	3448
204	0.280494	2.20E-05	7.63E-04	5.40E-05	2.37E-02	1.3E-03	1.46721	2.5E-05	1.886	1.4E-04	17.6	3383	21	0.280444	-81.02	-5.35	0.935	0.28059	3785
205	0.280498	2.30E-05	8.91E-04	7.40E-05	2.79E-02	1.9E-03	1.46719	2.8E-05	1.886	1.9E-04	18.6	3349	15	0.280441	-80.87	-6.30	0.965	0.28062	3792
206	0.280790	1.30E-05	3.30E-04	1.70E-05	9.99E-03	7.1E-04	1.46720	2.8E-05	1.886	1.7E-04	22.2	3164	29	0.280770	-70.55	1.06	0.688	0.28074	3354
207	0.280799	1.40E-05	3.12E-04	4.30E-06	8.80E-03	2.1E-04	1.46721	2.6E-05	1.887	1.6E-04	22.7	3084	22	0.280781	-70.23	-0.46	0.713	0.28079	3340
209	0.280874	1.60E-05	5.28E-04	1.70E-05	1.50E-02	6.4E-04	1.46721	2.8E-05	1.887	1.6E-04	18.8	2969	29	0.280844	-67.58	-0.93	0.765	0.28087	3259

	$^{176}Hf/^{177}Hf$	2SE	$^{176}Lu/^{177}Hf$	2SE	$^{176}Yb/^{177}Hf$	2SE	$^{178}Hf/^{177}Hf$	2SE	$^{180}Hf/^{177}Hf$	2SE	Total Hf beam	Age per spot	2SE	Initial	EHfpd	eHf (t)	2SE	CHUR	TDM
210	0.280927	1.50E-05	2.01E-04	2.60E-06	5.24E-03	1.3E-04	1.46720	2.6E-05	1.886	1.8E-04	19.1	2952	34	0.280916	-65.70	1.23	0.738	0.28088	3162
212	0.281105	2.60E-05	1.30E-03	8.20E-05	3.56E-02	2.5E-03	1.46722	3.1E-05	1.886	2.7E-04	10.9	2843	24	0.281034	-59.41	2.88	1.059	0.28095	3011
214	0.280443	1.30E-05	2.97E-04	3.20E-05	1.11E-02	1.6E-03	1.46721	2.9E-05	1.886	2.4E-04	15.6	3690	13	0.280422	-82.82	1.17	0.688	0.28039	3807
217	0.281016	1.60E-05	8.34E-04	4.00E-05	2.25E-02	1.1E-03	1.46721	2.8E-05	1.887	1.6E-04	18.9	2901	16	0.280970	-62.56	1.93	0.765	0.28092	3094
52	0.280926	1.80E-05	5.28E-04	1.70E-05	1.57E-02	4.4E-04	1.46722	2.7E-05	1.887	2.3E-04	15.2	2748	16	0.280898	-65.74	-4.21	0.819	0.28102	3190
53	0.281107	1.50E-05	9.03E-04	3.10E-05	2.41E-02	5.7E-04	1.46722	3.1E-05	1.887	1.8E-04	13.8	2763	18	0.281059	-59.34	1.89	0.739	0.28101	2977
55	0.281065	1.50E-05	2.91E-04	1.30E-05	8.43E-03	6.7E-04	1.46719	3.0E-05	1.887	2.3E-04	17.7	2767	22	0.281050	-60.82	1.64	0.738	0.28100	2986
56	0.281011	1.60E-05	4.06E-04	2.80E-05	1.09E-02	6.1E-04	1.46722	2.9E-05	1.887	2.0E-04	15.8	2855	16	0.280989	-62.73	1.54	0.765	0.28095	3067
57	0.281015	1.40E-05	4.60E-04	2.90E-05	1.29E-02	1.0E-03	1.46721	3.2E-05	1.887	2.7E-04	15.1	2854	16	0.280990	-62.59	1.57	0.713	0.28095	3066
59	0.281011	1.30E-05	4.10E-04	1.30E-05	1.28E-02	3.4E-04	1.46724	2.8E-05	1.887	2.0E-04	20.4	2800	19	0.280989	-62.73	0.24	0.688	0.28098	3067
60	0.281026	1.50E-05	4.73E-04	4.10E-06	1.35E-02	3.1E-04	1.46722	2.9E-05	1.887	2.2E-04	17.4	2806	12	0.281001	-62.20	0.81	0.738	0.28098	3052
61	0.281000	1.60E-05	3.55E-04	1.30E-05	1.12E-02	7.3E-04	1.46721	2.8E-05	1.887	2.2E-04	19.1	2798	14	0.280981	-63.12	-0.07	0.765	0.28098	3078
62	0.281014	1.80E-05	3.97E-04	1.00E-05	1.18E-02	1.8E-04	1.46721	3.5E-05	1.886	3.1E-04	15.8	2874	20	0.280992	-62.63	2.11	0.819	0.28093	3062
65	0.281024	1.50E-05	1.15E-03	2.20E-05	3.40E-02	7.4E-04	1.46722	3.0E-05	1.887	2.0E-04	14.2	2962	21	0.280959	-62.27	2.99	0.738	0.28087	3109
66	0.280392	1.50E-05	6.34E-04	1.00E-05	1.88E-02	2.0E-04	1.46720	2.4E-05	1.886	2.5E-04	22.2	3822	12	0.280345	-84.62	1.62	0.738	0.28030	3907
67	0.280377	1.70E-05	6.14E-04	1.80E-05	1.88E-02	3.5E-04	1.46720	2.4E-05	1.887	2.5E-04	21.0	3812	14	0.280332	-85.15	0.89	0.791	0.28031	3925
68	0.281066	1.50E-05	1.66E-03	1.50E-04	5.48E-02	5.8E-03	1.46718	4.1E-05	1.886	2.7E-04	15.7	2826	21	0.280976	-60.79	0.40	0.738	0.28096	3093
69	0.281033	1.70E-05	5.34E-04	2.40E-05	1.59E-02	1.1E-03	1.46722	3.2E-05	1.886	2.1E-04	14.9	2886	13	0.281003	-61.96	2.81	0.792	0.28092	3048
70	0.280762	1.60E-05	2.76E-04	1.70E-05	7.21E-03	5.4E-04	1.46720	2.7E-05	1.886	2.5E-04	16.4	3037	13	0.280746	-71.54	-2.81	0.764	0.28082	3386
71	0.280830	2.00E-05	1.71E-03	7.00E-05	4.78E-02	3.6E-03	1.46722	3.4E-05	1.887	2.7E-04	14.2	3017	14	0.280731	-69.13	-3.83	0.876	0.28084	3422
72	0.281050	1.50E-05	8.82E-04	6.50E-06	2.78E-02	4.5E-04	1.46721	2.3E-05	1.887	1.9E-04	17.3	2858	15	0.281002	-61.35	2.08	0.738	0.28094	3052
73	0.280478	1.50E-05	5.29E-04	7.30E-06	1.57E-02	1.1E-04	1.46718	2.9E-05	1.887	2.2E-04	20.1	3511	13	0.280442	-81.58	-2.38	0.738	0.28051	3784
74	0.280478	1.20E-05	3.53E-04	7.00E-07	1.04E-02	1.4E-04	1.46719	3.1E-05	1.886	2.4E-04	20.8	3524	16	0.280454	-81.58	-1.63	0.664	0.28050	3767
77	0.280814	1.20E-05	5.50E-04	1.70E-05	1.71E-02	4.8E-04	1.46720	3.0E-05	1.886	2.3E-04	19.0	2962	14	0.280783	-69.70	-3.28	0.665	0.28087	3341
80	0.281001	1.50E-05	4.13E-04	2.50E-06	1.20E-02	2.3E-04	1.46722	2.7E-05	1.887	2.8E-04	16.7	2879	15	0.280978	-63.09	1.73	0.738	0.28093	3081
81	0.281053	1.30E-05	5.92E-04	1.80E-05	1.77E-02	4.5E-04	1.46721	3.1E-05	1.886	2.0E-04	17.9	2800	17	0.281021	-61.25	1.40	0.688	0.28098	3025
82	0.280944	1.70E-05	5.78E-04	2.10E-05	1.73E-02	4.7E-04	1.46722	3.2E-05	1.886	2.2E-04	14.1	2846	21	0.280912	-65.10	-1.40	0.792	0.28095	3170
84	0.281041	1.90E-05	1.21E-03	4.40E-06	3.47E-02	4.4E-04	1.46723	3.0E-05	1.886	1.8E-04	14.8	2892	14	0.280974	-61.67	1.88	0.848	0.28092	3090
85	0.280774	1.70E-05	4.95E-04	1.20E-05	1.49E-02	3.3E-04	1.46722	2.8E-05	1.887	1.7E-04	18.3	3102	15	0.280744	-71.11	-1.32	0.791	0.28078	3389
86	0.280922	1.00E-05	4.42E-04	7.10E-06	1.15E-02	1.6E-04	1.46719	2.9E-05	1.887	1.5E-04	23.2	2961	15	0.280897	-65.88	0.76	0.621	0.28088	3188
87	0.281123	2.30E-05	1.48E-03	5.30E-05	3.99E-02	1.6E-03	1.46718	3.3E-05	1.886	2.7E-04	16.5	2705	15	0.281047	-58.77	0.07	0.966	0.28104	3000
88	0.281034	1.20E-05	3.14E-04	9.60E-07	8.12E-03	1.1E-04	1.46723	2.6E-05	1.887	2.5E-04	21.8	2728	15	0.281018	-61.92	-0.43	0.665	0.28103	3029
89	0.280871	1.40E-05	2.63E-04	2.00E-06	7.27E-03	9.7E-05	1.46720	3.2E-05	1.887	2.2E-04	16.9	2978	25	0.280856	-67.68	-0.28	0.713	0.28086	3241
90	0.280866	1.30E-05	4.94E-04	1.30E-05	1.39E-02	2.7E-04	1.46721	2.6E-05	1.886	2.3E-04	21.6	2881	15	0.280839	-67.86	-3.19	0.688	0.28093	3267
92	0.281119	1.50E-05	8.36E-04	6.20E-05	2.86E-02	2.7E-03	1.46720	2.3E-05	1.887	2.3E-04	19.4	2706	21	0.281076	-58.91	1.13	0.739	0.28104	2955
93	0.281066	1.50E-05	3.14E-04	2.60E-06	9.55E-03	5.0E-05	1.46717	2.5E-05	1.887	1.7E-04	19.6	2876	16	0.281049	-60.79	4.17	0.738	0.28093	2987
94	0.280929	1.40E-05	4.03E-04	1.00E-05	1.12E-02	2.5E-04	1.46723	2.7E-05	1.887	2.0E-04	18.3	3015	24	0.280906	-65.63	2.36	0.713	0.28084	3176
95	0.280994	1.60E-05	2.61E-04	6.40E-06	7.10E-03	2.6E-04	1.46722	2.8E-05	1.887	2.0E-04	17.8	2907	26	0.280979	-63.33	2.44	0.765	0.28091	3078
96	0.280996	1.50E-05	3.00E-04	5.80E-06	8.82E-03	1.5E-04	1.46720	2.7E-05	1.887	2.1E-04	18.2	2728	18	0.280980	-63.26	-1.75	0.738	0.28103	3079
98	0.281051	1.50E-05	9.74E-04	5.30E-06	2.91E-02	1.5E-04	1.46718	2.8E-05	1.887	1.9E-04	16.7	2812	17	0.280999	-61.32	0.87	0.738	0.28097	3058
SU20																			
0	0.280992	1.60E-05	6.76E-04	2.70E-05	2.03E-02	1.0E-03	1.46718	3.0E-05	1.887	1.8E-04	16.7	2733	17	0.280957	-63.41	-2.47	0.765	0.28103	3114
1	0.280979	1.30E-05	4.67E-04	1.60E-05	1.41E-02	4.0E-04	1.46722	3.1E-05	1.887	1.8E-04	18.6	2961	16	0.280952	-63.86	2.76	0.688	0.28088	3114
100	0.280914	1.20E-05	6.39E-04	1.20E-05	2.00E-02	2.6E-04	1.46721	3.2E-05	1.887	1.7E-04	20.4	2953	15	0.280878	-66.16	-0.10	0.665	0.28088	3215
101	0.280893	1.40E-05	3.09E-04	1.00E-05	9.21E-03	3.8E-04	1.46721	3.1E-05	1.886	2.1E-04	16.2	2960	19	0.280875	-66.91	-0.01	0.713	0.28088	3216
102	0.281024	1.50E-05	2.54E-04	5.30E-06	7.78E-03	3.2E-04	1.46720	2.7E-05	1.887	1.8E-04	18.2	2793	33	0.281010	-62.27	0.86	0.738	0.28099	3038
103	0.281101	1.30E-05	3.35E-04	1.40E-05	1.02E-02	2.8E-04	1.46722	2.4E-05	1.886	2.2E-04	17.6	2713	16	0.281084	-59.55	1.58	0.688	0.28104	2942

	$^{176}Hf/^{177}Hf$	2SE	$^{176}Lu/^{177}Hf$	2SE	$^{176}Yb/^{177}Hf$	2SE	$^{178}Hf/^{177}Hf$	2SE	$^{180}Hf/^{177}Hf$	2SE	Total Hf beam	Age per spot	2SE	Initial	EHfpd	eHf (t)	2SE	CHUR	TDM
104	0.281090	1.30E-05	1.80E-04	1.20E-06	5.03E-03	6.1E-05	1.46720	2.3E-05	1.887	1.8E-04	19.9	2710	23	0.281081	-59.94	1.41	0.688	0.28104	2945
105	0.281069	1.40E-05	8.90E-04	1.10E-04	2.68E-02	4.3E-03	1.46720	2.6E-05	1.886	2.3E-04	21.9	2834	16	0.281021	-60.68	2.19	0.713	0.28096	3027
106	0.280934	1.30E-05	7.88E-04	9.90E-06	2.52E-02	4.6E-04	1.46722	2.6E-05	1.886	2.1E-04	19.2	2715	19	0.280893	-65.46	-5.15	0.688	0.28104	3201
109	0.281211	4.30E-05	2.51E-03	2.60E-04	9.20E-02	1.3E-02	1.46720	3.6E-05	1.886	2.5E-04	13.9	2842	19	0.281074	-55.66	4.27	1.618	0.28095	2960
11	0.281142	1.80E-05	1.02E-03	3.30E-05	3.04E-02	1.2E-03	1.46717	2.6E-05	1.887	1.7E-04	17.7	2769	22	0.281088	-58.10	3.04	0.820	0.28100	2938
111	0.281094	1.50E-05	6.48E-04	1.80E-05	2.06E-02	9.5E-04	1.46718	2.9E-05	1.886	1.8E-04	18.4	2680	16	0.281061	-59.80	-0.01	0.739	0.28106	2975
112	0.281068	1.40E-05	7.40E-04	2.10E-05	2.27E-02	7.2E-04	1.46721	3.0E-05	1.886	1.8E-04	20.3	2767	18	0.281029	-60.72	0.89	0.713	0.28100	3017
115	0.280878	1.20E-05	5.57E-04	9.40E-06	1.60E-02	2.4E-04	1.46718	2.9E-05	1.886	1.7E-04	21.0	3018	13	0.280846	-67.44	0.31	0.665	0.28084	3256
117	0.281067	1.90E-05	8.70E-04	5.70E-05	2.38E-02	1.6E-03	1.46722	2.5E-05	1.887	2.2E-04	20.2	2829	26	0.281020	-60.75	2.04	0.848	0.28096	3028
12	0.281200	2.10E-05	1.73E-03	5.70E-05	5.33E-02	1.7E-03	1.46719	2.6E-05	1.887	1.7E-04	16.6	2792	19	0.281107	-56.05	4.27	0.906	0.28099	2914
120	0.281026	1.10E-05	2.35E-04	2.30E-05	7.38E-03	8.8E-04	1.46719	2.5E-05	1.887	1.7E-04	24.5	2863	17	0.281013	-62.20	2.59	0.642	0.28094	3034
121	0.280870	1.30E-05	4.62E-04	3.40E-05	1.21E-02	9.4E-04	1.46722	3.1E-05	1.887	2.2E-04	20.2	2865	18	0.280845	-67.72	-3.35	0.688	0.28094	3259
122	0.281070	1.50E-05	2.05E-04	4.10E-06	5.34E-03	9.0E-05	1.46720	2.9E-05	1.886	1.9E-04	18.6	2807	22	0.281059	-60.65	2.91	0.738	0.28098	2973
123	0.281007	1.10E-05	2.31E-04	2.20E-06	6.16E-03	1.1E-04	1.46720	2.8E-05	1.886	1.9E-04	17.8	2826	32	0.280994	-62.87	1.06	0.642	0.28096	3059
126	0.280850	2.10E-05	3.71E-04	9.80E-06	9.53E-03	2.1E-04	1.46722	3.0E-05	1.887	1.8E-04	12.3	2855	17	0.280830	-68.43	-4.12	0.906	0.28095	3278
13	0.280548	1.50E-05	9.85E-04	3.80E-06	3.23E-02	3.2E-04	1.46722	3.1E-05	1.887	1.8E-04	17.7	3341	16	0.280485	-79.11	-4.92	0.738	0.28062	3735
130	0.280952	1.60E-05	8.99E-04	3.60E-05	2.75E-02	1.5E-03	1.46720	3.0E-05	1.886	2.2E-04	17.1	2733	15	0.280905	-64.82	-4.31	0.765	0.28103	3186
131	0.281072	1.50E-05	3.78E-04	1.10E-05	1.02E-02	3.5E-04	1.46719	3.0E-05	1.886	1.8E-04	18.2	2786	20	0.281052	-60.58	2.16	0.738	0.28099	2984
134	0.280941	1.30E-05	1.42E-04	1.30E-06	4.71E-03	4.0E-05	1.46723	2.7E-05	1.887	1.6E-04	20.1	2928	15	0.280933	-65.21	1.28	0.688	0.28090	3139
135	0.280450	1.30E-05	7.15E-04	3.40E-05	2.37E-02	1.6E-03	1.46720	2.6E-05	1.886	1.8E-04	20.8	3568	12	0.280401	-82.57	-2.50	0.688	0.28047	3839
136	0.281080	1.90E-05	6.55E-04	3.30E-05	1.83E-02	8.3E-04	1.46720	3.2E-05	1.886	2.1E-04	13.1	2719	22	0.281046	-60.29	0.38	0.848	0.28104	2994
138	0.280993	1.30E-05	8.67E-04	2.60E-05	2.52E-02	5.7E-04	1.46718	3.2E-05	1.886	1.5E-04	19.5	2939	16	0.280944	-63.37	1.93	0.688	0.28089	3128
139	0.280984	1.30E-05	8.31E-04	1.50E-05	2.26E-02	3.5E-04	1.46721	2.2E-05	1.886	1.8E-04	18.5	2943	15	0.280937	-63.69	1.78	0.688	0.28089	3137
14	0.280993	1.10E-05	4.08E-04	1.10E-05	1.27E-02	5.8E-04	1.46720	3.0E-05	1.887	1.7E-04	17.6	2842	19	0.280971	-63.37	0.59	0.642	0.28095	3091
140	0.280761	1.40E-05	5.39E-04	2.00E-05	1.73E-02	8.2E-04	1.46719	3.0E-05	1.886	1.8E-04	17.4	3240	18	0.280727	-71.57	1.34	0.713	0.28069	3410
141	0.280944	1.30E-05	8.02E-04	4.60E-05	2.28E-02	1.7E-03	1.46721	2.9E-05	1.887	1.7E-04	18.8	3033	19	0.280897	-65.10	2.48	0.688	0.28083	3188
142	0.280998	1.60E-05	5.15E-04	2.70E-05	1.57E-02	7.0E-04	1.46721	2.5E-05	1.886	2.2E-04	19.1	2901	19	0.280969	-63.19	1.93	0.765	0.28092	3093
146	0.281077	1.70E-05	8.95E-04	6.50E-05	2.85E-02	2.2E-03	1.46723	2.6E-05	1.886	1.6E-04	22.3	2749	18	0.281030	-60.40	0.50	0.792	0.28102	3017
147	0.281011	1.20E-05	1.90E-04	7.90E-06	4.77E-03	3.1E-04	1.46720	2.6E-05	1.886	1.5E-04	17.5	2884	24	0.281000	-62.73	2.64	0.665	0.28093	3050
149	0.281039	1.40E-05	1.17E-03	1.30E-05	2.91E-02	1.9E-04	1.46723	2.3E-05	1.886	1.8E-04	20.4	2862	17	0.280975	-61.74	1.21	0.713	0.28094	3090
15	0.280750	1.50E-05	4.83E-04	1.60E-05	1.51E-02	4.1E-04	1.46720	2.9E-05	1.886	2.0E-04	16.7	2892	18	0.280723	-71.96	-7.05	0.738	0.28092	3420
152	0.281016	1.40E-05	3.88E-04	3.60E-05	1.17E-02	1.7E-03	1.46719	2.1E-05	1.887	1.6E-04	25.0	2849	19	0.280995	-62.56	1.62	0.713	0.28095	3059
155	0.281055	1.40E-05	6.16E-04	2.10E-05	1.80E-02	9.2E-04	1.46720	3.0E-05	1.886	1.9E-04	17.9	2719	14	0.281023	-61.18	-0.44	0.713	0.28104	3025
156	0.281024	1.60E-05	3.97E-04	1.20E-05	1.16E-02	4.6E-04	1.46722	3.4E-05	1.886	1.7E-04	19.6	2740	16	0.281003	-62.27	-0.66	0.765	0.28102	3049
158	0.280862	1.50E-05	8.50E-04	2.40E-05	2.39E-02	4.7E-04	1.46720	2.9E-05	1.886	1.5E-04	19.0	2840	17	0.280816	-68.00	-4.97	0.738	0.28096	3302
16	0.280987	1.40E-05	4.58E-04	1.20E-05	1.32E-02	2.5E-04	1.46720	3.4E-05	1.887	1.6E-04	16.7	2958	20	0.280961	-63.58	2.98	0.713	0.28088	3103
160	0.280825	1.20E-05	8.32E-04	1.50E-05	2.44E-02	6.0E-04	1.46721	2.5E-05	1.887	2.2E-04	23.8	2960	15	0.280778	-69.31	-3.51	0.665	0.28088	3350
163	0.281075	1.30E-05	6.16E-04	1.70E-05	1.71E-02	4.8E-04	1.46722	3.0E-05	1.886	2.2E-04	19.9	2790	18	0.281042	-60.47	1.92	0.688	0.28099	2998
166	0.281129	1.80E-05	1.70E-03	5.90E-05	5.10E-02	1.9E-03	1.46722	3.0E-05	1.887	2.1E-04	14.3	2702	14	0.281041	-58.56	-0.20	0.820	0.28105	3009
169	0.281022	1.30E-05	4.16E-04	3.90E-05	1.18E-02	1.1E-03	1.46722	2.5E-05	1.887	1.9E-04	23.3	2691	21	0.281001	-62.34	-1.90	0.688	0.28105	3053
17	0.281073	1.40E-05	5.00E-04	3.80E-05	1.85E-02	1.8E-03	1.46722	2.8E-05	1.886	2.3E-04	19.0	2740	14	0.281047	-60.54	0.91	0.713	0.28102	2992
171	0.281050	1.20E-05	7.02E-04	4.90E-05	2.22E-02	2.1E-03	1.46721	3.3E-05	1.886	2.2E-04	24.7	2795	14	0.281012	-61.35	0.97	0.665	0.28099	3038
172	0.281061	1.50E-05	9.52E-04	4.50E-05	2.76E-02	1.2E-03	1.46718	2.9E-05	1.886	2.6E-04	17.3	2809	20	0.281010	-60.97	1.21	0.738	0.28098	3043
175	0.280718	2.00E-05	6.54E-04	1.20E-05	1.90E-02	4.5E-04	1.46724	2.8E-05	1.887	2.1E-04	17.9	2950	15	0.280681	-73.09	-7.17	0.876	0.28088	3478
177	0.281060	1.60E-05	1.46E-03	3.30E-05	4.44E-02	1.4E-03	1.46720	2.2E-05	1.886	1.6E-04	18.8	2903	14	0.280979	-61.00	2.31	0.765	0.28091	3085
179	0.280891	1.40E-05	5.56E-04	7.50E-06	1.63E-02	3.8E-04	1.46720	2.8E-05	1.887	2.2E-04	18.9	2918	17	0.280860	-66.98	-1.55	0.713	0.28090	3239
18	0.280804	1.30E-05	3.04E-04	6.80E-07	8.69E-03	5.9E-05	1.46721	2.7E-05	1.887	1.6E-04	21.7	3153	17	0.280786	-70.05	1.35	0.688	0.28075	3333

	$^{176}Hf/^{177}Hf$	2SE	$^{176}Lu/^{177}Hf$	2SE	$^{176}Yb/^{177}Hf$	2SE	$^{178}Hf/^{177}Hf$	2SE	$^{180}Hf/^{177}Hf$	2SE	Total Hf beam	Age per spot	2SE	Initial	EHfpd	eHf (t)	2SE	CHUR	TDM
182	0.280806	1.40E-05	3.51E-04	1.20E-06	1.00E-02	8.1E-05	1.46719	3.3E-05	1.886	1.7E-04	15.9	3144	14	0.280785	-69.98	1.11	0.713	0.28075	3334
183	0.280808	1.40E-05	3.58E-04	7.30E-06	1.05E-02	3.1E-04	1.46722	2.2E-05	1.886	1.7E-04	20.6	3150	16	0.280786	-69.91	1.30	0.713	0.28075	3332
184	0.281052	1.60E-05	8.24E-04	4.20E-05	2.87E-02	1.7E-03	1.46720	2.6E-05	1.887	1.9E-04	23.8			0.281052	-61.28	-61.28	0.765	0.28279	3045
185	0.281043	1.60E-05	6.16E-04	2.80E-06	1.85E-02	2.4E-04	1.46722	2.5E-05	1.886	2.1E-04	20.7	2892	24	0.281009	-61.60	3.12	0.765	0.28092	3041
186	0.281055	1.80E-05	8.49E-04	3.40E-05	2.55E-02	1.4E-03	1.46720	3.2E-05	1.886	1.5E-04	17.4	2787	16	0.281010	-61.18	0.69	0.820	0.28099	3043
188	0.281108	1.40E-05	6.73E-04	2.30E-05	1.79E-02	5.5E-04	1.46722	2.9E-05	1.886	1.6E-04	18.4	2781	16	0.281072	-59.30	2.76	0.713	0.28099	2958
19	0.280819	1.70E-05	5.20E-04	8.50E-06	1.53E-02	2.7E-04	1.46722	2.7E-05	1.887	1.1E-04	18.7	3143	16	0.280788	-69.52	1.17	0.792	0.28075	3332
190	0.281089	1.30E-05	3.53E-04	3.20E-06	1.08E-02	2.0E-04	1.46720	2.5E-05	1.886	1.9E-04	19.3	2689	16	0.281071	-59.97	0.56	0.688	0.28106	2959
191	0.280878	1.20E-05	6.41E-04	2.20E-05	1.85E-02	5.2E-04	1.46718	2.5E-05	1.886	2.1E-04	21.3	2872	27	0.280843	-67.44	-3.27	0.665	0.28093	3263
193	0.281025	1.70E-05	6.81E-04	7.20E-05	2.38E-02	3.0E-03	1.46719	3.2E-05	1.887	3.1E-04	24.6	2823	19	0.280988	-62.24	0.77	0.792	0.28097	3070
194	0.280785	1.40E-05	4.29E-04	6.20E-06	1.27E-02	1.2E-04	1.46718	2.7E-05	1.886	2.2E-04	21.3	3218	16	0.280758	-70.73	1.92	0.713	0.28070	3369
197	0.280791	1.70E-05	7.63E-04	3.70E-05	2.39E-02	1.7E-03	1.46719	3.1E-05	1.886	3.8E-04	25.6	3177	19	0.280744	-70.51	0.45	0.792	0.28073	3390
198	0.281048	1.40E-05	6.24E-04	2.90E-05	1.78E-02	6.2E-04	1.46722	2.4E-05	1.887	1.4E-04	19.3	2775	15	0.281015	-61.42	0.59	0.713	0.28100	3035
199	0.280939	1.30E-05	5.40E-04	5.50E-06	1.27E-02	2.7E-04	1.46721	2.8E-05	1.887	1.7E-04	24.6	3017	13	0.280908	-65.28	2.47	0.688	0.28084	3174
2	0.280903	1.60E-05	6.73E-04	6.00E-05	1.92E-02	2.1E-03	1.46720	2.9E-05	1.887	1.6E-04	17.6	2857	16	0.280866	-66.55	-2.79	0.765	0.28094	3233
20	0.280802	1.90E-05	1.01E-03	1.10E-05	3.03E-02	3.2E-04	1.46721	2.6E-05	1.887	1.9E-04	16.7	3098	24	0.280742	-70.12	-1.51	0.848	0.28078	3397
200	0.280961	1.50E-05	9.62E-04	2.30E-05	2.67E-02	7.1E-04	1.46722	2.9E-05	1.886	2.0E-04	23.9	3026	15	0.280905	-64.50	2.59	0.738	0.28083	3179
21	0.281061	1.30E-05	3.20E-04	7.20E-07	9.51E-03	7.0E-05	1.46722	3.0E-05	1.887	1.7E-04	18.2	2757	16	0.281044	-60.97	1.20	0.688	0.28101	2994
22	0.281011	1.30E-05	4.37E-04	6.70E-06	1.34E-02	1.9E-04	1.46719	3.0E-05	1.887	1.9E-04	18.7	2879	19	0.280987	-62.73	2.04	0.688	0.28093	3069
24	0.281108	1.40E-05	5.00E-04	7.30E-06	1.52E-02	2.0E-04	1.46721	2.6E-05	1.887	2.3E-04	17.7	2710	18	0.281082	-59.30	1.46	0.713	0.28104	2945
25	0.281006	1.50E-05	2.60E-04	3.50E-06	7.37E-03	1.9E-04	1.46720	3.2E-05	1.887	1.8E-04	16.1	2827	16	0.280992	-62.91	0.99	0.738	0.28096	3062
27	0.281118	1.70E-05	5.70E-04	2.40E-06	1.72E-02	2.0E-04	1.46719	2.9E-05	1.887	2.0E-04	18.3	2721	21	0.281088	-58.95	1.93	0.792	0.28103	2937
28	0.281001	1.70E-05	7.26E-04	2.20E-05	2.06E-02	6.3E-04	1.46721	2.9E-05	1.887	1.6E-04	17.8	2929	28	0.280960	-63.09	2.27	0.792	0.28090	3106
3	0.280947	1.70E-05	1.53E-03	9.30E-05	5.24E-02	4.7E-03	1.46721	3.0E-05	1.887	1.7E-04	16.4	2839	21	0.280864	-65.00	-3.27	0.792	0.28096	3245
30	0.280905	1.60E-05	1.12E-03	2.00E-05	3.17E-02	6.3E-04	1.46722	3.2E-05	1.886	1.7E-04	17.9	2982	17	0.280841	-66.48	-0.71	0.765	0.28086	3267
31	0.281027	1.60E-05	1.01E-03	2.00E-05	3.20E-02	9.7E-04	1.46721	3.0E-05	1.887	2.0E-04	17.2	2883	17	0.280971	-62.17	1.57	0.765	0.28093	3093
32	0.281092	1.60E-05	8.58E-04	4.10E-05	2.50E-02	1.1E-03	1.46718	2.8E-05	1.887	1.8E-04	13.5	2760	17	0.281047	-59.87	1.38	0.765	0.28101	2994
33	0.280673	1.40E-05	5.74E-04	9.70E-06	1.86E-02	2.3E-04	1.46721	2.4E-05	1.887	1.5E-04	18.9	3347	13	0.280636	-74.69	0.63	0.712	0.28062	3530
34	0.280872	1.30E-05	2.38E-04	7.50E-06	6.37E-03	1.5E-04	1.46724	2.5E-05	1.887	1.8E-04	21.0	2908	19	0.280859	-67.65	-1.85	0.688	0.28091	3238
37	0.281033	1.50E-05	4.81E-04	1.90E-05	1.30E-02	4.1E-04	1.46721	2.7E-05	1.887	1.9E-04	17.6	2856	23	0.281007	-61.96	2.20	0.738	0.28094	3043
38	0.280788	1.60E-05	8.12E-04	7.40E-06	2.40E-02	4.1E-04	1.46719	3.3E-05	1.887	2.7E-04	18.2	2977	19	0.280742	-70.62	-4.37	0.764	0.28086	3398
39	0.280991	1.60E-05	3.48E-04	3.20E-06	8.31E-03	9.7E-05	1.46721	3.1E-05	1.887	2.1E-04	16.7	2751	17	0.280973	-63.44	-1.48	0.765	0.28101	3089
4	0.281002	1.40E-05	1.15E-03	3.70E-05	3.45E-02	1.5E-03	1.46721	2.9E-05	1.887	1.6E-04	17.7	2993	18	0.280936	-63.05	2.91	0.713	0.28085	3139
40	0.280983	1.20E-05	3.63E-04	4.50E-06	8.96E-03	2.0E-04	1.46722	3.1E-05	1.887	1.9E-04	17.5	2744	20	0.280964	-63.72	-1.96	0.665	0.28102	3101
42	0.281039	1.60E-05	7.86E-04	2.30E-05	2.22E-02	6.7E-04	1.46721	2.6E-05	1.886	1.8E-04	19.1	2734	18	0.280998	-61.74	-0.97	0.765	0.28103	3059
43	0.281064	1.20E-05	2.94E-04	7.90E-06	8.92E-03	3.4E-04	1.46721	2.8E-05	1.887	1.9E-04	19.5	2711	17	0.281049	-60.86	0.29	0.665	0.28104	2988
44	0.280862	1.60E-05	1.32E-03	2.80E-05	3.68E-02	7.0E-04	1.46721	3.1E-05	1.887	2.3E-04	17.0	3091	14	0.280783	-68.00	-0.20	0.765	0.28079	3343
45	0.280845	1.60E-05	1.01E-03	3.70E-05	3.26E-02	2.0E-03	1.46720	2.9E-05	1.886	1.8E-04	16.8	3097	17	0.280785	-68.60	-0.01	0.765	0.28079	3339
46	0.280903	1.30E-05	7.22E-04	8.20E-06	2.16E-02	1.2E-04	1.46721	2.6E-05	1.887	2.1E-04	18.0	2887	19	0.280863	-66.55	-2.19	0.688	0.28092	3237
47	0.281040	1.50E-05	7.31E-04	3.40E-05	2.61E-02	1.5E-03	1.46723	2.7E-05	1.887	1.7E-04	20.9	2784	17	0.281001	-61.71	0.30	0.738	0.28099	3054
48	0.281043	1.50E-05	3.94E-04	1.80E-05	1.25E-02	6.4E-04	1.46720	2.8E-05	1.887	1.8E-04	21.7	2798	18	0.281022	-61.60	1.37	0.738	0.28098	3023
49	0.280956	1.30E-05	5.77E-04	2.90E-06	1.53E-02	1.3E-04	1.46721	2.8E-05	1.887	1.8E-04	21.4	2882	15	0.280924	-64.68	-0.13	0.688	0.28093	3154
5	0.280985	1.60E-05	8.51E-04	1.70E-05	2.61E-02	4.0E-04	1.46718	2.8E-05	1.887	2.2E-04	18.0	2985	19	0.280936	-63.65	2.75	0.765	0.28086	3137
50	0.281101	1.50E-05	1.18E-03	7.30E-05	3.67E-02	2.6E-03	1.46723	2.5E-05	1.886	2.2E-04	18.6	2756	22	0.281039	-59.55	0.99	0.739	0.28101	3006
51	0.281051	1.80E-05	1.65E-03	1.80E-05	4.70E-02	5.6E-04	1.46719	2.5E-05	1.886	2.2E-04	17.6	2954	13	0.280958	-61.32	2.78	0.820	0.28088	3112
52	0.281120	1.50E-05	5.28E-04	1.40E-05	1.44E-02	2.0E-04	1.46720	3.3E-05	1.887	2.1E-04	18.9	2760	19	0.281092	-58.88	2.98	0.739	0.28101	2931

	$^{176}Hf/^{177}Hf$	2SE	$^{176}Lu/^{177}Hf$	2SE	$^{176}Yb/^{177}Hf$	2SE	$^{178}Hf/^{177}Hf$	2SE	$^{180}Hf/^{177}Hf$	2SE	Total Hf beam	Age per spot	2SE	Initial	EHfpd	eHf (t)	2SE	CHUR	TDM
53	0.281128	1.30E-05	7.43E-04	7.60E-06	1.98E-02	1.4E-04	1.46721	2.5E-05	1.887	1.8E-04	19.2	2739	20	0.281089	-58.60	2.39	0.688	0.28102	2936
54	0.281035	1.60E-05	9.83E-04	2.00E-05	2.91E-02	5.5E-04	1.46720	2.9E-05	1.887	1.8E-04	16.9	2871	17	0.280981	-61.88	1.64	0.765	0.28093	3080
55	0.281019	1.20E-05	3.44E-04	6.70E-06	1.03E-02	3.3E-04	1.46719	2.9E-05	1.887	2.3E-04	19.8	2863	15	0.281000	-62.45	2.13	0.665	0.28094	3051
56	0.280880	1.50E-05	3.57E-04	5.90E-06	9.46E-03	8.5E-05	1.46720	3.1E-05	1.887	1.9E-04	16.8	3048	14	0.280859	-67.37	1.48	0.738	0.28082	3237
58	0.281041	1.50E-05	5.13E-04	8.30E-06	1.45E-02	1.1E-04	1.46720	3.2E-05	1.886	1.9E-04	16.3	2850	18	0.281013	-61.67	2.29	0.738	0.28095	3035
59	0.281050	1.60E-05	5.24E-04	1.30E-05	1.58E-02	4.8E-04	1.46721	2.7E-05	1.887	2.2E-04	16.8	2832	15	0.281022	-61.35	2.16	0.765	0.28096	3024
60	0.281033	1.30E-05	4.91E-04	1.70E-05	1.45E-02	3.3E-04	1.46720	3.0E-05	1.887	2.5E-04	18.4	2759	19	0.281007	-61.96	-0.07	0.688	0.28101	3044
61	0.281009	1.70E-05	3.56E-04	1.70E-05	9.88E-03	4.0E-04	1.46723	3.7E-05	1.886	1.8E-04	13.1	2877	18	0.280989	-62.80	2.07	0.792	0.28093	3066
62	0.280954	2.00E-05	9.23E-04	1.50E-05	2.68E-02	4.7E-04	1.46724	3.7E-05	1.886	2.0E-04	21.5	3019	23	0.280900	-64.75	2.28	0.877	0.28084	3185
63	0.280989	1.40E-05	4.41E-04	4.30E-05	1.38E-02	1.3E-03	1.46722	2.9E-05	1.887	2.0E-04	22.8	2822	18	0.280965	-63.51	-0.08	0.713	0.28097	3099
64	0.281000	1.20E-05	2.64E-04	5.80E-06	8.14E-03	2.5E-04	1.46719	2.6E-05	1.887	1.6E-04	21.0	2884	17	0.280985	-63.12	2.10	0.665	0.28093	3070
65	0.281007	1.20E-05	3.63E-04	3.70E-06	1.06E-02	9.1E-05	1.46724	3.0E-05	1.887	2.1E-04	22.2	2864	20	0.280987	-62.87	1.70	0.665	0.28094	3069
66	0.280854	1.40E-05	6.02E-04	5.20E-06	1.74E-02	1.9E-04	1.46722	2.7E-05	1.886	2.2E-04	20.6	2875	13	0.280821	-68.29	-3.96	0.713	0.28093	3292
67	0.281036	1.40E-05	3.47E-04	4.90E-06	1.03E-02	2.3E-04	1.46720	3.0E-05	1.887	2.5E-04	21.3	2881	20	0.281017	-61.85	3.15	0.713	0.28093	3029
68	0.281033	1.20E-05	3.09E-04	6.10E-06	9.17E-03	1.7E-04	1.46722	2.7E-05	1.887	1.9E-04	22.3	2842	20	0.281016	-61.96	2.20	0.665	0.28095	3030
69	0.281127	1.90E-05	1.99E-03	7.50E-05	7.04E-02	3.0E-03	1.46722	3.1E-05	1.887	1.9E-04	19.5	2743	16	0.281023	-58.63	0.10	0.848	0.28102	3035
70	0.281062	1.70E-05	8.42E-04	2.70E-05	2.28E-02	6.9E-04	1.46720	3.8E-05	1.887	2.1E-04	15.4	2741	16	0.281018	-60.93	-0.11	0.792	0.28102	3033
72	0.281034	1.70E-05	7.95E-04	7.10E-05	2.88E-02	3.2E-03	1.46722	2.8E-05	1.887	2.0E-04	20.4	2799	18	0.280991	-61.92	0.33	0.792	0.28098	3067
74	0.281000	2.30E-05	1.77E-04	4.00E-06	4.72E-03	1.7E-04	1.46724	5.1E-05	1.886	2.4E-04	10.5	2845	17	0.280990	-63.12	1.36	0.966	0.28095	3064
75	0.280839	1.30E-05	5.75E-04	5.60E-06	1.60E-02	1.4E-04	1.46718	2.3E-05	1.887	2.3E-04	21.0	2869	14	0.280807	-68.82	-4.58	0.688	0.28094	3310
76	0.280932	1.50E-05	2.83E-04	7.00E-06	6.70E-03	1.7E-04	1.46720	3.1E-05	1.887	2.2E-04	15.6	2934	19	0.280916	-65.53	0.83	0.738	0.28089	3162
78	0.281044	1.70E-05	7.96E-04	2.00E-05	2.37E-02	5.4E-04	1.46719	3.6E-05	1.886	1.8E-04	13.2	2822	23	0.281001	-61.57	1.19	0.792	0.28097	3053
79	0.281073	2.00E-05	1.69E-03	3.50E-05	4.90E-02	6.8E-04	1.46721	2.9E-05	1.886	1.4E-04	16.1	2816	13	0.280982	-60.54	0.36	0.877	0.28097	3086
80	0.281049	1.80E-05	4.47E-04	1.10E-05	1.43E-02	4.1E-04	1.46721	3.2E-05	1.886	1.7E-04	13.6	2781	16	0.281025	-61.39	1.10	0.820	0.28099	3019
81	0.281061	1.40E-05	5.82E-04	6.40E-06	1.64E-02	2.8E-04	1.46722	2.8E-05	1.887	1.8E-04	18.1	2701	20	0.281031	-60.97	-0.58	0.713	0.28105	3014
83	0.280907	1.40E-05	9.44E-04	6.70E-05	3.33E-02	2.7E-03	1.46722	2.5E-05	1.887	1.7E-04	21.3	3048	15	0.280852	-66.41	1.21	0.713	0.28082	3250
84	0.280983	1.60E-05	7.72E-05	2.30E-06	2.41E-03	4.6E-05	1.46721	2.9E-05	1.887	2.2E-04	18.1	2874	18	0.280979	-63.72	1.64	0.765	0.28093	3078
85	0.281097	1.50E-05	3.63E-04	4.30E-06	1.07E-02	1.1E-04	1.46720	3.1E-05	1.886	2.0E-04	20.9	2711	18	0.281078	-59.69	1.33	0.739	0.28104	2949
86	0.281077	1.70E-05	8.17E-04	2.20E-05	2.13E-02	5.2E-04	1.46721	3.2E-05	1.886	2.6E-04	17.8	2829	15	0.281033	-60.40	2.48	0.792	0.28096	3011
87	0.281118	1.80E-05	1.30E-03	6.50E-05	3.70E-02	1.9E-03	1.46722	2.9E-05	1.887	2.0E-04	17.3	2832	16	0.281047	-58.95	3.08	0.820	0.28096	2993
88	0.280729	1.20E-05	3.91E-04	1.60E-05	1.17E-02	4.8E-04	1.46722	2.5E-05	1.887	1.4E-04	20.6	2982	15	0.280707	-72.71	-5.50	0.664	0.28086	3440
9	0.280483	1.20E-05	3.31E-04	1.60E-06	1.08E-02	1.0E-04	1.46721	2.6E-05	1.887	2.4E-04	23.1	3311	21	0.280462	-81.40	-6.43	0.664	0.28064	3758
90	0.281000	1.50E-05	7.16E-04	6.20E-05	2.17E-02	2.5E-03	1.46722	2.6E-05	1.887	2.2E-04	21.2	2754	13	0.280962	-63.12	-1.79	0.738	0.28101	3106
91	0.280805	1.60E-05	5.58E-04	2.50E-05	1.47E-02	8.3E-04	1.46721	2.7E-05	1.887	2.0E-04	18.4	2971	17	0.280773	-70.02	-3.41	0.764	0.28087	3353
92	0.280861	1.60E-05	1.25E-03	6.00E-05	3.31E-02	1.6E-03	1.46721	3.0E-05	1.887	1.9E-04	15.6	2959	17	0.280790	-68.04	-3.08	0.765	0.28088	3338
93	0.280916	2.10E-05	5.43E-04	2.00E-05	1.58E-02	6.1E-04	1.46721	2.4E-05	1.887	1.7E-04	17.1	2984	20	0.280885	-66.09	0.89	0.906	0.28086	3204
94	0.280789	2.10E-05	1.96E-03	1.10E-04	5.64E-02	2.8E-03	1.46721	2.6E-05	1.886	2.0E-04	18.1	3247	15	0.280667	-70.58	-0.66	0.906	0.28069	3500
95	0.280748	1.60E-05	1.35E-03	2.30E-05	4.02E-02	2.8E-04	1.46722	2.8E-05	1.887	2.1E-04	17.5	3233	16	0.280664	-72.03	-1.09	0.764	0.28069	3501
96	0.280809	1.20E-05	4.14E-04	1.30E-06	1.22E-02	7.8E-05	1.46721	2.3E-05	1.887	2.1E-04	23.5	3145	13	0.280784	-69.88	1.10	0.664	0.28075	3336
98	0.281083	1.50E-05	5.25E-04	4.20E-06	1.53E-02	4.3E-04	1.46721	3.2E-05	1.886	2.7E-04	24.3	2787	25	0.281055	-60.19	2.30	0.738	0.28099	2980
99	0.281084	1.50E-05	7.39E-04	5.30E-05	2.29E-02	1.9E-03	1.46723	3.1E-05	1.887	1.8E-04	20.0	2850	18	0.281044	-60.15	3.38	0.738	0.28095	2995
SU21																			
11	0.281104	1.30E-05	4.13E-04	1.70E-05	1.13E-02	4.4E-04	1.46720	2.7E-05	1.886	1.7E-04	21.7	2803	19	0.281082	-59.44	2.51	0.688	0.28101	2943
12	0.281095	1.20E-05	4.46E-04	8.90E-06	1.19E-02	3.0E-04	1.46720	2.8E-05	1.886	1.7E-04	23.2	2796	15	0.281071	-59.76	2.13	0.665	0.28101	2958
13	0.281112	1.20E-05	6.96E-04	2.20E-05	2.20E-02	1.2E-03	1.46721	2.4E-05	1.887	1.8E-04	21.8	2748	13	0.281075	-59.16	2.27	0.665	0.28101	2954
15	0.281120	1.90E-05	9.93E-04	9.70E-06	2.81E-02	2.5E-04	1.46721	4.1E-05	1.886	3.5E-04	16.4	2762	21	0.281068	-58.88	2.00	0.848	0.28101	2966
24	0.281098	1.60E-05	6.53E-04	7.70E-05	1.78E-02	2.3E-03	1.46722	3.2E-05	1.886	2.7E-04	20.8	2751	19	0.281064	-59.66	1.85	0.765	0.28101	2970

	$^{176}Hf/^{177}Hf$	2SE	$^{176}Lu/^{177}Hf$	2SE	$^{176}Yb/^{177}Hf$	2SE	$^{178}Hf/^{177}Hf$	2SE	$^{180}Hf/^{177}Hf$	2SE	Total Hf beam	Age per spot	2SE	Initial	EHfpd	eHf (t)	2SE	CHUR	TDM
28	0.281135	1.50E-05	9.96E-04	4.50E-05	2.97E-02	1.3E-03	1.46722	2.4E-05	1.886	1.5E-04	22.5	2726	19	0.281082	-58.35	2.52	0.739	0.28101	2946
3	0.281117	1.30E-05	9.24E-04	9.10E-06	2.54E-02	4.2E-04	1.46721	2.4E-05	1.886	1.7E-04	26.1	2743	16	0.281068	-58.98	2.02	0.688	0.28101	2965
35	0.281121	1.40E-05	6.87E-04	9.90E-06	2.09E-02	3.8E-04	1.46722	2.3E-05	1.886	1.6E-04	22.4	2710	16	0.281085	-58.84	2.61	0.713	0.28101	2941
4	0.281177	2.20E-05	1.78E-03	1.90E-04	5.74E-02	6.2E-03	1.46722	2.8E-05	1.886	1.9E-04	18.4	2748	26	0.281083	-56.86	2.54	0.936	0.28101	2949
43	0.281137	1.30E-05	1.08E-03	2.40E-05	3.29E-02	5.8E-04	1.46718	2.9E-05	1.886	1.9E-04	20.6	2780	19	0.281080	-58.28	2.43	0.689	0.28101	2950
6	0.281197	1.80E-05	2.45E-03	1.10E-04	7.39E-02	3.9E-03	1.46718	3.0E-05	1.887	1.8E-04	17.5	2756	15	0.281068	-56.16	2.00	0.820	0.28101	2975
8	0.281126	1.30E-05	1.06E-03	1.70E-05	3.16E-02	9.5E-04	1.46722	2.6E-05	1.887	2.2E-04	19.6	2775	20	0.281070	-58.67	2.09	0.688	0.28101	2963
SU06																			
13	0.281090	1.40E-05	8.22E-04	2.20E-05	2.19E-02	6.4E-04	1.46722	3.1E-05	1.886	1.6E-04	19.3	2788	25	0.281046	-59.94	2.23	0.713	0.28098	2994
15	0.281104	1.80E-05	1.46E-03	4.70E-05	4.12E-02	1.8E-03	1.46721	3.1E-05	1.886	2.1E-04	13.4	2711	26	0.281029	-59.44	-0.94	0.820	0.28106	3025
16	0.281077	1.30E-05	6.90E-04	3.40E-05	1.84E-02	9.6E-04	1.46719	2.7E-05	1.886	2.2E-04	22.0	2804	17	0.281040	-60.40	2.02	0.688	0.28098	3001
17	0.281087	1.90E-05	1.20E-03	3.00E-05	3.60E-02	1.2E-03	1.46721	3.8E-05	1.886	1.9E-04	16.7	2676	25	0.281025	-60.05	-1.06	0.848	0.28106	3027
19	0.281037	1.90E-05	9.63E-04	3.90E-05	2.78E-02	8.4E-04	1.46722	2.9E-05	1.886	3.3E-04	19.6	2740	31	0.280987	-61.81	-2.41	0.848	0.28106	3076
20	0.281011	2.40E-05	7.49E-04	1.30E-05	2.22E-02	4.3E-04	1.46718	4.0E-05	1.886	2.6E-04	14.6	2669	28	0.280972	-62.73	-2.94	0.996	0.28106	3094
21	0.281127	2.20E-05	1.69E-03	6.20E-05	5.18E-02	2.1E-03	1.46719	4.0E-05	1.886	2.6E-04	12.1	2702	19	0.281040	-58.63	-0.54	0.936	0.28106	3011
22	0.281136	3.90E-05	1.69E-03	1.00E-04	4.98E-02	2.9E-03	1.46719	4.6E-05	1.886	2.3E-04	6.5	2711	33	0.281049	-58.31	-0.22	1.483	0.28106	2999
23	0.281047	1.30E-05	5.65E-04	2.70E-05	1.51E-02	8.0E-04	1.46720	3.0E-05	1.887	1.9E-04	25.2	2677	23	0.281018	-61.46	-1.32	0.688	0.28106	3031
24	0.281026	1.90E-05	9.48E-04	2.40E-05	2.84E-02	8.9E-04	1.46720	2.8E-05	1.886	2.3E-04	13.8	2677	20	0.280977	-62.20	-2.77	0.848	0.28106	3090
32	0.281049	1.80E-05	5.20E-04	2.10E-05	1.43E-02	6.0E-04	1.46724	4.3E-05	1.886	2.5E-04	13.9	2665	32	0.281022	-61.39	-1.17	0.820	0.28106	3025
33	0.280998	1.90E-05	8.25E-04	2.00E-05	2.31E-02	6.3E-04	1.46718	3.6E-05	1.887	1.8E-04	12.3	2697	26	0.280956	-63.19	-3.54	0.848	0.28106	3118
34	0.281019	2.10E-05	7.88E-04	9.40E-06	2.11E-02	2.4E-04	1.46721	3.4E-05	1.886	2.8E-04	12.7	2734	25	0.280978	-62.45	-2.73	0.906	0.28106	3086
36	0.281124	1.40E-05	9.44E-04	1.80E-05	2.70E-02	7.9E-04	1.46720	2.5E-05	1.886	1.9E-04	20.5	2687	24	0.281075	-58.74	0.72	0.713	0.28106	2957
39	0.281080	2.30E-05	1.33E-03	6.50E-05	3.82E-02	2.4E-03	1.46721	3.2E-05	1.886	2.0E-04	13.7	2698	21	0.281012	-60.29	-1.54	0.966	0.28106	3047
57	0.281049	2.10E-05	1.05E-03	1.40E-04	3.29E-02	4.6E-03	1.46720	2.8E-05	1.886	1.8E-04	19.2	2712	43	0.280995	-61.39	-2.14	0.906	0.28106	3067
SU10B																			
1	0.281168	2.30E-05	2.03E-03	3.40E-04	6.90E-02	1.2E-02	1.46720	2.9E-05	1.886	2.4E-04	21.1	2658	26	0.281065	-57.18	-0.45	0.966	0.28108	2982
11	0.281144	1.20E-05	7.58E-04	7.60E-06	1.88E-02	1.6E-04	1.46721	2.4E-05	1.886	2.2E-04	21.8	2671	15	0.281106	-58.03	1.00	0.665	0.28108	2916
12	0.281107	1.40E-05	6.04E-04	2.40E-05	1.65E-02	8.4E-04	1.46722	2.9E-05	1.886	2.3E-04	20.4	2660	16	0.281076	-59.34	-0.04	0.713	0.28108	2954
16	0.281124	1.10E-05	8.34E-04	1.80E-05	2.51E-02	7.3E-04	1.46721	2.8E-05	1.886	1.9E-04	19.4	2646	16	0.281082	-58.74	0.15	0.642	0.28108	2949
19	0.281117	1.40E-05	3.83E-04	2.80E-05	9.59E-03	6.9E-04	1.46720	3.7E-05	1.887	1.8E-04	14.8	2671	19	0.281098	-58.98	0.71	0.713	0.28108	2924
20	0.281111	1.60E-05	4.19E-04	1.30E-05	1.02E-02	4.2E-04	1.46721	2.9E-05	1.886	1.6E-04	15.5	2653	17	0.281090	-59.20	0.43	0.765	0.28108	2935
21	0.281119	1.80E-05	5.16E-04	1.00E-05	1.29E-02	3.4E-04	1.46722	2.5E-05	1.886	1.9E-04	15.5	2649	12	0.281093	-58.91	0.54	0.820	0.28108	2931
24	0.281138	1.40E-05	8.08E-04	1.90E-05	2.14E-02	6.0E-04	1.46721	2.6E-05	1.886	1.9E-04	19.7	2666	19	0.281097	-58.24	0.69	0.713	0.28108	2928
25	0.281125	1.60E-05	1.03E-03	2.50E-05	2.94E-02	7.5E-04	1.46721	3.3E-05	1.886	1.8E-04	18.7	2651	15	0.281073	-58.70	-0.17	0.765	0.28108	2962
28	0.281142	1.50E-05	8.71E-04	3.80E-05	2.43E-02	1.2E-03	1.46722	3.2E-05	1.887	2.1E-04	18.6	2698	19	0.281098	-58.10	0.72	0.739	0.28108	2927
4	0.281130	1.40E-05	9.26E-04	2.00E-05	2.57E-02	7.2E-04	1.46721	2.8E-05	1.886	1.6E-04	19.5	2649	19	0.281083	-58.53	0.19	0.713	0.28108	2948
50	0.281109	1.30E-05	9.67E-04	2.40E-05	2.82E-02	7.5E-04	1.46722	2.8E-05	1.886	1.9E-04	21.0	2644	13	0.281060	-59.27	-0.63	0.688	0.28108	2979
SU15																			
1	0.281095	3.70E-05	3.15E-04	2.00E-05	8.61E-03	5.9E-04	1.46720	5.1E-05	1.886	2.3E-04	6.2	2675	19	0.281079	-59.76	0.56	1.416	0.28106	2948
11	0.281115	1.30E-05	1.78E-04	2.70E-06	5.05E-03	8.8E-05	1.46722	2.6E-05	1.887	1.5E-04	20.6	2677	19	0.281106	-59.06	1.52	0.688	0.28106	2911
13	0.281097	1.50E-05	1.84E-04	7.30E-06	5.38E-03	2.3E-04	1.46720	2.7E-05	1.886	2.3E-04	20.6	2664	17	0.281088	-59.69	0.87	0.739	0.28106	2936
16	0.281114	1.40E-05	2.33E-04	3.30E-06	6.78E-03	8.4E-05	1.46720	2.9E-05	1.886	2.0E-04	17.6	2679	19	0.281102	-59.09	1.39	0.713	0.28106	2917
17	0.281124	1.60E-05	2.39E-04	6.00E-06	6.86E-03	1.3E-04	1.46723	3.2E-05	1.886	1.5E-04	16.4	2667	19	0.281112	-58.74	1.74	0.765	0.28106	2904
18	0.281108	1.50E-05	2.33E-04	9.60E-06	6.57E-03	2.8E-04	1.46720	2.7E-05	1.886	2.2E-04	19.9	2690	28	0.281096	-59.30	1.18	0.739	0.28106	2925
20	0.281141	3.20E-05	4.75E-04	4.10E-05	1.38E-02	1.5E-03	1.46723	4.9E-05	1.886	3.1E-04	7.1	2668	29	0.281117	-58.14	1.91	1.251	0.28106	2899
21	0.281117	1.40E-05	3.56E-04	9.70E-06	1.03E-02	2.6E-04	1.46720	3.3E-05	1.886	2.7E-04	17.0	2683	20	0.281099	-58.98	1.27	0.713	0.28106	2922
22	0.281129	1.80E-05	2.99E-04	5.60E-06	8.46E-03	9.3E-05	1.46718	3.9E-05	1.887	2.3E-04	16.3	2679	17	0.281114	-58.56	1.80	0.820	0.28106	2902

	$^{176}Hf/^{177}Hf$	2SE	$^{176}Lu/^{177}Hf$	2SE	$^{176}Yb/^{177}Hf$	2SE	$^{178}Hf/^{177}Hf$	2SE	$^{180}Hf/^{177}Hf$	2SE	Total Hf beam	Age per spot	2SE	Initial	EHfpd	eHf (t)	2SE	CHUR	TDM
23	0.281107	1.70E-05	3.52E-04	1.60E-05	9.57E-03	5.1E-04	1.46723	3.9E-05	1.886	4.8E-04	14.8	2702	30	0.281089	-59.34	0.92	0.792	0.28106	2935
27	0.281132	1.30E-05	5.43E-04	4.60E-06	1.60E-02	1.9E-04	1.46721	2.4E-05	1.887	1.4E-04	18.1	2685	20	0.281104	-58.45	1.46	0.689	0.28106	2916
3	0.281114	1.10E-05	1.91E-04	9.20E-06	5.72E-03	3.0E-04	1.46723	2.4E-05	1.886	1.7E-04	26.9	2692	20	0.281104	-59.09	1.47	0.642	0.28106	2914
30	0.281122	1.30E-05	1.69E-04	3.30E-06	4.84E-03	1.3E-04	1.46721	2.6E-05	1.886	2.2E-04	20.4	2654	16	0.281113	-58.81	1.79	0.688	0.28106	2901
6	0.281122	1.40E-05	4.52E-04	9.40E-06	1.35E-02	3.2E-04	1.46719	2.5E-05	1.886	1.7E-04	18.8	2681	17	0.281099	-58.81	1.27	0.713	0.28106	2922
SU16																			
10	0.281129	1.00E-05	5.37E-04	1.10E-05	1.59E-02	4.8E-04	1.46720	2.8E-05	1.886	2.0E-04	22.6	2633	16	0.281102	-58.56	0.63	0.621	0.28108	2919
11	0.281148	1.70E-05	1.07E-03	6.60E-06	3.22E-02	3.9E-04	1.46722	2.9E-05	1.886	2.3E-04	19.1	2647	17	0.281094	-57.89	0.35	0.792	0.28108	2934
15	0.281129	1.50E-05	6.20E-04	9.40E-06	1.81E-02	2.1E-04	1.46722	3.1E-05	1.886	2.2E-04	20.4	2648	16	0.281098	-58.56	0.48	0.739	0.28108	2926
17	0.281128	1.20E-05	6.90E-04	9.90E-06	2.07E-02	3.8E-04	1.46722	2.9E-05	1.886	2.1E-04	17.9	2633	18	0.281093	-58.60	0.32	0.665	0.28108	2932
23	0.281133	1.50E-05	1.00E-03	2.50E-05	2.98E-02	7.9E-04	1.46721	2.6E-05	1.886	2.4E-04	19.7	2639	19	0.281082	-58.42	-0.06	0.739	0.28108	2949
24	0.281175	1.90E-05	1.40E-03	1.00E-04	4.35E-02	2.9E-03	1.46723	2.3E-05	1.886	2.6E-04	19.3	2646	22	0.281104	-56.93	0.71	0.848	0.28108	2923
25	0.281123	1.30E-05	6.37E-04	1.90E-06	1.87E-02	8.7E-05	1.46719	3.2E-05	1.886	2.9E-04	19.0	2655	17	0.281091	-58.77	0.24	0.688	0.28108	2935
26	0.281138	1.30E-05	6.04E-04	2.60E-05	1.75E-02	8.9E-04	1.46719	2.7E-05	1.886	2.5E-04	20.3	2634	16	0.281107	-58.24	0.83	0.689	0.28108	2912
38	0.281136	1.70E-05	7.60E-04	4.00E-05	2.35E-02	1.3E-03	1.46722	3.1E-05	1.886	2.3E-04	19.0	2638	22	0.281098	-58.31	0.48	0.792	0.28108	2927
40	0.281154	1.50E-05	9.69E-04	7.30E-05	3.04E-02	2.2E-03	1.46722	2.5E-05	1.886	2.8E-04	21.2	2641	18	0.281105	-57.68	0.74	0.739	0.28108	2918
41	0.281155	1.60E-05	1.04E-03	3.20E-05	3.24E-02	6.7E-04	1.46721	2.5E-05	1.886	2.4E-04	21.0	2653	20	0.281102	-57.64	0.65	0.765	0.28108	2922
5	0.281099	2.40E-05	6.25E-04	2.10E-05	1.76E-02	4.6E-04	1.46725	4.2E-05	1.886	2.1E-04	8.3	2646	19	0.281067	-59.62	-0.60	0.997	0.28108	2966
7	0.281154	1.60E-05	9.43E-04	1.60E-05	2.82E-02	6.5E-04	1.46723	2.7E-05	1.886	2.1E-04	20.6	2660	17	0.281106	-57.68	0.79	0.765	0.28108	2916
8	0.281161	1.50E-05	1.10E-03	2.60E-05	3.33E-02	7.4E-04	1.46722	2.4E-05	1.886	2.2E-04	19.6	2656	20	0.281105	-57.43	0.76	0.739	0.28108	2919
9	0.281141	1.40E-05	9.45E-04	4.20E-05	2.96E-02	1.5E-03	1.46721	2.7E-05	1.886	2.1E-04	20.7	2641	15	0.281093	-58.14	0.32	0.713	0.28108	2934
SU25																			
10	0.281145	1.90E-05	7.61E-04	1.70E-05	2.09E-02	5.0E-04	1.46721	4.3E-05	1.886	1.9E-04	13.0	2645	21	0.281106	-57.99	0.77	0.848	0.28108	2915
11	0.281124	2.60E-05	9.55E-04	2.80E-05	2.62E-02	7.9E-04	1.46719	4.0E-05	1.886	3.2E-04	11.7	2630	19	0.281076	-58.74	-0.32	1.059	0.28108	2958
12	0.281115	4.00E-05	7.59E-04	4.30E-05	2.13E-02	1.2E-03	1.46721	5.1E-05	1.886	3.8E-04	8.9	2638	38	0.281077	-59.06	-0.29	1.516	0.28108	2955
20	0.281117	1.80E-05	6.26E-04	1.60E-05	1.72E-02	3.6E-04	1.46721	4.2E-05	1.886	3.3E-04	18.3	2653	27	0.281085	-58.98	0.02	0.820	0.28108	2942
21	0.281124	1.50E-05	6.51E-04	3.30E-05	1.94E-02	1.1E-03	1.46720	2.8E-05	1.886	2.1E-04	19.4	2643	14	0.281091	-58.74	0.22	0.739	0.28108	2935
23	0.281140	1.90E-05	1.02E-03	1.50E-04	2.98E-02	4.7E-03	1.46721	3.6E-05	1.886	2.5E-04	13.8	2654	21	0.281088	-58.17	0.13	0.848	0.28108	2941
30	0.281167	3.70E-05	1.52E-03	1.30E-04	4.34E-02	4.0E-03	1.46728	5.4E-05	1.885	8.4E-04	8.5	2644	31	0.281090	-57.22	0.19	1.416	0.28108	2943
39	0.281153	3.20E-05	1.01E-03	3.30E-05	2.81E-02	9.3E-04	1.46722	6.0E-05	1.886	3.3E-04	7.9	2623	15	0.281102	-57.71	0.61	1.251	0.28108	2923
43	0.281140	1.60E-05	8.80E-04	1.90E-05	2.48E-02	6.5E-04	1.46725	2.2E-05	1.886	2.8E-04	20.2	2660	13	0.281095	-58.17	0.38	0.765	0.28108	2930
50	0.281143	1.30E-05	8.01E-04	7.70E-05	2.32E-02	2.2E-03	1.46723	3.3E-05	1.886	2.3E-04	19.6	2627	18	0.281102	-58.07	0.63	0.689	0.28108	2920
51	0.281132	1.40E-05	8.29E-04	7.30E-05	2.39E-02	2.1E-03	1.46721	2.8E-05	1.886	2.1E-04	21.6	2623	36	0.281090	-58.45	0.19	0.713	0.28108	2937
8	0.281122	1.40E-05	7.41E-04	6.20E-06	2.04E-02	2.1E-04	1.46720	2.2E-05	1.886	2.0E-04	24.8	2618	25	0.281085	-58.81	-0.01	0.713	0.28108	2944
9	0.281126	1.30E-05	7.43E-04	4.30E-05	2.15E-02	1.2E-03	1.46723	2.9E-05	1.886	1.7E-04	20.6	2635	19	0.281088	-58.67	0.13	0.688	0.28108	2939

Supplementary Material 2-5

Whole-rock analyses from the literature

CTR = Central Tanzania Region

ISGB = Iramba Sekenke greenstone belt

KGB = Kilimafheda greenstone belt

MMGB = Musoma Mara greenstone belt

NGB = Nzega greenstone belt

SGB = Sukulamand greenstone belt

Reference	Belt	Location	Sample	Harmonisation litho	Age (Ma)	2σ	WR Nd age (Ma)	SiO_2	Al_2O_3	Fe_2O_3	FeO	CaO	MgO	Na_2O	K_2O	TiO_2	MnO	P_2O_5	LOI
								%	%	%	%	%	%	%	%	%	%	%	%
Boniface and Mruma 2012	SGB	Geita	N12	Granite-Monzonite				71	14	2.3	2.03	2.24	0.79	3.75	3.63	0.28	0.04	0.08	0.85
Boniface and Mruma 2012	SGB	Geita	N28	Granite-Monzonite				72	15	1.6	1.42	2.37	0.55	5.35	1.45	0.23	0.03	0.08	0.89
Boniface and Mruma 2012	SGB	Geita	N29A	Granite-Monzonite				71	16	1.6	1.47	2.62	0.51	5.27	1.48	0.22	0.02	0.07	0.9
Boniface and Mruma 2012	SGB	Geita	N33	Granite-Monzonite				68	15	3.2	2.84	3.39	0.94	4.52	2.36	0.29	0.07	0.16	2.33
Boniface and Mruma 2012	SGB	Geita	N49	Mafic volcanics				50	15	13.7	12.30	12.06	4.63	2.67	0.33	1.19	0.18	0.09	0.82
Boniface and Mruma 2012	SGB	Geita	N50	Mafic volcanics				52	15	12.8	11.56	12.85	3.68	2.02	0.13	1.17	0.19	0.09	1.16
Boniface and Mruma 2012	SGB	Geita	N51	Felsic volcanics				68	15	2.9	2.64	2.69	1.16	3.40	3.83	0.26	0.06	0.13	1.41
Boniface and Mruma 2012	SGB	Geita	N52	Felsic volcanics				64	16	5.2	4.64	5.26	3.13	4.77	0.78	0.63	0.11	0.16	1.3
Boniface and Mruma 2012	SGB	Geita	N54	Felsic volcanics				68	16	1.9	1.74	4.93	1.23	4.38	1.72	0.65	0.06	0.17	0.93
Boniface and Mruma 2012	SGB	Geita	N59	Granite-Monzonite				77	13	0.7	0.64	0.31	0.10	4.05	4.42	0.04	0.04	0.02	0.52
Boniface and Mruma 2012	SGB	Geita	N69	Granite-Monzonite				71	13	3.1	2.79	1.50	0.47	3.15	5.34	0.44	0.05	0.12	0.8
Boniface and Mruma 2012	SGB	Geita	N69A	Mafic volcanics				46	11	22.4	20.13	12.42	6.18	0.96	0.51	0.68	0.63	0.05	1.02
Cloutier et al 2005	SGB	Tulawaka East	D0142	Granite-Monzonite			2500	76	15	0.6	0.58	0.97	0.06	6.71	0.42	0.00	7.00	0.02	0.44
Cloutier et al 2005	SGB	Tulawaka East	D0142-1	Sediment			2800	64	18	4.7	4.21	1.04	2.68	2.31	2.56	0.65	62.00	0.11	2.86
Cloutier et al 2005	SGB	Tulawaka East	D0146-1	Mafic volcanics			2800	49	13	14.6	13.11	10.04	6.53	2.24	0.17	1.24	0.22	0.12	1.41
Cloutier et al 2005	SGB	Tulawaka East	D0149-1	Sediment			2800	60	21	5.0	4.47	0.80	2.65	2.10	4.04	0.67	51.00	0.09	3.19
Cloutier et al 2005	SGB	Tulawaka East	D0149-10	Sediment			2800	54	24	5.7	5.15	2.27	2.85	3.78	3.03	0.72	56.00	0.09	3.42
Cloutier et al 2005	SGB	Tulawaka East	D0149-12	Sediment			2800	62	20	7.6	6.82	1.09	2.38	1.03	3.85	0.65	54.00	0.10	2.03
Cloutier et al 2005	SGB	Tulawaka East	D0149-13	Felsic volcanics			2800	53	14	23.5	21.11	5.83	2.99	0.24	0.19	0.46	0.20	0.11	0.28
Cloutier et al 2005	SGB	Tulawaka East	D0149-14	Sediment			2800	61	21	6.1	5.46	1.75	2.61	1.87	3.19	0.67	59.00	0.10	2.37
Cloutier et al 2005	SGB	Tulawaka East	D0149-17	Sediment			2800	62	21	5.1	4.55	1.01	2.52	1.47	3.59	0.66	56.00	0.11	3.22
Cloutier et al 2005	SGB	Tulawaka East	D0149-18	Sediment			2800	59	24	6.3	5.69	0.63	2.84	0.92	3.57	0.75	54.00	0.10	1.89
Cloutier et al 2005	SGB	Tulawaka East	D0149-19	Sediment			2800	57	24	6.2	5.60	0.50	2.97	0.86	4.28	0.76	47.00	0.10	2.76
Cloutier et al 2005	SGB	Tulawaka East	D0149-2	Sediment			2800	68	15	6.0	5.40	3.64	1.77	3.37	0.94	0.55	0.11	0.12	0.74
Cloutier et al 2005	SGB	Tulawaka East	D0149-20	Sediment			2800	63	13	17.5	15.70	2.42	2.77	0.33	0.28	0.47	82.00	0.11	0.19
Cloutier et al 2005	SGB	Tulawaka East	D0149-3	Felsic volcanics			2800	58	14	14.6	13.11	5.94	2.24	0.67	1.38	0.42	0.17	0.14	1.91
Cloutier et al 2005	SGB	Tulawaka East	D0149-4	Sediment			2800	63	16	9.3	8.36	4.56	2.10	1.95	1.94	0.48	0.13	0.12	0.71
Cloutier et al 2005	SGB	Tulawaka East	D0149-6	Sediment			2800	54	23	7.2	6.44	1.03	3.40	1.88	4.51	0.75	56.00	0.10	4.9
Cloutier et al 2005	SGB	Tulawaka East	D0149-7	Sediment			2800	68	16	4.1	3.67	0.95	2.19	2.04	2.65	0.55	42.00	0.08	2.94
Cloutier et al 2005	SGB	Tulawaka East	D0149-8	Sediment			2800	57	24	5.7	5.16	0.47	3.11	1.32	4.62	0.72	80.00	0.10	4.21
Cloutier et al 2005	SGB	Tulawaka East	D0159-1	Sediment			2800	61	20	5.8	5.19	1.37	2.99	2.93	2.42	0.70	63.00	0.09	2.9
Cloutier et al 2005	SGB	Tulawaka East	D0159-2	Sediment			2800	54	24	6.1	5.48	0.55	3.20	2.56	4.00	0.76	66.00	0.09	3.84
Cloutier et al 2005	SGB	Tulawaka East	D0159-3	Sediment			2800	61	21	6.8	6.14	0.87	2.60	1.04	3.96	0.68	42.00	0.12	2.42
Cloutier et al 2005	SGB	Tulawaka East	D0159-4	Sediment			2800	63	19	5.3	4.72	2.73	2.17	2.48	2.96	0.63	61.00	0.12	1.74
Cloutier et al 2005	SGB	Tulawaka East	D0159-5	Sediment			2800	64	19	5.2	4.68	1.80	2.30	2.37	2.67	0.63	55.00	0.10	1.6
Cloutier et al 2005	SGB	Tulawaka East	D0159-6	Sediment			2800	51	26	5.6	5.03	0.42	3.01	2.25	6.53	0.76	45.00	0.08	3.33
Cloutier et al 2005	SGB	Tulawaka East	D0185-1	Mafic volcanics			2800	53	13	14.7	13.25	6.42	4.71	4.50	0.63	2.21	0.29	0.17	0.66
Cloutier et al 2005	SGB	Tulawaka East	D0309-1	Mafic volcanics			2800	49	12	20.2	18.13	8.59	4.73	2.11	0.50	2.64	0.28	0.20	0.2
Cloutier et al 2005	SGB	Tulawaka East	D0309-2	Mafic volcanics			2800	52	15	13.7	12.29	7.11	3.32	3.78	0.43	1.45	0.16	0.24	2.83
Cloutier et al 2005	SGB	Tulawaka East	D0309-3	Mafic volcanics			2800	50	14	14.4	12.96	10.53	6.41	2.25	0.18	1.43	0.24	0.11	0.96
Cloutier et al 2005	SGB	Tulawaka East	D0310-1	Proterozoic granitoid			2500	76	14	1.3	1.17	0.43	0.18	3.79	3.35	0.04	0.25	0.03	1.05
Cloutier et al 2005	SGB	Tulawaka East	D0310-2	Sediment			2800	55	23	6.7	5.98	0.40	2.41	0.67	6.28	0.85	42.00	0.13	527
Cloutier et al 2005	SGB	Tulawaka East	D0310-3	Proterozoic granitoid			2500	75	15	0.7	0.61	0.65	0.12	5.43	2.50	0.03	60.00	0.06	0.69
Cloutier et al 2005	SGB	Tulawaka East	D03104	Proterozoic granitoid			2500	76	15	0.7	0.60	0.51	0.10	4.58	3.27	0.03	29.00	0.04	0.71
Cook et al 2016	SGB	Geita	E1	Mafic volcanics				49	15	16.4	14.79	9.47	7.56	2.56	0.42	1.12	0.22	0.10	
Cook et al 2016	SGB	Geita	E4	Mafic volcanics				49	14	15.9	14.34	9.95	7.00	2.09	0.32	1.18	0.21	0.11	

Reference	Belt	Location	Sample	Harmonisation litho	Age (Ma)	2σ	WR Nd age (Ma)	SiO_2	Al_2O_3	Fe_2O_3	FeO	CaO	MgO	Na_2O	K_2O	TiO_2	MnO	P_2O_5	LOI
								%	%	%	%	%	%	%	%	%	%	%	%
Cook et al 2016	SGB	Geita	E5	Mafic volcanics				54	15	9.9	8.93	9.97	6.69	3.49	0.14	0.89	0.21	0.10	
Cook et al 2016	SGB	Geita	E6	Mafic volcanics				52	14	14.1	12.70	12.68	5.35	1.32	0.12	1.03	0.25	0.12	
Cook et al 2016	SGB	Geita	IH11	Mafic volcanics			2800	48	13	16.1	14.48	10.30	7.11	2.94	0.14	1.18	0.22	0.12	
Cook et al 2016	SGB	Geita	IH12	Mafic volcanics				50	14	15.0	13.47	10.06	7.73	2.52	0.42	1.10	0.21	0.10	
Cook et al 2016	SGB	Geita	IH8	Mafic volcanics			2800	49	13	17.4	15.70	9.30	6.74	2.83	0.18	1.26	0.23	0.11	
Cook et al 2016	SGB	Geita	IH9	Mafic volcanics				48	15	15.6	14.07	9.57	6.81	2.78	0.16	1.09	0.21	0.10	
Cook et al 2016	SGB	Geita	K43	Mafic volcanics				49	13	16.9	15.22	8.31	6.07	2.73	0.14	1.07	0.24	0.11	
Cook et al 2016	SGB	Geita	K45	Mafic volcanics				49	13	14.3	12.84	12.33	9.06	1.74	0.21	0.65	0.18	0.07	
Cook et al 2016	SGB	Geita	K56	Mafic volcanics			2800	48	14	18.2	16.38	7.47	6.24	4.02	0.21	1.40	0.21	0.13	
Cook et al 2016	SGB	Geita	K73	Mafic volcanics				49	14	16.1	14.53	8.81	7.31	3.15	0.23	1.20	0.23	0.11	
Cook et al 2016	SGB	Geita	K75	Mafic volcanics				52	12	17.7	15.91	9.79	5.53	0.91	0.09	1.70	0.26	0.15	
Cook et al 2016	SGB	Geita	K76	Mafic volcanics				49	15	13.9	12.49	11.36	6.22	2.09	0.29	1.19	0.21	0.12	
Cook et al 2016	SGB	Geita	K82	Mafic volcanics			2800	50	15	15.4	13.87	8.76	7.11	3.55	0.22	1.06	0.20	0.10	
Cook et al 2016	SGB	Geita	K83	Mafic volcanics			2800	49	14	15.4	13.86	10.53	6.93	2.73	0.31	1.04	0.22	0.11	
Cook et al 2016	SGB	Geita	K84	Mafic volcanics			2800	48	15	17.3	15.56	10.92	6.67	2.30	0.18	1.15	0.22	0.13	
Cook et al 2016	SGB	Geita	KH14	Mafic volcanics			2800	48	15	16.2	14.60	9.35	7.02	3.01	0.14	1.32	0.20	0.12	
Cook et al 2016	SGB	Geita	KH15	Mafic volcanics				49	14	16.2	14.55	8.32	7.35	3.37	0.08	1.25	0.19	0.12	
Cook et al 2016	SGB	Geita	KH18	Mafic volcanics				49	16	16.0	14.41	9.28	6.58	3.31	0.10	1.32	0.22	0.14	
Cook et al 2016	SGB	Geita	KH2	Mafic volcanics				48	14	16.0	14.43	9.27	7.76	2.13	0.90	1.14	0.23	0.12	
Cook et al 2016	SGB	Geita	KH3	Mafic volcanics			2800	53	13	14.9	13.45	9.21	6.29	3.74	0.42	1.36	0.21	0.13	
Cook et al 2016	SGB	Geita	KH4	Mafic volcanics				55	14	12.8	11.51	10.53	4.80	2.91	0.14	1.17	0.19	0.11	
Cook et al 2016	SGB	Geita	KH7	Mafic volcanics				49	13	17.1	15.37	8.70	6.65	3.64	0.29	1.23	0.22	0.11	
Cook et al 2016	SGB	Geita	LH8	Mafic volcanics				48	14	13.7	12.36	10.61	8.42	2.23	0.50	0.71	0.19	0.07	
Kazimoto and Ikingura 2014	MMGB	North Mara	E 5	Intermediate volcanics				68	15	4.2	3.80	1.11	0.62	7.12	0.50	0.13	0.36	0.02	2.6
Kazimoto and Ikingura 2014	MMGB	North Mara	E 8	Intermediate volcanics				56	19	7.3	6.59	4.60	3.08	4.69	1.13	0.66	0.66	0.12	2.8
Kazimoto and Ikingura 2014	MMGB	North Mara	E 9	Intermediate volcanics				71	15	2.6	2.37	2.98	0.40	5.57	0.53	0.14	0.22	0.07	1.4
Kazimoto and Ikingura 2014	MMGB	North Mara	E12	Intermediate volcanics				57	18	7.2	6.46	4.56	3.84	3.75	1.07	0.64	0.86	0.11	3.4
Kazimoto and Ikingura 2014	MMGB	North Mara	E13	Intermediate volcanics				66	16	5.6	5.03	2.42	0.76	4.50	0.51	0.27	0.65	0.16	2.3
Kazimoto and Ikingura 2014	MMGB	North Mara	E14	Granite-Monzonite				71	15	2.4	2.13	2.21	0.61	4.42	2.71	0.23	0.03	0.06	1.3
Kazimoto and Ikingura 2014	MMGB	North Mara	E15	TTG				70	15	2.8	2.48	3.06	0.72	4.96	1.22	0.28	0.04	0.11	1.2
Kazimoto and Ikingura 2014	MMGB	North Mara	E16	Intermediate volcanics				65	17	5.7	5.10	2.10	0.69	5.64	0.53	0.27	0.95	0.08	2.3
Kazimoto and Ikingura 2014	MMGB	North Mara	E17	Intermediate volcanics				58	18	7.4	6.65	5.38	3.15	3.34	1.08	0.68	0.56	0.15	2
Kazimoto and Ikingura 2014	MMGB	North Mara	E22	Intermediate volcanics				65	15	4.3	3.89	3.45	3.90	2.66	0.56	0.26	2.11	0.12	2.4
Kazimoto and Ikingura 2014	MMGB	North Mara	E23	TTG				70	15	2.1	1.88	2.01	0.70	5.23	2.11	0.25	0.02	0.09	2.4
Kazimoto and Ikingura 2014	MMGB	North Mara	E25	TTG				70	16	2.0	1.84	2.20	0.63	5.25	2.16	0.23	0.04	0.07	1.7
Kazimoto and Ikingura 2014	MMGB	North Mara	E26	TTG				74	11	5.3	4.81	1.49	0.06	4.59	1.55	0.35	0.05	0.03	1.4
Kazimoto and Ikingura 2014	MMGB	North Mara	E34	Intermediate volcanics				68	14	5.9	5.32	1.48	0.39	6.88	0.43	0.12	0.49	0.03	2.7
Kazimoto and Ikingura 2014	MMGB	North Mara	E35	TTG				72	15	2.1	1.92	2.61	0.63	5.72	0.81	0.20	0.03	0.08	1.4
Kazimoto and Ikingura 2014	MMGB	North Mara	E36	Granite-Monzonite				72	14	1.7	1.50	1.75	0.39	4.02	3.81	0.18	0.02	0.05	1.6
Kazimoto and Ikingura 2014	MMGB	North Mara	E4	Granite-Monzonite				72	14	2.5	2.27	1.32	1.00	3.89	2.04	0.26	0.02	0.10	2.4
Kazimoto and Ikingura 2014	MMGB	North Mara	E43	Granite-Monzonite				72	15	2.3	2.07	0.96	0.76	5.11	2.57	0.26	0.02	0.09	1.4
Kazimoto and Ikingura 2014	MMGB	North Mara	E44	TTG				70	15	2.6	2.34	2.74	0.69	4.44	1.58	0.31	0.03	0.10	2.2
Kazimoto and Ikingura 2014	MMGB	North Mara	E47	Granite-Monzonite				72	15	1.9	1.66	1.61	0.44	4.47	2.55	0.18	0.02	0.06	1.5
Kazimoto and Ikingura 2014	MMGB	North Mara	E48	Granite-Monzonite				73	14	1.7	1.48	1.82	0.27	4.13	3.35	0.12	0.02	0.04	1.3
Kazimoto and Ikingura 2014	MMGB	North Mara	E54	Granite-Monzonite				71	15	2.1	1.84	1.96	0.44	4.16	3.32	0.2	0.03	0.06	2
Kazimoto and Ikingura 2014	MMGB	North Mara	E55	TTG				73	13	1.5	1.34	2.46	0.61	4.48	1.71	0.15	0.03	0.03	3.1
Kazimoto and Ikingura 2014	MMGB	North Mara	E59	Granite-Monzonite				70	15	1.9	1.66	2.23	0.55	4.36	2.83	0.21	0.03	0.07	2.6
Kazimoto and Ikingura 2014	MMGB	North Mara	E60	TTG				72	15	1.9	1.67	1.82	0.50	5.06	2.00	0.16	0.03	0.07	2

Reference	Belt	Location	Sample	Harmonisation litho	Age (Ma)	2σ	WR Nd age (Ma)	SiO_2	Al_2O_3	Fe_2O_3	FeO	CaO	MgO	Na_2O	K_2O	TiO_2	MnO	P_2O_5	LOI
								%	%	%	%	%	%	%	%	%	%	%	%
Kazimoto and Ikingura 2014	MMGB	North Mara	E64	Intermediate volcanics				68	16	3.0	2.65	0.62	0.22	8.72	0.51	0.13	0.19	0.01	2.4
Kazimoto and Ikingura 2014	MMGB	North Mara	E69	Intermediate volcanics				66	16	4.6	4.13	2.21	0.46	8.23	0.51	0.26	0.55	0.06	1.4
Kazimoto and Ikingura 2014	MMGB	North Mara	E70	Intermediate volcanics				58	19	5.1	4.59	4.86	4.14	4.15	1.14	0.70	0.72	0.09	2.2
Kazimoto and Ikingura 2014	MMGB	North Mara	E71	Intermediate volcanics				60	18	6.4	5.71	6.44	2.25	2.62	1.11	0.69	1.00	0.07	1.8
Kazimoto and Ikingura 2014	MMGB	North Mara	E73	Intermediate volcanics				58	18	6.5	5.88	5.01	3.57	3.59	1.05	0.65	1.13	0.10	2.8
Kazimoto and Ikingura 2014	MMGB	North Mara	E74	TTG				69	14	2.5	2.25	2.82	0.77	6.87	0.55	0.28	0.03	0.09	2.6
Kazimoto and Ikingura 2014	MMGB	North Mara	E75	TTG				73	13	1.6	1.40	2.10	0.65	4.90	1.70	0.15	0.03	0.05	2.5
Kazimoto and Ikingura 2014	MMGB	North Mara	EIO	Granite-Monzonite				73	13	1.5	1.30	2.39	0.39	4.24	2.1	0.12	0.02	0.05	3
Kazimoto and Ikingura 2014	MMGB	North Mara	El 8	Granite-Monzonite				72	14	2.3	2.11	2.23	0.56	4.12	2.01	0.23	0.03	0.07	2.5
Maboko et al 2006	SGB	everywhere	KM1	Granite-Monzonite				75	13	1.4	1.24	1.03	0.21	3.56	5.55	0.14	0.04	0.01	0.7
Maboko et al 2006	SGB	everywhere	KM3	Granite-Monzonite				71	15	2.0	1.81	1.49	0.35	4.33	4.32	0.23	0.05	0.04	1
Maboko et al 2006	SGB	everywhere	KM3*	Granite-Monzonite							0.00								
Maboko et al 2006	SGB	everywhere	KM30	TTG				68	17	3.1	2.81	3.51	1.22	5.28	1.13	0.41	0.05	0.12	0.6
Maboko et al 2006	SGB	everywhere	KM31	TTG				74	14	1.1	0.98	1.32	0.27	4.21	3.79	0.14	0.02	0.03	0.6
Maboko et al 2006	SGB	everywhere	KM32	TTG				70	16	2.3	2.06	2.98	0.73	5.16	1.25	0.33	0.03	0.09	0.5
Maboko et al 2006	SGB	everywhere	KM34	TTG				70	15	2.1	1.88	2.01	0.67	4.45	3.59	0.32	0.02	0.10	0.5
Maboko et al 2006	SGB	everywhere	KM46	TTG				73	15	0.9	0.78	2.14	0.30	3.84	3.69	0.09	0.01	0.01	0.9
Maboko et al 2006	SGB	everywhere	KM47	Granite-Monzonite				70	15	2.3	2.08	2.19	0.73	4.23	3.34	0.45	0.03	0.10	1.1
Maboko et al 2006	SGB	everywhere	KM48	Granite-Monzonite				67	16	3.4	3.03	1.90	0.70	4.09	5.61	0.53	0.05	0.14	0.9
Maboko et al 2006	SGB	everywhere	KM5	Granite-Monzonite				73 09	14	1.3	1.20	1.15	0.22	3.99	4.54	0.16	0.04	0.02	0.9
Maboko et al 2006	SGB	everywhere	KM52	Granite-Monzonite				68	14	3.5	3.17	2.05	0.76	3.97	4.75	0.58	0.05	0.17	1.2
Maboko et al 2006	SGB	everywhere	KM53	Granite-Monzonite				68	15	3.6	3.27	2.08	0.78	3.96	5.3	0.58	0.05	0.18	1
Maboko et al 2006	SGB	everywhere	KM54	Granite-Monzonite				75	13	1.8	1.62	1.15	0.33	3.23	5.13	0.22	2.00	0.01	0.4
Maboko et al 2006	SGB	everywhere	KM55	Granite-Monzonite				74	13	1.0	0.92	0.93	0.15	4.08	5.1	0.11	0.03	0.01	0.8
Maboko et al 2006	SGB	everywhere	KM56	Granite-Monzonite				74	13	1.8	1.62	0.56	0.16	5.29	4.51	0.19	0 04	0.01	0 60
Maboko et al 2006	SGB	everywhere	KM57	Granite-Monzonite				73	13	2.3	2.06	0.72	0.29	5.48	4.37	0.25	0.06	0.03	0.5
Maboko et al 2006	SGB	everywhere	R 14	TTG			2620	69	16	2.5	2.28	3.02	0.84	5.08	1.86	0.37	0.03	0.12	0.8
Maboko et al 2006	SGB	everywhere	R 15	TTG			2620	70	15	2.5	2.26	2.15	0.54	4.49	3.16	0.28	0.03	0.11	1.4
Maboko et al 2006	SGB	everywhere	R 16	TTG			2620	70	15	2.6	2.36	2.08	0.65	4.31	3.48	0.38	0.04	0.13	0.7
Maboko et al 2006	SGB	everywhere	R 17	TTG			2620	68	17	2.6	2.29	3.15	0.72	5.28	1.46	0.27	0.03	0.08	1
Maboko et al 2006	SGB	everywhere	R 18	TTG			2620	72	15	2.1	1.87	1.71	0.40	4.22	3.16	0.23	0.03	0.07	1.3
Maboko et al 2006	SGB	everywhere	R 19	TTG			2620	72	15	1.4	1.21	1.64	0.27	4.32	3.88	0.15	0.03	0.05	1
Maboko et al 2006	SGB	everywhere	R 2	TTG			2620	67	16	3.3	3.00	3.07	1.03	5.11	2.82	0.30	0.08	0.15	0.9
Maboko et al 2006	SGB	everywhere	R 20	TTG			2620	72	15	1.7	1.51	1.76	0.32	4.70	3.06	0.15	0.03	0.01	0.7
Maboko et al 2006	SGB	everywhere	R 21	TTG			2620	70	15	2.2	2.02	2.09	0.53	4.97	2.69	0.27	0.03	0.07	0.9
Maboko et al 2006	SGB	everywhere	R 21*	TTG				70	15	2.2	2.00	2.10	0.54	4.96	2.61	0.26	0.03	0.09	1
Maboko et al 2006	SGB	everywhere	R 26	TTG			2620	73	14	2.1	1.92	1.64	0.40	4.60	2.34	0.24	0.04	0.07	1
Maboko et al 2006	SGB	everywhere	R22	Granite-Monzonite			2620	73	14	2.0	1.80	1.07	0.32	3.82	4.29	0.2	0.08	0.07	0.9
Maboko et al 2006	SGB	everywhere	R23	Granite-Monzonite			2620	72	14	2.3	2.10	1.41	0.55	3.75	4.2	0.23	0.07	0.07	1.3
Maboko et al 2006	SGB	everywhere	R24	Granite-Monzonite			2620	71	14	2.7	2.42	1.99	0.70	3.93	3.61	0.28	0.06	0.08	0.6
Maboko et al 2006	SGB	everywhere	R25	Granite-Monzonite			2620	60	20	3.2	2.89	0.54	1.86	5.00	6.85	0.36	0.06	8.00	1.7
Maboko et al 2006	SGB	everywhere	R63	Granite-Monzonite			2620	68	14	2.9	2.57	2.84	1.41	3.20	4.52	0.4	0.04	0.11	3.3
Manya 2004	SGB	Bulyanhulu	PORP	Felsic volcanics				69	15	2.7	2.43	3.05	1.08	5.16	1.93	0.35	0.05	0.11	0.5
Manya 2004	SGB	Bulyanhulu	R06	Mafic volcanics				50	17	12.1	10.91	11.24	4.05	2.91	0.18	0.92	0.29	0.12	0.8
Manya 2004	SGB	Bulyanhulu	R07	Mafic volcanics				49	16	12.8	11.48	13.24	4.50	1.90	0.16	0.93	0.28	0.14	1.1
Manya 2004	SGB	Bulyanhulu	R08	Mafic volcanics				48	15	14.5	13.04	12.17	4.95	2.79	0.17	1.14	0.27	0.12	0.5
Manya 2004	SGB	Bulyanhulu	R09	Mafic volcanics				48	15	15.2	13.66	12.56	4.53	1.65	0.40	1.12	0.31	0.13	0.8

Reference	Belt	Location	Sample	Harmonisation litho	Age (Ma)	2σ	WR Nd age (Ma)	SiO_2	Al_2O_3	Fe_2O_3	FeO	CaO	MgO	Na_2O	K_2O	TiO_2	MnO	P_2O_5	LOI
								%	%	%	%	%	%	%	%	%	%	%	%
Manya 2004	SGB	Bulyanhulu	R10	Mafic volcanics				47	15	15.1	13.55	11.49	6.53	2.34	0.17	1.31	0.26	0.12	1
Manya 2004	SGB	Bulyanhulu	R11	Mafic volcanics				49	14	13.0	11.65	11.10	6.96	2.79	0.21	1.10	0.18	0.12	0.7
Manya 2004	SGB	Bulyanhulu	R12	Mafic volcanics				48	16	10.9	9.76	11.59	8.76	1.53	0.12	0.53	0.20	0.09	2.5
Manya 2004	SGB	Bulyanhulu	R13	Mafic volcanics				48	16	11.1	9.94	11.41	8.86	1.64	0.10	0.55	0.18	0.09	2.3
Manya 2004	SGB	Bulyanhulu	R38	Mafic volcanics				49	16	10.1	9.11	13.60	6.54	2.06	0.17	0.71	0.24	0.07	1.4
Manya 2004	SGB	Bulyanhulu	R39	Mafic volcanics				49	17	9.5	8.57	12.84	8.36	2.01	0.07	0.73	0.18	0.09	0.8
Manya 2004	SGB	Bulyanhulu	R40	Mafic volcanics				48	14	14.1	12.72	12.63	5.92	1.75	0.51	1.22	0.23	0.10	0.6
Manya 2004	SGB	Bulyanhulu	R42	Mafic volcanics				48	18	10.0	9.01	13.05	6.02	2.44	0.43	0.75	0.18	0.03	0.7
Manya 2004	SGB	Bulyanhulu	R44	Felsic volcanics				67	16	2.6	2.38	2.96	0.85	3.52	3.11	0.32	0.05	0.07	3.2
Manya 2004	SGB	Bulyanhulu	R45	Felsic volcanics				69	17	2.7	2.47	1.12	0.86	2.34	4.13	0.32	0.02	0.13	2.7
Manya 2004	SGB	Bulyanhulu	R46	Felsic volcanics				71	17	2.3	2.02	0.21	0.33	5.37	2.68	0.34	0.04	0.08	1.3
Manya 2004	SGB	Bulyanhulu	R65	Mafic volcanics				51	12	14.2	12.80	11.35	7.45	1.54	0.18	0.74	0.25	0.08	0.5
Manya 2004	SGB	Bulyanhulu	R66	Mafic volcanics				55	13	11.9	10.70	9.62	6.39	2.36	0.14	0.65	0.21	0.06	0.6
Manya 2004	SGB	Bulyanhulu	R67	Mafic volcanics				52	14	12.1	10.84	9.72	7.42	3.10	0.27	0.86	0.26	0.10	0.6
Manya 2004	SGB	Bulyanhulu	R68	Mafic volcanics				55	13	11.2	10.11	8.90	6.55	2.70	0.12	0.67	0.23	0.09	0.9
Manya 2004	SGB	Bulyanhulu	R69	Mafic volcanics				50	14	11.8	10.64	9.47	8.76	2.53	0.23	0.73	0.26	0.09	1.5
Manya 2004	SGB	Bulyanhulu	R75	Mafic volcanics				50	14	11.5	10.34	13.98	6.46	1.27	0.08	0.86	0.17	0.06	2.1
Manya 2004	SGB	Bulyanhulu	R76	Mafic volcanics				54	14	12.1	10.87	9.66	3.52	3.32	0.68	1.08	0.18	0.08	0.6
Manya 2004	SGB	Bulyanhulu	R78	Mafic volcanics				51	14	11.5	10.36	9.90	8.70	1.19	0.09	0.82	0.15	0.09	2.5
Manya 2011	CTR		IM01	Granite-Monzonite	2680	3	2680	78	13	0.7	0.60	0.75	0.05	4.39	3.77	0.06	0.02	0.02	0.07
Manya 2011	CTR		IM02	Granite-Monzonite			2680	68	16	3.2	2.86	2.71	0.99	4.83	2.67	0.38	0.05	0.18	0.83
Manya 2011	CTR		IM03	Granite-Monzonite			2680	76	13	1.2	1.09	1.13	0.13	3.75	4.52	0.13	0.02	0.03	0.26
Manya 2011	CTR		IM04	Granite-Monzonite			2680	74	13	1.8	1.61	1.01	0.25	3.41	5.36	0.15	0.03	0.05	0.43
Manya 2011	CTR		IM05	Granite-Monzonite			2680	74	14	2.0	1.78	1.54	0.40	3.75	4.3	0.22	0.03	0.08	0.52
Manya 2011	CTR		IM06	Granite-Monzonite			2680	72	13	2.5	2.26	1.19	0.47	3.52	4.73	0.34	0.05	0.10	0.54
Manya 2011	CTR		IM07	Granite-Monzonite			2680	73	13	1.6	1.41	0.80	0.23	3.16	5.92	0.1	0.02	0.08	0.33
Manya 2011	CTR		IM08	Granite-Monzonite			2680	73	13	2.1	1.87	0.97	0.25	3.18	5.27	0.22	0.04	0.06	0.47
Manya 2011	CTR		IM09	Granite-Monzonite			2680	74	13	1.9	1.73	0.96	0.24	4.23	3.5	0.09	0.04	0.05	0.42
Manya 2011	CTR		IM12	Granite-Monzonite			2680	67	14	5.5	4.94	2.75	0.86	3.66	4.08	0.69	0.07	0.21	0.5
Manya 2011	CTR		IM13	Granite-Monzonite			2680	73	13	2.0	1.82	1.05	0.25	3.22	5.21	0.23	0.05	0.05	0.64
Manya 2011	CTR		IM14	Granite-Monzonite			2680	71	14	3.0	2.68	1.74	0.72	3.30	4.7	0.39	0.04	0.14	0.52
Manya 2011	CTR		IM15	Granite-Monzonite			2680	70	15	3.2	2.86	3.23	1.11	4.31	1.48	0.38	0.04	0.10	0.63
Manya 2011	CTR		IM16	Granite-Monzonite			2680	66	17	3.5	3.19	3.63	1.22	5.05	1.47	0.52	0.03	0.19	0.79
Manya 2011	CTR		IM17	Granite-Monzonite			2680	77	13	0.8	0.75	0.95	0.10	4.10	3.89	0.08	0.01	0.02	0.32
Manya 2011	CTR		IM18	Granite-Monzonite			2680	77	13	0.9	0.79	0.85	0.09	4.27	4.15	0.08	0.01	0.03	0.13
Manya 2011	CTR		IM32	Gneiss			2680	64	16	6.2	5.62	2.67	1.17	4.56	3.91	0.83	0.09	0.33	0.64
Manya 2011	CTR		IMI0	Granite-Monzonite			2680	73	13	2.0	1.75	1.01	0.31	3.07	5.4	0.34	0.04	0.11	0.54
Manya 2011	CTR		IMII	Granite-Monzonite			2680	72	15	1.9	1.69	2.25	0.38	4.53	2.67	0.2	0.03	0.06	0.42
Manya 2016	NGB	Buzwagi	BZ 03	Granite-Monzonite				69	15	5.0	4.46	1.12	0.64	1.08	5.07	0.35	0.03	0.10	3.16
Manya 2016	NGB	Buzwagi	BZ 04	Granite-Monzonite				72	13	4.4	3.95	0.66	0.48	0.53	5.24	0.33	0.05	0.08	2.68
Manya 2016	NGB	Buzwagi	BZ 06	Granite-Monzonite				71	15	2.3	2.03	1.94	0.48	3.78	3.98	0.36	0.04	0.11	1.27
Manya 2016	NGB	Buzwagi	BZ 08	Granite-Monzonite	2674	18	2674	72	15	1.7	1.52	1.79	0.47	4.39	3.88	0.33	0.03	0.08	0.91
Manya 2016	NGB	Buzwagi	BZ 10	Granite-Monzonite				72	15	1.9	1.67	1.65	0.45	4.51	3.92	0.44	0.02	0.15	0.81
Manya 2016	NGB	Buzwagi	BZ 13	Granite-Monzonite				70	15	1.9	1.66	1.82	0.49	4.44	3.69	0.33	0.04	0.09	1.06
Manya 2016	NGB	Buzwagi	BZ 18	TTG				72	14	2.1	1.87	2.53	0.57	4.10	2.11	0.22	0.03	0.07	1.16
Manya 2016	NGB	Buzwagi	BZ 19	TTG	2713	8		72	15	2.0	1.81	2.46	0.65	4.54	2.37	0.24	0.05	0.06	1.3
Manya 2016	NGB	Buzwagi	BZ 23	TTG	2713	8	2713	66	16	3.7	3.37	4.06	1.80	4.79	2.14	0.48	0.08	0.14	139
Manya 2016	NGB	Buzwagi	BZ 24	TTG	2713	8	2713	642	16	4.7	4.21	2.57	1.06	4.88	3.24	0.58	0.07	0.18	1.74

Reference	Belt	Location	Sample	Harmonisation litho	Age (Ma)	2σ	WR Nd age (Ma)	SiO_2	Al_2O_3	Fe_2O_3	FeO	CaO	MgO	Na_2O	K_2O	TiO_2	MnO	P_2O_5	LOI
								%	%	%	%	%	%	%	%	%	%	%	%
Manya 2016	NGB	Buzwagi	BZ 25	TTG				68	17	2.3	2.11	2.87	0.62	5.56	1.99	0.24	0.06	0.09	1.21
Manya 2016	NGB	Buzwagi	BZ 34	TTG				71	15	2.1	1.90	2.42	0.62	5.16	1.00	0.24	0.03	0.05	1.93
Manya 2016	NGB	Buzwagi	BZ01	Granite-Monzonite				77	13	1.2	1.04	1.22	0.23	2.42	4.45	0.11	0.02	0.02	1.38
Manya 2016	NGB	Buzwagi	BZ02	Granite-Monzonite				67	12	7.0	6.31	0.60	0.57	0.59	4.54	0.31	0.03	0.08	5.33
Manya 2016	NGB	Buzwagi	BZ05	Granite-Monzonite				82	9	1.0	0.92	1.06	0.22	2.82	2.49	0.23	0.02	0.07	0.64
Manya 2016	NGB	Buzwagi	BZ09	Granite-Monzonite				72	15	1.6	1.40	1.44	0.33	4.17	4.33	0.33	0.03	0.07	0.79
Manya 2016	NGB	Buzwagi	BZ11	Granite-Monzonite	2674	18	2674	71	15	1.4	1.27	1.57	0.32	3.53	5.07	0.27	0.03	0.05	1.16
Manya 2016	NGB	Buzwagi	BZ20	TTG				72	15	2.1	1.86	2.42	0.60	4.82	2.10	0.23	0.04	0.08	1.19
Manya 2016	NGB	Buzwagi	BZ26	TTG				70	15	2.1	1.88	2.54	0.59	4.49	2.58	0.22	0.06	0.07	1.2
Manya 2016	NGB	Buzwagi	BZ27	TTG				73	15	1.9	1.70	1.75	0.47	3.85	323.00	0.28	0.04	0.07	1.42
Manya 2016	NGB	Buzwagi	BZ28	TTG				72	15	1.9	1.69	2.71	0.63	4.46	1.87	0.24	0.04	0.07	1.19
Manya 2016	NGB	Buzwagi	BZ29	TTG				71	15	1.8	1.65	2.82	0.57	4.39	1.97	0.23	0.04	0.07	1.18
Manya and Maboko 2008a	ISGB		SIN 07a	Mafic volcanics				51	14	14.2	12.78	8.29	4.89	3.80	0.23	1.40	0.23	0.24	0.82
Manya and Maboko 2008a	ISGB		SIN 07b	Mafic volcanics				51	14	14.4	12.96	8.54	4.91	3.78	0.23	1.42	0.23	0.24	0.57
Manya and Maboko 2008a	ISGB		SIN 08	Mafic volcanics				48	14	17.4	15.66	9.93	4.88	2.83	0.23	1.17	0.22	0.28	0.99
Manya and Maboko 2008a	ISGB		SIN 11	Mafic volcanics				51	14	10.6	9.54	12.90	5.64	0.98	2.07	1.01	0.24	0.15	0.85
Manya and Maboko 2008a	ISGB		SIN 12	Mafic volcanics				48	15	13.3	11.97	13.70	5.82	1.70	0.14	0.74	0.19	0.10	0.5
Manya and Maboko 2008a	ISGB		SIN 13	Mafic volcanics				48	16	12.4	11.16	13.50	4.68	2.81	0.68	0.80	0.21	0.11	0.54
Manya and Maboko 2008a	ISGB		SIN 15	Mafic volcanics				51	14	10.5	9.45	12.00	5.93	3.26	0.13	0.96	0.24	0.17	0.8
Manya and Maboko 2008a	ISGB		SIN 17	Mafic volcanics				50	15	11.1	9.99	14.00	4.95	2.61	0.13	0.70	0.19	0.09	
Manya and Maboko 2008a	ISGB		SIN 18	Mafic volcanics				47	16	13.2	11.88	11.30	5.17	2.46	0.57	1.13	0.19	0.26	1.96
Manya and Maboko 2008a	ISGB		SIN 19	Mafic volcanics				52	15	10.6	9.54	10.60	4.78	2.73	0.53	1.03	0.15	0.19	1.56
Manya and Maboko 2008a	ISGB		SIN 20	Mafic volcanics				53	18	9.6	8.67	9.40	4.79	3.61	0.24	1.08	0.23	0.20	1.45
Manya and Maboko 2008a	ISGB		SIN 21	Mafic volcanics				49	16	14.3	12.87	11.50	3.94	1.99	0.47	1.10	0.21	0.20	0.76
Manya and Maboko 2008a	ISGB		SIN 22	Mafic volcanics				50	16	13.5	12.15	10.70	4.37	2.67	0.18	0.86	0.28	0.15	1.04
Manya and Maboko 2008a	ISGB		SIN 23	Mafic volcanics				50	16	10.8	9.72	11.10	5.43	3.32	0.52	0.99	0.21	0.21	1.16
Manya and Maboko 2008a	ISGB		SIN 24	Mafic volcanics				52	15	10.5	9.45	10.00	5.48	3.32	0.39	1.28	0.23	0.22	1.26
Manya and Maboko 2008a	ISGB		SIN 25	Mafic volcanics				50	15	12.6	11.34	12.50	4.35	3.51	0.37	1.00	0.27	0.18	0.79
Manya and Maboko 2008a	ISGB		SIN 28	Mafic volcanics				49	15	12.7	11.43	9.59	7.05	3.83	0.38	0.86	0.22	0.13	0.95
Manya and Maboko 2008a	ISGB		SIN 29	Mafic volcanics				52	16	11.1	9.99	9.98	5.00	4.31	0.24	0.85	0.20	0.13	0.59
Manya and Maboko 2008a	ISGB		SIN IO	Mafic volcanics				49	14	17.2	15.48	7.91	6.10	3.35	0.16	1.22	0.18	0.23	1.02
Manya and Maboko 2008a	ISGB		SIN01	Mafic volcanics				49	14	14.1	12.69	12.30	4.21	1.86	0.18	1.26	0.25	0.22	2.17
Manya and Maboko 2008a	ISGB		SIN02	Mafic volcanics				49	14	13.9	12.51	11.80	4.67	2.46	0.25	1.24	0.25	0.21	1.84
Manya and Maboko 2008a	ISGB		SIN04	Mafic volcanics				50	14	12.6	11.34	10.00	4.19	3.11	0.19	1.74	0.31	0.28	3.32
Manya and Maboko 2008b	SGB	Geita	GT 02	Mafic volcanics				50	14	13.4	12.06	10.20	6.33	2.36	0.20	1.15	0.19	0.21	2.23
Manya and Maboko 2008b	SGB	Geita	GT 04	Mafic volcanics				50	14	11.8	10.62	12.00	5.41	3.72	0.30	1.15	0.23	0.16	0.9
Manya and Maboko 2008b	SGB	Geita	GT 06	Mafic volcanics			2821	47	14	13.9	12.51	12.50	6.41	2.66	0.36	1.19	0.27	0.20	1.44
Manya and Maboko 2008b	SGB	Geita	GT 08	Mafic volcanics				53	15	8.6	7.72	12.00	5.96	2.33	0.19	0.89	0.19	0.17	1.16
Manya and Maboko 2008b	SGB	Geita	GT 09	Mafic volcanics				50	16	9.0	8.10	11.30	7.64	2.25	0.44	0.88	0.21	0.18	1.33
Manya and Maboko 2008b	SGB	Geita	GT 12	Mafic volcanics				52	15	10.0	9.00	12.20	5.58	1.99	0.24	0.99	0.26	0.14	1.03
Manya and Maboko 2008b	SGB	Geita	GT 15	Mafic volcanics				51	14	10.5	9.45	12.00	5.93	3.26	0.13	0.96	0.24	0.17	1.8
Manya and Maboko 2008b	SGB	Geita	GT 18	Mafic volcanics				52	14	11.1	9.99	12.70	4.86	1.61	0.16	1.00	0.22	0.15	0.67
Manya and Maboko 2008b	SGB	Geita	GT 19	Mafic volcanics				50	14	12.8	11.52	10.10	6.18	3.22	0.21	0.95	0.18	0.15	1.57
Manya and Maboko 2008b	SGB	Geita	GT01	Mafic volcanics				47	15	14.7	13.23	10.40	6.26	1.95	0.25	1.19	0.19	0.14	1.89
Manya and Maboko 2008b	SGB	Geita	GT05	Mafic volcanics				49	14	13.6	12.24	10.20	6.20	2.41	0.32	1.16	0.20	0.20	1.83
Manya and Maboko 2008b	SGB	Geita	GT07	Mafic volcanics			2821	53	15	8.8	7.91	12.30	5.71	1.86	0.20	0.89	0.27	0.18	1.01
Manya and Maboko 2008b	SGB	Geita	GT10	Mafic volcanics				48	15	13.2	11.88	10.60	7.76	2.06	0.09	0.99	0.19	0.19	1.39
Manya and Maboko 2008b	SGB	Geita	GT11	Mafic volcanics			2821	52	15	10.2	9.18	12.00	5.12	2.20	0.16	1.01	0.22	0.15	0.89

Reference	Belt	Location	Sample	Harmonisation litho	Age (Ma)	2σ	WR Nd age (Ma)	SiO_2	Al_2O_3	Fe_2O_3	FeO	CaO	MgO	Na_2O	K_2O	TiO_2	MnO	P_2O_5	LOI
								%	%	%	%	%	%	%	%	%	%	%	%
Manya and Maboko 2008b	SGB	Geita	GT13	Mafic volcanics				51	15	10.9	9.81	12.20	4.84	2.08	0.28	1.00	0.24	0.18	1.1
Manya and Maboko 2008b	SGB	Geita	GT14	Mafic volcanics			2821	49	14	12.6	11.34	11.60	6.75	2.22	0.14	0.98	0.18	0.22	1.13
Manya and Maboko 2008b	SGB	Geita	GT16	Mafic volcanics			2821	56	16	7.3	6.56	10.10	4.40	3.95	0.10	1.02	0.21	0.15	0.49
Manya and Maboko 2008b	SGB	Geita	GT17	Mafic volcanics				47	14	12.9	11.61	9.67	6.87	2.19	0.13	0.91	0.16	0.15	5.49
Manya and Maboko 2008b	SGB	Geita	GT20	Mafic volcanics				50	14	13.3	11.97	10.00	6.94	1.68	0.09	1.06	0.17	0.18	1.8
Messo et al 2012	KGB		MU100	Intermediate volcanics				52	16	12.9	11.61	5.97	3.64	4.75	1.16	1.42	0.15	0.12	1.99
Messo et al 2012	KGB		MU109	Mafic volcanics				49	17	6.2	5.58	12.30	8.30	2.99	0.81	0.62	0.08	0.01	2.15
Messo et al 2012	KGB		MU12	Intermediate volcanics				55	13	9.3	8.37	7.54	6.00	5.14	0.79	1.53	0.25	0.07	0.92
Messo et al 2012	KGB		MU13	Intermediate volcanics				53	15	10.8	9.72	10.94	4.66	2.49	0.27	1.44	0.24	0.06	1.03
Messo et al 2012	KGB		MU14	Mafic volcanics				50	15	12.3	11.07	10.90	5.45	2.29	0.52	1.36	0.27	0.04	1.46
Messo et al 2012	KGB		MU15	Mafic volcanics				47	16	12.4	11.16	10.90	8.09	1.84	0.17	0.92	0.17	0.01	2.14
Messo et al 2012	KGB		MU16	Felsic volcanics				75	14	0.3	0.31	0.26	0.23	5.14	3.98	0.03	0.02	0.01	0.75
Messo et al 2012	KGB		MU17	Felsic volcanics				76	14	0.3	0.25	0.10	0.22	5.17	3.61	0.03	0.01	0.01	0.69
Messo et al 2012	KGB		MU18	Felsic volcanics				75	14	0.3	0.31	0.15	0.25	5.32	3.41	0.03	0.01	0.01	0.69
Messo et al 2012	KGB		MU19	Mafic volcanics				50	14	11.9	10.71	10.70	7.53	1.92	0.15	0.60	0.17	0.01	2.17
Messo et al 2012	KGB		MU20	Mafic volcanics				50	14	12.9	11.61	10.70	7.32	1.79	0.11	0.66	0.18	0.01	2.45
Messo et al 2012	KGB		MU21	Intermediate volcanics				53	15	11.2	10.08	8.54	5.58	1.74	1.45	0.84	0.16	0.01	2.29
Messo et al 2012	KGB		MU27	Intermediate volcanics				65	16	4.2	3.78	3.65	2.68	4.91	0.83	0.58	0.06	0.06	2.19
Messo et al 2012	KGB		MU33	Intermediate volcanics				61	17	6.7	6.03	2.73	3.57	6.15	0.31	0.67	0.10	0.08	2.53
Messo et al 2012	KGB		MU35	Intermediate volcanics				54	14	11.3	10.17	9.62	3.42	3.12	1.44	1.45	0.11	0.12	1.39
Messo et al 2012	KGB		MU36	Intermediate volcanics				55	13	12.0	10.80	6.25	3.71	4.96	1.09	1.46	0.14	0.12	1.34
Messo et al 2012	KGB		MU37	Intermediate volcanics				54	14	11.2	10.08	9.49	3.43	2.70	1.43	1.36	0.11	0.12	1.72
Messo et al 2012	KGB		MU38	Intermediate volcanics				54	14	11.9	10.71	6.41	3.46	4.02	1.88	1.54	0.14	0.15	1.81
Messo et al 2012	KGB		MU39	Intermediate volcanics				54	15	12.1	10.89	5.30	3.62	5.00	1.77	1.60	0.14	0.15	1.83
Messo et al 2012	KGB		MU43	Mafic volcanics				48	15	13.3	11.97	10.30	6.62	1.96	0.03	1.73	0.19	0.19	3.19
Messo et al 2012	KGB		MU49	Intermediate volcanics				54	14	12.1	10.89	5.69	3.85	5.34	1.34	1.46	0.15	0.13	1.75
Messo et al 2012	KGB		MU54	Intermediate volcanics				54	14	11.8	10.62	8.30	4.24	2.67	2.09	1.26	0.12	0.12	1.97
Messo et al 2012	KGB		MU57	Intermediate volcanics				54	13	11.3	10.17	6.40	3.53	4.69	1.44	1.35	0.12	0.13	3.3
Messo et al 2012	KGB		MU60	Intermediate volcanics				55	14	11.7	10.53	6.94	3.77	3.10	2.75	1.38	0.12	0.03	1.66
Messo et al 2012	KGB		MU64	Intermediate volcanics				56	15	9.1	8.19	6.28	5.27	3.85	0.37	0.91	0.19	0.01	2.93
Messo et al 2012	KGB		MU65	Intermediate volcanics				55	14	10.8	9.72	7.16	3.80	3.01	2.20	1.24	0.13	0.11	2
Messo et al 2012	KGB		MU66	Intermediate volcanics				55	14	12.0	10.80	7.43	3.50	3.94	0.73	1.41	0.13	0.13	1.69
Messo et al 2012	KGB		MU68	Intermediate volcanics				62	14	6.6	5.94	4.53	2.60	4.20	1.50	0.84	0.09	0.16	2.8
Messo et al 2012	KGB		MU69	Mafic volcanics				48	14	13.5	12.15	10.50	6.76	1.91	0.10	1.75	0.18	0.09	2.55
Messo et al 2012	KGB		MU76	Intermediate volcanics				52	15	12.4	11.16	7.36	4.40	3.66	1.25	1.42	0.14	0.11	2.48
Messo et al 2012	KGB		MU77	Intermediate volcanics				52	14	12.6	11.34	7.97	4.20	2.83	1.91	1.38	0.14	0.02	2.35
Messo et al 2012	KGB		MU78	Intermediate volcanics				53	14	12.2	10.98	8.36	4.04	2.88	1.48	1.34	0.14	0.11	1.78
Messo et al 2012	KGB		MU79	Intermediate volcanics				52	14	12.4	11.16	8.38	4.10	2.87	1.67	1.37	0.14	0.11	1.79
Messo et al 2012	KGB		MU80	Intermediate volcanics				53	14	12.5	11.25	6.74	3.88	4.32	1.60	1.49	0.14	0.12	1.59
Messo et al 2012	KGB		MU81	Intermediate volcanics				53	14	12.6	11.34	7.00	3.92	3.92	1.52	1.49	0.14	0.13	1.57
Messo et al 2012	KGB		MU82	Intermediate volcanics				54	15	8.2	7.38	8.87	6.47	3.14	0.57	0.70	0.13	0.11	2.46
Messo et al 2012	KGB		MU83	Intermediate volcanics				54	14	12.4	11.16	6.82	3.86	4.20	1.57	1.51	0.14	0.13	1.52
Messo et al 2012	KGB		MU84	Intermediate volcanics				52	15	13.0	11.70	6.01	3.89	4.63	1.79	1.62	0.14	0.14	1.49
Messo et al 2012	KGB		MU85	Intermediate volcanics				54	14	11.3	10.17	7.40	4.44	2.91	2.89	1.25	0.13	0.11	1.7
Messo et al 2012	KGB		MU86	Intermediate volcanics				55	14	11.3	10.17	6.36	3.60	5.57	1.27	1.35	0.14	0.12	1.4
Messo et al 2012	KGB		MU87	Intermediate volcanics				54	14	12.2	10.98	7.03	3.68	3.79	1.47	1.41	0.13	0.13	1.97
Messo et al 2012	KGB		MU89	Intermediate volcanics				56	14	11.8	10.62	6.39	3.72	3.73	1.91	1.41	0.13	0.14	1.65
Messo et al 2012	KGB		MU90	Intermediate volcanics				56	13	11.4	10.26	7.13	3.55	3.62	0.15	1.43	0.12	0.13	2.94

Reference	Belt	Location	Sample	Harmonisation litho	Age (Ma)	2σ	WR Nd age (Ma)	SiO_2	Al_2O_3	Fe_2O_3	FeO	CaO	MgO	Na_2O	K_2O	TiO_2	MnO	P_2O_5	LOI
								%	%	%	%	%	%	%	%	%	%	%	%
Messo et al 2012	KGB		MU91	Intermediate volcanics				53	14	13.5	12.15	6.32	3.82	4.63	0.95	1.52	0.16	0.13	1.7
Messo et al 2012	KGB		MU92	Intermediate volcanics				51	14	11.6	10.44	9.37	7.08	2.41	0.88	0.84	0.15	0.03	2.27
Messo et al 2012	KGB		MU93	Intermediate volcanics				53	14	12.5	11.25	5.66	4.89	4.53	2.06	1.20	0.19	0.09	1.87
Messo et al 2012	KGB		MU94	Intermediate volcanics				55	15	11.4	10.26	5.84	3.66	4.55	1.66	1.37	0.13	0.10	1.4
Messo et al 2012	KGB		MU95	Intermediate volcanics				54	14	11.6	10.44	5.56	4.10	4.00	2.57	1.41	0.14	0.13	1.63
Messo et al 2012	KGB		MU96	Intermediate volcanics				54	15	12.5	11.25	5.28	4.56	4.91	1.77	1.09	0.15	0.10	0.94
Messo et al 2012	KGB		MU97	Intermediate volcanics				55	14	11.3	10.17	5.40	4.26	5.04	1.62	1.07	0.17	0.09	1.5
Sanislav et al 2014a	SGB	Geita	GP-01	Granite-Monzonite	2652	10		64	16	5.2	4.72	3.43	1.56	4.03	3.73	0.76	0.07	0.25	1.14
Sanislav et al 2014a	SGB	Geita	GP-02	Granite-Monzonite	2634	41		69	14	3.8	3.41	2.25	0.66	3.63	4.71	0.64	0.05	0.16	0.74
Sanislav et al 2014a	SGB	Geita	GP-03	Granite-Monzonite	2661	14		73	14	1.7	1.56	1.31	0.47	3.66	4.71	0.29	0.03	0.05	0.51
Sanislav et al 2014a	SGB	Geita	GX-01	Granite-Monzonite	2642	32		68	15	3.8	3.45	2.67	1.03	3.85	3.91	0.55	0.05	0.16	1
Sanislav et al 2014a	SGB	Geita	XU-01	Granite-Monzonite	2617	11		70	14	3.7	3.33	1.96	0.59	3.64	4.89	0.6	0.05	0.15	0.56
Sanislav et al 2014a	SGB	Geita	XU-01A	Granite-Monzonite	2628	12		68	14	4.3	3.83	2.06	0.73	3.58	5.12	0.66	0.05	0.17	0.66
Sanislav et al 2014a	SGB	Geita	XU-02	Granite-Monzonite	2623	15		76	12	2.0	1.81	0.88	0.21	2.79	5.37	0.31	0.03	0.06	0.45
Wu et al 2023	SGB	Geita	18TGE01-1	TTG	2683	16	2683	71	16	1.4	0.66	2.76	0.70	5.16	1.71	0.29	0.03	0.09	0.7
Wu et al 2023	SGB	Geita	18TGE01-0	TTG				71	16	1.2	0.70	2.60	0.66	5.12	1.89	0.30	0.03	0.09	0.46
Wu et al 2023	SGB	Geita	18TGE01-2	TTG				72	15	1.2	0.58	2.24	0.55	5.08	2.05	0.25	0.03	0.08	0.88
Wu et al 2023	SGB	Geita	18TGE01-3	TTG			2683	72	15	1.1	0.55	2.06	0.50	5.15	2.37	0.26	0.03	0.08	0.55
Wu et al 2023	SGB	Geita	18TGE01-4	TTG				73	15	1.1	0.37	1.87	0.45	4.97	2.43	0.22	0.04	0.06	0.72
Wu et al 2023	SGB	Geita	18TGE01-5	TTG			2683	73	15	1.0	0.36	1.82	0.40	5.01	2.57	0.20	0.03	0.06	0.98
Wu et al 2023	SGB	Geita	18TGE01-6	TTG				75	14	0.6	0.20	1.22	0.24	4.74	3.26	0.11	0.03	0.03	0.54
Wu et al 2023	SGB	Geita	18TGE01-7	TTG	2708	12	2683	73	15	0.9	0.40	1.85	0.37	4.99	2.55	0.18	0.02	0.06	0.81
Wu et al 2023	SGB	Geita	18TGE01-8	TTG				73	15	0.9	0.47	1.81	0.42	5.03	2.51	0.20	0.03	0.06	0.75
Wu et al 2023	SGB	Geita	18TGE01-9	TTG	2710	9	2683	72	15	1.0	0.77	2.37	0.61	5.09	2.08	0.27	0.03	0.08	0.87
Manya 2012	MMGB			Mafic volcanics			2768	49	12	10.4	9.36	11.30	11.10	1.25	0.82	0.72	0.21	0.31	2.67
Manya 2012	MMGB			Mafic volcanics			2768	54	11	12.1	10.89	8.51	10.10	2.61	0.01	0.87	0.17	0.06	1.11
Manya 2012	MMGB			Mafic volcanics			2768	49	10	12.3	11.07	8.45	15.60	1.13	0.02	0.60	0.19	0.06	2.62
Manya 2012	MMGB			Mafic volcanics			2768	48	13	13.7	12.33	11.80	7.64	2.04	0.12	1.13	0.18	0.08	1.53
Manya 2012	MMGB			Mafic volcanics			2768	47	12	14.3	12.87	12.40	8.59	1.34	0.51	0.80	0.19	0.01	2.32
Manya 2012	MMGB			Mafic volcanics			2768	52	13	11.7	10.53	9.80	7.91	2.00	0.40	0.72	0.17	0.06	2.19
Kwelwa 2017	SGB	Kukuluma	KIC-01	Felsic volcanics	Syn tectonic			57	16	3.4	3.09	6.23	2.53	6.64	0.86	0.46	0.05	0.50	4.58
Kwelwa 2017	SGB	Kukuluma	KIC-02	Felsic volcanics	Syn tectonic			59	14	4.2	3.78	5.85	3.55	4.97	2.43	0.42	0.07	0.40	3.97
Kwelwa 2017	SGB	Kukuluma	KIC-03	Felsic volcanics	Syn tectonic			57	16	6.5	5.88	5.29	2.94	6.17	3.15	0.47	0.10	0.36	1.88
Kwelwa 2017	SGB	Kukuluma	KIC-04	Felsic volcanics	Syn tectonic			57	16	6.8	6.14	4.09	3.61	4.49	3.44	0.51	0.05	0.44	4.53
Kwelwa 2017	SGB	Kukuluma	KIC-05	Felsic volcanics	Syn tectonic			56	17	6.0	5.44	4.50	3.00	5.69	3.17	0.52	0.08	0.47	3.78
Kwelwa 2017	SGB	Kukuluma	KIC-06	Felsic volcanics	Syn tectonic			55	16	6.2	5.54	4.39	3.40	6.22	2.75	0.51	0.07	0.45	3.58
Kwelwa 2017	SGB	Kukuluma	KIC-07	Felsic volcanics	Syn tectonic			62	17	4.4	3.97	3.96	2.58	6.61	2.05	0.42	0.05	0.35	0.92
Kwelwa 2017	SGB	Kukuluma	KIC-08	Felsic volcanics	Syn tectonic			53	14	7.9	7.11	6.98	5.53	4.46	3.57	0.58	0.09	0.86	3.14
Kwelwa 2017	SGB	Kukuluma	KIC-09	Felsic volcanics	Syn tectonic			56	16	6.5	5.89	3.78	3.47	5.63	2.67	0.49	0.07	0.43	4.54
Kwelwa 2017	SGB	Kukuluma	KIC-10	Felsic volcanics	Syn tectonic			52	15	10.0	9.03	4.51	5.62	4.50	2.71	0.56	0.07	0.83	4.13
Kwelwa 2017	SGB	Kukuluma	KIC-11	Felsic volcanics	Syn tectonic			57	15	7.7	6.90	5.26	2.77	6.27	1.71	0.46	0.08	0.46	4.86
Kwelwa 2017	SGB	Kukuluma	KIC-12	TTG	Syn tectonic			58	16	8.3	7.49	2.92	2.04	5.11	2.84	0.39	0.04	0.15	3.38
Kwelwa 2017	SGB	Kukuluma	KIC-13	TTG	Syn tectonic			63	15	3.1	2.83	3.46	2.61	5.17	3.24	0.32	0.04	0.21	3.24
Kwelwa 2017	SGB	Kukuluma	KIC-14	TTG	Syn tectonic			63	14	3.4	3.02	4.20	2.70	5.61	2.18	0.33	0.05	0.20	3.92
Kwelwa 2017	SGB	Kukuluma	KIC-15	TTG	Syn tectonic			62	17	7.8	6.98	3.13	2.97	3.62	1.75	0.58	0.07	0.21	1.72
Kwelwa 2017	SGB	Kukuluma	KIC-16	TTG	Syn tectonic			53	17	8.7	7.82	6.26	4.16	3.56	1.67	0.67	0.10	0.24	5.24
Kwelwa 2017	SGB	Kukuluma	KIC-17	TTG	Syn tectonic			55	16	7.8	7.00	6.55	3.46	3.79	1.35	0.64	0.13	0.27	5.55
Kwelwa 2017	SGB	Kukuluma	KIC-18	TTG	Syn tectonic			59	16	7.7	6.91	4.38	2.70	3.36	2.74	0.51	0.12	0.20	4.16

Reference	Belt	Location	Sample	Harmonisation litho	Age (Ma)	2σ	WR Nd age (Ma)	SiO_2	Al_2O_3	Fe_2O_3	FeO	CaO	MgO	Na_2O	K_2O	TiO_2	MnO	P_2O_5	LOI
								%	%	%	%	%	%	%	%	%	%	%	%
Kwelwa 2017	SGB	Kukuluma	KIC-19	TTG	Syn tectonic			59	17	7.5	6.78	4.71	3.07	4.79	1.18	0.59	0.09	0.20	2.43
Kwelwa 2017	SGB	Kukuluma	KIC-20	TTG	Syn tectonic			57	17	8.1	7.33	3.65	3.17	3.84	2.45	0.61	0.06	0.31	1.44
Kwelwa 2017	SGB	Kukuluma	KIC-21	TTG	Syn tectonic			58	16	8.6	7.71	6.59	2.15	3.14	2.21	0.51	0.08	0.18	3.32
Kwelwa 2017	SGB	Kukuluma	KIC-22	TTG	Late to post			63	16	5.4	4.83	3.78	1.87	3.39	3.60	0.55	0.08	0.17	3.66
Kwelwa 2017	SGB	Kukuluma	KIC-23	TTG	Late to post			63	16	5.6	5.04	3.11	1.93	3.87	3.41	0.56	0.08	0.17	3.15
Kwelwa 2017	SGB	Kukuluma	KIC-24	TTG	Late to post			62	16	5.3	4.81	3.88	1.88	3.24	3.72	0.55	0.08	0.16	3.23
Kwelwa 2017	SGB	Kukuluma	KIC-25	TTG	Late to post			62	16	5.4	4.87	4.09	1.89	2.98	3.93	0.56	0.08	0.17	3.7

Reference	Sample	Harmonisation litho	Sc	V	Mn	Cr	Cu	Zn	Ga	Ge	As	Ta	Ni	Co	Rb	Sr	Y	Zr	Nb	Mo	Sn	Sb	Cs	Ba	La
			ppm	ppm	ppm	ppm	ppm	ppm	ppm	ppm	ppm	ppm	ppm	ppm	ppm	ppm	ppm	ppm	ppm	ppm	ppm	ppm	ppm	ppm	ppm
Boniface and Mruma 2012	N12	Granite-Monzonite		31		36		44.8	19.8			0.83		5	124	281	12	138	6.59				4.23		32.1
Boniface and Mruma 2012	N29A	Granite-Monzonite		23		4		44	21.1			0.09		4	52	686	3	111	0.9				3.6		7.55
Boniface and Mruma 2012	N33	Granite-Monzonite		53		10		80.4	24.6			0.75		6	64	1436	16	192	8.47				3.12		49.1
Boniface and Mruma 2012	N49	Mafic volcanics		341		120		131.00	19.40			0.26		49	8	147	27	71	2.79				0.58		5.04
Boniface and Mruma 2012	N51	Felsic volcanics		41		38		55.00	21.10			0.44		6	114	713	10	122	4.72				1.64		27.00
Boniface and Mruma 2012	N54	Felsic volcanics		88		153		47.00	19.80			0.48		20	32	407	14	149	4.17				1.86		15.40
Cloutier et al 2005	D0142	Granite-Monzonite	2									1.84			19	148	2	37	13.10					35	1.48
Cloutier et al 2005	D0142-1	Sediment	15	102		118						0.69	48	18	92	206	15	150	7.80					829	28.40
Cloutier et al 2005	D0146-1	Mafic volcanics	41	313		52						0.22	42	41	11	116	25	66	3.80					75	4.12
Cloutier et al 2005	D0149-1	Sediment	18	123		132						0.84	51	17	111	154	18	119	8.10					915	31.20
Cloutier et al 2005	D0149-10	Sediment	21	122		152						0.78	60	19	123	409	19	108	9.00					560	36.10
Cloutier et al 2005	D0149-12	Sediment	20	117		126						0.66	57	19	185	162	19	114	7.70					1240	30.40
Cloutier et al 2005	D0149-13	Felsic volcanics	14	76		71						0.53		9	5	24	14	92	5.10					26	16.20
Cloutier et al 2005	D0149-14	Sediment	19	119		128						0.70	53	17	146	267	19	121	7.80					659	32.00
Cloutier et al 2005	D0149-17	Sediment	20	121		128						0.67	52	18	124	241	20	131	7.90					806	30.60
Cloutier et al 2005	D0149-18	Sediment	25	155		164						0.76	71	22	145	190	21	102	8.80					741	34.90
Cloutier et al 2005	D0149-19	Sediment	25	155		168						0.77	75	24	142	242	21	105	8.40					790	34.60
Cloutier et al 2005	D0149-2	Sediment	9	82		78						0.27	29	14	32	389	10	84	3.20					328	9.37
Cloutier et al 2005	D0149-20	Sediment	13	70		84						0.45	36	13	27	73	14	85	5.70					82	18.00
Cloutier et al 2005	D0149-3	Felsic volcanics	7	51		33						0.22		6	106	114	11	91	3.60					240	11.70
Cloutier et al 2005	D0149-4	Sediment	12	79		83						0.36	39	12	105	231	13	83	4.30					540	18.80
Cloutier et al 2005	D0149-6	Sediment	25	152		170						0.73	88	20	147	229	18	104	7.90					848	36.30
Cloutier et al 2005	D0149-7	Sediment	13	85		112						0.55	43	15	93	209	18	148	6.60					625	31.90
Cloutier et al 2005	D0149-8	Sediment	23	142		158						0.75	64	19	153	186	21	115	8.40					951	37.30
Cloutier et al 2005	D0159-1	Sediment	18	114		138						0.77	37	18	82	263	14	110	8.80					662	17.50
Cloutier et al 2005	D0159-2	Sediment	26	158		191						0.83	76	29	129	247	23	116	23.00					920	43.00
Cloutier et al 2005	D0159-3	Sediment	22	126		133						0.97	57	17	135	173	20	113	8.20					972	30.60
Cloutier et al 2005	D0159-4	Sediment	19	104		116						0.65	49	18	126	366	17	128	7.50					622	28.80
Cloutier et al 2005	D0159-5	Sediment	18	107		126						0.66	104	15	119	279	17	117	7.80					653	31.10
Cloutier et al 2005	D0159-6	Sediment	28	173		186						0.88	82	33	191	172	25	99	21.20					1530	51.90
Cloutier et al 2005	D0185-1	Mafic volcanics	52	454								0.41		17	30	206	46	143	6.30					131	5.05
Cloutier et al 2005	D0309-1	Mafic volcanics	47	443		20						0.47	31	43	12	113	43	132	7.00					96	8.48

Reference	Sample	Harmonisation litho	Sc	V	Mn	Cr	Cu	Zn	Ga	Ge	As	Ta	Ni	Co	Rb	Sr	Y	Zr	Nb	Mo	Sn	Sb	Cs	Ba	La
			ppm	ppm	ppm	ppm	ppm	ppm	ppm	ppm	ppm	ppm	ppm	ppm	ppm	ppm	ppm	ppm	ppm	ppm	ppm	ppm	ppm	ppm	ppm
Cloutier et al 2005	D0309-2	Mafic volcanics	30	224								0.45	0	33	21	184	43	141	6.80					103	11.70
Cloutier et al 2005	D0309-3	Mafic volcanics	45	357		58						0.21	49	42	7	117	24	64	3.90					54	3.98
Cloutier et al 2005	D0310-1	Proterozoic granitoid	8			54						0.23			393	8	47	31	20.10					24	5.72
Cloutier et al 2005	D0310-2	Sediment	24	141		153						0.78	61	13	277	54	15	116	9.10					1050	20.70
Cloutier et al 2005	D0310-3	Proterozoic granitoid	4									5.49			290	7	51	40	23.30					10	10.50
Cloutier et al 2005	D03104	Proterozoic granitoid	5									5.52			350	7	41	30	25.00					13	10.70
Cook et al 2016	E1	Mafic volcanics	36	327		134	94	67.41	14.42	1.73	5.04				22	149	18	47	2.15	1.12	1.00	0.78	0.77	198	3.10
Cook et al 2016	E4	Mafic volcanics	40	327		159	94	73.04	14.63	1.72	1.96				13	108	21	57	2.57	0.95	1.29	0.69	1.00	65	3.28
Cook et al 2016	E5	Mafic volcanics	42	281		160	86	55.29	13.62	1.91	7.66				4	196	14	48	2.09	1.06	0.92	0.91	1.45	82	2.76
Cook et al 2016	E6	Mafic volcanics	41	292		117	118	68.08	14.23	1.65	15.03				4	99	20	58	2.61	1.42	1.20	1.36	1.54	40	3.79
Cook et al 2016	IH11	Mafic volcanics	47	339		241	89	80.05	18.49	2.02	3.06				3	69	24	65	2.98	1.36	1.18	0.74	0.55	24	3.98
Cook et al 2016	IH12	Mafic volcanics	40	303		82	21	59.35	12.18	1.67	1.56				17	129	20	52	2.66	0.84	0.87	0.85	5.18	50	3.23
Cook et al 2016	IH8	Mafic volcanics	41	348		108	109	87.68	14.30	2.01	1.35				1	91	22	60	2.93	1.26	1.05	0.61	0.46	36	3.97
Cook et al 2016	IH9	Mafic volcanics	41	307		202	106	78.44	13.95	1.53	1.89				2	105	19	53	2.58	1.04	0.99	0.47	0.67	43	3.43
Cook et al 2016	K43	Mafic volcanics	38	296		34	103	68.16	14.00	1.33	1.30				4	106	20	53	2.42	1.47	1.04	0.45	0.32	32	4.27
Cook et al 2016	K45	Mafic volcanics	47	263		178	175	54.67	11.70	1.90	1.21				4	96	14	31	1.31	1.23	1.07	0.64	0.42	36	1.98
Cook et al 2016	K56	Mafic volcanics	43	364		113	114	68.23	14.98	1.54	2.37				5	112	24	66	3.22	0.91	1.11	1.03	2.64	44	4.52
Cook et al 2016	K73	Mafic volcanics	43	336		201	84	73.84	14.71	1.81	12.20				5	109	22	61	2.75	0.98	1.17	1.13	0.61	42	3.54
Cook et al 2016	K75	Mafic volcanics	41	388		83	75	80.21	14.55	1.97	4.08				5	125	31	89	4.04	1.40	1.21	IAI	0.63	52	5.18
Cook et al 2016	K76	Mafic volcanics	43	350		163	99	80.10	15.63	1.26	10.10				13	125	24	60	2.70	1.37	1.44	3.65	1.91	39	3.95
Cook et al 2016	K82	Mafic volcanics	39	305		185	102	66.38	13.93	1.43	4.37				9	125	19	50	2.22	1.01	0.90	0.74	1.02	40	2.86
Cook et al 2016	K83	Mafic volcanics	42	303		212	109	86.42	14.25	1.48	7.38				7	76	20	56	2.60	1.07	1.09	1.81	2.89	46	3.62
Cook et al 2016	K84	Mafic volcanics	39	312		179	97	77.90	15.15	2.25	8.53				3	98	21	57	2.64	1.38	1.21	2.15	1.37	30	3.44
Cook et al 2016	KH14	Mafic volcanics	42	345		179	105	77.09	16.17	2.13	7.74				4	96	23	66	3.00	1.19	1.28	0.81	1.50	36	3.95
Cook et al 2016	KH15	Mafic volcanics	41	333		167	80	69.75	13.29	1.25	1.03				1	66	24	65	2.96	0.91	1.40	0.63	0.84	23	3.64
Cook et al 2016	KH18	Mafic volcanics	45	354		181	103	82.31	15.82	1.81	3.75				4	131	24	68	3.30	0.83	1.22	1.15	2.03	62	4.21
Cook et al 2016	KH2	Mafic volcanics	40	324		166	69	66.45	14.94	1.61	21.97				47	132	23	62	2.78	1.06	1.21	1.10	1.70	142	3.60
Cook et al 2016	KH3	Mafic volcanics	38	337		133	97	71.19	12.39	1.80	14.88				17	147	24	71	3.18	1.10	1.12	0.81	1.04	97	4.02
Cook et al 2016	KH4	Mafic volcanics	39	314		169	51	60.85	11.82	1.64	30.33				3	117	22	60	2.83	1.03	1.12	1.26	0.30	58	3.48
Cook et al 2016	KH7	Mafic volcanics	38	321		121	86	85.28	13.41	2.42	5.29				8	148	19	50	2.56	1.13	1.15	0.64	2.25	101	3.45
Cook et al 2016	LH8	Mafic volcanics	47	273		185	139	66.34	13.57	1.91	21.40				26	192	15	37	1.72	1.08	1.38	1.17	1.88	41	2.62
Kazimoto and Ikingura 2014	E 5	Intermediate volcanics	6	60		42						0.60	44	15	226	553	15	186	8.10				7.80	1699	50.50

Reference	Sample	Harmonisation litho	Sc	V	Mn	Cr	Cu	Zn	Ga	Ge	As	Ta	Ni	Co	Rb	Sr	Y	Zr	Nb	Mo	Sn	Sb	Cs	Ba	La
			ppm	ppm	ppm	ppm	ppm	ppm	ppm	ppm	ppm	ppm	ppm	ppm	ppm	ppm	ppm	ppm	ppm	ppm	ppm	ppm	ppm	ppm	ppm
Kazimoto and Ikingura 2014	E 8	Intermediate volcanics	12	116		36						1.30	31	18	118	760	34	358	21.30				5.90	1593	115.40
Kazimoto and Ikingura 2014	E 9	Intermediate volcanics	5	53		44						0.50	49	15	154	437	16	220	8.50				5.20	1674	50.50
Kazimoto and Ikingura 2014	E12	Intermediate volcanics	12	105		40						1.30	33	17	120	892	32	352	21.90				5.50	1436	102.10
Kazimoto and Ikingura 2014	E13	Intermediate volcanics	7	60		46						0.60	19	6	163	544	16	182	7.50				7.20	1307	47.30
Kazimoto and Ikingura 2014	E14	Granite-Monzonite	3	16		6						0.5	3	3	55	280	6	124	4.1				0.8	792	21.6
Kazimoto and Ikingura 2014	E15	TTG	2	12		7						0.60	2	3	61	215	6	127	414.00				0.70	772	39.30
Kazimoto and Ikingura 2014	E16	Intermediate volcanics	11	76		26						0.50	47	15	226	422	17	164	7.10				7.90	1248	47.70
Kazimoto and Ikingura 2014	E17	Intermediate volcanics	11	105		18						1.50	41	21	109	822	31	392	23.10				9.10	1209	99.80
Kazimoto and Ikingura 2014	E22	Intermediate volcanics	8	59		46						0.50	27	11	93	752	21	190	6.60				8.20	1120	54.30
Kazimoto and Ikingura 2014	E23	TTG	2	15		4						0.30	3	2	48	238	8	155	3.40				1.30	414	29.20
Kazimoto and Ikingura 2014	E25	TTG	2	17		8						0.30	4	4	61	331	6	129	3.40				1.00	867	23.10
Kazimoto and Ikingura 2014	E26	TTG	3	16		4						0.10	3	3	64	3848	7	144	4.80				0.80	537	23.90
Kazimoto and Ikingura 2014	E34	Intermediate volcanics	5	58		46						0.50	48	28	236	309	14	144	6.00				4.90	1470	40.70
Kazimoto and Ikingura 2014	E35	TTG	2	15		3						0.40	4	3	51	385	7	127	3.40				1.00	718	16.20
Kazimoto and Ikingura 2014	E36	Granite-Monzonite	3	13		6						0.4	5	4	16	270	6	132	6				0.2	204	27.2
Kazimoto and Ikingura 2014	E4	Granite-Monzonite	3	26		4						0.4	10	3	72	193	7	126	4.9				1	292	19.8
Kazimoto and Ikingura 2014	E43	Granite-Monzonite	5	B.D		4						1.1	1	1	31	96	70	702	14.5				2.1	746	25.9
Kazimoto and Ikingura 2014	E44	TTG	2	18		7						0.20	3	3	21	400	5	100	3.10				0.30	282	15.60
Kazimoto and Ikingura 2014	E47	Granite-Monzonite	2	14		7						0.4	2	2	78	273	4	95	3.2				0.9	1302	13.1
Kazimoto and Ikingura 2014	E48	Granite-Monzonite	2	17		7						0.4	5	3	64	228	5	138	3.6				0.8	681	16.2
Kazimoto and Ikingura 2014	E54	Granite-Monzonite	2	10		4						0.3	3	5	49	267	5	191	4.2				0.8	580	29.1
Kazimoto and Ikingura 2014	E55	TTG	2	9		5						0.30	3	2	55	300	5	108	3.70				1.10	1075	18.30
Kazimoto and Ikingura 2014	E59	Granite-Monzonite	1	B.D		4						0.3	1	1	59	203	2	68	3.9				0.8	1078	23.8
Kazimoto and Ikingura 2014	E60	TTG	2	11		5						0.40	2	2	71	289	4	108	2.80				1.00	1121	10.70
Kazimoto and Ikingura 2014	E64	Intermediate volcanics	8	67		43						0.50	46	19	251	419	15	153	7.60				10.00	1823	43.80
Kazimoto and Ikingura 2014	E69	Intermediate volcanics	8	66		45						0.60	34	10	244	231	17	168	7.10				2.60	1367	47.20

Reference	Sample	Harmonisation litho	Sc	V	Mn	Cr	Cu	Zn	Ga	Ge	As	Ta	Ni	Co	Rb	Sr	Y	Zr	Nb	Mo	Sn	Sb	Cs	Ba	La
			ppm	ppm	ppm	ppm	ppm	ppm	ppm	ppm	ppm	ppm	ppm	ppm	ppm	ppm	ppm	ppm	ppm	ppm	ppm	ppm	ppm	ppm	ppm
Kazimoto and Ikingura 2014	E70	Intermediate volcanics	11	99		9						0.04	27	15	141	984	35	420	23.70				21.40	1186	106.30
Kazimoto and Ikingura 2014	E71	Intermediate volcanics	10	92		13						1.30	32	19	44	586	30	367	21.70				1.20	1228	98.10
Kazimoto and Ikingura 2014	E73	Intermediate volcanics	12	110		40						1.30	37	23	72	787	31	348	21.70				2.60	1277	93.90
Kazimoto and Ikingura 2014	E74	TTG	2	9		4						0.30	1	2	64	220	5	90	4.60				1.20	515	37.50
Kazimoto and Ikingura 2014	E75	TTG	3	16		4						0.20	2	3	68	276	6	107	4.20				0.90	747	19.60
Kazimoto and Ikingura 2014	EIO	Granite-Monzonite	1	13		414						0.4	2	2	70	285	5	66	2.1				0.8	900	13.1
Kazimoto and Ikingura 2014	El 8	Granite-Monzonite	3	21		10						0.3	4	5	41	521	7	167	2.8				0.3	298	39.4
Maboko et al 2006	KM1	Granite-Monzonite											5	2	159	99	6	114	5.87					379	28.73
Maboko et al 2006	KM3	Granite-Monzonite											3	3	140	158	15	150	9.37					662	37.49
Maboko et al 2006	KM3*	Granite-Monzonite											3	3	162	166	16	150	9.48					679	39.46
Maboko et al 2006	KM30	TTG											11	8	79	866	10	144	5.27					703	29.92
Maboko et al 2006	KM31	TTG											6	1	132	562	5	111	4.22					940	21.17
Maboko et al 2006	KM32	TTG											4	5	62	761	9	146	4.45					960	21.54
Maboko et al 2006	KM34	TTG											6	4	99	1264	7	179	3.60					2156	55.15
Maboko et al 2006	KM46	TTG											1	3	101	565	6	78	2.50					2732	24.24
Maboko et al 2006	KM47	Granite-Monzonite											5	5	120	315	8	267	6.68					1066	44.29
Maboko et al 2006	KM48	Granite-Monzonite											4	5	289	319	21	355	19.1					808	87.08
Maboko et al 2006	KM5	Granite-Monzonite											3	1	267	126	20	121	12.81					416	28.93
Maboko et al 2006	KM52	Granite-Monzonite											3	5	215	326	24	398	23.64					675	98.13
Maboko et al 2006	KM53	Granite-Monzonite											4	6	259	321	25	321	24.29					718	73.48
Maboko et al 2006	KM54	Granite-Monzonite											1	2	116	176	9	169	4.62					882	69.04
Maboko et al 2006	KM55	Granite-Monzonite											3	0	293	112	9	114	13.16					475	21.34
Maboko et al 2006	KM56	Granite-Monzonite											2	1	331	53	19	405	35.47					133	46.07
Maboko et al 2006	KM57	Granite-Monzonite											3	3	353	74	20	199	28.41					266	98.15
Maboko et al 2006	R 14	TTG											8	5	100	465	3	167	3.47					609	38.00
Maboko et al 2006	R 15	TTG											13	4	110	551	9	152	5.91					1131	45.30
Maboko et al 2006	R 16	TTG											9	5	106	620	8	212	6.54					1694	89.00
Maboko et al 2006	R 17	TTG											7	5	56	603	4	99	3.82					418	29.40
Maboko et al 2006	R 18	TTG											7	4	103	490	2	139	2.13					1265	32.30
Maboko et al 2006	R 19	TTG											6	3	116	457	3	108	2.54					1330	27.90
Maboko et al 2006	R 2	TTG											8	5	85	737	13	144	7.70					1717	46.30

Reference	Sample	Harmonisation litho	Sc	V	Mn	Cr	Cu	Zn	Ga	Ge	As	Ta	Ni	Co	Rb	Sr	Y	Zr	Nb	Mo	Sn	Sb	Cs	Ba	La
			ppm	ppm	ppm	ppm	ppm	ppm	ppm	ppm	ppm	ppm	ppm	ppm	ppm	ppm	ppm	ppm	ppm	ppm	ppm	ppm	ppm	ppm	ppm
Maboko et al 2006	R 20	TTG											10	2	103	405	3	88	2.89					829	18.80
Maboko et al 2006	R 21	TTG											8	4	76	689	4	113	3.30					976	34.00
Maboko et al 2006	R 21*	TTG											9	4	74	669	4	110	3.33					973	32.80
Maboko et al 2006	R 26	TTG											9	4	73	449	6	139	5.00					587	25.70
Maboko et al 2006	R22	Granite-Monzonite											9	3	199	161	14	133	8.81					924	52.1
Maboko et al 2006	R23	Granite-Monzonite											8	4	254	196	15	122	11.3					547	31
Maboko et al 2006	R24	Granite-Monzonite											9	5	215	250	14	144	10.6					576	37.1
Maboko et al 2006	R25	Granite-Monzonite											8	5	365	194	13	268	14.9					937	56.2
Maboko et al 2006	R63	Granite-Monzonite											13	8	40	136	6	144	4.2					287	21
Manya 2004	PORP	Felsic volcanics	5	40		55						0.90	25	7	55	423	8	102	3.70					696	18.60
Manya 2004	R06	Mafic volcanics	34	250		492						0.20	166	27	3	114	14	37	1.65					78	2.80
Manya 2004	R07	Mafic volcanics	35	278		397						0.20	102	21	2	164	16	39	1.83					43	2.80
Manya 2004	R08	Mafic volcanics	36	330		147						0.30	88	13	3	146	23	61	2.88					37	4.20
Manya 2004	R09	Mafic volcanics	36	305		161						0.20	81	17	12	119	23	58	2.90					123	4.30
Manya 2004	R10	Mafic volcanics	40	327		184						0.30	78	14	3	98	27	68	3.40					52	4.70
Manya 2004	R11	Mafic volcanics	35	316		232						0.20	84	12	6	133	21	63	2.69					44	4.60
Manya 2004	R12	Mafic volcanics	35	232		220						0.10	99	23	4	92	15	31	1.05					28	2.00
Manya 2004	R13	Mafic volcanics	37	234		190						0.10	100	27	2	98	15	30	1.04					23	1.80
Manya 2004	R38	Mafic volcanics	33	222		270						0.20	177	24	2	169	19	41	1.98					117	3.10
Manya 2004	R39	Mafic volcanics	34	254		390						0.20	159	13	1	113	19	43	2.15					115	2.80
Manya 2004	R40	Mafic volcanics	36	317		138						0.50	115	15	9	122	32	80	3.71					538	6.10
Manya 2004	R42	Mafic volcanics	35	248		221						0.20	143	18	9	137	20	43	2.03					91	3.60
Manya 2004	R44	Felsic volcanics	3	36		88						0.20	25	7	82	294	5	118	2.51					973	16.10
Manya 2004	R45	Felsic volcanics	3	51		145						0.20	35	9	107	176	4	126	2.40					1289	20.90
Manya 2004	R46	Felsic volcanics	3	55		152						0.20	27	7	65	185	4	117	2.33					1175	19.50
Manya 2004	R65	Mafic volcanics	37	271		256						0.10	88	19	3	58	19	45	1.75					28	0.90
Manya 2004	R66	Mafic volcanics	33	228		313						0.10	78	21	3	111	17	42	1.68					75	2.80
Manya 2004	R67	Mafic volcanics	39	288		260						0.10	103	14	8	110	23	58	2.26					58	3.60
Manya 2004	R68	Mafic volcanics	34	272		289						0.10	103	18	2	130	19	44	1.92					58	2.60
Manya 2004	R69	Mafic volcanics	40	319		180						0.10	150	26	14	81	18	41	1.59					99	2.30
Manya 2004	R75	Mafic volcanics	39	237		212						0.40	59	42	3	298	19	45	2.30					21	3.50
Manya 2004	R76	Mafic volcanics	33	262		96						0.50	55	46	18	194	21	76	3.70					191	7.20

Reference	Sample	Harmonisation litho	Sc	V	Mn	Cr	Cu	Zn	Ga	Ge	As	Ta	Ni	Co	Rb	Sr	Y	Zr	Nb	Mo	Sn	Sb	Cs	Ba	La
			ppm	ppm	ppm	ppm	ppm	ppm	ppm	ppm	ppm	ppm	ppm	ppm	ppm	ppm	ppm	ppm	ppm	ppm	ppm	ppm	ppm	ppm	ppm
Manya 2004	R78	Mafic volcanics	45	268		116						0.40	74	51	10	125	18	40	1.80					23	2.40
Manya 2011	IM01	Granite-Monzonite				190						1.90			183	18	14	22	19.00					22	7.10
Manya 2011	IM02	Granite-Monzonite				170						1.8			146	332	10	177	11					320	36.9
Manya 2011	IM03	Granite-Monzonite				180						0.4			216	85	7	107	5					268	17.2
Manya 2011	IM04	Granite-Monzonite				180						0.5			234	130	9	143	8					457	36.9
Manya 2011	IM05	Granite-Monzonite				180						0.5			178	232	8	141	6					852	27.7
Manya 2011	IM06	Granite-Monzonite				120						1			266	137	24	268	19					611	66.7
Manya 2011	IM07	Granite-Monzonite				160						0.1			218	188	9	101	2					448	18.2
Manya 2011	IM08	Granite-Monzonite				220						0.4			201	81	11	206	6					373	55.8
Manya 2011	IM09	Granite-Monzonite				160						1.9			171	87	8	14	10					184	7.7
Manya 2011	IM12	Granite-Monzonite				130						0.9			114	275	34	467	16					1078	42.6
Manya 2011	IM13	Granite-Monzonite				150						0.7			283	106	17	221	13					515	58.5
Manya 2011	IM14	Granite-Monzonite				140						0.4			171	382	13	240	8					1282	63.8
Manya 2011	IM15	Granite-Monzonite				240						0.6			64	191	7	198	6					269	23.8
Manya 2011	IM16	Granite-Monzonite				210						0.2			52	886	5	252	3					981	21.2
Manya 2011	IM17	Granite-Monzonite				220						0.1			59	108	2	47	1					599	11.3
Manya 2011	IM18	Granite-Monzonite				170						0.1			78	98	7	58	4					628	11.1
Manya 2011	IM32	Gneiss				80						0.60			76	440	22	375	15.00					1293	62.60
Manya 2011	IMI0	Granite-Monzonite				180						1.4			219	148	17	257	12					375	31.2
Manya 2011	IMII	Granite-Monzonite				180						0.3			83	375	4	95	3					655	21.6
Manya 2016	BZ 03	Granite-Monzonite		37				30				0.5		2	320	168	4	150	5					387	9.1
Manya 2016	BZ 04	Granite-Monzonite		25				40				0.4			307	153	4	136	5					708	20.3
Manya 2016	BZ 06	Granite-Monzonite		30				50				0.5		2	161	571	4	148	3					1129	46.3
Manya 2016	BZ 08	Granite-Monzonite		28		20		70				0.4		3	154	743	4	141	4					1163	46.6
Manya 2016	BZ 10	Granite-Monzonite		29				70				0.3		3	121	1092	4	192	2					1644	71.6
Manya 2016	BZ 13	Granite-Monzonite		28				60				0.4		2	148	724	5	132	5					1121	42.8
Manya 2016	BZ 18	TTG		24		20		50.00				0.60		4	115	384	5	110	2.00					757	21.50
Manya 2016	BZ 19	TTG		26		20		140.00				0.60		3	110	386	5	113	4.00					760	23.40
Manya 2016	BZ 23	TTG		67		60		90.00				1.10	40	11	170	529	5	134	4.00					526	12.90
Manya 2016	BZ 24	TTG		57		20		120.00				0.50		19	180	751	7	185	7.00					622	69.90
Manya 2016	BZ 25	TTG		26		20		70.00				0.80		4	108	456	5	120	7.00					741	25.80
Manya 2016	BZ 34	TTG		28		20		50.00				0.60		4	98	347	5	115	6.00					550	22.70

Reference	Sample	Harmonisation litho	Sc	V	Mn	Cr	Cu	Zn	Ga	Ge	As	Ta	Ni	Co	Rb	Sr	Y	Zr	Nb	Mo	Sn	Sb	Cs	Ba	La
			ppm	ppm	ppm	ppm	ppm	ppm	ppm	ppm	ppm	ppm	ppm	ppm	ppm	ppm	ppm	ppm	ppm	ppm	ppm	ppm	ppm	ppm	ppm
Manya 2016	BZ01	Granite-Monzonite		15				<30				0.3			163	208	2	70	3					503	15.5
Manya 2016	BZ02	Granite-Monzonite		31				60				0.4		5	271	146	4	122	4					563	33.7
Manya 2016	BZ05	Granite-Monzonite		16				40				0.5		1	74	525	3	114	2					824	27.8
Manya 2016	BZ09	Granite-Monzonite		23				50				0.3		2	134	875	3	159	4					1533	56.9
Manya 2016	BZ11	Granite-Monzonite		22				40				0.4		2	199	532	4	114	4					1200	41.1
Manya 2016	BZ20	TTG		27		20		40.00				0.60		4	97	404	5	110	6.00					819	21.50
Manya 2016	BZ26	TTG		26		20		270.00				0.80		4	128	558	6	106	4.00					1145	22.80
Manya 2016	BZ27	TTG		23				80.00				0.50		3	150	383	5	132	5.00					1384	37.60
Manya 2016	BZ28	TTG		25				40.00				0.50		3	100	455	3	101	4.00					987	23.70
Manya 2016	BZ29	TTG		26				40.00				0.60		3	114	368	6	108	5.00					884	23.20
Manya and Maboko 2008a	SIN 07a	Mafic volcanics	42	375		150		130.00				0.20	100	58	6	62	33	81	3.00					68	3.60
Manya and Maboko 2008a	SIN 07b	Mafic volcanics	44	390		140		120.00				0.20	90	60	6	68	34	77	3.00					73	4.30
Manya and Maboko 2008a	SIN 08	Mafic volcanics	44	312		40		120.00				0.20	60	62	4	112	28	72	3.00					183	4.10
Manya and Maboko 2008a	SIN 11	Mafic volcanics	41	319		140		100.00				0.20	80	57	55	105	24	65	3.00					658	4.70
Manya and Maboko 2008a	SIN 12	Mafic volcanics	35	231		290		90.00				0.10	180	60	4	153	16	42	2.00					41	2.90
Manya and Maboko 2008a	SIN 13	Mafic volcanics	40	250		310		90.00				0.10	180	61	20	110	17	42	2.00					215	2.60
Manya and Maboko 2008a	SIN 15	Mafic volcanics	43	281		160		100.00				0.10	110	61	8	133	20	46	2.00					32	2.70
Manya and Maboko 2008a	SIN 17	Mafic volcanics	37	227		280		90.00				0.10	160	57	3	149	17	39	2.00					38	2.90
Manya and Maboko 2008a	SIN 18	Mafic volcanics	50	319		170		50.00				0.20	70	56	14	153	28	77	3.00					147	4.30
Manya and Maboko 2008a	SIN 19	Mafic volcanics	40	281		170		50.00				0.20	60	43	12	130	18	60	3.00					158	3.40
Manya and Maboko 2008a	SIN 20	Mafic volcanics	45	343		260		70.00				0.20	130	62	10	148	23	62	3.00					37	3.70
Manya and Maboko 2008a	SIN 21	Mafic volcanics	43	304		170		100.00				0.20	110	56	22	127	25	64	3.00					63	3.40
Manya and Maboko 2008a	SIN 22	Mafic volcanics	40	279		210		90.00				0.20	120	58	4	117	22	52	2.00					50	2.90
Manya and Maboko 2008a	SIN 23	Mafic volcanics	46	300		290		80.00				0.20	120	54	13	156	26	59	3.00					145	3.40
Manya and Maboko 2008a	SIN 24	Mafic volcanics	37	326		140		90.00				0.30	80	49	12	130	27	79	4.00					132	4.60
Manya and Maboko 2008a	SIN 25	Mafic volcanics	41	280		160		90.00				0.20	100	50	6	159	23	58	3.00					162	3.60
Manya and Maboko 2008a	SIN 28	Mafic volcanics	41	262		300		100.00				0.10	130	51	29	130	19	48	2.00					44	3.30
Manya and Maboko 2008a	SIN 29	Mafic volcanics	38	252		260		90.00				0.10	140	55	7	111	19	46	2.00					73	2.60
Manya and Maboko 2008a	SIN IO	Mafic volcanics	42	331		40		120.00				0.20	60	69	2	71	29	75	3.00					90	3.10
Manya and Maboko 2008a	SIN01	Mafic volcanics	41	317		200		130.00				0.20	120	63	3	200	29	68	3.00					111	3.70
Manya and Maboko 2008a	SIN02	Mafic volcanics	42	314		190		120.00				0.20	110	59	6	143	29	70	3.00					173	3.80
Manya and Maboko 2008a	SIN04	Mafic volcanics	44	396		150		120.00				0.20	70	53	3	154	33	86	4.00					169	5.10

Reference	Sample	Harmonisation litho	Sc	V	Mn	Cr	Cu	Zn	Ga	Ge	As	Ta	Ni	Co	Rb	Sr	Y	Zr	Nb	Mo	Sn	Sb	Cs	Ba	La
			ppm	ppm	ppm	ppm	ppm	ppm	ppm	ppm	ppm	ppm	ppm	ppm	ppm	ppm	ppm	ppm	ppm	ppm	ppm	ppm	ppm	ppm	ppm
Manya and Maboko 2008b	GT 02	Mafic volcanics	42	337		120	140	90.00				0.20	90	53	7	305	26	79	3.00				0.70	39	4.30
Manya and Maboko 2008b	GT 04	Mafic volcanics	45	309		110	190	120.00				0.20	80	48	6	107	25	67	3.00				0.60	101	4.70
Manya and Maboko 2008b	GT 06	Mafic volcanics	41	328		110	100	110.00				0.20	80	45	8	349	27	70	3.00				1.00	97	4.50
Manya and Maboko 2008b	GT 08	Mafic volcanics	41	248		120	260	70.00				0.20	70	52	6	105	14	48	2.00				2.70	74	2.90
Manya and Maboko 2008b	GT 09	Mafic volcanics	44	267		140	120	60.00				0.20	70	51	16	127	17	49	2.00				2.60	199	3.30
Manya and Maboko 2008b	GT 12	Mafic volcanics	41	287		100	50	80.00				0.20	60	40	9	117	24	62	3.00				2.00	96	4.50
Manya and Maboko 2008b	GT 15	Mafic volcanics	40	294		90	20	80.00				0.20	60	41	2	137	24	62	3.00				0.50	117	4.30
Manya and Maboko 2008b	GT 18	Mafic volcanics	46	315		120	100	80.00				0.20	70	53	3	107	23	62	3.00				0.50	37	4.40
Manya and Maboko 2008b	GT 19	Mafic volcanics	41	369		190	90	110.00				0.20	90	54	4	167	26	61	2.00				1.00	35	3.90
Manya and Maboko 2008b	GT01	Mafic volcanics	45	369		150	1000	130.00				0.30	100	131	8	132	28	74	4.00				0.60	46	5.10
Manya and Maboko 2008b	GT05	Mafic volcanics	41	315		110	170	100.00				0.20	70	70	10	121	27	69	3.00				0.70	59	4.80
Manya and Maboko 2008b	GT07	Mafic volcanics	42	261		150	20	80.00				0.20	80	39	6	109	16	52	2.00				3.20	133	3.20
Manya and Maboko 2008b	GT10	Mafic volcanics	38	254		250	40	90.00				0.20	130	46	2	97	22	53	2.00				0.50	18	3.40
Manya and Maboko 2008b	GT11	Mafic volcanics	41	297		100	90	70.00				0.20	60	46	3	120	24	65	3.00				1.00	82	4.70
Manya and Maboko 2008b	GT13	Mafic volcanics	40	277		90	110	70.00				0.20	60	46	9	150	23	62	3.00				1.40	67	4.20
Manya and Maboko 2008b	GT14	Mafic volcanics	37	279		100	80	60.00				0.30	60	44	3	151	20	61	3.00				0.70	38	4.00
Manya and Maboko 2008b	GT16	Mafic volcanics	43	308		130	30	70.00				0.20	70	42	2	124	21	76	3.00				0.50	102	4.70
Manya and Maboko 2008b	GT17	Mafic volcanics	40	367		120	130	90.00				0.20	70	57	3	143	23	61	3.00				0.80	45	4.10
Manya and Maboko 2008b	GT20	Mafic volcanics	37	349		130	110	110.00				0.20	70	51	2	92	27	66	3.00				0.50	14	4.10
Messo et al 2012	MU100	Intermediate volcanics		175		40						0.60	43		40	312	25	155	7.00					485	20.10
Messo et al 2012	MU14	Mafic volcanics		342		160						0.30	100		26	147	29	80	3.00					204	4.60
Messo et al 2012	MU15	Mafic volcanics		228		200						0.20	190		9	106	20	53	2.00					27	3.00
Messo et al 2012	MU16	Felsic volcanics		5		20						0.60	20		91	37	12	34	5.00					301	6.60
Messo et al 2012	MU17	Felsic volcanics		5		20						0.60	20		83	32	9	36	5.00					220	3.90
Messo et al 2012	MU18	Felsic volcanics		5		20						0.60	20		77	31	10	33	4.00					217	3.70
Messo et al 2012	MU19	Mafic volcanics		232		240						0.10	90		5	101	16	31	1.00					66	1.70
Messo et al 2012	MU27	Intermediate volcanics		76		30						0.40	30		16	428	15	126	4.00					1230	22.10
Messo et al 2012	MU36	Intermediate volcanics		171		40						0.60	80		35	236	23	163	8.00					418	26.20
Messo et al 2012	MU49	Intermediate volcanics		154		70						0.80	90		40	239	24	177	8.00					329	28.10
Messo et al 2012	MU57	Intermediate volcanics		162		40						0.60	60		2	293	21	147	7.00					97	23.80
Messo et al 2012	MU60	Intermediate volcanics		153		90						0.70	90		97	320	24	184	8.00					763	28.20
Messo et al 2012	MU68	Intermediate volcanics		108		20						0.50	30		18	423	24	176	7.00					755	33.70

Reference	Sample	Harmonisation litho	Sc	V	Mn	Cr	Cu	Zn	Ga	Ge	As	Ta	Ni	Co	Rb	Sr	Y	Zr	Nb	Mo	Sn	Sb	Cs	Ba	La
			ppm	ppm	ppm	ppm	ppm	ppm	ppm	ppm	ppm	ppm	ppm	ppm	ppm	ppm	ppm	ppm	ppm	ppm	ppm	ppm	ppm	ppm	ppm
Messo et al 2012	MU69	Mafic volcanics		249		170						0.30	120		5	214	23	88	4.00					140	9.20
Messo et al 2012	MU79	Intermediate volcanics		180		40						0.60	160		56	349	25	158	7.00					504	23.60
Messo et al 2012	MU87	Intermediate volcanics		155		70						0.70	90		48	398	24	179	9.00					415	27.40
Messo et al 2012	MU89	Intermediate volcanics		149		70						0.80	80		61	395	24	173	8.00					643	28.00
Messo et al 2012	MU94	Intermediate volcanics		163		30						0.60	80		54	296	23	137	6.00					626	22.80
Sanislav et al 2014a	GP-01	Granite-Monzonite	10	87	478		9	50	16.8			0.848	11	35	124	549	16	264	8.5		6.83		27.4	1349	50.4
Sanislav et al 2014a	GP-02	Granite-Monzonite	7	58	347		6	41.4	17.4			1.79	5	49	177	273	26	314	17.9		5.74		2.83	817	43.6
Sanislav et al 2014a	GP-03	Granite-Monzonite	4	40	201		5	20.2	13.1			1.68	8	36	190	169	14	127	9.25		7.45		2.94	494	32.2
Sanislav et al 2014a	GX-01	Granite-Monzonite	7	68	379		8	34.9	16.1			0.854	8	34	132	404	13	213	8.81		6.99		3.55	1040	51.5
Sanislav et al 2014a	XU-01	Granite-Monzonite	7	55	332		4	38.5	17.5			1.53	4	29	179	232	23	275	16.9		6.15		4.59	728	76.6
Sanislav et al 2014a	XU-01A	Granite-Monzonite	8	58	408		7	52.3	17.8			1.42	5	27	247	247	25	337	17		6.37		6.37	874	92.3
Sanislav et al 2014a	XU-02	Granite-Monzonite	3	36	166		3	20.8	14.2			1.72	4	43	209	87	22	166	11.7		5.35		3.56	233	39.2
Wu et al 2023	18TGE01-1	TTG	11	26		7	7	56.20	33.10			0.27	5	5	31	626	5	138	3.46				1.32	814	18.10
Wu et al 2023	18TGE01-10	TTG	11	25		7	16	49.40	34.80			0.24	5	4	32	545	5	134	3.12				1.19	930	18.00
Wu et al 2023	18TGE01-2	TTG	11	22		5	10	45.40	32.30			0.30	3	3	38	574	6	131	4.43				2.24	811	20.30
Wu et al 2023	18TGE01-3	TTG	10	19		3	5	46.20	36.40			0.36	3	3	51	538	6	130	4.91				2.18	975	28.30
Wu et al 2023	18TGE01-4	TTG	11	17		3	11	46.10	34.70			0.36	3	3	67	516	5	108	4.77				3.20	906	19.60
Wu et al 2023	18TGE01-5	TTG	10	14		12	9	33.80	32.70			0.18	3	2	59	482	3	101	2.88				1.46	844	19.80
Wu et al 2023	18TGE01-6	TTG	10	9		2	5	28.10	31.60			0.51	2	1	127	348	6	71	4.35				6.20	757	13.00
Wu et al 2023	18TGE01-7	TTG	9	15		5	5	35.40	36.10			0.17	3	2	68	572	3	112	2.83				1.98	975	17.60
Wu et al 2023	18TGE01-8	TTG	11	17		4	5	38.90	34.80			0.30	3	2	69	513	4	118	4.36				3.67	906	21.00
Wu et al 2023	18TGE01-9	TTG	10	22		7	7	45.30	38.50			0.37	4	4	38	477	5	126	4.45				1.93	1060	14.80
Manya 2012		Mafic volcanics		148		860	20	110.00				1.00	350	50	88	197	18	85	3.00				5.20	266	43.00
Manya 2012		Mafic volcanics		226		820	40	70.00				0.30	170	52	2	121	15	40	1.00				0.70	33	1.90
Manya 2012		Mafic volcanics		188		1590	10	100.00				0.20	510	64	6	76	13	32	1.00				1.10	39	1.80
Manya 2012		Mafic volcanics		265		370	60	90.00				0.50	150	50	9	203	25	72	3.00				0.60	49	4.70
Manya 2012		Mafic volcanics		294		140	110	60.00				0.30	100	54	56	231	14	14	1.00				1.70	173	1.00
Manya 2012		Mafic volcanics		247		180	80	60.00				0.40	80	44	37	157	18	42	2.00				1.30	36	2.40
Kwelwa 2017	KIC-01	Felsic volcanics		75		32							34		9	1447	15	186	6.00					237	121.78
Kwelwa 2017	KIC-02	Felsic volcanics		67		98							63		40	1563	13	149	4.61					1414	68.59
Kwelwa 2017	KIC-03	Felsic volcanics		88		83							35		48	1535	21	238	9.40					1899	102.61
Kwelwa 2017	KIC-04	Felsic volcanics		105		84							56		75	1263	15	139	5.53					1783	81.02

Reference	Sample	Harmonisation litho	Sc	V	Mn	Cr	Cu	Zn	Ga	Ge	As	Ta	Ni	Co	Rb	Sr	Y	Zr	Nb	Mo	Sn	Sb	Cs	Ba	La
			ppm	ppm	ppm	ppm	ppm	ppm	ppm	ppm	ppm	ppm	ppm	ppm	ppm	ppm	ppm	ppm	ppm	ppm	ppm	ppm	ppm	ppm	ppm
Kwelwa 2017	KIC-05	Felsic volcanics		105		47							26		84	1245	16	173	6.04					1601	82.68
Kwelwa 2017	KIC-06	Felsic volcanics		99		66							42		94	1075	15	170	5.80					1345	80.94
Kwelwa 2017	KIC-07	Felsic volcanics		72		49							34		28	1136	12	152	5.09					1722	57.01
Kwelwa 2017	KIC-08	Felsic volcanics		131		195							56		109	856	28	275	9.74					2545	166.15
Kwelwa 2017	KIC-09	Felsic volcanics		91		77							59		72	674	11	132	5.62					1386	77.27
Kwelwa 2017	KIC-10	Felsic volcanics		135		196							79		100	1082	30	284	9.82					750	184.12
Kwelwa 2017	KIC-11	Felsic volcanics		92		28							28		23	537	14	187	5.39					149	78.90
Kwelwa 2017	KIC-12	TTG		75		64							37		99	798	9	106	2.91					696	22.33
Kwelwa 2017	KIC-13	TTG		62		97							61		61	1025	8	109	2.98					1478	31.39
Kwelwa 2017	KIC-14	TTG		56		98							58		52	1062	9	107	3.32					1156	31.58
Kwelwa 2017	KIC-15	TTG		175		82							58		73	978	11	113	3.03					561	21.22
Kwelwa 2017	KIC-16	TTG		163		98							60		62	774	12	80	2.43					563	13.72
Kwelwa 2017	KIC-17	TTG		158		87							66		48	680	11	79	2.53					418	12.31
Kwelwa 2017	KIC-18	TTG		113		50							77		88	800	8	93	2.54					557	12.02
Kwelwa 2017	KIC-19	TTG		135		90							30		43	778	9	105	2.95					330	12.07
Kwelwa 2017	KIC-20	TTG		150		87							59		95	876	12	145	5.16					725	38.26
Kwelwa 2017	KIC-21	TTG		114		85							24		66	572	10	97	2.16					380	10.72
Kwelwa 2017	KIC-22	TTG		62		21							14		102	302	17	132	5.7					585	24.26
Kwelwa 2017	KIC-23	TTG		67		22							16		98	340	17	129	6.04					521	23.89
Kwelwa 2017	KIC-24	TTG		67		21							11		83	358	16	132	5.90					508	23.69
Kwelwa 2017	KIC-25	TTG		66		21							13		86	327	16	130	5.73					546	23.52

Reference	Sample	Harmonisation litho	Ce	Pr	Nd	Sm	Eu	Gd	Tb	Dy	Ho	Er	Tm	Yb	Lu	Hf	Pb	Th	U
			ppm	ppm	ppm	ppm	ppm	ppm	ppm	ppm	ppm	ppm	ppm	ppm	ppm	ppm	ppm	ppm	ppm
Boniface and Mruma 2012	N12	Granite-Monzonite	59	6.43	23.2	3.83	0.65	2.86	2.12	0.37	0.88	0.14	1.11	0.16	4.31			19.2	7
Boniface and Mruma 2012	N29A	Granite-Monzonite	11	1.4	5.36	0.88	0.33	0.92	0.5	0.07	0.18	0.02	0.4	0.03	3.16			0.85	0.58
Boniface and Mruma 2012	N33	Granite-Monzonite	96	11.4	45.1	7.57	1.57	4.78	2.98	0.54	1.2	0.17	1.33	0.19	5.24			16.1	7.01
Boniface and Mruma 2012	N49	Mafic volcanics	11	1.77	9.17	2.85	0.97	3.94	4.86	1.01	2.60	0.41	2.91	0.43	2.21			0.33	0.06
Boniface and Mruma 2012	N51	Felsic volcanics	51	6.05	24.10	4.30	0.84	2.74	1.91	0.35	0.82	0.12	0.95	0.14	3.83			7.16	2.99
Boniface and Mruma 2012	N54	Felsic volcanics	32	4.19	18.40	3.82	0.99	3.25	2.60	0.50	1.14	0.18	1.31	0.19	4.17			3.15	0.79
Cloutier et al 2005	D0142	Granite-Monzonite	4	0.63	3.30	2.29	0.15	2.30	0.26	0.63	0.04	0.06		0.04		35.00		9.01	16.80
Cloutier et al 2005	D0142-1	Sediment	55	6.36	23.90	4.26	1.00	3.29	0.47	2.58	0.50	1.56	0.23	1.50	0.23	5.20		10.30	3.13
Cloutier et al 2005	D0146-1	Mafic volcanics	11	1.62	8.40	2.66	0.98	3.40	0.64	4.08	0.88	2.68	0.42	2.53	0.39	2.50		0.93	0.27
Cloutier et al 2005	D0149-1	Sediment	645	7.50	28.60	5.12	1.08	4.08	0.60	3.25	0.63	1.85	0.28	1.72	0.25	4.20		11.20	3.32
Cloutier et al 2005	D0149-10	Sediment	73	8.49	32.50	5.95	1.52	4.41	0.63	3.45	0.66	2.05	0.30	1.97	0.29	4.10		13.40	3.57
Cloutier et al 2005	D0149-12	Sediment	61	7.00	26.90	4.83	0.87	3.88	0.58	3.28	0.64	1.88	0.29	1.84	0.27	4.10		11.40	3.21
Cloutier et al 2005	D0149-13	Felsic volcanics	34	4.06	16.20	3.11	0.87	2.67	0.40	2.31	0.47	1.43	0.22	1.36	0.21	3.20		6.67	1.88
Cloutier et al 2005	D0149-14	Sediment	65	7.53	28.90	5.25	1.14	4.33	0.63	3.48	0.66	1.89	0.28	1.67	0.26	4.40		11.80	3.25
Cloutier et al 2005	D0149-17	Sediment	62	7.28	27.70	5.18	1.20	4.20	0.61	3.44	0.66	2.08	0.32	2.00	0.31	4.40		11.80	3.21
Cloutier et al 2005	D0149-18	Sediment	71	8.40	32.50	5.80	1.10	4.31	0.66	3.69	0.72	2.22	0.34	2.13	0.31	3.80		13.10	3.44
Cloutier et al 2005	D0149-19	Sediment	71	8.23	32.00	5.79	1.29	4.53	0.68	3.66	0.69	2.04	0.30	1.90	0.28	3.80		12.60	3.37
Cloutier et al 2005	D0149-2	Sediment	20	2.56	10.90	226.00	0.76	2.01	0.31	1.64	0.31	0.88	0.12	1.79	0.11	2.80		1.60	0.47
Cloutier et al 2005	D0149-20	Sediment	37	4.31	16.50	3.08	0.84	2.61	0.40	2.31	0.46	1.41	0.21	1.33	0.20	3.20		7.06	2.09
Cloutier et al 2005	D0149-3	Felsic volcanics	24	2.96	12.20	2.39	1.00	2.07	0.29	1.58	0.31	0.91	0.12	0.84	0.12	3.00		3.13	0.88
Cloutier et al 2005	D0149-4	Sediment	38	4.48	17.50	3.26	1.01	2.76	0.39	2.13	0.41	1.19	0.17	1.11	0.17	2.90		6.28	1.85
Cloutier et al 2005	D0149-6	Sediment	77	9.21	36.00	6.64	1.23	5.06	0.69	3.46	0.63	1.85	0.27	1.71	0.25	3.80		9.67	3.77
Cloutier et al 2005	D0149-7	Sediment	62	6.98	26.40	4.50	1.04	3.61	0.52	2.92	0.57	1.70	0.26	1.57	0.23	5.00		11.00	3.34
Cloutier et al 2005	D0149-8	Sediment	75	8.61	32.70	5.84	1.17	4.73	0.71	3.97	0.76	2.26	0.34	2.16	0.32	4.30		13.00	3.44
Cloutier et al 2005	D0159-1	Sediment	37	4.29	16.60	3.22	0.93	2.74	0.43	2.43	0.46	1.41	0.21	1.36	0.20	4.00		9.50	3.01
Cloutier et al 2005	D0159-2	Sediment	81	10.00	35.20	6.41	1.35	4.82	0.76	4.25	0.89	2.31	0.35	2.20	0.32	3.50		10.60	3.09
Cloutier et al 2005	D0159-3	Sediment	62	7.28	28.10	5.04	0.87	4.04	0.59	3.27	0.66	2.05	0.31	1.96	0.29	4.20		11.50	3.25
Cloutier et al 2005	D0159-4	Sediment	58	6.64	25.10	4.52	1.18	3.65	0.54	2.98	0.56	1.66	0.25	1.58	0.23	4.60		10.70	3.19
Cloutier et al 2005	D0159-5	Sediment	61	6.82	25.60	4.45	1.26	3.72	0.53	2.92	0.57	1.76	0.24	1.55	0.23	4.20		10.50	2.93
Cloutier et al 2005	D0159-6	Sediment	95	11.70	41.10	7.36	1.35	5.46	0.82	4.68	0.95	2.47	0.37	2.35	0.33	3.20		11.20	3.13
Cloutier et al 2005	D0185-1	Mafic volcanics	14	2.18	12.10	4.35	1.29	6.14	1.19	7.47	1.58	4.79	0.78	4.65	0.70	5.20		1.55	0.56
Cloutier et al 2005	D0309-1	Mafic volcanics	22	3.24	16.20	4.99	1.74	6.26	1.14	7.24	1.51	4.55	0.70	4.41	0.67	4.80		2.02	0.60
Cloutier et al 2005	D0309-2	Mafic volcanics	27	3.88	18.80	5.28	1.83	6.45	1.17	7.15	1.50	4.49	0.70	4.28	0.64	5.00		2.63	1.09

Reference	Sample	Harmonisation litho	Ce	Pr	Nd	Sm	Eu	Gd	Tb	Dy	Ho	Er	Tm	Yb	Lu	Hf	Pb	Th	U
			ppm	ppm	ppm	ppm	ppm	ppm	ppm	ppm	ppm	ppm	ppm	ppm	ppm	ppm	ppm	ppm	ppm
Cloutier et al 2005	D0309-3	Mafic volcanics	10	1.56	8.00	2.56	1.00	3.33	0.64	4.01	0.84	2.57	0.40	2.44	0.37	2.40		0.88	0.25
Cloutier et al 2005	D0310-1	Proterozoic granitoid	14	1.83	6.90	2.40	0.07	2.92	0.82	6.25	1.37	4.82	1.03	7.84	1.23	2.70		8.50	2.00
Cloutier et al 2005	D0310-2	Sediment	45	5.34	20.80	4.02	0.77	3.29	0.45	2.46	0.48	1.48	0.23	1.52	0.24	4.40		9.66	5.24
Cloutier et al 2005	D0310-3	Proterozoic granitoid	29	3.99	17.00	6.70	0.05	6.81	1.37	7.82	1.43	4.36	0.76	4.90	0.73	3.60		16.90	8.51
Cloutier et al 2005	D03104	Proterozoic granitoid	28	3.77	15.50	5.31	0.03	5.51	1.06	6.31	1.19	3.68	0.66	4.17	0.62	3.00		12.91	5.10
Cook et al 2016	E1	Mafic volcanics	8	1.16	6.12	2.01	0.76	2.82	0.47	3.15	0.69	2.02	0.33	1.95	0.29	1.40	1.37	0.24	0.06
Cook et al 2016	E4	Mafic volcanics	9	1.39	7.33	2.42	0.86	3.29	0.57	3.64	0.80	2.39	0.36	2.23	0.34	1.67	0.97	0.28	0.07
Cook et al 2016	E5	Mafic volcanics	7	1.01	5.13	1.64	0.66	2.20	0.40	2.68	0.55	1.62	0.26	1.56	0.24	1.40	2.06	0.31	0.08
Cook et al 2016	E6	Mafic volcanics	10	1.40	7.11	2.19	0.80	3.08	0.51	3.47	0.74	2.30	0.36	2.15	0.33	1.69	2.01	0.38	0.09
Cook et al 2016	IH11	Mafic volcanics	10	1.56	8.43	2.76	0.90	3.72	0.64	4.35	0.93	2.79	0.43	2.56	0.42	1.99	1.43	0.37	0.12
Cook et al 2016	IH12	Mafic volcanics	9	1.33	6.87	2.25	0.82	3.04	0.52	3.48	0.74	2.31	0.37	2.21	0.34	1.52	1.50	0.37	0.09
Cook et al 2016	IH8	Mafic volcanics	10	1.55	8.19	2.65	0.87	3.40	0.58	3.79	0.80	2.48	0.38	2.45	0.37	1.78	1.07	0.33	0.09
Cook et al 2016	IH9	Mafic volcanics	9	1.37	7.02	2.26	0.81	3.02	0.51	3.45	0.72	2.22	0.33	2.15	0.31	1.54	1.29	0.31	0.07
Cook et al 2016	K43	Mafic volcanics	10	1.38	6.88	2.21	0.78	3.04	0.53	3.53	0.77	2.34	0.34	2.24	0.34	1.52	0.81	0.29	0.07
Cook et al 2016	K45	Mafic volcanics	5	0.81	4.15	1.54	0.55	2.05	0.35	2.36	0.53	1.62	0.26	1.45	0.24	0.91	0.98	0.18	0.13
Cook et al 2016	K56	Mafic volcanics	12	1.72	8.98	2.72	0.98	3.73	0.62	4.15	0.89	2.66	0.42	2.64	0.40	1.87	1.57	0.35	0.09
Cook et al 2016	K73	Mafic volcanics	9	1.46	7.89	2.64	0.95	3.59	0.63	4.02	0.87	2.60	0.41	2.59	0.39	1.84	6.32	0.32	0.08
Cook et al 2016	K75	Mafic volcanics	14	2.10	11.07	3.55	1.19	4.95	0.83	5.56	1.18	3.56	0.53	3.42	0.54	2.59	2.84	0.46	0.13
Cook et al 2016	K76	Mafic volcanics	10	1.53	8.20	2.54	0.86	3.60	0.60	4.02	0.86	2.58	0.39	2.45	0.38	1.74	5.87	0.29	0.08
Cook et al 2016	K82	Mafic volcanics	8	1.19	6.27	2.18	0.81	3.03	0.51	3.42	0.76	2.17	0.35	2.16	0.33	1.53	3.04	0.26	0.07
Cook et al 2016	K83	Mafic volcanics	10	1.41	7.45	2.33	0.79	3.22	0.56	3.65	0.77	2.39	0.36	2.20	0.34	1.67	4.10	0.34	0.09
Cook et al 2016	K84	Mafic volcanics	9	1.43	7.59	2.47	0.83	3.29	0.57	3.76	0.81	2.46	0.37	2.29	0.36	1.79	2.07	0.31	0.08
Cook et al 2016	KH14	Mafic volcanics	10	1.60	8.20	2.60	0.96	3.78	0.64	4.31	0.91	2.75	0.41	2.65	0.40	1.94	2.63	0.33	0.09
Cook et al 2016	KH15	Mafic volcanics	10	1.58	8.20	2.65	0.95	3.64	0.66	4.17	0.94	2.72	0.44	2.57	0.42	1.87	1.36	0.35	0.10
Cook et al 2016	KH18	Mafic volcanics	11	1.69	8.77	2.84		3.88	0.66	4.35	0.90	2.80	0.43	2.60	0.40	2.03	2.14	0.39	0.10
Cook et al 2016	KH2	Mafic volcanics	10	1.52	8.04	2.57	0.90	3.56	0.62	4.09	0.85	2.64	0.41	2.50	0.38	1.83	3.45	0.31	0.08
Cook et al 2016	KH3	Mafic volcanics	11	1.66	8.88	2.91	0.99	3.96	0.66	4.48	0.94	2.78	0.43	2.82	0.42	2.07	1.35	0.39	0.11
Cook et al 2016	KH4	Mafic volcanics	9	1.49	7.64	2.51	0.84	3.54	0.59	3.98	0.85	2.48	0.39	2.37	0.36	1.78	1.83	0.33	0.08
Cook et al 2016	KH7	Mafic volcanics	9	1.38	7.13	2.22	0.81	2.97	0.51	3.36	0.72	2.21	0.35	2.02	0.32	1.47	2.08	0.32	0.08
Cook et al 2016	LH8	Mafic volcanics	6	0.99	4.84	1.54	0.60	2.26	0.42	2.73	0.62	1.77	0.31	1.76	0.28	1.11	3.59	0.22	0.07
Kazimoto and Ikingura 2014	E 5	Intermediate volcanics	111	12.89	42.50	6.90	1.56	4.21	0.60	2.82	0.47	1.27	0.16	1.20	0.17	5.50		9.40	3.10
Kazimoto and Ikingura 2014	E 8	Intermediate volcanics	267	30.85	107.90	17.40	3.61	10.58	1.39	6.52	1.02	2.84	0.39	2.48	0.38	8.60		27.00	6.70
Kazimoto and Ikingura 2014	E 9	Intermediate volcanics	115	13.45	45.00	7.20	1.73	4.98	0.74	3.21	0.52	1.35	0.16	1.15	0.21	5.90		15.80	5.20

Reference	Sample	Harmonisation litho	Ce	Pr	Nd	Sm	Eu	Gd	Tb	Dy	Ho	Er	Tm	Yb	Lu	Hf	Pb	Th	U
			ppm	ppm	ppm	ppm	ppm	ppm	ppm	ppm	ppm	ppm	ppm	ppm	ppm	ppm	ppm	ppm	ppm
Kazimoto and Ikingura 2014	E12	Intermediate volcanics	242	27.89	102.70	16.00	3.42	9.71	1.47	6.54	0.99	2.72	0.36	2.48	0.38	7.80		26.40	6.00
Kazimoto and Ikingura 2014	E13	Intermediate volcanics	102	12.27	43.00	7.00	1.52	4.79	0.63	3.23	0.50	1.31	0.19	1.31	0.17	5.10		15.80	2.80
Kazimoto and Ikingura 2014	E14	Granite-Monzonite	42	4.19	13.6	2.3	0.46	1.74	0.28	1.04	0.18	0.61	0.1	0.48	0.11	3.4		9.3	3.6
Kazimoto and Ikingura 2014	E15	TTG	68	6.36	20.30	2.90	0.57	1.89	0.24	1.10	0.22	0.53	0.09	0.59	0.09	3.80		25.40	3.00
Kazimoto and Ikingura 2014	E16	Intermediate volcanics	107	12.54	45.10	7.30	1.69	4.96	0.72	3.56	0.55	1.46	0.17	1.37	0.21	5.00		14.70	3.10
Kazimoto and Ikingura 2014	E17	Intermediate volcanics	241	28.53	102.90	16.10	3.61	10.36	1.48	7.26	0.95	2.81	0.33	2.61	0.33	7.90		29.90	7.60
Kazimoto and Ikingura 2014	E22	Intermediate volcanics	120	14.67	51.20	9.60	2.10	6.46	0.78	4.24	0.61	1.77	0.20	1.69	0.28	5.50		17.40	3.90
Kazimoto and Ikingura 2014	E23	TTG	53	4.97	15.30	2.10	0.55	2.02	0.26	1.32	0.29	0.76	0.11	0.77	0.14	3.90		8.80	5.20
Kazimoto and Ikingura 2014	E25	TTG	46	4.78	13.90	2.00	0.52	1.53	0.26	1.04	0.16	0.54	0.08	0.58	0.09	3.70		9.80	1.90
Kazimoto and Ikingura 2014	E26	TTG	48	5.05	16.60	2.80	0.44	2.08	0.35	1.41	0.23	0.54	0.06	0.46	0.09	3.90		7.40	1.50
Kazimoto and Ikingura 2014	E34	Intermediate volcanics	89	9.78	38.70	6.40	1.56	4.12	0.61	2.58	0.40	1.09	0.18	1.04	0.17	3.90		7.90	2.90
Kazimoto and Ikingura 2014	E35	TTG	32	3.07	10.50	1.40	0.42	1.37	0.20	0.97	0.21	0.46	0.07	0.62	0.09	3.60		6.40	1.20
Kazimoto and Ikingura 2014	E36	Granite-Monzonite	50	5.13	16.9	2.4	0.59	1.54	0.28	0.91	0.17	0.51	0.06	0.36	0.09	3.8		7	1.6
Kazimoto and Ikingura 2014	E4	Granite-Monzonite	37	3.65	10.5	1.9	0.36	1.34	0.21	1.11	0.25	0.64	0.08	0.44	0.11	3.4		10.5	2.4
Kazimoto and Ikingura 2014	E43	Granite-Monzonite	67	9.07	37.4	8.4	3.42	9.74	1.92	12.04	2.22	7.29	0.98	7.2	1.38	16.4		9.6	3.5
Kazimoto and Ikingura 2014	E44	TTG	30	2.83	8.30	1.80	0.44	1.19	0.19	0.97	0.13	0.43		0.41	0.05	2.60		5.40	1.00
Kazimoto and Ikingura 2014	E47	Granite-Monzonite	27	2.56	10.2	1.6	0.55	1.11	0.17	0.67	0.08	0.34	0.06	0.31	0.07	2.8		6.9	2.1
Kazimoto and Ikingura 2014	E48	Granite-Monzonite	30	2.78	10.3	1.9	0.51	1.11	0.21	0.9	0.11	0.45		0.37	0.05	3.4		8.6	2.4
Kazimoto and Ikingura 2014	E54	Granite-Monzonite	51	4.47	14.4	2.1	0.59	1.28	0.19	0.92	0.13	0.46	0.09	0.39	0.11	5.7		12.9	1.5
Kazimoto and Ikingura 2014	E55	TTG	34	3.11	11.00	1.90	0.54	1.29	0.13	0.98	0.15	0.39		0.42	0.06	3.20		5.70	1.30
Kazimoto and Ikingura 2014	E59	Granite-Monzonite	43	3.7	12.1	2.1	0.44	0.65	0.12	0.42	0.07	0.17		0.17	0.03	2.6		12.2	1.1
Kazimoto and Ikingura 2014	E60	TTG	23	2.32	7.70	1.50	0.59	0.74	0.13	0.67	0.11	0.45		0.47	0.07	2.90		5.40	2.10
Kazimoto and Ikingura 2014	E64	Intermediate volcanics	99	11.35	45.00	7.90	1.34	4.68	0.54	2.56	0.38	1.18	0.14	1.09	0.20	4.70		10.50	3.70
Kazimoto and Ikingura 2014	E69	Intermediate volcanics	109	11.54	43.90	7.00	1.30	4.60	0.71	2.47	0.48	1.30	0.20	1.23	0.19	4.60		11.60	3.40
Kazimoto and Ikingura 2014	E70	Intermediate volcanics	277	29.48	108.90	17.90	3.63	11.19	1.77	6.88	1.11	2.72	0.39	2.21	0.32	8.90		30.80	8.50
Kazimoto and Ikingura 2014	E71	Intermediate volcanics	244	25.96	100.40	15.40	3.22	10.21	1.53	5.65	0.91	2.50	0.33	1.86	0.27	8.80		30.50	7.70
Kazimoto and Ikingura 2014	E73	Intermediate volcanics	235	25.90	102.30	15.50	3.08	10.42	1.45	5.35	0.88	2.48	0.34	2.02	0.32	7.70		24.70	5.30
Kazimoto and Ikingura 2014	E74	TTG	63	5.69	19.10	2.30	0.66	1.37	0.17	0.89	0.14	0.58	0.08	0.87	0.15	2.50		7.60	2.70
Kazimoto and Ikingura 2014	E75	TTG	37	3.64	12.20	2.30	0.46	1.52	0.20	1.37	0.19	0.59	0.08	0.38	0.09	2.70		7.70	1.30
Kazimoto and Ikingura 2014	EIO	Granite-Monzonite	27	2.7	8.6	1.4	0.31	0.74	0.15	0.84	0.15	0.39	0.06	0.36	0.07	2.2		7.2	1.5
Kazimoto and Ikingura 2014	El 8	Granite-Monzonite	76	7.7	23.3	2.9	0.63	1.83	0.24	1.23	0.2	0.46	0.06	0.47	0.11	4.8		12.5	1.2
Maboko et al 2006	KM1	Granite-Monzonite	52	3.97	17.38	5.05	0.45	1.67	0.25	1.51	0.32	0.84	0.13	0.78	0.09	3.34	29.02	0.65	
Maboko et al 2006	KM3	Granite-Monzonite	73	6.41	27.37	7.53	0.72	3.53	0.4	2.38	0.37	0.8	0.13	0.69	0.1	4.47	20.38	98	

Reference	Sample	Harmonisation litho	Ce	Pr	Nd	Sm	Eu	Gd	Tb	Dy	Ho	Er	Tm	Yb	Lu	Hf	Pb	Th	U
			ppm	ppm	ppm	ppm	ppm	ppm	ppm	ppm	ppm	ppm	ppm	ppm	ppm	ppm	ppm	ppm	ppm
Maboko et al 2006	KM3*	Granite-Monzonite	76	6.71	28.99	7.67	0.81	3.65	0.39	2.56	0.37	0.82	0.13	0.69	0.1	3.94	21.73	1.02	
Maboko et al 2006	KM30	TTG	57	7.26	23.14	5.87	1.02	2.17	0.39	1.53	0.29	0.54	0.11	0.56	0.08	3.22	18.22	2.13	
Maboko et al 2006	KM31	TTG	44	5.22	18.14	4.44	0.63	1.86	0.25	0.70	0.12	0.32	0.04	0.19	0.02	3.64	28.59	0.54	
Maboko et al 2006	KM32	TTG	42	5.51	19.30	4.19	1.02	2.48	0.36	1.39	0.28	0.77	0.08	0.64	0.06	3.65	16.36	1.67	
Maboko et al 2006	KM34	TTG	111	13.99	41.56	11.08	1.51	3.09	0.30	1.21	0.31	0.45	0.07	0.59	0.07	4.18	22.54	1.41	
Maboko et al 2006	KM46	TTG	44	4.45	14.96	4.35	0.61	1.24	0.21	1.07	0.15	0.26	0.03	0.17	0.02	2.58	11.33	0.26	
Maboko et al 2006	KM47	Granite-Monzonite	84	7.17	25.28	7.69	0.7	3.14	0.31	2.12	0.48	1.09	0.1	0.57	0.07	5.8	15.26	2.26	
Maboko et al 2006	KM48	Granite-Monzonite	176	16.62	57.39	17.34	1.34	6.09	0.31	3.25	0.58	1.47	0.14	0.73	0.11	8.01	28.37	2.54	
Maboko et al 2006	KM5	Granite-Monzonite	57	5.04	22.62	5.66	0.41	4.51	0.43	2.75	0.42	0.89	0.13	0.79	0.13	3.58	29.8	0.72	
Maboko et al 2006	KM52	Granite-Monzonite	206	19.08	68.5	20.33	1.35	6.51	0.38	3.71	0.72	1.43	0.15	0.88	0.12	9.59	33.55	2.94	
Maboko et al 2006	KM53	Granite-Monzonite	162	16.14	57.85	16.05	1.45	6.05	0.3	3.74	0.63	1.49	0.15	0.86	0.13	7.72	24.55	3.19	
Maboko et al 2006	KM54	Granite-Monzonite	135	12.48	43.59	13.38	1.05	3.12	0.39	1.47	0.32	0.8	0.14	0.81	0.12	3.98	18.84	0.98	
Maboko et al 2006	KM55	Granite-Monzonite	39	2.58	12.74	3.73	0.3	2.73	0.23	1.28	0.27	0.5	0.07	0.44	0.06	3.3	24.68	0.48	
Maboko et al 2006	KM56	Granite-Monzonite	101	6.87	22.27	8.69	0.45	6.81	0.33	2.08	0.34	1.05	0.13	0.82	0.13	9.79	49.35	1.09	
Maboko et al 2006	KM57	Granite-Monzonite	151	12	39.23	14.85	0.72	5.45	0.38	2.85	0.49	1.07	0.13	0.77	0.12	5.54	30.3	1.24	
Maboko et al 2006	R 14	TTG	62	6.02	18.70	2.30	0.52	1.80	0.18	0.65	0.09	0.27	0.05	0.27	0.04	3.80	3.59	8.60	
Maboko et al 2006	R 15	TTG	79	8.63	27.80	4.10	0.84	3.66	0.41	1.89	0.32	0.81	0.12	0.57	0.09	4.00	9.91	13.50	
Maboko et al 2006	R 16	TTG	158	16.30	50.10	5.80	0.89	4.66	0.31	1.41	0.28	0.58	0.09	0.52	0.09	4.80	13.10	22.00	
Maboko et al 2006	R 17	TTG	51	5.67	18.20	2.40	0.73	2.02	0.19	0.87	0.13	0.35	0.05	0.27	0.04	2.40	6.87	6.70	
Maboko et al 2006	R 18	TTG	58	5.68	17.60	2.20	0.51	1.80	0.16	0.60	0.08	0.27	0.05	0.17	0.03	3.50	8.16	7.60	
Maboko et al 2006	R 19	TTG	47	5.03	15.40	2.20	0.44	1.78	0.16	0.70	0.09	0.29	0.05	0.21	0.03	3.00	11.90	7.60	
Maboko et al 2006	R 2	TTG	87	10.30	37.20	5.90	1.39	4.79	0.54	2.55	0.44	1.19	0.17	0.93	0.17	4.10	16.20	14.20	
Maboko et al 2006	R 20	TTG	31	3.47	11.00	1.70	0.36	1.47	0.16	0.72	0.10	0.28	0.05	0.21	0.04	2.40	9.12	7.20	
Maboko et al 2006	R 21	TTG	64	7.21	24.40	3.10	0.70	2.28	0.21	0.93	0.14	0.41	0.05	0.30	0.05	3.00	7.20	9.10	
Maboko et al 2006	R 21*	TTG	62	7.18	24.60	3.20	0.68	2.27	0.23	0.97	0.13	0.37	0.05	0.30	0.05	3.10	7.62	9.10	
Maboko et al 2006	R 26	TTG	54	5.29	18.30	2.90	0.69	2.45	0.26	1.32	0.20	0.52	0.09	0.43	0.08	3.90	6.41	7.80	
Maboko et al 2006	R22	Granite-Monzonite	91	9.42	29.9	4.4	0.66	3.9	0.46	2.24	0.44	1.22	0.2	1.12	0.21	4	14.6	20.4	
Maboko et al 2006	R23	Granite-Monzonite	55	6.43	21.9	3.9	0.61	3.31	0.46	2.51	0.48	1.27	0.24	L36	0.25	4.1	13.2	20.7	
Maboko et al 2006	R24	Granite-Monzonite	66	7.52	24.3	3.9	0.75	3.27	0.46	2.36	0.49	1.27	0.2	1.28	0.24	4.3	12.8	23.3	
Maboko et al 2006	R25	Granite-Monzonite	97	10.7	33	4.9	0.57	3.91	0.49	2.38	0.46	1.27	0.16	0.79	0.12	7.2	10.4	36.3	
Maboko et al 2006	R63	Granite-Monzonite	38	4.4	17	2.5	0.78	2.2	0.2	1.3	0.2	0.5	0.1	0.5	0.1	3.1	2.1	2.8	
Manya 2004	PORP	Felsic volcanics	35	3.86	15.80	2.70	0.70	1.95	0.27	1.40	0.24	0.73	0.09	0.68	0.08	3.10		3.30	
Manya 2004	R06	Mafic volcanics	7	1.10	5.40	1.80	0.77	2.34	0.39	2.48	0.60	1.53	0.25	1.31	0.24	1.10		0.20	

Reference	Sample	Harmonisation litho	Ce	Pr	Nd	Sm	Eu	Gd	Tb	Dy	Ho	Er	Tm	Yb	Lu	Hf	Pb	Th	U
			ppm	ppm	ppm	ppm	ppm	ppm	ppm	ppm	ppm	ppm	ppm	ppm	ppm	ppm	ppm	ppm	ppm
Manya 2004	R07	Mafic volcanics	7	1.06	5.20	1.60	0.90	2.31	0.42	2.56	0.62	1.64	0.29	1.42	0.26	1.10		0.30	
Manya 2004	R08	Mafic volcanics	11	1.77	8.30	2.60	1.00	3.54	0.62	4.06	0.93	2.43	0.42	2.24	0.42	1.70		0.50	
Manya 2004	R09	Mafic volcanics	11	1.73	8.90	2.60	1.03	3.32	0.59	3.86	0.92	2.28	0.41	2.12	0.39	1.50		0.40	
Manya 2004	R10	Mafic volcanics	12	1.96	9.30	2.80	0.87	3.79	0.66	4.25	1.01	2.63	0.48	2.58	0.46	2.00		0.40	
Manya 2004	R11	Mafic volcanics	11	1.53	7.50	2.20	1.32	2.94	0.51	3.52	0.86	2.25	0.42	2.19	0.37	1.70		0.40	
Manya 2004	R12	Mafic volcanics	5	0.74	3.80	1.20	0.53	1.84	0.35	2.32	0.56	1.45	0.25	1.37	0.27	0.80		0.20	
Manya 2004	R13	Mafic volcanics	4	0.72	3.60	1.20	0.53	1.90	0.35	2.38	0.56	1.55	0.29	1.40	0.28	0.80		0.20	
Manya 2004	R38	Mafic volcanics	6	1.16	6.40	1.90	0.76	2.44	0.47	2.94	0.68	1.86	0.30	1.60	0.28	1.00		0.20	
Manya 2004	R39	Mafic volcanics	7	0.99	5.60	1.80	0.73	2.57	0.42	2.95	0.67	1.80	0.29	1.62	0.28	1.00		0.20	
Manya 2004	R40	Mafic volcanics	13	2.20	11.70	3.60	1.22	4.55	0.80	5.10	1.11	3.22	0.49	2.73	0.46	2.00		0.60	
Manya 2004	R42	Mafic volcanics	9	1.25	6.90	2.10	0.84	2.64	0.44	2.90	0.67	1.90	0.30	1.63	0.30	1.10		0.20	
Manya 2004	R44	Felsic volcanics	30	3.45	13.90	2.30	0.48	1.79	0.19	0.92	0.16	0.45	0.05	0.33	0.05	2.50		2.60	
Manya 2004	R45	Felsic volcanics	39	4.39	17.00	2.40	0.53	2.03	0.20	0.91	0.13	0.36	0.05	0.31	0.04	2.90		3.00	
Manya 2004	R46	Felsic volcanics	36	3.82	15.20	2.20	0.59	1.96	0.18	0.80	0.12	0.37	0.05	0.24	0.04	2.50		2.90	
Manya 2004	R65	Mafic volcanics	2	0.48	3.20	1.50	0.50	2.16	0.40	2.87	0.66	1.85	0.30	1.75	0.31	1.10		0.20	
Manya 2004	R66	Mafic volcanics	6	1.00	5.40	1.80	0.70	2.18	0.41	2.54	0.56	1.63	0.26	1.47	0.25	1.00		0.20	
Manya 2004	R67	Mafic volcanics	8	1.36	7.90	2.40	1.10	3.11	0.54	3.45	0.75	2.14	0.36	1.97	0.34	1.40		0.30	
Manya 2004	R68	Mafic volcanics	6	0.94	5.20	1.70	0.64	2.31	0.40	2.60	0.60	1.75	0.27	1.65	0.28	1.00		0.30	
Manya 2004	R69	Mafic volcanics	5	0.89	5.10	1.60	0.62	2.21	0.38	2.60	0.58	1.72	0.28	1.56	0.27	1.00		0.20	
Manya 2004	R75	Mafic volcanics	8	1.12	6.70	1.90	0.95	2.40	0.47	3.18	0.63	1.92	0.25	1.73	0.26	1.40		0.20	
Manya 2004	R76	Mafic volcanics	15	1.96	9.60	2.60	0.94	2.93	0.54	3.49	0.71	2.18	0.29	2.06	0.29	2.20		0.80	
Manya 2004	R78	Mafic volcanics	6	0.84	5.00	1.70	0.72	2.33	0.42	2.83	0.58	1.92	0.26	1.78	0.25	1.30		0.10	
Manya 2011	IM01	Granite-Monzonite	19	2.42	9.80	2.50	0.15	2.30	0.40	2.50	0.50	1.70	0.26	1.70	0.24	1.40	71.00	12.70	17.70
Manya 2011	IM02	Granite-Monzonite	70	7.96	26.6	5.3	0.87	4	0.5	2.8	0.5	1.2	0.17	1.1	0.15	5.5	31	13.5	8
Manya 2011	IM03	Granite-Monzonite	36	4.32	16	3.2	0.41	2.4	0.3	1.8	0.3	0.8	0.12	0.7	0.11	4.7	61	30.8	8.9
Manya 2011	IM04	Granite-Monzonite	74	8.23	24.5	4.3	0.43	3	0.4	2.1	0.3	0.9	0.12	0.7	0.1	5.2	78	40	19.4
Manya 2011	IM05	Granite-Monzonite	54	6.1	18.8	3.5	0.65	2.4	0.3	1.8	0.3	0.8	0.12	0.8	0.12	4.4	36	11.2	5.4
Manya 2011	IM06	Granite-Monzonite	142	16.2	52.4	9.2	0.64	6.9	1	5.2	0.9	2.4	0.32	1.9	0.27	9.1	41	28.6	11.8
Manya 2011	IM07	Granite-Monzonite	37	4.22	14.2	2.8	0.39	2.1	0.2	1.1	0.2	0.5	0.08	0.5	0.08	3.9	38	17	4.3
Manya 2011	IM08	Granite-Monzonite	118	13.6	43.1	7.8	0.48	5.1	0.6	2.6	0.4	1	0.15	0.9	0.14	7	45	44	7
Manya 2011	IM09	Granite-Monzonite	15	1.73	6.7	1.7	0.25	1.7	0.3	1.6	0.3	0.9	0.12	0.8	0.12	0.8	38	8.8	6.5
Manya 2011	IM12	Granite-Monzonite	104	14.5	55.2	12	1.92	9.9	1.4	7.2	1.3	3.4	0.47	2.9	0.39	13.2	37	2.7	1.3
Manya 2011	IM13	Granite-Monzonite	125	14.7	46.4	8.8	0.65	6.2	0.8	4.2	0.6	1.5	0.18	1	0.13	7.5	29	40.4	8

Reference	Sample	Harmonisation litho	Ce	Pr	Nd	Sm	Eu	Gd	Tb	Dy	Ho	Er	Tm	Yb	Lu	Hf	Pb	Th	U
			ppm	ppm	ppm	ppm	ppm	ppm	ppm	ppm	ppm	ppm	ppm	ppm	ppm	ppm	ppm	ppm	ppm
Manya 2011	IM14	Granite-Monzonite	123	13.3	37.8	6.1	1.13	3.8	0.5	2.7	0.5	1.3	0.18	1.1	0.15	7.3	13	23.3	1.6
Manya 2011	IM15	Granite-Monzonite	41	4.34	14.2	2.7	0.56	2.3	0.3	1.7	0.3	0.8	0.11	0.8	0.11	5.7	22	11.2	1.7
Manya 2011	IM16	Granite-Monzonite	34	4.55	15.2	2.8	0.97	2	0.2	1.1	0.2	0.4	0.06	0.4	0.06	7.1	10	3.6	0.5
Manya 2011	IM17	Granite-Monzonite	24	2.75	9	1.8	0.61	1.2	0.1	0.5	0.1	0.3	0.05	0.3	0.04	2	11	10.4	1
Manya 2011	IM18	Granite-Monzonite	25	3.21	12.3	2.6	0.54	2.1	0.3	1.5	0.3	0.7	0.11	0.7	0.11	2.8	17	11.2	3.8
Manya 2011	IM32	Gneiss	126	17.80	53.30	9.60	2.04	7.20	0.90	4.70	0.80	2.10	0.27	1.60	0.23	8.60	11.00	1.20	0.50
Manya 2011	IMI0	Granite-Monzonite	66	7.89	28	6	0.57	5.2	0.8	4.4	0.8	2.3	0.34	2	0.28	9.3	38	31.2	14
Manya 2011	IMII	Granite-Monzonite	42	4.57	13.1	2.1	0.48	1.3	0.2	0.8	0.1	0.4	0.06	0.4	0.06	3.2	22	13.9	1.2
Manya 2016	BZ 03	Granite-Monzonite	18	1.92	7.4	1.1	0.25	0.8	0.1	0.5	0.1	0.3	0.07	0.5	0.08	3.9	10	11.5	8.2
Manya 2016	BZ 04	Granite-Monzonite	37	3.93	13.3	1.8	0.39	1.4	0.1	0.7	0.1	0.3	0.05	0.3	0.05	3.5	27	12.6	23.6
Manya 2016	BZ 06	Granite-Monzonite	86	8.94	29.7	4	0.86	2.6	0.2	1	0.2	0.4	0.05	0.3	0.05	3.5	19	9	5.3
Manya 2016	BZ 08	Granite-Monzonite	89	9.72	33.2	4.5	1	2.8	0.2	1	0.2	0.4	0.06	0.4	0.05	4	27	12.1	3.9
Manya 2016	BZ 10	Granite-Monzonite	137	15.3	52.2	6.4	1.33	3.6	0.2	0.9	0.1	0.4	0.05	0.3	0.04	4.3	24	13.7	3.7
Manya 2016	BZ 13	Granite-Monzonite	81	8.81	30	4	0.9	2.4	0.2	0.9	0.1	0.4	0.05	0.3	0.05	3.7	22	12	4
Manya 2016	BZ 18	TTG	40	4.37	15.60	2.50	0.59	1.80	0.20	0.90	0.20	0.50	0.07	0.40	0.06	2.70	12.00	6.80	2.70
Manya 2016	BZ 19	TTG	42	4.50	16.60	2.60	0.69	1.90	0.20	1.10	0.20	0.50	0.07	0.40	0.07	3.20	160.00	7.50	2.90
Manya 2016	BZ 23	TTG	26	3.03	11.60	22.00	0.68	1.80	2.00	1.10	0.20	0.50	0.07	0.40	0.06	32.00	12.00	3.60	1.50
Manya 2016	BZ 24	TTG	129	13.80	45.70	5.80	1.28	3.80	0.30	1.50	0.20	0.60	0.09	0.50	0.07	5.10	24.00	15.50	3.20
Manya 2016	BZ 25	TTG	49	5.31	19.10	3.10	0.74	2.40	0.30	1.20	0.20	0.60	0.09	0.50	0.08	3.70	27.00	9.80	3.90
Manya 2016	BZ 34	TTG	42	4.56	16.10	2.50	0.63	1.90	0.20	1.00	0.20	0.40	0.06	0.40	0.06	3.20	16.00	7.50	2.20
Manya 2016	BZ01	Granite-Monzonite	28	3.01	10	1.3	0.33	1	0.1	0.4	0.1	0.3	0.05	0.3	0.04	2.3	22	12.5	4.6
Manya 2016	BZ02	Granite-Monzonite	62	6.57	21.6	2.7	0.53	1.8	0.1	0.6	0.1	0.4	0.05	0.4	0.05	3.5	10	10.2	10.8
Manya 2016	BZ05	Granite-Monzonite	54	5.81	20	2.5	0.54	1.4	0.1	0.6	0.1	0.3	0.05	0.3	0.04	2.5	14	6.6	1.5
Manya 2016	BZ09	Granite-Monzonite	110	12.2	41.5	5.3	1.1	2.9	0.2	0.7	0.1	0.3	0.05	0.2	0.04	4.2	25	11.8	2.8
Manya 2016	BZ11	Granite-Monzonite	77	8.24	28	3.7	0.82	2.4	0.2	0.8	0.1	0.4	0.05	0.3	0.05	3.3	39	11.7	4.5
Manya 2016	BZ20	TTG	40	4.55	15.70	2.60	0.70	1.90	0.20	1.00	0.20	0.40	0.06	0.40	0.06	3.10	16.00	7.00	3.00
Manya 2016	BZ26	TTG	42	4.61	16.20	2.70	0.70	2.20	0.20	1.10	2.00	0.50	0.07	0.40	0.07	3.00	203.00	7.60	72.00
Manya 2016	BZ27	TTG	71	7.68	26.20	3.80	0.78	2.50	2.00	1.00	0.20	0.40	0.05	3.00	0.05	3.70	52.00	15.20	3.90
Manya 2016	BZ28	TTG	44	4.81	17.00	2.60	0.62	1.80	0.20	0.90	0.20	0.40	0.06	0.40	0.06	2.90	13.00	72.00	2.60
Manya 2016	BZ29	TTG	42	4.68	16.80	2.60	0.58	2.00	0.20	1.00	0.20	0.50	0.08	0.50	0.08	3.20	21.00	8.10	3.40
Manya and Maboko 2008a	SIN 07a	Mafic volcanics	10	1.78	10.00	3.30	1.15	4.30	0.80	5.60	1.20	3.60	0.55	3.50	0.53	2.30		0.30	0.10
Manya and Maboko 2008a	SIN 07b	Mafic volcanics	10	1.89	10.40	3.40	1.19	4.60	0.90	5.60	1.20	3.50	0.55	3.60	0.55	2.30		0.30	0.10
Manya and Maboko 2008a	SIN 08	Mafic volcanics	11	1.88	10.10	3.20	1.19	4.00	0.70	4.80		3.10	0.46	3.00	0.47	2.10		0.40	0.10

Reference	Sample	Harmonisation litho	Ce	Pr	Nd	Sm	Eu	Gd	Tb	Dy	Ho	Er	Tm	Yb	Lu	Hf	Pb	Th	U
			ppm	ppm	ppm	ppm	ppm	ppm	ppm	ppm	ppm	ppm	ppm	ppm	ppm	ppm	ppm	ppm	ppm
Manya and Maboko 2008a	SIN 11	Mafic volcanics	12	1.78	8.90	2.60	0.99	3.50	0.60	4.10	0.90	2.60	0.39	2.50	0.39	1.80		0.50	0.20
Manya and Maboko 2008a	SIN 12	Mafic volcanics	7	1.09	5.70	1.70	0.69	2.30	0.40	2.80	0.60	1.80	0.27	1.80	0.27	1.20		0.30	0.20
Manya and Maboko 2008a	SIN 13	Mafic volcanics	7	1.08	5.40	1.80	0.70	2.50	0.50	3.00	0.60	1.90	0.29	1.90	0.28	1.20		0.30	0.10
Manya and Maboko 2008a	SIN 15	Mafic volcanics	8	1.20	6.40	2.00	0.85	2.90	0.50	3.30	0.70	2.10	0.32	2.00	0.31	1.30		0.20	0.20
Manya and Maboko 2008a	SIN 17	Mafic volcanics	7	1.14	5.80	1.70	0.70	2.30	0.40	2.80	0.60	1.80	0.27	1.80	0.26	1.20		0.30	0.10
Manya and Maboko 2008a	SIN 18	Mafic volcanics	12	1.88	10.30	3.00	0.98	3.80	0.70	4.60		3.00	0.46	3.00	0.46	2.20		0.30	0.30
Manya and Maboko 2008a	SIN 19	Mafic volcanics	10	1.47	7.60	2.30	0.81	2.80	0.50	3.10	0.60	2.00	0.30	2.00	0.31	1.70		0.30	0.20
Manya and Maboko 2008a	SIN 20	Mafic volcanics	10	1.62	8.70	2.70	0.98	3.50	0.60	4.00	0.80	2.50	0.39	2.50	0.37	1.80		0.30	0.20
Manya and Maboko 2008a	SIN 21	Mafic volcanics	10	1.48	8.00	2.50	0.96	3.40	0.60	4.10	0.90	2.70	0.40	2.50	0.37	1.80		0.30	0.10
Manya and Maboko 2008a	SIN 22	Mafic volcanics	8	1.25	7.00	2.30	0.86	3.00	0.60	3.60	0.70	2.30	0.34	2.20	0.33	1.50		0.20	0.10
Manya and Maboko 2008a	SIN 23	Mafic volcanics	10	1.52	8.20	2.50	1.02	3.50	0.60	4.10	0.90	2.70	0.40	2.60	0.39	1.70		0.30	0.10
Manya and Maboko 2008a	SIN 24	Mafic volcanics	13	2.01	10.30	3.20	1.11	4.10	0.70	4.70		2.90	0.44	2.90	0.44	2.20		0.40	2.70
Manya and Maboko 2008a	SIN 25	Mafic volcanics	10	1.53	8.00	2.50	0.91	3.40	0.60	4.00	0.80	2.50	0.38	2.40	0.37	1.70		0.30	0.10
Manya and Maboko 2008a	SIN 28	Mafic volcanics	7	1.20	6.10	1.90	0.83	2.60	0.50	3.20	0.70	2.00	0.31	2.10	0.31	1.40		0.20	0.10
Manya and Maboko 2008a	SIN 29	Mafic volcanics	7	1.12	6.00	1.90	0.75	2.70	0.50	3.20	0.70	2.00	0.30	1.90	0.29	1.30		0.20	0.10
Manya and Maboko 2008a	SIN IO	Mafic volcanics	9	1.52	8.60	2.80	1.08	3.80	0.70	4.60		3.00	0.46	3.00	0.45	2.10		0.30	0.20
Manya and Maboko 2008a	SIN01	Mafic volcanics	10	1.63	8.90	2.90	1.13	4.10	0.80	4.90		3.10	0.47	3.00	0.46	2.00		0.30	0.10
Manya and Maboko 2008a	SIN02	Mafic volcanics	10	1.76	9.70	3.10	1.12	4.00	0.80	4.80		3.10	0.48	3.10	0.46	2.00		0.30	0.20
Manya and Maboko 2008a	SIN04	Mafic volcanics	13	2.17	11.60	3.70	1.48	5.00	0.90	5.50	1.20	3.50	0.53	3.30	0.49	2.40		0.40	0.10
Manya and Maboko 2008b	GT 02	Mafic volcanics	12	1.76	9.00	2.80	1.02	3.80	0.70	4.10	0.90	2.60	0.39	2.60	0.39	2.00	5.00	0.50	0.20
Manya and Maboko 2008b	GT 04	Mafic volcanics	13	1.82	9.40	2.90	1.06	3.80	0.70	4.30	0.90	2.70	0.41	2.60	0.38	1.90	9.00	0.50	0.40
Manya and Maboko 2008b	GT 06	Mafic volcanics	12	1.84	9.20	2.90	1.07	3.70	0.70	4.60	1.00	2.90	0.44	2.80	0.42	1.90	5.00	0.50	0.20
Manya and Maboko 2008b	GT 08	Mafic volcanics	8	1.09	5.70	1.80	0.77	2.40	0.40	2.60	0.50	1.60	0.24	1.50	0.23	1.40	5.00	0.40	0.30
Manya and Maboko 2008b	GT 09	Mafic volcanics	9	1.25	6.40	2.00	0.86	2.70	0.50	3.10	0.60	2.00	0.31	2.00	0.29	1.50	5.00	0.40	0.20
Manya and Maboko 2008b	GT 12	Mafic volcanics	12	1.69	8.70	2.70	0.97	3.70	0.70	4.00	0.80	2.50	0.38	2.40	0.38	1.80	5.00	0.50	0.30
Manya and Maboko 2008b	GT 15	Mafic volcanics	12	1.66	8.50	2.70	1.06	3.60	0.60	4.00	0.80	2.60	0.39	2.50	0.38	1.80	5.00	0.50	0.30
Manya and Maboko 2008b	GT 18	Mafic volcanics	12	1.72	8.60	2.60	0.99	3.30	0.60	3.90	0.80	2.50	0.38	2.50	0.37	1.80	5.00	0.50	0.10
Manya and Maboko 2008b	GT 19	Mafic volcanics	10	1.56	7.90	2.40	0.94	3.40	0.60	4.20	0.90	2.80	0.43	2.80	0.43	1.70	5.00	0.40	0.20
Manya and Maboko 2008b	GT01	Mafic volcanics	14	1.99	10.20	3.10	1.10	4.20	0.70	4.70	1.00	2.90	0.44	2.90	0.43	2.10	50.00	0.60	0.40
Manya and Maboko 2008b	GT05	Mafic volcanics	13	1.86	9.80	3.10	1.11	4.20	0.70	4.50	0.90	2.90	0.44	2.80	0.44	2.00	8.00	0.50	0.40
Manya and Maboko 2008b	GT07	Mafic volcanics	8	1.16	5.70	1.80	0.79	2.30	0.40	2.80	0.60	1.80	0.28	1.70	0.26	1.50	7.00	0.40	0.40
Manya and Maboko 2008b	GT10	Mafic volcanics	9	1.40	7.50	2.50	0.90	3.40	0.60	3.70	0.80	2.40	0.35	2.30	0.36	1.60	5.00	0.30	0.20
Manya and Maboko 2008b	GT11	Mafic volcanics	12	1.72	8.40	2.60	1.00	3.40	0.60	4.20	0.90	2.60	0.40	2.50	0.38	1.90	5.00	0.50	0.20

Reference	Sample	Harmonisation litho	Ce	Pr	Nd	Sm	Eu	Gd	Tb	Dy	Ho	Er	Tm	Yb	Lu	Hf	Pb	Th	U
			ppm	ppm	ppm	ppm	ppm	ppm	ppm	ppm	ppm	ppm	ppm	ppm	ppm	ppm	ppm	ppm	ppm
Manya and Maboko 2008b	GT13	Mafic volcanics	11	1.59	8.40	2.60	0.97	3.50	0.60	3.90	0.80	2.50	0.37	2.40	0.36	1.70	5.00	0.50	0.20
Manya and Maboko 2008b	GT14	Mafic volcanics	10	1.50	7.40	2.30	0.88	2.90	0.50	3.60	0.70	2.20	0.34	2.20	0.33	1.80	5.00	0.50	0.20
Manya and Maboko 2008b	GT16	Mafic volcanics	12	1.76	8.30	2.60	1.01	3.30	0.60	3.80	0.80	2.30	0.34	2.10	0.31	2.10	5.00	0.50	0.10
Manya and Maboko 2008b	GT17	Mafic volcanics	11	1.59	8.20	2.50	0.94	3.20	0.60	3.80	0.80	2.50	0.38	2.50	0.37	1.70	5.00	0.50	2.00
Manya and Maboko 2008b	GT20	Mafic volcanics	11	1.61	8.40	2.70	1.01	3.70	0.70	4.70	1.00	3.00	0.47	3.10	0.48	2.00	5.00	0.40	0.10
Messo et al 2012	MU100	Intermediate volcanics	47	6.24	23.60	5.70	1.62	5.50	0.90	4.70	0.90	2.60	0.36	2.20	0.33	4.10	5.00	7.50	2.20
Messo et al 2012	MU14	Mafic volcanics	12	1.96	6.58	1.63	1.11	4.30	0.80	5.00	1.10	3.30	0.48	3.10	0.46	2.20	5.00	0.50	0.20
Messo et al 2012	MU15	Mafic volcanics	8	1.27	6.70	2.10	0.84	3.00	0.50	3.40	0.70	2.10	0.32	2.10	0.31	1.40	5.00	0.30	0.10
Messo et al 2012	MU16	Felsic volcanics	13	1.90	7.80	2.10	0.12	2.10	0.40	2.00	0.40	1.00	0.15	0.90	0.13	1.90	9.00	3.10	2.50
Messo et al 2012	MU17	Felsic volcanics	9	1.31	5.40	1.40	0.09	1.40	0.30	1.50	0.30	0.80	0.13	0.80	0.12	2.00	5.00	2.90	2.10
Messo et al 2012	MU18	Felsic volcanics	12	1.12	4.60	1.40	0.10	1.50	0.30	1.50	0.30	0.90	0.14	0.90	0.12	1.90	5.00	2.70	2.00
Messo et al 2012	MU19	Mafic volcanics	5	0.75	4.10	1.30	0.57	2.00	0.40	2.50	0.60	1.70	0.26	1.70	0.26	1.00	5.00	0.20	0.10
Messo et al 2012	MU27	Intermediate volcanics	42	4.99	17.90	3.50	1.06	3.30	0.50	2.60	0.50	1.50	0.22	1.40	0.22	3.20	7.00	3.90	1.30
Messo et al 2012	MU36	Intermediate volcanics	54	6.46	24.40	5.70	1.37	5.70	0.80	4.70	0.90	2.40	0.34	2.10	0.31	4.30	5.00	8.00	2.10
Messo et al 2012	MU49	Intermediate volcanics	60	7.74	28.10	6.40	1.66	5.80	0.90	4.70	0.90	2.50	0.35	2.20	0.31	4.90	9.00	8.70	2.90
Messo et al 2012	MU57	Intermediate volcanics	49	6.21	22.90	5.40	1.68	4.80	0.80	4.00	0.80	2.10	0.29	1.80	0.26	3.90	42.00	7.00	1.90
Messo et al 2012	MU60	Intermediate volcanics	60	7.49	28.50	6.20	1.65	6.10	0.90	4.80	0.90	2.50	0.34	2.10	0.30	4.70	6.00	8.90	2.50
Messo et al 2012	MU68	Intermediate volcanics	69	9.00	31.60	6.50	1.62	5.30	0.80	4.20	0.80	2.50	0.37	2.30	0.34	4.60	10.00	5.80	1.40
Messo et al 2012	MU69	Mafic volcanics	22	3.05	17.82	6.10	1.36	4.10	0.70	4.00	0.80	2.40	0.36	2.30	0.35	2.40	5.00	1.00	0.40
Messo et al 2012	MU79	Intermediate volcanics	51	6.35	24.40	5.80	1.78	6.00	0.90	4.90	0.90	2.60	0.36	2.20	0.32	4.30	5.00	7.80	2.20
Messo et al 2012	MU87	Intermediate volcanics	58	7.20	27.30	6.20	1.60	6.20	0.90	4.70	0.90	2.40	0.34	2.00	0.30	4.60	14.00	8.90	2.50
Messo et al 2012	MU89	Intermediate volcanics	60	7.68	27.90	6.60	1.81	5.70	0.90	4.70	0.90	2.50	0.36	2.20	0.31	4.90	18.00	8.80	3.10
Messo et al 2012	MU94	Intermediate volcanics	47	5.82	22.70	5.20	1.63	5.30	0.80	4.40	0.80	2.30	0.32	2.00	0.30	3.70	5.00	7.20	2.00
Sanislav et al 2014a	GP-01	Granite-Monzonite	99	10.9	41	6.81	1.5	4.53	0.609	3.32	0.594	1.62	0.22	1.34	0.185	5.82	16	9.02	2.39
Sanislav et al 2014a	GP-02	Granite-Monzonite	98	12	48.2	9.3	1.46	6.45	0.864	5.12	0.939	2.57	0.37	2.42	0.38	7.9	21.9	15.7	5.43
Sanislav et al 2014a	GP-03	Granite-Monzonite	62	6.7	24.4	4.2	0.457	2.7	0.469	2.44	0.52	1.19	0.2	1.37	0.237	3.9	20	18.5	6.26
Sanislav et al 2014a	GX-01	Granite-Monzonite	96	9.93	35.6	5.33	1.11	3.39	0.431	2.42	0.467	1.21	0.163	1.13	0.179	5.3	14.6	14.7	8.22
Sanislav et al 2014a	XU-01	Granite-Monzonite	151	15.9	57.7	8.8	1.35	5.95	0.823	4.61	0.871	2.36	0.342	2.08	0.355	7.36	25.4	23.5	6.62
Sanislav et al 2014a	XU-01A	Granite-Monzonite	181	19.2	66.8	10.3	1.53	6.62	0.867	5.13	0.936	2.52	0.335	2.64	0.37	7.39	23.1	23.3	4.79
Sanislav et al 2014a	XU-02	Granite-Monzonite	86	9.38	34	6.12	0.449	4.5	0.719	4.08	0.801	2.37	0.342	2.15	0.312	5.17	25.4	46.3	13.2
Wu et al 2023	18TGE01-1	TTG	34	3.94	14.80	2.56	0.89	2.07	0.26	1.15	0.19	0.54	0.08	0.45	0.07	3.73	12.10	3.96	0.90
Wu et al 2023	18TGE01-10	TTG	34	3.78	13.80	2.38	0.92	1.98	0.26	1.08	0.18	0.50	0.07	0.41	0.06	3.68	11.60	3.54	0.44
Wu et al 2023	18TGE01-2	TTG	38	4.25	15.40	2.70	0.85	2.11	0.27	1.19	0.20	0.56	0.07	0.44	0.07	3.73	13.30	5.33	2.54

Reference	Sample	Harmonisation litho	Ce	Pr	Nd	Sm	Eu	Gd	Tb	Dy	Ho	Er	Tm	Yb	Lu	Hf	Pb	Th	U
			ppm	ppm	ppm	ppm	ppm	ppm	ppm	ppm	ppm	ppm	ppm	ppm	ppm	ppm	ppm	ppm	ppm
Wu et al 2023	18TGE01-3	TTG	50	5.39	18.70	2.78	1.00	2.37	0.27	1.16	0.19	0.55	0.08	0.50	0.08	3.66	14.60	7.94	1.40
Wu et al 2023	18TGE01-4	TTG	35	3.88	13.60	2.10	0.78	1.76	0.22	0.91	0.15	0.44	0.06	0.41	0.07	3.13	16.20	5.47	1.45
Wu et al 2023	18TGE01-5	TTG	34	3.60	11.90	1.73	0.70	1.48	0.16	0.62	0.11	0.31	0.04	0.28	0.05	2.94	15.00	7.96	1.62
Wu et al 2023	18TGE01-6	TTG	24	2.67	9.74	1.73	0.61	1.47	0.22	1.01	0.18	0.51	0.08	0.54	0.07	2.50	15.20	4.65	2.12
Wu et al 2023	18TGE01-7	TTG	31	3.39	11.60	1.75	0.72	1.47	0.16	0.66	0.12	0.36	0.05	0.30	0.05	3.26	13.50	4.99	1.33
Wu et al 2023	18TGE01-8	TTG	37	3.91	13.40	1.93	0.77	1.68	0.19	0.78	0.14	0.40	0.06	0.38	0.06	3.47	17.00	7.94	3.91
Wu et al 2023	18TGE01-9	TTG	29	3.36	12.50	2.24	0.90	1.86	0.25	1.09	0.19	0.53	0.07	0.46	0.07	3.53	13.00	4.26	1.22
Manya 2012		Mafic volcanics	104	13.30	51.10	9.60	2.40	6.50	0.80	3.60	0.60	1.60	0.23	1.40	0.21	2.10	7.00	4.50	0.90
Manya 2012		Mafic volcanics	6	0.83	5.00	1.60	0.59	2.20	0.40	2.60	0.50	1.70	0.25	1.60	0.22	1.10	5.00	0.20	0.20
Manya 2012		Mafic volcanics	5	0.72	4.00	1.40	0.60	1.80	0.30	2.10	0.50	1.30	0.20	1.30	0.20	0.90	5.00	0.20	0.10
Manya 2012		Mafic volcanics	13	1.82	8.80	2.80	1.25	3.60	0.70	4.20	0.90	2.60	0.40	2.50	0.39	2.00	6.00	0.50	0.10
Manya 2012		Mafic volcanics	3	0.51	3.40	1.40	0.60	1.90	0.40	2.40	0.50	1.50	0.22	1.40	0.23	0.50	5.00	0.10	0.20
Manya 2012		Mafic volcanics	7	0.92	5.00	1.70	0.68	2.20	0.40	2.80	0.60	1.90	0.28	1.80	0.28	1.20	5.00	0.40	0.10
Kwelwa 2017	KIC-01	Felsic volcanics	235	25.95	96.49	13.96	2.80	7.17	0.79	3.34	0.52	1.38	0.19	1.25	0.18	4.41		20.30	3.75
Kwelwa 2017	KIC-02	Felsic volcanics	143	17.15	69.46	11.14	2.77	6.57	0.66	3.34	0.48	1.09	0.15	0.71	0.10	3.53		12.00	3.95
Kwelwa 2017	KIC-03	Felsic volcanics	212	24.48	95.99	15.46	3.73	9.21	1.04	4.73	0.73	1.80	0.22	1.33	0.17	5.30		18.25	4.59
Kwelwa 2017	KIC-04	Felsic volcanics	164	18.69	72.82	11.17	2.65	6.35	0.70	3.31	0.52	1.35	0.18	1.07	0.15	3.70		11.55	4.59
Kwelwa 2017	KIC-05	Felsic volcanics	169	19.48	75.62	11.85	3.01	6.99	0.78	3.60	0.57	1.36	0.18	1.17	0.17	4.12		16.89	4.26
Kwelwa 2017	KIC-06	Felsic volcanics	168	19.36	75.68	11.29	2.71	6.66	0.70	3.18	0.52	1.27	0.18	1.12	0.17	4.13		17.06	4.09
Kwelwa 2017	KIC-07	Felsic volcanics	116	13.28	52.45	8.25	2.05	5.15	0.57	2.74	0.46	1.05	0.15	0.85	0.13	3.61		11.95	3.47
Kwelwa 2017	KIC-08	Felsic volcanics	354	42.13	172.62	26.47	6.53	15.35	1.64	6.87	1.04	2.29	0.27	1.68	0.21	6.14		31.58	7.40
Kwelwa 2017	KIC-09	Felsic volcanics	158	18.30	71.57	10.25	2.28	5.42	0.51	2.64	0.42	1.09	0.16	0.99	0.16	3.23		17.52	8.36
Kwelwa 2017	KIC-10	Felsic volcanics	380	44.78	177.99	28.78	6.67	16.27	1.55	7.39	1.08	2.47	0.33	1.81	0.24	6.29		32.83	7.78
Kwelwa 2017	KIC-11	Felsic volcanics	162	18.43	74.67	11.76	2.54	6.61	0.64	3.27	0.51	1.35	0.18	1.05	0.17	4.08		16.22	5.24
Kwelwa 2017	KIC-12	TTG	43	4.59	17.11	2.96	0.86	2.23	0.32	1.75	0.31	0.86	0.14	0.94	0.14	3.05		434.00	1.31
Kwelwa 2017	KIC-13	TTG	66	7.65	30.62	5.07	1.22	3.14	0.36	1.62	0.28	0.61	0.09	0.50	0.08	2.83		6.90	2.39
Kwelwa 2017	KIC-14	TTG	66	7.92	32.22	5.94	1.42	3.78	0.44	2.05	0.34	0.88	0.12	0.61	0.08	2.91		6.92	2.68
Kwelwa 2017	KIC-15	TTG	46	5.74	24.19	4.86	1.31	3.55	0.46	2.41	0.45	1.19	0.18	1.04	0.17	2.99		2.45	0.86
Kwelwa 2017	KIC-16	TTG	31	4.01	17.65	3.74	1.11	3.21	0.44	2.39	0.46	1.27	0.19	1.19	0.18	227.00		1.64	0.57
Kwelwa 2017	KIC-17	TTG	29	4.05	17.04	3.70	1.15	3.13	0.46	2.27	0.44	1.08	0.16	0.94	0.15	2.31		1.49	0.48
Kwelwa 2017	KIC-18	TTG	27	3.54	14.47	3.08	1.07	2.53	0.35	1.67	0.32	0.76	0.12	0.66	0.11	2.53		1.68	0.61
Kwelwa 2017	KIC-19	TTG	27	3.53	16.21	3.47	1.19	2.78	0.35	1.93	0.36	0.99	0.14	0.79	0.12	2.88		1.53	0.52
Kwelwa 2017	KIC-20	TTG	76	8.76	34.33	5.77	1.51	3.90	0.49	2.53	0.45	1.29	0.18	1.09	0.16	3.73		5.25	1.64

Reference	Sample	Harmonisation litho	Ce	Pr	Nd	Sm	Eu	Gd	Tb	Dy	Ho	Er	Tm	Yb	Lu	Hf	Pb	Th	U
			ppm	ppm	ppm	ppm	ppm	ppm	ppm	ppm	ppm	ppm	ppm	ppm	ppm	ppm	ppm	ppm	ppm
Kwelwa 2017	KIC-21	TTG	22	2.80	12.69	2.65	0.85	2.33	0.31	1.84	0.35	0.94	0.14	0.75	0.10	2.54		1.09	0.40
Kwelwa 2017	KIC-22	TTG	52	6.15	23.64	4.45	0.96	3.61	0.5	3.17	0.57	1.87	0.25	1.56	0.26	3.89		8.3	2.82
Kwelwa 2017	KIC-23	TTG	51	5.79	22.66	4.21	0.86	3.70	0.49	3.08	0.55	1.69	0.26	1.57	0.25	3.92		8.12	2.76
Kwelwa 2017	KIC-24	TTG	51	5.89	22.88	4.36	1.05	3.63	0.52	2.46	0.62	1.71	0.29	1.61	0.24	3.81		8.10	2.83
Kwelwa 2017	KIC-25	TTG	49	5.79	22.49	4.31	1.15	3.46	0.48	2.86	0.56	1.63	0.25	1.54	0.23	3.76		7.67	2.62

Supplementary Material 2-6

U-Pb-Nd-Hf analyses from the literature

CTR = Central Tanzania Region

ISGB = Iramba Sekenke greenstone belt

KGB = Kilimafheda greenstone belt

MMGB = Musoma Mara greenstone belt

NGB = Nzega greenstone belt

SGB = Sukulamand greenstone belt

EAAO = East African Antarctica orogen, Mozambic belt

Table SM2-6.1. U-Pb dating results on magmatic and detrital zircon from the Tanzania Craton and its surrounding mobile belts.

Table SM2-6.2. Lu-Hf isotope composition of magmatic and detrital zircon from the Tanzania Craton and its surrounding mobile belts.

Table SM2-6.3. Sm-Nd isotope composition of magmatic and detrital zircon from the Tanzania Craton and its surrounding mobile belts.

Table SM2-6.1. U-Pb dating results on magmatic and detrital zircon from the Tanzania Craton and its surrounding mobile belts

Reference	Location	Harmonized classification	Sample	inheritance	Name	Comments	$^{207}Pb/^{206}Pb$ Age (Ma)	2SE
Borg and Krogh 1999	SGB	Felsic volcanic	16150.00		16150.00	Crystallization age	2808	3
Borg and Krogh 1999	SGB	Felsic volcanic	26150.00		26150.00	Crystallization age	2780	3
Borg and Krogh 1999	SGB	TTG	96056.00		96056.00	Crystallization age	2699	9
Borg and Krogh 1999	SGB	Felsic volcanic	35352.00		35352.00	Crystallization age	2654	15
Borg and Krogh 1999	SGB	TTG	96058		96058	Crystallization age	2644	3
Chamberlain and Tosdal 2007	SGB	Felsic volcanic				Crystallization age	2821	30
Chamberlain and Tosdal 2007	SGB	Felsic volcanic				Crystallization age	2779	13
Chamberlain and Tosdal 2007	SGB	Felsic volcanic				Crystallization age	2770	9
Chamberlain and Tosdal 2007	SGB	TTG				Crystallization age	2758	7
Chamberlain and Tosdal 2007	SGB	TTG				Crystallization age	2758	6
Chamberlain and Tosdal 2007	SGB	TTG				Crystallization age	2743	14
Chamberlain and Tosdal 2007	SGB	Mafic volcanic				Crystallization age	2743	12
Chamberlain and Tosdal 2007	SGB	TTG				Crystallization age	2738	9
Chamberlain and Tosdal 2007	SGB	Felsic volcanic				Crystallization age	2719	16
Chamberlain and Tosdal 2007	SGB	Granite-Monzonite				Crystallization age	2710	20
Chamberlain and Tosdal 2007	SGB	Sediment				Crystallization age of precursor	2702	8
Chamberlain and Tosdal 2007	SGB	Granite-Monzonite				Crystallization age	2700-3100	
Chamberlain and Tosdal 2007	SGB	Gneiss				Crystallization age	2698	12
Chamberlain and Tosdal 2007	SGB	Granitoid				Crystallization age	2697	10
Chamberlain and Tosdal 2007	SGB	Granite-Monzonite				Crystallization age	2695	18
Chamberlain and Tosdal 2007	SGB	TTG				Crystallization age	2686	13
Chamberlain and Tosdal 2007	SGB	Granite-Monzonite				Crystallization age	2670	21
Chamberlain and Tosdal 2007	SGB	Granite-Monzonite				Crystallization age	2667	14
Chamberlain and Tosdal 2007	SGB	Granitoid				Crystallization age	2666	8
Chamberlain and Tosdal 2007	SGB	Sediment				Crystallization age of precursor	2659	41
Chamberlain and Tosdal 2007	SGB	TTG				Crystallization age	2653	10
Chamberlain and Tosdal 2007	SGB	Sediment				Detrital zircons	2650-2700	
Chamberlain and Tosdal 2007	SGB	Sediment				Detrital zircons	2650-2700	
Chamberlain and Tosdal 2007	SGB	Granitoid				Crystallization age	2646	14
Chamberlain and Tosdal 2007	SGB	TTG				Crystallization age	2567	10
Chamberlain and Tosdal 2007	ISGB	TTG				Crystallization age	2751	17
Chamberlain and Tosdal 2007	NGB	Felsic volcanic				Crystallization age	2725	22
Chamberlain and Tosdal 2007	NGB	Felsic volcanic				Crystallization age	2717	10
Chamberlain and Tosdal 2007	NGB	Felsic volcanic				Crystallization age	2695	12
Chamberlain and Tosdal 2007	NGB	Granite-Monzonite				Crystallization age	2680	13
Chamberlain and Tosdal 2007	NGB	Sediment				Crystallization age	2655-3100	
Chamberlain and Tosdal 2007	NGB	TTG				Crystallization age	2655	16
Chamberlain and Tosdal 2007	NGB	TTG				Crystallization age	2765	25
Chamberlain and Tosdal 2007	NGB	Granitoid				Crystallization age	2680	9
Chamberlain and Tosdal 2007	NGB	Granitoid				Crystallization age	2656	11
Chamberlain and Tosdal 2007	MMGB	TTG				Crystallization age	2843	12
Chamberlain and Tosdal 2007	MMGB	Granitoid				Crystallization age	2842	6
Chamberlain and Tosdal 2007	MMGB	TTG				Crystallization age	2835	12
Chamberlain and Tosdal 2007	MMGB	TTG				Crystallization age	2825	20
Chamberlain and Tosdal 2007	MMGB	Granitoid				Crystallization age	2803	4
Chamberlain and Tosdal 2007	MMGB	TTG				Crystallization age	2743	28
Chamberlain and Tosdal 2007	MMGB	Granite-Monzonite				Crystallization age	2671	10

Reference	Location	Harmonized classification	Sample	inheritance	Name	Comments	$^{207}Pb/^{206}Pb$ Age (Ma)	2SE
Chamberlain and Tosdal 2007	MMGB	Granite-Monzonite				Crystallization age	2649	10
Chamberlain and Tosdal 2007	MMGB	TTG				Crystallization age	2648	9
Chamberlain and Tosdal 2007	NGB	Granite-Monzonite				Crystallization age	2640	17
Chamberlain and Tosdal 2007	MMGB	TTG				Crystallization age	2660	6
Chamberlain and Tosdal 2007	MMGB	Felsic volcanic				Crystallization age	2831	7
Chamberlain and Tosdal 2007	MMGB	Felsic volcanic				Crystallization age	2807	3
Chamberlain and Tosdal 2007	MMGB	Felsic volcanic				Crystallization age	2804	3
Chamberlain and Tosdal 2007	MMGB	Felsic volcanic				Crystallization age	2759	9
Chamberlain and Tosdal 2007	SGB	Felsic volcanic				Crystallization age	2710	10
Chamberlain and Tosdal 2007	SGB	Felsic volcanic				Crystallization age	2697	10
Chamberlain and Tosdal 2007	MMGB	Felsic volcanic				Crystallization age	2696	26
Chamberlain and Tosdal 2007	SGB	Felsic volcanic				Crystallization age	2695	18
Chamberlain and Tosdal 2007	MMGB	Felsic volcanic				Crystallization age	2692	18
Chamberlain and Tosdal 2007	SGB	Felsic volcanic				Crystallization age	2686	13
Chamberlain and Tosdal 2007	SGB	Felsic volcanic				Crystallization age	2684	21
Chamberlain and Tosdal 2007	NGB	Felsic volcanic				Crystallization age	2680	13
Chamberlain and Tosdal 2007	NGB	Felsic volcanic				Crystallization age	2675	25
Chamberlain and Tosdal 2007	SGB	Felsic volcanic				Crystallization age	2670	21
Chamberlain and Tosdal 2007	MMGB	Felsic volcanic				Crystallization age	2670	5
Chamberlain and Tosdal 2007	SGB	Felsic volcanic				Crystallization age	2667	14
Chamberlain and Tosdal 2007	MMGB	Felsic volcanic				Crystallization age	2657	8
Chamberlain and Tosdal 2007	MMGB	Felsic volcanic				Crystallization age	2653	7
Kabete et al 2012b	RTC	Sediment	JK-02			Zircon analysis	2702	14
Kabete et al 2012b	RTC	Sediment	JK-02			Zircon analysis	2702	18
Kabete et al 2012b	RTC	Sediment	JK-02			Zircon analysis	2702	46
Kabete et al 2012b	RTC	Sediment	JK-02			Zircon analysis	2702	14
Kabete et al 2012b	RTC	Sediment	JK-02			Zircon analysis	2702	14
Kabete et al 2012b	RTC	Sediment	JK-02			Zircon analysis	2702	14
Kabete et al 2012b	RTC	Sediment	JK-02			Zircon analysis	2702	22
Kabete et al 2012b	RTC	Sediment	JK-02	Inherited		Zircon analysis	2743	14
Kabete et al 2012b	RTC	Sediment	JK-02	Inherited		Zircon analysis	2738	18
Kabete et al 2012b	RTC	Sediment	JK-02			Zircon analysis	2702	14
Kabete et al 2012b	RTC	Sediment	JK-02			Zircon analysis	2702	22
Kabete et al 2012b	RTC	Granitoid	JK-01	Inherited		Zircon analysis	2718	32
Kabete et al 2012b	RTC	Granitoid	JK-01	Inherited		Zircon analysis	2892	20
Kabete et al 2012b	RTC	Granitoid	JK-01			Zircon analysis	2691	26
Kabete et al 2012b	RTC	Granitoid	JK-01			Zircon analysis	2691	20
Kabete et al 2012b	RTC	Granitoid	JK-01			Zircon analysis	2691	20
Kabete et al 2012b	RTC	Granitoid	JK-01			Zircon analysis	2691	14
Kabete et al 2012b	RTC	Granitoid	JK-01			Zircon analysis	2691	16
Kabete et al 2012b	RTC	Granitoid	JK-01			Zircon analysis	2691	14
Kabete et al 2012b	RTC	Granitoid	JK-01			Zircon analysis	2691	16
Kabete et al 2012b	RTC	Granitoid	JK-01			Zircon analysis	2691	26
Kabete et al 2012b	RTC	Granitoid	JK-01			Zircon analysis	2691	32
Kabete et al 2012b	RTC	Granitoid	JK-01			Zircon analysis	2691	24
Kabete et al 2012b	RTC	Granitoid	JK-01			Zircon analysis	2691	18
Kabete et al 2012b	RTC	Granitoid	JK-01			Zircon analysis	2691	24
Kabete et al 2012b	RTC	Granitoid	JK-01			Zircon analysis	2691	28

Reference	Location	Harmonized classification	Sample	inheritance	Name	Comments	$^{207}Pb/^{206}Pb$ Age (Ma)	2SE
Kabete et al 2012b	RTC	Sediment	JK-05			Zircon analysis	3611	14
Kabete et al 2012b	RTC	Sediment	JK-05			Zircon analysis	3828	8
Kabete et al 2012b	RTC	Sediment	JK-05			Zircon analysis	3641	18
Kabete et al 2012b	RTC	Sediment	JK-05			Zircon analysis	3657	16
Kabete et al 2012b	RTC	Sediment	JK-05			Zircon analysis	3698	14
Kabete et al 2012b	RTC	Sediment	JK-05			Zircon analysis	3699	10
Kabete et al 2012b	RTC	Sediment	JK-05			Zircon analysis	3603	14
Kabete et al 2012b	RTC	Sediment	JK-05			Zircon analysis	3735	14
Kabete et al 2012b	RTC	Sediment	JK-05			Zircon analysis	3720	10
Kabete et al 2012b	RTC	Sediment	JK-05			Zircon analysis	3611	10
Kabete et al 2012b	RTC	Sediment	JK-05			Zircon analysis	4013	8
Kabete et al 2012b	RTC	Sediment	JK-05			Zircon analysis	3612	16
Kabete et al 2012b	RTC	Sediment	JK-05			Zircon analysis	3797	18
Kabete et al 2012b	RTC	Sediment	JK-05			Zircon analysis	3631	14
Kabete et al 2012b	RTC	Sediment	JK-05			Zircon analysis	3860	8
Kabete et al 2012b	RTC	Sediment	JK-05			Zircon analysis	3820	2
Kabete et al 2012b	RTC	Sediment	JK-05			Zircon analysis	3656	10
Kabete et al 2012b	RTC	Sediment	JK-05			Zircon analysis	3652	10
Kabete et al 2012b	RTC	Sediment	JK-05			Zircon analysis	3622	10
Kabete et al 2012b	RTC	Sediment	JK-05			Zircon analysis	3735	8
Kabete et al 2012b	RTC	Sediment	JK-05			Zircon analysis	3762	8
Kabete et al 2012b	RTC	Sediment	JK-05			Zircon analysis	3719	16
Kabete et al 2012b	RTC	Sediment	JK-05			Zircon analysis	4007	12
Kabete et al 2012b	RTC	Sediment	JK-05			Zircon analysis	3622	18
Kabete et al 2012b	RTC	Sediment	JK-05			Zircon analysis	3708	10
Kabete et al 2012b	RTC	Sediment	JK-05			Zircon analysis	3668	20
Kabete et al 2012b	RTC	Sediment	JK-05			Zircon analysis	3633	12
Kabete et al 2012b	RTC	Sediment	JK-05			Zircon analysis	3635	10
Kabete et al 2012b	RTC	Sediment	JK-05			Zircon analysis	3688	16
Kabete et al 2012b	RTC	Sediment	JK-05			Zircon analysis	3870	18
Kabete et al 2012b	RTC	Sediment	JK-05			Zircon analysis	3638	12
Kabete et al 2012b	RTC	Sediment	JK-05			Zircon analysis	3650	12
Kabete et al 2012b	RTC	Sediment	JK-05			Zircon analysis	3658	10
Kabete et al 2012b	RTC	Sediment	JK-05			Zircon analysis	3654	16
Kabete et al 2012b	RTC	Sediment	JK-05			Zircon analysis	3733	10
Kabete et al 2012b	RTC	Sediment	JK-05			Zircon analysis	3645	18
Kabete et al 2012b	RTC	Sediment	JK-05			Zircon analysis	3727	14
Kabete et al 2012b	RTC	Sediment	JK-05			Zircon analysis	3649	18
Kabete et al 2012b	RTC	Sediment	JK-05			Zircon analysis	3598	10
Kabete et al 2012b	RTC	Sediment	JK-05			Zircon analysis	3675	8
Kabete et al 2012b	RTC	Sediment	JK-05			Zircon analysis	3706	10
Kabete et al 2012b	RTC	Sediment	JK-05			Zircon analysis	3671	30
Kabete et al 2012b	RTC	Sediment	JK-05			Zircon analysis	3640	16
Kabete et al 2012b	RTC	Sediment	JK-05			Zircon analysis	3744	10
Kabete et al 2012b	RTC	Sediment	JK-05			Zircon analysis	3692	22
Kabete et al 2012b	RTC	Sediment	JK-05			Zircon analysis	3711	12
Kabete et al 2012b	RTC	Sediment	JK-05			Zircon analysis	3708	8
Kabete et al 2012b	RTC	Sediment	JK-05			Zircon analysis	3663	10

Reference	Location	Harmonized classification	Sample	inheritance	Name	Comments	$^{207}Pb/^{206}Pb$ Age (Ma)	2SE
Kabete et al 2012b	RTC	Sediment	JK-05			Zircon analysis	4020	14
Kabete et al 2012b	RTC	Sediment	JK-05			Zircon analysis	3667	10
Kabete et al 2012b	RTC	Sediment	JK-05			Zircon analysis	3812	10
Kabete et al 2012b	RTC	Sediment	JK-05			Zircon analysis	3648	10
Kabete et al 2012b	RTC	Sediment	JK-05			Zircon analysis	3609	10
Kabete et al 2012b	RTC	Sediment	JK-05			Zircon analysis	3833	48
Kabete et al 2012b	RTC	Sediment	JK-05			Zircon analysis	3662	10
Kabete et al 2012b	RTC	Sediment	JK-05			Zircon analysis	3836	10
Kabete et al 2012b	RTC	Sediment	JK-05			Zircon analysis	3755	16
Kabete et al 2012b	RTC	Sediment	JK-05			Zircon analysis	3739	10
Kabete et al 2012b	RTC	Sediment	JK-05			Zircon analysis	3667	12
Kabete et al 2012b	RTC	Sediment	JK-05			Zircon analysis	3655	10
Kabete et al 2012b	RTC	Sediment	JK-05			Zircon analysis	3638	10
Kabete et al 2012b	RTC	Sediment	JK-05			Zircon analysis	3638	8
Kabete et al 2012b	RTC	Sediment	JK-05			Zircon analysis	3545	8
Kabete et al 2012b	RTC	Sediment	JK-05			Zircon analysis	3830	16
Kabete et al 2012b	RTC	Sediment	JK-05			Zircon analysis	3716	10
Kabete et al 2012b	RTC	Sediment	JK-05			Zircon analysis	3766	16
Kabete et al 2012b	RTC	Sediment	JK-05			Zircon analysis	3870	12
Kabete et al 2012b	RTC	Sediment	JK-05			Zircon analysis	3730	36
Kabete et al 2012b	RTC	Sediment	JK-05			Zircon analysis	3634	10
Kabete et al 2012b	RTC	Sediment	JK-05			Zircon analysis	3803	12
Kabete et al 2012b	RTC	Sediment	JK-05			Zircon analysis	3449	16
Kabete et al 2012b	RTC	Sediment	JK-05			Zircon analysis	3574	8
Manya 2016a	NGB	TTG	BZ-19		1	Zircon analysis	2713	8
Manya 2016a	NGB	TTG	BZ-19		3	Zircon analysis	2713	8
Manya 2016a	NGB	TTG	BZ-19		7	Zircon analysis	2713	8
Manya 2016a	NGB	TTG	BZ-19		12	Zircon analysis	2713	8
Manya 2016a	NGB	TTG	BZ-19		15	Zircon analysis	2713	8
Manya 2016a	NGB	Granite-Monzonite	BZ-11		1.00	Zircon analysis	2674	18
Manya 2016a	NGB	Granite-Monzonite	BZ-11		3.00	Zircon analysis	2674	18
Manya 2016a	NGB	Granite-Monzonite	BZ-11		4.00	Zircon analysis	2674	18
Thomas et al 2016	RTC	Granite-Monzonite	102_005	Inherited	102 051_029.1	Zircon analysis	2841	57
Thomas et al 2016	RTC	Granite-Monzonite	102_005	Inherited	102 051_019.2	Zircon analysis	2910	63
Thomas et al 2016	RTC	Granite-Monzonite	SK106	Inherited	SK106_17	Zircon analysis	2989	13
Thomas et al 2016	RTC	Sediment	FMP85AW		FMP85AW_32	Zircon analysis	2820	9
Thomas et al 2016	RTC	Sediment	FMP85AW		FMP85AW_18	Zircon analysis	2837	13
Thomas et al 2016	RTC	Sediment	FMP85AW		FMP85AW_49	Zircon analysis	2842	9
Thomas et al 2016	RTC	Sediment	FMP85AW		FMP85AW_51	Zircon analysis	2846	9
Thomas et al 2016	RTC	Sediment	FMP85AW		FMP85AW_13	Zircon analysis	2851	13
Thomas et al 2016	RTC	Sediment	FMP85AW		FMP85AW_42	Zircon analysis	2862	9
Thomas et al 2016	RTC	Sediment	FMP85AW		FMP85AW_46	Zircon analysis	2870	9
Thomas et al 2016	RTC	Sediment	FMP85AW		FMP85AW_53	Zircon analysis	2871	9
Thomas et al 2016	RTC	Sediment	FMP85AW		FMP85AW_40	Zircon analysis	2883	9
Thomas et al 2016	RTC	Sediment	FMP85AW		FMP85AW_48	Zircon analysis	2900	9
Thomas et al 2016	RTC	Sediment	FMP85AW		FMP85AW_28	Zircon analysis	2904	9
Thomas et al 2016	RTC	Sediment	FMP85AW		FMP85AW_43	Zircon analysis	2930	9

Table SM2-6.2. Lu-Hf isotope composition of magmatic and detrital zircon from the Tanzania Craton and its surrounding mobile belts

Reference	Location	Sample	Harmonized classification	Name	$^{207}Pb/^{206}Pb$ Age (Ma)	2SE	$^{176}Hf/^{177}Hf_{(i)}$	$^{176}Hf/^{177}Hf_{(t)}$	2SE	$^{176}Hf/^{177}Hf_{(i)}$	2SE	$^{176}Lu/^{177}Hf$	1SE	Ehfpd	$eHf_{(t)}$	2SE	T_{DM2}
Kwelwa et al 2018	SGB	KK01	TTG	KK01-06	2661		0.28107	0.28099	0.00002	0.28096	0.00002	0.00063	0.00003	-59.9	0.00	0.20	3109
Kwelwa et al 2018	SGB	KK01	TTG	KK01-07	2661		0.28103	0.28108	0.00001	0.28104	0.00001	0.00085	0.00004	-60.8	-1.50	0.40	3006
Kwelwa et al 2018	SGB	KK01	TTG	KK01-08	2661		0.28101	0.28108	0.00002	0.28102	0.00002	0.00128	0.00002	-59.4	-2.20	0.40	3043
Kwelwa et al 2018	SGB	KK03	TTG	KK03-1	2667		0.28106	0.28110	0.00001	0.28105	0.00001	0.00093	0.00001	-59.9	-0.20	0.30	2994
Kwelwa et al 2018	SGB	KK03	TTG	KK03-2	2667		0.28106	0.28108	0.00001	0.28107	0.00001	0.00029	0.00000	-60.2	-0.20	0.30	2966
Kwelwa et al 2018	SGB	KK01	TTG	KK01-01	2661		0.28096	0.28109	0.00001	0.28107	0.00001	0.00036	0.00000	-63.4	-4.00	0.80	2957
Kwelwa et al 2018	SGB	KK01	TTG	KK01-02	2661		0.28104	0.28107	0.00001	0.28103	0.00001	0.00069	0.00001	-60.2	-1.20	0.30	3015
Kwelwa et al 2018	SGB	KK01	TTG	KK01-03	2661		0.28102	0.28111	0.00001	0.28101	0.00001	0.00186	0.00008	-60.3	-2.10	0.60	3055
Kwelwa et al 2018	SGB	KK01	TTG	KK01-04	2661		0.28105	0.28109	0.00001	0.28106	0.00001	0.00053	0.00000	-59.7	-0.90	0.30	2970
Kwelwa et al 2018	SGB	KK01	TTG	KK01-05	2661		0.28107	0.28108	0.00001	0.28106	0.00001	0.00037	0.00000	-60.3	-0.30	0.20	2968
Kwelwa et al 2018	SGB	KK03	TTG	KK03-3	2667		0.28104	0.28106	0.00001	0.28104	0.00001	0.00047	0.00001	-60.9	-1.10	0.30	3001
Kwelwa et al 2018	SGB	KK03	TTG	KK03-4	2667		0.28103	0.28109	0.00002	0.28103	0.00002	0.00117	0.00003	-60.1	-1.60	0.60	3028
Kwelwa et al 2018	SGB	KK03	TTG	KK03-5	2667		0.28100	0.28107	0.00004	0.28100	0.00004	0.00125	0.00003	-60.7	-2.40	1.50	3058
Kwelwa et al 2018	SGB	KK04	TTG	KK04-1	2663		0.28104	0.28106	0.00001	0.28104	0.00001	0.00040	0.00001	-60.9	-1.10	0.30	2998
Kwelwa et al 2018	SGB	KK04	TTG	KK04-2	2663		0.28105	0.28113	0.00001	0.28105	0.00001	0.00146	0.00003	-58.7	-0.80	0.40	2996
Kwelwa et al 2018	SGB	KK04	TTG	KK04-3	2663		0.28105	0.28112	0.00001	0.28105	0.00001	0.00147	0.00004	-58.7	-0.80	0.40	2998
Kwelwa et al 2018	SGB	KK04	TTG	KK04-4	2663		0.28107	0.28111	0.00001	0.28107	0.00001	0.00082	0.00002	-59.3	-0.30	0.40	2971
Kwelwa et al 2018	SGB	KK04	TTG	KK04-5	2663		0.28105	0.28108	0.00001	0.28105	0.00001	0.00058	0.00002	-60.3	-0.80	0.30	2990
Kwelwa et al 2018	SGB	KK04	TTG	KK04-6	2663		0.28104	0.28107	0.00001	0.28104	0.00001	0.00054	0.00000	-60.6	-1.00	0.30	2999
Kwelwa et al 2018	SGB	KK04	TTG	KK04-7	2663		0.28108	0.28113	0.00001	0.28108	0.00001	0.00087	0.00001	-58.7	0.30	0.30	2949
Kwelwa et al 2018	SGB	KK04	TTG	KK04-8	2663		0.28107	0.28111	0.00001	0.28107	0.00001	0.00085	0.00001	-59.1	-0.10	0.30	2965
Kwelwa et al 2018	SGB	KK04	TTG	KK04-9	2663		0.28107	0.28111	0.00001	0.28107	0.00001	0.00085	0.00001	-59.1	-0.10	0.30	2965
Kwelwa et al 2018	SGB	MT20	TTG	MT20-1	2651		0.28107	0.28109	0.00001	0.28107	0.00001	0.00047	0.00002	-59.8	-0.40	0.30	2962
Kwelwa et al 2018	SGB	MT20	TTG	MT20-2	2651		0.28108	0.28120	0.00002	0.28108	0.00002	0.00233	0.00006	-56.2	0.00	0.60	2965
Kwelwa et al 2018	SGB	MT20	TTG	MT20-3	2651		0.28110	0.28115	0.00001	0.28110	0.00001	0.00105	0.00002	-57.9	0.50	0.40	2932
Kwelwa et al 2018	SGB	MT20	TTG	MT20-4	2651		0.28107	0.28113	0.00001	0.28107	0.00001	0.00118	0.00002	-58.5	-0.30	0.50	2965
Kwelwa et al 2018	SGB	MT20	TTG	MT20-5	2651		0.28107	0.28110	0.00001	0.28107	0.00001	0.00045	0.00000	-59.8	-0.30	0.20	2958
Kwelwa et al 2018	SGB	MT20	TTG	MT20-6	2651		0.28106	0.28110	0.00001	0.28106	0.00001	0.00086	0.00001	-59.7	-0.90	0.30	2985
Kwelwa et al 2018	SGB	MT20	TTG	MT20-7	2651		0.28107	0.28110	0.00001	0.28107	0.00001	0.00064	0.00001	-59.5	-0.40	0.30	2965
Kwelwa et al 2018	SGB	KK51	Felsic volcanic	KK51-1	2717		0.28108	0.28113	0.00001	0.28108	0.00001	0.00091	0.00001	-58.5	1.60	0.30	2947
Kwelwa et al 2018	SGB	KK51	Felsic volcanic	KK51-2	2717		0.28111	0.28116	0.00001	0.28111	0.00001	0.00097	0.00001	-57.4	2.60	0.30	2909
Kwelwa et al 2018	SGB	KK51	Felsic volcanic	KK51-3	2717		0.28110	0.28115	0.00001	0.28110	0.00001	0.00112	0.00001	-57.7	2.10	0.30	2931
Kwelwa et al 2018	SGB	KK51	Felsic volcanic	KK51-4	2717		0.28109	0.28115	0.00001	0.28109	0.00001	0.00108	0.00001	-57.9	1.90	0.40	2936
Kwelwa et al 2018	SGB	KK51	Felsic volcanic	KK51-5	2717		0.28110	0.28113	0.00001	0.28110	0.00001	0.00045	0.00001	-58.7	2.40	0.30	2917
Kwelwa et al 2018	SGB	KK51	Felsic volcanic	KK51-6	2717		0.28109	0.28114	0.00001	0.28109	0.00001	0.00081	0.00001	-58.3	2.00	0.40	2930
Kwelwa et al 2018	SGB	KK51	Felsic volcanic	KK51-7	2717		0.28110	0.28114	0.00001	0.28110	0.00001	0.00084	0.00001	-58.2	2.10	0.20	2927
Sanislav et al 2014	SGB	XU01	Granite-Monzonite	XU01-3	2617		0.28112	0.28113	0.00001	0.28109		0.00084	0.00002	−56.95	1.13	0.21	2941
Sanislav et al 2014	SGB	XU01	Granite-Monzonite	XU01-4	2617		0.28109	0.28111	0.00001	0.28109		0.00042	0.00000	−59.11	0.01	0.28	2937
Sanislav et al 2014	SGB	XU01	Granite-Monzonite	XU01-5	2617		0.28109	0.28117	0.00001	0.28112		0.00101	0.00000	−59.36	−0.03	0.25	2894
Sanislav et al 2014	SGB	XU01	Granite-Monzonite	XU01-6	2617		0.28110	0.28111	0.00001	0.28109		0.00042	0.00000	−58.58	0.20	0.25	2932
Sanislav et al 2014	SGB	XU01	Granite-Monzonite	XU01-7	2617		0.28110	0.28111	0.00001	0.28109		0.00030	0.00000	−58.72	0.36	0.25	2932
Sanislav et al 2014	SGB	XU01	Granite-Monzonite	XU01-8	2617		0.28110	0.28113	0.00001	0.28110		0.00061	0.00001	−58.37	0.30	0.32	2926
Sanislav et al 2014	SGB	XU01	Granite-Monzonite	XU01-9	2617		0.28109	0.28112	0.00001	0.28110		0.00045	0.00000	−58.97	0.05	0.25	2919
Sanislav et al 2014	SGB	XU01	Granite-Monzonite	XU01-1	2617		0.28109	0.28113	0.00001	0.28110		0.00068	0.00002	−58.51	−0.14	0.32	2923
Sanislav et al 2014	SGB	XU01	Granite-Monzonite	XU01-2	2617		0.28109	0.28112	0.00001	0.28109		0.00048	0.00000	−59.25	−0.14	0.28	2931

Reference	Location	Sample	Harmonized classification	Name	$^{207}Pb/^{206}Pb$ Age (Ma)	2SE	$^{176}Hf/^{177}Hf_{(i)}$	$^{176}Hf/^{177}Hf_{(t)}$	2SE	$^{176}Hf/^{177}Hf_{(i)}$	2SE	$^{176}Lu/^{177}Hf$	1SE	Ehfpd	$eHf_{(t)}$	2SE	T_{DM2}
Sanislav et al 2014	SGB	XU01	Granite-Monzonite	XU01A-1	2628		0.28109	0.28112	0.00001	0.28109		0.00063	0.00001	−58.86	−0.19	0.25	2938
Sanislav et al 2014	SGB	XU01A	Granite-Monzonite	XU01A-2	2628		0.28109	0.28111	0.00001	0.28109		0.00037	0.00000	−59.22	−0.08	0.25	2932
Sanislav et al 2014	SGB	XU01A	Granite-Monzonite	XU01A-3	2628		0.28112	0.28120	0.00001	0.28112		0.00143	0.00004	−56.21	1.05	0.32	2898
Sanislav et al 2014	SGB	XU01A	Granite-Monzonite	XU01A-4	2628		0.28109	0.28112	0.00001	0.28109		0.00064	0.00000	−58.72	−0.06	0.36	2934
Sanislav et al 2014	SGB	XU01A	Granite-Monzonite	XU01A-5	2628		0.28109	0.28112	0.00001	0.28109		0.00072	0.00002	−58.72	−0.20	0.32	2940
Sanislav et al 2014	SGB	XU01A	Granite-Monzonite	XU01A-6	2628		0.28109	0.28112	0.00001	0.28109		0.00056	0.00002	−58.90	−0.10	0.25	2935
Sanislav et al 2014	SGB	XU01A	Granite-Monzonite	XU01A-7	2628		0.28110	0.28112	0.00001	0.28110		0.00051	0.00000	−58.86	0.02	0.25	2930
Sanislav et al 2014	SGB	XU02	Granite-Monzonite	XU02-1	2623		0.28109	0.28112	0.00001	0.28109		0.00060	0.00000	−58.90	−0.46	0.50	2937
Sanislav et al 2014	SGB	XU02	Granite-Monzonite	XU02-2	2623		0.28111	0.28117	0.00001	0.28111		0.00126	0.00002	−57.13	0.13	0.32	2920
Sanislav et al 2014	SGB	XU02	Granite-Monzonite	XU02-3	2623		0.28117	0.28127	0.00001	0.28117		0.00211	0.00004	−53.45	2.32	0.39	2840
Sanislav et al 2014	SGB	XU02	Granite-Monzonite	XU02-4	2623		0.28110	0.28113	0.00001	0.28110		0.00058	0.00001	−58.44	0.04	0.28	2918
Sanislav et al 2014	SGB	GP02	Granite-Monzonite	GP02-1	2634		0.28110	0.28119	0.00001	0.28112		0.00142	0.00002	−57.87	0.46	0.32	2908
Sanislav et al 2014	SGB	GP02	Granite-Monzonite	GP02-2	2634		0.28109	0.28114	0.00001	0.28109		0.00091	0.00001	−58.97	−0.08	0.32	2940
Sanislav et al 2014	SGB	GP02	Granite-Monzonite	GP02-3	2634		0.28110	0.28115	0.00001	0.28109		0.00115	0.00001	−58.37	0.16	0.32	2937
Sanislav et al 2014	SGB	GP02	Granite-Monzonite	GP02-4	2634		0.28109	0.28114	0.00001	0.28108		0.00114	0.00000	−58.51	0.11	0.32	2948
Sanislav et al 2014	SGB	GP02	Granite-Monzonite	GP02-5	2634		0.28109	0.28113	0.00001	0.28108		0.00096	0.00002	−58.65	0.09	0.25	2954
Sanislav et al 2014	SGB	GP02	Granite-Monzonite	GP02-6	2634		0.28112	0.28112	0.00001	0.28109		0.00058	0.00001	−57.62	0.88	0.28	2940
Sanislav et al 2014	SGB	GP02	Granite-Monzonite	GP02-7	2634		0.28108	0.28113	0.00001	0.28110		0.00078	0.00001	−58.61	−0.31	0.32	2931
Sanislav et al 2014	SGB	GP02	Granite-Monzonite	GP02-8	2634		0.28108	0.28109	0.00001	0.28108		0.00019	0.00000	−59.60	−0.41	0.25	2945
Sanislav et al 2014	SGB	GP03	Granite-Monzonite	GP03-1	2661		0.28109	0.28115	0.00001	0.28110		0.00088	0.00004	−58.05	0.09	0.36	2919
Sanislav et al 2014	SGB	GP03	Granite-Monzonite	GP03-2	2661		0.28109	0.28112	0.00001	0.28109		0.00057	0.00001	−58.61	0.36	0.32	2938
Sanislav et al 2014	SGB	GP03	Granite-Monzonite	GP03-3	2661		0.28107	0.28113	0.00001	0.28110		0.00077	0.00003	−59.25	−0.47	0.32	2930
Sanislav et al 2014	SGB	GP03	Granite-Monzonite	GP03-4	2661		0.28106	0.28113	0.00001	0.28109		0.00072	0.00001	−58.76	−0.92	0.43	2932
Sanislav et al 2014	SGB	GP03	Granite-Monzonite	GP03-5	2661		0.28106	0.28113	0.00001	0.28109		0.00065	0.00001	−60.10	−0.68	0.28	2932
Sanislav et al 2014	SGB	GP03	Granite-Monzonite	GP03-6	2661		0.28107	0.28116	0.00001	0.28112		0.00078	0.00001	−59.04	−0.51	0.25	2903
Sanislav et al 2014	SGB	GP03	Granite-Monzonite	GP03-7	2661		0.28109	0.28113	0.00001	0.28108		0.00089	0.00002	−58.86	0.24	0.36	2949
Sanislav et al 2014	SGB	GP03	Granite-Monzonite	GP03-8	2661		0.28107	0.28110	0.00001	0.28108		0.00039	0.00000	−58.86	−0.38	0.36	2948
Sanislav et al 2014	SGB	GP01	TTG	GP01-1	2652		0.28112	0.28114	0.00001	0.28109		0.00116	0.00001	−56.49	1.41	0.46	2948
Sanislav et al 2014	SGB	GP01	TTG	GP01-2	2652		0.28109	0.28113	0.00001	0.28109		0.00069	0.00004	−58.33	0.48	0.36	2934
Sanislav et al 2014	SGB	GP01	TTG	GP01-3	2652		0.28109	0.28111	0.00001	0.28107		0.00080	0.00002	−57.80	0.59	0.36	2966
Sanislav et al 2014	SGB	GP01	TTG	GP01-4	2652		0.28108	0.28112	0.00001	0.28106		0.00133	0.00003	−58.08	0.32	0.43	2988
Sanislav et al 2014	SGB	GP01	TTG	GP01-5	2652		0.28108	0.28109	0.00001	0.28106		0.00044	0.00001	−58.61	0.12	0.32	2971
Sanislav et al 2014	SGB	GP01	TTG	GP01-6	2652		0.28109	0.28112	0.00001	0.28107		0.00094	0.00006	−59.00	0.40	0.32	2969
Sanislav et al 2014	SGB	GP01	TTG	GP01-7	2652		0.28110	0.28112	0.00001	0.28109		0.00062	0.00001	−58.37	0.68	0.32	2938
Sanislav et al 2014	SGB	GP01	TTG	GP01-8	2652		0.28108	0.28112	0.00001	0.28107		0.00097	0.00002	−59.92	0.19	0.28	2964
Sanislav et al 2014	SGB	GX01	TTG	GX01-1	2642		0.28109	0.28113	0.00001	0.28109		0.00096	0.00004	−58.37	−0.01	0.32	2945
Sanislav et al 2014	SGB	GX01	TTG	GX01-2	2642		0.28111	0.28115	0.00001	0.28111		0.00088	0.00001	−57.69	0.82	0.28	2913
Sanislav et al 2014	SGB	GX01	TTG	GX01-3	2642		0.28109	0.28114	0.00001	0.28109		0.00091	0.00001	−58.33	0.12	0.36	2940
Sanislav et al 2014	SGB	GX01	TTG	GX01-4	2642		0.28109	0.28115	0.00001	0.28109		0.00113	0.00001	−57.77	0.29	0.36	2935
Sanislav et al 2014	SGB	GX01	TTG	GX01-5	2642		0.28112	0.28128	0.00002	0.28112		0.00306	0.00003	−53.38	1.23	0.53	2911
Sanislav et al 2014	SGB	GX01	TTG	GX01-6	2642		0.28110	0.28113	0.00001	0.28110		0.00056	0.00001	−58.51	0.57	0.28	2920
Sanislav et al 2014	SGB	GX01	TTG	GX01-7	2642		0.28117	0.28124	0.00001	0.28117		0.00143	0.00004	−54.65	2.88	0.36	2837
Sanislav et al 2014	SGB	GX01	TTG	GX01-8	2642		0.28114	0.28121	0.00001	0.28114		0.00139	0.00003	−55.78	1.82	0.39	2878
Sanislav et al 2018b	SGB	PD01	Sediment	PD01-01	2702			0.28111	0.00001	0.28107	0.00001	0.00067	0.00001		0.97	0.2500	2956
Sanislav et al 2018b	SGB	PD01	Sediment	PD01-02	2646			0.28106	0.00001	0.28105	0.00001	0.00038	0.00002		-1.39	0.2400	2994
Sanislav et al 2018b	SGB	PD01	Sediment	PD01-03	2692			0.28107	0.00001	0.28103	0.00001	0.00069	0.00001		-0.69	0.2300	3011
Sanislav et al 2018b	SGB	PD01	Sediment	PD01-04	2668			0.28109	0.00001	0.28105	0.00002	0.00071	0.00002		-0.69	0.3700	2990

Reference	Location	Sample	Harmonized classification	Name	$^{207}Pb/^{206}Pb$ Age (Ma)	2SE	$^{176}Hf/^{177}Hf_{(i)}$	$^{176}Hf/^{177}Hf_{(t)}$	2SE	$^{176}Hf/^{177}Hf_{(i)}$	2SE	$^{176}Lu/^{177}Hf$	1SE	Ehfpd	$eHf_{(t)}$	2SE	T_{DM2}
Sanislav et al 2018b	SGB	PD01	Sediment	PD01-05	2696			0.28108	0.00001	0.28104	0.00002	0.00088	0.00001		-0.51	0.2800	3010
Sanislav et al 2018b	SGB	PD01	Sediment	PD01-06	2658			0.28110	0.00001	0.28106	0.00002	0.00091	0.00003		-0.70	0.2700	2984
Sanislav et al 2018b	SGB	PD01	Sediment	PD01-07	2681			0.28110	0.00001	0.28105	0.00002	0.00107	0.00001		-0.42	0.3600	2995
Sanislav et al 2018b	SGB	PD01	Sediment	PD01-08	2751			0.28108	0.00001	0.28105	0.00002	0.00058	0.00002		1.16	0.3100	2992
Sanislav et al 2018b	SGB	PD01	Sediment	PD01-09	2722			0.28109	0.00001	0.28104	0.00002	0.00094	0.00003		0.38	0.3400	2999
Sanislav et al 2018b	SGB	PD01	Sediment	PD01-10	2702			0.28114	0.00001	0.28107	0.00001	0.00124	0.00003		0.90	0.2500	2963
Sanislav et al 2018b	SGB	PD01	Sediment	PD01-11	2687			0.28107	0.00001	0.28102	0.00002	0.00090	0.00001		-1.26	0.3100	3030
Sanislav et al 2018b	SGB	PD01	Sediment	PD01-12	2684			0.28115	0.00001	0.28110	0.00002	0.00088	0.00001		1.59	0.3000	2920
Sanislav et al 2018b	SGB	PD01	Sediment	PD01-13	2685			0.28113	0.00001	0.28109	0.00001	0.00080	0.00001		0.97	0.2500	2943
Sanislav et al 2018b	SGB	PD01	Sediment	PD01-14	2718			0.28112	0.00001	0.28107	0.00002	0.00100	0.00001		1.02	0.3000	2971
Sanislav et al 2018b	SGB	PD01	Sediment	PD01-15	2672			0.28112	0.00001	0.28108	0.00002	0.00075	0.00002		0.52	0.3000	2948
Sanislav et al 2018b	SGB	PD01	Sediment	PD01-16	2695			0.28108	0.00002	0.28102	0.00003	0.00110	0.00002		-1.19	0.5800	3036
Sanislav et al 2018b	SGB	PD01	Sediment	PD01-17	2702			0.28110	0.00001	0.28106	0.00002	0.00093	0.00001		0.31	0.3400	2984
Sanislav et al 2018b	SGB	PD01	Sediment	PD01-18	2708			0.28112	0.00001	0.28107	0.00002	0.00107	0.00001		0.90	0.2800	2967
Sanislav et al 2018b	SGB	PD01	Sediment	PD01-19	2689			0.28110	0.00001	0.28105	0.00002	0.00095	0.00001		-0.12	0.3200	2988
Sanislav et al 2018b	SGB	PD01	Sediment	PD01-20	2721			0.28109	0.00001	0.28106	0.00002	0.00063	0.00000		0.75	0.2700	2981
Sanislav et al 2018b	SGB	PD01	Sediment	PD01-21	2734			0.28107	0.00001	0.28104	0.00002	0.00058	0.00001		0.52	0.3800	3000
Sanislav et al 2018b	SGB	PD01	Sediment	PD01-22	2731			0.28107	0.00001	0.28104	0.00002	0.00060	0.00001		0.26	0.2700	3009
Sanislav et al 2018b	SGB	PD01	Sediment	PD01-23	2674			0.28110	0.00001	0.28106	0.00001	0.00068	0.00000		-0.13	0.2500	2974
Sanislav et al 2018b	SGB	PD01	Sediment	PD01-24	2696			0.28112	0.00001	0.28108	0.00001	0.00080	0.00001		1.12	0.2400	2946
Sanislav et al 2018b	SGB	PD01	Sediment	PD01-25	2748			0.28110	0.00001	0.28105	0.00002	0.00099	0.00001		1.25	0.2700	2989
Sanislav et al 2018b	SGB	PD01	Sediment	PD01-26	2678			0.28111	0.00001	0.28108	0.00002	0.00071	0.00001		0.54	0.3500	2952
Sanislav et al 2018b	SGB	PD01	Sediment	PD01-27	2739			0.28108	0.00001	0.28105	0.00001	0.00055	0.00001		0.90	0.2500	2991
Sanislav et al 2018b	SGB	PD01	Sediment	PD01-28	2725			0.28107	0.00001	0.28105	0.00002	0.00056	0.00001		0.48	0.2600	2995
Sanislav et al 2018b	SGB	PD01	Sediment	PD01-29	2751			0.28112	0.00001	0.28108	0.00002	0.00073	0.00002		2.25	0.2900	2952
Sanislav et al 2018b	SGB	PD01	Sediment	PD01-30	2725			0.28108	0.00001	0.28106	0.00001	0.00045	0.00001		0.84	0.2600	2980
Sanislav et al 2018b	SGB	PD01	Sediment	PD01-31	2701			0.28113	0.00001	0.28108	0.00002	0.00088	0.00001		1.26	0.3000	2946
Sanislav et al 2018b	SGB	PD01	Sediment	PD01-32	2714			0.28111	0.00001	0.28108	0.00001	0.00059	0.00000		1.30	0.2200	2955
Sanislav et al 2018b	SGB	PD01	Sediment	PD01-33	2704			0.28114	0.00001	0.28110	0.00002	0.00079	0.00001		2.07	0.2800	2918
Sanislav et al 2018b	SGB	PD01	Sediment	PD01-34	273			0.28109	0.00001	0.28105	0.00001	0.00076	0.00001		0.79	0.2500	2986
Sanislav et al 2018b	SGB	PD01	Sediment	PD01-35	2719			0.28112	0.00001	0.28108	0.00001	0.00076	0.00001		1.49	0.2300	2952
Sanislav et al 2018b	SGB	PD01	Sediment	PD01-36	2768			0.28110	0.00001	0.28106	0.00002	0.00071	0.00001		2.01	0.2700	2975
Sanislav et al 2018b	SGB	PD01	Sediment	PD01-37	2744			0.28112	0.00001	0.28107	0.00002	0.00101	0.00001		1.68	0.2600	2969
Sanislav et al 2018b	SGB	PD01	Sediment	PD01-38	2714			0.28114	0.00001	0.28110	0.00001	0.00076	0.00000		2.02	0.2200	2928
Sanislav et al 2018b	SGB	PD01	Sediment	PD01-39	2759			0.28110	0.00001	0.28104	0.00002	0.00117	0.00004		1.06	0.3000	3006
Sanislav et al 2018b	SGB	PD01	Sediment	PD01-40	2715			0.28112	0.00001	0.28106	0.00002	0.00122	0.00004		0.74	0.2700	2980
Sanislav et al 2018b	SGB	PD01	Sediment	PD01-41	2747			0.28108	0.00001	0.28105	0.00002	0.00069	0.00002		0.99	0.2800	2996
Sanislav et al 2018b	SGB	PD01	Sediment	PD01-42	2722			0.28110	0.00001	0.28105	0.00002	0.00095	0.00002		0.54	0.3300	2993
Sanislav et al 2018b	SGB	PD01	Sediment	PD01-43	2755			0.28109	0.00001	0.28105	0.00001	0.00066	0.00002		1.38	0.2500	2987
Sanislav et al 2018b	SGB	PD01	Sediment	PD01-44	2716			0.28113	0.00001	0.28109	0.00002	0.00080	0.00002		1.90	0.2700	2935
Sanislav et al 2018b	SGB	PD01	Sediment	PD01-45	2715			0.28112	0.00001	0.28109	0.00001	0.00057	0.00002		1.90	0.2300	2933
Sanislav et al 2018b	SGB	PD01	Sediment	PD01-46	2755			0.28109	0.00001	0.28105	0.00001	0.00069	0.00003		1.39	0.2500	2988
Sanislav et al 2018b	SGB	PD01	Sediment	PD01-47	2732			0.28108	0.00001	0.28105	0.00001	0.00059	0.00001		0.74	0.2300	2992
Sanislav et al 2018b	SGB	PD01	Sediment	PD01-48	2718			0.28111	0.00001	0.28107	0.00001	0.00075	0.00003		1.32	0.2300	2958
Sanislav et al 2018b	SGB	PD01	Sediment	PD01-49	2740			0.28109	0.00001	0.28105	0.00002	0.00080	0.00001		0.85	0.2800	2996
Sanislav et al 2018b	SGB	PD01	Sediment	PD01-50	2730			0.28107	0.00001	0.28105	0.00002	0.00032	0.00000		0.94	0.2700	2980
Sanislav et al 2018b	SGB	PD01	Sediment	PD01-51	2704			0.28113	0.00001	0.28109	0.00002	0.00079	0.00002		1.63	0.2700	2934

Reference	Location	Sample	Harmonized classification	Name	$^{207}Pb/^{206}Pb$ Age (Ma)	2SE	$^{176}Hf/^{177}Hf_{(i)}$	$^{176}Hf/^{177}Hf_{(t)}$	2SE	$^{176}Hf/^{177}Hf_{(i)}$	2SE	$^{176}Lu/^{177}Hf$	1SE	Ehfpd	$eHf_{(t)}$	2SE	T_{DM2}
Sanislav et al 2018b	SGB	PD01	Sediment	PD01-52	2717			0.28112	0.00001	0.28108	0.00002	0.00078	0.00001		1.37	0.2800	2955
Sanislav et al 2018b	SGB	PD01	Sediment	PD01-53	2729			0.28111	0.00001	0.28106	0.00002	0.00083	0.00000		1.26	0.2700	2970
Sanislav et al 2018b	SGB	PD01	Sediment	PD01-54	2712			0.28111	0.00001	0.28108	0.00001	0.00063	0.00001		1.24	0.2500	2955
Sanislav et al 2018b	SGB	PD01	Sediment	PD01-55	2700			0.28112	0.00001	0.28109	0.00002	0.00066	0.00001		1.48	0.2900	2937
Sanislav et al 2018b	SGB	PD01	Sediment	PD01-56	2747			0.28107	0.00001	0.28104	0.00002	0.00063	0.00002		0.71	0.2900	3006
Sanislav et al 2018b	SGB	PD01	Sediment	PD01-57	2704			0.28113	0.00001	0.28109	0.00002	0.00087	0.00001		1.54	0.2700	2939
Sanislav et al 2018b	SGB	PD01	Sediment	PD01-58	2713			0.28111	0.00001	0.28108	0.00001	0.00058	0.00001		1.36	0.2500	2951
Sanislav et al 2018b	SGB	PD01	Sediment	PD01-59	2754			0.28108	0.00001	0.28104	0.00001	0.00078	0.00001		0.94	0.2600	3004
Sanislav et al 2018b	SGB	PD01	Sediment	PD01-60	2741			0.28108	0.00001	0.28105	0.00001	0.00054	0.00001		1.18	0.2300	2982
Sanislav et al 2018b	SGB	PD01	Sediment	PD01-61	2729			0.28110	0.00001	0.28106	0.00001	0.00085	0.00001		1.02	0.2500	2980
Sanislav et al 2018b	SGB	PD01	Sediment	PD01-62	2712			0.28113	0.00001	0.28109	0.00001	0.00065	0.00001		1.85	0.2400	2932
Sanislav et al 2018b	SGB	PD01	Sediment	PD01-63	2680			0.28113	0.00001	0.28108	0.00002	0.00097	0.00001		0.66	0.2600	2952
Sanislav et al 2018b	SGB	PD01	Sediment	PD01-64	2709			0.28110	0.00001	0.28104	0.00002	0.00116	0.00002		-0.16	0.3000	3010
Sanislav et al 2018b	SGB	PD01	Sediment	PD01-65	2718			0.28109	0.00001	0.28104	0.00001	0.00088	0.00002		0.13	0.2300	3005
Sanislav et al 2018b	SGB	PD01	Sediment	PD01-66	2701			0.28110	0.00001	0.28107	0.00002	0.00075	0.00002		0.63	0.2600	2969
Sanislav et al 2018b	SGB	PD01	Sediment	PD01-67	2702			0.28109	0.00001	0.28107	0.00002	0.00048	0.00001		0.73	0.2700	2965
Sanislav et al 2018b	SGB	PD01	Sediment	PD01-68	2714			0.28108	0.00001	0.28105	0.00001	0.00071	0.00001		0.26	0.2200	2994
Sanislav et al 2018b	SGB	PD01	Sediment	PD01-69	2736			0.28113	0.00001	0.28109	0.00001	0.00065	0.00001		2.40	0.2400	2932
Sanislav et al 2018b	SGB	PD01	Sediment	PD01-70	2731			0.28106	0.00001	0.28105	0.00001	0.00029	0.00001		0.64	0.2600	2993
Sanislav et al 2018b	SGB	PD01	Sediment	PD01-71	2714			0.28107	0.00001	0.28105	0.00001	0.00044	0.00001		0.39	0.2400	2988
Sanislav et al 2018b	SGB	PD01	Sediment	PD01-72	2728			0.28108	0.00001	0.28104	0.00002	0.00082	0.00001		0.28	0.2700	3006
Sanislav et al 2018b	SGB	PD01	Sediment	PD01-73	2747			0.28108	0.00001	0.28105	0.00002	0.00064	0.00001		1.18	0.2800	2987
Sanislav et al 2018b	SGB	PD01	Sediment	PD01-74	2752			0.28108	0.00001	0.28104	0.00002	0.00068	0.00000		0.91	0.2800	3003
Sanislav et al 2018b	SGB	PD01	Sediment	PD01-75	2735			0.28109	0.00001	0.28104	0.00002	0.00086	0.00001		0.63	0.2700	3001
Sanislav et al 2018b	SGB	PD01	Sediment	PD01-76	2712			0.28113	0.00001	0.28108	0.00002	0.00093	0.00000		1.52	0.2800	2947
Sanislav et al 2018b	SGB	PD01	Sediment	PD01-77	2753			0.28108	0.00001	0.28104	0.00002	0.00074	0.00001		0.93	0.2900	3003
Sanislav et al 2018b	SGB	PD01	Sediment	PD01-78	2716			0.28109	0.00001	0.28105	0.00002	0.00087	0.00001		0.36	0.3700	2993
Sanislav et al 2018b	SGB	PD01	Sediment	PD01-79	2687			0.28112	0.00001	0.28108	0.00002	0.00079	0.00001		0.67	0.3000	2956
Thomas et al 2016	RTC	102_005	Granite-Monzonite	6	2700	18		0.28110	0.01894			0.00080	0.00005		0.45	1.9	3449
Thomas et al 2016	RTC	102_005	Granite-Monzonite	7	2700	18		0.28106	0.01820			0.00069	0.00001		-0.74	1.8	3489
Thomas et al 2016	RTC	102_005	Granite-Monzonite	10	2700	18		0.28107	0.01831			0.00067	0.00001		-0.50	1.8	3482
Thomas et al 2016	RTC	102_005	Granite-Monzonite	21.3	2700	18		0.28110	0.01880			0.00063	0.00002		0.64	1.9	3452
Thomas et al 2016	RTC	102_005	Granite-Monzonite	27	2700	18		0.28109	0.01820			0.00088	0.00004		-0.23	1.8	3464
Thomas et al 2016	RTC	102_005	Granite-Monzonite	29.1	2700	18		0.28111	0.02023			0.00058	0.00001		1.09	2.0	3442
Thomas et al 2016	RTC	102_051	Granite-Monzonite	2	2612	14		0.28108	0.00569			0.00012	0.00001		-1.36	0.6	3433
Thomas et al 2016	RTC	102_051	Granite-Monzonite	3	2612	14		0.28112	0.00320			0.00052	0.00000		-0.61	0.3	3392
Thomas et al 2016	RTC	102_051	Granite-Monzonite	5	2612	14		0.28111	0.00462			0.00015	0.00000		-0.31	0.5	3402
Thomas et al 2016	RTC	102_051	Granite-Monzonite	8.2	2612	14		0.28109	0.00605			0.00014	0.00001		-0.75	0.6	3415
Thomas et al 2016	RTC	102_051	Granite-Monzonite	9	2612	14		0.28115	0.00640			0.00087	0.00000		-0.20	0.6	3363
Thomas et al 2016	RTC	102_051	Granite-Monzonite	16	2612	14		0.28110	0.00534			0.00012	0.00001		-0.46	0.5	3408
Thomas et al 2016	RTC	102_051	Granite-Monzonite	18	2612	14		0.28108	0.00534			0.00012	0.00000		-1.36	0.5	3433
Thomas et al 2016	RTC	102-216	Granite-Monzonite	6	2775	19		0.28110	0.01515			0.00074	0.00001		2.02	1.5	3494
Thomas et al 2016	RTC	102-216	Granite-Monzonite	12	2775	19		0.28107	0.01377			0.00047	0.00001		1.66	1.4	3518
Thomas et al 2016	RTC	102-216	Granite-Monzonite	31	2775	19		0.28107	0.01395			0.00035	0.00002		1.85	1.4	3519
Thomas et al 2016	RTC	102-216	Granite-Monzonite	33	2775	19		0.28108	0.01395			0.00025	0.00002		2.19	1.4	3515

Reference	Location	Sample	Harmonized classification	Name	$^{207}Pb/^{206}Pb$ Age (Ma)	2SE	$^{176}Hf/^{177}Hf_{(i)}$	$^{176}Hf/^{177}Hf_{(t)}$	2SE	$^{176}Hf/^{177}Hf_{(i)}$	2SE	$^{176}Lu/^{177}Hf$	1SE	Ehfpd	$eHf_{(t)}$	2SE	T_{DM2}
Thomas et al 2016	RTC	102-216	Granite-Monzonite	40	2775	19		0.28113	0.01377			0.00125	0.00003		2.18	1.4	3462
Thomas et al 2016	EAAO	AMB120	Gneiss	1.1	2693	28		0.28105	0.01894			0.00044	0.00000		-0.85	1.9	3496
Thomas et al 2016	EAAO	AMB120	Gneiss	1.2	2693	28		0.28104	0.01894			0.00057	0.00001		-1.53	1.9	3509
Thomas et al 2016	EAAO	AMB120	Gneiss	2.1	2693	28		0.28109	0.01971			0.00098	0.00003		-0.68	2.0	3464
Thomas et al 2016	EAAO	AMB120	Gneiss	3	2693	28		0.28111	0.02023			0.00058	0.00005		1.08	2.0	3435
Thomas et al 2016	EAAO	AMB120	Gneiss	5	2693	28		0.28107	0.02005			0.00046	0.00002		-0.27	2.0	3479
Thomas et al 2016	EAAO	AMB120	Gneiss	16.1	2693	28		0.28106	0.01810			0.00031	0.00001		-0.41	1.8	3491
Thomas et al 2016	EAAO	AMB120	Gneiss	17	2693	28		0.28107	0.01954			0.00038	0.00005		-0.05	2.0	3477
Thomas et al 2016	EAAO	AMB120	Gneiss	19.2	2693	28		0.28107	0.01867			0.00035	0.00002		-0.17	1.9	3482
Thomas et al 2016	EAAO	AMB14	Gneiss	1	2635	10		0.28105	0.00641			0.00036	0.00000		-2.21	0.6	3472
Thomas et al 2016	EAAO	AMB14	Gneiss	3	2635	10		0.28106	0.00676			0.00028	0.00001		-1.81	0.7	3465
Thomas et al 2016	EAAO	AMB14	Gneiss	8	2635	10		0.28109	0.00640			0.00044	0.00002		-1.03	0.6	3435
Thomas et al 2016	EAAO	AMB14	Gneiss	9	2635	10		0.28107	0.00783			0.00054	0.00001		-1.90	0.8	3454
Thomas et al 2016	EAAO	AMB14	Gneiss	11	2635	10		0.28112	0.00569			0.00089	0.00001		-0.78	0.6	3405
Thomas et al 2016	EAAO	AMB14	Gneiss	12	2635	10		0.28105	0.00712			0.00053	0.00000		-2.55	0.7	3473
Thomas et al 2016	EAAO	AMB14	Gneiss	15	2635	10		0.28104	0.00641			0.00018	0.00000		-2.32	0.6	3484
Thomas et al 2016	RTC	AMB178_58	Felsic volcanic	5	2725	22		0.28100	0.01831			0.00023	0.00001		-1.77	1.8	3570
Thomas et al 2016	RTC	AMB178_58	Felsic volcanic	8	2725	22		0.28095	0.01867			0.00064	0.00004		-4.02	1.9	3612
Thomas et al 2016	RTC	AMB178_58	Felsic volcanic	10.2	2725	22		0.28095	0.01880			0.00041	0.00003		-3.84	1.9	3619
Thomas et al 2016	RTC	AMB178_58	Felsic volcanic	15	2725	22		0.28094	0.01831			0.00067	0.00002		-4.66	1.8	3628
Thomas et al 2016	RTC	AMB178_58	Felsic volcanic	16.1	2725	22		0.28097	0.01784			0.00024	0.00000		-2.82	1.8	3599
Thomas et al 2016	RTC	AMB178_58	Felsic volcanic	16.5	2725	22		0.28094	0.01867			0.00061	0.00001		-4.29	1.9	3621
Thomas et al 2016	RTC	AMB178_58	Felsic volcanic	19	2725	22		0.28102	0.01854			0.00037	0.00001		-1.24	1.9	3548
Thomas et al 2016	RTC	AMB178_80	Gneiss	4	2782	15		0.28097	0.01867			0.00034	0.00001		-1.44	1.9	3621
Thomas et al 2016	RTC	AMB178_80	Gneiss	7.1	2782	15		0.28106	0.01842			0.00054	0.00002		1.14	1.8	3537
Thomas et al 2016	RTC	AMB178_80	Gneiss	7.3	2782	15		0.28099	0.01854			0.00026	0.00001		-0.67	1.9	3604
Thomas et al 2016	RTC	AMB178_80	Gneiss	9.1	2782	15		0.28104	0.01867			0.00045	0.00003		0.85	1.9	3550
Thomas et al 2016	RTC	AMB178_80	Gneiss	12	2782	15		0.28099	0.01894			0.00112	0.00003		-2.30	1.9	3604
Thomas et al 2016	RTC	AMB178_80	Gneiss	13.2	2782	15		0.28100	0.01800			0.00021	0.00000		-0.25	1.8	3595
Thomas et al 2016	EAAO	AMB203	Gneiss	1	2685	17		0.28107	0.01395			0.00108	0.00003		-1.60	1.4	3475
Thomas et al 2016	EAAO	AMB203	Gneiss	2	2685	17		0.28106	0.01395			0.00076	0.00005		-1.37	1.4	3485
Thomas et al 2016	EAAO	AMB203	Gneiss	6	2685	17		0.28103	0.01494			0.00087	0.00001		-2.72	1.5	3518
Thomas et al 2016	EAAO	AMB203	Gneiss	7	2685	17		0.28109	0.01313			0.00117	0.00007		-1.23	1.3	3460
Thomas et al 2016	EAAO	AMB203	Gneiss	12.2	2685	17		0.28103	0.01313			0.00030	0.00001		-1.61	1.3	3516
Thomas et al 2016	EAAO	AMB203	Gneiss	16	2685	17		0.28106	0.01344			0.00055	0.00003		-1.14	1.3	3489
Thomas et al 2016	EAAO	AMB203	Gneiss	17	2685	17		0.28102	0.01453			0.00032	0.00001		-2.17	1.5	3531
Thomas et al 2016	EAAO	AMB203	Gneiss	20	2685	17		0.28103	0.01344			0.00037	0.00001		-1.72	1.3	3516
Thomas et al 2016	EAAO	AMB203	Gneiss	21	2685	17		0.28103	0.01414			0.00061	0.00004		-2.30	1.4	3520
Thomas et al 2016	EAAO	AMB203	Gneiss	23	2685	17		0.28105	0.01328			0.00074	0.00002		-1.83	1.3	3499
Thomas et al 2016	EAAO	AMB203	Gneiss	31.1	2685	17		0.28104	0.01433			0.00039	0.00002		-1.30	1.4	3502
Thomas et al 2016	EAAO	AMB203	Gneiss	33.2	2685	17		0.28110	0.01414			0.00042	0.00004		0.48	1.4	3450
Thomas et al 2016	EAAO	AMB203	Gneiss	34.1	2685	17		0.28106	0.01328			0.00074	0.00000		-1.44	1.3	3488
Thomas et al 2016	EAAO	AMB203	Gneiss	34.2	2685	17		0.28107	0.01917			0.00032	0.00001		-0.28	1.9	3477

Reference	Location	Sample	Harmonized classification	Name	$^{207}Pb/^{206}Pb$ Age (Ma)	2SE	$^{176}Hf/^{177}Hf_{(i)}$	$^{176}Hf/^{177}Hf_{(t)}$	2SE	$^{176}Hf/^{177}Hf_{(i)}$	2SE	$^{176}Lu/^{177}Hf$	1SE	Ehfpd	$eHf_{(t)}$	2SE	T_{DM2}
Thomas et al 2016	EAAO	AMB203	Gneiss	37	2685	17		0.28103	0.01414			0.00046	0.00001		-1.89	1.4	3516
Thomas et al 2016	EAAO	AMB203	Gneiss	38	2685	17		0.28103	0.01360			0.00042	0.00001		-1.92	1.4	3519
Thomas et al 2016	EAAO	AMB203	Gneiss	39.2	2685	17		0.28102	0.01433			0.00035	0.00000		-2.08	1.4	3527
Thomas et al 2016	EAAO	AMB213	Gneiss	2.2	2651	5		0.28109	0.02732			0.00027	0.00006		-0.09	2.7	3435
Thomas et al 2016	EAAO	AMB213	Gneiss	4	2651	5		0.28109	0.01515			0.00150	0.00000		-2.49	1.5	3440
Thomas et al 2016	EAAO	AMB213	Gneiss	5	2651	5		0.28104	0.01414			0.00027	0.00001		-1.84	1.4	3484
Thomas et al 2016	EAAO	AMB213	Gneiss	6	2651	5		0.28105	0.01395			0.00056	0.00012		-2.01	1.4	3474
Thomas et al 2016	EAAO	AMB213	Gneiss	8	2651	5		0.28106	0.01377			0.00052	0.00001		-1.79	1.4	3470
Thomas et al 2016	EAAO	AMB213	Gneiss	9	2651	5		0.28107	0.01473			0.00083	0.00017		-2.04	1.5	3461
Thomas et al 2016	EAAO	AMB213	Gneiss	10	2651	5		0.28104	0.01313			0.00044	0.00011		-2.18	1.3	3485
Thomas et al 2016	EAAO	AMB213	Gneiss	11	2651	5		0.28102	0.01262			0.00048	0.00001		-2.93	1.3	3505
Thomas et al 2016	EAAO	AMB213	Gneiss	12	2651	5		0.28106	0.01313			0.00052	0.00017		-1.75	1.3	3469
Thomas et al 2016	EAAO	AMB213	Gneiss	13	2651	5		0.28104	0.01433			0.00043	0.00009		-2.31	1.4	3489
Thomas et al 2016	EAAO	AMB213	Gneiss	14	2651	5		0.28108	0.01473			0.00120	0.00013		-2.17	1.5	3446
Thomas et al 2016	EAAO	AMB213	Gneiss	16	2651	5		0.28103	0.01299			0.00046	0.00010		-2.57	1.3	3495
Thomas et al 2016	EAAO	AMB213	Gneiss	17	2651	5		0.28107	0.01274			0.00089	0.00003		-1.95	1.3	3456
Thomas et al 2016	EAAO	AMB213	Gneiss	18	2651	5		0.28111	0.01395			0.00146	0.00001		-1.50	1.4	3414
Thomas et al 2016	EAAO	AMB213	Gneiss	22	2651	5		0.28107	0.01414			0.00115	0.00002		-2.42	1.4	3456
Thomas et al 2016	EAAO	AMB213	Gneiss	27	2651	5		0.28116	0.01452			0.00227	0.00004		-1.49	1.5	3373
Thomas et al 2016	EAAO	AMB213	Gneiss	29	2651	5		0.28109	0.01654			0.00129	0.00001		-2.21	1.7	3443
Thomas et al 2016	EAAO	AMB213	Gneiss	32	2651	5		0.28116	0.01395			0.00216	0.00001		-1.30	1.4	3373
Thomas et al 2016	EAAO	AMB213	Gneiss	36	2651	5		0.28105	0.01299			0.00047	0.00006		-1.98	1.3	3478
Thomas et al 2016	EAAO	AMB213	Gneiss	38	2651	5		0.28106	0.01414			0.00081	0.00004		-2.35	1.4	3471
Thomas et al 2016	EAAO	AMB213	Gneiss	39	2651	5		0.28109	0.01452			0.00123	0.00001		-2.10	1.5	3443
Thomas et al 2016	EAAO	AMB213	Gneiss	40	2651	5		0.28110	0.01515			0.00132	0.00010		-1.64	1.5	3425
Thomas et al 2016	EAAO	AMB213	Gneiss	41.2	2651	5		0.28103	0.01377			0.00031	0.00004		-2.48	1.4	3500
Thomas et al 2016	Lupa block	AMB238	Granite-Monzonite	7	2731	5		0.28107	0.01831			0.00039	0.00005		0.90	1.8	3494
Thomas et al 2016	Lupa block	AMB238	Granite-Monzonite	8	2731	5		0.28110	0.01988			0.00069	0.00000		1.24	2.0	3469
Thomas et al 2016	Lupa block	AMB238	Granite-Monzonite	9	2731	5		0.28108	0.01908			0.00051	0.00000		0.72	1.9	3493
Thomas et al 2016	Lupa block	AMB238	Granite-Monzonite	10	2731	5		0.28112	0.01954			0.00096	0.00005		1.37	2.0	3451
Thomas et al 2016	Lupa block	AMB238	Granite-Monzonite	11.1	2731	5		0.28107	0.01938			0.00070	0.00003		0.23	1.9	3497
Thomas et al 2016	Lupa block	AMB238	Granite-Monzonite	12.2	2731	5		0.28105	0.01923			0.00047	0.00003		-0.25	1.9	3523
Thomas et al 2016	Lupa block	AMB238	Granite-Monzonite	13.2	2731	5		0.28108	0.01908			0.00052	0.00001		0.73	1.9	3492
Thomas et al 2016	Lupa block	AMB238	Granite-Monzonite	14	2731	5		0.28110	0.01954			0.00051	0.00004		1.58	2.0	3469
Thomas et al 2016	Lupa block	AMB238	Granite-Monzonite	15.1	2731	5		0.28108	0.01988			0.00047	0.00001		0.96	2.0	3488
Thomas et al 2016	Lupa block	AMB238	Granite-Monzonite	16	2731	5		0.28108	0.01880			0.00053	0.00001		0.76	1.9	3491
Thomas et al 2016	Lupa block	AMB364	TTG	4	1919	20		0.28158	0.01907			0.00120	0.00005		-0.75	1.9	2574
Thomas et al 2016	Lupa block	AMB364	TTG	6	1919	20		0.28158	0.01893			0.00064	0.00011		-0.27	1.9	2581
Thomas et al 2016	Lupa block	AMB364	TTG	8	1919	20		0.28156	0.01893			0.00055	0.00002		-0.65	1.9	2595
Thomas et al 2016	Lupa block	AMB364	TTG	10	1919	20		0.28157	0.01866			0.00077	0.00005		-0.76	1.9	2590
Thomas et al 2016	Lupa block	AMB364	TTG	13	1919	20		0.28158	0.01820			0.00084	0.00002		-0.41	1.8	2578
Thomas et al 2016	Lupa block	AMB364	TTG	14	1919	20		0.28154	0.01893			0.00064	0.00001		-1.55	1.9	2618
Thomas et al 2016	Lupa block	AMB364	TTG	18	1919	20		0.28106	0.01831			0.00042	0.00002		1.13	1.8	3518

Reference	Location	Sample	Harmonized classification	Name	$^{207}Pb/^{206}Pb$ Age (Ma)	2SE	$^{176}Hf/^{177}Hf_{(i)}$	$^{176}Hf/^{177}Hf_{(t)}$	2SE	$^{176}Hf/^{177}Hf_{(i)}$	2SE	$^{176}Lu/^{177}Hf$	1SE	Ehfpd	$eHf_{(t)}$	2SE	T_{DM2}
Thomas et al 2016	Lupa block	AMB364	TTG	28	1919	20		0.28159	0.01879			0.00107	0.00012		-0.39	1.9	2569
Thomas et al 2016	EAAO	ASM108	Gneiss	2	2674	14		0.28103	0.01174			0.00112	0.00006		-3.21	1.2	3506
Thomas et al 2016	EAAO	ASM108	Gneiss	3	2674	14		0.28111	0.01210			0.00186	0.00014		-2.01	1.2	3434
Thomas et al 2016	EAAO	ASM108	Gneiss	8	2674	14		0.28106	0.01530			0.00074	0.00010		-1.59	1.5	3480
Thomas et al 2016	EAAO	ASM108	Gneiss	9	2674	14		0.28104	0.00925			0.00150	0.00006		-3.58	0.9	3497
Thomas et al 2016	EAAO	ASM108	Gneiss	14	2674	14		0.28105	0.01530			0.00076	0.00004		-1.90	1.5	3487
Thomas et al 2016	EAAO	ASM108	Gneiss	16	2674	14		0.28102	0.00783			0.00072	0.00004		-3.03	0.8	3521
Thomas et al 2016	EAAO	ASM108	Gneiss	17	2674	14		0.28098	0.00783			0.00099	0.00005		2.03	0.8	3710
Thomas et al 2016	Lupa block	ASM271	Granite-Monzonite	23	1896	8		0.28145	0.01328			0.00022	0.00004		-4.77	1.3	2698
Thomas et al 2016	Lupa block	ASM271	Granite-Monzonite	26	1896	8		0.28150	0.01343			0.00070	0.00005		-3.47	1.3	2644
Thomas et al 2016	Lupa block	ASM271	Granite-Monzonite	30	1896	8		0.28148	0.01395			0.00036	0.00002		-3.82	1.4	2666
Thomas et al 2016	Lupa block	ASM271	Granite-Monzonite	33	1896	8		0.28145	0.01299			0.00017	0.00001		-4.57	1.3	2694
Thomas et al 2016	Lupa block	ASM271	Granite-Monzonite	35	1896	8		0.28148	0.01328			0.00027	0.00002		-3.74	1.3	2667
Thomas et al 2016	Lupa block	ASM271	Granite-Monzonite	40	1896	8		0.28150	0.01536			0.00022	0.00001		-3.10	1.5	2651
Thomas et al 2016	Lupa block	ASM271	Granite-Monzonite	44	1896	8		0.28148	0.01472			0.00004	0.00006		-3.59	1.5	2671
Thomas et al 2016	Lupa block	ASM271	Granite-Monzonite	45	1896	8		0.28145	0.01343			0.00009	0.00000		-4.68	1.3	2700
Thomas et al 2016	Lupa block	ASM271	Granite-Monzonite	46	1896	8		0.28144	0.01493			0.00008	0.00001		-5.09	1.5	2712
Thomas et al 2016	Lupa block	ASM271	Granite-Monzonite	47	1896	8		0.28151	0.01395			0.00097	0.00000		-3.71	1.4	2641
Thomas et al 2016	Lupa block	ASM271	Granite-Monzonite	48	1896	8		0.28147	0.01328			0.00020	0.00001		-4.04	1.3	2678
Thomas et al 2016	Lupa block	ASM271	Granite-Monzonite	51	1896	8		0.28145	0.01395			0.00009	0.00003		-4.43	1.4	2693
Thomas et al 2016	Lupa block	ASM271	Granite-Monzonite	52	1896	8		0.28146	0.01286			0.00008	0.00001		-4.27	1.3	2689
Thomas et al 2016	Lupa block	ASM271	Granite-Monzonite	53	1896	8		0.28147	0.01413			0.00087	0.00001		-5.03	1.4	2682
Thomas et al 2016	Lupa block	ASM271	Granite-Monzonite	54	1896	8		0.28147	0.01313			0.00011	0.00000		-3.93	1.3	2678
Thomas et al 2016	Lupa block	ASM271	Granite-Monzonite	56	1896	8		0.28147	0.01286			0.00030	0.00005		-4.10	1.3	2676
Thomas et al 2016	Lupa block	ASM271	Granite-Monzonite	59	1896	8		0.28146	0.01328			0.00012	0.00001		-4.18	1.3	2685
Thomas et al 2016	Lupa block	ASM470	Gneiss	1	1929	15		0.28148	0.01273			0.00102	0.00003		-4.00	1.3	2684
Thomas et al 2016	Lupa block	ASM470	Gneiss	2	1929	15		0.28155	0.01452			0.00198	0.00006		-2.61	1.5	2610
Thomas et al 2016	Lupa block	ASM470	Gneiss	5	1929	15		0.28154	0.01413			0.00181	0.00003		-2.82	1.4	2622
Thomas et al 2016	Lupa block	ASM470	Gneiss	6	1929	15		0.28155	0.01343			0.00223	0.00006		-3.15	1.3	2616
Thomas et al 2016	Lupa block	ASM470	Gneiss	10	1929	15		0.28157	0.01514			0.00205	0.00004		-2.03	1.5	2591
Thomas et al 2016	Lupa block	ASM470	Gneiss	11	1929	15		0.28154	0.01343			0.00182	0.00006		-2.72	1.3	2619
Thomas et al 2016	Lupa block	ASM470	Gneiss	16	1929	15		0.28153	0.01377			0.00149	0.00006		-2.94	1.4	2637
Thomas et al 2016	Lupa block	ASM470	Gneiss	17	1929	15		0.28154	0.01377			0.00160	0.00008		-2.65	1.4	2625
Thomas et al 2016	Lupa block	ASM470	Gneiss	18	1929	15		0.28151	0.01395			0.00104	0.00010		-2.84	1.4	2651
Thomas et al 2016	Lupa block	ASM470	Gneiss	19	1929	15		0.28148	0.01328			0.00092	0.00012		-3.96	1.3	2687
Thomas et al 2016	Lupa block	ASM470	Gneiss	20	1929	15		0.28153	0.01360			0.00170	0.00008		-3.20	1.4	2637
Thomas et al 2016	Lupa block	ASM470	Gneiss	30	1929	15		0.28150	0.01343			0.00105	0.00008		-3.21	1.3	2661
Thomas et al 2016	Lupa block	ASM470	Gneiss	28	1929	15		0.28151	0.01328			0.00151	0.00022		-3.53	1.3	2653
Thomas et al 2016	Lupa block	ASM470	Gneiss	29	1929	15		0.28150	0.01360			0.00148	0.00003		-3.88	1.4	2664
Thomas et al 2016	Lupa block	ASM470	Gneiss	31	1929	15		0.28147	0.01286			0.00075	0.00005		-4.07	1.3	2696
Thomas et al 2016	Lupa block	ASM470	Gneiss	32	1929	15		0.28150	0.01452			0.00143	0.00019		-3.67	1.5	2660
Thomas et al 2016	Ubendian	ASM496c	Gneiss	2	1815	5		0.28191	0.00674			0.00277	0.00009		6.47	0.7	2195
Thomas et al 2016	Ubendian	ASM496c	Gneiss	3	1435	5		0.28180	0.00461			0.00079	0.00020		-3.20	0.5	2106

Reference	Location	Sample	Harmonized classification	Name	$^{207}Pb/^{206}Pb$ Age (Ma)	2SE	$^{176}Hf/^{177}Hf_{(i)}$	$^{176}Hf/^{177}Hf_{(t)}$	2SE	$^{176}Hf/^{177}Hf_{(i)}$	2SE	$^{176}Lu/^{177}Hf$	1SE	Ehfpd	$eHf_{(t)}$	2SE	T_{DM2}
Thomas et al 2016	Ubendian	ASM496c	Gneiss	4	1435	5		0.28189	0.00745			0.00231	0.00020		-1.75	0.7	2023
Thomas et al 2016	Ubendian	ASM496c	Gneiss	6	1435	5		0.28188	0.00816			0.00160	0.00023		-1.35	0.8	2031
Thomas et al 2016	Ubendian	ASM496c	Gneiss	12	1435	5		0.28186	0.00639			0.00158	0.00014		-1.83	0.6	2045
Thomas et al 2016	Ubendian	ASM496c	Gneiss	13	1435	5		0.28190	0.00709			0.00238	0.00012		-1.36	0.7	2010
Thomas et al 2016	Ubendian	ASM496c	Gneiss	14	1435	5		0.28183	0.00603			0.00115	0.00021		-2.77	0.6	2084
Thomas et al 2016	Ubendian	ASM496c	Gneiss	16	1435	5		0.28188	0.00603			0.00222	0.00007		-1.73	0.6	2025
Thomas et al 2016	Ubendian	ASM496c	Gneiss	19	1435	5		0.28191	0.00709			0.00243	0.00016		-1.05	0.7	2000
Thomas et al 2016	Ubendian	ASM573	Gneiss	1	872	20		0.28145	0.01273			0.00024	0.00000		-5.58	1.3	2677
Thomas et al 2016	Ubendian	ASM573	Gneiss	3	872	20		0.28146	0.01313			0.00102	0.00001		-6.34	1.3	2671
Thomas et al 2016	Ubendian	ASM573	Gneiss	12	872	20		0.28147	0.01377			0.00123	0.00005		-6.31	1.4	2663
Thomas et al 2016	Ubendian	ASM573	Gneiss	15	872	20		0.28145	0.01286			0.00029	0.00001		-5.71	1.3	2679
Thomas et al 2016	Ubendian	ASM573	Gneiss	18	872	20		0.28148	0.01299			0.00037	0.00001		-4.78	1.3	2650
Thomas et al 2016	Ubendian	ASM573	Gneiss	19	872	20		0.28148	0.01343			0.00063	0.00003		-5.17	1.3	2652
Thomas et al 2016	Ubendian	ASM573	Gneiss	21	872	20		0.28144	0.01360			0.00046	0.00001		-6.38	1.4	2692
Thomas et al 2016	Ubendian	ASM573	Gneiss	22	872	20		0.28146	0.01299			0.00034	0.00002		-5.48	1.3	2671
Thomas et al 2016	Ubendian	ASM573	Gneiss	26	872	20		0.28150	0.01343			0.00093	0.00007		-4.80	1.3	2631
Thomas et al 2016	Ubendian	ASM573	Gneiss	27.2	872	20		0.28150	0.01452			0.00044	0.00006		-4.05	1.5	2627
Thomas et al 2016	Ubendian	ASM573	Gneiss	30	872	20		0.28146	0.01360			0.00049	0.00004		-5.42	1.4	2664
Thomas et al 2016	Ubendian	ASM573	Gneiss	32	872	20		0.28147	0.01273			0.00032	0.00002		-5.10	1.3	2661
Thomas et al 2016	Ubendian	ASM573	Gneiss	34	872	20		0.28147	0.01313			0.00037	0.00007		-4.99	1.3	2656
Thomas et al 2016	Ubendian	ASM573	Gneiss	35	872	20		0.28145	0.01273			0.00028	0.00001		-5.66	1.3	2678
Thomas et al 2016	Ubendian	ASM573	Gneiss	36	872	20		0.28146	0.01343			0.00037	0.00003		-5.37	1.3	2667
Thomas et al 2016	Ubendian	ASM573	Gneiss	37	872	20		0.28147	0.01313			0.00044	0.00002		-5.08	1.3	2656
Thomas et al 2016	Ubendian	ASM590	Gneiss	1	1871	8		0.28149	0.01678			0.00044	0.00009		-4.31	1.7	2648
Thomas et al 2016	Ubendian	ASM590	Gneiss	4	1871	8		0.28147	0.01432			0.00028	0.00001		-4.85	1.4	2669
Thomas et al 2016	Ubendian	ASM590	Gneiss	5	1871	8		0.28148	0.01728			0.00027	0.00001		-4.48	1.7	2659
Thomas et al 2016	Ubendian	ASM590	Gneiss	6	1871	8		0.28144	0.01377			0.00049	0.00001		-5.97	1.4	2693
Thomas et al 2016	Ubendian	ASM590	Gneiss	11	1871	8		0.28149	0.01703			0.00028	0.00002		-4.00	1.7	2645
Thomas et al 2016	Ubendian	ASM590	Gneiss	12	1871	8		0.28149	0.01452			0.00040	0.00005		-4.29	1.5	2649
Thomas et al 2016	Ubendian	ASM590	Gneiss	13	1871	8		0.28147	0.01432			0.00029	0.00001		-4.54	1.4	2660
Thomas et al 2016	Ubendian	ASM590	Gneiss	14	1871	8		0.28146	0.01653			0.00061	0.00001		-5.37	1.7	2672
Thomas et al 2016	Ubendian	ASM590	Gneiss	16	1871	8		0.28152	0.02114			0.00039	0.00004		-2.90	2.1	2610
Thomas et al 2016	EAAO	C182	Gneiss	1.4	607	2		0.28224	0.00496			0.00020	0.00001		-5.74	0.5	1240
Thomas et al 2016	EAAO	C182	Gneiss	1.5	607	2		0.28222	0.00567			0.00025	0.00002		-6.50	0.6	1261
Thomas et al 2016	EAAO	C182	Gneiss	1.6	607	2		0.28225	0.00496			0.00016	0.00000		-5.58	0.5	1236
Thomas et al 2016	EAAO	C182	Gneiss	1.7	607	2		0.28225	0.00567			0.00036	0.00000		-5.66	0.6	1236
Thomas et al 2016	EAAO	C182	Gneiss	2.1	607	2		0.28225	0.00461			0.00018	0.00000		-5.55	0.5	1235
Thomas et al 2016	EAAO	C182	Gneiss	3.1	607	2		0.28224	0.00602			0.00028	0.00000		-6.02	0.6	1247
Thomas et al 2016	EAAO	C182	Gneiss	5	607	2		0.28221	0.00532			0.00021	0.00000		-7.01	0.5	1276
Thomas et al 2016	EAAO	C182	Gneiss	7	607	2		0.28220	0.00354			0.00026	0.00000		-7.11	0.4	1278
Thomas et al 2016	EAAO	C182	Gneiss	8	607	2		0.28227	0.00673			0.00028	0.00002		-4.74	0.7	1211
Thomas et al 2016	EAAO	C182	Gneiss	9	607	2		0.28227	0.00461			0.00041	0.00001		-4.76	0.5	1210
Thomas et al 2016	EAAO	C182	Gneiss	11	607	2		0.28229	0.00708			0.00038	0.00001		-3.97	0.7	1187

Reference	Location	Sample	Harmonized classification	Name	$^{207}Pb/^{206}Pb$ Age (Ma)	2SE	$^{176}Hf/^{177}Hf_{(i)}$	$^{176}Hf/^{177}Hf_{(t)}$	2SE	$^{176}Hf/^{177}Hf_{(i)}$	2SE	$^{176}Lu/^{177}Hf$	1SE	Ehfpd	$eHf_{(t)}$	2SE	T_{DM2}
Thomas et al 2016	EAAO	C182	Gneiss	12	607	2		0.28223	0.00461			0.00022	0.00001		-6.28	0.5	1255
Thomas et al 2016	EAAO	C182	Gneiss	14	607	2		0.28221	0.00425			0.00027	0.00000		-6.83	0.4	1270
Thomas et al 2016	EAAO	C182	Gneiss	15	607	2		0.28226	0.00531			0.00026	0.00001		-5.16	0.5	1223
Thomas et al 2016	EAAO	F024	Granite-Monzonite	1	2670	6		0.28105	0.01842			0.00051	0.00004		-1.72	1.8	3491
Thomas et al 2016	EAAO	F024	Granite-Monzonite	2	2670	6		0.28107	0.01854			0.00053	0.00001		-0.83	1.9	3464
Thomas et al 2016	EAAO	F024	Granite-Monzonite	3	2670	6		0.28105	0.01908			0.00052	0.00001		-1.72	1.9	3491
Thomas et al 2016	EAAO	F024	Granite-Monzonite	4	2670	6		0.28111	0.01908			0.00112	0.00007		-0.62	1.9	3428
Thomas et al 2016	EAAO	F024	Granite-Monzonite	5.1	2670	6		0.28108	0.01842			0.00082	0.00004		-1.18	1.8	3459
Thomas et al 2016	EAAO	F024	Granite-Monzonite	6	2670	6		0.28107	0.01880			0.00087	0.00002		-1.69	1.9	3472
Thomas et al 2016	RTC	FMP106	Gneiss	2	2740	12		0.28112	0.01344			0.00022	0.00001		3.00	1.3	3454
Thomas et al 2016	RTC	FMP106	Gneiss	17	2740	12		0.28114	0.01494			0.00033	0.00005		3.43	1.5	3435
Thomas et al 2016	RTC	FMP106	Gneiss	20	2740	12		0.28113	0.01414			0.00050	0.00005		2.80	1.4	3444
Thomas et al 2016	RTC	FMP106	Gneiss	26	2740	12		0.28112	0.01494			0.00031	0.00001		2.69	1.5	3458
Thomas et al 2016	RTC	FMP273W	Gneiss	10.2	2823	4		0.28100	0.00605			0.00067	0.00001		0.13	0.4	3583
Thomas et al 2016	RTC	FMP273W	Gneiss	15	2823	4		0.28103	0.00569			0.00126	0.00010		-0.40	0.6	3597
Thomas et al 2016	RTC	FMP273W	Gneiss	20.1	2823	4		0.28102	0.00569			0.00120	0.00003		-0.21	0.7	3581
Thomas et al 2016	RTC	FMP273W	Gneiss	21	2823	4		0.28101	0.00676			0.00087	0.00003		-0.02	0.5	3572
Thomas et al 2016	RTC	FMP273W	Gneiss	22	2823	4		0.28103	0.00427			0.00107	0.00003		-1.20	0.6	3627
Thomas et al 2016	RTC	FMP273W	Gneiss	23	2823	4		0.28102	0.00641			0.00108	0.00003		0.12	0.9	3574
Thomas et al 2016	RTC	FMP273W	Gneiss	25	2823	4		0.28103	0.00712			0.00128	0.00010		-0.68	0.5	3620
Thomas et al 2016	RTC	FMP273W	Gneiss	26	2823	4		0.28104	0.00534			0.00135	0.00007		0.38	0.6	3594
Thomas et al 2016	RTC	FMP273W	Gneiss	27	2823	4		0.28099	0.00641			0.00095	0.00006		-0.50	0.5	3604
Thomas et al 2016	RTC	FMP273W	Gneiss	30	2823	4		0.28104	0.00854			0.00124	0.00016		-0.18	0.7	3595
Thomas et al 2016	RTC	FMP273W	Gneiss	31	2823	4		0.28099	0.00534			0.00080	0.00005		-0.06	0.6	3578
Thomas et al 2016	RTC	FMP273W	Gneiss	32	2823	4		0.28102	0.00569			0.00074	0.00003		0.32	0.6	3560
Thomas et al 2016	RTC	FMP273W	Gneiss	3.2	2823	4		0.28101	0.00463			0.00101	0.00004		-0.23	0.6	3615
Thomas et al 2016	RTC	FMP273W	Gneiss	4.1	2823	4		0.28102	0.00676			0.00101	0.00008		-0.25	0.6	3583
Thomas et al 2016	RTC	FMP273W	Gneiss	5.1	2823	4		0.28104	0.00640			0.00126	0.00002		-0.44	0.6	3592
Thomas et al 2016	RTC	FMP273W	Gneiss	8	2823	4		0.28105	0.00569			0.00140	0.00006		-0.05	0.7	3599
Thomas et al 2016	RTC	FMP78AW	Granite-Monzonite	24	2678	34		0.28109	0.01831			0.00036	0.00000		0.35	1.8	3449
Thomas et al 2016	RTC	FMP78AW	Granite-Monzonite	26	2678	34		0.28111	0.01854			0.00058	0.00003		0.73	1.9	3427
Thomas et al 2016	RTC	FMP78AW	Granite-Monzonite	27	2678	34		0.28108	0.01894			0.00039	0.00001		-0.24	1.9	3464
Thomas et al 2016	RTC	FMP78AW	Granite-Monzonite	32	2678	34		0.28114	0.01867			0.00057	0.00001		1.68	1.9	3401
Thomas et al 2016	RTC	FMP78AW	Granite-Monzonite	41	2678	34		0.28110	0.01938			0.00059	0.00001		0.03	1.9	3446
Thomas et al 2016	RTC	FMP78AW	Granite-Monzonite	43	2678	34		0.28110	0.01867			0.00088	0.00001		-0.42	1.9	3444
Thomas et al 2016	RTC	FMP85AW	Sediment	1	2744	6		0.28110	0.01395			0.00101	0.00002		0.79	1.4	3479
Thomas et al 2016	RTC	FMP85AW	Sediment	3	2744	6		0.28106	0.01395			0.00090	0.00002		-0.18	1.4	3512
Thomas et al 2016	RTC	FMP85AW	Sediment	4	2744	6		0.28112	0.01473			0.00232	0.00002		-0.69	1.5	3452
Thomas et al 2016	RTC	FMP85AW	Sediment	7	2744	6		0.28105	0.01473			0.00074	0.00003		-0.37	1.5	3526
Thomas et al 2016	RTC	FMP85AW	Sediment	20	2744	6		0.28095	0.01360			0.00069	0.00005		-3.81	1.4	3625
Thomas et al 2016	RTC	FMP85AW	Sediment	21	2744	6		0.28105	0.01453			0.00127	0.00005		-1.22	1.5	3522
Thomas et al 2016	RTC	FMP85AW	Sediment	19.1	2744	6		0.28110	0.01473			0.00071	0.00003		1.32	1.5	3480
Thomas et al 2016	RTC	FMP85AW	Sediment	5	2744	6		0.28103	0.01299			0.00062	0.00011		-0.83	1.3	3545

Reference	Location	Sample	Harmonized classification	Name	$^{207}Pb/^{206}Pb$ Age (Ma)	2SE	$^{176}Hf/^{177}Hf_{(i)}$	$^{176}Hf/^{177}Hf_{(t)}$	2SE	$^{176}Hf/^{177}Hf_{(i)}$	2SE	$^{176}Lu/^{177}Hf$	1SE	Ehfpd	$eHf_{(t)}$	2SE	T_{DM2}
Thomas et al 2016	Irumide	P032	paragneiss	4	1013	20		0.28141	0.00675			0.00038	0.00004		-4.81	0.7	2774
Thomas et al 2016	Irumide	P032	paragneiss	5	1013	20		0.28147	0.01386			0.00083	0.00003		-3.61	1.4	2706
Thomas et al 2016	Irumide	P032	paragneiss	7	1013	20		0.28144	0.00640			0.00031	0.00001		-25.06	0.6	2245
Thomas et al 2016	Irumide	P032	paragneiss	9	1013	20		0.28160	0.01598			0.00046	0.00011		-19.62	1.6	2099
Thomas et al 2016	Irumide	P032	paragneiss	21	1013	20		0.28141	0.00640			0.00092	0.00002		-6.63	0.6	2754
Thomas et al 2016	Irumide	P032	paragneiss	24	1013	20		0.28172	0.00887			0.00043	0.00004		-15.00	0.9	1989
Thomas et al 2016	Irumide	P032	paragneiss	27	1013	20		0.28143	0.01066			0.00115	0.00009		-6.01	1.1	2724
Thomas et al 2016	Irumide	P032	paragneiss	28	1013	20		0.28167	0.00604			0.00032	0.00000		-13.88	0.6	2104
Thomas et al 2016	Irumide	P032	paragneiss	30	1013	20		0.28145	0.00675			0.00065	0.00001		-20.39	0.7	2349
Thomas et al 2016	Irumide	P032	paragneiss	32	1013	20		0.28141	0.00711			0.00047	0.00001		-4.63	0.7	2777
Thomas et al 2016	Irumide	P032	paragneiss	33	1013	20		0.28168	0.00568			0.00026	0.00003		-14.46	0.6	2068
Thomas et al 2016	Irumide	P032	paragneiss	34	1013	20		0.28142	0.00817			0.00036	0.00002		-22.26	0.8	2359
Thomas et al 2016	Irumide	P032	paragneiss	35	1013	20		0.28168	0.00959			0.00032	0.00001		-17.48	1.0	1992
Thomas et al 2016	Irumide	P032	paragneiss	36	1013	20		0.28146	0.00959			0.00154	0.00013		-24.41	1.0	2250
Thomas et al 2016	Irumide	P032	paragneiss	37	1013	20		0.28172	0.00568			0.00035	0.00001		-14.14	0.6	1992
Thomas et al 2016	Irumide	P170	Gneiss	2	1083	6		0.28201	0.01580			0.00087	0.00004		-3.65	1.6	1715
Thomas et al 2016	Irumide	P170	Gneiss	4	1083	6		0.28207	0.01412			0.00123	0.00010		-2.10	1.4	1663
Thomas et al 2016	Irumide	P170	Gneiss	6.1	1083	6		0.28198	0.01343			0.00085	0.00001		-4.85	1.3	1749
Thomas et al 2016	Irumide	P170	Gneiss	7.1	1083	6		0.28198	0.01313			0.00036	0.00004		-4.52	1.3	1750
Thomas et al 2016	Irumide	P170	Gneiss	8	1083	6		0.28203	0.01285			0.00080	0.00006		-3.00	1.3	1698
Thomas et al 2016	Irumide	P170	Gneiss	9.1	1083	6		0.28198	0.01327			0.00050	0.00001		-4.62	1.3	1750
Thomas et al 2016	Irumide	P170	Gneiss	10.1	1083	6		0.28201	0.01299			0.00090	0.00004		-3.67	1.3	1715
Thomas et al 2016	Irumide	P170	Gneiss	12.1	1083	6		0.28200	0.01313			0.00057	0.00006		-4.11	1.3	1734
Thomas et al 2016	Irumide	P170	Gneiss	13	1083	6		0.28201	0.01394			0.00058	0.00006		-3.65	1.4	1721
Thomas et al 2016	Irumide	P170	Gneiss	15	1083	6		0.28198	0.01376			0.00050	0.00003		-4.73	1.4	1753
Thomas et al 2016	Irumide	P170	Gneiss	18	1083	6		0.28200	0.01313			0.00069	0.00005		-4.05	1.3	1730
Thomas et al 2016	Irumide	P170	Gneiss	19.1	1083	6		0.28195	0.01273			0.00062	0.00001		-5.77	1.3	1781
Thomas et al 2016	Irumide	P170	Gneiss	21	1083	6		0.28197	0.01286			0.00045	0.00005		-4.87	1.3	1758
Thomas et al 2016	Irumide	P170	Gneiss	23	1083	6		0.28204	0.01580			0.00086	0.00007		-2.90	1.6	1694
Thomas et al 2016	Irumide	P203	Sediment	1	1124			0.28225	0.01726			0.00119	0.00011		5.20	1.7	1501
Thomas et al 2016	Irumide	P203	Sediment	2	1223			0.28197	0.01913			0.00133	0.00005		-2.56	1.9	1833
Thomas et al 2016	Irumide	P203	Sediment	3	431			0.28266	0.01938			0.00093	0.00009		5.06	1.9	721
Thomas et al 2016	Irumide	P203	Sediment	4	1088			0.28200	0.01431			0.00076	0.00008		-4.13	1.4	1737
Thomas et al 2016	Irumide	P203	Sediment	5	1068			0.28198	0.01299			0.00054	0.00002		-5.03	1.3	1744
Thomas et al 2016	Irumide	P203	Sediment	6	1080			0.28198	0.01343			0.00058	0.00021		-4.87	1.3	1752
Thomas et al 2016	Irumide	P203	Sediment	7	2721			0.28109	0.01560			0.00076	0.00004		0.67	1.6	3469
Thomas et al 2016	Irumide	P203	Sediment	9	1042			0.28196	0.01376			0.00062	0.00013		-6.26	1.4	1748
Thomas et al 2016	Irumide	P203	Sediment	11	1130			0.28187	0.01376			0.00132	0.00005		-8.03	1.4	1883
Thomas et al 2016	Irumide	P203	Sediment	12	1052			0.28202	0.01451			0.00065	0.00005		-4.11	1.5	1697
Thomas et al 2016	Irumide	P203	Sediment	14	1116			0.28193	0.01394			0.00168	0.00006		-6.67	1.4	1822
Thomas et al 2016	Irumide	P203	Sediment	18	2064			0.28135	0.02264			0.00143	0.00020		-6.11	2.3	2882
Thomas et al 2016	Irumide	P203	Sediment	23	1106			0.28196	0.01451			0.00073	0.00003		-5.00	1.5	1782
Thomas et al 2016	Irumide	P203	Sediment	27	1082			0.28197	0.01376			0.00077	0.00016		-5.06	1.4	1756

Reference	Location	Sample	Harmonized classification	Name	$^{207}Pb/^{206}Pb$ Age (Ma)	2SE	$^{176}Hf/^{177}Hf_{(i)}$	$^{176}Hf/^{177}Hf_{(t)}$	2SE	$^{176}Hf/^{177}Hf_{(i)}$	2SE	$^{176}Lu/^{177}Hf$	1SE	Ehfpd	$eHf_{(t)}$	2SE	T_{DM2}
Thomas et al 2016	Irumide	P203	Sediment	29	2652			0.28098	0.01630			0.00077	0.00003		-5.05	1.6	3551
Thomas et al 2016	Irumide	P203	Sediment	30	2692			0.28095	0.01583			0.00083	0.00007		-5.14	1.6	3596
Thomas et al 2016	Irumide	P203	Sediment	33	1824			0.28167	0.01536			0.00167	0.00011		-0.45	1.5	2442
Thomas et al 2016	Irumide	P203	Sediment	34	1824			0.28169	0.01942			0.00212	0.00016		-0.27	1.9	2421
Thomas et al 2016	Irumide	P203	Sediment	35	2724			0.28102	0.01583			0.00071	0.00006		-1.77	1.6	3544
Thomas et al 2016	Irumide	P203	Sediment	38	1083			0.28225	0.01312			0.00083	0.00002		4.67	1.3	1477
Thomas et al 2016	Irumide	P203	Sediment	39	1134			0.28199	0.01492			0.00069	0.00005		-3.10	1.5	1761
Thomas et al 2016	Irumide	P203	Sediment	40	1103			0.28192	0.01604			0.00144	0.00004		-6.86	1.6	1817
Thomas et al 2016	Irumide	P203	Sediment	45	1147			0.28190	0.01558			0.00150	0.00023		-6.83	1.6	1865
Thomas et al 2016	Irumide	P204	paragneiss	5	1796	44		0.28189	0.01359			0.00032	0.00003		-7.62	1.4	1850
Thomas et al 2016	Irumide	P204	paragneiss	12	1796	44		0.28188	0.02026			0.00034	0.00003		-8.43	2.0	1839
Thomas et al 2016	Irumide	P204	paragneiss	13	1796	44		0.28188	0.02083			0.00023	0.00003		-8.72	2.1	1832
Thomas et al 2016	Irumide	P204	paragneiss	21	1796	44		0.28184	0.02537			0.00023	0.00001		-9.26	2.5	1889
Thomas et al 2016	Irumide	P204	paragneiss	26	1796	44		0.28186	0.01652			0.00092	0.00009		-9.50	1.7	1868
Thomas et al 2016	Irumide	P204	paragneiss	28	1796	44		0.28188	0.01752			0.00021	0.00005		-7.39	1.8	1864
Thomas et al 2016	Irumide	P204	paragneiss	30	1796	44		0.28191	0.01805			0.00048	0.00011		-4.70	1.8	1876
Thomas et al 2016	Irumide	P204	paragneiss	32	1796	44		0.28192	0.01412			0.00031	0.00009		-7.12	1.4	1801
Thomas et al 2016	Irumide	P204	paragneiss	36	1796	44		0.28174	0.01702			0.00084	0.00007		2.92	1.7	2366
Thomas et al 2016	Irumide	P204	paragneiss	37	1796	44		0.28188	0.01492			0.00054	0.00009		-8.96	1.5	1828
Thomas et al 2016	Irumide	P204	paragneiss	38	1796	44		0.28200	0.01451			0.00086	0.00001		2.10	1.5	1874
Thomas et al 2016	Irumide	P204	paragneiss	39	1796	44		0.28181	0.01558			0.00065	0.00005		1.86	1.6	2213
Thomas et al 2016	RTC	SK106	Granite-Monzonite	1	2675	15		0.28105	0.01908			0.00057	0.00004		-1.50	1.9	3485
Thomas et al 2016	RTC	SK106	Granite-Monzonite	3.1	2675	15		0.28110	0.01923			0.00091	0.00001		-0.52	1.9	3440
Thomas et al 2016	RTC	SK106	Granite-Monzonite	11	2675	15		0.28107	0.01880			0.00071	0.00005		-1.36	1.9	3474
Thomas et al 2016	RTC	SK106	Granite-Monzonite	14	2675	15		0.28106	0.01908			0.00061	0.00003		-1.39	1.9	3480
Thomas et al 2016	RTC	SK106	Granite-Monzonite	16	2675	15		0.28111	0.02182			0.00082	0.00019		0.11	2.2	3427
Thomas et al 2016	RTC	SK106	Granite-Monzonite	27	2675	15		0.28105	0.01867			0.00053	0.00011		-1.71	1.9	3493
Thomas et al 2016	RTC	SK106	Granite-Monzonite	30	2675	15		0.28117	0.02119			0.00200	0.00004		-0.12	2.1	3372
Thomas et al 2016	RTC	SK106	Granite-Monzonite	31	2675	15		0.28106	0.01842			0.00075	0.00004		-1.80	1.8	3484
Thomas et al 2016	RTC	SK256	Granite-Monzonite	1	2683	19		0.28105	0.01560			0.00043	0.00001		-1.29	1.6	3497
Thomas et al 2016	RTC	SK256	Granite-Monzonite	15	2683	19		0.28110	0.01606			0.00050	0.00001		0.58	1.6	3441
Thomas et al 2016	RTC	SK256	Granite-Monzonite	21	2683	19		0.28108	0.01560			0.00034	0.00002		0.00	1.6	3466
Thomas et al 2016	RTC	SK256	Granite-Monzonite	23	2683	19		0.28110	0.01433			0.00087	0.00001		-0.37	1.4	3449
Thomas et al 2016	RTC	SK256	Granite-Monzonite	35	2683	19		0.28108	0.01414			0.00046	0.00007		-0.27	1.4	3467
Thomas et al 2016	RTC	SK390	TTG	3	2742	6		0.28114	0.01537			0.00054	0.00008		3.23	1.5	3432
Thomas et al 2016	RTC	SK390	TTG	6	2742	6		0.28108	0.01473			0.00058	0.00002		1.01	1.5	3493
Thomas et al 2016	RTC	SK390	TTG	8	2742	6		0.28109	0.01515			0.00061	0.00001		1.38	1.5	3481
Thomas et al 2016	RTC	SK390	TTG	21	2742	6		0.28109	0.01360			0.00037	0.00003		1.61	1.4	3487
Thomas et al 2016	RTC	SK390	TTG	23	2742	6		0.28108	0.01452			0.00030	0.00004		1.55	1.5	3493
Thomas et al 2016	RTC	SK390	TTG	38	2742	6		0.28111	0.01494			0.00051	0.00001		2.12	1.5	3466
Thomas et al 2016	RTC	SK390	TTG	40	2742	6		0.28108	0.01494			0.00064	0.00002		1.01	1.5	3490
Thomas et al 2016	RTC	SK499	Sediment	1	3844			0.28027	0.01018			0.00050	0.00004		-1.89	1.0	4848
Thomas et al 2016	RTC	SK499	Sediment	6	3658			0.28044	0.00929			0.00088	0.00001		-1.20	0.9	4588

Reference	Location	Sample	Harmonized classification	Name	$^{207}Pb/^{206}Pb$ Age (Ma)	2SE	$^{176}Hf/^{177}Hf_{(i)}$	$^{176}Hf/^{177}Hf_{(t)}$	2SE	$^{176}Hf/^{177}Hf_{(i)}$	2SE	$^{176}Lu/^{177}Hf$	1SE	Ehfpd	$eHf_{(t)}$	2SE	T_{DM2}
Thomas et al 2016	RTC	SK499	Sediment	11	3702			0.28038	0.01018			0.00084	0.00001		-2.35	1.0	4674
Thomas et al 2016	RTC	SK499	Sediment	14	3155			0.28048	0.00929			0.00141	0.00006		-12.47	0.9	4295
Thomas et al 2016	RTC	SK499	Sediment	18	3584			0.28054	0.01144			0.00125	0.00006		-0.22	1.1	4449
Thomas et al 2016	RTC	SK499	Sediment	31	3365			0.28048	0.00972			0.00091	0.00002		-6.85	1.0	4409
Thomas et al 2016	RTC	SK499	Sediment	34	3637			0.28041	0.00995			0.00037	0.00000		-1.65	1.0	4612
Thomas et al 2016	RTC	SK499	Sediment	36	3749			0.28032	0.00972			0.00051	0.00004		-2.44	1.0	4753
Thomas et al 2016	RTC	SK499	Sediment	38	3365			0.28041	0.01092			0.00074	0.00001		-8.71	1.1	4471
Thomas et al 2016	RTC	SK499	Sediment	39	3557			0.28039	0.01067			0.00066	0.00005		-4.98	1.1	4593
Thomas et al 2016	RTC	SK499	Sediment	40	3862			0.28026	0.00930			0.00031	0.00008		-1.24	0.9	4865
Thomas et al 2016	RTC	SK499	Sediment	42	3620			0.28045	0.01018			0.00092	0.00007		-1.79	1.0	4558
Thomas et al 2016	RTC	SK499	Sediment	53	2819			0.28042	0.01401			0.00175	0.00014		-22.86	1.4	4185
Thomas et al 2016	RTC	SK499	Sediment	54	3476			0.28041	0.01145			0.00047	0.00003		-5.58	1.1	4530
Thomas et al 2016	RTC	SK499	Sediment	67	3333			0.28042	0.01172			0.00089	0.00002		-9.36	1.2	4443
Thomas et al 2016	RTC	SK499	Sediment	76	3634			0.28054	0.01118			0.00166	0.00002		-0.08	1.1	4474
Thomas et al 2016	RTC	SK499	Sediment	102	2811			0.28045	0.01118			0.00078	0.00024		-20.26	1.1	4155
Thomas et al 2016	RTC	SK499	Sediment	109	2986			0.28044	0.01461			0.00039	0.00002		-15.89	1.5	4255
Thomas et al 2016	RTC	SK499	Sediment	110	2768			0.28043	0.00995			0.00097	0.00007		-22.15	1.0	4147
Thomas et al 2016	RTC	SK553	Granite-Monzonite	1	2727	12		0.28108	0.02005			0.00209	0.00002		-2.02	2.0	3482
Thomas et al 2016	RTC	SK553	Granite-Monzonite	4	2727	12		0.28101	0.01938			0.00047	0.00002		-1.56	1.9	3554
Thomas et al 2016	RTC	SK553	Granite-Monzonite	5	2727	12		0.28101	0.01923			0.00083	0.00001		-2.21	1.9	3553
Thomas et al 2016	RTC	SK553	Granite-Monzonite	12	2727	12		0.28103	0.01923			0.00042	0.00001		-0.77	1.9	3534
Thomas et al 2016	RTC	SK553	Granite-Monzonite	19	2727	12		0.28100	0.01908			0.00058	0.00007		-2.34	1.9	3570
Thomas et al 2016	RTC	SK553	Granite-Monzonite	20	2727	12		0.28107	0.01867			0.00063	0.00007		0.31	1.9	3493
Wu et al 2023	SGB	18TGE01-1	TTG	18TGE01-1.2	2683			0.28118				0.00085	0.00002	-56.3	2.81	0.68	2983
Wu et al 2023	SGB	18TGE01-1	TTG	18TGE01-1.3	2683			0.28119				0.00051	0.00002	-55.9	3.83	0.61	2920
Wu et al 2023	SGB	18TGE01-1	TTG	18TGE01-1.4	2683			0.28111				0.00076	0.00002	-58.9	0.39	0.85	3130
Wu et al 2023	SGB	18TGE01-1	TTG	18TGE01-1.5	2683			0.28116				0.00070	0.00002	-57.2	2.18	0.71	3021
Wu et al 2023	SGB	18TGE01-1	TTG	18TGE01-1.7	2683			0.28111				0.00061	0.00002	-58.9	0.66	0.67	3113
Wu et al 2023	SGB	18TGE01-1	TTG	18TGE01-1.9	2683			0.28114				0.00067	0.00002	-57.8	1.68	0.64	3051
Wu et al 2023	SGB	18TGE01-1	TTG	18TGE01-1.10	2683			0.28110				0.00046	0.00002	-59.2	0.65	0.68	3114
Wu et al 2023	SGB	18TGE01-1	TTG	18TGE01-1.11	2683			0.28116				0.00079	0.00005	-57.1	2.09	1.78	3026
Wu et al 2023	SGB	18TGE01-1	TTG	18TGE01-1.12	2683			0.28111				0.00052	0.00002	-58.7	0.97	0.72	3095
Wu et al 2023	SGB	18TGE01-1	TTG	18TGE01-1.13	2683			0.28113				0.00045	0.00002	-57.9	1.91	0.61	3037
Wu et al 2023	SGB	18TGE01-1	TTG	18TGE01-1.15	2683			0.28115				0.00057	0.00002	-57.3	2.34	0.61	3011
Wu et al 2023	SGB	18TGE01-1	TTG	18TGE01-1.16	2683			0.28115				0.00063	0.00002	-57.6	1.95	0.57	3035
Wu et al 2023	SGB	18TGE01-1	TTG	18TGE01-1.19	2683			0.28114				0.00078	0.00002	-57.7	1.56	0.76	3059
Wu et al 2023	SGB	18TGE01-1	TTG	18TGE01-1.20	2683			0.28116				0.00058	0.00002	-57.1	2.50	0.57	3001
Wu et al 2023	SGB	18TGE01-1	TTG	18TGE01-1.21	2683			0.28117				*0.00052*	0.00002	-56.8	2.94	0.65	2975
Wu et al 2023	SGB	18TGE01-1	TTG	18TGE01-1.22	2683			0.28113				0.00062	0.00002	-58.1	1.43	0.8	3067
Wu et al 2023	SGB	18TGE01-1	TTG	18TGE01-1.24	2683			0.28109				0.00063	0.00002	-59.4	0.07	0.55	3149
Wu et al 2023	SGB	18TGE01-1	TTG	18TGE01-1.25	2683			0.28110				0.00048	0.00002	-59.3	0.47	0.69	3125
Wu et al 2023	SGB	18TGE01-1	TTG	18TGE01-1.26	2683			0.28122				0.00100	0.00002	-54.7	4.09	0.69	2905
Wu et al 2023	SGB	18TGE01-1	TTG	18TGE01-1.27	2683			0.28117				0.00057	0.00002	-56.8	2.83	0.56	2982
Wu et al 2023	SGB	18TGE01-1	TTG	18TGE01-1.30	2683			0.28112				0.00050	0.00002	-58.6	1.15	0.7	3084
Wu et al 2023	SGB	18TGE01-1	TTG	18TGE01-1.32	2683			0.28112				0.00059	0.00002	-58.3	1.28	0.59	3076

Reference	Location	Sample	Harmonized classification	Name	$^{207}Pb/^{206}Pb$ Age (Ma)	2SE	$^{176}Hf/^{177}Hf_{(i)}$	$^{176}Hf/^{177}Hf_{(t)}$	2SE	$^{176}Hf/^{177}Hf_{(i)}$	2SE	$^{176}Lu/^{177}Hf$	1SE	Ehfpd	$eHf_{(t)}$	2SE	T_{DM2}
Wu et al 2023	SGB	18TGE01-7	TTG	18TGE01-7.1	2708			0.28113				0.00069	0.00002	-58.1	0.68	1.27	3076
Wu et al 2023	SGB	18TGE01-7	TTG	18TGE01-7.2	2708			0.28115				0.00088	0.00002	-57.3	0.68	1.7	3050
Wu et al 2023	SGB	18TGE01-7	TTG	18TGE01-7.3	2708			0.28116				0.00079	0.00002	-57.0	0.84	2.2	3020
Wu et al 2023	SGB	18TGE01-7	TTG	18TGE01-7.4	2708			0.28121				0.00082	0.00003	-55.4	0.91	3.79	2923
Wu et al 2023	SGB	18TGE01-7	TTG	18TGE01-7.5	2708			0.28116				0.00074	0.00002	-56.9	0.75	2.38	3009
Wu et al 2023	SGB	18TGE01-7	TTG	18TGE01-7.6	2708			0.28115				0.00058	0.00002	-57.5	0.76	2.12	3025
Wu et al 2023	SGB	18TGE01-7	TTG	18TGE01-7.7	2708			0.28119				0.00072	0.00002	-56.0	0.66	3.37	2948
Wu et al 2023	SGB	18TGE01-7	TTG	18TGE01-7.8	2708			0.28116				0.00066	0.00002	-56.9	0.70	2.52	3000
Wu et al 2023	SGB	18TGE01-7	TTG	18TGE01-7.9	2708			0.28116				0.00093	0.00002	-57.0	0.70	1.91	3037
Wu et al 2023	SGB	18TGE01-7	TTG	18TGE01-7.10	2708			0.28119				0.00075	0.00002	-56.0	0.66	3.26	2955
Wu et al 2023	SGB	18TGE01-7	TTG	18TGE01-7.11	2708			0.28111				0.00075	0.00002	-58.9	0.63	0.36	3132
Wu et al 2023	SGB	18TGE01-7	TTG	18TGE01-7.12	2708			0.28115				0.00074	0.00002	-57.5	0.70	1.8	3044
Wu et al 2023	SGB	18TGE01-7	TTG	18TGE01-7.13	2708			0.28116				0.00079	0.00002	-56.9	0.68	2.31	3013
Wu et al 2023	SGB	18TGE01-7	TTG	18TGE01-7.14	2708			0.28117				0.00081	0.00002	-56.7	0.65	2.49	3002
Wu et al 2023	SGB	18TGE01-7	TTG	18TGE01-7.15	2708			0.28116				0.00077	0.00002	-57.1	0.59	2.2	3002
Wu et al 2023	SGB	18TGE01-7	TTG	18TGE01-7.16	2708			0.28114				0.00068	0.00002	-57.7	1.67	0.77	3052
Wu et al 2023	SGB	18TGE01-7	TTG	18TGE01-7.17	2708			0.28120				0.00094	0.00002	-55.6	3.34	0.64	2951
Wu et al 2023	SGB	18TGE01-7	TTG	18TGE01-7.18	2708			0.28114				0.00091	0.00003	-57.6	1.36	0.96	3071
Wu et al 2023	SGB	18TGE01-7	TTG	18TGE01-7.19	2708			0.28114				0.00086	0.00002	-57.9	1.18	0.65	3082
Wu et al 2023	SGB	18TGE01-7	TTG	18TGE01-7.20	2708			0.28114				0.00069	0.00002	-57.9	1.53	0.59	3060
Wu et al 2023	SGB	18TGE01-7	TTG	18TGE01-7.21	2708			0.28118				0.00070	0.00002	-56.4	2.98	0.63	2972
Wu et al 2023	SGB	18TGE01-7	TTG	18TGE01-7.22	2708			0.28114				0.00066	0.00002	-57.6	1.81	0.76	3043
Wu et al 2023	SGB	18TGE01-7	TTG	18TGE01-7.23	2708			0.28114				0.00069	0.00002	-57.9	1.54	0.74	3060
Wu et al 2023	SGB	18TGE01-7	TTG	18TGE01-7.24	2708			0.28116				0.00075	0.00002	-57.1	2.17	0.73	3022
Wu et al 2023	SGB	18TGE01-7	TTG	18TGE01-7.25	2708			0.28116				0.00077	0.00002	-57.1	2.20	0.6	3020
Wu et al 2023	SGB	18TGE01-7	TTG	18TGE01-7.26	2708			0.28113				0.00084	0.00002	-58.2	0.90	0.6	3099

Table SM2-6.3. Sm-Nd isotope composition of magmatic and detrital zircon from the Tanzania Craton and its surrounding mobile belts.

reference	Location	Sample	Harmonized classification	WR Sm-Nd isochron age	2SE	eNd(t)	1SE	TDM1	1SE	TDM2	1SE
Cloutier et al 2005	SGB	D0142-1	Sediment	2823	44	1.00					
Cloutier et al 2005	SGB	D0142-2	Sediment	2823	44	1.30					
Cloutier et al 2005	SGB	D0149-1	Sediment	2823	44	0.50					
Cloutier et al 2005	SGB	D0149-2	Sediment	2823	44	2.60					
Cloutier et al 2005	SGB	D0149-4	Sediment	2823	44	2.30					
Cloutier et al 2005	SGB	D0149-5	Sediment	2823	44	0.20					
Cloutier et al 2005	SGB	D0149-7	Sediment	2823	44	1.60					
Cloutier et al 2005	SGB	D0149-8	Sediment	2823	44	0.00					
Cloutier et al 2005	SGB	D0149-20	Sediment	2823	44	1.50					
Cloutier et al 2005	SGB	D0159-1	Sediment	2823	44	0.40					
Cloutier et al 2005	SGB	D0159-2	Sediment	2823	44	1.50					
Cloutier et al 2005	SGB	D0159-3	Sediment	2823	44	1.80					
Cloutier et al 2005	SGB	D0159-4	Sediment	2823	44	1.40					
Cloutier et al 2005	SGB	D0159-5	Sediment	2823	44	1.60					
Cloutier et al 2005	SGB	D0159-6	Sediment	2823	44	1.60					
Cloutier et al 2005	SGB	D0310-2	Sediment	2823	44	0.00					
Cloutier et al 2005	SGB	D0146-1	Mafic volcanic	2823	44	3.20					
Cloutier et al 2005	SGB	D0149-3	Mafic volcanic	2823	44	2.30					
Cloutier et al 2005	SGB	D0149-13	Mafic volcanic	2823	44	0.90					
Cloutier et al 2005	SGB	D0185-1	Mafic volcanic	2823	44	1.40					
Cloutier et al 2005	SGB	D0309-1	Mafic volcanic	2823	44	3.90					
Cloutier et al 2005	SGB	D0309-2	Mafic volcanic	2823	44	5.30					
Cloutier et al 2005	SGB	D0309-3	Mafic volcanic	2823	44	3.00					
Cloutier et al 2005	SGB	D0310-1	Granite-Monzonite	2543	15	3.90					
Cloutier et al 2005	SGB	D0310-3	Granite-Monzonite	2543	15	-0.70					
Cloutier et al 2005	SGB	D03I0-4	Granite-Monzonite	2543	15	5.80					
Cloutier et al 2005	SGB	D0310-1	Granite-Monzonite	2543	15	-12.60					
Cook et al 2016	SGB	IH8	Mafic volcanic	2819	18	2.17	0.83	3190			
Cook et al 2016	SGB	IHII	Mafic volcanic	2819	18	2.94	0.85	3037			
Cook et al 2016	SGB	K56	Mafic volcanic	2819	18	2.64	0.82	3050			
Cook et al 2016	SGB	K83	Mafic volcanic	2819	18	1.97	0.83	3275			
Cook et al 2016	SGB	K84	Mafic volcanic	2819	18	2.03	0.84	3367			
Cook et al 2016	SGB	KH3	Mafic volcanic	2819	18	2.93	0.84	3006			
Cook et al 2016	SGB	K82	Mafic volcanic	2819	18	2.41	0.86	3337			
Cook et al 2016	SGB	KH14	Mafic volcanic	2819	18	2.59	0.84	3142			
Maboko and Nakamura 1996	RTC	IRAI1	Granite-Monzonite	2611	58	-0.09	1.74	2950	26	2927	308
Maboko and Nakamura 1996	RTC	IRA12	Granite-Monzonite	2611	58	0.92	1.67	2832	19	2886	363
Maboko and Nakamura 1996	RTC	IRA14	Granite-Monzonite	2611	58	1.25	1.79	2873	31	2860	287
Maboko and Nakamura 1996	RTC	IRA17	Granite-Monzonite	2611	58	0.72	1.63	2821	14	2902	402
Maboko and Nakamura 1996	RTC	IRA19	Granite-Monzonite	2611	58	0.66	1.66	2845	16	2907	365
Maboko and Nakamura 1996	RTC	IRA24	Granite-Monzonite	2611	58	-3.62	1.65	3096	16	3249	375
Maboko and Nakamura 1996	RTC	IRA25	Granite-Monzonite	2611	58	2.13	1.79	2801	29	2789	282
Maboko et al 2006	SGB	R22	Granite-Monzonite	2620	30	1.57	0.89	2947	22	3012	209
Maboko et al 2006	SGB	R23	Granite-Monzonite	2620	30	0.87	0.92	2656	14	2670	229
Maboko et al 2006	SGB	R24	Granite-Monzonite	2620	30	0.46	0.91	2882	19	2948	212
Maboko et al 2006	SGB	R25	Granite-Monzonite	2620	30	1.99	0.88	2823	13	2919	236

reference	Location	Sample	Harmonized classification	WR Sm-Nd isochron age	2SE	eNd(t)	1SE	TDM1	1SE	TDM2	1SE
Maboko et al 2006	SGB	R63	Granite-Monzonite	2620	30	0.56	0.89	2848	16	2936	228
Maboko et al 2006	SGB	R2	TTG	2620	30	-0.56	0.91	2827	14	2925	238
Maboko et al 2006	SGB	R14	TTG	2620	30	3.71	0.86	2831	16	2906	225
Maboko et al 2006	SGB	R15	TTG	2620	30	0.23	0.89	2873	19	2941	216
Maboko et al 2006	SGB	R16	TTG	2620	30	0.61	0.85	2915	15	3036	227
Maboko et al 2006	SGB	R17	TTG	2620	30	0.38	0.87	2688	20	2700	208
Maboko et al 2006	SGB	R18	TTG	2620	30	0.53	0.85	2791	18	2841	219
Maboko et al 2006	SGB	R19	TTG	2620	30	0.76	0.87	2866	23	2897	202
Maboko et al 2006	SGB	ROO	TTG	2620	30	0.32	0.89	2881	22	2931	209
Maboko et al 2006	SGB	R21	TTG	2620	30	-0.86	0.86	2764	16	2808	216
Maboko et al 2006	SGB	R26	TTG	2620	30	3.34	0.91	2858	19	2922	217
Manya 2008	MMGB	TA11	Felsic volcanic					2975			
Manya 2008	MMGB	TA14	Felsic volcanic					3050			
Manya 2008	MMGB	TA15	Felsic volcanic					3393			
Manya 2008	MMGB	TA115	Felsic volcanic					2867			
Manya 2008	MMGB	TA113	Felsic volcanic					4015			
Manya 2011	RTC	IM01	Granite-Monzonite	2680	3	-0.17	0.39	3168	62	2997	167
Manya 2011	RTC	IM02	Granite-Monzonite	2680	3	-0.59	0.29	2954	22	2996	122
Manya 2011	RTC	IM03	Granite-Monzonite	2680	3	-0.42	0.30	2978	26	2990	128
Manya 2011	RTC	IM04	Granite-Monzonite	2680	3	-0.71	0.24	2926	16	2996	104
Manya 2011	RTC	IM05	Granite-Monzonite	2680	3	-0.79	0.25	2943	18	3007	106
Manya 2011	RTC	IM06	Granite-Monzonite	2680	3	-0.77	0.26	2943	18	3005	108
Manya 2011	RTC	IM07	Granite-Monzonite	2680	3	-0.32	0.28	2944	22	2976	120
Manya 2011	RTC	IM08	Granite-Monzonite	2680	3	-1.00	0.25	2954	18	3022	107
Manya 2011	RTC	IM09	Granite-Monzonite	2680	3	-1.14	0.40	3350	78	3078	172
Manya 2011	RTC	IMI0	Granite-Monzonite	2680	3	-0.45	0.30	2988	27	2994	128
Manya 2011	RTC	IMII	Granite-Monzonite	2680	3	-0.65	0.22	2897	13	2984	93
Manya 2011	RTC	IM12	Granite-Monzonite	2680	3	-0.24	0.29	2959	25	2975	125
Manya 2011	RTC	IM13	Granite-Monzonite	2680	3	-0.35	0.26	2926	19	2974	112
Manya 2011	RTC	IM14	Granite-Monzonite	2680	3	0.24	0.22	2843	12	2912	91
Manya 2011	RTC	IM15	Granite-Monzonite	2680	3	-3.67	0.27	3159	23	3241	116
Manya 2011	RTC	IM16	Granite-Monzonite	2680	3	0.08	0.24	2876	16	2933	102
Manya 2011	RTC	IM17	Granite-Monzonite	2680	3	-1.04	0.27	2974	20	3030	113
Manya 2011	RTC	IM18	Granite-Monzonite	2680	3	1.71	0.31	2826	27	2824	132
Manya and Maboko 2003	SGB	R06	Mafic volcanic	2823	44	2.26	1.66				
Manya and Maboko 2003	SGB	R07	Mafic volcanic	2823	44	2.63	1.68				
Manya and Maboko 2003	SGB	R09	Mafic volcanic	2823	44	2.49	1.65	3259	150	2935	228
Manya and Maboko 2003	SGB	RIO	Mafic volcanic	2823	44	2.70	1.61	3101	139	2918	222
Manya and Maboko 2003	SGB	Ril	Mafic volcanic	2823	44	2.74	1.65	3180	140	2915	228
Manya and Maboko 2003	SGB	R13	Mafic volcanic	2823	44	2.20	1.79				
Manya and Maboko 2003	SGB	R38	Mafic volcanic	2823	44	2.97	1.71				
Manya and Maboko 2003	SGB	R39	Mafic volcanic	2823	44	2.78	1.69				
Manya and Maboko 2003	SGB	R40	Mafic volcanic	2823	44	3.60	1.65	2911	136	2847	229
Manya and Maboko 2003	SGB	R41	Mafic volcanic	2823	44	2.52	3.36				
Manya and Maboko 2003	SGB	R42	Mafic volcanic	2823	44	2.56	1.73				
Manya and Maboko 2008a	ISGB	SIN02	Mafic volcanic	2742	27	2.65	1.13				
Manya and Maboko 2008a	ISGB	SIN07a	Mafic volcanic	2742	27	1.85	1.16				

reference	Location	Sample	Harmonized classification	WR Sm-Nd isochron age	2SE	eNd(t)	1SE	TDM1	1SE	TDM2	1SE
Manya and Maboko 2008a	ISGB	SIN08	Mafic volcanic	2742	27	2.17	1.10				
Manya and Maboko 2008a	ISGB	SIN17	Mafic volcanic	2742	27	2.52	1.09				
Manya and Maboko 2008a	ISGB	SIN18	Mafic volcanic	2742	27	2.18	1.09				
Manya and Maboko 2008a	ISGB	SIN27	Mafic volcanic	2742	27	2.54	0.81	2834	19	2865	218
Manya and Maboko 2008a	ISGB	SIN06	Felsic volcanic	2742	27	1.71	0.84	2915	23	2931	186
Manya and Maboko 2008a	ISGB	SIN30	Felsic volcanic	2742	27	2.08	0.80	2863	16	2901	203
Manya and Maboko 2008b	SGB	GT06	Mafic volcanic	2821	19	2.35	0.83	3265	143	2944	219
Manya and Maboko 2008b	SGB	GT07	Mafic volcanic	2821	19	2.53	0.83	3193	138	2930	217
Manya and Maboko 2008b	SGB	GTII	Mafic volcanic	2821	19	2.57	0.83	3158	147	2927	219
Manya and Maboko 2008b	SGB	GT14	Mafic volcanic	2821	19	2.58	0.84	3185	174	2926	229
Manya and Maboko 2008b	SGB	GT16	Mafic volcanic	2821	19	2.28	0.83	3233	162	2950	219
Manya et al 2007a	MMGB	TA21	Felsic volcanic	2669	9	1.27	0.43	2891	29	2906	156
Manya et al 2007a	MMGB	TA23	Felsic volcanic	2669	9	1.57	0.41	2865	26	2882	146
Manya et al 2007a	MMGB	TA26	Felsic volcanic	2673	8	0.44	0.45	2981	37	2975	171
Manya et al 2007a	MMGB	TA28	Felsic volcanic	2669	9	1.09	0.42	2899	28	2921	154
Manya et al 2007a	MMGB	TA96	Felsic volcanic	2676	12	1.81	0.45	2841	22	2868	144
Manya et al 2007a	MMGB	TA35	Felsic volcanic	2668	30	1.01	0.92	2894	24	2926	209
Manya et al 2007a	MMGB	TA65	Felsic volcanic	2668	30	1.39	0.90	2853	21	2896	217
Manya et al 2007a	MMGB	TA69	Felsic volcanic	2668	30	2.67	0.88	2760	19	2793	236
Manya et al 2007a	MMGB	TA72	Felsic volcanic	2668	30	1.66	0.88	2816	18	2874	238
Manya et al 2007a	MMGB	TA99	Felsic volcanic	2667	8	1.50	0.37	2860	23	2886	137
Manya et al 2007a	MMGB	TA105	Felsic volcanic	2667	8	1.18	0.42	2917	33	2911	157
Manya et al 2007a	MMGB	TA107	Felsic volcanic	2667	8	1.36	0.37	2863	23	2897	138
Manya et al 2007a	MMGB	TA108	Felsic volcanic	2667	8	1.21	0.39	2884	26	2909	147
Manya et al 2007a	MMGB	TA43	TTG	2668	11	1.72	0.44	2841	24	2869	150
Manya et al 2007a	MMGB	TA47	TTG	2668	11	1.47	0.41	2842	19	2889	135
Manya et al 2007a	MMGB	TA79	TTG	2668	11	1.91	0.42	2821	21	2854	142
Manya et al 2007b	MMGB	TA29	Granite-Monzonite	2649	36	1.70	1.06	2813	20	2855	249
Manya et al 2007b	MMGB	TAB	Granite-Monzonite	2649	36	1.50	1.29	3080	96	2871	213
Manya et al 2007b	MMGB	TA87	Granite-Monzonite	2649	36	0.69	1.11	2919	28	2936	226
Manya et al 2007b	MMGB	TA95	Granite-Monzonite	2649	36	0.54	1.05	2876	19	2948	259
Manya 2016a	NGB	BZ-08	Granite-Monzonite	2674	18	1.19		2855			
Manya 2016a	NGB	BZ-11	Granite-Monzonite	2674	18	1.22		2855			
Manya 2016a	NGB	BZ-23	Granite-Monzonite	2713	8	1.19		2949			
Manya 2016a	NGB	BZ-24	Granite-Monzonite	2713	8	1.77		2885			
Messo et al 2012	KGB	MU14	Mafic volcanic	2712	5	2.20	0.51	2962±80	2867±216		
Messo et al 2012	KGB	MU69	Mafic volcanic	2712	5	1.90	0.60				
Messo et al 2012	KGB	MU49	Felsic volcanic	2712	5	1.82	0.45	2913±44	2898±192		
Messo et al 2012	KGB	MU57	Felsic volcanic	2712	5	2.02	0.46	2897±45	2881±193		
Messo et al 2012	KGB	MU68	Felsic volcanic	2712	5	2.48	0.43	2835±34	2845±182		
Messo et al 2012	KGB	MU89	Felsic volcanic	2712	5	1.86	0.46	2912±45	2894±193		
Messo et al 2012	KGB	MU100	Felsic volcanic	2712	5	1.57	0.47	2958±52	2917±199		
Messo et al 2012	KGB	MU16	Felsic volcanic	2712	5	5.13	0.55	2529±107	2632±234		
Messo et al 2012	KGB	MU17	Felsic volcanic	2712	5	-0.47	0.57	3877±336	3079±240		
Mtoro et al 2009	MMGB	S14	Mafic volcanic	2755	1	2.13	0.52				
Mtoro et al 2009	MMGB	S18	Mafic volcanic	2755	1	2.11	0.52				
Mtoro et al 2009	MMGB	S143	Mafic volcanic	2755	1	1.75	0.51				

reference	Location	Sample	Harmonized classification	WR Sm-Nd isochron age	2SE	eNd(t)	1SE	TDM1	1SE	TDM2	1SE
Mtoro et al 2009	MMGB	S60	Felsic volcanic	2755	1	1.94	0.31	2919	27	2923	137
Mtoro et al 2009	MMGB	S03A	Felsic volcanic	2755	1	2.04	0.29	2893	22	2914	128
Mtoro et al 2009	MMGB	S19	Felsic volcanic	2755	1	2.10	0.29	2901	24	2910	129
Mtoro et al 2009	MMGB	S59	Felsic volcanic	2755	1	2.32	0.26	2863	18	2892	117
Mtoro et al 2009	MMGB	S65B	Felsic volcanic	2755	1	2.10	0.32	2885	24	2910	142
Mtoro et al 2009	MMGB	S131	Felsic volcanic	2755	1	2.00	0.25	2887	18	2918	111
Thomas et al 2016	RTC	FMP484	Mafic volcanic	2750		3.20	0.2			2761	
Wu et al 2023	SGB	18TGE01	TTG	2683	16	1.85	0.24	2850		2886	

Supplementary Material 4-1

Multiple-sulfur isotope analyses

			Drift corrected or raw ratios if no drift									Final Results			
Analysis Name	**Stage**	**Alteration zone**	**32S**	**33S**	**34S**	**33S/32S**	**S abs**	**36S/32S**	**S abs**	**$\delta^{33}S$**	**2σ**	**$\delta^{34}S$**	**2σ**	**$\Delta^{33}S$**	**2σ**
NY53_20															
1_1	D1a	Disseminated Py1a bands	1.01E+09	8.04E+06	4.60E+07	5.33	0.03	9.22	0.01	4.07	0.09	7.85	0.07	0.03	0.14
1_2	D1a	Disseminated Py1a bands	1.00E+09	8.00E+06	4.59E+07	9.01	0.03	16.40	0.01	7.74	0.08	15.03	0.07	0.03	0.08
1_3	D1a	Disseminated Py1a bands	1.00E+09	8.01E+06	4.61E+07	12.67	0.03	23.70	0.01	11.41	0.09	22.33	0.08	-0.03	0.09
1_4	D1a	Disseminated Py1a bands	9.84E+08	7.85E+06	4.50E+07	8.23	0.05	14.95	0.01	6.96	0.11	13.58	0.08	-0.01	0.11
1_5	D1a	Disseminated Py1a bands	1.01E+09	8.04E+06	4.61E+07	7.23	0.05	12.83	0.01	5.97	0.11	11.46	0.08	0.08	0.11
1_6	D1a	Disseminated Py1a bands	9.90E+08	7.90E+06	4.54E+07	9.69	0.05	17.75	0.04	8.42	0.11	16.38	0.11	0.02	0.11
1_7	D1a	Disseminated Py1a bands	9.72E+08	7.74E+06	4.43E+07	6.95	0.04	12.72	0.02	5.68	0.10	11.35	0.08	-0.15	0.10
1_9	D1a	Disseminated Py1a bands	9.95E+08	7.92E+06	4.53E+07	5.99	0.04	10.70	0.01	4.72	0.09	9.33	0.07	-0.07	0.09
1_9	D1a	Disseminated Py1a bands	9.95E+08	7.92E+06	4.53E+07	5.99	0.04	10.70	0.01	4.72	0.09	9.33	0.07	-0.07	0.09
1_10	D1a	Disseminated Py1a bands	9.93E+08	7.92E+06	4.54E+07	8.68	0.03	15.74	0.01	7.42	0.08	14.37	0.08	0.04	0.08
2_1	D1a	Disseminated Py1a bands	1.00E+09	7.97E+06	4.56E+07	6.38	0.03	11.26	0.01	5.11	0.09	9.89	0.07	0.03	0.09
2_2	D1a	Disseminated Py1a bands	9.66E+08	7.68E+06	4.39E+07	5.25	0.04	9.25	0.01	3.98	0.09	7.88	0.08	-0.07	0.09
2_3	D1a	Disseminated Py1a bands	9.81E+08	7.82E+06	4.47E+07	7.08	0.04	12.36	0.02	5.81	0.10	10.99	0.08	0.17	0.10
2_4	D1a	Disseminated Py1a bands	1.01E+09	8.08E+06	4.63E+07	6.82	0.04	12.06	0.02	5.55	0.09	10.69	0.08	0.06	0.09
2_5	D1a	Disseminated Py1a bands	1.02E+09	8.06E+06	4.60E+07	3.98	0.03	6.65	0.01	2.71	0.08	5.28	0.07	-0.01	0.08
2_6	D1a	Disseminated Py1a bands	9.88E+08	7.87E+06	4.51E+07	7.51	0.04	13.86	0.01	6.24	0.10	12.49	0.08	-0.18	0.10
2_7	D1a	Disseminated Py1a bands	1.01E+09	8.06E+06	4.63E+07	10.91	0.04	20.05	0.02	9.64	0.09	18.68	0.08	0.06	0.09
2_8	D1a	Disseminated Py1a bands	1.00E+09	8.00E+06	4.58E+07	6.75	0.04	12.27	0.01	5.49	0.10	10.90	0.07	-0.11	0.10
2_9	D1a	Disseminated Py1a bands	1.00E+09	7.95E+06	4.55E+07	6.08	0.04	10.61	0.01	4.81	0.09	9.24	0.07	0.06	0.09
2_10	D1a	Disseminated Py1a bands	1.01E+09	8.00E+06	4.58E+07	6.45	0.03	11.51	0.02	5.18	0.08	10.14	0.08	-0.03	0.08
3_1	D1b	Py1b overgrowths around Py1a	1.01E+09	8.04E+06	4.60E+07	6.83	0.04	12.16	0.01	5.57	0.09	10.79	0.07	0.02	0.09
3_02	D1b	Py1b overgrowths around Py1a	1.02E+09	8.08E+06	4.63E+07	6.75	0.04	12.15	0.01	5.49	0.10	10.78	0.07	-0.05	0.10
3_03	D1b	Py1b overgrowths around Py1a	1.01E+09	8.01E+06	4.59E+07	6.91	0.04	12.34	0.01	5.64	0.10	10.97	0.08	0.01	0.10
3_04	D1b	Py1b overgrowths around Py1a	1.01E+09	8.08E+06	4.63E+07	7.04	0.04	12.52	0.01	5.78	0.10	11.14	0.08	0.05	0.10
3_05	D1b	Py1b overgrowths around Py1a	1.01E+09	8.08E+06	4.63E+07	7.07	0.04	12.62	0.01	5.81	0.09	11.25	0.07	0.03	0.09
3_06	D1b	Py1b overgrowths around Py1a	9.95E+08	7.93E+06	4.54E+07	7.13	0.07	12.59	0.01	5.87	0.15	11.22	0.07	0.11	0.15
3_07	D1b	Py1b overgrowths around Py1a	1.01E+09	8.04E+06	4.60E+07	7.04	0.03	12.47	0.01	5.77	0.08	11.10	0.07	0.07	0.08
3_08	D1b	Py1b overgrowths around Py1a	1.01E+09	8.04E+06	4.61E+07	7.95	0.05	14.35	0.01	6.68	0.11	12.97	0.07	0.02	0.11
3_09	D1b	Py1b overgrowths around Py1a	1.01E+09	8.03E+06	4.59E+07	6.81	0.05	12.22	0.01	5.54	0.11	10.85	0.07	-0.03	0.11
3_10	D1b	Py1b overgrowths around Py1a	1.02E+09	8.10E+06	4.64E+07	6.97	0.03	12.50	0.01	5.70	0.09	11.13	0.07	-0.01	0.09
3_11	D1b	Py1b overgrowths around Py1a	9.95E+08	7.93E+06	4.54E+07	7.21	0.03	12.94	0.01	5.94	0.09	11.57	0.07	0.00	0.09
3_12	D1b	Py1b overgrowths around Py1a	1.01E+09	8.03E+06	4.60E+07	7.00	0.03	12.46	0.01	5.73	0.09	11.09	0.07	0.03	0.09
3_13	D1b	Py1b overgrowths around Py1a	1.01E+09	8.06E+06	4.62E+07	7.15	0.03	12.69	0.01	5.89	0.09	11.32	0.07	0.07	0.09
3_14	D1b	Py1b overgrowths around Py1a	1.02E+09	8.13E+06	4.65E+07	7.52	0.03	13.35	0.01	6.26	0.08	11.98	0.07	0.10	0.08
3_15	D1b	Py1b overgrowths around Py1a	1.02E+09	8.12E+06	4.65E+07	7.16	0.04	12.80	0.01	5.89	0.09	11.43	0.07	0.02	0.09
3_16	D1b	Py1b overgrowths around Py1a	1.01E+09	8.05E+06	4.61E+07	7.11	0.05	12.65	0.01	5.84	0.11	11.28	0.07	0.05	0.11
3_17	D1b	Py1b overgrowths around Py1a	1.00E+09	8.00E+06	4.58E+07	7.13	0.04	12.69	0.01	5.86	0.10	11.31	0.07	0.05	0.10
3_18	D1b	Py1b overgrowths around Py1a	1.01E+09	8.02E+06	4.59E+07	6.92	0.04	12.53	0.01	5.65	0.10	11.16	0.07	-0.08	0.10
3_19	D1a	Py1b overgrowths around Py1a	9.21E+08	7.32E+06	4.18E+07	4.95	0.05	8.19	0.02	3.68	0.11	6.82	0.08	0.17	0.11
3_20	D1a	Py1b overgrowths around Py1a	1.01E+09	8.03E+06	4.60E+07	7.07	0.04	12.40	0.01	5.80	0.10	11.03	0.08	0.13	0.10
NY53_01															
1_1	D1a	Disseminated Py1a bands	1.06E+09	8.46E+06	4.84E+07	5.76	0.04	10.17	0.01	4.50	0.09	8.80	0.07	-0.03	0.09
1_02	D1a	Disseminated Py1a bands	1.04E+09	8.27E+06	4.72E+07	5.20	0.04	8.94	0.01	3.93	0.10	7.57	0.07	0.04	0.10
1_03	D1a	Disseminated Py1a bands	1.02E+09	8.12E+06	4.64E+07	5.32	0.06	9.25	0.01	4.05	0.13	7.87	0.08	0.00	0.13
1_04	D1a	Disseminated Py1a bands	9.49E+08	7.58E+06	4.35E+07	10.20	0.04	18.97	0.01	8.93	0.10	17.59	0.07	-0.09	0.10

1_05	D1a	Disseminated Py1a bands	1.01E+09	8.09E+06	4.63E+07	8.26	0.04	15.06	0.01	6.99	0.10	13.69	0.07	-0.04	0.10
1_06	D1a	Disseminated Py1a bands	9.90E+08	7.88E+06	4.52E+07	7.34	0.04	13.01	0.01	6.07	0.09	11.64	0.07	0.09	0.09
1_07	D1a	Disseminated Py1a bands	9.93E+08	7.92E+06	4.55E+07	9.04	0.04	16.73	0.01	7.77	0.10	15.36	0.07	-0.11	0.10
1_08	D1a	Disseminated Py1a bands	8.59E+08	6.85E+06	3.93E+07	9.12	0.04	16.67	0.01	7.85	0.10	15.30	0.08	0.00	0.10
1_09	D1a	Disseminated Py1a bands	9.80E+08	7.85E+06	4.52E+07	12.80	0.04	24.09	0.02	11.53	0.09	22.72	0.09	-0.10	0.09
1_10	D1a	Disseminated Py1a bands	9.87E+08	7.88E+06	4.52E+07	9.08	0.03	16.58	0.01	7.82	0.09	15.21	0.08	0.01	0.09
1_11	D1a	Disseminated Py1a bands	1.00E+09	7.99E+06	4.58E+07	9.30	0.04	16.94	0.02	8.03	0.09	15.57	0.08	0.05	0.09
1_12	D1a	Disseminated Py1a bands	1.00E+09	8.02E+06	4.61E+07	10.98	0.04	20.57	0.01	9.71	0.09	19.20	0.07	-0.13	0.09
1_13	D1a	Disseminated Py1a bands	1.01E+09	8.02E+06	4.59E+07	5.77	0.03	10.14	0.03	4.50	0.08	8.77	0.09	-0.01	0.08
1_14	D1a	Disseminated Py1a bands	7.36E+08	5.84E+06	3.34E+07	4.88	0.05	8.66	0.02	3.61	0.12	7.29	0.08	-0.13	0.12
1_15	D1a	Disseminated Py1a bands	9.99E+08	7.94E+06	4.54E+07	5.72	0.04	9.99	0.01	4.46	0.11	8.62	0.07	0.03	0.11
2_1	D1b	Py1b overgrowths around Py1a	1.01E+09	8.03E+06	4.59E+07	5.21	0.03	9.10	0.01	3.95	0.09	7.73	0.07	-0.03	0.09
2_02	D1b	Py1b overgrowths around Py1a	1.01E+09	8.05E+06	4.59E+07	4.13	0.04	7.01	0.01	2.86	0.10	5.64	0.07	-0.04	0.10
2_03	D1b	Py1b overgrowths around Py1a	1.01E+09	8.02E+06	4.59E+07	5.21	0.04	9.15	0.01	3.94	0.09	7.78	0.07	-0.06	0.09
2_04	D1b	Py1b overgrowths around Py1a	1.00E+09	7.95E+06	4.55E+07	5.60	0.04	9.84	0.01	4.33	0.10	8.47	0.08	-0.02	0.10
2_05	D1b	Py1b overgrowths around Py1a	1.00E+09	7.98E+06	4.56E+07	6.51	0.05	11.42	0.01	5.24	0.12	10.05	0.07	0.08	0.12
2_06	D1b	Py1b overgrowths around Py1a	1.01E+09	8.00E+06	4.57E+07	5.43	0.06	9.31	0.01	4.16	0.14	7.94	0.07	0.08	0.14
2_07	D1b	Py1b overgrowths around Py1a	1.01E+09	8.01E+06	4.58E+07	5.65	0.05	9.83	0.01	4.38	0.12	8.46	0.07	0.04	0.12
2_08	D1b	Py1b overgrowths around Py1a	9.84E+08	7.82E+06	4.47E+07	5.42	0.04	9.38	0.01	4.15	0.10	8.00	0.08	0.04	0.10
2_09	D1b	Py1b overgrowths around Py1a	1.00E+09	7.97E+06	4.56E+07	5.55	0.03	9.60	0.01	4.28	0.09	8.23	0.07	0.05	0.09
2_10	D1b	Py1b overgrowths around Py1a	1.01E+09	8.02E+06	4.59E+07	5.40	0.05	9.42	0.01	4.13	0.11	8.05	0.08	-0.01	0.11
2_11	D1b	Py1b overgrowths around Py1a	1.01E+09	8.05E+06	4.60E+07	5.52	0.03	9.49	0.01	4.25	0.08	8.12	0.07	0.08	0.08
2_12	D1a	Py1b overgrowths around Py1a	9.89E+08	7.84E+06	4.47E+07	2.46	0.05	3.72	0.01	1.19	0.11	2.35	0.07	-0.02	0.11
2_13	D1a	Py1b overgrowths around Py1a	9.81E+08	7.78E+06	4.44E+07	2.77	0.04	4.14	0.01	1.51	0.10	2.77	0.07	0.08	0.10
2_14	D1b	Py1b overgrowths around Py1a	9.91E+08	7.88E+06	4.51E+07	5.42	0.03	9.30	0.01	4.15	0.08	7.93	0.07	0.08	0.08
2_15	D1b	Py1b overgrowths around Py1a	9.96E+08	7.92E+06	4.53E+07	5.37	0.03	9.30	0.01	4.11	0.09	7.93	0.08	0.03	0.09
_1	D1c	Py-Po-dominated vein	9.97E+08	7.94E+06	4.54E+07	6.40	0.04	11.38	0.01	5.13	0.10	10.01	0.07	-0.01	0.10
_02	D1c	Py-Po-dominated vein	1.00E+09	7.97E+06	4.56E+07	6.39	0.04	11.37	0.01	5.12	0.10	10.00	0.07	-0.01	0.10
_03	D1c	Py-Po-dominated vein	9.95E+08	7.92E+06	4.53E+07	6.49	0.07	11.51	0.01	5.22	0.15	10.14	0.07	0.02	0.15
_04	D1c	Py-Po-dominated vein	9.86E+08	7.85E+06	4.49E+07	6.44	0.04	11.43	0.01	5.17	0.09	10.06	0.07	0.00	0.09
_05	D1c	Py-Po-dominated vein	9.88E+08	7.87E+06	4.50E+07	6.61	0.04	11.57	0.01	5.35	0.10	10.20	0.07	0.11	0.10
_06	D1c	Py-Po-dominated vein	9.89E+08	7.87E+06	4.51E+07	6.38	0.06	11.54	0.01	5.12	0.13	10.17	0.07	-0.11	0.13
_07	D1c	Py-Po-dominated vein	1.00E+09	7.97E+06	4.56E+07	6.40	0.03	11.37	0.01	5.13	0.08	10.00	0.07	-0.01	0.08
_08	D1c	Py-Po-dominated vein	1.00E+09	7.96E+06	4.55E+07	6.50	0.04	11.56	0.01	5.23	0.10	10.19	0.07	0.00	0.10
_09	D1c	Py-Po-dominated vein	9.92E+08	7.89E+06	4.52E+07	6.33	0.04	11.21	0.01	5.06	0.10	9.84	0.07	0.01	0.10
_10	D1c	Py-Po-dominated vein	1.00E+09	7.96E+06	4.56E+07	6.41	0.04	11.42	0.01	5.14	0.10	10.05	0.08	-0.02	0.10
_11	D1c	Py-Po-dominated vein	1.00E+09	7.99E+06	4.57E+07	6.55	0.03	11.59	0.01	5.29	0.09	10.22	0.07	0.04	0.09
_12	D1c	Py-Po-dominated vein	1.00E+09	7.98E+06	4.57E+07	6.44	0.04	11.64	0.01	5.17	0.10	10.26	0.07	-0.11	0.10
_13	D1c	Py-Po-dominated vein	9.89E+08	7.87E+06	4.50E+07	6.53	0.04	11.58	0.01	5.26	0.09	10.21	0.08	0.01	0.09
_14	D1c	Py-Po-dominated vein	8.61E+08	6.85E+06	3.92E+07	6.26	0.04	11.15	0.02	4.99	0.09	9.78	0.08	-0.03	0.09
_15	D1c	Py-Po-dominated vein	9.90E+08	7.88E+06	4.51E+07	6.70	0.03	11.76	0.01	5.43	0.09	10.39	0.08	0.09	0.09
_16	D1c	Py-Po-dominated vein	9.85E+08	7.84E+06	4.49E+07	6.62	0.04	11.94	0.01	5.35	0.10	10.57	0.07	-0.08	0.10
_17	D1c	Py-Po-dominated vein	9.70E+08	7.72E+06	4.42E+07	6.69	0.03	11.94	0.01	5.43	0.08	10.57	0.08	0.00	0.08
_18	D1c	Py-Po-dominated vein	9.49E+08	7.55E+06	4.32E+07	6.72	0.04	12.07	0.01	5.45	0.10	10.70	0.08	-0.05	0.10
_19	D1c	Py-Po-dominated vein	9.53E+08	7.59E+06	4.35E+07	7.33	0.04	13.08	0.01	6.07	0.10	11.71	0.08	0.05	0.10
_20	D1c	Py-Po-dominated vein	9.37E+08	7.46E+06	4.27E+07	6.89	0.04	12.36	0.01	5.62	0.10	10.99	0.07	-0.02	0.10

NY278_07

1_1	D1c	Ga-bearing vein	9.24E+08	7.33E+06	4.19E+07	3.65	0.03	6.03	0.01	2.39	0.08	4.66	0.07	-0.01	0.08
1_2	D1c	Ga-bearing vein	8.79E+08	6.97E+06	3.98E+07	3.50	0.05	5.87	0.02	2.23	0.11	4.50	0.08	-0.08	0.11
1_3	D1c	Ga-bearing vein	9.35E+08	7.42E+06	4.24E+07	3.69	0.03	6.22	0.01	2.42	0.08	4.84	0.07	-0.07	0.08
1_4	D1c	Ga-bearing vein	9.13E+08	7.24E+06	4.14E+07	3.74	0.04	6.24	0.01	2.47	0.09	4.86	0.07	-0.03	0.09
1_5	D1c	Ga-bearing vein	9.05E+08	7.18E+06	4.10E+07	3.99	0.05	6.65	0.01	2.72	0.12	5.28	0.08	0.01	0.12
1_6	D1c	Ga-bearing vein	9.01E+08	7.15E+06	4.08E+07	4.04	0.04	6.81	0.01	2.77	0.10	5.44	0.07	-0.03	0.10
1_7	D1c	Ga-bearing vein	9.24E+08	7.33E+06	4.19E+07	3.96	0.04	6.75	0.01	2.70	0.11	5.38	0.07	-0.07	0.11
1_8	D1c	Ga-bearing vein	9.00E+08	7.14E+06	4.08E+07	3.93	0.04	6.62	0.01	2.66	0.10	5.25	0.08	-0.04	0.10
1_9	D1c	Ga-bearing vein	8.87E+08	7.04E+06	4.02E+07	4.10	0.04	6.70	0.01	2.83	0.10	5.33	0.07	0.09	0.10
1_10	D1c	Ga-bearing vein	8.63E+08	6.84E+06	3.91E+07	3.84	0.05	6.39	0.01	2.57	0.12	5.02	0.08	-0.01	0.12
2_1	D1c	Ga-bearing vein	9.27E+08	7.36E+06	4.20E+07	3.97	0.03	6.52	0.01	2.70	0.09	5.15	0.07	0.05	0.09
2_2	D1c	Ga-bearing vein	8.88E+08	7.05E+06	4.03E+07	4.25	0.03	6.97	0.01	2.98	0.08	5.60	0.07	0.10	0.08
2_3	D1c	Ga-bearing vein	9.24E+08	7.33E+06	4.19E+07	3.84	0.04	6.52	0.01	2.58	0.09	5.15	0.08	-0.07	0.09
03_1	D1c	Ga-bearing vein	9.62E+08	7.64E+06	4.36E+07	3.87	0.04	6.54	0.01	2.60	0.09	5.17	0.07	-0.05	0.09
03_2	D1c	Ga-bearing vein	9.02E+08	7.15E+06	4.09E+07	4.10	0.04	6.93	0.01	2.83	0.10	5.55	0.07	-0.02	0.10
03_3	D1c	Ga-bearing vein	9.36E+08	7.42E+06	4.24E+07	3.74	0.04	6.10	0.01	2.48	0.10	4.73	0.08	0.04	0.10
03_4	D1c	Ga-bearing vein	9.37E+08	7.43E+06	4.25E+07	3.88	0.04	6.51	0.01	2.61	0.10	5.14	0.07	-0.03	0.10
03_5	D1c	Ga-bearing vein	9.61E+08	7.63E+06	4.36E+07	4.04	0.04	6.84	0.01	2.77	0.10	5.47	0.07	-0.04	0.10
03_6	D1c	Ga-bearing vein	9.52E+08	7.56E+06	4.32E+07	4.00	0.04	6.70	0.01	2.73	0.10	5.33	0.07	-0.01	0.10
03_7	D1c	Ga-bearing vein	8.95E+08	7.10E+06	4.06E+07	3.84	0.05	6.19	0.01	2.58	0.11	4.82	0.07	0.10	0.11
03_8			*9.19E+08*	*7.26E+06*	*4.13E+07*	*-0.07*	*0.03*	*-1.29*	*0.01*	*-1.33*	*0.09*	*-2.66*	*0.07*	*0.04*	*0.09*
03_9	D1c	Ga-bearing vein	9.28E+08	7.37E+06	4.21E+07	4.08	0.05	6.78	0.01	2.81	0.12	5.41	0.08	0.03	0.12
04_1	D1c	Ga-bearing vein	9.26E+08	7.35E+06	4.20E+07	4.34	0.03	7.21	0.01	3.07	0.09	5.83	0.08	0.07	0.09
04_2	D1c	Ga-bearing vein	8.84E+08	7.01E+06	4.01E+07	4.25	0.05	7.14	0.01	2.99	0.11	5.77	0.08	0.02	0.11
04_3	D1c	Ga-bearing vein	9.14E+08	7.26E+06	4.15E+07	4.13	0.04	6.88	0.01	2.86	0.10	5.51	0.08	0.02	0.10
04_4	D1c	Ga-bearing vein	9.08E+08	7.21E+06	4.12E+07	4.18	0.04	7.00	0.01	2.91	0.09	5.62	0.08	0.02	0.09
04_5	D1c	Ga-bearing vein	9.17E+08	7.28E+06	4.16E+07	4.24	0.05	7.11	0.01	2.97	0.11	5.74	0.07	0.02	0.11
Galene_3			4.61E+08	3.57E+06	2.02E+07	-11.83	0.09	-24.38	0.10						
Galene_4			4.55E+08	3.52E+06	2.00E+07	-12.06	0.08	-24.74	0.11						
Galene_5			4.68E+08	3.63E+06	2.05E+07	-12.60	0.09	-25.12	0.07						
Spain-Py_1			9.72E+08	7.68E+06	4.37E+07	-0.43	0.03	-1.76	0.01						
Spain-Py_2			9.67E+08	7.64E+06	4.35E+07	-0.48	0.03	-1.83	0.01						
Spain-Py_3			9.66E+08	7.64E+06	4.34E+07	-0.38	0.03	-1.75	0.01						
Spain-Py_4			9.43E+08	7.45E+06	4.24E+07	-0.34	0.04	-1.69	0.02						
Spain-Py_7			9.36E+08	7.40E+06	4.21E+07	-0.27	0.03	-1.69	0.01						
Spain-Py_8			9.94E+08	7.86E+06	4.47E+07	-0.14	0.04	-1.38	0.01						
Spain-Py_9			8.68E+08	6.86E+06	3.90E+07	-0.29	0.04	-1.72	0.01						
Spain-Py_10			9.84E+08	7.78E+06	4.43E+07	-0.19	0.05	-1.45	0.01						
Spain-Py_11			1.00E+09	7.92E+06	4.51E+07	-0.09	0.03	-1.49	0.01						
Spain-Py_12			9.95E+08	7.87E+06	4.47E+07	-0.24	0.05	-1.51	0.01						
Spain-Py_13			1.07E+09	8.45E+06	4.80E+07	-0.24	0.03	-1.60	0.01						
Spain-Py_14			1.06E+09	8.41E+06	4.78E+07	-0.16	0.04	-1.44	0.01						
Spain-Py_15			1.06E+09	8.37E+06	4.76E+07	-0.26	0.04	-1.46	0.01						
Spain-Py_16			1.06E+09	8.37E+06	4.76E+07	-0.19	0.03	-1.56	0.01						
Spain-Py_17			1.07E+09	8.46E+06	4.81E+07	-0.14	0.03	-1.46	0.01						
Spain-Py_18			1.07E+09	8.47E+06	4.82E+07	-0.20	0.04	-1.48	0.01						

Supplementary Material 5-1

Matlab 3D-modeling of fold interference patterns

The interference of two folding stages appears to be at the heart of the structural complexity observed within the studied area. In fact, it appears that curving of the F_{1a} axial planes during the F_{1b} folding resulted in a multitude of apparent fold orientations and has overprinted the initial orientation of the F_{1a} folds and obscured the D_{1a} strain ellipsoid orientation. However, the use of 3D numerical modeling of refolding stages can provide insights into the initial orientation of the F_{1a} fold, by considering the final geometry of the folded volcanosediments at the two deposits and the known final orientation of the F_{1b} folds.

A Matlab script was used to model 3D iso-surfaces affected by two successive folding events. The script was kindly provided by Dr M. Schöpfer and is available online (Schöpfer, 2009; Schöpfer, 2018; Schagerl, 2022). An infinite number of refold structures can be modelled by using six parameters given as script entries. These are, for each fold set: (i) the direction of the fold axial plane, (ii) the dip of the fold axial plane, (iii) the pitch, or rake, that described the inclination of the fold axis from the horizontal. The script then generates the refolded 3D surface and provides the stereogram with the two-fold axial planes and axes. No modification of the initial script was necessary for our study.

The dips and directions of the fold axial planes, and the fold axis pitches for the F_{1a} and F_{1b} folds are provided as inputs in the script (Fig. A5-1). Given an F_{1b} 260-83 axial plane and 82/135 fold axis measured at the Nyanzaga deposit (Figs. 4.4e, A5-1a_2-f_2), the objectives were to achieve interference patterns exhibiting two key features: (i) a horizontal, progressive shift in orientation from north to south, resembling the curved axial plane of the Nyanzaga Anticline, shifting from NW-SE to NE-SW axes orientations and (ii) a global z-shaped refold structure, with NW-oriented long limbs and N- to NE-oriented short limbs (Fig. 5-1c).

The F_{1b} parameters are unchanged for all models, using the F_{1b} axial plane and fold axis described above (approximately 260-85 and 85/135 respectively), and the F_{1a} initial fold orientation was made variable, with vertical axial plane and horizontal axis (Fig. A5-1). Six different F_{1a} strike orientations were modeled: E-W, ESE-WNW, NW-SE, N-S, NE-SW and ENE-WSW (Fig. A5-1a_1, b_1, c_1, d_1, e_1, f_1, respectively). These parameters model 180° of F_{1a} orientations, the last one being the same orientation as the F_{1b} (Fig. A5-1f). All six orientations correspond to six different maximum shortening directions, perpendicular to the fold axial planes (black arrow in Fig. A5-1a_1-f_1).

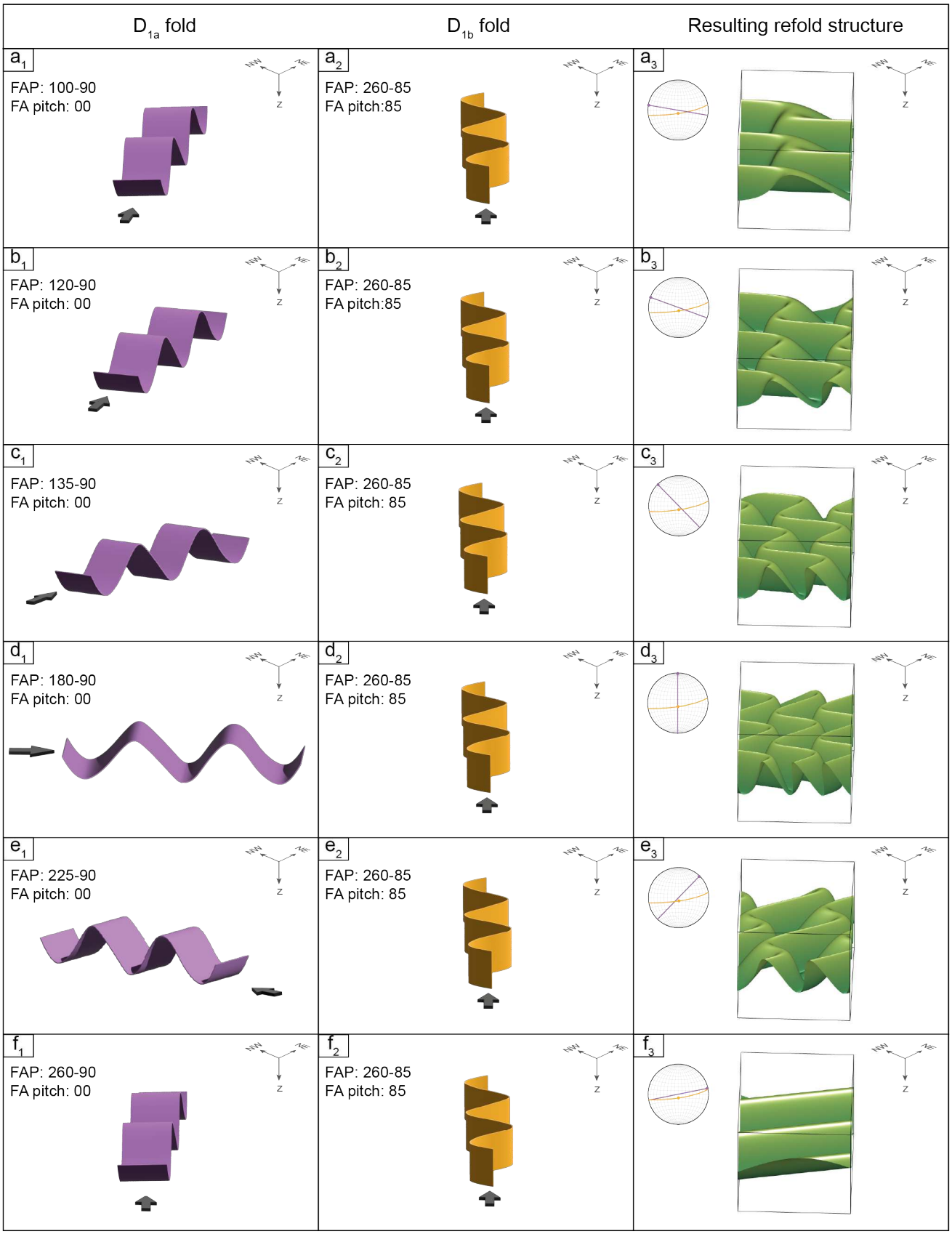

Figure A5-1. 3D Matlab modelling showing in violet the orientation of F_{1a} folds, in yellow the orientation of the F_{1b} folds and in green the refold structure resulting from the addition of both folds. The stereogram with both fold axial planes and fold axes are presented in the last column. Fold axial planes and fold axes follow the right hand rule. FAP = fold axial plane, FA = fold axis. Matlab script from Schöpfer (2009 and personnal communication).

A comparison between the two key features mapped in outcrop and all six models can be made: (i) to the exception of the last model, where the F_{1a} and F_{1b} fold axial planes are almost parallel (Fig. A5-1f), all refold structures demonstrate a curving of the F_{1a} axial plane, with NW- and NE-oriented limbs (Fig. A5-1a-e); (ii) z- and s-shaped asymmetry of refold structures are well developed when the difference of orientation of the two fold axial planes is above 45°, *i.e.*, well visible in the models a, b and e in Fig. A5-1 but poorly visible in models c and d. Finally, the distinctive z-shaped, with NW-oriented long limbs, only appears when the F_{1a} axial plane is roughly ESE-WNW (N100 and N120, Fig. A5-1a-b). Therefore, the Matlab modeling of refold structures indicate that the original orientation of the F_{1a} folds at the Nyanzaga and Kilimani deposits was confined between E-W to ESE-WNW, hence a N- to NNE-oriented maximal shortening during the D_{1a} deformation stage (Figs. A5-1a-b, A5-2).

However, while the Matlab script simulates refolding in two distinct stages, deformation during the D_{1a} to D_{1c} stages was progressive, as discussed in Section 5.2 of Chapter VI. The script is unable to model the continuous rotation that occurred alongside this progressive refolding, which may have impacted the overall geometry of the interference pattern.

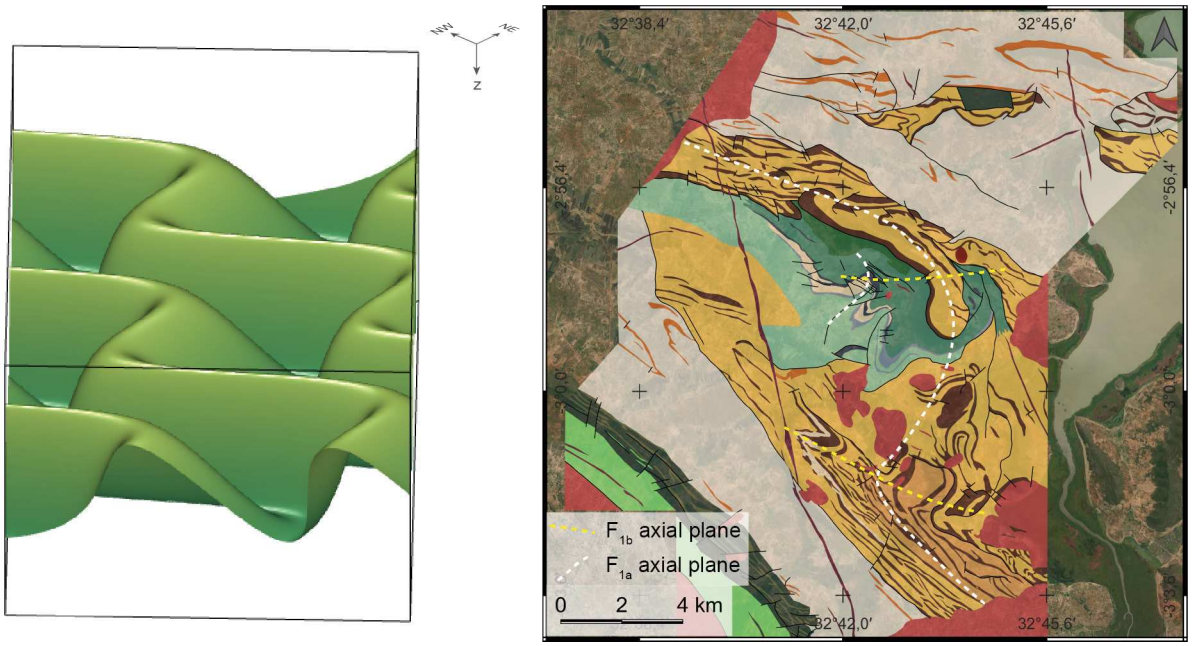

Figure A5-2. Comparison between the Matlab 3D model of refold structures and the district-scale map of the geological and structural framework near the Nyanzaga Project. Dotted lines represent the fold axes in the meta-volcanosediments, purple = first set, yellow = second set of folds.

~

References

~

A

Albarède, F., Scherer, E.E., Blichert-Toft, J., Rosing, M., Simionovici, A., and Bizzarro, M., 2006, γ-ray irradiation in the early Solar System and the conundrum of the 176Lu decay constant: Geochimica et Cosmochimica Acta, v. 70, p. 1261–1270.

Allibone, A. et al., 2002, Timing and Structural Controls on Gold Mineralization at the Bogoso Gold Mine, Ghana, West Africa: Economic Geology, v. 97, p. 949–969, doi:10.2113/gsecongeo.97.5.949.

Almeida, J. de A.C. de, Dall'Agnol, R., and Leite, A.A. da S., 2013, Geochemistry and zircon geochronology of the Archean granite suites of the Rio Maria granite-greenstone terrane, Carajás Province, Brazil: Journal of South American Earth Sciences, v. 42, p. 103–126, doi:10.1016/j.jsames.2012.10.008.

Alsop, G.I., Cheer, D.A., Strachan, R.A., Krabbendam, M., Kinny, P.D., Holdsworth, R.E., and Leslie, A.G., 2010, Progressive fold and fabric evolution associated with regional strain gradients: a case study from across a Scandian ductile thrust nappe, Scottish Caledonides: Geological Society, London, Special Publications, v. 335, p. 255–274, doi:10.1144/SP335.12.

Alt, J.C., Shanks, W.C., and Jackson, M.C., 1993, Cycling of sulfur in subduction zones: The geochemistry of sulfur in the Mariana Island Arc and back-arc trough: Earth and Planetary Science Letters, v. 119, p. 477–494, doi:10.1016/0012-821X(93)90057-G.

Amelin, Y., and Davis, W., 2005, Geochemical test for branching decay of 176Lu: Geochimica et Cosmochimica Acta, v. 69, p. 465–473.

Anderson, D.L., 1995, Lithosphere, asthenosphere, and perisphere: Reviews of Geophysics, v. 33, p. 125–149.

André-Mayer, A.-S., Eglinger, A., Fontaine, A., Combes, V., Perret, J., Thebaud, N., Berthier, C., Bosc, R., Feneyrol, J., and Chauvet, A., 2024, Les systèmes hydrothermaux aurifères: des archives géologiques de l'évolution du système Terre et des défis pour l'exploration minérale: Géologues, p. 26–33.

Anhaeusser, C.R., 2014, Archaean greenstone belts and associated granitic rocks – A review: Journal of African Earth Sciences, v. 100, p. 684–732, doi:10.1016/j.jafrearsci.2014.07.019.

Artemieva, I.M., 2006, Global 1°×1° thermal model TC1 for the continental lithosphere: Implications for lithosphere secular evolution: Tectonophysics, v. 416, p. 245–277, doi:10.1016/j.tecto.2005.11.022.

Arndt, N.T., 2013, The formation and evolution of the continental crust: Geochemical Perspectives, v. 2, p. 405–405.

Arndt, N.T., and Goldstein, S.L., 1987, Use and abuse of crust-formation ages: Geology, v. 15, p. 893–895.

Augustin, J., Gaboury, D., and Crevier, M., 2017, Structural and gold mineralizing evolution of the world-class orogenic Mana district, Burkina Faso: Multiple mineralizing events over 150 million years: Ore Geology Reviews, v. 91, p. 981–1012, doi:10.1016/j.oregeorev.2017.08.007.

Ávila, J.N., Ireland, T.R., Holden, P., Lanc, P., Latimore, A., Schram, N., Foster, J., Williams, I.S., Loiselle, L., and Fu, B., 2020, High-Precision, High-Accuracy Oxygen Isotope Measurements of Zircon Reference Materials with the SHRIMP-SI: Geostandards and Geoanalytical Research, v. 44, p. 85–102.

B

Balakrishnan, S., and Rajamani, V., 1987, Geochemistry and Petrogenesis of Granitoids around the Kolar Schist Belt, South India: Constraints for the Evolution of the Crust in the Kolar Area: The Journal of Geology, v. 95, p. 219–240, doi:10.1086/629121.

Balé, P., and Brun, J.-P., 1989, Late Precambrian thrust and wrench zones in northern Brittany (France): Journal of Structural Geology, v. 11, p. 391–405, doi:10.1016/0191-8141(89)90017-5.

Bark, G., Boyce, A.J., Fallick, A.E., and Weihed, P., 2021, Fluid and metal sources in the Fäboliden hypozonal orogenic gold deposit, Sweden: Mineralium Deposita, v. 56, p. 425–440, doi:10.1007/s00126-020-00977-7.

Barley, M., and Groves, D., 1992, Supercontinent cycles and the distribution of metal deposits through time: Geology, v. 20, p. 291–294.

Barnes, S.J., Van Kranendonk, M.J., and Sonntag, I., 2012, Geochemistry and tectonic setting of basalts from the Eastern Goldfields Superterrane: Australian Journal of Earth Sciences, v. 59, p. 707–735, doi:10.1080/08120099.2012.687398.

Barrick, 2024, Annual report 2023:, https://s25.q4cdn.com/322814910/files/doc_financial/annual_reports/2023/Barrick_Annual_Report_2023.pdf.

Barth, H., 1990, Provisional geological map of the Lake Victoria Goldfields, Tanzania.:

Bauer, A.B., Reimink, J.R., Chacko, T., Foley, B.J., Shirey, S.B., and Pearson, D.G., 2020, Hafnium isotopes in zircons document the gradual onset of mobile-lid tectonics: Geochemical Perspectives Letters, p. 1–6, doi:10.7185/geochemlet.2015.

Bédard, J.H., 2006, A catalytic delamination-driven model for coupled genesis of Archaean crust and sub-continental lithospheric mantle: Geochimica et Cosmochimica Acta, v. 70, p. 1188–1214, doi:10.1016/j.gca.2005.11.008.

Bedard, J.H. et al., 2012, Fault-mediated melt ascent in a Neoproterozoic continental flood basalt province, the Franklin sills, Victoria Island, Canada: Geological Society of America Bulletin, v. 124, p. 723–736, doi:10.1130/B30450.1.

Bédard, J.H., 2020, From the LIPS of a serial killer: Endogenic retardation of biological evolution on unstable stagnant-lid planets: Planetary and Space Science, v. 192, p. 105068, doi:10.1016/j.pss.2020.105068.

Bédard, J.H., 2018, Stagnant lids and mantle overturns: Implications for Archaean tectonics, magmagenesis, crustal growth, mantle evolution, and the start of plate tectonics: Geoscience Frontiers, v. 9, p. 19–49, doi:10.1016/j.gsf.2017.01.005.

Bédard, J.H., Brouillette, P., Madore, L., and Berclaz, A., 2003, Archaean cratonization and deformation in the northern Superior Province, Canada: an evaluation of plate tectonic versus vertical tectonic models: Precambrian Research, v. 127, p. 61–87, doi:10.1016/S0301-9268(03)00181-5.

Bédard, J.H., Harris, L.B., and Thurston, P.C., 2013, The hunting of the snArc: Precambrian Research, v. 229, p. 20–48, doi:10.1016/j.precamres.2012.04.001.

Begg, G.C. et al., 2009, The lithospheric architecture of Africa: Seismic tomography, mantle petrology, and tectonic evolution: Geosphere, v. 5, p. 29, doi:10.1130/GES00179.S2.

Bekker, A., Grokhovskaya, T.L., Hiebert, R., Sharkov, E.V., Bui, T.H., Stadnek, K.R., Chashchin, V.V., and Wing, B.A., 2016, Multiple sulfur isotope and mineralogical constraints on the genesis of Ni-Cu-PGE magmatic sulfide mineralization of the Monchegorsk Igneous Complex, Kola Peninsula, Russia: Mineralium Deposita, v. 51, p. 1035–1053, doi:10.1007/s00126-015-0604-1.

Belousova, E.A., Kostitsyn, Y.A., Griffin, W.L., Begg, G.C., O'Reilly, S.Y., and Pearson, N.J., 2010, The growth of the continental crust: Constraints from zircon Hf-isotope data: Lithos, v. 119, p. 457–466, doi:10.1016/j.lithos.2010.07.024.

Belousova, E.A., Reid, A.J., Griffin, W.L., and O'Reilly, S.Y., 2009, Rejuvenation vs. recycling of Archean crust in the Gawler Craton, South Australia: Evidence from U–Pb and Hf isotopes in detrital zircon: Lithos, v. 113, p. 570–582, doi:10.1016/j.lithos.2009.06.028.

Benning, L.G., and Seward, T.M., 1996, Hydrosulphide complexing of Au (I) in hydrothermal solutions from 150–400°C and 500–1500 bar: Geochimica et Cosmochimica Acta, v. 60, p. 1849–1871, doi:10.1016/0016-7037(96)00061-0.

Berthier, C., Perret, J., Eglinger, A., André-Mayer, A.-S., Feneyrol, J., Voinot, A., Teitler, Y., and Bosc, R., 2023, Pyrite as a Microtextural and Geochemical Tracer of Ore-Forming Processes, Central Zone Orogenic Gold Deposit, Gabgaba District, Sudan: Economic Geology, v. 118, p. 1031–1053, doi:10.5382/econgeo.5001.

Bierlein, F.P., Groves, D.I., Goldfarb, R.J., and Dubé, B., 2006a, Lithospheric controls on the formation of provinces hosting giant orogenic gold deposits: Mineralium Deposita, v. 40, p. 874–886.

Bierlein, F., and McKnight, S., 2005, Possible intrusion-related gold systems in the western Lachlan Orogen, southeast Australia: Economic Geology, v. 100, p. 385–398.

Bierlein, F.P., Murphy, F.C., Weinberg, R.F., and Lees, T., 2006b, Distribution of orogenic gold deposits in relation to fault zones and gravity gradients: targeting tools applied to the Eastern Goldfields, Yilgarn Craton, Western Australia: Mineralium Deposita, v. 41, p. 107–126, doi:10.1007/s00126-005-0044-4.

Bierlein, F.P., and Pisarevsky, S., 2008a, Plume-related oceanic plateaus as a potential source of gold mineralization: Economic Geology, v. 103, p. 425–430, doi:10.2113/gsecongeo.103.2.425.

Bierlein, F., and Pisarevsky, S., 2008b, Plume-related oceanic plateaus as a potential source of gold mineralization: Economic Geology, v. 103, p. 425–430.

Blackman, D.K. et al., 2002, Geology of the Atlantis Massif (Mid-Atlantic Ridge, 30° N): Implications for

the evolution of an ultramafic oceanic core complex: Marine Geophysical Researches, v. 23, p. 443–469, doi:10.1023/B:MARI.0000018232.14085.75.

Bleeker, W., 2015, Synorogenic gold mineralization in granite-greenstone terranes: the deep connection between extension, major faults, synorogenic clastic basins, magmatism, thrust inversion, and long-term preservation: 7852, 7852 p., doi:10.4095/296626.

Blichert-Toft, J., 2008, The Hf isotopic composition of zircon reference material 91500: Chemical Geology, v. 253, p. 252–257.

Blichert-Toft, J., and Albarède, F., 2008, Hafnium isotopes in Jack Hills zircons and the formation of the Hadean crust: Earth and Planetary Science Letters, v. 265, p. 686–702, doi:10.1016/j.epsl.2007.10.054.

Boniface, N., and Mruma, A.H., 2012, Structural analysis, metamorphism, and geochemistry of the Archean granitoids-greenstones of the Sukumaland Greenstone Belt around Geita Hills, Northern Tanzania: Natural Science, v. 04, p. 526–535, doi:10.4236/ns.2012.48070.

Borg, G., 1992, The Geita gold deposit in NW Tanzania - geology, ore petrology, geochemistry and timing of events, in Metallogenesis of selected gold deposits in Africa, Hannover, Geologisches Jahrbuch 100.

Borg, G., 1992, New aspects of the lithostratigraphy and evolution of the Siga Hills, an Archaean granite-greenstone terrain in NW Tanzania: Zeitschrift fur Angewandte Geologie, 38, 89-93.

Borg G., 1994, The Geita gold deposit in NW Tanzania - Geology, ore petrology, geochemistry and timing of events: Geologische Jahrbuch, v. D100, p. 545–595.

Borg, G., and Krogh, T., 1999, Isotopic age data of single zircons from the Archaæan Sukumaland Greenstone Belt, Tanzania: Journal of African Earth Sciences, v. 29, p. 301–312, doi:10.1016/S0899-5362(99)00099-8.

Borg, G., and Shackleton, R.M., 1997, The Tanzania and NE-Zaire Cratons, in The Tanzania and NE-Zaire Cratons, Oxford University Press, p. 608–619.

Bouhallier, H., 1994, Evolution structurale et métamorphique de la croûte continentale archéenne (craton de Dherwar, Inde du Sud) [PhD thesis in geology]: Université Rennes 1.

Bouhallier, H., Chardon, D., and Choukroune, P., 1995, Strain patterns in Archaean dome-and-basin structures: the Dharwar craton (Karnataka, South India): Earth and Planetary Science Letters, v. 135, p. 57–75.

Bouvier, A., Vervoort, J.D., and Patchett, P.J., 2008, The Lu–Hf and Sm–Nd isotopic composition of CHUR: Constraints from unequilibrated chondrites and implications for the bulk composition of terrestrial planets: Earth and Planetary Science Letters, v. 273, p. 48–57, doi:10.1016/j.epsl.2008.06.010.

Bowring, S.A., and Williams, I.S., 1999, Priscoan (4.00–4.03 Ga) orthogneisses from northwestern Canada: Contributions to Mineralogy and Petrology, v. 134, p. 3–16.

Brigden, J., 2020, Report on the Geological Controls and Geological Model Development for the Kilimani Mineralisation, Nyanzaga Project, Tanzania.:

Brigden, J., Sparrow, R., Titley, M., and Spora, P., 2017, Nyanzaga gold project, Tanzania: Small company approach, big company view.:

Brown, M., 2006, Duality of thermal regimes is the distinctive characteristic of plate tectonics since the Neoarchean: Geology, v. 34, p. 961–964.

Brown, M., 2007, Metamorphic Conditions in Orogenic Belts: A Record of Secular Change: International Geology Review, v. 49, p. 193–234, doi:10.2747/0020-6814.49.3.193.

Brown, M., and Johnson, T., 2019, Metamorphism and the evolution of subduction on Earth: American Mineralogist, v. 104, p. 1065–1082, doi:10.2138/am-2019-6956.

Brown, M., Johnson, T., and Gardiner, N.J., 2020, Plate Tectonics and the Archean Earth: Annual Review of Earth and Planetary Sciences, v. 48, p. 291–320, doi:10.1146/annurev-earth-081619-052705.

Buhemba Gold Company Limited, 2020, Feasability assessment on Buhemba gold mine project:

Burg, J.-P., Bouilhol, P., 2019, Timeline of the South Tibet-Himalayan belt: the geochronological record of subduction, collision, and underthrusting from zircon and monazite U-Pb ages: Canadian Journal of Earth Sciences, 56, 1318–1332.

Buzenchi, A., 2023, Changements de la composition de la croûte continentale au cours du temps et implications pour la dynamique terrestre: Apport de l'analyse à haute précision des isotopes du Sr, de l'U-Pb et de l'Hf par LA-MC-ICP-MS [PhD thesis in geology]: Geosciences Montpellier, 316 p.

C

Cabral, R.A., Jackson, M.G., Rose-Koga, E.F., Koga, K.T., Whitehouse, M.J., Antonelli, M.A., Farquhar, J., Day, J.M.D., and Hauri, E.H., 2013, Anomalous sulphur isotopes in plume lavas reveal deep mantle storage of Archaean crust: Nature, v. 496, p. 490–493, doi:10.1038/nature12020.

Cagnard, F., Durrieu, N., Gapais, D., Brun, J., and Ehlers, C., 2006, Crustal thickening and lateral flow during compression of hot lithospheres, with particular reference to Precambrian times: Terra Nova, v. 18, p. 72–78, doi:10.1111/j.1365-3121.2005.00665.x.

Cameron, E.M., and Hattori, K., 1987, Archean gold mineralization and oxidized hydrothermal fluids: Economic Geology, v. 82, p. 1177–1191, doi:10.2113/gsecongeo.82.5.1177.

Capitanio, F.A., Nebel, O., Cawood, P.A., Weinberg, R.F., and Clos, F., 2019, Lithosphere differentiation in the early Earth controls Archean tectonics: Earth and Planetary Science Letters, v. 525, p. 115755, doi:10.1016/j.epsl.2019.115755.

Carlson, R.W., Garçon, M., O'neil, J., Reimink, J., and Rizo, H., 2019, The nature of Earth's first crust: Chemical Geology, v. 530, p. 119321.

Carreras, J., and Druguet, E., 2019, Complex fold patterns developed by progressive deformation: Journal of Structural Geology, v. 125, p. 195–201, doi:10.1016/j.jsg.2018.07.015.

Caruso, S., Fiorentini, M.L., Champion, D.C., Lu, Y., Ueno, Y., and Smithies, R.H., 2022, Sulfur isotope systematics of granitoids from the Yilgarn Craton sheds new light on the fluid reservoirs of Neoarchean orogenic gold deposits: Geochimica et Cosmochimica Acta, v. 326, p. 199–213, doi:10.1016/j.gca.2022.03.023.

Cawood, P.A., Chowdhury, P., Mulder, J.A., Hawkesworth, C.J., Capitanio, F.A., Gunawardana, P.M., and Nebel, O., 2022, Secular Evolution of Continents and the Earth System: Reviews of Geophysics, v. 60, p. 67, doi:10.1029/2022RG000789.

Cawood, P.A., and Hawkesworth, C.J., 2015, Temporal relations between mineral deposits and global tectonic cycles, in The Geological Society of London London.

Cawood, P.A., Hawkesworth, C.J., and Dhuime, B., 2012, Detrital zircon record and tectonic setting: Geology, v. 40, p. 875–878, doi:10.1130/G32945.1.

Cawood, P.A., Hawkesworth, C.J., and Dhuime, B., 2013, The continental record and the generation of continental crust: Geological Society of America Bulletin, v. 125, p. 14–32, doi:10.1130/B30722.1.

Cawood, P.A., Hawkesworth, C.J., Pisarevsky, S.A., Dhuime, B., Capitanio, F.A., and Nebel, O., 2018, Geological archive of the onset of plate tectonics: Philosophical Transactions of the Royal Society A: Mathematical, Physical and Engineering Sciences, v. 376, p. 20170405, doi:10.1098/rsta.2017.0405.

Cawood, P., Kröner, A., and Pisarevsky, S., 2006, Precambrian Plate Tectonics: Criteria and Evidence Precambrian Plate Tectonics: Criteria and Evidence: GSA Today, v. 16, p. 4–10, doi:10.1130/GSAT01607.1.

Chamberlain, C.M., 2003, Geology and genesis of the Bulyanhulu gold deposit, Sukumaland greenstone belt, Tanzania [PhD thesis in geology]: University of London.

Chamberlain, C.M., and Tosdal, R.M., 2007, U–Pb Geochronology of the Lake Victoria Greenstone Terrane, Tanzania. Mineral Deposit Research Unit, The University of British Columbia: Unpublished report, p. 81.

Champion, D., and Cassidy, K., 2007, An overview of the Yilgarn Craton and its crustal evolution: Geoscience Australia Record, v. 14, p. 8–13.

Champion, D.C., and Huston, D.L., 2016, Radiogenic isotopes, ore deposits and metallogenic terranes: Novel approaches based on regional isotopic maps and the mineral systems concept: Ore Geology Reviews, v. 76, p. 229–256, doi:10.1016/j.oregeorev.2015.09.025.

Chappell, B.W., and White, A.J.R., 2001, Two contrasting granite types: 25 years later: Australian Journal of Earth Sciences, v. 48, p. 489–499, doi:10.1046/j.1440-0952.2001.00882.x.

Chardon, D., Bamba, O., and Traoré, K., 2020, Eburnean deformation pattern of Burkina Faso and the tectonic significance of shear zones in the West African craton: BSGF - Earth Sciences Bulletin, v. 191, p. 2, doi:10.1051/bsgf/2020001.

Chardon, D., Choukroune, P., and Jayananda, M., 1996, Strain patterns, décollement and incipient sagducted greenstone terrains in the Archaean Dharwar craton (south India): Journal of Structural Geology, v. 18, p. 991–1004.

Chardon, D., Jayananda, M., and Peucat, J.-J., 2011, Lateral constrictional flow of hot orogenic crust: Insights from the Neoarchean of south India, geological and geophysical implications for orogenic plateaux: LATERAL CONSTRICTIONAL FLOW OF OROGENS: Geochemistry, Geophysics, Geosystems, v. 12, p. n/a-n/a, doi:10.1029/2010GC003398.

Chardon, D., Rey, P., Teyssier, C., and Whitney, D.L., 2009, Hot orogens: Tectonophysics, v. 477, p. 103–104, doi:10.1016/j.tecto.2009.10.005.

Chauvet, A. (Ed.), 2019, Structural control of mineral deposits: theory and reality: Basel Beijing Wuhan Barcelona Belgrade, MDPI, Minerals, 244 p.

Chen, M., Campbell, I.H., Xue, Y., Tian, W., Ireland, T.R., Holden, P., Cas, R.A.F., Hayman, P.C., and Das, R., 2015, Multiple Sulfur Isotope Analyses Support a Magmatic Model for the Volcanogenic Massive Sulfide Deposits of the Teutonic Bore Volcanic Complex, Yilgarn Craton, Western Australia: Economic Geology, v. 110, p. 1411–1423, doi:10.2113/econgeo.110.6.1411.

Choukroune, P., Bouhallier, H., and Arndt, N.T., 1995, Soft lithosphere during periods of Archaean crustal growth or crustal reworking: Geological Society, London, Special Publications, v. 95, p. 67–86, doi:10.1144/GSL.SP.1995.095.01.05.

Chowdhury, P., Chakraborty, S., and Gerya, T.V., 2021, Time will tell: Secular change in metamorphic timescales and the tectonic implications: Gondwana Research, v. 93, p. 291–310.

Clos, F., Weinberg, R.F., Zibra, I., and Schwindinger, M., 2019, Magmatic and anatectic history of a large Archean diapir: Insights from the migmatitic core of the Yalgoo Dome, Yilgarn Craton: Lithos, v. 338–339, p. 18–33, doi:10.1016/j.lithos.2019.04.012.

Cloutier, J., Stevenson, R., and Bardoux, M., 2005, Nd isotopic, petrologic and geochemical investigation of the Tulawaka East gold deposit, Tanzanian Craton: Precambrian Research, v. 139, p. 147–163, doi:10.1016/j.precamres.2005.06.002.

Collins, W.J., Belousova, E.A., Kemp, A.I.S., and Murphy, J.B., 2011, Two contrasting Phanerozoic orogenic systems revealed by hafnium isotope data: Nature Geoscience, v. 4, p. 333–337, doi:10.1038/ngeo1127.

Collins, A.S., Reddy, S.M., Buchan, C., and Mruma, A., 2004, Temporal constraints on Palaeoproterozoic eclogite formation and exhumation (Usagaran Orogen, Tanzania): Earth and Planetary Science Letters, v. 224, p. 175–192, doi:10.1016/j.epsl.2004.04.027.

Collins, W., Van Kranendonk, and M., and Teyssier, C., 1998, Partial convective overturn of Archaean crust in the east Pilbara Craton, Western Australia: driving mechanisms and tectonic implications: Journal of Structural Geology, v. 20, p. 1405–1424.

Colvine, A.C., 1988, Archean lode gold deposits in Ontario: Ontario Ministry of Northern Development and Mines, v. 139.

Condie, K., 1981, Archean Greenstone Belts: v. 3, 434 p.

Condie, K.C., 2005, Earth as an evolving planetary system: Amsterdam, Elvesier, 447 p.

Condie, K.C., 1998, Episodic continental growth and super- continents: A mantle avalanche connection? Earth and Planetary Science Letters, v. 163, p. 97–108.

Condie, K.C., and Benn, K., 2006, Archean geodynamics: Similar to or different from modern geodynamics?, in Benn, K., Mareschal, J.-C., and Condie, K.C. eds., Geophysical Monograph Series, Washington, D. C., American Geophysical Union, v. 164, p. 47–59, doi:10.1029/164GM05.

Condie, K.C., and Kröner, A., 2008, When did plate tectonics begin? Evidence from the geologic record, in Special Paper 440: When Did Plate Tectonics Begin on Planet Earth?, Geological Society of America, v. 440, p. 281–294, doi:10.1130/2008.2440(14).

Cook, N.J., and Chryssoulis, A.L., 1990, Concentrations of invisible gold in the common sulfides: The Canadian Mineralogist, v. 28, p. 1–16.

Cook, N.J., Ciobanu, C.L., Spry, P.G., and Voudouris, P., 2009, Understanding gold-(silver)-telluride-(selenide) mineral deposits: Episodes Journal of International Geoscience, v. 32, p. 249–263.

Cook, Y.A., Sanislav, I.V., Hammerli, J., Blenkinsop, T.G., and Dirks, P.H.G.M., 2016, A primitive mantle source for the Neoarchean mafic rocks from the Tanzania Craton: Geoscience Frontiers, v. 7, p. 911–926, doi:10.1016/j.gsf.2015.11.008.

Cooke, D.R., and McPhail, D.C., 2001, Epithermal Au-Ag-Te Mineralization, Acupan, Baguio District, Philippines: Numerical Simulations of Mineral Deposition: Economic Geology, v. 96, p. 109–131, doi:https://doi.org/10.2113/gsecongeo.96.1.109.

Couture, J.-F., Pilote, P., Machado, N., and Desrochers,

J.-P., 1994, Timing of gold mineralization in the Val-d'Or District, southern Abitibi Belt; evidence for two distinct mineralizing events: Economic Geology, v. 89, p. 1542–1551.

Cox, S.F., 1995, Faulting processes at high fluid pressures: An example of fault valve behavior from the Wattle Gully Fault, Victoria, Australia: Journal of Geophysical Research: Solid Earth, v. 100, p. 12841–12859, doi:10.1029/95JB00915.

Cox, S.F., 2016, Injection-Driven Swarm Seismicity and Permeability Enhancement: Implications for the Dynamics of Hydrothermal Ore Systems in High Fluid-Flux, Overpressured Faulting Regimes—An Invited Paper: Economic Geology, v. 111, p. 559–587, doi:10.2113/econgeo.111.3.559.

Cox, S.F., and Etheridge, M.A., 1983, Crack-seal fibre growth mechanisms and their significance in the development of oriented layer silicate microstructures: Deformation processes in tectonics, v. 92, p. 147–170, doi:10.1016/0040-1951(83)90088-4.

Croharé, P., 2015, La production mondiale minière d'or en danger, ou : vers une pénurie d'or physique et une hausse record des cours de l'or:

Cutten, H., Johnson, S.P., and Waele, B.D., 2006, Protolith ages and timing of metasomatism related to the formation of whiteschists at Mautia Hill, Tanzania: implications for the assembly of Gondwana: The Journal of Geology, v. 114, p. 683–698.

Czarnota, K., Champion, D.C., Goscombe, B., Blewett, R.S., Cassidy, K.F., Henson, P.A., and Groenewald, P.B., 2010, Geodynamics of the eastern Yilgarn Craton: Precambrian Research, v. 183, p. 175–202, doi:10.1016/j.precamres.2010.08.004.

D

Davis, B.K., and Maidens, E., 2003, Archaean orogen-parallel extension: evidence from the northern Eastern Goldfields Province, Yilgarn Craton: Precambrian Research, v. 127, p. 229–248, doi:10.1016/S0301-9268(03)00189-X.

Davy, P., and Cobbold, P., 1991, Experiments on shortening of a 4-layer model of the continental lithosphere: Tectonophysics, v. 188, p. 1–25.

Deditius, A.P., Reich, M., Kesler, S.E., Utsunomiya, S., Chryssoulis, S.L., Walshe, J., and Ewing, R.C., 2014, The coupled geochemistry of Au and As in pyrite from hydrothermal ore deposits: Geochimica et Cosmochimica Acta, v. 140, p. 644–670, doi:10.1016/j.gca.2014.05.045.

Deditius, A.P., Utsunomiya, S., Ewing, R.C., Chryssoulis, S.L., Venter, D., and Kesler, S.E., 2009, Decoupled geochemical behavior of As and Cu in hydrothermal systems: Geology, v. 37, p. 707–710, doi:10.1130/G25781A.1.

Delavault, H., Chauvel, C., Thomassot, E., Devey, C.W., and Dazas, B., 2016, Sulfur and lead isotopic evidence of relic Archean sediments in the Pitcairn mantle plume: Proceedings of the National Academy of Sciences, v. 113, p. 12952–12956, doi:10.1073/pnas.1523805113.

DePaolo, D.J., 1981, Neodymium isotopes in the Colorado Front Range and crust–mantle evolution in the Proterozoic: Nature, v. 291, p. 193–196, doi:10.1038/291193a0.

Dhuime, B., Hawkesworth, C., and Cawood, P., 2011, When Continents Formed: Science, v. 331, p. 154–155, doi:10.1126/science.1201245.

Dhuime, B., Hawkesworth, C.J., Cawood, P.A., and Storey, C.D., 2012, A Change in the Geodynamics of Continental Growth 3 Billion Years Ago: Science, v. 335, p. 1334–1336, doi:10.1126/science.1216066.

Dhuime, B., Wuestefeld, A., and Hawkesworth, C.J., 2015, Emergence of modern continental crust about 3 billion years ago: Nature Geoscience, v. 8, p. 552–555, doi:10.1038/ngeo2466.

Dhuime, B., Hawkesworth, C.J., Delavault, H., and Cawood, P.A., 2017, Continental growth seen through the sedimentary record: Sedimentary Geology, v. 357, p. 16–32.

Dhuime, B., Hawkesworth, C.J., Delavault, H., and Cawood, P.A., 2018, Rates of generation and destruction of the continental crust: implications for continental growth: Philosophical Transactions of the Royal Society A: Mathematical, Physical and Engineering Sciences, v. 376, p. 20170403, doi:10.1098/rsta.2017.0403.

Dilek, Y., and Polat, A., 2008, Suprasubduction zone ophiolites and Archean tectonics: Geology, v. 36, p. 431–432.

Ding, T., Valkiers, S., Kipphardt, H., De Bièvre, P., Taylor, P.D.P., Gonfiantini, R., and Krouse, R., 2001, Calibrated sulfur isotope abundance ratios of three

IAEA sulfur isotope reference materials and V-CDT with a reassessment of the atomic weight of sulfur: Geochimica et Cosmochimica Acta, v. 65, p. 2433–2437, doi:10.1016/S0016-7037(01)00611-1.

Dirks P.H.G.M, Sanislav I.V., Van Ryt M.R., Huizenga J.-M., Blenkinsop T.G., Kolling S.L., Kwelwa S.D., and Mwazembe G., 2020, The World-Class Gold Deposits in the Geita Greenstone Belt, Northwestern Tanzania: Society of Economic Geologists, SEG Special Publications, v. 22, p. 163–183, doi:10.5382/SP.23.08.

Diwu, C., Sun, Y., Si, B., and Yan, M., 2024, Archean continental crustal growth and reworking of the North China Craton: Constraints from zircon U Pb age and Hf isotopic composition: Earth-Science Reviews, v. 248, p. 104624, doi:10.1016/j.earscirev.2023.104624.

Djeutchou, C., de Kock, M., Ernst, R.E., Ossa Ossa, F.G., and Bekker, A., 2024, A review of the Intraplate Mafic Magmatic Record of the Greater Congo craton: Earth-Science Reviews, v. 249, p. 104649, doi:10.1016/j.earscirev.2023.104649.

Dodson, M., Gledhill, A., Shackleton, R., and Bell, K., 1975, Age differences between Archaean cratons of eastern and southern Africa: Nature, v. 254, p. 315–318.

Dong, G., Morrison, G., and Jaireth, S., 1995, Quartz textures in epithermal veins, Queensland; classification, origin and implication: Economic Geology, v. 90, p. 1841–1856, doi:10.2113/gsecongeo.90.6.1841.

Dong, Y., Santosh, M., 2015, Tectonic architecture and multiple orogeny of the Qinling Orogenic Belt, Central China: Gondwana Research, 29. doi:10.1016/j.gr.2015.06.009.

Dong, C., Wan, Y., Xie, H., Nutman, A.P., Xie, S., Liu, S., Ma, M., and Liu, D., 2017, The Mesoarchean Tiejiashan-Gongchangling potassic granite in the Anshan-Benxi area, North China Craton: Origin by recycling of Paleo- to Eoarchean crust from U-Pb-Nd-Hf-O isotopic studies: Lithos, v. 290–291, p. 116–135, doi:10.1016/j.lithos.2017.08.009.

Doublier, M.P., Thébaud, N., Wingate, M.T.D., Romano, S.S., Kirkland, C.L., Gessner, K., Mole, D.R., and Evans, N., 2014a, Structure and timing of Neoarchean gold mineralization in the Southern Cross district (Yilgarn Craton, Western Australia) suggest leading role of late Low-Ca I-type granite intrusions: Journal of Structural Geology, v. 67, p. 205–221, doi:10.1016/j.jsg.2014.02.009.

Doublier, M.P., Thébaud, N., Wingate, M.T.D., Romano, S.S., Kirkland, C.L., Gessner, K., Mole, D.R., and Evans, N., 2014b, Structure and timing of Neoarchean gold mineralization in the Southern Cross district (Yilgarn Craton, Western Australia) suggest leading role of late Low-Ca I-type granite intrusions: Journal of Structural Geology, v. 67, p. 205–221, doi:10.1016/j.jsg.2014.02.009.

Dressel, B.C., Chauvet, A., Trzaskos, B., Biondi, J.C., Bruguier, O., Monié, P., Villanova, S.N., and Newton, J.B., 2018, The Passa Três lode gold deposit (Paraná State, Brazil): An example of structurally-controlled mineralisation formed during magmatic-hydrothermal transition and hosted within granite: Ore Geology Reviews, v. 102, p. 701–727, doi:10.1016/j.oregeorev.2018.09.007.

Dubé, B., and Gosselin, P., 2007, Greenstone-hosted quartz-carbonate vein deposits, in Mineral deposits of Canada: a synthesis of major deposit-types, district metallogeny, the evolution of geological provinces and exploration methods, Goodfellow, W.D., v. 5, p. 49–73.

Dubé, B., and Mercier-Langevin, P., 2020, Chapter 32: Gold Deposits of the Archean Abitibi Greenstone Belt, Canada, in Sillitoe, R.H., Goldfarb, R.J., Robert, F., and Simmons, S.F. eds., Geology of the World's Major Gold Deposits and Provinces, Society of Economic Geologists, p. 669–708, doi:10.5382/SP.23.32.

Dubé, B., Mercier-Langevin, P., Ayer, J., Pilote, J.-L., and Monecke, T., 2020, Chapter 3: Gold Deposits of the World-Class Timmins-Porcupine Camp, Abitibi Greenstone Belt, Canada, in Sillitoe, R.H., Goldfarb, R.J., Robert, F., and Simmons, S.F. eds., Geology of the World's Major Gold Deposits and Provinces, Society of Economic Geologists, p. 53–80, doi:10.5382/SP.23.03.

Duclaux, G., Rey, P., Guillot, S., and Ménot, R.-P., 2007, Orogen-parallel flow during continental convergence: Numerical experiments and Archean field examples: Geology, v. 35, p. 715, doi:10.1130/G23540A.1.

E

Eglinger, A., André-Mmayer, A.-S., Thébaud, N., and Masurel, Q., 2023, West African Leo-Man Shield Metallogenic Province: Metallic Resources 2: Geodynamic Framework and Remarkable Examples

in the World, p. 265–305.

Eglinger, A., Thébaud, N., Zeh, A., Davis, J., Miller, J., Parra-Avila, L.A., Loucks, R., McCuaig, C., and Belousova, E., 2017, New insights into the crustal growth of the Paleoproterozoic margin of the Archean Kéména-Man domain, West African craton (Guinea): Implications for gold mineral system: Precambrian Research, v. 292, p. 258–289.

Elbra, A., 2017, A History of Gold Mining in South Africa, Ghana and Tanzania, in Elbra, A. ed., Governing African Gold Mining: Private Governance and the Resource Curse, London, Palgrave Macmillan UK, p. 67–103, doi:10.1057/978-1-137-56354-5_3.

Elkins-Tanton, L.T., 2008, Linked magma ocean solidification and atmospheric growth for Earth and Mars: Earth and Planetary Science Letters, v. 271, p. 181–191, doi:10.1016/j.epsl.2008.03.062.

Elkins-Tanton, L.T., 2012, Magma oceans in the inner solar system: Annual Review of Earth and Planetary Sciences, v. 40, p. 113–139.

England, P., and Bickle, M., 1984, Continental thermal and tectonic regimes during the Archaean: The Journal of Geology, v. 92, p. 353–367.

Ernst, W.G., 2017, Earth's thermal evolution, mantle convection, and Hadean onset of plate tectonics: Journal of Asian Earth Sciences, v. 145, p. 334–348, doi:10.1016/j.jseaes.2017.05.037.

Ernst, W., Sleep, N.H., and Tsujimori, T., 2016, Plate-tectonic evolution of the Earth: bottom-up and top-down mantle circulation: Canadian Journal of Earth Sciences, v. 53, p. 1103–1120.

Evans, K.A., Phillips, G.N., and Powell, R., 2006, Rock-Buffering of Auriferous Fluids in Altered Rocks Associated with the Golden Mile-Style Mineralization, Kalgoorlie Gold Field, Western Australia: Economic Geology, v. 101, p. 805–817, doi:10.2113/gsecongeo.101.4.805.

F

Faleiros, F.M., Campanha, G.A.C., Pavan, M., Almeida, V.V., Rodrigues, S.W.O., Araújo, B.P., 2016, Short-lived polyphase deformation during crustal thickening and exhumation of a collisional orogen (Ribeira Belt, Brazil): Journal of Structural Geology 93, 106–130. doi: 10.1016/j.jsg.2016.10.006

Farquhar, J., Bao, H., and Thiemens, M., 2000, Atmospheric Influence of Earth's Earliest Sulfur Cycle: Science, v. 289, p. 756–758, doi:10.1126/science.289.5480.756.

Farquhar, J., Cliff, J., Zerkle, A.L., Kamyshny, A., Poulton, S.W., Claire, M., Adams, D., and Harms, B., 2013, Pathways for Neoarchean pyrite formation constrained by mass-independent sulfur isotopes: Proceedings of the National Academy of Sciences, v. 110, p. 17638–17643, doi:10.1073/pnas.1218851110.

Farquhar, J., and Wing, B.A., 2003, Multiple sulfur isotopes and the evolution of the atmosphere: Earth and Planetary Science Letters, v. 213, p. 1–13, doi:10.1016/S0012-821X(03)00296-6.

Farquhar, J., and Wing, B., 2005, Sulfur multiple isotopes of the Moon: 33S and 36S abundances relative to Canon Diablo Troilite, in p. 2380.

Farquhar, J., Wing, B.A., McKeegan, K.D., Harris, J.W., Cartigny, P., and Thiemens, M.H., 2002, Mass-Independent Sulfur of Inclusions in Diamond and Sulfur Recycling on Early Earth: Science, v. 298, p. 2369–2372, doi:10.1126/science.1078617.

Fennell, L.M., Iannelli, S.B., Encinas, A., Naipauer, M., Valencia, V., Folguera, A., 2019, Alternating contraction and extension in the Southern Central Andes (35°–37° S): American Journal of Science, 319, 381–429.

Fiorentini, M.L., LaFlamme, C., Denyszyn, S., Mole, D., Maas, R., Locmelis, M., Caruso, S., and Bui, T.-H., 2018, Post-collisional alkaline magmatism as gateway for metal and sulfur enrichment of the continental lower crust: Geochimica et Cosmochimica Acta, v. 223, p. 175–197, doi:10.1016/j.gca.2017.11.009.

Fischer, K.M., Ford, H.A., Abt, D.L., and Rychert, C.A., 2010, The lithosphere-asthenosphere boundary: Annual Review of Earth and Planetary Sciences, v. 38, p. 551–575.

Fisher, D.M., and Brantley, S.L., 1992, Models of quartz overgrowth and vein formation: deformation and episodic fluid flow in an ancient subduction zone: Journal of Geophysical Research: Solid Earth, v. 97, p. 20043–20061.

Fisher, C.M., Hanchar, J.M., Samson, S.D., Dhuime, B., Blichert-Toft, J., Vervoort, J.D., and Lam, R., 2011, Synthetic zircon doped with hafnium and rare earth elements: A reference material for in situ hafnium isotope analysis: Chemical Geology, v. 286, p. 32–47.

Fisher, C.M., and Vervoort, J.D., 2018, Using the magmatic

record to constrain the growth of continental crust—The Eoarchean zircon Hf record of Greenland: Earth and Planetary Science Letters, v. 488, p. 79–91.

Fisher, C.M., Vervoort, J.D., and Hanchar, J.M., 2014, Guidelines for reporting zircon Hf isotopic data by LA-MC-ICPMS and potential pitfalls in the interpretation of these data: Chemical geology, v. 363, p. 125–133.

Fontaine, A., Eglinger, A., Ada, K., André-Mayer, A.-S., Reisberg, L., Siebenaller, L., Le Mignot, E., Ganne, J., and Poujol, M., 2017, Geology of the world-class Kiaka polyphase gold deposit, West African Craton, Burkina Faso: Journal of African Earth Sciences, v. 126, p. 96–122, doi:10.1016/j.jafrearsci.2016.11.017.

Fossen, H., 2016, Structural geology: Cambridge university press.

Fossen, H., Cavalcante, G.C.G., Pinheiro, R.V.L., and Archanjo, C.J., 2019, Deformation – Progressive or multiphase? Journal of Structural Geology, v. 125, p. 82–99, doi:10.1016/j.jsg.2018.05.006.

Fossen, H., and Tikoff, B., 1998, Extended models of transpression and transtension, and application to tectonic settings: Geological Society, London, Special Publications, v. 135, p. 15–33, doi:10.1144/GSL.SP.1998.135.01.02.

Foucault, A., and Raoult, J.-F., 2010, Dictionnaire de Géologie: Dunod.

Fougerouse, D. et al., 2024, Dislocation-mediated interfacial re-equilibration of pyrite: An alternative model to interface-coupled dissolution-reprecipitation and gold remobilisation: Geochimica et Cosmochimica Acta, v. 374, p. 136–145, doi:10.1016/j.gca.2024.04.027.

Fougerouse, D. et al., 2016, Gold remobilisation and formation of high grade ore shoots driven by dissolution-reprecipitation replacement and Ni substitution into auriferous arsenopyrite: Geochimica et Cosmochimica Acta, v. 178, p. 143–159, doi:10.1016/j.gca.2016.01.040.

François, C., Philippot, P., Rey, P., and Rubatto, D., 2014, Burial and exhumation during Archean sagduction in the East Pilbara Granite-Greenstone Terrane: Earth and Planetary Science Letters, v. 396, p. 235–251, doi:10.1016/j.epsl.2014.04.025.

Frimmel, H.E., 2008, Earth's continental crustal gold endowment: Earth and Planetary Science Letters, v. 267, p. 45–55, doi:10.1016/j.epsl.2007.11.022.

Frimmel, H.E., 2018, Episodic concentration of gold to ore grade through Earth's history: Earth-Science Reviews, v. 180, p. 148–158, doi:10.1016/j.earscirev.2018.03.011.

Frimmel, H.E., and Hennigh, Q., 2015, First whiffs of atmospheric oxygen triggered onset of crustal gold cycle: Mineralium Deposita, v. 50, p. 5–23.

Frimmel, H.E., and Nwaila, G.T., 2020, Chapter 31: Geologic Evidence of Syngenetic Gold in the Witwatersrand Goldfields, South Africa, in Sillitoe, R.H., Goldfarb, R.J., Robert, F., and Simmons, S.F. eds., Geology of the World's Major Gold Deposits and Provinces, Society of Economic Geologists, p. 645–668, doi:10.5382/SP.23.31.

Frost, B.R., Barnes, C.G., Collins, W.J., Arculus, R.J., Ellis, D.J., and Frost, C.D., 2001, A Geochemical Classification for Granitic Rocks: Journal of Petrology, v. 42, p. 2033–2048, doi:10.1093/petrology/42.11.2033.

Furumoto, A.S., Webb, J.P., Odegard, M.E., and Hussong, D.M., 1976, Seismic studies on the Ontong Java Plateau, 1970: Tectonophysics, v. 34, p. 71–90, doi:10.1016/0040-1951(76)90177-3.

G

Gabert, G., 1990, Lithostratigraphic and tectonic setting of gold mineralization in the Archean cratons of Tanzania and Uganda, East Africa: Precambrian Research, v. 46, p. 59–69, doi:10.1016/0301-9268(90)90066-Y.

Gaboury, D., 2013, Does gold in orogenic deposits come from pyrite in deeply buried carbon-rich sediments?: Insight from volatiles in fluid inclusions: Geology, v. 41, p. 1207–1210, doi:10.1130/G34788.1.

Gaboury, D., 2019, Parameters for the formation of orogenic gold deposits: Applied Earth Science, v. 128, p. 124–133, doi:10.1080/25726838.2019.1583310.

Ganne, J., De Andrade, V., Weinberg, R.F., Vidal, O., Dubacq, B., Kagambega, N., Naba, S., Baratoux, L., Jessell, M., and Allibon, J., 2012, Modern-style plate subduction preserved in the Palaeoproterozoic West African craton: Nature Geoscience, v. 5, p. 60–65, doi:10.1038/ngeo1321.

Gao, L., Liu, S., Cawood, P.A., Hu, F., Wang, J., Sun, G., and Hu, Y., 2022, Oxidation of Archean upper mantle caused by crustal recycling: Nature Communications, v. 13, p. 3283, doi:10.1038/s41467-022-30886-4.

Gao, P., Zheng, Y.-F., and Zhao, Z.-F., 2016, Distinction between S-type and peraluminous I-type granites: Zircon versus whole-rock geochemistry: Lithos, v. 258–259, p. 77–91, doi:10.1016/j.lithos.2016.04.019.

Gard, M., Hasterok, D., and Halpin, J.A., 2019, Global whole-rock geochemical database compilation: Earth Syst. Sci. Data, v. 11, p. 1553–1566, doi:10.5194/essd-11-1553-2019.

Gardiner, N.J., Johnson, T.E., Kirkland, C.L., and Smithies, R.H., 2018, Melting controls on the lutetium–hafnium evolution of Archaean crust: Precambrian Research, v. 305, p. 479–488, doi:10.1016/j.precamres.2017.12.026.

Geological Survey of Tanzania, 2024, Geological and Mineral Information System of Tanzania:, https://www.gmis-tanzania.com.

Gerya, T., 2014, Precambrian geodynamics: Concepts and models: Gondwana Research, v. 25, p. 442–463, doi:10.1016/j.gr.2012.11.008.

Gillet, P., Choukroune, P., Ballevre, M., and Davy, P., 1986, Thickening history of the Western Alps: Earth and planetary science letters, v. 78, p. 44–52.

Gilligan, A., Priestley, K.F., Roecker, S.W., Levin, V., and Rai, S.S., 2015, The crustal structure of the western Himalayas and Tibet: Journal of Geophysical Research: Solid Earth, v. 120, p. 3946–3964, doi:10.1002/2015JB011891.

Godwin, A.M., 1996, Principles of Precambrian Geology: Academic Press, London.

Goldfarb, R.J., Baker, T., Dubé, B., Groves, D.I., Hart, C.J.R., and Gosselin, P., 2005, Distribution, character, and genesis of gold deposits in metamorphic terranes: Economic Geology, v. 100th anniversary, p. 407–450, doi:10.5382/AV100.14.

Goldfarb, R.J., Bradley, D., and Leach, D.L., 2010, Secular Variation in Economic Geology: Economic Geology, v. 105, p. 459–465, doi:10.2113/gsecongeo.105.3.459.

Goldfarb, R.J., and Groves, D.I., 2015, Orogenic gold: Common or evolving fluid and metal sources through time: Lithos, v. 233, p. 2–26, doi:10.1016/j.lithos.2015.07.011.

Goldfarb, R.J., Groves, D.I., and Gardoll, S., 2001, Orogenic gold and geologic time: a global synthesis: Ore Geology Reviews, v. 18, p. 1–75, doi:10.1016/S0169-1368(01)00016-6.

González-Partida, E., Carrillo-Chávez, A., Levresse, G., Tello-Hinojosa, E., Venegas-Salgado, S., Ramirez-Silva, G., Pal-Verma, M., Tritlla, J., and Camprubi, A., 2005, Hydro-geochemical and isotopic fluid evolution of the Los Azufres geothermal field, Central Mexico: Applied Geochemistry, v. 20, p. 23–39, doi:10.1016/j.apgeochem.2004.07.006.

Gourcerol, B., Kontak, D.J., Petrus, J.A., and Thurston, P.C., 2020, Application of LA-ICP-MS analysis of arsenopyrite to gold metallogeny of the Meguma Terrane, Nova Scotia, Canada: Gondwana Research, v. 81, p. 265–290, doi:10.1016/j.gr.2019.11.011.

Grasemann, B., Wiesmayr, G., Draganits, E., and Fusseis, F., 2004, Classification of Refold Structures: The Journal of Geology, v. 112, p. 119–125, doi:10.1086/379696.

Greber, N.D., Dauphas, N., Bekker, A., Ptáček, M.P., Bindeman, I.N., and Hofmann, A., 2017, Titanium isotopic evidence for felsic crust and plate tectonics 3.5 billion years ago: Science, v. 357, p. 1271–1274.

Green, D.H., Hibberson, W.O., Kovács, I., and Rosenthal, A., 2010, Water and its influence on the lithosphere–asthenosphere boundary: Nature, v. 467, p. 448–451.

Griffin, W., Belousova, E., O'Neill, C., O'Reilly, S.Y., Malkovets, V., Pearson, N., Spetsius, S., and Wilde, S., 2014, The world turns over: Hadean–Archean crust–mantle evolution: Lithos, v. 189, p. 2–15.

Griffin, W.L., Pearson, N.J., Belousova, E., Jackson, S. v, Van Achterbergh, E., O'Reilly, S.Y., and Shee, S., 2000, The Hf isotope composition of cratonic mantle: LAM-MC-ICPMS analysis of zircon megacrysts in kimberlites: Geochimica et cosmochimica acta, v. 64, p. 133–147.

Griffin, W.L., Wang, X., Jackson, S.E., Pearson, N.J., O'Reilly, S.Y., Xu, X., and Zhou, X., 2002, Zircon chemistry and magma mixing, SE China: In-situ analysis of Hf isotopes, Tonglu and Pingtan igneous complexes: Lithos, v. 61, p. 237–269, doi:10.1016/S0024-4937(02)00082-8.

Grootenboer, J., and Schwarcz, H.P., 1969, Experimentally determined sulfur isotope fractionations between sulfide minerals: Earth and Planetary Science Letters, v. 7, p. 162–166, doi:10.1016/0012-821X(69)90031-4.

Groves, D., Condie, K., Goldfarb, R., Hronsky, J., and Vielreicher, R., 2005, Secular changes in global tectonic processes and their influence on the temporal distribution of gold-bearing mineral deposits:

Economic Geology, v. 100, p. 203–224.

Groves, D.I., Goldfarb, R.J., Gebre-Mariam, M., Hagemann, S.G., and Robert, F., 1998, Orogenic gold deposits: A proposed classification in the context of their crustal distribution and relationship to other gold deposit types: Ore Geology Reviews, v. 13, p. 7–27, doi:10.1016/S0169-1368(97)00012-7.

Groves, D.I., Goldfarb, R.J., and Santosh, M., 2016, The conjunction of factors that lead to formation of giant gold provinces and deposits in non-arc settings: Geoscience Frontiers, v. 7, p. 303–314, doi:10.1016/j.gsf.2015.07.001.

Groves, D.I., Santosh, M., Deng, J., Wang, Q., Yang, L., and Zhang, L., 2020a, A holistic model for the origin of orogenic gold deposits and its implications for exploration: Mineralium Deposita, v. 55, p. 275–292, doi:10.1007/s00126-019-00877-5.

Groves, D.I., Santosh, M., Deng, J., Wang, Q., Yang, L., and Zhang, L., 2020b, A holistic model for the origin of orogenic gold deposits and its implications for exploration: Mineralium Deposita, v. 55, p. 275–292, doi:10.1007/s00126-019-00877-5.

Groves, D.I., Santosh, M., Goldfarb, R.J., and Zhang, L., 2018, Structural geometry of orogenic gold deposits: Implications for exploration of world-class and giant deposits: Geoscience Frontiers, v. 9, p. 1163–1177, doi:10.1016/j.gsf.2018.01.006.

Guillot, S., Garzanti, E., Baratoux, D., Marquer, D., Mahéo, G., and de Sigoyer, J., 2003a, Reconstructing the total shortening history of the NW Himalaya: Geochemistry, Geophysics, Geosystems, v. 4.

Guillot, S., Garzanti, E., Baratoux, D., Marquer, D., Mahéo, G., and de Sigoyer, J., 2003b, Reconstructing the total shortening history of the NW Himalaya: Geochemistry, Geophysics, Geosystems, v. 4, p. 2002GC000484, doi:10.1029/2002GC000484.

Guillot, S., Le Fort, P., Peˆcher, A., Barman, M.R., and Aprahamian, J., 1995, Contact metamorphism and depth of emplacement of the Manaslu granite (central Nepal). Implications for Himalayan orogenesis: Tectonophysics, v. 241, p. 99–119, doi:10.1016/0040-1951(94)00144-X.

Guo, J.-L., Wu, Y.-B., Gao, S., Jin, Z.-M., Zong, K.-Q., Hu, Z.-C., Chen, K., Chen, H.-H., and Liu, Y.-S., 2015, Episodic Paleoarchean-Paleoproterozoic (3.3–2.0Ga) granitoid magmatism in Yangtze Craton, South China: Implications for late Archean tectonics: Precambrian Research, v. 270, p. 246–266, doi:10.1016/j.precamres.2015.09.007.

H

Hagemann, S.G., Gebre-Mariam, M., and Groves, D.I., 1994, Surface-water influx in shallow-level Archean lode-gold deposits in Western, Australia: Geology, v. 22, p. 1067, doi:10.1130/0091-7613(1994)022<1067:SWIISL>2.3.CO;2.

Halla, J., van Hunen, J., Heilimo, E., and Hölttä, P., 2009, Geochemical and numerical constraints on Neoarchean plate tectonics: Precambrian Research, v. 174, p. 155–162, doi:10.1016/j.precamres.2009.07.008.

Hamilton, W.B., 2011, Plate tectonics began in Neoproterozoic time, and plumes from deep mantle have never operated: Secular variations in magmatism and tectonic implications, v. 123, p. 1–20, doi:10.1016/j.lithos.2010.12.007.

Harrison, T.M., Bell, E.A., and Boehnke, P., 2017, Hadean zircon petrochronology: Reviews in Mineralogy and Geochemistry, v. 83, p. 329–363.

Harrison, T., Blichert-Toft, J., Muller, W., Albarede, F., Holden, P., and Mojzsis, S., 2005, Heterogeneous Hadean hafnium: evidence of continental crust at 4.4 to 4.5 Ga: Science, v. 310, p. 1947–1950.

Harrison, T.M., Schmitt, A.K., McCulloch, M.T., and Lovera, O.M., 2008, Early (≥ 4.5 Ga) formation of terrestrial crust: Lu–Hf, δ18O, and Ti thermometry results for Hadean zircons: Earth and Planetary Science Letters, v. 268, p. 476–486.

Hart, C.J., 2005, Classifying, distinguishing and exploring for intrusion-related gold systems: The Gangue, v. 87, p. 9.

Hastie, A.R., Fitton, J.G., Bromiley, G.D., Butler, I.B., and Odling, N.W.A., 2016, The origin of Earth's first continents and the onset of plate tectonics: Geology, v. 44, p. 855–858, doi:10.1130/G38226.1.

Hawkesworth, C.J., Cawood, P.A., and Dhuime, B., 2016, Tectonics and crustal evolution: GSA Today, v. 26, p. 4–11, doi:10.1130/GSATG272A.1.

Hawkesworth, C.J., Cawood, P.A., and Dhuime, B., 2020, The Evolution of the Continental Crust and the Onset of Plate Tectonics: Frontiers in Earth Science, v. 8, p.

326, doi:10.3389/feart.2020.00326.

Hawkesworth, C.J., Cawood, P.A., Dhuime, B., and Kemp, T.I., 2017, Earth's continental lithosphere through time: Annual review of earth and planetary sciences, v. 45, p. 169–198.

Hawkesworth, C., Cawood, P.A., Dhuime, B., and Kemp, T., 2024, Tectonic processes and the evolution of the continental crust: Journal of the Geological Society, v. 181, p. jgs2024- 027, doi:10.1144/jgs2024-027.

Hawkesworth, C.J., Dhuime, B., Pietranik, A., Cawood, P.A., Kemp, A.I., and Storey, C., 2010, The generation and evolution of the continental crust: Journal of the Geological Society, v. 167, p. 229–248.

Hawkesworth, C., and Jaupart, C., 2021, Heat flow constraints on the mafic character of Archean continental crust: Earth and Planetary Science Letters, v. 571, p. 117091.

Hawkesworth, C., and Kemp, T., 2021, A Pilbara perspective on the generation of Archaean continental crust: Chemical Geology, v. 578, p. 120326, doi:10.1016/j.chemgeo.2021.120326.

Hawkesworth, C.J., and Kemp, A.I.S., 2006, Using hafnium and oxygen isotopes in zircons to unravel the record of crustal evolution: Chemical Geology, v. 226, p. 144–162, doi:10.1016/j.chemgeo.2005.09.018.

Haxel, G.B., Hedrick, J.B., Orris, G.J., Stauffer, P.H., & Hendley, J.W., 2002, Rare earth elements: critical resources for high technology: SGS Fact Sheet 087–02.

Heilimo, E., Halla, J., and Hölttä, P., 2010, Discrimination and origin of the sanukitoid series: Geochemical constraints from the Neoarchean western Karelian Province (Finland): Lithos, v. 115, p. 27–39, doi:10.1016/j.lithos.2009.11.001.

Helt, K.M., Williams-Jones, A.E., Clark, J.R., Wing, B.A., and Wares, R.P., 2014, Constraints on the Genesis of the Archean Oxidized, Intrusion-Related Canadian Malartic Gold Deposit, Quebec, Canada: Economic Geology, v. 109, p. 713–735, doi:10.2113/econgeo.109.3.713.

Henckel, J., Poulsen, K.H., Sharp, T., and Spora, P., 2016, Lake Victoria Goldfields: Episodes, v. 39, p. 135–154, doi:10.18814/epiiugs/2016/v39i2/95772.

Henderson, B., 2016, What do epsilon hafnium isotopic arrays tell us about Wilson cycle tectonics? Implications for the type area in the Appalachian-Variscan Orogen [PhD thesis in geology]: The Unversity of Adelaide, 340 p.

Herzberg, C., Condie, K., and Korenaga, J., 2010a, Thermal history of the Earth and its petrological expression: Earth and Planetary Science Letters, v. 292, p. 79–88, doi:10.1016/j.epsl.2010.01.022.

Herzberg, C., Condie, K., and Korenaga, J., 2010b, Thermal history of the Earth and its petrological expression: Earth and Planetary Science Letters, v. 292, p. 79–88, doi:10.1016/j.epsl.2010.01.022.

Hilgers, C., Dilg-Gruschinski, K., and Urai, J.L., 2003, Microstructures grown experimentally from advectivesupersaturated solution and their implication for natural vein systems: Journal of Geochemical Exploration, v. 78–79, p. 221–225, doi:10.1016/S0375-6742(03)00081-5.

Hodkiewicz, P.F., Groves, D.I., Davidson, G.J., Weinberg, R.F., and Hagemann, S.G., 2009, Influence of structural setting on sulphur isotopes in Archean orogenic gold deposits, Eastern Goldfields Province, Yilgarn, Western Australia: Mineralium Deposita, v. 44, p. 129–150, doi:10.1007/s00126-008-0211-5.

Hodkiewicz, P.F., Weinberg, R.F., Gardoll, S.J., and Groves, D.I., 2005, Complexity gradients in the Yilgarn Craton: Fundamental controls on crustal-scale fluid flow and the formation of world-class orogenic-gold deposits: Australian Journal of Earth Sciences, v. 52, p. 831–841, doi:10.1080/08120090500304257.

Hoefs, J., 2009, Stable isotope geochemistry: Springer, v. 285.

Hoffmann, J.E., Münker, C., Næraa, T., Rosing, M.T., Herwartz, D., Garbe-Schönberg, D., and Svahnberg, H., 2011, Mechanisms of Archean crust formation inferred from high-precision HFSE systematics in TTGs: Geochimica et Cosmochimica Acta, v. 75, p. 4157–4178, doi:10.1016/j.gca.2011.04.027.

Holdsworth, R.E., and Pinheiro, R.V.L., 2000, The anatomy of shallow-crustal transpressional structures: insights from the Archaean CarajaÂ s fault zone, Amazon, Brazil: Journal of Structural Geology, v. 22, p. 1105–1123.

Hopkins, M.D., Harrison, T.M., and Manning, C.E., 2010, Constraints on Hadean geodynamics from mineral inclusions in >4Ga zircons: Earth and Planetary Science Letters, v. 298, p. 367–376, doi:10.1016/j.epsl.2010.08.010.

Hopkins, M., Harrison, T.M., and Manning, C.E., 2008, Low heat flow inferred from >4 Gyr zircons suggests Hadean plate boundary interactions: Nature, v. 456, p. 493–496, doi:10.1038/nature07465.

Hronsky, J.M.A., Groves, D.I., Loucks, R.R., Begg, G.,C., 2012. A unified model for gold mineralisation in accretionary orogens and implications for regional-scale exploration targeting methods. Miner Deposita 47, 339–358. https://doi.org/10.1007/s00126-012-0402-y

Hu, R., Fu, S., Huang, Y., Zhou, M.-F., Fu, S., Zhao, C., Wang, Y., Bi, X., and Xiao, J., 2017, The giant South China Mesozoic low-temperature metallogenic domain: Reviews and a new geodynamic model: Journal of Asian Earth Sciences, v. 137, p. 9–34, doi:10.1016/j.jseaes.2016.10.016.

Huang, B., Kusky, T., Wang, L., Polat, A., Fu, D., Windley, B., Deng, H., and Wang, J., 2019, Structural relationships and kinematics of the Neoarchean Dengfeng forearc and accretionary complexes, southern North China craton: GSA Bulletin, v. 131, p. 966–996, doi:10.1130/B31938.1.

Huston, D.L., Doublier, M.P., Eglington, B., Pehrsson, S., Piercey, S., and Mercier-Langevin, P., 2023, Convergent margin metallogenic cycles: A window to secular changes in Earth's tectonic evolution: Earth-Science Reviews, v. 245, p. 104551, doi:10.1016/j.earscirev.2023.104551.

Hutchison, W., Finch, A.A., and Boyce, A.J., 2020, The sulfur isotope evolution of magmatic-hydrothermal fluids: insights into ore-forming processes: Geochimica et Cosmochimica Acta, v. 288, p. 176–198, doi:10.1016/j.gca.2020.07.042.

I-J

IAMGOLD, 2009, The Licenses relating to the Agreement to Redevelop the Buckreef Gold Mine (between the Government of the United Republic of Tanzania and East Africa Mines Limited:

Iizuka, T., Yamaguchi, T., Itano, K., Hibiya, Y., and Suzuki, K., 2017, What Hf isotopes in zircon tell us about crust–mantle evolution: Lithos, v. 274–275, p. 304–327, doi:10.1016/j.lithos.2017.01.006.

Jackson, J., 2002, Strength of the continental lithosphere: time to abandon the jelly sandwich? GSA today, v. 12, p. 4–10.

Jahn, B.-M., Glikson, A.Y., Peucat, J.J., and Hickman, A.H., 1981, REE geochemistry and isotopic data of Archean silicic volcanics and granitoids from the Pilbara Block, Western Australia: implications for the early crustal evolution: Geochimica et Cosmochimica Acta, v. 45, p. 1633–1652, doi:10.1016/S0016-7037(81)80002-6.

Jayananda, M., Martin, H., Peucat, J.-J., and Mahabaleswar, B., 1995, Late Archaean crust-mantle interactions: geochemistry of LREE-enriched mantle derived magmas. Example of the Closepet batholith, southern India: Contributions to Mineralogy and Petrology, v. 119, p. 314–329, doi:10.1007/BF00307290.

Jayananda, M., Moyen, J.-F., Martin, H., Peucat, J.-J., Auvray, B., and Mahabaleswar, B., 2000, Late Archaean (2550–2520 Ma) juvenile magmatism in the Eastern Dharwar craton, southern India: constraints from geochronology, Nd–Sr isotopes and whole rock geochemistry: Precambrian Research, v. 99, p. 225–254, doi:10.1016/S0301-9268(99)00063-7.

Jayananda, M., Santosh, M., and Aadhiseshan, K.R., 2018, Formation of Archean (3600–2500 Ma) continental crust in the Dharwar Craton, southern India: Earth-Science Reviews, v. 181, p. 12–42, doi:10.1016/j.earscirev.2018.03.013.

Jébrak, M., and Marcoux, E. Géologie des ressources minérales:

Jenkin, G.R., Lusty, P.A., McDonald, I., Smith, M.P., Boyce, A.J., and Wilkinson, J.J., 2015, Ore deposits in an evolving Earth: an introduction: The Geological Society of London London, v. 393.

Johnson, T.E., Brown, M., Gardiner, N.J., Kirkland, C.L., and Smithies, R.H., 2017, Earth's first stable continents did not form by subduction: Nature, v. 543, p. 239–242, doi:10.1038/nature21383.

Johnson, T.E., Brown, M., Kaus, B.J.P., and VanTongeren, J.A., 2014, Delamination and recycling of Archaean crust caused by gravitational instabilities: Nature Geoscience, v. 7, p. 47–52, doi:10.1038/ngeo2019.

Johnson, S., Cutten, H., Muhongo, S., and De Waele, B., 2003, Neoarchaean magmatism and metamorphism of the western granulites in the central domain of the Mozambique belt, Tanzania: U–Pb shrimp geochronology and PT estimates: Tectonophysics, v. 375, p. 125–145.

Johnson, T.E., Kirkland, C.L., Gardiner, N.J., Brown, M.,

Smithies, R.H., and Santosh, M., 2019, Secular change in TTG compositions: Implications for the evolution of Archaean geodynamics: Earth and Planetary Science Letters, v. 505, p. 65–75, doi:10.1016/j.epsl.2018.10.022.

Joly, A., Porwal, A., McCuaig, T.C., Chudasama, B., Dentith, M.C., and Aitken, A.R.A., 2015, Mineral systems approach applied to GIS-based 2D-prospectivity modelling of geological regions: Insights from Western Australia: Ore Geology Reviews, v. 71, p. 673–702, doi:10.1016/j.oregeorev.2015.06.007.

K

Kabete, J.M., Groves, D.I., McNaughton, N.J., and Mruma, A.H., 2012a, A new tectonic and temporal framework for the Tanzanian Shield: Implications for gold metallogeny and undiscovered endowment: Ore Geology Reviews, v. 48, p. 88–124, doi:10.1016/j.oregeorev.2012.02.009.

Kabete, J.M., McNaughton, N.J., Groves, D.I., and Mruma, A.H., 2012b, Reconnaissance SHRIMP U–Pb zircon geochronology of the Tanzania Craton: Evidence for Neoarchean granitoid–greenstone belts in the Central Tanzania Region and the Southern East African Orogen: Precambrian Research, v. 216–219, p. 232–266, doi:10.1016/j.precamres.2012.06.020.

Kamber, B.S., Whitehouse, M.J., Bolhar, R., and Moorbath, S., 2005, Volcanic resurfacing and the early terrestrial crust: Zircon U–Pb and REE constraints from the Isua Greenstone Belt, southern West Greenland: Earth and Planetary Science Letters, v. 240, p. 276–290, doi:10.1016/j.epsl.2005.09.037.

Kamenetsky, V.S., Everard, J.L., Crawford, A.J., Varne, R., Eggins, S.M., and Lanyon, R., 2000, Enriched End-member of Primitive MORB Melts: Petrology and Geochemistry of Glasses from Macquarie Island (SW Pacific): Journal of Petrology, v. 41, p. 411–430, doi:10.1093/petrology/41.3.411.

Kanehira, K., Yui, S., Sakai, H., and Sasaki, A., 1973, Sulphide globules and sulphur isotope ratios in the abyssal tholeiite from the Mid-Atlantic Ridge near 30°N latitude: Geochemical Journal, v. 7, p. 89–96, doi:https://doi.org/10.2343/geochemj.7.89.

Kazimoto, E.O., and Ikingura, J.R., 2014, Trace element geochemistry and petrogenesis of the granitoids and high-K andesite hosting gold mineralisation in the Archean Musoma-Mara Greenstone Belt, Tanzania: Journal of African Earth Sciences, v. 91, p. 66–78, doi:10.1016/j.jafrearsci.2013.12.003.

Keller, C.B., and Schoene, B., 2012, Statistical geochemistry reveals disruption in secular lithospheric evolution about 2.5 Gyr ago: Nature, v. 485, p. 490–493, doi:10.1038/nature11024.

Kelley, K.D., Romberger, S.B., Beaty, D.W., Pontius, J.A., Snee, L.W., Stein, H.J., and Thompson, T.B., 1998, Geochemical and geochronological constraints on the genesis of Au-Te deposits at Cripple Creek, Colorado: Economic Geology, v. 93, p. 981–1012.

Kemp, A.I.S., Hawkesworth, C.J., Paterson, B.A., and Kinny, P.D., 2006, Episodic growth of the Gondwana supercontinent from hafnium and oxygen isotopes in zircon: Nature, v. 439, p. 580–583, doi:10.1038/nature04505.

Kemp, A.I., Vervoort, J.D., Bjorkman, K.E., and Iaccheri, L.M., 2017, Hafnium isotope characteristics of palaeoarchaean zircon OG 1/OGC from the Owens Gully Diorite, Pilbara Craton, Western Australia: Geostandards and Geoanalytical Research, v. 41, p. 659–673.

Kemp, A., Wilde, S., Hawkesworth, C., Coath, C., Nemchin, A., Pidgeon, R., Vervoort, J., and DuFrane, S., 2010, Hadean crustal evolution revisited: new constraints from Pb–Hf isotope systematics of the Jack Hills zircons: Earth and Planetary Science Letters, v. 296, p. 45–56.

Kerr, A., 2003, Oceanic Plateaus, in Treatise on geochemistry, Pergamon, p. 537–565.

Kerrich, R., Goldfarb, R.J., and Richards, J.P., 2005, Metallogenic provinces in an evolving geodynamic framework: Economic Geology 100th Anniversary, v. 13, p. 1097–1136.

Kita, N.T., Ushikubo, T., Fu, B., and Valley, J.W., 2009, High precision SIMS oxygen isotope analysis and the effect of sample topography: Chemical Geology, v. 264, p. 43–57.

Kitayama, Y., 2018, Les quatre isotopes du soufre dans les kimberlites de Sibérie, traceurs du recyclage de croûte océanique et de sédiments Archéens dans le manteau terrestre [PhD thesis in geology]: Université de Lorraine, 333 p.

Klemm, R., and Klemm, D., 2013, Gold Production Sites

and Gold Mining in Ancient Egypt: Gold and Gold Mining in Ancient Egypt and Nubia: Geoarchaeology of the Ancient Gold Mining Sites in the Egyptian and Sudanese Eastern Deserts, p. 51–339.

Kolb, J., Dziggel, A., Bagas, L., 2015, Hypozonal lode gold deposits: A genetic concept based on a review of the New Consort, Renco, Hutti, Hira Buddini, Navachab, Nevoria and The Granites deposits, Precambrian Research, 262, 20-44. doi:10.1016/j.precamres.2015.02.022

Komiya, T., Maruyama, S., Masuda, T., Nohda, S., Hayashi, M., and Okamoto, K., 1999, Plate tectonics at 3.8–3.7 Ga: field evidence from the Isua accretionary complex, southern West Greenland: The Journal of Geology, v. 107, p. 515–554.

Korenaga, J., 2021, Was There Land on the Early Earth? Life, v. 11, p. 1142, doi:10.3390/life11111142.

Krapez, B., Brown, S.J.A., Hand, J., Barley, M.E., and Cas, R.A.F., 2000, Age constraints on recycled crustal and supracrustal sources of Archaean metasedimentary sequences, Eastern Goldfields Province, Western Australia: evidence from SHRIMP zircon dating: Tectonophysics, v. 322, p. 89–133, doi:10.1016/S0040-1951(00)00059-7.

Kröner, A., and Layer, P., 1992, Crust formation and plate motion in the early Archean: Science, v. 256, p. 1405–1411.

Kusky, T.M., Windley, B.F., and Polat, A., 2018, Geological Evidence for the Operation of Plate Tectonics throughout the Archean: Records from Archean Paleo-Plate Boundaries: Journal of Earth Science, v. 29, p. 1291–1303, doi:10.1007/s12583-018-0999-6.

Kusky, T., Windley, B.F., Polat, A., Wang, L., Ning, W., and Zhong, Y., 2021, Archean dome-and-basin style structures form during growth and death of intraoceanic and continental margin arcs in accretionary orogens: Earth-Science Reviews, v. 220, p. 103725, doi:10.1016/j.earscirev.2021.103725.

Kwelwa, S.D., 2017, Geological controls on gold mineralization in the Kukuluma Terrain, Geita Greenstone Belt, NW Tanzania [PhD thesis in geology]: James Cook University, 206 p.

Kwelwa, S.D., Sanislav, I.V., Dirks, P.H.G.M., Blenkinsop, T., and Kolling, S.L., 2018, Zircon U-Pb ages and Hf isotope data from the Kukuluma Terrain of the Geita Greenstone Belt, Tanzania Craton: Implications for stratigraphy, crustal growth and timing of gold mineralization: Journal of African Earth Sciences, v. 139, p. 38–54, doi:10.1016/j.jafrearsci.2017.11.027.

L

Labidi, J., Cartigny, P., and Moreira, M., 2013, Non-chondritic sulphur isotope composition of the terrestrial mantle: Nature, v. 501, p. 208–211, doi:10.1038/nature12490.

Labrosse, S., and Jaupart, C., 2007, Thermal evolution of the Earth: Secular changes and fluctuations of plate characteristics: Earth and Planetary Science Letters, v. 260, p. 465–481, doi:10.1016/j.epsl.2007.05.046.

LaFlamme, C. et al., 2016, In situ multiple sulfur isotope analysis by SIMS of pyrite, chalcopyrite, pyrrhotite, and pentlandite to refine magmatic ore genetic models: Chemical Geology, v. 444, p. 1–15, doi:10.1016/j.chemgeo.2016.09.032.

LaFlamme, C., Fiorentini, M.L., Lindsay, M.D., and Bui, T.H., 2018c, Atmospheric sulfur is recycled to the crystalline continental crust during supercontinent formation: Nature Communications, v. 9, p. 4380, doi:10.1038/s41467-018-06691-3.

LaFlamme, C., Jamieson, J.W., Fiorentini, M.L., Thébaud, N., Caruso, S., and Selvaraja, V., 2018b, Investigating sulfur pathways through the lithosphere by tracing mass independent fractionation of sulfur to the Lady Bountiful orogenic gold deposit, Yilgarn Craton: Gondwana Research, v. 58, p. 27–38, doi:10.1016/j.gr.2018.02.005.

LaFlamme, C., Sugiono, D., Thébaud, N., Caruso, S., Fiorentini, M., Selvaraja, V., Jeon, H., Voute, F., and Martin, L., 2018a, Multiple sulfur isotopes monitor fluid evolution of an Archean orogenic gold deposit: Geochimica et Cosmochimica Acta, v. 222, p. 436–446, doi:10.1016/j.gca.2017.11.003.

Lambeck, A., Mernagh, T.P., and Wyborn, L., 2011, Are Iron-Rich Sedimentary Rocks the Key to the Spike in Orogenic Gold Mineralization in the Paleoproterozoic? Economic Geology, v. 106, p. 321–330, doi:10.2113/econgeo.106.3.321.

Large, R.R., Gregory, D.D., Steadman, J.A., Tomkins, A.G., Lounejeva, E., Danyushevsky, L.V., Halpin, J.A., Maslennikov, V., Sack, P.J., and Mukherjee, I., 2015, Gold in the oceans through time: Earth and Planetary

Science Letters, v. 428, p. 139–150.

Laurent, O., 2012, Les changements géodynamiques à la transition Archéen-Protérozoïque: étude des granitoïdes de la marge Nord du craton du Kaapvaal (Afrique du Sud) [PhD thesis in geology]: Université Blaise Pascal, 532 p.

Laurent, O., Martin, H., Moyen, J.F., and Doucelance, R., 2014, The diversity and evolution of late-Archean granitoids: Evidence for the onset of "modern-style" plate tectonics between 3.0 and 2.5Ga: Lithos, v. 205, p. 208–235, doi:10.1016/j.lithos.2014.06.012.

Laurent, O., Moyen, J.-F., Wotzlaw, J.-F., Björnsen, J., and Bachmann, O., 2021, Early Earth zircons formed in residual granitic melts produced by tonalite differentiation: Geology, v. 50, p. 437–441, doi:10.1130/G49232.1.

Laurent, O., Zeh, A., Brandl, G., Vezinet, A., and Wilson, A., 2019, Granitoids and Greenstone Belts of the Pietersburg Block—Witnesses of an Archaean Accretionary Orogen Along the Northern Edge of the Kaapvaal Craton, in Kröner, A. and Hofmann, A. eds., The Archaean Geology of the Kaapvaal Craton, Southern Africa, Cham, Springer International Publishing, p. 83–107, doi:10.1007/978-3-319-78652-0_4.

Lawley, C., Selby, D., and Imber, J., 2013, Re-Os molybdenite, pyrite, and chalcopyrite geochronology, lupa goldfield, southwestern Tanzania: tracing metallogenic time scales at midcrustal shear zones hosting orogenic Au deposits: Economic Geology, v. 108, p. 1591–1613.

Le Maître, R.W., 1989, A classification of igneous rocks and glossary of terms. Recommandations of the International Union of Geological Sciences, Subcommission on the systematics of Igneous Rocks: Oxford, Blackwell, 193 p.

Le Mignot, E., Reisberg, L., André-Mayer, A.-S., Bourassa, Y., Fontaine, A., and Miller, J., 2017, Re-Os Geochronological Evidence for Multiple Paleoproterozoic Gold Events at the Scale of the West African Craton: Economic Geology, v. 112, p. 145–168, doi:10.2113/econgeo.112.1.145.

Lenardic, A., 2018, The diversity of tectonic modes and thoughts about transitions between them: Philosophical Transactions of the Royal Society A: Mathematical, Physical and Engineering Sciences, v. 376, p. 20170416.

Lewis, J.A., Hoffmann, J.E., Schwarzenbach, E.M., Strauss, H., Liesegang, M., and Rosing, M.T., 2021, Sulfur isotope evidence for surface-derived sulfur in Eoarchean TTGs: Earth and Planetary Science Letters, v. 576, p. 117218, doi:10.1016/j.epsl.2021.117218.

Li, N., Deng, J., Yang, L.-Q., Goldfarb, R.J., Zhang, C., Marsh, E., Lei, S.-B., Koenig, A., and Lowers, H., 2014, Paragenesis and geochemistry of ore minerals in the epizonal gold deposits of the Yangshan gold belt, West Qinling, China: Mineralium Deposita, v. 49, p. 427–449, doi:10.1007/s00126-013-0498-8.

Li, Y., and Liu, J., 2006, Calculation of sulfur isotope fractionation in sulfides: Geochimica et Cosmochimica Acta, v. 70, p. 1789–1795, doi:10.1016/j.gca.2005.12.015.

Liu, J., Liu, F., Ding, Z., Li, Y., Jin, W., and Tian, Z., 2024, Mesoarchean–Neoarchean coupled crust–mantle differentiation followed by gravity-driven lithospheric delamination and subduction initiation in the North China Craton: Precambrian Research, v. 404, p. 107349, doi:10.1016/j.precamres.2024.107349.

Ludwig, K.R., 2012, User's manual for Isoplot 3.75: A geochronological toolkit for Microsoft Excel: Berkeley Geochronology Center Special Publication, v. 5, p. 75.

M

Maboko, M., Pedersen, R., Manya, S., Torssander, P., and Mwache, M., 2006, The origin of late archaean granitoids in the Sukumaland greenstone belt of Northern Tanzania: geochemical and isotopic constraints: Tanzania Journal of Science, v. 32, p. 75–88, doi:10.4314/tjs.v32i1.18431.

Magayan A.A.M., 1998, Controls on lode-gold mineralisation at the Buhemba and Kilamongo deposits, Musoma greenstone belt, Tanzanian Craton [B.Sc]: University of Western Australia, 150 p.

Mallard, C., Coltice, N., Seton, M., Müller, R.D., and Tackley, P.J., 2016, Subduction controls the distribution and fragmentation of Earth's tectonic plates: Nature, v. 535, p. 140–143.

Manya, S., 2017, Characterization of geochemical alteration halo associated with gold mineralization at the Buzwagi mine, northern Tanzania: Journal of African Earth Sciences, v. 129, p. 136–145, doi:10.1016/j.

jafrearsci.2017.01.006.

Manya, S., 2004, Geochemistry and petrogenesis of volcanic rocks of the Neoarchaean Sukumaland Greenstone Belt, northwestern Tanzania: Journal of African Earth Sciences, v. 40, p. 269–279, doi:10.1016/j.jafrearsci.2004.12.006.

Manya, S., 2016b, Geochemistry of the mafic volcanic rocks of the Buzwagi gold mine in the Neoarchaean Nzega greenstone belt, northern Tanzania: Lithos, v. 264, p. 86–95, doi:10.1016/j.lithos.2016.08.016.

Manya, S., 2011, Nd-isotopic mapping of the Archaean–Proterozoic boundary in southwestern Tanzania: Implication for the size of the Archaean Tanzania Craton: Gondwana Research, v. 20, p. 325–334, doi:10.1016/j.gr.2011.01.002.

Manya, S., 2016a, Petrogenesis and emplacement of the TTG and K-rich granites at the Buzwagi gold mine, northern Tanzania: Implications for the timing of gold mineralization: Lithos, v. 256–257, p. 26–40, doi:10.1016/j.lithos.2016.03.025.

Manya, S., Kobayashi, K., Maboko, M.A.H., and Nakamura, E., 2006, Ion microprobe zircon U–Pb dating of the late Archaean metavolcanics and associated granites of the Musoma-Mara Greenstone Belt, Northeast Tanzania: Implications for the geological evolution of the Tanzania Craton: Journal of African Earth Sciences, v. 45, p. 355–366, doi:10.1016/j.jafrearsci.2006.03.004.

Manya, S., and Maboko, M.A.H., 2003, Dating basaltic volcanism in the Neoarchaean Sukumaland Greenstone Belt of the Tanzania Craton using the Sm–Nd method: implications for the geological evolution of the Tanzania Craton: Precambrian Research, v. 121, p. 35–45, doi:10.1016/S0301-9268(02)00195-X.

Manya, S., and Maboko, M.A.H., 2008a, Geochemistry and geochronology of Neoarchaean volcanic rocks of the Iramba–Sekenke greenstone belt, central Tanzania: Precambrian Research, v. 163, p. 265–278, doi:10.1016/j.precamres.2008.01.001.

Manya, S., and Maboko, M.A.H., 2008b, Geochemistry of the Neoarchaean mafic volcanic rocks of the Geita area, NW Tanzania: Implications for stratigraphical relationships in the Sukumaland greenstone belt: Journal of African Earth Sciences, v. 52, p. 152–160, doi:10.1016/j.jafrearsci.2008.06.003.

Manya, S., Maboko, M., and Nakamura, E., 2007a, Geochemistry and Nd-isotopic composition of potassic magmatism in the Neoarchaean Musoma-Mara Greenstone Belt, northern Tanzania: Precambrian Research, v. 159, p. 231–240, doi:10.1016/j.precamres.2007.07.001.

Manya, S., Maboko, M., and Nakamura, E., 2007b, The geochemistry of high-Mg andesite and associated adakitic rocks in the Musoma-Mara Greenstone Belt, northern Tanzania: Possible evidence for Neoarchaean ridge subduction? Precambrian Research, v. 159, p. 241–259, doi:10.1016/j.precamres.2007.07.002.

Marini, L., Moretti, R., and Accornero, M., 2011, Sulfur Isotopes in Magmatic-Hydrothermal Systems, Melts, and Magmas: Reviews in Mineralogy and Geochemistry, v. 73, p. 423–492, doi:10.2138/rmg.2011.73.14.

Martin, H., 1986, Effect of steeper Archean geothermal gradient on geochemistry of subduction-zone magmas: Geology, v. 14, p. 753, doi:10.1130/0091-7613(1986)14<753:EOSAGG>2.0.CO;2.

Martin, H., and Moyen, J.-F., 2002, Secular changes in tonalite-trondhjemite-granodiorite composition as markers of the progressive cooling of Earth: Geology, v. 30, p. 319–322, doi:10.1130/0091-7613(2002)030<0319:SCITTG>2.0.CO;2.

Martin, H., Moyen, J.-F., Guitreau, M., Blichert-Toft, J., and Le Pennec, J.-L., 2014, Why Archaean TTG cannot be generated by MORB melting in subduction zones: Lithos, v. 198–199, p. 1–13, doi:10.1016/j.lithos.2014.02.017.

Martin, H., Moyen, J.-F., and Rapp, R., 2009, The sanukitoid series: magmatism at the Archaean–Proterozoic transition: Earth and Environmental Science Transactions of the Royal Society of Edinburgh, v. 100, p. 15–33, doi:10.1017/S1755691009016120.

Martin, H., Smithies, R.H., Rapp, R., Moyen, J.-F., and Champion, D., 2005, An overview of adakite, tonalite–trondhjemite–granodiorite (TTG), and sanukitoid: relationships and some implications for crustal evolution: Lithos, v. 79, p. 1–24, doi:10.1016/j.lithos.2004.04.048.

Martinez-Serrano, R.G., Jacquier, B., and Arnold, M., 1996, The δ34S composition of sulfates and sulfides at the Los Humeros geothermal system, Mexico and their application to physicochemical fluid evolution: Journal of volcanology and geothermal research, v.

76, p. 99–118, doi:https://doi.org/10.1016/0377-0273(95)00083-6.

Maruyama, S., Santosh, M., and Azuma, S., 2018, Initiation of plate tectonics in the Hadean: Eclogitization triggered by the ABEL Bombardment: Geoscience Frontiers, v. 9, p. 1033–1048, doi:10.1016/j.gsf.2016.11.009.

Masurel, Q. et al., 2022, Paleoproterozoic gold events in the southern West African Craton: review and synopsis: Mineralium Deposita, v. 57, p. 513–537, doi:10.1007/s00126-021-01052-5.

McCuaig, T.C., and Hronsky, J.M.A., 2014, The Mineral System ConceptThe Key to Exploration Targeting, in Building Exploration Capability for the 21st Century, Society of Economic Geologists, doi:10.5382/SP.18.08.

Meffre, S., Large, R.R., Steadman, J.A., Gregory, D.D., Stepanov, A.S., Kamenetsky, V.S., Ehrig, K., and Scott, R.J., 2016, Multi-stage enrichment processes for large gold-bearing ore deposits: Ore Geology Reviews, v. 76, p. 268–279, doi:10.1016/j.oregeorev.2015.09.002.

Mériaud, N., Masurel, Q., Thébaud, N., and Tourigny, G., 2022, Fluid pressure–dominated orogenic gold mineralization under low differential stress: case of the Yaouré gold camp, Côte d'Ivoire, West Africa: Mineralium Deposita, v. 57, p. 539–556, doi:10.1007/s00126-019-00927-y.

Messo, C.W., Manya, S., and Maboko, M.A.H., 2012, Geochemistry of the Neoarchaean Volcanic Rocks of the Kilimafedha Greenstone Belt, Northeastern Tanzania: Journal of Geological Research, v. 2012, p. 1–18, doi:10.1155/2012/603971.

Middlemost, E.A.K., 1994, Naming materials in the magma/igneous rock system: Earth-Science Reviews, v. 37, p. 215–224, doi:10.1016/0012-8252(94)90029-9.

Mitchell, R.N., Bleeker, W., Van Breemen, O., Lecheminant, T.N., Peng, P., Nilsson, M.K., and Evans, D.A., 2014, Plate tectonics before 2.0 Ga: Evidence from paleomagnetism of cratons within supercontinent Nuna: American Journal of Science, v. 314, p. 878–894.

Mole, D.R., Kirkland, C.L., Fiorentini, M.L., Barnes, S.J., Cassidy, K.F., Isaac, C., Belousova, E.A., Hartnady, M., and Thebaud, N., 2019a, Time-space evolution of an Archean craton: A Hf-isotope window into continent formation: Earth-Science Reviews, v. 196, p. 102831, doi:10.1016/j.earscirev.2019.04.003.

Mole, D.R., Kirkland, C.L., Fiorentini, M.L., Barnes, S.J., Cassidy, K.F., Isaac, C., Belousova, E.A., Hartnady, M., and Thebaud, N., 2019b, Time-space evolution of an Archean craton: A Hf-isotope window into continent formation: Earth-Science Reviews, v. 196, p. 102831, doi:10.1016/j.earscirev.2019.04.003.

Mole, D.R., Thurston, P.C., Marsh, J.H., Stern, R.A., Ayer, J.A., Martin, L.A.J., and Lu, Y.J., 2021, The formation of Neoarchean continental crust in the south-east Superior Craton by two distinct geodynamic processes: Precambrian Research, v. 356, p. 106104, doi:10.1016/j.precamres.2021.106104.

Monroe, J., Wicander, R., and Hazlett, R., 2006, Physical Geology: Exploring the Earth: Pacific Grove, CA, United States, Brooks, 712 p.

Moore, W.B., Simon, J.I., and Webb, A.A.G., 2017, Heat-pipe planets: Earth and Planetary Science Letters, v. 474, p. 13–19.

Moreira, H., Seixas, L., Storey, C., Fowler, M., Lasalle, S., Stevenson, R., and Lana, C., 2018, Evolution of Siderian juvenile crust to Rhyacian high Ba-Sr magmatism in the Mineiro Belt, southern São Francisco Craton: Geoscience Frontiers, v. 9, p. 977–995, doi:10.1016/j.gsf.2018.01.009.

Moreira, H., Storey, C., Fowler, M., Seixas, L., and Dunlop, J., 2020, Petrogenetic processes at the tipping point of plate tectonics: Hf-O isotope ternary modelling of Earth's last TTG to sanukitoid transition: Earth and Planetary Science Letters, v. 551, p. 116558, doi:10.1016/j.epsl.2020.116558.

Moresi, L., and Solomatov, V., 1998, Mantle convection with a brittle lithosphere: thoughts on the global tectonic styles of the Earth and Venus: Geophysical Journal International, v. 133, p. 669–682.

Morris, P.A., and Kirkland, C.L., 2014, Melting of a subduction-modified mantle source: A case study from the Archean Marda Volcanic Complex, central Yilgarn Craton, Western Australia: Lithos, v. 190–191, p. 403–419, doi:10.1016/j.lithos.2013.11.016.

Moyen, J.-F., 2009, High Sr/Y and La/Yb ratios: The meaning of the "adakitic signature": Lithos, v. 112, p. 556–574, doi:10.1016/j.lithos.2009.04.001.

Moyen, J.-F., 2011, The composite Archaean grey gneisses: Petrological significance, and evidence for a non-unique tectonic setting for Archaean crustal

growth: Lithos, v. 123, p. 21–36, doi:10.1016/j.lithos.2010.09.015.

Moyen, J.-F., and Laurent, O., 2018, Archaean tectonic systems: A view from igneous rocks: Lithos, v. 302–303, p. 99–125, doi:10.1016/j.lithos.2017.11.038.

Moyen, J.-F., and Martin, H., 2012, Forty years of TTG research: Lithos, v. 148, p. 312–336, doi:10.1016/j.lithos.2012.06.010.

Moyen, J.-F., Martin, H., Jayananda, M., and Auvray, B., 2003, Late Archaean granites: a typology based on the Dharwar Craton (India): Archaean Tectonics, Volume 1, v. 127, p. 103–123, doi:10.1016/S0301-9268(03)00183-9.

Moyen, J.-F., Stevens, G., and Kisters, A., 2006, Record of mid-Archaean subduction from metamorphism in the Barberton terrain, South Africa: Nature, v. 442, p. 559–562.

Mshiu, E.E., and Maboko, M.A.H., 2012a, Geochemistry and petrogenesis of the late Archaean high-K granites in the southern Musoma-Mara Greenstone Belt: Their influence in evolution of Archaean Tanzania Craton: Journal of African Earth Sciences, v. 66–67, p. 1–12, doi:10.1016/j.jafrearsci.2012.03.002.

Mshiu, E.E., and Maboko, M.A.H., 2012b, Geochemistry and petrogenesis of the late Archaean high-K granites in the southern Musoma-Mara Greenstone Belt: Their influence in evolution of Archaean Tanzania Craton: Journal of African Earth Sciences, v. 66–67, p. 1–12, doi:10.1016/j.jafrearsci.2012.03.002.

Mshiu, E., Marobhe, I., and Maboko, M., 2009, Aerogeophysical, Geological and Geochemical Investigation of the Late Archaean Granitoids in the Musoma-Mara Greenstone Belt, NE Tanzania: Journal of Earth African sciences, v. 16, p. 279–279.

Mtoro, M., Maboko, M.A.H., and Manya, S., 2009, Geochemistry and geochronology of the bimodal volcanic rocks of the Suguti area in the southern part of the Musoma-Mara Greenstone Belt, Northern Tanzania: Precambrian Research, v. 174, p. 241–257, doi:10.1016/j.precamres.2009.07.006.

Muhongo, S., Tuisku, P., Mnali, S., Temu, E., Appel, P., and Stendal, H., 2002, High-pressure granulite-facies metagabbros in the Ubendian Belt of SW Tanzania: preliminary petrography and P–T estimates: Journal of African Earth Sciences, v. 34, p. 279–285, doi:10.1016/S0899-5362(02)00026-X.

Müller, R.D., Sdrolias, M., Gaina, C., and Roest, W.R., 2008, Age, spreading rates, and spreading asymmetry of the world's ocean crust: Geochemistry, Geophysics, Geosystems, v. 9.

Murray, S., Torvela, T., Bills, H., 2018, A geostatistical approach to gold distribution controlled by large-scale fault systems in Côte d'Ivoire: Journal of African Earth Sciences, 151, 351-370. doi:10.1016/j.jafrearsci.2018.12.019

Mvondo, H., Lentz, D., and Bardoux, M., 2017, Crustal shortening and thickening in Neoarchean granite-greenstone belts: A case study from the link between the ~ 2.7 Ga Elu and Hope Bay belts, northeast Slave craton, Canada: Journal of Structural Geology, v. 104, p. 6–20, doi:10.1016/j.jsg.2017.10.004.

N

Naeraa, T., Scherstén, A., Rosing, M., Kemp, A., Hoffmann, J., Kokfelt, T., and Whitehouse, M., 2012, Hafnium isotope evidence for a transition in the dynamics of continental growth 3.2 Gyr ago: Nature, v. 485, p. 627–630.

Nebel, O., Capitanio, F.A., Moyen, J.-F., Weinberg, R.F., Clos, F., Nebel-Jacobsen, Y.J., and Cawood, P.A., 2018, When crust comes of age: on the chemical evolution of Archaean, felsic continental crust by crustal drip tectonics: Philosophical Transactions of the Royal Society A: Mathematical, Physical and Engineering Sciences, v. 376, p. 20180103, doi:10.1098/rsta.2018.0103.

Nebel-Jacobsen, Y., Münker, C., Nebel, O., Gerdes, A., Mezger, K., and Nelson, D.R., 2010, Reworking of Earth's first crust: constraints from Hf isotopes in Archean zircons from Mt. Narryer, Australia: Precambrian Research, v. 182, p. 175–186.

Neuendorf, K.K., Mehl, J. J. P., and Jackson, J. A., 2005, Glossary of geology: Springer Science & Business Media, 779 p.

Neves, S.P., da Silva, J.M.R., and Mariano, G., 2005, Oblique lineations in orthogneisses and supracrustal rocks: vertical partitioning of strain in a hot crust (eastern Borborema Province, NE Brazil): Journal of Structural Geology, v. 27, p. 1513–1527, doi:10.1016/j.jsg.2005.02.002.

Nutman, A.P., Friend, C.R., and Bennett, V.C., 2002,

Evidence for 3650–3600 Ma assembly of the northern end of the Itsaq Gneiss Complex, Greenland: implication for early Archaean tectonics: Tectonics, v. 21, p. 5–1, doi:10.1029/2000tc001203.

O

Occhipinti, S., Metelka, V., Lindsay, M., Aitken, A., Pirajno, F., and Tyler, I., 2020, The evolution from plate margin to intraplate mineral systems in the Capricorn Orogen, links to prospectivity: Ore Geology Reviews, v. 127, p. 103811.

O'Connor, J.T., 1965, A classification for quartz-rich igneous rocks based on feldspar ratios: U.S. Geological Survey Professional Paper, v. 525B, p. 79–84.

Ohmoto, H., 1972, Systematics of Sulfur and Carbon Isotopes in Hydrothermal Ore Deposits: Economic Geology, v. 67, p. 551–578, doi:10.2113/gsecongeo.67.5.551.

O'Neil, J., and Carlson, R.W., 2017, Building Archean cratons from Hadean mafic crust: Science, v. 355, p. 1199–1202.

O'Neil, J., Rizo, H., Boyet, M., Carlson, R., and Rosing, M., 2016, Geochemistry and Nd isotopic characteristics of Earth's Hadean mantle and primitive crust: Earth and Planetary Science Letters, v. 442, p. 194–205.

OreCorp, 2017, ASX Pre-Feasibility Study Demonstrates Significant Potential of Nyanzaga Gold Project: ASX report.

OreCorp, 2020, Kilimani Mineral Resource Estimate and New Targets Identified Within Nyanzaga Special Mining Licence Application Area - Tanzania: JORC.

OreCorp, 2022, DFS Completion and Kilimani Mineral Resource Estimate update within the Nyanzaga Special Mining Licence – Tanzania: ASX release. https://perseusmining.com/asx-announcements/

Oriolo, S. et al., 2022, The petrologic and petrochronologic record of progressive vs polyphase deformation: Opening the analytical toolbox: Earth-Science Reviews, v. 234, p. 104235, doi:10.1016/j.earscirev.2022.104235.

Osei, K.P., Kirkland, C.L., and Mole, D.R., 2021, Nd and Hf isoscapes of the Yilgarn Craton, Western Australia and implications for its mineral systems: Gondwana Research, v. 92, p. 253–265, doi:10.1016/j.gr.2020.12.027.

P

Paces, J.B., and Miller Jr, J.D., 1993, Precise U-Pb ages of Duluth complex and related mafic intrusions, northeastern Minnesota: Geochronological insights to physical, petrogenetic, paleomagnetic, and tectonomagmatic processes associated with the 1.1 Ga midcontinent rift system: Journal of Geophysical Research: Solid Earth, v. 98, p. 13997–14013.

Palin, R.M., and Santosh, M., 2021, Plate tectonics: What, where, why, and when? Gondwana Research, v. 100, p. 3–24, doi:10.1016/j.gr.2020.11.001.

Palin, R.M., Santosh, M., Cao, W., Li, S.-S., Hernández-Uribe, D., and Parsons, A., 2020, Secular change and the onset of plate tectonics on Earth: Earth-Science Reviews, v. 207, p. 103172, doi:10.1016/j.earscirev.2020.103172.

Palin, J.M., and Xu, Y., 2000, Gilt by Association? Origins of Pyritic Gold Ores in the Victory Mesothermal Gold Deposit, Western Australia: Economic Geology, v. 95, p. 1627–1634, doi:0361-0128/00/2107/1627-8.

Parra, M., Mora, A., Jaramillo, C., Torres, V., Zeilinger, G., and Strecker, M.R., 2010, Tectonic controls on Cenozoic foreland basin development in the north-eastern Andes, Colombia: Basin Research, v. 22, p. 874–903, doi:10.1111/j.1365-2117.2009.00459.x.

Passchier, C.W., Trouw, R.A.J., 2005, Microtectonics: Berlin, New-York, v. econd ed. Springer.

Patchett, P.J., 1983, Importance of the Lu-Hf isotopic system in studies of planetary chronology and chemical evolution: Geochimica et Cosmochimica Acta, v. 47, p. 81–91, doi:10.1016/0016-7037(83)90092-3.

Paton, C., Woodhead, J.D., Hellstrom, J.C., Hergt, J.M., Greig, A., and Maas, R., 2010, Improved laser ablation U-Pb zircon geochronology through robust downhole fractionation correction: Geochemistry, Geophysics, Geosystems, v. 11.

Pearce, J.A., 2008, Geochemical fingerprinting of oceanic basalts with applications to ophiolite classification and the search for Archean oceanic crust: Lithos, v. 100, p. 14–48, doi:10.1016/j.lithos.2007.06.016.

Pearce, J.A., 2014, Immobile Element Fingerprinting of Ophiolites: Elements, v. 10, p. 101–108, doi:10.2113/gselements.10.2.101.

Pease, V., Percival, J., Smithies, H., Stevens, G., and Van Kranendonk, M., 2008, When did plate tectonics

begin? Evidence from the orogenic record: When did plate tectonics begin on planet Earth, v. 440, p. 199–228.

Perchuk, A.L., Zakharov, V.S., Gerya, T.V., and Brown, M., 2019, Hotter mantle but colder subduction in the Precambrian: What are the implications? Precambrian Research, v. 330, p. 20–34, doi:10.1016/j.precamres.2019.04.023.

Percival, J.A., 1994, Chapter 9 Archean High-Grade Metamorphism, in Condie, K.C. ed., Developments in Precambrian Geology, Elsevier, v. 11, p. 357–410, doi:10.1016/S0166-2635(08)70227-5.

Percival, J., Skulski, T., Sanborn-Barrie, M., Stott, G., Leclair, A.D., Corkery, M.T., and Boily, M., 2012, Geology and tectonic evolution of the Superior Province, Canada: Geological Association of Canada Special Paper, v. 49, p. 321–378.

Perret, J., 2021, Répartition spatio-temporelle du système métallogénique de l'or panafricain au sein du bouclier arabo-nubien: étude multiscalaire le long de la suture de Keraf (Soudan) [PhD thesis in geology]: Université de Lorraine, 562 p.

Perret, J., Eglinger, A., André-Mayer, A.-S., Aillères, L., Feneyrol, J., Hartshorne, C., Abanyin, E., and Bosc, R., 2020, Subvertical, linear and progressive deformation related to gold mineralization at the Galat Sufar South deposit, Nubian Shield, NE Sudan: Journal of Structural Geology, v. 135, p. 104032, doi:10.1016/j.jsg.2020.104032.

Perret, J., Feneyrol, J., Eglinger, A., André-Mayer, A.-S., Berthier, C., Ennaciri, A., and Bosc, R., 2021, Tectonic record and gold mineralization in the central part of the Neoproterozoic Keraf suture, Gabgaba district, NE Sudan: Journal of African Earth Sciences, v. 181, p. 104248, doi:10.1016/j.jafrearsci.2021.104248.

Perseus Mining, 2024, Annual report 2023:, https://perseusmining.com/storage/2024/08/Annual-Report-2024.pdf.

Peterson, E.C., and Mavrogenes, J.A., 2014, Linking high-grade gold mineralization to earthquake-induced fault-valve processes in the Porgera gold deposit, Papua New Guinea: Geology, v. 42, p. 383–386, doi:10.1130/G35286.1.

Petersson, A., Kemp, A.I., Hickman, A.H., Whitehouse, M.J., Martin, L., and Gray, C.M., 2019, A new 3.59 Ga magmatic suite and a chondritic source to the east Pilbara Craton: Chemical Geology, v. 511, p. 51–70.

Petrella, L., Thébaud, N., Fougerouse, D., Evans, K., Quadir, Z., and Laflamme, C., 2020a, Colloidal gold transport: a key to high-grade gold mineralization? Mineralium Deposita, v. 55, p. 1247–1254, doi:10.1007/s00126-020-00965-x.

Petrella, L., Thébaud, N., LaFlamme, C., Miller, J., McFarlane, C., Occhipinti, S., Turner, S., and Perazzo, S., 2020b, Contemporaneous formation of vein-hosted and stratabound gold mineralization at the world-class Dead Bullock Soak mining camp, Australia: Mineralium Deposita, v. 55, p. 845–862, doi:10.1007/s00126-019-00902-7.

Phillips, G.N., and Groves, D.I., 1983, The nature of Archean gold-bearing fluids as deduced from gold deposits of Western Australia: Journal of the Geological Society of Australia, v. 30, p. 25–39, doi:10.1080/00167618308729234.

Phillips, G.N., and Powell, R., 2010, Formation of gold deposits: a metamorphic devolatilization model: Journal of Metamorphic Geology, v. 28, p. 689–718, doi:10.1111/j.1525-1314.2010.00887.x.

Phillips, G.N., and Powell, R., 2009, Formation of gold deposits: Review and evaluation of the continuum model: Earth-Science Reviews, v. 94, p. 1–21.

Phillips, G., Vearncombe, J., and Eshuys, E., 2019, Gold production and the importance of exploration success: Yilgarn Craton, Western Australia: Ore Geology Reviews, v. 105, p. 137–150.

Piccolo, A., Palin, R.M., Kaus, B.J.P., and White, R.W., 2019, Generation of Earth's Early Continents From a Relatively Cool Archean Mantle: Geochemistry, Geophysics, Geosystems, v. 20, p. 1679–1697, doi:10.1029/2018GC008079.

Pidgeon, R., Nemchin, A., and Cliff, J., 2013, Interaction of weathering solutions with oxygen and U–Pb isotopic systems of radiation-damaged zircon from an Archean granite, Darling Range Batholith, Western Australia: Contributions to Mineralogy and Petrology, v. 166, p. 511–523.

Pidgeon, R., Nemchin, A., and Whitehouse, M.J., 2017, The effect of weathering on U–Th–Pb and oxygen isotope systems of ancient zircons from the Jack Hills, Western Australia: Geochimica et Cosmochimica Acta, v. 197, p. 142–166.

Pilia, S. et al., 2023, Intra-crustal Mantle in the Himalayan-

Tibetan Orogen: Research Square, doi:https://doi.org/10.21203/rs.3.rs-2981173/v1.

Pinna, P., Cocherie, A., Thieblemont, D., and Jezequel, P., 2000, The Kisii Group of western Kenya: an end-Archaean (2.53 Ga) late orogenic volcano sedimentary sequence: Journal of African Earth Sciences, v. 30, p. 79–97.

Pitcairn, I.K., 2011, Background concentrations of gold in different rock types: Applied Earth Science, v. 120, p. 31–38, doi:10.1179/1743275811Y.0000000021.

Pitcairn, I.K., Leventis, N., Beaudoin, G., Faure, S., Guilmette, C., and Dubé, B., 2021, A metasedimentary source of gold in Archean orogenic gold deposits: Geology, v. 49, p. 862–866, doi:10.1130/G48587.1.

Pitcairn, I.K., Teagle, D.A.H., Craw, D., Olivo, G.R., Kerrich, R., and Brewer, T.S., 2006, Sources of Metals and Fluids in Orogenic Gold Deposits: Insights from the Otago and Alpine Schists, New Zealand: Economic Geology, v. 101, p. 1525–1546, doi:10.2113/gsecongeo.101.8.1525.

Platt, J.P., and Behrmann, J.H., 1986, Structures and fabrics in a crustal-scale shear zone, Betic Cordillera, SE Spain: Journal of Structural Geology, v. 8, p. 15–33, doi:10.1016/0191-8141(86)90014-3.

Pokrovski, G.S. et al., 2015, Sulfur radical species form gold deposits on Earth: Proceedings of the National Academy of Sciences, v. 112, p. 13484–13489, doi:10.1073/pnas.1506378112.

Pokrovski, G.S., Akinfiev, N.N., Borisova, A.Y., Zotov, A.V., and Kouzmanov, K., 2014, Gold speciation and transport in geological fluids: insights from experiments and physical-chemical modelling: Geological Society, London, Special Publications, v. 402, p. 9–70, doi:10.1144/SP402.4.

Polat, A., 2012, Growth of Archean continental crust in oceanic island arcs: Geology, v. 40, p. 383–384, doi:10.1130/focus042012.1.

Poli, M.E., and Renner, G., 2004, Normal focal mechanisms in the Julian Alps and Prealps: seismotectonic implications for the Italian-Slovenian border region: Bollettino di Geofisica Teorica ed Applicata, v. 45, p. 51–69.

Pollack, H.N., 1986, Cratonization and thermal evolution of the mantle: Earth and Planetary Science Letters, v. 80, p. 175–182, doi:10.1016/0012-821X(86)90031-2.

Pollack, H.N., and Chapman, D.S., 1977, On the regional variation of heat flow, geotherms, and lithospheric thickness: Tectonophysics, v. 38, p. 279–296.

Poulsen, K.H., Barber, R., and Robert, F., 2020, Chapter 4: Hemlo Gold System, Superior Province, Canada, in Sillitoe, R.H., Goldfarb, R.J., Robert, F., and Simmons, S.F. eds., Geology of the World's Major Gold Deposits and Provinces, Society of Economic Geologists, p. 81–100, doi:10.5382/SP.23.04.

Pourteau, A., Doucet, L.S., Blereau, E.R., Volante, S., Johnson, T.E., Collins, W.J., Li, Z.-X., and Champion, D.C., 2020, TTG generation by fluid-fluxed crustal melting: Direct evidence from the Proterozoic Georgetown Inlier, NE Australia: Earth and Planetary Science Letters, v. 550, p. 116548, doi:10.1016/j.epsl.2020.116548.

Powell, R., Will, T., and Phillips, G., 1991, Metamorphism in Archaean greenstone belts: calculated fluid compositions and implications for gold mineralization: Journal of Metamorphic Geology, v. 9, p. 141–150.

Q-R

Quennell, A., McKinlay, A., and Aiken, W., 1956, Summary of the geology of Tanganyika: introduction and stratigraphy: v. Memoir 1 (Pt. 1), 264 p.

Rabeau, O., Royer, J.-J., Jébrak, M., and Cheilletz, A., 2013, Log-uniform distribution of gold deposits along major Archean fault zones: Mineralium Deposita, v. 48, p. 817–824, doi:10.1007/s00126-013-0470-7.

Ramberg, H., 1967, Gravity, Deformation and the Earth's Crust.: London, v. Academic Press.

Ramsay, J.G., 1962, Interference Patterns Produced by the Superposition of Folds of Similar Type: The Journal of Geology, v. 70, p. 466–481, doi:10.1086/626837.

Ramsay J.G. and Huber M.I., 1987, Modern structural geology Vol 2: Folds and Fractures: Academic Press, 406 p.

Rapp, R.P., Watson, E.B., and Miller, C.F., 1991, Partial melting of amphibolite/eclogite and the origin of Archean trondhjemites and tonalites: Precambrian Research, v. 51, p. 1–25, doi:10.1016/0301-9268(91)90092-O.

Reddy, S.M., Collins, A.S., Buchan, C., and Mruma, A.H., 2004, Heterogeneous excess argon and Neoproterozoic heating in the Usagaran Orogen, Tanzania, revealed by single grain 40Ar/39Ar

thermochronology: Journal of African Earth Sciences, v. 39, p. 165–176.

Reddy, S.M., Collins, A.S., and Mruma, A., 2003, Complex high-strain deformation in the Usagaran Orogen, Tanzania: structural setting of Palaeoproterozoic eclogites: Tectonophysics, v. 375, p. 101–123.

Reimink, J.R., Chacko, T., Carlson, R.W., Shirey, S.B., Liu, J., Stern, R.A., Bauer, A.M., Pearson, D.G., and Heaman, L.M., 2018, Petrogenesis and tectonics of the Acasta Gneiss Complex derived from integrated petrology and 142Nd and 182W extinct nuclide-geochemistry: Earth and Planetary Science Letters, v. 494, p. 12–22, doi:10.1016/j.epsl.2018.04.047.

Reimink, J.R., Chacko, T., Stern, R.A., and Heaman, L.M., 2014, Earth's earliest evolved crust generated in an Iceland-like setting: Nature Geoscience, v. 7, p. 529–533, doi:10.1038/ngeo2170.

Rey, P.F., Coltice, N., and Flament, N., 2014, Spreading continents kick-started plate tectonics: Nature, v. 513, p. 405–408, doi:10.1038/nature13728.

Rey, P.F., and Houseman, G., 2006, Lithospheric scale gravitational flow: the impact of body forces on orogenic processes from Archaean to Phanerozoic: Geological Society, London, Special Publications, v. 253, p. 153–167, doi:10.1144/GSL.SP.2006.253.01.08.

Richards, J.P., 2009, Postsubduction porphyry Cu-Au and epithermal Au deposits: Products of remelting of subduction-modified lithosphere: Geology, v. 37, p. 247–250, doi:10.1130/G25451A.1.

Richards, J.P., 2011, Magmatic to hydrothermal metal fluxes in convergent and collided margins,: Ore Geol. Rev. 40, 1–26. doi:10.1016/j.oregeorev.2011.05.006.

Richards, J.P., 2013, Giant ore deposits formed by optimal alignments and combinations of geological processes: Nat. Geosci. 6, 911.

Ridley, J.R., and Diamond, L.W., 2000, Fluid chemistry of orogenic lode gold deposits and implications for genetic models: Reviews in Economic Geology, v. 13, p. 141–162.

Rino, S., Komiya, T., Windley, B.F., Katayama, I., Motoki, A., and Hirata, T., 2004, Major episodic increases of continental crustal growth determined from zircon ages of river sands; implications for mantle overturns in the Early Precambrian: Physics of the Earth and Planetary Interiors, v. 146, p. 369–394.

Robb, L., 2005. Introduction to Ore-Forming Processes. Blackwell Publishing.

Robert, F., and Brown, A.C., 1986, Archean gold-bearing quartz veins at the Sigma Mine, Abitibi greenstone belt, Quebec; Part I, Geologic relations and formation of the vein system: Economic Geology, v. 81, p. 578–592, doi:10.2113/gsecongeo.81.3.578.

Rock, N.M., and Groves, D.I., 1988, Can lamprophyres resolve the genetic controversy over mesothermal gold deposits? Geology, v. 16, p. 538–541.

Rowe, M.L., 2021, Origin of late Archaean granite from the Narryer Terrane, Yilgarn Craton [PhD thesis in geology]: The University of Western Australia, 305 p.

Rowe, M.L., Kemp, A.I.S., Wingate, M.T.D., Petersson, A., Whitehouse, M.J., and van der Riet, C., 2022, Cratonisation of Archaean continental crust: Insights from U–Pb zircon geochronology and geochemistry of granitic rocks in the Narryer Terrane, northwest Yilgarn Craton: Precambrian Research, v. 372, p. 106609, doi:10.1016/j.precamres.2022.106609.

Rudnick, R., and Gao, S., 2003, Composition of the Continental Crust. Treatise Geochem 3:1-64: Treatise on Geochemistry, v. 3, p. 1–64, doi:10.1016/B0-08-043751-6/03016-4.

Rutter, E., 1986, On the nomenclature of mode of failure transitions in rocks: Tectonophysics, v. 122, p. 381–387.

S

Salier, B.P., Groves, D.I., Mcnaughton, N.J., and Fletcher, I.R., 2005, Geochronological and Stable Isotope Evidence for Widespread Orogenic Gold Mineralization from a Deep-Seated Fluid Source at ca 2.65 Ga in the Laverton Gold Province, Western Australia: Economic Geology, v. 100, p. 1363–1388, doi:https://doi.org/10.2113/gsecongeo.100.7.1363.

Salters, V.J.M., and Stracke, A., 2004, Composition of the depleted mantle: Geochemistry, Geophysics, Geosystems, v. 5, doi:10.1029/2003GC000597.

Sanislav, I.V., Blenkinsop, T.G., and Dirks, P.H.G.M., 2018a, Archaean crustal growth through successive partial melting events in an oceanic plateau-like setting in the Tanzania Craton: Terra Nova, v. 30, p. 169–178, doi:10.1111/ter.12323.

Sanislav, I.V., Blenkinsop, T.G., and Dirks, P.H.G.M., 2018b, Archaean crustal growth through successive partial

melting events in an oceanic plateau-like setting in the Tanzania Craton: Terra Nova, v. 30, p. 169–178, doi:10.1111/ter.12323.

Sanislav, I.V., Blenkinsop, T.G., and Dirks, P.H.G.M., 2018c, Archaean crustal growth through successive partial melting events in an oceanic plateau-like setting in the Tanzania Craton: Terra Nova, v. 30, p. 169–178, doi:10.1111/ter.12323.

Sanislav, I.V., Brayshaw, M., Kolling, S.L., Dirks, P.H.G.M., Cook, Y.A., and Blenkinsop, T.G., 2016, The structural history and mineralization controls of the world-class Geita Hill gold deposit, Geita Greenstone Belt, Tanzania: Mineralium Deposita, v. 52, p. 257–279, doi:10.1007/s00126-016-0660-1.

Sanislav, I.V., Dirks, P.H.G.M., Blenkinsop, T., and Kolling, S.L., 2018d, The tectonic history of a crustal-scale shear zone in the Tanzania Craton from the Geita Greenstone Belt, NW-Tanzania Craton: Precambrian Research, v. 310, p. 1–16, doi:10.1016/j.precamres.2018.02.025.

Sanislav, I.V., Dirks, P.H.G.M., Cook, Y.A., Blenkinsop, T.G., and Kolling, S.L., 2014a, A Giant Gold System, Geita Greenstone Belt, Tanzania: Acta Geologica Sinica - English Edition, v. 88, p. 110–111, doi:10.1111/1755-6724.12368_21.

Sanislav, I.V., Kolling, S.L., Brayshaw, M., Cook, Y.A., Dirks, P.H.G.M., Blenkinsop, T.G., Mturi, M.I., and Ruhega, R., 2015, The geology of the giant Nyankanga gold deposit, Geita Greenstone Belt, Tanzania: Ore Geology Reviews, v. 69, p. 1–16, doi:10.1016/j.oregeorev.2015.02.002.

Sanislav, I.V., Wormald, R.J., Dirks, P.H.G.M., Blenkinsop, T.G., Salamba, L., and Joseph, D., 2014b, Zircon U–Pb ages and Lu–Hf isotope systematics from late-tectonic granites, Geita Greenstone Belt: Implications for crustal growth of the Tanzania Craton: Precambrian Research, v. 242, p. 187–204, doi:10.1016/j.precamres.2013.12.026.

Santos, L.C.M. de L., Dantas, E.L., Vidotti, R.M., Cawood, P.A., dos Santos, E.J., Fuck, R.A., and Lima, H.M., 2017, Two-stage terrane assembly in Western Gondwana: Insights from structural geology and geophysical data of central Borborema Province, NE Brazil: Journal of Structural Geology, v. 103, p. 167–184, doi:10.1016/j.jsg.2017.09.012.

Sawkins, F.J., 1990, Metal Deposits in Relation to Plate Tectonics: Springer Berlin, Berlin.

Schagerl A., 2022, Strain distribution in refold structures:

Schmalholz, S.M., and Podladchikov, Y.Y., 2013, Tectonic overpressure in weak crustal-scale shear zones and implications for the exhumation of high-pressure rocks: Geophysical Research Letters, v. 40, p. 1984–1988.

Schmitz, M.D., Bowring, S.A., de Wit, M.J., and Gartz, V., 2004, Subduction and terrane collision stabilize the western Kaapvaal craton tectosphere 2.9 billion years ago: Earth and Planetary Science Letters, v. 222, p. 363–376, doi:10.1016/j.epsl.2004.03.036.

Schöpfer, M.P.J., 2008, A Matlab Script for Visualizing Structure Contours and Outcrop Patterns in Three Dimensions: Journal of Geoscience Education, v. 56, p. 142–148, doi:10.5408/1089-9995-56.2.142.

Schöpfer, M.P.J., 2009, Superposed folding papermodels: Fault analysis group, https://www.fault-analysis-group.ucd.ie/SuperPosedFolds/Superposed_PM_Index.html.

Schreefel, R. et al., 2024, Crustal growth in the Archean: Insights from zircon petrochronology of the far-east Yilgarn Craton, Western Australia: Precambrian Research, v. 401, p. 107253, doi:10.1016/j.precamres.2023.107253.

Seal, R.R., 2006, Sulfur Isotope Geochemistry of Sulfide Minerals: Reviews in Mineralogy and Geochemistry, v. 61, p. 633–677, doi:10.2138/rmg.2006.61.12.

Selvaraja, V., Fiorentini, Marco.L., Jeon, H., Savard, D.D., LaFlamme, C.K., Guagliardo, P., Caruso, S., and Bui, T.-H., 2017, Evidence of local sourcing of sulfur and gold in an Archaean sediment-hosted gold deposit: Ore Geology Reviews, v. 89, p. 909–930, doi:10.1016/j.oregeorev.2017.07.021.

Seward, T.M., 1973, Thio complexes of gold and the transport of gold in hydrothermal ore solutions: Geochimica et Cosmochimica Acta, v. 37, p. 379–399, doi:https://doi.org/10.1016/0016-7037(73)90207-X.

Shirey, S.B., and Hanson, G.N., 1984, Mantle-derived Archaean monozodiorites and trachyandesites: Nature, v. 310, p. 222–224, doi:10.1038/310222a0.

Shirey, S.B., Kamber, B.S., Whitehouse, M.J., Mueller, P.A., and Basu, A.R., 2008, A review of the isotopic and trace element evidence for mantle and crustal processes in the Hadean and Archean: Implications for the onset of plate tectonic subduction: When did plate tectonics

begin on planet Earth, v. 440, p. 1–29.

Shirey, S.B., and Richardson, S.H., 2011, Start of the Wilson Cycle at 3 Ga Shown by Diamonds from Subcontinental Mantle: Science, v. 333, p. 434–436, doi:10.1126/science.1206275.

Sibson, R.H., Robert, F., and Poulsen, K.H., 1988, High-angle reverse faults, fluid-pressure cycling, and mesothermal gold-quartz deposits: Geology, v. 16, p. 551, doi:10.1130/0091-7613(1988)016<0551:HARFFP>2.3.CO;2.

Sillitoe, R.H., 2005, Musings on Future Exploration Targets and Strategies in the Andes, in Sillitoe, R.H., Perelló, J., and Vidal, C.E. eds., Andean Metallogeny: New Discoveries, Concepts, and Updates, Society of Economic Geologists, v. 11, p. 0, doi:10.5382/SP.11.01.

Sims, P., Kotov, A., Neymark, L., Peterman, Z., 1997, Nd isotopic evidence for middle and early Archean crust in the Wawa subprovince of Superior Province, Michigan, USA: Geological Association of Canada, v. Annual meeting of the Geological Association of Canada, p. A137.

Sizova, E., Gerya, T., Stüwe, K., and Brown, M., 2015, Generation of felsic crust in the Archean: A geodynamic modeling perspective: Precambrian Research, v. 271, p. 198–224, doi:10.1016/j.precamres.2015.10.005.

Sleep, N.H., and Windley, B.F., 1982, Archean Plate Tectonics: Constraints and Inferences: The Journal of Geology, v. 90, p. 363–379, doi:10.1086/628691.

Smit, K., Shirley, S., Hauri, E., and Stern, R., 2019, Sulfur isotopes in diamonds reveal differences in continent construction: Science, v. 364, p. 383–385, doi:https://doi.org/10.1126/science.aaw954.

Smith, M., and Anderson, C., 2003, Gokona gold deposit, northern Tanzania:

Smithies, R.H., Champion, D.C., and Van Kranendonk, M.J., 2009, Formation of Paleoarchean continental crust through infracrustal melting of enriched basalt: Earth and Planetary Science Letters, v. 281, p. 298–306, doi:10.1016/j.epsl.2009.03.003.

Smithies, R.H., Champion, D.C., Van Kranendonk, M.J., Howard, H.M., and Hickman, A.H., 2005, Modern-style subduction processes in the Mesoarchaean: Geochemical evidence from the 3.12 Ga Whundo intra-oceanic arc: Earth and Planetary Science Letters, v. 231, p. 221–237, doi:10.1016/j.epsl.2004.12.026.

Smithies, R.H., Ivanic, T.J., Lowrey, J.R., Morris, P.A., Barnes, S.J., Wyche, S., and Lu, Y.-J., 2018, Two distinct origins for Archean greenstone belts: Earth and Planetary Science Letters, v. 487, p. 106–116, doi:10.1016/j.epsl.2018.01.034.

Smithies, R.H., Lu, Y., Kirkland, C.L., Johnson, T.E., Mole, D.R., Champion, D.C., Martin, L., Jeon, H., Wingate, M.T.D., and Johnson, S.P., 2021a, Oxygen isotopes trace the origins of Earth's earliest continental crust: Nature, v. 592, p. 70–75, doi:10.1038/s41586-021-03337-1.

Smithies, R., Lu, Y., Lowrey, J., Ivanic, T., Champion, D., and Wilde, S., 2021b, Variations in granite geochemistry in the southwest Yilgarn: Geological survey of Western Australia,.

Smithies, R., Van Kranendonk, M., and Champion, D., 2007, The Mesoarchean emergence of modern-style subduction: Gondwana Research, v. 11, p. 50–68.

Snoke, A.W., Tullis, J., and Todd, V.R., 1998, Fault-related rocks: a photographic atlas: Princeton University Press.

Söderlund, U., Hofmann, A., Klausen, M.B., Olsson, J.R., Ernst, R.E., and Persson, P.-O., 2010, Towards a complete magmatic barcode for the Zimbabwe craton: Baddeleyite U–Pb dating of regional dolerite dyke swarms and sill complexes: v. 183, p. 388–398, doi:10.1016/j.precamres.2009.11.001.

Spencer, C.J., Kirkland, C.L., Roberts, N.M.W., Evans, N.J., and Liebmann, J., 2020, Strategies towards robust interpretations of in situ zircon Lu–Hf isotope analyses: Geoscience Frontiers, v. 11, p. 843–853, doi:10.1016/j.gsf.2019.09.004.

Spencer, C.J., Roberts, N.M.W., and Santosh, M., 2017, Growth, destruction, and preservation of Earth's continental crust: Earth-Science Reviews, v. 172, p. 87–106, doi:10.1016/j.earscirev.2017.07.013.

Stern, R.J., 2005, Evidence from ophiolites, blueschists, and ultrahigh-pressure metamorphic terranes that the modern episode of subduction tectonics began in Neoproterozoic time: Geology, v. 33, p. 557, doi:10.1130/G21365.1.

Stern, R.J., 2018, The evolution of plate tectonics: Philosophical Transactions of the Royal Society A: Mathematical, Physical and Engineering Sciences, v. 376, p. 20170406.

Stern, R.A., Bodorkos, S., Kamo, S.L., Hickman, A.H., and

Corfu, F., 2009, Measurement of SIMS instrumental mass fractionation of Pb isotopes during zircon dating: Geostandards and Geoanalytical Research, v. 33, p. 145–168.

Stern, R.J., Leybourne, M., and Tsujimori, T., 2016, Kimberlites and the start of plate tectonics: Geology, v. 44, p. 799–802.

Stern, R.J., Tsujimori, T., Harlow, G., and Groat, L.A., 2013, Plate tectonic gemstones: Geology, v. 41, p. 723–726.

Stipp, M., Stünitz, H., Heilbronner, R., and Schmid, S.M., 2002a, Dynamic recrystallization of quartz: correlation between natural and experimental conditions: Geological Society, London, Special Publications, v. 200, p. 171–190, doi:10.1144/GSL.SP.2001.200.01.11.

Stipp, M., Stünitz, H., Heilbronner, R., and Schmid, S.M., 2002b, The eastern Tonale fault zone: a 'natural laboratory' for crystal plastic deformation of quartz over a temperature range from 250 to 700°C: Journal of Structural Geology, v. 24, p. 1861–1884, doi:10.1016/S0191-8141(02)00035-4.

van Straaten, P., 1984, Gold mineralization in Tanzania-a review.: Gold '82. Proceedings of a symposium, University of Harare, 1982, p. 673–685.

Suess, E., 1875, Die entstehung der Alpen: W. Braumüller.

Sugiono, D., LaFlamme, C., Thébaud, N., Martin, L., Savard, D., and Fiorentini, M., 2022, Fault-induced gold saturation of a single auriferous fluid is a key process for orogenic gold deposit formation: Economic Geology, v. 117, p. 1405–1414, doi:10.5382/econgeo.4923.

Sugiono, D., Martin, L., Thébaud, N., Fougerouse, D., LaFlamme, C.K., Fiorentini, M., Petrella, L., Guagliardo, P., Reddy, S., and Hu, S.-Y., 2025, Arsenic in pyrite acts as a catalyst for dissolution-reprecipitation reaction and gold remobilization: American Mineralogist, v. 110, p. 82–92.

Sugiono, D., Thébaud, N., LaFlamme, C., Fiorentini, M., Martin, L., Rogers, J., Lorusso, G., and McFarlane, C., 2021, Integration of multiple sulfur isotopes with structural analysis unveils the evolution of ore fluids and source of sulfur at the Kanowna Belle Archean orogenic gold deposit, Yilgarn Craton, Western Australia: Mineralium Deposita, v. 56, p. 1471–1490, doi:10.1007/s00126-020-01032-1.

Sumail, Thébaud, N., Masurel, Q., Fisher, C.M., Smithies, H., and Schreefel, R., 2024, Temporal constraints on gold mineralisation at the world-class Jundee deposit: Insights into the episodic nature of orogenic gold mineralisation in the Neoarchean Yilgarn Craton: Precambrian Research, v. 410, p. 107479, doi:10.1016/j.precamres.2024.107479.

Sun, S.-S., 1982, Chemical composition and origin of the earth's primitive mantle: Geochimica et Cosmochimica Acta, v. 46, p. 179–192, doi:10.1016/0016-7037(82)90245-9.

Sun, K. et al., 2018, Episodic crustal growth in the Tanzania Craton: evidence from Nd isotope compositions: China Geology, v. 1, p. 210–224, doi:10.31035/cg2018025.

Süssenberger, A., Schmidt, S.T., Wemmer, K., Baumgartner, L.P., Grobety, B., 2018, Timing and thermal evolution of fold-and-thrust belt formation in the Ultima Esperanza District, 51°S Chile: constraints from K-Ar dating and illite characterization: Geological Society of America Bulletin, 130, 975–998.

Sylvester, P.J., 1994, Chapter 7 Archean Granite Plutons, in Condie, K.C. ed., Developments in Precambrian Geology, Elsevier, v. 11, p. 261–314, doi:10.1016/S0166-2635(08)70225-1.

T

Tang, M., Chen, K., and Rudnick, R.L., 2016, Archean upper crust transition from mafic to felsic marks the onset of plate tectonics: Science, v. 351, p. 372–375.

Taylor, S.R., and McLennan, S.M., 1985, The Continental Crust: Its Composition and Evolution: Boston, 312 p.

Temporim, F.A. et al., 2023, Vertical deformation partitioning across a collapsing large and hot orogen: Terra Nova, v. 35, p. 23–31, doi:10.1111/ter.12625.

Tenczer, V., Hauzenberger, C., Fritz, H., Hoinkes, G., Muhongo, S., and Klötzli, U., 2013, Crustal age domains and metamorphic reworking of the deep crust in Northern-Central Tanzania: a U/Pb zircon and monazite age study: Mineralogy and Petrology, v. 107, p. 679–707.

Tenczer, V., Hauzenberger, C., Fritz, H., Whitehouse, M., Mogessie, A., Wallbrecher, E., Muhongo, S., and Hoinkes, G., 2006, Anorthosites in the Eastern Granulites of Tanzania—New SIMS zircon U–Pb age data, petrography and geochemistry: Precambrian Research, v. 148, p. 85–114.

Thébaud, N., Allibone, A., Masurel, Q., Eglinger, A., Davis,

J., André-Mayer, A.-S., Miller, J., Ouedrago, M.F., and Jessell, M., 2020, Chapter XX The Paleoproterozoic (Rhyacian) Gold Deposits of West Africa: Society of Economic Geologists, SEG Special Publications, p. 18.

Thébaud, N., Sugiono, D., LaFlamme, C., Miller, J., Fisher, L., Voute, F., Tessalina, S., Sonntag, I., and Fiorentini, M., 2018, Protracted and polyphased gold mineralisation in the Agnew District (Yilgarn Craton, Western Australia): Precambrian Research, v. 310, p. 291–304, doi:10.1016/j.precamres.2018.02.013.

Thode, H.G., 1970, Sulfur isotope geochemistry and fractionation between coexisting sulfide minerals: Mineralogical society of America, v. Special paper 3, p. 133–144.

Thomas, R.J. et al., 2016, Geochronology of the central Tanzania Craton and its southern and eastern orogenic margins: Precambrian Research, v. 277, p. 47–67, doi:10.1016/j.precamres.2016.02.008.

Thomas, H.V., Large, R.R., Bull, S.W., Maslennikov, V., Berry, R.F., Fraser, R., Froud, S., and Moye, R., 2011, Pyrite and Pyrrhotite Textures and Composition in Sediments, Laminated Quartz Veins, and Reefs at Bendigo Gold Mine, Australia: Insights for Ore Genesis: Economic Geology, v. 106, p. 1–31, doi:10.2113/econgeo.106.1.1.

Thompson, J., Sillitoe, R., Baker, T., Lang, J., and Mortensen, J., 1999, Intrusion-related gold deposits associated with tungsten-tin provinces: Mineralium Deposita, v. 34, p. 323–334.

Tikoff, B., Teyssier, C., 1994, Strain modeling of displacement-field partitioning in transpressional orogens: Journal of Structural Geology, 16, 1575–1588.

Tomkins, A.G., 2013, On the source of orogenic gold: Geology, v. 41, p. 1255–1256, doi:10.1130/focus122013.1.

Tomkins, A.G., 2010, Windows of metamorphic sulfur liberation in the crust: Implications for gold deposit genesis: Geochimica et Cosmochimica Acta, v. 74, p. 3246–3259, doi:10.1016/j.gca.2010.03.003.

Traoré, Y.D., Siebenaller, L., Salvi, S., Béziat, D., and Bouaré, M.L., 2016, Progressive gold mineralization along the Syama corridor, southern Mali (West Africa): Ore Geology Reviews, v. 78, p. 586–598, doi:10.1016/j.oregeorev.2015.11.003.

Travers, L., 2023, Distribution and structural control of the hydrothermal events within the Barberton greenstone belt (South Africa, Eswatini): implications for gold mineralisation formation [PhD thesis in geology]: 374 p.

Travers, L., Chauvet, A., and Lehmann, J., 2023, Structure and Distribution of the Gold-Related Quartz Vein Systems in the Southwestern Part of the Barberton Greenstone Belt (South Africa, Eswatini): Minerals, v. 13, p. 1034, doi:10.3390/min13081034.

Tremblay, A., Ruffet, G., and Lemarchand, J., 2020, Timing and duration of Archean orogenic gold deposits in the Bourlamaque pluton, Val d'Or mining camp, Abitibi, Canada: Ore Geology Reviews, v. 127, p. 103812, doi:10.1016/j.oregeorev.2020.103812.

Tripp, G.I., Tosdal, R.M., Blenkinsop, T., Rogers, J.R., and Halley, S., 2020, Chapter 33: Neoarchean Eastern Goldfields of Western Australia, in Sillitoe, R.H., Goldfarb, R.J., Robert, F., and Simmons, S.F. eds., Geology of the World's Major Gold Deposits and Provinces, Society of Economic Geologists, p. 709–734, doi:10.5382/SP.23.33.

Turner, S., Rushmer, T., Reagan, M., and Moyen, J.-F., 2014, Heading down early on? Start of subduction on Earth: Geology, v. 42, p. 139–142, doi:10.1130/G34886.1.

Turner, S., Wilde, S., Wörner, G., Schaefer, B., and Lai, Y.-J., 2020, An andesitic source for Jack Hills zircon supports onset of plate tectonics in the Hadean: Nature Communications, v. 11, p. 1241, doi:10.1038/s41467-020-14857-1.

V

Valley, J.W. et al., 2005, 4.4 billion years of crustal maturation: oxygen isotope ratios of magmatic zircon: Contributions to Mineralogy and Petrology, v. 150, p. 561–580, doi:10.1007/s00410-005-0025-8.

Valley, J.W., Kinny, P.D., Schulze, D.J., and Spicuzza, M.J., 1998, Zircon megacrysts from kimberlite: oxygen isotope variability among mantle melts: Contributions to Mineralogy and Petrology, v. 133, p. 1–11, doi:10.1007/s004100050432.

Van der Voo, R., 1982, Pre-Mesozoic paleomagnetism and plate tectonics: Annual Review of Earth and Planetary Sciences, Vol. 10, p. 191, v. 10, p. 191.

Van Kranendonk, M.J., 2011, Onset of Plate Tectonics: Science, v. 333, p. 413–414, doi:10.1126/science.1208766.

Van Kranendonk, M.J., Collins, W.J., Hickman, A., and Pawley, M.J., 2004, Critical tests of vertical vs. horizontal tectonic models for the Archaean East Pilbara Granite–Greenstone Terrane, Pilbara Craton, Western Australia: Archaean Tectonics, Volume 2, v. 131, p. 173–211, doi:10.1016/j.precamres.2003.12.015.

Van Kranendonk, M.J., Hugh Smithies, R., Hickman, A.H., and Champion, D., 2007, secular tectonic evolution of Archean continental crust: interplay between horizontal and vertical processes in the formation of the Pilbara Craton, Australia: Terra Nova, v. 19, p. 1–38.

Van Kranendonk, M.J., Kirkland, C.L., and Cliff, J., 2015, Oxygen isotopes in Pilbara Craton zircons support a global increase in crustal recycling at 3.2Ga: Lithos, v. 228–229, p. 90–98, doi:10.1016/j.lithos.2015.04.011.

Van Ryt, M.R., Sanislav, I.V., Dirks, P.H.G.M., Huizenga, J.M., Mturi, M.I., and Kolling, S.L., 2017, Alteration paragenesis and the timing of mineralised quartz veins at the world-class Geita Hill gold deposit, Geita Greenstone Belt, Tanzania: Ore Geology Reviews, v. 91, p. 765–779, doi:10.1016/j.oregeorev.2017.08.023.

Van Ryt, M.R., Sanislav, I.V., Dirks, P.H.G.M., Huizenga, J.M., Mturi, M.I., and Kolling, S.L., 2019, Biotite chemistry and the role of halogens in Archaean greenstone hosted gold deposits: A case study from Geita Gold Mine, Tanzania: Ore Geology Reviews, v. 111, p. 102982, doi:10.1016/j.oregeorev.2019.102982.

Van Ryt, M.R., Sanislav, I.V., Dirks, P.H.G.M., and Huizenga, J., 2020, Trace element associations in magnetite and hydrothermal pyrite from the Geita Hill gold deposit, Tanzania: Journal of Geochemical Exploration, v. 209, p. 106418, doi:10.1016/j.gexplo.2019.106418.

Vandenburg, E.D. et al., 2023, Spatial and temporal control of Archean tectonomagmatic regimes: Earth-Science Reviews, v. 241, p. 104417, doi:10.1016/j.earscirev.2023.104417.

Vanderhaeghe, O., and Teyssier, C., 2001, Partial melting and flow of orogens: Tectonophysics, v. 342, p. 451–472.

Vearncombe, J., and Zelic, M., 2015, Structural paradigms for gold: do they help us find and mine? Applied Earth Science, v. 124, p. 2–19, doi:10.1179/1743275815Y.0000000003.

Velásquez, N.Z., 2023, Lithostratigraphic, structural and gold metallogenic evolution of the Mungari gold camp, Western Australia [MSc]: University of Western Australia, 163 p.

Velasquez, G., Beziat, D., Salvi, S., Siebenaller, L., Borisova, A.Y., Pokrovski, G.S., and De Parseval, P., 2014, Formation and Deformation of Pyrite and Implications for Gold Mineralization in the El Callao District, Venezuela: Economic Geology, v. 109, p. 457–486, doi:10.2113/econgeo.109.2.457.

Velásquez, G., Salvi, S., Siebenaller, L., Béziat, D., and Carrizo, D., 2018, Control of Shear-Zone-Induced Pressure Fluctuations on Gold Endowment: The Giant El Callao District, Guiana Shield, Venezuela: Minerals, v. 8, p. 430, doi:10.3390/min8100430.

Vervoort, J.D., Kemp, A.I., and Fisher, C.M., 2018, Hf isotope constraints on evolution of the depleted mantle and growth of continental crust, in v. 2018, p. V23A-07.

Vervoort, J., and Weisberger, B., 2004, Origin and evolution of the Kilimafedha Greenstone Belt, Eastern Tanzania Craton: evidence from Nd and Pb Isotopes: GSA Annual Meeting, Denver. Denver, v. 36.

Vezinet, A., 2016, Différenciation et stabilisation de la croûte continentale archéenne, l'exemple de la marge Nord du craton du Kaapvaal en Afrique du Sud [Sciences de la Terre]: Université de Lyon; Universiteit Stellenbosch, 323 p.

Vielreicher, N., Groves, D., McNaughton, N., and Fletcher, I., 2015, The timing of gold mineralization across the eastern Yilgarn craton using U–Pb geochronology of hydrothermal phosphate minerals: Mineralium Deposita, v. 50, p. 391–428, doi:10.1007/s00126-015-0589-9.

Virnes, A.B., Fiorentini, M.L., Caruso, S., Baublys, K., Masurel, Q., and Thebaud, N., 2024, Sulfur isotopes in Archaean crustal reservoirs constrain the transport and deposition mechanisms of nickel-sulfides in komatiites: Mineralium Deposita, v. 59, p. 1155–1183, doi:10.1007/s00126-024-01253-8.

Voisey, C.R., Willis, D., Tomkins, A.G., Wilson, C.J.L., Micklethwaite, S., Salvemini, F., Bougoure, J., and Rickard, W.D.A., 2020, Aseismic Refinement of Orogenic Gold Systems: Economic Geology, v. 115, p. 33–50, doi:10.5382/econgeo.4692.

Vos, I.M.A., Bierlein, F.P., Standing, J.S., and Davidson, G., 2009, The geology and mineralisation at the Golden Pride gold deposit, Nzega Greenstone Belt, Tanzania:

Mineralium Deposita, v. 44, p. 751–764, doi:10.1007/s00126-009-0245-3.

Voute, F., and Thébaud, N., 2015, Structural, mineralogical and geochemical constraints on the atypical komatiite-hosted Turret deposit in the Agnew–Mt. White district, Western Australia: Mineralium Deposita, v. 50, p. 697–716, doi:10.1007/s00126-014-0566-8.

W

Walker, A.T., Evans, K.A., Kirkland, C.L., and Polito, P.A., 2022, Multiple modes of sulphur cycling within a mineralised orogen: A case study from the Fraser Zone, Western Australia: Lithos, v. 408–409, p. 106536, doi:10.1016/j.lithos.2021.106536.

Wang, S.-R., Yang, L.-Q., Wang, J.-G., Wang, E.-J., Xu, Y.-L, 2019, Geostatistical Determination of Ore Shoot Plunge and Structural Control of the Sizhuang World-Class Epizonal Orogenic Gold Deposit, Jiaodong Peninsula, China; Minerals, 9, 214. doi:10.3390/min9040214

Watine, H., Masson, V., Fontaine, A., Bonnetti, C., Feneyrol, J., Berthier, C., Furic, R., and Bosc, R., 2023, Cartographie prédictive des métaux critiques à l'échelle du Craton Ouest-Africain: Conference: Réunion des Sciences de la Terre - RST 2023.

Weinberg, R.F., and Podladchikov, Y.Y., 1995, The rise of solid-state diapirs: Journal of Structural Geology, v. 17, p. 1183–1195.

Whalen, J.B., Currie, K.L., and Chappell, B.W., 1987, A-type granites: geochemical characteristics, discrimination and petrogenesis: Contributions to Mineralogy and Petrology, v. 95, p. 407–419, doi:10.1007/BF00402202.

White, A.J.R., Waters, D.J., and Robb, L.J., 2015, Exhumation-Driven Devolatilization as a Fluid Source for Orogenic Gold Mineralization at the Damang Deposit, Ghana: Economic Geology, v. 110, p. 1009–1025, doi:10.2113/econgeo.110.4.1009.

Whymark, W.E., and Frimmel, H.E., 2018, Regional gold-enrichment of conglomerates in Paleoproterozoic supergroups formed during the 2.45 Ga rifting of Kenorland: Ore Geology Reviews, v. 101, p. 985–996, doi:10.1016/j.oregeorev.2017.04.003.

Wiedenbeck, M., Alle, P., Corfu, F., Griffin, W.L., Meier, M., Oberli, F. v, Quadt, A. von, Roddick, J., and Spiegel, W., 1995, Three natural zircon standards for U-Th-Pb, Lu-Hf, trace element and REE analyses: Geostandards newsletter, v. 19, p. 1–23.

Wiedenbeck, M., Hanchar, J.M., Peck, W.H., Sylvester, P., Valley, J., Whitehouse, M., Kronz, A., Morishita, Y., Nasdala, L., and Fiebig, J., 2004, Further characterisation of the 91500 zircon crystal: Geostandards and Geoanalytical Research, v. 28, p. 9–39.

Wiemer, D., Schrank, C.E., Murphy, D.T., Wenham, L., and Allen, C.M., 2018, Earth's oldest stable crust in the Pilbara Craton formed by cyclic gravitational overturns: Nature Geoscience, v. 11, p. 357–361, doi:10.1038/s41561-018-0105-9.

Wilde, S.A., Valley, J.W., Peck, W.H., and Graham, C.M., 2001, Evidence from detrital zircons for the existence of continental crust and oceans on the Earth 4.4 Gyr ago: Nature, v. 409, p. 175–178, doi:10.1038/35051550.

Wilkinson, J.J., and Johnston, J.D., 1996, Pressure fluctuations, phase separation, and gold precipitation during seismic fracture propagation: Geology, v. 24, p. 395, doi:10.1130/0091-7613(1996)024<0395:PFPSAG>2.3.CO;2.

Williams-Jones, A.E., Bowell, R.J., and Migdisov, A.A., 2009, Gold in Solution: Elements, v. 5, p. 281–287, doi:10.2113/gselements.5.5.281.

Windley, B.F., Kusky, T., and Polat, A., 2021, Onset of plate tectonics by the Eoarchean: Precambrian Research, v. 352, p. 105980, doi:10.1016/j.precamres.2020.105980.

de Wit, M.J., 1998, On Archean granites, greenstones, cratons and tectonics: does the evidence demand a verdict? Precambrian Research, v. 91, p. 181–226.

Witt, W.K., Cassidy, K.F., Lu, Y.-J., and Hagemann, S.G., 2020, The tectonic setting and evolution of the 2.7 Ga Kalgoorlie–Kurnalpi Rift, a world-class Archean gold province: Mineralium Deposita, v. 55, p. 601–631, doi:10.1007/s00126-017-0778-9.

Wood, B.J., Walter, M.J., and Wade, J., 2006, Accretion of the Earth and segregation of its core: Nature, v. 441, p. 825–833.

Woodcock, N.H., and Fischer, M., 1986, Strike-slip duplexes: Journal of Structural Geology, v. 8, p. 725–735, doi:10.1016/0191-8141(86)90021-0.

Woodhead, J.D., and Hergt, J.M., 2005, A preliminary appraisal of seven natural zircon reference materials

for in situ Hf isotope determination: Geostandards and Geoanalytical Research, v. 29, p. 183–195.

Wu, X., Liu, X., Sun, K., Xu, K., Sun, H., Gong, P., He, S., and Machumu, G., 2023, Petrogenesis and tectonic setting of TTG rocks from the Katoro area, Sukumaland Greenstone Belt, NW Tanzania: Evidence from zircon U-Pb geochronology, Lu-Hf isotopes, whole-rock geochemistry, and Sr-Nd isotopes: Precambrian Research, v. 385, p. 106943, doi:10.1016/j.precamres.2022.106943.

Wyborn, L., 1997, Australian mineral systems; a National Geoscience Mapping Accord Project: Australian Geological Survey Organisation Record, v. 56.

Wyborn, L., Heinrich, C., and Jaques, A., 1994, Australian Proterozoic mineral systems: essential ingredients and mappable criteria, in Australasian Institute of Mining and Metallurgy, p. 109–115.

Wyman, D.A., 2019, 2.8 Ga Subduction-related magmatism in the Youanmi Terrane and a revised geodynamic model for the Yilgarn Craton: Precambrian Research, v. 327, p. 14–33, doi:10.1016/j.precamres.2019.02.008.

Wyman, D.A., Cassidy, K.F., and Hollings, P., 2016, Orogenic gold and the mineral systems approach: Resolving fact, fiction and fantasy: Ore Geology Reviews, v. 78, p. 322–335, doi:10.1016/j.oregeorev.2016.04.006.

Y-Z

Yakymchuk, C., Kirkland, C.L., and Clark, C., 2018, Th/U ratios in metamorphic zircon: Journal of Metamorphic Geology, v. 36, p. 715–737, doi:10.1111/jmg.12307.

Yang, L.-Q. et al., 2024, Mantle-rooted fluid pathways and world-class gold mineralization in the giant Jiaodong gold province: Insights from integrated deep seismic reflection and tectonics: Earth-Science Reviews, v. 255, p. 104862, doi:10.1016/j.earscirev.2024.104862.

Yuan, Y., Li, S., Peng, J., Si, J., Cheng, H., Sun, J., Wei, J., Shao, J., and ,No. 2 Institute of Geological and Mineral Resources Survey of Henan, Zhengzhou 450001, China, 2019, An integrated ore prospecting model for the Nyasirori gold deposit in Tanzania: China Geology, v. 3, p. 1–15, doi:10.31035/cg2018127.

Zhang, J., 2021, Equilibrium sulfur isotope fractionations of several important sulfides: Geochemical journal, v. 55, p. 135–147, doi:10.2343/geochemj.2.0623.

Zhang, H., Li, Y., Zheng, J., Zhao, L., Wang, K., and Brouwer, F.M., 2024, The Archean crust-mantle interaction in the Jiaoliao microblock, North China Craton: Constraints on the Neoarchean subduction regime: Earth-Science Reviews, v. 255, p. 104827, doi:10.1016/j.earscirev.2024.104827.

Zhong, R., Brugger, J., Tomkins, A.G., Chen, Y., and Li, W., 2015, Fate of gold and base metals during metamorphic devolatilization of a pelite: Geochimica et Cosmochimica Acta, v. 171, p. 338–352, doi:10.1016/j.gca.2015.09.013.

Zibra, I., Lu, Y., Clos, F., Weinberg, R.F., Peternell, M., Wingate, M.T.D., Prause, M., Schiller, M., and Tilhac, R., 2020, Regional-scale polydiapirism predating the Neoarchean Yilgarn Orogeny: Tectonophysics, v. 779, p. 228375, doi:10.1016/j.tecto.2020.228375.

~ Abstract ~

Structurally-controlled, epigenetic gold deposits can be defined as small-scale expressions of a sequence of geological processes that occur across different temporal and spatial scales. Notably, some factors influencing mineralization may have involved lithospheric-scale processes, active well before the ore-forming events, up to one or more orogenic cycles. These processes governed the initial enrichment of the crust, the transport of ore-bearing fluids to deposition sites and controlled gold deposition. Conversely, insights into the mechanisms of deposit formation can significantly contribute to our understanding of the Earth's system, specifically mineral systems requiring large-scale and long-term processes such as orogenic gold. A multi-scale and multi-method approach was followed to reconstruct the gold mineral system and constrain crustal growth mechanisms in the northern Sukumaland granite-greenstone belt (SGGB) of the Archean Tanzania Craton, host of the Nyanzaga and Kilimani gold deposits.

The journey of gold in the northern SGGB, from initial fertilization of the crust to economic concentration at the Nyanzaga and Kilimani gold deposits, results from nearly 200 million years of magmatic activity, deformation, metamorphism and hydrothermal circulation. Gold was extracted from the mantle during the earliest record of crustal growth in the SGGB. This episode consisted of mantle-derived mafic-ultramafic magmatism in a mantle-plume oceanic plateau setting, between 2820 and 2800 Ma. Between 2800 and 2700 Ma, crustal reworking was likely driven by dripping processes, before transitioning to subduction-like processes around 2700 Ma. The convergent tectonics ultimately led to collision between the SGGB and an exotic terrane during the 2700-2660 Ma period. A hot and weak lithosphere controlled shortening and crustal thickening that resulted in transpression and vertical flattening, contrasting with the localized strain typical of modern cold orogens. The absence of crustal-scale thrusts and significant topography, along with the presence of granulite-facies metamorphism and lateral crustal flow suggests that the SGGB evolved through prolonged transpression in a hot orogen setting. Crustal anatexis is recorded between 2660 and 2620 Ma. The resulting partial melting, reworking and/or metamorphism of the gold-enriched mafic lithologies likely triggered gold release from its source rock around 2645 Ma. Refolding processes shaped the meta-volcanosediments of the SGGB to provide favorable geometries for strike-slip faulting with favorable opening rates for ore-bearing fluid circulation and gold precipitation after 2645 Ma. Gold fertilization and gold release and concentration processes are therefore temporally disconnected of more than 150 Ma. Mixing of fluids may have contributed to the precipitation of gold.

The mineral system approach had dual implications, synchronously constraining (i) the tectonic processes that drove crustal growth and differentiation in a Neoarchean granite-greenstone terrane and (ii) the magmatic, tectonic, hydrothermal and to a smaller extent metamorphic processes that controlled the journey of gold within this juvenile crustal segment.